Springer Atmospheric Sciences

Costas G. Helmis
Panagiotis T. Nastos *Editors*

Advances in Meteorology, Climatology and Atmospheric Physics

Volume 2

Springer

Advances in Meteorology, Climatology and Atmospheric Physics

Springer Atmospheric Sciences

For further volumes:
http://www.springer.com/series/10176

Costas G. Helmis • Panagiotis T. Nastos
Editors

Advances in Meteorology, Climatology and Atmospheric Physics

Springer

Editors
Costas G. Helmis
Department of Physics
University of Athens
University Campus
Athens
Greece

Panagiotis T. Nastos
Department of Physics
University of Athens
University Campus
Athens
Greece

ISBN 978-3-642-29171-5 ISBN 978-3-642-29172-2 (eBook)
DOI 10.1007/978-3-642-29172-2
Springer Heidelberg New York Dordrecht London

Library of Congress Control Number: 2012939847

Printed on acid-free paper

Springer is part of Springer Science+Business Media (www.springer.com)

Preface

The Conference on Meteorology, Climatology and Atmospheric Physics (COMECAP) is organized on a biennial basis holding a long history of 22 years, dating back to the early 1990s. This year it is co-organized by the National and Kapodistrian University of Athens (Department of Atmospheric Physics – Meteorology and Laboratory of Climatology and Atmospheric Environment), the Hellenic Meteorological Society and the Mariolopoulos-Kanaginis Foundation for the Environmental Sciences. COMECAP Conferences provide the opportunity for the dissemination of new knowledge in the framework of Meteorology, Climatology and Atmospheric Physics, hosting experts, scientists and mainly young researchers to present their recent research studies and share their innovating ideas.

COMECAP 2012 covers various topics related to the science of the Atmospheric Environment, which is in fact an interdisciplinary field, giving the opportunity to understand the physical systems and environmental processes in an integrated manner. The papers presented at COMECAP 2012 cover a spectrum of topics that include Atmospheric Physics and Radiation, Dynamic and Synoptic Meteorology, Applied Meteorology and Climatology, Climate Dynamics and Changes, Weather Analysis and Forecasting and Extreme Events, Mesoscale and Micro-meteorology, Remote Sensing and Satellite Meteorology, Air Quality (Indoor and Outdoor), Biometeorology and Bioclimatology, Agricultural Meteorology, Hydrology and Hydrometeorology. It is worth mentioning that 177 full papers were finally accepted to be published at the Conference Proceedings after peer revision against 210 abstracts initially submitted. The published papers in this book are classified into three main sections, as reflected in the title of the Conference: 50 papers in Meteorology, 67 in Climatology and 60 in Atmospheric Physics.

Finally, it is my pleasure and privilege to acknowledge the contribution of the authors, the members of the Scientific Committee, the appointed reviewers and especially the members of the Organizing Committee, for their valuable efforts on the production of this book, as well as our Sponsors.

I wish you all a fruitful Conference and a pleasant stay at the beautiful city of Athens.

The Conference Chairman — Professor Costas G. Helmis

Address of the Hellenic Meteorological Society (HMS)

The Hellenic Meteorological Society, member of the European Meteorological Society, proudly presents the Proceedings of the International Conference on Meteorology, Climatology and Atmospheric Physics (COMECAP 2012), in collaboration with the Department of Atmospheric Physics – Meteorology and Laboratory of Climatology and Atmospheric Environment of the National and Kapodistrian University of Athens. For the first time, the accepted scientific papers are published, after peer revision, in Springer book series under the title "Advances in Meteorology, Climatology and Atmospheric Physics". This fact improves the level of the Conference as far as the quality of presentations and the dissemination of recent knowledge of our climate system from the regional to the global scale are concerned.

The Hellenic Meteorological Society has co-organized the previous biennial conferences in Thessaloniki (May 21–23, 1992, and September 29–30, 1994), Athens (September 25–27, 1996, and September 22–25, 1998), Thessaloniki (September 28–30, 2000), Ioannina (September 25–28, 2002), Nicosia (September 28–30, 2004), Athens (May 24–26, 2006), Thessaloniki (May 28–31, 2008) and Patras (May 25–28, 2010). All these conferences have been carried out by the members of the Hellenic Meteorological Society and our foreign colleagues from disciplines associated with the study of atmospheric environment.

The achievement of COMECAP 2012 is due to the great efforts of the Organizing Committee towards the success and quality of the Conference as well as the Sponsors who granted this scientific event. The Hellenic Meteorological Society wishes to express its gratitude to everybody mentioned and the participants, who presented their scientific papers, contributing to the better understanding of the physical processes of our climate system.

On behalf of Hellenic Meteorological Society

The President
Associate Professor Panagiotis T. Nastos

Organizing Committee

Chairman

Helmis Costas, Professor (University of Athens)

Vice Chairman

Nastos Panagiotis, Associate Professor (University of Athens), President of the Hellenic Meteorological Society

General Secretary

Flocas Helena, Assistant Professor (University of Athens)

Treasurer

Founda Dimitra, Senior Researcher (National Observatory of Athens)

Members

Paliatsos Athanasios, Professor (Technological Education Institute of Piraeus)
Moustris Costas, Lecturer (Technological Education Institute of Piraeus)
Hatzaki Maria, Ph.D., Research Assistant (University of Athens)
Katavoutas Giorgos, Ph.D., Research Assistant (University of Athens)
Larissi Ioanna, Research Assistant (Technological Education Institute of Piraeus)

Scientific Committee of COMECAP 2012

Chairman: Prof. D. N. ASIMAKOPOULOS, University of Athens

ARGIRIOU A., Assoc. Professor	University of Patras, Greece
BAIS A., Professor	University of Thessaloniki, Greece
BALARAS C., Research Director	National Observatory of Athens, Greece
BARTZOKAS A., Assoc. Professor	University of Ioannina, Greece
BENISTON M., Professor	University of Geneva, Switzerland
BLOUTSOS A. Professor	University of Thessaloniki, Greece
BOLAND J., Assoc. Professor	University of South Australia, Australia
CHARANTONIS T, Deputy Director	Hellenic National Weather Service, Greece
CHRONOPOULOU A., Professor	Agricultural University of Athens, Greece
FOUNDA D., Senior Researcher	National Observatory of Athens, Greece
GERASOPOULOS E., Senior Researcher	National Observatory of Athens, Greece
GIANNAKOPOULOS C., Senior Researcher	National Observatory of Athens, Greece
HADJIMITSIS D., Assoc. Professor	Cyprus University of Technology, Cyprus
HELMIS C., Professor	University of Athens, Greece
JACOVIDES K., Assoc. Professor	University of Athens, Greece
KALABOKAS P., Research Director	Academy of Athens, Greece
KALLOS G., Professor	University of Athens, Greece
KAMBEZIDIS H., Research Director	National Observatory of Athens, Greece
KANAKIDOU M., Professor	University of Crete, Greece
KARACOSTAS T., Professor	University of Thessaloniki, Greece
KASSOMENOS P., Assoc. Professor	University of Ioannina, Greece
KERKIDIS P., Professor	Agricultural University of Athens, Greece
KOTRONI V., Senior Researcher	National Observatory of Athens, Greece
KOURTIDIS K., Assoc. Professor	University of Thrace, Greece
KOUSSIS A., Research Director	National Observatory of Athens, Greece
KOUTSOYIANNIS D., Professor	National Technical University of Athens, Greece
KUTIEL H., Professor	University of Haifa, Israel
LAGOUVARDOS K., Senior Researcher	National Observatory of Athens, Greece
LAZARIDIS M., Assoc. Professor	Technical University of Crete, Greece
LELIEVELD J., Professor	Cyprus Institute, Cyprus
LIONELLO P., Assoc Professor	University of Lecce, Italy
LUTERBACHER J. Professor	Liebig University of Giessen, Germany
MATZARAKIS A., Professor	University of Freiburg, Germany
MELAS D., Assoc. Professor	University of Thessaloniki, Greece

MICHAELIDES S. Director	Cyprus Weather Service, Cyprus
MICHALAKAKOU G., Professor	University of Ioannina, Greece
MIHALOPOULOS N., Professor	University of Crete, Greece
NASTOS P., Assoc. Professor	University of Athens, Greece
NENES A., Assoc. Professor	Georgia Institute of Technology, USA
PALIATSOS A., Professor	Technol Education Institute of Piraeus, Greece
PANDIS S., Professor	University of Patras, Greece
PAPAYANNIS A., Professor	National Technical University of Athens, Greece
PETRAKIS M., Research Director	National Observatory of Athens, Greece
PHILANDRAS C., Senior Researcher	Academy of Athens, Greece
PILINIS C., Professor	University of Aegean, Greece
PSILOGLOU B., Senior Researcher	National Observatory of Athens, Greece
RETALIS A., Senior researcher	National Observatory of Athens, Greece
SANTAMOURIS M., Professor	University of Athens, Greece
SCHAEFER K., Professor	Karlsruhe Institute of Technology, Germany
SIMMONDS I., Professor	University of Melbourne, Australia
TOMBROU M., Assoc. Professor	University of Athens, Greece
TRIANTAFYLLOU A., Professor	Technol Educ Inst of West Macedonia, Greece
TSIROS J., Assoc. Professor	Agricultural University of Athens, Greece
VAROTSOS C., Professor	University of Athens, Greece
ZIOMAS I., Professor	National Technical University of Athens, Greece
ZOUMAKIS E., Professor	Technol Educ Inst of Thessaloniki, Greece

Contents

Part II Climatology

Part I
Meteorology

Application of GIS and Remote Sensing Techniques for Flood Risk Assessment in Cyprus

D.D. Alexakis, D.G. Hadjimitsis, S. Michaelides, I. Tsanis, A. Retalis, C. Demetriou, A. Agapiou, K. Themistokleous, S. Pashiardis, K. Aristeidou, and F. Tymvios

Abstract Flooding is one of the most common natural disasters leading to economic losses and death. This paper strives to highlight the hydrological effects of land use changes in flood risk in a catchment area in Cyprus (Yialias river) through the application of ArcSWAT (Soil and Water Assessment Tool) in GIS environment. The model is used to simulate the main components of the hydrologic cycle, in order to study the effects of land use changes. For the implementation of the model, land use, soil and hydrometeorological data were used. The climatic and stream flow data were derived from hydrometeorological stations located in the wider area of the basin under study. In addition the land use and soil data were extracted from the analysis of multispectral satellite images such as those of Aster after the application of sophisticated classification algorithms. The results denoted the increase of runoff in the catchment area due to the recorded extensive urban sprawl phenomenon of the last decade.

DD. Alexakis (✉) • DG. Hadjimitsis • A. Agapiou • K. Themistokleous
Cyprus University of Technology, Limassol 3603, Cyprus
e-mail: dimitrios.alexakis@cut.ac.cy

S. Michaelides • S. Pashiardis • F. Tymvios
Meteorological Service of Cyprus, Nicosia, Cyprus

I. Tsanis
Technical University of Crete, Chania-Crete, Greece

A. Retalis
National Observatory of Athens, Athens, Greece

C. Demetriou • K. Aristeidou
Water Development Department of Cyprus, Nicosia, Cyprus

C.G. Helmis and P.T. Nastos (eds.), *Advances in Meteorology, Climatology and Atmospheric Physics*, Springer Atmospheric Sciences,
DOI 10.1007/978-3-642-29172-2_1,

1 Introduction

Ecosystem and floods are closely related and any changes in the ecosystem, such as urbanization across the catchment's area, may trigger off a sequence of flood occurrence causes are closely related and any changes in the ecosystem, such as urbanization across the catchment's area, may trigger off a sequence of flood occurrence causes (Hadjimitsis 2010). Simulation models are essential tools to evaluate potential consequences of proposed strategies and to facilitate management decisions. One of the most common used river basin models is ArcSWAT, which mainly focuses on spatial data mining, facilitating construction of a hydrologic model, computation and visualization of modeling output. According to Fürst et al. (2004) the GIS-support for hydrological models is classified into the following levels: assessment, estimation of hydrological parameters, hydrological modeling, coupling of GIS and hydrological models. SWAT belongs to the group of deterministic hydrological models. In SWAT the spatial heterogeneity of the watershed is taken into account, considering information from the elevation map (DEM), the soil and land use maps. The computed runoff from each sub-basin is routed through the river network o the main basin outlet.

This paper strives to present an analysis of the sensitivity of the distributed hydrological model soil and water assessment tool (SWAT, Arnold et al. 1993) to the land and soil use parameterization in order to simulate run off processes in a catchment area in Cyprus. Specifically there was an effort to highlight the potential of remote sensing in providing the GIS based hydrological softwares with adequate, reliable and updated land use data. The major flood event that occurred at 12–13 February of 2003 is successively simulated with the use of land use data of the specific period (data of 2000) and land use data of 2010 (keeping the same meteorological parameters) in order to assess the impact of land use changes to the run off processes.

2 Study Area and Data

Located in the central part of the island of Cyprus the study area is about 110 km^2 in size with an average slope value of 7.19% (Fig. 1). Specifically the study area is situated between longitudes 33° 11′ 24, 28″ and 33° 26′ 31, 52″ and latitudes 34° 54′ 36, 74″ and 35° 2′ 52, 16″ (WGS' 84, 36°N). The island of Cyprus is located in the northeastern most corner of the Mediterranean Sea and, therefore, has a typical eastern Mediterranean climate: the combined temperature–rainfall regime is characterized by cool-to-mild wet winters and warm-to-hot dry summers (Michaelides et al. 2009).

For the purposes of the study the following satellite and digital spatial data were incorporated: (a) Two Aster images, (b) a Digital Elevation Model (DEM) of 25 m pixel size provided by the Department of Land and Surveys of Cyprus and created with the use of ortho-rectified stereo-pairs of aerial photos covering the study area.

The acquired Aster images had a 10 year time interval in order the multi-temporal monitoring of urban sprawl to be guaranteed. For this study, the first three spectral bands were used (VNIR and SWIR) with spatial resolution of 15 m. The exact acquisition dates of the images were: 12 of May/2000 and 06 of April 2010.

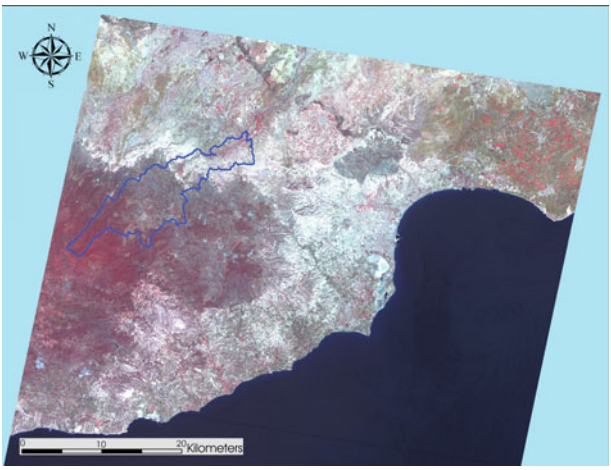

Fig. 1 Aster image (RGB – 321) of the study area. With blue outline the Yialias catchment area is indicated

3 Pre and Post-processing Techniques of Satellite Imagery Data

Initially geometric corrections were carried out using standard techniques with ground control points and a first order polynomial fit. For this purpose topographical maps were used to track the position of ground control points in conjunction with the digital shoreline of Cyprus extracted from the provided DEM. In this study, the darkest pixel atmospheric correction method was applied to every image (Hadjimitsis et al. 2004). It has been found that atmospheric effects contribute significantly to the classification technique.

In order to search the diachronic expansion of urban cover in the watershed basin, classification algorithms such as Maximum Likelihood, Minimum Distance, Mahalanobis Distance and Spectral Angle Mapper were applied to both Aster images through the Erdas Imagine v.10 and ENVI v.4.8 image analysis softwares. The time period to be searched was 2000 and 2010 when considerable construction and urban development was recorded to the whole island of Cyprus. The training classes that were used for the supervised algorithms were: (1) urban cover, (2) vegetation 1, (3) bare soil, (4) forest, (5) geologic formation of marl/chalk (6) vegetation 2 (Fig. 2). During the supervised classification process the authors had to strive with the problem of similar spectral response of chalk/marls geologic formations and urban constructions that affected the validity of the final results.

At the next step the overall accuracy of each method was calculated using the kappa coefficient which indicates whether mapping results are significantly better than randomly generated results (Martinez and Toan 2009). The values of coefficient vary from 0 to 1. The kappa value of 0.80 for Maximum Likelihood (ML) classification algorithm suggested a good agreement above chance between classified pixels

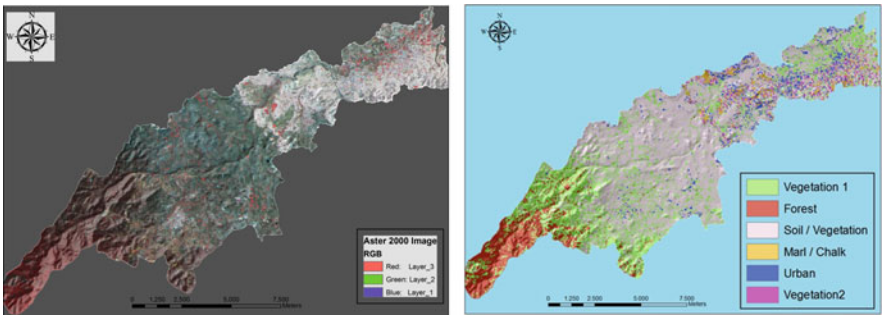

Fig. 2 False color composite of Aster image (3,2,1: RGB) of the catchment area during 2000 (*left*). Land use thematic map derived from ML classification method applied to 2000 Aster image (*right*)

Table 1 Statistics of urban expansion during the period of 2000–2010 in Yialias catchment area

	2000	2010
Urban area (km^2)	4.0359	19.128

and reference pixels. Regarding ML, at the specific algorithm the statistical probability is computed for each training class to determine the membership of the cells to the class. The classification results (Table 1) concerning urban sprawl phenomenon denoted a major urban area expansion during the time period of 2000–2010.

4 Set Up of Hydrological Model

According to Neitsch et al. (2005) SWAT is a conceptual semi-distributed model for watershed hydrology and water quality operating on a daily step. A crucial factor that is usually taken into account is the spatial heterogeneity of the model considering information for elevation (Digital Elevation Model/DEM), soil and land use. The research team proceeded to the model parameterization using the ArcGIS interface for SWAT which provides a graphical support for the disaggregation scheme and this way facilitates the data handling.

Initially, after the delineation of the DEM the watershed was divided to 13 individual sub-basins (Fig. 3 upper left, upper right). The next step required the land use and soil input, overlay and characterization for each sub-basin. As it was mentioned, the generalized land use maps derived from the Aster images of 2000 and 2010 were incorporated to the same hydrological model consecutively. All the other data (such as soil, precipitation and temperature) were related to the catchment regime during the 2003 flood event. Concerning soil data these were extracted from the integrated search of CORINE and FAO (Food and Agriculture Organization of the United States) soil map datasets. Regarding meteorological data, the research team had access to precipitation data from "Kionia" and "Mantra tou Kampiou" rain gauges which are spatially limited only to the southwestern

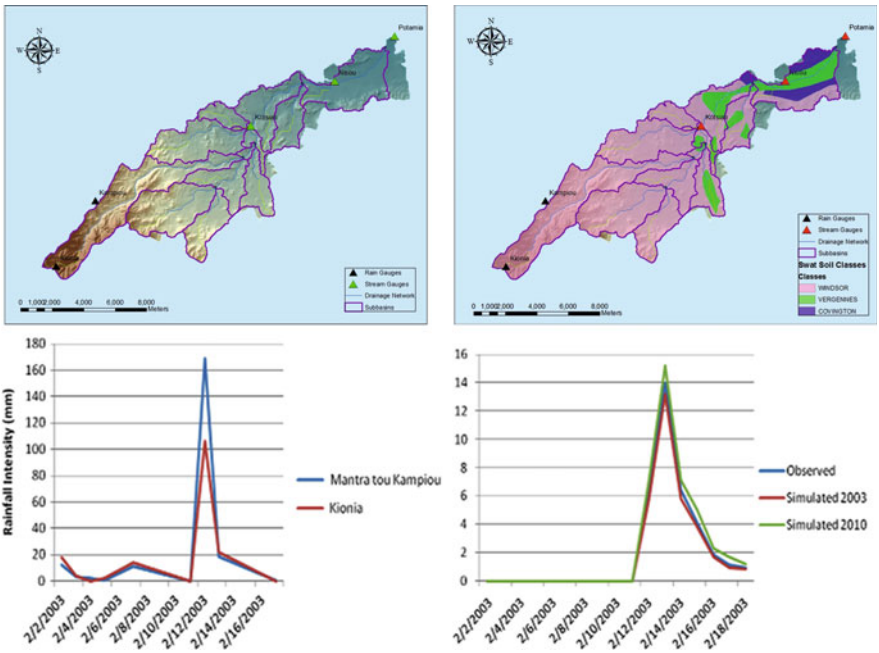

Fig. 3 Map of the stream and rain gauges of the watershed area (*upper left*). Soil map of the study area derived from the SWAT program default classes (*upper right*). Precipitation diagram for the flood period event (*lower left*). Diagram of observed and simulated flow results for the period 2003 and 2010 (*lower right*)

(mountainous) part of the catchment area (Fig. 3 lower left). Similarly, temperature data were provided from "Politiko" and "Kornos" weather stations that are established in close vicinity to the study area. The meteorological data covered a period of 3 years in total (2 years before and 1 year after the event). In addition, concerning the calibration process and assessment of the accuracy of simulated runoff results, observed flow data from "Potamia", "Kotsiatis" and "Nisou" stream gauges for the same period were used. The results reflected the high rate of affection of urban sprawl phenomenon to the hydrological response of catchment area as it is indicated in flow diagram of Fig. 3 lower right. Specifically, the simulated flow measurements with the use of 2010 land use datasets are steadily higher from both 2003 observed and simulated measurements.

5 Conclusions

The preliminary results in Yialias catchment area denoted the crucial role of urban sprawl phenomenon in the increase of runoff rate within the spatial limits of a catchment area and highlighted the importance of searching land use regime with

the use of satellite remote sensing imageries. The comparison of observed flow results concerning the flood event of 2003 with the simulated flow results (with the use of different land use data concerning 2000 and 2010 land use regime) proved that in the case of "2010" model the run off rates were steadily higher due to the expanded urban area cover that increases the phenomenon of surface run off. However, the research team will continue to search the hydrological response of the catchment area with more updated meteorological and stream data as well as satellite images of higher spatial resolution.

Acknowledgments The project is funded by the Cyprus Research Promotion Foundation in the frameworks of the project "SATFLOOD".

References

Arnold JG, Engel BA, Srinivasan R (1993) Continuous-time, grid cell watershed model. In: Proceedings of application of advanced information technologies for the management of natural resources. Sponsored by ASAE, 17–19 June 1993, Spokane, Washington

Fürst C, Klins U, Knoke T, Suda M, Bitter AW (2004) Multifunctional demands to forestry – societal background, evaluation approaches and adapted inventory methods for the key functions protection, production, diversity and recreation. In: Andersson F, Birot Y, Päivinen R (eds) Towards the sustainable use of Europe's forests – forest ecosystem and landscape research: scientific challenges and opportunities, EFI Proceedings 49, Saarijarvi, Finland, pp 113–124

Hadjimitsis D (2010) Determination of urban growth in catchment areas in Cyprus using multi-temporal remotely sensed data: risk assessment study. Nat Hazards Earth Syst Sci 10:2235–2240. doi:10.5194/nhess-10-2235-2010

Hadjimitsis DG, Clayton CRI, Hope VS (2004) An assessment of the effectiveness of atmospheric correction algorithms through the remote sensing of some reservoirs. Int J Remote Sens 25 (18):3651–3674. doi:http://dx.doi.org/10.1080/01431160310001647993

Martinez JM, Toan T (2009) Mapping of flood dynamics and spatial distribution of vegetation in the Amazon floodplain using multi-temporal SAR data. Remote Sens Environ 108:209–223

Michaelides S, Tymvios F, Michaelidou T (2009) Spatial and temporal characteristics of the annual rainfall frequency distribution in cyprus. Atmos Res 94:606–615. doi:http://dx.doi.org/10.1016/j.atmosres.2009.04.008

Neitsch SL, Arnold JG, Kiniry JR, Williams JR (2005) Soil and water assessment tool. Theoretical documentation, version 2005. Blackland Research Center, Texas Agricultural Experiment Station, Temple

Estimating Flash Flood Discharge in a Catchment Area with the Use of Hydraulic Model and Terrestrial Laser Scanner

D.D. Alexakis, D.G. Hadjimitsis, and A. Agapiou

Abstract A flood can be determined as a mass of water that produces runoff on land that is not normally covered by water. This paper aims to define the potential utility of terrestrial laser scanning data and hydraulics for improving flood risk assessment models in Yialias catchment area in Cyprus. Recently, terrestrial scanners have been used to capture 3D point cloud data of high accuracy for inundation models. Thus, different methods are used to process the scanning data in order to extract hydraulically relevant information. For this reason a variety of Digital Elevation Models (DEMs) of different spatial resolution was derived. The combined use of a two dimensional (2D) numerical hydraulic model and a terrestrial laser scanner can give the opportunity of estimation of peak discharge of a recent flash flood. Hence, the approach used in this study demonstrated the potential of hydraulics and laser scanner for flood risk assessment in catchments with infrastructure and vulnerable goods.

1 Introduction

The last years the urgent demand for flooding predictions caused by events of different return periods has increased markedly (Hall et al. 2005; Dawson et al. 2005). The practically instantaneous occurrence of flash floods together with their capacity of transport renders flash floods which is one of the most significant weather-related hazards in many parts of the world, causing considerable economic and human losses every year (Gaume et al. 2009).

Recently the growing understanding of the interaction between surface morphology and geomorphological processes as well as the awareness of the wide spatial and temporal processes take place, have increased the need for accurate and continuous three dimensional descriptions of topography (Lane et al. 1998). Thus

D.D. Alexakis (✉) • D.G. Hadjimitsis • A. Agapiou
Cyprus University of Technology, Limassol 3603, Cyprus
e-mail: dimitrios.alexakis@cut.ac.cy

C.G. Helmis and P.T. Nastos (eds.), *Advances in Meteorology, Climatology and Atmospheric Physics*, Springer Atmospheric Sciences,
DOI 10.1007/978-3-642-29172-2_2,

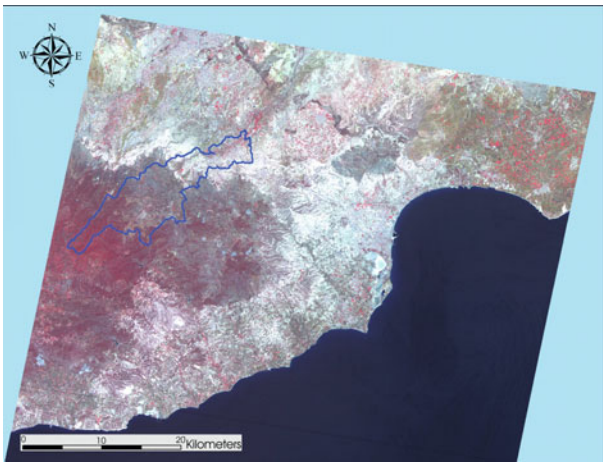

Fig. 1 Aster image (RGB – 321) of the study area. With blue outline the Yialias catchment area is indicated

a detailed description of fluvial topography is essential to accurately model the extent of the flooded areas. Currently the most accurate method for collecting elevation data for the production of Digital Elevation Model (DEM) is laser scanning (Cavalli et al. 2008). Terrestrial laser scanners (TLS) offer a high potential for the 3D mapping of smaller areas with high detail, a range accuracy of up to 1–2 mm and a scanning speed of up to 1M pts/s. The principle of TLS is simple, involving highly collimated laser-beam scans over a predefined solid angle in a regular scan pattern and the measurement of the time of flight of the laser signal.

This study strived to demonstrate in preliminary stage the potential of hydraulics and laser scanner for flood risk assessment in catchments with infrastructure and vulnerable goods. Specifically, after the extraction of major hydrologic parameters in GIS environment with the use of medium resolution DEM the research team proceeded to the construction of a high resolution DEM in the downstream of the basin in order to incorporate it in HEC-HMS software and implement a detailed hydraulic/hydrologic study of the area.

2 Study Area and Data

Located in the central part of the island of Cyprus the study area is about 110 km^2 in size with an average slope value of 7.19% (Fig. 1). Specifically the study area is situated between longitudes 33° 11′ 24, 28″ and 33° 26′ 31, 52″ and latitudes 34°54′36, 74″ and 35°2′ 52, 16″ (WGS' 84, 36°N). The island of Cyprus is located in the northeastern most corner of the Mediterranean Sea and, therefore, has a typical eastern

Fig. 2 Map of the catchment area indicating the subbasins, the rain and the stream gauges (*left*). Bridge in the downstream area of the basin where extreme inundation phenomena have taken place during 1992, 2003 and 2009 (*right*)

Mediterranean climate: the combined temperature–rainfall regime is characterized by cool-to-mild wet winters and warm-to-hot dry summers (Michaelides et al. 2009).

For the purposes of the study a Digital Elevation Model (DEM) of 25 m pixel size provided by the Department of Land and Surveys of Cyprus was used. The specific DEM was created with the use of ortho-rectified stereo-pairs of aerial photos covering the study area. At a next step the DEM was incorporated in GIS environment in order to delineate the basin's drainage network and extract the subbasins (13 subbasins) (Fig. 2). Moreover, flow accumulation, slope and elevation maps were produced in order to support the hydrological study of the area.

The elevation of the basin ranges from 194 to 1,408 m. In the upstream area the topography is steep though in the downstream is smooth. The geology of the basin is mainly volcanic with pillow lavas and basal group formations. Moreover, there are extended areas with marl/chalk formations of low hydropermeability and alluvium/colluviums deposits in the downstream. During the last 20 years three extreme floods have occurred in the basin, especially in the downstream area. According to historical data the most extreme events took place on 2 December 1992, February 2003 and 27 October 2009. All these extreme floods caused significant damage to properties and constructions.

3 DEM Creation

The Leica ScanStation C10 laser scanner was used for documentation of Yialias catchment area at the area where its bank gets really narrow due to anthropogenic interventions. This laser scanner may scan up to 50,000 points per second, while the accuracy – as provided by the developer – is ±6 mm/50 m distance. The field of view of the Scan Station is 360° × 270°. Laser Scanner was used in conjunction

Fig. 3 Rover GPS equipment (*left*). Use of the Leica ScanStation C10 laser scanner in Yialias catchment area (*right*)

with differential GPS instrument. The Leica GNSS Viva was used for this purpose. A reference base was set up at a triangulation pillar of the local reference system of Cyprus (WGS 84, Local Transverse Mercator). A rover GPS equipment was used in order to measure characteristics points of the Yialas basin (Fig. 3). The accuracy of the measurements was less than 2 cm (3D measurements).

The laser scanner allows acquiring the reflected beam intensity and RGB colours. Tripods and the HDS scan targets are the main accessories of the instrument. The post-processing of the laser scanning includes some standard procedure. To accurately model the flow of water over the floodplain the DEM derived from the TLS point data must preserve all the important geometric details affecting the flow. At first, after the data are downloaded to the computer the registration of the point's clouds was applied in the Cyclone software. The registration was performed automatically using the special targets. Afterwards, an ICP (Iterative Closest Point) algorithm was applied in order to achieve a highest accuracy of registration of the point clouds in the same software. The relative accuracy of scans was up to 2 cm (RMS) between the point clouds. After the ICP algorithm was applied the accuracy was found to be less than 1.5 cm (Fig. 4). However, the accuracy of the registration can only be evaluated by using Check Points (CP) not used for the estimation for the registration parameters. The next step of the post-processing is the automatic and manual cleaning of the data. This is a necessary step in order to minimize the noise which appears in the point clouds and to define a perimeter of the area of interest. In order to model the water flow accurately it is important to include the channel bathymetry in the model as well as the objects that affect the direction and velocity of water flow in the over bank situation such as buildings, bridges etc. (Mandlburger et al. 2009). After the cleaning of the data the mesh procedure can be performed using all the points' clouds. A 3D mesh was created in the 3D Reshaper software.

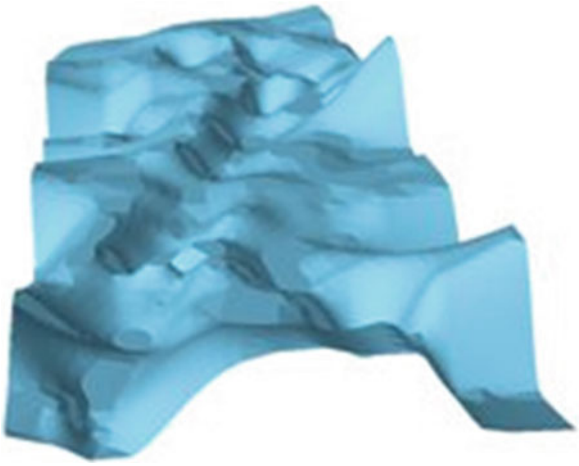

Fig. 4 Preliminary result of the DEM output in the downstream with the use of only the elevation data derived from the GPS survey

4 Run-off Model Description

The runoff process is modeled using the Hydrologic Engineering Center's Hydrologic Modeling System (HEC-HMS). The specific software was developed by the US Army Corps of Engineers and is designed to simulate the precipitation – runoff processes of dendritic watershed systems. Moreover it gives the chance to the end user to choose between numerous infiltration losses parameterizations (Knebla et al. 2005).

The final hydraulic model requires as input the hydrographs derived from HMS. The parameters of the model are representative cross-sections including left and right bank locations roughness coefficients (Manning's coefficient) and finally contraction and expansion coefficients. The roughness coefficients are crucial for the implementation of the model (they represent a surface's resistance to flow and are integral parameters for the calculation of water depth) and are calculated by combining land use data with tables of Manning's *n* values.

As it was mentioned the rainfall-runoff models simulate the runoff response of an area to a given amount and distribution of precipitation over a certain period of time. The output of the model is the discharge hydrograph at each sub-basin outlet which defines each sub-basin's unique runoff response due to differences in watershed properties such as geomorphology, geology and anthropogenic effects. The research team will incorporate the spatial data (DEM from laser scanner) and precipitation data from the meteorological stations in and outside of the basin in order to simulate the hydrologic/hydraulic response of Yialias river during extreme weather phenomena.

5 Conclusions

This review of the application of laser scanning in fluvial studies has shown that laser scanner data have great potential to improve the effectiveness of topographical data acquisition and the accuracy and resolution of DEMs. The integration of hydraulic geometry methods and 3D scanner with the use of bed roughness and high quality topographic data have proved to be a great alternative for searching the watershed regime in flood prone areas. The detailed DEM constructed by 3D laser scanner provides the model with reliable data related to the geometry of the cross-sections.

Acknowledgments The project is funded by the Cyprus Research Promotion Foundation in the frameworks of the "SATFLOOD" project. In addition the authors would like to acknowledge the Cyprus University of Technology/Department of Civil Engineering and Geomatics (Remote Sensing Laboratory) for supporting this study.

References

Cavalli M, Tarolli P, Marchi L, Fontana GD (2008) The effectiveness of airborne LiDAR data in the recognition of channel-bed morphology. Catena 73:249–260

Dawson RJ, Hall JW, Sayers PB, Bates PD, Rosu C (2005) Sampling-based flood risk analysis for fluvial dike systems. Stoch Environ Res Risk A 19(6):388–402. doi:10.1007/s00477-005-0010-9

Gaume E, Bain V, Bernardara P, Newinger O, Barbuc M, Bateman A, Blaskovicova L, Bloschl G, Borga M, Dumitrescu A, Daliakopoulos I, Garcia J, Irimescu A, Kohnova S, Koutroulis A, Marchi L, Matreata S, Medina V, Preciso E, Sempere-Torres D, Stancalie G, Szolgay J, Tsanis I, Velasco D, Viglione A (2009) A compilation of data on European flash floods. J Hydrol 367 (1–2):70–78. doi:10.1016/j.jhydrol.2008.12.028

Hall JW, Sayers PB, Dawson RJ (2005) National-scale assessment of current and future flood risk in England and Wales. Nat Hazards 36(1–2):147–164. doi:10.1007/s11069-004-4546-7

Knebla MR, Yanga ZL, Hutchisonb K, Maidment DC (2005) Regional scale flood modeling using NEXRAD rainfall, GIS, and HEC-HMS/RAS: a case study for the San Antonio river basin summer 2002 storm event. J Environ Manage 75:325–336

Lane SN, Chandler JH, Richards KS (1998) Landform monitoring, modelling and analysis: landform in geomorphological research. In: Lane SN, Richards KS, Chandler JH (eds) Landform monitoring, modelling and analysis. Wiley, Chichester, pp 1–18

Mandlburger G, Hauer C, Hofle B, Habersack H, Pfeifer N (2009) Optimization of LiDAR derived terrain models for river flow modelling. Hydrol Earth Syst Sci 13:1453–1466. doi:10.5194/hess-13-1453-2009

Michaelides S, Tymvios F, Michaelidou T (2009) Spatial and temporal characteristics of the annual rainfall frequency distribution in Cyprus. Atmos Res 94:606–615

On the Role of Potential Vorticity Perturbations in the Spontaneous Generation of Gravity Waves

N.A. Bakas and B.F. Farrell

Abstract Mechanisms of internal gravity wave generation have been intensively studied because of the role of gravity waves in the large-scale atmospheric circulation. One source of gravity waves that is poorly understood is spontaneous wave generation by the low frequency mesoscale and large scale motions in the atmosphere. In this work, we study the interaction among potential vorticity perturbations and gravity waves in a stably stratified, horizontally sheared zonal flow, with the goal of clarifying the role of these interactions in the process of spontaneous wave generation. We find that vorticity perturbations amplify in energy due to downgradient Reynolds stress when their phase lines tilt towards the west with increasing latitude for a northward increasing shear flow. For a Froude number of order one, there is strong coupling between the vorticity perturbations and the gravity wave manifold. As a result, the large growth attained by vorticity perturbations is transferred to propagating gravity waves. When the flow geometry permits wave propagation, significant gravity wave emission occurs.

1 Introduction

Mechanisms of gravity wave generation have been intensively studied in the past in order to obtain an estimate of internal wave energy rates in the atmosphere. In this work we study the interaction of potential vorticity perturbations with gravity waves for a stably stratified horizontal shear flow and investigate its role in spontaneous gravity wave generation.

Spontaneous generation of gravity waves has been studied in the past for shallow water equations (Ford et al. 2000) and for sheared disturbances in the *f*-plane (Vanneste and Yavneh 2004; Kalashnik et al. 2006). The term spontaneous

N.A. Bakas (✉) • B.F. Farrell
School of Engineering and Applied Sciences, Harvard University, Cambridge, MA 02138, USA
e-mail: nikos.bakas@gmail.com

C.G. Helmis and P.T. Nastos (eds.), *Advances in Meteorology, Climatology and Atmospheric Physics*, Springer Atmospheric Sciences,
DOI 10.1007/978-3-642-29172-2_3,

generation refers to emission of gravity waves occurring abruptly during the evolution of an initially balanced flow and is distinct from emission of gravity waves during geostrophic adjustment of an initially unbalanced flow. The process of spontaneous generation is underlying emission of gravity waves during baroclinic life cycles (O'Sullivan and Dunkerton 1995; Plougonven and Snyder 2007), a source of gravity waves that has not yet been adequately understood.

In this work we perform a generalized stability analysis (Farrell and Ioannou 1996) of a linear three dimensional stably stratified model with a constant Brunt-Väisälä frequency and a meridional shear flow and make use of closed form asymptotic solutions to study the role of potential vorticity perturbations in the process of spontaneous wave generation.

2 Gravity Wave-Vorticity Wave Interactions

The linearized, nondimensional momentum and thermodynamic equations governing the evolution of small perturbations in a stably stratified zonal flow $U(y)$ with constant buoyancy frequency in the vertical are given by:

$$\begin{aligned}(\partial_t + U\partial_x)\zeta &= -\frac{dU}{dy}\partial_z v + S\partial_x \rho + \frac{1}{\mathrm{Re}}\nabla^2\zeta \\ (\partial_t + U\partial_x)v &= \frac{d^2U}{dy^2}\partial_x v + S\partial_{yz}\rho + \frac{1}{\mathrm{Re}}\nabla^4 v \\ (\partial_t + U\partial_x)\left(\partial_x^2 + \partial_z^2\right)\rho &= -\partial_x\zeta - \partial_{yz}v + \frac{1}{\mathrm{Re}}\nabla^2\left(\partial_x^2 + \partial_z^2\right)\rho \end{aligned} \tag{1}$$

where $\zeta = \partial_z u - \partial_x w$, v, are the meridional components of vorticity and velocity, ρ is the density, S is the static stability and Re is the Reynolds number.

Consider first an inviscid, unbounded, constant shear flow $U(y) = y$, for which the sheared disturbances of the form $[\zeta(t), v(t), \rho(t)]e^{ikx+i(l-kt)y+imz}$ reduce the partial differential equations to the single second order non-homogeneous differential equation:

$$\frac{d^2\rho}{dt^2} + (l - kt)a(t)\frac{d\rho}{dt} + \left[S\omega^2(t) + ka(t)\right]\rho = -\frac{ika(t)}{m}q(0) \tag{2}$$

where $a(t) = 2\,km^2/[k^2 + (l - kt)^2]K^2(t)$, $\omega^2(t) = [k^2 + (l - kt)^2]/K^2(t)$, $K^2(t) = k^2 + (l - kt)^2 + m^2$ and $q(0)$ is the initial potential vorticity $q = \partial_x v - \partial_y u + \partial_z \rho$. The solution of the homogeneous equation consists of propagating gravity waves having zero potential vorticity (Bakas and Farrell 2009a). The interaction of these propagating waves with the non-propagating initial potential vorticity perturbation is described by the particular solution. Therefore the following question arises: if we consider oscillation free initial conditions, what portion of the initial energy will radiate away as gravity waves? To address this question, we calculate the evolution of $\rho(t)$ containing a vorticity and a gravity wave component: $\rho(t) = \rho_{vort}(t) + \rho_{wave}(t)$ and we start with gravity wave free initial conditions $\rho_{wave}(0) = 0$.

The coupling strength between vorticity dynamics and gravity waves is determined by the Froude number that is defined as $F = (m/k)/S^{1/2}$. We can therefore distinguish two regimes that will be studied separately.

2.1 Weak Coupling Regime ($F << 1$)

In this regime, we can seek a solution for the vorticity wave of the form: $\zeta_z(t) = \zeta_0(t) + F^2\zeta_1(t) + F^4\zeta_2(t) + \ldots$, $\rho_{vort}(t) = (1/S)\rho_1(t) + (1/S^2)\rho_2(t) + \ldots$, for the vertical component of vorticity and for the density perturbation of the vorticity wave respectively. The leading order term is $\zeta_0(t) = \zeta_z(0)$. That is, the vertical component of vorticity is conserved, leading due to kinematic deformation of ζ_z by the shear, to transient growth of the meridional and zonal velocity fields for perturbations with constant phase surfaces oriented against the shear. This is the mechanism of growth in planar shear flow discussed by Orr (1907) and it will be referred to as the Orr mechanism. Using a similar expansion for $\rho_{wave}(t)$ and asymptotic matching in the complex t-plane (Hakim 1998), it can be shown that the solution to leading order in $1/S$ and at large times is given by (Bakas and Farrell 2009b):

$$\rho(t) = \frac{2k^2 mq(0)}{iS\left[k^2 + (l - kt)^2\right]^2} + \frac{q(0)\sqrt{\pi}e^{(i\phi_0 - \beta)\sqrt{S}}}{k\sqrt{2}S^{1/4}}\left(e^{i\sqrt{S}\int \omega^2(s)ds} + e^{-i\sqrt{S}\int \omega^2(s)ds}\right) \tag{3}$$

The first term is the first order correction to the non-propagating vorticity wave and corresponds to a large density amplification that might lead to a localized convective overturning of the vorticity perturbation itself. The last two terms are propagating gravity waves excited abruptly at time $t = l/k$. Like in the case of sheared disturbances in the f-plane (Vanneste and Yavneh 2004), these gravity waves are generated through a Stokes phenomenon (Olver 1974) in which the subdominant solution (waves) is switched on by the dominant solution (potential vorticity perturbation) when time crosses a Stokes line. These spontaneously generated waves are exponentially small for large values of static stability. Thus, the overall effect of potential vorticity perturbations in this regime is an amplification of density and vertical velocity of the non-propagating vorticity wave itself and a weak excitation of propagating gravity waves.

2.2 Strong Coupling Regime ($F \sim O(1)$)

In this regime, gravity waves generated through the Stokes phenomenon are order one. The evolution of the particular solution φ_p with time for $m/k = 5$ is shown in Fig. 1. The forced waves' amplitudes remain at very low values until time

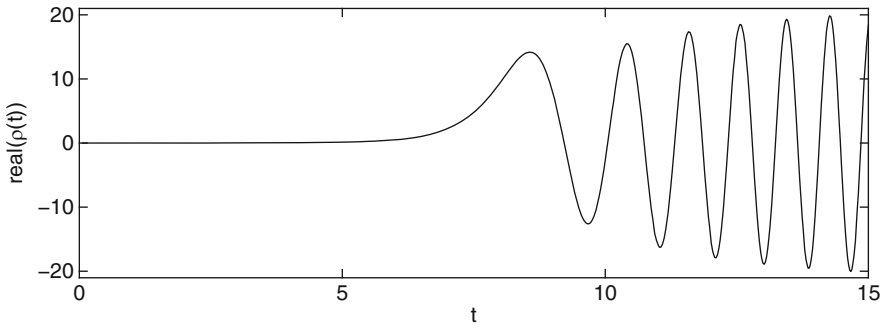

Fig. 1 Evolution of perturbation density for sheared wave perturbations with $(k, l, m) = (1, 8, 5)$. The static stability is $S = 100$ and the initial conditions are $(\zeta, v, \rho) = (-90\mathrm{i}, 1.6, 1)$

$t = l/k = 8$. At that time, the large amplification of the vorticity wave's meridional velocity due to the Orr mechanism is transferred to vertical velocity, exciting in this case gravity waves. The amplitude of these forced waves increases rapidly and saturates at large values as illustrated in Fig. 1. The amplitude of the forced waves can be calculated in closed form (Bakas and Farrell 2009b) and is of order $q(0)FS^{1/4}$ for $F \sim \mathrm{O}(1)$ showing that a large initial potential vorticity perturbation leads to substantial excitation of waves.

3 Emission of Gravity Waves from a Shear Layer

As discussed in the previous section, the excitation mechanism of gravity waves by vorticity perturbations is robust for Froude number of order one, leading to a large energy transfer to propagating waves. While in a constant shear flow these waves are bounded by their trapping levels, in a flow with shear varying with latitude, the possibility arises that the energy tapped in propagating waves may leak and lead to enhanced gravity wave activity in regions with low shear. In order to investigate this possibility, we use the mean velocity profile $U(y) = \tanh(y/\delta)$ plotted in Fig. 2a. It consists of a shear flow region bounded by two regions of uniform velocity.

To address the question of what portion of initial energy remains trapped in the shear layer and what portion radiates to infinity we calculate the evolution of an initial perturbation of unit energy that is confined inside the shear layer. The evolution is calculated numerically, through discretization of the differential operators in system (1) in a meridional channel, introduction of sponge layers at the boundaries in the form of Rayleigh damping imposing radiation conditions and numerical integration of the resulting matrix equations. The energy evolution inside and outside of the shear layer is shown in Fig. 2b for $S = 1$. A large amplification occurs within the shear layer followed by wave excitation. We can see that around

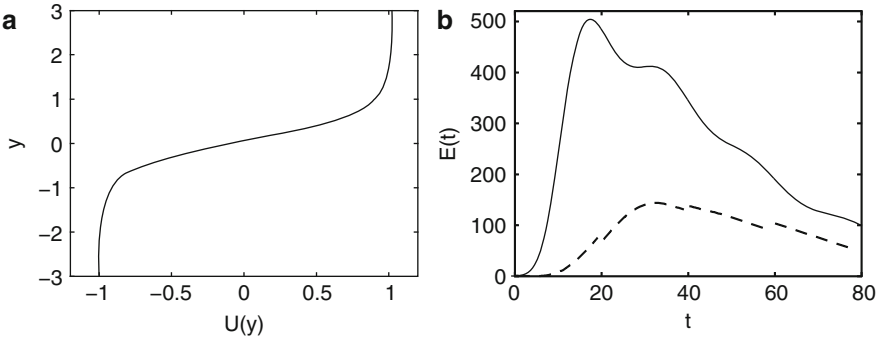

Fig. 2 (**a**) Zonal velocity profile of a meridional shear layer $U(y) = \tanh(y/\delta)$ with $\delta = 0.6$. (**b**) Energy evolution of an initial perturbation confined inside the shear layer. The initial perturbation is monochromatic in y and z with $(k, m) = (1, 1)$ and has a unit initial energy. The *solid line* shows the energy within the shear layer and the *dashed line* shows the energy outside of the shear. The static stability is $S = 1$ and the Reynolds number is $\mathrm{Re} = 10^3$

30% of the energy is radiated away leading to substantial emission of wave activity. Note that even though the percentage of energy leakage is moderate, an initial perturbation of unit energy leads to the emission of gravity waves of energy $E = 150$. Further investigation is needed though in the nonlinear regime to verify this hypothesis and examine the amount of emitted energy.

4 Conclusions

Interaction of non-propagating potential vorticity perturbations with internal gravity waves within a meridionally varying shear flow was investigated. For small Froude number, a weak coupling was found that nevertheless led to spontaneous gravity wave excitation by vorticity perturbations. In the case of oscillation free initial conditions, while the density field of potential vorticity perturbation was significantly amplified leading possibly to local convective overturning, two counter propagating gravity waves with an exponentially small amplitude of order $\exp(-\beta S^{1/2})$ were spontaneously generated through a Stokes phenomenon. For Froude number of order one, a strong coupling was found and gravity wave excitation by vorticity perturbations clearly manifests. Vorticity perturbations were found to amplify due to the Orr mechanism when their phase lines are tilted against the shear ($l/k > 0$) and the acquired energy is then transferred to gravity waves excited at $t = l/k$ through a Stokes phenomenon. These spontaneously generated waves finally emerge with an amplitude of order $q(0)FS^{1/4}$.

For an unbounded shear, all of the wave activity is confined in a region determined by the waves' trapping levels and convective collapse of this region is expected. For a finite shear layer a significant amount of wave activity was also found to be emitted from the shear layer. The results in this work suggest that the

interaction of vorticity and internal wave manifolds in the presence of shear is expected to play a significant role in the process of spontaneous gravity wave emission during baroclinic life cycles (Plougonven and Snyder 2007). Investigation of the role of the excitation mechanism during baroclinic life cycles for more realistic flows will be addressed in future work.

Acknowledgments This research was supported by the NSF ATM-0736022 grant.

References

Bakas NA, Farrell BF (2009a) Gravity waves in a barotropic shear flow. Part I: growth mechanisms in the absence of potential vorticity perturbations. J Phys Oceanogr 39:481–496. doi:10.1175/2008JPO3836.1

Bakas NA, Farrell BF (2009b) Gravity waves in a barotropic shear flow. Part II: interaction between gravity waves and potential vorticity perturbations. J Phys Oceanogr 39:497–511. doi:10.1175/2008JPO3836.1

Farrell BF, Ioannou PJ (1996) Generalized stability theory. Part I: autonomous operators. J Atmos Sci 53:2025–2040. doi:10.1175/1520-0469(1996) 053<2025:GSTPIA>2.0.CO;2

Ford R, McIntyre ME, Norton WA (2000) Balance and the slow quasi-manifold: some explicit results. J Atmos Sci 57:1236–1254. doi:10.1175/15200469(2000) 057<1236:BATSQS>2.0.CO;2

Hakim V (1998) Asymptotic techniques in nonlinear problems: some illustrative examples. In: Godreche C, Manneville P (eds) Hydrodynamics and nonlinear instabilities. Cambridge University Press, Cambridge, pp 295–386

Kalashnik MV, Mamatsashvili GR, Chagelishvili GD, Lominadze JG (2006) Linear dynamics of non-symmetric perturbations in geostrophic horizontal shear flows. Q J R Meteor Soc 132:505–518. doi:10.1256/qj.04.105

O'Sullivan D, Dunkerton TJ (1995) Generation of inertia-gravity waves in a simulated life cycle of baroclinic instability. J Atmos Sci 52:3695–3716. doi:10.1175/1520-0469(1995) 052<3695:GOIWIA>2.0.CO;2

Olver FWJ (1974) Asymptotics and special functions. Academic Press, New York, p 572

Orr WMF (1907) The stability or instability of the steady motions of a perfect liquid and of a viscous liquid. Proc R Irish Acad Ser A 27:9

Plougonven R, Snyder C (2007) Inertia-gravity waves spontaneously generated by jets and fronts. Part I: different baroclinic life cycles. J Atmos Sci 64:2502–2520. doi:10.1175/JAS3953.1

Vanneste J, Yavneh I (2004) Exponentially small inertia-gravity waves and the breakdown of quasigeostrophic balance. J Atmos Sci 61:211–223. doi:10.1175/1520-0469(2004) 061< 0211:ESIWAT>2.0.CO;2

On a Dynamical Mechanism Underlying the Intensification of Tropical Cyclones

N.A. Bakas and P.J. Ioannou

Abstract Tropical cyclones are among the most life threatening and destructive natural phenomena on Earth. A dynamical mechanism for cyclone intensification that has been proposed is based on the idea that patches of high vorticity associated with individual convective systems are quickly axisymmetrized, feeding their energy into the circular vortex. In this work, Stochastic Structural Stability Theory (SSST) is used to achieve a comprehensive understanding of this physical mechanism. According to SSST, the distribution of momentum fluxes arising from the field of asymmetric eddies associated with a given mean vortex structure, is obtained using a linear model of stochastic turbulence. The resulting momentum flux distribution is then coupled with the equation governing the evolution of the mean vortex to produce a closed set of eddy/mean vortex equations. We apply the SSST tools to a two dimensional, non-divergent model of stochastically forced asymmetric eddies. We show that the process intensifying a weak vortex is shearing of asymmetric eddies with small azimuthal scale that produces upgradient fluxes. For stochastic forcing with amplitude larger than a certain threshold, these upgradient fluxes lead to a structural instability of the eddy/mean vortex system and to an exponentially growing vortex.

1 Introduction

Tropical cyclones are among the most life threatening and destructive natural phenomena on Earth. However, despite our knowledge of the climatological conditions favoring tropical cyclogenesis, a widely accepted theory for tropical cyclone formation and intensification does not exist. Early theoretical work suggested that tropical depressions intensify by utilizing cooperative feedbacks

N.A. Bakas (✉) • P.J. Ioannou
National and Kapodistrian University of Athens, Athens 15784, Greece
e-mail: nikos.bakas@gmail.com

C.G. Helmis and P.T. Nastos (eds.), *Advances in Meteorology, Climatology and Atmospheric Physics*, Springer Atmospheric Sciences,
DOI 10.1007/978-3-642-29172-2_4,

between cumulus clouds and the large scale flow (Charney and Eliasen 1964), or between surface heat fluxes and the surface wind (Rotunno and Emanuel 1987). Another theory is based on the idea that patches of high vorticity associated with individual convective systems are quickly axisymmetrized, feeding their energy into the vortex scale flow (Montgomery and Enagonio 1998), a process that can be described in terms of the interaction between Vortex Rossby Waves (VRW) and the circular vortex (Montgomery and Kallenbach 1997).

The goal of this work is to provide a theory for the systematic organization of the turbulent fluxes intensifying the vortex, based on the interaction between VRW and the mean vortex and building on results from linear stochastic turbulence modeling that has led to a novel framework for investigating the organization of eddy fluxes in turbulent zonal flows called Stochastic Structural Stability Theory (SSST, Farrell and Ioannou 2003). In the context of SSST, the forcing of VRW, that can be traced to highly intermittent, short time scale processes (e.g. convection), is modeled stochastically (Farrell and Ioannou 1993a, b; DelSole and Farrell 1996). Furthermore, the VRW-VRW interactions are ignored, yielding a linear stochastic model for the VRW evolution. The resulting momentum flux distribution arising from the VRW is coupled with the mean vortex momentum equations to obtain a closed dynamical system for the joint evolution of the VRW statistics and the mean vortex. The dynamics of this system that will be derived in detail in Sect. 2, will be investigated in order to address whether axisymmetrization can lead to the transformation of a small depression into a tropical cyclone of sufficient intensity, focusing on the VRW-mean vortex dynamics leading to such intensification.

2 Evolution Equations for a Barotropic Vortex

Consider a forced non-divergent, flow in which the Coriolis parameter f is set to a local, constant value. A streamfunction ψ can be defined such that: $[u,v] = [-(1/r)\psi_\theta,\psi_r]$, where u, v are the radial, r, and azimuthal, θ, components of velocity. Since we are interested in the effect of asymmetric perturbations on a circular vortex, we decompose the streamfunction into an axi-symmetric component (indicated with upper case) and an asymmetric eddy component that is typically termed as Vortex Rossby Waves (VRW) (indicated with a tilde): $\psi(r,\theta,t) = \Psi(r,t) + \tilde{\psi}(r,\theta,t)$. Harmonic VRW of the form $\tilde{\psi}(r,\theta,t) = \psi'(r,t)\, e^{im\theta}$, where m is the azimuthal wavenumber, evolve according to:

$$\left(\partial_t + im\frac{V}{r}\right)\zeta' - \frac{1}{r}\frac{dZ}{dr} im\Delta^{-1}\zeta' = -\mu\zeta' + f_{ext} + f_{eddy} \tag{1}$$

where $V = \Psi_r$ is the azimuthal averaged tangential wind, $\zeta' = \Delta\psi'$ is the relative vorticity of the VRW, $Z = \Delta\Psi$ is the vorticity of the mean flow, Δ is the Laplacian in polar coordinates, μ is the coefficient of linear dissipation, f_{ext}, is the external

forcing and f_{eddy} is the forcing term from the eddy-eddy interactions. On the other hand, the circular vortex is forced by the radial vorticity fluxes and evolves as:

$$\partial_t V = -\overline{u'\zeta'} - \mu V \tag{2}$$

Following previous studies of stochastic turbulence modeling (Farrell and Ioannou 1993a, b; DelSole and Farrell 1996), we parameterize the eddy forcing term $f_{ext} + f_{eddy}$ as a stochastic process. We also discretize the differential operators with finite differences on a radial channel $[0,R]$, imposing zero boundary conditions for the streamfunction at the boundaries. The operators then, become finite dimensional matrix approximations of the continuous operators and the variables ζ', V become column vectors with elements the values of the variables at the grid points defined by the elements of the radial vector $\mathbf{r}$. In matrix notation, (1) takes the form:

$$\frac{d\zeta}{dt} = \mathbf{A}\zeta + \mathbf{F}\xi \tag{3}$$

where the spatial structure of the forcing is given by the columns of $\mathbf{F}$ and $\boldsymbol{\xi}$ is a vector giving the time variation of the forcing. $[Notdefined]$ is the matrix form of the linear dynamics of VRW:

$$\mathbf{A} = -imdiag(V)\mathbf{R}^{-1} - im\mathbf{R}^{-1}\mathbf{D}\mathbf{Z}\Delta^{-1} - \mu\mathrm{I} \tag{4}$$

where $\mathbf{R} = \mathrm{diag}(\mathbf{r})$, $\mathbf{I}$ is the identity matrix and diag(●) denotes the diagonal matrix with diagonal elements the vector ●. The dynamics of VRW comprise of advection of the vorticity of VRW by the vortex, advection of the vorticity gradient $\mathbf{DZ}$ by VRW and dissipation. Similarly, (2) is written as:

$$\frac{d\mathbf{V}}{dt} = \mathbf{M} - \mu\mathbf{V} = -\frac{m}{2}\mathrm{Im}\left[\Delta^{-1}\zeta\zeta^{\dagger}\right] - \mu\mathbf{V} \tag{5}$$

where $\mathbf{M}$ are the radial vorticity fluxes, † denotes the Hermitian transpose and vecd denotes the operation of extracting the diagonal elements of a matrix. The random vector process ξ has statistically independent elements and is a Gaussian white noise in time with zero mean and unit variance: $<\xi> = 0$, $<\xi_i\ \xi_j> = \delta_{ij}\delta(t-s)$, where the angle brackets denote an ensemble average over realizations of the forcing. The spatial localization of the excitation is dictated by the matrix $\mathbf{F}$ which is chosen to have l columns and elements $F_{ij} = J_m(k_j r_i/R)$, where J_m is the Bessel function of order m and k_j is the jth zero of J_m. This specification leads to a statistically homogeneous excitation with forcing that is coherent over a distance inversely proportional to k_l. Finally, the forcing is normalized to have input power ε.

The system of (3), (5) describes the dynamics of a single realization of the stochastically excited VRW interacting with the circular mean vortex. Assuming a large number of independent realizations of the forcing and taking an ensemble

average of the excited wave fields, we obtain a deterministic equation governing the evolution of the ensemble average enstrophy covariance matrix $\mathbf{C} = <\boldsymbol{\zeta}\boldsymbol{\zeta}^\dagger>$:

$$\frac{d\mathbf{C}}{dt} = \mathbf{A}\mathbf{C} + \mathbf{C}\mathbf{A}^\dagger + \varepsilon\mathbf{Q} \tag{6}$$

where $\mathbf{Q} = \mathbf{F}\mathbf{F}^\dagger$. Under an ergodic assumption, the ensemble average of the eddy vorticity fluxes is equal to the azimuthal mean vorticity fluxes and the vortex therefore evolves as:

$$\frac{d\mathbf{V}}{dt} = \mathbf{M} - \mu\mathbf{V} = -\frac{m}{2}\mathrm{Im}\left[\Delta^{-1}\mathbf{C}\right] - \mu\mathbf{V} \tag{7}$$

Equations (6), (7) form a deterministic, autonomous, nonlinear system for the evolution of the mean vortex under the influence of its consistent field of VRW. The fixed points $\mathbf{V}^E$ and $\mathbf{C}^E$, if they exist, define statistical equilibria in the presence of an eddy field with covariance $\mathbf{C}^E$. The stability of the VRW-vortex equilibria $\mathbf{V}^E$ and $\mathbf{C}^E$ can then be determined by considering the evolution of small perturbations $\delta\mathbf{V}$, $\delta\mathbf{C}$ about the equilibrium. Because of the operator Im in (6), we must write separate equations for the evolution of the real, $\delta\mathbf{C}^R$, and imaginary part, $\delta\mathbf{C}^I$, of the covariance. The resulting stability equations for the evolution of $\delta\mathbf{V}$, $\delta\mathbf{C}^R$, $\delta\mathbf{C}^I$ can be written in the form:

$$\frac{d}{dt}\begin{bmatrix} vec(\delta\mathbf{C}^R) \\ vec(\delta\mathbf{C}^I) \\ \delta\mathbf{V} \end{bmatrix} = \mathbf{L}\begin{bmatrix} vec(\delta\mathbf{C}^R) \\ vec(\delta\mathbf{C}^I) \\ \delta\mathbf{V} \end{bmatrix} \tag{8}$$

where vec is the vector representation of a matrix obtained by stacking sequentially the columns of a matrix on top of each other. The structural stability operator $\mathbf{L}$ determines the stability of the VRW-vortex equilibria.

3 Structural Instability for an Equilibrium with No Mean Vortex

The state with $\mathbf{V}^E = 0$ and $\mathbf{C}^E = \varepsilon\mathbf{Q}/2\,\mu$, is a fixed point of the system (5)–(6) and the goal is to determine the stability of this statistical equilibrium state. It can be readily shown that $\mathbf{L}$ has a large number of decaying eigenmodes with $\delta\mathbf{V} = 0$ that do not modify the mean vortex. The remaining eigenvalues are given by:

$$\lambda_n = -\frac{3\mu}{2} \pm \frac{1}{2}\sqrt{2\mu^2 + 4s_n^2}, n = 1, 2, ..., N \tag{9}$$

where s_n are the eigenvalues of matrix $\mathbf{S}$ that determines the sensitivity of the vorticity fluxes to small changes in the vortex velocity $\mathbf{S} = \partial\mathbf{M}/\partial\mathbf{V}$. As a result, the

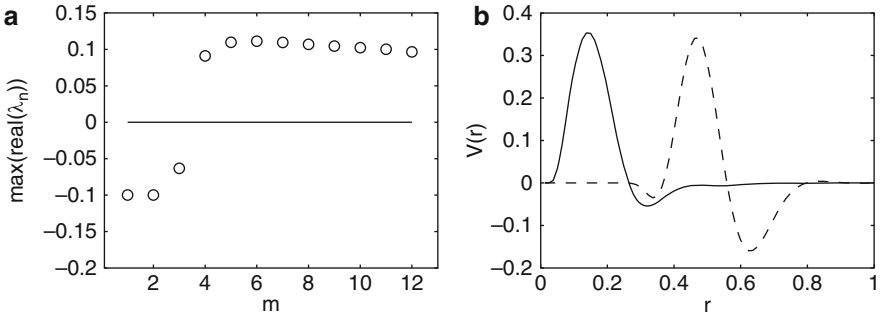

Fig. 1 (**a**) Maximum growth rate as a function of azimuthal wavenumber m. (**b**) The tangential velocity of the most unstable eigenfunction for $m = 4$ (*solid line*) and $m = 12$ (*dashed line*). For both panels, the power input is $\varepsilon = 10^{-3}$, $\mu = 0.1$ and $l = 40$

state with no mean vortex becomes unstable and a vortex emerges and intensifies only if the eigenvalues of $\mathbf{S}$ are positive, that is only if the VRW are organized by the vortex perturbation in such a way to yield upgradient vorticity fluxes.

The sensitivity operator can be explicitly calculated in terms of $\mathbf{Q}$, $\mathbf{R}$ and $\mathbf{\Delta}$ and is given as the sum of two commuting operators $\mathbf{S} = \mathbf{S}^{ad} - \mathbf{S}^{vg}$. The first operator, $\mathbf{S}^{ad}$, determines the sensitivity of the fluxes to changes in the advection of the vorticity of VRW, and the second operator, $\mathbf{S}^{vg}$, determines the sensitivity of the fluxes to changes in the advection of the mean vorticity gradient by the VRW. The eigenvalues of $\mathbf{S}^{ad}$, $\mathbf{S}^{vg}$ were numerically calculated and were both found to be positive. Consequently, advection of the eddy vorticity by the perturbed vortex yields upgradient fluxes and is destabilizing, while advection of the perturbed mean vorticity gradient by the VRW yields downgradient fluxes and has a stabilizing tendency. For $m > 2$, the eigenvalues of $\mathbf{S}^{ad}$ are larger, resulting in an overall destabilizing tendency.

Calculation of the eigenvalues λ_n revealed that another necessary condition for instability, is that the input power ε should be above a certain threshold, so that the eddy forcing, as measured by s_n can overcome the mean vortex dissipation. When the two necessary conditions are met, there is an emerging vortex whose mean tangential velocity grows exponentially. The maximum growth rate as a function of m is shown in Fig. 1a for a given forcing and eddy dissipation and roughly saturates at a constant value for large m, showing that small scale VRW are the most unstable. Figure 1b shows the most unstable mean flow perturbation, for $m = 4$ and $m = 10$. We observe that as m increases, the core of the vortex moves away from $r = 0$.

4 Conclusions

Axisymmetrization of VRW has been proposed as a dynamical mechanism for the intensification of a circular vortex. The VRW-circular vortex system is examined in this work within the framework of SSST. In the context of SSST, the average VRW

field and the circular vortex form a coupled system, in which the evolution of VRW is obtained using a linear stochastic model and the resulting vorticity fluxes force the mean vortex. Using SSST, the structural stability of a vortex with no velocity, subjected to homogeneous stochastic excitation was examined. The eigenvalues of the linear operator governing the evolution of mean vortex perturbations and the associated VRW statistics around the equilibrium state were calculated. The structural stability was found to depend on the sensitivity of the vorticity fluxes to changes in the vortex. Calculation of the eigenvalues of the sensitivity operator revealed two mechanisms underlying the instability: shearing of VRW by the vortex that is destabilizing, and advection of the mean vorticity gradient by the VRW that is stabilizing. VRW with small (large) azimuthal scales were found to be destabilizing (stabilizing) and a threshold for the amplitude of the excitation was found, above which an infinitesimal vortex is intensified. The maximum growth rate saturates for small azimuthal scales. It occurs for a vortex, whose core is at a radial distance proportional to the azimuthal wavelength of the VRW.

Acknowledgments This research is supported by the IRG-230958 Marie Curie Grant.

References

Charney JG, Eliasen A (1964) On the growth of hurricane depression. J Atmos Sci 21:68–75

DelSole T, Farrell BF (1996) The quasi-linear equilibration of a thermally maintained, stochastically excited jet in a quasigeostrophic channel. J Atmos Sci 53:1781–1797. doi:10.1175/1520–0469(1996) 053<1781:TQLEOA>2.0.CO;2

Farrell BF, Ioannou PJ (1993a) Stochastic dynamics of baroclinic waves. J Atmos Sci 50:4044–4057. doi:10.1175/1520–0469(1993) 050<4044:SDOBW>2.0.CO;2

Farrell BF, Ioannou PJ (1993b) Stochastic forcing of perturbation variance in unbounded shear and deformation flows. J Atmos Sci 50:200–211. doi:10.1175/1520–0469(1993) 050<0200:SFOPVI>2.0.CO;2

Farrell BF, Ioannou PJ (2003) Stochastic structural stability of turbulent jets. J Atmos Sci 60:2101–2118. doi:10.1175/1520–0469(2003) 060<2101:SSOTJ>2.0.CO;2

Montgomery MT, Enagonio J (1998) Tropical cyclogenesis via convectively forced Rossby waves in a three dimensional quasi-geostrophic model. J Atmos Sci 55:3176–3207. doi:10.1175/1520–0469(1998) 055<3176:TCVCFV>2.0.CO;2

Montgomery MT, Kallenbach RJ (1997) A theory for vortex Rossby waves and its application to spiral bands and intensity changes in hurricanes. Quart J Roy Meteor Soc 123:435–465. doi:10.1002/qj.49712353810

Rotunno R, Emanuel KA (1987) An air-sea interaction theory for tropical cyclones. Part II: evolutionary study using a nonhydrostatic axisymmetric numerical model. J Atmos Sci 44:542–561. doi:10.1175/1520–0469(1987) 044<0542:AAITFT>2.0.CO;2

Radar Derived Storm Characteristics Over Central Greece

D. Bampzelis and T. Karacostas

Abstract Individual storm measurements are obtained from the C-band weather radar, located close to the area of interest, using the cell tracker TITAN (thunderstorm identification, tracking, analysis, and nowcasting). The study aims in analyzing certain storm characteristics over central Greece, as a tool for investigating possible rain enhancement feasibility potential. The objective on this study is two folded: firstly, to analyze and describe storm characteristics and secondly, to identify differences in storm characteristics, structure and their behavior, among distinct synoptic situation patterns. The radar-based storm characteristics are extracted using certain thresholds. Storm characteristics include: storm initiation time, storm duration, storm motion, cloud top, reflectivity, storm volume and storm area. Frequency analyses of the aforementioned findings bring out evidences of the storm characteristics, their extends and limitations, providing thus an integrated view of the experienced isolated storms over the examined area. Moreover, the classification of the storm days reveals certain differences in several storm properties, indicating how isolated storms over central Greece vary under different synoptic situation patterns.

1 Introduction

Convective storms are meteorological phenomena of great importance as they are associated with extreme events, while at the same time are not captured accurately by any conventional observation system, since they exhibit small-scale characteristics, lifetime and size. The purpose on this study is to analyze and describe radar-based storm characteristics and to identify differences in

D. Bampzelis (✉) • T. Karacostas
Department of Meteorology and Climatology, School of Geology, Aristotle University of Thessaloniki, Thessaloniki 541 24, Greece
e-mail: babzel@geo.auth.gr

C.G. Helmis and P.T. Nastos (eds.), *Advances in Meteorology, Climatology and Atmospheric Physics*, Springer Atmospheric Sciences,
DOI 10.1007/978-3-642-29172-2_5,

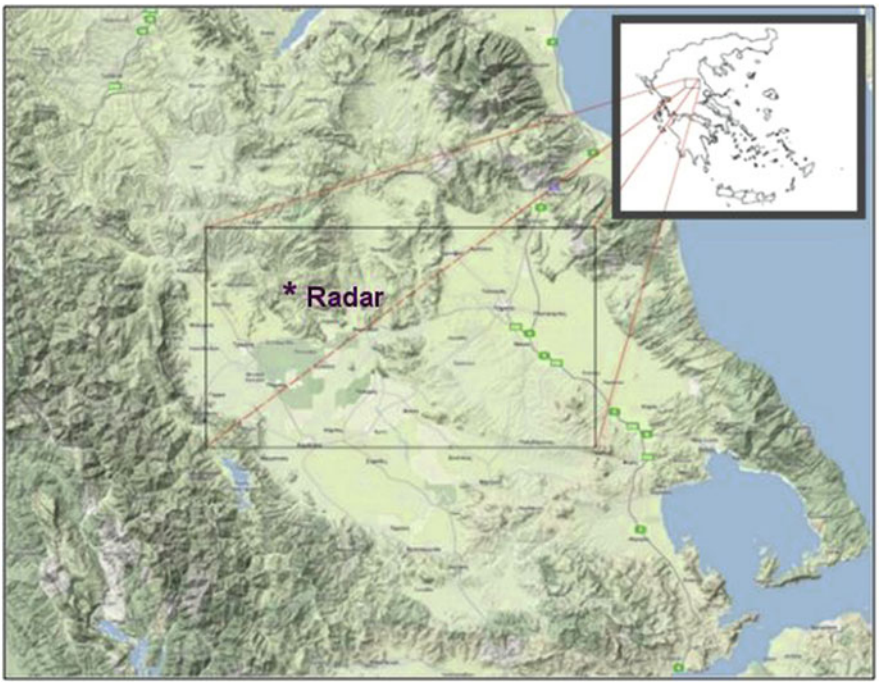

Fig. 1 The study area over Thessaly, Greece

storm characteristics among distinct synoptic situation patterns over central Greece.

Radar data-based storm characteristics studies appeared in the USA in the 1950s following the invention and first use of weather radars (Braham 1958). In Greece, radar-based storm studies have been performed by Karacostas (1991), who investigated convective cells characteristics after the first 2 years (1984 and 1985) of operations of the Greek National Hail Suppression Program (NHSP), Sioutas and Flocas (2003) who analyzed the hailstorm characteristics in northern Greece through synoptic typing and thermodynamic environment and Foris et al. (2006) who performed a kinematic study of hailstorms in central Macedonia.

Storm characteristics are obtained and identified from weather radar reflectivity images taken and analyzed from a C-band (5-cm) weather radar, being located at Liopraso area, within the area of interest. Such information is considered as diagnostic, since it can assist – as a very useful tool – for investigating rain enhancement potential over the area. The area selected for the analysis covers 4,000 km^2 (rectangular 50 $\times$ 80 km) and is mostly plain, within the eastern part of Thessaly (Fig. 1). Only storm cells that initiated (gave their first radar echo) within the area of interest are used in this analysis.

2 Data and Methodology

The dataset that is used in the analysis includes radar reflectivity measurements for the time period of April 2006 to September 2010, focusing only on the month period April to September, for each year. The radar reflectivity measurements have 750 × 750 m spatial and 3.5 min temporal, resolution. Storm characteristics are obtained from reflectivity measurements using the cell tracker TITAN (Thunderstorm Identification, Tracking, Analysis, and Nowcasting) (Dixon and Wiener 1993). Storm characteristics include: storm initiation time (UTC hour), storm duration (minutes), storm direction (°), storm speed (km/h), storm volume (km^3), storm mass (ktons), storm maximum reflectivity (dBz) and storm cloud top (km).

The cell tracker TITAN is developed for automatic identification, tracking and forecasting of convective cells. The algorithm, at a given reflectivity image, defines a convective cell as a 3D region in which reflectivity values exceed a given threshold and match convective storms between two successive radar images. To be considered a valid storm, a track must satisfy a set of criteria and threshold values, regarding its own characteristics. Hence, the following have been set for the current analysis:

1. A storm track is rejected if it begins or ends after or before a missing radar file.
2. A storm track is discarded if its top is missing, since it lies too close to the radar (within the cone of silence).
3. The storm minimum volume must be at least 15 km^3.
4. A storm track must have a minimum duration of 15 min (five successive radar scans).
5. The storm volume area reflectivity must exceed 35 dBz.
6. A storm track must have maximum top above 3.5 km.

For criterion 5 the 35 dBz was chosen, since that value is the threshold for the storms to be seeded during the NHSP (Karacostas 1984) and it correlates well with the development of mature cumulonimbus clouds (Roberts and Rutledge 2003). With respect to criterion 6, a cloud with maximum top below 3.5 km is discarded, since it is likely not to be a convective storm.

3 Results

3.1 Storm Characteristics

Following the above procedure and selection criteria, a total number of 514 valid storm cells are identified by the algorithm. The percent relative frequency of the storm characteristics is depicted in Fig. 2.

As seen in Fig. 2, convective cells that affect the area of interest develop during the afternoon hours, with a peak at 14:00 UTC indicating that surface heating is the

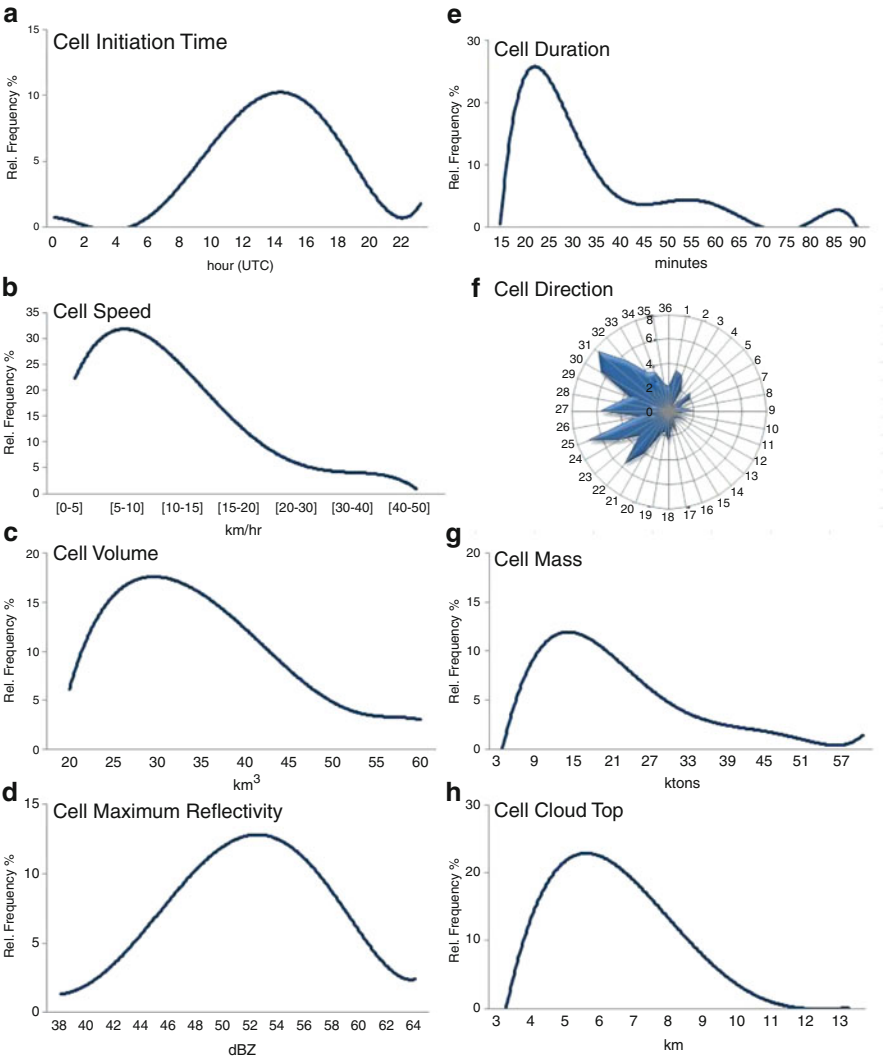

Fig. 2 The percent relative distribution of the observed convective cell characteristics

dominant factor for storm initiation. The identified secondary maximum in storm initiation time at 00:00 UTC is most probably due to cells that have developed during the previous day and continue to exist after midnight. Cells exhibit a lifetime up to 40 min in a percentage of 72%, with a peak at 25 min, indicating that cells that affect the area are short lived. It is noted that lifetime is defined as the time elapsed from the first radar echo of 35 dBz until the disappearance of that.

Cell motion peak speed is between 6 and 10 km/h and cell direction of movement is from northwest and southwest, which is mostly related to the 500 hPa upper

Table 1 Number of cells per synoptic circulation type

	Number of cells	Number of cells with duration 15–35 min
Southwest flow (SW)	61	34
Short wave trough and closed low (L2-CLO)	157	93
Northwest flow (NW)	135	84
Cut off low (CUT)	17	13

air winds. Regarding cell's volume and mass it is found that cell volume ranges between 20 and 45 km^3 in a percentage of 64% and cell mass between 6 and 21 ktons in a percentage of 55%. Finally, cell's reflectivity peaks at 54 dBz with 73% of cells ranging between 46 and 58 dBz and cell cloud top most frequently encountered at 7 km, with 55% of cells having cloud tops between 6 and 8 km.

3.2 Storm Characteristic Differences Among Synoptic Types

In order to study the connection of atmospheric circulation with convective activity over the examined area the manual classification scheme proposed by Karacostas et al. (1992) is used, which is based on the isobaric charts of 500 hPa and the position and orientation of the trough axis. Furthermore, circulation patterns that produced storms over the examined area, are grouped into the following four types: (1) southwest flow (SW), a long wave trough to the west of the examined area, (2) short wave trough and closed low (L2-CLO), referring mostly on storms produced during the developing stage of a surface low pressure system, (3) northwest flow (NW), along wave trough located to the east of the area, and (4) cut off low (CUT), referring on storms developing during the mature phase and dissipating stage of an upper air and surface low system.

The number of cells grouped under the four types is indicated in Table 1. In order to study cells of similar duration, a second grouping is performed only for cells that exhibit lifetime between 15 and 35 min. Cut off low (CUT) cases are excluded from the results due to their small sample size.

It can be seen that most cases of cell development refer to two different synoptic types, the short wave trough – closed low (L2-CLO) and the northwest flow (NW). Results indicate the following: cell characteristics between these two synoptic types differ in initiation time; later peak in relative frequency for cells developing at NW synoptic type, and cell direction; NW type cells follow the northwest to southeast direction, while L2-CLO type cells do not have a clear direction (Fig. 3a, b). Although the rest of cell characteristics (volume, max reflectivity and cloud top) do not show remarkable differences, from the diagrams (Fig. 3c, e, f) it is observed that cells developing at L2-CLO synoptic type exhibit two maximum peaks; almost at the same level; while cells developing at NW synoptic type have only one maximum. This fact indicates a more scattered behavior of cells that develop at

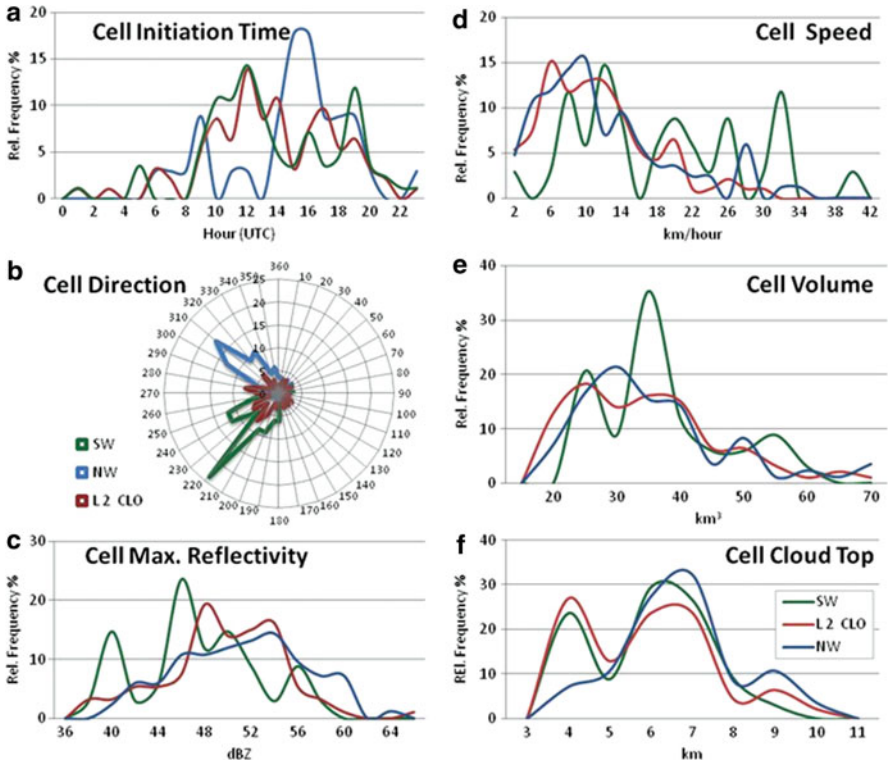

Fig. 3 The relative frequency distribution of the observed cell characteristics per synoptic type

L2-CLO synoptic type, with air masses coming from various directions and having different properties, than those developed at NW synoptic type, where air mass potential is probably restricted. Concerning the cells develop at southwest (SW) synoptic type, they move quite faster, from southwest to northeast, exhibit lower maximum reflectivity values and higher volume and mass content.

4 Conclusions

An attempt is made to analyze and describe storm characteristics, obtained from weather radar measurements for a specific plain area in eastern Thessaly. Frequency distribution of cell characteristics indicated their extends and limitations, providing an integrated view of storms' behavior over the examined area. It appears that convective cells occur mostly in the afternoon. Cells are mostly short lived, with a mean peak at 20–25 min. Cell motion is consistent with upper air winds at 500 hPa. Cell characteristics, such as: volume, mass, max reflectivity and cloud top, follow almost a normal distribution. Furthermore, the storm characteristics are examined

in relation to the synoptic types. Certain differences are observed between L2-CLO and NW synoptic types, with cells developing at L2-CLO synoptic type to exhibit more scattered characteristics.

Acknowledgments The authors wish to thank the Meteorological Application Center of the Greek Agricultural Insurance Organization (ELGA) and 3D S.A. for the free provision of weather radar data.

References

Braham RR (1958) Cumulus cloud precip. as revealed by radar-Arizona. J Meteor 15:75–83

Dixon M, Wiener G (1993) Titan: thunderstorm identification, tracking, analysis and nowcasting – a radar-based methodology. J Atmos Ocean Technol 10:785–797

Foris DV, Karacostas TS, Flocas AA, Makrogiannis TI (2006) Hailstorm in the region of central Macedonia, Greece: a kinematic study. Meteorol Z 15:317–326

Karacostas TS (1984) The design of the Greek National Hail Suppression Program. Ninth conference on weather modification. American Meteorological Society, Park City, UT

Karacostas TS (1991) Some characteristics of convective cells in the Greek National Hail Suppression Program. Geofizika 8:43–50

Karacostas TS, Flocas AA, Flocas HA, Kakaliagou O, Rizou C (1992) A study of the synoptic situations over the area of Eastern Mediterranean. Proceedings, 1st Greek conferences on meteorology-climatology-physics of the atmosphere, Thessaloniki, Greece, pp 469–477 (in Greek)

Roberts RD, Rutledge S (2003) Nowcasting storm initiation and growth using GOES-8 and WSR-88D data. Weather Forecast 18:62–584

Sioutas MV, Flocas HA (2003) Hailstorms in Northern Greece: synoptic patterns and thermodynamic environment. Theor Appl Climatol 75:189–202. doi:10.1007/s00704-003-0734-8

Synoptic Aspects of the Eastern Mediterranean Explosive Cyclogenesis of 22 January 2004

D. Brikas, T. Karacostas, and I. Pytharoulis

Abstract The synoptic environment of the Eastern Mediterranean explosive cyclogenesis (ECG) of 22 January 2004, is described from a Sutcliffe-type viewpoint. ECG lasted 30 h. It began as warm-frontal cyclogenesis, forced by the advection of a cold and cyclonically rotating upper air mass, above an unstable marine boundary layer. The cold air mass was cut off its polar reservoir 2 days before ECG, followed a route above the Iberian Peninsula and the Sahara desert and approached the Libyan Sea from the southwest. When the bomb entered the Eastern Mediterranean, an arctic-type front penetrated from the north and turned the former into an intense frontal cyclone.

1 Introduction

The Eastern Mediterranean explosive cyclogenesis (ECG) of January 22 was associated with heavy rainfall, snow depths up to 1 m, even on Aegean islands, damaging winds exceeding 40 m/s and record low pressures. It has been already studied by Lagouvardos et al. (2007), Pytharoulis (2008), Karacostas et al. (2010).

The associated synoptic environment is portrayed in Fig. 1. Upper tropospheric flow is inferred by 500 hPa geopotential height. Combined with the

D. Brikas (✉)
Regional Meteorological Centre Makedonia, Thessaloniki, International Airport Makedonia, Thessaloniki 551 03, Greece
e-mail: dimibrik@otenet.gr

T. Karacostas • I. Pytharoulis
Department of Meteorology and Climatology, School of Geology, Aristotle University of Thessaloniki, Thessaloniki 541 24, Greece

C.G. Helmis and P.T. Nastos (eds.), *Advances in Meteorology, Climatology and Atmospheric Physics*, Springer Atmospheric Sciences,
DOI 10.1007/978-3-642-29172-2_6,

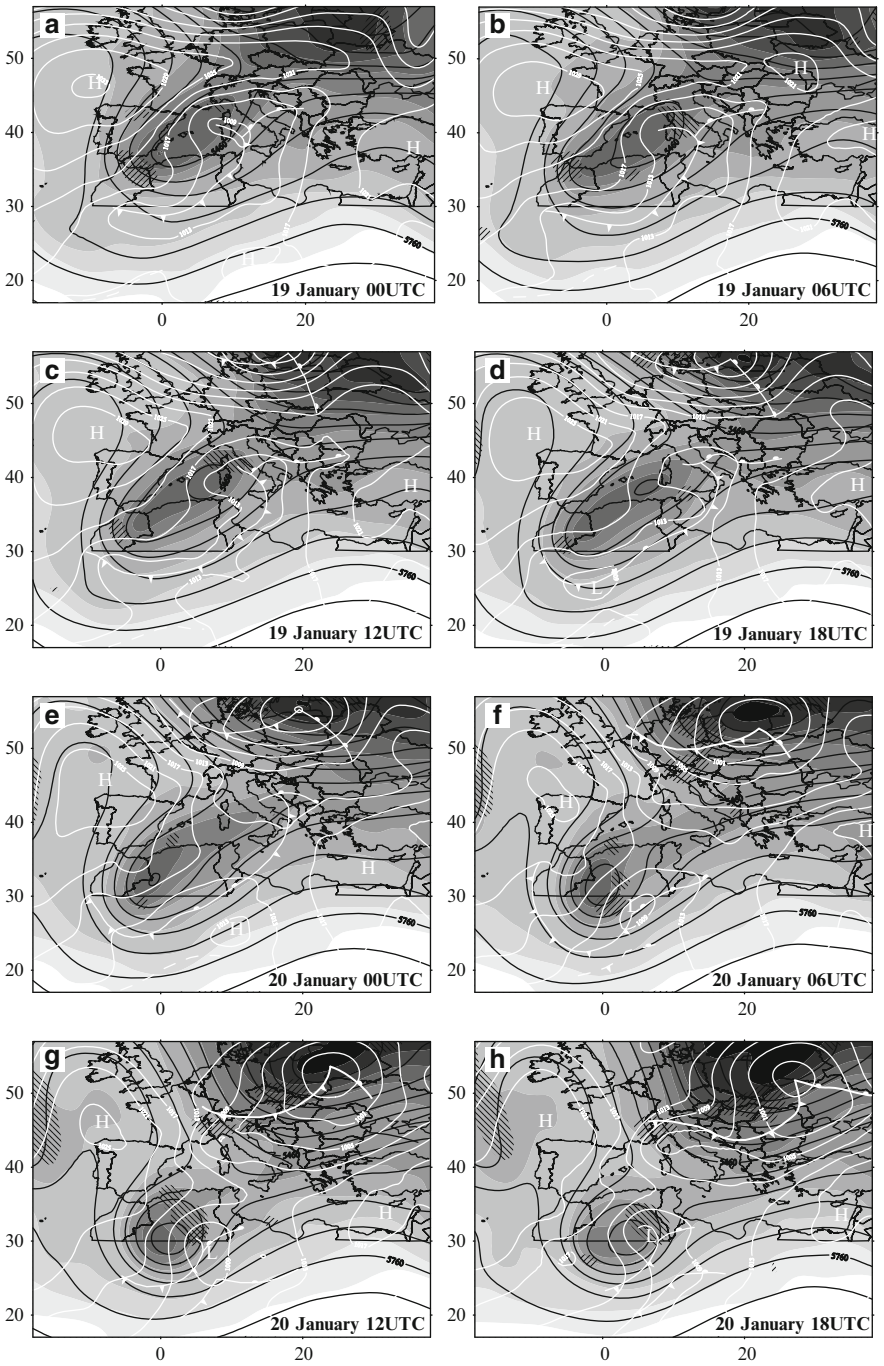

Fig. 1 (continued)

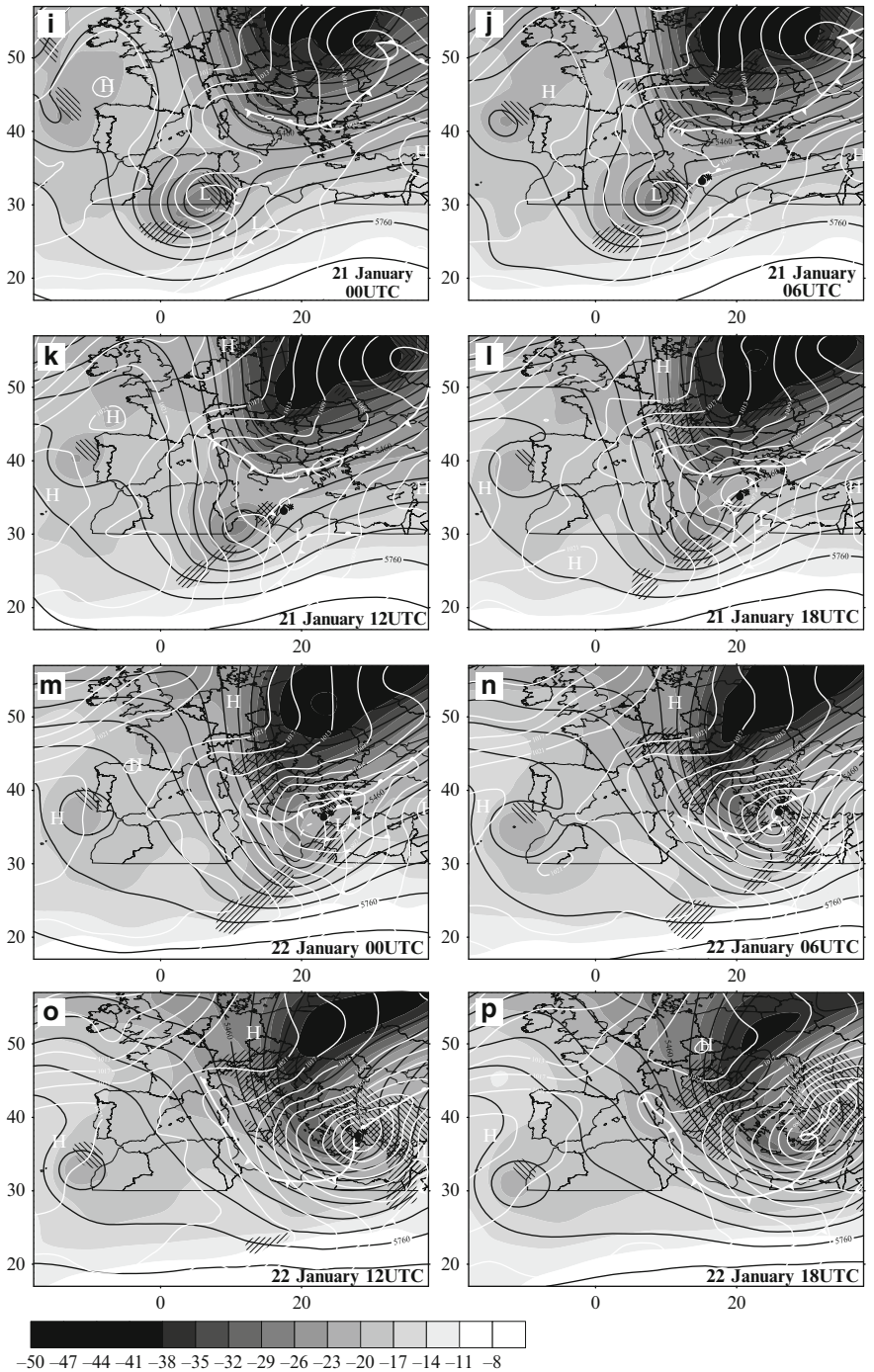

Fig. 1 Sea level pressure (*white*, every 4 hPa), 500 hPa heights (*black*, every 60 gpm), temperature (*shaded*, every 3°C, see bar in next page), cold air advection (*hatching*, //) and cyclonic vorticity advection (*reverse hatching*, \cr) for 00UTC 19–18UTC 22 January 2004

thermal field of the same level, the upper level forcing (hereafter ULFng) is inferred. To quantify the latter, areas where cold air advection (CAA, $\vec{u}\nabla T$) is stronger than 10°C/day and those where cyclonic vorticity advection (CVA, $-\vec{u}\nabla\zeta_{abs}$) is in excess of 10^{-8} s^{-2} are hatched at right angles. Thus, cross hatching indicates ULFng favorable for development downstream. Assuming negligible advection at low levels and non-negative absolute vorticity [$\zeta_{abs} \geq 0$ (1)] and stratification [$\partial\theta/\partial p \geq 0(2)$], multiplying CAA and CVA by (1) and (2), respectively, and adding by parts, positive potential vorticity (PV) advection ($-\vec{u}\nabla PV > 0$) is obtained.

A gross inspection of Fig. 1 points out two major troughs: one amplifying above the Iberian Peninsula on the 19th and another one in Eastern Europe on the 21st. According to Lagouvardos et al. (2007), ECG began at ~18UTC 21 January (hereafter 21 18), with the merger of the two troughs, and lasted merely 24 h. A closer inspection of Fig. 1j, k reveals a weak warm-frontal cyclone in the Libyan Sea, already deepening explosively downstream its parental low (big size L), 12 h before trough merger. This credits the bomb under study at least 30 h of duration. Cold-frontal cyclogenesis also takes place along the northern Mediterranean coast at 21 00 (Fig. 1i), in association with the advancing Eastern European trough. One might say that the cold-frontal cyclones seen in Fig. 1k merge with the bomb 6 h later. However, they do not deepen explosively until this hypothetical merger, so, in that respect the Eastern Mediterranean bomb is *not* related with the Eastern European trough, at least initially. Even if trough merger is important in maintaining ECG during the rapid intensification phase (RIP) of the bomb, the Saharan trough *alone* is responsible for triggering ECG in the Libyan Sea. Motivated by this observation, a synoptic picture of the Saharan system, the bomb and the associated features, is intended to be given in the present study. The study period is extended back to January 19 (Fig. 1a), when the original trough of the Saharan system is cut off the westerlies at the longitude of the Iberian Peninsula and progresses southwards into North Africa.

2 Pre- and Initial Cyclogenetic Period (19 00–21 18)

With the beginning of the study period (19 00), a deep polar air mass outbreak occurs behind the tail of the cold front of a mature occluded low (Fig. 1a). The latter subsequently fills up above Central Europe (20 06), while its trailing cold front triggers orographic cyclogenesis by the end of the 19th (Fig. 1d), as the northerly flow impinges on the east–west oriented Atlas range. This cyclone, L, begins to occlude on the 20th (Fig. 1f) and is no other than the parental low of the bomb. The upper low compacts into a more circular shape. As vorticity increases, an

appreciable area of CVA forms just downstream the upper low, above and to the N–NE of the surface low.

Despite the weakening of the Saharan system by the 21st, CVA is combined with CAA at 21 06–12 (Fig. 1j, k), to trigger ECG along the warm front, above the Libyan Sea. The developing cyclone is in a marine area of reduced (equivalent) static stability (figure not shown). This favors the penetration of the ULFng down to the low levels. The bomb subsequently travels towards the NE. Its low level circulation is not strong at these initial stages in association with the rather weak baroclinicity and stability. These factors favor the strong moist convection observed on satellite pictures (not shown) during 21 00–22 00, which is largely how the bomb is maintained near the end of this period.

3 Associated Features

After giving birth to the bomb, its parental low, L, fills up and its associated North African trough moves ahead of the bomb, towards the ENE. However, another daughter low, denoted with small L (Fig. 1i–m), still follows the bomb from the south, all the way from the initial stages of ECG (21 06) to the time cyclolysis begins (22 12). Its role is to advect warm and moist air ahead of the bomb, sharpening the frontal character of the latter and triggering moist convection in its warm sector. The associated front is traceable back to the beginning of the study period, as a diffuse baroclinic zone (broken white line) in the southwest corner of Fig. 1a. Because of its position below a trough of the subtropical jet (hereafter SJ, not shown), this front is improperly called ‘subtropical’. Cyclogenesis occurs along the subtropical front (hereafter SF) at 20 12 (Fig. 1f). As Thorncroft and Flocas point out (1997), such fronts form as Saharan cold air outbreaks converge along the pre-existing low level baroclinic zone of the heat low.

The polar front that enters from the top of Fig. 1c plays the most important role in the rapid intensification of the bomb. As the low level (geostrophic) flow veers with time behind the front, the advected air masses become arctic. Nevertheless, this front is a deep feature, accompanied by a short wave trough aloft, that quickly amplifies in the westerlies. Meridionality above the eastern part of the map indeed increases steadily for the rest of the study period. Orographic cyclones form downstream the Alps at 21 00, which in the next day (21st) travel east, then NEwards along the front (see Fig. 1i–l) and decay. By the end of the 21st, the arctic front is very close to the bomb, the ascending branch of its direct transverse circulation (not shown) being the major forcing to explosive deepening. Frontal merger with the original front of the bomb is completed at 22 06, as seen in Fig. 1n.

4 Rapid Intensification: Mature Phase (22 00–22 18)

The bomb rapidly intensifies at ~22 00 in the Aegean Sea (Fig. 1m), when the arctic front approaches from continental Greece. The bomb undergoes significant changes. Until now it was maintained mainly via ULFng and moist convection shooting upwards from an unstable boundary layer. Low level frontogenetical forcing was less important, not insignificant though. From now on, ULFng is less important, mostly because the invading arctic air masses increase the stability. Low level frontogenetical forcing is at least three times stronger than before (Karacostas et al. 2010). Condensation now is mostly due to slantwise ascent along the gently tilted warm frontal part of the polar/arctic front. Strong low level baroclinicity and stability in the expanding cold sector are associated with a gradual increase of the low-mid level kinetic energy of the bomb.

Steered by the almost 100 m/s strong subtropical jet (hereafter SJ, not shown) SF reaches the Middle East at 22 06 (Fig. 1n). However, its occlusion stretches backwards to the Southeast Aegean Sea, still providing the bomb with warm and humid air at mid levels. The remnants of the bomb associated original cold front easily trigger a squall line (Lagouvardos et al. 2007) in the convectively unstable warm sector of the bomb, especially since polar air masses, spreading aloft from the NW, act to enhance instability.[1] At 22 12 the bomb achieves its lowest MSLP, ~972 hPa, above the island of Ikaria, a record low value for the Southern Aegean area. By this time the bomb is located right under the 500 hPa trough. This neutral tilt of the vortex is unfavorable for development. Physically, cyclogenesis stops because the bomb is gradually deprived of its low level warm air supply. Low level convergence associated with the arctic front is absolutely greater than the upper level divergence (Pytharoulis 2008), reflecting the fill up of the bomb after 22 12.

The intense circulation of the bomb has distorted the thermal field towards a pattern of a cold and a warm strip, spiraling cyclonically in one another. With the SJ superimposed on this pattern, cyclonically rotating cold air is advected above the warm front of the bomb. The resulting ULFng (see cross hatching in Fig. 1o, p) is associated with vigorous cyclogenesis in the Black Sea, beginning at 22 18. A similar process takes place, to a much lesser extent though, above extreme Eastern Mediterranean and the Middle East, where a rejuvenation of the SF associated low occurs at 22 12 (see Fig. 1o).

[1] Or, from a large-scale view point, the 500 hPa thermal pattern resembles the cyclonically wrapping baroclinic wave of Thorncroft and Hoskins (1990, see their Fig. 7a, b). The difference here is that, at 22 12, the structure is not that much cyclonically wrapped, as in the above authors' Fig. 7b, consistent with the locally kata-front character of the present cold front. In contrast, the Saharan trough evolution during 19 00–21 18 resembles the anticyclonic shear jet side paradigm of the same authors (see their Fig. 7d–f). The contrasting evolving patterns of the present real atmosphere cases, are indeed associated with opposite signs of the mean jet horizontal shear.

References

Karacostas T et al (2010) Dynamic processes of the Mediterranean 'bomb' of 2004. In: Proceedings of the 10th international conference on meteorology and climatology, Patra, Greece

Lagouvardos K, Kotroni V, Defer E (2007) The 21–22 January 2004 explosive cyclogenesis over the Aegean Sea: observations and model analysis. Q J R Meteorol Soc 133:1519–1531. doi:10.1002/qj.121

Pytharoulis I (2008) Numerical study of the Eastern Mediterranean 'bomb' of Jan 2004. In: Proceedings of the 8th annual meeting of EMS and ECAC, 1–3 October, Amsterdam, Holland

Thorncroft C, Flocas H (1997) A case study of Saharan cyclogenesis. Mon Weather Rev 125:1147–1165. doi:10.1175/1520-0493(1997) 125<1147:ACSOSC>2.0.CO;2 DOI:dx.doi.org

Thorncroft C, Hoskins B (1990) Frontal cyclogenesis. J Atmos Sci 47:2317–2336. doi:10.1175/1520-0469(1990) 047<2317:FC>2.0.CO;2 DOI:dx.doi.org

Wind Energy in NW Greece

D.C. Chaskos, A. Bartzokas, and J.D. Pnevmatikos†

Abstract In this paper the wind energy in northwestern Greece is studied at 80 m above ground level. The MM5 meteorological model is used to obtain the necessary wind data to estimate the wind energy potential. This model is used operationally by the Laboratory of Meteorology of Ioannina University for daily weather forecast. The model runs in 3 domains (Europe–Greece–Epirus) with the one-way nesting technique. The third domain contains 12,544 (112 × 112) grid points with a spatial resolution of 2 × 2 km. By using a statistical analysis for 1 year wind data, the mean annual power density map and the resultant wind direction map at 80 m above ground level is calculated for NW Greece. The mean annual power density is calculated from the average 2-h wind data of MM5 from the 1st of June 2007 until the 31st of May 2008. The highest values of wind energy are found in the mountainous areas. The maximum estimated value is 815 W/m^2.

1 Introduction

Wind energy is created by the movement of air parcels and is one of the renewable energy sources which are naturally replenished. The wind is very variable in time and space, thus the wind resource varies with the time of day, the season of year and even from year to year.

The power P_a, available in a cross-sectional area, A, perpendicular to the wind stream moving at speed, V, is the kinetic energy flux

D.C. Chaskos (✉) • A. Bartzokas • J.D. Pnevmatikos†
Laboratory of Meteorology, Department of Physics, University of Ioannina, Ioannina 45110, Greece
e-mail: dchaskos@grads.uoi.gr

C.G. Helmis and P.T. Nastos (eds.), *Advances in Meteorology, Climatology and Atmospheric Physics*, Springer Atmospheric Sciences,
DOI 10.1007/978-3-642-29172-2_7,

$$P = 0.5\rho V^3 A \tag{1}$$

where ρ is the air density.

One method for characterizing the available wind energy of various sites of interest is via their average available wind energy per unit area

$$\langle P_a \rangle / A = 0.5\rho \langle V^3 \rangle \tag{2}$$

where the angular brackets indicate an averaging process, and ρ is taken to be effectively constant $\rho \simeq \langle \rho \rangle$ (Justus 1985).

Because of the wind variability, the wind resource estimation is a very important part of wind energy applications. There are many methods to estimate the wind resource of an area. One of them is the method of mesoscale meteorological modeling. By using this method, obtaining wind data with longer than 1 year time series, would be very time consuming. Usually a few months of the year are used in order to estimate the wind energy (Dvorak et al. 2007). The most common mesoscale models used for wind energy calculations are KAMM (Karlsruhe Atmospheric Mesoscale Model), MM5 (Mesoscale Model 5) and MC2 (Mesoscale Compressible Community) (Landberg et al. 2003).

In Greece, wind speed presents maximum values over the Aegean Sea, especially during summer, when the northerly Etesian winds prevail. This is why most research works on wind energy refer to this area (see e.g. Oikonomou et al. 2009; Fyrippis et al. 2010; Palaiologou et al. 2011). For the western Greece the available research works are rather limited maybe due to the lower values of wind speed (see e.g. Bagiorgas et al. 2008). The aim of the present work is to estimate the wind energy over NW Greece. For this reason, the Penn State/National Center for Atmospheric Research Mesoscale Model version 5 (MM5), which is operationally used for daily weather forecast in the University of Ioannina, is applied to obtain the necessary meteorological data in order to estimate the wind energy potential.

2 Data and Methodology

The MM5 model (version 3.6.3) is a limited-area, terrain following sigma coordinate, non-hydrostatic, model designed to simulate or predict mesoscale atmospheric circulation. The MM5 model is used to simulate the winds of NW Greece at high resolution for 1 year period from 1 June 2007 to 31 May 2008. The results of the global model GFS (Global Forecast System), provided by NCEP (National Centers for Environmental Prediction) with 1×1 degree resolution, are used to create initial and boundary conditions for MM5, updated every 6 h.

For the daily weather forecast, the following 1-way nesting technique is adopted: Domain 1 covers the major part of Europe and the Mediterranean, Domain 2 covers Greece and the surrounding waters and Domain 3 covers NW Greece. The horizontal grid increments of the three domains are: 24, 8 and 2 km, respectively. The vertical

resolution of the model is 23 sigma levels while the domain 3 consists of 12,544 (112 × 112) grids. In the present study, the microphysical scheme described by Schultz (1995) and the convective parameterization scheme of Kain and Fritsch 2 (Kain 2004) are selected. For the atmospheric boundary layer the MRF scheme (Hong and Pan 1996) is used. This configuration of MM5 model has been verified for daily weather forecast by the Laboratory of Meteorology of Ioannina University. The results of verification of wind speed at 10 m height, for three main towns of NW Greece at 12:00 UTC, have shown that wind speed is overestimated by the model by 0.8–1.6 m/s (Bartzokas et al. 2010).

Because of 20 missing daily weather forecasts during the study period, the NCEP FNL 1 × 1 degree Operational Model Global Tropospheric Analyses data, updated every 6 h (dataset ds.083.2), is used as input data. The MM5 model operates in order to obtain meteorological data for 1 day while the spin-up of the model is not removed. Because of the differences in the data bases four additional runs are performed for 1 June 2007, 1 September 2007, 1 December 2007 and 1 March 2008 for the determination of a correlation between these two bases. These days have been selected so that they belong to different season of the year.

The MM5 forecast for domain 3, every 2 h, contains all the meteorological parameters on sigma levels. A linear interpolation method is used to calculate the wind speed at 80 m above ground level for all grid points and for all time series of data. The height of 80 m is selected in order to be in agreement with the new wind turbines which have been introduced in energy market. Taller turbine hubs take the advantage of higher wind speeds aloft due to reduced surface friction and produce more wind power.

3 Results

For a comparison of the GFS and the FNL results, the daily average wind components (U, V) are calculated at each grid point, at 80 m above ground level, for the four selected days. Then, the correlation coefficients of the daily average wind components are calculated for all grid points (Table 1).

In Figs. 1 and 2 the maps of differences of wind components resulted from the different input databases are presented for 1-6-2007 and 1-12-2007. It is seen that the majority of differences range from −1 to 1 m/s. The high values of correlation coefficients and the low values of wind component differences imply that the FNL database highly resembles the GFS database and therefore, it is proper to be used for filling the missing input data.

Table 1 Correlation coefficients of the daily average wind components at 80 m for two different input databases (GFS, FNL)

	1-6-2007	1-9-2007	1-12-2007	1-3-2008
U wind component	0.84	0.93	0.96	0.97
V wind component	0.94	0.96	0.94	0.98

All correlation coefficients are statistically significant at 99% confidence level

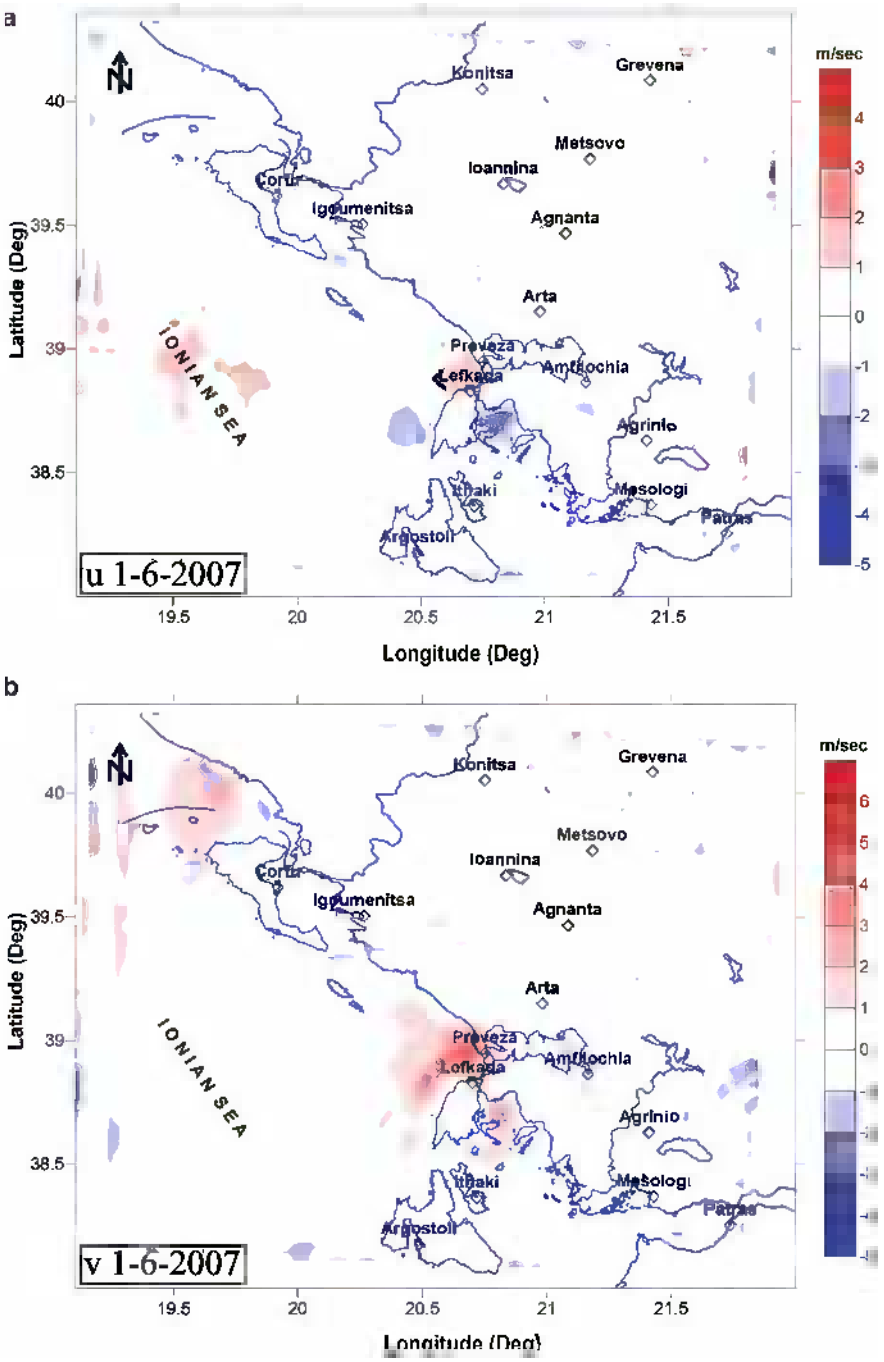

Fig. 1 Maps of differences of wind components, at 80 m above ground level, resulted from different input databases [U(FNL)-U(GFS) and V(FNL)-V(GFS)] for 1 June 2007. (**a**) U component, (**b**) V component

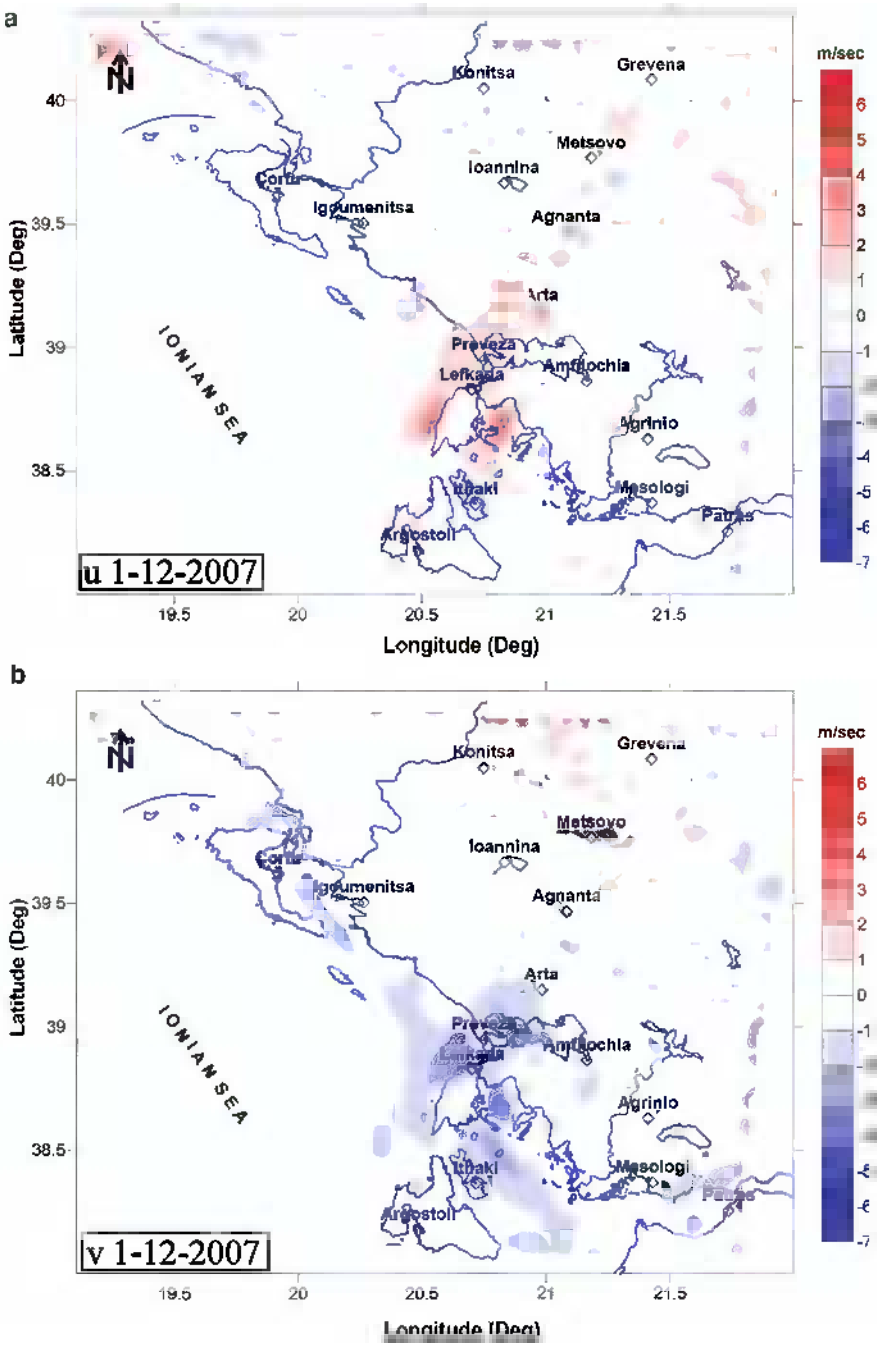

Fig. 2 As in Fig. 1 but for 1 December 2007

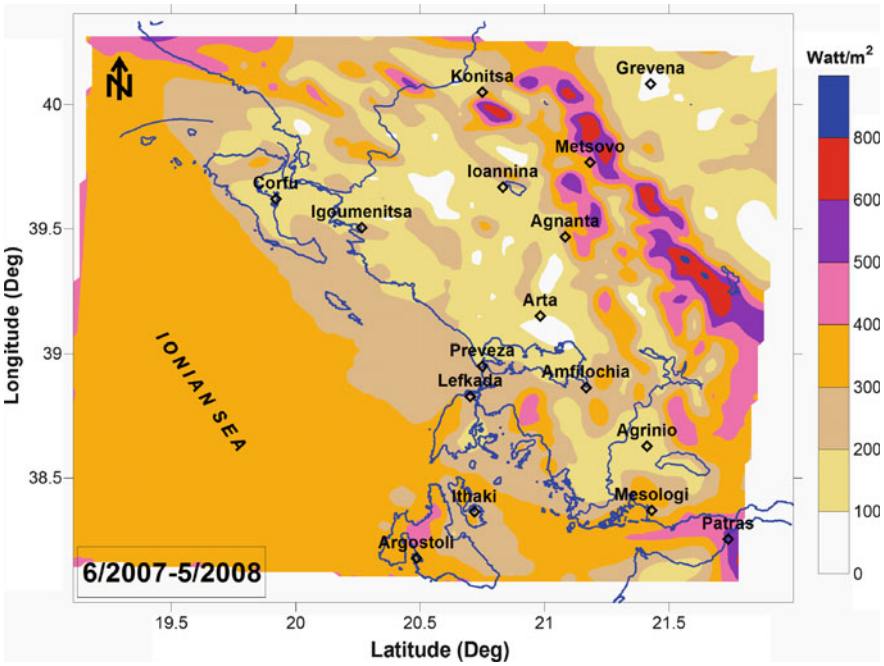

Fig. 3 Annual average available wind energy per unit area at 80 m height above ground level for the period 1 June 2007–31 May 2008

The 1-year period of the wind data is considered sufficient to predict the long term trend in wind velocity with an accuracy of 10% at a confidence level of 90% (Jamil et al. 1995; Mathew et al. 2002). The wind data resulted by the MM5 model could be used in order to draw useful conclusions on the wind energy characteristics in NW Greece.

From the mean annual wind velocity, by using (2), the map of average available wind energy per unit area is calculated at hub height 80 m, assuming that the air density is constant and equal to $\rho = 1.225\ \mathrm{kg/m^3}$ (Fig. 3). In addition, the resultant wind directions calculated by the vector sum of all the 2-h vectors of wind velocity at each grid point is estimated (Fig. 4). The resultant wind direction defines the directions for which the wind turbines receive the highest values of energy.

In Fig. 3 the areas with high and low values of annual average wind energy per unit area can be seen. The maximum estimated value is 815 $\mathrm{W/m^2}$. Satisfactory values of wind energy are found over Timfi Mountain (near Konitsa), Lakmos Mountain (near Metsovo), Athamanika and Akarnanika mountains. The rest continental areas of NW Greece are characterized by low values of wind energy. Wind energy in the Ionian Sea ranges from 300 to 400 $\mathrm{W/m^2}$ while at the coastal areas of Epirus it ranges from 200 to 300 $\mathrm{W/m^2}$. The map of resultant wind directions (Fig. 4) indicates the variability of wind direction over the continental areas while in Ionian Sea the resultant wind direction is almost constant, westerly.

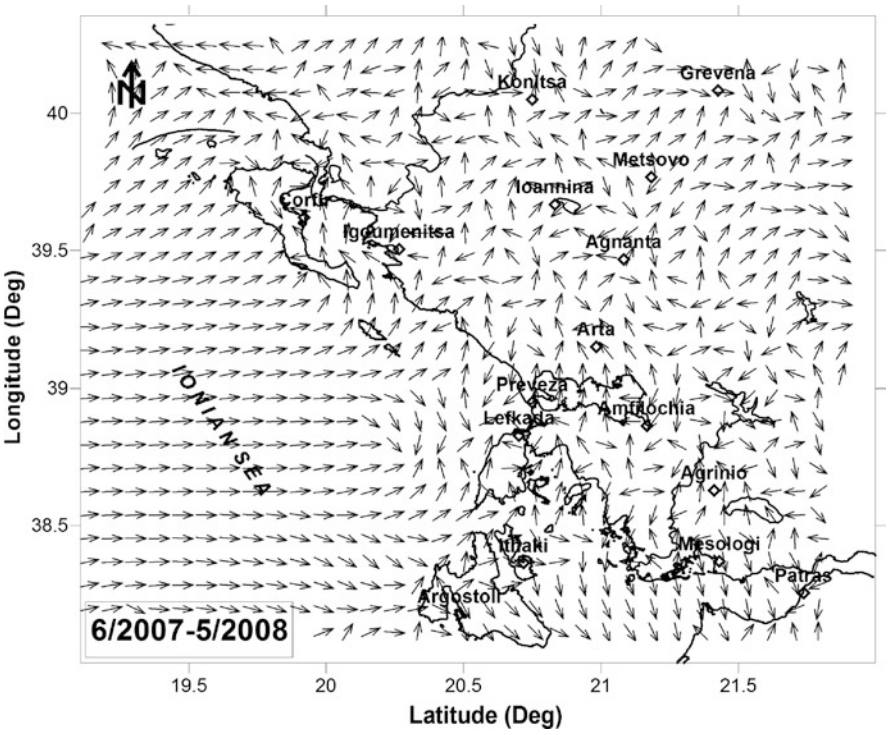

Fig. 4 Resultant wind directions at 80 m height above ground level for the period 1 June 2007–31 May 2008

4 Conclusions

This study analyzed the wind energy potential over NW Greece at a hub height of 80 m. The meteorological model MM5 was used due to the absence of meteorological stations at mountainous areas. This method has the advantage of not introducing errors due to wind data extrapolation from surface to the desired height. The FNL input data of the model MM5 was found proper for replacing of the missing original time series which use GFS input data, with wind data at 80 m. Wind energy values greater than 400 W/m^2 were found over mountainous regions indicating areas for best wind energy applications. The resultant wind directions were found very variable over continental areas expect over the Ionian Sea where they were found almost constant, westerly.

References

Bagiorgas HS, Mihalakakou G, Matthopoulos D (2008) A statistical analysis of wind speed distributions in the area of Western Greece. Int J Green Energy 5(1–2):120–137. doi:10.1080/15435070701839488

Bartzokas A, Kotroni V, Lagouvardos K, Lolis CJ, Gkikas A, Tsirogianni MI (2010) Weather forecast in North-Western Greece: RISKMED warnings and verification of MM5 model. Nat Hazard Earth Syst 10:383–394. doi:10.5194/nhess-10-383-2010

Dvorak MJ, Jacobson MZ, Archer CL (2007) California offshore wind energy potential. Proceedings from Windpower 2007: American Wind Energy Association Windpower 2007 conference & exhibition, AWEA, Los Angeles, CA, 3–6 June 2007

Fyrippis I, Axaopoulos PJ, Panayiotou G (2010) Wind energy potential assessment in Naxos Island, Greece. Appl Energy 87(2):577–586. doi:10.1016/j.apenergy.2009.05.031

Hong SY, Pan HL (1996) Nonlocal boundary layer vertical diffusion in a medium-range forecast model. Mon Weather Rev 124:2322–2339. doi:10.1175/1520-0493(1996) 124 <2322: NBLVDI>2.0.CO;2

Jamil M, Parsa S, Majidi M (1995) Wind power statistics and an evaluation of wind energy density. Renew Energy 6(5–6):623–628. doi:10.1016/0960-1481(95)00041-H

Justus CG (1985) Wind energy. In: Houghton DD (ed) Handbook of applied meteorology, vol 33. Wiley, New York, pp 915–944

Kain JS (2004) The Kain-Fritsch convective parameterization: an update. J Appl Meteorol 43:170–181. doi:10.1175/1520-0450(2004) 043<0170:TKCPAU>2.0.CO;2

Landberg L, Myllerup L, Rathmann O, Petersen EL, Jørgensen BH, Badger J, Mortensen NG (2003) Wind resource estimation – an overview. Wind Energy 6:261–271

Mathew S, Pandey KP, Kumar A (2002) Analysis of wind regimes for energy estimation. Renew Energy 25:381–399. doi:10.1016/S0960-1481(01)00063-5

Oikonomou EK, Kilias V, Goumas A, Rigopoulos A, Karakatsani E, Damasiotis M, Papastefanakis D, Marini N (2009) Renewable energy sources (RES) projects and their barriers on a regional scale: the case study of wind parks in the Dodecanese islands, Greece. Energy Policy 37(11):4874–4883. doi:10.1016/S0960-1481(01)00063-5

Palaiologou P, Kalabokidis K, Haralambopoulos D, Feidas H, Polatidis H (2011) Wind characteristics and mapping of power production in the Island of Lesvos, Greece. Comp Geosci 37(7):962–972. doi:10.1016/j.cageo.2010.05.025

Schultz P (1995) An explicit cloud physics parameterization for operational numerical weather prediction. Mon Weather Rev 123:3331–3343

Agrometeorological Remote Sensing of High Resolution for Decision Support in Precision Agriculture

N.R. Dalezios, N. Spyropoulos, A. Blanta, and S. Stamatiades

Abstract Precision agriculture or operational agriculture is a dynamically developing field of agricultural science, which is based on geoinformatics. Agrometeorological remote sensing contributes through processing and analysis of high resolution satellite images to decision support at field level. In this paper, in HYDROSENSE project, the classification of organic matter zones is presented aiming at the assessment of water and fertilizer operational needs per zone for cotton crops in Thessaly during the phenological cycle. Two pan-sharpened satellite images WorldView-2 (0.5 m) of the region are used, one before planting and the other at the maximum plant cover, as well as one pan-sharpened reference satellite image (2007) IKONOS-2 (1 m). The methodological processing approach includes image filtering and preprocessing, as well as processing, which involves principal component analysis and clustering leading to the production of thematic maps. These maps are combined with mapping through geostatistical analysis of weekly periodic field measurements in three selected cotton fields referring to NDVI, Red/Red edge, NIR/Red and the development of a mini GIS. The results of this combined analysis lead to organic matter zones of the whole region for decision support in precision agriculture.

N.R. Dalezios (✉) • A. Blanta
Laboratory of Agrometeorology, Department of Ichthyology and Aquatic Environment, School of Agriculture Sciences, University of Thessaly, Fytoko, 38446 Volos, Greece
e-mail: dalezios@uth.gr

N. Spyropoulos
Department of Natural Resource and Agricultural Engineering, Agricultural University of Athens, Athens, Greece

S. Stamatiades
Goulandri Natural History Museum, Centre Gaia, Athens, Greece

C.G. Helmis and P.T. Nastos (eds.), *Advances in Meteorology, Climatology and Atmospheric Physics*, Springer Atmospheric Sciences,
DOI 10.1007/978-3-642-29172-2_8,

1 Introduction

Remote sensing applications are designed to provide farmers with timely crop monitoring and production information for large and geographically dispersed areas. Such information can be used to identify crop health problems, monitor food supplies and assess famine risks. The "new-generation satellite birds" can provide better to one-meter resolution and near real time information that will offer numerous benefits in agriculture at field level (Spyropoulos 1999). Operational agro-environment and related business at farm scale is often related to precision farming (Koch and Khosla 2003). On the other hand the revolution of electronics of the last several decades has spawned two additional technologies that also impact agriculture in this decade. These are the Geographic Information Systems (GIS) and the Global Positioning System (GPS). Along with GIS and GPS there is also a wide range of sensors, monitors and controllers for agricultural equipment such as shaft monitors, pressure transducers and servo motors. Very high spatial resolution satellite imagery, GIS and GPS together with field instruments are enabling farmers to use electronic guidance aids to direct equipment movements more accurately, provide precise positioning for all equipment actions and chemical applications and analyze all data in association with other sources such as climate. This will add up to a new and powerful toolbox of management techniques for the progressive farm manager. Precision farming technologies will affect the entire production function (and by extension, the management function) of the farm (Yang et al. 2006). In this paper, two very high spatial resolution WorldView-2 (0.5 m) images were acquired and used one before planting and the other at the maximum plant cover. The derived satellite data products were compared and combined with vegetation indices generated by portable spectrometer in order to introduce and demonstrate the utilization of satellite imagery in *precision farming* tasks that deal with the estimation of water and nitrogen needs.

2 Data and Methodology

Several satellite data were investigated to be procured for the purpose of this research study. Finally, one IKONOS-2 image, acquired on 4-March-2007 was selected as reference and two WorldView-2 pan-sharpened images were programmed to be acquired in order to depict the diachronic changes of vegetation (phenological cycle) and soil. The WorldView-2 (WV-2) images were scheduled for acquisition, one before sowing of the crop (26-March-2010) and another during the maximum growth (22-July-2010). Both images were almost vertical and cloud free with excellent spatial and spectral information content. Additionally, four map sheets of 1/50.000 scale identified from the Hellenic Army Geographical Service were used as the main cartographic background that covers the entire AOI (Larissa, Platikampos, Gonnoi and Rapsani map sheets).

The definition of the following methodological steps, stems from the hypothesis that by using very high spatial resolution satellite data in pan-sharpened multispectral mode, it is possible to map and categorize the land-use of experimental agricultural fields according to the spectral behaviour of soil and vegetation during the growing season (phenological cycle). Three cotton fields were used as the experimental test sites of the project: Mitsoyannis field covering an area of 0.4 ha, Vardoulis field (0.24 ha) and Samaras field (0.42 ha). These fields are located in the Gonni-Sikourion-Platikambos sub-basin, an area of 120 sq. km, which belongs to the Pinios river watershed. The intensive nature of agricultural practices in the area has led to excessive fertilizer and pesticide inputs. As a result, soil and water nitrate concentrations often exceed EU limits. The aforementioned conditions and overuse of irrigation water accelerates the leaching of agrochemicals leading to groundwater contamination. The satellite data are atmospherically and geometrically corrected (Lanzl and Richter 1991; Updike and Comp 2010) and then processed using Principle Components and Tasseled Cap Transformations to delineate subtle changes in the imagery. Several vegetation based processing methodologies are implemented such as NDVI, NIR/RED Index, SAVI, LAI and FPAR (Colombo et al. 2003). The data then is categorized in zones using specific Clustering approaches (Horne 2003). Ground measurements were performed on a weekly basis to collect NDVI, CI, Red/Red edge indices in each agricultural experimental field. The data were collected using a portable spectrometer and a GPS providing its signals in ITRF format (OmniStar HP system). Almost 10.000 point measurements were collected for each field per week and then geostatistically analyzed to create solid raster representations/bitmaps or user defined zones (Fig. 1). Kriging on Geomatica software package was used to analyze the data. The Kriging technique for estimating a surface over an area of interest is a statistical technique that minimizes the error variance for the estimated values. It calculates the value at a specific point as a weighted sum of the known points. The weights are determined by considering the co-variance between each pair of the known points, and the co-variance between the specific point and each of the known points. The geostatistical data are then compared with the satellite derivative products. A GIS database was developed to correlate the spatiotemporal relationships between the spectral characteristics of satellite imagery and the organic matter and soil and plant moisture (Dalezios et al. 2010).

3 Results

NDVI, NIR/RED and RED/Red Edge indices are produced by field measurements. A geostatistical interpolation and analysis is then performed in order to produce three zones per field for soil, crop and N requirement prediction. These data are then compared with the NDVI, NIR/RED, PCA, SAVI, LAI and FPAR indices derived from the WV-2 data. March field measurements applied before crop plantation have shown similar soil patterns with satellite derivative products such as SAVI (Soil Adjusted Vegetating Index) and the produced zones also coincided. July field

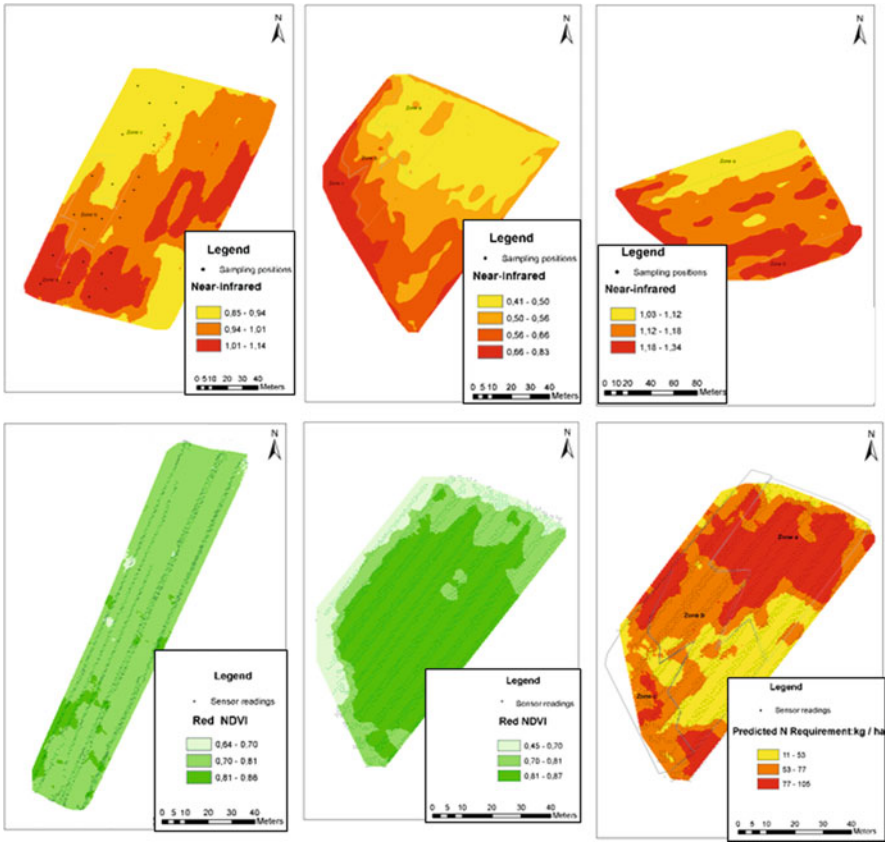

Fig. 1 From *upper left*: Soil map of Mitsoyannis field (March), soil map of Valrdoulis field (March), soil map of Samaras field (March). From *lower left*: Red NDVI of Mitsoyannis field (July), Red NDVI of Vardoulis field (July), predicted N requirements of Vardoulis field (July)

measurements applied during maximum plant cover have shown similar vegetation patterns with satellite derivative products such as NDVI and NIR/RED index (Figs. 1 and 2).

Both Principal Components (PC2 and PC3) and Photosynthetically Active Radiation applied onto March and July WV-2 data are also exhibiting similar results with field measurements. All March WV-2 indices and derivative products were compared and verified with the same products generated by the IKONOS-2 reference image. ISODATA clustering was applied to NIR/RED indices (produced by WV-2 data) in order to generate three-zone thematic maps for the entire region of interest. This index exhibited very similar patterns to ground measurements and helped to extract the cotton area coverage and the variation of its growth in each field with great accuracy enabling farmers not only to control the rate of irrigation application but also to differentially distribute it within the same cotton field.

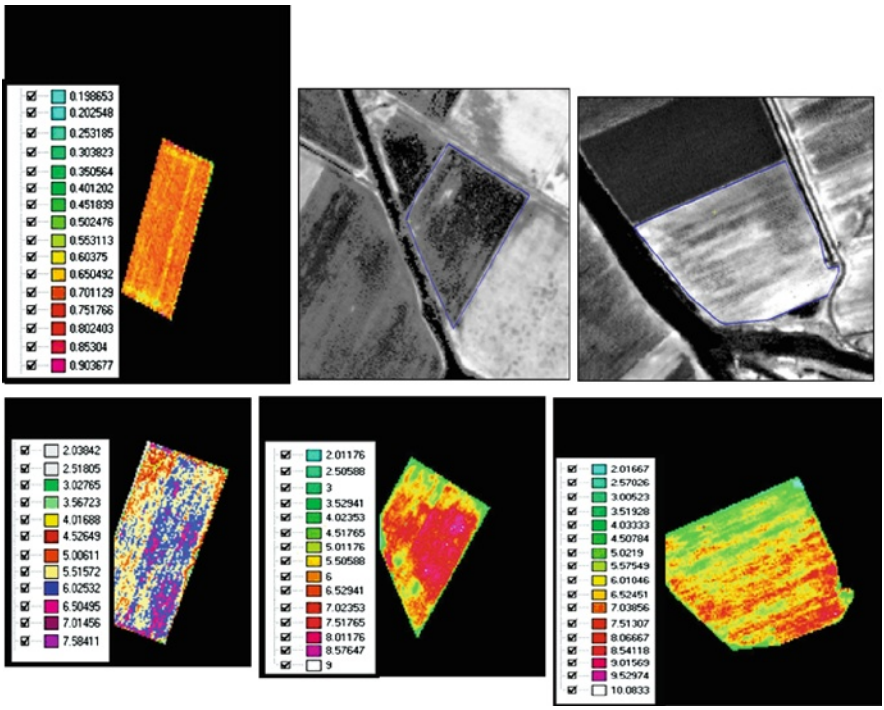

Fig. 2 From *upper left*: IKONOS NDVI index of Mitsoyannis field, WV-2 SAVI index of Vardoulis field (March), WV-2 SAVI index of Samaras field (March). From *lower left*: WV-2 NIR/Red index of Mitsoyannis field (July), WV-2 NIR/Red index of Vardoulis field (July), WV-2 NIR/Red index of Samaras field (July)

The latter index was selected as the most representative to produce the generalization map of the whole region for decision support in precision agriculture.

4 Conclusions

The present research effort is the first attempt to deploy the principles of precision agriculture for integrated crop management of combined inputs from satellite data and field measurements. The development and implementation of an efficient site-specific management system for reducing irrigation and chemical inputs is possible by combining field measurements and satellite data. Satellites proved to be ideal due to their global repetitive coverage over an area of interest (every 2–3 days), spatial and spectral resolution. The comparison of satellite data and field measurements has shown that the utilization of WorldView-2 is definitely a useful tool for Greek farmers, allowing not only the extraction of crop area but also the derivation of crop water needs based on crop area. Spatial resolution (0.5 m),

together with spectral capacity play an important role in the precision farming applications where the scale and crop separability are of key issues at field level (Spyropoulos 2002). High resolution satellites such as WorldView-2 can be used in an operational mode for crop area extraction and estimation of water needs for each crop type according to its phenological stage. Cotton Greek farmers exhibited a positive reaction on the image clarity and sharpness of WorldView-2 satellite data. In that respect and prior to any irrigation programme Greek farmers may consult WorldView-2 images to estimate the necessary water quantity for their crops. Variable-rate irrigation is expected to reduce water consumption by 20% in comparison with conventional management with uniform irrigation. Similarly variable-rate fertilization is expected to reduce N inputs by 20%. Pesticide and herbicide inputs are expected to be reduced by 50% when principles of Integrated Crop Management and precision technologies are implemented.

Acknowledgments This research effort was executed in the premises of Laboratory of Agrometeorology of the University of Thessaly and co-financed by the European Commission Life + Programme, HYDROSENSE project.

References

Colombo R, Bellingeri D, Dante Fasolini D, Marino MC (2003) Retrieval of leaf area index in different vegetation types using high-resolution satellite data. Remote Sens Environ 86 (1):120–131. doi:10.1016/S0034-4257(03)00094-4

Dalezios RN, Spyropoulos VN, Mplanta A (2010) Hydrosense project. Annual report. European commission, life + programme

Horne JH (2003) A tasseled cap transformation for IKONOS images. In: ASPRS annual conference proceedings, Anchorage, Alaska

Koch B, Khosla R (2003) The role of precision agriculture in cropping systems. J Crop Prod 9 (1–2):361–381. doi:10.1300/J144v09n01_02

Lanzl F, Richter R (1991) A fast atmospheric correction algorithm for small swath angle satellite sensors. ICO topical meeting on atmospheric, volume, and surface scattering and propagation, Florence, Italy, August 1991

Spyropoulos VN (1999) The benefits of high-resolution earth imagery in agriculture – The Ikonos system and its applications to agri-environment schemes. 1st workshop on the management and monitoring of agri-environment schemes. Joint Research Center (JRC) Ispra, Italy, 23–24 Nov 1999

Spyropoulos VN (2002) Image segmentation, classification and feature extraction. XXII FIG international congress. ACSM-ASPRS conference and technology exhibition Washington, D.C, April 19–26, 2002

Updike T, Comp C (2010) Radiometric use of WorldView-2 Imagery. Technical Note DigitalGlobe, 1601 Dry Creek Drive Suite 260 Longmont, Colorado, USA, 80503

Yang C, Everitt HJ, Bradford MJ (2006) Comparison of QuickBird satellite imagery and airborne imagery for mapping grain sorghum yield patters. Precis Agric 7(1):33–44. doi:10.1007/s11119-005-6788-0

Surface Meso High and Wake Low Associated with Pre-Monsoon Thunderstorm Over the Kharagpur Region

S. Dawn and M. Mandal

Abstract Observations recorded under the national coordinated STORM (Severe Thunderstorm Observations and regional Modeling) Programme have been used to study the surface parameters associated with tropical squall line (thunderstorm) with trailing stratiform precipitation. A number of studies indicated the presence of three well known features—a pre-squall meso-low, a squall meso-high and a wake low in the surface pressure field associated with a midlatitude squall with trailing stratiform precipitation. In this paper, an attempt is made to identify these meso-scale features, if any, associated with thunderstorms over Indian region. The study is conducted over Kharagpur region, a part of the Gangetic West Bengal frequently affected by thunderstorms during the pre-monsoon season. The observations from 50 m instrumented micro-meteorological tower and upper air sounding at Kharagpur are used in the study. Doppler Weather Radar (DWR) (at Kolkata) imageries are used to identify the squall line with trailing stratiform precipitation. It is observed that in the squall line with trailing stratiform precipitation shield, the meso-high (MH) is associated with convective line and wake low (WL) exists in the rear of the storm. The position of the meso-high is typically found in the vicinity of the heavy rain directly beneath the downdraft.

1 Introduction

Mesohigh and wake lows are mesoscale phenomena associated with mid-latitude thunderstorms (Fujita 1955). These result to strong and sometimes severe winds. Johnson (2001) has shown that wake lows typically form during the decaying stage of a mesoscale convective system (MCS) near the rear edge of the trailing

S. Dawn • M. Mandal (✉)
Centre for Oceans, Rivers, Atmosphere and Land sciences, Indian Institute of Technology, Kharagpur, West Bengal 721302, India
e-mail: duttasoma4u@gmail.com; mmandal@coral.iitkgp.ernet.in

C.G. Helmis and P.T. Nastos (eds.), *Advances in Meteorology, Climatology and Atmospheric Physics*, Springer Atmospheric Sciences,
DOI 10.1007/978-3-642-29172-2_9,

stratiform precipitation region. Zipser (1977) has observed that the thermodynamic state of the atmosphere that supports the development of wake low shows "onion" structure in the upper-air sounding.

The Gangetic West Bengal gets frequently affected by thunderstorms known as 'Noŕwester' in the summer months (March–May). These weather events are locally called 'Kalbaisaki'. Severe thunderstorms create great damages to property, crops, human and animal fatalities over small areas through strong surface wind squalls, large hails, frequent lightning and heavy rain showers. They also cause serious aviation hazards. A nationally coordinated program, named Severe Thunderstorm Observation and Regional Modeling (STORM), has been initiated by the Department of Science and Technology (DST) and the Ministry of Earth Sciences of the Government of India, in order to improve the present understanding of the pre-monsoon thunderstorms over the eastern and north-eastern part of India. The objective of this paper is to examine whether the meso-high and wake-low features are also present in the tropical trailing stratiform squall-line thunderstorms and the thermodynamic environment associated with these features.

2 Data

The datasets that have been used in the present study are the 50 m micrometeorological tower observations during the pre-monsoon period (15th April–31st May) under the STORM field experiment in 2007, 2009 and 2010. The upper-air sounding at Kharagpur and the imageries from Kolkata Doppler Weather Radar (DWR) are also utilized in the study. The NCEP/NCAR reanalysis dataset is used to check the prevailing synoptic situation over the region.

3 Analysis

The DWR imageries suggested that 12 squall line thunderstorms affected Kharagpur and adjoining areas during STORM field experiment periods in 2007, 2009 and 2010. The observational datasets mentioned above are analyzed for all the 12 cases. The data analysis of one (5th May 2010 thunderstorm case) of these 12 cases is presented in some detail in this section. The maximum variation in pressure and wind gust associated with the other cases is summarized in Table 1.

3.1 5th May 2010

The large-scale circulation during pre-monsoon months is characterized by ascending motion over Indian landmass and descending motion over the surrounding seas. This leads to a shallow inflow of warm moist air from the sea (the Bay of Bengal) along the east coast. Thus the air in the southeastern part of India is moist, whereas, in the

Table 1 Wake low and meso high cases in this study along with the maximum pressure drop, rise and wind gust for each

Date	Maximum pressure drop (hPa)	Maximum pressure rise (hPa)	Maximum wind gust (m/s)
26-04-2007	13	0	14.37
27-04-2007	6	5	10.62
06-05-2009	4	3	8.51
11-05-2009	4	6	9.2
12-05-2009	7	2	12.28
15-05-2009	9	7	11.92
03-05-2010	3	4	6.57
05-05-2010	7	5	6.8
07-05-2010	14	3	9.27
14-05-2010	9	7	11.39
29-05-2010	4	2	9.8
30-04-2010	10	2	13.41

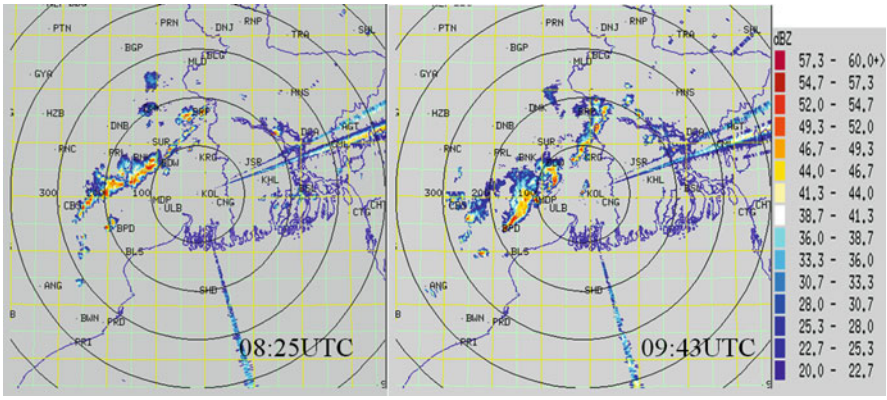

Fig. 1 MAX (Z) display of life cycle of thunderstorm occurred on 5th May 2010

northwestern part it is relatively dry and cold. This favors development of thunderstorm activity. This favors development of thunderstorm activity. On 5th May 2010, a trough of low pressure area formed extending from North West India to West Bengal across the Bihar, Jharkhand and Orissa (figure not shown). This trough of low pressure persists up to Jharkhand till 06:00 UTC. The DWR imageries (Fig. 1) show the squall line having a southwest-northeast orientation at 08:25 UTC. The squall-line reached Kharagpur region around 0943 UTC. The structure of the convective line was trailing stratiform type as observed from the DWR imageries.

The passage of this trailing stratiform squall line is illustrated in a time series of surface observations (Fig. 2) obtained from 50 m micrometeorological tower at Kharagpur. The arrival of the convective line over Kharagpur was marked by sudden increase in surface wind speed by 3–4 m/s and in pressure by 5 hPa and is followed by heavy rainfall. The maximum surface pressure was recorded at the time

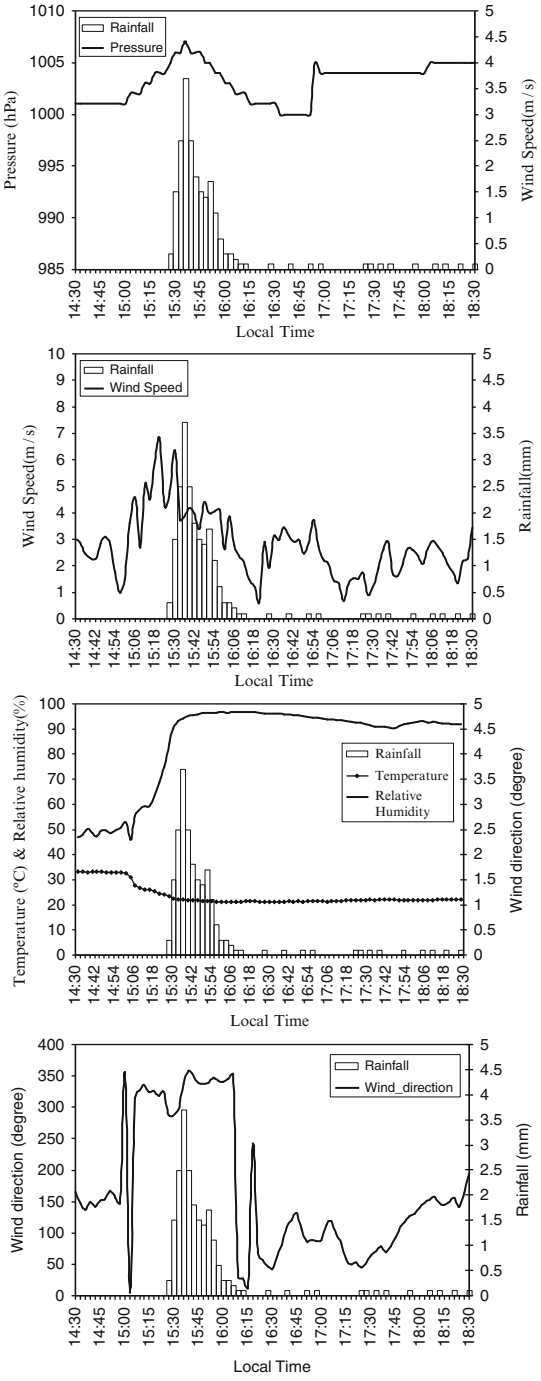

Fig. 2 Temporal variation of pressure, wind speed, wind direction, rainfall, temperature and relative humidity on 5th May 2010 at Kharagpur

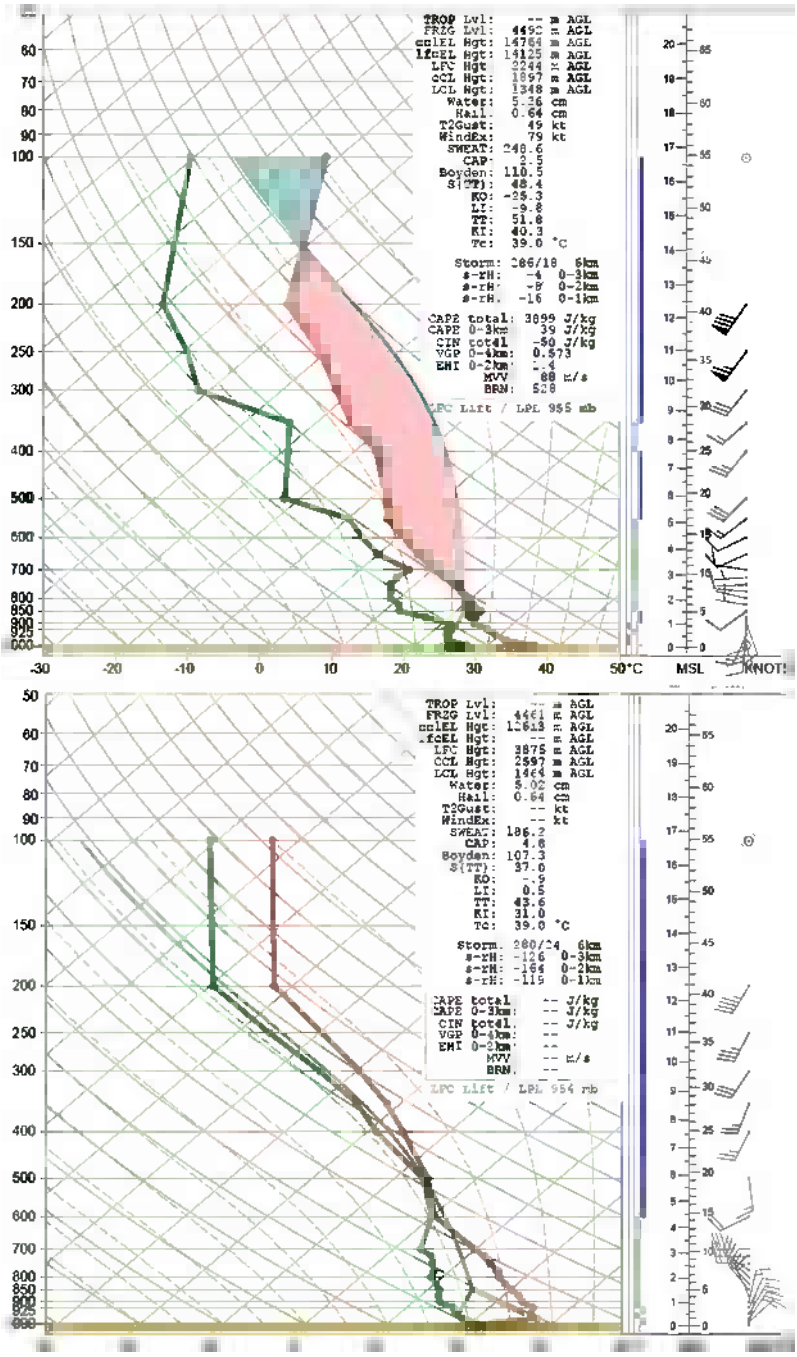

Fig. 3 Skew-T plots of temperature and dewpoint at Kharagpur at 06:00 and 12:00 UTC on 5th May, 2010

of maximum rainfall intensity. This clearly indicates the passage of a meso-high. The passage of the meso-high is followed by drop in pressure of 7 hPa in 1 h. During this time, the pressure decreased first slowly and then rapidly, reaching a minimum at about 20 min after the rainfall ends. This is a clear indication of wake low. During the process of wake low, the wind direction was slowly changed from northeasterly to south of southeasterly (clockwise). The end of the wake low is characterized by an abrupt increase in pressure (5 hPa) and gradual wind shift [In the process wind gradually veered from south of southeasterly to northeasterly (anticlockwise)]. The convective rainfall continued for about 45 min due to the presence of convective clouds in the front-end of the squall-line. The stratiform cloud let to light stratiform rain for next 2 h.

Radiosonde observations at 06:00 UTC at Kharagpur revealed a large unstable layer above the 900 hPa (Fig. 3). The post-squall upper-air sounding (at 12:00 UTC) at Kharagpur resembles the 'onion shape' suggested by Zipser (1969).

4 Summary and Conclusions

The analysis of surface pressure, temperature, relative humidity, winds and rainfall associated with trailing stratiform squall-line thunderstorm at Kharagpur reveals two mesoscale phenomena, namely a meso-high and a wake low. The meso-high was observed during the period of heavy downdrafts. A pressure rise up to 7 hPa was recorded at the time of maximum rainfall. The wake low is found after the completion of heavy rainfall i.e. just behind the convective line. The drop of pressure up to 12 hPa was recorded during the wake low period. It is also observed that the maximum pressure fall was recorded when the stratiform cloud of the squall-line crossed over the station (Kharagpur). This observation agrees well with that of the mid-latitude squall-line, where a meso-high forms near the convective line and a wake low in the rear i.e. within the trailing stratiform region.

The post-squall sounding of Skew-T and log P plot at Kharagpur depicted mid-tropospheric cooling and lower tropospheric warming. Maybe, these are due to the dominance of evaporative cooling in the mid levels and dynamically forced decent leading to adiabatic warming in the low levels. These observations indicate that the trailing stratiform precipitation region of the squall-line thunderstorm provides significant mesoscale weather phenomena in the tropical region, also.

Acknowledgments The authors are thankful to the Department of Science and Technology (DST), Govt. of India, for organizing STORM program from which the required data were made available.

References

Fujita TT (1955) Results of detailed synoptic studies of squall lines. Tellus 7:405–436. doi:10.1111/j.2153-3490.1955.tb01181.x

Johnson HR (2001) Surface mesohighs and mesolows. Bull Am Meteorol Soc 82:13–32. doi:10.1175/1520-0477(2001) 082<0013:SMAM>2.3.CO;2

Zipser EJ (1969) The role of organized unsaturated convective downdrafts in the structure and rapid decay of an equatorial disturbance. J Appl Meteorol 8:799–814. doi:10.1175/1520-0450(1969) 008<0799:TROOUC>2.0.CO;2

Zipser EJ (1977) Mesoscale and convective-scale downdrafts as distinct components of squall-line structure. Mon Weather Rev 105:1568–1589. doi:10.1175/1520-0493(1977)105<1568:MACDAD>2.0.CO;2

Evaluation of WRF-ARW Model in Reproducing a Heavy Rainfall Event Over Chalkidiki, Greece: The Effect of Land-Surface Features on Rainfall

G. Efstathiou, D. Melas, N. Zoumakis, and P.A. Kassomenos

Abstract A record breaking 24 h accumulated rainfall event was observed in Chalkidiki Peninsula, Greece on the 8th of October 2006. Intense precipitation was associated with strong low level convergence imposed by a low pressure system developed over the Aegean Sea and topographical lifting in the area of interest. Severe flooding and damage was reported especially in the east coast of Chalkidiki. The ability of WRF model to simulate this extreme precipitation episode using three different operational microphysical schemes was tested by comparing the high resolution results with available raingauge data. The verification results indicate that WRF configuration using ETA Ferrier microphysics provides better statistical scores for heavy hourly precipitation rates while it was able to reproduce the spatial rainfall distribution of this event. PLIN scheme captures the measured 24 h accumulations especially where maximum precipitation is observed. Sensitivity experiments suggest that highly localized heavy rainfall was the result of an interaction between synoptic conditions and the topographical features, with large scale forcing imposing a low-level convergent flow field that

G. Efstathiou (✉)
Laboratory of Meteorology, University of Ioannina, Ioannina 45 110, Greece

Environmental Process Laboratory, Atmospheric Physics Group, Alexander Technological Educational Institution of Thessaloniki, Thessaloniki, Greece
e-mail: gefstath@cc.uoi.gr

D. Melas
Laboratory of Atmospheric Physics, Department of Physics, Aristotle University of Thessaloniki, Thessaloniki, Greece

N. Zoumakis
Environmental Process Laboratory, Atmospheric Physics Group, Alexander Technological Educational Institution of Thessaloniki, Thessaloniki, Greece

P.A. Kassomenos
Laboratory of Meteorology, University of Ioannina, Ioannina 45 110, Greece

C.G. Helmis and P.T. Nastos (eds.), *Advances in Meteorology, Climatology and Atmospheric Physics*, Springer Atmospheric Sciences,
DOI 10.1007/978-3-642-29172-2_10,

produced heavy rain and topography enhancing highly localized precipitation maxima.

1 Introduction

An atmospheric disturbance affected Greece on 8–12 October 2006 which resulted in prolonged heavy rainfalls in Northern and Central Greece and severe thunderstorms over the island of Crete. On 8 October 2006 heavy rainfall occurred over northern Greece and especially over Chalkidiki peninsula causing severe problems and extensive flooding. A meteorological station situated on the east side of Chalkidiki (Skouries station at 40.47°N, 23.71°E) recorded 268 mm 24 h accumulated precipitation with a maximum rainfall intensity of 140 mm 3 h^{-1}. This heavy precipitation episode, associated with a case of cyclogenesis over the Aegean Sea in connection with mid-level vorticity advection and strong low-level moisture convergence over the area of interest, was simulated using the Weather Research and Forecasting (WRF) model. The high resolution model results were compared with available raingauge measurements, in order to investigate the ability of three microphysical parameterizations to reproduce the heavy rainfall event over the highly complex topography of Chalkidiki peninsula. In addition, sensitivity simulations excluding orography and replacing land surface with water over Chalkidiki, were used to establish the impact of synoptic scale forcing and land surface features on this high-impact precipitation event.

2 Data and Methodology

The numerical simulations are carried out using the Advanced Research Weather Research and Forecasting (WRF) model version 3.2. The WRF model is a fully compressible non-hydrostatic, primitive – equation model with multiple nesting capabilities (Skamarock et al. 2008). Three one – way nested grids have been defined for this work (Fig. 1b): Grid 1 covers the major part of Europe, the Mediterranean and northern Africa coasts with a grid spacing of 27 km. Grid 2 has a 9 km grid increment covering a large part of the eastern Mediterranean and Grid 3 is covering northern and central Greece and a large part of the Balkans with a grid spacing of 3 km. In the vertical dimension, 28 unevenly spaced sigma levels were selected. The simulations were initialized at 00:00 UTC 7 October 2006 and lasted for 48 h. The GFS $1^\circ \times 1^\circ$ gridded analysis fields at 6-h intervals have been used for initial and boundary conditions.

The bulk microphysical schemes examined in this study are used operationally and have been evaluated in many numerical experiments (Jankov et al. 2007; Hong et al. 2009; Lin and Colle 2009). The PLIN and WSM6 are six-class single-moment schemes that are based on common parameterizations (see Hong et al. 2009). The ETA Ferrier (Ferrier et al. 2002) scheme is designed to be computationally efficient

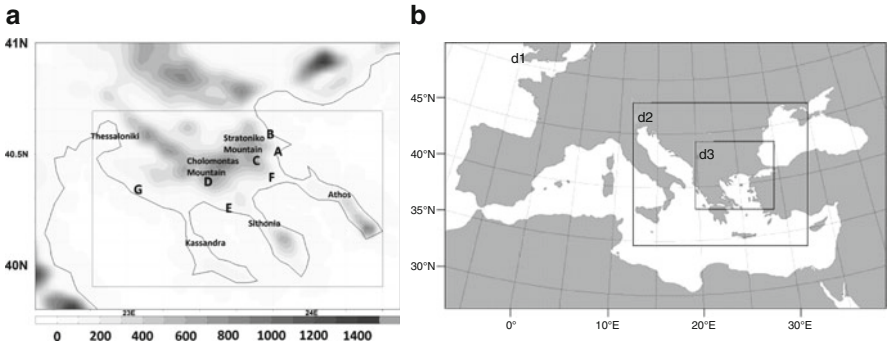

Fig. 1 (**a**) Orography (terrain height in meters) of Chalkidiki Peninsula as interpreted by WRF model. *Capital letters* indicate the positions of meteorological stations. A: Stratoni, B: Olympiada, C: Skouries, D: Polygyros, E: Vatopaidi, F: Gomati and G: Agios Pavlos. (**b**) WRF domains used in this study

for use in a wide range of numerical weather prediction models (Skamarock et al. 2008).

Precipitation observations from seven meteorological stations in Chalkidiki peninsula (see Fig. 1a) were used to compare with the model results from the high resolution grid (3 × 3 km) and conduct the forecast verification for this heavy rainfall episode. The available stations are Stratoni, Olympiada, Skouries operated by Hellas-Gold Company, Gomati station operated by the School of Agriculture of the Aristotle University of Thessaloniki, Vatopaidi and Ag. Pavlos stations operated by the Greek Ministry of Rural Development and Food and Polygyros station operated by the National Observatory of Athens (www.meteo.gr). It should be noted that only 24 h accumulated rainfall values are available for Polygyros station. Although the highest accumulations were observed in the eastern part of the peninsula high precipitation was also recorded at the other stations causing severe widespread flooding in many areas. Large damages in private properties and infrastructure were reported especially on the regional transportation network where some bridges collapsed.

For the evaluation of the model skill using different microphysical schemes, hourly rain rates were compared with model results in order to capture the high temporal variability of the heavy rainfall event. The model grid point spatially closest to the raingauge location is taken as the corresponding value to build up each model – observational pair. The observed precipitation values are verified against the corresponding model predicted values, creating a dataset that consists of 288 model – observational pairs for the six stations and for the 48h simulation period. This dataset is used for the calculation of Quantity Bias (QB) and Mean Absolute Error (MAE) for five ranges: 0.1–2.5, 2.5–5.0, 5.0–10, 10–20 and >20 mm h^{-1}.

In addition, two sensitivity experiments (using PLIN scheme) were carried out in order to identify the role of land-surface features on surface precipitation amounts

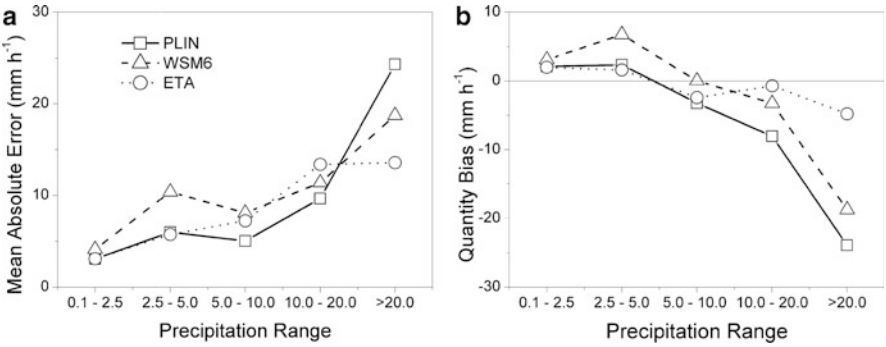

Fig. 2 (**a**) Mean absolute error and (**b**) quantity bias for the hourly precipitation forecasts for the different microphysical schemes

over the highly complex area of Chalkidiki peninsula: a simulation with the topography (NOTOPOHAL) of the peninsula eliminated (area in dashed box in Fig. 1a) and replaced by a constant value equal to mean sea level (z = 0) and a simulation where land surface is replaced and treated as water (AQUAHAL).

3 Results

Figure 2 presents MAE and QB for this heavy precipitation event. All schemes overpredict the amounts of rain for the 2.5 and 5 mm h^{-1} thresholds and underpredict for the 5–10 and 10–20 mm h^{-1} range with PLIN showing the lowest MAE. For heavy precipitation thresholds (>20 mm h^{-1}) all schemes underestimate precipitation and show a large negative bias. ETA exhibits the best statistical scores with lower mean absolute error and small negative bias when high rainfall intensity was observed (>20 mm h^{-1}).

The spatial distribution of the observed 24 h accumulated precipitation for 8 October 2006 and comparison with available measurements is presented in Figs. 3 and 4a respectively. PLIN simulation captures the 24 h accumulated rainfall at Skouries (see Fig. 4a) were heaviest rainfall was reported although maximum rainfall is predicted in central Chalkidiki as can be seen in Fig. 3a. WSM6 overestimates rainfall at eastern Chalkidiki producing a nearly 500 mm maximum in Gomati station where 62 mm were observed (see Fig. 3b). This station is only 11 km southeast of Skouries suggesting that this rain event had significant spatial heterogeneity. Both schemes generate large accumulations in stations in western and central Chalkidiki. ETA also overestimates rainfall at stations where intense rainfall was observed but places maximum 24 h accumulations near Skouries (where maximum rates and accumulation were measured – see Fig. 3c). It should be noted that due to the very limited number of available observations and the spatial heterogeneity of this event it is difficult to evaluate the ability of the microphysical schemes to simulate the spatial distribution of 24 h accumulated precipitation.

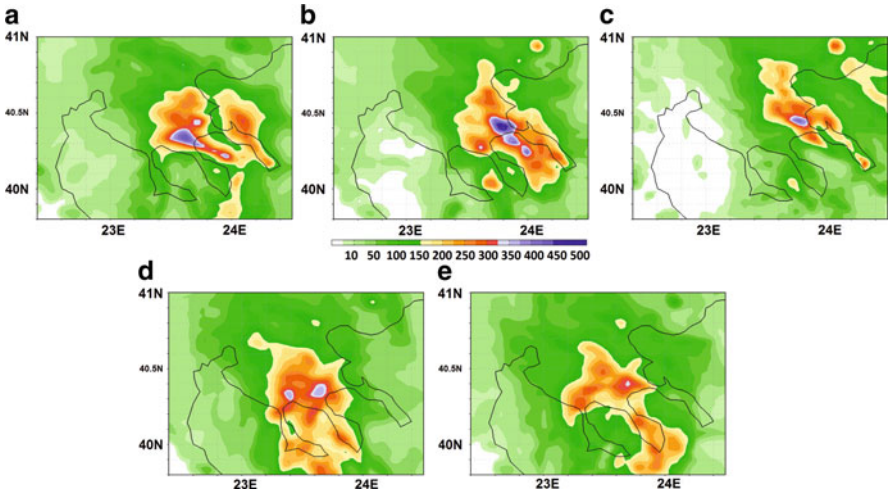

Fig. 3 Spatial distribution of 24 h accumulated rainfall (mm) over Chalkidiki for 8/10/2006 using (**a**) PLIN, (**b**) WSM6, (**c**) ETA microphysical schemes, (**d**) NOTOPOHAL using PLIN experiment and (**e**) AQUAHAL using PLIN experiment

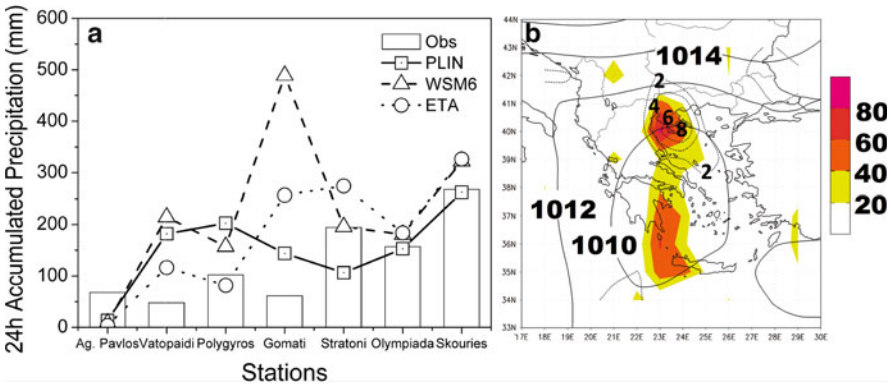

Fig. 4 (**a**) Comparison between measured and modeled 24 h accumulated rainfall. (**b**) Contours of mean sea level pressure hPa (*solid*), 1,000 hPa convergence 10^{-5} s^{-1} (*dotted*) and 500 hPa vorticity advection 10^{-10} s^{-2} (*shaded*) from GFS analysis valid at 00:00 UTC 8/10/2006

The 24 h accumulated rainfall for the NOTOPOHAL and AQUAHAL experiments is shown in Fig. 3d and e respectively. As can be seen from the plots there is significant change in the distribution of surface precipitation compared to the control (PLIN) run in Chalkidiki peninsula, reducing maximum 24 h accumulations. Intense rainfall is moved westwards as topography is removed and maximum precipitation is further reduced as land is replaced with water (AQUAHAL see Fig. 3e). However total rain volume (see Table 1) calculated over Chalkidiki (area confined in box in Fig. 1a) is

Table 1 Maximum accumulated rainfall and rain volume for the control and sensitivity simulations

Simulation	Max accumulated 24 h precipitation (mm)	Rain volume (km^3)
PLIN	450	2.4
PLIN_NOTOPOHAL	372	2.6
PLIN_AQUAHAL	340	2.5

almost unaffected by the changes in land-surface features indicating that the total precipitation amount over the 48h simulation period has not changed significantly.

4 Conclusions

In this study, preliminary results from the simulation of a heavy rainfall event using three operational microphysical schemes over the mountainous area of Chalkidiki are presented. The comparison of high resolution model results with available raingauge measurements demonstrated that:

1. All microphysical schemes overestimate light to moderate and underestimate heavy precipitation hourly rates (e.g. Mazarakis et al. 2009). ETA provides best scores for the highest rainfall rates with small negative bias.
2. WSM6 and ETA schemes produce high accumulations and overestimate 24 h rainfall in all stations. PLIN captures 24 h accumulated rainfall at Olympiada and Skouries where maximum rainfall was observed.
3. Sensitivity experiments revealed that topography controls the surface distribution of rainfall and enhances maximum 24 h rainfall accumulations. Total precipitation amounts over the area of interest remain almost unaffected indicating the importance of large scale forcing during this high-impact event, as can be seen by examining vorticity advection and divergence fields (see Fig. 4b).

Acknowledgments This work is co-funded by the European Union – European Social Fund (ESF) & National Sources, in the framework of the program "HRAKLEITOS II" of the "Operational Program Education and Life Long Learning" of the Hellenic Ministry of Education, Life Long Learning and religious. The authors would like to thank Hellas-Gold Company for providing available raingauge datasets.

References

Ferrier BS, Jin Y, Lin Y, Black T, Rogers E, DiMego G (2002) Implementation of a new grid-scale cloud and precipitation scheme in the NCEP eta model. In: Proceedings of 19th conference on weather analysis and forecasting/15th conference on numerical weather prediction. American Meteorological Society, San Antonio, TX, pp 280–283

Jankov I, Schultz PJ, Anderson CJ, Koch SE (2007) The impact of different physical parameterizations and their interactions on cold season QPF in the American River Basin. J Hydrometeorol 8:1141–1151. doi:10.1175/JHM630.1

Lin Y, Colle BA (2009) The 4–5 December 2001 IMPROVE-2 event: observed microphysics and comparisons with the weather research and forecasting model. Mon Weather Rev 137:1372–1392. doi:10.1175/2008MWR2653.1

Hong SY, Lim KS, Kim JH, Lim JO, Dudhia J (2009) Sensitivity study of cloud-resolving convective simulations with WRF using two bulk microphysical parameterizations: ice-phase microphysics versus sedimentation effects. J Appl Meteorol Climatol 48:61–76. doi:10.1175/2008JAMC1960.1

Mazarakis N, Kotroni V, Lagouvardos K, Argiriou AA (2009) The sensitivity of numerical forecasts to convective parameterization during the warm period and the use of lightning data. Atmos Res 94:704–714. doi:10.1016/j.atmosres.2009.03.002

Skamarock WC, Klemp JB, Dudhia J, Gill DO, Barker DM, Wang W, Powers JG (2008) A description of the advanced WRF version 3. NCAR technical note NCAR/TN/u2013475+STR

On the Effect of Land Use Change on the Meteorological Parameters Above the Greater Athens Area

K.M. Fameli, V.D. Assimakopoulos, and V. Kotroni

Abstract The rapid land use changes that took place in the Greater Athens Area (GAA) the past decades, due to the expansion of the urban grid, have changed the landscape of Attica significantly. Areas that were covered by low vegetation in the past are now replaced by roads (e.g. Attiki Odos) and new towns. On the other hand, accurate and updated data of land use are necessary for simulating the meteorological fields above urban areas, which in turn are given as input to photochemical models in order to study the dispersion of pollutants above urban areas. The purpose of the present work is to study the effects of land use changes on the meteorological parameters, such as wind speed profiles and temperature. For this reason, the meteorological mesoscale model MM5 was applied, using updated land use data. The model ran with the grid nesting method using two grids, the fine one covering the GAA with a spatial resolution of $5 \times 5\,km^2$. Results showed that the land use changes affected wind and temperature fields. Wind velocities decreased above areas covered by urban grid that were previously characterised as shrub land, while above the rapidly developing eastern suburbs of Attica an increase in velocities appeared.

1 Introduction

Rapid Land Use/Land Cover (LULC) changes that take place in urban areas affect the local environment and human activities to such extent that updating data sets used in meteorological models is necessary in order to simulate accurately the

K.M. Fameli (✉)
Division of Environmental Physics and Meteorology, Department of Physics, University of Athens, Building Physics V, University Campus, Athens 157 84, Greece
e-mail: kmfameli@phys.uoa.gr

V.D. Assimakopoulos • V. Kotroni
Institute for Environmental Research and Sustainable Development, National Observatory of Athens, Athens, Greece

C.G. Helmis and P.T. Nastos (eds.), *Advances in Meteorology, Climatology and Atmospheric Physics*, Springer Atmospheric Sciences,
DOI 10.1007/978-3-642-29172-2_11,

current state (Lee et al. 2009). In many studies the relationship between land use change and meteorological fields, such as wind velocity and direction and surface temperature, has been described (Civerolo et al. 2000; Tokairin et al. 2010). As for the Greater Athens Area (GAA), the land use changes that occurred the past decade due to the organization of the Olympic Games of 2004 and the population shift to the eastern areas of Attica, is not well represented in the traditional LULC data sets used by meteorological models. Moreover, meteorological data used in photochemical models affect the predicted pollutants concentrations (Jackson et al. 2006) so the development of accurate meteorological fields is of great importance. The purpose of the present study is to examine the contribution of the LULC updated data on the meteorological pattern with the use of the mesoscale meteorological model MM5 for the GAA.

2 Meteorological Model Description

For the present study the meteorological simulations were performed with MM5, a widely used non-hydrostatic, primitive equation model using terrain-following coordinates. The model setup for the physical parameterizations includes: the combination of Kain-Fritsch (Kain and Fritsch 1993) convective scheme, with the highly efficient and simplified microphysical scheme proposed by Schultz (1995), and the MRF scheme proposed by Hong and Pan (1996) for the boundary layer.

For the simulations performed, two one-way nested grids were used: Grid1 (220 $\times$ 180 grid points with a 15-km horizontal grid increment) covering most of Europe, the Mediterranean and the northern African coast, Grid2 (52 $\times$ 46 grid points, 5-km grid spacing) covering the entire Athens area and the adjacent water bodies. In the vertical direction, 23 unevenly spaced full sigma levels are selected, (σ = 1.00, 0.99, 0.98, 0.96, 0.93, 0.89, 0.85, 0.80, 0.75, 0.70, 0.65 0.60, 0.55, 0.50, 0.45, 0.40, 0.35, 0.30, 0.25, 0.20, 0.15, 0.10, 0.05, 0.00). For the initialization and nudging of the boundaries of Grid1 the European Centre of Medium Range Weather Forecasts (ECMWF) analyses at 0.5-degree lat/lon horizontal grid increment were used. Finally the topography and land cover (25-categories) were derived from the 30-arcsec global USGS global coverage file.

3 Methodology

The simulation period started at 00.00 (UTC) on June 19th, 2006 and ended at 24.00 (UTC) on June 19th, 2006. The temporal resolution was 120 min for Grid1 and 60 min for Grid2. MM5 ran for two land use cases: (a) LULC data provided by USGS Global LULC v.2.0 Database were used for the year 1992 and (b) an updated land use field for the fine grid was used (Fig. 1).

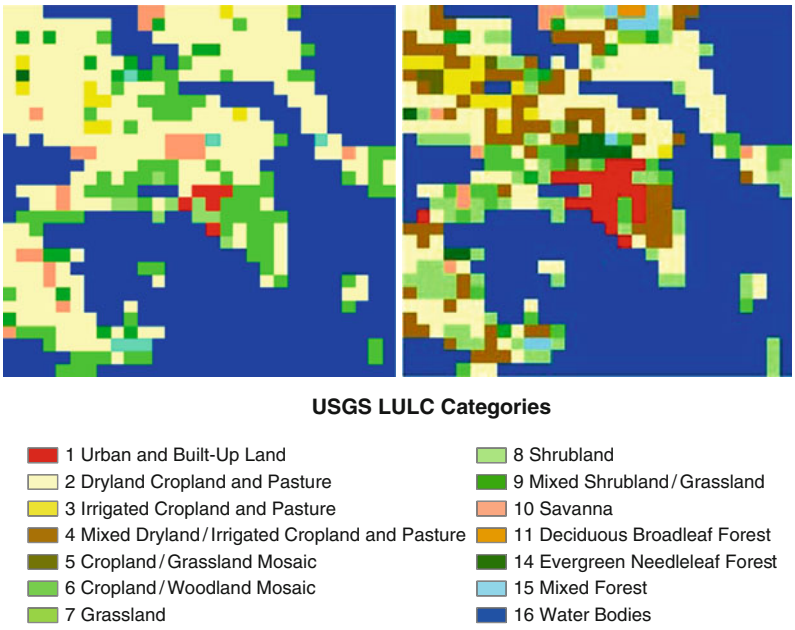

Fig. 1 USGS LULC field (1992) (*left*), updated LULC field (2006) (*right*)

Table 1 Description of selected LULC USGS categories and physical parameters for N.H. summer (15 April–15 October).

LU value	Land use category	Albedo (%)	Moisture avail. (%)	Emissivity (% at 9 μm)	Roughness length (cm)	Thermal inertia (cal cm^{-2} k^{-1} $s^{-1/2}$)
1	Urban	15	10	88	80	0.03
2	Drylnd crop. past.	17	30	98.5	15	0.04
8	Shrubland	37.2	39.2	41.9	10	0.03
15	Mixed forest	13	30	94	50	0.04
16	Water bodies	8	100	98	.01	0.06

The updating process was fulfilled only for the fine grid having 29 cells on each direction. Each cell was assigned one land use type based upon the predominant category within that cell. The land use classes are depicted in Table 1. From the 25-LULC categories only 13 describe this study area of interest. It is obvious from Figs. 2 and 3 that areas previously covered by low vegetation are now covered by urban land in the GAA and cells covered by irrigated croplands have increased in Boeotia and NE Peloponnese.

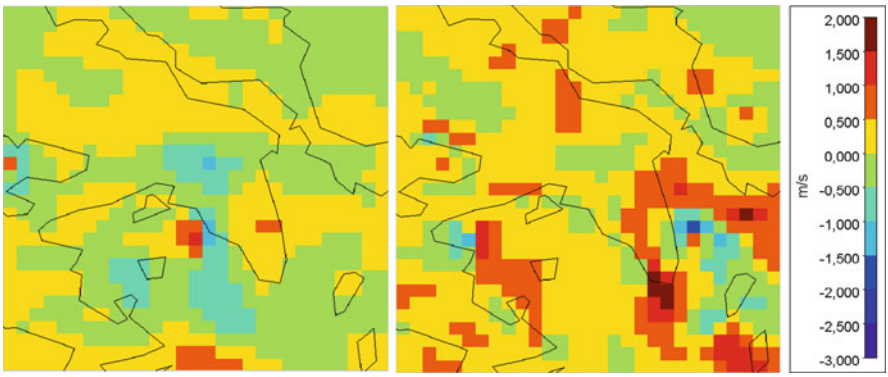

Fig. 2 Difference in wind velocity between the updated and the old LULC fields, at 6.00 UTC (*left*) and 15.00 UTC (*right*)

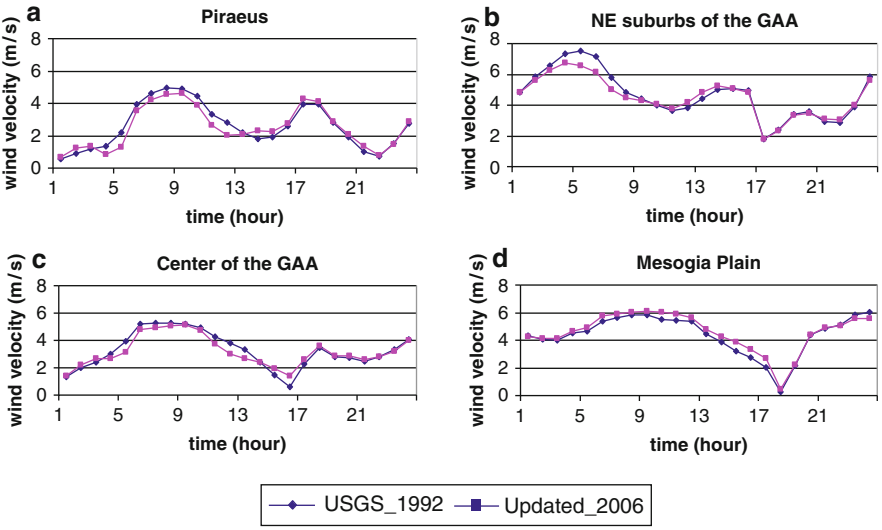

Fig. 3 Wind velocity for the old and the updated LULC fields at selected cells

4 Results

The new land use field modified the surface roughness of the area significantly and as a consequence meteorological parameters such as wind velocity and direction were affected. To illustrate the effects of the land use changes, the wind velocity differences were plotted; case B–case A (Fig. 2).

Generally, the wind velocity decreased in urban cells previously covered by low vegetation as the surface roughness length is higher for the urban class (80 cm – class 1, 15 cm – class 2). The decrease was mainly noticed in the morning and

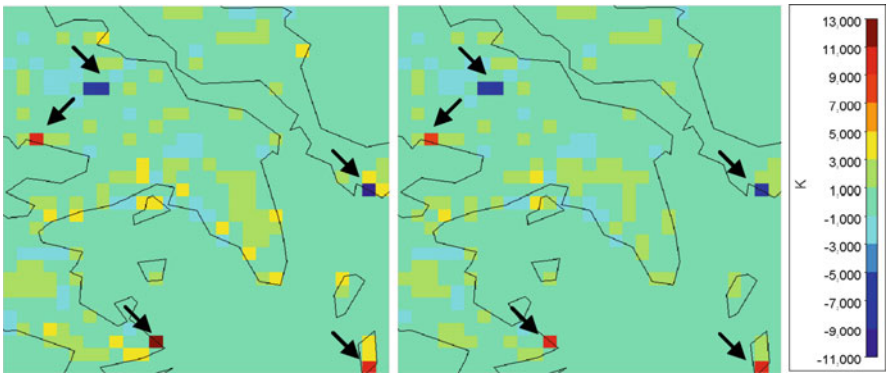

Fig. 4 Difference in temperature between the updated and the old LULC fields, at 6.00 UTC (*left*) and 15.00 UTC (*right*) – at cells pointed with arrows the land use changed from sea to land and vice versa so temperature appeared to have the major differences at these areas (~10 K)

varied from 0.1 to 1 m/s. A great change in wind velocity appeared above urban areas at the edges with coastal ones (Piraeus, Fig. 3a), as the previously low surface in combination with the sea favored the development of higher velocities, or to the NE suburbs of the GAA as shown in Fig. 3b. Wind velocity in urban areas whose land use category was unchanged was also affected thanks to the increase of the urban grid (Fig. 3c). It is worth mentioning that during the simulation period low winds occurred (about 1–5 m/s) so changes in land use played a significant role to the development of the new wind field.

On the other hand, wind velocity increased at eastern Attica due to the fact that areas previously characterized as cropland/woodland mosaic are now croplands and pastures (Fig. 3d). Differences in wind direction appeared at the southern edges of the urban grid with the Saronic Gulf where a shift from NW to NNW was made (not shown here).

The expansion of the urban grid led to a small rise in temperature at the NE suburbs of the GAA (Fig. 4). On the contrary, regarding the new land use field, urban cells close to the sea appeared to be cooler. In the Mesogia Plain, the surface temperature was higher by 2 K on average, which may be attributed to the decreased soil moisture availability (35% at USGS land use field – 25% at the updated land use field).

5 Conclusions

In the present study the effects of updated land use input data to the MM5 model were examined. The most important results may be summarized as follows:

- The wind velocity decreased while its direction presented a shift due to the expansion of the urban grid.

- The surface temperature at areas of the GAA that underwent rapid urbanization increased by 2 K.
- The meteorological parameters changed significantly at the border between cells whose land use category was unchanged with the ones where new data existed.

Concluding, land use patterns should be taken into consideration when using models in order to simulate meteorology as the latter is sensitive to the surface characteristics, thus affecting input data given to photochemical models

Acknowledgments This research has been co-financed by the European Union (European Social Fund – ESF) and Greek national funds through the Operational Program "Education and Lifelong Learning" of the National Strategic Reference Framework (NSRF) – Research Funding Program: Heracleitus II. Investing in knowledge society through the European Social Fund.

References

Civerolo KL, Sistla G, Rao ST, Nowak DJ (2000) The effects of land use in meteorological modeling: implications for assessment of future air quality scenarios. Atmos Environ 34:1615–1621. doi:10.1016/S1352-2310(99)00393-3

Hong SY, Pan HL (1996) Nonlocal boundary layer vertical diffusion in a medium – range forecast model. Mon Weather Rev 124:2322–2339. doi:10.1175/1520-0493(1996)124<2322: NBLVDI>2.0.CO;2

Jackson B, Chau D, Gurer K, Kaduwela A (2006) Comparison of ozone simulations using MM5 and CALMET/MM5 hybrid meteorological fields for the July/August 2000 CCOS episode. Atmos Environ 40:2812–2822. doi:10.1016/j.atmosenv.2006.01.020

Kain, JS, Fritsch JM (1993) Convective parameterization for mesoscale models: the Kain-Fritsch scheme. The representation of cumulus in numerical models. American Meteorological Society, Meteor Monogr 46:165–177

Lee SM, Princevac M, Mitsutomi S, Cassmassi J (2009) MM5 simulations for air quality modeling: an application to a coastal area with complex terrain. Atmos Environ 43:447–457. doi:10.1016/j.atmosenv.2008.07.067

Schultz P (1995) An explicit cloud physics parameterization for operational numerical weather prediction. Mon Weather Rev 123:3331–3343. doi:10.1175/1520-0493(1995)123<3331: AECPPF>2.0.CO;2 DOI:dx.doi.org

Tokairin T, Sofyan A, Kitada T (2010) Effect of land use changes on local meteorological conditions in Jakarta, Indonesia: toward the evaluation of the thermal environment of megacities in Asia. Int J Climatol 30:1931–1941. doi:10.1002/joc.2138

Study of a Mesoscale Convective Complex Over Balkans with Meteosat Data

H. Feidas

Abstract Large size mesoscale convective systems (MCSs) with long duration such as Mesoscale Convective Complexes (MCCs) are rare in the Mediterranean basin. On May 24, 2009 one MCC crossed western and southern Balkan Peninsula causing severe weather, heavy precipitation, hail and strong wind. The case was analyzed using Meteosat Second Generation (MSG) satellite data. First, an automatic algorithm for detecting and tracking convective cloud cells on infrared MSG images was applied to monitor the time evolution of several radiative, morphological and positional cloud parameters that express the MCC cloud top microphysics, structure, development and movement. Then successive multispectral MSG imagery was analyzed to reveal the organization and the cloud top microphysics of the system in different phases of its lifecycle. Visible images from the MSG satellite were used to identify the overshooting tops while infrared brightness temperature revealed the cloud top temperature structure. Composite imagery obtained from single channels or from various channel differences were analyzed to investigate the spatial distribution of convection and cloud top microphysics as well as the air mass type in middle troposphere. It is concluded that cloud tracking algorithms along with composites of satellite and lightning data has proved very valuable in assessing important features of a severe MCC in operational terms.

1 Introduction

Mesoscale convective complexes (MCCs) are important well-organized, midlatitude convective storm systems due to their large size and long duration. They are large, long-lived convective systems with a quasi-circular cold cloud shield as

H. Feidas (✉)
Department of Meteorology and Climatology, School of Geology, Aristotle University of Thessaloniki, Thessaloniki, 54124, Greece
e-mail: hfeidas@geo.auth.gr

C.G. Helmis and P.T. Nastos (eds.), *Advances in Meteorology, Climatology and Atmospheric Physics*, Springer Atmospheric Sciences,
DOI 10.1007/978-3-642-29172-2_12,

defined in satellite infrared (IR) images. More precisely, what is required is (a) a continuous cloud shield with IR temperature $<-32°C$ that must have an area $>100{,}000$ km^2, (b) an interior cold cloud region with IR temperature $<-52°C$ that must have an area $>50{,}000$ km^2, (c) these conditions must be met for a period of 6 h, and (d) the eccentricity (minor axis/major axis) of its shape must be >0.7 at the time of maximum extent (Maddox 1980).

On May 24, 2009 a MCC crossed western and southern Balkans causing severe weather, heavy rainfall, hail and strong wind. This study aims to analyze this case using the high spectral resolution of Meteosat Second Generation (MSG) data.

2 Data and Methodology

The structure and development of the MCC were studied with satellite data obtained from Spinning Enhanced Visible and Infrared Imager (SEVIRI) instrument of the MSG satellite. First, an automatic algorithm for detecting and tracking convective cloud cells on infrared MSG images (Feidas 2002) was applied to monitor the time evolution of several radiative, morphological and positional cloud parameters that express cloud top microphysics, structure and development. Then successive multispectral MSG imagery was analyzed to reveal the organization and the cloud top microphysics of the system in different phases of its lifecycle. MSG data were visualized as single channel or RGB images using the MSGView software (Ertürk 2010).

3 Results

The lifecycle of the MCC is displayed with sequential enhanced IR (10.8 μm) images in Fig. 1. The development of the MCC started as an orogenic mesoscale convective system at 5:00 UTC over the Austrian Alps moving towards southeast (Fig. 1a–c). The system developed with a rapidly growing internal cold area until 13:00 UTC (Fig. 1b–d), when it merged with four neighboring new convective cells developed next and behind of the existing cell (Fig. 1e) to form a large system. Over the next 3 h the MCC developed rapidly heading towards Greece (Fig. 1f, g) where started to decline and finally dissipated as a mesoscale convective vortex over the Aegean Sea.

Most of the favorable large-scale meteorological preconditions found by Maddox (1983) were met in our case. A few hours before the convective initiation, a high pressure system dominated the area where the system developed (Fig. 2a). The system was born and developed (a) in the right entry of a jet-streak in the upper troposphere where high upper-level divergence supported instability (Fig. 2b), (b) in an area of strong low-level warm advection occurred in the boundary between a warm, humid air mass and cold polar air mass (Fig. 2c), (c) in an area with a large amount of low-level moisture (Fig. 2d). The triggering mechanism was the orographic uplift along a line between the Austrian and the Dinaric Alps.

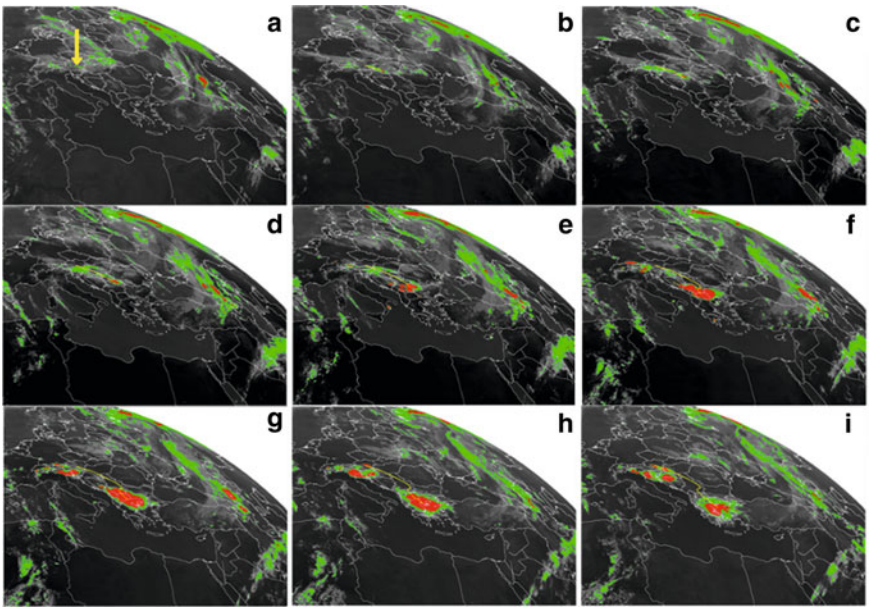

Fig. 1 Snapshots of enhanced IR images adapted to the definition of the MCC shown in 2-h intervals (5:00–23:00 UTC). *Red* and *green* colors indicate $T_{10.8}$ lower than −32°C and −52°C, respectively. *Yellow arrow* in (**a**) shows the initial convective cell

Figure 3a presents the time evolution of cloud shield system area, interior cold region area and eccentricity using the automatic cloud tracking algorithm of Feidas (2002). It is clear that the system met the MCC criteria set by Maddox (1980) having a cloud shield with an areal extent and an interior cold cloud region exceeding 100,000 and 50,000 km^2, respectively, for a period longer than 6 h. In addition, the eccentricity of its shape is >0.7 at the time of maximum extent.

The next step was to investigate the time evolution of several radiative, morphological and positional parameters of the MCC. Figure 3a reveals that the internal cold cloud area peaks 30 min earlier than the cloud shield system area of the MCC. Moreover, the maximum of the internal cold cloud fractional coverage, defined as the ratio of the internal cold area to the cloud shield system area, occurred about 3 h earlier than the area of the MCC (Fig. 3b). This pattern is in fully agreement with the evolution of the mean brightness temperature (BT) at $IR_{10.8}$ that expresses the vertical development of the system (Fig. 3b).

This time lag between the cloud top temperature and cloud shield area defines the three phases of the MCC lifecycle (Fig. 3d): (1) a growing phase where both cloud top height and cloud shield area are increasing rapidly, (2) a phase of maturity where the cloud shield area is still increasing while cloud top height is decreasing, and (3) the dissipation phase where both parameters decrease.

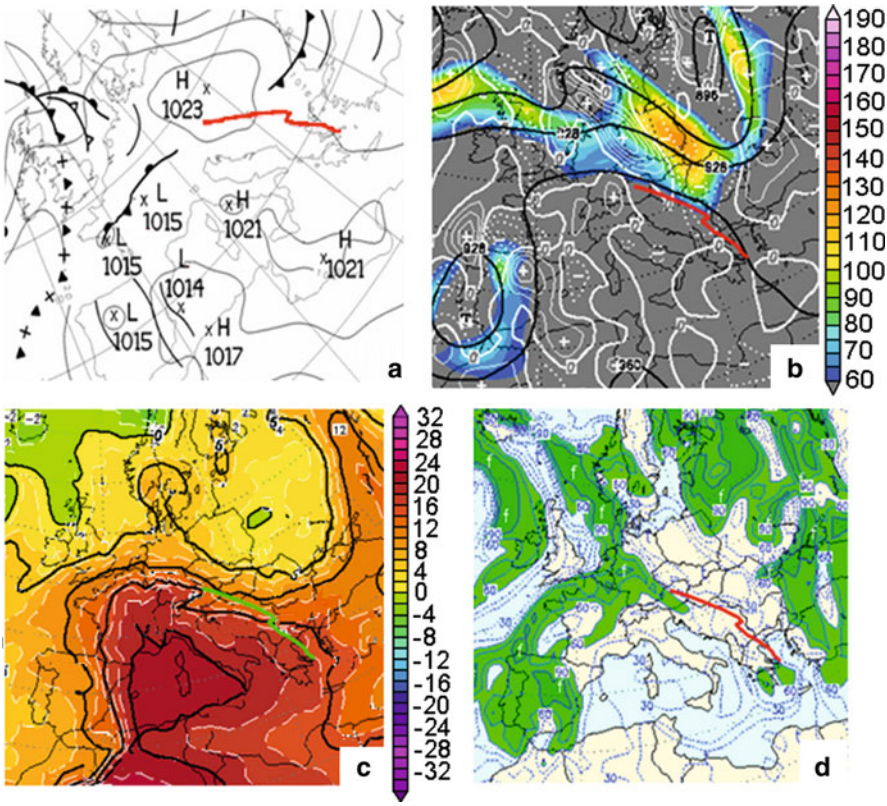

Fig. 2 (**a**) Mean sea-level pressure weather chart, (**b**) wind and divergence at the 300 hPa level, (**c**) temperature at the 850 hPa level and (**d**) relative humidity at the 850 hPa level, at 00:00 UTC, 24/5/2009. The trajectory of the MCC is also indicated in the charts

Brightness temperature differences (BTDs) in the thermal infrared channels can be used to gain implicit information about cloud top microphysics. BTD between the 6.2 and 10.8 μm channels ($T_{6.2}$–$T_{10.8}$) is effective in distinguishing between high-level and mid-level clouds (Lutz et al. 2003). It usually takes very small negative values for upper level thick clouds and positive differences for convective cloud tops (Schmetz et al. 1997). Mean $T_{6.2}$–$T_{10.8}$ at the time of maximum extent of the MCC is very close to zero, with a time evolution in fully agreement with the BT10.8 pattern (Fig. 3c). This implies that intense convective cloud tops are penetrating the tropopause.

BTD between the 8.7 and 10.8 μm channels ($T_{8.7}$–$T_{10.8}$) can be utilized to gain information about the cloud phase (Strabala et al. 1994). For ice clouds, $T_{8.7}$–$T_{10.8}$ tends to be positive in sign (Baum and Platnick 2006). Mean $T_{8.7}$–$T_{10.8}$ for the MCC are positive, increasing almost steadily with time (Fig. 3c). This implies an increasing ice formation in the MCC throughout its entire lifecycle.

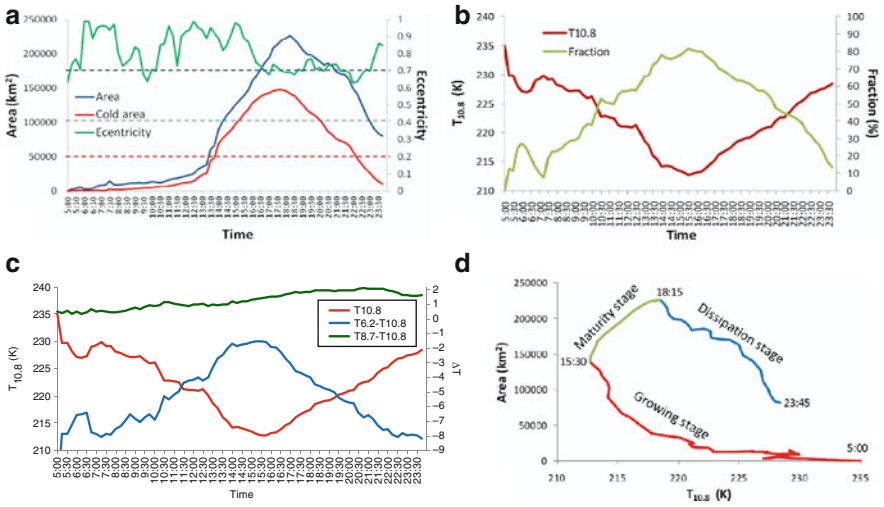

Fig. 3 Time evolution of (**a**) cloud shield system area, interior cold region area and eccentricity, (**b**) internal cold cloud fraction along with the mean BT at $IR_{10.8}$ (*Dotted lines* denote the threshold values of the MCC criteria), (**c**) mean $T_{6.2}$–$T_{10.8}$ and $T_{8.7}$–$T_{10.8}$ BTDs along with the mean BT at $IR_{10.8}$, (**d**) relation of cloud shield area with mean cloud top BT at $IR_{10.8}$. Colours denote different lifecycle stages

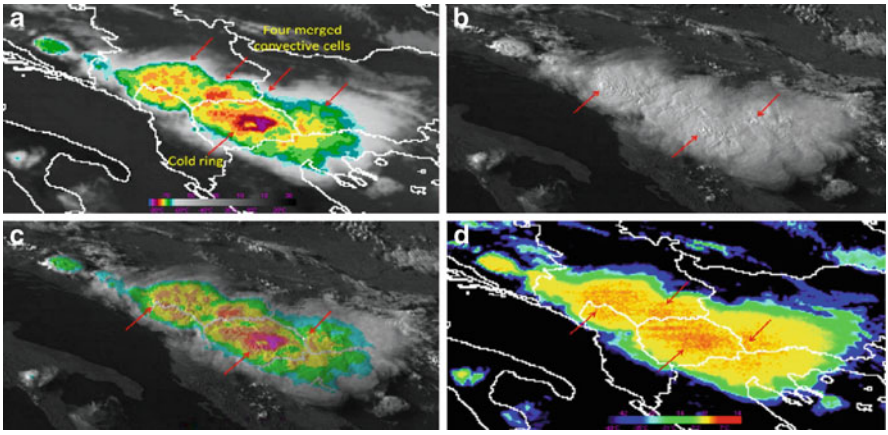

Fig. 4 (**a**) Enhanced $IR_{10.8}$ image, (**b**) HRV image, (**c**) merged HRV and enhanced $IR_{10.8}$ image, and (**d**) $T_{6.2}$–$T_{10.8}$ BTD image at 16:00 UTC. *Red arrows* show the overshooting tops

The enhanced $IR_{10.8}$ image at 16:00 UTC shows that the MCC is an aggregation of four merged convective cells (Fig. 4a). A "Cold ring" structure is observed in the central convective cell, which is often characteristic of a severe system. In the low sun angle high resolution visible (HRV) image of Fig. 4b one can easily discern three overshooting tops in the cloud shield of the MCC, each of which corresponding to one of the four merged cells.

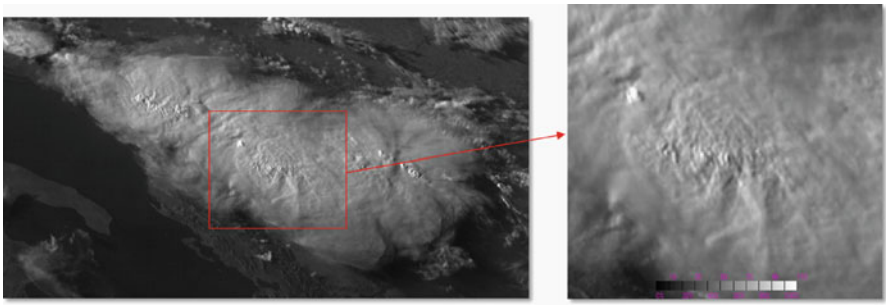

Fig. 5 HRV image at 16:30 UTC

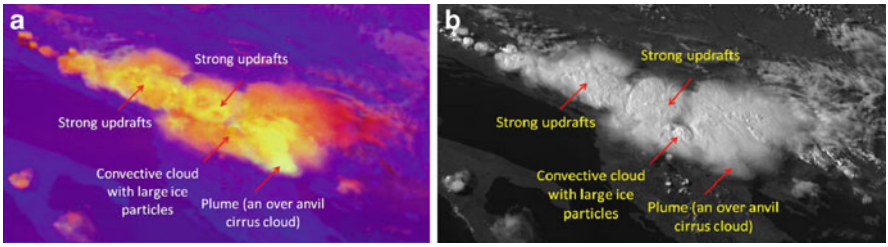

Fig. 6 (**a**) Convective storms RGB image and (**b**) HRV image at 15:00 UTC

The image merging the HRV and IR108 channels shows that the overshooting top is situated within the upwind side of the cold ring (Fig. 4c). The MSG HRV image in Fig. 5 shows gravity wave generation at the top of the MCC system, which could be connected to the strength and oscillations of the updraft.

The $T_{6.2}$–$T_{10.8}$ BTD image reveals the warm moisture distribution above cloud tops. High positive $T_{6.2}$–$T_{10.8}$ values represent lower stratospheric moisture above storm tops. Their comparison with $IR_{10.8}$ window shows a close correlation between the $T_{6.2}$–$T_{10.8}$ maxima and IR BT minima (Fig. 4d).

The "convective storms RGB" product (6.2–7.3, 3.9–10.8, 1.6–0.6) visualizes the particle size features of high-level cloud tops with good contrast. Yellowish cloud tops indicate opaque ice cloud with small particles which can serve as an indicator of storm severity. High-level opaque ice cloud tops with large particles are reddish. In the RGB image of Fig. 6a, there are two distinct yellowish areas indicating ice cloud with small particles formed by strong updrafts. The first one located in the central convective cell outlines a "Cold ring" structure. The bright yellowish area at the southernmost part of the MCC shows a broad plume (an over anvil cirrus cloud), with its source being several overshooting tops on the southern part of the MCC. The comparison with the HRV image (Fig. 6b) reveals a small convective cell with large ice particles, as indicating by the reddish color in the RGB product and the corresponding distinct overshooting top in the HRV image.

Successive multispectral MSG imagery can be used to visualize the development of the MCC in different phases of its lifecycle. The evolution of the MCC in

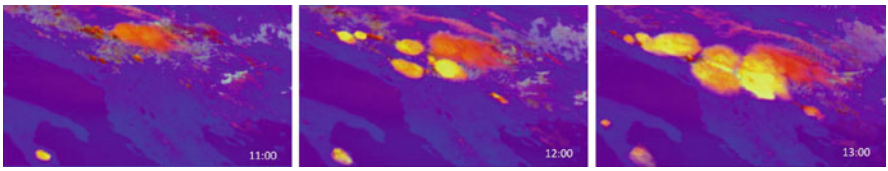

Fig. 7 Evolution of the MCC from 11:00 to 13:00 UTC using "Convective storms" RGB images at 1 h interval

Fig. 7 revealed that the MCC actually formed by the merge of a MCS with four new developed convective cloud cells characterized by strong updrafts.

4 Conclusions

The features exhibited by the system of May 24, 2009 in SE Europe met the requirements of a MCC conceptual model. It is shown how MSG imagery can be used to analyze the development and structure of a MCC. First, the evolution of the system was described, in terms of the track, timing, and development. Then multispectral MSG imagery was analyzed to reveal the organization and the cloud top microphysics of the system in different phases of its lifecycle. The main conclusion is that MSG data has proven to be a valuable tool not only in studying a MCC but also in detecting and nowcasting the severity and location of convection.

References

Baum BA, Platnick S (2006) Introduction to MODIS cloud products. In: Qu JJ, Gao W, Kafatos M, Murphy RE, Salomonson VV (eds) Earth science satellite remote sensing: science and instruments. Springer, Berlin

Ertürk AG (2010) MSGView: an operational and training tool to process, analyze and visualization of MSG SEVIRI data. In: Proceedings of the 10th EUMETSAT conference, Cordoba, Spain

Feidas H (2002) A software tool for monitoring the features of convective cloud systems with the use of Meteosat images. Environ Modell Softw 18:1–12

Lutz H-J, Inoue T, Schmetz J (2003) NOTES AND CORRESPONDENCE Comparison of a split-window and a multi-spectral cloud classification for MODIS observations. J Meteorol Soc Jpn 81(3):623–631. doi:10.2151/jmsj.81.623

Maddox RA (1980) Mesoscale convective complexes. Bull Am Meteorol Soc 61:1374–1387

Maddox RA (1983) Large-scale meteorological conditions associated with midlatitude, mesoscale convective complexes. Mon Weather Rev 111:1475–1493

Schmetz J, Tjemkes SA, Gube M, van de Berg L (1997) Monitoring deep convection and convective overshooting with METEOSAT. Adv Space Res 19:433–441

Strabala KI, Ackerman SA, Menzel WP (1994) Cloud properties inferred from 8–12-μm data. J Appl Meteorol 33:212–229. doi:10.1175/1520-0450(1994) 033<0212:CPIFD>2.0.CO;2

Numerical Wave Modeling and Wave Energy Estimation

G. Galanis, G. Zodiatis, D. Hayes, A. Nikolaidis, G. Georgiou, S. Stylianou, G. Kallos, C. Kalogeri, P.C. Chu, A. Charalambous, K. Savvidou, and S. Michaelides

Abstract In a rapidly evolving operational and research framework concerning the global energy resources, new frontiers have been set for the scientific community working on environmental and renewable energy issues. In particular, new numerical techniques supporting the accurate estimation of renewable energy sources are highly emphasized. In this framework, wave energy – the energy that can be captured from sea waves – provides an alternative option with critical advantages. In the present paper, recent advances and some preliminary results obtained in two European projects will be discussed: Marina Platform and E-wave projects are focusing on the estimation of the wave energy potential in North Atlantic coastline of Europe and in Eastern Mediterranean Sea, respectively. Special emphasis is given to the utilization of numerical atmospheric and wave modeling systems able to accurately monitor the atmospheric and sea conditions in the area of interest.

G. Galanis (✉)
Atmospheric Modeling and Weather Forecasting Group, Department of Physics, University of Athens, University Campus, Building Physics V, Athens, Greece

Oceanography Centre, University of Cyprus, P.O. Box 20537, Nicosia, Cyprus
e-mail: ggalanis@mg.uoa.gr

G. Zodiatis • D. Hayes • A. Nikolaidis • G. Georgiou • S. Stylianou
Oceanography Centre, University of Cyprus, P.O. Box 20537, Nicosia, Cyprus

G. Kallos • C. Kalogeri
Atmospheric Modeling and Weather Forecasting Group, Department of Physics, University of Athens, University Campus, Building Physics V, Athens, Greece

P.C. Chu
Department of Oceanography, Naval Postgraduate School, Monterey, CA 93943, USA

A. Charalambous
Cyprus Energy Agency, 20 Lefkonos str, Strovolos, Nicosia, Cyprus

K. Savvidou • S. Michaelides
Meteorological Service of Cyprus, 28 Nikis Avenue, Nicosia, Cyprus

C.G. Helmis and P.T. Nastos (eds.), *Advances in Meteorology, Climatology and Atmospheric Physics*, Springer Atmospheric Sciences,
DOI 10.1007/978-3-642-29172-2_13,

On the other hand, advanced statistical techniques are utilized for the local adaptation of the results and the estimation of the spatial and temporal distribution of the wave energy potential.

1 Introduction

During the last decade most of the developed European and American countries have set as a primary target the adaptation of novel policies and methodologies that will lead to a substantial increase of the use of renewable resources for energy production. The recent global economic crisis further strengthened this political decision leading to a reduced dependence of oil products. Within this framework, the exploitation of wave energy potential, that is the energy produced by the sea waves, seems to be one of the most promising solutions especially for countries with extended coastline like Greece and Cyprus.

Wave energy has some critical advantages compared to other renewable sources: it is far more stable than wind power and, therefore, it is easier to be merged into the general grid. Moreover, wave power can be produced even in the absence of local winds by exploiting the swell component of the waves while ecological damages or consequences appear negligible. Still, there are issues that should be taken into consideration in order to ensure the successful exploitation of this type of "clean" energy: The wave energy potential in the area of interest should be monitored in a credible way and local activities that could be affected (fisheries, touristic companies, marine structures, wildlife, hazards to navigation) must be taken into account.

In the present work, the main activities and results of two European projects dealing with wave energy potential estimation are presented. The E-wave project, coordinating by the Oceanography Centre of the University of Cyprus and the MARINA project, in which the Atmospheric Modeling and Weather Foreacting Group of the University of Athens is participating, focusing on the development and application of novel methodologies for the accurate estimation of the wave energy potential in the Mediterranean and the North Atlantic coastline of Europe. Towards this target, state of the art numerical atmospheric and wave simulation systems are utilized while novel statistical approaches are developed and exploited in order to support the credible monitoring of the wave energy potential in the areas of interest.

The present work is organized as follows: In Sect. 2 the main directions and components of the above mentioned projects are presented. The models and the techniques employed are discussed in Sect. 3, while some first results that have been reached are outlined in Sect. 4.

2 The Projects

The primary objectives and methodologies of the Marina and E-wave projects are outlined in this section. Special emphasis is given to the components relevant with the wave power estimation.

2.1 The E-Wave Project

In January 2011, a research project started in Cyprus focusing on the opportunities for exploitation of wave energy in the Eastern Mediterranean Sea with special emphasis to the Exclusive Economical Zone (EEZ) of Cyprus. The E-wave project is co-funded by the Republic of Cyprus and the European Regional Development Fund of the EU through the National Framework Programme for Research and Technological Development & Innovation 2009–2010 by the Research Promotion Foundation of Cyprus. It is coordinated by the Oceanographic Centre (University of Cyprus) while a number of research and operational groups participate: the Atmospheric Modeling and Weather Forecasting Group of the University of Athens, Greece (http://www.mg.uoa.gr), the Ocean Analysis Lab – USA Naval Postgraduate School (http://www.oc.nps.edu/~chu/noap.html), the Cyprus Energy Agency (http://www.cea.org.cy/), and the Meteorological Service of Cyprus (http://www.ms.moa.gov.cy). The duration of the project is 24 months.

The main aim of E-wave is the development of an integrated, fully operational high resolution system for monitoring the energy potential from sea waves at the EEZ of Cyprus and the wider eastern Levantine basin, coupled with the well-established Cyprus Coastal Ocean Forecasting System (CYCOFOS). The new system will include:

- A complete, high resolution digital atlas consisting of detailed maps for the coastal and offshore areas of the EEZ of Cyprus, in which sea wave and wind climatological characteristics as well as the distribution of the wave energy potential will be monitored.
- Novel models for the prediction and quantification of wave energy in short and long forecasts, a tool of significant value for grid designers and regulators.

More details for the E-wave can be found in the project's web page: http://www.oceanography.ucy.ac.cy/ewave/.

2.2 The MARINA Project

The Atmospheric Modeling and Weather Forecasting Group of the University of Athens participates in the Marine Renewable Integrated Application Platform (MARINA) project, with 16 other research groups and companies from 12 European countries. MARINA project is funded within the Seventh Framework Program for R&D of the European Union.

The main objective is to support the development of offshore deepwater structures in the Mediterranean and the North Atlantic coastline of Europe that can exploit the energy from wind, wave, tidal and ocean currents. In particular, novel criteria will be defined ensuring the successful integration and the development of innovative and viable new concepts. In this context a set of solutions are

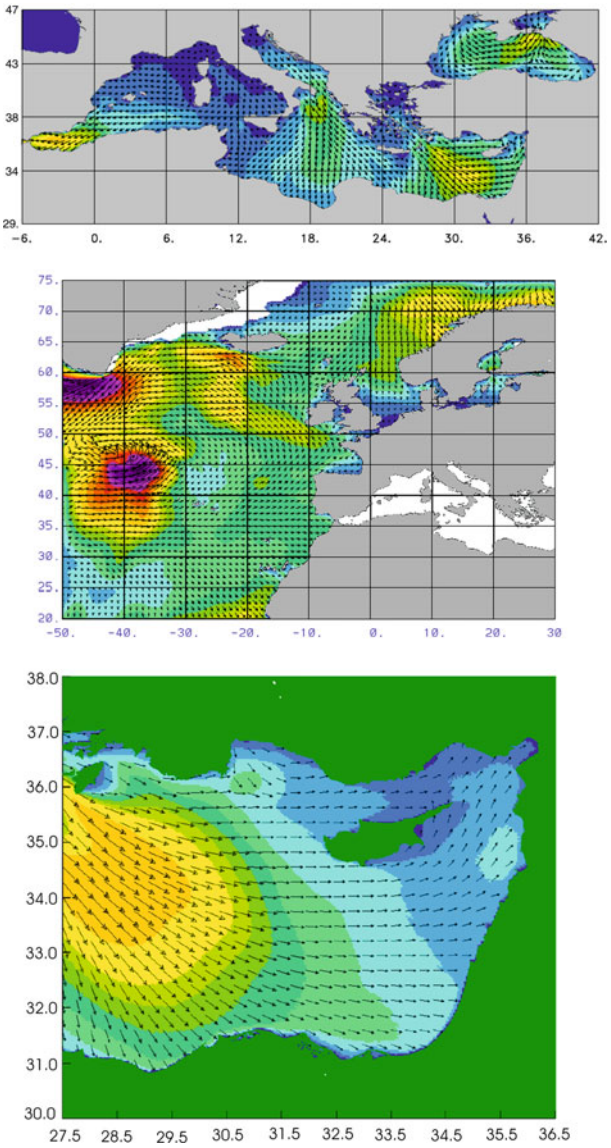

Fig. 1 The study area of the E-wave and the MARINA project

being investigated for: working principle, design, manufacturing, installation (including mooring and grid connection), operation and maintenance, and decommissioning (Fig. 1).

One of the most important effects to be accounted for is the coupling between wind- and wave-induced motions. Non-linear platform mechanics and hydrodynamic effects need to be modeled at different levels of approximation according to

the physics of the problem and the accuracy required. MARINA project will contribute in assessing the adequate level of approximation for such applications and will conduct risk assessments concerning safety, environment and survivability. Further details for the MARINA project can be found in the project's web site: http://www.marina-platform.info/.

3 Models and Methodologies

The objectives of both projects, described in the previous section, are essentially based on the accurate knowledge of the local wind and wave climate over the area of interest. The main tools that the research community utilizes today to obtain such information are based on physical and statistical numerical models that simulate the wind/wave evolution.

Within the framework of the E-wave and the MARINA projects, the atmospheric parameters required for the wind power estimation (e.g., wind speed, turbulence, atmospheric pressure) are provided by the regional atmospheric modeling system SKIRON (Kallos 1997). The high horizontal grid of the model configuration

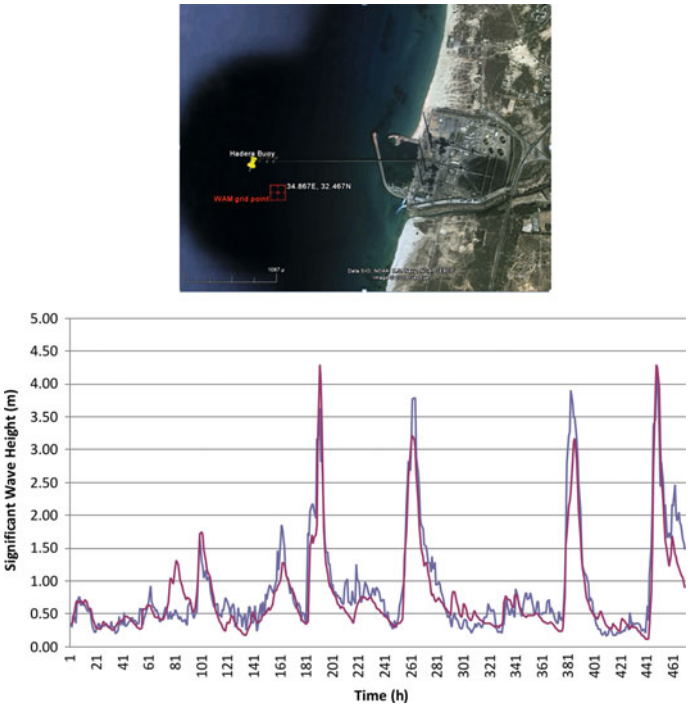

Fig. 2 Evaluation of the SWH in the framework of the E-wave project. The *blue line* corresponds to in-situ observation wave data and the *red* to the models corresponding outputs

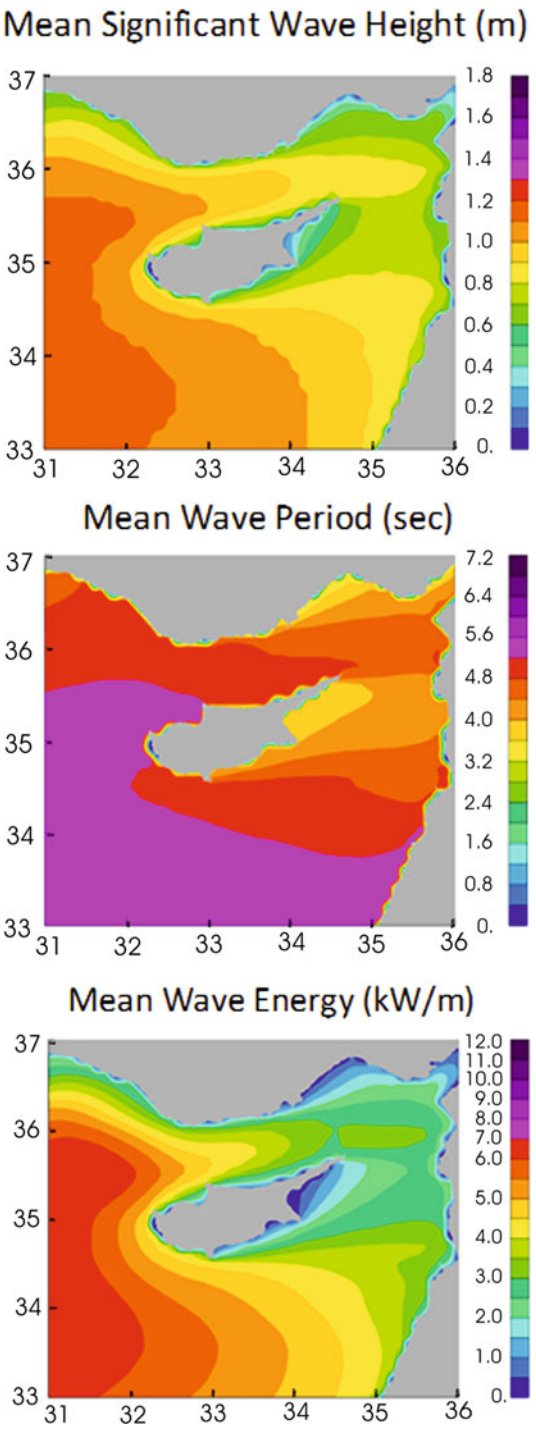

Fig. 3 Mean values of significant wave height, wave period and wave energy

(5 km × 5 km) allows the detailed description of the atmospheric fields and the provision of highly resolved atmospheric data.

Concerning the sea wave simulation, the latest version of the wave model WAM (WAMDIG 1988; Bidlot et al. 2007; Janssen 2000) is utilized at the same resolution. The model provides a number of integrated wave parameters (e.g. the significant wave height, mean and peak wave period, wind driven and swell components of the waves) that are crucial for the wave power estimation. Moreover, the full wave spectrum at specific preselected locations is also available.

The results of the above numerical models are compiled by a combination of statistical procedures – Kolmogorov-Zurbenko (KZ) and Kalman filters (Eskridge et al. 1997; Rao et al. 1997) – to remove possible biases and provide accurate wind and wave information and resource mapping. The Kalman filter, in particular, recursively combines observations and model simulations based on least square methods. The main advantage is the easy adaptation to new conditions and the

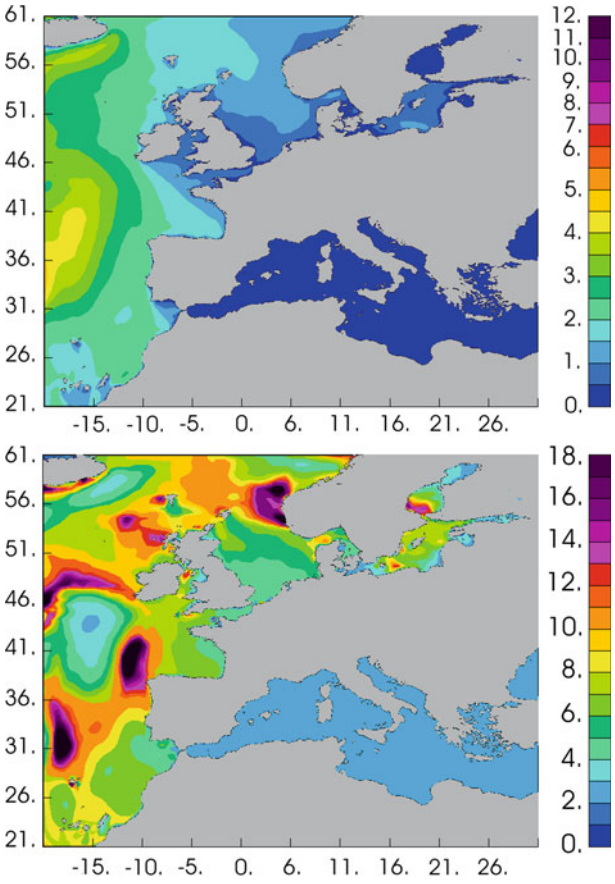

Fig. 4 The shape and scale parameter values of the Weibull distribution

limited background information needed. KZ filters, on the other hand, support the homogenization of the time series used and the removal of high frequencies and noisy intervals.

4 Results and Conclusions

Some preliminary results obtained within the framework of the MARINA and E-wave projects are presented here focusing on the wave characteristics over the areas under study and the corresponding distribution of the wave energy potential.

A first point that is worth noticing is the high accuracy of the wave simulations. A characteristic evaluation is presented in Fig. 2. It concerns the area of Hadera port in Israel where, despite the fact that the observational platform was located very close to the coastline – a fact that theoretically poses extra difficulties to an offshore system – the simulated and observed time series are almost identical.

Some characteristic results for the main wave parameters that affect the wave power estimation, i.e. the significant wave height and the mean wave period in the NE Levantine area for a period of 3 months are presented in Fig. 3.

Increased values of wave energy at the west coastline of Cyprus can be attributed to the prevailing swell waves in the area and the elevated values of Significant Wave Height (SWH). SWH values are well fitted by the Weibull distribution. However, the corresponding shape and scale parameters emerge a non-trivial spatial variation (Fig. 4).

The distribution of SWH is close to the usually adopted Rayleigh probability density function (shape parameter 2) near shores. However, it deviates offshore. On the other hand, increased scale parameter values are revealed near Spain and Norway. This spatial distribution is information of potential value for grid designers and researches working on wave energy issues.

Acknowledgments This work was supported by the E-wave project (funded by the Research Promotion Foundation of Cyprus, http://www.oceanography.ucy.ac.cy/ewave/) and the MARINA project (Seventh Framework Programme, Grant agreement number: 241402, http://www.marina-platform.info/).

References

Bidlot JR, Janssen P, Abdalla S, Hersbach H (2007) A revised formulation of ocean wave dissipation and its model impact. ECMWF Technical Memorandum 509. ECMWF, Reading, UK, 27pp

Eskridge RE, Ku JY, Rao ST, Porter PS, Zurbenko IG (1997) Separating different scales of motion in time series of meteorological variables. Bull Am Meteorol Soc 78(7):1473–1483. doi:10.1175/1520-0477(1997) 078<1473:SDSOMI>2.0.CO;2

Jansen PAEM (2000) ECMWF wave modeling and satellite altimeter wave data. In: Halpern D (ed.), Satellites, oceanography and society, Elsevier, New York, pp 35–36

Kallos G (1997) The regional weather forecasting system SKIRON. In: Proceedings, symposium on regional weather prediction on parallel computer environments, Athens, Greece, 9pp, 15–17 Oct 1997

Rao ST, Zurbenko IG, Neagu R, Porter PS, Ku JY, Henry RF (1997) Space and time scales in ambient ozone data. Bull Am Meteorol Soc 78(10):2153–2166. doi:10.1175/1520-0477(1997)078<2153:SATSIA>2.0.CO;2

WAMDIG, The WAM-Development and Implementation Group: Hasselmann S, Hasselmann K, Bauer E, Bertotti L, Cardone CV, Ewing JA, Greenwood JA, Guillaume A, Janssen PAEM, Komen GJ, Lionello P, Reistad M, Zambresky L (1988) The WAM model - a third generation ocean wave prediction model. J Phys Oceanogr 18(12):1775–1810

Delineation of Convective and Stratiform Rainy Clouds Based on Their Spectral and Textural Features on Meteosat Data

A. Giannakos and H. Feidas

Abstract In the present study two schemes were developed for the delineation of convective and stratiform clouds based on the high spectral resolution of the Meteosat Second Generation (MSG). Two classification methods were proposed that use spectral cloud parameters along with textural cloud parameters. The first model is an empirical algorithm based on the estimation of the probability of convective rainfall (PCR) for each pixel of the satellite data and the second is a statistical approach (Artificial Neural Network, ANN) based on the correlation of spectral and textural parameters with convective and stratiform rain. It was found that the introduction of textural parameters as additional information tends to improve the discrimination between convective and stratiform clouds for the models in the training and validation dataset. The PCR algorithm based on spectral and textural parameters shows the best performance among all the rain classification models for the training dataset. When evaluating against the independent dataset, the ANN model based on both spectral and textural parameters produces scores significantly better than the other rain classification algorithms. All algorithms overestimate the convective rain occurrences detected by the rain stations network.

1 Introduction

Convective and stratiform rain area classification algorithms applied to single channel infrared (IR) satellite data are based on the cloud top temperatures. In general, these IR techniques are most applicable for deep cold convective clouds in the Tropics. In order to overcome the difficulty of these single IR techniques to

A. Giannakos (✉) • H. Feidas
Department of Meteorology and Climatology, School of Geology, Aristotle University of Thessaloniki, 54124 Thessaloniki, Greece
e-mail: agiannas@geo.auth.gr

C.G. Helmis and P.T. Nastos (eds.), *Advances in Meteorology, Climatology and Atmospheric Physics*, Springer Atmospheric Sciences,
DOI 10.1007/978-3-642-29172-2_14,

distinguish convective from stratiform rain clouds in mid-latitudes, the contribution of more than one single channel is needed. The high spectral resolution of the Spinning Enhanced Visible and Infrared Imager (SEVIRI) on board the MSG satellites, offers the possibility of an improved discrimination between convective and stratiform rain areas.

The objective of this study is to investigate the contribution of the SEVIRI high spectral resolution to the classification of convective and stratiform precipitating clouds over Greece. Two kinds of techniques were proposed to develop the classification models that use spectral along with textural cloud parameters. The first model is an empirical algorithm based on the estimation of the probability of convective rainfall (PCR) for each pixel of the satellite data and the second is a statistical approach (ANN) relied on the correlation of spectral and textural parameters with convective and stratiform rain. Models' training and validation are carried out by comparing spectral and textural cloud parameters with rain gauge observations.

2 Data and Methodology

2.1 Data

In this study the convective/stratiform rain classification schemes were trained and validated using spatio-temporally matched 15 min SEVIRI observation datasets and rain gauge data for the area of Greece. SEVIRI datasets included seven infrared channels acquired at 15 min time intervals with a spatial resolution of 4×5 km^2 at the area of study. Rain gauge data from 88 stations of the National Observatory of Athens for 20 rainy days with convective activity from September 2008 to February 2009 were used as a reference to train the models. These cases were selected to cover the wet season in Greece and have adequate amounts of heavy rain, in order to give reliable statistics. Models were validated against six independent rainy days during the same period, which were not used for training the models.

Seven spectral parameters were used as cloud information from the SEVIRI thermal infrared satellite data: (a) Brightness temperature (BT) at the 10.8 μm channel ($BT_{10.8\ \mu m}$) is used to estimate the vertical extent of the cloud. (b) Brightness temperature difference (BTD) between the 10.8 and 12.1 μm channels ($BT_{10.8}$–$BT_{12.1}$) is a good indicator of the cloud optical thickness and is very effective in discriminating optically thick cumuliform clouds from cirrus clouds (Inoue et al. 2001). (c) BTD between the 8.7 and 10.8 μm channels ($BT_{8.7}$–$BT_{10.8}$) is used to gain information about the cloud phase (Thies et al. 2008). For ice clouds $BT_{8.7}$–$BT_{10.8}$ tends to be positive in sign, whereas for low-level water clouds, tends to be small negative. (d) The BTD between the 6.2 μm channel and the 7.3 μm channel ($BT_{6.2}$–$BT_{7.3}$) can give information about the cloud height and the early detection of convective activity. Low clouds tend to give large negative temperature differences while positive differences may occur for very high clouds reaching the

stratosphere. The $BT_{6.2}$–$BT_{7.3}$ difference is effective in distinguishing between high-level and mid-level clouds. (e) For low-level clouds the BTD between the 6.2 μm channel and the 10.8 μm channel ($BT_{6.2}$–$BT_{10.8}$) tends to be very negative while positive differences may occur for convective clouds (Lutz et al. 2003). (f) BTD between the 13.4 μm channel and the 10.8 μm channel ($BT_{13.4}$–$BT_{10.8}$) provides estimation of cloud top height and detection of cumulus cloud growth development. (g) The BTD between the 8.7 μm channel and the 12.1 μm channel ($T_{8.7}$–$T_{12.1)}$ can provide information about clouds' optical thickness. It exhibits high values for large cloud particle size and large optical thickness. (h) BTD between the 9.7 μm channel and the 13.4 μm channel ($T_{9.7}$–$T_{13.4}$) is an indicator of cloud top height that produces negative difference values for low level clouds while for high level clouds yields positive BTD values (Kwon et al. 2010).

Two different procedures were applied to calculate texture measures from MSG satellite data in the thermal infrared: (1) Brightness Temperature Level Co-occurrence Matrix (BTLCM) and (2) Brightness Temperature Level Difference Vector (BTLDV). The SEVIRI datasets were spatially and temporally collocated with rain gauge observations. Each rain observation was classified as convective or stratiform using a rain rate threshold value of 3 mm/h. This value was chosen because it gives comparable amounts of convective and stratiform rain for most cases, and thus provides more reliable statistics. Furthermore the values of each spectral and textural cloud parameter were divided into two parts based on the categorical dichotomous statement of "convective/stratiform rain". Four texture parameters were finally used in the classification models, after rejecting textural measures exhibiting high correlations: (1) Homogeneity, (2) Contrast, (3) Angular Second Moment, and (4) BTLDV Entropy.

2.2 Methodology

Two different schemes were used to develop convective/stratiform rain type classification models. The PCR1 scheme is computed as a function of the value combinations of the eight spectral variables. The same technique was applied using both the spectral and the textural parameters (PCR2). The PCR is calculated as a function of the different variables $x_1, x_2, \ldots, x_i$:

$$PCR(x_1, x_2, ..., x_i) = \frac{Nconvective(x_1, x_2, ..., x_i)}{Nconvective(x_1, x_2, ..., x_i) + Nstratiform(x_1, x_2, ..., x_i)} \quad (1)$$

where $i = 8$ for PCR1 and $i = 12$ for PCR2 model, $x_1, x_2, \ldots, x_i$ denote the spectral and textural variables and $N_{convective}$ and $N_{stratiform}$ are the numbers of convective and stratiform raining pixels, respectively, in each distinct interval in the $(x_1, x_2, \ldots, x_i)$ space (Thies et al. 2008). Then, an i-dimensional contingency matrix is constructed based on the PCR value and each pixel is flagged as a "convective" or "stratiform" if PCR is exceeding a lower threshold.

The second technique was based on ANN Multilayer Perceptron (MLP) scheme that approximates the best nonlinear function between spectral and textural features of satellite data and convective/stratiform rain information to classify rain clouds. Two MLP models were created, using 8 spectral parameters (MLP1) and 12 spectral and textural cloud parameters (MLP2), respectively.

3 Results

3.1 Models' Training

The statistical measures POD, FAR, POFD, BIAS, CSI, ETS and HK were computed by applying the PCR and MLP algorithms for the 20 convective rainy days (Table 1). PCR2 model has the best overall performance (POD = 79.4%, FAR = 43.6%, POFD = 38.8%) during the training phase, followed at a short distance by PCR1, while the worst scores are obtained for MLP1. It seems that the addition of the textural parameters into a model improves the discrimination between convective and stratiform rain clouds for both PCR2 and MLP2 models.

3.2 Models' Validation

The rain events chosen for the evaluation phase are independent from the rain events used to train the models. The results of the verification analysis are presented in Table 2. The MLP2 model performs best among the four algorithms for the validation dataset. MLP1 model shows the second best performance followed by the two PCR models. More precisely, the best skilled MLP2 algorithm for the validation dataset correctly identifies the 73.8% (POD) of the convective rain

Table 1 Verification scores computed from MLP1 and MLP2 algorithms during the training phase

Models	POD	FAR	POFD	BIAS	CSI	ETS	HK
PCR1	77.9	46.3	40.2	1.48	0.373	0.184	0.377
PCR2	79.4	43.6	38.8	1.54	0.386	0.197	0.406
MLP1	73.2	47.8	41.3	1.65	0.327	0.168	0.319
MLP2	75.6	45.8	37.6	1.73	0.336	0.181	0.38

Table 2 Verification scores computed for the four models during the evaluation phase

Models	POD	FAR	POFD	BIAS	CSI	ETS	HK
PCR1	68.4	51.5	46.4	1.55	0.316	0.123	0.22
PCR2	70.4	49.3	43.7	1.62	0.322	0.15	0.267
MLP1	72.5	44.2	41.9	1.69	0.308	0.156	0.306
MLP2	73.8	42.6	39.5	1.77	0.325	0.167	0.343

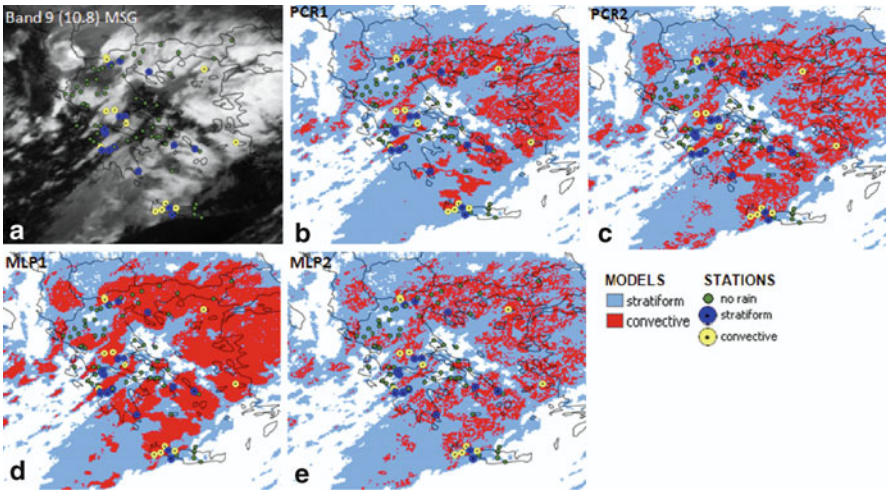

Fig. 1 (**a**) SEVIRI brightness temperature at the 10.8 μm channel and classified rain area by (**b**) PCR1, (**c**) PCR2, (**d**) MLP1 and (**e**) MLP2 models, for February 12, 2009 at 17:00 UTC

occurrences whereas it misclassifies as convective rain cases the 42.6% (FAR) of the estimates and the 39.5% (POFD) of the observed stratiform events. The MLP2 overestimates the rain occurrences detected by the rain stations network, as indicated by the bias of 1.77**.** The PCR1 algorithm during the evaluation phase exhibits the worst scores with the highest FAR (51.5%) and POFD (46.4%) values among the four convective detection models.

The classified rain area derived by the four detection schemes for a scene at 17:00 UTC, February 12, 2009, is shown in Fig. 1. In general PCR1 model tends to assign connective pixels to the cold and uniform parts of the cloud whereas these convective pixels are reduced when using textural data as additional information in PCR2. At the same time, more convective pixels are assigned to the rugged and uneven parts of the cloud tops. The convective rain area delineated by MLP1 model is considerable larger than the actual convective rain area defined by gauges. This area becomes significantly smaller with the MLP2 model as a result of a better discrimination of non-convective uniform cloud tops from their convective uneven parts.

4 Conclusions

The training and validation of the convective/stratiform rain classification models based on spectral parameters showed that the use of MSG SEVIRI channels in the thermal infrared gives encouraging results for the detection of convective rain clouds in the mid-latitudes. The incorporation of textural cloud parameters increased the performance in the discrimination between convective and stratiform

rain clouds. The algorithms based on both spectral and textural parameters generally produce better verification scores than the algorithms based on spectral parameters alone and provide improved convective rain area detection skill. Between the two schemes validated in this study, ANN algorithms seem to outperform the PCR algorithms. Finally, all schemes clearly overestimate the convective rain occurrences detected by the rain stations for both the training and validation dataset.

Acknowledgments This research has been co-financed by the European Union (European Social Fund – ESF) and Greek national funds through the Operational Program "Education and Lifelong Learning" of the National Strategic Reference Framework (NSRF) – Research Funding Program: Heracleitus II. Investing in knowledge society through the European Social Fund. The authors also wish to thank the National Observatory of Athens for providing the precipitation data.

References

Inoue T, Wu X, Bessho K (2001) Life cycle of convective activity in terms of cloud type observed by split window. In: Proceedings of 11th conference on satellite meteorology and oceanography, Madison, WI, USA

Kwon E, Sohn B, Schmetz J, Watts P (2010) Intercomparison of height assignment methods for opaque clouds over the tropics. J Atmos Sci 46:11–19. doi:10.1007/s13143-010-0002-7

Lutz H, Inoue T, Schmetz J (2003) Comparison of a split-window and a multi-spectral cloud classification for MODIS observations. J Meteorol Soc Jpn 81:623–631

Thies B, Nauss T, Bendix J (2008) Discriminating raining from non-raining cloud areas at mid-latitudes using meteosat second generation SEVIRI night-time data. J Meteorol Appl 15:219–230. doi:10.1002/met.56

Development of a Modeling System for Urban Heat Islands: An Application to Athens and Thessaloniki, Greece

T.M. Giannaros, D. Melas, I. Keramitsoglou, and I.A. Daglis

Abstract The urban heat island (UHI) is one of the most well known forms of localized, inadvertent anthropogenic climate modification. The study of urban climate problems, such as the UHI, is possible through the implementation of numerical models. In this context, numerical weather prediction models are thought to be a significant supporting tool with a wide area of successful applications for studying the UHI effect. The current paper aims to present the development of a numerical modeling system that could be used for forecasting the UHI and its impacts on human thermal comfort. The modeling system is based on the mesoscale meteorological Weather Research and Forecasting (WRF) model. Major innovations include the incorporation of high resolution land use data, the use of satellite data for defining land surface parameters, and the development of a downscaling mask for increasing the spatial resolution. The modeling system was evaluated against ground-based data during selected dates in summer 2010 for the cities of Athens and Thessaloniki. The estimated average bias of the model in terms of air temperature simulation was found to approximate $\pm 1^{\circ}$C.

1 Introduction

Over the past decade we have witnessed significant progress in urban surface modeling (e.g. Masson 2006). As a result, mesoscale meteorological models coupled with urban canopy parameterizations are increasingly used to examine the structure of

T.M. Giannaros (✉) • D. Melas
Laboratory of Atmospheric Physics, Aristotle University of Thessaloniki, 54124 Thessaloniki, Greece
e-mail: thgian@auth.gr

I. Keramitsoglou • I.A. Daglis
Institute for Space Applications and Remote Sensing, National Observatory of Athens, 15236 Athens, Greece

C.G. Helmis and P.T. Nastos (eds.), *Advances in Meteorology, Climatology and Atmospheric Physics*, Springer Atmospheric Sciences,
DOI 10.1007/978-3-642-29172-2_15,

the urban boundary layer (UBL). In particular, an intensive effort has been carried out for the mesoscale meteorological Weather Research and Forecasting (WRF) model to improve its skills over urban areas for assessing environmental problems such as the urban heat island (UHI). Up to nowadays, the WRF model has been extensively used to study the UHI effect in many cities (e.g. Lin et al. 2008; Miao et al. 2009; Shem and Sheperd 2009). A review of the applications of the WRF modeling system for studying the urban environment can be found in Chen et al. (2011).

The purpose of this paper is to present the development of a modeling system for UHI and its application over two major cities in Greece: Athens and Thessaloniki. The modeling system is built around the WRF model, properly modified to allow for the more accurate representation of urban processes. The overall performance of the model, in terms of predicting the near-surface air temperature, is evaluated during selected dates in summer 2010.

2 Modeling System Description and Application

The meteorological model used for the development of the modeling system is WRF-ARW, version 3.1.2. A detailed description of the model can be found in Skamarock et al. (2008).

2.1 Model Configuration and Physics

Four one-way nested modeling domains with horizontal grid resolutions of 30-km (D01; mesh size of 199 $\times$ 175), 10-km (D02; mesh size of 214 $\times$ 175), and 2-km (D03 and D04; mesh sizes of 76 $\times$ 76 and 56 $\times$ 56, respectively) are specified. The outermost 30-km domain covers the entire European continent and is used for simulating large-scale meteorological conditions. The inner three domains with finer resolutions are used to simulate meso-scale and local-scale features, of which the innermost two domains focus on the study areas: Athens and Thessaloniki. All modeling domains have 33 layers in the vertical dimension. The lowest layer is at approximately 10 m above ground level (AGL), while the model top is defined at 100-hPa with radiative boundary conditions for all domains. Standard WRF physics options for microphysics, cumulus convection, short-wave and long-wave radiation, and boundary layer parameterization are used.

Land surface processes are parameterized using the advanced Noah land surface model (LSM). The Noah LSM is a four-layer soil temperature and moisture model with canopy moisture and snow cover prediction. It is also enhanced with a simple urban parameterization based on the bulk roughness approach of Liu et al. (2006). It has been widely used for studying the UHI effect (e.g. Miao et al. 2007).

2.2 Model Modifications and Adjustments

In the coupled WRF/Noah modeling system, land use is one of the primary variables that controls land surface processes. The importance of land use in mesoscale simulations has been demonstrated in earlier studies, such as the ones of Cheng and Byun (2008), Foy et al. (2006), Lin et al. (2008), and Lo et al. (2007).

With this in mind, the original 1-km resolution U.S. Geological Survey (USGS) 24-category land use data were replaced by the 250-m resolution European Environment Agency (EEA) CORINE land use (CLC) data. Based on this improvement, satellite remote sensing data were used to define more realistic values for the key land surface properties, including albedo, emissivity, roughness length and green vegetation cover.

The UHI is a local-scale urban effect and as such, its study requires the conduction of high spatial resolution simulations. Taking this into account, artificial neural networks (ANN) were employed to develop a statistical downscaling mask that allows for increasing the spatial resolution of the modeled 2-m air temperature field. For each study area, an ANN was designed and trained to predict air temperature at 250-m resolution. The proxy data used for the training of the ANNs include the original 2-km modeled air temperature data, time of the day, and 250-m EEA CLC data. A preliminary evaluation of the performance of the downscaling ANN over the city of Athens was presented by Daglis et al. (2010).

2.3 Model Initialization and Application

In the present study, the modeling system is initialized using the $0.5^\circ \times 0.5^\circ$ spatial resolution and 6-h temporal resolution global operational atmospheric forecasts (GFS) provided by the U.S. National Centre for Environmental Predictions (NCEP). Soil moisture and temperature data used in the Noah LSM are also initialized from the NCEP forecasts.

84-h simulations were carried out operationally, on a daily basis, covering the time period from 0000 UTC 01 July through 2300 UTC 31 August 2010 and providing output at hourly intervals. The first 12 h of each 84-h simulation are discarded as the model's spin-up period. The remaining 72 h are used for carrying out the evaluation of the modeling system.

2.4 Evaluation Methods

The observational data used for the evaluation of the modeling system were collected during the period from 0000 UTC 15 August to 2300 UTC 17 August 2010. During this time period, both study areas were affected by a heat wave.

In Athens, 2-m air temperature observations were collected from seven stations belonging to the network of stations of the Hydrological Observatory of Athens, operated by the National and Technical University of Athens. In Thessaloniki, observational data were collected from three stations belonging to the network of stations operated by the Laboratory of Atmospheric Physics of the Aristotle University of Thessaloniki.

The downscaled model results for Athens and Thessaloniki are horizontally interpolated onto the respective observational sites using bilinear interpolation. The interpolated model results are compared against observations. Several model performance statistics are computed, including: (a) the mean bias error (MBE), (b) the root mean squared error (RMSE), (c) the index of agreement (IOA), (d) the hit rate (HR), and (e) the Pearson correlation coefficient. The criterion for the calculation of the HR in the present study is for model-observation agreement within 2°C (Cox et al. 1998).

3 Results and Discussion

Tables 1 and 2 summarize the computed model performance metrics for the 2-m air temperature, in Athens and Thessaloniki, respectively. The modeling system is found to be biased cold over both study areas. As it would be expected, the model performs better during the first day and worse during the last day of the forecast period. However, the calculated statistics indicate that the modeling system performs better over Athens than over Thessaloniki. This could be due to the performance of the corresponding downscaling ANN, which depends strongly on the availability of observational data during the training phase. For the city of Athens, such data were available at higher spatial and temporal resolution than for the city of Thessaloniki.

Table 1 Model performance statistics computed for 2-m air temperature, for Athens

Day	MBE	RMSE	IOA	HR	R
15/08/2010	−0.48	1.71	0.84	0.79	0.88
16/08/2010	−0.38	1.83	0.83	0.74	0.87
17/08/2010	0.43	2.33	0.76	0.59	0.79
Overall	−0.15	1.97	0.81	0.71	0.84

Table 2 Same as Table 1, but for Thessaloniki

Day	MBE	RMSE	IOA	HR	R
15/08/2010	−1.05	1.75	0.80	0.72	0.87
16/08/2010	−1.10	1.78	0.74	0.71	0.87
17/08/2010	−1.67	2.36	0.69	0.54	0.89
Overall	−1.27	1.97	0.75	0.66	0.86

Table 3 Model performance statistics computed for 2-m UHI intensity, for Athens

Day	MBE	RMSE	IOA	HR	R
15/08/2010	0.07	0.63	0.40	1.00	0.61
16/08/2010	0.11	0.74	0.30	1.00	0.70
17/08/2010	0.01	0.94	0.44	0.96	0.56
Overall	0.06	0.77	0.44	0.99	0.59

Table 3 presents a compilation of the calculated model performance statistics for 2-m UHI intensity (UHII) in Athens. The UHII is defined as the spatially averaged temperature difference between urban and rural areas that share similar topographic features (Kim and Baik 2005). In this study, the definition of urban and rural areas is based on the model-resolved land use in the finest resolution domains (D03). Measuring locations with significantly different topographic features (e.g. elevation) are excluded from the UHII computation. Unfortunately, this analysis was not carried out for Thessaloniki due to the limited number of observational sites, which could not be considered as representative of either urban or rural conditions.

As seen in Table 3, the model simulates successfully the magnitude of the UHII (low MBE and RMSE values). On the other hand, it appears that the model lacks ability in capturing the phase of the diurnal cycle of the UHII (moderate R values). This could be due to a number of reasons, mainly related to the simulation of the surface energy budget of urban and rural areas. However, because of the unavailability of detailed energy budget measurements, the actual causes for this model behavior cannot be speculated.

4 Conclusions

This study presents the development of a modeling system for UHI. The main components and key features of the system include the coupled WRF/Noah modeling system, the use of high-resolution land use data and satellite-derived land surface properties data, and the implementation of a statistical downscaling mask, built on the basis of ANNs. The performance of the modeling system in terms of near-surface air temperature and UHII prediction is evaluated using in situ data during a 3-day period in August 2010. The evaluation results reveal that the model performs reasonably well over the study areas, showing a cold bias ranging from $-0.15°C$ (Athens) to $-1.27°C$ (Thessaloniki). The computed statistics indicate that the performance of the modeling system may depend on the availability of observational data for training the downscaling ANNs. The model is also found to simulate the magnitude of the UHII in Athens very well, showing an average bias close to zero. The calculated correlation coefficients between simulated and observed UHII values reveal that the model may not simulate accurately enough the energy budgets of urban and rural areas.

Acknowledgments This work was supported by the European Space Agency (ESA) Contract 21913/08/I-LG for the project "Urban Heat Islands and Urban Thermography (UHI)".

References

Chen F, Kusaka R, Bornstain J et al (2011) The integrated WRF/urban modeling system: development, evaluation, and applications to urban environmental problems. Int J Climatol 31:273–288. doi:10.1002/joc.2158

Cheng FY, Byun DW (2008) Application of high resolution land use and land cover data for atmospheric modeling in the Houston-Galveston metropolitan area, part I: meteorological simulation results. Atmos Environ 42:7795–7811. doi:10.1016/J.Atmos Env. 2008.04.055

Cox R, Bauer BL, Smith T (1998) Mesoscale model intercomparison. Bull Am Meteorol Soc 79:265–283. doi:http://dx.doi.org/10.1175/2010MWR3523.1

Daglis IA, Rapsomanikis S, Kourtidis K et al (2010) Results of the DUE THERMOPOLIS campaign with regard to the urban heat island (UHI) effect in Athens. In: Proceedings of the ESA living planet symposium, Bergen, Norway, 28 June–2 July 2010

Foy B, Molina LT, Molina MJ (2006) Satellite-derived land surface parameters for mesoscale modeling of the Mexico city basin. Atmos Chem Phys 6:1315–1330. doi:10.5194/acpd-5-9861-2005

Kim YH, Baik JJ (2005) Spatial and temporal structure of the urban heat island in Seoul. J Appl Meteorol 44:591–605. doi:10.1175/JAM2226.1

Lin CY, Chen F, Huang JC, Chen WC, Liou YA, Chen WN, Liu SC (2008) Urban heat island and its impact on boundary layer development and land-sea circulation in northern Taiwan. Atmos Environ 42:5635–5649. doi:10.1016/J.Atmos Env. 2008.03.015

Liu Y, Chen F, Warner T, Basara J (2006) Verification of a mesoscale data-assimilation and forecasting system for the Oklahoma city area during the Joint Urban 2003 field project. J Appl Meteorol Climatol 45:912–929. doi:10.1175/JAM2383.1

Lo JCF, Lau AKH, Chen F, Fung JCH, Leung KKM (2007) Urban modification in a mesoscale model and the effects on the local circulation in the Pearl River Delta region. J Appl Meteorol Climatol 46:457–476. doi:10.1175/JAM2477.1

Masson V (2006) Urban surface modeling and the meso-scale impact of cities. Theor Appl Climatol 84:35–45. doi:10.1007/s00704-005-0142-3

Miao S, Chen D, Borne K (2007) Evaluation and comparison of Noah and Pleim-Xiu land surface models in MM5 using GOTE2001 data: spatial and temporal variations in near-surface air temperature. J Appl Meteorol Climatol 46:1587–1605. doi:10.1175/JAM2561.1

Miao S, Chen F, LeMone MA, Tewari M, Li Q, Wang Y (2009) An observational and modeling study of characteristics of urban heat island and boundary layer structures in Beijing. J Appl Meteorol Climatol 48:484–501. doi:10.1175/2008JAMC1909.1

Shem W, Shepherd M (2009) On the impact of urbanization on summertime thunderstorms in Atlanta: two numerical model case studies. Atmos Res 92:172–189. doi:10.1016/J.Atmos Res. 2008.09.013

Skamarock WC, Klemp JB, Dudhia J et al (2008) A description of the advanced research WRF version 3. NCAR Technical Note (NCAR/TN-475+STR), Boulder, CO

Using Synoptic Classification to Evaluate an Operational Weather Forecasting System

F. Gofa, D. Tzeferi, and A. Raspanti

Abstract Verifying forecast quality over extended periods, i.e. monthly, seasonally or annually, can provide misleading results since performance is averaged over a wide range of meteorological conditions. The danger is that differences in forecast quality can be masked or results can be biased when the data are not homogeneous, even in terms of flow regimes. A relevant weather classification scheme must therefore be developed and applied. The aim of the study is to identify weather situation-dependent weaknesses and strengths of the COSMOGR model that is used operationally at the Hellenic National Meteorological Service (HNMS). A tailor-made weather classification was constructed focusing mainly on the origin of the air masses that are responsible for the presence of certain weather regimes in the region. The period between December 2009 and June 2011 was categorized and the model outputs were subsequently verified, with a particular emphasis on the predicted precipitation, cloudiness and temperature.

1 Introduction

With the multiplicity of weather prediction models and their fast-growing evolution, it is sometimes difficult for the forecaster to have an objective opinion regarding their quality. Verification analysis issued by the modelers is often not precise enough to be used as a guideline for a correct forecast. Verification is carried out to analyze the general skill of a model either over a large area or over a very long period of time. On the one hand, the forecaster would like to know when they can trust the model, on the other hand, the modeler would like to know when

F. Gofa (✉) • D. Tzeferi
Hellenic National Meteorological Service (NHMS), Athens, Greece
e-mail: fgofa@hnms.gr

A. Raspanti
Italian Meteorological Service (USAM), Roma, Italy

C.G. Helmis and P.T. Nastos (eds.), *Advances in Meteorology, Climatology and Atmospheric Physics*, Springer Atmospheric Sciences,
DOI 10.1007/978-3-642-29172-2_16,

the model is not performing well in order to make improvements. To answer these questions, it is necessary to differentiate between different weather situations. This kind of differentiated evaluation is achieved by appropriately stratifying the verification dataset.

One might suspect that the performance in winter and in summer could be different, or that, for instance, model performance in anticyclonic conditions may differ from that in a vigorous northerly flow. These differences may depend on the geographical location, especially with respect to the presence of a land-sea border or mountains. Monthly, seasonal and annual statistical verifications are limited in that their performance is averaged over the whole spectrum of weather types the atmosphere can produce. The danger is that they can mask differences in forecast quality when the data are not homogeneous, even in terms of flow regimes.

During this study, a weather-based stratification was applied before the verification process took place. In this way, systematic model errors during the various synoptic situations could be identified. The Hellenic National Meteorological Service (HNMS) operates a high-resolution Numerical Weather Prediction system (COSMO-GR) that provides detailed deterministic forecasts for an extended area around Greece on a daily basis. The verification is performed with state-of-the art software called VERification System Unified Survey (Gofa et al. 2010). The VERSUS software was developed as a unified tool capable of performing standard operational verification, conditional operational verification as well as experimental verification, in both batch and interactive model.

2 Methodology of Classification

A weather type classification is a method which distinguishes between meteorological situations describing them in accordance with circulation parameters (e.g. zonality, cyclonality, position of low and high pressure systems, etc.) or local weather elements such as temperature or precipitation. Circulation parameters are often preferred since such parameters can be used very easily to relate certain features of the atmospheric circulation with local weather by statistical methods. The large number of different methods applied for classification of weather types implies open challenges to the meteorological-climatological communities (Maheras 1988). The type of classification is usually adapted to a specific region and is not easily transferable to another region, or it is focused on the analysis of a specific problem so the temporal and spatial scales are adjusted accordingly.

With the aim of gaining a better understanding of model behavior for the various types of weather that influence our area, a subjective classification was adopted that is based mainly on the basic circulation patterns that the forecasters at HNMS come across in their daily experience. This tailor-made classification scheme comprises 12 different weather classes which describe the synoptic situation of the 500 hPa at 12 UTC on a daily basis, with a geographical focus on the Greek region. These

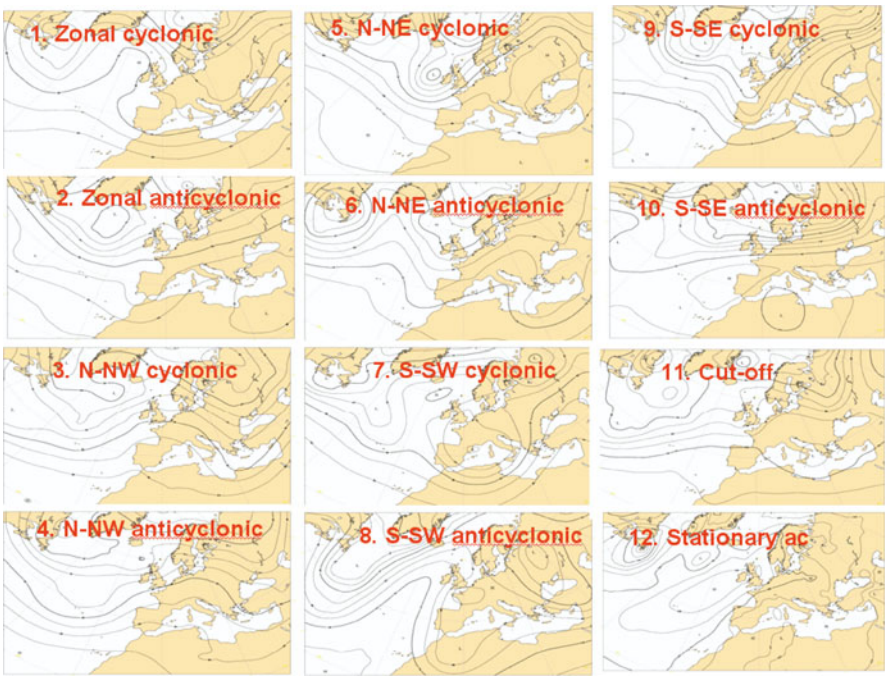

Fig. 1 Graphical representation of the weather classes used

Table 1 Percentage of days in each weather regime (total number of days 577)

Zonal C	Zonal AC	N-NW C	N-NW AC	N-NE C	N-NE AC	S-SW C	S-SW AC	S-SE C	S-SE AC	Cut-off low	Stat/ry AC
28	14	10	2	2	1	21	6	1	1	11	4

classes roughly separate the different weather situations into advective classes (e.g. *northwest*, *southeast*) and the accompanied convective classes *anticyclonic* and *cyclonic*.

Each of these categories is related to specific weather phenomena, the intensity and amplitude of which depend greatly on the season. The categories used are presented in Fig. 1 with an example of the graphical representation of the circulation. The time period covered by the study was 1 December 2009 to 30 June 2011.

Table 1 shows the relative percentage of days that fall into each weather category. Particular attention must be given to gathering large enough samples to provide trustworthy verification results, i.e. interpretation of verification results for classes ‘N-NE’ and ‘S-SE’ for both convective classes is limited.

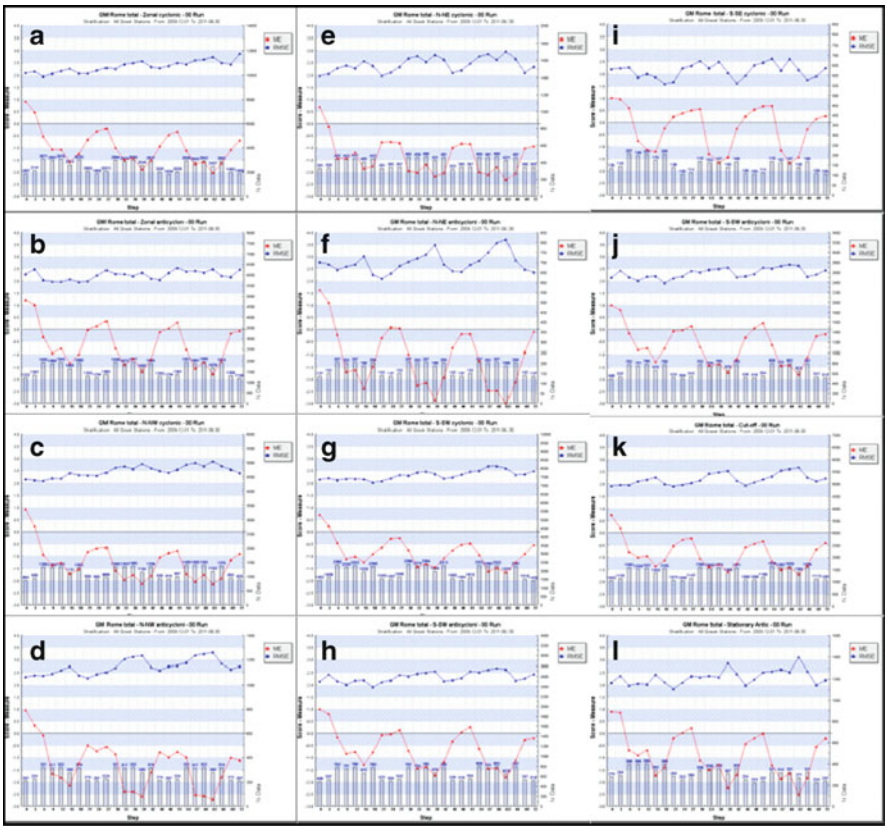

Fig. 2 2 m temperature verification of stratified forecasts against 80 weather stations

3 Results

The following section presents some of the results of the verification of the continuous and non-continuous surface parameters for the period: December 2009–June 2011. The verification of continuous variables (e.g. T2m, Td2m, MSLP, wind speed) is typically performed using statistics that show the degree to which the forecast values differ from the observations. The Mean Error (ME) and the Root Mean Square Error (RMSE) are simple indices that provide useful information about the model's performance for a given weather parameter for a given location. Thus, for all continuous weather parameters, 3-hourly forecast values for a horizon of 72 h of the 00 UTC model runs were compared against the respective SYNOP data.

Looking at the overall 2 m temperature verification graphs (Fig. 2) for each classification class, one can identify some characteristics common to all classes. These include the distinct daily cycle of both Bias and RMSE and the general trend

of underestimation of temperature by the forecast model. Looking into characteristics that are related to each circulation, it can be noted that for the northern weather systems (Fig. 2c–f), there is a colder bias (underprediction) of the 2 m temperature in comparison with the weather systems originating from the south. The value of ME is respectively a bit higher, and in general terms the model has a discrepancy of approximately 2–3°C.

A similar analysis was performed for the 10 m wind speed but is not presented here due to space limitations. The forecasted wind speed exhibits a general overestimation for all classes, but the error was significantly reduced for all anticyclonic convective classes. A weather parameter that most if not all NWP models fail to predict correctly is the amount of clouds. COSMO-GR produces subgrid scale cloudiness using an empirical function that depends on relative humidity and height. Looking the calculated BIAS and RMSE for each weather type (Fig. 3), we can see large differences in the ability of the model to correctly estimate the amount of clouds for each weather pattern. The error seems to be connected mainly with the cyclonality with improved performance during the passage of low pressure systems versus stable anticyclonic conditions.

Precipitation is commonly accepted as the most difficult weather parameter to correctly predict in terms of its spatial and temporal structure due to its stochastic behavior and any connection with specific weather systems is greatly appreciated by forecasters. The 12 h-hour precipitation amounts were verified for this study and the thresholds for the precipitation amounts ranged from 0.2 mm up to 30 mm accumulated over each time interval. For each threshold a number of scores were calculated that provide insight into model behaviour, the most representative of which are shown in Fig. 4.

The Frequency Bias (FBI) is a measure of comparison between the frequency of forecasts to the frequency of occurrences (range: 0–∞, perfect score $= 1$, FBI > 1 indicates over-forecast) while the Equitable Threat Score (ETS) is a measure of the fraction of correctly predicted events, adjusting for random hits (range: $-1/3$ to 1, perfect score $= 1$). In the case of precipitation, statistical indexes worsen when model resolution is increased as it produces better defined mesoscale structures, higher amplitude features and larger gradients, and inevitably leads to increased spatial and temporal errors. The results indicate that the COSMO-GR model performs well for the thresholds corresponding to small amounts of precipitation, but it fails to accurately predict large rainfall events. In cases that there was precipitation during a substantial number of days, FBI index results indicate that there is an overprediction for the lower thresholds during all cyclonic circulations, independent of the origin of the system, meaning that the model was giving us more often precipitation than truly occurred. On the other hand, the model underforecasts precipitation during heavy rainfall events (>8 mm), especially during anticyclone circulations. The ETS index, which provides a measure of the general performance of the model, reduces dramatically as the precipitation threshold increases. After measuring this index for all the statistically significant weather classes, it was discovered that precipitation forecasts were more successful for weather systems

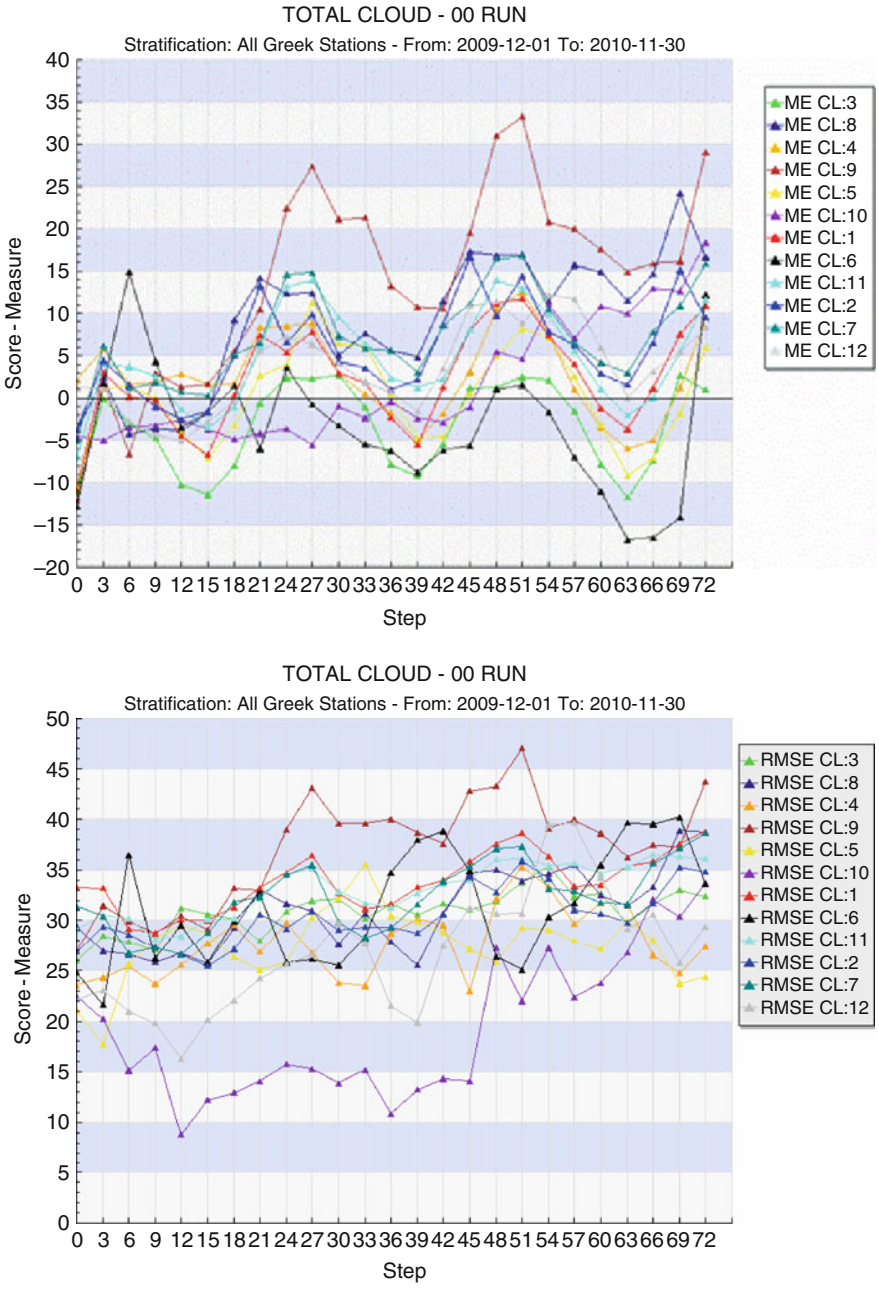

Fig. 3 Cloud cover: BIAS (*left*) and RMSE (*right*) values for all weather classes

Fig. 4 FBI (*two left columns*) and ETS (*two right columns*) for 12 h precipitation forecasts

originating from the south-west, but this behavior can only be better understood if a seasonal analysis is performed.

4 Conclusions

A systematic weather situation-dependent comparison of forecast weather parameters with synoptic station measurements has been presented for the period of 2010–2011. In summary, the analysis identified: a colder bias of the 2 m temperature during the passage of weather systems originating from the north, a reduced 10 m wind speed error for all anticyclonic convective classes, an improved performance of cloud cover prediction when low pressure systems are present and, finally, an overprediction of the precipitation for all cyclonic circulations for the lower thresholds of precipitation, independent of the origin of the system. The limitations of this study are related to the lack of large samples for every weather class. Moreover, the weather classification scheme that was followed is not specifically geared to a specific weather parameter and may, therefore, not be the optimal choice every time.

References

Gofa F, Raspanti A, Charantonis T (2010) Assessment of the performance of the operational forecast model COSMOGR using a conditional verification tool. In: Proceedings of 10th COMECAP conference of meteorology, Hellenic Meteorological Society, Patras, Greece

Maheras P (1988) The synoptic weather types and objective delimitation in the winter period in Greece. Weather 43:40–45

MODIS Data for Monitoring RedScale (*Aonidiella aurantii*) Population: The Development of a Regression Model Using Temperature Measurements from Satellite and Meteorological Stations

D.G. Hadjimitsis, A. Agapiou, and A. Papachristodoulou

Abstract The aim of the "RedScale ID" research program which is funded by the CRPF is to develop an automated, energy-independent trap for continuous monitoring/identification of the RedScale population and in addition to record other relevant parameters related to the population. Such kind of parameter is temperature which is related to day-degrees growth calculation for estimating RedScale population. For this purpose MODIS satellite image data were used in order to estimate LST and then to correlate with air surface temperature. The use of satellite data has many advantages against traditional techniques such as local meteorological stations located in agricultural areas, since they can provide a synoptic coverage on a systematic daily basis. From the statistical regression analysis between the satellite images MODIS LST product for the year 2010 with data from 47 meteorological stations in Cyprus, it has been found that satellite images can accurate estimate air surface temperature. From the linear regression model, a high correlation coefficient $R^2 \approx 0.77$ was found. By categorizing observations acquired at an altitude of 100–200 m the correlation coefficient was improved up to 0.87. Seasonal regression analysis will be performed in the near future.

1 Introduction

"*Aonidiella aurantii*" or red scale is an armored scale insect and a major pest of citrus (Fig. 1). They are found on all parts of the plant but are most noticeable on the fruit. Heavy infestations may cause discolouration, shoot distortion and leaf drop. The fruit may become pitted and unmarketable. The tree's bark may split and the twigs and branches may die back and this sometimes results in the death of the tree.

D.G. Hadjimitsis • A. Agapiou (✉) • A. Papachristodoulou
Department of Civil Engineer and Geomatics, Cyprus University of Technology, Limassol 3603, Cyprus
e-mail: athos.agapiou@cut.ac.cy

C.G. Helmis and P.T. Nastos (eds.), *Advances in Meteorology, Climatology and Atmospheric Physics*, Springer Atmospheric Sciences,
DOI 10.1007/978-3-642-29172-2_17,

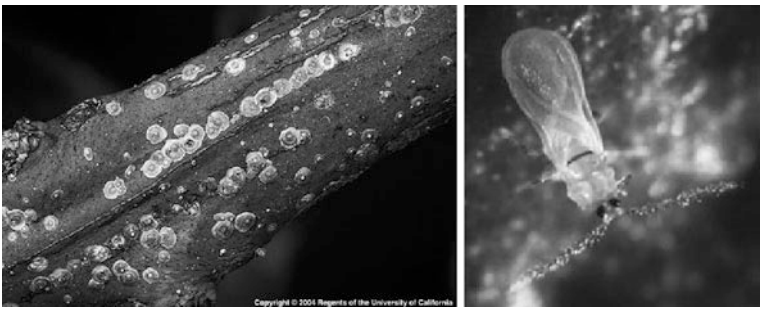

Fig. 1 Red scale ("*Aonidiella aurantii*") (Image from Center for Invasive Species Research)

Chemical control is difficult because the insects are protected by their hard waxy covers. They are also becoming resistant to many insecticides and indiscriminate use of pesticides has adverse effects on their natural predators (Center for Invasive Species Research).

The project "RedScale ID" funded by the Cyprus Research Promotion Foundation, concerns the development, for the first time in a global scale, of a novel automated and energetically autonomous trap for monitoring the Red Scale "*Aonidiella aurantii*" and of an automated system for its continuous identification and population monitoring. The system records also major environmental parameters that can affect Red Scale population (see further details at http://www.redscaletrap.com).

A significant climatic parameter is the temperature which is related to day-degrees growth calculation for estimating Red Scale population. The aim of this study is to evaluate the potential of using remote sensing techniques and data in order to be able to monitor in a systematic and near-real time basis, the temperature for vast agricultural areas. The use of satellite data has many advantages against traditional techniques such as local meteorological stations located in agricultural areas, since they can provide a synoptic coverage on a systematic daily basis.

Indeed the retrieval of surface temperature from satellite images has been widely used for several applications (Coll et al. 2005; Papadavid et al. 2011; Retalis et al. 2010). Wan (2008) argues the land-surface temperature (LST) is a key parameter in the physics of land-surface processes on regional and global scales, since it combines the results of all surface–atmosphere interactions and energy fluxes between the atmosphere and the ground. Jacob et al. (2004) mentioned that the knowledge of land surface temperature is of prime interest when studying energy and water balance of Earth, biosphere and atmosphere. Mapping surface temperature in large lakes with low resolution satellite data was evaluated by Reinart and Reinhold (2008) while Vancutsem et al. (2010) have investigated the potential of using Moderate Resolution Imaging Spectroradiometer (MODIS) data for estimating air surface temperature in different ecosystems over Africa.

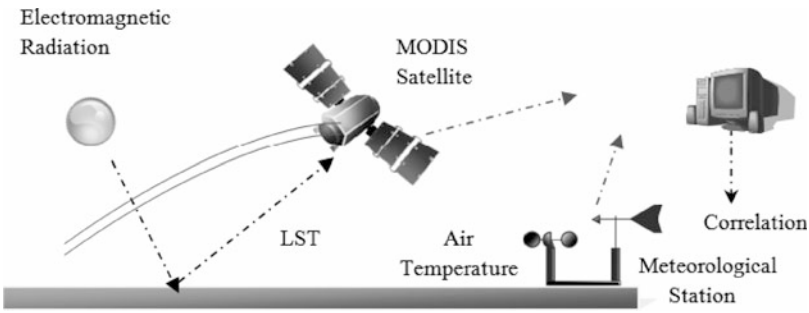

Fig. 2 Methodology applied in this study

In this paper the contribution of MODIS data was used for estimating LST for different areas of Cyprus with heterogeneous characteristics (e.g. elevation) and then to correlate with air surface temperature.

2 Data and Methodology

2.1 Methodology

In order to correlate temperature from satellite sensors and ground measurements, both MODIS satellite imagery and data from meteorological stations (air surface temperature) were used. MODIS data are freely available to the web while meteorological data were kindly provided form the Meteorological Service of Cyprus. Extraction of LST temperature was performed from the satellite imagery, at a GIS environment and then a correlation was performed. Furthermore the authors examined the correlation of LST – air surface temperature for several elevations in order to achieve a higher correlation coefficient. Figure 2 indicates the methodological framework of this study.

2.2 Data

For the calculation of LST temperature collected from Aqua MODIS 11 (MYD 11) sensors all images of 2010 (day and night, >700 images) have been acquired (MODIS LST product). These data are retrieved based on the «split-window» (GSW) algorithm which was firstly developed by Wan and Dozier (1996). This algorithm recovers the ground temperature at 1 km spatial resolution based on: (a) the satellite brightness temperatures T31 and T32 (spectral channels 31 and 32 of the MODIS sensor) and (b) the values of emissivity (e) for the respective channels. The correlation coefficients for determining the appropriate equations are based on radiation's diffusion simulations in a range of different surface and atmospheric conditions. The emissivity for the

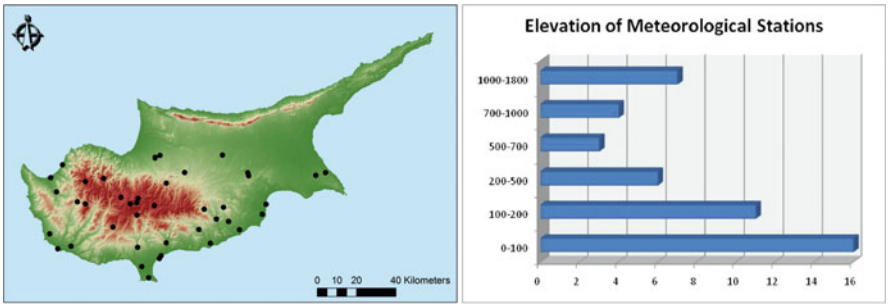

Fig. 3 Distribution of meteorological stations (*left*) and characteristics of the stations (*right*)

Table 1 Statistics from meteorological and satellite data

	Ground data from meteorological stations (°C)	Data from MODIS sensor (°C)
Mean temperature (°C)	33.7	36.3
Max temperature (°C)	46.2	55.0
Min temperature (°C)	−4.5	0.9
St. dev. (°C)	7.8	10.0

spectral channels 31 and 32 defined in this method (GSW) are based to land cover types derived from the classification system MODIS.

In addition meteorological data from ground meteorological stations were acquired. More than 45 stations were used for the aims of this study. The stations are distributed at the whole island, and they cover both valleys and mountainous regions (Fig. 3). Some basic statics from these two databases are shown in Table 1.

LST values may vary during a day and therefore this phenomenon is difficult to be observed from polar-orbited satellites (e.g. MODIS) which capture an area of interest about twice a day.

3 Results

Before the LST retrieval from the MODIS satellite imagery some basics pre-processing steps were performed at the ERDAS Imagine and ArcGIS softwares. All images have been georeferenced to the WGS 84 datum and then the digital values were converted to LST values. Linear regression between ground data (meteorological stations, $n > 12{,}500$ measurements) and satellite LST values ($n > 6{,}500$ measurements) indicates a strong correlation. Indeed the R^2 correlation coefficient was found approximately 0.77 as indicated in Fig. 4.

Finally, the data were categorized according to height. This was performed since air surface temperature is affected by the altitude of the area of interest.

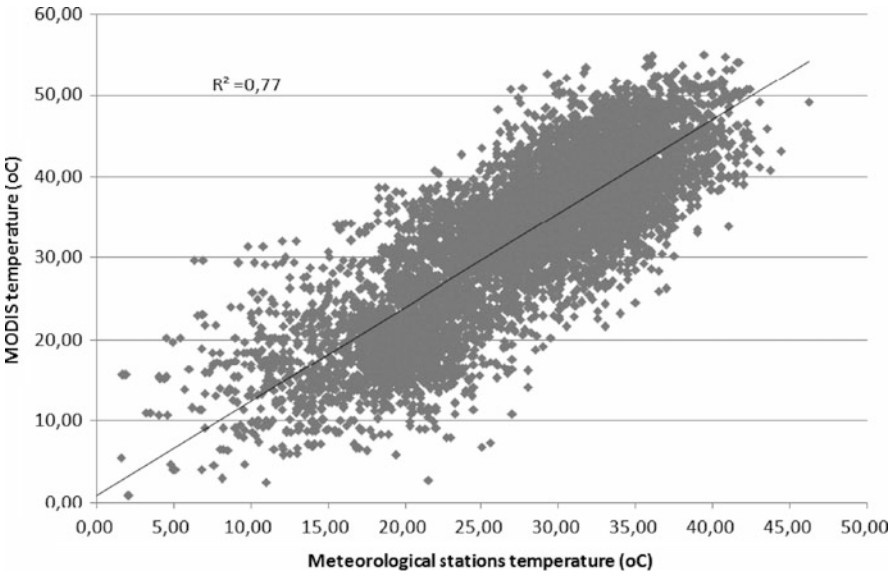

Fig. 4 Linear regression between ground and satellite data

Table 2 Correlation (left) and cumulative correlation (right) according to elevation

Elevation (m)	R^2	N	Slope	Intercept	Elevation (m)	R^2	N
<100	0.79	731	0.47	12.74	<100	0.79	731
100–300	0.80	1,123	0.66	5.75	<300	0.79	1,854
300–400	0.57	841	0.28	18.63	<400	0.69	2,695
400–500	0.87	525	0.61	7.09	<500	0.72	3,220
500–700	0.86	1,344	0.59	8.50	<700	0.76	4,564
700–1,000	0.71	560	0.43	14.93	<1,000	0.75	5,124
>1,000	0.85	1,589	0.59	7.22	<1,700	0.77	6,713

Seven different categories were created (<100 m; 100–300 m; 300–400 m; 400–500 m; 500–700 m; 700–1,000 m and >1,000 m). Linear regression was improved when the data were categorized according to elevation. R^2 can be as 0.87 in contrast to 0.77 of the whole dataset. Table 2 indicates these results. Based on these results, the cumulative correlation was found (Table 2). If we ignore measurements between 300 and 400 m (low correlation) then the final linear regression can be as 0.82.

4 Conclusions

Based on ground temperatures from meteorological stations and LST values from MODIS satellite data, a high correlation ($R^2 = 0.77$) was found. The data used for this purpose were more than 6,500 measurements. Higher correlation was achieved

($R^2 = 0.82$) when some stations (with altitude between 300 and 400 m) were excluded. Seasonal regression analysis will be performed in the near future.

During the "RedScale ID" project, new meteorological stations will be placed in areas of interest, and new validations will be performed. The results are found very promising since air surface temperature is highly correlated with LST values retrieved from satellite sensors. Near-real time estimations of air surface temperature are possible to be estimated, and therefore a systematic monitoring tool can be developed. Indeed the final aim of the project is to develop a Web-GIS system which can map risky areas and alert end-users.

Acknowledgments "RedScale ID" project is funded by the Cyprus Promotion Research Foundation. Thanks are given to the Remote Sensing Laboratory of the Department of Civil Engineering & Geomatics at the Cyprus University of Technology for the support (http://www.cut.ac.cy/) and the Meteorological Service of Cyprus for providing climate data.

References

Coll C, Caselles V, Galve MJ, Valor E, Niclòs R, Sánchez MJ, Rivas R (2005) Ground measurements for the validation of land surface temperatures derived from AATSR and MODIS data. Remote Sens Environ 97(3):288–300, 10.1016/j.rse.2005.05.007

Jacob F, Petitcolin F, Schmugge T, Vermote E, French A, Ogawa K (2004) Comparison of land surface emissivity and radiometric temperature derived from MODIS and ASTER sensors. Remote Sens Environ 90(2):137–152. doi:10.1016/j.rse.2003.11.015

Papadavid G, Hadjimitsis DG, Toulios L, Michaelides S (2011) Mapping potato crop height and leaf area index through vegetation indices using remote sensing in Cyprus. J Appl Remote Sens 5:053526. doi:10.1117/1.3596388 (2011)

Reinart A, Reinhold M (2008) Mapping surface temperature in large lakes with MODIS data. Remote Sens Environ 112(2):603–611. doi:10.1016/j.rse.2007.05.015

Retalis A, Paronis D, Michaelides S, Tymvios F, Charalambous D, Hadjimitsis DG, Agapiou A (2010) Urban Heat Island and heat wave events in Cyprus. In: Proceedings of 10th COMECAP conference, University of Patras, 15–21/5/2010

Vancutsem C, Ceccato P, Dinku T, Connor JS (2010) Evaluation of MODIS land surface temperature data to estimate air surface temperature in different ecosystems over Africa. Remote Sens Environ 114(2):449–465. doi:10.1016/j.rse.2009.10.002

Wan Z (2008) New refinements and validation of the MODIS land-surface temperature/emissivity products. Remote Sens Environ 112(1):59–74. doi:10.1016/j.rse.2006.06.026

Wan Z, Dozier J (1996) A generalized split-window algorithm for retrieving land surface temperature from space. IEEE Trans Geosci Remote Sens 34:892–905. doi:10.1109/36.508406

Studying Surface Observed Meteorological Characteristics Under Different Synoptic Scale Circulation Patterns

C.H. Halios, C.G. Helmis, H.A. Flocas, S. Nyeki, and D.N. Asimakopoulos

Abstract This work aims to study surface meteorological patterns under different synoptic scale categories. Multivariate Data Analysis techniques were applied on two datasets including surface meteorological elements, and meteorological variables in the lower troposphere (850 and 700 hPa). For the former, three principal components were found, related to the thermodynamic status of the surface environment and the two components of the wind speed. For the lower troposphere dataset three principal components were related with: (1) the thermodynamic status, (2) the wind field at 850 hPa, and (3) the direction of the flow at 700 hPa. Principal components from the surface dataset were related with atmospheric circulation categories via Correspondence Analysis. Canonical Correlation Analysis between the surface and upper air datasets revealed: (1) the strong thermodynamic connection of the surface and the upper air environment and (2) a very weak connection between the surface flow field and the upper air circulation indicating the influence of the local topography.

C.H. Halios (✉)
Department of Environmental Physics and Meteorology, University of Athens, Athens 15784, Greece

Physikalisch-Meteorologisches Observatorium Davos/World Radiation Center, Davos, Switzerland
e-mail: c_halios@phys.uoa.gr

C.G. Helmis • H.A. Flocas • D.N. Asimakopoulos
Department of Environmental Physics and Meteorology, University of Athens, Athens 15784, Greece

S. Nyeki
Physikalisch-Meteorologisches Observatorium Davos/World Radiation Center, Davos, Switzerland

C.G. Helmis and P.T. Nastos (eds.), *Advances in Meteorology, Climatology and Atmospheric Physics*, Springer Atmospheric Sciences,
DOI 10.1007/978-3-642-29172-2_18,

1 Introduction

Multivariate data analysis (MDA) refers to the simultaneous observation and analysis of more than one statistical variable, and in the context of atmospheric physics includes simultaneous observations of multiple meteorological variables at one location, or an atmospheric field as represented by a set of gridpoint values at a particular time (Wilks 2006). Multivariate data analysis (MDA) refers to techniques such as Correspondence Analysis (CA), Principal Component Analysis (PCA) and Factor Analysis, Canonical Correlation Analysis (CCA), Cluster Analysis, and Discriminant Analysis (Wilks 2006; Sharma 1996). During the past years MDA has been applied to simultaneous observations of multiple meteorological variables in numerous studies with the aim of identifying various features of surface climate. For example, Bartzokas and Metaxas (1995) employed Factor Analysis as an objective investigation of the interrelation of various climatological parameters in Athens; Statheropoulos et al. (1998) performed a combination of PCA and CCA on simultaneous observations of multiple meteorological and air pollution variables at one location in Athens in order to find simple underlying components and attribute physical meaning to them.

The aim of the paper is to examine the surface meteorological characteristics as observed by a single meteorological station under different synoptic scale atmospheric circulation patterns. Surface meteorological characteristics were analyzed by PCA and CA. The response of the surface meteorological conditions to atmospheric circulation forcing was also examined by means of PCA and CCA. The combination of PCA with CA as employed here is an innovative approach.

2 Data and Methods

Two datasets from the time period 2000–2006 were used. The first, consists of surface measured meteorological parameters measured at the University of Athens (37° 58′ 10″ N, 23° 47′ 11″ S, 240 m ASL), on a daily basis including: atmospheric pressure (P, hPa), temperature (T, °C), relative humidity (RH, %), global horizontal solar irradiance (SR, W m^{-2}), mean prevailing wind velocity components of WNW-ESE and SSW-NNE directions (perpendicular and parallel to Hymettus mountain – u and v respectively, m s^{-1}), standard deviations of the wind direction (wd sd, degrees) and wind speed (ws sd, m s^{-1}), and wind shear between 5 and 10 m (m s^{-1}). Standard deviations of the wind speed and wind direction were used in order to account for the persistence of the atmospheric flow.

The second dataset consists of meteorological variables obtained from radiosondes (http://weather.uwyo.edu/upperair/sounding.html), which are routinely carried out twice per day at Ellinikon airport, by the Greek National Meteorological Service. It includes geopotential height at 850 hPa (GH, m), temperature at 850 hPa (T-850, °C), equivalent potential temperature at 850 hPa (theta-850, °C), wind

speed and direction at 850 hPa (ws-850, m s^{-1}, and wd-850, degrees respectively) and wind direction at 700 hPa (wd-700, degrees).

A day-by-day analysis of the synoptic scale circulation during the period 2000–2006 was performed following the classification scheme described in Kassomenos et al. (1998a). According to this classification scheme, synoptic conditions that prevail over GAA (Greater Athens Area) are divided into eight categories, according to the general circulation patterns at the 850 and 700 hPa isobaric levels and the position and orientation of the trough or ridge axes. These categories are: (1) South-westerly flow (SW), (2) North-westerly flow (NW), (3) Long-wave Trough (LW), (4) Closed Low (CL), (5) Zonal Flow (ZONAL), (6) Open Anticyclone (OA), (7) Closed Anti-cyclone (CA) and (8) High Low Category (H-L) (a high-pressure system or a ridge is combined with a low pressure system or a trough over the eastern Mediterranean).

Principal Component Analysis (PCA) was applied to the two datasets. PCA reduces a dataset which contains a large number of variables to a new dataset containing fewer variables (principal components) which are linear combinations of the original ones, and are chosen to represent the maximum possible fraction of the variability contained in the original data (Wilks 2006). Then, Correspondence Analysis (CA), designed to analyze simple contingency tables containing a measure of correspondence between the rows and columns (Silveira 1997), was applied to the results of the PCA (PCs scores) in order to explore the relationship of the surface meteorological patterns with the eight synoptic circulation types; biplots were produced by taking into account the proportion of the total variability explained by the first two factors. Finally, Canonical Correlation Analysis (CCA) that allows the investigation of the interrelationships between two datasets, by identifying a sequence of pairs of patterns in the two datasets, was applied to the results of the PCA (obtained PCs of the upper air and surface meteorological datasets) in order to examine the response of the surface environment to the forcing imposed by upper air atmospheric circulation patterns.

3 Results

Three Principal Components (PCs) of the surface data set with eigenvalues higher than 1 were rotated with varimax rotation; they account for 69.4% of the total variance. PC1 contrasts temperature and solar radiation to humidity (correlation coefficients 0.9, −0.85 and 0.9 respectively); it accounts for 28.8% of the total data variability (before rotation). The other two PCs are related with the along-axis (v) and across-axis (u) mountain components of the wind speed (PC2 and PC3 respectively), and account for 25.8% and 14.8% of the total variance respectively (before rotation). The PC related to the along-mountain wind speed component is highly correlated with intense changes in the wind speed ($R = -0.61$) and wind shear

(R = −0.63). Furthermore, for PC2, high values of the v-component, wind shear and wind speed standard deviation are contrasted with low values of wind direction standard deviation (R = −0.61), indicating constant flows, characterized by high surface wind shear. Therefore, PC2 may indicate channeling of the wind flow due to the local topography. PC3 is correlated mainly with the u-component of the wind speed (R = 0.88), intense changes in the wind speed (R = 0.63) and is slightly anti-correlated with atmospheric pressure (R = −0.41), characterizing a variable (not intense neither constant) flow. Our results are in accordance with the results of Bartzokas and Metaxas (1995) and also correspond well with the results obtained from Statheropoulos et al. (1998).

Correspondence Analysis results are presented in Fig. 1a, b and c. In these plots the axes represent the two main factors (dimensions) which account for the highest percentage of variability (inertia). The distance between points representing different categories is a measure of similarity with regard to the examined PC scores: if the points representing categories are situated close to each other, the relevant categories show similar behavior in relation to the examined PC score; otherwise, the categories show deviating behavior in relation to the examined PC scores. Ranges for correspondences of PC1 scores (Fig. 1a) are: a: $x < -1.2$, b: $-1.2 < x < -0.6$, c: $-0.6 < x < 0$, d: $0 < x < 0.6$, e: $0.6 < x < 1.2$, f: $x > 1.2$, PC2 scores (Fig. 1b): a: $x < -1.2$, b: $-1.2 < x < -0.5$, c: $-0.5 < x < 0.2$, d: $0.2 < x < 0.9$, e: $x > 0.9$, PC3 scores (Fig. 1c): a: $x < -1.2$, b: $-1.2 < x < -0.5$, c: $-0.5 < x < 0.2$, d: $0.2 < x < 0.9$, e: $x > 0.9$

Categories LW and CL present similar, negative PC1 scores (i.e. close to PC score class “a”), indicating low temperature and solar radiation accompanied by high relative humidity values. On the contrary, category H-L is correlated with high positive values, which are indicative of high temperature, solar radiation and low relative humidity values. These results are in accordance with Kassomenos et al. (1998a), who found that the LW category is combined at the surface with a cyclonic pattern, a low-pressure centre or a cold front, and the CL category with a low pressure centre at the surface. PC2 scores, associated with the along-mountain wind component are similar for categories CL and HL (Fig. 1b). On the other hand, category OA is contrasted with categories CL and H-L: high PC2 scores are observed for the OA category, indicative of low values of the v-component, wind shear, and rapid wind speed changes. High wind direction standard deviations are observed for the same category, indicative of non steady low winds. For categories CL and H-L the pattern is reversed, corresponding to high, steady v-component winds and wind shear. Regarding PC3 which relates to the across-mountain component of the wind speed, PC scores for ZONAL category contrast the respective scores of CL category (Fig. 1c). Low PC scores are observed for the H-L category indicating that at that particular site under that category the prevailing meso-scale flow lies almost entirely parallel to the along-mountain axis.

PCA applied to the upper air dataset revealed three PCs accounting for 70.4% of the observed variance. PC1 relates to the thermodynamic status of the atmosphere at 850 hPa (R = 0.94 and 0.91 for temperature and equivalent potential

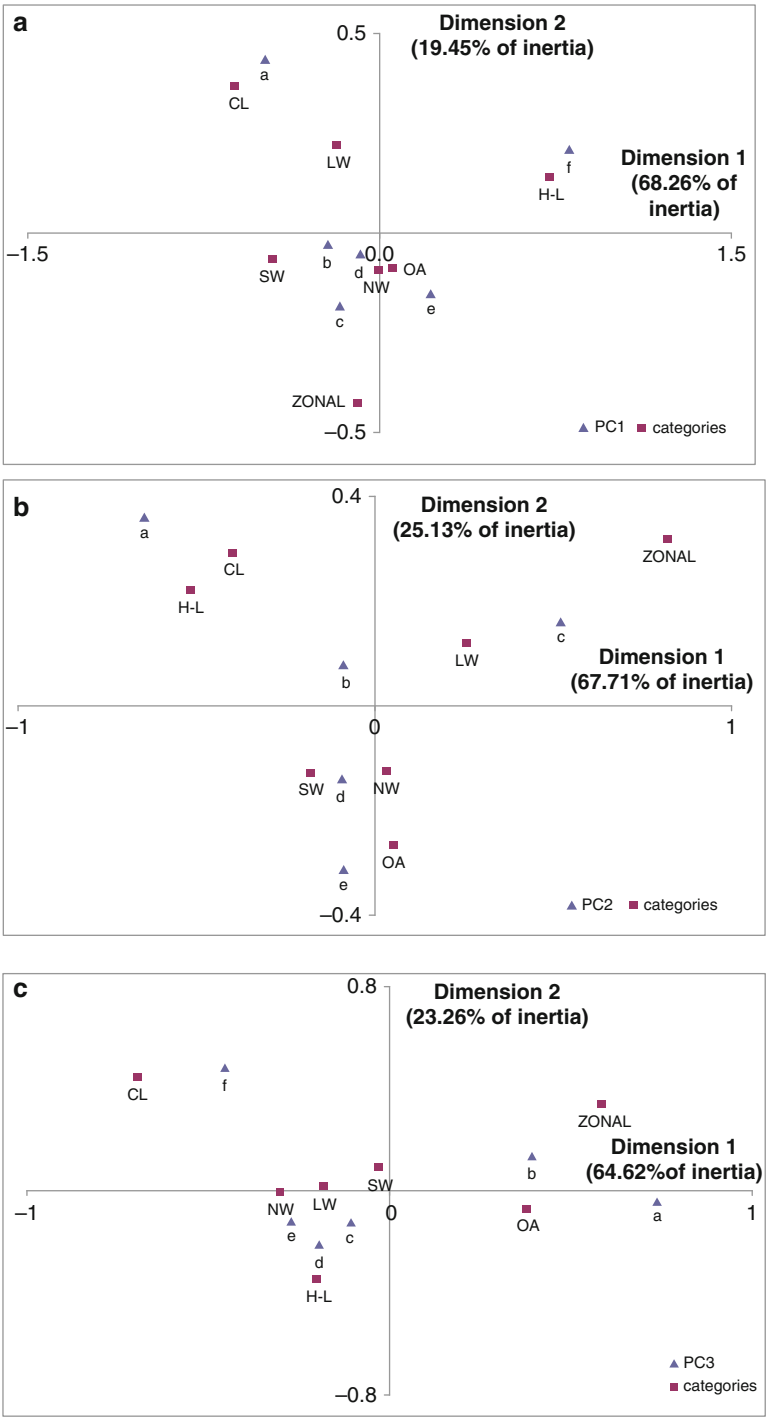

Fig. 1 Biplots of the correspondence analysis for: (**a**) PC1, (**b**) PC2, (**c**) PC3 scores

temperature), PC2 is related mainly to the wind direction at 700 hPa (R = 0.86) and the geopotential height at 850 hPa (R = 0.68), while PC3 gives the wind field at 850 hPa (R = 0.72 and −0.75 for wind direction and wind speed at 850 hPa).

From CCA it was obtained that CV1 correlates highly with PC1 of the surface meteorological and upper air datasets (canonical correlation 0.44), indicating that surface solar radiation, temperature and relative humidity are strongly connected with upper air temperature and equivalent potential temperature. CV2 is associated with PC3 of the meteorological dataset, which is related to the across-mountain component of the wind speed, and is also related to PC3 of the upper air dataset (reflecting 700 hPa wind direction), and to a lesser extent PC2. CV3 correlates surface PC2, which is related to the along-mountain component of the wind speed and upper air PC2, associated with the wind speed and direction at 850 hPa and to a lesser extent PC3. CV2 and CV3 explain a very small portion of the total variance (1.1% and 0.8% respectively), probably indicating that PC2 and PC3 of the surface meteorological datasets are highly influenced by aspects other than synoptic, topographic/atmospheric features, on the local or mesoscale scale.

4 Conclusions

In this study, a combined MDA approach was applied, aiming to examine the response of the surface environment to different atmospheric synoptic forcing. Cyclonic LW and CL categories are characterized by similar surface radiation, temperature, and humidity values. These categories are contrasted with the anti-cyclonic H-L category. NW and OA categories present similar surface radiation, temperature, and humidity values. It was also found that the along-mountain component of the wind speed (v) is similar for the CL and H-L categories, which contrast the OA category. The surface temperature, relative humidity and solar radiation are closely related to the thermodynamic status of the atmosphere at 850 hPa. A very weak connection between the across-mountain wind component and the wind field at 850 hPa is observed, pointing to the role of local/mesoscale topographic atmospheric features; this connection was moderate for the ZONAL and SW categories. Finally, the along mountain wind component was poorly related to the wind direction at 700 hPa and geopotential height at 850 hPa, further indicating the significance of local topographic processes.

Acknowledgments The authors would like to thank Mr. Nikos Kaltsounidis for his contribution to the data collection and support. The upper air dataset were obtained from http://weather.uwyo.edu/upperair/sounding.html.

References

Bartzokas A, Metaxas DA (1995) Factor analysis of some climatological elements in Athens, 1931–1992: covariability and climatic change. Theor Appl Climatol 52:195–205

Kassomenos P, Flocas HA, Lykoudis S, Petrakis M (1998) Analysis of mesoscale patterns in relation to synoptic conditions over an urban Mediterranean basin. Theor Appl Climatol 59:215–229. doi:10.1007/s007040050025

Sharma S (1996) Applied multivariate techniques. Wiley, USA, 229p

Silveira L (1997) Multivariate analysis in hydrology: the factor correspondence analysis method applied to annual rainfall data. Hydrol Sci J 42(2):215–224. doi:10.1080/02626669709492021

Statheropoulos M, Vassiliadis N, Pappa A (1998) Principal component and canonical correlation analysis for examining air pollution and meteorological data. Atmos Environ 32 (6):1087–1095. doi:10.1016/S1352-2310(97)00377-4

Wilks DS (2006) Statistical methods in the atmospheric sciences, 2nd edn. Academic, Burlington

Forest Fire Modeling and the Effect of Fire-Weather in Landscape Fire Behavior for the Region of Attica, Greece

N. Iliopoulos, K. Kalabokidis, G. Kallos, H. Feidas, A. Malounis, and E. Mavromatidis

Abstract The knowledge of meteorological conditions is critical for the description of fire weather. In this paper, the mesoscale numerical meteorological model RAMS has been used to simulate the surface wind and temperature in two fire events in the region of Attica in Greece. The FARSITE (Fire Area Simulator) fire model, for the description of forest fire behavior, taking into consideration the influence of fuels, topography and weather conditions. The accuracy of the results was evaluated and confirmed that the use of suitable fuel models is very important for achieving reliable simulations for the devastating fires.

N. Iliopoulos (✉)
Department of Geography, University of the Aegean, GR-81100 Mytilene, Greece

Coordinative Operational Centre of Fire Brigade Services, Mikras Asias and Rizareiou 1, GR-15233 Chalandri, Athens, Greece
e-mail: hlnic@rocketmail.com

K. Kalabokidis
Department of Geography, University of the Aegean, GR-81100 Mytilene, Greece

G. Kallos
University of Athens, GR-15784 Athens, Greece

H. Feidas
Department of Geology, Aristotle University of Thessaloniki, GR-54124 Thessaloniki, Greece

A. Malounis
Coordinative Operational Centre of Fire Brigade Services, Mikras Asias and Rizareiou 1, GR-15233 Chalandri, Athens, Greece

E. Mavromatidis
Harokopion University, 70 El. Venizelou, Kallithea, Athens GR-17671, Greece

C.G. Helmis and P.T. Nastos (eds.), *Advances in Meteorology, Climatology and Atmospheric Physics*, Springer Atmospheric Sciences,
DOI 10.1007/978-3-642-29172-2_19,

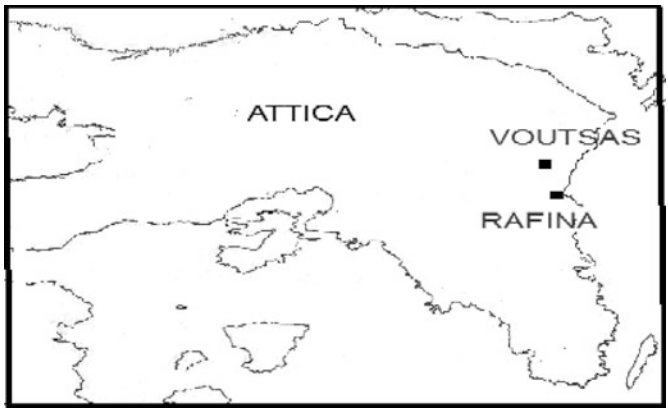

Fig. 1 Attica region in Greece

1 Introduction

Forest fires have been a very common phenomenon in Mediterranean climates for years. The change in land utilization in the Mediterranean has increased the frequency of destructive fires (Piñol et al. 1998). In Greece, Attica (Fig. 1) is one of the regions that are influenced by the increase in fire frequency. In this work we use the numeral meteorological model RAMS (Regional Atmospheric Modeling System) to simulate the wind factor and the surface temperature as well as their temporal change for the period 25–30 July 2005. The meteorological data that arise can be the input in a fire model such as FARSITE (Fire Air Simulation) for the description of the behavior of forest fire. More specifically two forest fires in Rafina and Voutsas in Eastern Attica on 28th July 2005 are simulated by FARSITE, taking into consideration the effect of fuel, using different fuel models, the terrain and the weather conditions.

2 Methodology

2.1 Climatic Conditions: Vegetation

Rafina and Voutsas (Fig. 1), the places where big forest fires broke out on 28th July 2005, have a distance of 28 km and are located in Eastern Attica in Greece (N: 38° 01′, E: 24° 00′), 100 m above sea level. Eastern Attica is characterized by the typical dry Mediterranean climate. It does not rain most of the times except for the autumn and winter months. The total yearly rainfall is 397 mm, the average yearly temperature is 17.3°C but during the summer period the average maximum temperature reaches 30.9°C according to the climatic data of the 1986–1997 period, which were

collected from the meteorological station in Marathonas (approximately 9 km north from the areas of the fires). The average wind speeds are high in the winter and in the summer and the prevailing wind directions are typically north and north-east. The topography and the breeze are likely to diversify in many cases the direction of the winds. The burnt land (about 9,000 m^2) was covered with the typical Mediterranean vegetation, the dominant kinds of which were *Pinus halepensis*, *Quercus coccifera*, *Phillyrea latifolia*, *Pistacia lentiscus* and *Genista acanthoclada*.

2.2 Meteorological Model RAMS: Fire Model FARSITE

The numeral Atmospheric Model RAMS (Regional Atmospheric Modeling System) simulate atmospheric phenomena on a scale ranging from a few meters to some thousands meters. Rams is very often used as a model of a limited area (Pielke et al. 1992). Some of the RAMS feature can be summarized as follows: Two-way interactive nested grid structure, terrain following coordinate surfaces, various options for upper and lateral boundary conditions, radiative transfer parameterizations (short and long wave), various levels of complexity for surface-layer parameterization and cloud microphysics parameterization.

The Fire Area Simulation (FARSITE) can calculate the intensity of the fire and the speed of the spreading for numerous places along the landscape by using the fire behavior model of Rothermel (Rothermel 1972). FARSITE, includes existing fire behavior models for surface, crown, spotting, point-source fire acceleration, and fuel moisture. The space data of the raster type that are used by the FARSITE model are the elevation, the slope, the aspect, the fuel, the canopy cover, the canopy height, the crown base height and the crown bulk density.

3 Outcome

3.1 RAMS Simulation

RAMS simulated the atmospheric conditions in Rafina and Voutsas in Eastern Attica for the period 25–30 July 2005 (120 h) on four nested grids in polar stereographic coordinates. Indeed, the computational domain of the model consisted of (1) the outer grid, with 48 km horizontal resolution (110 × 94 analyses), (2) the second grid with 16 km horizontal grid interval (86 × 77 analyses), (3) the third grid with 4 km horizontal resolution (82 × 74 analyses) and (4) the inner grid with 1 km horizontal resolution (80 × 72 analyses). 35 levels are used until the height of 18 km for the vertical analysis. The temporal step for the simulation is 60s. RAMS simulated the wind and the temperature for the period of the two fires. On 28th July 2005 at 10:00 local time, the wind was N.E. with a speed of 12 m/s and the temperature was 26°C. At 13:00 local time the wind continued to

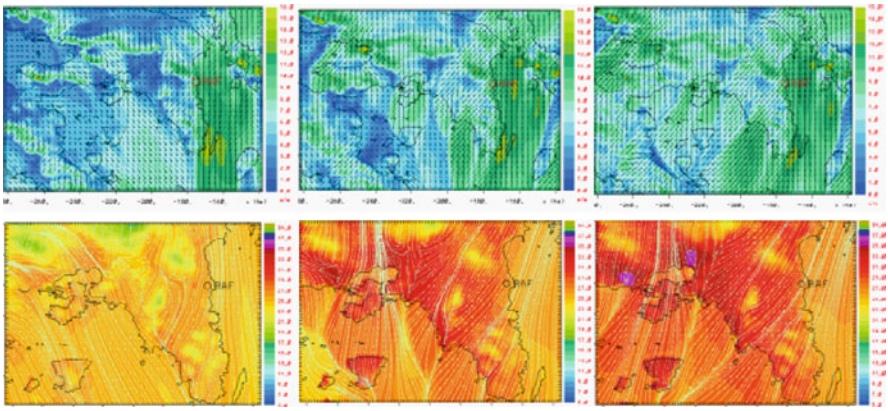

Fig. 2 Simulation of the wind and the temperature streamlines from the inner grid of the Rams model for Rafina region on 28-07-2005 and for the time 10:00, 13:00 and 15:00

be S.E. with a speed of 12 m/s whereas the temperature rose to 19°C. At 15:00 the wind continued to be S.E. with a speed of 12 m/s whereas the temperature rose to 30°C (Fig. 2).

3.2 FARSITE Simulation

A digital model of the ground was used with a horizontal analysis of 25 × 25 m for the place of interest. Apart from the information concerning the altitude, the necessary information about the slope and the aspect was obtained from this model. For the specific area the canopy height was bibliographically evaluated at 10.0 m, the crown base height was evaluated at 4.8 m and the crown bulk density at 0.16 kg/m^3 (Mitsopoulos and Dimitrakopoulos 2006). Next the included humidities of the living and dead fuels per fuel model are introduced into FARSITE (calculation by Mr. Xanthopoulos – Institute of Forest Research). Included humidity of dead fuels: 1 – h TL: 5%, 10 – h TL: 6% and 100 – h TL: 10%. In the case of the fire under study, 30 m was defined as the time step, 1 h the visual step, 60 m the analysis of the perimeter and 30 m the analysis of the distance of the spreading. It was evaluated approximately that the fires started in the area with co-ordinates N: 38° 01′, E: 24° 00′.

The fire in Rafina started at 10:45 local time on 28-07-2005 and was controlled at 18:00 local time on the same day. The fire started from bushes and next it preceded burning pine halepensis. The fire in Voutsas started at 13:25 local time on 28-07-2005 and was under control at 20:00 local time on the same day. The meteorological conditions used were obtained from the RAMS model and the closest meteorological stations. The use of FARSITE on areas different from those where the model was originally developed requires a local calibration. To

Fig. 3 Simulation of FARSITE for the fire in Rafina on 28-07-2005 for the tests 1, 2 and 3 of fuel models. The *black line* is the real burnt land whereas the *red line* shows the simulated burnt land of the fire per hour

Fig. 4 Simulation of FARSITE for the fire in Voutsas on 28-07-2005 for the test 1, 2 and 3 of fuel models. The *black line* is the real burnt land whereas the *red line* shows the simulated burnt land of the fire per hour

perform FARSITE calibration an appropriate set of fuel models for each fire is needed. FARSITE simulated fires in Rafina and Voutsas using the following fuel models: 2, 7, 8 and 10 (Andrews 1986) – next test 1 of the fuel models: 8,122 and 164 (Scott and Burgan 2005) – test 2 and finally the fuel models: 7 and 10 (Corine) – test 3. The simulated burnt area by FARSITE corresponds to 34.14% of the real burnt area for test 1, 62.93% for test 2 and 53.77% for test 3 (Fig. 3).

FARSITE simulated the burnt area of the Voutsas fire at a 96.22% of the real burnt area for test 1, at 35.6% for the test 2 and at 29.49% for test 3 (Fig. 4).

To check the accuracy of the simulation, the asymmetric statistical indicator Sorensen (SC) was used (1), which calculates the correlation between the real and the simulated burnt land (Bachisio et al. 2007):

$$SC = \frac{2a}{2a + b + c} \tag{1}$$

where a is the number of the cells which have been characterized as burnt in both the real and the simulated fires, b is the number of the cells that were characterized as burnt in the simulated fire but were not burnt in the real fire and c is the number of the cells that were characterized as unburnt in the simulated fire but were burnt in the real fire.

Finally, x^2 tests were performed to examine the zero hypotheses for the independence of the simulated and the real burnt land (Ludwig and Reynolds 1988). For the

fire in Rafina SC was calculated as follows: 0.35 for tests 1, 2 and 0.58 for test 3. For the fire in Voutsas SC saw calculated in the same way as follows: 0.75, 0.46 and 0.45 for tests 1, 2 and 3 respectively with the x^2 test showing a significant correlation of the simulated and the real burnt land at a significance level of a = 0.01.

4 Conclusion

By using the proper models of fuels, the burnt land of the fire in Rafina was simulated with the FARSITE model with 62.93% accuracy for test 2, whereas for the fire in Voutsas at 96.22% of the really burnt land for test 1, with the co-efficient SC taking the 0.58 and 0.75 values respectively. It was estimated that the SC values would be bigger (it takes values from 0.00 to 1.00) if the fire fighters didn't influence the real burnt land. The burnt land in Voutsas was better simulated than that in Rafina, according to co-efficient SC, due to its most complicated topography and the biggest heterogeneity of the fuels in the fire in Rafina. The results recommend that the use of appropriate fuel models is crucial to obtain reasonable simulation of devastating fires that occur in the vegetation of the Mediterranean, during the dry season.

References

Andrews PL (1986) BEHAVE, fire behavior prediction and fuel modeling system-BURN subsystem, Part 1. USDA Forest Service, Intermountain Forest and Range Experiment Station, General Technical Report INT-194, Odgen, UT

Bachisio A, Duce P, Laconi M, Pellizzaro G, Salis M, Spano D (2007) Evaluation of FARSITE simulator in Mediterranean maquis. Int J Wildland Fire 16:563–572. doi:dx.doi.org/10.1071/WF06070

Ludwig JA, Reynolds JF (1988) Statistical ecology: a primer on methods and computing. Wiley, New York

Mitsopoulos ID, Dimitrakopoulos AP (2006) Canopy fuel characteristics and potential crown fire behavior in Aleppo pine (*Pinus halepensis* Mill.) forests. Ann For Sci 64:287–299. doi:10.1051/forest:2007006

Pielke RA, Cotton WR, Walko RL, Tremback CJ, Lyons WA, Grasso LD, Nicholls ME, Moran MD, Wesley DA, Lee TJ, Copeland JH (1992) A comprehensive meteorological modeling system rams. Meteorol Atmos Phys 49:69–91. doi:10.1007/BF01025401

Piñol J, Terradas J, Lloret F (1998) Climate warming, wildfire hazard, and wildfire occurrence in oastal eastern Spain. Clim Chang 38:345–357. doi:10.1023/A:1005316632105

Rothermel RC (1972) A mathematical model for predicting fire spread in wildland fuels. Res. USDA Forest Service, Intermountain Forest and Range Experiment Station. Pap. INT-115, Odgen, UT

Scott JH, Burgan RE (2005) Standard fire behavior fuel models: a comprehensive set for use with Rothermel's surface fire spread model. US Department of Agriculture, Forest Service, Rocky Mountain Research Station, General Technical Report RMRS-GTR-153, Fort Collins, CO

Mobile Radar Network Measurements for Flood Applications During the Field Campaign of HydroRad Project

J. Kalogiros, M. Anagnostou, F.S. Marzano, E. Picciotti, G. Cinque, M. Montopoli, L. Bernardini, E. Anagnostou, A. Volpi, and A. Telleschi

Abstract The main aim of the HydroRad European project was to develop an innovative dual-polarization X-band mini-radar system and software support tools like rainfall estimation, nowcasting, precipitation classification and integration with hydrological and meteorological models for the use in weather and flood applications. These mini-radars are low cost, easy to deploy and, thus, ideal for the setup of radar networks to cover areas with complex terrain. In order to test the system an experimental campaign took place during autumn 2011 in Moldova. A network of three mini-radars was setup and tested against an advanced mobile polarimetric radar (XPol) in the center of the network and in-situ rain measurements from a video disdrometer and raingauges. Original polarimetric algorithms for attenuation correction and rainfall estimation were applied and their results were compared to the reference in-situ data for moderate widespread and intense convective rain events. The results show that mini-radars can produce high quality and accurate rain fields in difficult to cover complex terrain areas.

J. Kalogiros (✉) • M. Anagnostou
NOA, National Observatory of Athens, Athens, Greece
e-mail: jkalog@noa.gr

F.S. Marzano • E. Picciotti • G. Cinque •
M. Montopoli • L. Bernardini
HIMET, High Innovation in Meteorology, L'Aquila, Italy

E. Anagnostou
Department of Civil and Environmental Engineering, University of Connecticut, Storrs, CT, USA

A. Volpi • A. Telleschi
ELDES, ELI International Company, Florence, Italy

C.G. Helmis and P.T. Nastos (eds.), *Advances in Meteorology, Climatology and Atmospheric Physics*, Springer Atmospheric Sciences,
DOI 10.1007/978-3-642-29172-2_20,

1 Introduction

Rainfall estimates based on classical weather radar observations have quantitative limitations mainly due to the lack of uniqueness in the relationship of the single radar measurable (reflectivity) to the associated rainfall intensity. The polarization diversity capability of modern weather radars is expected to moderate this effect (Anagnostou et al. 2004). High-frequency/low-power polarization-diversity mini-radars can constitute a low-cost solution to the problem of hydrologic forecasting for urban and small-scale flood-prone basins and coastal areas not well covered by operational weather radar networks. Thus, short-wavelength radar systems (like X-band radars) became more attractive also for research purposes and they can either be mobile (trailer mounted, containerized or airborne) or static. Their limitations are the smaller range due to low power and the significant signal attenuation at X-band in heavy rain, which must be corrected because it introduces errors in the rainfall estimation.

Within the context of the HydroRad project, the aim of this study was to test an innovative dual-polarization X-band mini-radar system for use in weather and hydrologic applications. Three mini-radars were tested in an experimental campaign against a state-of-the-art radar (XPol) and in-situ (raingauges and disdrometer) rain measurements.

2 Experimental Setup

The data used in this work were collected during Moldova Operational Field campaign (MOF), which took place in September and October 2011. The target area for the MOF campaign is the region around the Moldovan capital Chisinau. This region includes the basin of the river Bic with its tributaries and smaller rivers (Fig. 1). The terrain is characterized by low elevations up to 300 m.

The three mini-radars (Fig. 2) were installed in locations around Chisinau in order to cover the basin. XPol and the 2D-video disdrometer were installed in the center of mini-radars triangle in Chisianu in order to provide a reference basis for comparison with the mini-radars. In addition six pairs of tipping raingauges were installed in different positions along the river (see Fig. 3 for their positions relative to XPol). The range of the radars was 60 km with a resolution of 120 m. Radar observations included the horizontal reflectivity Z_h, the differential reflectivity Z_{dr} and the differential phase Φ_{dp}, which is insensitive to radar calibration.

PPI scans at low elevation angles (up to 3.5°) were performed as well as RHI scans in selected azimuth angles in order to estimate the vertical structure of the rain field. The time period for a full volume scan was about 3 min. The disdrometer data

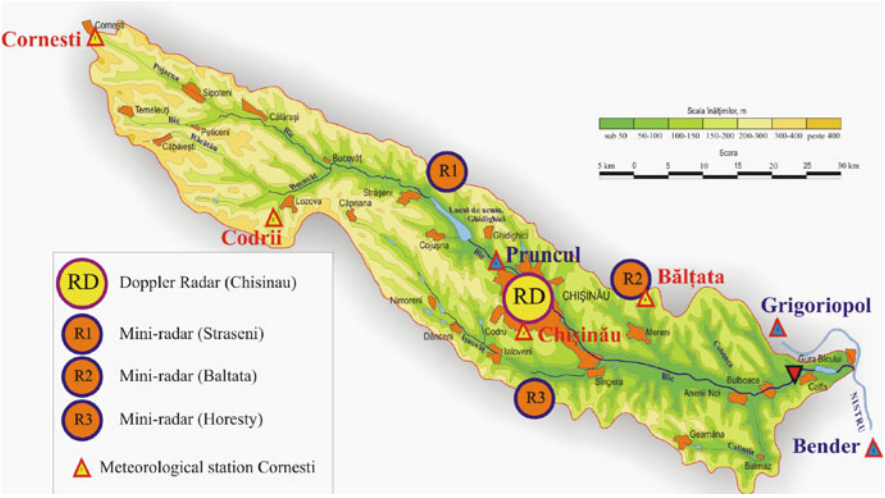

Fig. 1 The basin of the Bic river in central Moldova. The locations of the radars are shown

Fig. 2 A mini-radar (*left*) and the XPol mobile radar with disdrometer and gauges (*right*)

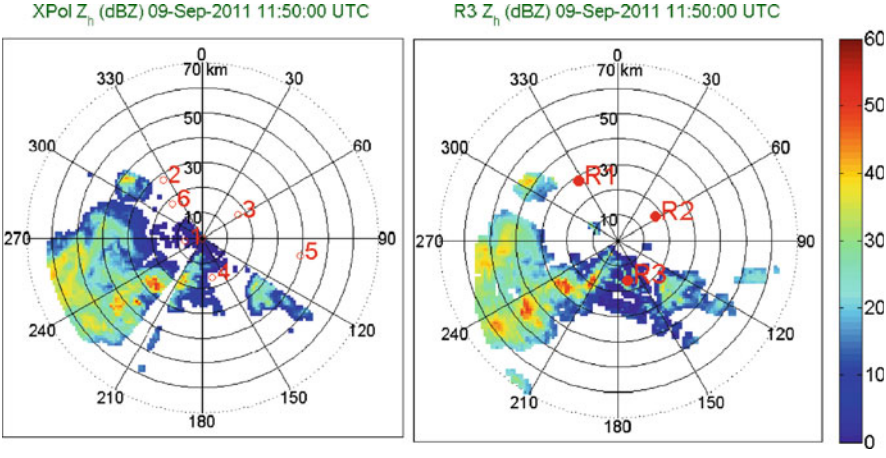

Fig. 3 A PPI of horizontal reflectivity Z_h measured from the XPol and the R3 mini-radar at an elevation angle of 1.5°. The locations of the three mini-radars and the six pairs of raingauges relative to XPol are also shown

was used for the analysis of droplet size distribution, shape (axis ratio) and orientation of rain droplets, and the theoretical estimation (simulation) of polarimetric radar products.

3 Data Processing

At X-band frequencies attenuation of radar signal by rain can be quite significant and it can be larger than 10 dB in heavy rain. There are a number of rain attenuation correction algorithms like the ZPHI algorithm (Testud et al. 2000) used in this study, which is based on Φ_{DP} measurements, and its extension with the additions of a $\Phi_{DP} - Z_{DR}$ constraint (Bringi et al. 2001). The calibration of the reflectivity measurements of mini-radars was carried out by comparison with the radar products estimated from the disdrometer data (not shown here).

Rainfall rate R is estimated from radar measurements using polarimetric relations of rainfall parameters at X-band, which combine Z_h, Z_{dr} and specific differential phase K_{dp}, which is half the gradient of Φ_{dp} along the radar ray, as described in Matrosov et al. (2002) and Park et al. (2005). In this study we evaluated three rainfall estimators. The first one is a classic Z-R estimator with steady coefficients which were evaluated from historic XPol data:

$$R = 3.36 \times 10^{-2} Z_h^{0.58} \tag{1}$$

where R is in mm h^{-1} units and Z_h is in linear units instead of dBZ. The second estimation is a polarimetric estimator which is based the N_w normalization approach. Its constants were estimated from electromagnetic scattering simulations. N_w is the intercept parameter (units mm^{-1} m^{-3}) of rain droplet size distribution (DSD), which is approximated with a normalized Gamma distribution (Bringi and Chandrasekar 2001). N_w is obtained also from polarimetric relations found from the simulations. The polarimetric rainfall rate R estimator is:

$$R = 1.305 \times 10^{-3} N_w (Z_h / N_w)^{0.58} \tag{2}$$

The third rainfall estimator is a new polarimetric estimator which minimizes the approximation error using the theoretical Rayleigh scattering limit with the addition of a rational polynomial function of reflectivity-weighted droplet diameter to approximate the Mie character of scattering (Kalogiros et al. 2012):

$$R = 0.8106 F_R(\mu) N_w D_0^{4.67} f_R(D_0) \tag{3}$$

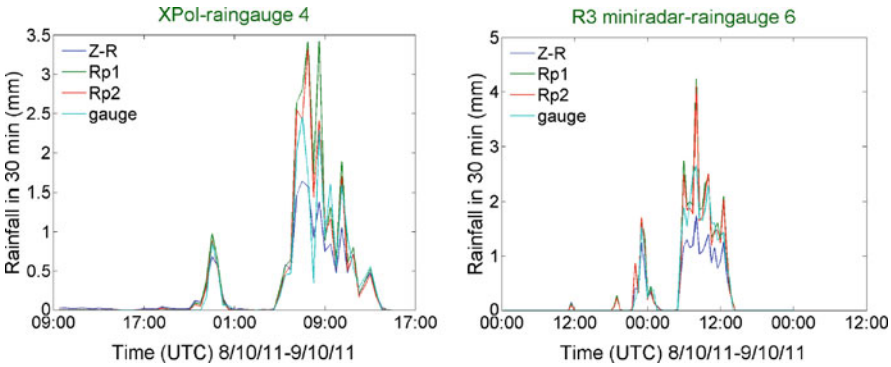

Fig. 4 Time series comparison of XPol and mini-radars rainfall estimators with raingauges

D_0 and μ are the median volume diameter and the shape parameter of the DSD, respectively, d F_R is a function of μ, which is included in the Gamma approximation of the DSD, and f_R is a third degree rational polynomial of D_0 with constants evaluated by the simulations.

4 Results

Figure 3 shows an example of near simultaneous Z_h PPI from XPol and the R3 mini-radar. Both radars sense well convective rain cells coming from southwest. However, there are some differences which are due to the vertical profile of rain field and the different altitude of each volume of measurements from the two radars which are separated by a distance of 16 km.

Figure 4 shows time series of comparison of accumulated rain in 30 min intervals from the two radars with raingauges. The polarimetric estimators Rp1 and Rp2 correspond to (2), (3), respectively, and follow well the raingauges reference measurements. The classic Z-R estimator shows lower values which is due to the fact that the constants in (1) were estimated from historic XPol data in Athens, Greece, where rain microphysics differ from Moldova region.

Figures 5 and 6 show the comparison of total accumulated rain in the experimental area from XPol and R3 mini-radar (classic and Rp2 estimators) during the rain event of 8–9 September 2011. The correlation coefficient is r, NB is the normalized bias and NSE in the normalized standard error. R3 rainfall estimates are similar with XPol but with a small overestimation by R3, which is probably due to errors in the calibration of the radars, and significant scatter probably due to the differences in the time and altitude of the measurement volume of the two radars.

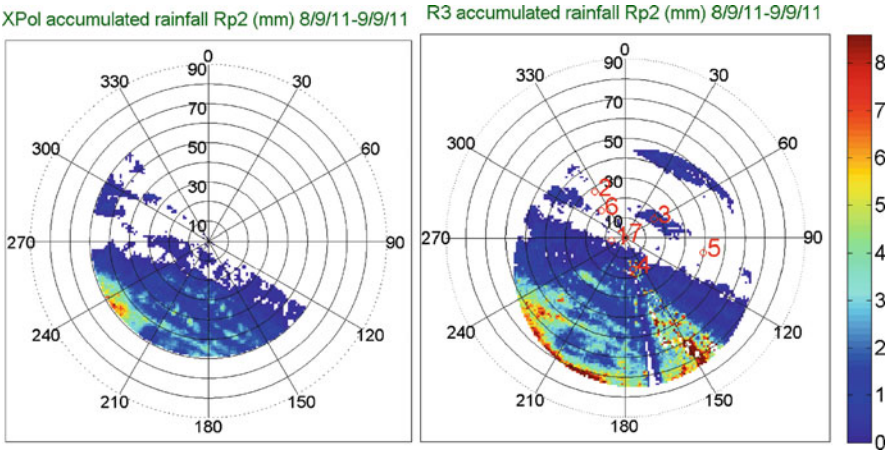

Fig. 5 PPI of total accumulated rain estimated using (3) from XPol and R3 in 8–9/9/2011

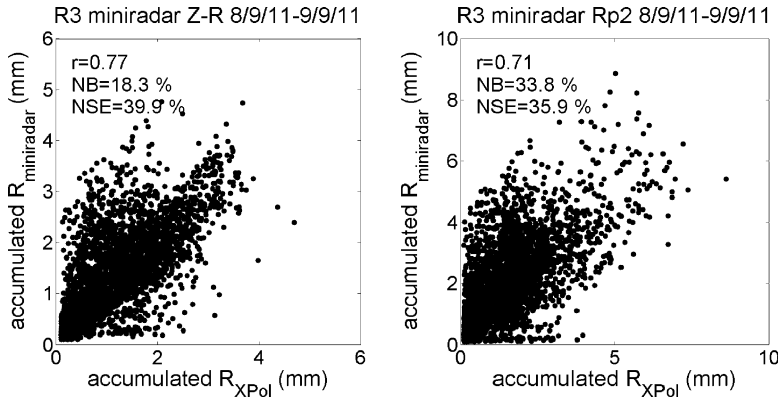

Fig. 6 Scatter plots of accumulated rain from XPol and R3 corresponding to Fig. 5

5 Conclusions

Weather and hydrologic hazards are at the top of environmental issues world-wide. X-band mini-radars are low cost mobile radar systems for weather and flood monitoring in small scales. Limitations in the operating characteristics of mini-radars (like the 3° wide beam-width compared to 1° of XPol) question the usefulness of their measurements. Our first results show that mini-radars can give reliable estimates of rainfall. Networks of mini-radars can cover broader areas in complex terrain where large expensive systems cannot achieve this.

Acknowledgments This work is part of the HYDRORAD project (Research for SMEs category–Grand agreement number FP7-SME-2008-1-232156) funded by EC 7th Framework Program.

References

Anagnostou E, Anagnostou M, Krajewski W, Kruger A, Miriovsky B (2004) High-resolution rainfall estimation from X-band polarimetric radar measurements. J Hydrometeorol 5:110–128. doi:10.1175/1525-7541(2004) 005<0110:HREFXP>2.0.CO;2 DOI:dx.doi.org

Bringi V, Chandrasekar V (2001) Polarimetric Doppler weather radar. Cambridge University Press, Cambridge. doi:10.2277/0521623847

Bringi V, Keenan T, Chandrasekar V (2001) Correcting C-band radar reflectivity and differential reflectivity data for rain attenuation: a self consistent method with constraints. IEEE Trans Geosci Remote Sens 39:1906–1915. doi:10.1109/36.951081

Kalogiros J, Anagnostou M, Anagnostou E, Montopoli M, Picciotti E, Marzano FS (2012) Optimum estimation of rain microphysical parameters from X-band dual-polarization radar observables. IEEE Trans Geosci Remote Sens (under revision)

Matrosov S, Clark K, Martner B, Tokay A (2002) X-band polarimetric radar measurements of rainfall. J Appl Meteorol 41:941–952. doi:10.1175/1520-0450(2002) 041<0941:XBPRMO> 2.0.CO;2

Park S, Maki M, Iwanami K, Bringi V, Chandrasekar V (2005) Correction of radar reflectivity and differential reflectivity for rain attenuation at X-band, part II: evaluation and application. J Atmos Ocean Technol 22:1633–1655. doi:10.1175/JTECH1804.1

Testud J, Le Bouar E, Obligis E, Ali-Mehenni M (2000) The rain profiling algorithm applied to polarimetric weather radar. J Atmos Ocean Technol 17:332–356. doi:10.1175/1520-0426 (2000) 017<0332:TRPAAT>2.0.CO;2

Synoptic, Dynamic and Thermodynamic Characteristics of the 10th August 2008 Intensive Storm Over North-Central Greece

T. Karacostas, V. Spiridonov, D. Bampzelis, I. Pytharoulis, G. Karoutsos, and C. Sideropoulou

Abstract The synoptic, dynamic and thermodynamic characteristics of the intensive storm that occurred over the north-central Greece on the 10th August 2008 are studied. The event started as two individual cells that formed over the Vermion mountainous area moved northeastwards and eventually merged into one cell, growing spontaneously and developing very strong storm characteristics. Both cells were seeded before and after merging. The study is based on data derived through: ECMWF gridded analyses, synoptic charts, radiosonde, and mostly on measurements recorded and analyzed by the cell tracker TITAN. Synoptic, dynamic and thermodynamic analysis revealed favourable conditions for storm development over the area. The analysis of storm characteristics obtained from the weather radar depicted in a realistic way an integrated view of the storm triggering, development and dissipation pointing out the importance of weather radars and the powerful tool of the cell tracker TITAN.

1 Introduction

Northern Greece is an area frequently affected by severe storms accompanied by hail during the warm period of the year (April to September). For this reason, the Greek National Hail Suppression Program (NHSP) operates in this area since 1984, with the objective to reduce hail damages on agricultural production. Several studies of convective storm characteristics and hailstorms over northern Greece have been based on the NHSP program (Karacostas 1984, 1991; Foris et al. 2006).

T. Karacostas (✉) • D. Bampzelis • I. Pytharoulis • G. Karoutsos • C. Sideropoulou
Department of Meteorology and Climatology, School of Geology, Aristotle University of Thessaloniki, Thessaloniki 541 24, Greece
e-mail: karac@geo.auth.gr

V. Spiridonov
Republic Hydrometeorological Service, Skupi bb 1000, Skopje, Macedonia

C.G. Helmis and P.T. Nastos (eds.), *Advances in Meteorology, Climatology and Atmospheric Physics*, Springer Atmospheric Sciences,
DOI 10.1007/978-3-642-29172-2_21, © Springer-Verlag Berlin Heidelberg 2012

The purpose on this study is to analyze and depict the storm event that took place on August 10th 2008, incorporating several available datasets, in order to specify atmospheric conditions responsible for the development of such storms and to point out the use of weather radar as a powerful and useful tool in storm tracking and analysis.

2 Data and Methodology

The study is based on ECMWF and UKMO analyses, radiosonde data information and weather radar images. The 6-hourly ECMWF gridded analyses were available at a horizontal resolution of 0.25° × 0.25°. The utilized variables include the geopotential height, air temperature, divergence, relative vorticity, vertical velocity, relative humidity and u, v horizontal wind components, at 850, 700, 500 and 300 hPa.

The 12 UTC sounding of that day for the Thessaloniki synoptic station was used for the thermodynamic analysis and study. Five instability indices are calculated, such as: the K (KI) and Totals Total (TT) (Miller 1967) indices that provide an expression of an air mass thunderstorm activity potential through vertical temperature lapse rate and lower moisture extend calculations. The Showalter index (SI) (Showalter 1953), which is defined as the difference in environmental temperature at 500 hPa with the temperature of an air parcel lifted adiabatically from 850 to 500 hPa. Convective Available Potential Energy (CAPE) (Moncrieff and Green 1972), which is a measure of the vertically integrated positive buoyancy of a rising air parcel and the Severe Weather Threat Index (SWEAT), an index that discriminates ordinary and severe convection by incorporating thermodynamic and kinetic formation mechanisms (Binder 1970). Moreover, the dataset includes weather radar reflectivity measurements from a C-band (5-cm) weather radar located at Fyliro mountainous area, close to Thessaloniki. Radar reflectivity measurements have 750 m × 750 m spatial and 3.5 min temporal resolution. Storm characteristics are obtained using the cell tracker TITAN (Thunderstorm Identification, Tracking, Analysis, and Nowcasting) (Dixon and Wiener 1993).

3 Results

3.1 Synoptic and Dynamic Analysis

The UKMO surface analyses show that during the occurrence of the hail event (12 UTC 10/08/2008), northern Greece was affected by the edge of a cold front (Fig. 1a). In the middle troposphere (500 hPa) a trough is observed, with its axis located a few degrees to the west of the area of interest (Fig. 1b). Upward motions

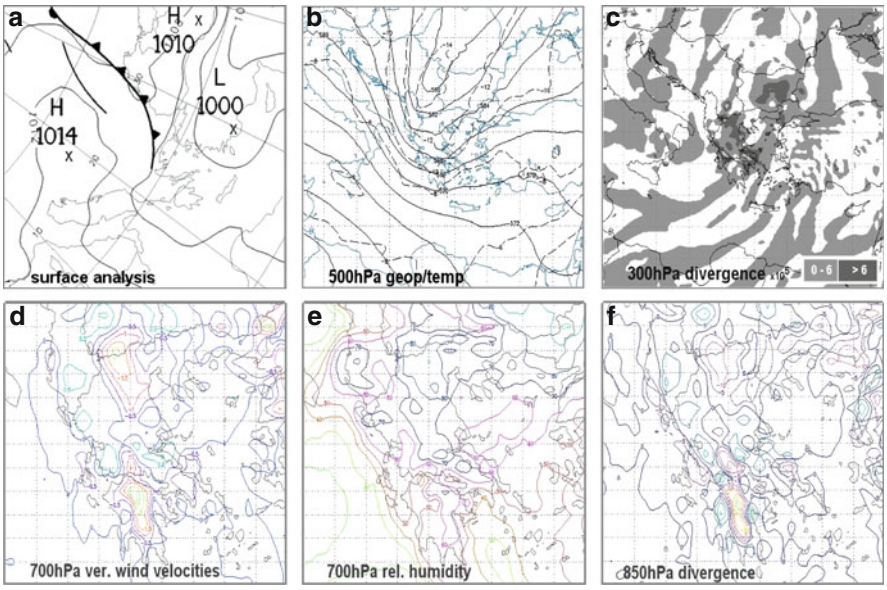

Fig. 1 Horizontal analyses of (**a**) mean sea-level pressure (hPa), (**b**) 500 hPa geopotential height (gpm) – *solid lines* and temperature (C) – *dashed lines*, (**c**) 300 hPa divergence ($\times 10^5$ s^{-1}), (**d**) 700 hPa vertical wind ($\times 10^5$ Pa/s), (**e**) 700 hPa relative humidity (%) and (**f**) 850 hPa divergence ($\times 10^5$ s^{-1}), at 1,200 UTC on 10 August 2008

are favored downstream of the trough (that is on its eastern flank), due to positive vorticity advection. The geopotential height and temperature over Central Macedonia at this level were about 5,630 gpm and −13°C, respectively. The trough is extended all the way to the upper troposphere (300 hPa), being associated with divergence over northern Greece (Fig. 1c). Convergence is observed in the lower troposphere, 700 and 850 hPa (Fig. 1f). The combination of these promotes the ascending motion (Fig. 1d) of moist lower tropospheric air masses (RH > 80–90%; Fig. 1e), triggering thus deep convection.

3.2 Thermodynamic Analysis

The development of severe storms and hailstorms requires the presence of thermodynamic instability related to moisture availability in the lower troposphere and vertical temperature lapse rate. A lifting mechanism must also be present in order to raise an air parcel to reach the level of free convection (LCL) (Johns and Doswell 1992). The calculated values of the five instability indices, using the Thessaloniki 1,200 UTC 10/08/08 sounding, are presented on Table 1. It is obvious that moderate to severe convection is expected over the area. CAPE suggests limited probability

Table 1 Instability indices at Thessaloniki synoptic station at 12:00 UTC on 10/08/2008

Index	Value	Description
K-index (KI)	39.2	KI > 30: atmospheric conditions potential for numerous thunderstorms to occur
Totals Total Index (TT)	53.8	TT > 52 indicates convective potential for severe thunderstorm developments
Showalter Index (SI)	−3.0	0 < SI < −3: unstable conditions and thunderstorm activity, SI < −3: extremely unstable conditions and severe thunderstorms
Convective Available Potential Energy (CAPE)	671.0	CAPE < 1,000 J/kg: restricted probability of severe thunderstorms.
Severe Weather Threat Index (SWEAT)	249.2	SWEAT > 250: strong potential for severe storm development

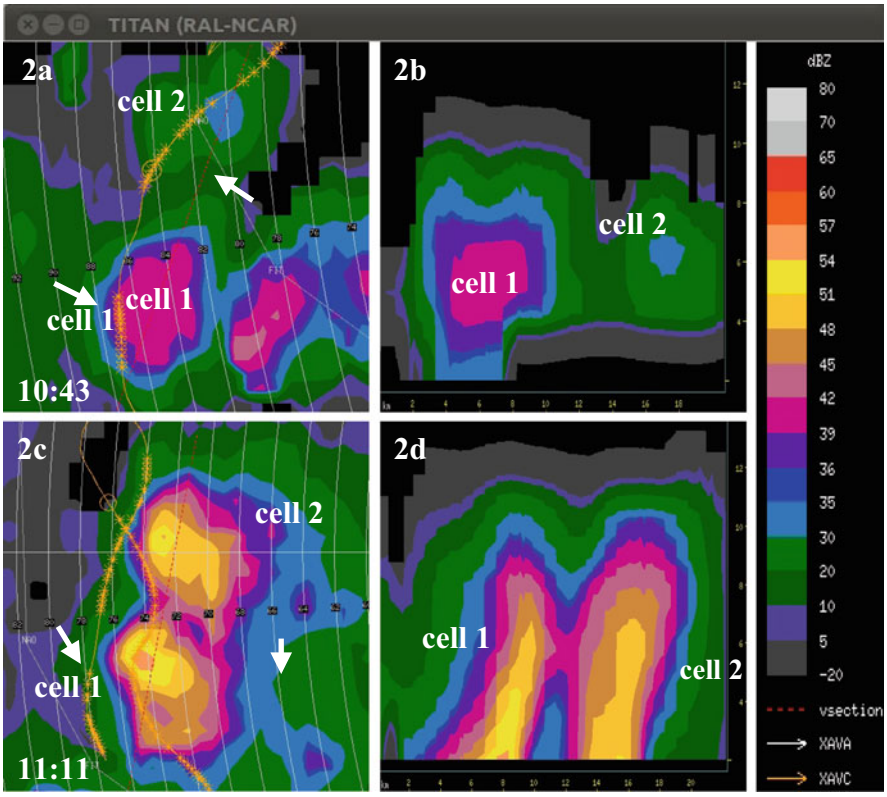

Fig. 2 PPI (composite) and RHI images of the storm at 10:43 UTC (**a** and **b**) and 11:11 UTC (**c** and **d**). RHI images are along the storm direction SW to NE (*dotted red line* in **a** and **c** images). Aircraft track position and seeding spots are also clearly marked

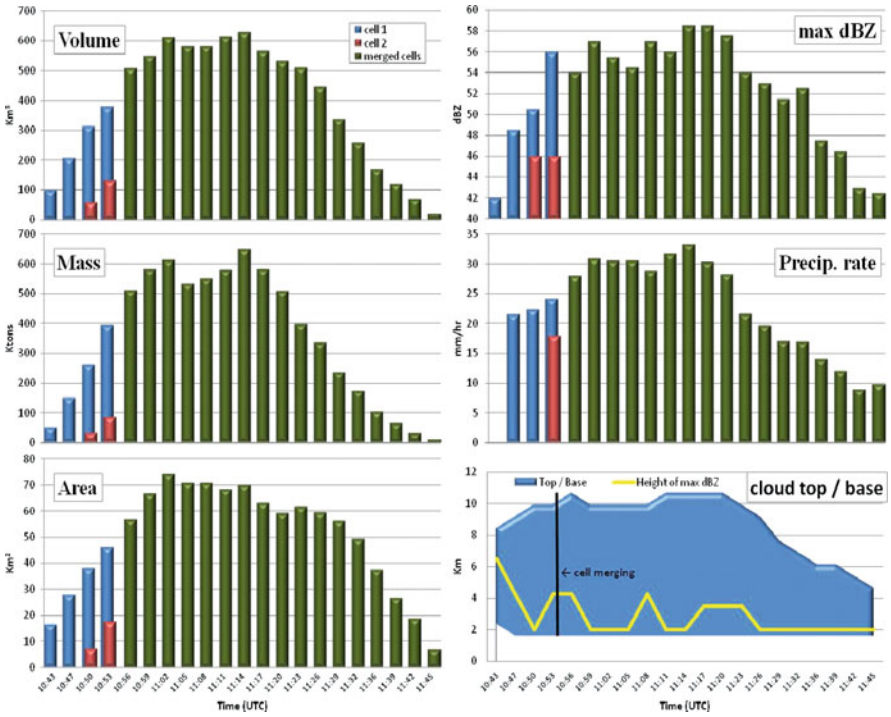

Fig. 3 Distribution of cell characteristics from 10:43 until 11:45 UTC on 10/08/2008 storm event

of severe thunderstorms. Consequently, the thermodynamic indices values clearly denote increased convection activity potential over the studied area.

3.3 Radar Analysis

The sequence of radar reflectivity images provides the storm characteristics necessary for the analysis and gives a realistic view of the storm development and motion. The event started as two individual cells (Fig. 2a and b, cell 1 and cell 2) formed over Vermion mountainous area and gave their first echo over 35 dBz at 10:43 and 10:50 UTC, respectively. At 10:56 UTC, 6–8 min after the cell 2 formation, the two cells merged into one multicell storm. Figure 2 shows the storm at two different times (before and after merger).

The total storm duration (above 35 dBz value) was about an hour (from 10:43 until 11:45 UTC). Its direction of movement was from southwest to northeast (230°), with an average speed of 25 km/h. Average values of the storm characteristics were: volume 361 km^3, mass 323 ktons, area 46.4 km^2, precipitation rate 24.9 mm/h, mean maximum reflectivity 51.7 dBz and mean maximum top

8.9 km. Instantaneous values of cell characteristics for each successive radar scan appear in Fig. 3. The cells were seeded several times before and after merging, since their direction was towards the protected by the NHSP area. Seeding took place three times on cell 1 and one time on cell 2, before merging. After the merger, the storm continued to develop, hence, it was seeded again three more times. Although the effects of seeding are not within the concept of this paper, a weakening was observed at 11:05 UTC (Fig. 3).

4 Conclusions

The synoptic, dynamic and thermodynamic characteristics of the storm event that occurred on the 10th August 2008 over central Macedonia were studied. Moreover, storm characteristics were obtained from weather radar reflectivity images for cell 1 further analysis and a more realistic view of the storm. Results of synoptic and dynamic analysis indicated that synoptic atmospheric conditions were favorable for storm development as low-level convergence and upper air divergence were present, along with increased moisture in the lower troposphere. These mechanisms, along with the surface heating, triggered storm development. These findings are in accordance with thermodynamic analysis and instability indices values.

References

Binder A (1970) The Air Force Global Weather Central Severe Weather Threat (SWEAT) index – a preliminary report. Air Weather Service Sciences Review, AWS 015–2 No. 70-3, pp 2–5

Dixon M, Wiener G (1993) TITAN: thunderstorm identification, tracking, analysis and nowcasting – a radar-based methodology. J Atmos Ocean Technol 10:785–797

Foris DV, Karacostas TS, Flocas AA, Makrogiannis TI (2006) Hailstorm in the region of Central Macedonia, Greece: a kinematic study. Meteorol Z 15:317–326

Johns RH, Doswell CA (1992) Severe local storms forecasting. Weather Forecast 7:588–612

Karacostas TS (1984) The design of the Greek National Hail Suppression Program. In: Proceedings of 9th conference on weather modif, AMS, Park City, UT

Karacostas TS (1991) Some characteristics of convective cells in the Greek National Hail Suppression Program. Geofiz 8:43–50

Miller RC (1967) Note on analysis and severe storm forecasting procedures of the Military Weather Warning Center, AWSTR 200, USAF

Moncrieff MW, Green JSA (1972) The propagation of steady convective overturning in shear. Q J R Meteorol Soc 98:336–352. doi:10.1002/qj.49709841607

Showalter AK (1953) A stability index for thunderstorm forecasting. Bull Am Meteorol Soc 34:250–252

A Three-Dimensional Simulation of the 10th August 2008 Storm Occurred Over Greece: AgI Seeding of Cell Merger by Using a Cloud Resolving Model

T. Karacostas, V. Spiridonov, S. Stolaki, I. Pytharoulis, and I. Tegoulias

Abstract A three-dimensional cloud resolving model is used to study the 10th of August intensive storm. This convective case occurred over north-central Greece and resembled similar characteristics of a cell merger, causing heavy rainfall, hailfall and high-frequency lightning. Three distinct numerical experiments have been performed. In the unseeded case, the structural and evolutionary properties of the reflectivity are analyzed, horizontally and vertically, in different simulation times. The 3-d numerical simulations suggest that the merger process occurred from two or three isolated single-cells, formed during their SW-NE motion. The merging process apparently alters the dynamical and microphysical properties through low and middle level forcing, increasing cloud diameters and cloud depths, enhancing convection, producing more graupel and ice particles and increasing radar reflectivity values. The resolved TITAN radar imageries depict a similar view of the storm structure, evolution and interactions of such merging processes. The model calculated maximum radar reflectivity values coincide with the recorded ones. For these specific cell mergers, two distinct seeding experiments were conducted, to find out the optimal seeding parameters, related to seeding criteria. Specific storm characteristics are demonstrated for the stages: before and after seeding, and before and after merging.

T. Karacostas (✉) • S. Stolaki • I. Pytharoulis • I. Tegoulias
Department of Meteorology and Climatology, School of Geology, Aristotle University of Thessaloniki, Thessaloniki 541 24, Greece
e-mail: karac@geo.auth.gr

V. Spiridonov
Faculty of Natural Sciences and Mathematics, Institute of Physics, Gazi Baba bb 1000, Skopje, Macedonia

C.G. Helmis and P.T. Nastos (eds.), *Advances in Meteorology, Climatology and Atmospheric Physics*, Springer Atmospheric Sciences,
DOI 10.1007/978-3-642-29172-2_22,

1 Introduction

An important aspect in the study of cumulonimbus convection is the identification of situations such as cloud splitting or merging which lead to intense hailfall and rainfall (Curic et al. 2009; Spiridonov et al. 2010). These processes are found to depend on the variation of wind with height, the relative stage of development of the two clouds-cells and their initial separation. Interaction between convective cells may alter cells on longevity, intensity, and propagation characteristics. A case similar to that is examined, where two initially separate clouds interact and merge. The objective on this numerical experiment is, firstly to reproduce, then to study, and most importantly to conduct an airborne seeding experiment, similar to those performed during the Greek National Hail Suppression Program (NHSP). Numerical sensitivity tests have been performed in order to reproduce the operational seeding carried out for the same case study, evaluating thus the seeding hypothesis and the optimal results, through seeding convective cloud in different phase of their evolution.

2 The Model

The convective cloud (resolving) model has been used to simulate the cloud seeding. The model is a three-dimensional, non-hydrostatic, time-dependant, compressible, homogeneous system using the dynamic scheme from Klemp and Wilhelmson (1978). The thermodynamic energy equation is based on Orville and Kopp (1977). The bulk microphysical parameterization is according to Lin et al. (1983), with a treatment of all water categories: water vapor, cloud water, cloud ice, rain, snow and graupel or hail. Two governing equations of the mixing ratio of the ice crystals number concentration (Ni) and seeding agent (Xs) are accomplished by using additional conservation equations. The activation of AgI is parameterized by the three nucleation mechanisms, based on Hsie et al. (1980) and Kopp (1988). Since the AgI agent is released in respect to the model on a sub-scale, its advection and turbulence are parameterized by using turbulent spreading of puff as function of the turbulent diffusion coefficient (Georgopoulos and Seinfeld 1986). More detail information about the model, initial and boundary conditions, numerical technique and initialization and seeding module, could be found in Telenta and Aleksic (1988) and Spiridonov and Curic (2006).

3 Initial Data and Methodology

Model uses homogeneous meteorological fields with artificial initiation of convection, using a thermal bubble and temperature perturbation. Topography of the terrain is not represented in the present version of the model. The model is

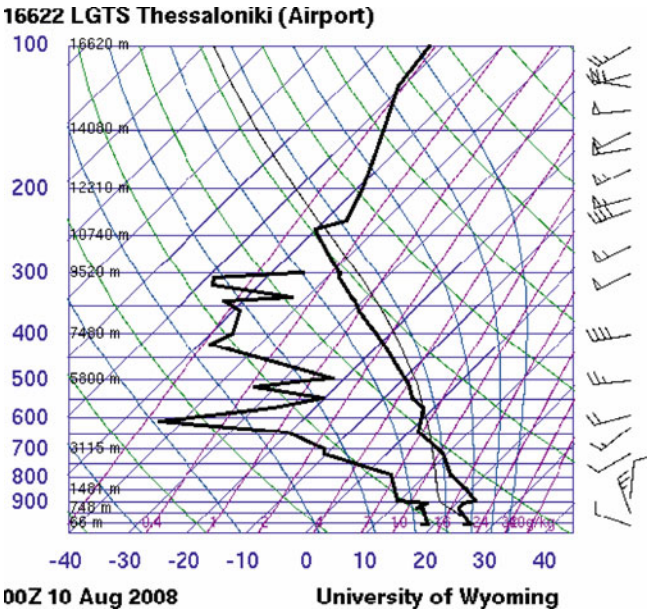

Fig. 1 Upper air sounding for Thessaloniki on 10th August 2008, 00 UTC (University of Wyoming)

initialized on upper air sounding representing initial vertical profiles of meteorological data for the 10th August 2008 for Thessaloniki, Greece (Fig. 1). Upper air sounding indicates unstable atmospheric conditions favorable for convection. Main characteristic of the upper air sounding is a weak wind veering condition in the surface layer and strong wind shear at the middle and upper part of the atmosphere. Vertical profile indicates moisture deficit at 500 hPa pressure level, and increase moisture content at 700 and 300 hPa levels.

Cloud seeding experiments have been performed following the Greek NHSP, adopted by Karacostas (1984, 1989). Three distinct numerical experiments have been performed in this study. The first numerical experiment is an unseeded case simulation, where it is tested the performance of the cloud resolving model to adequately reproducing this specific convective case study occurred on 10 August 2008, being associate with a cell splitting and merging processes.

The second experiment run is a numerical simulation of cloud seeding of splitting cells, before they start merging. Modeling of cloud seeding approach follows the Greek operational seeding procedures already conducted during daily airborne seeding operations.

The third numerical experiment is designed on cloud seeding of cell merging.

4 Model Results

The first run of this convective case shows the development and evolution of a typical ordered multicell convective storm. Figure 2 shows a three dimensional depictions of the cloud life cycle, viewed form SW to NE, at 20 min intervals, starting at 20 min simulation time. The convective cloud seems to start its development with the appearance of two individual cells. In this developing stage, the convective cells interact mutually in a gradually entering merging phase. After cell merging, cloud exhibits more intensive growth and change its structure by altering its internal dynamical and microphysical characteristics. This merging process intensified the cloud growth, accelerated the precipitation formation processes and increased the rainfall and hailfall at the ground. The life cycle of this intensive convective system was continuously monitored by C-band weather radar, using the TITAN (Thunderstorm Identification, Tracking, Analysis, and Nowcasting) visualization tool (Dixon and Wiener 1993).

Figure 3 shows radar scanned PPI data in three different observation times versus model calculated radar data. It is important to note that the radar image domain shown on Fig. 2a is consistent with the model integration domain. The cell splitting and merging processes are easily detected by PPI and RHI radar images. The horizontal transects of the modeled reflectivity fields show a very good agreement with observations.

Additional research is pursued with the examination of the capability of the cloud resolving model, for the simulation of the cloud seeding applied through different seeding strategies. The first seeding experiment is focused on seeding the two splitting cells, 20 min of the simulation time before merging. The trajectories of airborne seeding for both cases are shown in Fig. 4. These individual splitting cells are seeded at height 5.25 km, on the upshear side, above the 25 dBz reflectivity zones, with the seeding rate of two flares within 5 min. The second seeding

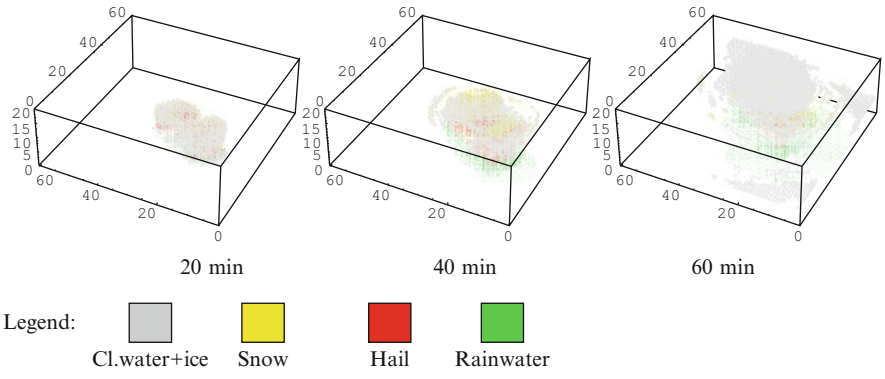

Fig. 2 3-D depictions of convective cloud occurred over Greece on 10th August, 2008 in 20, 40 and 60 min of the simulation time. Plot areas with *grey*, *yellow*, *red* and *green* colors denote mixing ratios of total cloud water, snow, hail and rainwater, with threshold value 0.1 (g/kg)

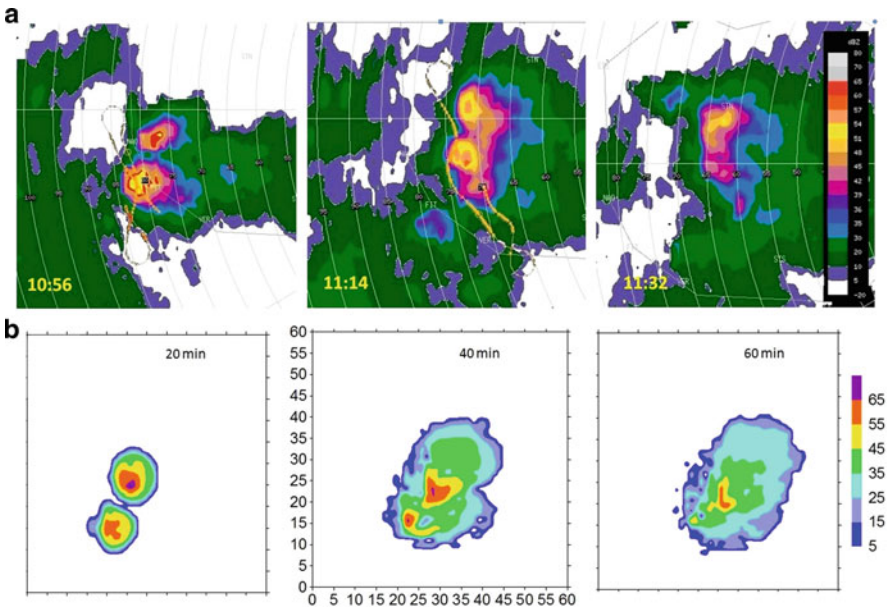

Fig. 3 (**a**) PPI radar images provided by TITAN tracking algorithm in three distinct radar observation times. (**b**) Modeled radar reflectivity horizontal transects at 5.2 km height.

experiment is conducted 35 min of the simulation time after initial cell merging, in cloud developing stage at height 4.75 km, with the same seeding rate.

Figure 5 shows the three dimensional depictions of the convective cloud, in 50 min of the simulation time of unseeded cloud, seeded before merging and after merging.

Although it is quite difficult – on the first sight – to identify remarkable changes, there are some differences in the microphysical structure. It is demonstrated that cloud seeding modified the cloud shape and caused a decrease of hail and rainwater mixing ratio, with more remarkable results in case of seeding the cloud before it's merging.

Seeding the cloud before merging has resulted to an increase for cloud ice mixing ratio and to a decrease on hailfall. The calculated percentages reach to the levels of 21% and 9% in both seeded cases, respectively.

5 Conclusions

A three-dimensional cloud resolving model is used to study the 10th of August 2008 intensive storm occurred over Greece. The main storm dynamical characteristics (splitting and merging), during the whole life cycle of the convective cloud, are correctly simulated by the adopted model resembling great similarities to the observed radar reflectivity fields images. The two seeding experiments show optimistic results in respect to the seeding effects of such convective case, where

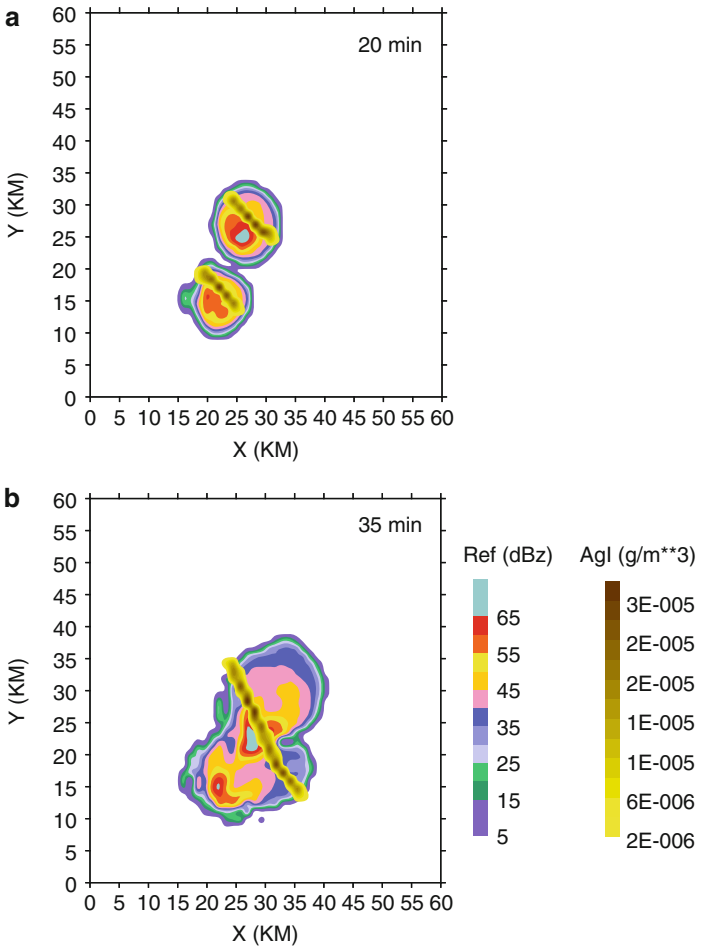

Fig. 4 Horizontal cross section of radar reflectivity at 5.2 km height and airborne seeding trajectories: (**a**) before merging, (**b**) after initial cell merging

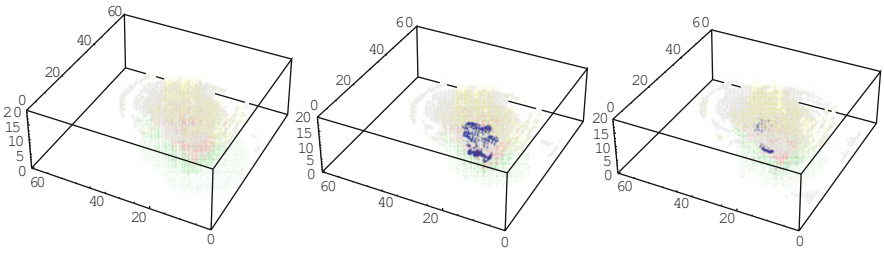

Fig. 5 Same as Fig. 2, but with added mixing ratio for AgI, with threshold values 0.1 (g/kg)

cell merging plays a crucial role in the intensification of storm evolution, producing intensive rainfall and hailfall at the ground. Seeding the cloud before it's merging, shows more positive effects to the hail suppression. The calculated results suggest that seeding before and after merging causes 21% and 9% hailfall decrease, respectively. These findings are quite important information for both: (a) to document the value of the cloud resolving model and its capability to adequately simulate and well reproduce the realistic storm processes and its behavior and (b) to provide with the potential knowledge for the design of the operational daily seeding strategy, during the Greek NHSP.

References

Curic M, Janc D, Vuekovic V (2009) The influence of merging and individual storm splitting on mesoscale convective system formation. Atmos Res 93(1–3):21–29

Dixon M, Wiener G (1993) TITAN: thunderstorm identification, tracking, analysis and nowcasting – a radar-based methodology. J Atmos Ocean Technol 10:785–797

Georgopoulos PG, Seinfeld JH (1986) Mathematical modeling of turbulent reacting plumes – general theory and model formulation. Atmos Environ 20:1791–1802

Hsie E-Y, Farley RD, Orville HD (1980) Numerical simulation of ice-phase convective cloud seeding. J Appl Meteorol 19:950–977

Karacostas TS (1984) The design of the Greek NHSP. In: Proceeding of the 9th conference on weather modification, AMS, Park City, UT

Karacostas TS (1989) The Greek National Hail Suppression Program, 1989: design and conduct of the experiment. In: Proceedings of 5th WMO science conference on weather modification and applied cloud physics, WMO/TD-269, Beijing, pp 605–608

Klemp JB, Wilhelmson RB (1978) The simulation of three-dimensional convective storm dynamics. J Atmos Sci 35:1070–1096

Kopp FJ (1988) A simulation of Alberta cumulus. J Appl Meteorol 27:626–641

Lin Y-L, Rarley RD, Orville HD (1983) Bulk parameterization of the snow field in a cloud model. J Appl Meteorol 22:1065–1092

Orville HD, Kopp FJ (1977) Numerical simulation of the history of a hailstorm. J Atmos Sci 34:1596–1618. doi:10.1175/1520-0469(1977) 034<1596:NSOTLH>2.0.CO;2

Spiridonov V, Curic M (2006) A three-dimensional modeling studies of hailstorm seeding. J Weather Modif 38:31–37

Spiridonov V, Dimitrovski Z, Curic M (2010) A three-dimensional simulation of supercell convective storm. Adv Meteorol 15. doi: 10.1155/2010/234731

Telenta B, Aleksic N (1988) A three-dimensional simulation of the 17 June 1978 HIPLEXcase with observed ice multiplication. 2nd International cloud modeling workshop, Toulouse, 8–12 August 1988. WMO/TD No. 268, pp 277–285

The Meteorological Setting of a Particulate Air Pollution Episode During November 2009, in Western Macedonia Industrial Area, Greece

A.F. Karagiannidis, A.G. Triantafyllou, and T. Karacostas

Abstract A particulate air pollution episode of relatively long duration was recorded in the industrial basin of Western Macedonia, Greece, during November of 2009. A case study of the meteorological aspects of this episode is presented in this paper, based on the combined utilization of PM10 concentration measurements, surface and lower atmosphere parameters and simulations. An Omega blocking pattern which gradually transformed to a high-over-low pattern prevailed over central and southern Europe during the episode's period. The absence of significant convection in the middle and lower troposphere combined with a weak horizontal wind field near the surface and the reduced mixing height, resulted in the pollutants' trapping and the increased PM10 concentrations. The change of the synoptic setting marked the end of the episode.

1 Introduction

In western Macedonia/Greece region and especially in the complex terrain basin of Amyntaio–Ptolemais–Kozani (BAPK), PSs and mines are operated, resulting in large amount of particulate matter (PM) emissions and atmospheric pollution episodes under specific atmospheric conditions (Triantafyllou 2003). The relation of the meteorological conditions to the atmospheric pollution helps to successfully forecast extreme air pollution episodes, in order for governments and civilians, to prepare for, or even avoid them (Kallos et al. 1993; Triantafyllou 2001; Flocas et al.

A.F. Karagiannidis (✉) • A.G. Triantafyllou
Laboratory of Atmospheric Pollution and Environmental Physics, School of Technological Applications, TEI of Western Macedonia, 50100 Kozani, Greece
e-mail: thankar@live.com

T. Karacostas
Department of Meteorology and Climatology, School of Geology, Aristotle University of Thessaloniki, Thessaloniki, Greece

C.G. Helmis and P.T. Nastos (eds.), *Advances in Meteorology, Climatology and Atmospheric Physics*, Springer Atmospheric Sciences,
DOI 10.1007/978-3-642-29172-2_23,

2009). The meteorological setting during a particulate air pollution episode during November 2009 is investigated in the present paper. The episode is identified by means of PM10 concentration values in specific sites along the BAPK axis. The data used are: (a) mean daily PM10 concentrations from the atmospheric pollution stations network of the Greek Public Power Corporation (PPC) and the Laboratory of Atmospheric Pollution and Environmental Physics of the School of Technological Applications of TEI of Western Macedonia, (b) operational ECMWF analyses data, (c) soundings data and (d) vertical profiles of the basic meteorological parameters, produced by a prognostic local scale meteorological model.

2 The Area

The BAPK is situated in a mountainous area of western Macedonia, Greece. It presents a NW to SE orientation, with Amyntaio at the north and Kozani at the south end. Figure 1a depicts a topographic map of the area, the measuring stations (1,. . .13) and the power plants sites (PS1, PS6).

3 Data and Methodology

Hourly observational data from stations belonging to the Greek Power Corporation (GPC) and to the Laboratory of Atmospheric Pollution and Environmental Physics of the School of Technological Applications of TEI of Western Macedonia are one of the primary data sets used. These data include surface wind speed and direction and PM10 concentration measurements, extending from 1/11/2009 to 30/12/2009. Based on the hourly observations, mean daily values are also computed. Monthly PM10 values have been derived for November and December of 2006 to 2009 using archived data. Operational ECMWF analysis data of horizontal resolution of 0.25×0.25 degrees and temporal resolution of 6 h, at all the basic pressure levels, are used to produce the required synoptic charts by means of Grid Analysis and Display System (GrADS). The Mean Sea Level Pressure (MSLP) and the 500 hPa geopotential height field are examined to define the synoptic conditions of the episode. The meteorological component of The Air Pollution Model (Hurley et al. 2001, 2005; Triantafyllou et al. 2011) is also used to produce hourly vertical profiles of specific atmospheric parameters like temperature, potential temperature, wind speed and direction and other useful variables like the mixing height for selected sites of the area. Finally, sounding data from the nearest sounding station (Thessaloniki) are used, mainly to determine the presence of vertical forcing through the examination of stability indices such as the Total Totals Index (TTI), the Lifted Index (LI), the K-Index (KI) and the Showalter Index (SI).

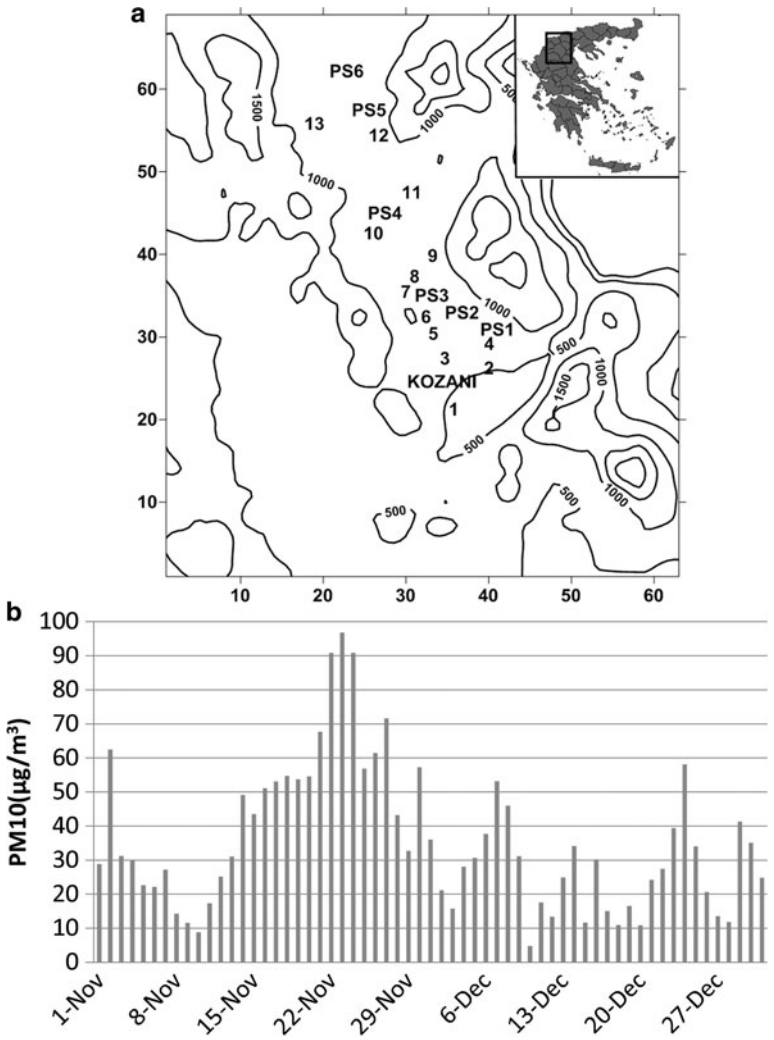

Fig. 1 (**a**) Measuring stations (1, 2, 3,. . .) and power plants sites (PS1,PS2,. . .); (**b**) daily PM10 concentration values, averaged over all available measuring stations

4 Results

The definition of the exact time period of the episode is not a straightforward task, due to the diversity of the measuring sites. Daily PM10 mean values from November of 2006 to November of 2009 are used to calculate the November 3rd quartile PM10 daily value for each measuring site. Any day with mean PM10 value exceeding this value is considered to be part of the episode.

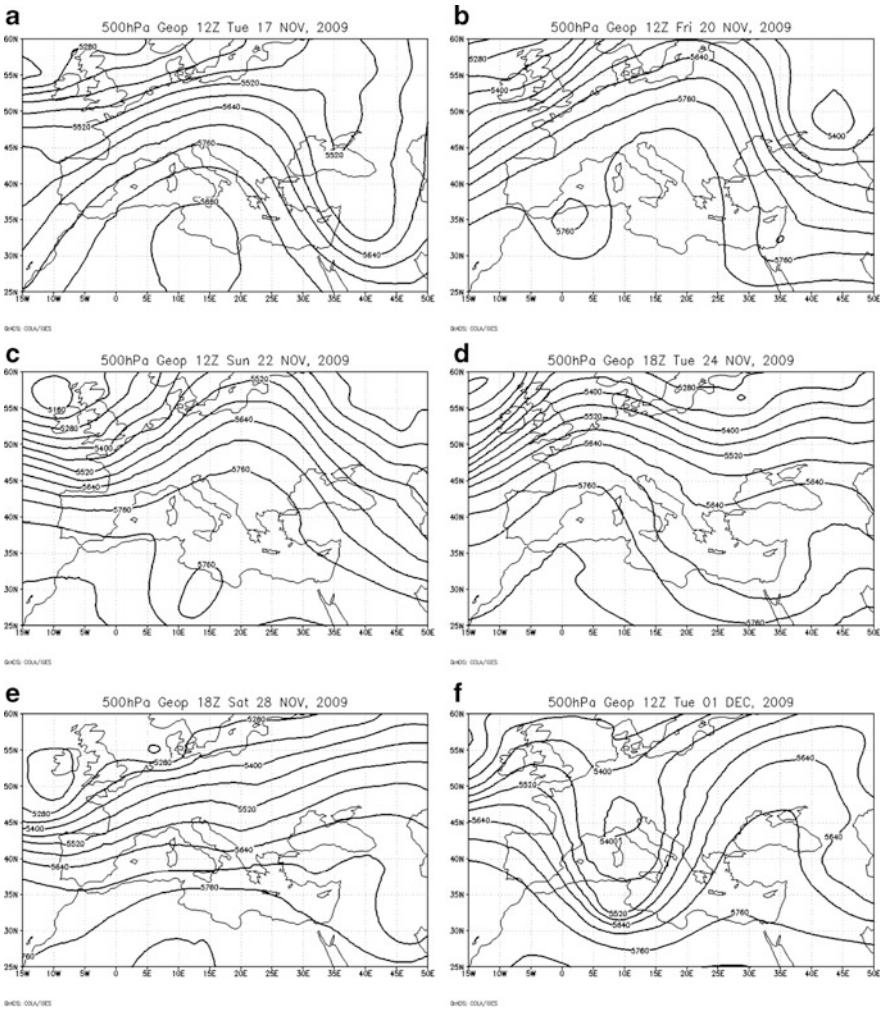

Fig. 2 Geopotential height at the 500 hPa level during significant time instances of the episode

The studied episode starts at the 14th of November for half of the stations (1 or 2 days later for the rest) and ends after the 27th, showing a peak between the 22nd and the 24th. This is denoted in Fig. 1b, where the time evolution of the daily average PM10 concentration amongst all the measuring sites is depicted. Concluding, the episode is considered to extend from the 14th to the end of November 2009.

The synoptic setting in Europe is investigated based on MSLP and 500 hPa synoptic charts. Southern Europe is dominated by an Omega block (Huschke 1959; Karacostas et al. 2006) from 17/11 to 20/11 as it can be seen in Fig. 2a and b. During the 21st and 22nd the Omega block gradually transforms to a high-over-low pattern (Fig. 2c) that lasts until the night of the 23rd of November. At the afternoon of the

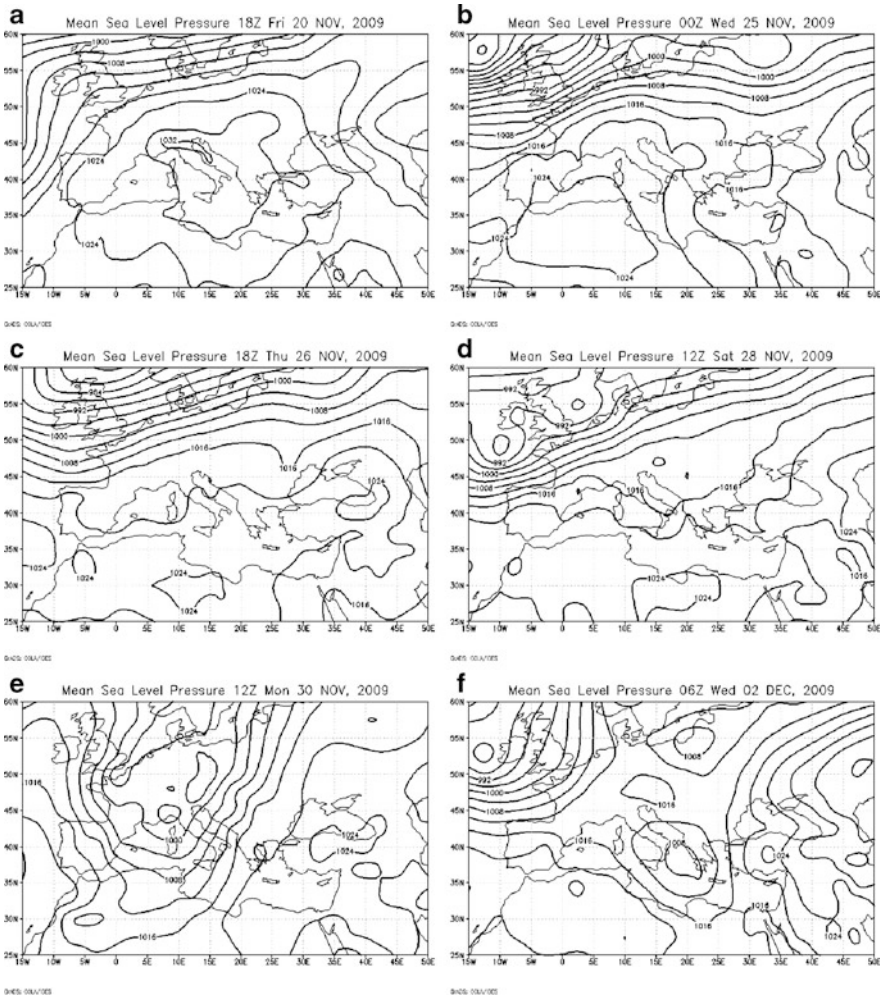

Fig. 3 MSLP during significant time instances of the episode

24th (Fig. 2d) a short wave embedded on the almost stagnant long wave passes over Western Macedonia and reinforces temporarily the surface wind field. Another short wave passes over the area during the afternoon of the 28th (Fig. 2e) causing light rainfall. A trough associated with a deep depression, approaches Greece during the 1st of December (Fig. 2f) establishing a strong southeasterly flow and producing significant rainfall in western Macedonia during the 1st and 2nd of December.

Due to the Omega block that dominates the area, MSLP and therefore the associated surface wind field, is quite weak (Fig. 3a), strengthening during the passing of the first short wave on the 25th of November (Fig. 3b). The horizontal

wind field in the lower troposphere weakens again during the 26th of November (Fig. 3c) and strengthens again due to the second short wave of the 28th (Fig. 3d). The approach of the trough preserves the strong surface horizontal wind (Fig. 3e) until the first days of December when the depression reaches the examined area (Fig. 3f).

An almost constant increase of PM10 concentrations is recorded as the surface wind remains quite weak. During the 25th of November when the wind field strengthens temporarily, PM10 values drop significantly at most of the measuring sites. The same pattern appears after the 28th of November when the wind field presents another significant increase (Fig. 4a).

Hourly mixing height values are calculated by TAMP at various sites. Figure 5 shows the diurnal variation of this parameter from 15th to 30th of November at Petrana (2, Fig. 1a) and Pontokomi (5, Fig. 1a). Low mixing height values are recorder during most hours of the days, increasing only around midday. Moreover, a gradual decrease of the top of the mixing height until 22nd of November is recorder. Another significant feature is the increased mixing height during the last hours of the 25th and the first ones of the 26th of November.

The examination of the diurnal variation vertical profiles produced by TAPM, (an example is presented in Fig. 4b) shows a strong surface temperature inversion existing during late afternoon, night and morning hours. The base of the inversion is lifted only around the warm hours of the day and in some cases a shallow convective boundary layer is formed. In general, the diurnal variation of the bottom of the inversion follows a pattern similar to that of the mixing height. It becomes evident that pollutants are practically trapped in the lower boundary layer.

The sounding examination of the nearest station (Macedonia airport, Thessaloniki) confirms the lack of significant synoptic forcing. Four of most common stability indices, TTI, SI, KI and LI, are calculated indicating relative stability, during the episode period.

5 Conclusions

The evaluation and synthesis of the results presented in the previous section can be summarized in the following:

- The PM10 intensive pollution episode that was recorded in the BAPK during the last 15 days of November 2009 is the result of the synoptic setting that prevailed in the middle and lower troposphere. An Omega block followed by a high-over-low pattern in the southern Europe formed such an ABL structure in the area of interest, which favored high PM10 concentrations.
- A ground based temperature inversion persisted during most of the days, except the warm hours of the day, when a shallow convective layer was developed.

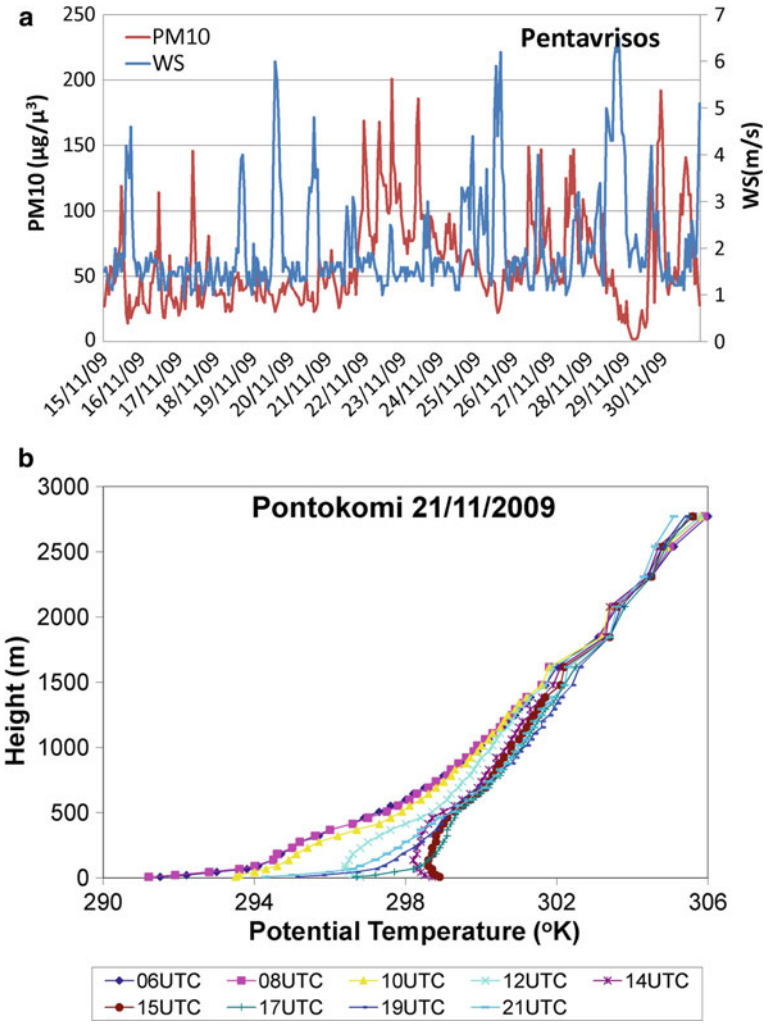

Fig. 4 (**a**) Wind speed (m/s) and PM10 (μg/m^3) hourly values at Pentavrisos (Fig. 1a measuring station 9) from 15th to 30th of November; (**b**) vertical profile of potential temperature at Pontokomi (Fig. 1a measuring station 5)

The lack of significant synoptic forcing allowed the lingering of the pollutants inside the boundary layer.

- The wind field in the surface and lower troposphere was very weak and assisted to the trapping of pollutants in the lowest part of the boundary layer increasing thus the PM10 concentrations values.
- The PM10 values were related satisfactory with the mixing height variation in the area, during the episode period.

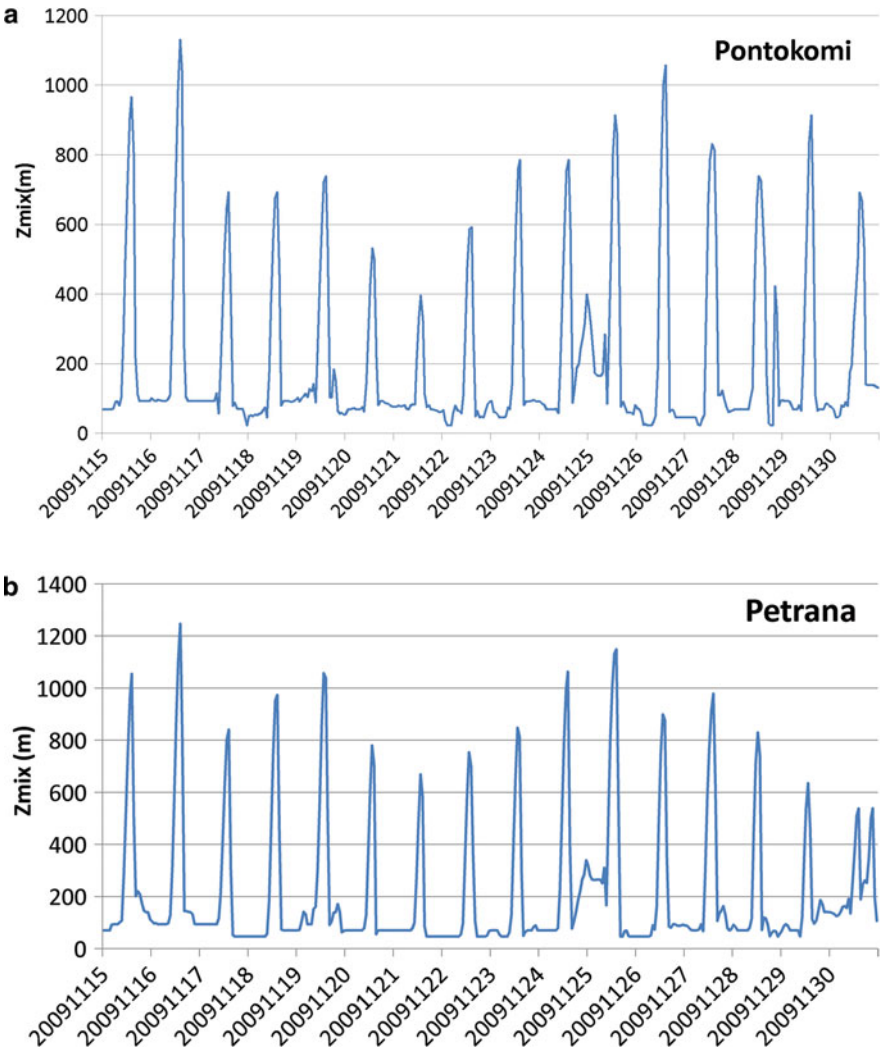

Fig. 5 Mixing height (m) hourly values at (**a**) Pontokomi and (**b**) Petrana from the 15th to the 30th of November

- The change of the synoptic setting during the last days of the episode caused the development of significant synoptic forcing and the strengthening of the horizontal wind field near the surface, resulting in a significant decrease of PM10 concentration. The rainfall that followed marked the end of the episode.

Acknowledgments The authors would like to thank the Greek Public Power Corporation for providing the data.

References

Flocas H, Kelessis A, Helmis C, Petrakakis M, Zoumakis M, Pappas K (2009) Synoptic and local scale atmospheric circulation associated with air pollution episodes in an urban Mediterranean area. Theor Appl Climatol 95:265–277. doi:10.1007/s00704-008-0005-9

Hurley P, Blockley A, Rayner K (2001) Verification of a prognostic meteorological and air pollution model for year-long predictions in the Kwinana region of Western Australia. Atmos Environ 35:1871–1880. doi:10.1016/S1352-2310(00)00486-6

Hurley P, Physick W, Luhar A (2005) TAPM – a practical approach to prognostic meteorological and air pollution modeling. Environ Model Softw 20:737–752. doi:10.1016/j.envsoft.2004.04.006

Huschke RE (1959) Glossary of meteorology. American Meteorological Society, Boston

Kallos G, Kassomenos P, Pielke RA (1993) Synoptic and mesoscale weather conditions during air pollution episodes in Athens, Greece. Bound-Lay Meteorol 62:163–184. doi:10.1007/BF00705553

Karacostas Th, Kontogianni P, Roupa P, Lysitsa E, Brikas D, Mitas C (2006) Study of the characteristics of omega blocking episodes over the major area of south-east Europe. In: Proceedings of eighth Panhellenic conference of meteorology, climatology and atmospheric physics, Hellenic Meteorological Society, Athens, pp 233–242

Triantafyllou AG (2001) PM10 pollution episodes as a function of synoptic climatology in a mountainous industrial area. Environ Pollut 112(3):91–500. doi:10.1016/S0269-7491(00)00131-7

Triantafyllou AG (2003) Levels and trend of suspended particles around large lignite power stations. Environ Monit Assess 89:15–34. doi:10.1023/A:1025829907390

Triantafyllou AG, Skordas S, Diamantopoulos Ch, Mattheos S (2011) EAP/WMAQIS: the new dynamic atmospheric quality information system and its application in western Macedonia, Hellas. In: 16th International symposium on environmental pollution and its impact on life in the Mediterranean region, Ioannina, Greece, organized by MESAEP

A First Comparative Analysis of Temperature Data Collected from Automatic and Conventional Weather Stations in Greece

N. Karatarakis, A. Sarantopoulos, T. Charantonis, P.T. Nastos, K. Lianos, and K. Petsa

Abstract A new automatic system of meteorological observations has become operational at Hellenic National Meteorological Service. This new system attempts to overcome the problems of shortage of personnel and limited budget in recent years. The data collected from both systems of observation are analysed to detect any differences between them, understand these better, and perform any necessary adjustments. These differences may become important in evaluating normal values, developing homogenized data and examining climate variability and change. A first analysis of common temperature synoptic data collected from 11 Meteorological Stations is analyzed, for a period of 18 months. Dry, minimum, and maximum temperatures are studied. Results show that, in most cases, there is a very good correlation for all parameters; however, there are significant biases between corresponding values of new Automatic Weather Stations (AWS) and the Conventional Weather Stations (CWS).

1 Introduction

The automatic system of meteorological observations with the use of electronic sensors has been becoming operational at Hellenic National Meteorological Service.

There are a few published studies on comparison of data from Automated Weather Stations (AWS) and Conventional Weather Stations (CWS). Differences

N. Karatarakis • A. Sarantopoulos (✉) • T. Charantonis
Hellenic National Meteorological Service, Hellinikon 16777, Greece
e-mail: sarantopoulos@gmail.com

P.T. Nastos • K. Lianos
National and Kapodistrian University of Athens, Athens, Greece

K. Petsa
University of the Aegean, Mytilene, Greece

C.G. Helmis and P.T. Nastos (eds.), *Advances in Meteorology, Climatology and Atmospheric Physics*, Springer Atmospheric Sciences,
DOI 10.1007/978-3-642-29172-2_24,

in sitings of AWS and CWS systems can cause variations in respective datasets. According to Davey and Pielke (2005), the collocation of the station sites can be useful in reducing siting errors on climatological datasets, which play a critical role in assessment of regional changes of climate.

The Guttman and Baker (1996) study, which analyzed data from AWS and CWS, resulted in a conclusion that, even though variability in datasets is caused by different sensors and observation techniques, the most significant differences between the two datasets come from the distance separating the stations and from the differences in land usage and topography.

In this study, a first analysis of temperature data collected from 11 Meteorological Stations is attempted. The study period is 18 months and data from common synoptic hours is examined. Specifically, the parameters of dry temperature for three main synoptic hours of observation (06, 12, 18 UTC) and minimum and maximum temperature are studied.

Most of the conventional weather stations of the Hellenic National Meteorological Service have been operating since early 1950s. Recently, a system of automated weather stations has been developing. This automated system of collecting meteorological data has been expanded in National Observatory of Athens, Ministry of Agriculture and several academic and research institutes.

Results show that, in general, there is a very good correlation for dry temperature, maximum temperature, and minimum temperature for most stations studied. However, in some cases, there are significant differences which indicate that fine-tuning of AWS sensors is needed.

2 Data and Methodology

2.1 Data

The temperature data used in this study covers a period of 18 months (January 2010 to June 2011) and was collected from 11 co-located AWS and CWS of the Greek territory. The stations studied are: Andravida (LGAD), Ioannina (LGIO), Kozani (LGKZ), Lamia (LAMI), Aghialos (LGBL), Kefalonia (LGKF), Siteia (LGST), Tripoli (LGTP), Thessaloniki (LGTS), Naxos (NAXO), and Larisa (LGLR).

Only available common observations for the main three synoptic hours of observation (06, 12, 18 UTC) were examined.

2.2 Methodology

From the recorded observations, three time series were created for each station studied, corresponding to dry, maximum, and minimum temperature.

For each observed temperature variable, the difference $\Delta T(x) = T_{CWS}(x) - T_{AWS}(x)$ was computed. T_{CWS} is the measured variable from the conventional weather stations (CWS) and T_{AWS} is the measured variable from the automatic weather stations (AWS) and x the type of temperature variable, $x \in \{dry, max, min\}$.

From the above data, basic statistics were computed along with histograms of the differences and scatter diagrams. The Pearson correlation coefficients were calculated between $T_{CWS}(x)$ and $T_{AWS}(x)$.

3 Results

Examining the differences $\Delta T(x)$ we realized that:

Dry temperatures of AWS are generally higher than those of CWS. The means of $\Delta T(dry)$ do not exceed $-1°C$, $[-1 < \Delta T(dry) < 0]$ except for MS Aghialos and Kozani, where means of $\Delta T(dry)$ are positive (+0.2°C and +0.3°C respectively).

With respect to maximum temperatures, AWS data are generally higher than those of CWS. The means of the difference $\Delta T(max)$ are very small and do not exceed $-1°C$, except for MS Ioannina, where difference is $-1.3°C$.

Finally, minimum temperature is underestimated by the AWS in all cases, expect for MS Kefalonia. The differences $\Delta T(min)$ in the means do not exceed +1°C except for MS Kefalonia, where this difference is $-0.1°C$. In general, differences in standard deviation follow the same pattern with means with some exceptions.

Statistics for the matched variables resulting from the difference of the CWS and AWS data, namely, $\Delta T(dry)$, $\Delta T(max)$, and $\Delta T(min)$ were computed. In general, a negative difference in the temperature values indicates that AWS overestimate temperature and a positive difference indicates that AWS underestimate temperature.

Results for $\Delta T(dry)$ show that there is a bias ranging from $-0.7°C$ (Thessaloniki) to 1.4°C (Naxos). In addition, the standard deviation for $\Delta T(dry)$ ranged from 0.5°C (Siteia) to 7.7°C (Naxos). $\Delta T(max)$ ranges from $-3.3°C$ (Thessaloniki) to 1.4°C (Naxos). Also, the standard deviation for $\Delta T(max)$ ranges from 0.4°C (Aghialos) to 6.0°C (Naxos). Finally, the $\Delta T(min)$ ranges from 0.1°C (MS Kozani) to 2.2°C (MS Naxos). Also, the standard deviation for $\Delta T(min)$ ranges from 0.4°C (Siteia) to 12.0°C (Naxos).

95% confidence intervals of the differences were computed along with Pearson correlation coefficients, r, of CWS and AWS data. Results show a strong correlation for all stations except Naxos which exhibited moderate correlation for Tdry, Tmax, and Tmin. Also, in all cases, correlation is significant at the 0.01 level (two-tailed). This is in agreement with findings of Holder et al. (2006) which state that without correcting the data for differing observations times, daily temperature observations are generally in good agreement.

Finally, histograms with the normal curve were generated for the differences between CWS and AWS data. Three of them are shown in Figs. 1, 2, 3 (left). The histograms indicate that there is a shift to the left or to the right of 0. This is due to

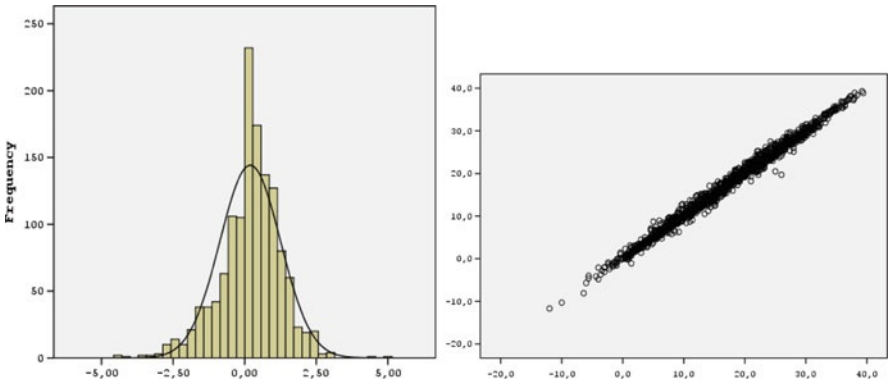

Fig. 1 (*left*) ΔTdry (LGTP); (*right*) T_{AWS}(dry) versus T_{CWS}(dry) (LGLR)

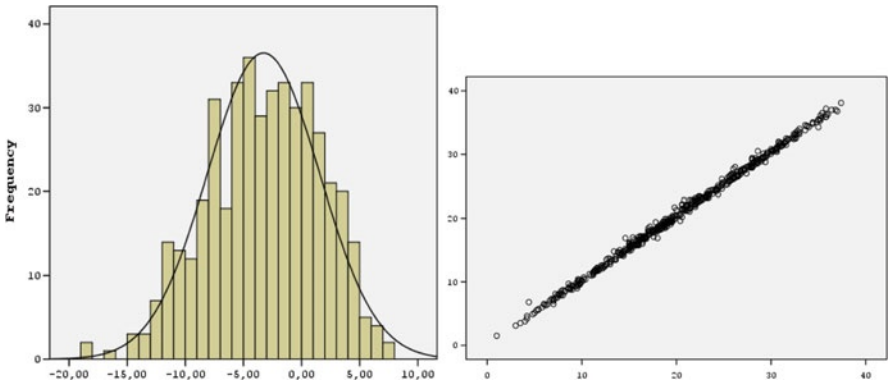

Fig. 2 (*left*) ΔTmax (LGTS); (*right*) T_{AWS}(max) versus T_{CWS}(max) (LGBL)

bias between AWS and CWS data. Also, some graphs are skewed to the left or to the right. According to Lucas et al. (2010), the comparative study of observed meteorological data from automatic and conventional stations typically shows satisfactory results in statistical indices applied. However, changes in average level of bias occur frequently and are associated with systematic errors that can vary from interruptions in the data series and crash sensors on the automatic station. Results found in this study are consistent with above findings. Finally, scatter plots are generated three of which are shown in Figs. 1, 2, 3 (right).

As mentioned earlier, correlation between AWS and CWS data is strong for all meteorological stations except Naxos. However, in some scatter plots, one can see that, there are outliers. By examination the raw data, in some cases, the AWS sensor underestimated the values of the observed parameters, while in others, it overestimated them. However, in most cases, the discrepancies were observed at the start of operation of the AWS.

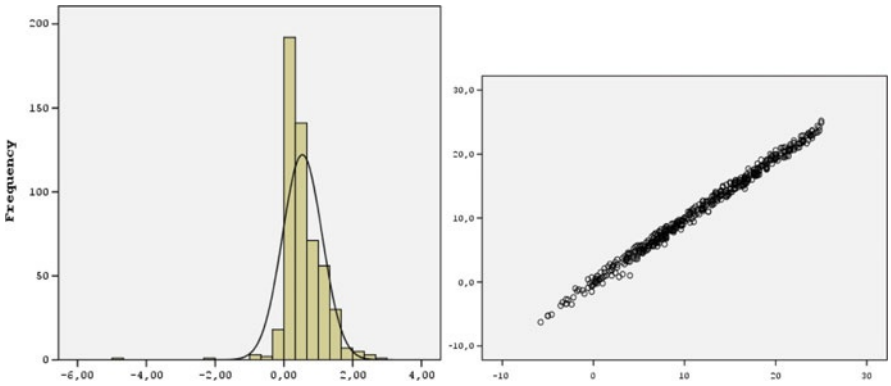

Fig. 3 (*left*) ΔTmin (LGLR); (*right*) T_{AWS}(min) versus T_{CWS}(min) (LGTS)

4 Conclusions

Overall, results showed that there are pronounced differences between CWS and AWS data. Also, some stations did better than others. Assuming conventional thermometers were well-calibrated this difference can be attributed to errors in fine-tuning the sensors of the AWS equipment. AWS can be programmed and delicate calibration procedures must be done to minimize biases, thus making the station fully-operational. In the case of temperatures, even small fractions of deviations in degrees are very important. No station should be put to operation if its temperature sensor is not carefully adjusted. Of course, the same holds true for all other parameters recorded.

Another possible source of error may be the differences in exact location between AWS and CWS. During a day, reflections from nearby buildings or varying landscape may cause significant variation (increase or decrease) in recorded temperatures. Thus, surrounding areas should be free of obstacles, if accurate readings are to be taken.

There is a need to combine, with some caution, datasets from different instrumentation platforms and observation methods, since not all data are homogenous. The observational data from heterogeneous measurement networks might have significant inconsistencies and a unification of datasets should not be done, without the proper quality control and the necessary adjustments that account for inherent system biases. These adjustments refer to location and environment characteristics, sensor characteristics, differences in data observation time, etc.

Finally, during an observation, the observer usually takes one reading off the thermometer. Automatic weather stations usually take the average temperature during a 5- or 10-min interval, depending on their settings. Within this short period of observation, temperature variations may happen, affecting recorded values.

In closing, one must overemphasize the importance of very good calibration of both automatic sensors and conventional instruments. Automatic weather stations

require maintenance according to tight schedules and cannot be left unattended. Results in this study prove that there are issues, which must be resolved before any attempt is made to replace conventional stations with automatic. Both systems should work in parallel for a long period of time, in order to synchronize measurements.

This study was a first investigation on the AWS and CWS observational systems. As such, it was mostly an explanatory study, to the extent that, the main emphasis was to search for general patterns in differences between AWS and CWS observed data.

A comparison for the chosen period of operation was made for three main synoptic hours. It will be very interesting to examine the performance of automatic weather stations in variations of temperatures within a day. Also, further research is needed to compare night observations with observations made during daytime.

Furthermore, the influence of the local environment surrounding the AWS and the distance between the AWS and CWS can be studied. In other words the "site bias" should be researched, in addition to "instrument bias".

Finally, performance of automatic weather stations with respect to other meteorological parameters is an area for further study. So far, nothing to this end has been done at HNMS or other institution. However, this work is planned for the near future.

References

Davey CA, Pielke RA Sr (2005) Microclimate exposures of surface-based weather stations: implications for the assessment of long-term temperature trends. Bull Am Meteorol Soc 86:497–504. doi:10.1175/BAMS-86-4-497

Guttman N, Baker B (1996) Exploratory analysis of the difference between temperature observations recorded by ASOS and conventional methods. Bull Am Meteorol Soc 77:865–2873

Holder C, Boyles R, Syed A, Niyogi D, Raman S (2006) Comparison of collocated automated (NCECONet) and manual (COOP) climate observations in North Carolina. J Atmos Ocean Technol 23(5):671–682. doi:10.1175/JTECH1873.1

Lucas EWM, Rodrigues JE, Rezende JM, Abreu SF, Braga AP (2010) Comparative analysis of observed meteorological data in the conventional and surface automatic station at Brazilian National Institute of Meteorology. Instituto Nacional de Meteorologia–INMET

Thermal Comfort in Hot Outdoor Environment Under Unsteady Conditions

G. Katavoutas, H.A. Flocas, and M. Tsitsomitsiou

Abstract One of the major problems of outdoor thermal comfort assessment is the quantification of thermophysiological parameters in order to model human heat balance, especially under unsteady conditions. In this context, the aim of this study is to investigate the thermophysiological parameters involved in human heat balance and their contribution to heat fluxes associated with the human body. This applies for a person leaving a typical indoor environment and seating quite under the shade of a tree for 30 min. In order to achieve these simulations, the Instationary Munich Energy-Balance Model (IMEM) is employed. Body temperatures and heat fluxes are modelled for a standard male at intervals of 1 min, using meteorological measurements carried out during ten experimental days under hot summer conditions. Although the current study reveals that the temporal pattern of mean skin temperature has a similar form, there are found marked quantitative differences among the experimental days, varying from 2°C to 3.2°C. This variation depends primarily on the increase of the air temperature.

1 Introduction

A complex issue concerning thermal comfort is the evaluation of thermal effects of the atmospheric environment on the human body under unsteady conditions. The term "unsteady conditions" refers to significant changes of the factors involved in human heat balance in time scale of minutes. These factors summarized in the main four climatic parameters (air temperature, relative humidity, mean radiant temperature and air velocity) as well as the level of activity and the clothing insulation. In real life, the transition from an indoor to the outdoor environment is such a case.

G. Katavoutas (✉) • H.A. Flocas • M. Tsitsomitsiou
Department of Environmental Physics-Meteorology, University of Athens, University Campus-Zografou, 15784 Athens, Greece
e-mail: geokat@phys.uoa.gr

C.G. Helmis and P.T. Nastos (eds.), *Advances in Meteorology, Climatology and Atmospheric Physics*, Springer Atmospheric Sciences,
DOI 10.1007/978-3-642-29172-2_25,

More specifically, Höppe (2002) showed that for a person leaving a neutral indoor climate and walks slowly under hot conditions, steady state of mean skin and body core temperature is reached approximately after half an hour and 1 h, respectively, concluding that steady state thermal comfort models cannot provide sufficient information for persons staying outdoors for less than half an hour. In this sense, Katavoutas et al. (2009, 2010) studied the human heat balance based on the experimental measurements of skin temperature and metabolic heat production, while Shimazaki et al. (2011) examined the application of human thermal load into unsteady condition for improvement of outdoor thermal comfort.

This study aims to investigate the thermophysiological parameters involved in human heat balance under unsteady conditions and to further identify the contribution to heat fluxes, for a person leaving a typical indoor environment and seating quite under the shade of a tree for 30 min, during hot summer days.

2 Data and Methodology

In order to investigate the effects of the atmospheric environment on the human body under unsteady conditions, the Instationary Munich Energy balance Model (IMEM) was employed. The dynamic model IMEM is a two-node model based on human heat balance, quantifying realistic values of the thermophysiological parameters and the human heat fluxes (Höppe 1993, 2002).

Simulations concern an "average" male individual 30 years old, weighting 70 kg and 1.75 m tall, according to ISO 8996 (2004). The model subject stays for more than 1 h in a typical indoor environment, with climatic conditions of air temperature 23°C, relative humidity 50%, air velocity 0.1 ms^{-1} and mean radiant temperature equals air temperature. During this period, the model subject performs sedentary activity assuming work metabolism 80 W of light activity. Further, the heat resistance of clothing assumes a typical summer clothing ensemble consisting of straight trousers, T-shirt, socks and shoes, including briefs, providing a clothing insulation at 0.41 clo according to ASHRAE (2004). Under this typical indoor setting, the steady state mean skin temperature and body core temperature for the model subject is formed at 33.5°C and 36.9°C, respectively. These body temperatures constitute the starting values for the model subject leaving the indoor environment and seating quite (work metabolism 80 W, mechanical efficiency 0%) under tree shade conditions for 30 min.

Meteorological measurements used in these simulations were obtained from field experiments conducted during the second half of July 2008. In this sense, the greater experimental site constitutes the outdoor setting where the model subject enters. Particularly, meteorological datasets of ten experimental days were employed in this analysis, in intervals of 1 min (Table 1). Mean radiant temperature is modeled employing Rayman model (Matzarakis et al. 2007, 2010), according to climatic conditions, suburban landscape and terrain of the experimental site.

Table 1 Average meteorological parameters under tree shade conditions

	15/7	16/7	17/7	18/7	21/7	22/7	23/7	24/7	25/7	28/7
Air temperature (°C)	37.5	28.7	30.2	31.7	36.4	35.5	33.8	28.1	28.5	29.3
Vapour pressure (hPa)	10.1	11.4	11.4	13.3	12.2	14.3	11.4	10.6	12.2	16.5
Wind speed (ms^{-1})	0.9	1.7	1.3	1.1	1.3	1.2	1.1	1.0	1.0	1.0
Air pressure (hPa)	984.3	982.9	984.5	984.2	983.8	980.0	976.8	979.8	979.5	976.3
Mean radiant temperature (°C)	47.1	35.8	37.3	40.1	44.6	45.8	40.5	36.2	36.7	36.3

Body temperatures, skin wettedness and human heat fluxes are modeled under tree shade conditions for 30 min, in time intervals of 1 min, based on 5 min average of the meteorological parameters employing IMEM model.

3 Results

3.1 Body Temperatures and Skin Wettedness

The temporal pattern of mean skin temperature (T_s) reveals an increasing course during the time frame of 30 min under the shade on each experimental day. In particular, mean skin temperature difference (ΔT_s) between the initial (1st minute) and the final (30th minute) value of T_s holds a positive sign and varies from 2.0°C to 3.2°C (Fig. 1a). Within this range, air temperature (T) increment about 10°C results in an increase of ΔT_s by 1.2°C. Thus, air temperatures higher than 35°C indicate ΔT_s higher than 3.0°C. The relationship between mean skin temperature difference versus air temperature is well fitted by a linear equation with relatively high coefficient of determination R^2 (0.91), at the confidence level of 95%.

On the other hand, the relationship between body core temperature difference (ΔT_c) versus air temperature reveals a positive correlation as well (Fig. 1b). Nevertheless, a visual inspection of the results (Fig. 1b) implies a negative ΔT_c (−0.1°C) for air temperatures lower than 29.0°C and a positive ΔT_c up to 0.3°C for air temperatures higher than 32.0°C. Moreover, no change of ΔT_c is observed for air temperatures between 29°C and 32°C. It is worth noting that the above result does not preclude the variation of T_c during the time frame of 30 min but indicate that after 30 min seating quite under tree shade conditions, T_c is formed at the initial value. The relationship between body core temperature difference and air temperature is well fitted by a linear equation with high coefficient of determination R^2 (0.95), determined at the confidence level of 95%.

Further, the relationship between initial and final clothing surface temperature (T_{cl}) versus air temperature (T) are shown in Fig. 2a. A visual inspection of the results indicate that air temperature (T) increment of about 10°C results in an increase of initial and final T_{cl} by 3.4°C and 4.9°C, respectively. In particular, initial T_{cl} varies from 33.0°C to 36.4°C and final T_{cl} from 33.7°C to 38.6°C. The

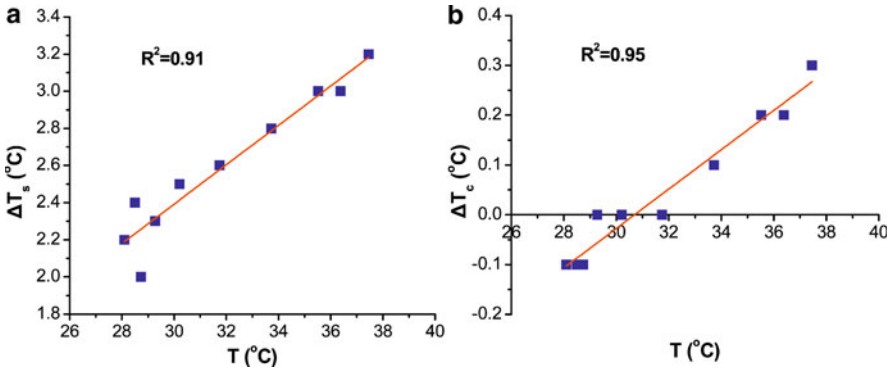

Fig. 1 Scatter plot of difference of (**a**) mean skin temperature (ΔT_s) and (**b**) body core temperature (ΔT_c) versus air temperature (T) under tree shade conditions for 30 min. The regression lines are also illustrated

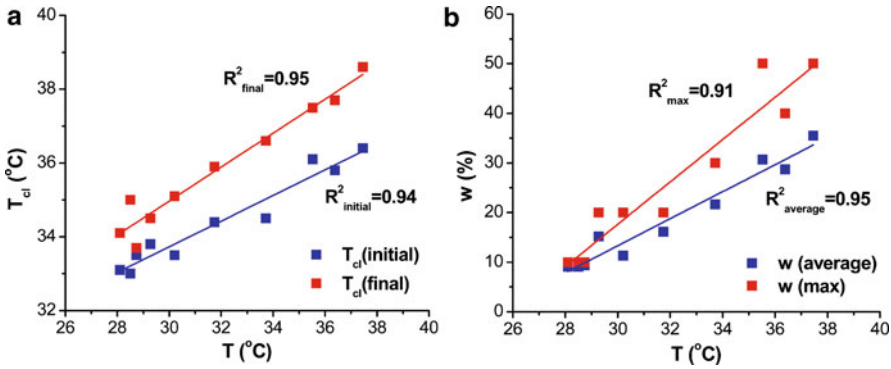

Fig. 2 Scatter plot of (**a**) initial and final clothing surface temperature (T_{cl}) and (**b**) average and maximum skin wettedness (w) versus air temperature (T) under tree shade conditions for 30 min. The regression lines are also illustrated

relationship between initial and final clothing surface temperature versus air temperature is well fitted by a linear equation, with coefficients of determination up to $R^2 = 0.95$, statistically significant at the 95% confidence level.

Figure 2b illustrates the relationship between average and maximum skin wettedness (w) versus air temperature (T). The level of wettedness over the skin surface is defined as the ratio of skin evaporative heat loss to the maximum evaporative capacity of the environment if the skin surface were completely wet. In this sense, within the examined air temperature range, average and maximum w varies from 9.0% to 35.5% and from 10% to 50%, respectively. Moreover, for air temperature lower than 29.0°C average and maximum w does not exceed 10%. On the other hand, for air temperature higher than 33.0°C average and maximum w exceeds 22%, which constitute the comfort limit at rest (Nishi and Gagge 1977).

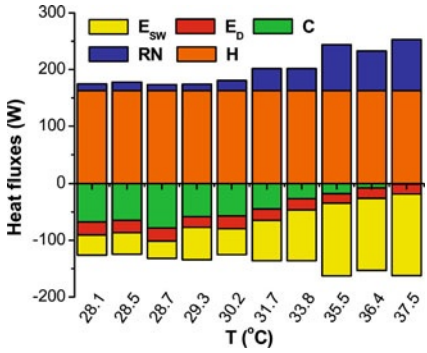

Fig. 3 Average human heat fluxes versus air temperature under tree shade conditions for 30 min

3.2 Human Heat Fluxes

It is further constructive to study the variation of heat fluxes to and from the human body among the experimental days. For this purpose, average human heat fluxes consist of internal heat production (H), convective heat (C), radiative heat (RN), evaporation heat due to sweating (E_{sw}) and latent heat to evaporate water into water vapour diffusing through skin (E_D) are presented in Fig. 3 from lower to higher air temperatures. In particular, H is formed at 162.7 W on each experimental day due to constant work metabolism and mechanical efficiency. On the other hand, average RN increases as air temperature increases and varies between 10.8 and 81.4 W under tree shade conditions. This variation is related to the difference of mean radiant temperature with mean skin or/and clothing surface temperature.

At the same time, average C decreases as air temperature increases and varies from −78.6 to −0.9 W. This result is related to the corresponding decrease of the difference of air temperature with mean skin or/and clothing surface temperature as air temperature increases. On the other hand, average E_D indicates small fluctuation among the days and varies from −22.9 to −16.8 W. On the contrary, average E_{sw} displays significant variation among the days and varies from −30.7 to −143.8 W, even under tree shade conditions. This result is consistent with the corresponding increase of T_s and T_c, especially for air temperatures higher than 30°C.

4 Conclusions

Body temperatures, skin wettedness and human heat fluxes have been analyzed in order to further clarify outdoor thermal comfort especially under unsteady conditions. The study reveals that mean skin temperature difference (ΔT_s), body core temperature difference (ΔT_c), initial and final clothing surface temperature (T_{cl}) and average and maximum skin wettedness (w) vary for an "average" person going out under hot summer conditions, as coming from a typical indoor environment with steady body temperatures. In particular, ΔT_s increases with air

temperature and varies from 2.0°C to 3.2°C. On the contrary, no change of ΔT_c is observed for air temperatures between 29°C and 32°C, a negative ΔT_c for air temperatures lower than 29.0°C and a positive ΔT_c for air temperatures higher than 32.0°C. Further, air temperature increment about 10°C results in an increase of initial and final T_{cl} by 3.4°C and 4.9°C, respectively. For air temperature higher than 33.0°C average and maximum w exceeds 22%, which constitute the comfort limit at rest. On the other hand, the above variations result significant fluctuation on human heat fluxes, especially for evaporation heat due to sweating (E_{sw}), convective heat (C) and radiative heat (RN), even under tree shade conditions for 30 min.

Acknowledgments Prof. Matzarakis A. of the University of Freiburg and Prof. Höppe P., for providing the model IMEM are highly acknowledged.

References

ASHRAE (2004) Thermal environmental conditions for human occupancy. ASHRAE standard 55, Atlanta

Höppe PR (1993) Heat balance modelling. Experientia 49:741–746. doi:10.1007/BF01923542

Höppe P (2002) Different aspects of assessing indoor and outdoor thermal comfort. Energy Build 34:661–665. doi:10.1016/S0378-7788(02)00017-8

ISO 8996 (2004) Ergonomics of the thermal environment – determination of metabolic rate. International Organization for Standardization, Geneva

Katavoutas G, Theoharatos G, Flocas HA, Asimakopoulos DN (2009) Measuring the effects of heat wave episodes on the human body's thermal balance. Int J Biometeorol 53:177–187

Katavoutas G, Theoharatos G, Flocas HA, Asimakopoulos DN (2010) A field study of heat stress under different thermal and radiation conditions. In: Proceedings of 10th international conference of meteorology, climatology and atmospheric physics, Patras, pp 486–494

Matzarakis A, Rutz F, Mayer H (2007) Modelling radiation fluxes in simple and complex environments – application of the RayMan model. Int J Biometeorol 51:323–334

Matzarakis A, Rutz F, Mayer H (2010) Modelling radiation fluxes in simple and complex environments: basics of the Rayman model. Int J Biometeorol 54:131–139

Nishi Y, Gagge AP (1977) Effective temperate scale for use in hypo- and hyperbaric environments. Aviat Space Environ Med 48:97–107

Shimazaki Y, Yoshida A, Suzuki R, Kawabata T, Imai D, Kinoshita S (2011) Application of human thermal load into unsteady condition for improvement of outdoor thermal comfort. Build Environ 46:1716–1724. doi:10.1016/j.buildenv.2011.02.013

Heat Island and Thermal Bioclimate in Athens, Greece

G. Katavoutas, G.K. Georgiou, D.N. Asimakopoulos, and G. Theoharatos

Abstract Urbanization and industrialization are the main causes of the well documented climatic phenomenon called heat island. As the problem is worse in big cities, more urban residents complain about discomfort conditions. In this context, the aim of the present study is a combinational approach of heat island and thermal bioclimate in the city of Athens. For this purpose meteorological data of air temperature, relative humidity, wind speed, solar radiation and cloud cover data have been employed for 3 years, by a network of stations, as obtained by the Hellenic National Meteorological Service, the National Observatory of Athens and the National Technical University of Athens. Thermal comfort was assessed through Physiologically Equivalent Temperature (PET), a thermal index derived from human heat balance, utilizing the Rayman model.

1 Introduction

A number of studies have been devoted to the well documented climatic phenomenon known as the urban heat island (Arnfield 2003). Human-made modifications in the physical characteristics of natural surfaces through urbanization and industrialization constitute the main cause of urban heat island. As consequence, urban and suburban air temperature is higher than nearby rural areas. Indications of the urban heat island in the greater Athens area have been noted by Katsoulis and Theoharatos (1985), while Philandras et al. (1999) conclude that urbanization increased the maximum temperatures by about 2°C mainly in spring and summer. The central and western parts of the city of Athens develop the urban heat island effect intensely

G. Katavoutas (✉) • G.K. Georgiou • D.N. Asimakopoulos • G. Theoharatos
Department of Environmental Physics-Meteorology, University of Athens, University Campus-Zografou, 15784 Athens, Greece
e-mail: geokat@phys.uoa.gr

C.G. Helmis and P.T. Nastos (eds.), *Advances in Meteorology, Climatology and Atmospheric Physics*, Springer Atmospheric Sciences,
DOI 10.1007/978-3-642-29172-2_26,

Table 1 Geographical characteristics of stations

No.	Station name	Lon	Lat	Alt (m)	Description
1	Ano Liosia	23° 04′	38° 03′	184	Urban complex (S, SE), highway nearby
2	Galatsi	23° 45′	38° 01′	176	In a park, surrounded by high building density
3	Elefsina	23° 33′	38° 04′	30	Open field, heavy industries nearby
4	Ag. Kosmas	23° 43′	37° 52′	6	Coastal, urban complex (N)
5	Zografou	23° 46′	37° 58′	219	Urban complex (W, SW, NW), mountain (E, SE)
6	Ilioupoli	23° 45′	37° 54′	206	Urban complex (N, W, S), mountain (E)
7	Athens	23° 43′	37° 58′	107	On a hill at the centre of Athens
8	Mandra	23° 33′	37° 07′	258	Mountain (N), open field (S)
9	Menidi	23° 43′	38° 06′	248	Urban complex (S), mountain (N)
10	Penteli	23° 51′	38° 04′	729	Upland
11	Pikermi	23° 55′	37° 58′	133	Rural area

(Livada et al. 2002), while the morning urban heat island is formed during the 2/3 of the days, yearly (Kassomenos and Katsoulis 2006).

From the perspective of human biometeorology, Mayer and Höppe (1987) revealed higher heat stress in urban structures in the city of Munich in comparison to the nearby forest. Recently, Matzarakis et al. (2009) showed that the urban center of Strasbourg is more affected by heat events than the rural areas, especially at night-time. The frequency of hot days and heat waves in urban regions is increased in comparison to nearby rural areas, while urban heat island is directly responsible for heat-related mortality in urban areas (Tan et al. 2010). Consequently, the residents in urbanized and industrialized areas experience heat stress, especially during heat waves (Theoharatos et al. 2010; Mavrakis et al. 2011).

Within this context, the aim of the present study is a combinational approach of heat island and thermal bioclimate in the greater Athens area, employing a thermal index such as PET instead of air temperature.

2 Data and Methodology

The meteorological data employed in this study are 3 h measurements of air temperature, relative humidity, wind speed, global solar radiation and cloud cover for the time period of October 2006 to October 2009. The aforementioned meteorological datasets were obtained for 11 stations by the National Technical University of Athens (NTUA), the National Observatory of Athens (NOA) and the Hellenic National Meteorological Service (HNMS) (Table 1).

Thermal comfort was assessed through Physiologically Equivalent Temperature (PET), a thermal index derived from human heat balance, which incorporates the main four climatic parameters (air temperature, relative humidity, wind speed and mean radiant temperature) as well as clothing and activity. PET is defined as the equivalent air temperature in a typical setting at which the human heat balance is maintained with body temperatures equal to those in the assessed conditions

Table 2 Physiologically equivalent temperature classification (Matzarakis and Mayer 1996)

Thermal sensation	Very cold	Cold	Cool	Slightly cool	Comfortable	Slightly warm	Warm	Hot	Very hot
PET (°C)	<4	8	13	18	23	29	35	41	>41

(Table 2) (Mayer and Höppe 1987; Matzarakis and Mayer 1996). Clothing insulation was computed as a function of air temperature, while PET was estimated for an average male walking slowly, utilizing Rayman model (Matzarakis et al. 2007).

In this analysis the 3 h results of PET are separated into three subsets; the Winter Period (WP) consisting of December, January, February and March, the Summer Period (SP) consisting of June, July, August and September and the Transitional Period (TP) consisting of April, May, October and November.

3 Results

In order to analyze the bioclimatic features in terms of urban, suburban and exurban characteristics of each station, the differences between the mean PET values of each station with the mean PET value of all stations and for each period are displayed in Fig. 1. The estimated differences have been ordered from a maximum to a minimum range and the stations with a positive sign can be defined with urban or suburban characteristics and those with a negative sign with exurban characteristics (Livada et al. 2002).

A visual inspection of the results (Fig. 1) indicates that stations 8, 9, 10 and 11 come up with exurban characteristics due to negative variation. It is clear that the highest negative difference, more than 4°C, is observed for station 10, as it is located at the highest altitude. Station 11 shows the highest negative variation during SP (−0.81°C) and is positioned in a rural area with low building density. Stations 8 and 9 are located at the north boundaries of Thriassion Plain and urban complex of Athens, respectively. Both stations indicate the highest negative variation during the WP, at −0.70°C for station 8 and at −0.72°C for station 9.

On the other hand, stations 2, 3, and 7 imply urban characteristics in terms of thermal comfort due to positive variation, especially during the summer and the transitional period (Fig. 1b, c). In particular, station 3 shows the highest positive variation, 2.10°C and 1.63°C during the SP and TP, respectively, despite the fact that it is located in the Thriassion plain and it could be characterized as open field due to its position. That result can be explained by the fact that it's surrounded by more than 2,200 large and small industries (Mavrakis et al. 2011). Furthermore, station 7 is positioned on a hill at the centre of urban complex of Athens indicating the third positive variation at 1.29°C during the WP, the second at 1.22°C during the SP and the fourth at 0.92°C during the TP. On the other hand, the positive variation at station 2 exceeds 0.88°C indicating the highest positive variation at 1.24°C

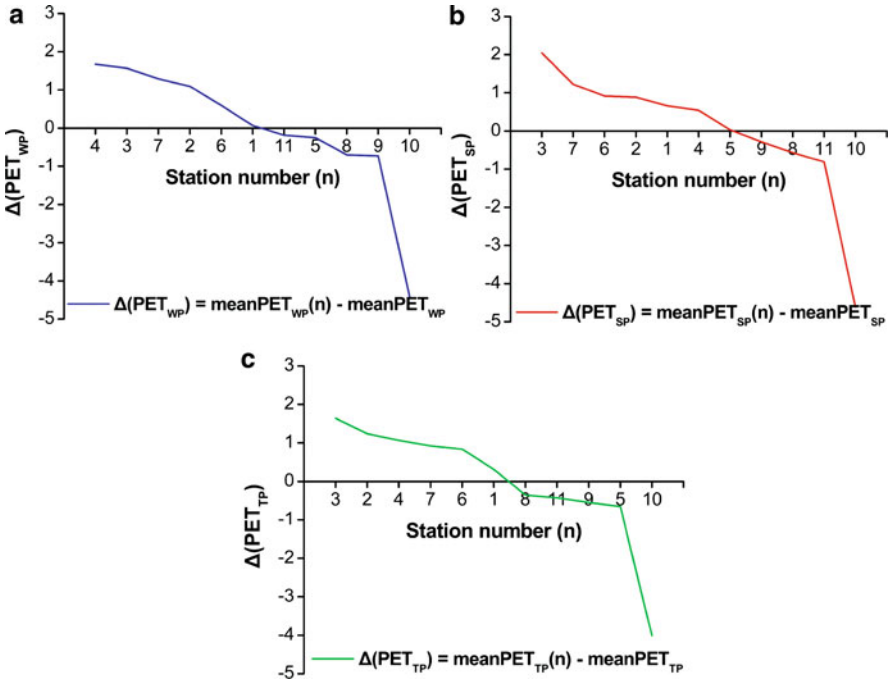

Fig. 1 Differences between the mean PET value of each station (n) with the mean PET value of all stations for (**a**) winter period (WP), (**b**) summer period (SP) and (**c**) transitional period (TP)

during the TP. Station 2 is located at the boundaries of a park, with the surrounding area being characterized by high building density.

On the contrary, stations 1, 4, 5 and 6 imply combined features during the examined periods. In particular, station 1 shows small variation during the WP and TP and only during the SP period it indicates positive variation at 0.66°C implying urban characteristics in terms of thermal comfort. Moreover, station 4 indicates the highest positive variation (1.67°C) during the WP and the third highest (1.07°C) during the TP implying urban characteristics. However during the SP shows the lowest positive variation. That result can be rationalized according to station position (next to the sea) and is an outcome of the sea influence (Livada et al. 2002). Finally, station 5 indicates small variation during the WP and SP, while during the TP it shows exurban characteristics in terms of thermal comfort. The station is situated in the foot of Hymettus mountain, approximately 6 km east-southeast from the city center and the influence of the mountain in the bioclimatic characteristics of the station is obvious. South of the station 5 but still in the foot of Hymettus mountain is located station 6, which indicates urban characteristics with the highest variation during the SP (0.91°C). That station is probably also influenced by the sea, as it is positioned closest to the coast.

Moreover, in order to determine the percentage frequency distribution, a bioclimatic chart has been produced according to PET limits for all stations and for each

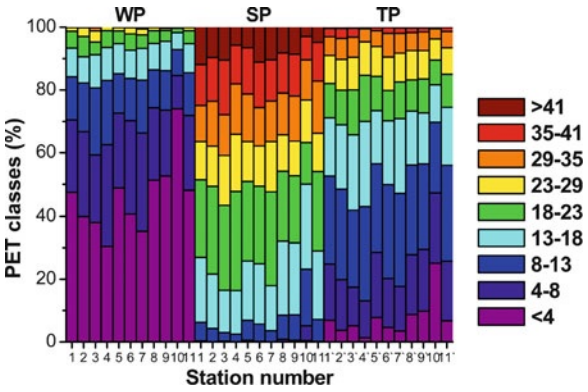

Fig. 2 Percentage frequency distribution of PET for each station (1–11) and for each period (WP, SP, TP)

Table 3 PET differences between stations 2 and 7 versus station 11 at 0200 and 1400 LST

Hour (LST)	WP	WP	SP	SP	TP	TP
	2	7	2	7	2	7
0200	0.83	1.61	0.75	1.85	1.13	1.67
1400	2.22	2.12	3.19	3.43	3.16	2.10

period (Fig. 2). Stations 2, 3 and 7 indicate the lowest percentage frequency (67%, 59% and 66%) among the stations, for PET values lower than 8°C (cold and very cold) during the WP. Furthermore, those stations also reveal the maximum percentage frequency (2.9%, 4.8% and 2.5%) for PET values higher than 23°C (slightly warm to very hot). On the other hand, stations 2, 3, 4 and 7 present the lowest percentage frequency (4.3%, 3.0%, 2.5% and 3.5%) among the stations, for PET values lower than 13°C (cool to very cold) during the SP. However the low percentage frequency for the station 4 is owed to its position as already mentioned. The above results imply further urban characteristics for these stations in terms of thermal comfort.

Taking into consideration the above results and the fact that stations 2 and 7 are located inside the urban complex of Athens, while station 11 is positioned outside of it in a rural area, PET differences during each period at 0200 and 1400 LST are given in Table 3. It is obvious that stations 2 and 7 indicate higher PET values in comparison to station 11. In particular, the highest differences are observed at 1400 LST, when the difference values exceed 3°C during the SP and 2°C during the WP and TP. On the other hand, the difference values at 0200 LST exceed 0.7°C for station 2 and 1.6°C for station 7, while the highest values are observed during the SP (1.85°C) for station 7 and during the TP (1.13°C) for station 2.

4 Conclusions

The present study deals with a combinational approach of heat island and thermal comfort in the greater Athens area, employing a thermal index (PET). The results show that PET can be used to study the heat island, as it incorporates four climatic

parameters which can be affected by urbanization and industrialization. The study reveals that stations 8, 9, 10, 11 indicate exurban characteristics in terms of thermal comfort. On the contrary, stations 2, 3, 7 show urban characteristics. Although the exact locations of stations 2 and 7 could be characterized as semi-suburban or semi-urban, they are influenced by the urban complex that surrounds them. Likewise, station 3 is affected by the industrialization of the area nearby. The remaining stations indicate mixed results, as they are located at the boundaries of the urban complex and they are spotted close to either mountains or to the sea.

References

Arnfield JA (2003) Two decades of urban climate research: a review of turbulence, exchanges of energy and water and the urban heat island. Int J Climatol 23:1–26. doi:10.1002/joc.859

Kassomenos PA, Katsoulis BD (2006) Mesoscale and macroscale aspects of the morning urban heat island around Athens, Greece. Meteorol Atmos Phys 94:209–218

Katsoulis BD, Theoharatos GA (1985) Indications of the urban heat island in Athens, Greece. J Clim Appl Meteorol 24:1296–1302. doi:10.1175/1520-0450(1985) 024<1296:IOTUHI>2.0.CO;2

Livada I, Santamouris M, Niachou K, Papanikolaou N, Mihalakakou G (2002) Determination of places in the greater Athens area where the heat island effect is observed. Theor Appl Climatol 71:219–230

Matzarakis A, Mayer H (1996) Another kind of environmental stress: thermal stress. WHO Newsl 18:7–10

Matzarakis A, Rutz F, Mayer H (2007) Modelling radiation fluxes in simple and complex environments-application of the RayMan model. Int J Biometeorol 51:323–334. doi:10.1007/s00484-006-0061-8

Matzarakis A, De Rocco M, Najjar G (2009) Thermal bioclimate in Strasbourg – the 2003 heat wave. Theor Appl Climatol 98:209–220

Mavrakis A, Spanou A, Pantavou K, Katavoutas G, Theoharatos G, Christides A, Verouti E (2011) Biometeorological and air quality assessment in an industrialized area of eastern Mediterranean: the Thriassion Plain. Greece Int J Biometerol. doi:10.1007/s00484.011.0475.9

Mayer H, Höppe PR (1987) Thermal comfort of man in different urban environments. Theor Appl Climatol 38:43–49. doi:10.1007/BF00866252

Philandras CM, Metaxas DA, Nastos PTh (1999) Climate variability and urbanization in Athens. Theor Appl Climatol 63:65–72. doi:10.1007/s007040050092

Tan J, Zheng Y, Tang X, Guo C, Li L, Song G, Zhen X, Yuan D, Kalkstein AJ, Li F, Chen H (2010) The urban heat island and its impact on heat waves and human health in Shanghai. Int J Biometeorol 54:75–84. doi:10.1007/s00484-009-0256-x

Theoharatos G, Pantavou K, Mavrakis A, Spanou A, Katavoutas G, Efstathiou P, Mpekas P, Asimakopoulos D (2010) Heat waves observed in 2007 in Athens, Greece: synoptic conditions, bioclimatological assessment, air quality levels and health effects. Environ Res 110:152–161. doi:10.1016/j.envres.2009.12.002

Seasonal Forecasts for the 2010 Russian Heat Wave Using an Atmospheric General Circulation Model

P. Katsafados, E. Papadopoulou, A. Papadopoulos, and E. Mavromatidis

Abstract In this study the capabilities of a state-of-the-art Atmospheric General Circulation Model (AGCM) for the estimation of the atmospheric conditions on seasonal scale are examined. Seasonal simulations were carried out using the NCAR Community Atmosphere Model (CAM 3). The unusual weather patterns prevailed over Europe and Asia during July and August of 2010, which led in the development of the Russian heat wave and provoked severe rainfall in Pakistan, were simulated by using an ensemble based methodology. The ensemble was consisting of 61 independent members and it has been produced by consecutive simulations performed for each day of January and April 2010. Each hindcast has been integrated for 8 and 5 months ahead. The model outputs have been statistically processed in order to estimate the monthly average temperature anomalies and the monthly accumulated precipitation probability of exceedance. Preliminary results suggest that the system is able to reproduce the large scales of the atmospheric circulation indicating that it can be a useful tool for better understanding the mechanisms of atmospheric variations on seasonal scale.

1 Introduction

In 2011, the Hellenic Centre for Marine Research (HCMR) in cooperation with the Department of Geography at Harokopion University introduced the dynamical seasonal simulations based on a state-of-the-art AGCM. Seasonal simulations have been carried out using the NCAR (National Center for Atmospheric Research) Community

P. Katsafados (✉) • E. Papadopoulou • E. Mavromatidis
Department of Geography, Harokopion University of Athens, 70 El. Venizelou Street, Athens 17671, Greece
e-mail: pkatsaf@hua.gr

A. Papadopoulos
Institute of Inland Waters, Hellenic Centre for Marine Research, Anavyssos, Attiki, Greece

C.G. Helmis and P.T. Nastos (eds.), *Advances in Meteorology, Climatology and Atmospheric Physics*, Springer Atmospheric Sciences,
DOI 10.1007/978-3-642-29172-2_27,

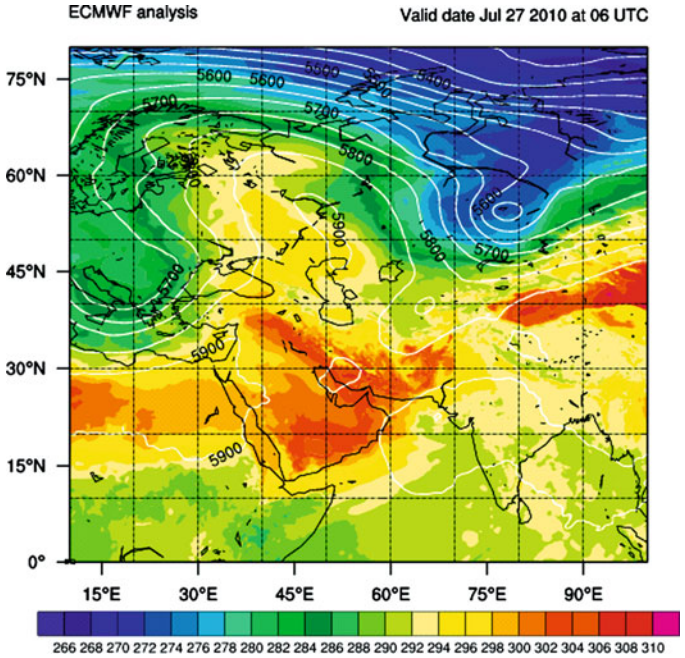

Fig. 1 Temperature at 850 hPa and geopotential height at 500 hPa for July 27 at 06:00 UTC based on ECMWF analysis

Atmosphere Model (CAM version 3) coupled with the Community Land Model (CLM). The principal aim of this study is to present the developed methodology of the seasonal simulations and to evaluate the system by examining a large scale heating wave that hit Russia in July and August of 2010, which resulted into intensive fires and deaths of many people in the area and provoked severe rainfall in Pakistan (Gilbert 2010). The heat wave, that exceeded 40°C in early August, resulted in more than 1,500 deaths, including more than 1,600 drowning deaths as people entered to the water in an attempt to escape the heat and more than 600 wildfires (Matsueda 2011). To the east of the heat wave anomalously cool temperatures resulted in intensifying the monsoon period over the northern part of the Indian subcontinent, causing also devastating floods in Pakistan (Dole et al. 2011).

2 Description of the Synoptic Conditions

The Russian heat wave was mainly due to internal atmospheric dynamical processes that produced and maintained a strong and long-lived blocking event. The nature of the heat wave and its origins were associated to the upper-level atmospheric flow. An "omega" blocking pattern characterized the 500 hPa July flow. The blocking high is visible in the geopotential height of the European Centre for Medium-Range Weather Forecasts (ECMWF) analysis field (Fig. 1). The highest

July 2010 surface temperature anomalies occurred near the center of the block, where northward displaced subtropical air, descending air motions and reduced cloudiness all contributed to abnormally warm surface temperatures.

To the east of the omega block anomalously cool temperatures occurred in conjunction with an upper level trough and southward transport of polar air (Dole et al. 2011) that resulted in intensifying the monsoon period over the northern part of the Indian subcontinent, causing also devastating floods in Pakistan. This upper level jet drove polar air masses towards the Indian Ocean which interacted with low-level warm and humid air and initiated the heavy rainfall in Pakistan. During July 2010 the monsoon over the northern part of the Indian subcontinent was "active" with rainfall extending across the Gangetic Plains between the Bay of Bengal in the east to northern Pakistan in the west. In late July, over a 4-day period, some Pakistan stations recorded rainfall exceeding 300 mm (Webster et al. 2011).

3 Model Characteristics and Methodology

The NCAR CAM3 is a global AGCM designed to produce simulations with high fidelity for several different dynamical cores and horizontal resolutions. The formulation of the physics and dynamics of CAM3 is detailed by Collins et al. (2006). The standard version, used in this study, has 26 vertical levels and an 85-wave triangular spectral truncation (T85L26). The specific Eulerian truncation corresponds to a zonal resolution of $1.41° \times 1.41°$. CAM3 also includes the CLM for the treatment of land surface energy exchanges (Oleson et al. 2004).

The performance of the model has been evaluated by examining the Russian heating wave in July and August of 2010. To this end, seasonal simulations of the CAM3 coupled with the CLM have been carried out using a time-variant climatological SST dataset for the definition of the sea surface boundary condition. Model simulations were initialized by the Global Forecasting System (GFS) global analyses on 00:00 UTC for a period of 31 consecutive days at January 2010 and 30 days at April 2010 producing 31 and 30 ensemble members on hindcast mode. Each member has been integrated for 8 and 5 months ahead having as starting months the January and the April, respectively. In this way, 31 members were produced with 5–7 months lead time for the period June, July, August (JJA) and 30 members were produced with 2–4 months lead time for the same period (Fig. 2). Moreover, spaghetti plots of the temperature at 850 hPa are also included as a guidance of each member uncertainty. Each member was compared against long-term monthly means valid for the period of 1968–1996, released by the National Center for Environmental Predictions (NCEP) and NCAR (Kalnay et al. 1996). In the framework of cumulative frequency analysis for discrete variables, a probabilistic approach was followed for the assessment of the extreme precipitation event in Pakistan. This method was based on the estimation of the probability that monthly precipitation will exceed a trace rainfall amount (Mason et al. 2007).

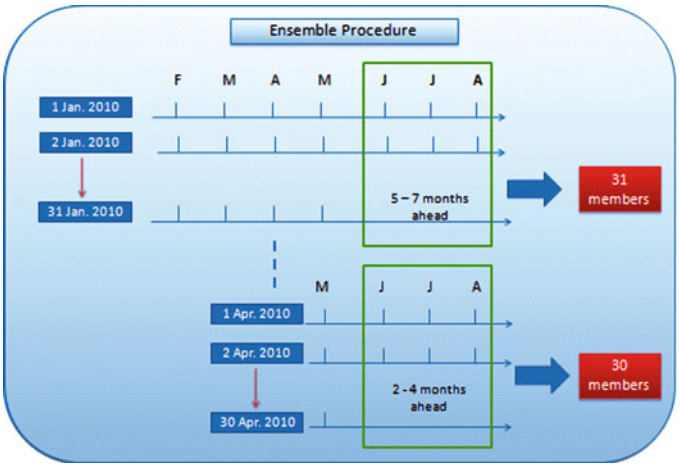

Fig. 2 A schematic representation of the ensemble procedure

4 Preliminary Results and Discussion

The temperature at 850 hPa has been chosen as a representative field of the synoptic scale motions into the atmosphere because this level is usually located above the atmospheric boundary layer and due to its proximity to the surface. Thus, the long-term mean monthly isothermal values of both 283 K (10°C) and the 278 K (5°C) was compared against the mean monthly 283 K isothermal surfaces obtained from the 31 members of January 2010 (Fig. 3 upper) and the 30 members of April 2010 (Fig. 3 lower) respectively.

This comparison suggests whether the estimated temperatures will exceed or not the relevant climatological values for the period under consideration. According to Fig. 3, the entire ensemble members exceeded NCEP long-term mean monthly temperature at 283 K for August. Moreover a sufficient number of members went beyond or lied closely to the 278 K one. This is a strong indication that unusual and higher than normal temperatures are likely to occur in the entire area. Despite the fact of the long lead period, both January and April members provided similar confidence for the temperature anomaly.

In order to investigate model capability to simulate the devastating precipitation over Northern Pakistan mean monthly accumulated precipitation has been extracted from the ensemble members and they were compared against the records from 12 surface meteorological stations located over the affected area. According to the Pakistan Meteorological Office the most of the stations recorded monthly precipitation amounts that exceeded the 400 mm (Table 1 and Fig. 4).

In Fig. 5 (upper) the July accumulated precipitation based on the April 2010 ensemble members indicated local precipitation maxima up to 720 mm at the western coastal areas of India. Despite the fact that the averaged precipitation for July exceeded the 200 mm in the areas of Northern Pakistan the model did not

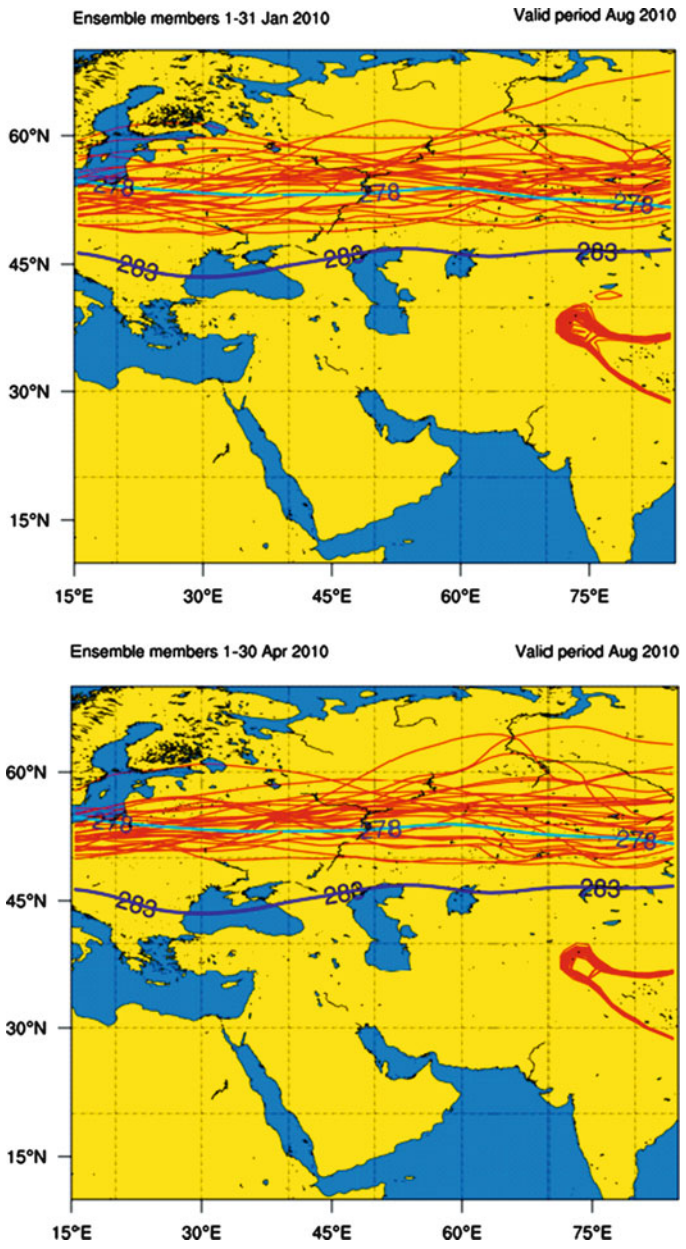

Fig. 3 Spaghetti plots of the mean monthly temperature at 850 hPa for August 2010 based on January 2010 (*upper*) and April 2010 ensemble members (*lower*). Ensemble contours at 283 K are denoted by red color and the long-term mean monthly temperatures of 283 and 278 K are denoted in *blue* and *cyan* respectively

Table 1 Accumulated precipitation (mm) recorded from 12 surface stations for July 2010

Stations in Pakistan	Rainfall recorded in July 2010	Normal rainfall amount	Recorded to normal rainfall percentage (%)
Lahore A/P	308	217.9	141.35
Lahore PBO	287	212.1	135.31
Murree	579	364.1	159.02
Sialkot Cantt	373	304.1	122.66
Garhi Dupatta	570	265.6	214.61
Kotli	417	285.8	145.91
Muzaffarabad	579	359.4	161.10
Cherat	388	93.4	415.42
Dir	317	154.1	205.71
Kakul	389	263.6	147.57
Peshawar A/P	402	46.1	872.02
SAIDU SHARIF	471	152.6	308.65

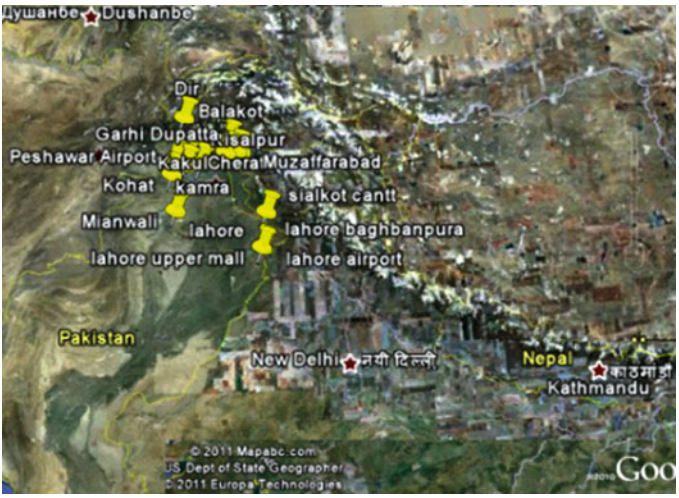

Fig. 4 The *yellow pins* stand for the locations of the meteorological stations in Table 1

reproduce the observed precipitation maxima. This could be possible attributed to the coarse horizontal resolution of the model domain and the inadequate resolve of the mesoscale atmospheric patterns. The probability map of the accumulated precipitation greater than 200 mm for July 2010 depicts areas with increased uncertainty (values lower than 0.6) and areas with high confidence that the monthly accumulated rainfall will exceed the predefined threshold (values greater than 0.8). According to Fig. 5 (lower) the increased probability of high precipitation amounts over Northeastern Pakistan is a strong indicator of extreme precipitation event.

Summarizing, CAM3 model with the developed methodology for seasonal simulations were able to reproduce the main features of the Russian blocking

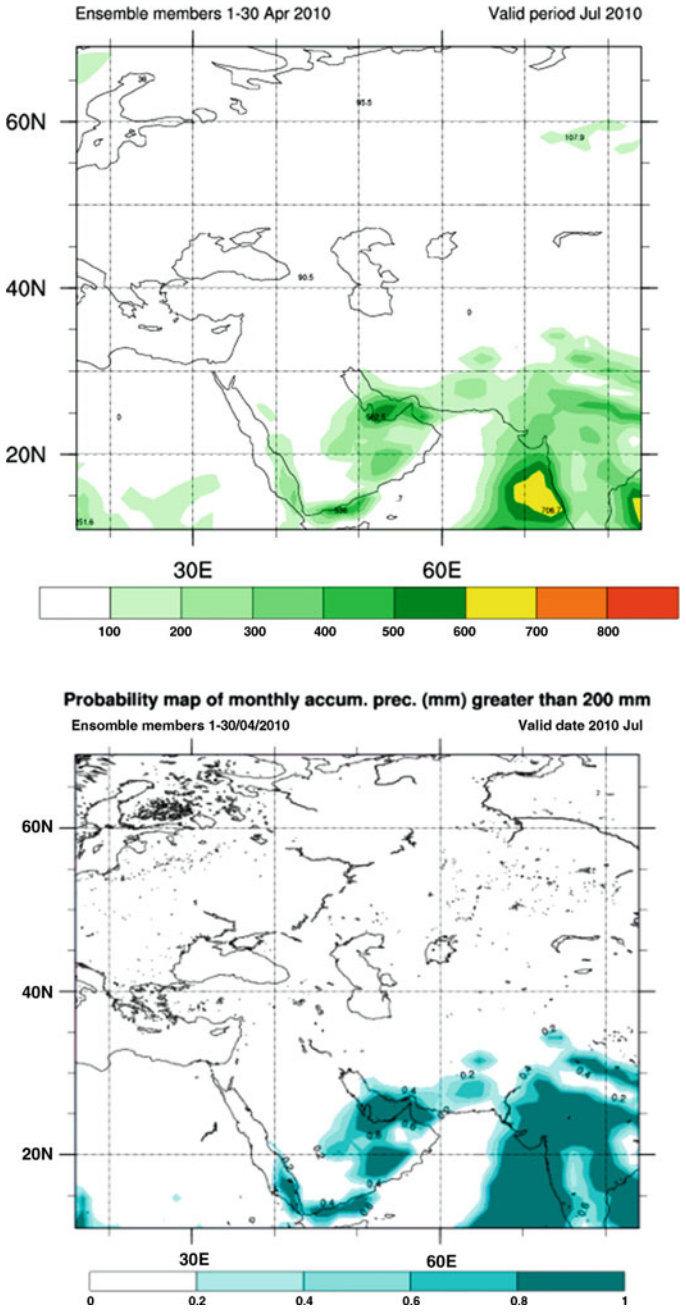

Fig. 5 (*upper*) Average accumulated precipitation (mm/month) for July 2010 of April 2010 ensemble members and (*lower*) probability map of monthly accumulated precipitation greater than 200 mm for July 2010 based on the April 2010 ensemble members

system even though in a forecast period 4–7 months before the event. The above diagnoses characterize the system as a reliable tool for simulating the large and synoptic scale atmospheric patterns. However, the system has to be further evaluated under different weather patterns on both hindcasting and forecasting modes.

References

Collins WD et al (2006) The formulation and atmospheric simulation of the Community Atmosphere Model: CAM3. J Climate 19:2144–2161. doi:10.1175/JCLI3760.1

Dole R, Hoerling M, Perlwitz J, Eischeid J, Pegion P, Zhang T, Quan XW, Xu T, Murray D (2011) Was there a basis for anticipating the 2010 Russian heat wave? Geophys Res Lett 38:L06702. doi:10.1029/2010GL046582

Gilbert N (2010) Russia counts environmental cost of wildfires. Nat News 12: doi:10.1038/news2010.404

Kalnay E et al (1996) NCEP/NCAR 40-year reanalysis project. Bull Am Meteorol Soc 77:437–470

Mason SJ, Galpin JS, Goddard L, Graham NE, Rajaratnam B (2007) Conditional exceedance probabilities. Mon Weather Rev 135:363–372. doi:10.1175/MWR3284.1

Matsueda M (2011) Predictability of Euro-Russian blocking in summer of 2010. Geophys Res Lett 38:L06801. doi:10.1029/2010GL046557

Oleson KW et al (2004) Technical description of the Community Land Model (CLM). NCAR/TN-461 + STR, National Center for Atmospheric Research, Boulder, CO, p 174

Webster PJ, Toma VE, Kim HM (2011) Were the 2010 Pakistan floods predictable? Geophys Res Lett 38:40806. doi:10.1029/2010GL046346

Nowcasting a Mesoscale Convective System Over Greece with a Satellite-Based Algorithm

S. Kolios and H. Feidas

Abstract On June 16, 2011, a Mesoscale Convective System (MCS) was developed in central Greece, over the area of Magnesia. Lightnings data from of the National Observatory of Athens along with the satellite images of that day, provide clear evidence for the convective nature of the cloud system that was developed during that day. In this study, a fully automated nowcasting algorithm based on Meteosat thermal infrared imagery was applied, which is capable of detecting and forecasting the evolution of MCSs over the Mediterranean basin. We evaluate the capability of the algorithm to early detect and especially to forecast the cloud system evolution and its convective potential from the remote sensing point of view. The results showed that the algorithm was capable of producing a satisfactory forecasting accuracy and illustrated the effectiveness of its operational use for nowcasting MCSs.

1 Introduction

Mesoscale Convective Systems (MCSs) are significant cloud systems since they can cause loss of human lives and property by producing severe weather conditions such as heavy precipitation, hail, strong winds and lightning (Gaye et al. 2005; Correoso et al. 2006). MCSs can occur worldwide, in many sizes and shapes (Jirak et al. 2003), with horizontal scales ranging from a few hundred kilometres in length to many thousand kilometres (Fujita 1986). Their life cycles can range from a few hours to almost 1 day (Morel and Senesi 2002). The forecast of these systems is

S. Kolios (✉)
Department of Geography, University of the Aegean, Mytilene 81100, Greece
e-mail: stkolios@geo.aegean.gr

H. Feidas
Department of Meteorology and Climatology, School of Geology, Aristotle University of Thessaloniki, Thessaloniki, Greece

C.G. Helmis and P.T. Nastos (eds.), *Advances in Meteorology, Climatology and Atmospheric Physics*, Springer Atmospheric Sciences,
DOI 10.1007/978-3-642-29172-2_28,

difficult because they have complicated internal dynamics and develop under various favourable conditions depending on topography, synoptic weather conditions, humidity of the atmosphere, atmospheric instability and wind shear. Mesoscale numerical models still have significant problems in forecasting MCSs (Rakesh et al. 2009). Nevertheless, the use of modern geostationary meteorological satellites, with their high time and space sampling, has become an excellent alternative way to face uncertainness and restrictions of most of the numerical models in MCS forecasting and provide the capability to track and forecast the rapid evolution of dynamic phenomena such as MCSs.

In this study, we examined the efficiency of a satellite-based automatic nowcasting algorithm in detecting, monitoring and finally short-range forecasting the physical properties of a MCS developed over Thessaly, Greece, on May 16, 2011.

2 Data and Methodology

2.1 Data

The nowcasting algorithm make use of infrared imagery obtained with the Spinning Enhanced Visible and InfraRed Imager (SEVIRI) instrument on board Meteosat Second Generation (MSG) satellites with a 15-min temporal sampling rate and about 5×6 km^2 spatial resolution at the area of study. The dataset used includes images from the infrared spectral channel of SEVIRI, with centre at 10.8 μm, which is commonly used to identify convective cloud tops. Moreover, lightning data (temporal resolution of msec and spatial resolution of about 40 km in the study area) of the Long Range Lightning Detection System (ZEUS), provided by the National Observatory of Athens, were used to detect the MCS.

2.2 Methodology

The nowcasting algorithm is capable of detecting and tracking cloud cells, defined as clusters of contiguous pixels with brightness temperatures lower than 228 K and size over 100 km^2 in the 10.8 μm channel. For each detected cloud cell, the algorithm can track the detected convective cloud cells based on an area overlap method and then forecast the movement and the evolution of their physical properties through their entire lifecycle, at 15-min intervals. The forecasting procedure combines a linear extrapolation method of the MCS life cycle history and information extracted from conceptual models derived from a local climatology. It is implemented in three steps: (a) forecast of the life cycle phase and duration based on the areal expansion rate at the initiation time of the MCS, (b) linear extrapolation of the MCS displacement and shape, and (c) forecast of the evolution of the physical properties of the MCS based on a linear extrapolation technique combined with a MCS conceptual life cycle model. For a more detailed description of the algorithm, readers may refer to the study of Kolios and Feidas (2010b).

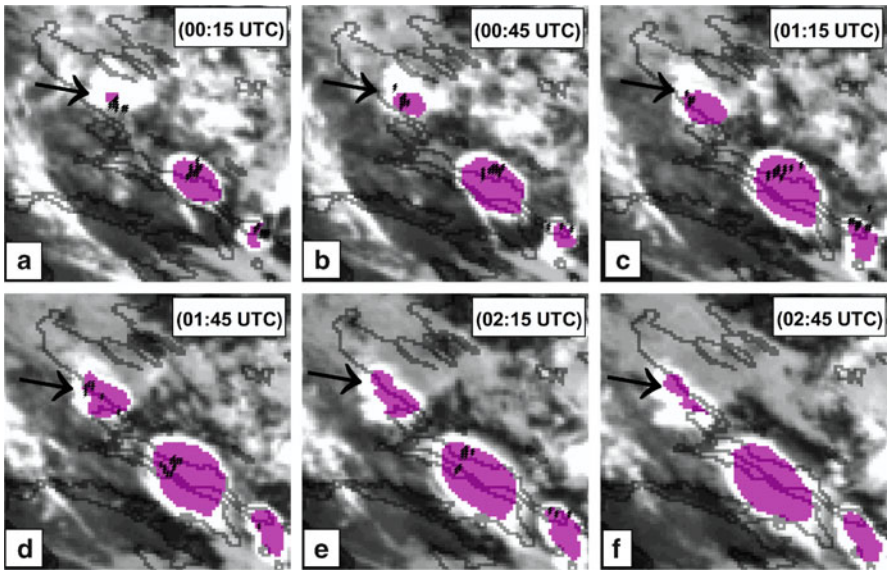

Fig. 1 Sequence of SEVIRI infrared images (10.8 μm channel) from 00:15 UTC to 2:45 UTC. Convective cloud cells (*purple colored*) identified by the algorithm along with the recorded lightning events are also indicated (*black dots*). *Arrow* denotes the MCS examined in the study

A complete forecast of the MCS evolution (forecast cycle) is provided every 15 min, in accordance to the acquisition of a new satellite image. Moreover, the algorithm is capable of spatially and temporally correlating cloud cells with lightning data in a separate module (Kolios and Feidas 2007). The lightnings were chosen as ground truth data in order to verify the convective character of the cloud system.

3 Results

In the early hours of June 16, 2011, a group of mesoscale convective cells developed over central Greece (Fig. 1). The synoptic situation at the surface at 00:00 UTC is characterized by a weak pressure gradient over Greece (Fig. 2a). The MCSs were triggered by a strong upper-level trough stretched over the eastern Mediterranean with its axis extending over Greece (Fig. 2b). Upward vertical motion caused by the release of instability when the cold upper-level air masses advected over the warm and humid air of the heated surface (Fig. 2c).

We chose to study a small convective cloud system in order to assess the capability of the algorithm to detect and forecast small MCSs (Fig. 1). The MCS of interest was detected by the algorithm for the first time at 00:15 UTC over the Aegean sea, northeast of the Magnesia gulf (Thessaly). It moved southwest over the land and dissipated at 03:15 UTC. Lightning activity was detected during the growing phase of the MCS lifecycle (00:15 UTC–01:45 UTC) (Fig. 3) confirming

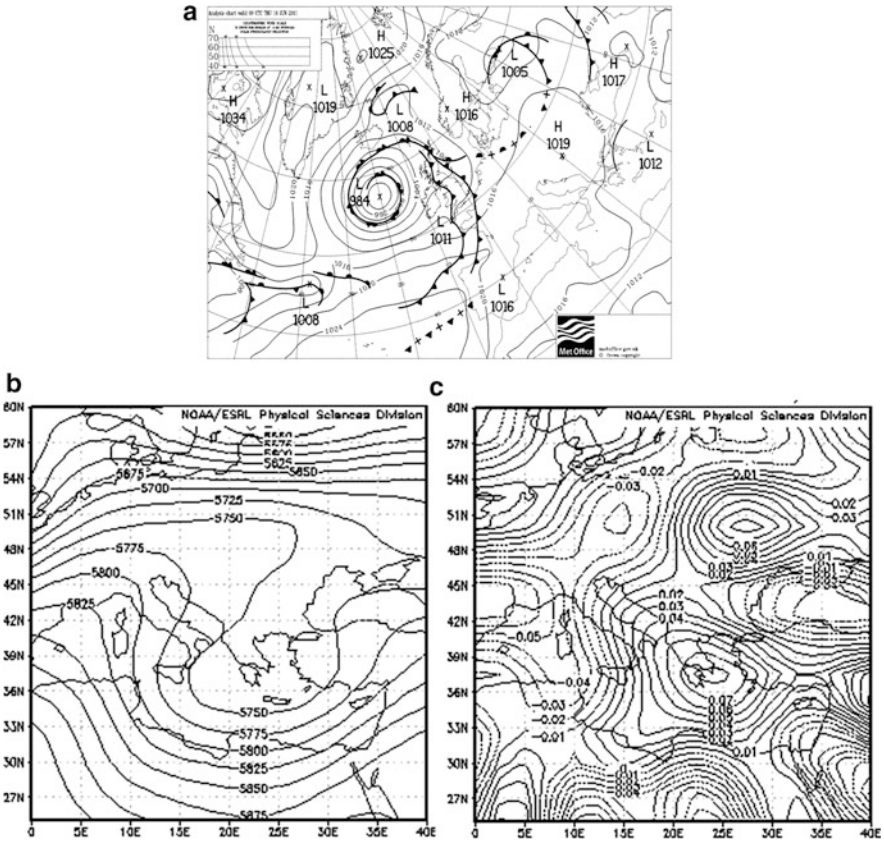

Fig. 2 (**a**) Surface weather map, (**b**) 500 hPa height analysis and (**c**) vertical (omega) velocities (Pa/s) for June 16, 2011, at 00:00 UTC

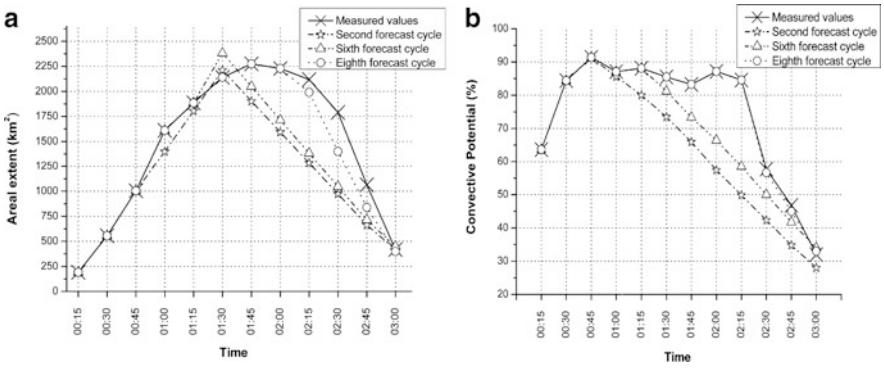

Fig. 3 Comparison between the forecasted and observed life cycle of the examined MCS (June 16, 2011) expressed as the time evolution of two characteristic parameters: (**a**) areal extent (km^2), (**b**) convective potential (%). Forecasts are presented for three forecast cycles (second, sixth and eighth)

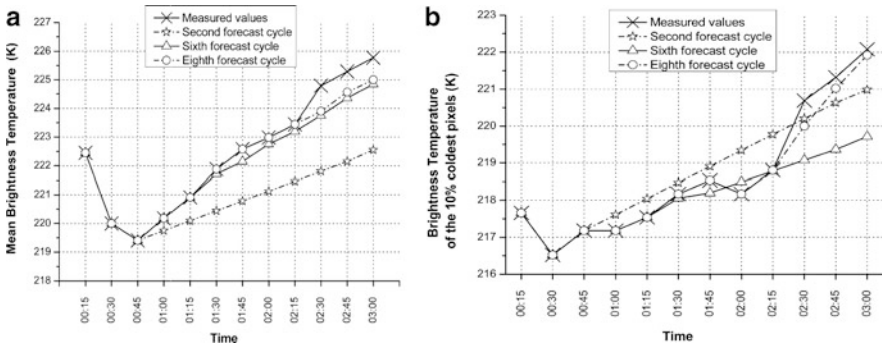

Fig. 4 (**a**) Mean temperature (K) at the 10.8 μm channel, (**b**) temperature of the 10% coldest pixels at the 10.8 μm channel (K). Forecasts are presented for three forecast cycles (second, sixth and eighth)

the convective nature of the system. Figure 3 exhibits the comparison between the forecasted and observed MCS life cycle expressed as the time evolution of two characteristic parameters (areal extent and temperature of the 10% coldest pixels in the 10.8 μm channel) for three forecast cycles (second, sixth and eighth). The evolution of the MCS areal extent reveals a growing phase lasting 90 min and a shorter dissipation phase lasting 60 min. There is a gradual transition between these two phases which is not well represented by the forecast due to the linear extrapolation method used by the forecast system. Nevertheless, the time lag between the measured and forecasted maximum areal extent is only 15 min. However, there is a good correspondence between the time evolution of forecasted and observed areal extent in the development phase. The main discrepancy is discerned in the dissipation phase, during which the MCS dissipated slower than forecast. This discrepancy is improved only after the sixth forecast cycle when observations from the dissipation phase became available to the forecasting system.

The areal extent as well as the convective potential (Kolios and Feidas 2010a) forecasts (Fig. 3a, b, respectively) were improved significantly in subsequent forecast cycles. The Mean Absolute Error (MAE) and Mean Error (ME) scores for all the eight forecast cycles were quite low for both parameters (MAE = 215.8, ME = 187.4 km^2 for the areal extent, MAE = 7.68%, ME = 3.15% for convective potential). According to Fig. 4a, mean brightness temperature is predicted efficiently only after the second forecast cycle. MAE and ME scores, however, for all the eight forecast cycles are very low (0.92 and 0.86 K, respectively). The general pattern of the 10% coldest cloud pixels temperature evolution was predicted efficiently, however, forecasts did not improve with increasing forecast cycles (Fig. 3b). Indeed, there is a notable deterioration of forecast skill in the last three time steps of the sixth forecast cycle. However, the general forecast accuracy can be characterized as satisfactory given that the MAE and ME for all the forecast cycles were only 0.43 and 0.21 K, respectively.

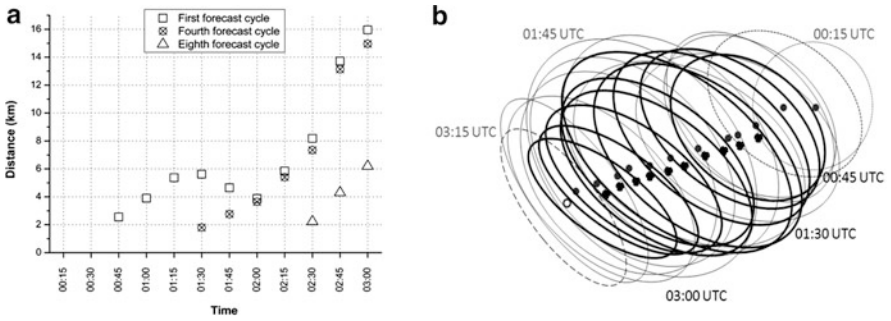

Fig. 5 (**a**) Time evolution of the distance between detected and estimated cloud centers of mass for three forecast cycles (first, second, and eighth). (**b**) Observed (*gray colour*) and forecasted ellipses (*black colour*) for the first forecast cycle. The *dotted gray* ellipses represent the MCS history and the *dash dotted* ellipse (at 03:15 UTC) denotes the last observed timestep that is not predicted by the forecasting procedure. *Gray and black dots* indicate the observed and the estimated centers of the ellipses, respectively

According to Fig. 5a, the error in the position of the forecasted MCS is in overall small, being of the order of two MSG pixels (less than 10 km), at least up to the eighth lead-time (2:30 UTC) of the first forecast cycle. This error is ameliorated in subsequent forecast cycles when more MCS life history observations are ingested into the model.

Figure 5b presents a comparison between the observed and forecasted MCS track in terms of best fitted ellipses, showing the recent MCS history and the forecast for the first forecast cycle. The forecasted MCS lifespan is 15-min shorter that the observed life cycle duration. There is, however, a very good spatial match between forecasted and observed ellipses of the MCS and a remarkable agreement in the direction of movement, as indicated by the centres of the ellipses.

4 Conclusions

The capability of a satellite-based MCS nowcasting system to forecast the evolution of a small MCS developed in June 16, 2011, in Thessaly (Greece), was assessed in this study. The pattern of the time evolution of some main MCS parameters, such as areal extent, convective potential and the mean and 10% coldest cloud pixels temperatures were well predicted by the system with quite low errors. The movement of the MCS is also well predicted considering the small error in the position of the forecasted MCS (less than 10 km). A tendency for a slight improvement in the forecast skill is observed as we proceed to the next forecast cycles. The system provided a notably accurate forecast of the MCS track in terms of direction of movement and spatial match of forecasted and observed MCSs. To sum up, the presented case study demonstrated the value of the forecasting system in early detecting a small MCS and then predicting its movement and intensity.

Acknowledgments The authors would like to thank Dr. V. Kotroni and K. Lagouvardos, researchers in the National Observatory of Athens, for providing the lightning data.

References

Correoso FJ, Hernndez E, Garcia-Herrera R, Barriopedro D, Paredes D (2006) A 3-year of cloud-to-ground lightning flash characteristics of mesoscale convective systems over the Western Mediterranean Sea. Atmos Res 79:89–107. doi:10.1016/j.atmosres.2005.05.002

Fujita T (1986) Mesoscale classifications: their history and their application to forecasting. In: Ray PS (ed) Mesoscale meteorology and forecasting. American Meteorological Society, Boston

Gaye A, Viltard A, De Felice P (2005) Squall lines and rainfall over Western Africa during 1986 and 1987. Meteorol Atmos Phys 90:215–224

Jirak IL, Cotton WR, McAnelly RL (2003) Satellite and radar survey of mesoscale convective system development. Mon Weather Rev 131:2428–2449. doi:10.1175/1520-0493(2003)131<2428:SARSOM>2.0.CO;2

Kolios S, Feidas H (2007) Correlation of lightning activity with spectral features of clouds in Meteosat-8 imagery over the Mediterranean basin. In: Proceedings of the 8th Pan-Hellenic geographic conference, Athens, 4–7 October 2007

Kolios S, Feidas H (2010a) A warm season climatology of mesoscale convective systems in the Mediterranean basin using satellite data. Theor Appl Climatol 102:29–42

Kolios S, Feidas H (2010b) An automated short-range forecasting system of mesoscale convective systems for the Mediterranean basin using satellite imagery. In: Proceedings of 10th COMECAP, Patras, Greece

Morel C, Senesi S (2002) A climatology of mesoscale convective systems over Europe using satellite infrared imagery. II. Characteristics of European mesoscale convective systems. Q J R Meteorol Soc 128:1973–1995. doi:10.1256/003590002320603494

Rakesh V, Singh R, Joshi CP (2009) Intercomparison of the performance of MM5/WRF with and without satellite data assimilation in short-range forecast applications over the Indian region. Meteorol Atmos Phys 105:133–155. doi:10.1007/s00703-009-0038-3

openmeteo.org: A Web Service for the Dissemination of Free Meteorological Data

S. Kozanis, A. Christofides, N. Mamassis, and D. Koutsoyiannis

Abstract Individuals or organizations managing meteorological or hydrological stations typically need to either collect the data on personal computers or bear the costs required to setup a server. As an alternative, the openmeteo.org database provides users and organizations the option to upload their time series, on condition that their data will be available to the public under a free license (the Open Database License and the Creative Commons Attribution-ShareAlike License, depending on the type of data). Each user has write access to his own data, whereas the public has read access to all the data. *Enhydris*, the software that powers openmeteo.org, is also free, available under the GNU General Public License v.3, and provides several useful features like time series graphs and plots, display of online data, maps etc. The purpose of openmeteo.org is not only to enable people to manage their data more easily, but also to bring people into a community and encourage a spirit of openness and sharing.

1 Introduction

A major task in meteorology, climatology and hydrology is finding and collecting measurement data. The conventional procedure is to contact an organization such as a meteorological office, a research institution, a ministry, an electric supply company, a water supply company, and so on. Data, whenever they exist, are then provided either for free or for a fee and usually they are copyrighted by the supplying organization, with restrictions on the use or publication of the data.

On the other hand, many organizations and individuals, amateurs and professionals, wish to offer their data to the public in order to help the scientific

S. Kozanis (✉) • A. Christofides • N. Mamassis • D. Koutsoyiannis
National Technical University of Athens, Zografos 157 80, Greece
e-mail: S.Kozanis@itia.ntua.gr

C.G. Helmis and P.T. Nastos (eds.), *Advances in Meteorology, Climatology and Atmospheric Physics*, Springer Atmospheric Sciences,
DOI 10.1007/978-3-642-29172-2_29,

community or just to build an information service, for example, with the current weather conditions, but either they lack the expertise or the resources to build it.

openmeteo.org is a new concept implemented as an internet web service, with the goals: (a) to provide to such individuals and organizations a free hosting service for meteorological data supported by a robust and user-friendly system, helping them share their data with the public; and (b) to create a pool of free data available to everyone. The owner of the data keeps the copyright, but the data are provided under a free license.

The service consists of many elements, the most important of them being: (a) The server software and the database for the storage; (b) the server computer itself running the software, web application services and data storage and backup; and (c) users, submitting and downloading data in the form of meteorological or hydrometeorological time series. The web address for the service is http://openmeteo.org/db/.

2 Data, Licensing and Copyright

Besides the technological implementation, a crucial factor for the success of the objectives is the adoption of appropriate licensing schemes for data, which should help the dissemination of free information and redistribution of data allow derivative works.

We have chosen two licenses for user submissions, depending on the nature of data: (a) for time series, the Open Database License (http://opendatacommons.org/licenses/odbl/), with the individual records that comprise the time series being licensed under the Database Contents License; and (b) for images, audio-video material, and substantial pieces of text, the Creative Commons Attribution ShareAlike License (http://creativecommons.org/licenses/by-sa/2.5/). The database as a whole is also licensed under the Open Database License.

When a user submits material to the openmeteo.org site, he acknowledges either that (a) the user submissions are in the public domain; or, (b) he is the copyright holder; or, (c) he has permission from the copyright holder to upload the data and license it to openmeteo.org.

(See http://openmeteo.org/db/terms_of_service/ for the full Terms of Service).

3 Software and Setup

The software that powers the openmeteo.org web site is *Enhydris*, a database system for the storage and management of hydrological and meteorological data. It allows the storage and retrieval of raw data, processed time series, model parameters, curves and meta-information such as measurement stations overseers, instruments, events etc. *Enhydris* implementation is based on the experience gained from several research projects, especially from the database design of the "National Data Bank for

Hydrological and Meteorological Information" of Greece (Papakostas et al. 1994; Tsakalias and Koutsoyiannis 1994).

The *Enhydris* database is accessible through a web interface, which includes several data representation features such as tables, graphs and maps. Data access is configurable to allow or to restrict user groups and/or privileged users to contribute or download data. With these capabilities, *Enhydris* can be used either as a public repository of free data or as a fully secured – restricted system for data storage. Time series can be downloaded in plain text format that can be directly loaded to *Hydrognomon* (http://hydrognomon.org/), a free tool for analysis and processing of meteorological time series.

Enhydris is free software, developed mainly by the National Technical University of Athens, and it is an active project with continuous development. It is available under the GNU Affero General Public License version 3. It is written in Python/Django and C and uses PostgreSQL and PostGIS. It can run on UNIX and Windows; currently all known installations use Debian GNU/Linux. Anyone can obtain a copy of *Enhydris* from openmeteo.org and install it to his own servers. *Enhydris* is already installed and run by several services beyond openmeteo.org, such as Hydroscope (National Greek database of hydrological and meteorological data), the Athens Water Supply Company (EYDAP), the Hydrological Observatory of Athens (hoa.ntua.gr), and WQ Dreams (funded by the European Environmental Agency). Such applications of *Enhydris* were extensively presented in the recent past (Christofides et al. 2011b); the free public database presented in this text is a new application, announced officially to the public on July 25, 2011.

Enhydris is modular and extensible; new applications can be written which extend the core functionality. Such applications which have already been developed and are bundled with the core code are: (a) **hchart,** for chart plots of meteorological variables; (b) **hrain,** for analysis and plotting (surface and line charts) of rainfall events; (c) **hprocessor,** for automatic – scheduled processing of time series such as aggregation, curve interpolation etc.; (d) **contourplot,** for surface plots of meteorological variables such as precipitation or temperature; and (e) **gis_objects,** which installs special entities for the management of water supply systems. The installation of these applications is optional; for example, only hchart and hprocessor are currently installed in openmeteo.org.

Part of the setup is our experimental automatic meteorological station (meteo.ntua.gr) which is active by serving online data for 20 years. The data of this station is automatically entered to the openmeteo.org database. The logging is executed by a separate computer with a modem connection to the station. Logging intervals are of 10 min, and logged data are immediately available to the public via openmeteo.org.

4 Methodology

Enhydris, the server software application behind the openmeteo.org database service implements a typical Model – View – Controller software architecture pattern (Reenskaug 1979). The "domain logic" (the application layer for the user) is

isolated from the User Interface (input and presentation), permitting independent development, testing and maintenance of each. Model View Controller (MVC) pattern creates applications that separate the different elements of the application (input logic, business logic, and UI logic), while providing a loose coupling between them.

The MVC is implemented with a web application framework the so-called *Django*. *Django* implements MVC business logic by the extensive use of the Python Programming Language which is the core of the application framework. *Django* also provides a custom web template language to build the "presentation layer" or "input logic". The "model layer" is supported by the database "backend" for data retrieval and storage. *Django* applications can cooperate with a range of RDMSes (Relational Database Management Systems) such as *PostgreSQL*, *mySQL* and *Oracle*. Finally, "presentation layer" needs a web server to function which is the *Apache* in our case. *Apache* serves web service static data (pictures and files) but also invokes the *Enhydris* processes to run the service.

RDMS of choice is *PostgreSQL*, a free database system with good in overall performance, used widely and well adopted by information technology business. PostgreSQL is scalable and can work in distributed RDMS environments as well as in load balancing schemes for high availability services. One of the main aspects of RDMSes that *PostgreSQL* implements in a strict way is the so-called RDMS *Referential Integrity* (Dates 1981), a crucial feature for our service that should be satisfied.

openmeteo.org meta-data such as information about stations and time series are stored in ordinary character, text, integer, floating point or logical (Boolean) fields. For the storage of time series data, consisted sometimes of millions of records, a non-ordinary storage process is implemented and this is one of the major advantages of the system. By brief describing the algorithm, a few records from the beginning and the end of the time series are stored in ordinary text fields allowing the fast retrieval of time series bounds as well as, for example, last 24 h weather conditions. The rest – big part of the time series is stored in a *bytea* (binary) database field, compressed then with the LZ77 algorithm (Ziv and Lempel 1977). This storage methodology is a good compromise between storage space and performance.

Each one of the time series record is a line of text containing three fields of information separated by comma (,). The first field is the representation of the time series records time stamp in the widely adopted ISO 8601 format. The second field can be a floating point value representing the actual measurement or just an empty string to denote null values; null values represent absence of measurement due to several factors such as malfunctions of the logging devices or sensors etc. Last field of the record is a list of possible flags separated by white-space. Flags are special marks for time series records to denote e.g. values suspect for errors or values inserted by infilling etc.

Backend system is not only accessible by the *Django* system but also by special scripts such as the *loggertodb* script that we developed in order to communicate with meteorological stations data loggers and to store measurements in the database

system. *loggertodb* can be installed to the main server or to separate servers where MODEMs are installed for the communication with the stations loggers. Another option for access to the backend is the use of special developed APIs (Application Programming Interface) allowing the interoperability with other web services that can retrieve our data and presented them in other manners and custom interfaces.

Some data operations are executed automatically by the main core (business logic) of the *Enhydris* system. These automatic operations can be triggered by a *cron* process of the operating system, which is a time scheduler that invokes system or user commands. Automatic operations have full access to the backend system to read and write data. Some of these operations are time series aggregation (e.g. calculations of monthly mean values from 10-min measurements), discharge calculations in water streams from the measured water stage, reservoir storage from stage level measurements, barometric formula – barometric pressure reduction by elevation and temperature and finally assessment of bioclimatic indices such as heat index by temperature, humidity and wind speed measurements.

Time series data are exported in several ways. The first and obvious is the download capability by the appropriate web page. In addition to simple downloads the system can provide data for special requests i.e. for specific time periods. Special data requests are served in the *JSON* data format and contain not only time series records but also some useful statistics for the dataset such as mean values (vector mean values for wind direction data), min and max, sums etc. The *JSON* service can be used by external services beyond openmeo.org to retrieve data; however it is used preliminary to support charting and contour plotting of meteorological and hydrometerological variables of openmeteo.org.

5 The Web Site

The free database is available at http://openmeteo.org/db/. The web site was first announced as a part of a framework with free software applications (Christofides et al. 2011a), where only download was possible in this preliminary version. In the current, full functional version, anyone can browse the meteorological stations, instruments etc., and download historical data. Registration to the web site is optional for read access and required in order to create meteorological stations in the database and generally to submit content. Each registered user can modify the information for the stations he creates; he can provide write access to other users by defining a list “maintainers” of his stations.

6 Conclusions

With openmeteo.org we wish to enlarge the publicly available pool of data and provide appropriate tools to people who cannot otherwise afford them, such as amateurs and small organizations. In this way, we also hope to raise awareness of the benefits of the free public sharing of information, and contribute to the establishing of a spirit of openness and co-operation within the meteorological community.

Acknowledgments The authors wish to acknowledge the Ministry of Public Works and the Hydroscope Systems Consortium for funding the initial development of *Enhydris* and openmeteo.org.

References

Christofides A, Kozanis S, Karavokiros G, Koukouvinos A (2011) Enhydris, Filotis & openmeteo.org: free software for environmental management, FLOSS conference 2011, Athens, http://conferences.ellak.gr/2011/, 2011

Christofides A, Kozanis S, Karavokiros G, Markonis Y, Efstratiadis A (2011) Enhydris: a free database system for the storage and management of hydrological and meteorological data, European Geosciences Union General Assembly 2011, Geophysical Research Abstracts, vol 13. European Geosciences Union, Vienna

Dates C (1981) Referential integrity. In: Proceedings of the 7th international VLDB conference, France, 1981

Papakostas N, Nalbantis I, Koutsoyiannis D (1994) Modern computer technologies in hydrologic data management. In: Tsakiris G, Santos MA (eds) Proceedings of the 2nd European conference on advances in water resources technology and management, Lisbon, Balkema, Rotterdam, pp 285–293

Reenskaug T (1979) MVC XEROX PARC 1978–79. http://heim.ifi.uio.no/~trygver/themes/mvc/mvc-index.html. Accessed 28 Dec 2011

Tsakalias G, Koutsoyiannis D (1994) Hydrologic data management using RDBMS with differential-linear data storage, Hydraulic Engineering Software V. In: Blain WR, Katsifarakis KL (eds) Proceedings of the 5th international conference HYDROSOFT'94, Sithonia, vol 2. Computational Mechanics Publications, Southampton, pp 317–326

Ziv J, Lempel A (1977) A universal algorithm for sequential data compression. IEEE Trans Inform Theory 23(3):337–343

Numerical Investigation of the Role of Topography in Tornado Events in Greece

I.T. Matsangouras, I. Pytharoulis, and P.T. Nastos

Abstract Several tornadic events have been reported in Greece during the last decades and are usually associated with strong synoptic scale forcing. Although most of them occur over the sea (waterspouts), a number of events appear over the land, causing serious damages to the nearby infrastructure and posing an important threat to human beings. It is well known that the meteorological conditions over Greece are affected at various scales by the significant variability of topography. However, there is still uncertainty regarding its importance on tornadoes. The aim of this study is to investigate the relative role of topography and synoptic scale forcing in the occurrence of tornadoes in Greece. Two events that occurred during the last years at Thiva (Boeotia, 17/11/2007) and Vrastera (Chalkidiki, 12/02/2010) were selected for numerical experiments. These events were associated with frontal activity and caused serious damages. The non-hydrostatic WRF-ARW atmospheric numerical model is utilized at very high resolution using telescoping nests in order to perform the sensitivity experiments. Two sets of experiments are conducted: (a) with the actual topography and (b) without it.

1 Introduction

Tornadoes are associated with strong winds, causing extended damage and in many cases loss of life. Wind whirl events occur in many parts of the world (Fujita 1973) and several publications during the last two decades indicate their occurrence in many

I.T. Matsangouras (✉) • P.T. Nastos
Laboratory of Climatology and Atmospheric Environment, University of Athens, Panepistimiopolis, GR-15784 Athens, Greece
e-mail: john_matsa@geol.uoa.gr

I. Pytharoulis
Department of Meteorology and Climatology, School of Geology, Aristotle University of Thessaloniki, University Campus, GR-54124 Thessaloniki, Greece

C.G. Helmis and P.T. Nastos (eds.), *Advances in Meteorology, Climatology and Atmospheric Physics*, Springer Atmospheric Sciences,
DOI 10.1007/978-3-642-29172-2_30,

European countries (Dessens and Snow 1987; Reynolds 1999; Gayà et al. 2000; Dotzek 2001; Holzer 2001; Bertato et al. 2003; Dotzek 2003; Giaiotti et al. 2007).

Regarding tornadic variability in Greece, significant research has been carried out during the last years, such as the 300 years (1709–2010) study of historical records of tornadoes – waterspouts – funnel clouds (see Matsangouras et al. 2011b), a 10 year climatology (Sioutas 2011) and the twentieth century climatology (Nastos and Matsangouras 2010). In addition to the above climatologic publications, analysis of several catastrophic case studies were carried out from a synoptic scale point of view (Matsangouras and Nastos 2010; Matsangouras et al. 2010, 2011a) in order to understand the relation between the complex Greek terrain and the vulnerability of several geographical places for tornado development.

The aim of this study is to investigate the relative role of topography and synoptic scale forcing in the occurrence of tornadoes in Greece as uncertainty exists regarding its importance on tornado generation and development. Two events that occurred during the last years in Thiva (Boeotia, 17/11/2007) and Vrastera (Chalkidiki, 12/02/2010) were selected for numerical experiments. These tornadic events were associated with synoptic scale forcing, their intensity was T4–T5 (Torro scale) and caused significant damages.

2 Data and Methodology

Tornado event simulations were performed using the non-hydrostatic Weather Research and Forecasting (WRF) model, in order to determine whether the model is able to indicate the occurrence of these events by modifying the topography. The simulations concern runs with and without topography.

An analysis of severe weather variables were conducted for every simulation. These variables concern the Bulk Richardson number shear (BRNSHR), the energy helicity index (EHI), the storm-relative environmental helicity (SREH) and maximum convective available potential energy (MCAPE, for parcel with maximum theta-e). The selection of these parameters is consistent with the approach adopted in previous studies (Droegemeier et al. 1993; Johns et al. 1993; Rasmussen and Blanchard 1998; Brooks et al. 2003; Doswell and Evans 2003; Thompson et al. 2003; Shafer et al. 2009).

The WRF-ARW V3.2.0 non-hydrostatic numerical model (Skamarock et al. 2008; Wang et al. 2010) was used in order to simulate the weather conditions regarding tornadic activity on 17/11/2007 and 12/02/2010. Three one-way nested domains were utilised. The spatial resolution of the model was 12 km for D1 (381×301 grid-points), 4 km for D2 (310×301) and 1.333 km for D3 (202×202). All nests were integrated in non-hydrostatic mode. The 6-hourly analyses from European Centre for Medium-Range Weather Forecasts (ECMWF) with a spatial resolution of $0.25^\circ \times 0.25^\circ$ were used as initial and lateral boundary conditions for the domain D1. The sea-surface temperatures (SSTs) were derived from the daily NCEP SST files at a very high horizontal resolution of $0.083^\circ \times 0.083^\circ$. The model was initialised at 00:00 UTC on 17/11/2007 (~24 h

before the event) and at 00:00 UTC on 12/02/2010 (~18 h before the event), in the simulations of the November 2007 and February 2010 cases, respectively. In both case studies domain D1 covered Europe and northern Africa and D2 covered southern Balkans, while D3 was setup over each area of interest. In the sensitivity experiments, topography was removed only in D3. In the vertical, 39 sigma levels (up to 25 hPa) with increased resolution in the boundary layer were used by all nests.

The Ferrier (Ferrier et al. 2002), RRTMG scheme (Mlawer et al. 1997), the Monin-Obukhov (Eta) (Monin and Obukhov 1954), the Mellor-Yamada-Janjic (Janjic 2002) level 2.5 and the NOAH Unified model (Chen et al. 1996) were used in all nests to represent microphysics, longwave/shortwave radiation, surface layer, boundary layer and soil physics, respectively. Cumulus convection was parameterized only in nests D1 and D2 by the Betts-Miller-Janjic (Betts and Miller 1993; Janjic 1994) scheme (operational Eta model).

The model outputs were available at 10 min interval. This interval was chosen to investigate the ability of the WRF to simulate severe weather events, providing qualitative and quantitative evidence as to the degree of synoptic scale involvement, influenced by topography modifications.

3 Synoptic Conditions

The first event concerns the tornado which formed approximately at 21:20 UTC on 17/11/2007, over Loutoufi, a small village located 9 km SW of Thiva's city (Lat: 38.28°N, Lon: 23.28°E).

The tornado dissipated at Thiva's NW urban area (Piri district), its path was 10 km and scattered broken branches of olive trees were found along it. Additionally, significant damages were documented in Loutoufi village and in Thiva city (structural damages). Regarding tornado's force scale it could be characterized as a T4–T5 of Torro scale (Meaden 1976), based on tornado's damage survey.

ECMWF reanalysis at 500 hPa at 18:00 UTC 17/11/2007 (not shown) presents a closed cyclonic circulation over central Italy causing a SW upper air stream over central Greece. The short wave trough is located east of Italy accompanied by a cold air mass of −24°C at the level of 500 hPa. Six hours later, at 00:00 UTC 18/11/2007 the short wave trough is located over the west coast of Greece (not shown). MSL analysis of UK Met Office (UKMO), at 18:00 UTC 17/11/2007, depicts a shallow low (1,004 hPa) located over Brindisi accompanied by a cold front located over Ionian Sea (not shown). UKMO Mean Sea Level (MSL) analysis of 00:00 UTC 18/11/2007 presents the cold front along the east coasts of central Greece (Fig. 1a).

The second event concerns a tornado that occurred 2.5 km south of Chalkidiki's Vrastama village, a non urban area 45 km southeast of Thessaloniki in northern Greece (Lat: 40.36°N, Lon: 23.54°E), on 12/02/2010. The tornado developed approximately between 17:10 and 17:35 UTC, caused significant damages. Based on the caused damages it could be characterized at least as an F2 (Fujita scale) or T4–T5 of TORRO scale (Meaden 1976). Along the tornado path, several metallic

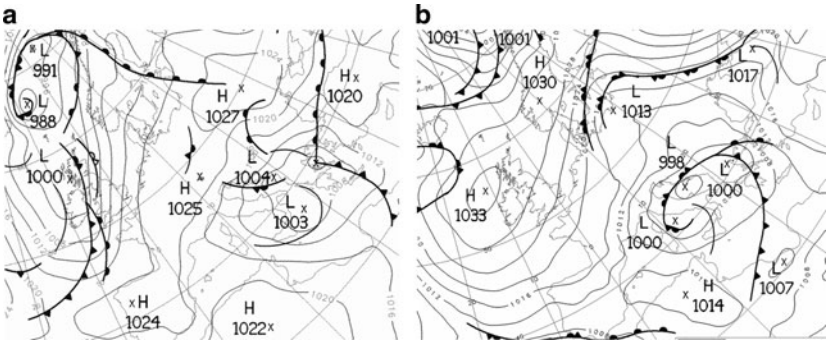

Fig. 1 UKMO's MSL analysis: (**a**) at 00:00 UTC 18/11/2007 and (**b**) at 18:00 UTC 12/02/2010

parts of an olive oil processing building and scattered broken branches of olive trees were found, revealing the tornado's force.

ECMWF's reanalysis, at the isobaric level of 500 hPa (12:00 UTC 12/02/2010) presents a closed cyclonic circulation over central Italy associated with cold air masses of −35°C at this level (not shown). The closed low induced a SW upper air stream over the area of interest. UKMO MSL analysis depicts a low pressure system (998 hPa) over central Adriatic Sea, associated with a cold front (over west Greece) at 12:00 UTC (not shown). At 18:00 UTC the UKMO's MSL pressure analysis shows that the cold front is extended from northern Greece to Peloponnesus (south Greece) and northern Libya through the area of interest (Fig. 1b).

4 Numerical Results and Conclusions

Simulation results of 12/02/2010 tornado event revealed that topography did not affect significantly the calculated variables of EHI, BRNS, SREH and MCAPE. These light differences could be attributed to (a) the short distance (less than 8 km) of tornado location from the coast line and (b) the low height contrast regarding the above mention horizontal distance (slope).

It is worth mentioning that both simulations (with topography and no topography) exhibited the maximum values of EHI, SREH and MCAPE with a horizontal offset of 20 km W-SW from the tornado's developed location.

However, the simulations of 17/11/2007 case presented significant differences of the aforementioned variables, as they were calculated with topography and without topography. The maximum values (at 21:20 UTC, time of the tornado event) were located 10 km E-SE to the tornado's development location. These maximum values in the topography simulation run were almost 50% higher than the calculated values with no topography (Fig. 2a, b, EHI).

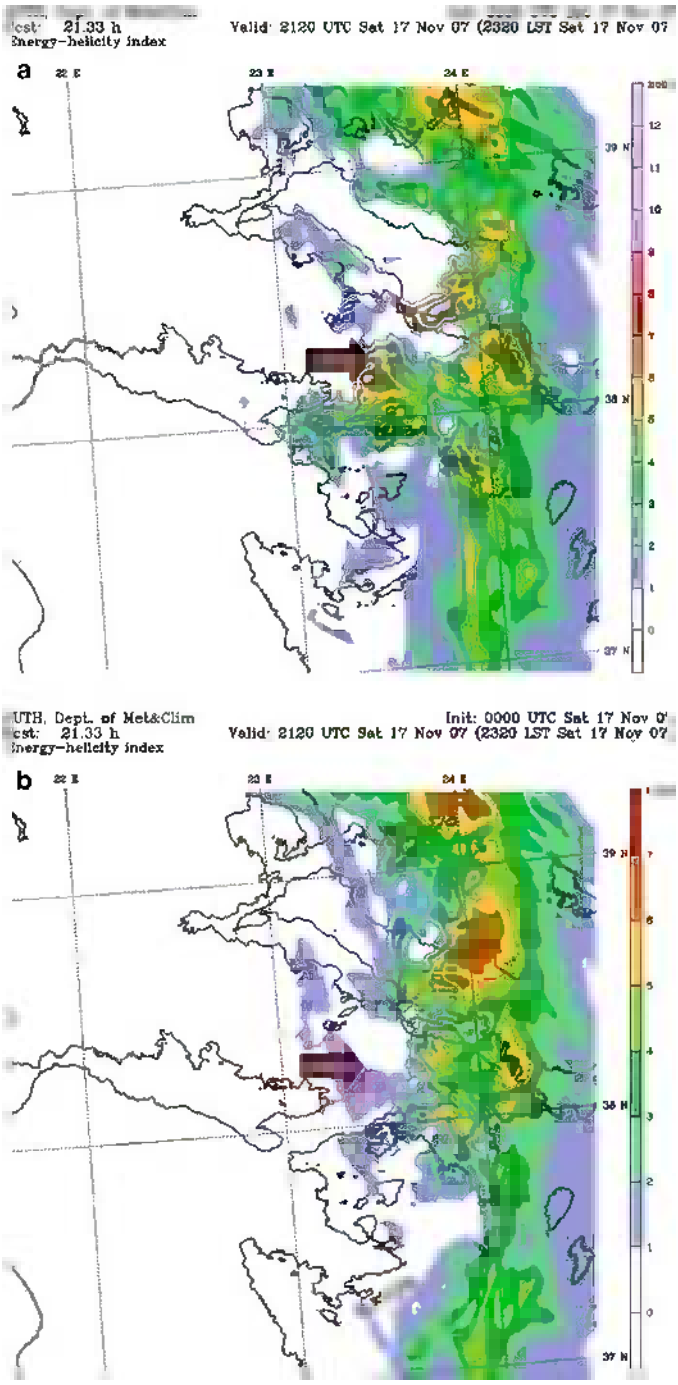

Fig. 2 Horizontal sections of WRF-ARW Energy Helicity Index (EHI) for 17/11/2007 tornado event: (**a**) with topography and (**b**) with no topography, valid at 21:20 UTC 17/11/2007. The *red arrow* represents the actual tornado location

Authors firmly believe that although the tornado in Thiva (17/11/2007) developed over an area within less than 12 km far from the coast, the significant differences in EHI, SREH, MCAPE and BRNS, as they were calculated with topography and without topography, were due to the steep slope of the terrain regarding the direction of air flow. Further analysis will be performed in order to quantify these results.

Acknowledgments The authors would like to acknowledge the European Centre for Medium Range Weather Forecasts (ECMWF), the UK Met Office (UKMO) and the Hellenic National Meteorological Service (HNMS) for the processed data that were used in order to complete this study. Additionally, we would like to thank NCAR for providing the WRF-ARW model.

References

Bertato M, Giaiotti D, Manzato A, Stel F (2003) An interesting case of tornado in Friuli-Norteastern Italy. Atmos Res 67:3–21. doi:10.1016/S0169-8095(03)00043-7

Betts A, Miller M (1993) The Betts-Miller scheme. The representation of cumulus convection in numerical models. Meteorol Monogr Am Meteorol Soc 24:107–121

Brooks H, Lee J, Craven JP (2003) The spatial distributions of severe thunderstorm and tornado environments from global reanalysis data. Atmos Res 67:73–94

Chen F, Mitchell K, Schaake J, Xue Y, Pan H, Koren V, Duan Y, Ek M, Betts A (1996) Modeling of land-surface evaporation by four schemes and comparison with FIFE observations. J Geophys Res 101:7251–7268. doi:10.1029/95JD02165

Dessens J, Snow J (1987) Tornadoes in France. Weather Forecast 4:110–132

Doswell C III, Evans J (2003) Proximity sounding analysis for derechos and supercells: an assessment of similarities and differences. Atmos Res 67:117–133

Dotzek N (2001) Tornadoes in Germany. Atmos Res 56:233–251

Dotzek N (2003) An updated estimate of tornado occurrence in Europe. Atmos Res 67:153–161

Droegemeier K, Lazarus S, Davies J (1993) The influence of helicity on numerically simulated convective storms. Mon Weather Rev 121:2005–2029

Ferrier B, Lin Y, Black T, Rogers E, DiMego G (2002) Implementation of a new grid-scale cloud and precipitation scheme in the NCEP Eta model. Preprints, 15th conference on numerical weather prediction, American Meteorological Society, San Antonio, TX, pp 280–283

Fujita T (1973) Tornadoes around the world. Weatherwise 26:56–83

Gayà M, Homar V, Romero R, Ramis C (2000) Tornadoes and waterspouts in the Balearic Islands: phenomena and environment characterization. Atmos Res 56:253–267

Giaiotti D, Giovannoni M, Pucillo A, Stel F (2007) The climatology of tornadoes and waterspouts in Italy. Atmos Res 83:534–541. doi:10.1016/j.atmosres.2005.10.020

Holzer A (2001) Tornado climatology of Austria. Atmos Res 56:203–211

Janjic Z (1994) The step-mountain eta coordinate model: further development of the convection, viscous sublayer and turbulence closure schemes. Mon Weather Rev 122:927–945

Janjic Z (2002) Nonsingular implementation of the Mellor-Yamada level 2.5 scheme in the NCEP Meso model. NCEP Office Note 437:61

Johns R, Davies J, Leftwich P (1993) Some wind and instability parameters associated with strong and violent tornadoes. Part II: variations in the combinations of wind and instability parameters. The tornado: its structure, dynamics, prediction and hazards. Geophys Monogr 79:583–590

Matsangouras I, Nastos P (2010) The 27 July 2002 tornado event in Athens, Greece. Adv Sci Res 4:9–13. doi:10.5194/asr-4-9-2010

Matsangouras I, Nastos P, Nikolakis D (2010) Study of meteorological conditions related to the tornado activity on 25-3-2009 over NW Peloponnesus, Greece. In: Proceedings of 10th international conference on meteorology, climatology and atmospheric physics (COMECAP), Patra, pp 417–425 (in Greek), 25–38 May 2010

Matsangouras I, Nastos P, Pytharoulis I (2011a) Synoptic-mesoscale analysis and numerical modeling of a tornado event on 12 February 2010 in northern Greece. Adv Sci Res 6:187–194. doi:10.5194/asr-6-187-2011

Matsangouras I, Nastos P, Sioutas M (2011b) 300 years historical records of tornadoes waterspouts and funnel clouds over Greece. In: Proceedings of 6th European conference on severe storms (ECSS), Palma de Mallorca, Spain, 3–7 October 2011

Meaden G (1976) Tornadoes in Britain: their intensities and distribution in space and time. J Meteorol 1:242–251

Mlawer E, Taubman S, Brown P, Iacono M, Clough S (1997) Radiative transfer for inhomogeneous atmospheres: RRTM, a validated correlated-k model for the longwave. J Geophys Res 102:16663–16682. doi:10.1029/97JD00237

Monin A, Obukhov A (1954) Basic laws of turbulent mixing in the groundlayer of the atmosphere. Trans Geophys Inst Akad Nauk USSR 151:163–187

Nastos P, Matsangouras I (2010) Tornado activity in Greece within the 20th century. Adv Geosci 26:49–51. doi:10.5194/adgeo-26-49-2010

Rasmussen E, Blanchard D (1998) A baseline climatology of sounding-derived supercell and tornado forecast parameters. Weather Forecast 13:1148–1164

Reynolds D (1999) European tornado climatology, 1960–1989. J Meteorol 24:376–403

Shafer C, Mercer A, Doswell C III, Richman M, Leslie L (2009) Evaluation of WRF forecasts of tornadic and nontornadic outbreaks when initialized with synoptic-scale input. Mon Weather Rev 137:1250–1271. doi:10.1175/2008MWR2597.1

Sioutas M (2011) A tornado and waterspout climatology for Greece. Atmos Res 100:344–356

Skamarock W, Klemp J, Dudhia J et al (2008) A description of the advanced research WRF version 3. National Center for Atmospheric Research MMM Division, Boulder

Thompson R, Edwards R, Hart J, Elmore K, Markowski P (2003) Close proximity soundings with supercell environments obtained from the Rapid Update Cycle. Weather Forecast 18:1243–1261. doi:10.1175/1520-0434(2003) 018<1243:CPSWSE>2.0.CO;2

Wang W, Bruyere C, Duda M, Dudhia J, Gill D, Lin H, Michalakes J, Rizvi S, Zhang X, Beezley J, Coen J, Mandel J (2010) ARW version 3 modeling system user's guide. National Center for Atmospheric Research MMM Division, Boulder

Biometeorological Conditions in the Urban Park of Nea Smirni in the Greater Region of Athens, Greece During Summer

A. Matsoukis, A. Kamoutsis, A. Bollas, and A. Chronopoulou-Sereli

Abstract The aim of this study was to investigate the biometeorological environment in relation with different types of ground cover in the urban park area of Nea Smirni in the greater region of Athens in Greece. Five sites were selected, including irrigated (IPS) and non irrigated plant species (NIPS) and the adjacent build-up area (ABA). The thermal condition of the environment around the examined sites was evaluated using an infrared thermografic camera in the summer of the years 2009–2011. Also, data loggers with temperature and humidity sensors were placed in the aforementioned sites during the experimental period. Results showed that the environment of NIPS appeared, in general, to have a warmer trees foliage in relation to IPS by about 2°C. Higher surface temperature conditions were detected in sites covered with structural materials. On the other hand, lower temperature conditions were observed in the shaded sites and in the water surfaces. For the period between 11:00 and 19:00 h, more favorable human thermal comfort conditions among the examined types of ground cover, as were evaluated by the thermohygrometric index, were observed at the environment with IPS, especially in July, rendering the aforementioned environment more friendly to the visitors.

1 Introduction

Local climate in big cities has been changed in many cases due mainly to urbanization effect. This status has a negative impact on the quality of human life and particularly on the public health at the warm season of the year (Clarke and Bach 1971), e.g. the case of Athens in Greece where people must defend themselves against heat stress in the summer months July and August (Matsoukis et al. 2009).

A. Matsoukis (✉) • A. Kamoutsis • A. Bollas • A. Chronopoulou-Sereli
Laboratory of General and Agricultural Meteorology, Department of General Sciences, Agricultural University of Athens, Athens 118 55, Greece
e-mail: armatsoukis@aua.gr

C.G. Helmis and P.T. Nastos (eds.), *Advances in Meteorology, Climatology and Atmospheric Physics*, Springer Atmospheric Sciences,
DOI 10.1007/978-3-642-29172-2_31,

Human life quality is closely associated with human thermal comfort which is defined as the condition of mind that expresses satisfaction with the thermal environment, absence of thermal discomfort or conditions in which 80% or 90% of humans do not express dissatisfaction (Yilmaz et al. 2007). One easily and widely applied index for the evaluation of human thermal comfort conditions, that is to say biometeorological conditions, is the thermohygrometric index (THI). According to its categories, the optimum comfort occurs between THI values of 15.0°C and 19.9°C (Toy et al. 2007).

It has long been recognized that parks contribute, in a high degree, noticeable benefits to the physical and aesthetic quality of urban neighborhoods (Walker 2004). Also, large urban parks, e.g. the National Garden in Athens, under certain circumstances, exhibit favorable biometeorological conditions inside them and partially in their nearby area (Chronopoulou-Sereli and Chronopoulos 2011) and therefore, improve human life quality.

Nea Smirni (NS) is a municipality located at the Athens basin, with one of the highest population densities in Greece according to the census of 2011 (Greek Statistical Authority 2011). There is an urban park in the center of NS, recently renovated, which accepts many visitors throughout the year and its importance is particular. Taking this into account, purpose of this study is the evaluation of biometeorological conditions of the aforementioned park.

2 Materials and Methods

2.1 Study Region and Measurement Sites

This study was carried out at the urban park of NS which occupies an area of approximately 5 ha. For the study of the biometeorological conditions of NS park, five sites, each one of western orientation, were selected. These sites were placed in three sets and each set represented a different type of ground cover for the whole studied place. Thus, the first set comprised the sites s1 (37° 57′ 01.6″ N, 23° 42′ 57.2 E) and s2 (37° 57′ 00.9″ N, 23° 43′ 01.3 E) which were surrounded by irrigated plant species (IPS), the second set comprised s3 (37° 57′ 04.8″ N, 23° 43′ 00.6 E) and s4 (37° 57′ 03.0″ N, 23° 42′ 55.9 E), surrounded by non irrigated plant species (NIPS) and the third set comprised the site s5 (37° 57′ 00.4″ N, 23° 42′ 50.4 E) in the adjacent build-up area (ABA).

2.2 Analysis of Thermal and Meteorological Data

The thermal condition of the environment around each study site, with regard to surface temperature, was visualized with the aid of a high sensitive infrared radiometric camera (Thermo tracer model TH9100MR/WR, Japan, operation air

temperature from −15°C to 50°C, relative humidity 90% or less, not condensed) in the summer (1 June–31 August) of the years 2009–2011 and for the period between 14:00 and 15:00 h, local standard time. The thermal images of the same visual images were similar for each study site among the examined years.

Also, air temperature and relative humidity were monitored simultaneously every 15 min by sensors with dataloggers (Hobo type Pro, H08-032-08, USA, accuracy ±0.2°C at 25°C and ±3% relative humidity over 0–50°C), one for each site, for the experimental period.

For air temperature and relative humidity data, means on hourly basis were calculated for each study site, separately for each examined month. These means were used for the calculation of the average hourly values of THI. The average THI value of each set of the examined sites, as mentioned above, was calculated from the average THI values of its individual sites. Average THI values of the sets were used for the evaluation of human thermal comfort category (Toy et al. 2007).

In this paper, results for the month July, which is characterized by 'extreme' temperature conditions (heat stress) in the examined area and for the period between 6:00 and 23:00 h, local standard time (visiting hours for the NS urban park) are presented. Statistics was performed using MS Excel and SPSS 11.0.

3 Results

The thermal images of the examined environments of the NS park area in combination with their respective visual images revealed a diversity of temperature conditions. In the case of IPS (Fig. 1 upper left, right), it is obvious that the water surface of the artificial pool in this environment, presented lower temperature values compared to trees foliage while the vertical stone-structure surface of the pool wall exhibited the highest temperature values as did the non-shaded parts of the trees trunks.

The situation in the case of the NIPS (Fig. 1 middle left, right) was different in relation to IPS regarding the trees foliage. Non irrigated plant species appeared, in general, to have a warmer trees foliage in relation to IPS by about 2°C. The shaded parts of the trees trunks in NIPS were cooler than the respective non-shaded parts, as in the case of irrigated plant species. Also, the temperature of the ground surface in the environment of NIPS reached the value of 64.4°C, which was the maximum temperature value in all examined area, attributed to direct effect of solar radiation.

The adjacent build-up area (Fig. 1 lower left, right) was appeared, in general, warmer in greater extension, than the environments of IPS and NIPS because of the large presence of the structural materials. Thus, the asphalt road along with the non-shaded parked cars appeared temperatures between 51.4°C and 54.4°C. The existed plants of ABA appeared lower temperature values than the aforementioned temperature values, reaching 42.4°C in their non shaded parts.

The relative frequencies of classes of hourly THI values for the presented period and for the three sets of the examined sites for the urban park of NS are shown in Fig. 2. Totally, two classes of THI values, the 'Hot' and 'Very Hot', were detected.

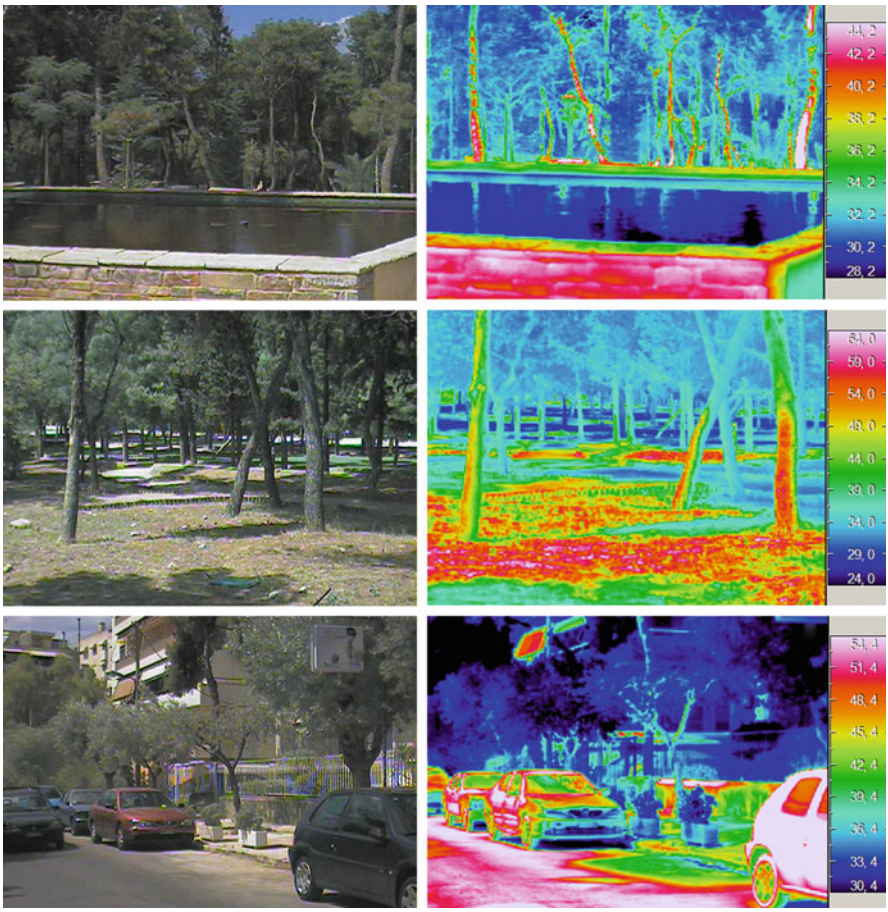

Fig. 1 Visual and respective thermal images of the environment with irrigated plant species (*upper left, right*), of the environment with non irrigated plant species (*middle left, right*) and of the adjacent build-up area (*lower left, right*) of the urban park of Nea Smyrni, Greece in 1 July 2011 from 14:00 until 15:00 h, local standard time

At all the examined environments, the whole percentage of THI values (100%) occupied the 'Hot' class from 6:00 until 9:00 h and from 22:00 until 23:00 h. Therefore, these environments did not differ, biometeorologically, according to THI classes, at both aforementioned periods.

As regards to the IPS (Fig. 2a), the 'Very Hot' class made its appearance at 11:00 h with a small percentage of THI values which progressively increased, reaching its maximum values (45.2%) at both 13:00 and 15:00 h and therefore, the majority of THI values was classified as 'Hot' with noticeable percentages for the time period between 11:00 and 20:00 h.

At the environment with NIPS (Fig. 2b), a considerable percentage of THI values was lying in the 'Very Hot' class at 11:00 and 18:00 h (35.5% and 41.9%, respectively) while in the hours between the aforementioned ones, THI values were

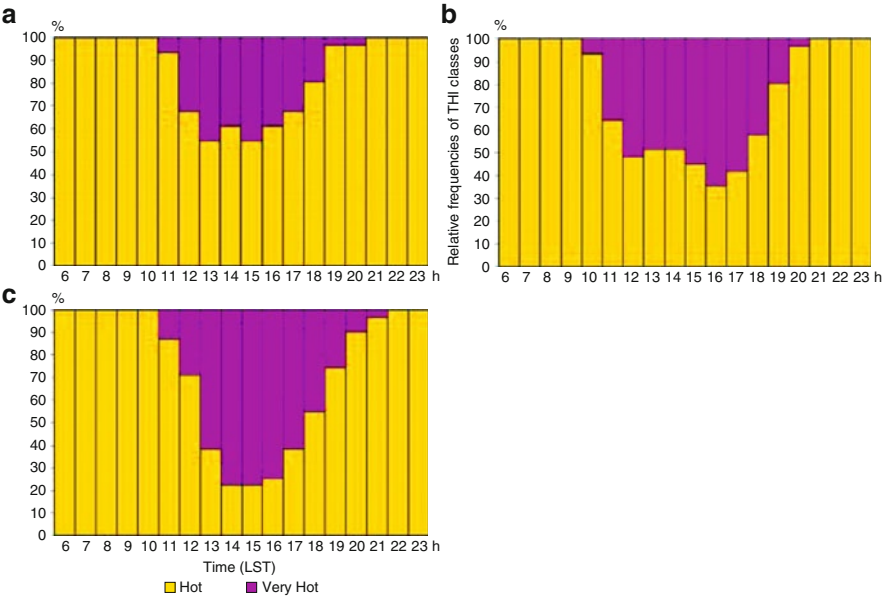

Fig. 2 Relative frequencies of different categories of thermohygrometric index (THI) values on hourly basis in the environment with irrigated plant species (**a**), in the environment with non irrigated plant species (**b**) and in the adjacent built-up area (**c**) of the urban park of Nea Smyrni, Greece during July 2009–2011 (LST: Local Standard Time = Greenwich Meridian Time + 2 h)

classed as 'Very Hot' in percentages ranged from 48.4% up to 64.5%. It is clear that for the period between 11:00 and 19:00 h, IPS presented better biometeorological conditions in relation to NIPS because of the occurrence of the 'Very Hot' class in smaller percentages in IPS compared to NIPS, for the same time period.

In the case of ABA, the 'Very Hot' class percentage progressively increased from 11:00 h, reaching a maximum value at both 14:00 and 15:00 h (77.4%), while decreasing afterwards until 21:00 h. In this environment, for the period between 13:00 and 17:00 h, the majority of THI values belonged to the aforementioned class. For the period between 10:00 and 21:00 h where the THI values lied in both 'Hot' and 'Very Hot' classes, for at least one examined environment, ABA was characterized by more disadvantageous biometeorological conditions than IPS and NIPS, because, in general, the 'Very Hot' class occupied considerably higher percentages in ABA in relation to the examined environments inside the park.

4 Conclusions

The thermal analysis with the infrared radiometric camera for the park area of NS in the hotter month of the year (July) revealed that NIPS appeared, in general, to have a warmer trees foliage in relation to IPS by about 2°C. Higher temperature

conditions were detected in sites covered with structural materials and in sites which were affected by the direct solar radiation. On the other hand, lower temperature conditions were observed in the shaded sites and in the water surfaces.

As for the biometeorological conditions of the examined area during the experimental period and especially in July, determined by the classes percentages of THI values, we can conclude that the examined environments of the NS park area did not differ biometeorologically from 6:00 until 9:00 h and from 22:00 until 23:00 h. For the rest period (10:00–21:00 h), ABA was characterized, in general, by more disadvantageous biometeorological conditions than IPS and NIPS. The environment of IPS presented better biometeorological conditions in relation to NIPS for the period between 11:00 and 19:00 h, and thus, the IPS environment was more friendly to the visitors for the aforementioned period.

Acknowledgments Thanks are due to Mr. M. Pagonis, Technical Assistant of the Laboratory of General and Agricultural Meteorology, Agricultural University of Athens for his help with the graphs.

References

Chronopoulou-Sereli A, Chronopoulos I (2011) Biometeorology-bioclimatology, applications to the configuration of outdoor spaces. Ziti Publications, Thessaloniki (in Greek)

Clarke JF, Bach W (1971) Comparison of the comfort conditions in different urban and suburban microenvironments. Int J Biometeorol 15:1–54. doi:10.1007/BF01804717

Greek Statistical Authority (2011) Press bulletin, Announcement of temporary results of population census 2011, Greek democracy. http://www.tovima.gr/files/1/2011/07/22/apografh 22.pdf. Accessed 14 Dec 2011

Matsoukis A, Kamoutsis A, Chronopoulou-Sereli A (2009) Air temperature and thermal comfort conditions in mountainous and urban regions. Int J Sustain Dev Plan 4:357–363. doi:10.2495/SDP-V4-N4-357-363

Toy S, Yilmaz S, Yilmaz H (2007) Determination of bioclimatic comfort in three different land uses in the city of Erzurum, Turkey. Build Environ 42:1315–1318. doi:10.1016/j.buildenv.2005.10.031

Walker C (2004) The public value of urban parks. Beyond recreation, a broader view of urban parks. The Urban Institute, The Wallace Foundation. http://www.urban.org/Uploaded PDF/311011_urban_parks.pdf. Accessed 14 Dec 2011

Yilmaz S, Toy S, Yilmaz H (2007) Human thermal comfort over three different land surfaces during summer in the city of Erzurum, Turkey. Atmósfera 20:289–297

Forest Fire Indices in Greece During the Forest Fire Events of Summer 2007

A. Mavrakis, A. Agelakis, and G. Theoharatos

Abstract During the summer of 2007 the entire Greek territory was subject to a great number of forest fires, which caused many casualties. The purpose of this paper is to investigate the levels of two prognostic forest fire risk indices, the Angstrom index and the Nesterov index. We used hourly data from five surface stations of the Hellenic National Meteorological Service, obtained from the website of the University of Wyoming, as well as upper level NCEP/NCAR data, for the period June 1st to August 31st, 2007. The analysis showed that both indices reached values indicating a high probability of fire occurrence during the entire examined period. In addition by the end of August the level of the Nesterov index was 18 times higher than the respective threshold limits. Finally, the deviation of certain upper atmospheric parameters from their average values was also examined.

1 Introduction

During the summer of 2007 the entire Greek territory was threatened by huge forest fires, which caused many casualties (Lazaridis et al. 2008; Miliaresis 2008). The purpose of this paper is to investigate the levels of two prognostic forest fire risk indices, the Nesterov index and the Angstrom index (Mantzavelas et al. 2006). As reference events we choose the 12 most serious forest fires (European Environment Agency 2007) and Center for Satellite Based Crisis Information (ZKI 2007), presented in Table 1.

A. Mavrakis (✉)
Institute of Urban Environment and Human Resources, Department of Economic and Regional Development, Panteion University, 136 Syngrou Av., 176 71 Athens, Greece
e-mail: mavrakisan@yahoo.gr

A. Agelakis • G. Theoharatos
Department of Environmental Physics and Meteorology, University of Athens, University Campus, Athens, Greece

C.G. Helmis and P.T. Nastos (eds.), *Advances in Meteorology, Climatology and Atmospheric Physics*, Springer Atmospheric Sciences,
DOI 10.1007/978-3-642-29172-2_32,

Table 1 Forest fire's reference events for summer 2007 in Greece

Forest fires location	Beginning (LST – date)	Duration (days)	Burnt area (acres)
1. Parnitha mount/mountain	19:30 – 27/06/2007	3	5,045
2. Ymytos mount/mountain	14:50 – 16/07/2007	<1	41
3.1 Akrokorinthos, Korinthos perfecture	16:00 – 17/07/2007	<1	1,605
3.2 Chiliomodi, Korinthos perfecture	14:30 – 18/07/2007	2	
4. Aegion, Achaia perfecture	21:30 – 23/07/2007	5	14,306
5. Penteli mount/mountain	10:30 – 16/08/2007	<1	950
6. Megalopoli, Arcadia perfecture	12:20 – 24/08/2007	3	44,841
10. Doriza, Arcadia perfecture	23:00 – 24/08/2007	6	43,328
7. Andritsaina, Ileia perfecture	14:30 – 24/08/2007	5	1,144,744
8. Palaiochori, Ileia perfecture	14:35 – 24/08/2007	9	
9. Valmis, Ileia perfecture	17:30 – 24/08/2007	6	
11. Klindias Oleni, Ileia perfecture	01:00 – 25/08/2007	7	

For the last four fire events, the total burn area is given. There is also a missing value for 3.2

2 Data and Methodology

2.1 Data

For the calculation of Nesterov and Angstrom indices the daily values of air temperature, relative humidity dew point and precipitation were used. Five stations of the Hellenic National Meteorological Service, namely Thessaloniki, Corfu, Helliniko, Kalamata and Heraklion were selected. The data were obtained from the website of the University of Wyoming (http://weather.uwyo.edu/). Upper level reanalysis data were also used and adopted from the NCEP/NCAR for the period from June 1 to August 31/1st June to 31st August 2007.

2.2 Methodology

The calculation of Nesterov index is based on the following formula:

$$N = \sum_{i=1}^{w} (t_i - D_i) \times t_i$$

where N is the Nesterov index, w the number of days since last rainfall >3 mm, t_i the mid-day temperature (°C), and Di the dew point temperature (°C). The Sum is calculated for positive temperatures for a sequence of days with precipitation less

Table 2 Categories for Nesterov and Angstrom indices

A	Nesterov index	Fire danger	B	Angstrom index	Fire occurrence
	0–300	Zero		$I > 4.0$	Unlikely
	301–1,000	Low		$4.0 > I > 2.5$	Unfavorable
	1,001–4,000	Medium		$2.5 > I > 2.0$	Favorable
	4,001–10,000	High		$I < 2.0$	Very favorable
	>10,000	Extreme			

than 3 mm. Rainfall above 3 mm resets the index N to zero. It is a cumulative index and reflects drying potential for fuels. High values of the index indicate long periods without rain. The values of Nesterov index and their correspondence to fire hazard are shown in Table 2A.

The index Angstrom (I) is calculated by the formula

$$I = \left(\frac{R}{20}\right) + \left(\frac{27 - T}{10}\right)$$

where R is relative humidity and T is the air temperature °C. The values of I correspond to a fire hazard as shown in Table 2B.

Then we examine the deviation of monthly values of Air Temperature and the Geodynamic Height, from the normal climatic values. Figure 1 were derived from reanalysis data and were adopted from the interactive plots provided by the NOAA/NCEP online at http://www.esrl.noaa.gov/psd/cgi-bin/data/composites/ and refer to 500 hPa geopotential height anomaly and to 1,000 hPa air temperature anomaly.

3 Results

Figure 2a shows the results for Nesterov index. In all cases that the large forest fires of 2007 were observed and for the data of the five representative stations, the Nesterov index indicated "extreme fire danger" and the values were up to the lower limit of this zone. The only exceptions were observed at the station of Thessaloniki for the fire event of 28th August, 2007.

Excluding again the station of Thessaloniki, the Nesterov index as calculated for the remaining stations indicates "extreme fire danger" from 22/06/2007 until 31/08/2007. The exception was on 01/08/2007 for the station of Heraklion, where the value of Nesterov index is zero, (i.e. the station is under "zero risk of fire") to soar the next day 02/08/2007 to the value of 5,476.1, (i.e. after a short period of time, the station is under extreme fire risk). The station of Thessaloniki does not coincide with the remaining stations.

The maximum value of the Nesterov index regarding all the stations was estimated in the summer of 2007 in Kalamata on 24/08/2007. On the same day wildfires broke out in neighboring areas with tragic consequences for our country.

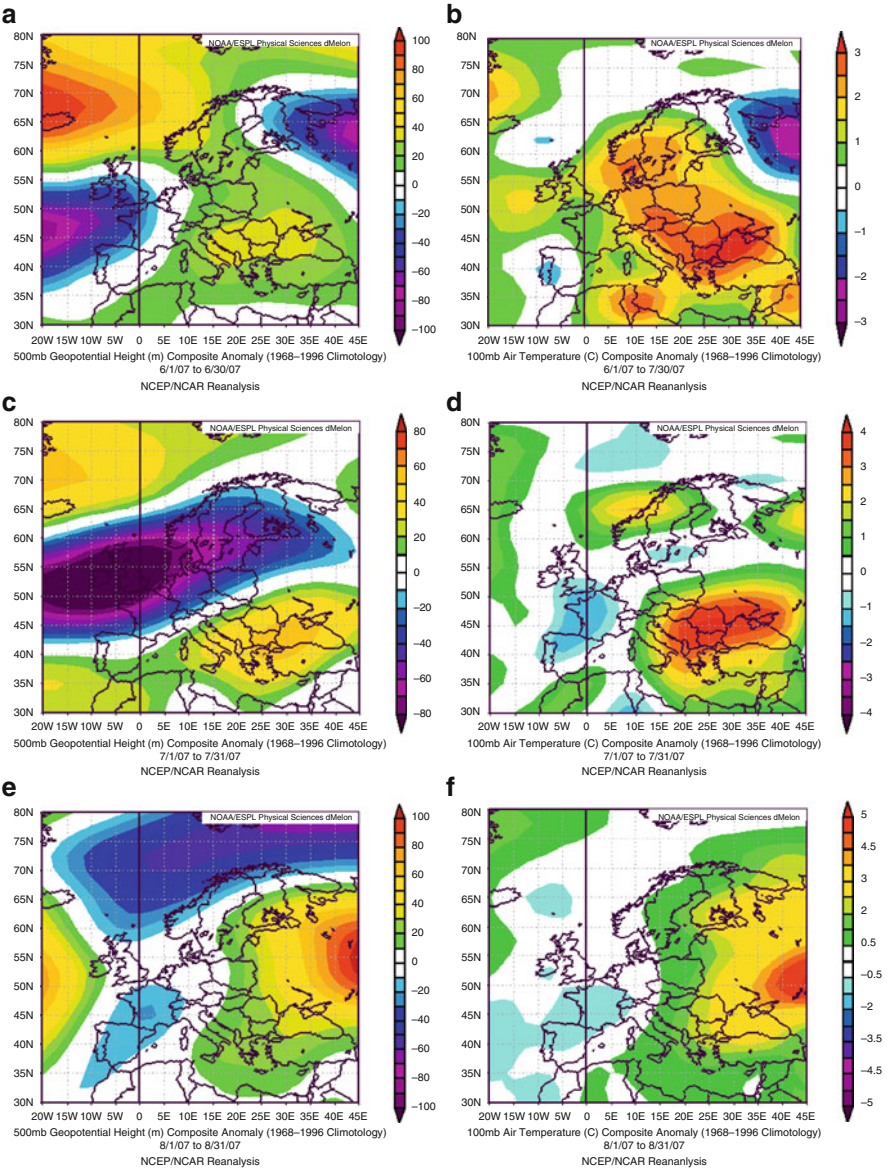

Fig. 1 *Left panels*: geopotential height anomalies for June (**a**), July (**c**) and August (**e**). *Right panels*: air temperature anomalies for June (**b**), July (**d**) and August (**f**)

In other stations, the maximum summer, and thus annual, Nesterov index value recorded 1–3 days before or after the onset of a forest fire.

The figure including all graphs of Nesterov index we notice that – with the exception of station of Thessaloniki – followed a similar course for the period from

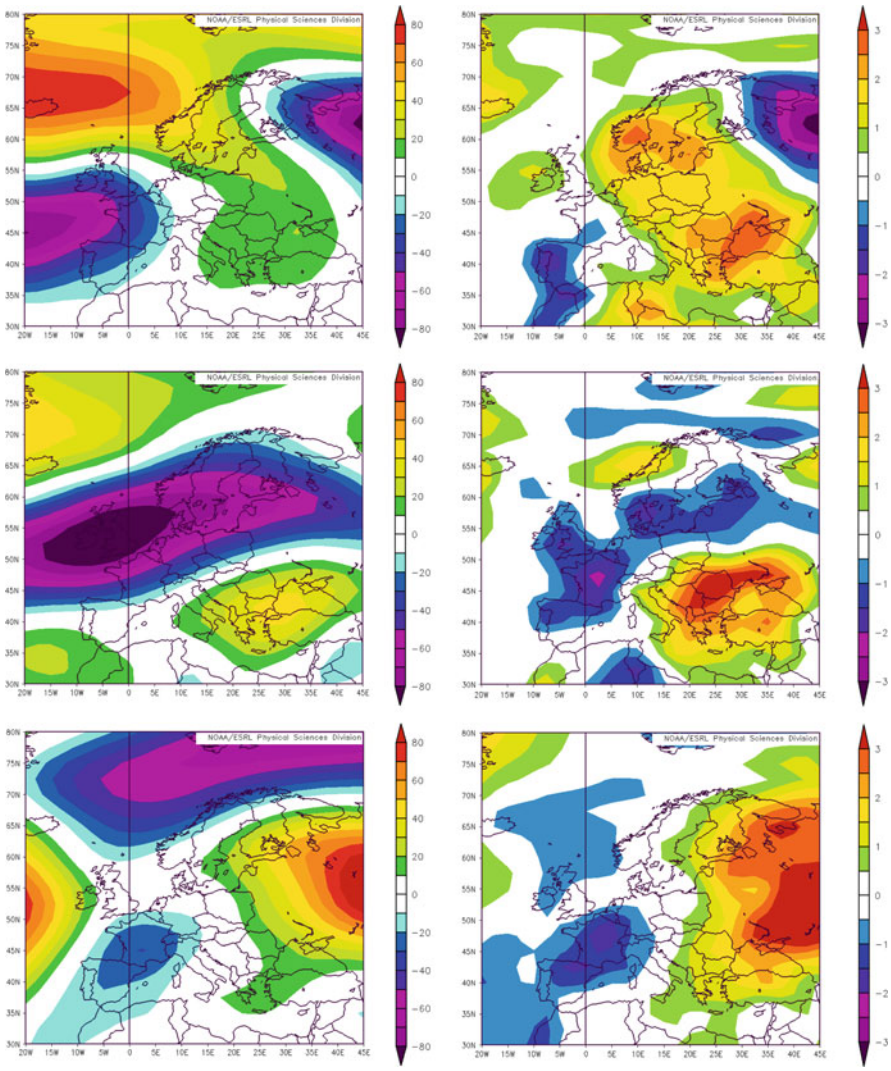

Fig. 2 (**a**) Nesterov fire index, (**b**) Angstrom fire index for summer 2007 in Greece

5/08/2007 to 20/08/2007. We also observe that for the stations Kalamata and Hellinikon the course of the index is similar.

Figure 2b shows the results for the Angstrom index. On 09–10/06/2007, from 15/06/2007 until 31/08/2007 (except 02/08/2007) and from 06/08/2007 to 08/08/2007 the calculated values for the Angstrom index indicate "Very Favorable" or "Favorable" conditions for fire.

In four of the five cases Angstrom index I located in Zone "Very Favorable". In the case of 28/08/2007 the Angstrom's index area "Favorable", located very near the area

"Very Favorable". It should be noted that in all cases of the forest fires during the period of study was preceded by a period of time (2 days) with very high temperatures, very low humidity and intense winds. Those conditions contribute to the start and the expansion of forest fires of 2007, resulting in tragic consequences for Greece.

According to the above chart we can see that when the pointer is in Angstrom bands "Unlikely" and "Not Favorable" there is no records of wildfire. In the case of forest fires in the summer of 2007, the Angstrom index is in the danger zones "Favorable" and "Very Favorable". Therefore, we can conclude that the Angstrom index is a very good predictor of the risk of a forest fire.

The maximum value of the index Nesterov for all stations in the summer of 2007 was recorded in Kalamata on 24/08/2007. On the same day an outbreak of wildfires in neighboring areas was recorded with tragic results for our country. In other stations, the maximum summer values for Nesterov index value recorded 1–3 days before or after starting a forest fire.

Then for the months of June, July and August, we examine the variations of monthly values of Air Temperature Anomaly at 1,000 hPa and the Geopotential Height Anomaly at 500 hPa, from the normal climatic values.

The results confirm the prevalence of conditions with significant positive deviation from the corresponding climatic values. Those conditions were favorable the entry of large forest fires and contributed to the difficulty of extinguishing them.

4 Conclusions

The wild forest fires of summer 2007 in Greece which caused extreme disasters and human casualties were an exceptional event for the country.

The outbreaks of these events were estimated using two forest fire indices, Nesterov and Angstrom. Both indices show that the meteorological conditions were very favorable for forest fires outbreak. The Nesterov index during late summer was calculated to be above the extreme limits level 18 times. The same is true for Angstrom index as well.

The results confirm the prevalence of conditions with significant positive deviation from the corresponding climatic values. Those conditions favored the outbreak of large forest fires and contributed to the difficulty of controlling them.

References

Center for Satellite Based Crisis Information (ZKI) (2007) Website http://www.zki.dlr.de/article/857

European Environment Agency (2007) Website http://www.eea.europa.eu/data-and-maps/figures/number-of-forest-fires-and-burnt-area-in-the-eu-mediterranean-countries

Lazaridis M, Latos M, Aleksandropoulou V, Hov Ø, Papayannis A, Tørseth K (2008) Contribution of forest fire emissions to atmospheric pollution in Greece. Air Qual Atmos Health 1:143–158. doi:10.1007/s11869-008-0020-0

Mantzavelas A, Apostolopoulou I, Lazaridou T, Partozis T, Topaloudis T, Lampin C, Borgniet L, Bouillon C, Brewer S, Curt T, Ganteaume A, Jappiot M, Defossé G, Gómez Fernán M, Lencinas DJ (2006) Project title FIRE PARADOX: an innovative approach of integrated wildland fire management regulating the wildfire problem by the wise use of fire: solving the fire paradox. Project no. FP6-01850

Miliaresis GC (2008) Monitoring/impact of wild fires of the August 2007 in the mountain region of Ilia prefecture (Western Greece) from web spatial (no cost) GIS databases. Geographic Information and Earth Observation for the Sustainable Development, ICIMOD, 14–25 Jan 2008

Satellite Based Estimation of Urban Surface Emissivity with the Use of Sub-Pixel Classification Techniques

Z. Mitraka and N. Chrysoulakis

Abstract Information about the spatial distribution of urban surface emissivity is essential for surface temperature estimation which is an important component of urban microclimate and it is critical in many applications, like turbulent sensible and latent heat fluxes estimation, energy budget, urban canopy modeling, bioclimatic studies and urban planning. The proposed method presents an improvement in emissivity estimation as compared with existing methods, such as the look-up table approach, wherein emissivity and other biophysical parameters are assigned to grid cells based on land cover types. The basic premise of this method is a sub-pixel classification of urban surface into vegetation, impervious and soil, based on spectral mixture analysis. The proposed approach was applied to Landsat-7 ETM + observations over the area of Athens, Greece. Spatial distributions of surface emissivity, as well as land surface temperature in the spectral region of 10.4–12.5 μm were derived. ASTER (Advanced Spectral Reflection and Emission Radiometer) emissivity and surface temperature products were used for evaluation.

Z. Mitraka (✉)
Foundation for Research and Technology – Hellas, Institute of Applied and Computational Mathematics, N. Plastira 100, Vassilika Vouton, 70013 Heraklion, Greece

European Space Agency, Directorate of Earth Observation Programmes, ESA/ESRIN, Via Galileo Galilei, Casella Postale 64, 00044 Frascati, Italy
e-mail: mitraka@iacm.forth.gr

N. Chrysoulakis
Foundation for Research and Technology – Hellas, Institute of Applied and Computational Mathematics, N. Plastira 100, Vassilika Vouton, 70013 Heraklion, Greece

C.G. Helmis and P.T. Nastos (eds.), *Advances in Meteorology, Climatology and Atmospheric Physics*, Springer Atmospheric Sciences,
DOI 10.1007/978-3-642-29172-2_33,

1 Introduction

The knowledge of urban energy budget characteristics and surface temperatures is essential to a range of topics in earth sciences, including urban climatology (Voogt and Oke 2003), global environmental change, human–environment interactions and planning and management practices (Chrysoulakis et al. 2009). The energy budget of the urban surface is mainly defined by its albedo and Land Surface Temperature (LST), both of which can be derived from satellite observations (Chrysoulakis 2003). To retrieve LST from satellite observations, the angular, atmospheric and emissivity effects have to be considered and corrected. LST errors increase almost linearly, and may reach 6 K in absolute magnitude for fairly small errors in emissivity (Yu et al. 2008).

Emissivity is a measure of the inherent efficiency of the surface to convert heat energy into radiant energy. Satellite-based emissivity estimates depend largely on the composition, roughness and other physical parameters of the surface, such as its moisture content. There are several issues to be dealt when measuring emissivity from satellite observations. The main problem in determining emissivity from satellite data is the observation of emissivity of land surfaces at satellite spectral and spatial resolution (Mitraka et al. 2011). The dimension of ground pixels in a satellite image is such that the characteristics of the surface may display substantial variation within a pixel. This scale mismatch also makes validation against "ground truth" difficult.

Dash et al. (2002) summarize different emissivity estimation techniques and analyzed their main constraints. ASTER higher level emissivity and LST products are derived using the Temperature Emissivity Separation method (TES) (Gillespie et al. 1998). TES products have been validated and were found to perform within the specification of ± 0.015 for emissivity and ± 1.5 K for LST.

Mapping the urban environment in terms of its physical components preserves the heterogeneity of urban land cover better than traditional land-use classification, characterizes urban land cover independent from analyst-imposed definitions and captures accurately changes through time. The Vegetation–Impervious–Soil (VIS) model (Ridd 1995) considers the combination of impervious surfaces, green vegetation, and exposed soil as the fundamental components of urban ecosystems if water surfaces are ignored.

In this study, a methodology for land surface emissivity estimation using Landsat satellite imagery is proposed. The urban land cover is modeled using a variant of VIS model (Ridd 1995) and the sub-pixel components of land cover are mapped using Spectral Mixture Analysis (SMA). Assuming that land surface emissivity can be expressed as a linear combination of the emissivities of all components inside a pixel, the spatial distribution of emissivity is derived from visible and near infrared satellite observations.

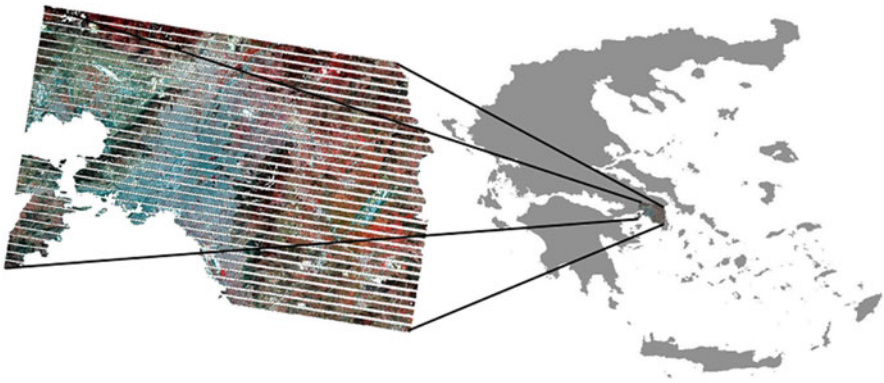

Fig. 1 The study area – the broader area of the city of Athens, Greece

2 Data and Methodology

2.1 Study Area and Data

The study area covers the broader area of Athens, Greece (Fig. 1). A Landsat-7 ETM + terrain corrected image (Level 1T) acquired on July 2, 2004 (acquisition time 08:54:08 UTC) under clear weather conditions, was used in this study (Fig. 1). Landsat-7 ETM + imagery contains six visible, near infrared and shortwave infrared (VNIR, SWIR) bands, one thermal infrared (TIR) band and one panchromatic band of spatial resolution 30 m × 30 m, 60 m × 60 m and 15 m × 15 m respectively. Landsat-7 ETM + presented a failed scan line corrector in May 31, 2003, resulting in images that have high geometric and radiometric fidelity, but no data present for wedges of the image (Wuldera et al. 2011).

Advanced Spaceborne Thermal Emission and Reflection Radiometer (ASTER) emissivity and temperature products were used to evaluate the performance of the proposed method. ASTER imagery acquisition time was nearly concurrent to Landsat-7 ETM + (09:22:10).

2.2 Methodology

The fraction of each land cover component in the scene was computed using SMA, emissivity density functions were created for these components based on the ASTER Spectral Library Version 2.0 (Baldridge et al. 2009) and the combination of those were used to estimate the spatial distribution of surface emissivity.

A pre-processing of the available Landsat-7 ETM + image was necessary, before applying SMA. Digital numbers of VNIR and SWIR bands were converted to radiance values. Athens is a coastal city and thus water is an important

component of the scene. In this study it was treated separately, since dark pixels corresponding to sea water are highly degenerate and they cannot be modeled accurately using SMA (Mitraka et al. 2011). In addition, pixels corresponding to sensor failure were excluded from the analysis.

Linear Spectral Mixture Analysis (LSMA) (Mitraka et al. 2011) was used to analyze the mixed pixels of the urban environment. The underlying urban landscapes are assumed to be composed of a few fundamental components, called endmembers. The fractional cover of each urban component is estimated by solving a linear regression problem, using a least squares algorithm.

In this study, land cover was modeled using a variation of the VIS model (Ridd 1995). Vegetation component refers to green vegetation while the impervious component to manmade surfaces which vary widely in spectral response, so two main categories of impervious surface components were assumed: a high-albedo (bright impervious surfaces) and a low-albedo (dark impervious surfaces) component.

Each urban land cover component is assigned an endmember. The Pixel Purity Index (Mitraka et al. 2011) was used as a first step to identify spectrally pure pixels. Pixels regarded as possible endmembers were then visually inspected using the higher resolution Ikonos orthophotomap as reference.

Following, the fraction images derived using LSMA were combined with representative emissivity values for the urban land cover components to estimate urban surface emissivity. Specifically, a unique emissivity value ε for each pixel was obtained using $\varepsilon = \varepsilon_V \cdot f_V + \varepsilon_{HA}\, f_{HA} + \varepsilon_{LA} \cdot f_{LA} + \varepsilon_S \cdot f_S$, where ε_V, ε_{HA}, ε_{LA} and ε_S are the endmembers emissivities.

Spectra information of both natural and man-made materials included in the ASTER Spectral Library version 2.0 (Baldridge et al. 2009) was utilized to derive endmembers emissivity values. The mean value of green vegetation types (0.988) was considered representative of the vegetation component. Seven soil types were selected (Fig. 2a) as representative for the soil component of the study area with a mean emissivity value of 0.979. Ten bright and five dark construction materials (Fig. 2b) were selected for the high-albedo and low albedo components with mean emissivity values of 0.956 and 0.985 respectively.

The accuracy of the proposed method was assessed by comparing the estimated emissivity and LST maps to the ASTER emissivity high level products (Gillespie et al. 1998). Estimated maps using the proposed method were spatially averaged from 30 m × 30 m to 90 m × 90 m to match the ASTER high level products spatial resolution.

3 Results

The derived emissivity map in the 10.4–12.5 μm spectral window using the proposed method is shown in Fig. 3. The topography of the area is clearly outlined in the derived emissivity map. Low emissivity values (dark in Fig. 3) appear in the commercial and residential areas, whereas even lower values were estimated for

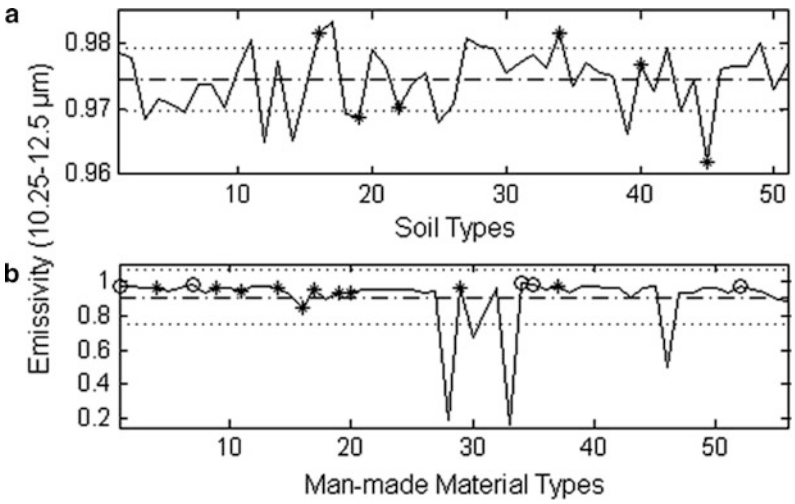

Fig. 2 Emissivities in 10.4–12.5 μm spectral window of (**a**) soil and (**b**) man-made materials types included in the ASTER Spectral Library. Marked values correspond to those that were selected ('*' used for the high-albedo and 'o' for low-albedo material types)

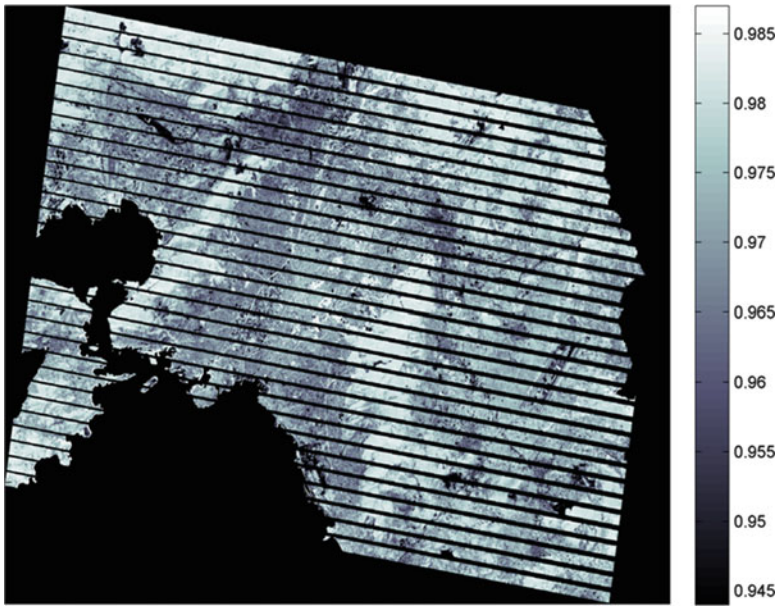

Fig. 3 Map of estimated emissivity values in the 10.4–12.5 μm spectral window produced for the study area using the proposed methodology

quarries included in the study area. In addition, high emissivity values (bright in Fig. 3) are observed in vegetated areas, which are mainly forested areas in the mountains of Imittos, Parnitha and Penteli, or crops in the eastern part.

Table 1 Error measurements for emissivity and LST differences between estimated and reference values from ASTER high level products

	Estimated emissivity versus ASTER emissivity product	Estimated LST versus ASTER LST product
MSE[a]	0.0036	2.1585
RMSE[a]	0.0605	1.1692
Bias[a]	0.0372	1.0390

[a] $MSE = mean(S_i - R_i)^2$, $RMSE = \sqrt{mean(S_i - R_i)^2}$, $Bias = mean(S_i - R_i)$

Table 1 presents measures of accuracy computed for estimated emissivity and LST versus the respective ASTER high level products. Low error measurements values indicate good agreement of estimated emissivity and LST compared to the respective ASTER high level products. A deviation of the magnitude of 0.06 in emissivity leads to more than 1 K deviation in LST.

4 Conclusions

In this paper, a methodology for deriving land surface emissivity over urban areas using Landsat-7 ETM + data based on spectral unmixing is presented. Visible and near infrared bands are utilized for spectral unmixing which enables direct derivation of emissivity maps from all Landsat satellites. In addition, since the proposed method is image-based it is considered suitable for time series derivation. Finally, a main advantage of the proposed approach is mixed pixel handling, which is essential for deriving biophysical parameters over urban areas using satellite imagery of this spatial resolution. The emissivity dependence on surface type and its physical conditions are taken into account in sub-pixel level.

References

Baldridge AM, Hook SJ, Grove CI, Rivera G (2009) The ASTER spectral library version 2.0. Remote Sens Environ 113:711–715. doi:10.1016/j.rse.2008.11.007

Chrysoulakis N (2003) Estimation of the all-wave urban surface radiation balance by use of ASTER multispectral imagery and in situ spatial data. J Geophys Res 108(D18):4582. doi:10.1029/2003JD003396

Chrysoulakis N, Vogt R, Young D, Grimmond CSB, Spano D, Marras S (2009) ICT for urban metabolism: the case of BRIDGE. In: Proceedings of EnviroInfo2009: environmental informatics and industrial environmental protection: concepts, methods and tools, Hochschule für Technik und Wirtschaft, Berlin, pp 183–193

Dash P, Gottsche FM, Olesen FS, Fischer H (2002) Land surface temperature and emissivity estimation from passive sensor data: theory and practice – current trends. Int J Remote Sens 23:2563–2594. doi:10.1080/01431160110115041

Gillespie A, Rokugawa S, Matsunaga T, Cothern JS, Hook S, Kahle AB (1998) A temperature and emissivity separation algorithm for advanced spaceborne thermal emission and reflection

radiometer (ASTER) images. IEEE Trans Geosci Remote Sens 36:1113–1126. doi:10.1109/36.700995

Mitraka Z, Chrysoulakis N, Kamarianakis N, Partsinevelos P, Tsouchlaraki A (2011) Improving the estimation of urban surface emissivity based on sub-pixel classification of high resolution satellite imagery. Remote Sens Environ 117:125–134. doi:10.1016/j.rse.2011.06.025

Ridd MK (1995) Exploring a V-I-S (vegetation-impervious surface-soil) model for urban ecosystem analysis through remote sensing: comparative anatomy for cities. Int J Remote Sens 16:2165–2185. doi:10.1080/01431169508954549

Voogt JA, Oke TR (2003) Thermal remote sensing of urban climates. Remote Sens Environ 86:370–384. doi:10.1016/S0034-4257(03)00079-8

Wuldera MA, Whitea JC, Masekb JG, Dwyerc J, Royd DP (2011) Continuity of Landsat observations: short term considerations. Remote Sens Environ 115(2):747–751. doi:10.1016/j.rse. 2010.11.002

Yu Y, Privette JL, Pinheiro AC (2008) Evaluation of split-window land surface temperature algorithms for generating climate data records. IEEE Trans Geosci Remote Sens 46:179–192. doi:10.1109/TGRS.2007.909097

Comparison of Actual Thermal Vote with Two Objective Human-Biometeorological Indices Values

K. Pantavou, E. Chatzi, and G. Theoharatos

Abstract In July 2010, a field study on the biometeorological conditions and human thermal comfort was carried out in Athens. The experiment was conducted during six different days in three different sites, Syntagma Square, Ermou Street and Flisvos coast. The collected data included measurements of meteorological parameters and subjective assessments of thermal sensation from morning to evening for each site. A mobile meteorological station collected data of air temperature, relative humidity, wind speed, total solar radiation, surface ground temperature and globe temperature while a group of five healthy and acclimatized subjects exposed to the environmental conditions completed every 30 min a questionnaire about their thermal sensation at the moment of measurement. Two biometeorological indices, Thermal Sensation (TS) and Heat Load (HL), were calculated in order to compare the indices values with the actual thermal vote of the five subjects. The analysis showed that TS underestimates the thermal sensation of the five subjects when their thermal vote is 'hot' or 'very hot' while TS overestimates the thermal sensation of the subjects when their thermal vote is 'neutral'. The HL index overestimates the thermal sensation of the subjects.

1 Introduction

The climate zone, the topography and orography are the main factors that define the thermal climate of an area. These background meteorological conditions can be modified when urbanization changes the characteristics of the land surface and atmosphere as it happens in cities, the phenomenon that is called urban heat island effect (Basara et al. 2010; Giannopoulou et al. 2011). Moreover there has been observed an increase in temperature (Philandras et al. 2008), changes in

K. Pantavou (✉) • E. Chatzi • G. Theoharatos
Department of Environmental Physics and Meteorology, University of Athens, Athens, Greece
e-mail: kpantav@phys.uoa.gr

C.G. Helmis and P.T. Nastos (eds.), *Advances in Meteorology, Climatology and Atmospheric Physics*, Springer Atmospheric Sciences,
DOI 10.1007/978-3-642-29172-2_34,

precipitation patterns (Philandras et al. 2010) and a greater number of extreme events over the last decades (Matzarakis and Nastos 2011). Most models predict that future climate change could include higher maximum temperatures and more hot days in nearly all land areas, more intense precipitation events over northern hemisphere, higher minimum temperatures and fewer cold days, reduced diurnal temperature range across most land areas, summer continental drying in some areas and associated drought risks (WMO).

The urban heat island effect combined with the climate change may lead to extreme thermal conditions in the cities, which affect many aspects of human life (Baccini et al. 2008; Theoharatos et al. 2010; Pantavou and Lykoudis 2011). A very important issue that requires a multi-disciplinary approach is human health. One approach is the use of a valid index to predict the possible human health effects by means of physiological stress.

The aim of this study was to evaluate two existing thermal indices designed for outdoor use when applied to predicting thermal sensation. A multi factor regression formula, expressing thermal sensation (TS) as a function of air temperature (Ta-°C), relative humidity (RH-%), wind speed (WS-m/s), solar radiation (SR-W/m^2) and surrounding ground temperature (ST-°C) was generated by an experimental research monitoring the thermal sensation and overall comfort of subjects staying outdoors in urban places. The experiment consisted of questionnaire surveys on the subjects' sensory responses and measurement of physical quantities (Givoni and Noguchi 2000; Givoni et al. 2003). The TS is the perception of heat or cold on a 7-point scale of 1–7 (1 very cold, 2 quite cold, 3 cold, 4 neutral, 5 hot, 6 quite hot, 7 very hot).

The calculation of HL index is based on MENEX model that assesses physiologically significant components of the heat exchange between man and environment (Blazejczyk 2001). According to MENEX the net heat storage is the sum of metabolic heat production (M), solar radiation absorbed by human body (R), evaporative heat loss (E), heat exchange by convection (C), heat exchange by long wave radiation (L) and respiratory heat loss (Res). The HL of an organism is calculated by the three principal heat fluxes: net heat storage (S), absorbed solar radiation (R) and evaporative heat loss (E) and expresses the warm and cold stress of the organism. The HL classifies the load of central thermoregulation system due to adaptation processes involved in an organism in order to be adjusted to the thermal environment in seven classes ranged from extreme cold stress (HL $\leq$ 0.25) to extreme hot stress (HL $\geq$ 1.751) (extreme cold stress, great cold stress, slight cold stress, thermoneutral, slight hot stress, great hot stress, extreme hot stress).

2 Data and Methodology

The data include meteorological measurements and subjective measurements of thermal sensation during six days of July 2010 in three sites of the greater area of Athens, Syntagma square, Ermou street and Flisvos coast. Five healthy volunteers,

three males and two females, were simultaneously exposed to the climatic conditions for 2 days for each site so as to include data from the morning to the evening. Syntagma square and Ermou street are the most central spots in the center of Athens surrounded by buildings and streets while Flisvos coast is an open space located south of the city of Athens.

2.1 Data

The environmental conditions were recorded using a mobile meteorological station around the subjects and at height 1.1 m above the ground, which it considers to be the average height of center of gravity of the body of an adult (Mayer and Hoppe 1987). The meteorological parameters, air temperature and relative humidity, ground temperature, wind speed and total solar radiation were measured per minute.

Each subject completed a questionnaire every 30 min throughout his or her exposure. The subjects were mainly standing with light activity, which corresponds, to a metabolic rate of 93 W/m^2 (ISO 7730 1994) and with clothing appropriate for the season, which corresponds to clothing insulation of 0.5 clo. The mean age, height and weight of the subjects were 31.4 years, 1.75 m and 72 kg respectively. The questionnaire contained a question on subjects' thermal sensation at the moment of the measurement based on the ISO seven-point thermal scale ranged from −3 to +3 (cold, cool, slightly cool, neutral, slightly warm, warm, hot) to which the participants gave ratings of their thermal sensation.

2.2 Methodology

The HL index was estimated using Bioklima software while TS was estimated by the formula:

$$TS = 1.7 + 0.1118 \cdot Ta + 0.0019 \cdot SR - 0.322 \cdot WS - 0.0073 \cdot RH + 0.0054 \cdot ST$$

TS and HL input values were the average of the recorded meteorological parameters of the first three minutes from the time of beginning completion of the questionnaire. The estimated time of completion of the questionnaire was at 3 min.

3 Results

The range of the environmental conditions is presented in Table 1. The maximum and minimum air temperatures, 37.46°C and 30.29°C respectively, were recorded at Flisvos coast as well as the mean maximum air temperature, which was estimated

Table 1 Mean environmental conditions over the measurement period

	Syntagma square				Ermou street				Flisvos coast			
	Morning		Evening		Morning		Evening		Morning		Evening	
	(10:20–13:25)		(16:48–19:33)		(10:53–14:05)		(16:48–19:33)		(11:35–13:20)		(16:48–19:33)	
	Mean	Range	Mean	Range	Mean	Range	Mean	Range	Mean	Range	Mean	Range
Ta (°C)	33.1	3.0	34.3	2.7	33.5	3.3	32.4	3.2	35.9	2.6	31.8	3.0
RH (%)	39.5	12.7	42.9	7.8	38.9	14.3	40.4	8.8	28.2	12.4	28.0	8.2
WS (m/s)	1.0	2.8	0.7	1.2	1.3	18.1	2.0	15.0	2.2	15.4	1.9	16.3
SR (W/m^2)	377.9	817.2	173.8	628.1	404.9	913.7	53.3	412.8	713.2	798.8	28.5	164.3

Table 2 Percentage of thermal sensation votes

Thermal vote	Percentage (%)	Percentage in males (%)	Percentage in females (%)
Cold	0.0	0.0	0.0
Cool	0.0	0.0	0.0
Slightly cool	0.0	0.0	0.0
Neutral	16.6	16.5	16.7
Slightly warm	38.3	9.6	9.0
Warm	35.8	38.3	38.5
Hot	35.8	35.7	35.9
Total	100.0	100.0	100.0

Table 3 Thermal sensation vote and TS and HL values crosstabulation

			Thermal sensation vote				
			Neutral	Slightly warm	Warm	Hot	Total
TS	Comfort	Percentage (%)	1.0	1.6	2.1	1.0	5.7
	Hot		13.5	7.3	28.5	13.0	62.2
	Quite hot		1.0	0.5	6.7	7.8	16.1
	Very hot		1.0	0.0	1.0	14.0	16.0
	Total		16.5	9.4	38.3	35.8	100.0
HL	Great hot stress		13.5	6.7	28.5	10.9	59.6
	Extreme hot stress		3.1	2.6	9.8	24.9	40.4
	Total		18.6	9.3	38.3	35.8	100.0

Statistical significance <0.05

35.9°C. A light breeze was blowing the most days of the measurements. Maximum mean relative was estimated during the evening in Syntagma square, while maximum mean solar radiation was estimated at Flisvos coast.

The participants completed 193 questionnaires. The maximum number of the questionnaires was obtained in Ermou street where the overall length of staying was longer. The 59.6% of the votes were by men. The thermal votes were ranged from 0 (neutral) to +3 (very hot) (Table 2). The 74.1% of the votes were ranged over +2 (hot) while a negligible difference was observed between the percentage of votes per scale in males and females.

The calculated TS values ranged from 4 (comfort) to 7 (very hot) in accordance to thermal votes. The Table 3 shows the percentage frequency distribution of the actual sensation votes of the participants for the different values of TS scale. For each class of TS scale the reported thermal sensation ranged from 'neutral' to 'very hot'. The 5.7% of the TS values indicated thermal comfort corresponding to about one third of the reported comfort as their sensation (16.6%) while only the 1.0% of the votes was well distributed. The greater variation of the predicted thermal sensation and the actual thermal sensation is observed in the case of 'hot' class where the 62.2% of the TS values indicated hot thermal sensation while the 7.3% of the participants reported their sensation as 'hot'. The TS index tends to classify the thermal sensation into the 'hot' class. Totally the 29% of the votes were predicted correctly by the TS index while the 54% of the votes were underestimated.

The mean value of TS index that corresponded to 'comfort' or 'hot' actual thermal sensation was 4.68 and 4.55 respectively. Actual thermal sensation 'quite hot' corresponded to 5.1 mean TS value and 'very hot' actual sensation vote corresponded to 6.0 mean TS value.

The estimated HL values were classified in 'great hot stress' (+2) and 'extreme hot stress' (+3) unlike the reported actual sensation votes that ranged between 'neutral' (0) and 'extreme hot stress' (Table 3). The mean value of HL for each class of the actual thermal sensation vote was estimated about 1.80 (extreme hot stress). The 53.4% of votes were properly predicted by the HL index while about 36% of the votes were overestimated.

4 Conclusions

The present study used in situ meteorological measurements and questionnaire responses to evaluate two indices predicting thermal sensation and stress. Even though the survey was conducted under normal meteorological conditions for the season and so as to include data during the whole day, over 70% of the thermal sensation votes were ranged over the point of +2 in the seven-point thermal sensation scale. It has been found that TS underestimated while HL overestimated the actual thermal sensation of the subjects. This is a primary finding that reveals the importance of verifying and determining the predictive model that can be properly used for predicting outdoor thermal comfort.

References

Baccini M, Biggeri A, Accetta G, Kosatsky T, Katsouyanni K, Analitis A, Anderson HR, Bisanti L, D'Ippoliti D, Danova J, Forsberg B, Medina S, Paldy A, Rabczenko D, Schindler C, Michelozzi P (2008) Heat effects on mortality in 15 European cities. Epidemiology 19:711–719. doi:10.1097/EDE.0b013e318176bfcd

Basara BJ, Basara GH, Illston GB, Crawford CK (2010) The impact of the urban heat Island during an intense heat wave in Oklahoma city. Adv Meteorol. doi:10.1155/2010/230365, Article ID 230365, 10 pp

Blazejczyk K (2001) Assessment of recreational potential of bioclimate based on the human heat balance. In: Matzarakis A, de Freitas CR (eds) Proceedings of the first international workshop on climate, tourism and recreation. International Society of Biometeorology. 5–10 October 2001, Halkidiki, Greece, pp 133–152

Giannopoulou K, Livada I, Santamouris M, Saliari M, Assimakopoulos M, Caouris YG (2011) On the characteristics of the summer urban heat island in Athens, Greece. Sustain Cities Soc 1:16–28. doi:10.1016/j.scs.2010.08.003

Givoni B, Noguchi M (2000) Issues in outdoor comfort research. In: Proceedings of PLEA 2000, Cambridge, pp 562–564

Givoni B, Noguchi M, Saaroni H, Pochter O, Yaacov Y, Feller N, Becker S (2003) Outdoor comfort research issues. Energy Build 35:77–86. doi:10.1016/S0378-7788(02)00082-8

ISO 7730 (1994) Moderate thermal environments-determination of the PMV and PPD indices and specification of the conditions for thermal comfort. ISO, Geneva

Matzarakis A, Nastos PT (2011) Human-biometeorological assessment of heat waves in Athens. Theor Appl Climatol 105:99–106. doi:10.1007/s00704-010-0379-3

Mayer H, Hoppe P (1987) Thermal comfort of man in different urban environment. Theor Appl Climatol 38:43–49. doi:10.1007/BF00866252

Pantavou K, Lykoudis S (2011) Environmental exposure and human health effects related to heat exhaustion-a field study of heat stress. In: Proceedings of the twelfth international conference on environmental science and technology, Rhodes, Greece, Global Nest and University of the Aegean, pp 807–812

Philandras CM, Nastos PT, Repapis CC (2008) Air temperature variability and trends over Greece. Glob NEST J 10:273–285

Philandras CM, Nastos PT, Paliatsos AG, Repapis CC (2010) Study of the rain intensity in Athens and Thessaloniki, Greece. Adv Geosci 23:7–45. doi:10.5194/adgeo-23-37-2010

Theoharatos G, Pantavou K, Mavrakis A, Spanou A, Katavoutas G, Efstathiou P, Mpekas P, Asimakopoulos D (2010) Heat waves observed in 2007 in Athens, Greece: synoptic conditions, bioclimatological assessment, air quality levels and health effects. Environ Res 110:152–161. doi:10.1016/j.envres.2009.12.002

WMO (2011) Climate change, Elements of change. World Meteorological Organization. Available at: http://www.wmo.int/pages/themes/climate/elements_climate_change.php. Accessed 2 Nov 2011

A Comparison of a Hydrological and an Energy Balance Model for Estimating Evapotranspiration of Chickpeas at Paphos (SW Cyprus) Agricultural Area

G. Papadavid, D.G. Hadjimitsis, S. Michaelides, L. Toulios, and A. Agapiou

Abstract The objective of this paper is to describe a methodological tool in order to improve the performance of irrigation demand based on the integration of remote sensing techniques and simulation modeling of irrigation water in Cyprus. For this purpose two different models were examined for specific annual crops (chickpeas) cultivated in the agricultural area of Mandria (SW Cyprus). The first one is a dynamic water budget model that supports multi-criteria optimization of water allocation and use. Estimating evapotranspiration involves irrigation demand estimation models which are based on predicted or observed meteorological data, crops and cropping patterns and individual crop physiological water demand. The second model is a fully based satellite image technique (SEBAL). SEBAL is a direct method to estimate evapotranspiration without a priori knowledge on soil, crop, and management conditions. Although evapotranspiration is very difficult to be calculated since it is not a straightforward procedure the comparison of the two different methods indicates similar results between them. The results had no any statistical significance difference using the *T*-test.

G. Papadavid
The Agricultural Research Institute (ARI), Nicosia, Cyprus

D.G. Hadjimitsis
Department of Civil Engineer and Geomatics, Cyprus University of Technology, Limassol 3603, Cyprus

S. Michaelides
Cyprus Meteorological Service, Nicosia, Cyprus

L. Toulios • A. Agapiou (✉)
National Agricultural Research Foundation (NAGREF), Larissa, Greece
e-mail: athos.agapiou@cut.ac.cy

C.G. Helmis and P.T. Nastos (eds.), *Advances in Meteorology, Climatology and Atmospheric Physics*, Springer Atmospheric Sciences,
DOI 10.1007/978-3-642-29172-2_35,

1 Introduction

Evapotranspiration (ET) is a term used to describe the sum of evaporation and plant transpiration from the Earth's land surface to atmosphere. In detail, in the first process water is lost from the soil and plant surfaces by evaporation and in the second from the crop by transpiration (FAO 1998). The actual estimation and calculation of ET, is a basic and crucial need for climate studies, weather forecasts, hydrological surveys, ecological monitoring, and water resource management (Hoedjes et al. 2008). Further to ET, actual Evapotranspiration ET_a is one of the most useful indicators to explain whether the water is used as 'intended' or not. However the estimation of ET_a is still under scientific study since many parameters are involved. This complexity associated with the estimation of ET has lead to the development of various methods for estimating this parameter over time (Doorenbos and Pruitt 1977; Allen et al. 1998). In Cyprus there is a great need for estimating ET using systematic and cost-effective techniques. Indeed many studies during the last years focused in order to determine the exact quantity of irrigated water needed for each specific crop (Papadavid et al. 2009, 2011; Hadjimitsis et al. 2008). The determination of ET for irrigation purposes can be used as a vital tool for supporting the decision-making process in the management of water resources, on a technocratic level, and on the other hand will have a positive effect on the rest of water resources of Cyprus.

2 Case Study Area

The study area is located in the area of Mandria village, in the vicinity of Paphos International Airport in Cyprus (Fig. 1). The selected area is a traditionally agricultural area with a diversity of annual cultivations and is irrigated by Asprokremnos Dam, one of the biggest dams of Cyprus. The area is characterized by mild climate which provides the opportunity for early production of leafy and annual crops. An advantage of the area of interest is that there is little cloud cover or cloud free during the year especially on spring and summer time. This fact enables and empowers the use of field spectroscopy in the area.

3 Methodology

Two different models have been examined for specific annual crops (chickpeas) cultivated in the agricultural area of Mandria (Cyprus). The first one is a dynamic water budget model that supports multi-criteria optimization of water allocation and use, named as 'WaterWare'. Estimating ET involves irrigation demand estimation models which are based on predicted or observed meteorological data, crops

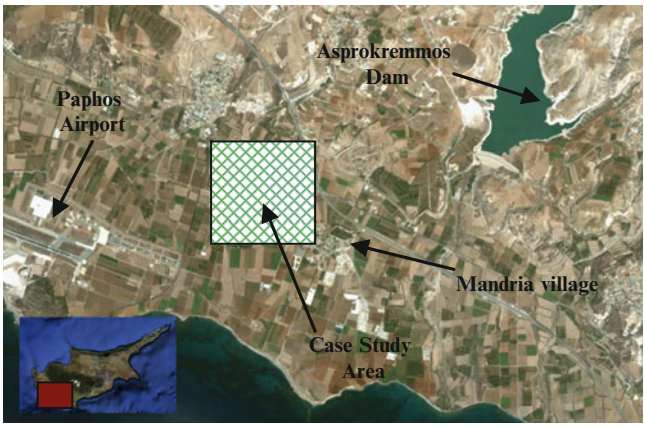

Fig. 1 Case study area (Google Earth ©)

and cropping patterns and individual crop physiological water demand. SEBAL the second model, is a fully satellite image based technique. SEBAL is a direct method to estimate ET without a priori knowledge on soil, crop, and management conditions and has been developed by Bastiaanssen et al. (1998).

3.1 Dynamic Water Budget Model (Water Ware)

WaterWare (Harmancioglu et al. 2008; Fedra et al. 2007) is a dynamic water budget model that supports multi-criteria optimization of water allocation and use. The model system uses a topological network structure to represent water resources systems (river basins including inter-basin transfers); cascading sub-models describe the dynamic mass budget in terms of hydro-meteorology rainfall-runoff modeling for sub-catchments, reservoir operations, irrigation water demand, and water quality. Economic valuation of water use and the costs of water supply include social and environmental criteria.

3.2 Remote Sensing Model (SEBAL)

SEBAL computes a complete radiation and energy balance along with the resistances for momentum, heat and water vapour transport for each pixel (Bastiaanssen et al. 1998; Bastiaanssen 2000). The key input data for SEBAL consists of spectral radiance in the visible, near-infrared and thermal infrared part of the spectrum. So, the model can be applied using satellite sensors having a thermal band. Landsat TM and ETM + images were used in this study. In addition to satellite images, the SEBAL model requires weather parameters (wind speed,

Table 1 Satellite versus WaterWare ET_c estimates

Observation date	RS ET_c mean	WaterWare/IWD
26-02-2008	2.25	2.20
28-07-2008	2.78	3.20
13-08-2008	2.84	3.20
29-08-2008	3.03	2.40
04-12-2008	2.65	2.70

Table 2 Results of ET_c (mm/day) for the different methods

Satellite image	SEBAL	E_{pan}
12-07-2008	5.6	5.5
28-07-2008	5.7	5.5
13-08-2008	5.1	4.2
29-08-2008	4.2	4.2
29-06-2009	3.8	2.3
7-07-2009	4.8	5.5
15-07-2009	6.1	5.5
23-07-2009	5.4	5.5
16-08-2009	3.3	4.2

humidity, solar radiation, air temperature). These meteorological parameters were used as inputs for the algorithm and they were provided from the national meteorological station next to the area of interest. SEBAL model is applied for the first time in Cyprus. In order to be as accurate as possible, all crop related parameters for SEBAL were adapted to the soil, geomorphological and meteorological conditions of the island using ground spectroradiometric measurements. Then SEBAL methodology was employed to estimate ET_c of chickpeas at the places of interest.

4 Results

The estimated ET_c are summarised below in Table 1. WaterWare estimates ET_c based on 'optimal' soil moisture maintained by supplementary irrigation during the growing season. Estimates represent the daily average rather than an instantaneous value, which will also vary considerably during the day. ET_c also varies from day to day with the meteorological conditions. Table 2 indicates the results from the SEBAL methodology.

$T_{observed}$ for both cases (Tables 3 and 4) was smaller than the $T_{statistical}$, which implies that at a confidence level of 95%, the ET_c derived from the different methods has no significant statistical difference.

The resulting water demand for the irrigation areas is then used in a dynamic water budget model of the overall basin, reservoir and groundwater. This allocates the water to different competing water uses considering hydrological, economic, and environmental criteria and objectives as well as alternative water supply from desalination. The purpose is to maximize overall net benefits as the basis for more

Table 3 T-test analysis for ET_c derived from RS and water ware

Crop	$T_{observed}$	$T_{statistical}$	n (sample)
Chickpeas	−0.991	2.139	5

Table 4 T-test analysis for ET_c derived from SEBAL and Epan

Crop	$T_{observed}$	$T_{statistical}$	n (sample)
Chickpeas	0.711	1.859	8

efficient and cooperative win-win strategies of water allocation that not only improve the economic performance, but also meet sustainability criteria. Of course both techniques have a sound base: WaterWare has a hydrological model as a base and remote sensing has an energy balance base and uses energy fluxes to estimate ET_c. The differences are in logical margins since the method estimating ET_c is different for each technique.

5 Conclusions

Although ET is difficult to be calculating, different algorithms and models are available for this purpose. This paper preset the result of two different methods for estimating ET at an agricultural area of Cyprus. Chickpeas crops were analyzed in this paper and the results have shown that the combination of remote sensing techniques and other models can be a systematic tool for monitoring irrigation demand over Cyprus. The integration of modeling and remote sensing can provide accurate results on a systematic basis in order to develop irrigation management and provide scientific data to policy makers.

Acknowledgments Thanks are given to the Remote Sensing Laboratory of the Department of Civil Engineering & Geomatics at the Cyprus University of Technology for the support (http://www.cut.ac.cy/) and the Meteorological Service of Cyprus for providing climate data. This study is part of G. Papadavid Ph.D. Thesis which is both supported by 'Cyprus Research Promotion Foundation fund (PENEK/ENISX/0308/13') and the Cyprus University Research Committee fund ('Integration'/Internal project).

References

Allen RG, Pereira LS, Raes D, Smith M (1998) Crop evapotranspiration, guidelines for computing crop water requirements. FAO Irrigation and Drainage, vol 56. Food and Agriculture Organization of the UN (FAO), Rome, p 300

Bastiaanssen WGM (2000) SEBAL-based sensible and latent heat fluxes in the irrigated Gediz Basin, Turkey. J Hydrol 229:87–100. doi:10.1016/S0022-1694(99)00202-4

Bastiaanssen WGM, Menenti M, Feddes RA, Holtslag AAM (1998) A remote sensing surface energy balance algorithm for land (SEBAL). Part 1: Formulation. J Hydrol 212–213:198–212. doi:10.1016/S0022-1694(98)00253-4

Doorenbos J, Pruitt WO (1977) Crop water requirements. FAO irrigation and drainage 24. FAO, Rome, 144pp (revised)

FAO (1998) Crop evapotranspiration – guidelines for computing crop water requirements. Food and Agricultural Organization Irrigation and Drainage 56. Food and Agriculture Organization of the United Nations, Rome

Fedra K, Kubat M, Zuvela-Aloise M (2007) Web-based water resources management: economic valuation and participatory multi-criteria optimization. In: Proceedings of the second IASTED international conference water resources management, 20–22 Aug 2007, Honolulu, HI

Hadjimitsis DG, Papadavid G, Themistocleous K, Kounoudes A, Toulios L (2008) Estimating irrigation demand using satellite remote sensing: a case study of Paphos District area in Cyprus. In: Neale CMU, Owe M, D'Urso G (eds) Remote sensing for agriculture, ecosystems, and hydrology. Proceedings of SPIE Europe remote sensing, vol 7104. University of Wales Institute, Cardiff, p 71040I. doi:10.1117/12.800366

Harmancioglu N, Fedra K, Barbaros F (2008) Analysis of sustainability in management of water scarce basins: the case of the Gediz River Basin in Turkey. Desalination 226:175–182

Hoedjes JCB, Chehbouni A, Jacob F, Ezzahar J, Boulet G (2008) Deriving daily evapotranspiration from remotely sensed instantaneous evaporative fraction over olive orchard in semi-arid Morocco. J Hydrol 354:53–64. doi:10.1016/j.jhydrol.2008.02.016

Papadavid G, Agapiou A, Michaelides S, Hadjimitsis DG (2009) The integration of meteorology and remote sensing for monitoring irrigation demand in Cyprus. Nat Hazard Earth Sys 9 (6):2009–2014. doi:10.5194/nhess-9-2009-200

Papadavid G, Hadjimitsis DG, Perdikou S, Michaelides S, Toulios L, Sereaphides N (2011) Use of field spectroscopy for exploring the impact of atmospheric effects on Landsat 5 TM/7 ETM + satellite images intended for hydrological purposes in Cyprus. GIScience Remote Sens 48 (2):280–298. doi:10.2747/1548-1603.48.2.280

High Resolution Gridded Meteorological Data Across the Mediterranean Basin

A. Papadopoulos, P. Katsafados, and I. Pytharoulis

Abstract The knowledge on the climatology and the statistics of extreme events is of central interest for a broad range of practical applications. To obtain such information long-term and homogeneous meteorological databases are needed. However, such time series of direct observations are not always available for sufficient long period. For regions that do not have adequate historical observations or measurements are not available or lack homogeneity, the application of advanced atmospheric numerical models is often an alternative solution. In this study a sophisticated downscaling procedure that was applied to reproduce high resolution historical records of the atmospheric conditions across the Mediterranean region is presented. This was accomplished by the dynamical downscaling of the ERA-40 reanalyses with the aid of the atmospheric model of the POSEIDON weather forecasting system. The full three dimensional atmospheric fields with 6 h of temporal resolution and the surface meteorological parameters at hourly intervals were produced for a 10-year period (1995–2004). The meteorological variables are readily available at 10 km resolution and may constitute the atmospheric forcing to drive wave, ocean hydrodynamic and hydrological models, as well as the baseline data for environmental impact assessment studies.

A. Papadopoulos (✉)
Institute of Inland Waters, Hellenic Centre for Marine Research, Anavyssos Attikis, Greece
e-mail: tpapa@hcmr.gr

P. Katsafados
Department of Geography, Harokopion University of Athens, Athens, Greece

I. Pytharoulis
Department of Meteorology and Climatology, School of Geology,
Aristotle University of Thessaloniki, Thessaloniki, Greece

C.G. Helmis and P.T. Nastos (eds.), *Advances in Meteorology, Climatology and Atmospheric Physics*, Springer Atmospheric Sciences,
DOI 10.1007/978-3-642-29172-2_36,

1 Introduction

Data assimilation is an advanced numerical method to combine background or "first-guess" gridded field for a short period (typically 6 h) with all available observations for this period in order to produce the analysis at regular temporal intervals (i.e., hourly). Global analyses are produced by large operational centers, like the European Centre for Medium-Range Weather Forecasts (ECMWF) and the US National Centers for Environmental Prediction (NCEP). The operational analyses contain many discontinuous changes due to the improvements in the numerical methods used to produce them (Trenberth and Olson 1988), introducing artificial changes in the apparent climate record. This problem has been addressed by the "reanalysis" projects. Reanalysis products are generated by the assimilation of all available observational data, incorporating data that had not been used in the operational analyses, using the same most recent assimilation method for the entire period of coverage (Kalnay et al. 1996). The ERA project has produced a 45-year second-generation reanalysis dataset, the ERA-40 (Uppala et al. 2005). Currently, ERA-40 is the main reanalysis product and is widely used. However, the spatial resolution of the ERA-40 data is rather coarse (about 125 km grid); consequently, they only describe the large-scale atmospheric features and provide limited representation of the mesoscale atmospheric processes, highly affected by topography and land-sea distribution. Thus, an appropriate downscaling technique is required to resolve the desired fine-scale meteorological fields.

The downscaling methods can be based on statistical schemes or can be conducted within a dynamical framework by nesting a high-resolution limited area model to the coarser resolution reanalysis output. Several studies have discussed a number of issues related to the appropriate choice of the downscaling method for a particular application (e.g., Kidson and Thompson 1998; Diez et al. 2005; Xue et al. 2007). However, the application of statistical downscaling schemes is restricted to data-rich regions, since most statistical downscaling methods cannot be applied unless observed data are available for model calibration. Therefore, the dynamical downscaling methods have the potential to outperform statistical methods, particularly when no observed data contribute to the analysis and assumptions have to be adapted in order to interpolate a sparse station network over complex terrain.

This paper presents the dynamical downscaling methodology which was undertaken to produce high-resolution atmospheric conditions over the Mediterranean basin and the surrounding countries. The motivation of this work was the need to provide fine scale atmospheric forcing usable to drive wave, ocean hydrodynamic and hydrological models as well as the baseline data for environmental impact assessment studies. The mesoscale atmospheric model of the POSEIDON weather forecasting system has been appropriately configured to run at 10 km grid spacing (as opposed to 125 km grid spacing of the ERA-40). The ECMWF ERA-40 reanalysis data and the ECMWF operational analyses were used to force the mesoscale model at its boundaries and thereafter the mesoscale model downscales

the global data by producing fine-scale weather patterns consistent with the coarse-resolution features in the forcing data. Due to the computational cost, the mesoscale model was run for a period of 10 years, namely 1995–2004.

2 Data and Methodology

In the current dynamical downscaling approach we used an advanced mesoscale atmospheric model, based on the Eta model, which was forced by the most popular global atmospheric reanalysis dataset, the ERA-40.

The ERA-40 data are available through public internet access to a comprehensive set of $2.5^\circ \times 2.5^\circ$ resolution and through authorized access to the ECMWF's Meteorological Archive and Retrieval System (MARS) to a regular $1.125^\circ \times 1.125^\circ$ latitude/longitude grid spacing products. For the Mediterranean region this grid spacing corresponds to a computational grid length of about 125 km in latitude and 95 km in longitude.

The atmospheric model is a modified version of the non-hydrostatic workstation Eta model (Janjic et al. 2001) and it constitutes the core of the second generation POSEIDON weather forecasting system (Papadopoulos and Katsafados 2009, and references therein). It is fully parallelized to run efficiently on any parallel computer platform and uses a two-dimensional scheme for partitioning grid-point space to Message Passing Interface (MPI) tasks.

2.1 Model Setup: Downscaling Experiment

The mesoscale model was integrated over a domain large enough to include all terrain features which might influence the mesoscale flow. Namely, the model domain covers the Mediterranean Sea and the surrounding countries, with latitude roughly between 24.4°N and 51.0°N, and longitude between 21.0°W and 51.0°E (Fig. 1).

The model had a horizontal grid increment of $0.1^\circ \times 0.1^\circ$ (about 10 km) resulting to 247×231 semi-staggered E grid points within the rotated transformed latitude-longitude coordinate system of the Eta model. In the vertical, 38 unevenly spaced levels were used covering the atmospheric layers from the surface to roughly 20 km height, with the maximum resolution within the planetary boundary layer. The fundamental time step of the model was defined to 30 s. Moreover, the six soil layers have been defined at the depths of 5, 15, 28, 50, 100, and 255 cm.

The ERA-40 reanalysis data are organized in four analyses per day (for 00, 06, 12, and 18 UTC) for the period from September 1957 to August 2002. Therefore, the ERA-40 reanalysis was the source used for the definition of the initial and the boundary conditions for the simulations from January 1995 to August 2002 while the operational ECMWF analysis fields were used for the simulations from January

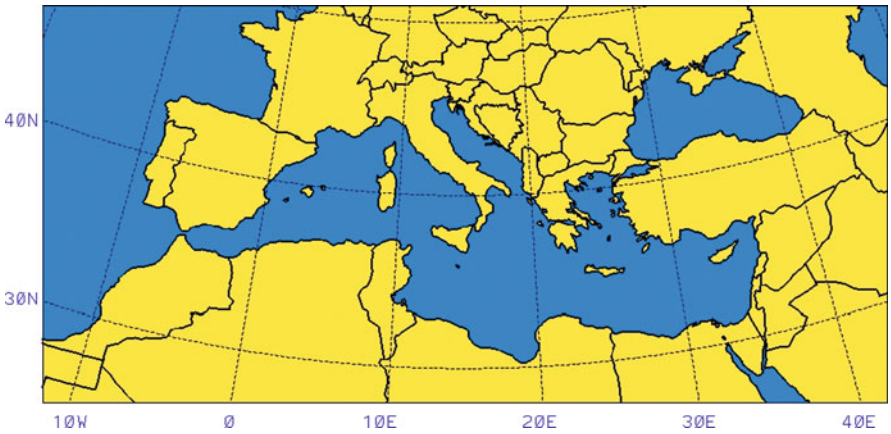

Fig. 1 Model domain

2002 to December 2004. It is worth noting, that the subsequent archived operational ECMWF analyses were based on the same data assimilation system as the ERA-40, but the resolution of the atmospheric model had increased to a spectral representation of $T_L511L60$, which is about 40 km horizontal grid spacing. The simulations for the common period (January 2002 till August 2002), have been performed in order to investigate later on any influence caused by the different initial and boundary conditions. Both reanalysis and operational analysis fields (geopotential, wind components and humidity) were available for 16 standard pressure levels and were interpolated to a regular $0.5^\circ \times 0.5^\circ$ horizontal grid increment using the ECMWF model's own reduced Gaussian grid (Persson 2001). The lateral boundaries of the model domain were updated at each model's time step from the ECMWF data available every 6 h. For the fields of the sea surface temperature (SST), soil temperature and soil moisture, the ECMWF data at a $0.5^\circ \times 0.5^\circ$ horizontal grid increment were used.

The model was configured to a 30-h forecasting mode and 3,896 simulations (including the common time period) were conducted to cover the 10-year period (1995–2004). For each simulation, starting at 00 UTC, the initial conditions for the atmosphere and the SST were reinitialized while the soil moisture and temperature were initialized from the previous simulation. The length of each simulation was set to 30 h in order to avoid a 6-h model spin-up time. Therefore, the model outputs from 6-h to 30-h of each simulation have been used to create the 10-years dataset of atmospheric forcing. The completeness of such demanding simulations would not have been feasible without the high-performance computing capabilities of the Hellenic National Meteorological Service (HNMS) which supported the available computing resources of the Hellenic Centre for Marine Research (HCMR). The two computing systems were combined to optimize computing workloads, data management, data processing and data mining and eventually the overall time of producing the final database was approximately 16 months.

3 Results

The atmospheric variables produced by the dynamical downscaling of the ERA-40 data can be grouped in upper air parameters, soil parameters, surface parameters and single level parameters (such as low, medium, high cloud cover, top atmosphere longwave and shortwave radiation).

The upper-air parameters have been saved at each of the 38 model levels for 00, 06, 12, and 18 UTC of each day for the 10-year period. These parameters include geopotential height, air temperature, specific humidity and wind components. The soil parameters, thus soil temperature and soil moisture, have been also stored at each of the six soil layers with 6 h of temporal resolution. Meanwhile, the surface and the single level parameters have been archived for every hour of the entire time period. The data volume of the complete archive is more than 4 TB. The format of the files is either FORTRAN binary or GRIB (Gridded Binary) both saved on the model grid. However, experience gained by disseminating the products from the POSEIDON weather forecasting system suggests that the majority of the users are mostly interested in the near surface meteorological variables. Thus, a smaller and more practical dataset has been formed consisting of the following surface meteorological variables

- Air temperature at 2 m
- Wind speed and direction at 10 m
- Humidity (relative or specific) at 2 m
- Mean sea level pressure
- Sensible and latent heat fluxes
- Ground fluxes of shortwave and longwave radiation
- Amount of precipitation,

The Eta model is defined over the semi-staggered E grid. To overcome this inconvenience advanced software has been developed in order to process the model-generated fields and bilinearly interpolate them in unstaggered grid form. In the unstaggered grids all variables are placed on a common and rectangular grid, taking also into account the wind rotation so that vector data are properly projected. This smaller dataset of surface meteorological variables is approximately 300 GB and is ready for use by other applications across the Mediterranean.

4 Conclusions

This study presents a sophisticated downscaling procedure that was applied to reproduce high resolution historical records of the atmospheric conditions across the Mediterranean region. This was accomplished by the dynamical downscaling of the European Center for Medium-Range Forecasts ERA-40 reanalyses with the aid of the atmospheric model of the POSEIDON weather forecasting system.

In the authors' future plans is to provide quantitative estimates of the potential benefit of the new 10-year dynamical downscaling dataset.

Acknowledgments The authors would like to thank Ms. Anna Mamara of the Hellenic National Meteorological Service (HNMS) who downloaded the ECWMF data through the operational dissemination system (MARS-Meteorological Archive and Retrieval System).

References

Diez E, Primo C, Garcia-Moya JA, Gutierrez JM, Orfila B (2005) Statistical and dynamical downscaling of precipitation over Spain from DEMETER seasonal forecasts. Tellus 57A:409–423. doi:10.1111/j.1600-0870.2005.00130.x

Janjic ZI, Gerrity JP Jr, Nickovic S (2001) An alternative approach to nonhydrostatic modeling. Mon Weather Rev 129:1164–1178. doi:10.1175/1520-0493(2001) 129<1164:AAATNM> 2.0.CO;2

Kalnay E, Kanamitsu M, Kistler R, Collins W, Deaven D, Gandin L, Iredell M, Saha S, White G, Woollen J, Zhu Y, Chelliah M, Ebisuzaki W, Higgins W, Janowiak J, Mo KC, Ropelewski C, Wang J, Leetmaa A, Reynolds R, Jenne R, Joseph D (1996) The NCEP/NCAR 40-year reanalysis project. Bull Am Meteorol Soc 77:437–471. doi:10.1175/1520-0477(1996) 077<0437: TNYRP>2.0.CO;2

Kidson JW, Thompson CS (1998) A comparison of statistical and model-based downscaling techniques for estimating local climate variations. J Clim 11:735–753

Papadopoulos A, Katsafados P (2009) Verification of operational weather forecasts from the POSEIDON system across the Eastern Mediterranean. Nat Hazard Earth Sys 9:1299–1306

Persson A (2001) User guide to ECMWF forecast products. Meteorological Bull M3.2, ECMWF, Reading, United Kingdom

Trenberth K, Olson J (1988) An evaluation and intercomparison of global analyses from the National Meteorological Center and the European Centre for Medium Range Weather Forecasts. Bull Am Meteorol Soc 69:1047–1057. doi:10.1175/1520-0477(1988) 069<1047: AEAIOG>2.0.CO;2

Uppala SM, Kallberg PW, Simmons AJ, Andrae U, Da Costa BV, Fiorino M, Gibson JK, Haseler J, Hernandez A, Kelly GA, Li X, Onogi K, Saarinen S, Sokka S, Allan RP, Andersson E, Arpe K, Balmaseda MA, Beljaars ACM, Van De Berg L, Bidlot J, Bormann N, Caires S, Chevallier F, Dethof A, Dragosavac M, Fisher M, Fuentes M, Hagemann S, Holm E, Hoskins BJ, Isaksen L, Janssen PAEM, Jenne R, Mcnally AP, Mahfouf JF, Morcrette JJ, Rayner NA, Saunders RW, Simon P, Sterl A, Trenberth KE, Untch A, Vasiljevic D, Viterbo P, Woollen J (2005) The ERA-40 re-analysis. Q J R Meteorol Soc 131:2961–3012. doi:10.1256/qj.04.176

Xue Y, Vasic R, Janjic Z, Mesinger F, Mitchell KE (2007) Assessment of dynamic downscaling of the continental U.S. regional climate using the Eta/SSiB regional climate model. J Clim 20:4172–4193. doi:10.1175/JCLI4239.1

Performance Assessment of an Integrated Sensor for Simultaneous Measurements of Global and Diffuse Radiation Components at Athens Area

B. Psiloglou, S. Lykoudis, and D. Kouvas

Abstract The proper design of installations utilizing solar radiation requires the accurate knowledge of solar radiation availability on horizontal and tilted surfaces as well as its direct/total and diffuse components. The measurement of diffuse radiation normally requires a sun tracking or shading device. However, a new integrated instrument, model SPN1, has been presented by Delta-T Devices, incorporating seven miniature thermopile sensors, a built-in microprocessor, and an internal shading device with no moving parts. SPN1 sensor is able to perform simultaneously measurements of both the global and diffuse solar radiation reaching a horizontal surface and can also estimate sunshine duration. Such a sensor was installed at NOA's actinometric station at Penteli site, during summer 2011, to assess its performance against classic measurements of global irradiance by thermopile pyranometer and diffuse with a shading ring. Stated accuracies are easily verified for 1-min measurements of total solar radiation, with RMSE values varying between 2.6% and 3.6%, whereas for the diffuse radiation, stated accuracies were not possible to verify, with RMSE values varying between 10.8% and 17.0%. This may be due to measurement inaccuracies, yet for the diffuse component there might be a need for a correction factor to improve accuracies.

B. Psiloglou (✉) • S. Lykoudis
Institute for Environmental Research and Sustainable Development, National Observatory of Athens, P. Penteli, Athens GR-15236, Greece
e-mail: bill@meteo.noa.gr

D. Kouvas
ScientAct S.A., 16 Kanari Street, Thessaloniki GR-54644, Greece

C.G. Helmis and P.T. Nastos (eds.), *Advances in Meteorology, Climatology and Atmospheric Physics*, Springer Atmospheric Sciences,
DOI 10.1007/978-3-642-29172-2_37,

1 Introduction

The advent of technological advances in the photovoltaic industry combined with the increased awareness and adoption of policies aiming at the reduction of greenhouse gas emissions has increased the demand for accurate data on solar energy availability at different locations around the globe. Solar data, on the other hand, are nowadays used in diverse disciplines, including climatology, micrometeorology, biology, agriculture, glaciology, urban planning, architecture, mechanical and environmental engineering. The proper design of installations utilizing solar radiation requires the knowledge of solar radiation availability on horizontal and tilted surfaces as well as its direct/total and diffuse components.

The measurement of diffuse radiation normally requires a sun tracking or shading device, which, usually, is either expensive or requires frequent adjustment by the operator. However, a new integrated instrument, model type SPN1 (Sunshine Pyranometer), has been presented recently by Delta-T Devices Ltd. as an affordable alternative to shade-ring pyranometers, pyrheliometers and traditional sunshine recorders (Fig. 1). It incorporates seven miniature thermopile sensors, mounted under cosine-corrected diffusers, an internal shading device with no complex electro-mechanical assemblies. More details on the optical design of the SPN1 are available through its predecessor BF2–BF3 sensor, from the Delta-T Devices (2001). The SPN1 is a meteorological class instrument, which matches the WMO "Good Quality" pyranometer classification, with a built-in microprocessor and an internal heater, and is designed for long-term outdoor exposure. It needs no routine adjustment or polar alignment and works at any latitude (Delta-T Devices 2007).

The SPN1 sensor is able to perform simultaneously measurements of both global and diffuse solar radiation reaching a horizontal surface. Also, sunshine duration can be estimated using an internal algorithm. The instrument provides two analog voltage outputs for global and diffuse radiation measurements, and a digital output for sunshine duration, which can be connected to most data loggers. Also an embedded RS232 port is included for digital recording.

SPN1's resolution is 0.6 W/m^2, with response time less than 200 ms, and spectral response between 400 and 2,700 nm, covering the whole solar spectrum with

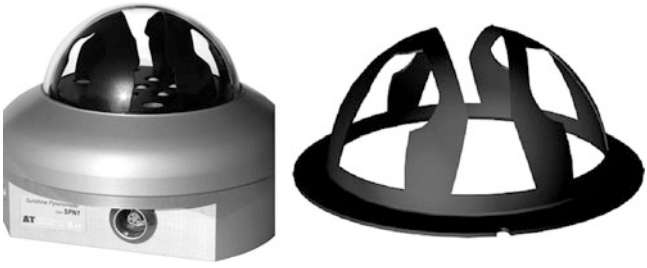

Fig. 1 SPN1 Sunshine Pyranometer (*left*) and its internal shading device (*right*) (Delta-T Devices 2007)

typical spectral sensitivity variation of 10% (Delta-T Devices 2007). According to the manufacturer, the overall accuracy for either total or diffuse radiation individual readings is $\pm(8\% + 10\ W/m^2)$, which is reduced to $\pm(5\% + 10\ W/m^2)$ for hourly averages. First results on SPN1's relative performance against other solar radiation sensors, for February to May 2008, are given by Wilcox and Myers (2008).

Such a sensor was installed at NOA's actinometric site at Penteli, during summer 2011, to test its performance against classical measurements of global radiation by CM11 Kipp & Zonen's (K&Z) thermopile pyranometers and diffuse with a shading ring, type CM121. The results of this assessment are presented here.

2 Data and Methodology

In order to evaluate the performance of the Sunshine Pyranometer, 1-min averaged total and diffuse horizontal solar irradiance data (Wm^{-2}) from NOA's actinometric-meteorological station at Penteli site (38.049°N, 23.863°E, 495 m asl) were used, covering the period from June, 1 till the end of September 2011.

The actinometers for measuring total and diffuse horizontal radiation are K&Z CM11 pyranometers; the diffuse radiation is measured using a CM121 K&Z shadow ring. A geometrical correction, based on an isotropic sky, was applied to diffuse radiation measurements, using tabulated correction factors (Kipp and Zonen 2004).

To establish a valid set of measurements, the 1-min mean total and diffuse horizontal irradiance values were thoroughly examined for errors. A routine quality control procedure (CIE 1994) was applied; all erroneous data were excluded. The quality tests screened out all cases of (1) diffuse irradiance greater than 110% of the corresponding total irradiance; (2) total irradiance greater than 120% of the seasonally corrected solar constant; (3) diffuse irradiance greater than 80% of the seasonally corrected solar constant; (4) total irradiance equal to or less than 5 Wm^{-2} to account for the pyranometers' sensitivity; (5) data below 5 deg solar altitude due to the cosine effect of the pyranometers' dome; and (6) data with the direct beam component exceeding the extraterrestrial solar irradiance. The quality control yielded a total of 88,375 valid 1-min data points. Finally, using night-time measurements, the "dark signal" (due to thermal losses) of each K&Z pyranometer was estimated on a daily basis, and removed from the measurements.

The Root Mean Square Error (RMSE) and the Mean Absolute Error (MAE), expressed as percentage of the measured mean reference values, were used as indicators of the SPN1's performance.

3 Results

The RMSE(%) and MAE(%) results for total and diffuse radiation at Penteli site, and the mean monthly values of reference total and diffuse radiation are presented in Table 1. The RMSE values for the four summer months examined vary between

Table 1 RMSE% and MAE%, for the SPN1 total and diffuse horizontal radiation components along with the monthly mean values from reference Kipp & Zonen sensors at Penteli

	June	July	August	September
Number of 1-min values	22,301	23,860	21,769	20,445
Average total hor. (W/m^2)	515	606	580	521
Average diffuse hor. (W/m^2)	170	123	115	113
MAE total hor. (%)	2.5	2.2	2.6	2.1
MAE diffuse hor. (%)	11.7	15.1	13.7	9.1
RMSE total hor. (%)	3.6	2.8	3.1	2.6
RMSE diffuse hor. (%)	13.7	17.0	15.9	10.8

2.6% and 3.6% for the total radiation, and from 10.8% to 17.0% for the diffuse radiation, while the MAE was found to vary between 2.1% and 2.6% and 9.1% and 15.1% for the total and diffuse radiation, respectively.

Considering that accuracies provided by manufacturers refer to standard deviations of some form of residuals, we can safely consider RMSE% as a valid representative of the instrument's accuracy. Thus, the stated accuracy for total solar radiation is more or less verified by our measurements, yet for diffuse radiation we obtain lower accuracies than those stated by the manufacturer.

To further investigate this discrepancy and better illustrate the performance of the intergraded SPN1 sensor, Figs. 2 and 3 present the comparison between the reference (K&Z CM11) and tested (Delta-T SPN1) 1-min values of total and diffuse solar radiation on a horizontal surface. Upper and lower accuracy limits according to manufacturer (red dashed lines), the optimal regression lines (black lines) as well as the determination coefficient values (R^2) are also included.

In Fig. 2, SPN1's total radiation measurements show good agreement with the CM11 values, with most values (>97%) lying well within the SPN1 specification limits of $\pm(8\% + 10\ W/m^2)$ (shown as red dashed lines). In Fig. 3, SPN1's diffuse measurements show more variability compared to the shade ring CM11 values, with the SPN1 giving lower values than the shading ring at low absolute values (typically clear blue sky) and higher values than the shade ring at higher absolute values (typically hazy or partly cloudy conditions). Only 62% of the 1-min readings conformed to the specified accuracy limits. However, this may be very well due partly to errors in the SPN1 measurements and partly to the inaccuracy of our diffuse radiation measurements, caused by the thermal losses inherent in the type of instrument we are using, and errors in shade-ring corrections due to deviations from the isotropic sky assumption.

For total solar radiation, the slope of the best-fit lines is the same (about 1.0) in all 4 months, as well as the coefficient of determination (about 0.997). The offset varies between +6.1 and +11.8 W/m^2, i.e. 1–2% of the average values.

For diffuse solar radiation measurements, the slope of the best-fit lines is almost the same, between 0.96 and 1.0 in all months. The coefficient of determination ranges between 0.960 and 0.982 and the offset varies between +7.6 and +22.1 W/m^2. This is a rather large offset (6–17% of the average values) suggesting that a correction factor might improve the sensor's performance.

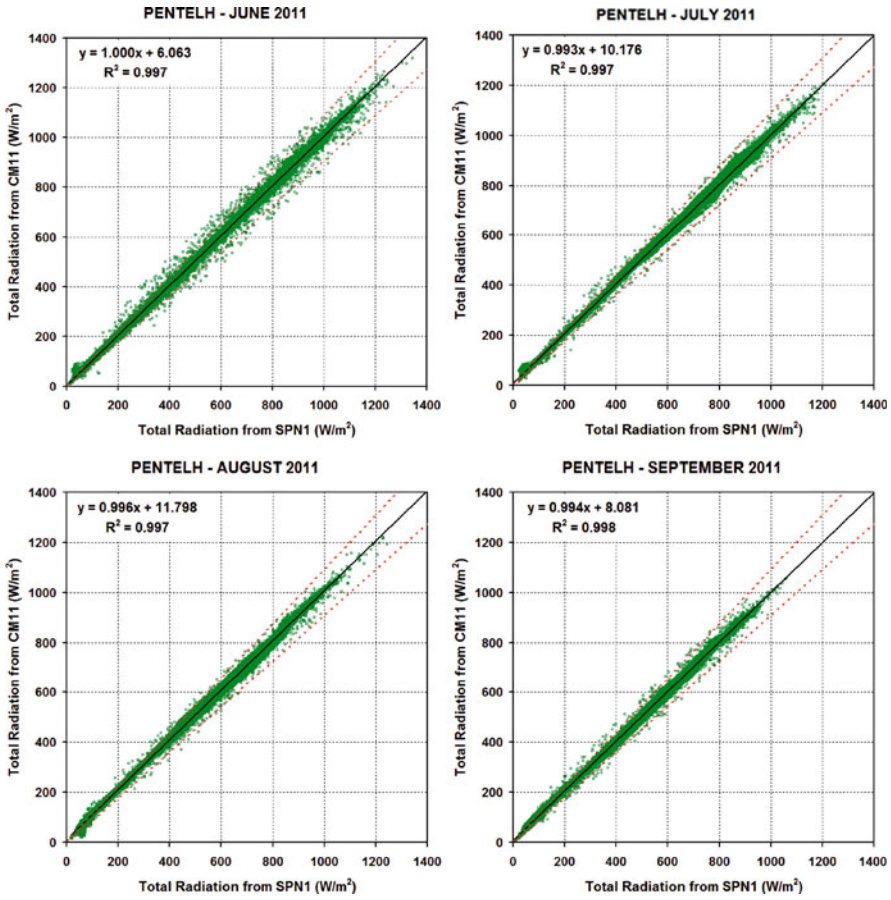

Fig. 2 Reference (Kipp & Zonen CM11 sensor) and tested (Delta-T SPN1 sensor) measurements of total horizontal solar radiation

4 Conclusions

The close agreement between the reference (K&Z CM11 sensors) and tested (Delta-T SPN1 sensor) values of total and diffuse solar radiation on a horizontal surface, suggests that SPN1 would be a valid candidate for basic solar radiation measurements, especially when cost and low operational requirements are considered.

Stated accuracies are easily verified for 1-min data of total horizontal solar radiation, yet for the diffuse component, stated accuracies could not be verified. This may be due to measurement inaccuracies, yet for the diffuse component there might be a need for some kind of correction factor to improve accuracies.

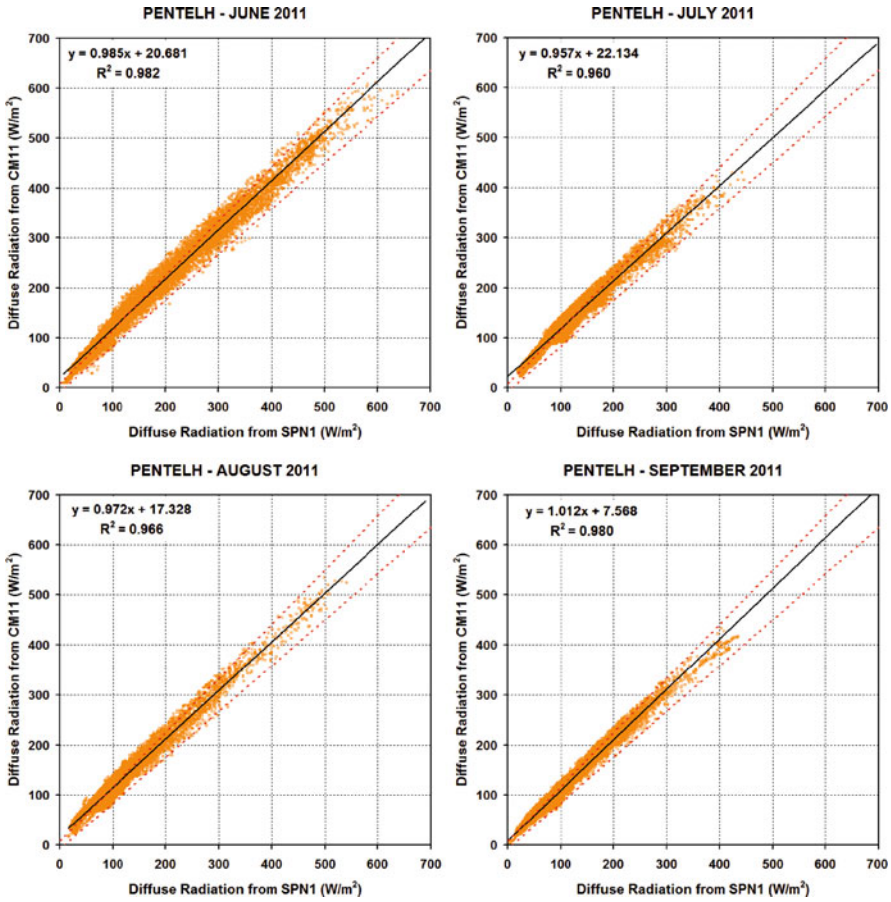

Fig. 3 Reference (Kipp & Zonen CM11 sensor) and tested (Delta-T SPN1 sensor) measurements of diffuse horizontal solar radiation

Acknowledgments Special thanks to Delta-T Devices Ltd. UK for lending us the SPN1 sensor for testing and comparison with classical thermopile sensors.

References

CIE (1994) Guide to recommended practice of daylight measurement. No. 108, Vienna, Austria

Delta-T Devices Ltd (2001) BF2 and BF3 optical design. Available from www.delta-t.co.uk

Delta-T Devices Ltd (2007) User manual for the Sunshine pyranometer type SPN1. Available from www.delta-t.co.uk

Kipp & Zonen (2004) CM121 Shadow Ring instruction manual. Ver. 0706, Delft

Wilcox SM, Myers DR (2008) Evaluation of radiometers in full-time use at the National Renewable Energy Laboratory Solar Radiation Research Laboratory. Technical report NREL/TP-550-44627

Study of the August 2010 Heat Event in Cyprus

A. Retalis, D. Paronis, S. Michaelides, F. Tymvios, D. Charalambous, D.G. Hadjimitsis, and A. Agapiou

Abstract An intense heat wave lasting for several days occurred in Cyprus during August 2010. Record high surface air temperatures were monitored. The aim of this study is to present the intensity and spatial extent of this event for four major districts, based on the analysis of MODIS Aqua satellite images along with surface air temperature data. Emphasis was given in the estimation of the urban heat island intensity and the differences from the respective mean intensity for August 2002–2008.

1 Introduction

Land surface temperature (LST) refers to the skin temperature retrieved by satellites. LST is a measure of how hot is the ground to the touch and is depended on the type of the ground surface. As derived from a variety of remotely sensed data (AVHRR, MODIS, ASTER, Landsat), LST has been used for urban heat island (UHI) studies by several researchers (Cheval et al. 2009; Tomlinson et al. 2010; Tran et al. 2006; Trigo

A. Retalis (✉)
Institute for Environmental Research and Sustainable Development,
National Observatory of Athens, Athens, Greece
e-mail: adrianr@meteo.noa.gr

D. Paronis
Institute for Space Applications and Remote Sensing, National Observatory of Athens, Athens, Greece

S. Michaelides • F. Tymvios • D. Charalambous
Meteorological Service, Nicosia, Cyprus

D.G. Hadjimitsis • A. Agapiou
Department of Civil Engineering and Geomatics, Remote Sensing Laboratory,
Cyprus University of Technology, Limassol, Cyprus

C.G. Helmis and P.T. Nastos (eds.), *Advances in Meteorology, Climatology and Atmospheric Physics*, Springer Atmospheric Sciences,
DOI 10.1007/978-3-642-29172-2_38,

et al. 2008). Remotely sensed data along with meteorological data has also been used for studying heat waves (Retalis et al. 2010a, b; Kotroni et al. 2011).

The Moderate Resolution Imaging Spectroradiometer (MODIS) sensor, aboard Terra and Aqua polar satellites, provides one day and one night image under clear sky conditions. MODIS LST product is ideal due to its global coverage, high calibration accuracy and radiometric resolution. MODIS LST products are based on the generalised split-window (GSW) algorithm (Wan and Dozier 1996), using as input the MODIS thermal bands 31 (10.78–11.28 μm) and 32 (11.77–12.27 μm). The parameters in the MODIS GSW depend on the satellite zenith view angles, column water vapour and also on the low atmosphere boundary temperature. The band emissivities rely on the classification-based method (Snyder et al. 1998) according to land cover types in the pixel (Monteiro et al. 2007). MODIS LST product has an accuracy of 1 K yielded for materials with known emissivities (Wan 1999).

The August 2010 heat wave event in Cyprus was a particularly intense one, commencing by the end of July. It is pointed out that July 2010 was particularly warm with the heat index being constantly at heavy discomfort levels during maximum heating hours, both inland and over coastlines. On 1 August, the heat event manifested the utmost, leading to the recording of the highest temperature ever recorded in 14 of the 63 stations of the Cyprus Meteorological Service's stations, with an absolute record high measured at Athalassa station near Nicosia with 45.6°C.

During this period, a surface trough of low surface pressure extending from the Tibetan plateau was dominant over Middle East, providing the island of Cyprus with a strong and warm northeasterly flow evident up to 700 hPa. The subsidence due to the upper ridge conditions prevailing over the area contributed to the further heating of the airmass (an indicative height at 500 hPa over Cyprus was 5,088 geopotential metres).

The aim of the paper is to assess the urban heat island effect in terms of its intensity and spatial extent for four major cities in Cyprus for the intense heat wave event of August 2010.

2 Data and Methodology

The methodology adopted consists of testing the suitability of using MODIS Aqua data for generating LST maps and to assess the impact of urban heat island effect during the specific intense heat wave event in Cyprus.

2.1 Data

Daily maximum temperatures at 2 m recorded from a variety of meteorological stations (operated by the Meteorological Service of Cyprus) for the period 23 July–28 August 2010 were considered in this study, in order to identify the days with maximum heat wave intensity.

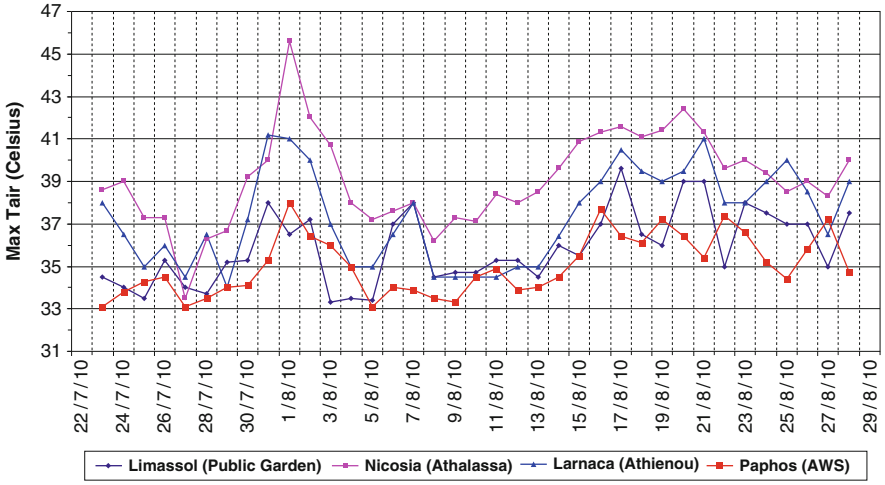

Fig. 1 Variation of maximum surface air temperature for selected stations located in the corresponding districts of Cyprus

A selection of available Aqua MODIS LST (MYD11A1) images at a spatial resolution of 1 × 1 km^2 corresponding to overpass times for the study area between 2230 and 0030 UTC were retrieved for the study period as well as for the period 2002–2008.

2.2 Methodology

The identification of the heat wave events was based on the selection of the station which recorded maximum daily temperatures (Fig. 1) for each one of the four districts (Nicosia, Larnaca, Limassol and Paphos) of Cyprus.

The UHI intensities were estimated by subtracting the LST value for each rural area (as identified from the position of a pre-selected rural meteorological station) from the respective values falling within the urban boundary of each district on a pixel-by-pixel basis (Fig. 2) (Tomlinson et al. 2010).

The temporal variation of the UHI intensity for each district was studied for the period 23 July–28 August 2010 (Fig. 3). The spatial patterns of the UHI effect for two cases when high air surface temperature had been recorded were analyzed and compared to the mean UHI estimated for the years 2002–2008 (Fig. 4).

3 Results

Figure 1 depicts the variation of the maximum temperatures for the study period and for each of the selected stations. It is noticed that on 1 August 2010, a maximum of around 46°C was recorded in Nicosia, while a secondary major event was observed later in August.

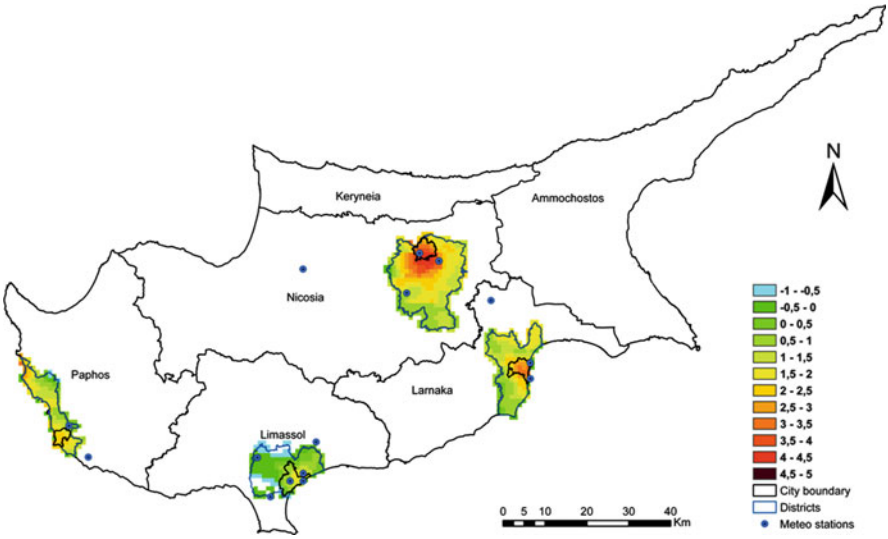

Fig. 2 Mean UHI estimated from MODIS Aqua nocturnal images for the period 2002–2008 for four districts of Cyprus: Nicosia, Larnaca, Limassol and Paphos

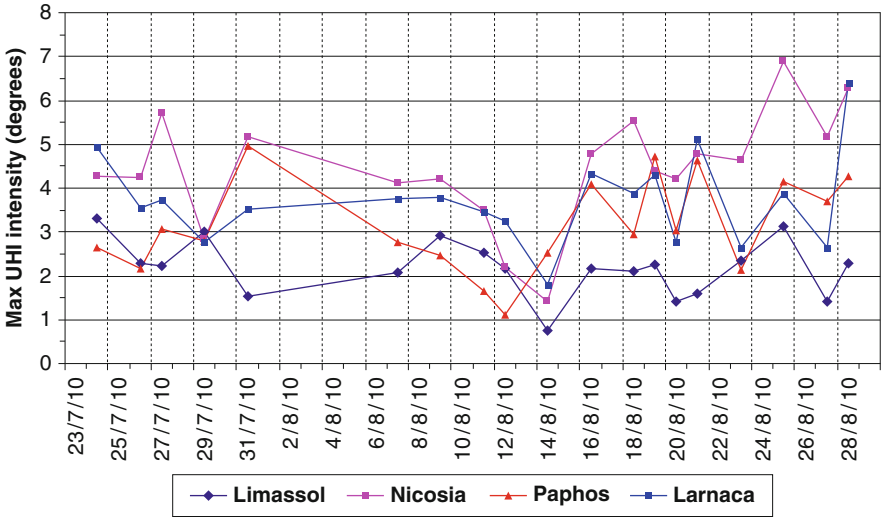

Fig. 3 Temporal variation of maximum UHI intensity for the four districts of Cyprus, as derived from the analysis of Aqua nocturnal data for the period 23 July–28 August 2010

Figure 2 presents the spatial mean UHI intensity for the four districts for the period 2002–2008. As noticed, Nicosia and Larnaca are more vulnerable to UHI, since both the spatial extent and intensity are higher compared to the other two districts. It is characteristic that the maximum mean UHI intensity for Nicosia and

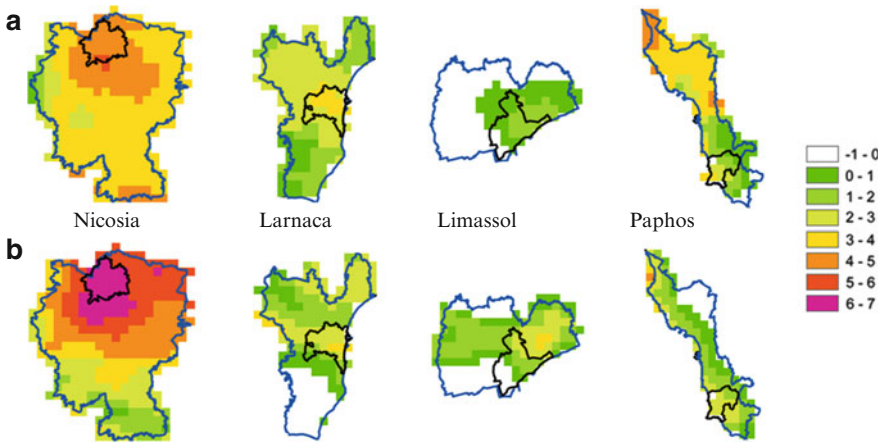

Fig. 4 UHI estimated from MODIS Aqua nocturnal images for the period (**a**) 31 July and (**b**) 28 August 2010, for the four districts of Cyprus: Nicosia, Larnaca, Limassol and Paphos

Larnaca is 4.6° and 3.4°, respectively, while in Limassol and Paphos is estimated at 1.9° and 3.1°, respectively.

Figure 3 shows the temporal variation of the maximum UHI intensity as estimated from the available nocturnal Aqua MODIS images for the period of study for all districts of Cyprus. It is noticed that for most cases the curves follow a similar trend. Two major peaks were observed on 31 July and 25 August 2010.

Figure 4 depicts the intensity and spatial extent of the UHI for the above dates. The results are consistent with the patterns observed for the mean UHI shown in Fig. 2, although the magnitude of intensity was found to be greater due to the heat wave event. More specifically, the maximum intensities of UHI for each district were 5.2 (Nicosia), 3.5 (Larnaca), 1.5 (Limassol), and 5.0 (Paphos) degrees on 31 July and 6.9 (Nicosia), 3.9 (Larnaca), 3.1 (Limassol), and 4.2 (Paphos) degrees on 25 August 2010. Thus, an increase of UHI intensity of about 0.5–2.3° is noticed for Nicosia, 0.1–0.5° for Larnaca, 1.2° for Limassol and 1.1–1.9° for Paphos.

4 Conclusions

An analysis of Aqua MODIS LST data along with surface air temperature measurements were used for studying the extensive heat wave event of August 2010 in Cyprus. The intensity of UHI was calculated for the study period as well as for the period 2002–2008. It was found that the UHI spatial pattern during the heat wave follows that of the mean period (2002–2008) although higher intensities were noticed in all districts. The UHI intensity was stronger in Nicosia and Larnaca while Limassol and Paphos were less affected.

At a later stage, we intend to expand our study to include more heat wave events for better understanding the role of LST evaluation in terms of seasonal and spatial variations.

Acknowledgments Partial support was received from the Cyprus Research Promotion Foundation under contract No. AEIFORIA/ASTI/0308(BE)/01. MODIS LST data were distributed by the Land Processes Distributed Active Archive Center (LP DAAC), located at the U.S. Geological Survey (USGS) Earth Resources Observation and Science (EROS) Center (lpdaac.usgs.gov).

References

Cheval S, Dumitrescu A, Bell A (2009) The urban heat island of Bucharest during the extreme high temperatures of July 2007. Theor Appl Climatol 97:391–401. doi:10.1007/s00704-008-0088-3

Kotroni V, Lagouvardos K, Retalis A (2011) The heat wave of June 2007 in Athens, Greece. Part 2: modeling study and sensitivity experiments. Atmos Res 100:1–11. doi:10.1016/j.atmosres.2010.12.007

Monteiro I, Trigo IF, Kebasch E, Olesen F (2007) Validation of land surface temperature retrieved from Meteosat Second Generation Satellites. In: Proceedings of the Joint 2007 EUMETSAT meteorological satellite conference and the 15th satellite meteorology and oceanography conference of the American Meteorological Society, Amsterdam, The Netherlands, 24–28 Sep 2007. http://www.eumetsat.int/Home/Main/Publications/index.htm. Accessed 24 June 2011

Retalis A, Paronis D, Lagouvardos K, Kotroni V (2010a) The heat wave of June 2007 in Athens, Greece. Part 1: study of satellite derived land surface temperature. Atmos Res 98:458–467. doi:10.1016/j.atmosres.2010.08.005

Retalis A, Paronis D, Michaelides S, Tymvios F, Charalambous D, Hadjimitsis D, Agapiou A (2010b) Urban heat island and heat wave events in Cyprus. In: Proceedings of the 10th conference of meteorology, climatology and atmospheric physics, Laboratory of Atmospheric Physics, Department of Physics, University of Patras, Patras, Greece. Hellenic Meteorological Society, pp 552–560

Snyder WC, Wan Z, Zhang Y, Feng YZ (1998) Classification-based emissivity for land surface temperature measurement from space. Int J Remote Sens 19:2753–2774. doi:10.1080/014311698214497

Tomlinson C, Chapman L, Thornes J, Baker C (2010) Derivation of Birmingham's summer surface urban heat island from MODIS satellite images. Int J Climatol. doi:10.1002/joc.2261

Tran H, Uchihama D, Ochi S, Yasuoka Y (2006) Assessment with satellite data of the urban heat island effects in Asian mega cities. Int J Appl Earth Obs Geoinf 8:34–48. doi:10.1016/j.jag.2005.05.003

Trigo IF, Monteiro IT, Olesen F, Kabsch E (2008) An assessment of remotely sensed land surface temperature. J Geophys Res 113:1–12. doi:10.1029/2008JD010035

Wan Z (1999) MODIS land-surface temperature algorithm theoretical basis document, version 3.3. NASA documents. http://modis.gsfc.nasa.gov/atbd/atbd_mod11.pdf. Accessed 24 June 2011

Wan Z, Dozier J (1996) A generalized split-window algorithm for retrieving land-surface temperature from space. IEEE Trans Geosci Remote Sens 34:892–905

Stable Isotopic Composition of Atmospheric Water Vapor in Greece

V. Salamalikis, A.A. Argiriou, and E. Dotsika

Abstract Water stable isotopes are applicable as tracers since these are present in the various processes of the hydrological cycle. Due to their mass differences the heavy isotopic species of water are preferentially distributed in the condensed phases, while the lighter isotope species are preferentially evaporated. The isotopic composition of atmospheric water vapor provides information on moisture transport processes and phase changes in the atmosphere. The study of the isotopic composition of water vapor is of great interest because water vapor is recognized as one of the most important greenhouse gases with a positive feedback in global warming. This paper presents the results of a 3-year sampling of the isotopic composition ($\delta^{18}O$) of atmospheric water vapor in Greece. The temporal variation of $\delta^{18}O$ and its link to various meteorological parameters is investigated. Finally, a statistical model for the estimation of atmospheric water vapor $\delta^{18}O$ is proposed, in order to capture the dependence of $\delta^{18}O$ on the concurrent meteorological conditions. The results of the isotopic model are compared with measurements.

1 Introduction

The knowledge of the isotopic composition of atmospheric water vapor is of great significance since atmospheric water vapor is strongly related with precipitation. Stable isotopes in atmospheric water vapor are useful tracers for the determination of moisture transport and phase changes in the atmosphere (Gat 1996). The variations

V. Salamalikis (✉) • A.A. Argiriou
Laboratory of Atmospheric Physics, Department of Physics, University of Patras, Patras GR-26500, Greece
e-mail: vsalamalik@upatras.gr

E. Dotsika
Institute of Material Science, National Center of Scientific Research "Demokritos", Ag. Paraskevi, Attikis, Greece

C.G. Helmis and P.T. Nastos (eds.), *Advances in Meteorology, Climatology and Atmospheric Physics*, Springer Atmospheric Sciences,
DOI 10.1007/978-3-642-29172-2_39,

in stable isotope content are strongly affected by isotopic fractionation effects, caused by condensation and evaporation processes during the course of an air mass. Under equilibrium conditions, the isotopic composition of water vapor can be estimated from that of precipitation (Jacob and Sonntag 1991). This assumption fails in arid and semi-arid climates as well as in light rains where partial evaporation of raindrops during their trip from the cloud base through the un-saturated atmosphere takes place (Stewart 1975; Zhang et al. 1998). This process enhances the isotopic composition of the remaining raindrops since the lighter water isotope species are preferentially distributed in the vapor phase.

Most studies concentrate on the isotopic composition of precipitation since precipitation can be directly collected. In this study, the results of the 3-year sampling of the isotopic composition ($\delta^{18}O$) of water vapor in Patras, Greece are presented and the correlation between $\delta^{18}O$ and the concurrent meteorological parameters is investigated.

2 Data and Methodology

Water vapor was sampled in the Laboratory of Atmospheric Physics, University of Patras (38° 16′ 48″N/21° 47′ 24″E/100 m.a.s.l.) for a 3-years period (2007–2010). Atmospheric water vapor was collected by cryogenic trapping at −160°C using the sampling device shown in Fig. 1.

The ambient air is sucked by an air pump into the condensate trap which is pre-cooled by immersion in a Dewar flask containing LN_2. Temperature is kept very low during the sampling procedure in order to avoid fractionation effects that may occur in the captured water vapor. Water vapor freezes under the low temperature conditions and an ice cube is formed in the condensate trap. Then, the condenser is removed from the Dewar and the ice cube is liquefied under room temperature conditions. The resulting water is then stored in airtight vials. Ambient temperature and relative humidity together with sampling duration were also recorded during sampling.

The water vapor samples were analyzed at the National Centre of Scientific Research 'Demokritos', Athens, Greece. The meteorological data used in this analysis are arithmetic mean values during the sampling period. Vapor pressure data were calculated using the Magnus-Tetens formula (Lawrence 2005),

$$e_{sat}(T) = 6.1094\,exp[17.625T/(243.04+T)], (hPa) \tag{1}$$

with T the ambient temperature (°C). Assuming that the water vapor is described by an exponential distribution in the atmosphere, the precipitable water can be derived from air temperature and the surface water vapor partial pressure via Butler's formula (Butler 1998),

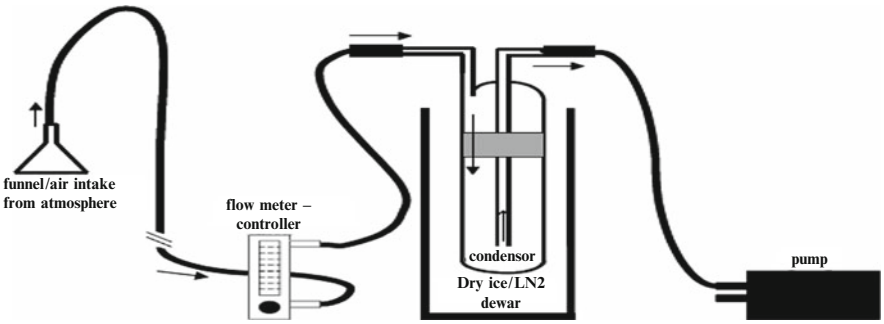

Fig. 1 Water vapor sampling device

$$h = \frac{m_w H P_0}{\rho_l k T} \approx \frac{3P_0}{T}, (mm) \tag{2}$$

where H = 1.5 km, m_w = 18, ρ_l = 1 kg/m^3, k = 1.38 10^{-23} m^2 kg/s^2. Temperature (T) is in K and P_0 is the water vapor partial pressure. P_0 can be calculated using the formula:

$$P_0(T, RH) = 2.409 \times 10^{12} RH (300/T)^4 exp(-6792/T), (\ \mu bar) \tag{3}$$

with T expressed in K and RH in percent.

Stable isotope data of monthly precipitation for Patras, Greece were obtained through the GNIP/ISOHIS databases (IAEA 2010).

3 Results

The temporal variations of meteorological parameters and $\delta^{18}O$ in atmospheric water vapor are shown in Fig. 2. The isotopic composition of water is highly correlated with the water vapor amount in the atmosphere (Yin et al. 2008). According to the Rayleigh distillation process which is temperature dependent, the heavy isotopes depletion is lower with higher water vapor content in the atmosphere and therefore higher condensation temperature.

The relationships between $\delta^{18}O$ and the meteorological parameters are shown in Fig. 3. The 'temperature' effect, namely the depletion of stable isotopic composition with descending temperature, is described by a quadratic equation for $\delta^{18}O$ in water vapor. On the other side, there is a linear relationship between air temperature and $\delta^{18}O$ in precipitation with a slope equal to 0.24‰/°C. The correlation between the isotopic composition and relative humidity is very low since the p-value of the linear fit is greater than 0.001 and the correlation coefficient approaches zero. The saturation vapor pressure and the precipitable water show

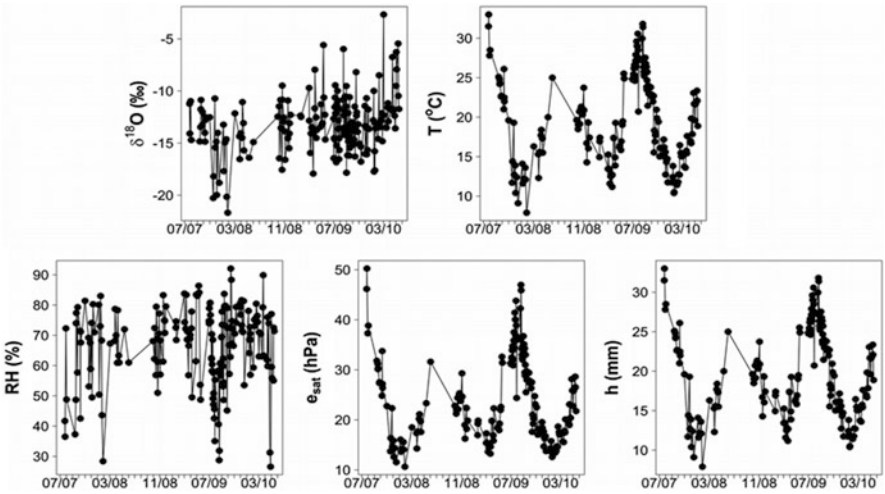

Fig. 2 Temporal variation of $\delta^{18}O$, temperature, relative humidity, saturation vapor pressure and precipitable water for the complete sampling period

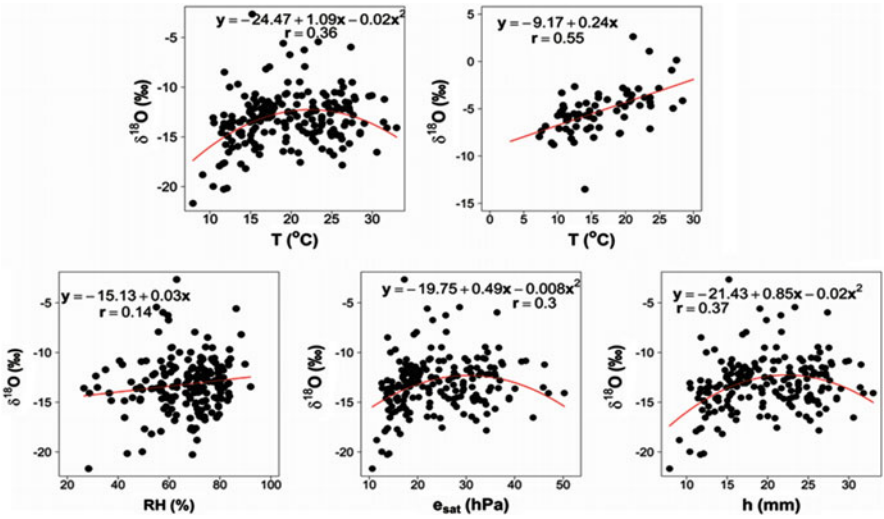

Fig. 3 Scatter diagrams between $\delta^{18}O$ and atmospheric variables

quadratic relationships with $\delta^{18}O$ since the air temperature plays a major role in their calculation.

In order to estimate the isotopic composition of atmospheric water vapor a model is proposed. This has two parts. The first describes the relationship between $\delta^{18}O$ and the meteorological parameters. Stepwise linear regression is used for the elimination of non-significant contributions. The second part of the model is

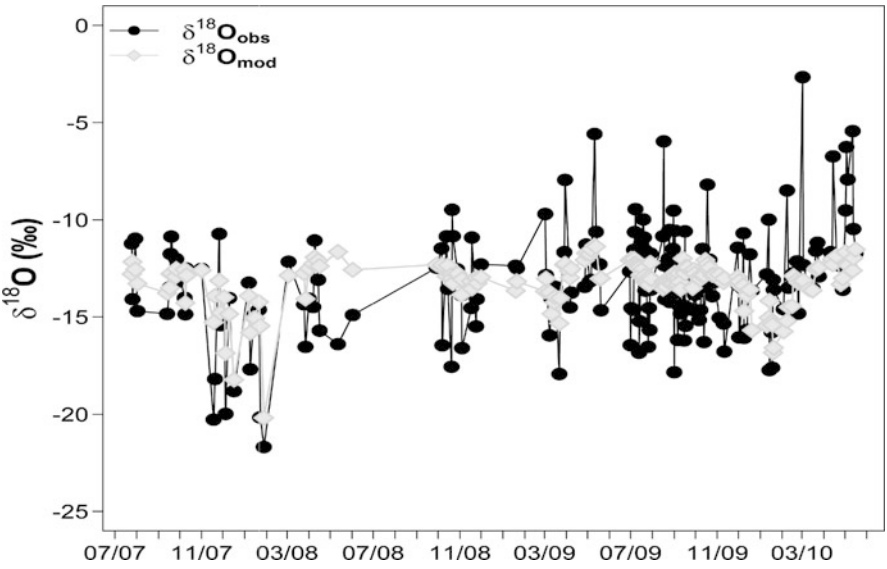

Fig. 4 Temporal variation of calculated and measured isotopic composition of atmospheric water vapor

a harmonic term added in order to express the temporal variation of $\delta^{18}O$. The final isotopic model is described by the following expression,

$$\delta^{18}O_{mod} = -65 + 1.48T - 0.2T^2 + 4.36e + 0.07h - cos\left(\frac{2\pi Jd}{365}\right) \quad (4)$$

where Jd is the day of the year (Julian day).

The isotopic model results are plotted against the sampling date together with the measurements (Fig. 4).

It is obvious that the modeled values follow the temporal variation of measurements. However it is very difficult to simulate the actual isotopic composition of atmospheric water vapor with high accuracy. The model represents successfully the low values of $\delta^{18}O$ but in less depleted values the differences between the model's results and the measurements are very high. In rainy days the isotopic composition of water vapor depends of the isotopic composition of rainfall and vice versa resulting to intensive depletion of the heavy water vapor isotope content. In rain episodes with high precipitation amount the isotopic composition of water vapor can be better related to that of precipitation events. In light rains the secondary evaporation phenomena take place and the resulting water vapor becomes further depleted in heavy isotopes since the lighter water isotopologues are distributed in the vapor phase. These effects could not be included in the isotope model. Therefore, the differences between the fitted and the actual isotope values cannot be explained by the isotope model during precipitation events revealing the weakness to describe the isotopic composition of ground level vapor.

4 Conclusions

In this paper the isotopic composition of atmospheric water vapor in Patras, Greece is studied and its link to atmospheric parameters is investigated. Isotope values of atmospheric water vapor differ from those of precipitation in Patras, Greece. The $\delta^{18}O$ in water vapor ranges between $-21.00‰$ and $-2.66‰$, while in precipitation the range of $\delta^{18}O$ is $-13.51‰ \leq \delta^{18}O \leq 2.62‰$. This results from the fact that lighter isotope species are preferentially distributed in the vapor phase. The distribution of stable isotopes in water vapor is mainly controlled by air temperature according to the Rayleigh distillation process. In order to derive explicit and adequate information for the isotopic composition of water vapor, continuous sampling on a daily basis is required. A possible remedy of future work will be the simultaneous sampling of precipitation and water vapor in order to explain their relation and their partition in the secondary evaporation effects occurred during the rainfall events.

References

Butler B (1998) Precipitable water at the VLA – 1990–1998. MMA memo no. 237. Available from http://www.alma.nrao.edu/memos/html-memos/abstracts/abs237.html

Gat JR (1996) Oxygen and hydrogen isotopes in the hydrological cycle. Annu Rev Earth Planet Sci 24:225–262. doi:10.1146/annurev.earth.24.1.225

IAEA (2010) Isotope hydrology information system: the ISOHIS database. Available from: http://isohis.iaea.org

Jacob H, Sonntag C (1991) An 8-year record of the seasonal variation of ^{2}H and ^{18}O in atmospheric water vapor and precipitation in Heidelberg, Germany. Tellus B Chem Phys Meteorol 43(3):291–300

Lawrence MG (2005) The relationship between relative humidity and the dew point temperature in moist air: a simple conversion and applications. Bull Am Meteorol Soc 86(2):225–233

Stewart MK (1975) Stable isotope fractionation due to evaporation and isotopic-exchange of falling waterdrops: application to evaporation processes and evaporation of lakes. J Geophys Res 80(9):1133–1146

Yin CL, Yao TD, Tian LD, Liu DN, Yu WS, Qu DM (2008) Temporal variations of $\delta^{18}O$ of atmospheric water vapor at Delingha. Sci China D Earth Sci 51(7):966–975

Zhang XP, Xie ZH, Yao TD (1998) Mathematical modeling of variations on stable isotopic ratios in falling raindrops. Acta Meteorol Sin 12:213–220

Hailstorm Characteristics Over the Area of Central Macedonia During the Period 1998–2008

E. Sfiri and T. Karacostas

Abstract The objective of this study is the analysis of the mesoscale thermodynamic characteristics of the hailstorms, which occurred over the region of Central Macedonia, where the National Hail Suppression Program is applied, during the period 1998–2008, except for the year 2003. The data used are derived through the C-band weather radar at Filyro and from the representative soundings of the synoptic station of Thessaloniki. The frequency of hailstorms' occurrence, their movement, intensity and the maximum development are studied. The radar data are analyzed and studied through the software TITAN (Thunderstorm Identification, Tracking, Analysis, and Nowcasting), for the period 2006–2008.

1 Introduction

The Greek National Hail Suppression Program (NHSP) has been applied over a region of Central Macedonia by the Greek Agricultural Insurance Organization (ELGA) since 1984. For the first 5 years, the program was run on an experimental mode (1984–1988) and afterwards on an operational basis (Karacostas 1984, 1989). The main purpose of this project is the hail suppression from hailstorm clouds. The hail suppression is performed by seeding the clouds properly with AgI particles. The protected and seeding areas of Central Macedonia include parts of the prefectures of Pieria, Thessaloniki and Kilkis, totaling to 2,670 km^2. The study and understanding of the hailstorm characteristics within the protected area of Central Macedonia is of great importance and usefulness, since this area is one of the largest agricultural areas and most crop productive – due to the potentiality of agricultural cultivations – and at the same time of a very high frequency of

E. Sfiri (✉) • T. Karacostas
Department of Meteorology and Climatology, School of Geology, Aristotle University of Thessaloniki, Thessaloniki 541 24, Greece
e-mail: esfiri@physics.auth.gr

C.G. Helmis and P.T. Nastos (eds.), *Advances in Meteorology, Climatology and Atmospheric Physics*, Springer Atmospheric Sciences,
DOI 10.1007/978-3-642-29172-2_40,

Fig. 1 The area of the NHSP, along with the three specifically chosen areas (P2, P3 and P4) for a distinctive examination of the hailstorm characteristics

occurrence of hailstorms, resulting to very high economic compensations paid by ELGA. Most frequently, hail appears over northern Greece during the warm period of the year, from April to September (Sioutas 1999). The seeding area (Fig. 1) is surrounded by mountainous ranges to its northwest, west and southwest boundaries. Specifically, the mountain range of Vermion extending to the west side of the area, can be considered as a storm influencing mechanism, due to the conglomeration of the cold and dry upper air with the warm and humid low level air. In this study, an attempt is made to investigate and study the characteristics of the hailstorms developed within the area of interest (P2, Fig. 1), and particularly over two specifically defined areas (P3 and P4, Fig. 1), thus distinguishing the orographic effect to hailstorm development from the thermal-convective influence on the development.

2 Data and Methodology

A storm is characterized as hailstorm when it produces hailstones, which have significant size and can reach the ground. According to NHSP, a storm is seeded when it reaches reflectivity values greater or equal than 35 dBz, between the −5°C and −30°C isotherms, over the study area or the transition zone (Karacostas 1984). In this study, the examined hailstorms must fulfill the following specific criteria: (1) the reflectivity to be at least 45 dBz above the isotherm of −5°C and (2) at least one damaged hailpad was identified within the area of interest. The need to overcome and distinguish the effect of the seeding on the hailstorms intense and frequency, leaded to the definition of two categories, based upon the two previous criteria. Category A incorporates all hailstorms that fulfill at least one criterion, while hailstorms that fulfill both criteria simultaneously determine category B. It is obvious that there are more hailstorms in category A, since B category is a subset of A. The archived data from ELGA, which have been collected during the 1998–2008 operational years (April–September) and concern 237 hailstorms, have been used. The studied variables are: the maximum reflectivity, which demonstrates the intensity of the hailstorm, the height (identified by the weather radar), and the level of the −5°C isotherm (derived from the 12:00 UTC radiosonde). Moreover, using the software

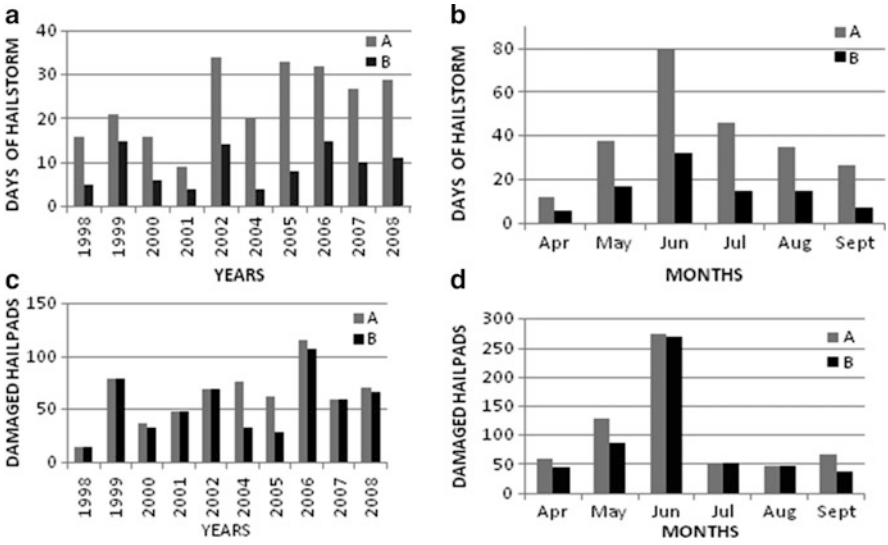

Fig. 2 Frequency of hailstorms and the damaged hailpads, per year and month, for categories A and B

TITAN, more hailstorm characteristics are retrieved, such as the average motion (speed and direction) of the identified cells, along with the maximum height of cells (max top), but only for the period 2006–2008.

2.1 Initial Analysis of Hailstorms

The 237 hailstorms are studied and their characteristics are analyzed for the two categories A and B. The frequency of occurrence of hailstorms (first row) and the number of damaged hailpads (second row) are depicted as a function of the examined years within the hail season in Fig. 2. The frequency of hailstorm occurrence is larger at the latest years for category A, while such indication is not obvious for category B. Most hailstorms seem to take place during June, for both categories. Probably, that is the reason for the very high values of the damaged hailpads in the same month. Although the hailstorm frequencies indicate big differences between the categories A and B, this is not identified in the distributions of the damaged hailpads. The years 2006 and 1998 represent the two extremes, indicating the maximum and minimum number of damaged hailpads, respectively. As far as the limits are concerned, the categories A and B are in agreement, although B exhibits lower or equal frequencies than A, in all circumstances.

The frequency of maximum reflectivity as a function of the examined years is depicted in Fig. 3, for the categories A and B. Moreover, the identified height of the maximum reflectivity values and the $-5°C$ isotherm are indicated, as a function of

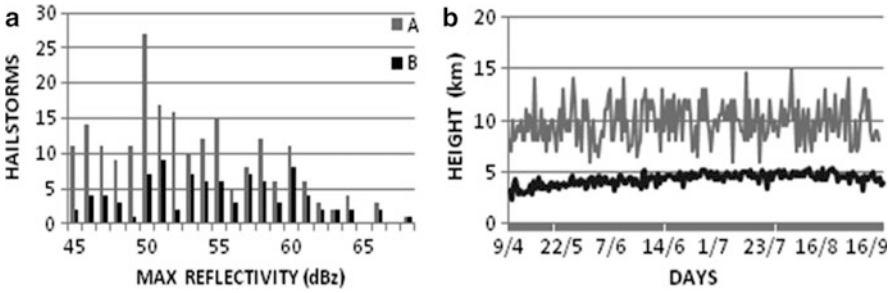

Fig. 3 Frequency of maximum reflectivity (**a**) and its height (*grey*) along with the −5°C isotherm (*black*) variation (**b**) through the period April–September for categories A and B (2006–2008)

the hail season, for the categories A and B. As referred to above, the height of the maximum reflectivity must exceed that of the −5°C isotherm; this is shown in Fig. 3b. The frequency of the maximum reflectivity maximizes at 50 dBz for category A and at 51 dBz for category B. Generally, high frequencies appear between 45 and 60 dBz. Beyond 60 dBz, the frequencies are very low or even zero, indicating the scarcity of very severe storms over the examined area (Foris et al. 2005).

2.2 *Data Analysis from TITAN Archives*

The software TITAN quantifies storm characteristics and determines storm motion, location and evolution (Pinto et al. 2007). The protected area includes few sub-areas with high altitude. The mountain range to the west side of the area contributes to the development of severe orographic hailstorms that affect the whole of area. These storms are expected to be significantly different from the ones developed over the plains. It has long been known that there is a general relationship between the area of a thunderstorm and its precipitation output (Ćurić and Janc 1992). Therefore, in this study, a sub-area (P2) over the plains has been chosen (Fig. 1), in order to achieve homogeneity in the characteristics of the hailstorms.

From the total 1,127 thunderstorm cells recorded by TITAN in the period 2006–2008, the 221 hailstorm cells developed over area P2 are studied. Figure 4a indicates that 33% of the hailstorm cells move from the WSW, with second preference that from north-north-west. According to Fig. 4b, which depicts the frequency of the hailstorm cells as a function of the mean speed of motion, the peak corresponds to the 11–19 km/h range, while only 22 hailstorm cells move with mean speed more than 38 km/h. The cloud heights, measured by radar, serve as a proxy for convective strength and precipitation, with reasonable success, as predicted by simple models (Sherwood et al. 2004). The highest percentage (39%) of the hailstorm cells is associated with maximum top at 6 km (Fig. 4d). For the examined period (2006–2008), the maximum top height rarely reached the height of 11 km, with only one category (on 1/9/2007) reaching 15 km and

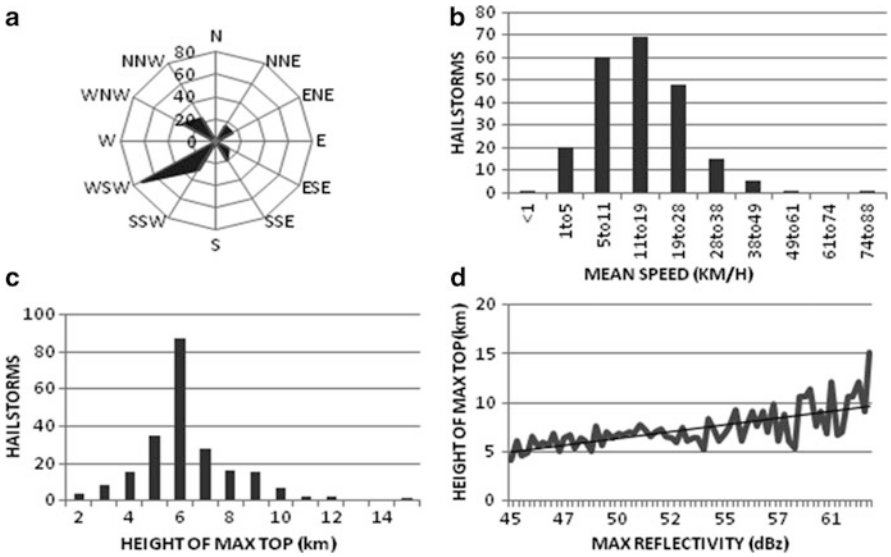

Fig. 4 Frequency of hailstorms mean direction (**a**), of mean speed (**b**), max top (**c**) and max top/reflectivity correlation (**d**) for 2006–2008

maximum reflectivity 71 dBz. The regression analysis between maximum reflectivity values and heights of maximum tops (Fig. 4d) exhibits a positive trend with R = 0.68. It is worth noting the increased deviations (above 52 dBz) towards the highest values.

2.3 Hailstorm Differences Over Two Distinct Areas

Two distinct areas (P3 and P4, see Fig. 1), with respect to their geomorphology, but of the same size, were chosen, in order to study and compare their respective hailstorm characteristics. Area P3 has a low altitude and is located close to the center of the protected area, where 20 hailstorm cells were recorded and studied. Also, the P4 mountainous area is located to the west side of the protected area, where 67 hailstorm cells were recorded and studied. Figure 5 depicts the frequency of occurrence of the hailstorm cells as a function of maximum reflectivity values (Fig. 5a) and the mean speed of their motion (Fig. 5b), for the plain (P3) and orographic (P4) hailstorm cells. As expected, the cells over the mountainous area exhibit broader spectra for maximum reflectivity values and mean speed motion. The frequencies appear to be higher for values between 45 and 60 dBz, with the peak occurring at 46 dBz, while the maximum reflectivity reaches 67.5 dBz. This variation exhibits quite a few similarities with the one corresponding to the whole protected area (Fig. 3a). On the contrary, the frequency of the hailstorm cells

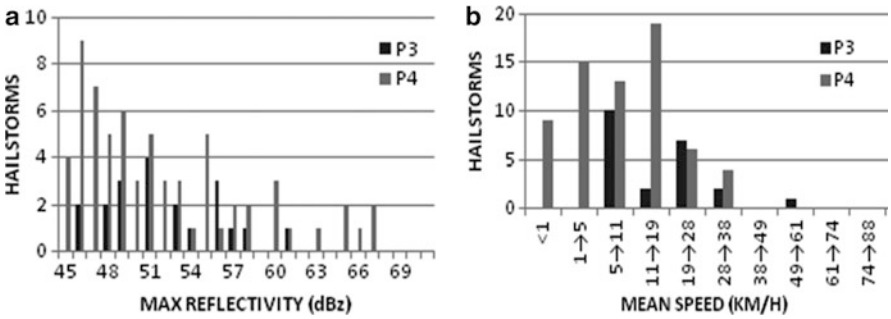

Fig. 5 Frequency of hailstorms as a function of maximum reflectivity (**a**) and their mean speed (**b**), for the plain (P3) and orographic (P4) hailstorm cells, for the examined period 2006–2008

over the plain area (P3) peaks at 51 dBz and between 5 and 11 km/h. The recorded maximum reflectivity and larger mean speed of cell motion were 61 dBz and 49.4 km/h.

3 Conclusions

Although the variation of hailstorm cells through the examined years (1998–2008) does not show important range for the categories A and B, the month with the highest activity is June. This is in good agreement with earlier studies (Sioutas et al. 2007), reporting 26% of hailstorms occurring in June and 25% in May. A study with more homogeneous areas, with respect to hailstorm cells development, life time and motion, would be very useful and quite indicative for hailstorm characteristics in these areas. It is concluded that the protected area is frequently affected by orographic hailstorms that are developed over its west side. These orographic hailstorms are more severe than the ones over the plain, and their speed does not exceed 36 km/h during the study period.

References

Ćurić M, Janc D (1992) Mountain influence on the areal characteristics of types of convective precipitation. Theor Appl Climatol 45:71–76. doi:10.1007/BF00865997

Foris D, Karacostas T, Flocas A, Makrogiannis T (2005) Hailstorm in the region of Central Macedonia, Greece: a kinematic study. Meteorol Z 15(3):317–326. doi:10.1127/0941-2948/2006/0134

Karacostas TS (1984) The design of the Greek NHSP, In: Proceedings of the 9th conference on weather modification. American Meteorological Society, Park City, UT

Karacostas TS (1989) The Greek National Hail Suppression Program: design and conduct of the experiment. In: Proceedings of 5th WMO scientific conference on weather modification and applied cloud physics, Beijing, China, pp 605–608

Pinto J, Kessinger C, Hendrickson B, Megenhardt D (2007) Storm characterization and short term forecasting using a phase array radar.NCAR/research applications. In: Proceedings of 33rd conference on radar meteorology, Cairns, Queensland, Australia

Sherwood S, Minnis P, McGill M (2004) Deep convective cloud-top heights and their thermodynamic control during CRYSTAL-FACE. J Geophys Res 109:D20119. doi:10.1029/2004JD004811

Sioutas M (1999) Contribution to the study of hailstorms in central Macedonia. Ph.D. dissertation, Aristotle University of Thessaloniki

Sioutas M, Meaden G, Webb J (2007) Hail frequency distribution and intensity in Northern Greece. Atmos Res 93:526–533. doi:10.1016/j.atmosres.2008.09.023

The Impact of Topography on the Precipitation Regime over Epirus, NW Greece, During the Cold Period of the Year

O.A. Sindosi, A. Bartzokas, V. Kotroni, and K. Lagouvardos

Abstract The aim of this study is to investigate the impact of orography on the distribution and the amount of precipitation in Epirus, NW Greece, during the cold period of the year. For this reason, a precipitation event with typical wintertime characteristics is considered; i.e. a low pressure system centered northwest of Epirus and moving southeastwards, generating southerly winds and causing extended and heavy precipitation over the area. The case is firstly simulated by applying the numerical meteorological model MM5 in a high resolution grid (2×2 km), in which the actual topographical data are incorporated. Then, the model is applied again incorporating modified data of topography, in order to study the differentiations in the fields of the most important meteorological parameters, which are directly related with precipitation. According to the results, the modification of topography changes the flows near the surface, causing a displacement of the convergence zones and thus a new distribution of vertical velocities, which, combined with the new water vapor field, has a direct impact on precipitation.

1 Introduction

The impact of mountains on air flow and precipitation regime has been investigated either theoretically by using simplified flow systems and trying to solve the basic equations (Smith 1979; Houze 1993) or by using numerical models which simulate the various atmospheric processes (Doyle and Durran 2001; Pathirana et al. 2005;

O.A. Sindosi (✉) • A. Bartzokas
Laboratory of Meteorology, Department of Physics, University of Ioannina, Ioannina 45110, Greece
e-mail: osintosi@cc.uoi.gr

V. Kotroni • K. Lagouvardos
Institute of Environmental Research and Sustainable Department, National Observatory of Athens, Athens 15236, Greece

C.G. Helmis and P.T. Nastos (eds.), *Advances in Meteorology, Climatology and Atmospheric Physics*, Springer Atmospheric Sciences,
DOI 10.1007/978-3-642-29172-2_41,

Minder et al. 2008). In the vast majority of the latter studies, the numerical models use idealized settings, as for example constant wind and humidity fields, which provide the distribution of precipitation around isolated and symmetrical obstacles with certain geometric characteristics. But, in reality, the cases are much more complex. It is not so evident how and to what extent the various mountain ridges affect the precipitation amounts and precipitation distribution in an orographically complex area. It is obvious that, in many cases, the real weather conditions may differ significantly in time and space from a theoretical approach, since the various obstacles are neither symmetric nor isolated. Thus, the only way to assess the contribution of mountains on the spatiotemporal distribution of precipitation is to perform sensitivity experiments with numerical models.

In this work, the mesoscale numerical model MM5 is used in order to investigate the role of topography in a precipitation case with typical wintertime characteristics over Epirus, NW Greece. Epirus is frequently called "the gate of the cyclones to Greece" as the eastwards travelling Mediterranean depressions, in combination with its mountainous topography favour the development of severe precipitation events and thunderstorms. In order to meet the aims of this study, the selected case is simulated using the actual topography and then a sensitivity test with reduced elevations is performed. Thus, the differentiations of the fields of some of the most important meteorological parameters, which are related to precipitation, are studied in order to understand how the elevation of the mountains affects the flow around them, the humidity distribution and thus the precipitation.

2 Data and Methodology

The case under study is the precipitation event of 3 November 2009. This day presents almost all the typical wintertime synoptic characteristics for central and eastern Mediterranean (see e.g. Trigo et al 2002), i.e. a low pressure system centered northwest of Greece is moving southeastwards causing southerly winds and transferring humid air masses over Epirus (Fig. 1).

These conditions are responsible for the high amounts of precipitation recorded over the area by a network of 14 automatic meteorological stations. Specifically, the rain started at the beginning of the day and considerable amounts fell during its second 6-h interval, when precipitation exceeded 40 mm in half of the meteorological stations. Thereinafter, precipitation was reduced and increased again during the last 6-h interval of the day. For the simulation of the atmospheric conditions, of the event, the non-hydrostatic model MM5 is applied by using as initial and boundary conditions, 6-hourly analysis data, provided by ECMWF. These data are interpolated in a coarse grid with 24 km horizontal grid increment, which covers most of Europe and the Mediterranean using 23 σ-levels in height. The model runs by utilizing the microphysical scheme described by Schultz (1995) and the MRF scheme of Hong and Pan (1996) for the parameterization of atmospheric boundary layer. The outputs of this simulation are used on a subsequent run, with a finer grid

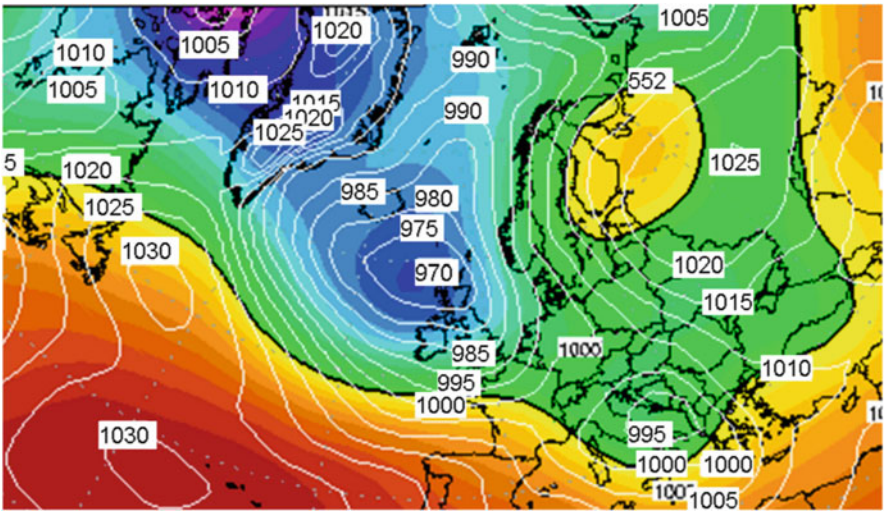

Fig. 1 The synoptic conditions on 3 November 2009 (12:00 UTC). Sea level pressure (hPa) and 500 hPa height (gpdm). (http://www.wetterzentrale.de/topkarten/fsrea2eur.html)

spacing, covering Greece (8 × 8 km), following the one-way nesting technique. Finally, a third simulation is carried out using the outputs of the latter for the finest grid of 2 × 2 km, which covers the region of Epirus. The topography fields are derived from a terrain data file with 30 arc sec resolution provided by the U.S. Geological Survey (USGS). In order to simulate the case as best as possible, various sensitivity experiments are performed, searching for the model initialization time and the convective parameterization scheme (CPS) leading to the smallest verification errors in terms of precipitation. Then, the topography of Epirus is modified southwest of an axis being parallel to Pindus and passing from Ioannina city (39° 40′ lat., 20° 51′ long.), which is located in the central plateau of Epirus and relatively close to the mountain range. All elevations, southwest of the axis and above 480 m are reduced to 480 m, which is the altitude of Ioannina city. Thus, a new simulation, with modified topography, is carried out by using the initialization time and the CPS which gave the best results in the previous stage of the study.

3 Results

The sensitivity experiments show that the case is simulated best if the initialization time is set at 18:00 UTC of 02-11-2009, i.e. approximately 12 h before the start of the intense rain. Also, best results are obtained when the Kain-Fritsch 2 parameterization scheme (Kain 2004) is applied even in the finest resolution grid. The distributions of precipitation over Epirus for the 6-h time interval 06:00–12:00

UTC of 03-11-2009 (not shown) resulted from the simulations of the case with (a) the actual (NRD) and (b) the modified (RD) topographical data show that the maxima are more intense in the NRD simulation while there are areas between them where the rain presents low values (rain shadows). The maxima in the RD simulations are generally weaker and in many cases shifted because the modification of the altitude of the mountains affect the wind field and as a consequence the areas of convergence and convection. In general, the rain field is more homogeneous in RD type as it was expected.

Because of the continuous changes of the atmospheric conditions during the 6-h interval, the distribution of the accumulated precipitation, for this period, cannot be directly connected with the fields of some meteorological parameters as, for example, wind, vertical velocities, humidity, etc. For this reason, the study is also carried out for each 2-h interval. In order to reveal the role of certain mountains on precipitation, the research is focused on the areas where the differentiations of the two types of topography are significant. Figure 2a presents the NRD rain distribution (06:00–08:00 UTC) and Fig. 2b the differences in precipitation between NRD and RD simulations. In Fig. 3c the actual topography for Epirus is shown as well as the three areas in which the research is focused.

In Fig. 3, precipitation forecast is presented for 06:00–08:00 UTC for a "Test Area" (see Fig. 2c) for the two simulations. The sub-areas presenting maximum differences are encircled. The maximum of rain which, in the NRD simulation, is located over sub-area Z, is moved slightly northeastwards, in sub-area 5, where, in the RD simulation, it appears more extended but weakened. In sub-area 6, the rain increases while the maximum at the windward side of Acarnanian Mountain (sub-area H), weakens substantially (about 20 mm) in the reduced altitude simulation.

In order to associate precipitation results with other important meteorological fields, the distribution of vertical velocities at 700 hPa level (Fig. 4a, d) and precipitable water (Fig. 4c, f) at 08:00 UTC are shown for the Test Area. In these figures the 10-m wind is also presented. Figure 4b and e, present the cross-section of vertical velocities along Line 1 as well as the wind projection on the corresponding vertical plane, for the NRD and RD simulations respectively. Line 1 is selected to be as parallel as possible to the prevailing wind in this site. As it can be seen in Fig. 4b, the Acarnanian Mountain forces the flow to uplift in NRD simulation (relatively high vertical velocities in the windward side), resulting in water vapour condensation. This condition combined with the relatively high amounts of humidity in the area (Fig. 4c) produces the maximum of rain. The humidity is rapidly reduced on the top of the mountain. Despite the fact that the southerly flow at the northern lee side of the mountain convergences (Fig. 4a) causing uplift, humidity is not enough to produce high rainfall, creating a rain shadow. In RD simulation, the uplift in the windward side weakens, causing a decrease in the rain in this area. Thus, the humidity at the top and in the lee of the mountain is higher, producing a smaller rain-shadow than in NRD.

When the topography is modified, it is seen (Fig. 4a, d) that, the vertical velocities in sub-area Z are reduced and the main core is moved northeastwards,

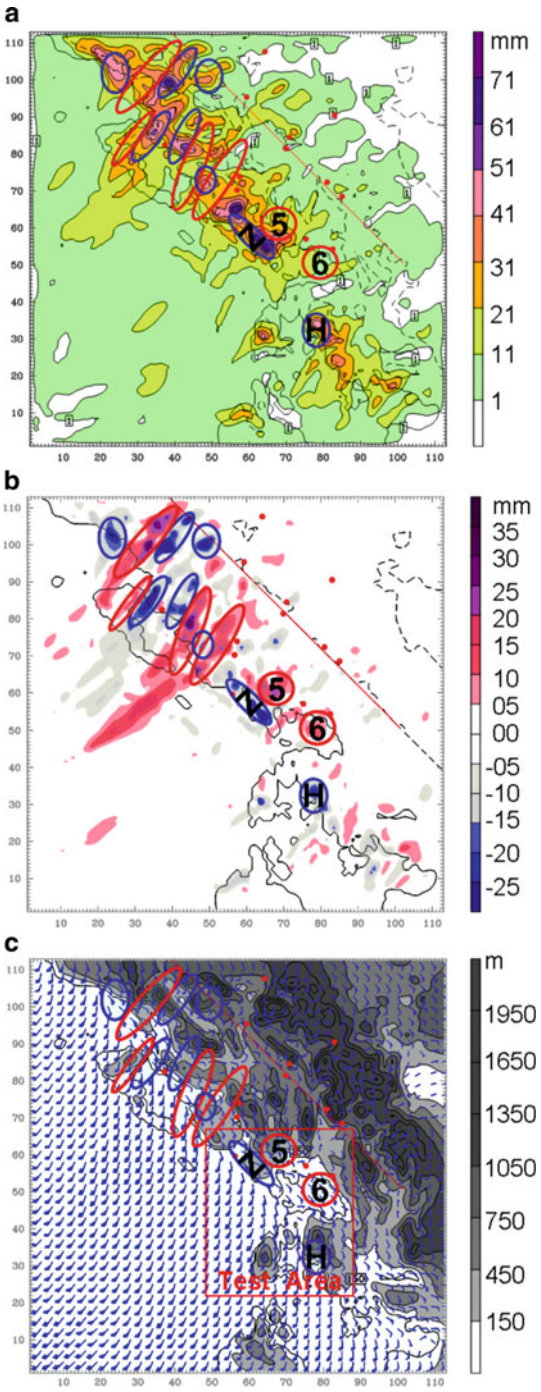

Fig. 2 (**a**) Spatial distribution of precipitation forecast (06:00–08:00 UTC) using the original elevation, (**b**) precipitation differences (mm). *Red colours* indicate areas where the modification of the altitudes causes an increase in precipitation while *blue colours* areas where the modification causes a decrease. The *red line* represents the axis that separates the modified from the unmodified area in the RD type of topography, (**c**) topography of Epirus and 10-m wind field at 06:00 UTC 03-11-09. The Test Area is also indicated

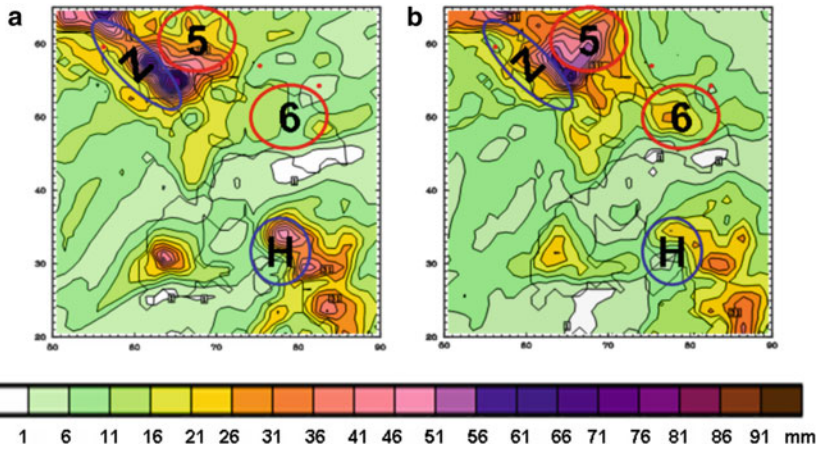

Fig. 3 Spatial distribution of precipitation forecast (06:00–08:00 UTC) in the Test Area (see Fig. 2), with: (**a**) the actual and (**b**) the modified topography. With the modification of topography, rain is reduced in the areas encircled by *solid curves*, while it is increased in the areas encircled by *dashed curves*

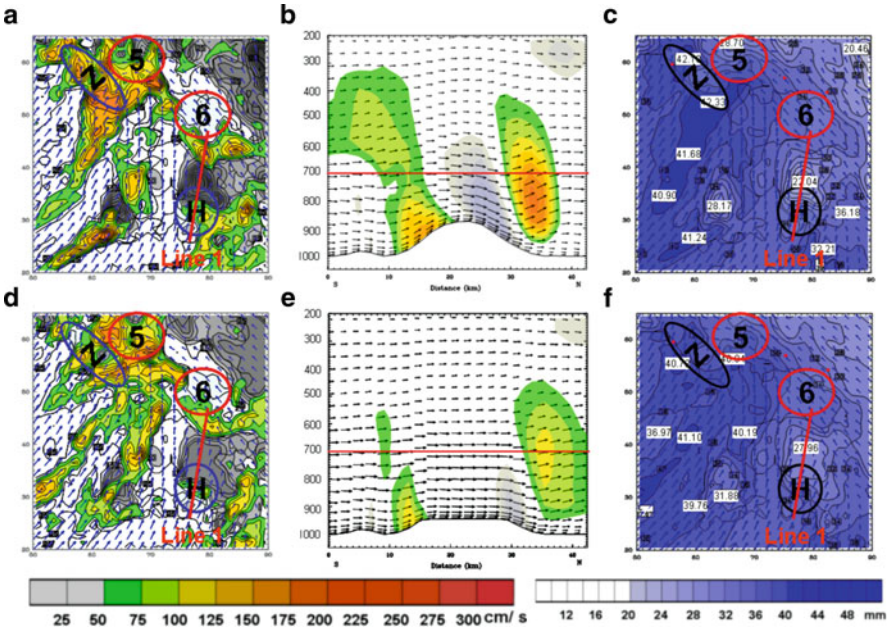

Fig. 4 08:00 UTC 03-11-2009: (**a**) vertical velocities at 700 hPa and 10-m wind for the Test Area, (**b**) cross section for vertical velocities and wind projection on the vertical plane of Line 1, (**c**) spatial distribution of precipitable water for the Test Area, (**d**), (**e**) and (**f**) as in (**a**), (**b**) and (**c**) but after the modification of topography

causing a similar movement in the rain maxima (Fig. 3a, b). In other words, the modification of the terrain (mainly north of sub-area 5) affects the air flow near the surface displacing the zones of convergence and transmitting more humidity inland.

4 Conclusions

In this work, the role of topography on the precipitation distribution over Epirus was investigated. A typical case of the cold period of the year with high precipitation over N.W. Greece, was analytically investigated, by incorporating in the numerical model MM5 firstly, the actual topographical data and then data of modified topography. The results show that when the height of the mountains is reduced, the precipitation field is more homogeneous, with weakened maxima on the windward side and above the ridges of mountains. As a consequence, less rain falls in these areas and the humid air can easily pass to the lee side eliminating the rain shadows. Finally, the modification of topography changes the flows near the surface, causing a displacement of the convergence zones and thus a new distribution of vertical velocities, having a direct impact on precipitation distribution.

Acknowledgments The research work is co-funded by the European Union – European Social Fund (ESF) & National Sources, in the framework of the program "HERAKLEITOS II" of the "Operational Program Education and Life Long Learning" of the Hellenic Ministry of Education, Life Long Learning and religious affairs.

References

Doyle JD, Durran DR (2001) The dynamics of mountain-wave induced rotors. J Atmos Sci 59:186–201

Hong S, Pan H (1996) Nonlocal boundary layer vertical diffusion in a medium-range forecast model. Mon Weather Rev 124:2322–2339

Houze RAJ (1993) Cloud dynamics. Academic, San Diego

Kain JS (2004) The Kain-Fritsch convective parameterization: an update. J Appl Meteorol 43:170–181

Minder JR, Durran DR, Roe GH, Andres AM (2008) The climatology of small-scale orographic precipitation over the Olympic Mountains: patterns and processes. Q J R Meteorolog Soc 134:817–839

Pathirana A, Herath S, Yamada T (2005) Simulating orographic rainfall with a limited-area, non-hydrostatic atmospheric model under idealized forcing. Atmos Chem Phys 5:215–226

Schultz P (1995) An explicit cloud physics parameterization for operational numerical weather prediction. Mon Weather Rev 123:3331–3343

Smith RB (1979) The influence of mountains of the atmosphere. Adv Geophys 21:87–230

Trigo IF, Bigg GR, Davies TD (2002) Climatology of cyclogenesis mechanisms in the Mediterranean. Mon Weather Rev 130:549–569

Meteorological Conditions Associated with Strong Tornadoes in Greece

M. Sioutas, P.T. Nastos, I.T. Matsangouras, and H.A. Flocas

Abstract Tornadoes are associated with deep convection and severe thunderstorm activity, representing extremely dangerous phenomena. Strong tornadoes, considered those of an intensity of F2 (Fujita scale) or T4 (TORRO scale) or greater, although rarely occur in Greece, however can pose a significant hazard to the community, including property, infrastructure, agricultural damage, injuries even and fatalities. In this study, an analysis is performed of meteorological conditions associated with strong tornado occurrences during the last decade, a period with systematic tornado recording in Greece. Selected cases include a sample of strongest and most damaged tornado cases as have been evaluated in the 12-year Greek tornado database (2000–2011). Synoptic and mesoscale features favourable for the development of such severe incidents, including upper-air patterns, thermo dynamic, wind parameters and convective instability indices, are examined. Thus, a contribution is offered to increase the ability to identify and anticipate such extreme weather events, critical to the mission of operational meteorologists.

1 Introduction

Tornadoes are one among the most severe weather phenomena, with high impacts on society in terms of damage to property, infrastructures, agriculture, even in injuries and loss of life. About 30 events, including tornadoes, waterspouts and funnel clouds have been recorded in Greece, in 19 days on average, during the last decade (2000–2009), a period of systematic tornado data recording (Sioutas 2003, 2011). Based on this database, the annual tornado number is determined as 1.4 days

M. Sioutas (✉)
ELGA – Meteorological Applications Centre, Airport Macedonia, Thessaloniki, Greece
e-mail: sioutas@elga.gr

P.T. Nastos • I.T. Matsangouras • H.A. Flocas
National and Kapodistrian University of Athens, Athens, Greece

C.G. Helmis and P.T. Nastos (eds.), *Advances in Meteorology, Climatology and Atmospheric Physics*, Springer Atmospheric Sciences,
DOI 10.1007/978-3-642-29172-2_42,

per 10^4 km^2, a rather high frequency between European countries (Homar et al. 2001; Dotzek 2003; Tyrrell 2003; Giaiotti et al. 2007). Tornadoes are much localized and short-lived phenomena, occurring during severe thunderstorm activity and hence difficult to detect and record. The tornado database has been started developing since 2000 in Greece, relying on observations and reports from various sources including tornado damage information from ELGA Organization (Hellenic National Agricultural Insurance), other services and authorities, amateurs and the media and internet sources (Sioutas 2002, 2003). These databases are subject to some biases, such as population density biases and a more frequently reporting of the intense and most damaged events. In this study, an analysis is presented of meteorological environments associated with strong tornado occurrences, based on synoptic data, thermodynamic parameters and severe weather indices. Section 2 contains the data and the methodology, Sect. 3 the results of analyses of synoptic and mesoscale features favour for the development of such severe incidents, and in Sect. 4 a summary and conclusions are provided.

2 Data and Methodology

Atmospheric circulation patterns leading to strong tornado formation were identified according to a four synoptic typing scheme, namely: South west flow (SW), shortwave trough (SWT), closed low (CLOSED) and longwave trough (LW). This classification was based on the 500 hPa level circulation patterns in conjunction to surface features as it has been described in Sioutas and Flocas (2003) and Sioutas and Keul (2007). Radiosonde data closest in time and space, preferably upwind to the tornado location were used. Synoptic maps were extracted by NOAA (National Oceanic Atmospheric Administration-Global Data Assimilation System), radiosonde data were gathered by the University of Wyoming (www.uwyo.edu) and further analyzed by using the SHARP workstation program (Hart and Korotky 1991). In Table 1, a list of the strong tornado events studied is provided.

3 Results

3.1 Synoptic Environment

Southwest flow (SW) and short wave trough (SWT) were the dominant synoptic types followed by CLOSED type, for the strong tornado 10 cases examined. Similar distributions have been determined for the 10-year Greek tornado database (2000–2009), with SWT (Short Wave Trough) and SW (south west) synoptic types accounting for 74% and CLOSED (Closed Low) and LW (Longwave trough) types for the 24% of the total tornado cases (Sioutas 2011).

Table 1 Strong tornado dates, locations and intensity by using of F (Fujita) and T (TORRO-Tornado and Storm Research Organization) tornado scales

Strong tornado event	Date	Location	Intensity level F (Fujita) and T (TORRO) scale
1	19 November 2000	Issos, Kerkyra Isl.	F2-3 (T5-6)
2	16 December 2001	Lassi, Kefalonia Isl.	F2-3 (T5-6)
3	11 July 2002	Mikro Monastiri, Thessaloniki	F2 (T4-5)
4	6 November 2002	Monemvasia, Lakonia	F2 (T4)
5	19 June 2003	Amaliada, Ilia	F3 (T6-7)
6	19 July 2003	Kefalovryso, Larissa	F2 (T4)
7	5 May 2004	Marathoupoli, Messinia	F2 (T4)
8	26 January 2005	Orfani, Kavala	F2-3 (T5-6)
9	6 November 2007	Mandriko, Rhodes Isl.	F2 (T5)
10	14 October 2010	Kythnos Isl., Cyclades	F2-3 (T5-6)

Synoptic settings of 500 hPa contours with Convective Available Potential Energy (CAPE) values and 250/300 hPa contours with isotachs, are displayed in Fig. 1 for two tornado events (numbered 8 and 9 in Table 1). On 26 January 2005 at 17:30 UTC (19:30 local time) an F2-3 (T5-6) tornado occurred in Orfani, Kavala, northern Greece. SW flow was the synoptic type prevailed on 26 January 2005 18 UTC, with a CAPE of 100–200 J/kg and a jetstreak left exit locating over northern Greece, favoring an increase of vorticity and vertical wind shear (Fig. 1a, b). On 6 November 2007 at 04:00 UTC (06:00 local time) an F2 (T5) tornado occurred in Mandriko, Rhodes Isl. Conditions of SWT synoptic type was prevailed (Fig. 1c), with a CAPE value of 1650 J/kg, according the 00:00 UTC Iraklion sounding. Upper level wind pattern revealed a jetstreak axis over Rhodes Sea, with a maximum wind speed of 100–110 kts (Fig. 1d).

3.2 Thermodynamic, Wind and Instability Indices

Thermodynamic, wind parameters and instability indices, based on radiosonde data are presented in Table 2. CAPE defining the vertically integrated positive buoyancy of an adiabatically rising parcel is averaged at 1,105.9 J/kg, with a minimum of 41 J/kg and a maximum of 3,276 J/kg, indicative of a thunderstorm potential but of a low likelihood for strong tornado occurrence (Thompson et al. 2003).

In conditions of severe storm activity Lifting Condensation Level (LCL) and Convective Inhibition (CIN) can be used as discriminators of non tornadic supercells and tornadoes. LCL heights less than 800 m are associated with supercell and significant tornado potential, while LCL above 1,200 m are not associated with strong tornadoes (Rasmussen and Blanchard 1998). In the data set examined, mean LCL was determined at 880.2 m, while in 5 out of 10 cases LCL heights were ranged between 230 and 599 m, indicative of an increase likelihood of supercell and strong tornado occurrence. CIN values of the tornado sample examined were

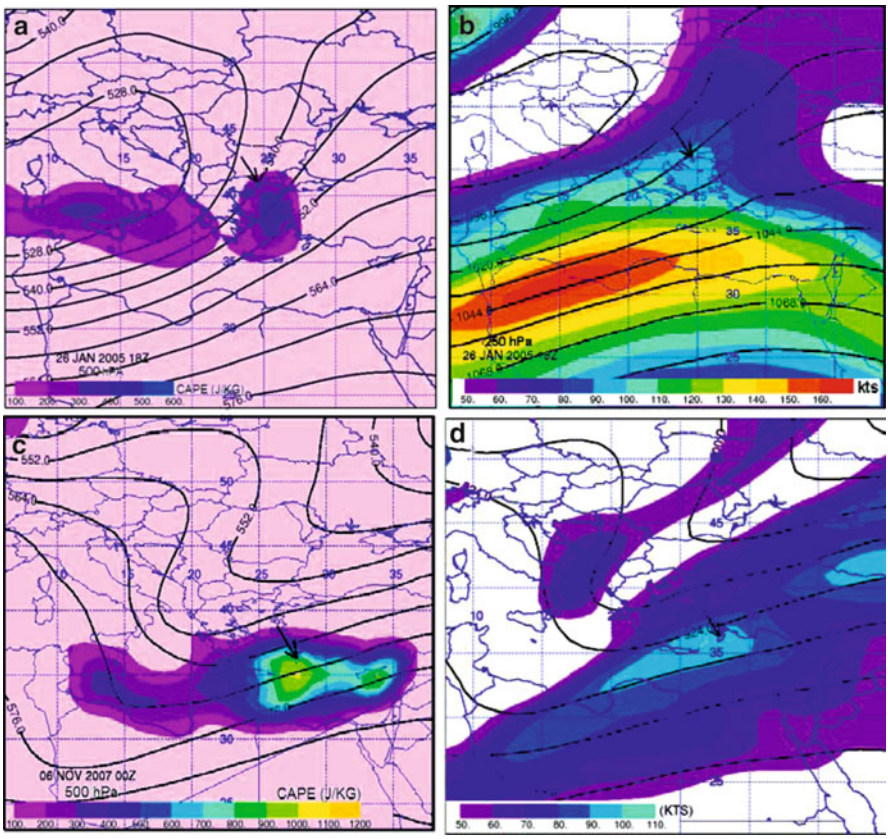

Fig. 1 500 hPa level contours (gpm) with convective available potential energy (CAPE) (J/kg), and 250/300 hPa level contours (gpm) with wind speed (kts), for strong tornado occurrences: (**a**, **b**) 26 January 2005, Orfani, Kavala, and (**c**, **d**) 6 November 2007, Mandriko, Rhodes. Tornado approximate locations are indicated by *arrows*

Table 2 A summary of thermodynamic, wind parameters and instability indices, for strong tornado environments in Greece

Parameters/indices	Mean	Min	Max	St. Dev.
CAPE (J/kg)	1,105.9	41	3,276	1,093.5
CIN (J/kg)	27	5	95	25.5
LCL (m)	880.2	230	1,767	528.9
0–2 km wind shear (10^{-3} s^{-1})	8.3	1.6	20	5.1
BRN shear (m^2 s^{-2})	55.4	4	148	45.4
BRN	83.3	0	500	157.2
0–3 km SRH (m^2 s^{-2})	157.7	−9	591	181.6
EHI	0.5	0.03	2.2	0.4
KI	32.2	23	40	4.9
LI	−3.4	−10	2	4.2
SW	−0.6	−8	4	3.7
TT	52.3	47	61	4.9

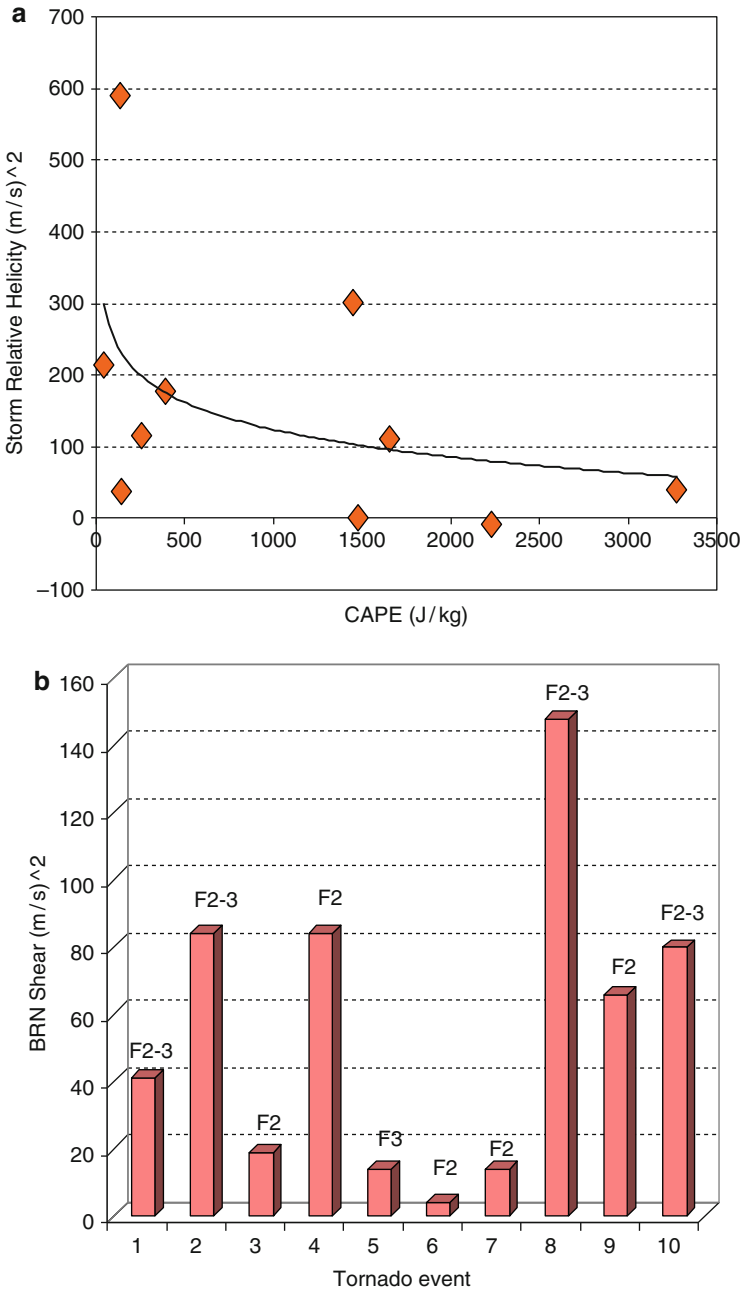

Fig. 2 (**a**) Scatter diagram of 0–3 km storm relative helicity (SRH) versus convective available potential energy (CAPE), and (**b**) Bulk Richardson number shear (BRN shear), for strong tornado events in Greece

averaged at 27 J/kg with the majority of events associated with CIN < 22 J/kg, indicating an increased likelihood for severe isolated convection.

The magnitude of the 0–2 km wind shear was greater than 6×10^{-3} s^{-1}, for 7 out of the 10 strong tornado cases examined. It implies that a horizontal vorticity present in the tornado environment had contributed to thunderstorm rotation, even with low amounts of storm relative helicity (SRH). The 0–3 km SRH was averaged at 157.7 m^2 s^{-2} with a maximum of 591 m^2 s^{-2}, and in 3 out of 10 cases with a SRH greater than 200 m^2 s^{-2} (Table 1). In Fig. 2, the relationship of 0–3 km SRH with CAPE (Fig. 2a) and the BRN shear for the tornado events, are illustrated (Fig. 2b).

Bulk Richardson Number (BRN), incorporating CAPE and vertical wind shear in the lowest 6 km, was averaged at 83.3 a value higher than that of the supercell threshold of 50 (Weisman and Klemp 1982). Mean BRN shear was 55.4 m s^{-1}, with 6 out of 10 cases exhibiting higher values than the threshold of 40 m s^{-1} for tornado occurrences (Stensrud et al. 1997). Energy Helicity Index (EHI), a dimensionless parameter combining CAPE with SRH in the lowest 3 km, is proved to be one of the best discriminators for rotating and non-rotating thunderstorms (Hart and Korotky 1991). Mean EHI was 0.5, with a maximum of 2.2, while in 3 out of the 10 strong tornado cases EHI was greater than 0.5. Conventional instability indices KI, LI, SW and TT generally were indicative of an increased instability and severe thunderstorm and tornado potential. Notable maximum values of the data sample included KI $= 40$ and TT $= 61$, with minimum values of LI $= -10$ and SW $= -8$ (Table 2).

4 Summary and Conclusions

Meteorological conditions associated with strong tornadoes in Greece, based on synoptic and mesoscale features were examined. SW flow and SWT were the dominant synoptic types with a contribution of the jetstream in increasing vorticity and vertical wind shear. A set of 12 severe weather parameters, including thermodynamic, wind and instability indices was examined for assessing of the meso- and storm-scale conditions favorable for the tornado occurrence. The 0–2 km wind shear, BRN shear, LCL and CIN were most related to the strong tornado environment for the majority of the examined cases. Following in performance, the 0–3 km SRH, EHI and the convective instability indices KI, SW, LI and TT, but were also indicative to a tornado supportive environment. These results can be useful in tornado forecasting, providing a basic guidance for identifying and assessing of the Greek tornado meteorological environment.

Acknowledgments The authors are grateful to anonymous people, media, services and authorities provided tornado information.

References

Dotzek N (2003) An updated estimate of tornado occurrence in Europe. Atmos Res 67–68: 153–161. doi:10.1016/S0169-8095(03)00049-8

Giaiotti DB, Giovannoni M, Pucillo A, Stel F (2007) The climatology of tornadoes and waterspouts in Italy. Atmos Res 83:534–541. doi:10.1016/j.atmosres.2005.10.020

Hart JA, Korotky W (1991) The SHARP workstation v1.50 users guide. National Weather Service, NOAA, US Department of commerce, 30pp

Homar V, Gaya M, Ramis C (2001) A synoptic and mesoscale diagnosis of a tornado outbreak in Balearic Islands. Atmos Res 56:31–55

Rasmussen EN, Blanchard DO (1998) A baseline climatology of sounding-derived supercell and tornado forecast parameters. Weather Forecast 13:1148–1164

Sioutas MV (2002) Damaging tornadoes in Greece: July and September 2001. J Meteorol 27:17–22

Sioutas MV (2003) Tornadoes and waterspouts in Greece. Atmos Res 67–68:645–656

Sioutas MV (2011) A tornado and waterspout climatology for Greece. Atmos Res 100:344–356

Sioutas MV, Flocas HA (2003) Hailstorms in northern Greece: synoptic patterns and thermodynamic environment. Theor Appl Climatol 75:189–202. doi:10.1007/s00704-003-0734-8

Sioutas MV, Keul AG (2007) Waterspouts of the Adriatic. Ionian and the Aegean Sea and their meteorological conditions. Atmos Res 83:542–557

Stensrud DJ Jr, Cortinas JV, Brooks HE (1997) Discriminating between tornadic and nontornading thunderstorms using mesoscale model output. Weather Forecast 13:304–326

Thompson RL, Edwards R, Hart JA, Elmore KL, Markowski P (2003) Close proximity soundings within supercell environments obtained from the Rapid Update Cycle. Weather Forecast 18:1243–1261. doi:10.1175/1520-0434(2003) 018<1243:CPSWSE>2.0.CO;2

Tyrrell J (2003) A tornado climatology for Ireland. Atmos Res 67–68:671–684

Weisman ML, Klemp JB (1982) The dependence of numerical simulated convective storms on wind shear and buoyancy. Mon Weather Rev 110:504–520

An Attempt for Teaching Meteorological Instruments to the Students of Agriculture by Using Self-Constructions

S. Spanos and X. Vatsios

Abstract The paper is a concise description of an attempt to teach laboratory meteorology in the school of agriculture at the University of Thessaly by using self-made meteorological instruments. After a thorough description of the operational principles and an exhibition of model constructions, students were asked to repeat the construction using ordinary materials and simple tools. A calibration procedure and sample measurements were also required in order to complete their project. Increased enthusiasm and interest from the students was especially encouraging for the future repetition of the attempt.

1 Introduction

Teaching of elementary meteorology in the Greek Universities incorporates a laboratory part (Hofstein and Lunetta 1982) in which students are familiarized with basic instruments and measurement procedures. Many of these instruments are still the traditional mechanical instruments that were used decades or centuries ago. This seems to be controversial with instrument evolution which has turned the old infrastructure to electronic devices. In modern instrumentation of meteorological stations the shrinking of the electronic sensors and the integration with data loggers produced small devices in which measurements are automated. This evolution has led to cheaper, more reliable and easy to maintain meteorological stations. On the other hand, this evolution has obscured the physical principles on which measurements are based. For a student with elementary knowledge of physics these devices are "black boxes" which receive and store data. It is therefore

S. Spanos (✉)
School of Agriculture, University of Thessaly, Volos 38446, Greece
e-mail: Seraf@sch.gr

X. Vatsios
EKFE Magnisias, Volos, Greece

C.G. Helmis and P.T. Nastos (eds.), *Advances in Meteorology, Climatology and Atmospheric Physics*, Springer Atmospheric Sciences,
DOI 10.1007/978-3-642-29172-2_43,

of great pedagogical value for students to become familiarized with traditional instruments and the measurement procedures. The problem has been realized by the majority of university schools which incorporate in their curricula the teaching of traditional instruments (Flocas 1998; Karapiperis 1966).

These instruments, which keep the names of their inventors, guide the students to discover the physical principles and laws on which measurements are based. Moreover, the historical value (Seroglou and Koumaras 2008) of these instruments introduces the student to the evolution of ideas in physics. Furthermore, the traditional instruments are still operational in many stations as a reference and for the continuity of the of time series. The construction simplicity of the traditional instruments offers the obvious advantage of an easy reproduction (Bohren 2001) with ordinary materials and simple tools. Based on this fact a series of instrument substitutes have been produced and tested in the Laboratory Education Centre (EKFE) of Magnesia. The reconstruction of these instruments was proposed to the students of agriculture in the University of Thessaly as a part of their course in elementary meteorology. The introduced procedure and a first evaluation of the results is presented in this paper. A short description of the motivation on which this attempt is based follows. In the third paragraph a brief description of the self-constructions is presented. In the fourth paragraph the grading of student's constructions is described and finally conclusions are drawn.

2 Motivation of the Attempt

Although the school of agriculture in the University of Thessaly owns a number of automatic meteorological stations, it does not operate a traditional meteorological station. As a result, students of meteorology were asked for their practical training to access the data from automatic stations in order to extract information and draw conclusions. This process was not popular among the students. On the other hand many students have shown a profound lack of understanding about the physical principles on which measurements were based. In the final tests many students for example believed that when a thermometer is exposed to the sunshine it measures the air temperature. For other students it was hard to realize that water volume per unit of collecting surface provides the rain depth.

A detailed study on the preconceptions that ordinary life supplies the students of atmospheric physics is not available in literature. However, the problem exists and cannot be addressed through lectures and demonstrations (Roth et al. 1997). In order to confront a well-established preoccupancy, only approaches based on new experiences can help. It has been proved that constructing an instrument from scratch and calibrating it in order to become operational is a very strong experience (Michaelides and Tsigris 2004). Such an experience has the power to demolish preoccupancy and restructure the previously gained experiences as a new formation. This is how knowledge is built according to constructivism.

Ordinary meteorological instruments were described during the lectures and each description was also accompanied by an exhibition of a constructed substitute. A calibration procedure followed the exhibition and at the end of the lectures, students were asked to select one of the proposed instruments for self-construction. When a prototype instrument was lacking, instead of the calibration procedure, students were asked to produce a series of measurements (Tsigris and Michaelides 2002) that can be easily reproduced by the teacher. Finally, the delivered self-constructions were graded on the basis of the accuracy of measurements and secondarily on robustness of the construction, aesthetics and innovation (Michaelides and Tsigris 2004).

3 Description of Self-Constructions

The first construction is a reproduction of an Arago-Davy actinometer by using twin thermometers (Fig. 1). One of these thermometers, which measure in the range between −10°C and 110°C and can easily be obtained in the market, was modified by blackening the Hg tank with the flame of a candle (left one in Fig. 1). When the combination is exposed to the sun there is always a difference in the readings which

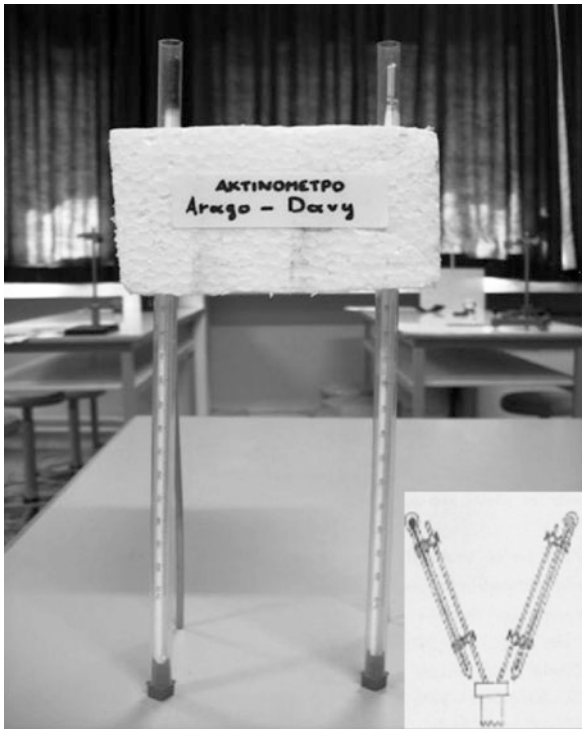

Fig. 1 A reproduction of an Arago-Davy actinometer (Model instrument at *lower right*)

Fig. 2 The reproduction of a water thermometer (Model instrument at *lower right*)

is proportional to the intensity of the solar radiation. During the night or when the combination is in the shade the readings are equal and the difference is zero.

The second construction is a water thermometer (Fig. 2) which is based on thermal expansion of a colored water mass inside a straw. The construction is calibrated with the help of an ordinary alcohol thermometer and its accuracy depends on variations of the atmospheric pressure. When atmospheric pressure remains constant, it is relatively accurate. A refrigerator and a boiler are used for the calibration of the instrument.

The third construction is a reproduction of a simple rain gage (Fig. 3) by using a plastic water bottle. The upper part of the bottle is cut off and adapted to the rest of the bottle with its neck upside down. Calibration is performed by adding measurable water volumes and measuring the corresponding water depth. The surface of the collecting area is also calculated in the process.

The forth construction is an evaporation meter of "wild" type (Fig. 4) which is a self-construction based on an electronic weighting device with a water tank on it. The day by day difference in weight readings provides an estimation of evaporation capacity of the atmospheric environment. To calculate the evaporation depth, mass difference is transformed to volume difference with the help of water density and the result is divided by the evaporating surface.

Fig. 3 The reproduction of a rain gage (Model instrument at *lower right*)

The fifth self-construction is an anemometer of "Daloz" type (Fig. 5). It consists of a wooden mast, which is able to revolve around a vertical axis, with a semi-circle goniometer on the top of it and full-circle goniometer at the bottom. A small Styrofoam piece with a spindle shape is hanged from the centre of the semi-circle goniometer through a thin strand. The angle between the vertical axis and the strand depends on wind speed. The direction on the full-circle goniometer is the wind direction.

4 Results

For the majority of the students it was the first time that they tried to construct something which is above all functional. Therefore, they expressed their enthusiasm and satisfaction. Although the grading of the construction contributed only a 20% to the final grading, their participation reached the 90%. The feeling that they are contributing to a new, innovating means of teaching was probably a strong motivation. In contrast with our initial expectations female students were more enthusiastic than the male ones. The students delivered their self-constructions along with a report containing the calibration curve and/or sample measurements.

Fig. 4 The reproduction of an evaporation meter (Model instrument at *lower right*)

There were several constructions with functional problems and bad calibration. For example most of the constructed anemometers suffered from friction problems in the revolving vertical mast and lubrication was required. Other students who constructed the water thermometers had to cope with the non linear response of water expansion to temperature variation. All these problems were discussed at the end of the semester where everybody had the opportunity to see and examine the constructions of the others.

5 Conclusions

1. We conclude that the attempt showed several encouraging elements of learning motivation and stimulated the interest of the students on the subject.
2. In order to investigate the learning outcome, a better formalization of the entire procedure has to be established.
3. As a final step the design and carry out of an evaluation experiment is required to investigate the knowledge transformation that the students incorporated. A random separation of the students in two groups, from which the first attends only lectures and exhibitions and the second delivers the calibrated self-constructions, is a fine proposal in the design of such experimentation. In this case the evaluation will be based on groups performance differences.

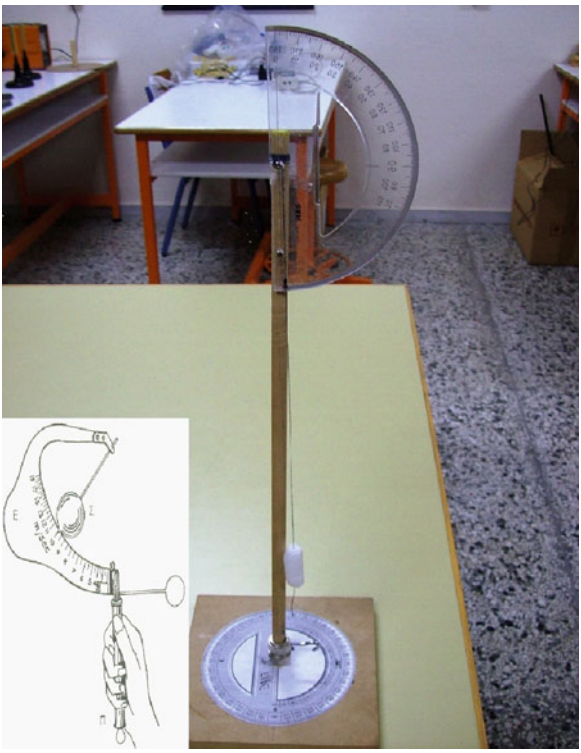

Fig. 5 The reproduction of a "Daloz" anemometer (Model instrument at *lower left*)

References

Bohren C (2001) Clouds in a glass of beer. Simple experiments in atmospheric physics. Dover Publications Inc., Mineola, NY

Flocas A (1998) Laboratory and preparatory exercises in meteorology and climatology. Ziti Publications, Thessaloniki

Hofstein A, Lunetta VN (1982) The role of the laboratory in science teaching: neglected aspects of research. Rev Educ Res 52(2):201–217. doi:10.2307/1170311

Karapiperis L (1966) Practical meteorology. University of Athens, Athens

Michaelides P, Tsigris M (2004) Science teaching with self-made apparatus. In: First international conference on hands on science Hsci2004 – teaching and learning science in the 21st century, Ljubljana, Slovenia, pp 47–52

Roth WM, McRobbie C, Lucas KB, Boutonné S (1997) Why may students fail to learn from demonstrations? A social practice perspective on learning in physics. J Res Sci Teach 34:509–533. doi:10.1002/(SICI)1098-2736(199705)34:5<509::AID-TEA6>3.0.CO;2-U

Seroglou F, Koumaras P (2008) Investigating the contribution of the history of physical sciences to the didactics of physical sciences. A research model and two applications. Physics Surveillance. Contribution to the didactics of physical sciences. Greek Physicists Association Publications, pp 7–18

Tsigris M, Michaelides P (2002) Measurements with self-constructions. Experimental layouts in the didactics of physical sciences. In: Proceedings of the third panellenic conference on the didactics of physical sciences and application of new technologies in education, University of Crete, pp 442–447

Contribution to the Study of Regional Actual Evapotranspiration with the Use of Surface Energy Balance and Remote Sensing for Central Greece

M. Spiliotopoulos, A. Loukas, and H. Michalopoulou

Abstract Actual Evapotranspiration (ET_a) is one of the main components of the hydrologic cycle and a continuous effort arises in order to improve its estimation. In this study in-situ data from selected meteorological stations over central Greece are used to calculate daily ET_a values during the warm season. These values then are combined with ET_a values computed with SEBAL (Surface Energy Balance Algorithm for Land) method. SEBAL is an image-processing model comprised of 25 computational submodels that computes ET_a and other energy exchanges as a component of energy balance. A series of Landsat-7 Enhanced Thematic Mapper Plus (ETM+) satellite images were acquired and used for the estimation of ET_a on a pixel-by-pixel basis. Landsat images consist of eight spectral bands with a spatial resolution of 30 m for Bands 1–7. ET_a values generated from two different sources are then analyzed and annotated. Finally ET_a values are mapping provided a useful and efficient tool for the estimation of regional actual evapotranspiration used for water resources and irrigation scheduling and management.

1 Introduction

Regional Actual Evapotranspiration (ET_a) is one of the main components of the hydrological balance and its impact to hydrology, agriculture, forestry and environmental studies is very crucial. Very special attention is given to ET_a for water resources management to regional scale as well. ET_a is difficult to access in space

M. Spiliotopoulos (✉) • A. Loukas
Laboratory of Hydrology and Aquatic Systems Analysis, Department of Civil Engineering, University of Thessaly, Volos, Greece
e-mail: spilioto@civ.uth.gr

H. Michalopoulou
Division of Environmental Physics and Meteorology, Department of Physics, University of Athens, Athens, Greece

C.G. Helmis and P.T. Nastos (eds.), *Advances in Meteorology, Climatology and Atmospheric Physics*, Springer Atmospheric Sciences,
DOI 10.1007/978-3-642-29172-2_44,

and time because it depends on the water status and energy processes at the earth surface. These processes are highly variable and dependent on land use, relief, soil properties, climatic properties, irrigation and many other parameters. Thus, there is a special need to develop a spatio-temporal operational monitoring of ET_a especially in regional scale. ET_a computational techniques consist of hydrological, micrometeorological and climatological methodologies (Penman 1963; Priestley and Taylor 1972; Liakatas and Anadranistakis 1992; Shuttleworth 1993). Traditional methods prevailed until recent years (Tsakiris 1995), but since the early 90s where thermal infrared wavebands from satellites have been proposed for ET-mapping, satellite derived methods have been added together with Soil-Vegetation-Atmosphere Transfer (SVAT) models to the most powerful ET_a-mapping tools (Olioso et al. 1999). Satellite derived methodologies proposed the residual method where ET_a can be estimated from the estimation of available energy and sensible heat flux using surface radiation balance (Morse et al. 2004; Li et al. 2009). Surface Energy Balance Algorithm for Land (SEBAL) methodology is proposed for this study been already used in several studies in many countries around the world with high accuracy (Bastiaanssen et al. 1998a, b; Li et al. 2009). SEBALbu was originally applied in Egypt (Bastiaanssen 2000; Bastiaanssen et al. 2005) and later to other Mediterranean countries like Turkey (Bastiaanssen 2000), Greece (Alexandridis et al. 2008; Spiliotopoulos et al. 2008) and recently Cyprus (Papadavid et al. 2011).

2 Data and Methodology

In this study in-situ data from two meteorological stations over eastern Thessaly, central Greece are utilized and daily ET_a values are calculated during the growing season (May–September) of 2008 combining FAO Penman-Monteith (PM) and modified Priestley Taylor (PT) ET models. Additionally, SEBAL method is applied to time series of Landsat-7 Enhanced Thematic Mapper Plus (ETM+) satellite images (max spatial resolution 30 m) which were acquired and used for the estimation of ET_a on a pixel-by-pixel basis. Meteorological data were available from the National Observatory of Athens and Centre for Research and Technology, Thessaly (Volos and Velestino station respectively). Wind, air temperature, relative humidity data as well as radiation values used as input parameters in the SEBAL methodology and for the initial calculation of ET_a.

ENVI 4.8 and ERDAS Imagine 9.2 software are used for the interpretation and analysis of images. Erdas Modeler has been used for the computation of all the intermediate models needed for the final computation of ET_a on a pixel-by-pixel basis. The basic concept in SEBAL is the equation of surface energy balance:

$$LE = \lambda ET = R_n - H - G \quad (1)$$

where LE is the latent heat flux (W/m^2), R_n is net radiation (W/m^2), G is soil heat flux (W/m^2) and H is sensible heat flux (W/m^2). W/m^2 in latent heat flux can easily later converted to mm. R_n can be computed from the land surface radiation balance:

$$R_n = (1 - a)R_{Si} + R_{Li} - R_{Lo} - (1 - \varepsilon_o)R_{Li} \tag{2}$$

where a is surface albedo, R_{Si} (W/m^2) is incoming solar radiation, R_{Li} (W/m^2) is incoming long wave radiation, R_{Lo} (W/m^2) is outcoming long wave radiation and ε_o is broad band surface emissivity. Soil Heat Flux G (W/m^2) can be empirically estimated using a function by Bastiaanssen (2000) which is based on albedo, surface temperature and NDVI:

$$G = \left\{T_s/a\ \left(0.0038a + 0.0074a^2\right)\left(1 - 0.98NDVI^4\right)\right\} * R_n \tag{3}$$

where T_s is surface temperature in K and NDVI is the normalized difference vegetation index. The third parameter is sensible heat flux (W/m^2):

$$H = pC_p(\alpha + \beta T_s)/r_{ah} \tag{4}$$

where p is air density (kg/m^3) related with atmospheric pressure, C_p is air specific heat capacity (1,004 $Jkg^{-1}\ K^{-1}$), T_s is surface temperature in K, and r_{ah} is aerodynamic resistance to heat transport (sm^{-1}). The definition of the function dT versus T_s is maybe the most significant philosophy of SEBAL. dT is the difference between the air temperature very near the surface (at 0.1 m above the zero plane displacement height) and the air temperature at 2 m above the zero plane displacement height (Waters et al. 2002). SEBAL methodology suggests linear change in dT with T_s (Bastiaanssen et al. 1998a). Equation 4 has two unknown parameters (α and β). This is where initial values from the selection of "cold" and "hot" pixels are used. These pixels serve as a solution for defining dT versus T_s.

"Cold" pixel can be defined as a generally wet, well-irrigated crop surface with full ground cover by vegetation. It is assumed that all energy is used to evaporate water, thus there is no sensible heat flux in this pixel (H = 0 and ET = R_n – G). ET at the "cold" pixel is closely predicted by the ET rate from a large expanse of alfalfa vegetation (Bastiaanssen et al. 1998a). For the selection of "cold" pixel a very moist terrain has to be found and a pixel with high NDVI, low temperature and low albedo seems to apply this specification. On the other hand, "hot" pixel is defined as a pixel which has low NDVI, high Albedo and high temperature. "Hot" pixel can be defined as a dry, bare agricultural field. It is assumed that all the energy is used to heat the surface in such a way that there is no latent heat flux there (ET = 0). In other words, a very dry terrain is selected as a "hot" pixel. It seems that the selection of a "hot" pixel is more difficult than the selection of "cold" pixel because there is a broader range of temperatures for "hot" pixel candidates.

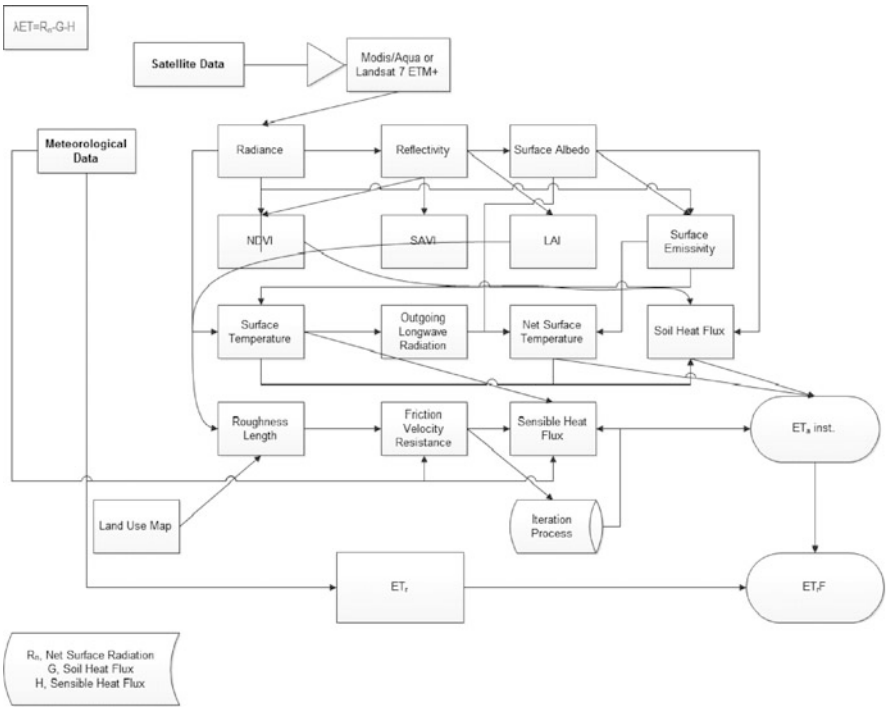

Fig. 1 SEBAL methodology flowchart

After the selection of "hot" and "cold" pixels the boundary conditions are now ready for solving the H. This is the first estimation of H assuming neutral atmospheric conditions. SEBAL, then, uses an iterative process to correct for atmospheric instability caused by buoyancy effects of surface heating applying Monin and Obukhov (1954). More details can be found at the original SEBAL papers (Bastiaanssen et al. 1998a, b). After the initial computation of H, new values of dT are computed for the "cold" and "hot" pixels and new values of α and β are derived. A corrected value for H is then computed and the stability correction is repeated until H stabilizes. The final step is the calculation of λET from (1). The evaporative fraction (ET_rF) can be defined as the fraction of the actual ET_a by the potential ET_r on an instantaneous basis assuming that is constant over the day:

$$ET_rF = ET_{a\,inst}/ET_r \tag{5}$$

REF-ET (Reference Evapotranspiration) Calculation software (Allen 2000) has been used to calculate hourly ET_r values. For this reason, air temperature (at 2 m above surface altitude), wind speed and humidity values from the available meteorological stations were utilized. Finally, the whole SEBAL methodology is depicted in Fig. 1.

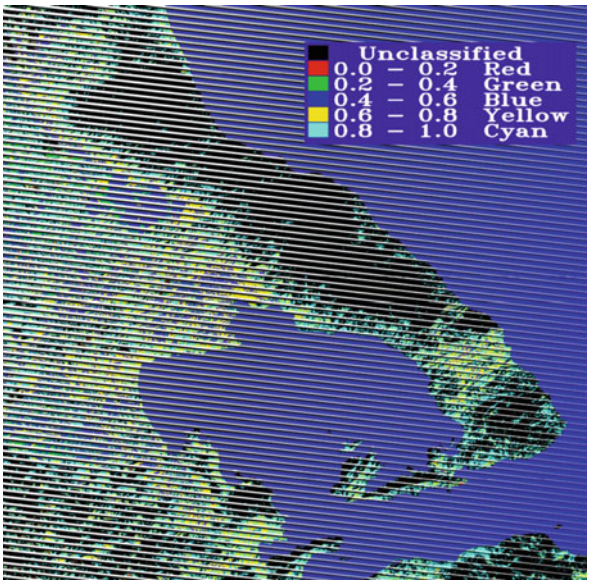

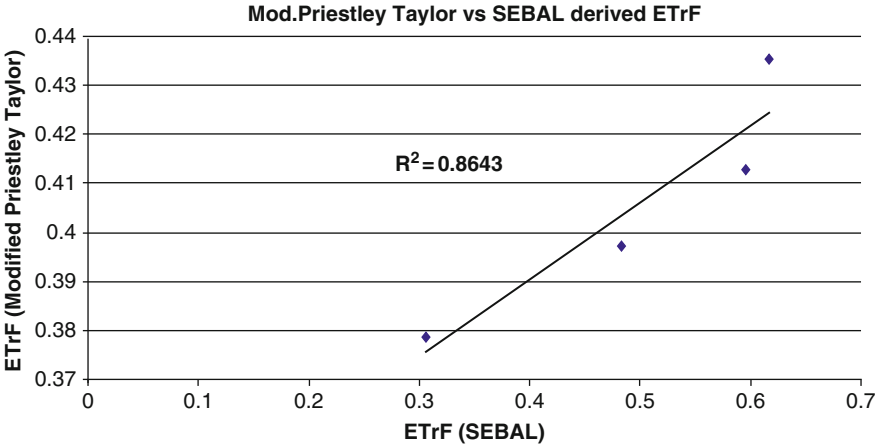

Fig. 2 (*upper*) SEBAL derived ET_rF for August 14, 2008. (*lower*) Correlation between SEBAL and modified Priestley-Taylor derived ET_rF

3 Results

After running all the above submodels, an image file indicating instantaneous ET_a is produced for each day. Applying (5) ET_rF or (K_c) coefficient is computed, considering that ET_r can easily computed for every hour applying ET-REF Software. ET_rF for August 14, 2008 is illustrated in Fig. 2 (upper). It should be reminded that ET_rF is considered constant for the duration of the day. SEBAL

methodology gives ET_rF values ranging between 0.31 and 0.62 while Modified Priestley-Taylor methodology gives values ranging between 0.38 and 0.44. Correlation between the two methodologies is very high ($R^2 = 0.86$). Figure 2 (lower) illustrates this relationship. It seems that SEBAL follows the trend of ET_rF but for some reasons overestimates ET_a.

4 Conclusions

SEBAL methodology is applied in eastern Thessaly Greece utilizing Landsat 7 ETM + image files with 30 m × 30 m spatial resolution. This case study utilizes only the free-available Landsat 7 ETM + images for the summer period of 2008. The first results seem to be very satisfactory with a very encouraging R^2. Thus, there is a strong indication that the combination of Landsat satellite data with surface meteorological data could provide an efficient tool for the estimation of regional ET_a used for water resources and irrigation scheduling and management. An overestimation of ET_a values in SEBAL maybe caused by the complex climate and soil conditions which are prevailing and affect significantly the methodology of selection the "cold" and "hot" pixels. Further work in the philosophy of SEBAL e.g. SEBTA (Gao et al. 2011) has to be applied in the future for a better ET_a computation performance adjusted to the regional Thessaly conditions.

Acknowledgments This work is supported by EFP7's "Sustainable use of irrigation water in the Mediterranean Region" (SIRIMED). The authors acknowledge National Observatory of Athens, and Centre for Research and Technology, Thessaly, Greece for the provided meteorological data as well as NASA Warehouse Inventory Search Tool for the provided satellite data.

References

Alexandridis TK, Chemin Y, Cherif I, Tsakoumis G, Galanis G, Arampatzis G, Zalidis GC, Silleos NG, Stavrinos E (2008) Improving spatial resolution of agricultural water use estimation using ALOS AVNIR-2 imagery. In: Proceedings of the ALOS principal investigators symposium, Rhodes, Greece, 8pp, 3–7 Nov 2008

Allen RG (2000) REF-ET: reference evapotranspiration calculation software for FAO and ASCE standardized equations, University of Idaho, www.kimberly.uidaho.edu/ref-et/

Bastiaanssen WGM (2000) SEBAL-based sensible and latent heat fluxes in the irrigated Gediz Basin, Turkey. J Hydrol 229:87–100. doi:10.1016/S0022-1694(99)00202-4

Bastiaanssen WGM, Menenti M, Feddes RA, Holtslag AAM (1998a) A remote sensing surface energy balance algorithm for land (SEBAL): 1. Formulation. J Hydrol 212–213:198–212

Bastiaanssen WGM, Pelgrum H, Wang J, Ma Y, Moreno J, Roerink GJ, van der Wal T (1998b) The surface energy balance algorithm for land (SEBAL): part 2 validation. J Hydrol 212–213:213–229

Bastiaanssen WGM, Noordman EJM, Pelgrum H, Davids G, Thoreson BP, Allen RG (2005) SEBAL model with remotely sensed data to improve water resources management under actual field conditions. J Irrig Drain E-ASCE 131:85–93

Gao ZQ, Liu CS, Gao W, Chang NB (2011) A coupled remote sensing and the surface energy balance with topography algorithm (SEBTA) to estimate actual evapotranspiration over heterogeneous terrain. Hydrol Earth Syst Sci 15:119–139

Li ZL, Tang R, Wan Z, Bi Y, Zhou C, Tang B, Yan G, Zhang X (2009) A review of current methodologies for regional evapotranspiration estimation from remotely sensed data. Sensors 9:3801–3853. doi:10.3390/s90503801

Liakatas A, Anadranistakis M (1992) Derived meteorological parameters: evapotranspiration, hydroscope: creation of a National Databank for Hydrological and Meteorological Information, Contractor: Department of water resources, hydraulic and maritime engineering – N.T.U. A, Report 5/4, Hellenic National Meteorological Service, Athens, 31 Dec 1992, p 31

Monin AS, Obukhov AM (1954) Basic laws of turbulent mixing in the surface layer of the atmosphere. Tr Akad Nauk SSSR Geofiz Inst 24:163–187

Morse A, Kramber WJ, Allen RG, Tasumi M (2004) Use of the METRIC evapotranspiration model to compute water use by irrigated agriculture in Idaho. In: Proceedings of the 2004 international geophysical and remote sensing symposium; Anchorage, AK

Olioso A, Chauki H, Courault D, Wigneron JP (1999) Estimation of evapotranspiration and photosynthesis by assimilation of remote sensing data into SVAT models. Remote Sens Environ 68:341–356. doi:10.1016/S0034-4257(98)00121-7

Papadavid G, Hatjimitsis D, Toulios L (2011) Estimating evapotranspiration of groundnuts using remote sensing; a modified SEBAL model under the current Cypriot conditions. Hydrol Sci J (in press)

Penman HL (1963) Vegetation and Hydrology. Technical Communication No. 53, Commonwealth Bureau of Soils, Harpenden, UK

Priestley CHB, Taylor RJ (1972) On the assessment of surface heat flux and evaporation using large-scale parameters. Mon Weather Rev 100(2):81–92

Shuttleworth WJ (1993) Evaporation. In: Maidment DR (ed) Handbook of hydrology. McGraw Hill, New York, pp 4.1–4.53

Spiliotopoulos M, Loukas, Vasiliades L (2008) Actual evapotranspiration estimation from satellite-based surface energy balance model in Thessaly, Greece. In: Fifth EGU General Assembly, Geophysical Research Abstracts 10, p 08278

Tsakiris G (1995) Water Resources: 1. Technical Hydrology (in Greek). Simmetria Publications, Athens, Greece

Waters R, Allen R, Bastiaanssen W (2002) SEBAL. Surface Energy Balance Algorithms for Land. Idaho Implementation. Advanced Training and Users Manual, Idaho, USA

The Effects of Naturally Produced Dust Particles on Radiative Transfer

C. Spyrou, G. Kallos, C. Mitsakou, P. Athanasiadis, and C. Kalogeri

Abstract Mineral dust has a profound effect on the radiative budget and energy distribution of the atmosphere. By absorbing and scattering the solar radiation aerosols reduce the amount of energy reaching the surface. In addition aerosols enhance the greenhouse effect by absorbing and emitting longwave radiation. Desert dust forcing exhibits large regional and temporal variability due to its short lifetime and diverse optical properties further complicate the quantification of the Direct Radiative Effect (DRE). The complexity of the above processes, indicate the need of an integrated approach in order to examine these impacts. To this end the radiative transfer module RRTMG has been incorporated into the framework of the SKIRON model. The updated system was used to perform a 6-year long simulation over the Mediterranean region. As it was found, the most profound effect dust clouds have in areas away from the sources is the surface cooling through the "shading" effect. The long wave radiation forcing below and above the dust cloud is considerable and drives changes in the tropospheric temperature. In general dust particles cause warming near the ground and at mid-tropospheric layers and at the same time cooling of the lower troposphere.

1 Introduction

Large amounts of mineral dust are produced from arid and semi-arid areas under favorable conditions. Aerosols interact strongly with solar and terrestrial radiation in several ways (Tegen et al. 1996; Haywood et al. 2003; Yoshioka et al. 2005; IPCC 2007; Kallos et al. 2009), also known as "Direct Aerosol Effect – DRE" (IPCC 2007). By absorbing and scattering the solar radiation, aerosols reduce

C. Spyrou (✉) • G. Kallos • C. Mitsakou • P. Athanasiadis • C. Kalogeri
Atmospheric Modeling and Weather Forecasting Group, Department of Physics, University of Athens, University Campus, Building Physics V, Athens, Greece
e-mail: cspir@mg.uoa.gr

C.G. Helmis and P.T. Nastos (eds.), *Advances in Meteorology, Climatology and Atmospheric Physics*, Springer Atmospheric Sciences,
DOI 10.1007/978-3-642-29172-2_45,

the amount of energy reaching the surface (Kaufman et al. 2005; Tegen 2003; Spyrou et al. 2010). Moreover, aerosols enhance the greenhouse effect by absorbing and emitting outgoing longwave radiation (Dufrense et al. 2001; Tegen 2003).

Aerosols act as a cloud condensation nuclei or ice nuclei, thus modifying the microphysical, microchemical, and, hence, optical properties of clouds (Levin et al. 2005; Solomos et al. 2011). Collectively changes in cloud processes due to aerosols are referred to as aerosol indirect effects. Finally, absorption of solar radiation by particles contributes to the reduction in cloudiness, a phenomenon referred to as the semi-direct effect. This occurs because absorbing aerosol warms the atmosphere, which changes the atmospheric stability, and reduces surface flux (IPCC 2007).

The magnitude of the feedback on the radiative transfer depends strongly on the optical properties of particles (single scattering albedo, asymmetry parameter, extinction efficiency), which in turn depend on the size, shape and refractive indexes of dust particles (Tegen 2003; Helmert et al. 2007). The mineral composition of the dust source areas (Tegen 2003), as well as the chemical composition and transformation of aerosols during their transportation (Astitha et al. 2010) are all factors on the optical intensity of dust. Furthermore the vertical distribution of dust, the presence of clouds and the albedo of the surface all contribute to the DRE (Sokolik and Toon 1996; Tegen and Lacis 1996; Liao and Seinfeld 1998; Helmert et al. 2007).

In the present study, the main objective is to quantify the contribution of dust particles on the DRE. To this end, the radiative transfer module – RRTMG (Mlawer et al. 1997; Oreopoulos and Barker 1999; Iacono et al. 2003; Pincus et al. 2003; Barker et al. 2003; Clough et al. 2005; Morcrette et al. 2008; Iacono et al. 2008) has been incorporated into the framework of the SKIRON/DUST model. The SKIRON/Dust system has already the capability to adequately simulate the desert dust cycle using state of the art parameterizations for the uplift, transportation and deposition of aerosols (Spyrou et al. 2010). The addition of the RRTMG radiative scheme has made it possible to model and study the effects of desert dust particles to the radiation balance of the atmosphere.

2 Experimental Design

In order to study the effects of desert dust particles to the radiation balance of the atmosphere, simulations for a 6-year period (2002–2007) were carried out with the implementation of the improved SKIRON/Dust modeling system.

The model was integrated over an extended area that covers the European continent, the Mediterranean Sea and northern Africa, as well as a major part of Middle East and Turkey. The horizontal grid increment was 0.24° and in the vertical direction 38 levels were used stretching from the ground surface up to 20 km. A high resolution reanalysis dataset (horizontal resolution of 0.15°) that has been developed in the framework of CIRCE project (Climate Change and Impact

Research: the Mediterranean Environment), was used for the initial and lateral boundary conditions for the meteorological parameters.

The model runs were carried out using two different setups: (a) by neglecting the effects of dust particles on the radiative parameters (NDE) and (b) by including the dust-radiation interaction mechanisms (WDE).

In order to evaluate the SKIRON/Dust model calculations related to air temperature for the 6-year period comparisons are realized between model results and actual data. The observations for the comparisons were retrieved from ~600 monitoring stations of ECMWF.

3 Results

Using model outputs from the two different simulations and temperature data from the ECMWF stations a number of statistical scores (Wilks 1995) were calculated for each season (Fig. 1). By including the DRE processes the SKIRON/Dust model manages to reproduce the surface temperature in greater detail, thus improving the model performance.

In order to quantify the energy redistribution in the atmosphere the average vertical temperature difference (WDE-NDE) was calculated. The vertical cross-sections of daily average dust concentration and temperature along the pathline at 18°E are illustrated in Fig. 2 upper right, lower respectively. The section was created to include source areas that are particularly active during March to May, specifically Lake Chad. This way we are able to examine the dust feedback in greater detail.

The presence of dust particles in the atmosphere drives changes in the tropospheric temperature as seen in the vertical cross-section of temperature difference between the two model setups (WDE-NDE) for the transient months of the 6-year studied period (Fig. 2 lower). The feedbacks are more profound near source areas, but are present in mid-latitude areas as well.

More specifically a temperature decrease in the upper-troposphere near the top of the dust layer is observed due to reflection. The dust particles reflect the incoming solar radiation back towards the top of the atmosphere (Fig. 2 lower). On the contrary, in the mid-troposphere there is an increase in temperature due to solar radiation absorption from the dust layer. During the day the energy absorbed by the dust layer raises its temperature while at night long-wave radiation is emitted toward the ground surface. The combined effect of these processes is the reduction in the air temperature near ground over dust source areas.

Furthermore, over dust affected African areas the long-wave radiation emitted by the dust layer toward the ground superimposed with the long-wave radiation emitted from the ground surface increases the temperature near to the surface (Fig. 2 lower).

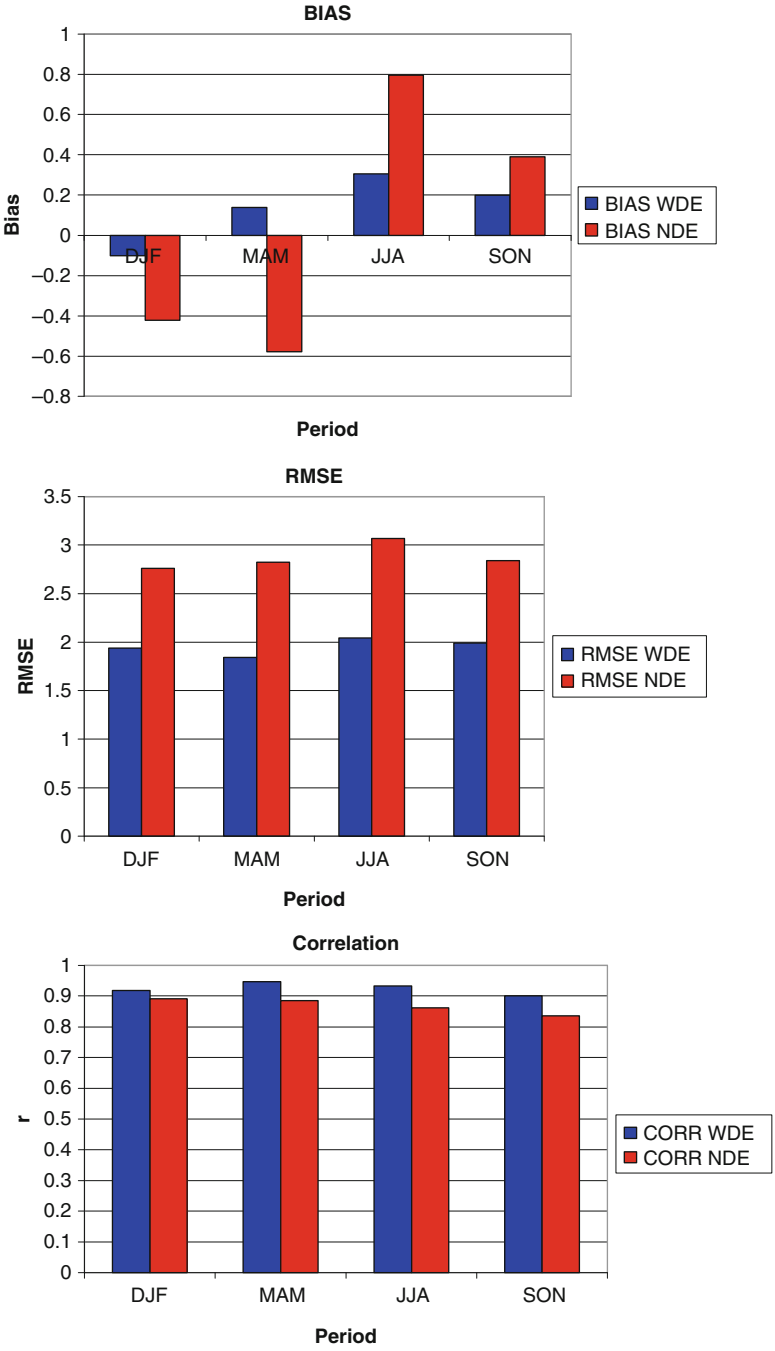

Fig. 1 Statistical parameters: Bias (*upper*), RMSE (*middle*), correlation coefficient (*lower*) for the 6-year period of simulations (2002–2007) with dust effects (WDE) and without dust effects (NDE)

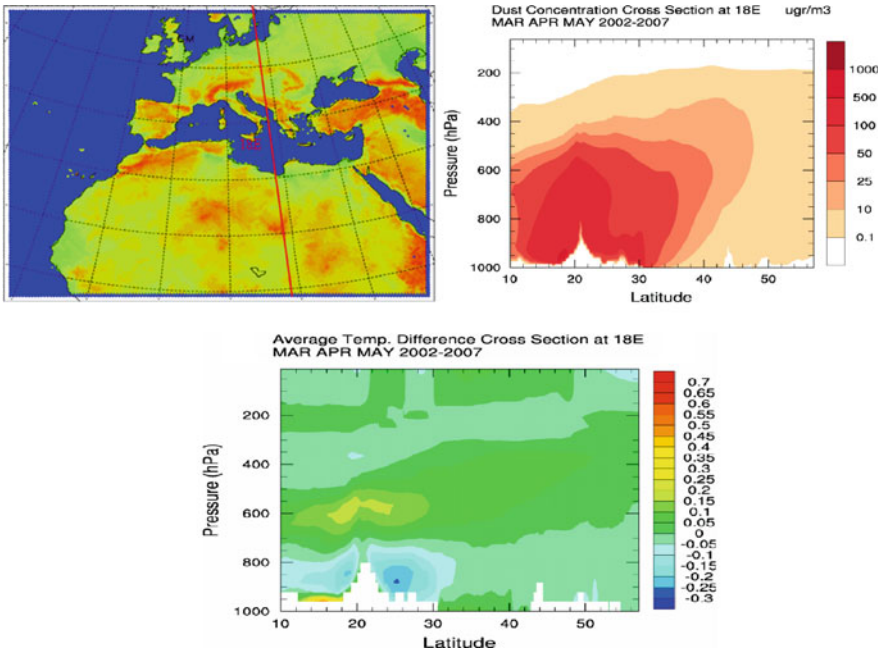

Fig. 2 Daily average dust concentration (*upper right*) and temperature differences (*lower*) cross section at 18°E (*upper left*) for the months March–April–May during the 6-year period (2002–2007)

4 Conclusions

In the present study, the effects of desert dust particles to the radiation balance of the atmosphere across the Greater Mediterranean Region were investigated with the implementation of SKIRON/Dust modelling system. The extensive analysis of the 6-year model runs covering the period 2002–2007 revealed important findings, as summarized below:

1. The suspension of desert dust particles decreases the calculated energy amounts reaching the ground.
2. The air temperature is decreased above the dust layer due to reflection.
3. On the contrary heating rates inside the dust plume are increases due to radiation absorption.
4. The extinction of incoming solar radiation causes lower tropospheric cooling.
5. The absorbed energy is emitted towards the ground increasing the temperature of surface layers with high dust concentration.
6. By including the dust feedbacks in the radiative calculations the model performance is improved.

In general desert dust is a significant climate factor. The direct feedback of natural aerosols on radiative transfer changes the energy distribution in the atmosphere and cannot be neglected in weather and climate studies.

References

Astitha M, Kallos G, Spyrou C, O'Hirok W, Lelieveld J, Denier van der Gon HAC (2010) Modelling the chemically aged and mixed aerosols over the eastern central Atlantic Ocean – potential impacts. Atmos Chem Phys 10:5797–5822. doi:10.5194/acp-10-5797-2010

Barker HW, Pincus R, Morcrette JJ, The Monte-Carlo Independent Column Approximation (2003) Application within large-scale models. In: Proceedings of the GCSS/ARM workshop on the representation of cloud systems in large-scale models, Kananaskis, Alberta, Canada, 10pp

Clough SA, Shephard MW, Mlawer EJ, Delamere JS, Iacono MJ, Cady-Pereira K, Boukabara S, Brown PD (2005) Atmospheric radiative transfer modeling: a summary of the AER codes. J Quant Spectrosc Radiat Transf 91:233–244

Dufrense JL, Gautier C, Ricchiazzi P (2001) Longwave scattering of mineral aerosols. J Atmos Sci 59:959–1966

Haywood JM et al (2003) Radiative properties and direct Radiative effect of Saharan dust measured by the C-130 aircraft during SHADE: 1. Solar spectrum. J Geophys Res 108 (D18):8577. doi:10.1029/2002JD002687

Helmert J, Heinold B, Tegen I, Hellmuth O, Wendisch M (2007) On the direct and semidirect effects of Saharan dust over Europe: a modelling study. J Geophys Res 112. doi:10.1029/2006JD007444

Iacono MJ, Delamere JS, Mlawer EJ, Clough SA (2003) Evaluation of upper tropospheric water vapor in the NCAR community climate model (CCM3) using modeled and observed HIRS radiances. J Geophys Res 108(D2):4037. doi:10.1029/2002JD002539

Iacono MJ, Delamere JS, Mlawer EJ, Shephard MW, Clough SA, Collins WD (2008) Radiative forcing by long-lived greenhouse gases: calculations with the AER radiative transfer models. J Geophys Res 113:D13103. doi:10.1029/2008JD009944

Intergovernmental Panel on Climate Change (IPCC) (2007), Climate change 2007: the physical science basis, Cambridge University Press, UK

Kallos G, Spyrou C, Astitha M, Mitsakou C, Solomos S, Kushta J, Pytharoulis I, Katsafados P, Mavromatidis E, Papantoniou N, Vlastou G (2009) Ten-year operational dust forecasting – recent model development and future plans. IOP Conf Ser Earth Environ Sci 7(2009). doi:10.1088/1755-1307/7/1/012012

Kaufman YJ, Koren I, Remer LA, Rosenfeld D, Rudich Y (2005) The effect of smoke, dust and pollution aerosol on shallow cloud development over the Atlantic 160 Ocean. Proc Natl Acad Sci USA 102:11207–11212

Levin Z, Teller A, Ganor E, Yin Y (2005) On the interactions of mineral dust, sea-salt particles and clouds: a measurement and modelling study from the Mediterranean Israeli Dust Experiment campaign. J Geophys Res 110:D20202. doi:10.1029/2005JD005810

Liao H, Seinfeld JH (1998) Radiative forcing by mineral dust aerosols: sensitivity to key variables. J Geophys Res 103(D):31637–31645

Mlawer EJ, Taubman SJ, Brown PD, Iacono MJ, Clough SA (1997) RRTM, a validated correlated-k model for the longwave. J Geophys Res 102:16,663–16,682

Morcrette JJ, Barker HW, Cole JNS, Iacono MJ, Pincus R (2008) Impact of a new radiation package, McRad, in the ECMWF integrated forecast system. Mon Weather Rev 136 (12):4773–4798, doi: 10.1175/2008MWR2363.1

Oreopoulos L, Barker HW (1999) Accounting for subgrid-scale cloud variability in a multi-layer 1-D solar radiative transfer algorithm. Q J R Meteor Soc 125:301–330

Pincus R, Barker HW, Morcrette JJ (2003) A fast, flexible, approximate technique for computing radiative transfer in inhomogeneous clouds. J Geophys Res 108(D13):4376. doi:10.1029/2002JD003322

Sokolik IN, Toon OB (1996) Direct radiative forcing by anthropogenic airborne mineral aerosols. Nature 381:681–683

Solomos S, Kallos G, Kushta J, Astitha M, Tremback C, Nenes A, Levin Z (2011) An integrated modeling study on the effects of mineral dust and sea salt particles on clouds and precipitation. Atmos Chem Phys 11:873–892. doi:10.5194/acp-11-873-2011

Spyrou C, Mitsakou C, Kallos G, Louka P, Vlastou G (2010) An improved limited area model for describing the dust cycle in the atmosphere. J Geophys Res 115:D17211. doi:10.1029/2009JD013682

Tegen I (2003) Modeling the mineral dust aerosol cycle in the climate system. Q Sci Rev 22:1821–1834

Tegen I, Lacis AA (1996) Modeling of particle size distribution and its influence on the radiative properties of mineral dust aerosol. J Geophys Res 101:19,237–19,244

Wilks DS (1995) Statistical methods in the atmospheric sciences, Academic Press NY, pp 233–277

Yoshioka M, Mahowald N, Dufresne JL, Luo C (2005) Simulation of absorbing aerosol indices for African dust. J Geophys Res 110:D18S17. doi:10.1029/2004JD005276

Numerical Study of an Intense Episode of Vardaris Wind

L. Tsopouridis, I. Pytharoulis, T. Karacostas, P. Zanis, and I. Tegoulias

Abstract This paper presents a case study of an episode of Vardaris that occurred on 10 November 2007 and caused widespread problems in Central Macedonia. It uses surface data including four stations along Axios valley (Evzonoi, Aksioupoli, Akropotamos, and Kymina), analyses and the nonhydrostatic Weather Research and Forecasting model. The episode was associated with the combination of a transient depression over Greece and an anticyclone in Western Europe. Maximum sustained wind speeds of 20.5 m/s with gusts up to 28.2 m/s appeared along Axios and at Thessaloniki airport (24 m/s with gusts up to 31.9 m/s). The model simulations with a horizontal resolution of 1 km were in good agreement with observations. The strongest winds, in excess of 30–35 m/s, were simulated between 750 and 900 hPa in the form of a jet streak. A numerical experiment showed that the occurrence of the episode was determined by the synoptic scale flow, but its maximum intensity was specified by the local conditions due to channeling.

1 Introduction

The wind called Vardaris is a strong northwesterly local wind that blows along the area of Axios Valley in southern Balkans. Vardaris is created in Axios river (Vardar) in FYROM, appearing in Greece and Central Macedonia through the central ridge of Paiko and Kerkini. Following the valley of Axios it affects Thessaloniki as a strong northwesterly wind. It is characterized by its direction, strong intensity, low temperatures and low humidity. It is of particular interest because it affects both humans and the local environment.

L. Tsopouridis (✉) • I. Pytharoulis • T. Karacostas • P. Zanis • I. Tegoulias
Department of Meteorology and Climatology, School of Geology, Aristotle University of Thessaloniki, Thessaloniki 54124, Greece
e-mail: ltsopour@geo.auth.gr

C.G. Helmis and P.T. Nastos (eds.), *Advances in Meteorology, Climatology and Atmospheric Physics*, Springer Atmospheric Sciences,
DOI 10.1007/978-3-642-29172-2_46,

Despite its importance, there are only a few studies about the Vardaris wind (Angouridakis et al. 1981; Maheras et al. 1984; Psarri 2005). More specifically, there is a lack of detailed high-resolution investigation of its spatiotemporal distribution and the relative role of the synoptic and local conditions in its development, providing a strong motivation to study this phenomenon.

A case study of an episode of the Vardaris that took place on 10 November 2007 and caused widespread problems in central Macedonia is presented. The objectives of this study are:

- To study the characteristics and causes of this event
- To investigate the relative role played by the synoptic scale meteorological conditions versus the local topography.

2 Data and Methodology

This research has been based on numerical simulations, observational data and gridded analyses. The nonhydrostatic Weather Research and Forecasting model with the Advanced Research dynamic solver (WRF-ARW Version 3.2.0) was utilized in the simulations (Wang et al. 2010). The observations are the routinely available surface measurements of the networks of the Hellenic National Meteorological Service (HNMS), the Department of Meteorology and Climatology (DMC/AUTH) and the School of Agriculture of the Aristotle University of Thessaloniki, the National Observatory of Athens (NOA), the Greek Agricultural Insurance Organization (ELGA), the Region of Central Macedonia and from four automatic meteorological stations that operated along Axios Valley in a common project between DMC/AUTH and NOA (Fig. 1). These four stations were installed at Evzonoi, Aksioupoli, Akropotamos and Kymina covering the whole area of interest within Greece. The data of Gevgeli (FYROM) were retrieved from GTS in order to cover the upstream region. The observations were used along with United Kingdom Meteorological Office (UKMO) mean sea-level pressure analyses and gridded 6-hourly operational surface and upper-air analyses of the European Centre for

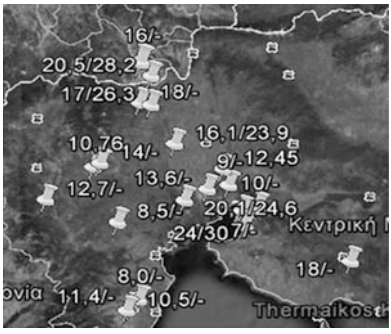

Fig. 1 Maximum observed sustained wind speed (m/s) and gust (m/s) at 10 m

Medium-Range Weather Forecasts (ECMWF). They were available at a regular grid of 0.25° lat × 0.25° lon at the pressure levels of 1,000, 925, 850, 700, 500, 400, 300, 250, 200, 150, 100, 70 and 50 hPa.

3 Synoptic and Mesoscale Analysis

Figure 1 depicts the spatial distribution of the maximum observed 10 m sustained wind speed and wind gusts. The measurements at Evzonoi, Aksioupoli, Akropotamos and Kymina and those of HNMS were recorded at 10 m above surface. The other wind observations were transformed to a height of 10 m using the wind profile power low. Maximum wind speeds appeared along Axios river (20.5 m/s with gusts up to 28.2 m/s at Evzonoi) and at Thessaloniki airport (24 m/s with gusts up to 31.9 m/s). It is hypothesized that the latter station exhibited the strongest winds because of the existence of the sea-surface (with low friction) upstream.

The temporal evolution of the 10 m wind speed along Axios and at Thessaloniki is presented in Fig. 2. The phenomenon appeared at about 0440 UTC at Evzonoi and about 1–1.5 h later at Kymina (located about 55 km south of Evzonoi). In all stations the sustained wind speed exceeded 15 m/s, while it exceeded 10–11 m/s (corresponding to strong winds in the Beaufort scale; ≥6 BF) for about 12, 10, 10, 5, 10 h at Evzonoi, Aksioupoli, Akropotamos, Kymina and Thessaloniki airport, respectively.

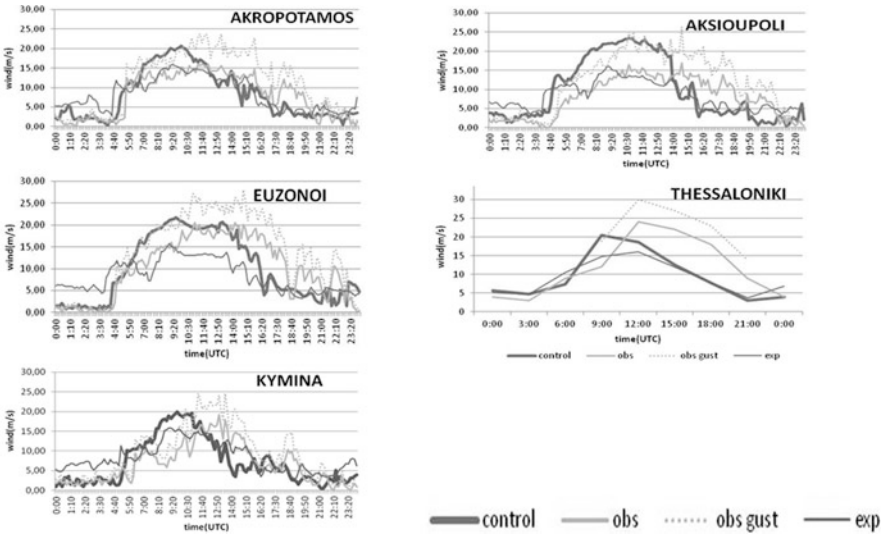

Fig. 2 Sustained wind speed (m/s) and wind gust (m/s) at 10 m above surface at (**a**) Akropotamos, (**b**) Aksioupoli, (**c**) Evzonoi, (**d**) Kymina and (**e**) Thessaloniki airport

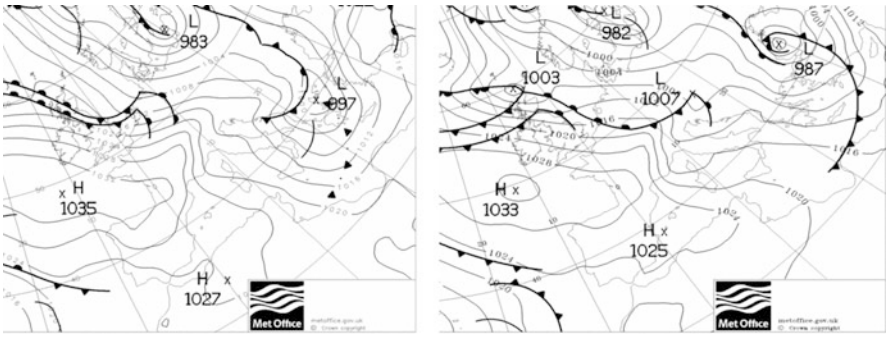

Fig. 3 UKMO mean sea-level pressure analyses (hPa) at (*left*) 06 UTC and (*right*) 18 UTC on 10/11/07

The synoptic conditions associated with this event were characterized by a low pressure system with a minimum pressure of 997 hPa centered over Thermaikos Gulf at 06 UTC on 10/11/07 (during the onset of the event) (Fig. 3 left). During the subsequent hours it moved eastward-northeastward while deepening (987 hPa at 18 UTC 10/11/07; Fig. 3 right). The interaction of the transient depression with a well-organized anticyclone over Western Europe and eastern Atlantic created a strong pressure gradient that triggered and maintained the strong northwesterlies over central Macedonia that is the Vardaris episode. A deepening trough, with geopotential heights of around 5,360 gpm, was located over Greece at 500 hPa at 12 UTC on 10/11/07 (Fig. 4 upper) and was associated with the surface cyclone. Cold air masses with temperatures below 0°C were advected at 850 hPa over the area of interest (Fig. 4 lower) behind the passage of the cold front of the cyclone (Fig. 3).

4 High Resolution Simulations

Three one-way nested domains were utilized (Fig. 5) in the simulations. The spatial resolution of the model was 15 km for D1, 5 km for D2 and 1 km for D3. The 6-hourly ECMWF analyses with a spatial resolution of 0.25° × 0.25° were used as initial and lateral boundary conditions for the domain D1. The model was initialised at 00 UTC on 9 November 2007, which is the day before the event.

Domains D2 and D3 were initialised 6 h later in order to minimize the model spin-up. The sea-surface temperatures were derived from daily NCEP SST files at the very high horizontal resolution of 0.083° × 0.083° and were kept fixed to their initial values throughout the simulations. In the vertical, 39 sigma levels (up to 50 hPa) with increased resolution in the boundary layer were used by all nests. High-resolution land use and topography (30 × 30 arc sec) were used in the control run. The WRF results have been derived from D3 in 10-min intervals.

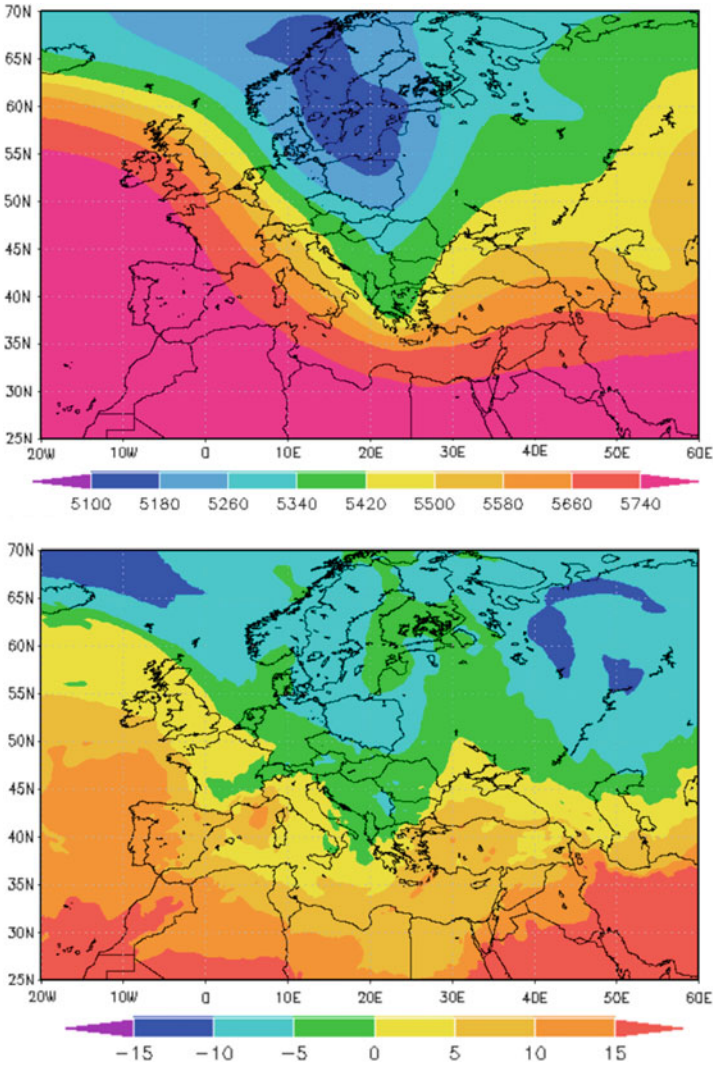

Fig. 4 Synoptic charts of (*upper*) geopotential height (gpm) at 500 hPa and (*lower*) temperature (°C) at 850 hPa, at 10/11/07 12 UTC (ECMWF analyses)

The model simulated the occurrence of the event and its onset in very good agreement with observations (Fig. 2). However, it underestimated its duration (~3 h) and generally overestimated its maximum intensity by about 1–7 m/s (except from Thessaloniki airport where underestimation occurred). The statistical analysis of the 10 m wind speed (at 10 min intervals) at Evzonoi, Axioupoli, Akropotamos and Kymina between 00 UTC 10/11 and 00 UTC 11/11 showed that the BIAS and the Mean Absolute Error ranged from −0.25 to 1.82 m/s and from 2.80 to 5.38 m/s,

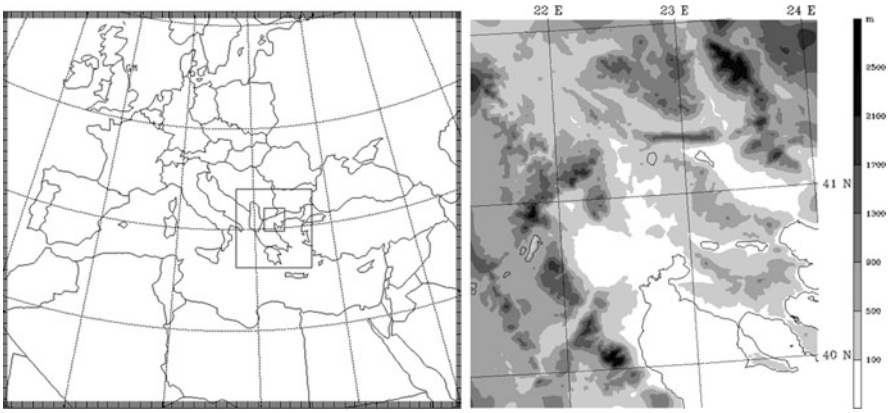

Fig. 5 The three nests used by WRF-ARW in the numerical experiments and the topography of the inner domain (d03)

respectively. Although these values seem to be higher than usual, one must take into account that the average observed 10 m wind speed was much higher than climatology and ranged from 8.0 to 10.2 m/s in the same period.

In the control run the Vardaris episode commenced at 05:00 UTC on 10/11/07 from the Greece-FYROM borders with strong northwesterly winds. In the subsequent hours it gradually affected the whole area of interest and maximum wind speeds up to about 20–24 m/s (not shown) were predicted at about 09 UTC in the areas of Evzonoi and the southern coast of Thermaikos Gulf where the airport is located (in agreement with observations). Therefore, within a few hours the wind conditions in the valley changed from absolute calm to stormy.

The temporal evolution of the vertical structure of v-wind and potential temperature at the locations of Euzonoi and Thessaloniki airport (Fig. 6) shows clearly that the initiation of the episode took place just after the passage of the cold front. The strongest winds, in excess of 30–35 m/s, were predicted between 750 and 900 hPa in the form of a jet streak. It is interesting to note the increase in the depth of the well-mixed layer and the establishment of low-static stability conditions, caused by the strong turbulence, after the episode during night hours.

Finally, the role of the synoptic scale meteorological conditions versus the local topography was investigated through a numerical experiment. The model setup was identical to the one of the control run, but the topography of the inner domain (D3) was removed (set equal to zero). Figure 2 shows that a Vardaris episode took place in the no-topography experiment about 0.5–1 h before the control run. Although the 10 m wind speed reached 15–16 m/s at all stations, the episode was weaker by about 4–7 m/s than in the control run. These results indicate that the occurrence of the episode was determined by the synoptic flow, but its maximum intensity was specified by the local conditions due to channeling in Axios valley.

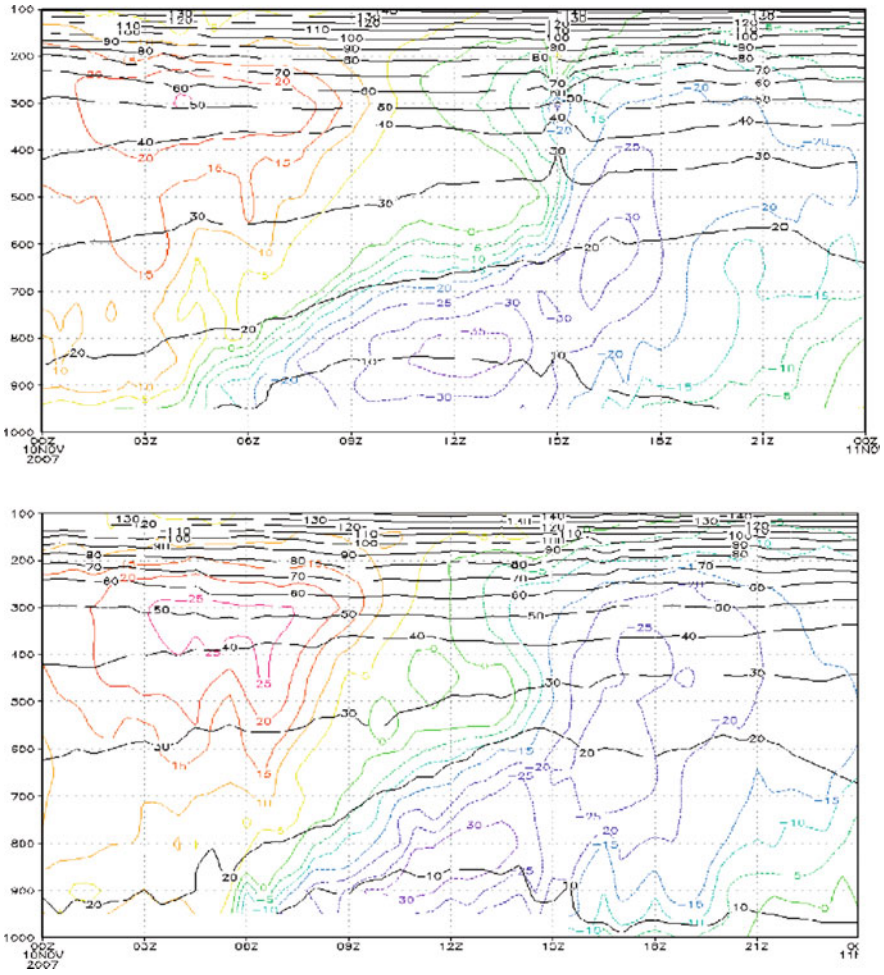

Fig. 6 Hovmoller diagrams of WRF simulated v-wind speed (m/s; coloured contours) and potential temperature (°C; *black* contours) at the locations of: (*upper*) Euzonoi (41.1°N, 22.5°E) and (*lower*) Thessaloniki airport (40.5°, 22.9°) from 00 UTC on 10/11/07 to 00 UTC on 11/11/07

5 Conclusions

The maximum wind speeds of the Vardaris wind episode that occurred on 10 November 2007 were recorded along Axios (20.5 m/s with gusts up to 28.2 m/s) and at the southern coast of Thermaikos Gulf (24 m/s with gusts up to 31.9 m/s).

The episode was associated with the combination of a transient depression over Greece and an anticyclone in Western Europe.

WRF model simulated the strongest winds, in excess of 30–35 m/s, between 750 and 900 hPa in the form of a jet streak.

A numerical experiment showed that the occurrence of the episode was determined by the synoptic scale flow, but its maximum intensity was specified by the local conditions due to channeling in Axios valley.

Acknowledgments The authors would like to thank NOA (and especially Dr. Lagouvardos and Dr. Koletsis), HNMS, the School of Agriculture of AUTH, ELGA, the Region of Central Macedonia, ECMWF, UKMO and NCEP for the availability of the necessary data as well as NCAR for providing the WRF-ARW model.

References

Angouridakis V, Balafoutis Ch, Maheras P (1981) Les Vents de NW, et "Vardaris" a Thessalonique. Essai statistique. Eaux et Climats. Melanges offerts en homage a ChPEGUE. Grenoble

Maheras P, Flocas A, Karacostas Th (1984) La structure de la basse troposphere pendant le vent Vardaris a Thessalonique. Zbornik 10:241–243

Psarri L (2005) The local wind of Thesaloniki, Vardaris – an approach to the problem with classical methods and the use of artificial neural networks. MSc thesis, AUTH

Wang W, Bruyère C, Duda M, Dudhia J, Gill D, Lin H-C, Michalakes J, Rizvi S, Zhang X (2010) ARW Version 3 modeling system user's guide. NCAR-MMM, p 312

A Comparison of Storm Characteristic Between Mountainous and Plain Areas within Central Macedonia

K. Tymbanidis, D. Bampzelis, T. Karacostas, and E. Chatzi

Abstract A comparison of storm characteristics between two selected areas (one mountainous and one plain) of Imathia-Pella region is performed, using radar-derived data taken from the C-band weather radar situated at Fyliro area, close to Thessaloniki and the cell tracker TITAN (Thunderstorm Identification, Tracking, Analysis, and Nowcasting – NCAR). The objective on this study is: firstly, to analyze, describe and compare storm characteristics between the two examined areas, and secondly, to identify monthly differences among them. The TITAN algorithm is used to obtain storm measurements during the months April to September for the 3-year period of 2008–2010. The radar-based storm information is compiled using certain storm-tracking thresholds. Following this approach, the total storm days and cell number, were identified. Results indicate that convective cells that affect both areas differ in number as well as in their characteristics. Cells develop over the mountainous area earlier within the day, move slower, have higher maximum reflectivity values and 35% of them do not precipitate at all. Monthly distribution of relative frequencies also revealed certain differences among transitional and summer months.

1 Introduction

Convective storms are significant meteorological phenomena of great importance, since, despite their local-scale characteristics, are associated with extreme events like heavy rainfall, hail, gusty winds that can cause considerable damage to

K. Tymbanidis (✉) • D. Bampzelis • T. Karacostas
Department of Meteorology and Climatology, School of Geology, Aristotle University of Thessaloniki, Thessaloniki 541 24, Greece
e-mail: ktymp@geo.auth.gr

E. Chatzi
Meteorological Application Center, Hellenic Agricultural Insurance Organization (ELGA), Thessaloniki 551 03, Greece

C.G. Helmis and P.T. Nastos (eds.), *Advances in Meteorology, Climatology and Atmospheric Physics*, Springer Atmospheric Sciences,
DOI 10.1007/978-3-642-29172-2_47,

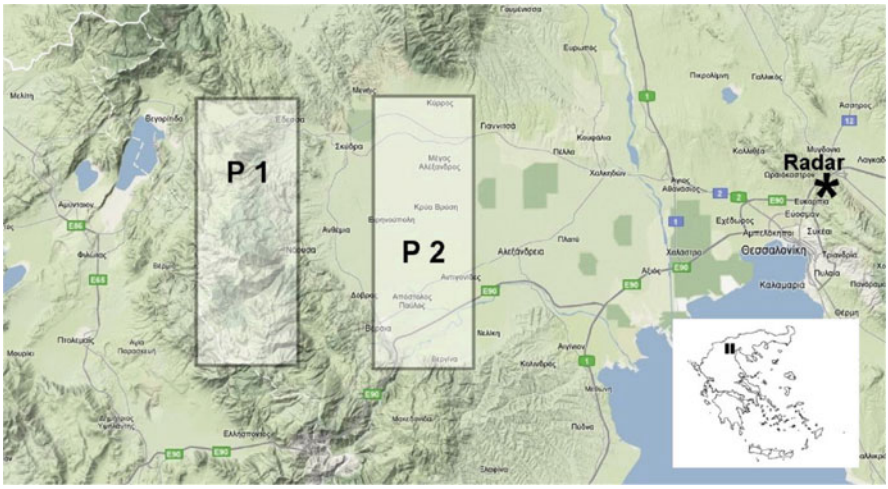

Fig. 1 The P1 and P2 areas of study in northern Greece

agriculture and infrastructure facilities. The purpose on this study is the analysis of radar data, digitally recorded during the Greek National Hail Suppression Program (NHSP) and the comparison of convective cell characteristics between two selected regions (one mountainous and one plain) in Imathia-Pella region. Concurrently, the analysis seeks to identify and compare mechanisms that affect their creation, movement and severity between the two selected areas.

Radar-based storm studies have been conducted by several researchers over the area of northern Greece, such as: Karacostas (1991), Sioutas and Flocas (2003) and Foris et al. (2006). They generally studied convective cell characteristics, and hailstorm characteristics, through synoptic situations, dynamic and thermodynamic environment.

Two areas were defined and are used (Fig. 1) in this analysis and comparisons of the storm characteristics between them is performed. The area P1 is a mountainous area which covers 150 km^2 (mean altitude 927 m), mainly over the mountainous range of Vermion, being to the west, and the plain and agricultural area of P2, which also covers 150 km^2 of Imathia-Pella region (mean altitude 51 m).

2 Data and Methodology

The dataset used for this radar analysis and comparison of storm characteristics between the two selected areas comes from a C-band weather radar situated at Fyliro mountain, close to Thessaloniki, with 750 m × 750 m spatial and 3.5 min temporal resolution during the April to September months of 2008–2010. The cell tracker TITAN (Thunderstorm Identification, Tracking, Analysis, and Nowcasting – NCAR), (Dixon and Wiener 1993) is used to identify storm tracks and extract storm

characteristics. The cell tracker TITAN is developed for automatic identification, tracking and forecasting of convective cells based on radar reflectivity measurements. The algorithm, at a given reflectivity image, defines a convective cell as a 3D region in which reflectivity values exceed a given threshold. Following that, the algorithm matches convective storms between two successive radar images using combinational optimization. The algorithm can also deal with cells that merge or split, classifying them as complex (multicells) or simple (singlecells). The storm characteristics include the following: cell lifetime or duration (mins), hour of start (in UTC time), cell speed (km/h), direction of motion (°), mean cell volume (km^3), mean cell mass (ktons), mean cell area (km^2), mean cell precipitating area (km^2), mean maximum cell reflectivity (dBz), maximum cloud top (km) and maximum height of 35 dBz echo (km).

A number of threshold values are set during the identification procedure by the algorithm, in order to capture only valid convective storms and to eliminate several non-meteorological echoes (i.e. ground clatter). These thresholds include the following: (1) a storm track is rejected if it begins or ends after or before a missing radar file, (2) the storm's minimum volume must be at least 15 km^3, (3) a storm track with a minimum duration less than 15 min (five successive radar scans), (4) a maximum duration of more than 2.5 h and maximum top below 3.5 km is discarded, since it is likely not to be a convective storm, and (5) the storm volume area reflectivity must exceed 35 dBz.

It must be stated that only cells developed within each one of the defined areas (P1 or P2) (give their first echo above 35 dBz) are considered in the analysis. Storms that might have developed elsewhere and passed through one or both areas, are not included in the analysis.

3 Results

With the application of all criteria and threshold values, a total number of 106 storm days with 289 valid cells are defined for area P1 (mountainous area) and 77 storm days with 141 valid cells for area P2 (plain area). It is obvious that mountainous area experiences more storm days and far more cells than the plain one. From the monthly distribution of the number of storm days (Fig. 2, left) and the number of cells developed per storm day (Fig. 2, right) is observed that this difference is mainly due to summer months. The number of cells per storm day for both areas exhibit similar behavior, except for July and August.

3.1 Comparison of Cell Characteristics Between the Two Areas

For the comparison between the two areas, relative frequency distributions were calculated for each cell characteristic and for each area. The comparison diagrams are presented in Fig. 3. The results reveal certain differences in some cell

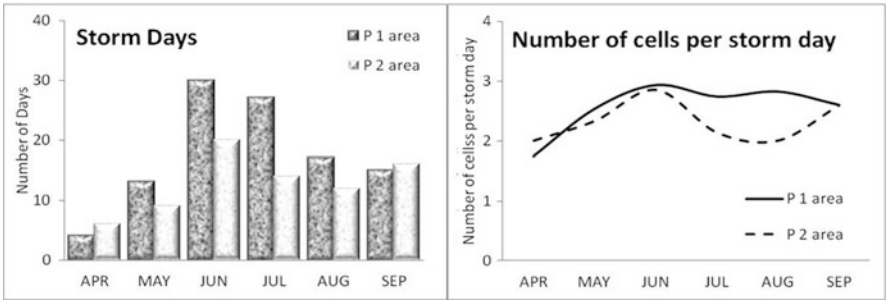

Fig. 2 Monthly distribution of the total number of storm days (*left*) and number of cells developed per storm day (*right*) for P1 and P2 areas

characteristics and similar behavior with some others. Cells initiate mainly during the day but they peak at different hours. As it was expected, in mountainous area (P1) they occur earlier than in the plain area (P2). The secondary maximum in storm initiation time at 00:00 UTC is most probably due to cells that have developed during the previous day and continue to exist after midnight.

Cell speed differs significantly between the two areas, as relative frequency of speed peaks at 6 km/h for P1 and at 14 km/h and 20 km/h for P2. Thus, cells travel slower in mountainous area, probably due to the complex terrain and the existing obstacles. Cell direction of movement for both areas is common and mainly from southwest and northwest to northeast and southwest.

Cell precipitating area is another characteristic that also exhibits certain differences. Particularly, for non precipitating cells the relative frequency is 35% for P1 and only 15% for P2, indicating that a certain number of cells that develop over the mountainous area do not precipitate at all. Another noticeable difference appears on maximum reflectivity and cloud top values compared as a whole. Although cloud top appear to have similar behavior between the two areas, maximum reflectivity differs, with the relative frequency to peak at 52–54 dBz for area P1 and at 48 dBz for area P2, indicating that the mountainous area experiences more severe storms than the plain one. The rest of the cell characteristics, such as: cell direction, duration, volume, mass and area, show similar behavior between the two examined areas.

3.2 Monthly Comparison of Relative Frequencies

Cell characteristics that do not revealed different behavior between the two areas are further analyzed in an attempt to compare the monthly distribution of these characteristics. Therefore, the higher relative frequency values of each cell characteristic are grouped for each area and their total frequencies are monthly compared between them.

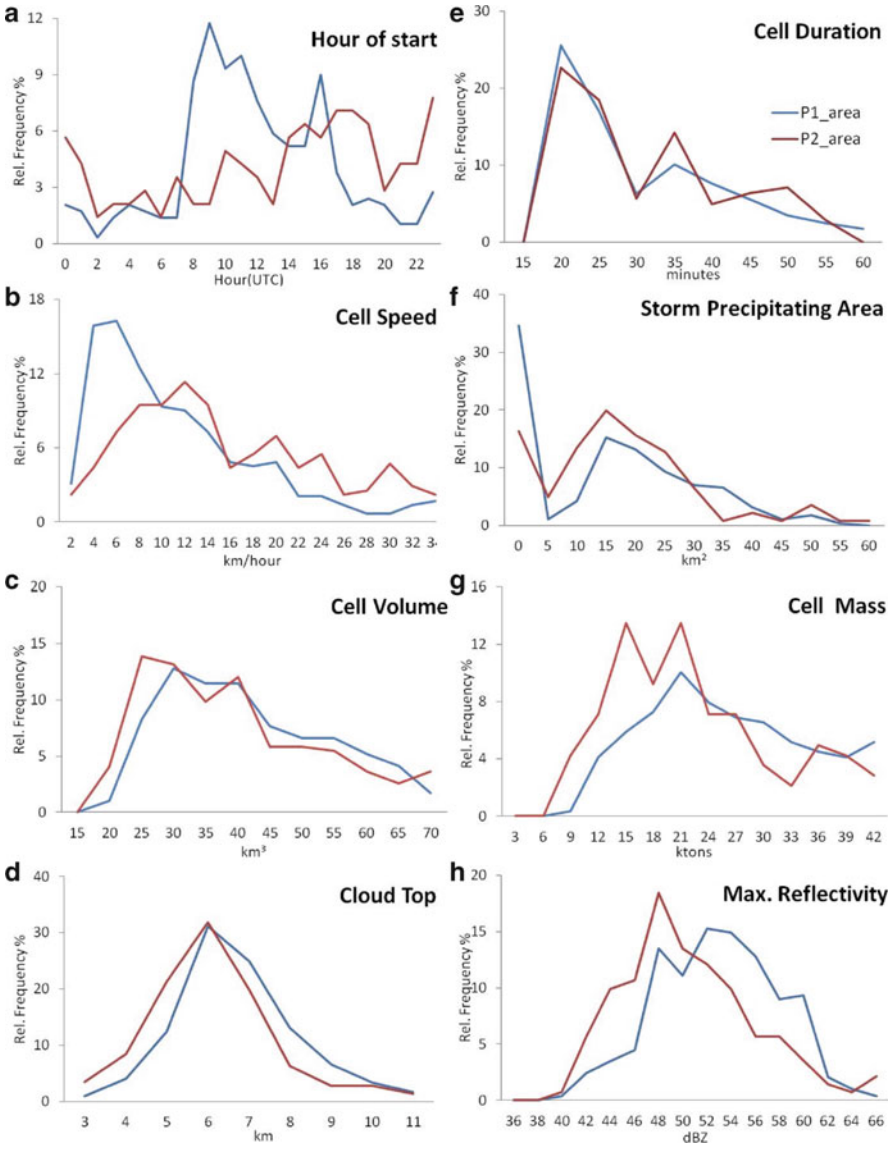

Fig. 3 Comparison of cells' relative frequencies between the two areas

Storm relative frequencies are grouped as follows: duration 15–30 min; cell volume 20–40 ktons and cell mass 10–30 km^3, for each area. The results are illustrated in Fig. 4. From the diagram of the monthly comparison of relative frequency distributions, it is observed that cell mass and volume have almost identical behavior between the two areas. Thus, cells having volume between 20 and 40 km^3 and mass 10–30 ktons appear to have lower relative frequencies in area

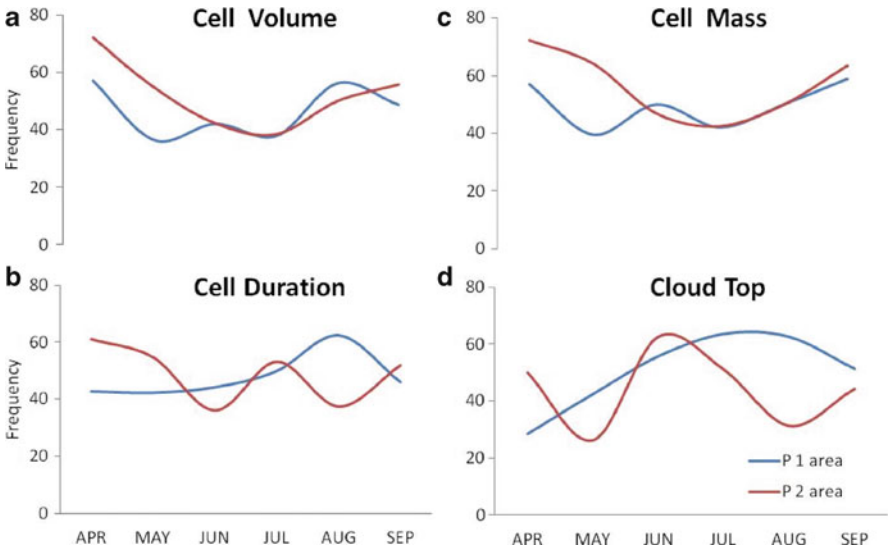

Fig. 4 Monthly distribution of relative frequencies of cell characteristics between the two areas

P1 during April and May than in area P2. Further analysis of that indicate the development of more cells with increased volume and mass during summer months for both areas, but this phenomenon is more intense for area P2.

The relative frequency of the cell duration as a function of the summer months for the two areas, also reveal some differences as seen in Fig. 4. It is observed that durations between 15 and 30 min are more frequently apparent for area P1 in August and for area P2 in April.

4 Conclusions

Cell characteristics that developed between two distinct areas in central Macedonia (mountainous and plain) are analyzed and compared. As it was expected, mountainous area experiences far more cells than the plain area, especially on July and August. Cell characteristics exhibit certain differences between the two areas of study. Cells that develop over the mountainous area (P1) appear earlier within the day, move slower and have higher maximum reflectivity values. On the other hand, cells that develop over the plain area (P2) appear later in the afternoon hours, move faster and have lower maximum reflectivity values. The 35% of the cells that develop over the mountainous area do not precipitate at all, while this percentage is only 16% over the plain area. Although cell volume and mass do not exhibit apparent differences, a closer investigation in monthly frequencies reveals that cells develop over the plain area differ more between transitional and summer months

than those who develop over mountainous area. Finally, cell lifetime is almost common for both areas (20 min), but their peaks appear in August for the mountainous area and in April for the plain area.

Acknowledgments The authors thank Meteorological Application Center of the Greek Agricultural Insurance Organization and 3D S.A. for the free provision of weather radar data.

References

Dixon M, Wiener G (1993) TITAN: thunderstorm identification, tracking, analysis and nowcasting – a radar-based methodology. J Atmos Ocean Technol 10:785–797

Foris DV, Karacostas TS, Flocas AA, Makrogiannis TI (2006) Hailstorm in the region of Central Macedonia, Greece: a kinematic study. Meteor Z 15:317–326. doi:10.1127/0941-2948/2006/0134

Karacostas TS (1991) Some characteristics of convective cells in the Greek National Hail Suppression program. Geofizika 8:43–50

Sioutas MV, Flocas HA (2003) Hailstorms in Northern Greece: synoptic patterns and thermodynamic environment. Theor Appl Climatol 75:189–202. doi:10.1007/s00704-003-0734-8

ANN-Based Modeling of Daily Global UV, PAR and Broadband Solar Radiant Fluxes in Cyprus

F. Tymvios, A. Georgiou, M. Pelecanou, and C.P. Jacovides

Abstract In this study, Artificial Neural Network (ANN) techniques for estimating daily global UV, PAR and broadband solar radiant fluxes have been developed. The data used in this analysis are global ultraviolet UV (G_{UV}), global photosynthetic photon flux density (PAR-G_{PAR}), broadband global radiant flux (G), extraterrestrial radiant flux E_0, air temperature (T), relative humidity (Rh), sunshine duration (n), daylength (N), precipitable water (w) and O_3 column density. By using different combinations of the above variables as inputs, numerous ANN-models have been developed. For each model, the output is the daily global UV, PAR and broadband radiant fluxes. Firstly, a set of 2 × 365 points (2 years) has been used for training each network–model, whereas a set of 365 points (1 year) has been engaged for testing and validating the ANN-models. It has been found that ANN-models' accuracy depends on the parameters used as well as spectral range considered. Moreover, results obtained reveal that the ANN methodology is a promising tool for estimating both broadband and spectral radiant fluxes.

1 Introduction

The increasing global energy demands and the increasing fossil fuel prices stimulate countries to downsize energy consumption and exploit renewable energy sources. On the other hand, environmental problems caused by mass consumption of fossil energy (e.g. global warming) are also reason for concern. Reliable solar radiant flux measurements for estimating the dynamic behavior of solar energy

F. Tymvios
Meteorological Service of Cyprus, Nicosia, Cyprus

A. Georgiou • M. Pelecanou • C.P. Jacovides (✉)
Department of Environmental Physics and Meteorology, Athens University Campus, Athens 15784, Greece
e-mail: kiakovid@phys.uoa.gr

C.G. Helmis and P.T. Nastos (eds.), *Advances in Meteorology, Climatology and Atmospheric Physics*, Springer Atmospheric Sciences,
DOI 10.1007/978-3-642-29172-2_48,

systems' process and for simulating long-term operations are required. For thermal analysis performance through transient simulation algorithms, a crucial input is the solar radiant energy components incident on the collector surfaces. Nevertheless, direct measurements of solar radiant components at the site of interest are not available in many instances so only the use of either modeling simulations or empirically derived estimates can fill this gap (Lopez et al. 2001).

Further, plants require solar radiation for photosynthesis and their growth is proportional to the amount received, assuming that other environmental factors are not limiting. Specifically, the portion of solar spectrum utilized by plant biochemical processes in photosynthesis for converting light energy into biomass is a composite of wavelengths between 400 and 700 nm. These wavelength limits define the so-called photosynthetically active radiation-PAR (McCree 1972; Ross and Sulev 2000), covering both photon and energy terms.

On the other hand, the depletion in the concentration of ozone layer in the stratosphere may significantly increase the UV radiant flux reaching the earth's surface. These modifications have raised concern among scientists and policy makers during recent decades. This spectral UV component has deleterious effects in many biological systems: disrupts protein (DNA), causes skin cancer and eye cataracts in humans, losses of productivity and other destructing effects in plants (Parisi et al. 2007; Jacovides et al. 2009).

Bearing the above in mind, the purpose of this research is to establish ANN-models which making use of a limited number of widely available input variables, both radiometric and atmospheric, predict daily values of solar radiant components, namely broadband global, PAR and UV on a horizontal surface in Cyprus.

2 Data and Methodology

This analysis is based on hourly radiometric data collected at the semi-rural Athalassa site, Cyprus (35°15′N, 33°40′E, 165 m a.m.s.l.) for a 3-year period (2004–2006). Global (G) radiant flux (305–2,800 nm) was measured using the Kipp & Zonen model CM11 pyranometer (Delft, The Netherlands). The PAR (G_{PAR}) radiant flux (400–700 nm) was measured with a Licor quantum sensor LI-190SA (Lincoln, Nebraska, USA), while the UV (G_{UV}) radiant flux (280–380 nm) readings were obtained by adding Skye's sensors SKU-430 and 420 (Skye, Powys, UK) outputs. Daily values for all the radiometric components have been computed by summing the individual radiant fluxes over the course of a day.

Global radiant measurements have an estimated experimental error of about 3%, while spectral PAR data have an error less than 5% relative to measured values. The spectral UV data errors associated with the experimental data are conservatively estimated to be less than 9% (Jacovides et al. 2012). Air temperature (T), relative humidity (Rh), sunshine hours (n) and ozone column amount (O_3) are also available supplementing the radiometric data. It is noted that the ozone column amount has been extracted from the TOMS website (http://toms.gsfc.nasa.gov). Finally,

the database was extended with the daily precipitable water content (w), air mass (m), and daylength (N). For the purpose of developing and testing the ANN-models, the whole database was divided into two subsets following a uniformly random distribution. The training data set contained 730 days and the test data set comprised 365 days.

3 Results

The computer codes for each ANN-model were developed in the MATLAB-software, whereas the architecture chosen is the feed-forward back propagation. All ANN-models used in this analysis are trained until the best performance is obtained. Once this criterion is achieved the optimal weights and biases are saved for further use to testing and validating the models. It also is noted here that in all ANN-models, one hidden layer was sufficient for modeling and estimating the daily global solar radiant fluxes (Tymvios et al. 2005; Benghanem et al. 2009).

Further, the performance of the ANN-models was assessed by means of the widely used statistical indicators, MBE and RMSE, which are normalized and they are expressed as a percentage of the corresponding mean values of the measured radiant fluxes. In addition, to indicate objectively whether the estimates of ANN-models are statistically significant, a supplementary statistical indicator, the *t-test*, combining both MBE and RMSE in their original form, is used (Jacovides and Kontogianis 1995).

Figure 1 displays predicted global radiant flux values through ANN-4 (Fig. 1a) and ANN-5 (Fig. 1b) models versus measured values. Figure 1c shows statistics of all ANN-models' developed here; this figure clearly indicates that ANN-4 and ANN-5 models provide the lower MBE and RMSE, while ANN-3, ANN-2 and ANN-1 models follow in that order. Results obtained through the five ANN-models developed here are statistically significant at the particular confidence level 97.5%, since their *t-test* values are less than the critical one ($t_{crit} = 1.96$).

Figure 2 displays a comparison between measured and predicted daily global G_{PAR} radiant flux obtained through ANN-4 model employing simple variables (Fig. 2a) and ANN-3 model using both solar and atmospheric variables (Fig. 2b), whereas statistics of the eight ANN-models developed are given in Fig. 2c. From these figures an acceptable agreement between measured and predicted daily global PAR radiant flux is obtained through all ANN-models. That is, all ANN-models' predictions are statistically significant at the particular confidence level 97.5%.

Viewing further ANN-models' statistics it is clear that the simple ANN's model making use of sunshine, daylength and precipitable water as inputs variables predicts accurately the daily global radiant flux, while the ANN-3 performed best when comparing against all ANN-models developed here. Earlier studies showed that G_{PAR} is strongly correlated with G (Ge et al. 2011) further implying the crucial role of the global radiant flux in modeling spectral radiant fluxes (Tymvios et al. 2008; Jacovides et al. 2009).

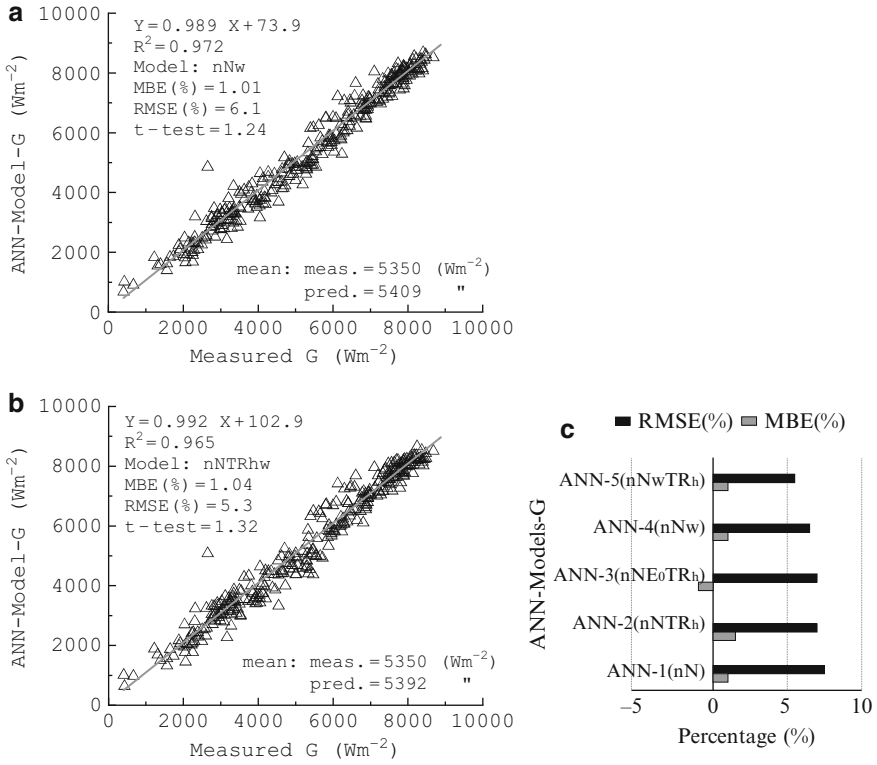

Fig. 1 ANN-4 (**a**) and ANN-5 (**b**) models' predictions for G radiant flux along with all ANN-models' statistics (**c**)

Further, Fig. 3 displays selected examples of scatter plots between ANN-3 (Fig. 3a) and ANN-4 models versus measured UV radiant flux, while ANN-models' statistics are given in Fig. 3c. It is well known that UV radiant flux is affected by cloudiness, optical air mass and ozone column amount (Junk et al. 2007; Bilbao et al. 2010), whereas numerous studies reported on the effective correlation between global G radiant flux and G_{UV} (Foyo-Moreno et al. 2003; Alados et al. 2004; Jacovides et al. 2009).

Further comparison between the two ANN-models given in Fig. 3a, b reveals that effective predictors affecting the ultraviolet solar portion may be included in modeling UV studies. It is clear that all statistical indicators MBE(%), RMSE(%) and *t-test* have been substantially improved when predictors, namely n, N, m, G, O_3 T and Rh are included in the ANN-model, further verifying earlier findings reported by various workers (i.e. Barbero et al. 2006; Junk et al. 2007).

Moreover, it is underlined here that RMSE and MBE values obtained through all ANN-models are consistent with those reported by other researchers for the UV radiant flux. Thus, Alados et al. (2004) reported RMSE (%) values ranging between

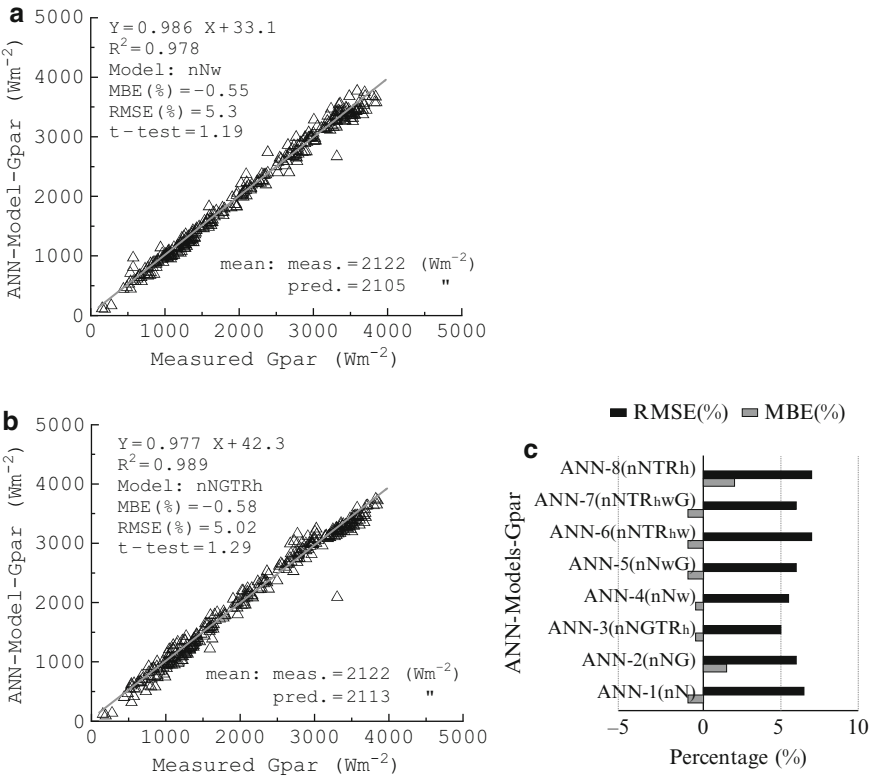

Fig. 2 ANN-4 (**a**) and ANN-3 (**b**) models' results for G_{PAR} radiant flux along with all ANN-models' statistics(**c**)

14.4% and 20.9% with relevant ANN-models applied for the Spanish environment. In contrast, MBE values reported for Spain are much less than that found here, whereas the present ANN-3, 4-models' results seem to be exceptions.

Further commenting on the ANN-models' performance, it is clear that the simplest ANN-model used as inputs n and N. Results on RMSE and MBE reveal that for both G and G_{PAR}, this combination is sufficient in producing acceptable radiant fluxes values; by contrast, this combination is not true for G_{UV}. Interestingly, by adding O_3 amount the simple ANN-model substantially improved, further revealing that ozone amount may be taken into account for modeling UV studies. The important role of O_3 on ANN's predictions is further demonstrated through ANN-6 versus ANN-5 comparison. That is, in ANN-6 model n, N and m are the inputs with RMSE and MBE of about 14% and −3.5% respectively; while in ANN-5 model by adding O_3 amount model's predictions are improved, with RMSE ~ 12.4% and MBE ~ −1.05%. It also is clear that ANN-4 model's performance is the best since numerous effective parameters, both solar and atmospheric, are included.

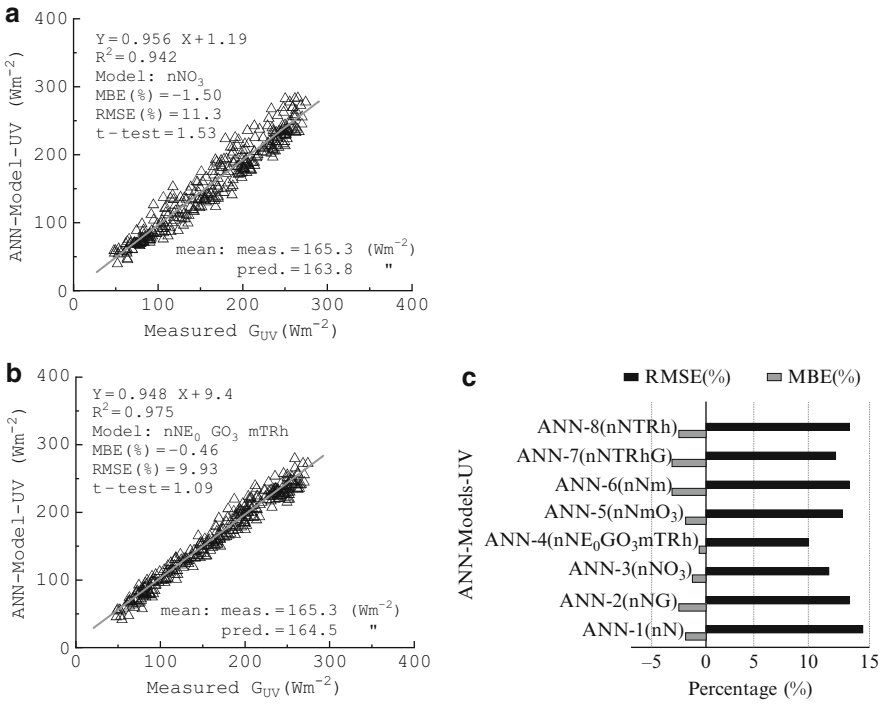

Fig. 3 ANN-3 (**a**) and ANN-4 (**b**) models results for G_{UV} radiant flux along with all ANN-models' statistics (**c**)

In principle, as reported by numerous researchers worldwide, most of the parameters likely affecting radiant components (ozone, cloudiness, trace gases, dust aerosols, site's characteristics, ground albedo, geometrical factors, etc.) may result in dissimilar variability on spectral PAR and UV modeling tools. Nevertheless, these parameters could have simultaneous changes which may add up resulting in spectral fluxes changes up to 30% or even more. On the other hand, several other parameters may inversely impact on the spectral radiant fluxes changes so that the net result may have an opposite sign compared to the above one, further reflecting the models' predictions. Therefore, for modeling accuracy of the spectral radiant fluxes it is essential to have as many measurements as possible of these radiant fluxes under diverse environmental conditions.

4 Conclusions

Design and analysis of artificial neural network models based on multilayer perceptron for the estimation of daily solar radiant components reveal the feasibility of this tool for predicting G, G_{PAR} and G_{UV} radiant fluxes. In this study case only

one hidden layer is sufficient for estimating daily global spectral radiant fluxes through both solar and atmospheric parameters. Sunshine duration plays an important role in obtaining accurate results, whereas other parameters used may have conflicting influences on the ANN-models' predictions. Comparing statistical performances for all ANN-models' presented in this analysis, it can be seen that the models ANN-(nNTRhw) for G, ANN-(nNGTRh) for G_{PAR} and ANN-($nNE_0GO_3m\ TR_h$) for G_{UV} exhibit the best results. Moreover, results obtained in this study render the ANN methodology as a promising alternative for estimating both broadband and spectral radiant fluxes.

References

Alados I, Mellado JA, Ramos F, Alados-Arboledas L (2004) Estimating UV erythemal irradiance by means of neural networks. Photochem Photobiol 80:351–358

Barbero FJ, Lopez G, Batlles FJ (2006) Determination of daily solar ultraviolet radiation using statistical models and artificial neural networks. Ann Geophys 24:2105–2114

Benghanem M, Mellit A, Alamri SN (2009) ANN-based modeling and estimation of daily global solar radiation data: a case study. Energy Convers Manage 50:1644–1655

Bilbao J, Mateos-Villan D, de Miguel A (2010) Analysis and cloudiness influence on UV total radiation. Int J Climatol 31:451–460

Foyo-Moreno I, Alados I, Olmo FJ, Alados-Arboledas I (2003) The influence of cloudiness on UV global irradiance (295–385 nm). Agric For Meteorol 1(20):101–111

Ge S, Smith RG, Jacovides CP, Kramer MG, Carruthers RI (2011) Dynamics of photosynthetic photon flux density (PPFD) and estimates in coastal northern California. Theor Appl Climatol 105(1–2):107–118

Jacovides CP, Kontogianis H (1995) Statistical procedure for the evaluation of evapotranspiration computing models. Agric Water Manage 27:365–371

Jacovides CP, Tymvios FS, Asimakopoulos DN, Kaltsounides NA (2009) Solar global UVB (280–315 nm) and UVA (315–380 nm) radiant fluxes and their relationships with broadband global radiant flux at an eastern Mediterranean site. Agric For Meteorol 149:1188–1200

Jacovides CP, Boland J, Rizou D, Kaltsounides NA, Theoharatos GA (2012) School Students participation in monitoring solar radiation components: preliminary results for UVB and UVA solar radiant fluxes. Ren Energy 39:367–374

Junk J, Feister U, Helbig A (2007) Reconstruction of daily solar UV irradiation from 1893 to 2002 in Potsdam, Germany. Int J Biometeorol 5:505–512

Lopez G, Rubio MA, Martinez M, Batlles FJ (2001) Estimation of hourly global photosynthetically active radiation using artificial neural network models. Agric For Meteorol 107:279–291

McCree KJ (1972) Test of current definitions of photosynthetically active radiation against leaf photosynthesis data. Agric Meteorol 10:443–453

Parisi AV, Turnbull DJ, Turner J (2007) Calculation of cloud modification factors for the horizontal plane eye damaging ultraviolet radiation. Atmos Res 86:278–285

Ross J, Sulev M (2000) Sources of errors in measurements of PAR. Agric For Meteorol 10:103–125

Tymvios FS, Jacovides CP, Michaelides SC, Scouteli C (2005) Comparative study of Angstrom's and artificial neural networks' methodologies in estimating global solar radiation. Sol Energy 78:752–762

Tymvios FS, Michaelides SC, Scouteli C (2008) Estimation of surface solar radiation with artificial neural networks. In: Badescu V (ed) Modeling solar radiation at the Earth's surface: recent advances. Springer, Berlin

Cloud Detection and Classification with the Use of Whole-Sky Ground-Based Images

P. Tzoumanikas, A. Kazantzidis, A.F. Bais, S. Fotopoulos, and G. Economou

Abstract A simple whole sky imaging system, based on a commercial digital camera with a fish-eye lens and a hemispheric dome, is used for the automatic estimation of total cloud coverage and classification. For the first time, a multi color criterion is applied on sky images, in order to improve the accuracy in detection of broken and overcast clouds under large solar zenith angles. The performance of the cloud detection algorithm is successfully compared with ground based weather observations. A simple method is presented for the detection of raindrops standing on the perimeter of hemispheric dome. Based on previous works on cloud classification, an improved k-Nearest-Neighbor algorithm is presented. The successful detection percentage of the classifier ranges between 78% and 95% for seven cloud types.

1 Introduction

Surface observations made at weather stations provide the longest available records of cloud cover changes and cloud type determination. Despite their unquestionable usefulness, these observations are associated with inhomogeneities in observation times and methodology. Additionally, the introduction of human factor and a rough measuring system (in octas or tenths of the sky dome) in the estimation of cloud cover and type weaken their credibility.

P. Tzoumanikas • A. Kazantzidis (✉)
Laboratory of Atmospheric Physics, University of Patras, Patras, Greece
e-mail: akaza@upatras.gr

A.F. Bais
Laboratory of Atmospheric Physics, Aristotle University of Thessaloniki, Thessaloniki, Greece

S. Fotopoulos • G. Economou
Electronics Laboratory, University of Patras, Patras, Greece

C.G. Helmis and P.T. Nastos (eds.), *Advances in Meteorology, Climatology and Atmospheric Physics*, Springer Atmospheric Sciences,
DOI 10.1007/978-3-642-29172-2_49,

In recent years, ground-based sky imaging systems have been developed and used for obtaining continuous information about the cloud conditions over specific sites. In some cases, these instruments are commercial, like the Whole Sky Imager (Shields et al. 1998; Feister and Shields 2005; Cazorla et al. 2008) and the Total Sky Imager (Long et al. 2006). Additionally, some scientific teams have developed low-cost alternatives for their research activities (Pfister et al. 2003; Kreuter et al. 2009; Kalisch and Macke 2008).

Some attempts have been made to develop algorithms for cloud type classification from whole sky images. Most of those methods are used for the estimation of cloud base height (Kassianov et al. 2005) or the identification of high or low clouds (Long et al. 2008; Cazorla et al. 2008; Parisi et al. 2008). Heinle et al. (2010) presented a cloud classification algorithm, based on a set of mainly statistical features describing the color as well as the texture of an image. They proposed the use of a k-Nearest-Neighbor (kNN) classifier, due to its high performance in solving complex issues, simplicity of implementation and low computational complexity. They distinguished seven different types of sky conditions (cumulus, cirrus and cirrostratus, cirrocumulus and altocumulus, clear sky, stratocumulus, stratus and altostratus, cumulonimbus and nimbostratus) and reported an accuracy of about 75% on a test run of random images.

In this study, whole-sky images from a commercial digital camera are processed. For the first time, a multi-color criterion is used for the determination of total cloud coverage. Additionally, an improved cloud classification, based on the work of Heinle et al. (2010) is presented including also a metric for the existence of rain in the digital images.

2 Data and Methodology

2.1 Data

The images used in this study were obtained with a commercial compact digital camera (Canon IXUS II), operating at the building roof of the Laboratory of Atmospheric Physics, of the Aristotle University of Thessaloniki, Greece (40.63°N, 22.96°E, 60 m amsl). A fish-eye lens (field of view = 180°) was mounted in front of the entrance optics of the camera. The system is enclosed in a water and weather resistant box with a glass dome pointing to the zenith and connected via RS-232 cable to a personal computer for external automated control. The camera is programmed to acquire one image every 5 min, stored in 8-bit JPEG format with spatial resolution 640 × 480 pixels. The whole sky is depictured as a circle. No shadowing mechanism for obscuring the direct solar radiation is used.

2.2 Methodology

The method for the detection of clouds and the estimation of total cloud coverage is based on the fact that color is the primary property that allows the visual detection of clouds on the sky. Using a diverse set of images with a variety of cloud conditions (including cases with different types and coverage) under different solar zenith angles, we found that the use of a ratio or a difference of Red (R) and Blue (B) intensities results in errors for cases of broken or overcast cloudiness under large solar zenith angles. In order to set a suitable threshold for discriminating cloud areas also under these conditions, we used a multi color threshold taking also into account the Green (G) intensity of the image. For the detection of cloudy pixels, the proposed threshold is defined as follows:

$$\mathbf{B}<\mathbf{R}+\mathbf{20}\ \&\ \mathbf{B}<\mathbf{G}+\mathbf{20}\ \&\ \mathbf{B}<\mathbf{60}.$$

Heinle et al. (2010) developed a cloud classifier, based on the k-Nearest-Neighbor (kNN) method. They selected 12 features, separated in three teams, containing the color information (at R, G, B) and grey levels of each image. Our method is based on that cloud classifier. We used, apart from the proposed features, the existence of raindrops in the image as an additional metric.

For the detection of raindrops in our images, we take advantage of the hemispherical shape and structure of the dome and of the fact that it is not self-cleaned during rain. As a result, we can clearly observe the raindrops standing on the perimeter of the hemispheric dome, which distort the circular shape of the perimeter of the image during dry conditions. In all cases, we calculate the "circle factor" (CF), a factor indicative of the circle's perfectness. For each image we calculate the average perimeter (P) and the area (A) of the corresponding circle (right). CF is calculated from the equation $CF = \frac{4\pi A}{P^2}$. For a perfect circle CF should be equal to one.

A set of 2,550 (out of 50,000) images was used for training and testing the cloud classifier. All images were selected by visual inspection to be representative for different cloud types that we would like to identify and for a variety of solar zenith angles and fractions of the solar disk. Additionally, the selected images were carefully inspected to comprise clouds of only one class. A subset of 1,050 images (with 150 images per cloud class) was selected for training the cloud classifier. The rest of the images (1,500 with at least 150 images per cloud class) were used to assess the methodology.

3 Results

The total cloud coverage values, derived from the proposed method, were compared to the SYNOP observations at the airport of Thessaloniki. The station is located towards the south-west of the camera site on a flat area near the seashore.

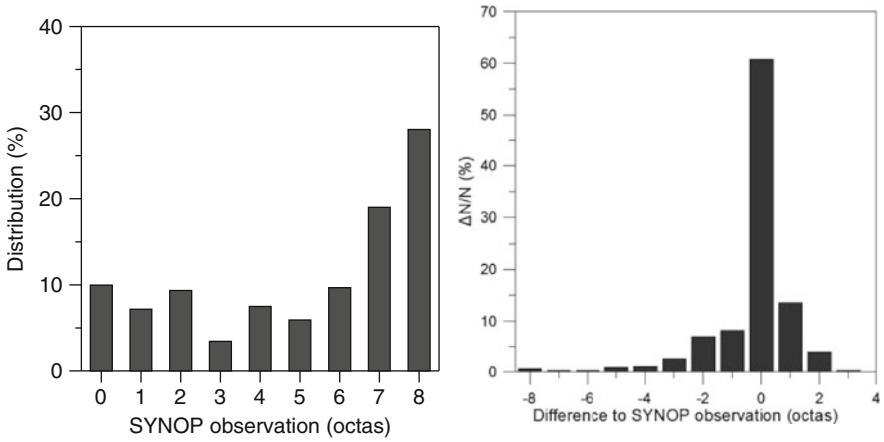

Fig. 1 The frequency distribution (%) of the selected SYNOP observations for the comparison with the sky camera estimations of total cloud coverage (*left panel*). Percentage (%) of total cloud cover estimations from the whole-sky camera images against the difference from the SYNOP observations (*right panel*)

Although this is the nearest meteorological station, the distance between the two sites is about 10 km. The available SYNOP observations at 6, 9, 12 and 15 UT were compared with the camera images at the same time. Images corresponding to solar zenith angles above 80° were excluded from this comparison. Additionally, we excluded images obtained during the period May–September, when most images are taken under clear skies of under skies with very few clouds. The frequency distribution of the selected SYNOP cloud coverage observations is presented in Fig. 1 (left panel). The lowest (3.5%) and highest (28%) values appear for 3 and 8 octas respectively, and 51% of the observations are between 6 and 8 octas. The distribution of the differences between the two datasets is presented in Fig. 1 (right panel). The 83% and the 94% of the analyzed images agree with the SYNOP observations to within 1 and 2 octas respectively.

The accuracy of the classifier (the correctly classified images from the 1500 images) ranges between 78% and 95% (Table 1). The rate of successful detection of cumulus clouds is 91.9%. The remaining images are assigned as cirrus-cirrostratus and cirricumulus-altocumulus (5.1% and 3% respectively). The misclassified cases correspond to whole-sky images with only a few clouds close to the horizon, far away from the camera site. Cirrus-cirrostratus clouds are successfully detected in the 94.6% of the images. Some images picturing overcast skies with these high clouds are classified to one of the three kinds of cumulus clouds. The lowest performance of the classifier (78%) is revealed for cirrocumulus-altocumulus. In this case, the rest of the images are distributed in all classes except stratus and cumulonimbus-nimbostratus. Stratocumulus and cumulonimbus-nimbostratus are correctly detected in 92.9% and 82.6% of cases respectively. There is a small confusion between these two cloud classes, since the rest of images are classified

Table 1 Classification matrix of the selected cloud types

	Cloud classification						
True cloud class	1	2	3	4	5	6	7
1. Cumulus	91.9	5.1	3.0	0.0	0.0	0.0	0.0
2. Cirrus-cirrostratus	1.8	94.6	3.0	0.6	0.0	0.0	0.0
3. Cirrocumulus-altocumulus	8.5	8.4	78.0	5.1	0.0	0.0	0.0
4. Stratocumulus	0.0	0.0	0.0	92.9	1.8	5.3	0.0
5. Straus-altostratus	0.0	0.0	0.0	6.9	93.1	0.00	0.0
6. Cumulonimbus-nimbostratus	0.0	0.0	0.0	17.4	0.0	82.6	0.0
7. Clear sky	0.0	5.0	0.0	0.0	0.0	0.0	95.0

The average performance of the classifier is 87.9%

to the other class and not the correct one. A high score or our classifier (93.1%) is revealed also for stratus-altostratus, while the rest of them (6.9%) are assigned as stratocumulus. Finally, the clear skies can be successfully detected in 95% of cases. The rest of the images correspond to days with considerably high values of aerosol optical depth, an optical parameter that has not been taken into account in the classification algorithm. According to aerosol measurements from a CIMEL sun photometer at the same site, the aerosol optical depth values were above 0.8 (at 440 nm) when these sky images were taken.

4 Conclusions

A whole-sky image system, based on a commercial digital camera has been used and characterized with respect to detecting the total cloud cover and classifying the digital images in seven cloud classes. For the first time, a multi color criterion is proposed for the estimation of total cloud coverage leading to improved results for broken or overcast cloudiness and for large solar zenith angles. According to this method, 83% and the 94% of the analyzed images agree to within ± 1 and ± 2 octas respectively with visual weather observations at a close by meteorological station.

An improved cloud classification algorithm, based on the work of Heinle et al. (2010), is also proposed. For the first time, we present a method to detect raindrops on sky images and include it as a metric to a cloud classifier. The classifier can detect correctly seven cloud types in 78–95% of the cases.

Acknowledgments We gratefully acknowledge the Hellenic National Meteorological Service for supplying the SYNOP cloud observations. We would like to thank the research staff of the Laboratory of Atmospheric Physics, Aristotle University of Thessaloniki, Greece, for maintaining the sky camera. This work was inspired by the activities of COST Action ES1002, "Weather Intelligence for Renewable Energies". This study was conducted in the frame of project "Hellenic Network of Solar Energy" (HNSE), funded by the General Secretariat for Research and Technology, Greek Ministry of Education, Lifelong Learning and Religious Affairs.

References

Cazorla A, Olmo FJ, Alados-Arboledas L (2008) Development of a sky imager for cloud cover assessment. J Opt Soc Am A 25(1):29–39

Feister U, Shields J (2005) Cloud and radiance measurements with the VIS/NIR Daylight Whole Sky Imager at Lindenberg (Germany). Meteorol Z 14(5):627–639

Heinle A, Macke A, Srivastav A (2010) Automatic cloud classification of whole sky images. Atmos Meas Tech 3:557–567

Kalisch J, Macke A (2008) Estimation of the total cloud cover with high temporal resolution and parametrization of short-term fluctuations of sea-surface insolation. Meteorol Z 17:603–611

Kassianov E, Long CN, Christy J (2005) Cloud-base-height estimation from paired ground-based hemispherical observations. J Appl Meteorol 44:1221–1233

Kreuter A, Zengerl M, Schwarzmann M, Blumthaler M (2009) All-sky imaging: a simple, versatile system for atmospheric research. Appl Opt 48(6):1091–1097

Long CN, Sabburg JM, Calbó J, Pagès D (2006) Retrieving cloud characteristics from ground-based daytime color all-sky images. J Atmos Ocean Technol 23:633–652

Parisi AV, Sabburg J, Turner J, Dunn PK (2008) Cloud observations for the statistical evaluation of the UV index at Toowoomba, Australia. Int J Biometeorol 52:159–166

Pfister G, Mc Kenzie RL, Liley JB, Thomas A, Forgan BW, Long CN (2003) Cloud coverage based on all-sky imaging and its impact on surface solar irradiance. J Appl Meteorol 42:1421–1434

Shields JE, Johnson RW, Karr ME, Wertz JL (1998) Automated day/night whole sky imagers for field assessment of cloud cover distributions and radiance distributions. In: Proceedings of the 10th Symposium on meteorological observations and instrumentation, Boston, MA, 11–16 Jan 1998

Factors Determined Snow Accumulation Over the Greater Athens Area During the Latest Snowfall Events

A. Voudouri and D. Kotta

Abstract Snowfall events accompanied with snow accumulation over the Greater Athens Area (GAA) are not common. The last event in GAA took place between 7th and 9th of March 2011 (case 1). The prevailing synoptic conditions that forced this snowfall, namely the entrainment of arctic air masses, accompanied by moister and warmer air masses from the Aegean following the north-northeasterly flow, were quite similar to those of the previous intense snowfall in GAA between the 16th and 18th of February 2008 (case 2). However the effects as well as the intensity of case 1 were less than expected compared to those recorded in case 2. This study is focused not only to further investigate the mechanisms that may generate snowfall events over GAA, but mainly the key-factors that restrained the snowfall in GAA in case 1 from being intense, affecting also operational forecast. This is made through the intercomparison of both cases using available observations and numerical weather prediction products such as ensemble prediction and deterministic forecasts.

1 Introduction

Snowfall over the Greater Athens Area (GAA) in not common especially in cases where snow is persistent more than 24 h and accumulates, disrupting everyday life. According to Houssos et al. (2007) more than 50% of snow events that occurred in Athens during the period 1958–2001 lasted for one day, while only once did the event last for 4 days. Only one snow event occurred in November while the others occurred during the months December, January, February and March.

A. Voudouri (✉) • D. Kotta
Hellenic National Meteorological Service, Elliniko 16777, Greece
e-mail: a.voudouri@yahoo.gr

C.G. Helmis and P.T. Nastos (eds.), *Advances in Meteorology, Climatology and Atmospheric Physics*, Springer Atmospheric Sciences,
DOI 10.1007/978-3-642-29172-2_50,

The last snowfall event in GAA was recorded between the 7th and 9th of March 2011 (case 1) and has lasted for more than 30 h over GAA. According to the Hellenic National Meteorological Service (HNMS) data, during this interval it was snowing with small interruptions for more than 33 h over Tatoi, 24 h over Elefsina and 12 h over Spata stations. Although there are no records of significant snow accumulation over the HNMS stations, several observations across GAA reported up to 10 cm snow locally over west and north suburbs.

The synoptic evolution of the barometric systems that cause snowfall in Athens has been studied in several cases. According to Prezerakos and Angouridakis (1984) the specific characteristics of the snowfall in Athens are related to the synoptic evolution of two types, A and B. In type A, a quasi-stationary ridge on 500 hPa is established over the British Isles and north-western Europe, while in type B the ridge is over the Scandinavian countries. In both types arctic air masses are advected over Greece. A strong anticyclone, over western Europe in type A and over eastern Europe in type B, is combined with low surface pressures over eastern Mediterranean inducing a northerly surface flow. Lagouvardos and Kotroni (2002) pointed out the significance of jet streak and vorticity advection in sustaining a snowfall. Houssos et al. (2007) statistically classified snowfall events in five clusters extracting also the average values for specific meteorological characteristics of the first snow day. Louka et al. (2010) identified and analysed three stages on the physical processes that forced the 16th–18th of February 2008 (case 2) intense snowfall over the GAA.

Synoptic conditions prevailing in case 1, were quite similar to those in case 2 however both the intensity and the effects of case 1 were less than expected compared to those recorded in case 2. It should be noted that both cases originally follow type A pattern. This study is focused not only to further investigate the mechanisms that may generate snowfall events over GAA, but mainly the key-factors that restrained the snowfall in GAA in case 1 from being intense, effecting also operational forecast. This is made through the intercomparison of both cases using available observations and numerical weather prediction products.

2 Data and Synoptic Analysis

HNMS operational weather forecasts are mainly based on numerical weather prediction products (NWP) as well as upper air observations and ground-based observations obtained through a wide network of stations all over Greece. ECMWF provides daily deterministic forecasts with horizontal resolution 16 km twice per day, namely the 0000 UTC and 1200 UTC cycles. Although ECMWF provides operational medium and long range weather predictions these data can adequately describe the synoptic conditions that favor snowfall over GAA.

Ground-based observations from meteorological stations over GAA, namely Tatoi, Spata, Helliniko and Elefsina have been used in the present study. The soundings performed over Helliniko Station during case 1, as well as satellite

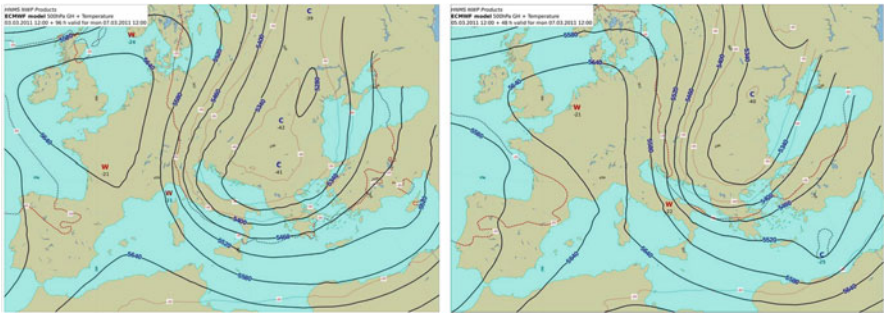

Fig. 1 ECMWF forecast of 500 hPa geopotential height and temperature for 7 March 2011 1200 UTC based on 3 March 2011 (*left panel*) and 5 March 2011 (*right panel*) 1200 UTC cycle

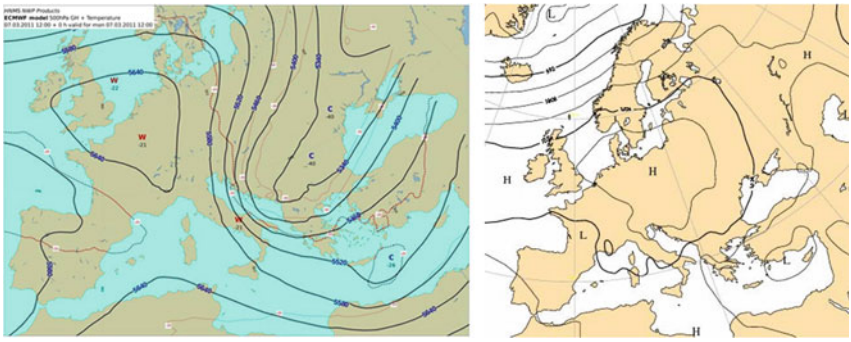

Fig. 2 ECMWF analysis of 500 hPa geopotential height and temperature for 7 March 2011 1200 UTC and MSL for the same time

images during the days of the event were gathered. Deterministic and ensemble forecasts from ECMWF forecasts based on all 0000 UTC and 1200 UTC cycles from 3 March 2011 to 7 March 2011 and analyses during the days of the event were also examined. The prevailing synoptic conditions that forced case 1 snowfall were early identified on the 3 March 2011 1200 UTC based simulation.

Figure 1 illustrates the ECMWF forecasts of 500 hPa geopotential height and temperature for 7 March 2011 1200 UTC (12 h before the beginning of the event) based on the 3 March 2011 and 5 March 2011 1200 UTC simulations, while the 7 March 2011 1200 UTC analyses of 500 hPa geopotential height, temperature and MSL pressure are presented in Fig. 2. A ridge over Western Europe and the British Isles and a low centered over NE Europe associated with an elongated trough and arctic air masses advecting towards Greece were evident. Cold surges were also predicted at 850 hPa with less than 0°C air masses covering Greece. In addition the entrainment of arctic air masses was accompanied by moister and warmer air masses from the Aegean initially following the surface northeasterly flow (Fig. 2). A considerable precipitation amount combined with low 2 m temperature was also early forecasted using the ECMWF ensemble prediction system (EPS). Figure 3 illustrates the Athens EPSgram for total precipitation, 10 m wind speed and 2 m

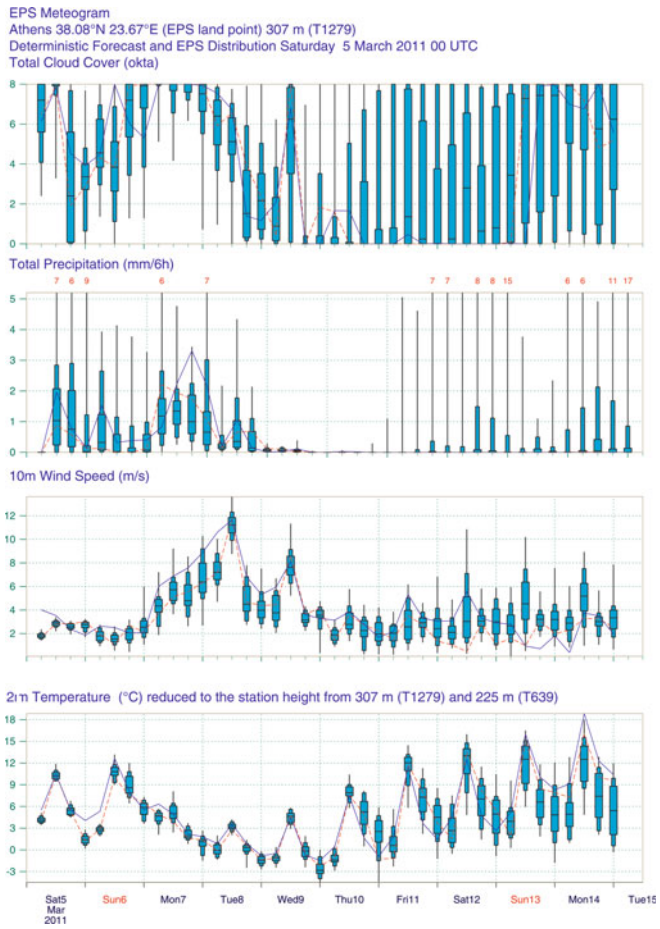

Fig. 3 Athens EPSgram based on the 5 March 2011 0000 UTC-cycle. The *red* line represents the control run (31 km resolution) of the EPS, the *blue* line represents the deterministic model run (16 km resolution) while the bars represent the percentiles of the ensemble prediction. EPS location is 12 km NW of the city centre

temperature respectively based on the 5 March 2011 0000 UTC-cycle for the control run (31 km resolution) of the EPS, the deterministic model run (16 km resolution) and the percentiles of the ensemble prediction. These conditions were quite similar to those of the previous intense snowfall in GAA of case 2 (Louka et al. 2010) indicating a forthcoming intense snowfall event of type A.

3 Discussion

The occurrence of a snowfall over GAA but mainly its intensity is important to be forecasted due to snowfall impacts on everyday life. Therefore an intercomparison of case 1 with the intense snowfall of case 2 is also performed. The average values

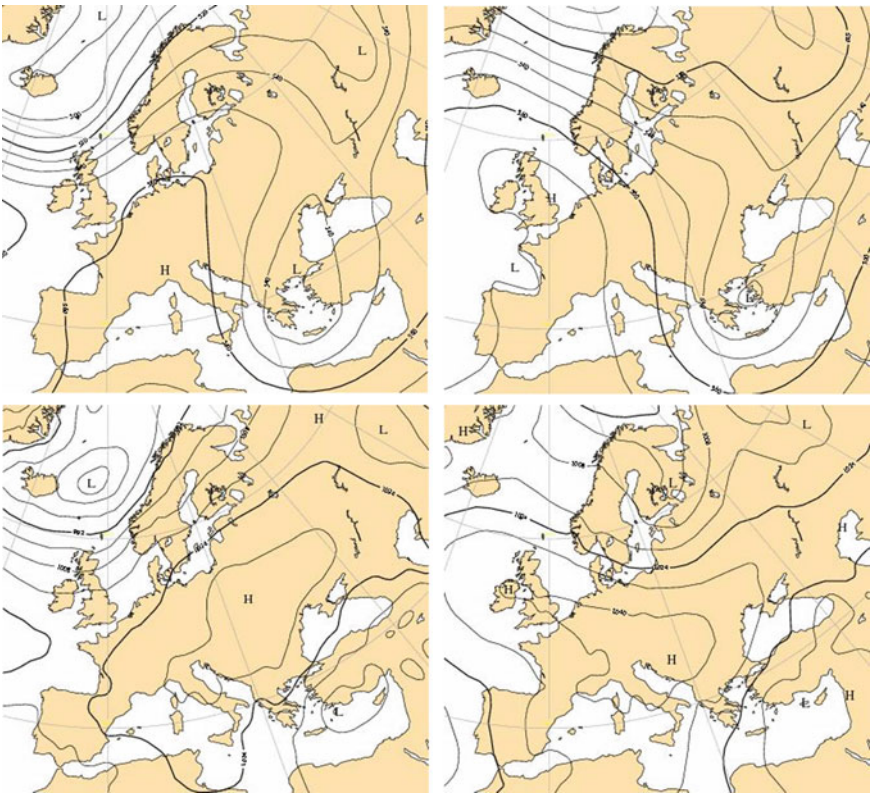

Fig. 4 Analyses of the 500 hPa geopotential height and MSL pressure on 8 March 2011 1200 UTC for case 1 (*left panels*) and for case 2 (*right panels*) on 17 February 2008 1200 UTC

of meteorological characteristic according to Houssos et al. (2007) statistical analysis as well as the synoptic conditions required according to Prezerakos and Angouridakis (1984) were fulfilled in both cases. At both cases initiation cold air masses were advected at 500 hPa with temperatures −33°C over GAA with geopotential heights in case 2 being much lower. Cold air masses intrusion was favoured (−40°C at 500 hPa) in case 2, while in case 1 the 500 hPa ridge moved eastwards and the formation of an extended cut-off low over Greece (Fig. 4) resulted to a weaker cold air masses feedback (−35°C at 500 hPa), suggesting a key-factor. It should be noted that although case 1 started as a type A event, ended as type B. Regarding the 850 hPa temperature, it reached −12°C in case 2, while in case 1 it was not lower than −8°C, with the surface temperature being also higher. Moreover the surface anticyclone in case 1 quickly extended over NE Europe establishing a NNE surface flow (strong NNE surface winds reached up to 50 kt over Central Aegean Sea). This eastwards movement of the surface anticyclone establishing the intense NNE flow in case 1 as shown in Fig. 4 could favour neither the enrichment of the atmosphere with moisture nor the "Aegean Snow effect".

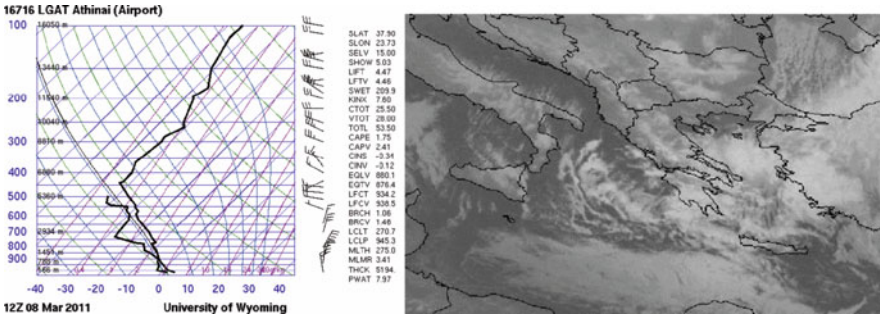

Fig. 5 Sounding at Helliniko station (lon: 23.73, lat: 37.89) on 8 March 2011 at 1200 UTC (*left panel*) (Source: University of Wyoming) and infrared satellite image on 8 March 2011 at 0600 UTC (*right panel*) (Source: Meteosat)

For snowfall events over GAA the "Aegean Snow effect" is important. As Louka et al. (2010) suggested this effect is similar to the "Great Lakes effect" (Niziol 1984) and is the main factor for intense snowfall events as in case 2. The necessary conditions according to Niziol (1984) are an unstable surface layer up to 850 mb with temperature difference $T_{sfc} - T_{850} > 13°C°$, directional wind shear between the planetary boundary layer (PBL) and 700 mb less than 30° with speeds less than 40 kt and significant moisture between the surface and 700 mb. These conditions were partly satisfied in case 1.

The sounding over Elliniko station at southern GAA at 1200 UTC on 8 March 2011 indicated a weak presence of humid air up to 750 mb (relative humidity between 56% and 98%), as well as a strong directional wind shear up to 40° and wind speed more than 40 kt between PBL and 700 mb suggesting key-factors for the intensity of the event (Fig. 5). Thus snow-band formation occurred in a much smaller scale as shown in the infrared satellite image in Fig. 5. However on 9 March 0000 UTC when snow was recorded over Elliniko station (Niziol 1984) necessary conditions were almost satisfied.

4 Conclusions

Operational forecast of the intensity of snowfall events over GAA is not an easy task. During the latest two cases the intensity of snowfall was strongly influenced by the position of the 500 hPa ridge west of Greece and the eastwards movement of the surface anticyclone. Favoring conditions for the 'Aegean snow effect', such as the temperature difference between surface and upper layers, specific wind shear and speed and the existence of significant moisture, should also be satisfied for intense snowfalls over GAA.

Acknowledgments The authors would like to acknowledge G. Mouxasiri and M. Plioutsas for providing figures of ECMWF forecasts and satellite images respectively and I. Mallas for providing the ECMWF EPSgrams.

References

Houssos EE, Lolis CJ, Bartzoka A (2007) The atmospheric conditions over Europe and the Mediterranean, favoring snow events in Athens, Greece. Adv Geosci 12:127–135. doi:10.5194/adgeo-12-127-2007

Lagouvardos K, Kotroni V (2002) The 4–6 January 2002 heavy snowfall over Central and Southern Greece: assessment of MM5 model forecasts. In: Proceedings of the 4th EGS plinius conference, Mallorca, Spain

Louka P, Boucouvala D, Gofa F, Balami M, Ziakopoulos D (2010) Operational forecasting of a snowfall event over the Greater Athens Area. Adv Geosci 23:25–30. doi:10.5194/adgeo-23-25-2010

Niziol TA (1984) Operational forecasting of lake effect snowfall in western and central New York. Weather Forecast 2:310–321. doi:10.1175/1520-0434(1987) 002<0310:OFOLES>2.0.CO;2 DOI:dx.doi.org

Prezerakos NG, Angouridakis VE (1984) Synoptic consideration of snowfall in Athens. J Climatol 4(3):269–285. doi:10.1002/joc.3370040305

Part II
Climatology

Simulating the Climatology of Extreme Events for the Central Asia Domain Using the RegCM 4.0 Regional Climate Model

H. Altinsoy, T. Ozturk, M. Turkes, and M.L. Kurnaz

Abstract In this work, future changes in the frequency of the seasonal extreme climate events such as number, frequency, duration and intensity of heat waves (5 consecutive temperature days above the maximum temperature calendar day 90th percentiles, number of days per year that is above the same percentiles and greatest number of consecutive days above these percentiles) for the period of 2071–2100 over Central Asia (18.56°–70.13° East and 7.28°–142.4° North) with respect to the present period of 1971–2000 were studied in detail. Regional Climate Model RegCM 4.0 of Abdus Salam International Center for Theoretical Physics (ICTP) with ECHAM5 forcing data was used for hindcast and forecast projection. This region will very likely be affected by heat waves in winter and spring seasons and heat wave frequency, intensity and duration will increase significantly over the Arabian Peninsula in summer. On the other hand, cold spells will not change as much as heat waves over the region in all seasons.

1 Introduction

Central Asia region consists of mostly arid and semi-arid lands, grasslands, rangelands, deserts and some woodlands (Türkeş 2010a, b; Lioubimtseva 2002). Particularly because of the semi-arid nature of the region, Central Asia's

H. Altinsoy (✉) • M.L. Kurnaz
Department of Physics, Bogazici University, Istanbul 34342, Turkey
e-mail: hamza.altinsoy@boun.edu.tr

T. Ozturk
Department of Physics, Bogazici University, Istanbul 34342, Turkey

Department of Physics, Isik University, Istanbul 34980, Turkey

M. Turkes
Physical Geography Division, Department of Geography, Canakkale Onsekiz Mart University, Canakkale 17020, Turkey

C.G. Helmis and P.T. Nastos (eds.), *Advances in Meteorology, Climatology and Atmospheric Physics*, Springer Atmospheric Sciences,
DOI 10.1007/978-3-642-29172-2_51,

environmental and socio-economic systems are under serious threat of the climate change according to Intergovernmental Panel on Climate Change (IPCC) Fourth Assessment Report.

There are several investigations about the analysis of extreme events and their impacts for Europe, Americas, and the Mediterranean basin, etc. (e.g., Easterling et al. 1999; Deque 2007; Beniston et al. 2007) with future projections. However, there are very few studies on climatic extreme events, covering the Central Asia domain (Klein Tank et al. 2006). Most of these analyses include only specific regions such as China, Tibet Plateau, India etc. (You et al. 2008) without any future projections. In this work the frequency, intensity and duration of heat waves have been analyzed for the Central Asia region using both hindcast and forecast data.

2 Data and Methodology

Extreme temperature events can be identified by various ways and several temperature extremes studies are performed according to different definitions such as those by Peterson et al. (2001).

2.1 Data

In this study, Regional Climate Model (Giorgi et al. 1993a, b) of the Abdus Salam International Center for Theoretical Physics (ICTP), RegCM version 4.0 with CLM community land model (Oleson et al. 2007) option was used to simulate temperature extremes for the Central Asia domain with a horizontal resolution of 50 km. ECHAM5 (Roeckner et al. 2003) global climate model data set, with a resolution of $2.5^\circ \times 2.5^\circ$ was used to obtain initial and boundary conditions for present climate (1970–2000 period) and for future climate simulations (2070–2100 period) with A1B greenhouse gases emission scenario. We chose 50 km resolution because of the reason that RegCM resolution can be at most one over five of global data set. RegCM 4.0 mainly includes CCSM3 (Kiehl et al. 1996) for radiation package, MM5 (Grell et al. 1994) for dynamical structure, BATS (Dickinson et al. 1993) for surface processes (Holtslag et al. 1990) PBL scheme and (Grell 1993) convective precipitation scheme.

2.2 Methodology

We estimated the intensity, duration and frequency of heat waves for the period 1970–2000 and 2070–2100 for each climatological season by applying the indices (Beniston et al. 2007) shown in Table 1. The 90th percentile values are calculated for each calendar day of the period 1970–2000.

Table 1 Definitions of the extreme temperature indices used in the study

Variable	Period	Indices
Maximum air temperature (t2max)	1970–2000 (past) 2070–2100 (future)	Number of days per year that is above the 90th percentile of calendar day t2max-pastvalue (HWNY90-period) Greatest number of consecutive days in past/future period with t2max-past/future above the 90th percentile of value t2max-past value (GHW90-period) Number of consecutive HWNY90-period with more than 5 days (HWN590-period)

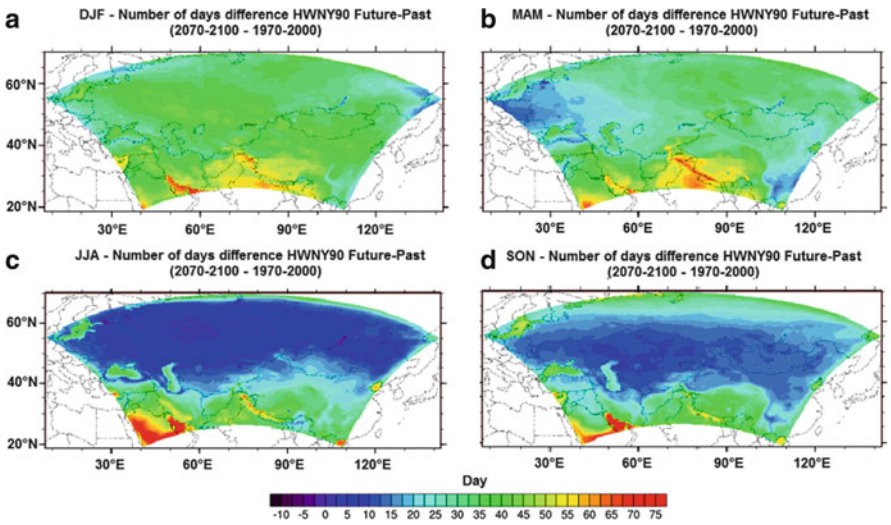

Fig. 1 The difference of "number of days per year that daily maximum air temperature is above 90th percentile value of daily maximum air temperature of 1970–2000 period" (**HWNY90**) between future (2070–2100) and past (1970–2000) period for (**a**) winter, (**b**) spring, (**c**) summer, (**d**) autumn

3 Results

We found that the intensity and frequency of heat waves increase for the whole domain. Southwest Iran, Pakistan, Afghanistan and Northern India in winter and spring season, Arabian Peninsula and Southwest Iran in summer and autumn season will be affected by heat waves more seriously. The number of hot days in the Arabian Peninsula in summer will increase in the future period compared to the reference period. In Northern India, 65% of days in winter and spring season will be extremely hot days in the future in comparison to the reference period as shown in Fig. 1. In Central Asia, the frequency of hot days will increase more than four times of past amount in winter season (Figs. 2 and 3).

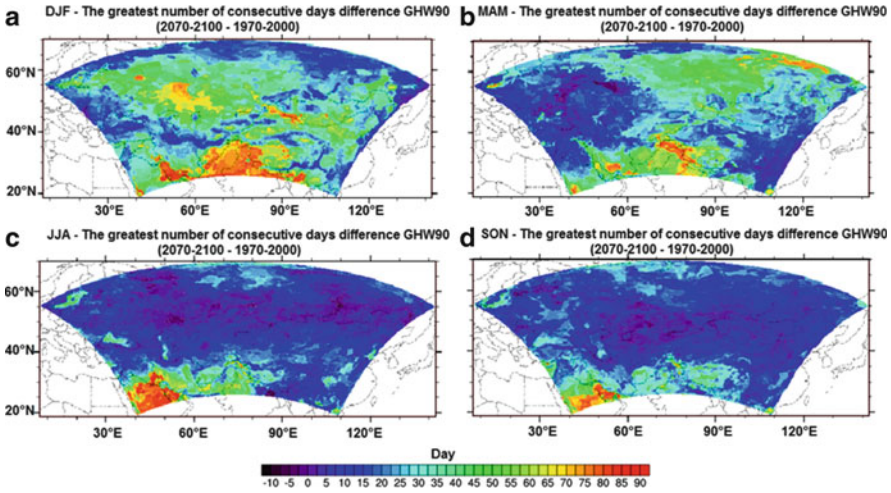

Fig. 2 The difference of "the greatest number of consecutive days per time period with daily maximum air temperature above 90th percentile value of daily maximum air temperature of 1970–2000 period" (**GHW90**) between future (2070–2100) and past (1970–2000) period for (**a**) winter, (**b**) spring, (**c**) summer, (**d**) autumn

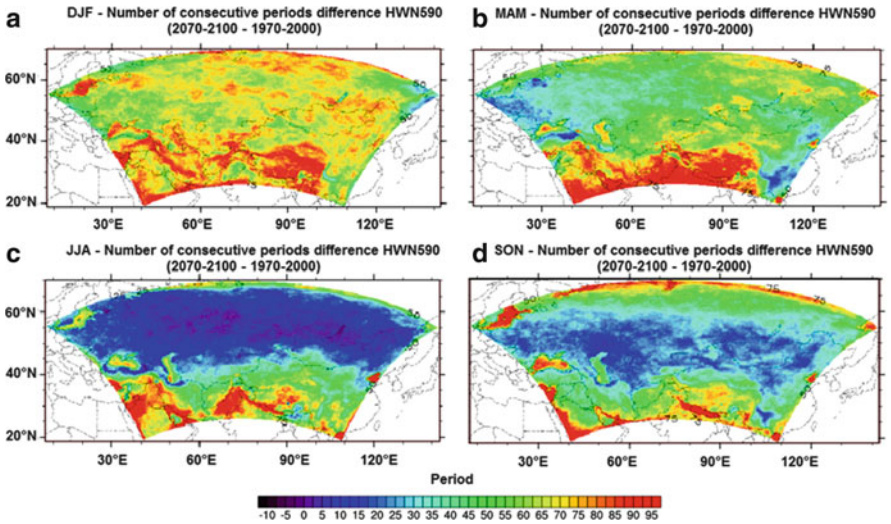

Fig. 3 The difference of "the number of consecutive periods in a given time period with more than 5 days that daily maximum air temperature is above 90th percentile value of daily maximum air temperature of 1970–2000 period" (**HWN590**) between future (2070–2100) and past (1970–2000) period for (**a**) winter, (**b**) spring, (**c**) summer, (**d**) autumn

4 Conclusions

In this study, we investigated the changes in heat waves over large Central Asia domain using the RegCM 4.0 regional climate model. Strong heat waves have recently affected the public health and taiga forests, and resulted in dryness and forest fires in a large domain including eastern Russia and Siberia during the 2010 July and August. Daily maximum air temperatures of Turkey also corresponded to a longer warm period characterized with heat wave conditions particularly in August 2010 (Acar and Türkeş 2011). Heat waves during this period affected all of Turkey, while increases in the number of tropical days over the Black Sea Region were remarkable. In future, Arabian Peninsula and Northern India will also be affected more frequently and strongly by heat waves. Moreover, at least 30% of days in all seasons will be extremely hot days over most of the region in the future.

Acknowledgments This work has been supported by Bogazici University BAP under project number 5130.

References

Acar DZ, Türkeş M (2011) Climatology of hot days of the 2010 summer in Turkey and analysis of its atmospheric causes. In: Proceedings of the national geographical congress with international participation (CD-R), 7–10 Sep 2011, Türk Coğrafya Kurumu, İstanbul University (in Turkish with an English abstract). ISBN 978-975-6686-04-1

Beniston M, Stephenson DB, Christensen OB, Frei C, Schöll R, Halsnaes K, Holt T, Palutikof J, Jylha K, Koffi B, Semmler T, Woth K (2007) Future extreme events in European climate: an exploration of regional climate model projections. Clim Change 81:71–95

Deque M (2007) Frequency of precipitation and temperature extremes over France in an anthropogenic scenario: model results and statistical correction according to observed values. Global Planet Change 57:16–26

Dickinson RE, Henderson-Sellers A, Kennedy PJ (1993) Biosphere-atmosphere transfer scheme (bats) version 1e as coupled to the NCAR community climate model. Technical report, National Center for Atmospheric Research, Boulder, CO

Easterling DR, Evans JL, Groisman PY, Karl TR, Kunkel KE, Ambenje P (1999) Observed variability and trends in extreme climate events: a brief review. Bull Am Meteorol Soc 81:417–425. doi:10.1175/1520-0477(2000)081<0417:OVATIE>2.3.CO;2

Giorgi F, Bates GT, Nieman SJ (1993a) The multi-year surface climatology of a regional atmospheric model over the western United States. J Climate 6:75–95

Giorgi F, Marinucci MR, Bates GT (1993b) Development of a second generation regional climate model (RegCM2). Part I: boundary layer and radiative transfer processes. Mon Weather Rev 121:2794–2813

Grell G (1993) Prognostic evaluation of assumptions used by cumulus parameterizations. Mon Weather Rev 121:764–787

Grell GA, Dudhia J, Stauffer DR (1994) Description of the fifth generation Penn State/NCAR mesoscale model (MM5). Technical report TN-398+STR. NCAR, Boulder, p. 121

Holtslag AAM, de Bruijn EIF, Pan H-L (1990) A high resolution air mass transformation model for short range weather forecasting. Mon Weather Rev 118:1561–1575

Kiehl JT, Hack JJ, Bonan GB, Boville BA, Breigleb BP, Williamson D, Rasch P (1996) Description of the NCAR community climate model (CCM3). Technical report NCAR/TN-420+STR. NCAR, Boulder

Klein Tank AMG, Peterson TC, Quadir DA, Dorji S, Zou X, Tang H, Santhosh K, Joshi UR, Jaswal AK, Kolli RK, Sikder AB, Deshpande NR, Revadekar JV, Yeleuova K, Vandasheva S, Faleyeva M, Gomboluudev P, Budhathoki KP, Hussain A, Afzaal M, Chandrapala L, Anvar H, Amanmurad D, Asanova VS, Jones PD, New MG, Spektorman T (2006) Changes in daily temperature and precipitation extremes in central and south Asia. J Geophys Res 111:D16105

Lioubimtseva E (2002) Arid environments. In: Shahgedanova M (ed) Physical geography of Northern Eurasia. Oxford University Press, Oxford, p 571

Oleson KW, Niu GY, Yang ZL, Lawrence DM,Thornton PE, Lawrence PJ, Stockli R, Dickinson RE, Bonan GB, Levis S (2007) Community land model version 3.5 (CLM 3.5) documentation, NCAR report. Available at http://www.cgd.ucar.edu/tss/clm/distribution/clm3.5/CLM3_5_documentation.pdf

Peterson TC, Folland C, Gruza G, Hogg W, Mokssit A, Plummer N (2001) Report on the activities of the working group on climate change detection and related rapporteurs 1998–2001. Report WCDMP-47, WMO-TD 1071. World Meteorological Organization, Geneva

Roeckner E, Bäuml G, Bonaventur L, Brokopf R, Esch M, Giorgetta M, Hagemann S,Kirchner I, Kornblueh L, Manzini E, Rhodin A, Schlese U, Schulzweida U, Tompkins A (2003) The atmospheric general circulation model ECHAM5. Part I: Model description. Max Planck Institute for Meteorology Report 349, 127pp

Türkeş M (2010a) Climatology and meteorology, 1st edn. Kriter Publisher, Istanbul. Publication no. 63, Physical geography series no. 1, ISBN 978-605-5863-39-6, 650 + XXII pp (in Turkish)

Türkeş M (2010b) Analysis of the UN convention to combat desertification with respect to the climate. Climate change and drought, and applications in Turkey. Invited panel paper. In: Proceedings of Çölleşme İle Mücadele Sempozyumu Tebliğler Kitabi, 17–18 June 2010, Çorum, pp 601–616 (in Turkish with an English abstract)

You Q, Kang S, Aguilar E, Yan Y (2008) Changes in daily climate extremes in the eastern and central Tibetan Plateau during 1961–2005. J Geophys Res Atmos 113:D07101

The Precipitation and Temperature Regime Over Three European Sub-regions as a Result of Climate Change

H. Altinsoy, A. Yuncu, and M.L. Kurnaz

Abstract In this research, regional climate models' (RCMs) simulation data set of PRUDENCE project is used to analyze the uncertainties, direction and magnitude of the expected changes of precipitation, temperature, maximum and minimum air temperature with two different scenarios (B2 and A2) in the period 2070–2100 and 1960–1990 for three different sub-regions of Europe (1.75°–15.75° East and 47.75°–55.75° North; 15.75°–25.75° East and 45.75°–55.75° North; 5.75°–13.75° East and 45.75°–47.75° North). SVM (support vector machine) is used to classify the models in order to choose the most appropriate ensembles with weighted coefficients from the multi model ensemble. The results are checked with ensemble-mean approach. In this study, we propose a new approach to multi-model ensemble. In general, the performance of our methodology is better than ensemble-mean approach. SVM can eliminate the models which have big amounts of absolute error and select the best ones that have small amounts of absolute error, with big coefficients. Moreover, our proposed methodology gives better results than ensemble-mean approach nearly in all cases.

1 Introduction

There are various statistical approaches to predict past and future temperature, precipitation and other climatological variables. Taylor Diagram (Gleckler et al. 2008), probability density functions (Ruosteenoja et al. 2007; Boberg et al. 2010), and weighted averages (Coppola and Giorgi 2010) are most common ones that have been enforced to find the best representative sample among multi-ensemble climatological data. SVM has been recently used in climatological studies for downscaling climatological variables (Tripathi et al. 2006; Chen et al. 2010; Anandhi et al. 2008),

H. Altinsoy (✉) • A. Yuncu • M.L. Kurnaz
Department of Physics, Bogazici University, Istanbul, Turkey
e-mail: hamza.altinsoy@boun.edu.tr

C.G. Helmis and P.T. Nastos (eds.), *Advances in Meteorology, Climatology and Atmospheric Physics*, Springer Atmospheric Sciences,
DOI 10.1007/978-3-642-29172-2_52,

runoff modeling (Behzad et al. 2009), soil moisture data assimilation (Kashif Gill et al. 2007) etc. The genuine part of our work stems from the fact that SVM is used as a classification tool instead of other statistical methods (e.g. PDF, Taylor diagram, ensemble-mean, ANN etc.) and usage of SVM in other climatological studies. More detailed explanation and theory can be found in Vapnik (1995, 1998), Cortes and Vapnik (1995).

2 Data

In this study, PRUDENCE (Prediction of Regional scenarios and Uncertainties for Defining EuropeaN Climate change risks and Effects, EVK2-CT2001-00132), Fifth Framework European programme project (2002–2005), European research project (Christensen and Christensen 2007; Christensen et al. 2002) simulation results of 22 regional climate models and CRU data set are used to propose a new methodology for the multi-model ensemble researches. SVM (Support Vector Machine) is used with its classification option for three different sub-domains in Europe (AL:1.75°–15.75° East and 47.75°–55.75° North; EA:15.75°–25.75° East and 45.75°–55.75° North; ME:5.75°–13.75° East and 45.75°–47.75° North).

3 Methodology

There are two main procedures in the usage of SVM. In the first step, SVM determines the classification regions and the hyperplane (multidimensional linear decision surfaces) which separates the regions by using the train data. While it determines the discriminant function of the hyperplane, $f(x_i) = 0$, it assumes that one region satisfies $f(x_i) < 0$ and the other satisfies $f(x_i) > 0$. To simplify the constraint of the hyperplane we label regions with $y = +1$ and $y = -1$ so the constraint becomes $yf(\vec{x}_i) < 0$. Then, it calculates the perpendicular distance between hyperplane and the closest points of both regions and determines the most efficient $f(x_i)$ by maximizing the sum of these distances. In the second step, it uses the test data, chooses the suitable region and it determines the coefficients with a hyperplane function.

In our study, we used seasonal spatial averages of climatic variables (as shown in Table 1) of the CRU (Climatic Research Unit) for 1961–1990 period as train data. We use all the combinations of 40 and 60 percentile values as accepted region ($y = +1$) and all the combinations of 10 and 90 percentile values as rejected region ($y = -1$). We try various percentile values for accepted and rejected regions as shown in Table 1 and obtain three different hyperplanes which separate the space in two main regions. In second step, test data sets are used to determine the classes of each data points. Thirty year averages of the same period (1961–1990) of Regional Climate Model (RCM) results of PRUDENCE project are used as data points of the

Table 1 The definitions of SVM train data set

	Accepted region boundaries	Rejected region boundaries	Definition
SVM-1	49 and 51 percentiles	1 and 99 percentiles	Weighted averages of models in the accepted region with respect to their coefficients
SVM-5	45 and 55 percentiles	5 and 95 percentiles	
SVM-10	40 and 60 percentiles	10 and 90 percentiles	
SVM-BEST-1	49 and 51 percentiles	1 and 99 percentiles	Weighted averages of models that have coefficients bigger than 0.8
SVM-BEST-5	45 and 55 percentiles	5 and 95 percentiles	
SVM-BEST-10	40 and 60 percentiles	10 and 90 percentiles	
ENS-1	49 and 51 percentiles	1 and 99 percentiles	Equally weighted averages of models in the accepted region
ENS-5	45 and 55 percentiles	5 and 95 percentiles	
ENS-10	40 and 60 percentiles	10 and 90 percentiles	
ENS	–	–	Equally weighted averages of all models

Table 2 Biases of different methods over AL region for Spring (MAM) season

AL	ENS	ENS-1	ENS-5	ENS-10	SVM-1	SVM-5	SVM-10	SVM-BEST-1	SVM-BEST-5	SVM-BEST-10
PRE	−0.365	−0.333	−0.314	−0.660	0.469	0.557	0.434	0.487	−0.819	0.289
TMN	0.537	0.458	0.298	0.552	−0.553	−0.728	−0.507	0.260	0.250	0.153
TMP	0.981	1.310	1.185	0.675	−0.268	−0.978	0.016	−0.249	0.079	0.064
TMX	−0.714	0.213	0.417	1.087	−0.081	−0.914	0.250	−0.260	0.223	0.237

test data sets. The result of SVM shows the strength of each model by assigning positive and negative coefficients. These coefficients then determine the classes of each model. The models with positive or negative coefficients are respectively in the accepted or rejected region. We claim that models in the accepted region can represent the climatological specialties more accurately because their spatial averages are closer to observation (CRU) data set. Precipitation, air temperature, maximum and minimum air temperature are climatological variables that we observed for three selected regions (AL, EA and ME). By this way, we obtained the best representative models for each domain with respect to different variables. Moreover, the positive or negative coefficients of the models represent how correlated they are to the observation data set.

The main purpose of using SVM is to classify the models in two groups. After the classification, we try three simple methods by using the results and coefficients of the program. First of all, we calculate weighted averages of all models in the accepted region with respect to their coefficients (described in Table 1 as SVM-10, SVM-5, SVM-1). Secondly, equally weighted averages of these models are calculated. (Ens-10, Ens-5 and Ens-1) Then, we repeated the same process by using the models that have greater coefficients (greater than 0.8) and named them as SVM-Best-1 (SVM-Best-5 and SVM-Best-10) At last, we take the averages of all models in two regions to compare the efficiency of these new methodologies with a classical approach. We take the differences between the results that we obtained and the spatial averages of observation (CRU) data set for selected period and variable over each domain to determine the biases as shown in Table 2 for spring

Table 3 Absolute errors of precipitation (PRE) and max air temperature (TMX) of different methods over AL region for Spring (MAM) season

AL	ENS	ENS-1	ENS-5	ENS-10	SVM-1	SVM-5	SVM-10	SVM-BEST-1	SVM-BEST-5	SVM-BEST-10
PRE	0.693	0.672	0.712	0.673	0.678	0.656	0.659	0.650	1.007	0.616
TMX	0.691	0.760	0.959	0.672	0.832	0.671	0.694	1.012	1.216	1.279

season. Although the biases of the new methodologies are lower than the classical approach (ENS) results, this doesn't mean that using SVM gives more accurate results than the ENS method. The main reason behind this fact is taking spatial averages and positive and negative biases on different grids over a selected domain can cancel each other. Therefore, we calculated the absolute errors of each grid and took the spatial averages of the absolute errors.

As an example, SVM-10 and SVM-1 have the least mean biases of spring air temperature (e.g. 0.016) and maximum air temperature (e.g. −0.081) over AL domain, respectively. However, SVM-BEST-10 has the least absolute error of spring air temperature and absolute error of SVM-5 of maximum air temperature of the same season is the lowest one. The spatial means of absolute errors have to be small in contrast to the other methodologies to find the most appropriate method. Hence, the results in Table 3 are essential to claim the accuracy and success of SVM usage in this sort of studies. In most of the samples, the differences between the errors of proposed methods and ENS are not very significant. It stems from the fact that the distributions of absolute errors of RCM data in PRUDENCE project are very close to each other.

Finally, we choose the SVM method that has the minimum absolute error for each domain and then calculate its differences between the absolute errors of the ENS method. We can show only the spring season results of precipitation percentage and maximum air temperature results due to lack of space.

4 Results

We obtained significant correction in precipitation percentage amounts by using the best representative SVM as shown in the Fig. 1. The correction amount increases to 20–25% over Germany, Poland and East-Netherlands. In the northern part of the domain, ENS method can estimate the precipitation pattern over some parts such as Bosnia-Herzegovina. However, spatial average of the whole domain is positive (6.69%). The correction in the air temperature results and minimum air temperature results are not as much as the correction in maximum air temperature results. ENS method gives better results over the Western Poland, Northern Germany, Northern Slovenia and Netherlands. On the other hand, the most suitable SVM methodology (has minimum absolute error) corrects the maximum air temperature by 0–1.5°C over the rest of the domain.

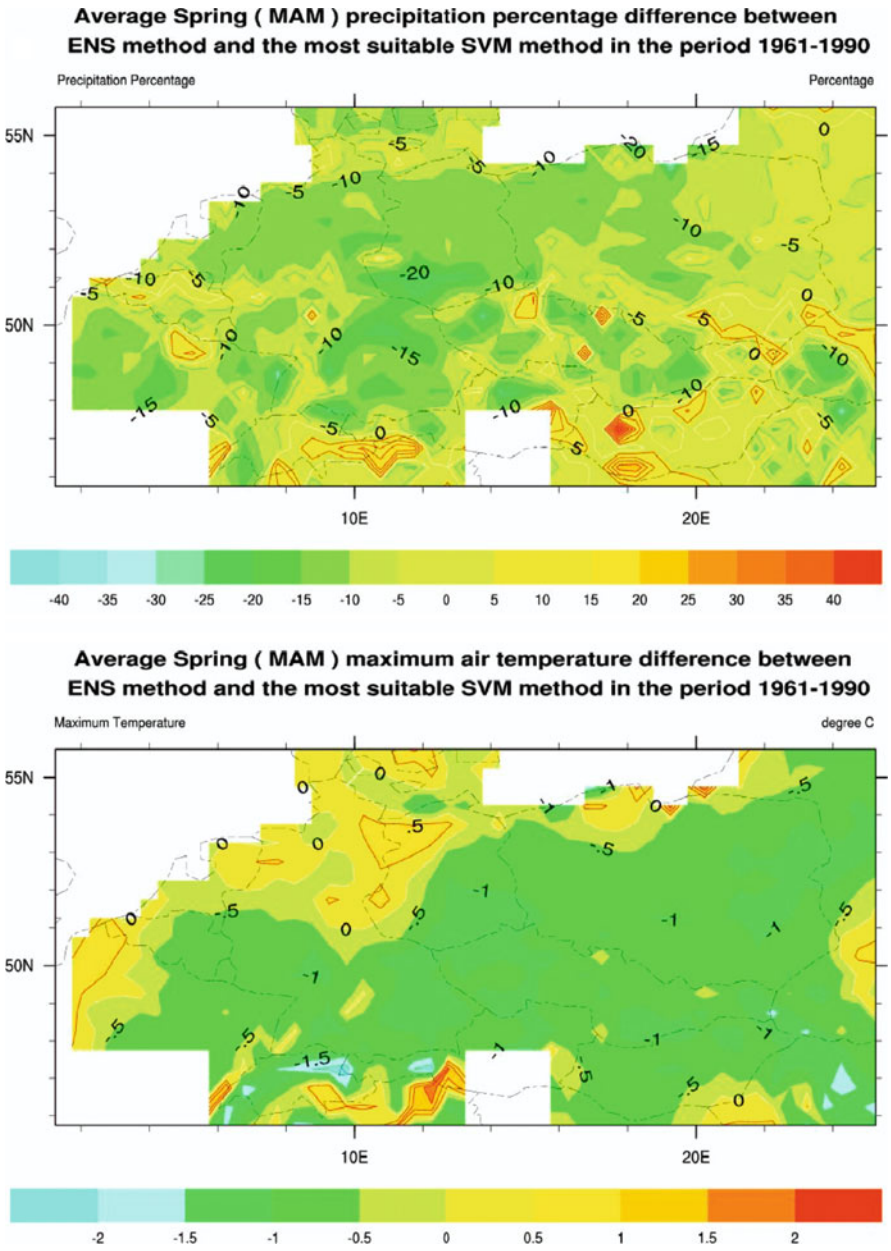

Fig. 1 The difference of absolute precipitation percentage and *max air temperature* error between ENS method and the SVM method over three (AL, EA, ME) domain

5 Conclusions

We have proposed a new methodology for representing the selected climatological variable over a specific domain in a more precise way. In general, the performance of our methodology is better than ENS approach. SVM effectively optimizes the model results by the usage of coefficients representing the level of correspondence with the observational data. With the analysis of the coefficients, the best model can easily be picked for different regions and/or seasons. The correction amount of absolute error changes in parallel with selected climatological variable, region and season. For some circumstances, there is a very small correction in selected region, because absolute errors of models are very close to each other. In order to increase the correction amounts, more Regional or Global Climate model results can be used. This type of methodology can be used to make further analysis of projections of the climatological variables.

Acknowledgments This work has been supported by Bogazici University BAP under project number 5130.

References

Anandhi A, Srinivas VV, Nanjundiahb RS, Kumara DN (2008) Downscaling precipitation to river basin in India for IPCC SRES scenarios using support vector machine. Int J Climatol 28:401–420. doi:10.1002/joc.1529

Behzad M, Asghari K, Eazi M, Palhang M (2009) Generalization performance of support vector machines and neural networks in runoff modeling. Expert Syst Appl 36:7624–7629. doi:10.1016/j.eswa.2008.09.053

Boberg F, Berg P, Thejll P, Gutowski WJ, Jens HC (2010) Improved confidence in climate change projections of precipitation further evaluated using daily statistics from ENSEMBLES models. Clim Dyn 35:1509–1520. doi:10.1007/s00382-009-0683-8

Chen S-T, Yu P-S, Tang Y-H (2010) Statistical downscaling of daily precipitation using support vector machines and multivariate analysis. J Hydrol 385:13–22. doi:10.1016/j.jhydrol.2010.01.021

Christensen JH, Christensen OB (2007) A summary of the PRUDENCE model projections of changes in European climate by the end of this century. Clim Chang 81:7–30

Christensen JH, Carter TR, Giorgi F (2002) PRUDENCE employs NEW methods to assess European climate change. EOS 83:147

Coppola E, Giorgi F (2010) An assessment of temperature and precipitation change projections over Italy from recent global and regional climate model simulations. Int J Climatol 30:11–32

Cortes C, Vapnik V (1995) Support vector networks. Mach Learn 20:273–297

Gleckler PJ, Taylor KE, Doutriaux C (2008) Performance metrics for climate models. J Geophys Res 113:D06104. doi:10.1029/2007JD008972

Kashif Gill M, Kemblowski MW, McKee M (2007) Soil moisture data assimilation using support vector machines and ensemble Kalman filter. J Am Water Resour Assoc 43:1004–1015. doi:10.1111/j.1752-1688.2007.00082.x

Ruosteenoja K, Tuomenvirta H, Jylhä K (2007) GCM-based regional temperature and precipitation change estimates for Europe under four SRES scenarios applying a super-ensemble pattern-scaling method. Clim Chang 81:193–208. doi:10.1007/s10584-006-9222-3

Tripathi S, Srinivas VV, Nanjundiah RS (2006) Downscaling of precipitation for climate change scenarios: a support vector machine approach. J Hydrol 330:621–640. doi:10.1016/j.jhydrol.2006.04.030
Vapnik VN (1995) The nature of statistical learning theory. Springer, New York
Vapnik VN (1998) Statistical learning theory. Wiley, New York

Analysis of the Effect of Climate Change on the Yield of Crops in Turkey Using a Statistical Approach

H. Altinsoy, C. Kurt, and M.L. Kurnaz

Abstract In this study, simulation data set from ENSEMBLE project is used to set up a statistical model to estimate the yield of crops according to climatic variables and conditions. We chose fig as an example crop. Fig is grown around Aydın in Turkey. The number of days above 40°C between June and October, the number of days below −1°C between October and November, the mean of the maximum air temperature between June and September, the mean of minimum air temperature between October and November, annual total precipitation amount, annual mean of relative humidity and annual mean of cloud cover in that region are chosen as independent variables for multiple regression to estimate yield of fig for the period 1991–2000.

1 Introduction

Global surface temperature has increased by about 0.8°C during the past century (Solomon et al. 2007; Houghton et al. 2001). Furthermore it is expected that the global surface temperature may increase by more than 2–6°C in the next century, unless the human contribution of greenhouse gases stops immediately (Houghton et al. 2001). The alteration of various dynamical factors that constitute the climate system stems from the increases in the global temperatures. These changes can easily be observed in a local base and have some crucial negative effects on ecological balance, especially. This fact is dreadful because this balance is obtained over thousands of years. Since the industrial revolution, there has been a substantial growth in population. The estimated population amount was approximately one

H. Altinsoy (✉) • ML. Kurnaz
Department of Physics, Bogazici University, Istanbul 34342, Turkey
e-mail: hamza.altinsoy@boun.edu.tr

C. Kurt
Institute of Environmental Sciences, Bogazici University, Istanbul 34342, Turkey

C.G. Helmis and P.T. Nastos (eds.), *Advances in Meteorology, Climatology and Atmospheric Physics*, Springer Atmospheric Sciences,
DOI 10.1007/978-3-642-29172-2_53,

billion just before the industrial revolution. However it reached seven billion in 2011 and it is expected to exceed nine billion by 2050 (U.S. Census Bureau 2012). On the other hand, agricultural lands continue to vanish and it is very difficult to produce sufficient amount of food to feed the growing population in near future. Already, 925 million people, which is approximately 13.6% of about seven billion population, suffer from lack of food or hunger (FAOSTAT 2010).

The changes in climate conditions force many plant species to migrate from places where they used to survive to places where they can survive. Hence, many forests and many plant species are in danger of extinction. Similarly, agricultural products are also affected by climate changes. Although agriculture can be controlled by human-beings, notwithstanding it has not been possible to adapt adequately to the changing conditions for farmers. Moreover, governments are not successful to renew the agricultural policies with the changing climate. By reason of changing climate, agricultural lands have to be shifted to the more favorable areas and agricultural policies have to be renewed (Hunger Notes 2011).

In general, various types of crops will not be farmed in the future as much as today. On the contrary, the amount of yields of some types of crops will increase according to the new climatological features by climate change in specific regions (FAOSTAT 2010). For instance, the increase in mean temperature causes the respiration increase. As a consequence of this, germination time is shorter and then total biomass of the plant is decreased which means that the productivity is directly decreased (Adams et al. 1998). In contrast to this example, an increase in the atmospheric carbon dioxide concentration rises productivity by increasing the rate of photosynthesis (Cure and Acock 1986; Allen et al. 1987).

Agriculture has a high sensitivity to climate. In other words, alterations in the climate variability can have some significant effects on agricultural productivity (Parry and Carter 1985; Carter and Parry 1986) and these effects vary regionally (Anderson and Hazell 1989). Therefore there is a potential yield reduction for many agricultural products (Houghton et al. 2001) and this circumstance will pose a serious problem for the future of mankind. Responses of agricultural products will vary with respect to the climatic conditions in the future.

In order to be able to make high accuracy estimates, proposed methods should be properly determined and used. There are many crop yield estimation models e.g. Palosuo et al. (2011) and Özdoğan (2011). Some of these models are dynamic models which are called biophysical crop models or crop growth models. These models express the vital activities of a plant as coefficients and dynamically estimate the yield by including temperature, humidity, solar radiation and so forth. These variables are needed during the growing period of plant (Boogaard et al. 1998). Although it is reported that most of these models and studies are very useful to determining the effects of climate change on yield, there are also some flaws in these models. For example, biophysical crop models ignore the effects of pests and disease on plants (Lobell et al. 2007). Also, these models do not contain all crop types. Instead of crop growth models, statistical models are also used to estimate yield. These are based on the relation between past climate data and yield data. Statistical crop models demonstrate net effects of all the climatological factors

on productivity. In spite of the fact that statistical models do not cover biophysical processes of a plant (e.g. photosynthesis and respiration) as crop growth models do, they can calculate the net effect of climate on the plant. The most important defect of statistical approach is the lack of observation data set. Because of that reason, this sort of approach cannot estimate the response of the crops to a situation that has never been preexisting (e.g. doubling the carbon dioxide amount), since the accuracy and sensitivity of statistical models depend upon the past climatological conditions (Lobell et al. 2007).

2 Data and Methodology

In the first part of this study, statistical crop model is applied to various crops' yield amounts and climatological variables over the selected regions of Turkey. Crops can be farmed in specific regions and climatic effects vary regionally. Because of that reason, the various spatial means of climate variables are taken according to the region where crops are farmed.

2.1 Data

Climatic Research Unit (CRU) data set and crop production statistics of Turkish Statistical Institute are used for agricultural data (TUİK 2010) in this part of the study. CRU data set consist of monthly averaged climatological variables with 0.5° resolution. In addition to this, we also used one of the Regional Climate Model (ETH-CLM) simulation results of ENSEMBLE project which is forced by ERA40 data set with a 50 km resolution. We select the specific regions which specific crops are cultivated.

2.2 Methodology

By using multiple regression method, the relationship between air temperature, annual total precipitation amounts, annual maximum air temperature, annual minimum air temperature of CRU data set and annual yields of the crops over selected regions are analyzed. R^2 values are shown in Table 1.

Many past studies e.g. White et al. (2006) have shown that instead of taking the climate averages, taking the crops growing season and its ecological needs into consideration gives higher accuracy results. Therefore, unlike the first part of this paper, we use climatological variables that are effective in growing of plant. We choose these variables according to ecological features of fig over the Aydin (27.25°–28.25° East and 37.25°–38.25° North) province. Climatological variables

Table 1 Coefficients of determination (R^2) between CRU data set and annual crop yields of specific crops

Crop	R^2	Crop	R^2	Crop	R^2
Pistachio	0.26	Fig	0.18	Cotton	0.65
Wheat	0.18	Apricot	0.27	Rice	0.27
Tea	0.66	Flax	0.6	Soy bean	0.69
Hazelnut	0.23	Banana	0.32	Peach	0.19

Table 2 The climatological boundary conditions of fig that are highly effective for production

Number of days above 40°C	After formation of flower and fruit (June–October totals)
Number of days below −1°C	October–November total amounts
Number of days below −9°C	December–March total amounts
Maximum temperature	June–September averages
Minimum temperature	October–November averages
Precipitation	Annual total amounts
Cloud cover	Annual averages
Relative humidity	Annual averages

of ETH-CLM simulation results of ENSEMBLE project used in model are given in Table 2. The main reason to choose the fig as observed crop is that multiple regression results show us that annual averages of climatological variables don't correlate with the yield amount (R^2 coefficient is 0.18). We propose that climatological variables that are significant in growing of crop are more effective than annual means of climatological variables. If these variables correlate with yield amount more substantially, then we can easily claim that it is better to use specific features of crops as climatological variables in statistical crop models.

3 Results

We obtain R^2 coefficient as 0.92 if the climatological variables in Table 2 are used in multiple regression. Moreover, the coefficients in these regression equations are meaningful. The number of days below −1°C, the number of days below −9°C and the number of days above 40°C have negative coefficients that show us that the increase in these amounts will affect the yield amount negatively. In addition to this, there is a strong negative correlation between the cloud cover and the fig yield. The increase in the cloud cover amount causes a decrease of the solar irradiance and indirectly causes a decrease in the amount and rate of photosynthesis.

In addition to these, the estimated and observed yield amounts are very close to each other in every year for the period 1991–2000 as shown in Fig. 1. The difference between these two yield amounts is at most 3.1 in whole year. By this way, we claim that the equation of multiple regression can be used to estimate yield of fig using this particular data set.

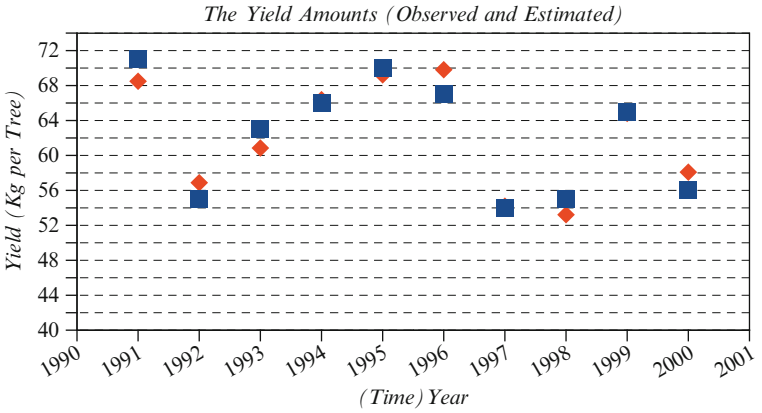

Fig. 1 Yield of fig for the period 1991–2000. The *red symbols* represent the estimated values and the *blue ones* represent the observed values

4 Conclusions

In this study, first of all, we tried to show that there can be a statistical correlation between the yield amounts of various crops and climatological variables. Twelve types of crops are selected as we claim that the yield amount of specific crops is more correlated with the effective climatological variables. We chose fig as the crop and we obtained significant corrections by using these variables instead of CRU data set (e.g. R^2 coefficient is 0.92 in contrast to 0.18) Regional Climate Model (ETH-CLM) results in Table 2 can be used for this type of research. According to results in reference period, future crop yield can be estimated.

Acknowledgments This work has been supported by Bogazici University BAP under project number 5130. We thank to Ayşe Rumeysa Muş for her help in preparation of regions' coordinates. We want to give special thanks to Murat Türkeş for giving suggestions during the preparation of project.

References

Adams RM, Hurd BH, Lenhart S, Leary N (1998) Effects of global climate change on agriculture: an interpretative review. Clim Res 11:19–30. doi:10.3354/cr011019

Allen LH Jr, Boote KJ, Jones JW, Jones PH, Valle RR, Acock B, Rogers HH, Dahlman RC (1987) Response of vegetation to rising carbon dioxide: photosynthesis, biomass and seed yield of soybean. Global Biogeochem Cycles 1:1–14. doi:10.1029/GB001i001p00001

Anderson JR, Hazell PBR (eds) (1989) Variability in grain yields. Johns Hopkins University, Baltimore

Boogaard HL, Van Diepen CA, Rötter RP, Cabrera JMCA, Van Laar HH (1998) WOFOST 7.1; user's guide for the WOFOST 7.1 crop growth simulation model and WOFOST Control Center 1.5. Technical Document 52, DLO Winand Staring Centre, Wageningen, p 144

Carter TR, Parry ML (1986) Climatic changes and yield variability. In: Hazell PBR (ed) Summary proceedings of a workshop on cereal yield variability. International Food Policy Research Institute, Washington, DC

Cure JD, Acock B (1986) Crop responses to carbon dioxide doubling: a literature survey. Agric For Meteorol 38:127–145. doi:10.1016/0168-1923(86)90054-7

FAOSTAT (2010) Agriculture updated. http://www.fao.org/corp/statistics/

Houghton JT, Ding Y, Griggs DJ, Noguer M, van der Linden PJ, Dai X, Maskell K, Johnson CA (eds) (2001) Climate change 2001: the scientific basis. Cambridge University Press, Cambridge

Hunger Notes (2011) World hunger and poverty facts and statistics, World Hunger Education Service. http://www.worldhunger.org

Lobell DB, Cahill KN, Field CB (2007) Historical effects of temperature and precipitation on California crop yields. Clim Chang 81:187–203. doi:10.1007/s10584-006-9141-3

Özdogan M (2011) Modeling the impacts of climate change on wheat yields in Northwestern Turkey. doi:10.1016/j.agee.2011.02.001

Palosuo T, Kersebaum KC, Angulo C, Hlavinka P, Moriondo M, Olesen JE, Patil RH, Ruget F, Rumbaur C, Takáč J, Trnka M, Bindi M, Çaldağ B, Ewert F, Ferrise R, Mirschel W, Şaylan L, Šiška B, Reimund R (2011) Simulation of winter wheat yield and its variability in different climates 3 of Europe: a comparison of eight crop growth model. Eur J Agron 35:103–114. doi:10.1016/j.eja.2011.05.001

Parry ML, Carter TR (1985) The effect of climatic variations on agricultural risk. Clim Chang 7:95–110. doi:10.1007/BF00139443

Solomon S, Qin D, Manning M, Chen Z, Marquis M, Averyt KB, Tignor M, Miller HL (eds) (2007) Climate change 2007: the physical science basis, Contribution of working group I to the fourth assessment report of the intergovernmental panel on climate change. Cambridge University Press, Cambridge

TUIK Turkish Statistical Institute (2010) Agriculture statistics (Crop production statistics, 2008). Available at: http://www.tuik.gov.tr

U.S. Census Bureau, Population Devision (2012) International data base. World population: 1950-2050. Available at http://www.census.gov/population/international/data/idb/worldpopgraph.php

White MA, Diffenbaugh NS, Jones GV, Pal JS, Giorgi F (2006) Extreme heat reduces and shifts United States premium wine production in the 21st century. Proc Natl Acad Sci USA 103 (30):11217–11222

Drought Index Over Greece as Simulated by a Statistical Downscaling Model

C. Anagnostopoulou, K. Tolika, and P. Maheras

Abstract Drought is the least understood of all weather phenomena, since it differs from other natural hazards in several ways. The hazardous of drought can be better understood by analyzing drought indices. The Standardized Precipitation Index (SPI) has been one of the most widely used indices for drought studies, as it can provide satisfactorily results for the appearance, variability and intensity of drought. Moreover, SPI has been developed in order to quantify and record drought episodes on multiple time scales (3 months, 6 months, 1 year, 2 years). In the present study a statistical downscaling technique based on artificial neural network was employed for the estimation of SPI over Greece. The aim of the study is to evaluate the simulated SPI index against the observational one. The performance of the statistical downscaling model is assessed utilizing biases, standard deviation and correlation coefficient between observed and simulated indices. An overestimation of the simulated mean SPI indices accompanied by a decrease in standard deviation is evident for all stations and all time periods. The reproduction of SPI3 and SPI6 for winter, spring seasons display rather promising results.

1 Introduction

Precipitation, as well as drought, is a major climatological concern particularly for their impacts on natural and human systems. Recent European and Mediterranean studies indicate that there will be an increase of precipitation in Europe and a decrease in Mediterranean Basin (IPCC 2007). Drought episode is unique, characterized by different climatological parameters and have different impacts. Drought indices are developed in order to overcome the difficulties in determination

C. Anagnostopoulou (✉) • K. Tolika • P. Maheras
Department of Meteorology and Climatology, Aristotle University of Thessaloniki, Thessaloniki 54124, Greece
e-mail: chanag@geo.auth.gr

C.G. Helmis and P.T. Nastos (eds.), *Advances in Meteorology, Climatology and Atmospheric Physics*, Springer Atmospheric Sciences,
DOI 10.1007/978-3-642-29172-2_54,

of the main characteristic of drought such as intension, duration and spatial distribution. Drought indices can be computed using a numerous parameters: precipitation total, the height of snowfall, evapotranspiration, wind, the ground water supply. The drought index is a pure number that can be easily used in the analysis of the drought. The most well known drought indices are the Palmer Drought Severity Index (PDSI) (Palmer 1965), the Crop Moisture Index (Palmer 1968; Hayes 1999) and the Standardize precipitation Index (McKee et al. 1993).

General Climate Models GCMs reproduce quite well the synoptic circulation however they fail to reproduce the rainfall regime (Giorgi 1995). The well known relationship between local climate variable such as precipitation and large scale circulation drive us to adopt a statistical downscaling technique to simulate the drought index SPI. Vasiliadis et al. (2009) applied a statistical downscaling method to simulate monthly precipitation and then they develop SPI index using the downscaled precipitation. Contrarily, in the present study the selected statistical model downscaled directly the SPI index. Finally, the study is motivated by an interest in evaluating statistical downscaling results to reproduce drought in Greek region.

2 Data

The study is based on daily rainfall totals from a dense 20 stations network located at the Greek region covering the 1961–1990 period. All the rainfall time series used are complete without missing values and they are tested for homogeneity utilizing Alexandersson test (Alexanderson 1986) in order to ensure the validity of the conclusions. For the downscaling procedure, large scale predictor 500 hPa geopotential height from the NCEP-NCAR reanalysis database were employed (Kalnay et al. 1996). The selected window covers the European area from 30°N to 55°N and from 0°E to 32.5°E with a spatial resolution of 2.5° × 2.5° for the same period 1961–1990.

3 Methodology

Gamma distribution is appropriate to most cases of the analysed rainfall records (Thom 1958; Lana et al. 2001). The probability density function of incomplete Gamma distribution is

$$G(x) = \frac{1}{\Gamma(\hat{a})} \int_0^x t^{\hat{a}-1} e^{-t} dx \quad \text{where} \quad t = \frac{x}{\hat{\beta}}$$

Shape parameter: $\hat{\alpha} = \frac{1}{4A}\left(1 + \sqrt{1 + \frac{4A}{3}}\right)$; $A = \ln(\bar{x}) - \frac{\sum \ln(x)}{n}$ and

Scale parameter: $\hat{\beta} = \frac{\bar{x}}{\hat{\alpha}}$,

where x is the precipitation amount and n the number of observations.

Because Gamma function is undefined for zero values, while precipitation can be zero, the cumulative distribution function become to $H(x) = q + (1-q)\, G(x)$, where q is the probability of no precipitation.

In order to calculate the Standardized Precipitation Index (McKee et al. 1993) an equiprobable transformation is used, going from gamma cumulative distribution H (x) to the standardized normal distribution of z with null mean and unit standard deviation. This z value is the SPI index. The index calculated on multiple time scales, 3 months, 6 months, 1 year and 2 years.

3.1 Statistical Downscaling Method: ANN

The Artificial Neural Network (ANN) Model used in the study is based on a "quickprop" algorithm, it adopts a feed-forward configuration and its learning process is based on the back – propagation method (Tolika et al. 2007). The most optimal results were obtained when the model had one hidden layer with 12 nodes. The period of analysis of the downscaling model was divided into two sub-periods. The calibration period covers the years from 1961 to 1980 (20 years) in order for the model to be trained and the rest of the years (1981–1990) were used for the validation of the results.

4 Results

Initially, the SPI was calculated for the observed data of the 20 stations for different time scales and in a seasonal basis. The predictor for the statistical downscaling model of this study is the 500 hPa geopotential heights at seasonal time resolution. For SPI3, the seasonal 500 hPa geopotential heights were used, for SPI12 the annual 500 hPa values, etc. To validate the skill of the ANN model in simulating the SPI values the biases of the mean and the standard deviation differences between the observed and the simulated data are estimated per station and per time period. Additionally the correlation coefficients between observed and simulated time-series were calculated.

Figure 1 shows the averaged indices for all stations for the observed and simulated datasets. The simulated mean values of the SPI indices consistently exceed the observed ones. The seasonal statistical significant differences between the simulated and the observed indices for SPI3, (estimated using the *t*-test at a level of significance 0.05), range from −0.5 (summer) to −1.9 (autumn). Spring and summer present the highest number of non statistical significant biases. The differences are smaller during the wet period SPI6 where none of the stations shows statistical significant differences, while the difference were high for SPI12. For SPI24, 40% of the stations present statistical significant differences. Moreover,

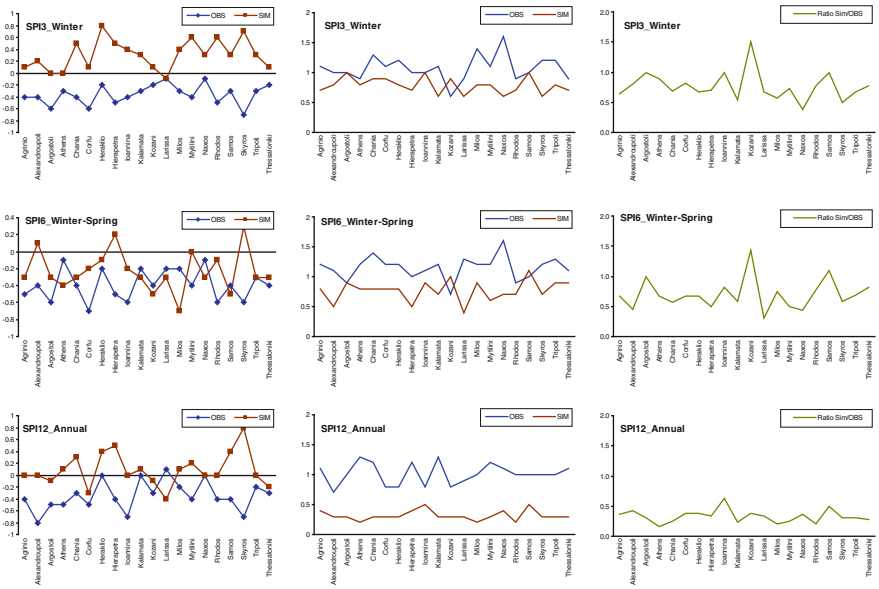

Fig. 1 SPI mean values (*first column*), SPI mean standard deviation (*second column*) and ratio between simulated and observed standard deviation (*third column*) for the 20 stations and the selected drought indices SPI3, SPI6 and SPI12

the simulated standard deviation is underestimated by the statistical downscaling model (Fig. 1, second column). Additionally, the ratio of the simulated to observed standard deviation of SPI was estimated (Fig. 1, third column). For SPI3 and SPI6 during the wet period, in the majority of the cases the computed ratio presents value close to 0.6 (2/3). On the other hand in the case of SPI12 this value is lower of 0.25 (1/4). The underestimation is larger for the southern stations suggesting the lack of uniformity of the drought distribution.

To identify the optimum combination between the predictor and the range of SPI indices and to evaluate the skill of the model, the correlation coefficient between simulated and observed seasonal values were calculated. Table 1 shows the skill of the model in simulating each of the individual SPI values for different time periods for each station under study. The correlation coefficients between the simulated and the observed SPI indices are generally high especially during the wet time period. SPI3 in winter is well predicted by the ANN downscaling model, since the correlation coefficients vary between 0.4 and 0.9. Thessaloniki and Athens are the two stations presenting the lowest coefficients. In contrast, the correlation coefficients for summer and autumn are relatively low, e.g. 25% of the stations present correlation coefficient lower than 0.1 in summer signifying the rainfall absence during the dry season. The majority of the stations in autumn present negative correlation coefficients probably due to the high variability of the predictor (500 hPa) during this season.

Table 1 Correlation coefficient values between simulated and observed SPI values for the 20 stations

	SPI3	SPI3	SPI3	SPI3	SPI6	SPI6	SPI6	SPI12
	Winter	Spring	Summer	Autumn	Winter Spring	Spring Summer	Summer Autumn	12 months
Agrinio	0.9	0.5	0.6	−0.2	0.8	0.4	0.5	0.5
Alexandroupoli	0.7	0.6	0.3	0.1	0.7	0	−0.1	0.2
Argostoli	0.8	0.7	0	−0.2	0.9	−0.3	0.2	0.1
Athens	0.4	0.3	−0.4	−0.1	0.5	−0.4	−0.1	−0.6
Chania	0.8	0.5	−0.8	−0.1	0.8	−0.2	−0.1	−0.5
Corfu	0.8	0.5	0.4	0.1	0.9	−0.1	0.2	0.2
Heraklio	0.5	0.4	−0.3	0	0.6	0.2	−0.1	−0.2
Hierapetra	0.6	−0.1	−0.5	−0.2	0.4	0.2	−0.2	−0.5
Ioannina	0.9	0.2	0.4	0.1	0.9	0.5	0.4	0.7
Kalamata	0.8	0.5	0.2	−0.3	0.7	−0.4	0.2	0.1
Kozani	0.6	0.1	0	−0.2	0.5	−0.3	0.2	0.3
Larissa	0.6	−0.3	0.1	−0.4	0.6	−0.8	−0.1	0
Milos	0.7	0.7	0	−0.7	0.8	−0.3	0.3	−0.2
Mytilini	0.9	0.8	0.2	−0.1	0.8	−0.3	0.1	0.4
Naxos	0.7	0.6	0	−0.6	0.7	−0.3	0.3	−0.3
Rhodos	0.5	0.7	0.2	0	0.6	−0.5	−0.7	−0.8
Samos	0.8	0.7	0.5	−0.2	0.8	−0.1	−0.1	0.1
Skyros	0.8	0.6	0.4	−0.4	0.7	−0.5	0.2	−0.1
Tripoli	0.9	0.6	0.3	−0.2	0.8	−0.4	0.2	0.4
Thessaloniki	0.4	0.5	0.7	−0.1	0.5	0.1	−0.2	−0.1

A similar behavior of SPI3 for winter was also found for SPI6 during the wet period. Contrarily, the downscaling skill of the model for SPI6 for spring–summer and summer–autumn is generally much lower. This is not surprising, as in general, the averaging of predictors (mean 6 month 500 hPa, etc.) smooth the geopotential heights fields and increase the uncertainty of the predictant. Finally, the correlation coefficient does not exceed the value of 0.6 for SPI12, while in the case of SPI24 the correlations reach up to 0.8 (25% of the stations).

5 Conclusions

In the present study an attempt is made to evaluate a statistical downscaling model based in the ANN approach in simulating the SPI (drought index) on multiple time scale. The evaluation analysis shows that the performance of the model varies substantially from station to station and from season to season. Nevertheless, a clear pattern emerges with respect to the simulation of index values. All stations for all time periods show an overall increase in the mean values of SPI indices accompanied by a general decrease of standard deviation. However, a Student *t*-test revealed that only SPI6 for the wet period (winter–spring) were not statistically

significant for all stations. The results show an improvement when compared to those obtained by Loukas et al. (2007) for central Greece because the direct downscaling of SPI does not include the uncertainties of the downscaling precipitation amounts. The predictor was proved to be relevant to drought index which is in coherent with the results from Anagnostopoulou (2003) who noted that SPI over Greece was highly connected with synoptic situations over Europe and especially the surface of 500 hPa. Additional research is required to determine the appropriate way on downscaling drought indices, as well as generating statistical downscaling results to develop future drought indices are planned for future studies.

References

Alexanderson H (1986) A homogeneity test applied to precipitation data. J Climatol 6:661–675

Anagnostopoulou C (2003) A contribution of drought analysis in Greece. Ph.D. dissertation, Aristotle University of Thessaloniki, Thessaloniki, 215pp

Giorgi F (1995) Perspectives for regional earth system modelling. Global Planet Change 10:23–43

Hayes M (1999) Drought indices, National Drought Mitigation Center. (Available on line: http://www.civil.utah.edu/~cv5450/swsi/indices.htm#deciles

IPCC (2007) IPCC fourth assessment report: climate change 2007. Working group I report, "the physical science basis", Chapter 11 "Regional climate projections". pp 847–940

Kalnay E, Kanamitsou M, Kistler R, Collins W, Deaven D, Gandin L, Irebell M, Saha S, White G, Woollen J, Zhu Y, Leetmaa A, Reynolds R, Chelliah M, Ebisuzaki W, Huggins W, Janowiak J, Mo KC, Ropelewski C, Wang J, Jenne R, Joseph D (1996) The NCEP/NCAR 40-year Reanalysis project. Bull Amer Meteor Soc 77:437–471

Lana X, Serra C, Burgueno A (2001) Patterns of monthly rainfall shortage and excess in terms of the Standardized Precipitation Index for Catalonia (Spain). Int J Climatol 21:1669–1691

Loukas A, Vasiliadis L, Tzabiras J (2007) Evaluation of climate change on drought impulses in Thessaly, Greece. Eur Water J 1:17–18

McKee TB, Doesken NJ, Kleist J (1993) The relationship of drought frequency and duration to time scale. In: Proceedings of the 8th conference of applied climatology, American Meteorological Society, Boston, pp 179–184

Palmer WC (1965) Meteorological drought. Research paper no. 45, U.S. Department of Commerce Weather Bureau, Washington, DC

Palmer WC (1968) Keeping track of crop moisture conditions, nationwide: the new crop moisture index. Weatherwise 21:156–161. doi:10.1080/00431672.1968.9932814

Thom HCS (1958) A note on the gamma distribution. Mon Weather Rev 86:117–122

Tolika K, Maheras P, Vafiadis M, Flocas HA, Arseni-Papadimitriou A (2007) Simulation of seasonal precipitation and raindays over Greece: a statistical downscaling technique based on artificial neural networks (ANNs). Int J Climatol 27:861–881. doi:10.1002/joc.1442

Vasiliadis L, Loukas A, Patsonas G (2009) Evaluation of a statistical downscaling procedure for the estimation of climate change impacts on droughts. Nat Hazards Earth Syst Sci 9:879–894. doi:10.5194/nhess-9-879-2009

Hellenic Network for Solar Energy

A.F. Bais, A. Kazantzidis, C.S. Zerefos, D. Melas, E. Kosmidis, S. Kazadzis, E. Nikitidou, T.M. Giannaros, M.-M. Zempila, K. Fragkos, and V. Salamalikis

Abstract We introduce the "Hellenic Network for Solar Energy", a system for supporting applications of solar energy with the combined use of measurements from the ground, satellite images, theoretical calculations with radiative transfer models and predictions. This study presents the design of the Network which is currently under development, the supporting networking applications, and preliminary results from basic methodologies that have been developed relating to the assessment of solar energy in near real-time using satellite images, and the forecast of solar energy using a meteorological forecasting model. In addition, preliminary results of the evaluation of these methods by comparison with ground based measurements from the stations of the Network are shown.

1 Introduction

Greece is a country with proven solar potential and with short-term objectives to increase the production from renewable energy sources to at least 20% of the total national energy production. Due to the low efficiency of solar energy collection

A.F. Bais (✉) • D. Melas • T.M. Giannaros • M.-M. Zempila • K. Fragkos
Laboratory of Atmospheric Physics, Aristotle University of Thessaloniki, Thessaloniki 54124, Greece
e-mail: abais@auth.gr

A. Kazantzidis • E. Nikitidou • V. Salamalikis
Laboratory of Atmospheric Physics, University of Patras, Rio 26504, Greece

C.S. Zerefos
National and Kapodistrian University of Athens, Athens 15784, Greece

E. Kosmidis
Draxis – Environmental Technologies, Thessaloniki 54623, Greece

S. Kazadzis
Institute of Environmental Research and Sustainable Development, National Observatory of Athens, Athens 11810, Greece

C.G. Helmis and P.T. Nastos (eds.), *Advances in Meteorology, Climatology and Atmospheric Physics*, Springer Atmospheric Sciences,
DOI 10.1007/978-3-642-29172-2_55,

systems, improving the accuracy of the available information on the availability of solar radiation is of primary importance for the design, implementation, and efficient operation of such systems.

In this study we present a general description of the system and its aims, and we focus on the calculation of solar energy at the surface using model calculations and satellite images, and the forecasting of solar energy levels using a meteorological forecasting model. Finally we present results from the evaluation of these methodologies.

2 Data and Methodologies

The network is under development and currently pyranometers have been installed in different locations in Greece (Orestiada, Xanthi, Thessaloniki, Ioannina, Preveza, Kozani, Volos, Athens, Argos, Patras, Pylos, Heraklion, Rhodes, Mytilini), to measure the shortwave solar irradiance reaching the surface. The network is expected to expand with the addition a few more sites in the near future. The data are collected locally and transmitted in real time (every minute) to a central server at the University of Thessaloniki.

Data from a Kipp & Zonen pyranometer (model CM21) operating at the University of Thessaloniki are used for the validation of the model estimates. The data are acquired continuously and recorded every 1 min. For the validation of the forecasting model we have used data for a short period spanning from February to May 2011.

Short-term forecasts of solar radiation at Earth's surface are produced with the middle-scale atmospheric model WRF (Weather Research and Forecasting). WRF is a latest generation numerical weather prediction model, which is designed for operational weather forecasting and atmospheric research. It consists of multiple dynamic "cores", supported by a 3-D system for the variational data assimilation. It contains pre-processing procedures for the definition of the simulation fields and the spatial extrapolation or interpolation of static (e.g., topography, land use) and meteorological data in these fields, and the ARW model for the numerical integration. The architecture of the code allows the exploitation of the computational capabilities of GRID infrastructures. The WRF model is suitable for a wide range of applications and provides estimates in spatial resolution ranging from a few meters to thousands of kilometres.

For the simulation of solar radiation, the radiation scheme MM5-SW (Dudhia 1989) is used, including absorption, scattering and reflection in the entire solar spectrum. Solar radiation interacts with the distribution of clouds and water vapour (Lacis and Hansen 1974) simulated by the model, as well as with specific climatic distributions of CO_2, O_3 and other trace gases. In the model, each atmospheric column is treated independently to calculate the solar flux at the surface.

The highest resolution is 2 km and is used for predictions in Athens and Thessaloniki. The WRF model initialization (definition of initial and boundary conditions) is performed using data from the European Centre for medium-term

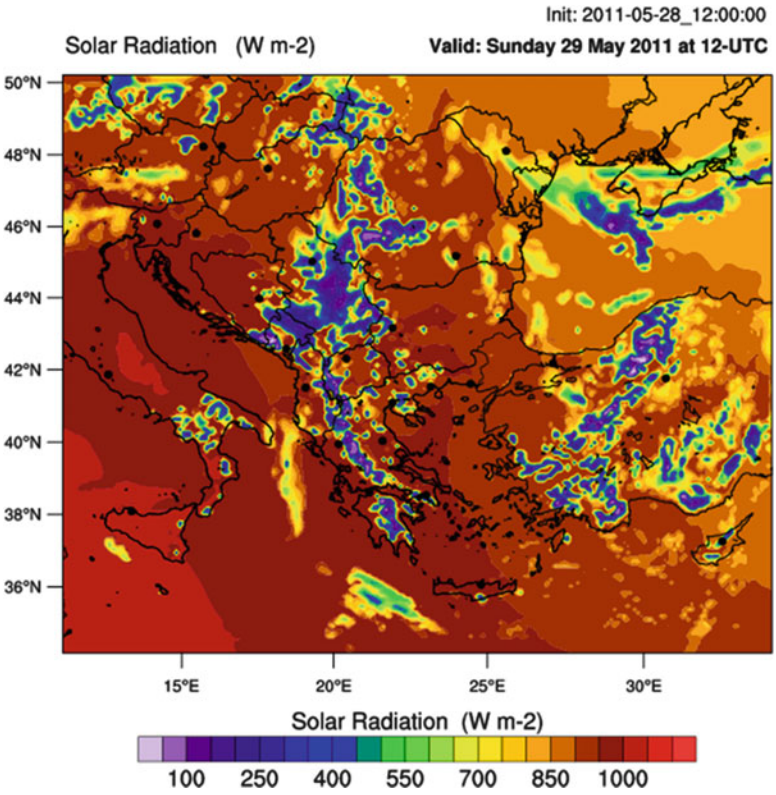

Fig. 1 Example of forecasted solar irradiance field over Greece under all weather conditions

Forecasts – ECMWF. The numerical model starts at 12 UT each day and predictions are produced for 84 h. The first 12 h are considered as a warm-up period of the model hence actual forecasts are given for up to 72 h (3 days). Operationally forecasts of solar radiation are provided at 1 h time steps. Figure 1 shows an example of a forecasted solar radiation field.

The concept for the estimation of solar radiation from satellite images was based on the derivation of the Cloud Modification Factor (CMF), which is the ratio of solar radiation under real cloud conditions with the corresponding cloud-free value. The algorithm was based on the methodology of Verdebout (2000), modified accordingly for solar radiation. Satellite images from the Spinning Enhanced Visible and Infrared Imager (SEVIRI) of MSG at 0.6 and 12 μm were used for the estimation of cloudiness and the identification of snow covered terrain respectively. Look Up Tables (LUTs), derived from the LibRadtran software package (Mayer and Kylling 2005) were used for the estimation of the scattered radiation to the imager for different values of solar and satellite zenith and azimuth angles, surface reflectivity, altitude, and aerosol and cloud optical properties. For each satellite pixel, the algorithm could provide the CMF, since all other parameters

were known or assumed from climatological values. LibRadtran LUTs, including solar irradiance under cloud-free conditions, were used also for the estimation of the irradiance incident on the ground. The later is equal with to the irradiance under cloud-free conditions multiplied with the CMF.

3 Results and Discussion

Figure 2 shows the comparison between model-derived and measured solar irradiance at Thessaloniki for the spring months of 2011 under all weather conditions and times of the day. The comparison is good, with the model overestimating the measurements on the average by 10%. More than 60% of the data pairs agree to within 10%. If measurements taken under very low solar zenith angles are excluded, then the comparison improves appreciably. When model estimates in a grid of 10×10 km^2 are considered, then the comparison improves further. It should be mentioned here that the model cannot capture the localized variations of solar irradiance that are measured by the pyranometer.

Satellite derived CMF values are compared with ground-based solar irradiance measurements (1-min averages at the same time with the satellite images) at Thessaloniki for the validation of the methodology described above. The measurements were divided by the model derived solar irradiance for cloud-free conditions to estimate the CMF at the ground. CMF values greater than unity were excluded from the comparison, since they correspond to enhancement of radiation by clouds. Such situations cannot be detected from the analyses of satellite images.

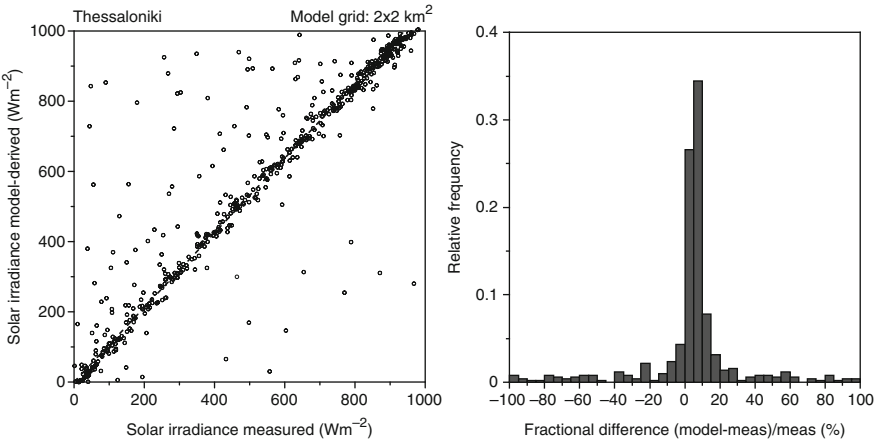

Fig. 2 (*Left*) Comparison of model-derived and measured hourly total solar irradiance at Thessaloniki, for days 148–241 of year 2011. The *dashed line* represents the linear regression of the data. (*Right*) Frequency distribution of the fractional differences between model-derived and measured irradiance

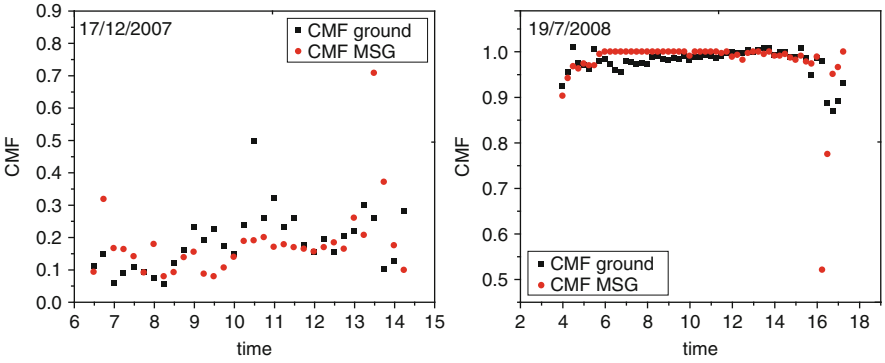

Fig. 3 Comparison of the Cloud Modification Factor, derived from MSG images (*red circles*) and ground-based measurements (*black rectangles*) at Thessaloniki, during 2 days with mostly clear skies (*left*) and overcast conditions (*right*)

Typical results, during 2 days with mostly clear and overcast conditions, are presented in Fig. 3. In general, the preliminary analysis shows that higher differences are revealed during broken cloudiness (when a cloud covers the sun and shades the instrument at the ground) and in cases with very thick clouds (with CMF < 0.2). There is no dependence on solar zenith angle, indicating that the change in surface reflectivity and the position of the satellite relative to the sun were simulated successfully. On monthly basis, the percentage differences between the satellite-derived and the ground-based CMF lay within $\pm 10\%$.

4 Conclusions

The "Hellenic Network for Solar Energy", which is currently in development phase, aims at providing real time data and simulations of solar energy over the Greece. These products will be produced by combining ground-based solar irradiance measurements, satellite images, as well as model simulations and predictions. The validation of the WRF derived forecasts of solar irradiance at the surface provided satisfactory results. Although the comparison is better for the coarser resolution of $10 \times 10\ \text{km}^2$ than for the fine resolution of $2 \times 2\ \text{km}^2$, the agreement is good as most of the model estimates agree to within 10% with the measurements. The model overestimates the irradiance probably because the local pollution of Thessaloniki cannot be represented in the model very accurately.

Images of the MSG satellite are used to derive the cloud modification factor which is employed for the simulation of the actual solar irradiance at the surface and in turn for the estimation of the available solar energy. The uncertainty of these estimations is within $\pm 10\%$, when compared with monthly averages of ground-based measurements.

Acknowledgments This work is conducted in the framework of the action "Cooperation 2009" of the Operational Programme "Competitiveness and Entrepreneurship" of the Hellenic Ministry of Development Competitiveness and Shipping, contract no. 09ΣΥΝ-32-778. MSG images were provided by EUMETSAT. The authors are indebted to Dr. Jean Verdebout (JRC, Ispra) for providing the original algorithm.

References

Dudhia J (1989) Numerical study of convection observed during the winter monsoon experiment using a mesoscale two-dimensional model. J Atmos Sci 46:3077–3107. doi:10.1175/1520-0469(1989) 046<3077:NSOCOD>2.0.CO;2

Lacis AA, Hansen JE (1974) A parameterization for the absorption of solar radiation in the Earth's atmosphere. J Atmos Sci 31:118–133. doi:10.1175/1520-0469(1974) 031 <0118: apftao>2.0.co;2

Mayer B, Kylling A (2005) Technical note: the libRadtran software package for radiative transfer calculations – description and examples of use. Atmos Chem Phys 5:1855–1877. doi:10.5194/acpd-5-1319-2005

Verdebout J (2000) A method to generate surface UV radiation maps over Europe using GOME, Meteosat, and ancillary geophysical data. J Geophys Res 105(D4):5049–5058. doi:10.1029/1999JD900302

The Climate and Bioclimate of Nevşehir from the Perspective of Tourism

O. Çalışkan and A. Matzarakis

Abstract Climate is an important resource for tourism and an equally important element that needs to be included in tourism purposes. This study reveals Nevşehir's human-bioclimatological and tourism climatological conditions. These conditions were identified by using physiologically equivalent temperature and Climate-Tourism-Information-Scheme over 10-day periods and analyzing the mean thermal perception values that emerged. Evaluating bioclimatic conditions and meteorological parameters such as thermal bioclimate issues, duration of sunshine, number of wet days, amount of precipitation and wind, from the perspective of tourism will help people choose the best holiday times depending on their individual needs and circumstances.

1 Introduction

Tourism is one of the world's largest and fastest growing economic sectors. Usually, the weather conditions and climate of a specific region are perceived, among other natural resources, as determining factors for tourism and recreation potential (de Freitas 2003; Matzarakis 2006). In recent years, tourism has become a fast growing economic sector attracting big investments in Turkey. The contribution of tourism to Turkish Gross National Product (GNP) leapt from approximately $7.8 billion in 1998 (net revenues) to approximately $22 billion in 2008 (Turkish Statistical Institute, TSI 2009). Although there is a big potential for tourism in many different parts of the country, the tourism industry has mostly been appeared in Southern and Western Anatolia. While promoting the potential of these regions,

O. Çalışkan (✉)
Ankara University, Izmir, Turkey
e-mail: ocaliskan@ankara.edu.tr

A. Matzarakis
Meteorological Institute, Albert-Ludwigs-University of Freiburg, Freiburg, Germany

C.G. Helmis and P.T. Nastos (eds.), *Advances in Meteorology, Climatology and Atmospheric Physics*, Springer Atmospheric Sciences,
DOI 10.1007/978-3-642-29172-2_56,

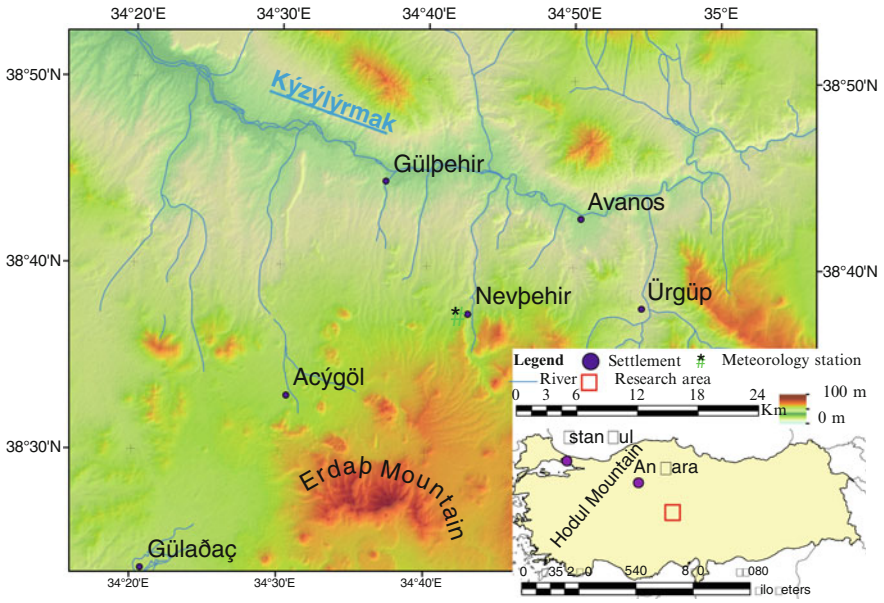

Fig. 1 Location map of Nevşehir

the sole focus remains on the triple S (sea, sand and sun trio). However, Nevşehir and its environs in Central Turkey comprise a natural recreational region with their diverse tourism opportunities, including culture, nature, sports and health tourism (Fig. 1). In 2008 a total 253,532 tourists (80,136 domestic and 173,396 foreign) visited and stayed on an average 1.4 days in Nevşehir (TSI 2009).

2 Data

The climatic and bioclimatological conditions of Nevşehir have been analyzed by using data (air temperature, humidity, wind speed and frequencies, global radiation, cloudiness, sunshine duration) belonging to the time period between 1975 and 2008 obtained from the General Directorate of State Meteorology Affairs for Nevşehir Meteorology Station.

3 Methodology

In order to present the potential of Nevşehir for tourism climate and bioclimate of the city has been analysed. In order to explain the bioclimatic conditions of the research area, thermal perception over a year were given in 10-day intervals at 7, 14 and 21

LST, and the formation frequency of different thermal perceptions was revealed for more detailed bioclimatological analyses. In addition, the meteorological variables important for tourism were given in 10-day periods over a year in the Nevşehir bioclimatology brochure. The meteorological parameters taken in 10-day time resolution were evaluated under three main heading parameters that affect tourism on thermal (thermal perception), physical (precipitation, snow, wind) and aesthetic dimensions (daylight and clouds) were treated together (de Freitas 1990; de Freitas and Matzarakis 2005). Climate variables were presented by using mean, minimum and maximum air temperature and the number of days with different threshold values. Days with a maximum temperature over 25°C (Tmax $>$ 25°C) were classified as hot days, those with a maximum temperature over 30°C (Tmax $>$ 30°C) were classified as tropical days. Days with a minimum temperature below 0°C (Tmin $<$ 0°C) were classified as frost days, those with a minimum temperature over 20°C (Tmin $>$ 20°C) were classified as tropical nights, and their annual distribution was given with 10-day intervals (Zaninović and Matzarakis 2009). Thermal conditions were also analyzed by using the PET values.

The aesthetic weather conditions in the brochure included parameters such as cloudiness, daylight periods, and the number of clear and overcast days. Similarly, the number of foggy days was also included among aesthetic weather conditions. Physical factors in the brochure were the number of days with precipitation and rain. Wind conditions were shown by using a wind vane. In addition to climatological and bioclimatological parameters, the Climate-Tourism-Information-Scheme (CTIS) (Matzarakis 2007; Lin and Matzarakis 2008; Zaninović and Matzarakis 2009) was used in the brochure in order to be able to offer a more holistic picture of tourism and recreation conditions. CTIS includes detailed climate information for tourists to use as they plan their holidays, such as thermal comfort conditions over a year, or aesthetic and physical weather conditions. The components of CTIS are:

Thermal components

1. Hot stress (PET $>$ 35°C)
2. Cold stress (PET $<$ 0°C)
3. Thermally comfortable conditions (18°C $<$ PET $<$ 29°C)

Aesthetic components

4. Cloudiness (cloud age $<$ 4 okta)
5. Fog (relative humidity $>$ 93%)

Physical components

6. Wind (wind speed $>$ 8 m/s)
7. Consistent rain (precipitation $>$ 5 mm)
8. Dry days (precipitation $<$ 1 mm)
9. Sultriness (vapor pressure $>$ 15 hPa)

4 Results

Nevşehir is an area with a high potential for tourism and recreational activities. In addition to areas conducive to outdoor activities such as trekking and mountaineering, it also has camp sites. For the correct timing of activities, knowing about the bioclimatological conditions would be useful. An analysis of Nevşehir 10-day mean thermal perception (PET) values between 1975 and 2008 shows that extreme cold stress may be experienced in morning and evening hours during the cold season (from the middle of November through the end of March; approximately 130 days), which is relatively less in the afternoon. Spring (18 days) and fall (17 days) have better thermal comfort conditions. In May, June, September and October, PET values seem to be comfortable mostly throughout the day. In July and August, mornings have more comfortable hours than evenings. During noon in these months, a hot stress can be seen. Therefore, it would not be wrong to say that morning hours have more appropriate bioclimatological conditions for walking and sports activities. One advantage of the bioclimatology of Nevşehir is that heat and excessive heat periods are rare and almost exclusively limited to the afternoon. In the summer, it is possible to stay outdoors at morning and evening hours (nearly all day except noon hours) thanks to comfortable weather conditions. During the hottest times of the day, it is necessary to stay in cool places as much as possible (Fig. 2).

Nevşehir's CTIS shows that there is a probability for thermo-physiologically severe cold from November through April. The probability is much higher between December and January. While early April to late October seems to be a favorable period as regards cold stress, there is an increased risk of cold after this. In contrast, heat stress occurs between the end of June and mid-August, and causes uncomfortable conditions during this period. Thermally favorable conditions last from mid-April to the end of October, and unfavorable (uncomfortable) conditions emerge once again in July and August. Except a very short time period in the summer, clouds of different degrees are seen at all times throughout the year. With respect to fog Nevşehir has very favorable conditions but strong winds can cause uncomfortable conditions especially during the cold season. Apart from the winter precipitation, there is a slight possibility of precipitation more than 5 mm almost anytime throughout the year (Fig. 2).

The climatological characteristics of Nevşehir with respect to tourism show that the season with cold stress (PET $< 0°C$) lasts from late October to early May, and the highest frequencies (75–100%) are seen in January and February. Excessive cold is not seen between May and September. The possibility of thermally comfortable conditions ($18°C <$ PET $< 29°C$) is highest (75–100%) between May and September, which is a transition between the warm and cold seasons. Hot stress (PET $> 35°C$) is observed between late May and late September, with a 75–100% of extreme heat stress possibility in July and August. Such thermal conditions (PET values) are not possible in the period between December and late March. There is a 50% and 27% possibility of sky conditions with less cloudiness than

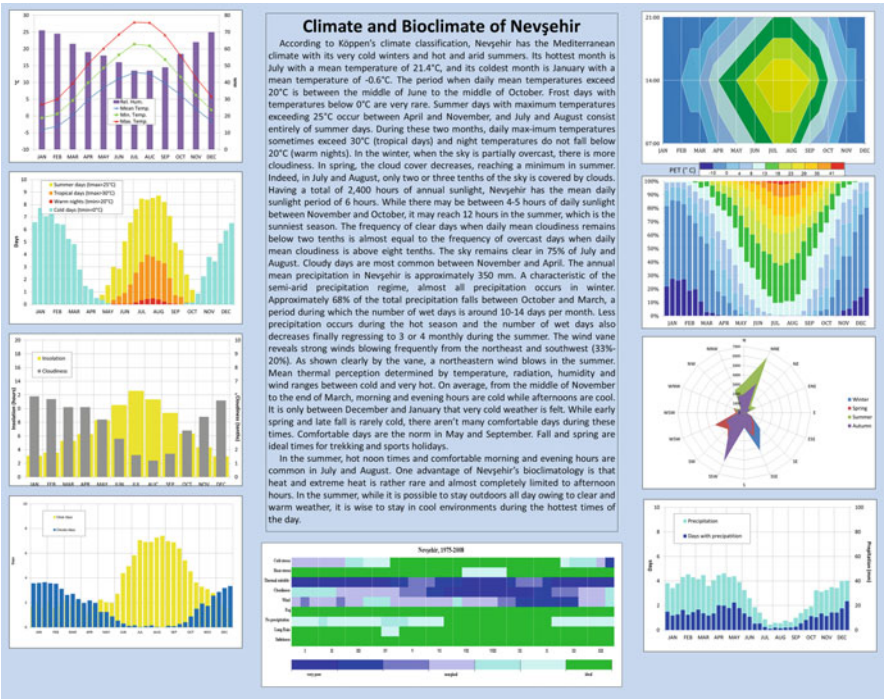

Fig. 2 Climate information scheme of Nevşehir

4 octa in the cold season, while in the warm season the possibility increases to 75–100%. The wind speed surpasses 8 m/s in Nevşehir during cold season, and relative humidity very rarely exceeds 93%. Throughout the year, there is a possibility of precipitation less than 1 mm (except summer). The possibility of consistent rain (precipitation $>$ 5 mm) is approximately 15%. There is no such possibility in June, July and August. Conditions of water vapor pressure higher than 18 hPa only appear in the summer. It is estimated that in June, July and August, there is a 15–50% possibility of water vapor pressure (sultriness) higher than 18 hPa (Fig. 2).

When the tourism potential appropriateness of climatological and bioclimatic conditions is analyzed, it is calculated that cold stress is felt from early November to late March. Ideal tourism conditions are seen in the period between early April and late October as the cold stress disappears. Heat stress is experienced most in July and August, and is almost nonexistent outside of summer months. Nevşehir does not have a time period when most appropriate thermal conditions for people increase to ideal levels of tourism. Still, thermally comfortable conditions are taking place from mid-April to late October. Regarding cloudiness, the ideal conditions appear in the summer. The most ideal sky conditions are seen in July and late August. Another advantage for tourism is that ideal wind speed and fog parameters exist in Nevşehir throughout the year. Even though the high possibility

of precipitation in Nevşehir in the cold season may imply unfavorable conditions, the conditions in the warm season are conducive to tourism activities. Excessive heat is only experienced between mid-June and early September and the rest of the year does not have excessive weather conditions (Fig. 2).

5 Conclusions

With this study, Nevşehir's climatic and bioclimatological conditions, and their change and distribution over the year were analyzed in order to be used in the tourism as well as tourism industry. The findings obtained were used to prepare a simple and clear bioclimate and tourism climate brochure that can be understood by everyone. Being well-suited to be used as part of tourism promotions, this brochure is important for the evaluation of not only the sea, sand, sun trio but also various natural resources and alternatives. Offering thermo physiologically comfortable conditions in May and September, Nevşehir is suitable for different health, culture, recreation and nature tourism activities from May to September. In July and August, there are hot noon hours and comfortable morning and evening hours. One advantage of Nevşehir's bioclimatic conditions is that rare heat and excessive heat periods are almost exclusively limited to the afternoon. In the summer, it is possible to stay outdoors all day owing to comfortable weather conditions. The proximity of Nevşehir to the sea and its low altitude prevent extreme thermal conditions.

References

de Freitas CR (1990) Recreation climate assessment. Int J Climatol 10:89–103. doi:10.1002/joc.3370100110

de Freitas CR (2003) Tourism climatology: evaluating environmental information for decision making and business planning in the recreation and tourism sector. Int J Biometeorol 48:45–54. doi:10.1007/s00484-003-0177-z

de Freitas CR, Matzarakis A (2005) Recent developments in tourism climatology. Bull Ger Meteorol Soc 1:2–4

Lin TP, Matzarakis A (2008) Tourism climate and thermal comfort in Sun Moon Lake, Taiwan. Int J Biometeorol 52:281–290. doi:10.1007/s00484-007-0122-7

Matzarakis A (2006) Weather and climate related information for tourism. Tour Hosp Plan Dev 3:99–115. doi:10.1080=14790530600938279

Matzarakis A (2007) Assessment method for climate and tourism based on daily data. In: Matzarakis A, de Freitas CR, Scott D (eds) Developments in tourism climatology. German Meteorological Society, Freiburg, pp 52–58

Turkish Statistical Institute (2009) Konaklama İstatistikleri (Mahalli İdarelerce Belgelendirilen), Yayın No. 209/2 Ankara (in Turkish)

Zaninović K, Matzarakis A (2009) The bioclimatological leaflet as a means conveying climatological information to tourists and the tourism industry. Int J Biometeorol 53:369–374. doi:10.1007/s00484-009-0219-2

Indications of Stability of Occurrence of Halcyon Days in the Ancient Greek Drama

C. Chronopoulou and A. Mavrakis

Abstract The aim of this paper is to examine the stability of the presence of the Halcyon days in the fifth and fourth century B.C. at Attica through the study of Greek tragedy and comedy. The dramas were being taught during the Lenaia – a celebration to honor Lenaius Dionysus, during the winter attic month Gamelion (15 January–15 February) – in open space firstly and then at the open theatre of Dionysus south of the Acropolis. The dramas did not saw references of sudden meteorological phenomena. On the contrary, they remark references of the clear weather of Attica and they notice the helpful presence of Halcyon days. In conclusion, the stable appearance of Halcyon days allowed Athens of classical years to organise dramatic festivals regularly, during the Gamelion without any signs of postponement or cancellation due to sudden weather phenomena, like sudden rainfall.

1 Introduction

This paper concerns the indications of stable weather conditions during the performance of dramatic festivals in Gamelion, attic month (15 January–15 February) in Athens of fifth and fourth century by studying the ancient Greek drama. The dramas of Aeschylus, Sophocles Euripides and comedies of Aristophanes provide testimonies about the clear, cloudiness, without indications of sudden weather phenomena and signs of stability in the appearance of the Halcyon days, in order

C. Chronopoulou (✉)
Theatre on Education, Educational Department of Primary Education, National and Kapodestrian University of Athens, 13A Navarinou Street, Athens 106 80, Greece
e-mail: chris_chron@yahoo.com

A. Mavrakis (✉)
Department of Economic and Regional Development, Institute of Urban Environment and Human Resources, Panteion University, 136 Syngrou Avenue, Athens 176 71, Greece
e-mail: mavrakisan@yahoo.gr

C.G. Helmis and P.T. Nastos (eds.), *Advances in Meteorology, Climatology and Atmospheric Physics*, Springer Atmospheric Sciences,
DOI 10.1007/978-3-642-29172-2_57,

the dramatic festivals of the Lenaia to be performed in an open space like the theatre of Dionysus. The Halcyon days were named from the myth of Greek mythology "The halcyon breeds at the season of the winter solstice. Accordingly, when this season is marked with calm weather, the name of 'halcyon days' is given to the 7 days preceding, and to as many following, the solstice" (Aristotle's, *Histories about animals*, 5.8, 350 B.C., (Wentworth Tompson (trans) 2007)).

"Halcyon days" is a phenomenon that happens in Greece till the latitude of southeast Europe between 15 December and 15 February but more frequently 15–31 January (HNMS 2011). This happens because it is observed the same barometric pressure (equality pressure) and so there are no winds due to anticyclonic condition and the weather is cold but sunny (Ziakopoulos 2008).

We reckon that the dramas of classical years can be used as eyewitness, giving information which can be useful to the study of the climate in Attica of the classical era and others paleoclimatological studies. The writer of these plays provide us with descriptions of weather conditions which are objective testimonies seen through the eye of a simple observer.

2 Data and Methodology

Study of classical dramas of Aeschylus, Sophocles, Euripides, Aristophanes. In the 43 plays, 7 of Aeschylus, 7 of Sophocles, 18 of Euripides and 11 of Aristophanes (Lesky 1988) we notice seven references which they give information about the weather in Athens from 458 B.C. until 401 B.C., providing direct and indirect indications which are related to the clear weather and the beneficial Halcyon days in midwinter.

3 Results

The ancient Greeks used to forecast, looking at the signs the *diosimies* = phenomena caused by Zeus. Meteorological calendars the *parapigmata* were being circulated in ancient Agora (a place of gathering and market) since the fifth century. Philosophers, combining meteorology and astronomy were observing from high mounts like Mithimna, Idi and Lycabettus (Theophrastus, third–fourth century) and they composed *Parapigmata*, a kind of forecast report. In *Agamemnon* (4–7) 458 B.C., (Sommerstein (trans) 2008), Aeschylus refers;

I've spent my nights on the Atreides roof – resting on my elbows like a dog, and come to know – thoroughly the throng of stars of the night, – and also those bright potentates, conspicuous – In the sky, which bring winter and summer to mortals <observing> them as some set and others rise (Fig. 1).

Dramatic festivals were being organized at the Lenaia in the winter specifically in the 12th day of Gamelion (26th of January). Besides this particular month was

φρουρᾶς ἐτείας μῆκος, ἣν κοιμώμενος – στέγαις Ἀτρειδῶν ἄγκαθεν – κυνός δίκην – ἄστρων κάτοιδα νυκτέρων ὁμήγυριν – καί τούς φέροντας χεῖμα καί θέρος βροτοῖς – λαμπρούς δυνάστας – ἐμπρέποντας αἰθέρι – ἀστέρας, ὅταν φθίνωσιν, ἀνατολάς τε τῶν.

Fig. 1 Aeschylus in *Agamemnon*, 458 B.C.

Ὁ δ᾽ἀμφιθαλής Ἔρως-χρυσόπτερος ἡνίας-ηὔθυνε παλιντόνους-Ζηνός πάροχος γάμων-τῆς τ᾽εὐδαίμονος Ἥρας.-Ὑμήν ὦ,Ὑμέναι᾽ὦ-Ὑμήν ὦ, Ὑμέναι᾽ὦ!

Fig. 2 Aristophanes in *Birds*, 414 B.C.

ἀλκυονίδας τ᾽ἄν ἤγεθ᾽ἡμέρας ἀεί.

Fig. 3 Aristophanes in *Birds*, 414 B.C.

the month of holy marriage of Zeus and Hera and thus the ideal month for the mortals to marry under the full moon of Gamelion. Aristophanes in *Birds* (1737–1743) 414 B.C., (Sommerstein (trans) 1987) refers;

And blooming young Eros – of the golden wings guided – the tautened reins – as groomsman at the wedding of Zeus – and the blessed Hera. Hymen O, Hymenaeus O! – Hymen O, Hymenaeus O! (Fig. 2).

Because the Attic weddings were lasted for 3 days and the ceremony was usually happening in an open area in order the newly weds to harmonize their life to nature, we conclude that in particular days of Gamelion offered suitable weather conditions (Michailidou 1997). Aristophanes referred to the beneficial Halcyon days for the couple who had been married in Gamelion, (Aristophanes, *Birds*, 1591).

Enjoy Halcyon days the whole time (Fig. 3).

The ancient Greeks used to observe the stability of the presence of summery days in the winter, so they decided to include dramatic festivals at Lenaia, one of the four celebrations to honor Dionysus, which was one of the most famous deities not only at Attica but in many other places in Greece. Three of the four celebrations were combined to dramatic festivals; City Dionysian, Rural Dionysian and Lenaia which they related to the maenads "*λήναι*" and "*ληναΐζω*" and that means that I participate to the dance of Bacchus (History of Greek Nation 1972). The dramatic festivals were accompanied by dramatic contests probably in 440 B.C. (Pickard-Cambridge 1988) in which many poets participated. We cannot be sure when the Lenaia celebrations first began, but the fact that the dramatic contests were included many years after the beginning of these celebrations indicates that the winter month Gamelion offered the security in the stability of weather conditions which allowed people to watch theatre performances somewhere in the ancient Agora and then at the theatre that Lycurgus was built in the south slope of the Acropolis on the fourth century B.C. There is no evidence of existence of some kind of covered place in Agora for the dramas to be

Ἐγὼ δὲ λέξω δεινὰ μὲν δίκαια δε – Οὐ γάρ με νῦν γε διαβαλεῖ Κλέων ὅτι – ξένων παρόντων τὴν πόλιν κακῶς λέγω – αὐτοὶ γάρ ἐσμεν οὐπὶ Ληναίῳ τ᾽ἀγών, κοὔπω ξένοι πάρεισιν. Οὔτε γὰρ φόροι – ἥκουσιν οὔτ᾽ ἐκ τῶν πόλεων οἱ ξύμμαχοι – ἀλλ᾽ἐσμὲν αὐτοὶ νῦν γε περιεπτισμένοι – τοὺς γὰρ μετοίκους ἄχυρα τῶν ἀστῶν λέγω

Fig. 4 Aristophanes in *Acharnians*, 425 B.C.

taught according to American excavations (Pickard-Cambridge 1988). Also, we have no serious evidence about some kind of shelter close to the theatre of Dionysus in case of sudden rain during these years. The stoa of Eumenus at the south of the theatre was built at about the second century. We could assume that the weather did not troubled people of the earlier years who used to organise dramatic contests at the Lenaia and the reason was surely not that they did not care about the performance. Lenaia was less highly regarded than the City Dionysian because there were not foreign but only the citizens of Athens and resident allies due to stop sailing from December until February (Pickard-Cambridge 1988). Aristophanes in *Acharnians* (501–507), 425 B.C., a lenaian play refers;

And what I say will be shocking, but right. – This time Cleon will not accuse me of – defaming the city in the presence of foreigners; – for we are by ourselves; it's the Lenean – competition, and no foreigners are here yet; – neither tribute nor troops have arrived from the – allied cities. This time we are by ourselves. – Clean – hulled for I count the resident – foreigners as the bran of our populace (Fig. 4).

Despite the above, contests of the Lenaia were important because they were organized under the Archon Basileus, the supreme religious officer in the city, and so the rich citizens as the resident allies were *khoroigoi*, they sponsored these dramas, and they surly did not want their offering to loose its glamour because of postponement or cancellation. The competitive spirit was very important for them in order to achieve prestige and glory (Bardy 1971). Evidence that makes Lenaia a festival of significance is that excavations south of Acropolis have found marble slabs with graven names of the winners of the dramatic contests in Gamelion (Pickard-Cambridge 1988). Lenaia seemed to be the second more populate celebration after Great Dionysian. Famous plays especially comedies like those of Aristophanes won the first or second prize at the dramatic contests at Lenaia like *Acharnians* (425 B.C.) first prize, *Knights* (425 B.C.) first prize, *Wasps* (422 B.C.) second prize, *Lysistrata* (411 B.C.) no information for prize, *Frogs* (405 B.C.) first prize. The weather was mild and stable enough to allow these performances to be presented in the midwinter. Euripides in *Medea* (824–833) (Kovacs (trans) 1994) talks about the clear, pleasant and harmonic climate;

From ancient times the sons of Erechteus have been favored; they are children – of the blessed gods sprung from a – holy land never pillaged the enemy. – They feed on wisdom most glorious, always stepping gracefully through the bright air, where once, it is said, he nine Pierian Muses gave birth to fair haired Harmonia. – Men celebrate in song how Aphrodite, filling her pail at the streams of the fair flowing Cephisus, blew down upon the land temperate and sweet breezes (Fig. 5).

Ἐρεχθεΐδαι τὸ παλαιὸν ὄλβιοι – καὶθεῶν παῖδες μακάρων, ἱερᾶς – κλεινοτάταν σοφίαν, αἰεί διὰ λαμπροτάτου – Βαίνοντες ἁβρῶς αἰθέρος, ἔνθα ποθ' ἁγνὰς ἐννέα Πιερίδας Μούσας λέγουσι – ξανθὰν Ἁρμονίαν φυτεῦσαι. – τοῦ καλλινάου τ' ἐπί Κηφισοῦ ῥοαῖς – τὰν Κύπριν κλῄζουσιν ἀφυσσαμέναν – Χώραν καταπνεῦσαι μετρίας ἀνέμων ἡδυπνόους αὔρας.

Fig. 5 Euripides in Medea

Ἀλκυόνες, αἱ παρ' ἀενάοις θαλάσσης κύμασι – κύμασι στωμύλλετε

Fig. 6 Aristophanes in *Frogs*, 405 B.C.

Εὐίππου, ξένε, τᾶσδε χώρας ἵκου τὰ κράτιστα γᾶς ἔπαυλα, in white τὸν ἀργῆτα Κολωνόν, ἔνθ' – ἁ λίγεια μινύρεται θαμίζουσα μάλιστ' ἀηδών χλωραῖς ὑπὸ βάσσαις, – τὸν οἰνῶπα νέμουσα κισσὸν καὶ τὰν ἄβατον θεοῦ φυλλάδα μυριόκαρπον ἀνήλιον – ἀνήνεμόν τε πάντων χειμώνων.

Fig. 7 Sophocles in *Oedipus at Colonus*, 410 B.C.

Aristophanes implies that he is particularly grateful for the presence of the Halcyon days because his comedies especially those who criticize the Athenian democracy were mainly presented in Lenaia and that is the reason why he invokes their appearance in his comedy *Frogs* (1309–1310) 405 B.C., (Henderson (trans) 2002).

You halcyons, – who chatter by the everflowing – waves of the sea (Fig. 6).

Moreover, there are indications of low rainfalls in Attica. There was ability to predict rainfalls by observing the small Hymettos (a mountain of Athens). Small Hymettus used to be called as "Ἄνυδρος", dry Hymettus. Theophrastus refers; If the lesser Mount Hymettus, which is called the Dry Hill, has cloud in its hollows, it is a sign of rain. *On the signs of Waters, Winds and Storms* 20. Athens seemed to have mild weather and it was "the best place on earth that never meet heavy winter" as the tragic poet Sophocles refers to *Oedipus at Colonus* (668–678), 410 B.C., (Banks (trans) 1956).

Noble the breed of horses here – in white Colonus, the land of our birth. The loveliest land in all the earth. – A distant music, pure and clear. Rises from green, secluded vales. – The constant trill of the nightingales deep in their haunts of tangled vine, – of sacred ivy, dark as wine, thick is the god's inviolate wood, – rich in berries and rich in fruit. The sun is curtained; the wind is mute in winter (Fig. 7).

4 Conclusions

In this work we attempted to extract information about the stability of the weather phenomena in the Athens of the classical years by studying the fully surviving theatrical plays of the three tragic poets Aeschylus, Sophocles, Euripides and the comedian writer Aristophanes and particularly about the stability in the presence of Halcyon days. The comedies of Aristophanes especially those who they have been taught at Lenaia they often invoke the presence of the Halcyon days. Combining the fact that dramatic contests were held in the midwinter without any indications of postponement and references from the dramas about the clear weather and mild winters in Attica we could assume that particular days of almost every January were summery in the fifth and maybe in the fourth century. All these references are concerning indications of the fifth century. We found no weather indications in the fourth century's dramas but dramatic contests continue to happen and in this century because when Aristotle talks about Lenaia, he refers to the fourth century.

References

Banks TH (Trans) (1956) Sophocles. Three Theban plays, Antigone, Oedipus the King, Oedipus at Colonus. Oxford University Press, New York

Bardy HC (1971) The tragic theater in Greece (Trans: George Christodoulou-Liana Chatzikosta, 1992). Kardamitsas editions (in Greek), Athens

Hellenic National Meteorological Service (2011) Introduction in meteorology from ancient Greece to today (n.d.). Retrieved 2 Oct 2011 from the website http://www.hnms.gr/hnms/greek/meteorology/full_story_html?dr_url=%2Fdocs%2Fmisc%2FArxaia

Henderson J (ed) (Trans) (2002) Aristophanes (Loeb Classical Library) Frogs, Assemblywoman, Wealth. Harvard University Press, Cambridge/London

History of Greek Nation (1972) Vol C2:256–257, Ekdotiki Athinon (in Greek)

Hort FA (Trans) (1926) Theophrastus (Loeb Classical Library) De signis: Vol II in the Enquire into plants. Harvard University Press, Cambridge

Kovacs D (ed) (Trans) (1994) Euripides (Loeb Classical Library) Cyclops, Alcestis, Medea. Harvard University Press, Cambridge, MA/London

Lesky A (1988) History of ancient Greek literature (Trans: Tsopanakis A), 5th edn. Kyriakidis bros, Thessaloniki (Original edition in 1975, in Greek)

Michailidou E (1997) Marital ceremonies according to ancient Greek customs. Diipetes 42. Retrieved 2 Oct 2011 from the website: http://www.diipetes.gr/htmlIdx_25htm

Pickard-Cambridge A (1988) THE LESSER FESTIVALS. B. The Lenaia. In: Gould J, Lewis DM (eds) The dramatic festivals of Athens, 2nd ed revised. Oxford University Press, Oxford

Sommerstein AH (ed) (Trans) (1987) The comedies of Aristophanes. Vol 6: Birds. Aris and Phillips Ltd. Harvard University Press, Cambridge

Sommerstein AH (ed) (Trans) (2008) Aeschylus. Oresteia: Agamemnon, libation – bearers, Eumenides. Harvard University Press, Cambridge, MA/London

Wentworth Tompson A (2007) The history of animals by Aristotle. Retrieved Nov 2011. Available from ebooks@Adelaide Web site: http://books,adelaide.edu./a/aristotle/history

Ziakopoulos D (2008) Weather. The son of earth and sun. Vol 2. Private Edition, Athens, Greece. ISBN: 960-92667-0-3

Remotely Sensed Spatiotemporal Features of Agrometeorological Drought

N.R. Dalezios, A. Blanta, and N. Spyropoulos

Abstract The growing number and efficiency of earth observation satellite systems, along with the increasing reliability of remote sensing methodologies, provide a range of new capabilities in monitoring and assessing drought. For the quantitative assessment of agrometeorological or agricultural drought as well as the computation of spatiotemporal features, one of the most reliable and widely used indices is applied, namely the Vegetation Health Index (VHI). The computation of VHI is based on satellite data of temperature and the Normalized Difference Vegetation Index (NDVI). The spatiotemporal features of drought, which are extracted from VHI are: areal extent, onset and end time, duration and severity. In this paper, a 20-year (1981–2001) time series of NOAA/AVHRR satellite data is used, where monthly images of VHI are extracted. Application is implemented in Thessaly, which is the major agricultural region of Greece characterized by vulnerable and drought-prone agriculture. The results show that there are episodes of mild to moderate, as well as severe to extreme droughts, respectively. Also, there is an increase in the areal extent of each drought episode with peaks appearing usually during the summer. Finally, the areas with diachronic drought persistence can be located.

N.R. Dalezios (✉) • A. Blanta
Laboratory of Agrometeorology, School of Agriculture Sciences, University of Thessaly, Fytoko 38445, Volos, Greece

Institute ITEMA/CERETETH, Technology Park of Thessaly, 1st Industrial Area, Volos, Greece
e-mail: dalezios@uth.gr

N. Spyropoulos
Department of Natural Resource Development and Agricultural Engineering, Agricultural University of Athens, Athens, Greece

C.G. Helmis and P.T. Nastos (eds.), *Advances in Meteorology, Climatology and Atmospheric Physics*, Springer Atmospheric Sciences,
DOI 10.1007/978-3-642-29172-2_58,

1 Introduction

Drought is one of the major natural hazards with significant impact to environment, agriculture, economy and society. It is difficult to determine the effects of drought as it constitutes a complicated phenomenon evolving gradually in any single region. Monitoring and assessing drought conditions are usually performed through drought indicators and indices (Keyantash and Dracup 2002).

There are several widely used drought indices using conventional and/or remote sensing data (Kanellou et al. 2008). Historically, drought quantification methods are based on conventional hydrometeorological data, such as precipitation and temperature, which are limited, often inaccurate and unavailable in near real-time (Heim 2002; Thenkabail et al. 2004). On the other hand, satellite-based data are consistently available and can be used to detect several features. Over the last decades, remote sensing has gradually become an important tool for the detection of the spatial and temporal distribution and characteristics of drought at different scales (Steven and Jaggard 1995). Thus, the growing number and effectiveness of earth observation satellite systems, along with the increasing reliability of remote sensing methods and techniques, present a wide range of new capabilities in monitoring and assessing droughts.

In order to assess and monitor drought episodes and to alleviate the impacts of droughts it is necessary to detect several drought features such as severity, duration, periodicity, areal extent, onset and end time and to link drought variability to climate and its variability (Loukas et al. 2002). In this paper, the remote sensing potential in terms of data and methods is explored in order to quantify drought and classify drought severity based on several drought features by using VHI. Specifically, areal extent and severity during drought episodes signify the spatiotemporal variability of droughts in Thessaly. VHI is a combination of Vegetation Condition Index (VCI) and Temperature Condition Index (TCI) derived by NOAA/AVHRR satellite data. In Greece, VCI and TCI have proven to be useful tools for the detection of agricultural drought (Domenikiotis et al. 2002; Tsiros et al. 2004). The paper is organized as follows: in Sect. 2 classification of drought severity is presented; in Sect. 3 the methodology is developed and Sect. 4 delineates the analysis and discussion of results.

2 Study Area and Database

The region of Thessaly overtakes the central-Eastern department of continental Greece and overtakes a total areal extent of 14,036 km^2 (10.6% of total extent of the country). The 36.0% of ground are in a plain, the 17.1% semi-mountain, while the 44.9% is mountainous. The main watershed in Thessaly water district is the Pinios basin which covers 9,500 km^2 (Fig. 1). Thessaly plain is a drought-prone area, which is also the main agricultural region of Greece. The increase in agricultural

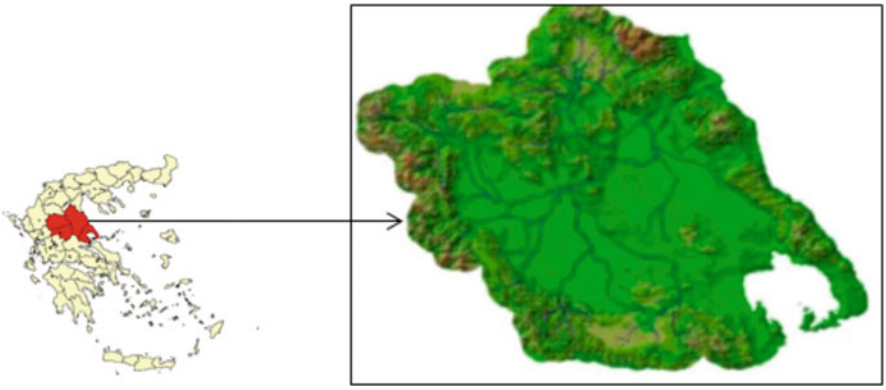

Fig. 1 Location and geographical map of Thessaly region

activities and the intensive type of agricultural practices applied in Thessaly, require more than the available natural resources. Low and irregular amount of rain during the summer period lead to regional drought events which in combination with the oversized pumping and the bad management of irrigation water have led to degradation of water resources and lowering of the ground water table. Thus, there is a necessity for identifying areas which are capable to fulfill crop water needs without aggravating the current conditions.

The database consists of NOAA/AVHRR satellite data and conventional data for 20 hydrological years, from October 1981 to September 2001. In specific: Normalized difference vegetation index (NDVI), channel 4 (CH4) and channel 5 (CH5) brightness temperature (BT) 10-day composite satellite images (8×8 km spatial resolution); Mean monthly air temperature measurements from Larissa meteorogical station (National Meteorological Service, NMS); Soil map of the study area (Yassoglou 2004); Digital elevation model derived from 100 m contours.

3 Methodology

The methodology includes data preprocessing and computation of VHI.

Preprocessing: Before using NDVI and BT images, fluctuations induces by noise must be removed. The combination of the filtering and the Maximum Value Composite (MVC) can significantly reduce the noise from residual clouds, fluctuating transparency of the atmosphere, target/sensor geometry, and satellite orbital drift. Other noise can be related to processing, data errors, or simple random noise. In the current study, a "4253 compound twice" median filter is applied to NDVI images, whereas a "conditional" statistical mean spatial filter (window size ranging from 3×3 to 7×7, according to image needs) has been used from smoothing the BT series (Tsiros et al. 2008, 2009). The BT series presented

Table 1 VHI drought classification schemes (Kogan 2001)

VHI values	Vegetative drought classes
<10	Extreme drought
<20	Severe drought
<30	Moderate drought
<40	Mild drought
>40	No drought

continuous spatial fluctuations, and thus, a spatial filter (statistical mean) has been preferred for smoothing channel 4 and channels 5 BTs. "Conditional" means that the filter is applied only to the pixels that present errors.

Computation of VHI: Remotely sensed Vegetation Condition Index (VCI) is based on NDVI, which is obtained by combining the channels 1 and 2, visible and near infrared respectively of NOAA/AVHRR. After a stressed condition, significant reduction in NDVI of the field is expected and values corresponding to complete lack of chlorophyll elements are sometimes anticipated. Maximum amount of vegetation is developed in years with optimal weather conditions. Conversely, minimum vegetation amount develops in years with extremely unfavourable weather (mostly dry and hot). This can be expressed by the vegetation condition index (VCI) and the temperature condition index (TCI) given by the equations:

$$VCI = 100^{*}\frac{NDVI - NDVI_{\min}}{NDVI_{\max} - NDVI_{\min}} \quad and \quad TCI = 100^{*}\frac{BT_{\max} - BT}{BT_{\max} - BT_{\min}}$$

where NDVI, $NDVI_{max}$ and $NDVI_{min}$ are the smoothed 10-day normalized difference vegetation index, BT, BT_{max} and BT_{min} are the smoothed 10-day radiant temperature, its multi-year maximum and its multi-year minimum respectively, for each pixel, in a given area. VCI and TCI vary from zero, for extremely unfavorable conditions, to 100, for optimal conditions. Kogan (2001) proposed the Vegetation Health Index (VHI) which represents overall vegetation health and used it for drought mapping. The five classes of VHI that represent vegetative and agrometeorological or agricultural drought (Bhuiyan et al. 2006) are illustrated in Table 1. VHI is expressed by the equation: $VHI = 0.5^{*}(VCI) + 0.5^{*}(TCI)$

In VHI computation, an equal weight has been assumed for both VCI and TCI since moisture and temperature contribution during the vegetation cycle is currently not known.

4 Results and Discussion

The results are presented in Table 2 and Fig. 2. At first, it can be stated (Table 2) that there are 8 hydrological years with drought episodes as in similar studies dealing with different types of drought (Dalezios et al. 2011).

Table 2 Areal extent of drought severity classes

Drought years	Class 1 (<10)	Class 2 (11–20)	Class 3 (21–30)	Class 4 (31–40)	Total
1984–1985	17.0	65.0	215.0	323.0	620.0
1987–1988	13.0	39.0	181.0	298.0	531.0
1989–1990	17.0	64.0	226.0	373.0	680.0
1991–1992	12.0	5.0	80.0	366.0	463.0
1992–1993	12.0	10.0	84.0	310.0	416.0
1996–1997	12.0	3.0	113.0	258.0	386.0
1999–2000	12.0	18.0	135.0	308.0	473.0
2000–2001	12.0	15.0	107.0	279.0	413.0

Fig. 2 Indicative VHI maps of Thessaly

However, there are differences in the values of various drought features such as duration areal extent, severity, on set and end time, as expected. From Table 2 it can also be noticed that there is a decreasing areal extent towards severe to extreme drought, which occur mainly during the summer. Finally, for illustrative purposes, two monthly VHI maps of Thessaly are presented in Fig. 2.

5 Conclusions

In this paper drought quantification is conducted through the estimation of remotely sensed monthly VHI in Thessaly, central Greece. Moreover, the remote sensing potential is explored by assessing several drought features towards drought severity

classification. The analysis has indicated the increasing potential and capabilities into assessing the variations of vegetative drought with the use of remote sensing techniques. Specifically, the results have shown that the region of Thessaly is affected by mild to moderate agrometeorological or agricultural drought in most of the cases mainly during the summer. Moreover, there is a decreasing trend in the areal extent of drought as long as drought severity is increasing during the summer again.

Acknowledgments This research was funded by Pleiades, Smart and Hydrosense EC projects. The conventional meteorological data was provided by the National Meteorological Service of Greece. The precipitation maps were provided by the Joint Research Center (JRC) of EC, Ispra, Italy. The satellite data was provided by NOAA.

References

Bhuiyan C, Singh RP, Kogan FN (2006) Monitoring drought dynamics in the Aravalli region (India) using different indices based on ground and remote sensing data. Int J Appl Earth Obs 8:289–302

Dalezios NR, Blanta A, Spyropoulos N, Pismichos N, Boukouvala E (2011) Spatiotemporal classification of drought severity. In: Proceedings of the international conference on ICT in agriculture HAICTA 2011, Skiathos, 14–17 Sep 2011

Domenikiotis C, Spiliotopoulos M, Tsiros E, Dalezios NR (2002) Application of NOAA/AVHRR VCI for drought monitoring in Thessaly. In: Proceedings of 6th international conference of protection and restoration of the environment, Skiathos, Greece, pp 1663–1670

Heim RR Jr (2002) A review of twentieth-century drought indices used in the United States. Bull Am Meteorol Soc 83:1149–1165

Kanellou E, Domenikiotis C, Tsiros E, Dalezios NR (2008) Satellite-based drought estimation in Thessaly. Eur Water 23(24):111–122

Keyantash J, Dracup JA (2002) The quantification of drought: an analysis of drought indices. Bull Am Meteorol Soc 88:1167–1180

Kogan FN (2001) Operational space technology for global vegetation assessment. Bull Am Meteorol Soc 82:1949–1964

Loukas A, Vasiliades L, Dalezios NR (2002) Hydroclimatic variability of regional droughts in Greece using the Palmer Moisture Anomaly Index. Nord Hydrol 33:425–442

Steven MD, Jaggard KW (1995) Advances in crop monitoring by remote sensing. In: Danson FM, Plummer SE (eds) Advances in environmental remote sensing. Wiley, Chichester, pp 143–156

Thenkabail PS, Gamage MSDN, Smakhtin VU (2004) The use of remote sensing data for drought assessment and monitoring in southwest Asia. Research report, vol 85. International Water Management Institute, Colombo, pp 1–25

Tsiros E, Domenikiotis C, Spiliotopoulos M, Dalezios NR (2004) Use of NOAA/AVHRR-based vegetation condition index (VCI) and temperature condition index (TCI) for drought monitoring in Thessaly, Greece. In: EWRA symposium on water resources management, Izmir, Turkey, 2–4 Sep 2004, pp 769–782

Tsiros E, Domenikiotis C, Kanellou E, Dalezios NR, Tzortzios S (2008) Identification of water limited growth environment zones using NOAA/AVHRR data. In: 4th international conference on information and communication technologies in bio and earth sciences HAICTA 2008, Athens, Greece, 18–20 Sep 2008, pp 150–155

Tsiros E, Domenikiotis C, Dalezios NR (2009) Sustainable production zoning for agroclimatic classification using GIS and remote sensing. IDŐJÁRÁS 113:55–68

Yassoglou N (2004) Soil map of Greece. National Committee against Desertification, Agricultural University of Athens, Athens, Greece

Characterization of Dust Storm Sources in Western Iran Using a Synthetic Approach

A. Darvishi Boloorani, S.O. Nabavi, R. Azizi, and H.A. Bahrami

Abstract Encountering numerous problems, many areas of the world experience dust storms every year. The west of Iran is considered as an area with numerous dust events because of vast deserts in Syria, Iraq, and the Arabian Peninsula. In recent years, the number of dust storms and the affected areas has remarkably increased. The present study is an attempt to identify west of Iran's dust sources using a synthetic approach including remote sensing technique of dust detection, physical–meteorological model called HYSPLIT, and analysis of the studied area's soil texture, land covering, and wind velocity data. Results show that there are two main dust storm sources affecting western Iran: The first region is the area between the west bank of Euphrates and east bank of Tigris, and the second one is the east and south eastern Arabian Peninsula a region called Rub' Al Khali.

1 Introduction

Concerning the definition of World Meteorological Organization, dust storms are resultant of weather turbulences which introduce a high mass of dust in the atmosphere, and consequently decrease the horizontal visibility to less than 1,000 m (Goudie and Middleton 2006). In a general perspective, primary sources

A.D. Boloorani
Department of Cartography, University of Tehran, Tehran, Iran

S.O. Nabavi (✉)
Department of Physical Geography, University of Tehran, Tehran, Iran
e-mail: s.o.nabavi@gmail.com

R. Azizi
Department of Mathematical Science, Sharif University of Technology, Tehran, Iran

H.A. Bahrami
Department of Soil Science, Tarbiat Modares University, Tehran, Iran

C.G. Helmis and P.T. Nastos (eds.), *Advances in Meteorology, Climatology and Atmospheric Physics*, Springer Atmospheric Sciences,
DOI 10.1007/978-3-642-29172-2_59,

of generating dust storms are located in the world's desert regions in Asia, Middle East, Europe, Latin America, North America, Australia, east and south Africa, and Sahara. Among them, Middle East has various sources of generating dust such as Arabian Peninsula, Syria, Egypt, Iraq and Iran (Shao et al. 2011).

Dramatic increase in occurrence of this phenomenon in the world's various regions, such as Iran, has led to the increasing attention of researchers to do numerous studies from various viewpoints. Li et al. (2010) have analyzed the greatest dust in the east of Australia using both satellite images, MODIS satellite, and Brightness Temperature Differences (BTD); denoting the significant effectiveness of this method in identification of dust masses, recognized how this phenomenon is occurred. Gerivani et al. (2011) characterized the source of dust storms in Iran based on geological maps and information on wind erosion of susceptible lands. Dust storm tracking is also a way of detecting dust sources which is primarily done by implementing remote sensing techniques and satellite imagery in short intervals, but another effective and convenient way to detect dust storm sources is HYSPLIT physical model (Draxler and Hess 1998) being used in areas with no access to satellite images to increase the validity of results acquired from satellite imagery. Kutiel and Furman (2003) have mainly studied temporal–spatial features of dust storms in Middle East. Summer was mentioned to be the time dust storms frequently occurred in Iran, north-east Iraq, Syria, Persian Gulf, south Arabia, Yemen, and Oman. Although each of the aforementioned studies have suggested remarkable results, the fact that dust events result from various factors necessitates adopting synthetic approaches and utilization of different sciences. Using various methods and information sources such as scientific techniques of remote sensing, specific physical model of wind tracking, and also soil texture, land cover and wind velocity data, current research attempts to achieve identification of dust sources in the area west of Iran.

2 Data and Methodology

2.1 Data

To study the effective conditions in which dust storms affect west of Iran, daily visibility data of ten synoptic stations, located in studied area, in the period of 2000–2008 have been used. Daily Visibility data were derived from Iran's Meteorology Organization archived database. The wind data for 1,000 hPa level is taken from National Centers for Environmental Prediction of US (Kalnay et al. 1996). MODIS satellite images are derived from http://rapidfire.sci.gsfc.nasa.gov/realtime website. Data used in HYSPLIT model are accessible at http://ready.arl.noaa.gov/ready2-bin/extract/extracta.pl. Soil texture data of studied area is extracted from the Harmonized World Soil Database (FAO/IIASA/ISRIC/ISSCAS/JRC 2009) and land cover data are accessible at www.esa.int/esaEO/SEM5N3TRJHG_index_0.html.

2.2 Methodology

In the present study, the dust storms that had been recorded in at least three synoptic stations were only studied with a non-local origin and leading to horizontal visibility of 1,000 m or less. The occurrence time of dust storms and detection of suspected dust clouds were determined by analysis of satellite images utilizing specific dust detection method (Ackerman 1997; Kaskaoutis et al. 2007). HYSPLIT physical model and its backward method are used to track air masses, as dust transporter, for approval whether the wind is blowing through the dust plumes to our given region. As it was mentioned, wind trajectory method is so helpful for situation lacking in satellite images with short time interval to identify main dust carrying paths and consequently their sources. Tracing the wind starts from stations affected by dust storms simultaneous with the formation of first dust core which terminates at the end of a day before dust occurrence, in altitude of 1,000 m. In fact, tracing the wind leads us to detect approximate dust sources. In the more precise identification phase of dust sources, the Harmonized World Soil Database, surface land cover, and wind velocity data of 1,000 hPa level (lower troposphere) are used in spite of reusing satellite images.

3 Results

Having examined the dust data of the local stations in our study from 2000 to 2008 and analyzed satellite images, and finally, based on the predetermined definition of dust storms, a number of 12 dust storm events have been investigated to identify western Iran's dust storm sources. Dust storm occurrence times and suspected dust clouds were identified by using dust detection method for all 12 dust cases. Generally, all events follow two formation and relocation regimes, from Iraq and Saudi Arabia to the west of Iran, shown for two cases from June 30 to July 3, 2008 and March 1–3, 2007 in Fig. 1.

Wind trajectory maps which are especially used for cases that satellite images are not accessible introduce two paths for carrying dust plumes into the west of Iran. Figure 2 shows two paths for the aforementioned examples determined by wind trajectory model:

1. North-west (west)–South-east (east) trajectory: The formed dust plumes in Iraq and Syria are carried to the west region of Iran by North-Westerly (Westerly) wind. Of 12 dust storms, 10 dust events were carried along this route (Fig. 2a, dust storm of Jun 30, 2008).
2. Southern-northern trajectory: It begins from southern coastline of Persian Gulf and ends at western Iran. Of 12 cases of dust storms, only 2 cases took this path and moved toward the west of Iran (Fig. 2b, dust storm of Mar 1, 2007).

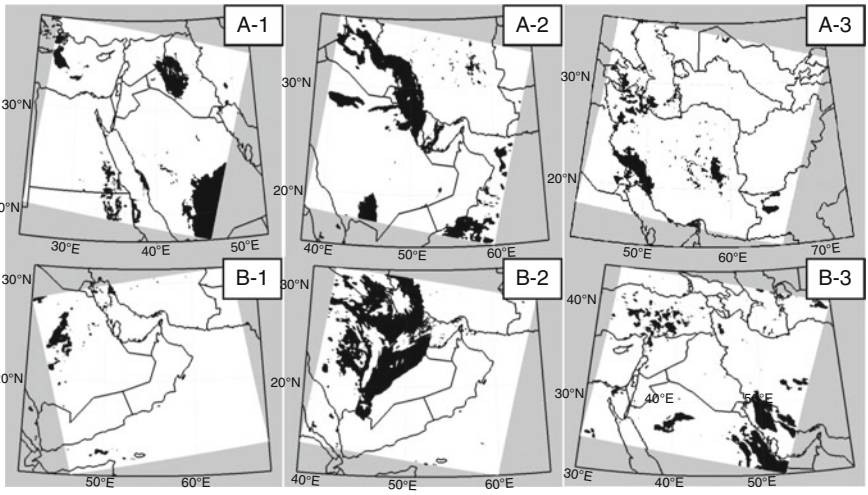

Fig. 1 Formation of dust storm from the area between the eastern bank of Euphrates and the western bank of Tigris on Jun 30, 2008; its expansion on Iran through Jul 2–3, 2008 (**a-1**, **a-2**, **a-3**) and from the eastern and southeastern deserts of Arabia Saudi Arabia on Mar 1, 2007 to Mar 3, 2007 (**b-1**, **b-2**, **b-3**)

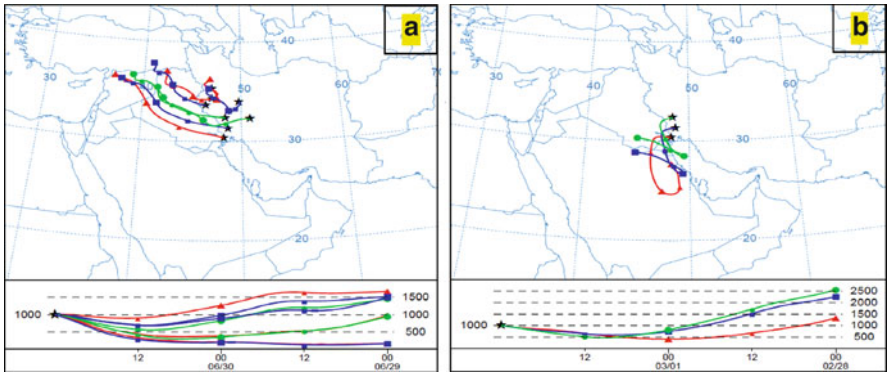

Fig. 2 Two examples of wind trajectory maps on Jun 30, 2008 (**a**) and Mar 1, 2007 (**b**) using HYSPLIT model. The *symbol (*)* shows the locations of synoptic stations affected by dust storm

Having done wind trajectory and known main dust transportation routes, the sources of dust storms are sought based on simultaneous study of Iraq, Syria, and Saudi Arabia's soil texture, land covering and wind velocity data along predetermined paths. In other word, determination of dust sources is due to identifying most influenced regions by wind velocity, with a superfine texture to be blown away by wind and also those without sufficient vegetation and humidity.

According to the Harmonized World Soil Database, along the first path determined by HYSPLIT model, there is an area with gypsum sediments in the northwest

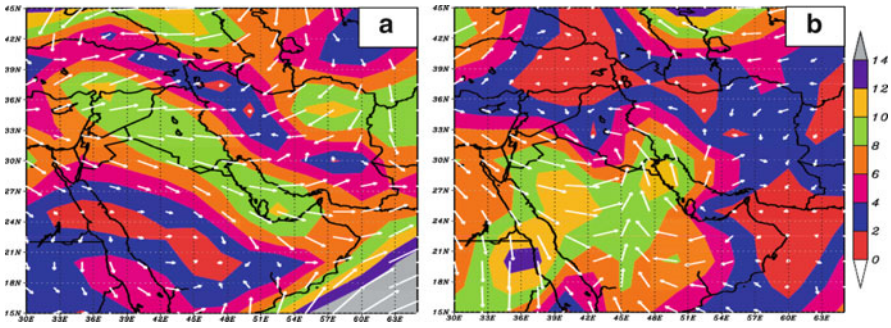

Fig. 3 Two examples of wind velocity maps on Jun 30, 2008 (**a**) and Mar 1, 2007 (**b**). *Vectors* show wind directions and *colored background* represents wind speed (ms^{-1})

of Iraq and the east of Syria called Gypsisols that is mostly developed in arid regions with sporadic vegetation. Presence of having such soil type prepares conditions for wind erosion, whereas southernmost area of the trajectory, i.e. the southeast of Iraq, consists of Solonchaks soil which is also found in arid and semi-arid regions; But one of its significant features is that the water table is high and the soil is moist; A condition that sometimes leads to water stillness on the soil surface Thus, such regions are less liable to develop extensive dust sources. About 20–23% of soil texture in the western bank of Euphrates and the eastern bank of Tigris consists of clay. In addition, the region has got a 50 unit of soil moisture, which is sometimes lowered to 15 units in some areas. These types of soil texture, with low moisture and sporadic vegetation, provide necessary conditions for wind erosion. Although this type of soil texture is also found in the southeast of Iraq (southern area of the trajectory), due to high soil moisture (almost 150 units), grasslands, and brushes, the surface soil is less likely to be removed from this region. The second trajectory includes Persian Gulf and its southern coast. Therefore, the only dust-prone areas along this trajectory are located in its southern parts, i.e. eastern and southeastern areas of Arabia (the desert region of Rub-Al-Khali). This part of Arabia consists of Regosol soil, the most texture of which is composed of gravel and sand coverings. In some parts of this region, more than 30% of soil texture is clay and could be considered as one of the most arid regions (the soil moisture is calculated as negligible, relatively zero) without vegetation (FAO/IIASA/ISRIC/ISSCAS/JRC 2009; IUSS 2007; Global Land Cover 2010). Though, due to coarse soil particles in this region, regional dust occurrence requires winds with higher velocity rather than the northwest of Iraq and the east of Syria ones. This is why we observe winds with velocity of more than 10 and even 12 m/s during dust events originated from the east of Arabia while in most cases in which dust storms originated from the northwest of Iraq and the east of Syria, a velocity of between 8 and 10 m/s is recorded in the region (Fig. 3).

4 Conclusions

Using the data from synoptic stations in the region, satellite images, and also tracking wind flows during dust events in the western stations in Iran, two main trajectories of dust transfer were recognized: The northwest-southeast trajectory which starts from the northwest of Iraq and the east of Syria, ends in the west of Iran, and the south–north trajectory that starts from the southern banks of Persian Gulf leads to the west of Iran through a south–north path. Utilizing the results of previous section, the simultaneous study of soil maps, land cover, and wind velocity along determined paths, led us to identify two main sources of dust storms in the west of Iran: The area between the eastern bank of Euphrates and the western bank of Tigris as the main dust sources; out of 12 dust storms, 10 cases were formed in this region and the eastern and southeastern deserts of Arabia. Considering more coarse soil texture of the eastern and southeastern deserts of Arabia rather than the first source, higher-velocity winds are required to form dust in this region.

References

Ackerman SA (1997) Remote sensing aerosols using satellite infrared observation. J Geophys Res 102:17069–17079. doi:10.1029/96JD03066

Draxler RR, Hess GD (1998) An overview of the HYSPLIT_4 modeling system for trajectories, dispersion, and deposition. Aust Meteorol Mag 47:295–308

FAO/IIASA/ISRIC/ISSCAS/JRC (2009) Harmonized World Soil Database (version 1.1). FAO, Rome, Italy and IIASA, Laxenburg, Austria

Gerivani H, Lashkaripour GR, Ghafoor IM, Jalili N (2011) The source of dust storm in Iran: a case study based on geological information and rainfall data. Carpathian J Earth Environ Sci 6(1):297–308

Global Land Cover (2010) Accessible at www.esa.int/esaEO/SEM5N3TRJHG_index_0.html

Goudie AS, Middleton NJ (2006) Desert dust in the global system. Springer, Berlin

IUSS Working Group WRB (2007) World reference base for soil resources 2006, first update 2007. World soil resources reports no. 103. FAO, Rome

Kalnay E, Kanamitsu M, Kistler R, Collins W, Deaven D, Gandin L, Iredell M, Saha S, White G, Woollen J, Zhu Y, Leetmaa A, Reynolds B, Chelliah M, Ebisuzaki W, Higgins W, Janowiak J, Mo KC, Ropelewski C, Wang J, Jenne R, Joseph D (1996) TheNCEP/NCAR 40-year reanalysis project. Bull Am Meteorol Soc 77:437–472

Kaskaoutis DG, Kosmopoulos P, Kambezidis HD, Nastos P (2007) Aerosol climatology and discrimination of different types over Athens, Greece based on MODIS data. Atmos Environ 41(34):7315–7329. doi:10.1016/j.atmosenv.2007.05.017

Kutiel H, Furman H (2003) Dust storms in the middle East: sources of origin and their temporal characteristics. Indoor Built Environ 12:419–426. doi:10.1177/1420326X03037110

Li X, Ge L, Dong Y, Chang HC (2010) Estimating the greatest dust storm in eastern Australia with MODIS satellite images. In: Proceedings of IEEE international geoscience and remote sensing symposium (IGARSS), Honolulu, HI, 25–30 July, pp 1039–1042

Shao Y, Wyrwoll K-H, Chappell A, Huang J, Lin Z, McTainsh GH, Mikami M, Tanaka TY, Wang X, Yoon S (2011) Dust cycle: an emerging core theme in Earth system science. Aeolian Res 2:181–204. doi:10.1016/j.aeolia.2011.02.001

Objective Recognition of Low Pressure Systems and Their Characteristics in the Area of Greece

K. Douvis, G. Tselioudis, M. Bauer, and C.S. Zerefos

Abstract The new dataset MCMS (MAP Climatology of Mid-latitude Storminess) of NASA-GISS performs objective recognition of the extra-tropical low pressure systems for the time period 1979–2010 based on the sea level pressure fields of NCEP-II re-analysis. The credibility of the dataset is considered to be very high as the fields of surface pressure, as well of geopotential height, are the most reliable among the fields of the re-analysis products. We focus on the characteristics of low pressure systems in the region of Greece. The seasonal signal is clear in both the frequency and the intensity of cyclones. Indications occur about the characteristics of the different prevailing circulations in the area of Greece from November–March and April–May.

1 Introduction

Cyclones are major features of the extra-tropical weather and climate. They regulate to a large degree the atmospheric circulation and the most vital atmospheric characteristics such as temperature, clouds, precipitation and winds.

A number of researchers have tried to perform objective recognition on data produced by analysis or reanalysis. That is the cyclones are recognized by an algorithm that is fed with analysis data. The most usual choice of input data is

K. Douvis (✉) • C.S. Zerefos
Research Center for Atmospheric Physics and Climatology, Academy of Athens, Athens, Greece
e-mail: cdouvis@geol.uoa.gr

G. Tselioudis
Research Center for Atmospheric Physics and Climatology, Academy of Athens, Athens, Greece

NASA-GISS, New York, NY, USA

M. Bauer
NASA-GISS, New York, NY, USA

C.G. Helmis and P.T. Nastos (eds.), *Advances in Meteorology, Climatology and Atmospheric Physics*, Springer Atmospheric Sciences,
DOI 10.1007/978-3-642-29172-2_60,

sea level pressure, but low-level vorticity (850 hPa) has been used as well. The algorithms usually identify the local minima of pressure as the centers of the cyclones. Many researchers have also used tracking algorithms that identify the centers with centers of the following time step thus allowing for the tracking of the cyclones. This way they calculated objectively the location, the velocity and the sea level pressure of the centers of extra-tropical cyclones. These data can afterwards be used by the researchers for various reasons such as the study of the statistical properties of weather and the evaluation of global circulation models (GCMs). A review of the past attempts in the field of objective recognition of low pressure systems was published relatively recently (Ulbrich et al. 2009).

Interest in the field has been renewed lately with a number of researchers focusing on the area of the Mediterranean. Campins et al. (2011) applied an algorithm on the 2.5° × 2.5° ERA-40 re-analysis data in order to create a climatology of the Mediterranean cyclones. The vertical structure of the cyclones was considered as well. Flocas et al. (2010) used the same data and the Melbourne University algorithm to create a climatology of cyclones in the eastern Mediterranean. They studied the differences in the features of the cyclones depending on their origin. Kouroutzoglou et al. (2010) used the same methodology in order to study the explosive cyclones in the Mediterranean. They found that explosive cyclones occur during the cold season, they form mainly along the northern coast of the Mediterranean and they studied the different features of those that form in the western and in the eastern Mediterranean. Kouroutzoglou et al. (2011) used the same methodology based on the 1° × 1° ERA-40 data and studied the differences in the created climatology. They found that the effect is very important, as in the high resolution case about four times as many cyclones were detected with several new tracks and with higher intensity in terms of deepening rates.

2 Data and Methodology

MCMS (MAP Climatology of Mid-latitude Storminess) is a new database developed in NASA-GISS, New York, USA (Bauer et al. 2012). It was created by applying an objective recognition algorithm on the 6-hourly sea level pressure fields of NCEP-2 Reanalysis for years 1979–2010. It is available for downloading at http://gcss-dime.giss.nasa.gov/mcms/mcms.html.

The MCMS database is more advanced than similar research attempts in the field of objective recognition. Earlier algorithms were focused mostly on the location of the centers of the low pressure systems and on the storm tracks, i.e. on the tracking in time of the centers. In addition to that the MCMS algorithm recognizes the grid points that belong to the area of influence of each low pressure center thus identifying the area, along with the shape of the area, the perimeter, the depth and the intensity. The area of influence of the depressions can be defined as the area of the depression bowl. This approach that was used is similar to the approach of Wernli and Schwierz (2006). The most important difference is that for the creation of the MCMS database the small depressions near a larger and deeper one were

attributed to it, given that certain criteria were met, thus allowing for the consideration of multi-center systems. In this case the area attributed to the storm is defined by the outermost closed contour that contains all the centers.

Note that in any reanalysis project the fields of geopotential height and pressure can be considered more credible than the other fields, such as precipitation and cloud properties due to the greater spatial and temporal homogeneity, the direct observations and the straightforward simulation. Although reanalysis products are not perfect and discrepancies cannot be ruled out in the small scale, the large scale features such as baroclinic cyclones can be considered to be represented with a high degree of accuracy.

3 Results

The low-pressure systems that affected Greece were isolated in order to be studied. It was considered that Greece is affected by the systems whose centers pass during their lifetime through a square defined by 35–43°N and 20–29°E.

Figure 1 presents the number of systems that affected Greece per 30 days. The strong seasonal variation was expected given that the climate of Greece is Mediterranean with strong seasonal variability in precipitation. The winter months

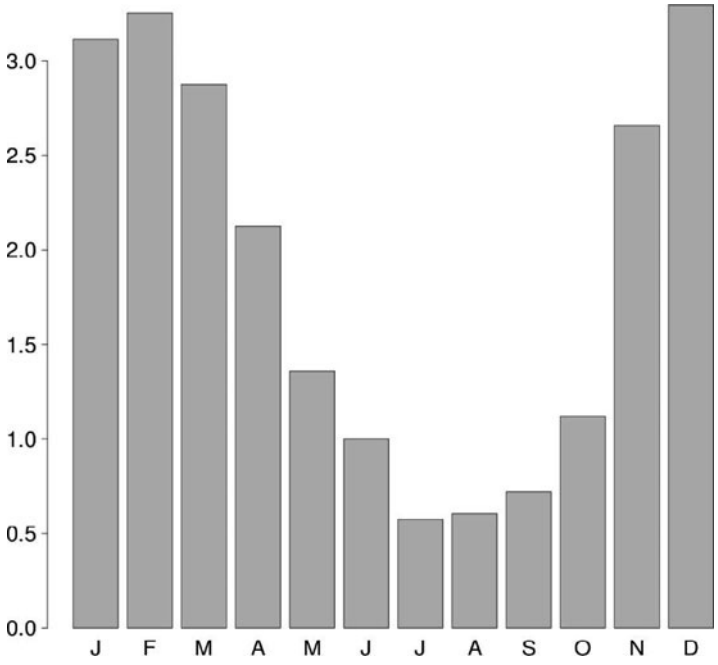

Fig. 1 Monthly variation of the number of low-pressure systems that affected Greece. Units are number of systems per 30 days

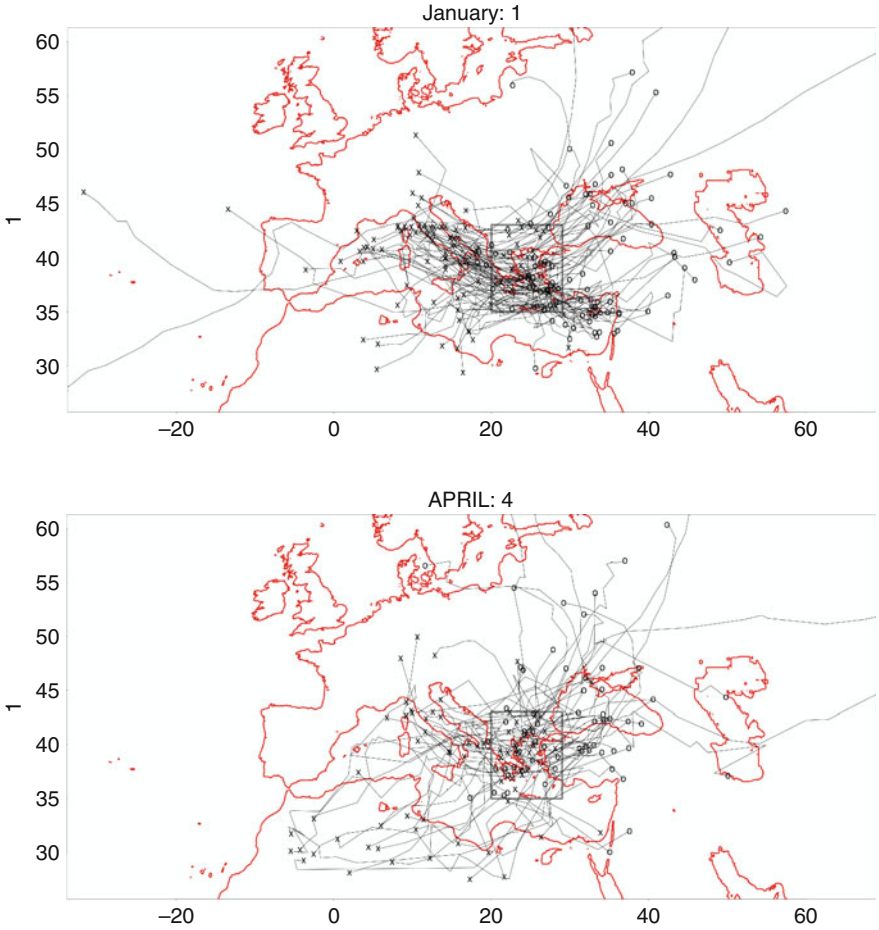

Fig. 2 The storm tracks observed on January (*top*) and on April (*bottom*)

along with March and November received about three low-pressure systems. July to September are the months of minimum activity with about 0.6 systems per month. The rest 4 months can be considered transitional, with April being closer to the winter values and the other 3 months being closer to the summer values. The autumn transition, located between October and November, is much more abrupt compared to the much more gradual transition observed during spring.

Figure 2 presents the tracks of the low-pressure systems that affected Greece on January and April for all the years with data. The "X" marks denote the origin of the depressions and the circles denote their end. In January most storms originate from the western Mediterranean and head eastwards, roughly along the northern coast of the Mediterranean and towards Greece. After they pass through Greece many of

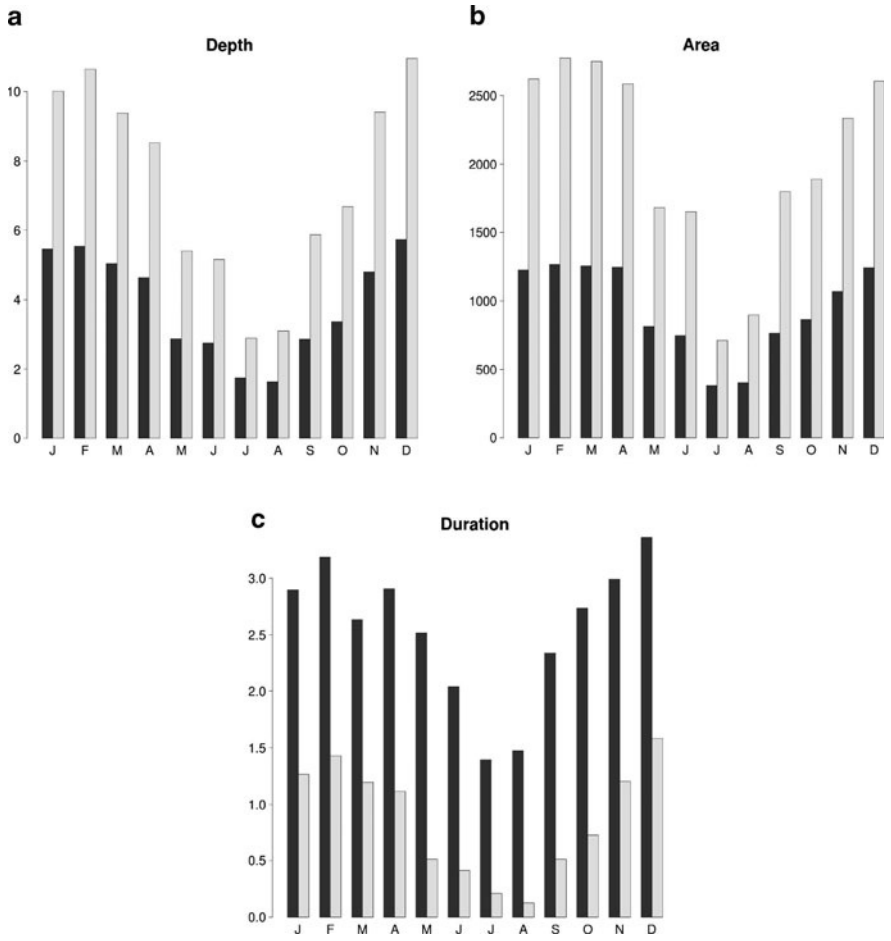

Fig. 3 Monthly variation of depressions characteristics: (**a**) mean lifetime depth and mean maximum depth in hPa, (**b**) mean lifetime area and mean maximum area in 1,000 km^2, and (**c**) mean duration and mean duration with a depth larger greater the 5 hPa in days

them continue on the same route until they dissipate near Cyprus but others divert to a more northward direction towards the Black Sea. The same description applies for all the other months from November to March (not shown).

In April many of the storms originate from the western Mediterranean as well but all of them follow the northern route after they pass Greece and very few head close to Cyprus. Another difference is that many storms originate in northern Africa. The picture is similar on May (not shown) except with less storms. The same description applies for May (not shown) except with fewer storms.

The summer months and September (not shown) are characterized by the very small number of storms. The origin of the storms is at Greece or very close to Greece although some of them proceed northwards and dissipate in the area of the Baltic Sea.

Figure 3 presents the seasonal variation of parameters concerning the intensity of the observed cyclones that affect Greece. It can be seen that there is a strong seasonal variation in the cyclone intensity similar to the variation in the frequency of occurrence. The mean lifetime depth of the depressions is (Fig. 3a) about double in the winter than in the summer. The same is valid about the mean maximum depth of the cyclones (Fig. 3a) and about the respective parameters on the area of the depressions (Fig. 3b). The seasonal variation in the mean lifetime (Fig. 3c) is slightly smoother with the winter values being less than double of the summer values but it is stronger concerning the duration of depressions deeper than 5 hPa because of very rare occurrences in the summer.

4 Conclusions

A new database with information on the extra-tropical low-pressure systems is used to study the impact of depressions in Greece. It contains information on the location of the centers of the systems and on a series of important characteristics.

1. The signal of the seasonal variation is clear in the cyclones that affect Greece. The frequency of occurrence, the depth, the area and the lifetime of cyclones is about double in the winter than in the summer.
2. The storm tracks indicate different dominant circulation patterns for November to March, than for April to May which can be considered a transitional season. There is not a similar transitional season in the autumn as the change of the circulation patterns as the change that occurs between summer-like October and winter-like November is very abrupt.

Future work on objective recognition of extra-tropical cyclones may take several different directions. The MCMS data should undergo extensive statistical analysis. Datasets of cloudiness and precipitation should be correlated with the passage of storm tracks and their age, depth, intensity, area of influence, orientation etc. It is of particular interest to investigate for a possible signal of a poleward shift of the storm tracks and of the arid climatic zone of northern Africa as has been predicted by GCM simulations (Meehl et al. 2007).

References

Bauer M, Tselioudis G, Rossow WB (2012) A new climatology for investigating storminess influences on the extratropics. J Clim (submitted)

Campins J, Genoves A, Picornell MA, Jansa A (2011) Climatology of Mediterranean cyclones using the ERA-40 dataset. Int J Climatol 31:1596–1614. doi:10.1002/joc.2183

Flocas HA, Simmonds I, Kouroutzoglou J, Keay K, Hadzaki M, Bricolas V, Asimakopoulos D (2010) On cyclonic tracks over the eastern Mediterranean. J Clim 23:5243–5257. doi:10.1175/2010JCLI3426.1

Kouroutzoglou J, Flocas HA, Keay K, Simmonds I, Hatzaki M (2010) Climatological aspects of explosive cyclones in the Mediterranean. Int J Climatol 31:1785–1802. doi:10.1002/joc.2203

Kouroutzoglou J, Flocas HA, Simmonds I et al (2011) Assessing characteristics of Mediterranean explosive cyclones for different data resolution. Theor Appl Climatol 105:263–275. doi:10.1007/s00704-010-0390-8

Meehl GA, Stocker TF, Collins WD, et al (2007) Global climate projections. In: Solomon S et al (eds) Climate change 2007: the physical science basis. Contribution of WG I to the AR4 of the IPCC. Cambridge University Press, Cambridge/New York

Ulbrich U, Leckebusch GC, Pinto J (2009) Extra-tropical cyclones in the present and future climate: a review. Theor Appl Climatol 96:117–131. doi:10.1007/s00704-008-0083-8

Wernli H, Schwierz C (2006) Surface cyclones in the ERA-40 dataset (1958–2001). Part I: novel identification method and global climatology. J Atmos Sci 63:2486–2507

Relating Climatic Variables to Geographic Features in Greece

H. Feidas, A.F. Karagiannidis, S. Keppas, G. Marougianni, M. Vaitis, Th. Kontos, I. Kioutsioukis, D. Melas, P. Zanis, and E. Anadranistakis

Abstract This study aims at investigating the relationship of climatic variables with geographic features over Greece. Seasonal and annual climate normals of temperature, rainfall and relative humidity covering the period from 1975 to 2004, from 85 meteorological stations of the Hellenic National Meteorological Service network are included in the analysis. Several geographical and environmental parameters such as altitude, location, slope, aspect, distance to coast, sea/land ratio and vegetation index obtained from a coastline dataset, a digital elevation model and a land cover database were examined for their dependencies with climatic elements. The relationship of a climate element with each geographical variable was investigated by means of graphical (e.g. scatter plots) and statistical scores. The results were used to assess the ability of each geographical parameter to explain part of the spatial variability of a climate variable. Backward stepwise linear regression was used to obtain a surface that gives the best fit to the measured climatic data. The adjusted determination coefficient (R^2_{adj}) was computed to evaluate the efficiency of each model. Elevation, latitude and NDVI were found to be the most important predictors, whereas other geographical parameters contribute less to the model predictability.

H. Feidas (✉) • A.F. Karagiannidis • S. Keppas • P. Zanis
Department of Meteorology and Climatology, School of Geology, Aristotle University of Thessaloniki, Thessaloniki 54124, Greece
e-mail: hfeidas@geo.auth.gr

G. Marougianni • I. Kioutsioukis • D. Melas
Laboratory of Atmospheric Physics, Department of Physics, Aristotle University of Thessaloniki, Thessaloniki, Greece

M. Vaitis • T. Kontos
Department of Geography, University of the Aegean, Mytilene, Greece

E. Anadranistakis
Hellenic National Meteorological Service, Ellinikon, Greece

C.G. Helmis and P.T. Nastos (eds.), *Advances in Meteorology, Climatology and Atmospheric Physics*, Springer Atmospheric Sciences,
DOI 10.1007/978-3-642-29172-2_61,

1 Introduction

Climate regime is strictly depended on various geographic and environmental features. However, the exact mechanisms and the quantitative expression of this dependence are neither always clear nor simple. The present study aims at the investigation of the relationship between specific climatic parameters and geographic features of the Greek area. Backward stepwise linear regression analysis is utilized in order to develop numerical relationships between the seasonal and annual climatic normals of temperature, precipitation and relative humidity and a variety of geographical parameters. Analogous efforts have been made around the world (Dyras et al. 2005; Hay et al. 1998; Ninyerola et al. 2007a, b; Vicente-Serrano et al. 2003).

2 Data and Methodology

Monthly averages of temperature (T) and relative humidity (RH), and monthly totals of precipitation (P) from 85 stations of the Hellenic National Meteorological Service (HNMS) network were used in this study. The dataset comprises time-series extending from 1975 to 2004, covering a 30-year period. Figure 1 shows the spatial distribution of the stations. These monthly values are used to derive T, P and RH seasonal and annual climate normal values.

A coastline dataset, a Digital Elevation Model (DEM) and ArcGIS 9.3 software were utilized to extract a series of geophysical parameters at each station's site. Based on scatter plots and statistical scores, like Pearson's correlation coefficients, the parameters that explained a significant part of the spatial variability of each climate variable were finally selected to be used in the analysis. These parameters are presented in Table 1 along with their abbreviations and units.

Seasonal and annual NDVI values are also used as an environmental parameter (Table 1). These values were calculated based on the MODIS Aqua NDVI monthly values, publicly available by NASA. The product generally named MYD13C2, includes gridded monthly NDVI values at $0.05^\circ \times 0.05^\circ$ horizontal resolution and currently extends from July 2002 to August 2011 (Huete et al. 1999).

Backward stepwise linear regression analysis was employed to build linear relations between the climatic variables and the geographical and environmental predictors. For a detailed description of the methodology readers may refer to Draper and Smith (1998) and Miles and Shevin (2001). The aim of the analysis is to develop predicting models of the form $Y = B_1X_1 + B_2X_2 + \ldots + B_nX_n + B_0$, where Y is the independent climatic variable, X_i the independent geographical and environmental predictors, B_i are the Beta coefficients and B_o the intercept. The backward elimination method was used to select entry of predictor variables.

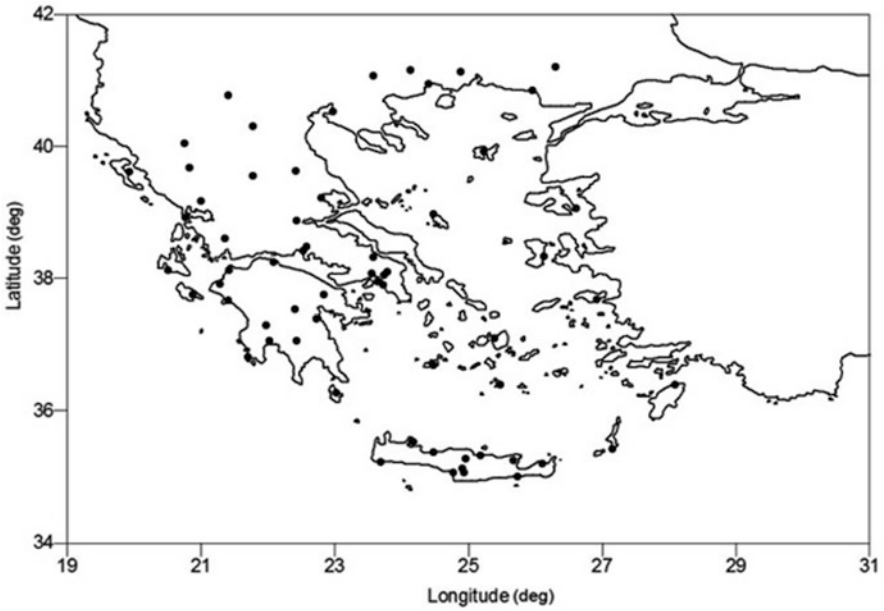

Fig. 1 Spatial distribution of meteorological stations used

Table 1 The geographical parameters used as independent predictors in the multiple regression models, along with their abbreviations and units

Geographical parameter	Abbreviation	Unit
Latitude/longitude	Lat/long	Degrees
Mean elevation over a cyclic buffer area of 5 km radius	ME	Meters
Euclidian distance to coast	Ds	Kilometers
Euclidian distance to Aegean coast	DsA	Kilometers
Euclidian distance to Ionian coast	DsI	Kilometers
North–South (East–West) component of direction to sea	DrNS (DrEW)	–
North–South (East–West) component of aspect of a cyclic buffer area of 10 km radius	AspNS (AspEW)	–
Slope of a cyclic area of 5 km radius	Sl	Degrees
Curvature of a cyclic area of 5 km radius	Cur	–
Sea to land surface ratio of a 20 km radius area	Rat	–
Maximum elevation of the northern (eastern/southern/western) sector of a cyclic area of 50 km radius	MaxEN (MaxEE/MaxES/MaxEW)	Meters
NDVI	NDVI	–

The efficiency of the model is evaluated by means of scatter plots of predicted versus observed values of each climatic variable and by statistical scores like the adjusted coefficient of determination R^2_{adj}. The R^2_{adj} values range from 0 to 1, with values close to 0 and 1 indicating very poor and perfect fitting, respectively.

3 Results

Seasonal and annual temperature, precipitation and relative humidity normals were analyzed by means of backward stepwise linear regression. The models developed, along with their R^2_{adj} are presented in Table 2.

Temperature is modeled quite successfully in all cases, with R^2_{adj} ranging from 0.82 to 0.91, except from summer when it presents significantly poorer predictability ($R^2_{adj} = 0.55$). Regarding the geographical parameters that contribute most to the temperature variability, and therefore affect significantly the temperature regime, latitude and mean elevation were found to be the more important. Longitude takes the place of latitude in the model of summer, while six more geographic parameters were included as predictors in the other models.

Summer and autumn precipitation R^2_{adj} is equal to 0.75 and 0.74 respectively, indicating significant prediction skill. However, models for the other seasons and the annual precipitation present weaker predictability, as indicated by the low R^2_{adj} values. Various geographical parameters appear as major predictors amongst the

Table 2 Multiple regression models for seasonal and annual temperature, precipitation and relative humidity and adjusted coefficient of determination (R^2_{adj}) for each model

Temperature (celsius degrees)		R^2_{adj}
Year	$T = -0.57832Lat - 0.00679ME + 0.1616Sl + 39.94439$	0.82
Winter	$T = -0.99412Lat + 0.00513ME + 0.03016Ds + 0.00695DsA + 0.14421Rat + 47.9329$	0.91
Spring	$T = -0.50584Lat - 0.00562ME + 0.00464DsA + 0.14485Sl + 0.0004MaxEE - 3.25158NDVI + 34.93659$	0.85
Summer	$T = -0.63112Lon + 0.00427ME + 0.00695DsI + 0.00074MaxEN + 11.81525$	0.55
Autumn	$T = -0.70276Lat - 0.00753ME + 0.20454Sl + 45.7376$	0.86
Precipitation (mm)		R^2_{adj}
Year	$P = 41.9007Lon + 2.74299DsA + 899.61215NDVI - 912.84749$	0.51
Winter	$P = 30.17969Lon + 0.18973ME - 1.47903Ds + 1.37177DsA + 418.77876NDVI - 729.369$	0.57
Spring	$P = 7.01492Lat + 8.79512Lon + 0.5639DsA + 0.02454MaxES - 392.69975$	0.43
Summer	$P = 9.63992Lat - 14.78388Lon + 0.19467DsI + 0.01617MaxEW - 33.76905$	0.75
Autumn	$P = -0.6426Ds + 0.94963DsA + 293.49362NDVI + 26.06933$	0.74
Relative humidity (%)		R^2_{adj}
Year	$RH = 0.62144Lat + 0.7765Rat + 1.70032Ds + 21.35591NDVI + 32.10645$	0.35
Winter	$RH = 0.60742Lat + 0.00388ME - 289.49537Cur + 2.25956AspNS + 10.28393NDVI + 45.93153$	0.40
Spring	$RH = 0.58852Lat - 0.07130Ds + 0.58957Rat + 234.57400Cur + 21.76651NDVI + 34.88233$	0.43
Summer	$RH = -3.54561Lon - 0.18624Ds + 0.04265DsI + 1.02673Rat - 0.00252MaxEN + 32.58999NDVI + 124.06562$	0.52
Autumn	$RH = 0.50715Lat + 0.76167Rat - 281.26748Cur + 23.00499NDVI + 38.38241$	0.44

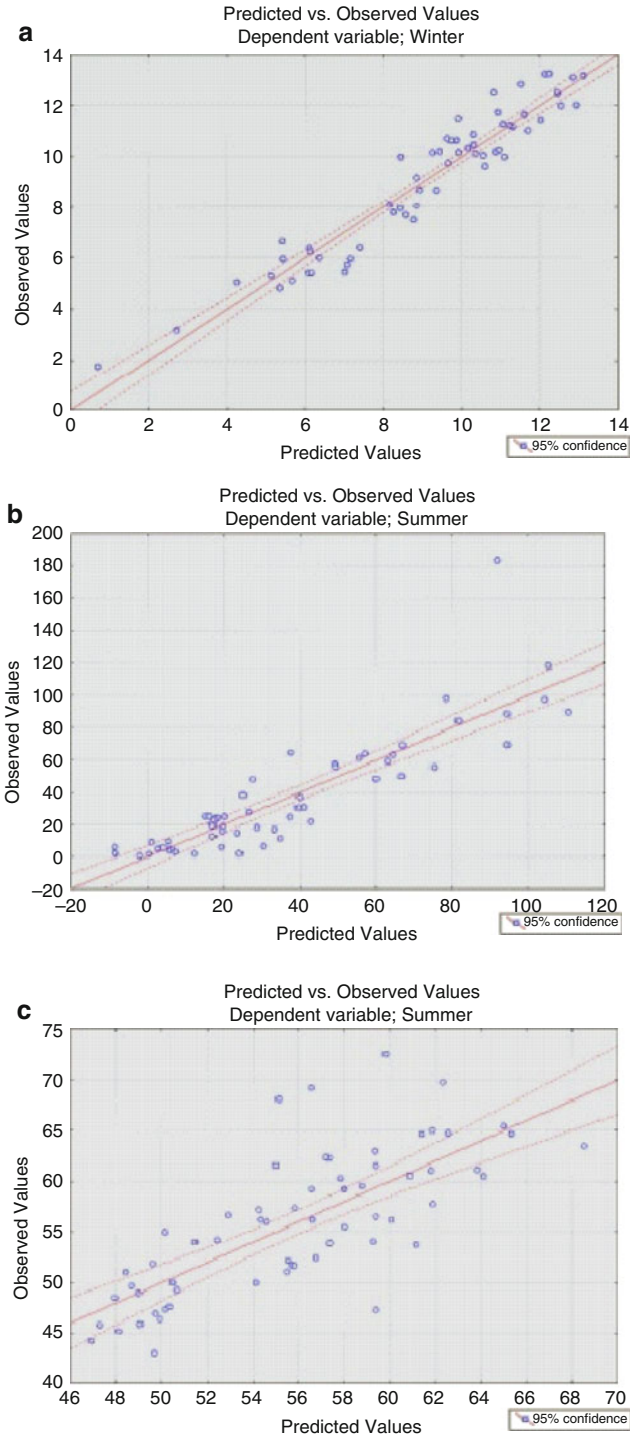

Fig. 2 Predicted versus observed scatter plots for (**a**) winter temperature, (**b**) summer precipitation and (**c**) summer relative humidity

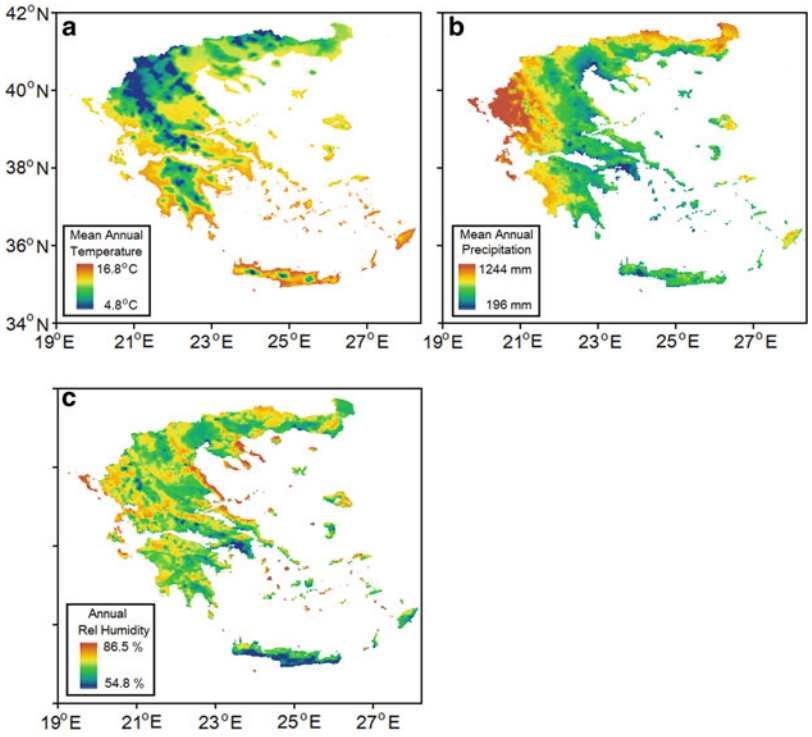

Fig. 3 Maps of annual (*upper left*) temperature, (*upper right*) precipitation and (*lower*) relative humidity using the developed regression models

five precipitation models. Longitude and distance to Aegean are involved in all models, indicating a meridional distribution of precipitation.

The regression models for relative humidity are not as efficient as for the other two climatic variables. As seen in Table 2, R^2_{adj} ranges from 0.35 for the annual normals to 0.52 for the summer ones. Latitude and NDVI seem to be the most important geographic and environmental parameters. As for temperature, latitude is replaced by longitude in summer. Eight more parameters, carrying lesser variability, are involved in the models.

Predicted versus observed scatter plots are created for each model. The efficiency of each model is assessed through the degree of dispersion of points in the plot. Figure 2 depicts the scatter plots of the most efficient model of each variable. The winter temperature model fitting is remarkably good, while the summer relative humidity plot presents significantly higher dispersion than temperature and precipitation, as indicated by their coefficients of determination.

Figure 3 depicts the map of annual temperature, precipitation and relative humidity using the developed regression models. Temperature is clearly dependent on latitude and elevation. A meridional distribution of precipitation is evident while the spatial pattern of relative humidity is more complicated. The temperature map seems to be quite realistic, while the annual precipitation model presents higher than expected

dependence on longitude. The relative humidity map is rather unrealistic and needs to be corrected by means of local interpolation methods.

4 Conclusions and Discussion

The results of the multiple regression correlation analysis of seasonal and annual temperature, precipitation and relative humidity normals can be summarized as follows:

- Temperature spatial distribution can be predicted successfully enough using specific geographic parameters, in contrast to precipitation and especially relative humidity. These two parameters may be strongly dependent on local features of spatial scales smaller than those examined, or on features not included in the present study.
- Latitude is the most important factor in the formation of the climate regime of the Greek area regarding temperature and relative humidity.
- During summer, longitude takes the place of latitude for all three climatic variables, indicating a meridional spatial distribution.
- Elevation affects significantly temperature as expected.
- The meridional distribution is dominant for precipitation in all cases.
- Relative humidity is substantially influenced by the vegetation strength of an area, as it is expressed by NDVI.
- The presence of sea in the close vicinity of an area, expressed through the sea to land ratio, increases relative humidity in all cases except winter.

Acknowledgments The research has been co-financed by the European Union (European Regional Development Fund) and Greek national funds through the Operational Program "Competitiveness and Entrepreneurship" of the National Strategic Reference Framework (NSRF) – Research Funding Program COOPERATION 2009 (no. 09COP-31-1094, Title "Development of a Geographic Climate Information System").

References

Draper NR, Smith H (1998) Applied regression analysis, Wiley series in probability and statistics. Wiley, New York

Dyras I, Dobesch H, Grueter E, Perdigao A, Tveito OE, Thornes JE, van der Well F, Bottai L (2005) The use of geographic information systems in climatology and meteorology: COST 719. Meteorol Appl 12:1–5. doi:10.1017/S1350482705001544

Hay L, Viger R, McCabe G (1998) Precipitation interpolation in mountainous regions using multiple linear regression. In: Proceedings of the hydrology, water resources and ecology in headwaters, HeadWater'98 conference, vol 248. IAHS Publication, pp 33–38

Huete A, Justice Ch, Van Leeuwen W (1999) MODIS vegetation index (MOD 13): algorithm theoretical basis document (version3). http://modis.gsfc.nasa.gov/data/atbd/atbd_mod13.pdf. Accessed on 28 April 2012

Miles J, Shevin M (2001) Applying regression and correlation: a guide for students and researchers. SAGE, London

Ninyerola M, Pons X, Roure JM (2007a) Monthly precipitation mapping of the Iberian Peninsula using spatial interpolation tools implemented in a Geographic Information System. Theor Appl Climatol 89:195–209. doi:10.1007/s00704-006-0264-2

Ninyerola M, Pons X, Roure JM (2007b) Objective air temperature mapping for the Iberian Peninsula using spatial interpolation and GIS. Int J Climatol 27:1231–1242. doi:10.1002/joc.1462

Vicente-Serrano SM, Saz-Sánchez MA, Cuardet JM (2003) Comparative analysis of interpolation methods in the middle Ebro Valley (Spain): application to annual precipitation and temperature. Clim Res 24:161–180. doi:10.3354/cr024161

The Contribution of Urban Effect to the Warming Trends of Air Temperature in Athens

D. Founda, F. Pierros, M. Petrakis, and C.S. Zerefos

Abstract Mediterranean is identified as one of the most vulnerable areas in the context of future climate projections and global warming. Greece in particular, has experienced significant warming over the past 3 decades, which is more pronounced in summer. At urban areas, air temperature trends are the result of the additive effect of global warming and urbanization. The study focuses on the city of Athens and aims to investigate and quantify the contribution of the urban effect to the recent significant warming, observed at the area. Although spatial distribution of urban heat island in Athens is extensively studied, its temporal variability hasn't been investigated. Long term observations of surface air temperature at stations of different characteristics (urban, suburban, coastal, neighbor rural etc.) are analysed in order to estimate the evolution of urban heat island (UHI) intensity over time. Temporal variability of UHI at the different stations provides information on increasing/decreasing or stabilized urban effect and enables the estimation of the rates of background warming. Analysis is performed on an annual and seasonal basis.

1 Introduction

Urban environment is almost always warmer than surrounding rural environment, mainly due to anthropogenic heat release and physical properties of the buildings and other structures (Oke 1973). This phenomenon, known as Urban Heat Island (UHI), is a well documented phenomenon in big cities and its intensity is highly

D. Founda (✉) • F. Pierros • M. Petrakis
Institute for Environmental Research and Sustainable Development, National Observatory of Athens, P. Penteli, Athens GR-15236, Greece
e-mail: founda@noa.gr

C.S. Zerefos
Research Center for Atmospheric Physics and Climatology, Academy of Athens, Athens, Greece

C.G. Helmis and P.T. Nastos (eds.), *Advances in Meteorology, Climatology and Atmospheric Physics*, Springer Atmospheric Sciences,
DOI 10.1007/978-3-642-29172-2_62,

variable depending on a number of factors such as the nature of urban environment, human activity and meteorological conditions. Urban heat islands link in a complex way with climatic change, as historical meteorological stations used for the estimation of large scale air temperature trends, are usually located in urban areas and hence urban effect is added to regional warming.

In their effort to estimate global warming, scientists worldwide have adopted several techniques to remove urban influence from temperature data; either by removing urban stations from observation network or by applying appropriate statistical adjustments. Stone (2007) however stresses that such approaches fail to accurately reflect rates of warming at the places of the greatest impacts: large cities.

Athens is a large urban area of the Eastern Mediterranean, experiencing both, urbanization effects and global warming. Although the possible impact of urbanization on Athens climate had been stressed even at the very early studies concerning temperature evolution in Athens (e.g. Karapiperis 1954), a first quantitative study was conducted by Katsoulis and Theoharatos (1985) suggesting a UHI of the order of 2–3°C in the minimum air temperature. Philandras et al. (1999) found that urban effect on air temperature of Athens is larger in summer. Santamouris et al. (2001) report a pronounced intensity of UHI in Athens that can reach up to 10°C between rural areas and the central zone of the city as regards the summer maximum temperature, while Livada et al. (2002) report a UHI intensity of 4–5°C between urban and suburban areas. The aforementioned studies concern the spatial distribution of UHI within the broader Athens area. However, in the light of future climate projections and development of adaptation and mitigation approaches, it is quite important to know the evolution of UHI over time, and how it contributes to the rates of warming in the Athens area (Founda 2011).

The present study investigates the temporal evolution of the intensity of UHI in Athens by comparing air temperature trends between urban, suburban and nearby rural stations and discusses how UHI changes link with background global warming in the area.

2 Data and Methodology

The study of the UHI can be considered in three scales: Mesoscale (corresponding to the size of a city), local scale (size of a park) and microscale (corresponding to the influence of e.g. a building). From the three scales, local and microscale can affect more the intensity of UHI (Peterson 2003). The present study considers UHI evolution on the mesoscale, by analyzing air temperature data from a sparse network of meteorological stations and nearby rural stations. It is mentioned that only a limited number of meteorological stations with long term observational data is available around the area of interest. Six routine meteorological stations of different characteristics were selected:

The historical meteorological station of the National Observatory of Athens (NOA) was selected to represent the ‘background’ urban conditions in Athens, as

the station is located on a small hill in the center of the city, but with its direct surroundings unchanged over the years. The stations of Hellinikon (HEL) (coastal urban), the Philadelfia (PHIL) (urban), Tatoi (TAT) (suburban/rural) to the northern border of the city, Tanagra (TAN) (rural) approximately 50 km to the north, and Aliartos (ALI) (rural) approximately 70 km northwest, from the network of the National Meteorological service were also selected for the analysis.

Mean monthly values of daily average, maximum and minimum air temperature at the aforementioned stations were used. The analysis was conducted for the period from 1975 and onwards. Actually mid-1970s correspond to the beginning of a period characterized by an ongoing and significant warming in the air temperature of Athens (especially pronounced in summer) according to NOA observations (Founda 2011). It is vital to know the contribution of UHI development to these warming rates. For some stations, data were available until 2004 securing a 30-year period for analysis, for some others (e.g. NOA, HEL) until 2009, while for ALI, time series is limited to 2001 due to the interruption of its operation.

Standard quality control and the homogeneity tests of Pettitt (1979) and Buishand (1982) were performed to test quality and homogeneity of the time series while the Mann-Kendall test was performed to test the statistical significance of trends.

The intensity of the urban heat island was estimated as the temperature difference between the urban stations and the rural or suburban stations.

3 Results

Poor quality was found in the time series of PHIL, so the station was excluded from the analysis. All time series passed successfully the Pettitt test, however, the critical value set by the Buishand range test was exceeded (marginally in some cases) as regards the time series of the maximum and minimum air temperature, so the analysis was mainly based on average air temperature.

As already stated, due to its location in the center of the city and also due to limited influence on the local and microscale, the station of NOA is considered to represent the background urban conditions of Athens on the mesoscale. NOA experiences pronounced warming during at least the last 30 decades. A dominant perception supported by several researchers (e.g. Philandras et al. 1999) is that the significant increase observed in the summer maximum temperature at NOA is related to the weakening and warming of the sea breeze as it travels from the coast over the urbanized environment. Figure 1 displays the variation of the summer maximum temperature from 1975 to 2009 at NOA and HEL, the coastal station open to the sea breeze. It is remarkable that both stations, even the coastal one, experience the same warming rates, amounting roughly to 1°C/decade, indicating that the warming at NOA is due to a number of additional factors, apart from the degraded impact of sea breeze.

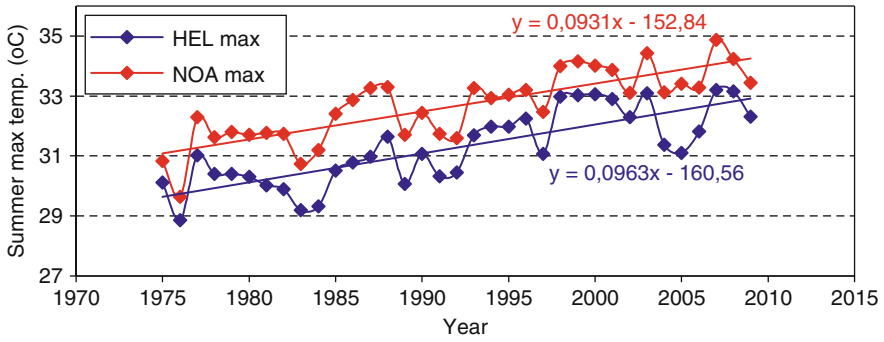

Fig. 1 Variation of the summer maximum temperature at NOA and the coastal station, HEL

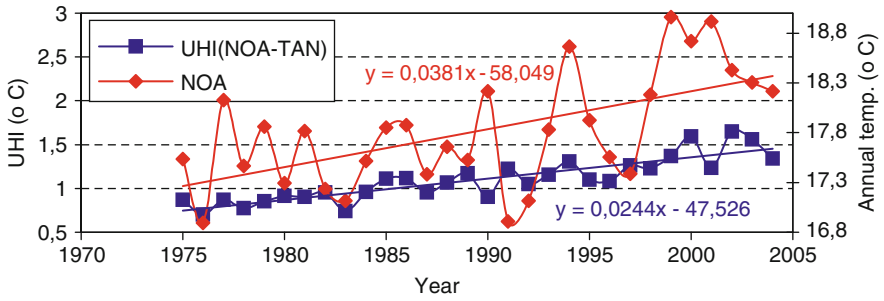

Fig. 2 Evolution of the annual mean air temperature at NOA along with the evolution of UHI intensity compared to TAN mean annual temperature

Figure 2 displays the temporal evolution of the annual air temperature at NOA along with the evolution of UHI intensity when comparison is performed with Tanagra (TAN) annual temperature. The overall linear trend here indicates a statistically significant (at 0.05 CL) increase of UHI intensity (~0.24°C/decade) that accounts for more than half of the warming rate of the annual temperature at NOA (~0.38°C/decade). Similar results were found when comparison id performed with Tatoi (TAT) suburban station.

It is interesting to see the results on a seasonal base. It was estimated (not shown) that both rural stations ALI and TAN reveal a statistically significant positive trend of the order of +0.5°C/decade in the average summer temperature, suggesting evidence of climatic change in the area, introduced by others than urban factor. As regards the progress of summer UHI, Fig. 3a–c displays the evolution of UHI intensity in summer, expressed as the difference between the average summer temperature at the two urban stations of NOA and HEL and the stations of TAT, TAN and ALI.

According to Fig. 3a–c, no development of UHI is discerned during the first years of our analysis, on the contrary, an attenuation of UHI intensity until mid-1980s is observed, when comparisons are based on TAT station. UHI intensity

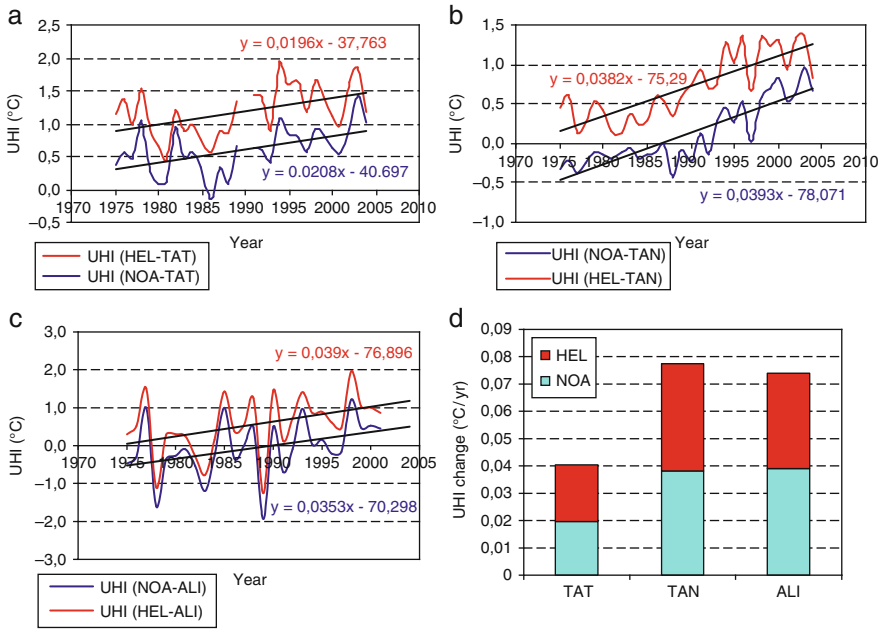

Fig. 3 (**a**–**d**) Temporal evolution of summer UHI expressed as the difference of air temperature at the urban stations NOA and HEL and (**a**) TAT, (**b**) TAN and (**c**) ALI. Rates of UHI changes (**d**)

increases progressively afterwards, while the overall linear trend amounts to ~+0.2/+0.4°C per decade concerning the suburban/rural stations respectively (Fig. 3d). Given that the warming rates in summer at the two urban stations of NOA and HEL are of the order of 1°C/decade it can be said that urban effect roughly accounts for 40% of the observed warming rates of summer air temperature in Athens.

The same analysis when applied to winter (not shown), suggested that UHI increases over the years, too, but at lower rates. A positive trend of the order of +0.1°C/decade was found in the UHI concerning the suburban station of TAT and +0.2°C/decade as regards the comparisons with the rural stations of TAN and ALI.

4 Conclusions

In an effort to highlight the degree of urban influence on the warming rates of the air temperature in Athens we investigated the evolution of the intensity of UHI on the mesoscale over the period from 1975 and onwards, by examining monthly air temperature data at stations of different characteristics.

It is rather certain that all meteorological stations, even rural ones, have undergone a kind of artificial influence due to land use/land cover changes or

other reasons. Moreover, different local conditions and distances from the sea introduce quite local climates making the interpretation of the results hard.

The analysis indicated similar warming rates at a coastal (HEL) and inland (NOA) station in Athens. On an annual base, the intensity of UHI was found to have increased by approximately +0.2°C/decade when comparing urban with rural or suburban stations. On a seasonal basis, the rate of UHI changes is more pronounced in summer than in winter, amounting to approximately +0.4/+0.2°C/decade when compared to rural/suburban stations respectively and accounting for almost 40% of the observed warming rates of summer temperature in Athens.

Acknowledgments The authors are grateful to the Hellenic National Meteorological Service for providing climatic data from its network.

References

Buishand TA (1982) Some methods for testing the homogeneity of rainfall records. J Hydrol 58:11–27. doi:10.106/0022-1694(82)90066-X

Founda D (2011) Evolution of the air temperature in Athens and evidence of climatic change: a review. Adv Build Energy Res 5:7–41. doi:10.1080/175/2549-2011-582332

Karapiperis PP (1954) Trends in Athens temperature. Pure Appl Geophys 29:212–217. doi:10.1007/BF01988615

Katsoulis BD, Theoharatos GA (1985) Indications of the urban heat island in Athens, Greece. J Clim Appl Meteorol 24:1296–1302

Livada I, Santamouris M, Niachou K, Papanikolaou N, Mihalakakou G (2002) Determination of places in the great Athens area where the heat island effect is observed. Theor Appl Climatol 71:219–230. doi:10.1007/s007040200006

Oke TR (1973) City size and the urban heat island. Atmos Environ 7:769–779

Peterson TC (2003) Assessment of urban versus rural in situ surface temperatures in the contiguous United States: no difference found. J Clim 16:2941–2959

Pettitt AN (1979) A non-parametric approach to the change-point detection. Appl Stat 28:126–135. doi:10.2307/2346729

Philandras CM, Metaxas D, Nastos P (1999) Climate variability and urbanization in Athens. Theor Appl Climatol 63:65–72. doi:10.1007/s007040050092

Santamouris M, Papanikolaou N, Livada I, Koronakis I, Georgakis C, Argiriou A, Assimakopoulos DN (2001) On the impact of urban climate to the energy consumption of buildings. Sol Energy 70:201–216

Stone BJ (2007) Urban and rural temperature trends in proximity to large US cities: 1951–2000. Int J Climatol 27:1801–1807. doi:10.1002/joc.1555

Modeling of Changes in Human Thermal Bioclimate Resulting from Changes in Urban Design: Example Based on a Popular Place in Freiburg, Southwest Germany

D. Fröhlich and A. Matzarakis

Abstract The place of the old Synagogue, a popular place in the central area in Freiburg, southwest Germany, is going to be redesigned soon. According to the plans of the city administration, most of the big trees will be removed, some new trees will be planted and the ground coverage will be changed. All of those changes may influence thermal human bioclimate. To analyze changes due to the redesign, a set of three micro scale models has been utilized. The SkyHelios Model was used as a quick overview of the changes in sky view factor (SVF), whereas RayMan was applied to show the changes in the frequency of thermal stress. Finally spatial distribution of heat stress on the place of interest was calculated with ENVI met. Results show that the area with high SVF slightly increases. The frequency of thermal stress, especially heat stress, also increases. The spatial distribution of heat stress shows the highest increases in heat stress due to the changes in ground coverage and shading.

1 Introduction

Urban street design has a strong influence on human thermal bioclimate. Especially shading and ground coverage show great impact (Lin et al. 2010a, b). Thus, if the design of a popular urban place is changed, human thermal bioclimate on the place may be seriously affected. Facing the impact of global climate change especially heat stress should be reduced (Matzarakis and Endler 2010). According to the "ideal urban climate" a thermal bioclimate with "lot of spatial variation, but avoiding extrema" (Mayer 1989) is to be preferred.

Area of investigation: For this study, the place of the old synagogue in Freiburg was selected as an area of interest. This decision is based on several reasons.

D. Fröhlich • A. Matzarakis (✉)
Meteorological Institute, Albert-Ludwigs University, Freiburg, Germany
e-mail: andreas.matzarakis@meteo.uni-freiburg.de

C.G. Helmis and P.T. Nastos (eds.), *Advances in Meteorology, Climatology and Atmospheric Physics*, Springer Atmospheric Sciences,
DOI 10.1007/978-3-642-29172-2_63,

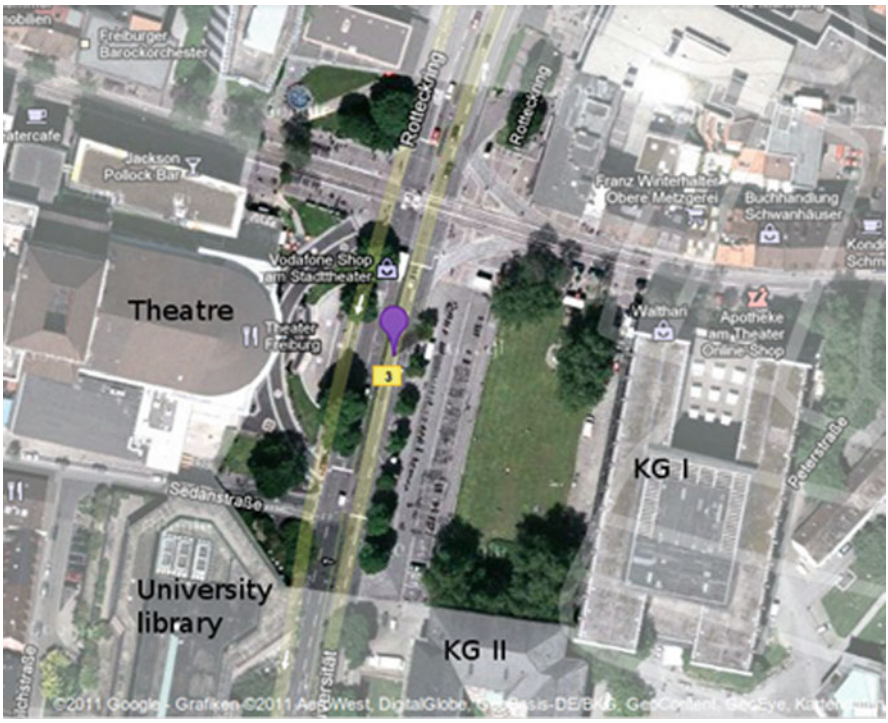

Fig. 1 The current place of the old synagogue (Modified after Google Maps)

Freiburg, a medium sized city in southwest Germany, is calling itself a "green city" and has already taken some effort in human bioclimate in the past (Matzarakis and Mayer 2008). Furthermore it is the warmest city in Germany (Nübler 1979; Rudloff 1993) and studies on climate change predict an increase of heat stress for Freiburg (Matzarakis and Endler 2010). The place of the old synagogue is a popular place in the western part of the inner city. Due to the university and the theater around it, there are lots of people on the place (Fig. 1). This place is now going to be redesigned by the city administration (Fig. 2). As the redesign is a matter of a very controversial public debate, it is a very interesting subject for the present study.

2 Data and Methodology

The changes in thermal bioclimate due to the redesign have been calculated using numerical models. For this study, the three models SkyHelios (Matzarakis and Matuschek 2011), RayMan (Matzarakis et al. 2007; Matzarakis and Rutz 2010) and ENVI-met (Bruse 1999) have been applied. Each model has been used to calculate

Fig. 2 The blueprint of the place of the old synagogue after the redesign (Modified after city administration of Freiburg)

two situations, one for the current place and one for the planned one. Afterwards the results have been compared to show and quantify the changes.

2.1 Data

To allow numerical calculations there are some input data required. For this study an aerial photograph of the current place, the blueprint of the redesigned place (Fig. 2), an elevation raster covering the area of interest, as well as ESRI® shapefiles

Table 1 Thermal stress classes for humans with an internal heat production of 80 W and a heat transfer resistance of the clothing of 0.9 clo (Modified after Matzarakis and Mayer (1996))

PET	Thermal perception	Grade of physical stress	Combined class
<4	Very cold	Extreme cold stress	Cold
4–8	Cold	Strong cold stress	Cold
8–13	Cool	Moderate cold stress	Cold
13–18	Slightly cool	Slight cold stress	Comfortable
18–23	Comfortable	No thermal stress	Comfortable
23–29	Slightly warm	Slight heat stress	Comfortable
29–35	Warm	Moderate heat stress	Hot
35–41	Hot	Strong heat stress	Hot
>41	Very hot	Extreme heat stress	Hot

of the surrounding buildings have been used. Also two ENVI-met surface models for the current and the redesigned place were used from a former project (Röckle et al. 2010). The 10 year period dataset of the urban climate station of the Albert-Ludwigs University Freiburg (Matzarakis and Mayer 2008) was used to provide the required meteorological input.

2.2 Methodology

For a first overview over the changes, the SVF was calculated by the SkyHelios model. As it is very time consuming to create RayMan obstacle files manually in the RayMan Editor, SkyHelios was also used to calculate fisheye images, that can be used in RayMan instead of obstacle files (RayMan buildings and vegetation files).

Although calculating SVF is good for a first overview, there are many more parameters influencing thermal bioclimate (Mayer and Höppe 1987). Thus conclusions are drawn from changes in physiologically equivalent temperature (PET) (Höppe 1999; Matzarakis et al. 1999). First PET was calculated for a 10 year period at seven Points on the current and the redesigned place using RayMan. Results from those calculations have been classified into nine classes of thermal perception, using the assessment table from Matzarakis and Mayer (1996). To even more facilitate the results, the three classes of cold stress, the three classes for comfortable conditions, as well as the three classes of heat stress have been merged into a cold, a comfortable, and a hot thermal stress class (Table 1).

To analyze the spatial distribution of thermal stress over the place calculations with ENVI-met for a hot and dry 7 day period in 2003 have been performed for the current and the redesigned place. This period was selected because thermal stress is mainly a problem during the summer months as people are more adapted to cold conditions in winter. Therefore an additional module called “CalcPET” was used, as the ENVI-met version 3.1BETA4 can’t calculate PET itself. As ENVI-met is a prognostic model, it was not possible to use a 7 day record from the urban climate station, but only initial conditions.

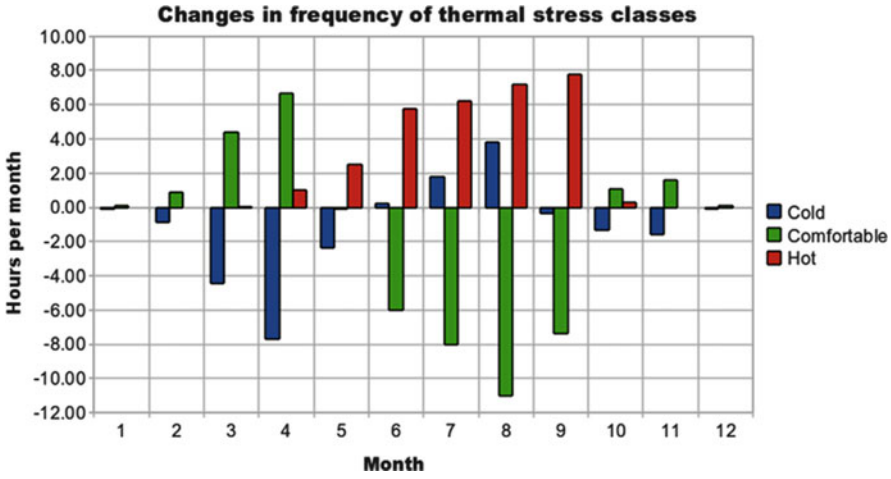

Fig. 3 Changes in the frequency of thermal stress classes at all points due to the redesign of the place of the old synagogue

3 Results

Results of the calculations are summarized as following:

- Changes in distribution of SVF calculated with SkyHelios,
- Changes in long term frequency of thermal stress calculated by RayMan,
- Changes in distribution of heat stress calculated by ENVI-met.

Changes in SVF calculated with SkyHelios: Comparing the SVF on the current and the redesigned place calculated by SkyHelios, it can be seen, that the central area of the place with high SVF, the area with high energy balance, that is likely to suffer thermal stress, is only little larger after the redesign.

Changes in long term frequency of thermal stress calculated by RayMan: The calculations with RayMan show a strong decrease of cold stress in spring and fall, with a maximum of nearly 8 h/month in April (Fig. 3). In summer, an increase in colder conditions with a maximum of nearly 4 h/month in August is calculated (Fig. 3). During the winter months cold stress is little decreased by less than 1 h/month. Looking at the class of thermal comfort (Fig. 3) there is a certain increase in spring and fall. During the summer months, the frequency of thermally comfortable conditions is calculated to be severely decreased by up to 12 h/month in August. There can be nearly no strong changes seen for the winter months. A much more interesting development is shown by the classes of heat stress (Fig. 3), as it only shows an increase. Especially in the summer months the frequency of heat stress is calculated to be severely increased by up to 8 h/month in September.

Changes in distribution of heat stress calculated by ENVI-met: Comparing the ENVI-met results for the current and the redesigned place on the third day, a difference of over 10°C (PET) between places with and without shading can be

seen. Because of the trees in the central area of the place that will be removed during the redesign, the area with very high PET of around 51°C will become larger. The new water basins on the redesigned place show slightly reduced PET compared to the lawn on the current place, but only inside the basins. A severe increase in PET of about 6°C is shown in the area in front of the KG II that is currently covered with grass and will be covered with stone plates after the redesign.

4 Conclusions

Even though the SVF does not increase significantly, results show that thermal bioclimate is strongly influenced by the redesign. According to the "ideal urban climate" (Mayer 1989) the reduction in the frequency of cold stress and the increase in the frequency of thermally comfortable conditions in spring and fall is to be seen as an advantage. The strong decrease in frequency of thermally comfortable conditions and the severe increase in frequency of heat stress in summer is, in contrast, a big disadvantage. Both developments are caused by the larger area without shading on the redesigned place, as well as by the change in ground coverage. This also can be seen in the results of the spatial analysis.

Acknowledgments The authors want to thank "iMA Richter & Röckle GmbH & Co. KG" for providing the surface models, the calculations with ENVI-met are based on.

References

Bruse M (1999) Die Auswirkungen kleinskaliger Umweltgestaltung auf das Mikroklima. Entwicklung des prognostischen numerischen Modells ENVI-met zur Simulation der Wind-, Temperature-, und Feuchtverteilung in städtischen Strukturen. Dissertation, University of Bochum, Germany

Höppe PR (1999) The physiological equivalent temperature – a universal index for the bioclimatological assessment of the thermal environment. Int J Biometeorol 43:71–75

Lin TP, Matzarakis A, Hwand RL (2010a) Shading effect on long-term outdoor thermal comfort. Build Environ 45:213–221. doi:10.1016/j.buildenv.2009.06.002

Lin TP, Matzarakis A, Hwang RL, Huang YC (2010b) Effect of pavements albedo on long-term outdoor thermal comfort. In: Matzarakis A, Mayer H, Chmielewski FM (eds) Proceedings of the 7th conference on biometeorology, Freiburg, Germany, 12–14 April 2010. Berichte des Meteorologischen Institutes der Universität Freiburg, vol 20. Meteorological Institute, Albert-Ludwigs-University of Freiburg, pp 498–504

Matzarakis A, Endler C (2010) Climate change and thermal bioclimate in cities: impacts and options for adaptation in Freiburg, Germany. Int J Biometeorol 54:479–483. doi:10.1007/s00484-009-0296-2

Matzarakis A, Matuschek O (2011) Sky view factor as a parameter in applied climatology – rapid estimation by the SkyHelios model. Meteorol Z 20:39–45

Matzarakis A, Mayer H (1996) Another kind of environmental stress: thermal stress. WHO Newsl 18:7–10

Matzarakis A, Mayer H (2008) Importance of urban meteorological stations – the example of Freiburg, Germany. Ber Meteorol Inst Univ Freiburg 17:119–128

Matzarakis A, Mayer H, Izimon M (1999) Application of a universal thermal index: physiological equivalent temperature. Int J Biometeor 43:76–84. doi:10.1007/s004840050119

Matzarakis A, Rutz F (2010) Application of the RayMan model in urban environments. In: Ninth symposium on the urban environment of the American Meteorological Society, 1–6 Aug 2010, Keystone, CO

Matzarakis A, Rutz F, Mayer H (2007) Modelling radiation fluxes in simple and complex environments – application of the RayMan model. Int J Biometeorol 51:323–334

Mayer H (1989) Workshop "Ideales Stadtklima" am 26. Oktober 1988 in München. DMG Mitteilungen 3:52–54, in German (http://www.geographie.uni-freiburg.de/publikationen/fgh-index)

Mayer H, Höppe P (1987) Thermal comfort of man in different urban environments. Theor Appl Climatol 38:43–49. doi:10.1007/BF00866252

Nübler W (1979) Konfiguration und Genese der Wärmeinsel der Stadt Freiburg, Freiburger. Geographische Hefte, 16 (in German)

Röckle R, Hermsdörfer K, Richter CJ (2010) Mikroklimatische Untersuchung Platz der Alten Synagoge im Zuge der Stadtbahnplanung mit Umgestaltung Kronenstrasse, Werthmannstrasse, Rotteckring und Friedrichring. iMA Richter & Röckle GmbH & Co. KG, 09-12-05-FR II (in German)

Rudloff H (1993) Beiträge zum Klima Freiburgs. Lingg Druck (in German), Freiburg

Evaluation of Potential Evapotranspiration in Central Macedonia by EmPEst

S. Gebhart, K. Radoglou, G. Chalivopoulos, and A. Matzarakis

Abstract The differentiation and the determination of reference potential evapotranspiration (PET_{ref}) is important for many geo scientifically relevant questions. The ASCE (American Society of Civil Engineers)-Penman-Monteith approach provides a facility for the estimation of PET_{ref} using meteorological input parameters. However, the equation needs a lot of different input parameters. Hence this work compares 13 different alternative equations using fewer input parameters of four meteorological stations in Central Macedonia. The stations Loutra, and Skotina are located in the South of central Macedonia, while the stations Gumenissa and Grisopigi are situated in the north. Six statistical goodness of fit measures, including mean absolute error (MAE), mean square error (MSE), relative mean absolute error (MRAE), relative mean square error (MRSE), mean bias error (MBE) and the root square mean error (RMSE), where used. Additionally a Welch *t*-test was applied to test significance of the results. Results were analyzed for monthly timescale. The calculation of the 13 different approaches of evapotranspiration has been performed by the EmPEST software.

1 Introduction

By virtue of perennially stronger to the force coming changes of the climatic conditions within the Mediterranean climate zones and therewith attended impacts on flora and fauna and due to this of the humans as part of the global ecosystem, questions about transpiration and evaporation are of eminent importance for the

S. Gebhart • A. Matzarakis (✉)
Meteorological Institute, Albert-Ludwigs-University Freiburg, Werthmannstr. 10, Freiburg D-79085, Germany
e-mail: andreas.matzarakis@meteo.uni-freiburg.de

K. Radoglou • G. Chalivopoulos
Forest Research Institute, NAGREF, Vassilika, Thessaloniki 57006, Greece

C.G. Helmis and P.T. Nastos (eds.), *Advances in Meteorology, Climatology and Atmospheric Physics*, Springer Atmospheric Sciences,
DOI 10.1007/978-3-642-29172-2_64,

understanding of coherences of interactions of earth's surface and the atmosphere. Especially for agricultural issues, which also include forestry as well as hydrological issues, there is a larger growing demand for information on quantified data of transpiration and evaporation.

Related to the modelling of the impacts of a changing climate as a basis of the before mentioned, attainment about evapotranspiration is of arbitrative interest for an adequate appraisement of changes within ecosystems over the time and herefrom deducible risks. In areas where irrigation is a major component of agriculture due to slightly precipitation, it is also of economic importance to ascertain ET as accurate as possible; in fact that ET is in these regions the most significant component of the hydrological budget together with precipitation (Alexandris et al. 2008).

Due to the high complexity, which is necessary to measure humidification it has to be harked back to mathematical functions for the determination of ET. These functions are often the only possibility to accomplish detailed analysis and modelling. The most accurate model for any climate condition is considered to be the ASCE-Penman-Monteith equation (Fontenot 2004). But due to the high number of input parameters it is in many cases impossible or very difficult to use this equation.

This work is focused on the estimation and analysis of 13 different PET_{ref} equations for four meteorological stations in the region of central Macedonia, Greece, compared with the ASCE-Penman-Monteith model. Meteorological input data for the used equations were prepared under use of MS Excel respectively Libre Office Calc. For the calculation of the equation the program EmPEst was used (Kostinakis et al. 2011). Statistical analysis is made by EmPEst for PET_{ref} equations output. Moreover R was used for additional statistical analysis.

2 Data and Methodology

2.1 Data

This elaboration was made for four meteorological stations owned by the Forest Research Institute (FRI), Thessaloniki. All stations, excluding Loutra which is situated next to the building of the Forest Research Institute near Vasilika and Thessaloniki, are located in forested areas. Therefore it is to reckon with a stronger influenced by the sea for the station in Loutra. The station Grisopigi is located in the north-east of Central Macedonia in the prefection of Serres, within the foothill of the Rhodopes. The station is to find on an east-oriented side of this mountainous area. Station Gumenissa, is situated in the north of Central Macedonia between Gumenissa and Livadia in the Prefecture of Kilikis. The station is located within the Paiko mountain range with north-east orientation. The station in Skotina is with 1,040 m located at the highest duties. It is situated in the south-west of Central

Table 1 Geographical coordinates and climate of the meteorological stations

Name	Elevation (m)	Latitude	Longitude	Climate
Loutra	30	40° 30′	23° 04′	Semi-arid
Grisopigi	605	41° 10′	23° 34′	Sub-humid
Gumenissa	1,140	40° 58′	22° 20′	Humid
Skotina	600	40° 12′	22° 14′	Humid

Macedonia on a north-west orientated slope in the south-west of Skotina. Detailed geographic coordinates for all stations can be found in Table 1.

All stations collect calculation relevant input parameters, which are

- Air temperature
- Relative humidity
- Wind speed
- Solar radiation

The available meteorological input data had a time series resolution of 1 h. For station Loutra and station Grisopigi data series for a time range of 8 years (2002–2010) where extracted, for station Gumenissa and station Skotina time series of 5 years (2005–2010) where exploited. Commitment for the length of the time series has been made due to the available data records and their condition. Not measured or missing input data were calculated with Excel as mentioned in Allen et al. (1998) and include:

- Net radiation (R_n)
- Extraterrestrial radiation (R_a)
- Day length (DL)
- Dew point temperature (T_{dew})

As default value for the albedo 0.23, the average value for grassland, was used (Allen et al. 1998). PET_{ref} equations, wind speed correction to a height of 2 m above ground level, and all necessary goodness of fit calculations according to this issue were determined by the software EmPEst for PET_{ref} calculation (Kostinakis et al. 2011; Xystrakis and Matzarakis 2011). Additional statistics (Welch *t*-test, RMSE) where determined under use of R. Inhomogenities in the data where corrected as mentioned in Allen et al. (1998).

2.2 Methodology

Thirteen reference potential evapotranspiration models including the approaches of Hargreaves, McGuiness, Jensen, Hansen, Caprio, Romanenko, Tuc, Makkink, de Bruin, McCloud and three versions of Hamons approach, where calculated under use of EmPEsT (Kostinakis et al. 2011; Xystrakis and Kostinakis 2010). For statistical evaluation of the model performance mean absolute error (MAE), mean relative square error (MRSE), mean relative absolute error (MRAE), mean bias

error (MBE) and root mean square error (RMSE) where used. It was renounced to use regression models for the PET_{ref} model comparison in addition to the other used methods, like it can be found in many similar studies. As Willmott (1982) remarked, these methods are often inappropriate or misleading for model comparison (Alexandris et al. 2008; Willmott 1982). Also it is evident that all the used methods of the uncertainty analysis cannot make any statement about the significance of model performance. To take account of this fact a Welch *t*-test was used to determine further information on model performance and to compensate the reasonable omission of the correlation coefficient.

3 Results

Exemplary the results for integrated monthly values of the station in Gumenissa (Table 2) will be discussed. Temperature based models show relatively diffuse results. $PET_{Hargreaves}$ performed best for MSE, while $PET_{McGuiness}$ gave the best results for MRSE and $PET_{Romananko}$ for MRAE. For all other statistical tests PET_{Hamon1} performed best. An additionally made Spearman correlation showed highest correlations of this model to the mean, minimum and maximum air temperature. A graphical analysis of the MBE showed a constant underestimation of McClouds model and Hamons equation version 3. $PET_{Romanenko}$ overestimated PET_{ASCE} constantly with exception of May. All other temperature based equations underestimated PET_{ref} mainly during the colder month and tended to overestimate during growing season. PET_{Hamon1} which has to be seen as the best temperature

Table 2 Results of all goodness of fit measures including Welch *t*-test results for integrated monthly values of PET_{ref} for Gumenissa

Stat. method	Har	McG	Rom	Ham1	Ham2	Ham3	McC
Air temperature based							
MSE	834.200	871.900	1649.700	472.700	610.200	1019.000	2280.500
MAE	24.456	24.578	138.778	17.842	19.486	27.317	42.267
MRSE	0.088	0.041	0.044	0.058	0.042	0.189	1.251
MRAE	0.259	0.174	0.159	0.184	0.163	0.350	0.821
MBE	−21.183	22.722	19.203	−5.142	9.397	−25.789	−37.872
RMSE	28.882	29.527	40.616	21.742	24.702	31.921	47.755
t-value	−2.579	2.332	1.691	−0.553	0.900	−2.934	−3.786
Radiation based							
	Cap	Jen	Han	Mak	Turc	deB	
MSE	1580.500	2102.200	364.500	31.000	139.400	748.300	
MAE	32.117	38.453	18.103	4.344	10.650	25.611	
MRSE	0.047	0.055	0.020	0.004	0.009	0.032	
MRAE	0.195	0.219	0.134	0.042	0.084	0.175	
MBE	29.394	37.464	18.103	−3.139	9.578	25.611	
RMSE	39.755	45.850	19.091	5.571	11.807	27.356	
t-value	2.357	2.993	1.851	−0.346	0.984	2.471	

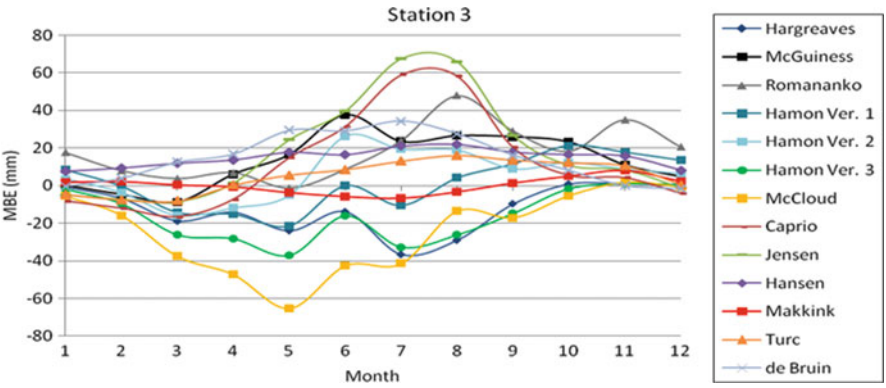

Fig. 1 MBE for integrated monthly values of PET_{ref} for Gumenissa (station 3)

based alternative to PET_{ASCE} underestimated for the first half of a year and overestimated during the second half in nearly the same range what leads to the good performance of this model also in comparison with the radiation based equations. Results for the radiation-based models show that $PET_{Makkink}$ performed outstandingly best for all statistical tests. With a MBE of -3.139 mm month^{-1}, a MAE of 4.344 mm month^{-1} and a MSE of 31.000 mm month^{-1} this equation gave by far the best results and is therefore without any alternative, also with view on the less amount on input parameters. The outstanding good performance of $PET_{Makkink}$ has also to be related to the elevation of this station and the associated climate conditions. However Makkink's model underestimated constantly what has to be fixed by an adjustment (Fig. 1).

4 Conclusions

Actually the study found different best performing models for different regions of central Macedonia as it was expected due to the results of other studies as for example Lu et al. (2005), or specific on Crete in Greece, Xystrakis and Matzarakis (2011). Hence, a north south gradient in model performance could be determined which is mainly a result of the solar radiation as the evaluation shows.

For nearly all statistical evaluations the radiation based equations performed better than the air temperature based once. This might also be due to the large influence of solar radiation. The only noticeable air temperature based equations are therefore PET_{Hamon3} for the south situated areas and $PET_{McGuiness}$ respectively $PET_{Hargreaves}$ for the north situated areas. Due to the low need on input parameters Hargreaves' equation can be seen as a good alternative.

On side of the radiation based approaches $PET_{Makkink}$ for the northern located stations in the north and PET_{Turc} respectively PET_{Hansen} for the stations in the south of central Macedonia gave the clearly best results. Nevertheless, none of the used

equations gave overall best results. The good estimated of PET_{Turc} is comparable to the latest study on PET_{ref} for Crete by Xystrakis and Matzarakis (2011).

An additionally performed correlation analysis of the PET_{ref} results and the used input parameters showed a relatively high correlation of the equations with solar radiation, what points out the big influence of solar radiation for evapotranspiration within the region of central Macedonia. Therefore it is to aspire to fall back on one of the mentioned radiation based approaches as an alternative for PET_{ASCE}. For further estimations it should be thought about an adjustment of the proposed models to get even better results.

Summed up PET_{Turc} and $PET_{Makkink}$ are the suggested alternatives to the ASCE-Penman-Monteith equation for central Macedonia, Makkink's equation for the northern regions, Turc's equation for the southern regions.

References

Alexandris S, Stricevic R, Petcovic S (2008) Comparative analysis of reference evapotranspiration from the surface of rainfed grass in central Serbia, calculated by six empirical methods against the Penman-Monteith formula. Eur Water 21(22):17–28

Allen R, Pereira L, Raes D, Smith M (1998) Crop evapotranspiration – guidelines for computing crop water requirements. FAO irrigation and drainage paper 5. FAO, Rome

Fontenot R (2004) An evaluation of reference evapotranspiration models in Louisiana. Master thesis, Luisiana State University and A&M College, Louisiana

Kostinakis K, Xystrakis F, Theodoropoulos K, Stathis D, Eleftheriadou E, Matzarakis A (2011) Estimation of reference potential evapotranspiration with focus on vegetation science – the EmPEst software. J Irrig Drain E-ASCE 137:616–619

Lu J, Sun G, McNulty SG, Amatya DM (2005) A comparison of six potential evapotranspiration methods for regional use in the southeastern United States. J Am Water Resour Assoc 41:621–633. doi:10.1111/j.1752-1688.2005.tb03759.x

Willmott C (1982) Some comment on the evaluation of model performance. Bull Am Meteorol Soc 63:1309–1313. doi:10.1175/1520-0477(1982) 063<1309:SCOTEO>2.0.CO;2

Xystrakis F, Kostinakis K (2010) EmPEst – empirical reference potential evaporation estimation: user's guide. Available at http://empest.wordpress.com/

Xystrakis F, Matzarakis A (2011) Evaluation of 13 empirical reference potential evapotranspiration equations on the island of Crete in southern Greece. J Irrig Drain E-ASCE 137:211–222

Impacts of Climate Change Over the Eastern Mediterranean and Middle East Region Using the Hadley Centre PRECIS RCM

C. Giannakopoulos, E. Kostopoulou, P. Hadjinicolaou, M. Hatzaki, A. Karali, J. Lelieveld, and M.A. Lange

Abstract The Eastern Mediterranean and Middle East (EMME) region is a vulnerable region regarding global warming and therefore likely to be greatly affected by climate change and its associated impacts. This study uses daily climate projections based on the Hadley Centre PRECIS regional climate model (RCM) to assess climate change impacts in the Eastern Mediterranean and Middle East. The PRECIS RCM uses boundary and initial conditions from the HadCM3Q0 global climate model, employing the IPCC SRES A1B emission scenario. The control run represents the base period 1961–1990 and is used here as reference for comparison with future projections. We study the future period 2040–2069 specifically chosen for the needs of policy makers, so as to assist their planning in the mid-term future. Using daily PRECIS output, we examine climatic changes with the aim to identify regions in the study area that are likely to undergo significant changes in impact sectors, such as thermal comfort, energy demand, and agriculture. More specifically, vulnerable regions per sector of interest are identified, using appropriately constructed indices and impact models.

1 Introduction

The Eastern Mediterranean and Middle East (EMME) is a vulnerable region regarding global warming and therefore likely to be greatly affected by climate change and associated impacts in several activity sectors such as energy demand,

C. Giannakopoulos (✉) • M. Hatzaki • A. Karali
Institute for Environmental Research and Sustainable Development, National Observatory of Athens, Athens, Greece
e-mail: cgiannak@meteo.noa.gr

E. Kostopoulou
Department of Geography, University of the Aegean, Mytilene 81100, Greece

P. Hadjinicolaou • J. Lelieveld • M.A. Lange
Energy, Environment and Water Research Center, The Cyprus Institute, Nicosia, Cyprus

C.G. Helmis and P.T. Nastos (eds.), *Advances in Meteorology, Climatology and Atmospheric Physics*, Springer Atmospheric Sciences,
DOI 10.1007/978-3-642-29172-2_65,

agriculture and thermal comfort. Since the region is diverse and extreme climate conditions already common, the impacts will be disproportional. In summer, furthermore, the EMME is hot, and climate change may intensify heat waves with consequences for human health, energy use and economic activity, including the tourist sector, which have yet received little attention.

In this work, we present projections of climate change impacts for 2040–2069 based on the intermediate A1B scenario of the Special Report on Emissions Scenarios (SRES) of the Intergovernmental Panel on Climate Change (Nakićenović and Swart 2000). Our projections are based on the output of the PRECIS regional climate model (RCM), based on the United Kingdom (UK) Meteorological Office Hadley Centre HadRM3P model (Jones et al. 2004). RCMs serve as a dynamical downscaling tool to refine the global climate simulations onto a finer mesh that more realistically describe the surface topography. The model simulations were performed at the Cyprus Institute within the framework of the CIMME project (www.cyi.ac.cy/climatechangemetastudy), which studies 'Climate Change and Impacts in the Eastern Mediterranean and Middle East'. The model has a horizontal resolution of 25 km. The area of interest extends from 22° to 46°N and from 10° to 62°E, covering a large portion of the EMME region.

Two time periods are employed. The control run represents the base period 1961–1990 and is used here as reference for comparison with future projections. The future period studied is 2040–2069, specifically chosen for the needs of policy makers to assist their planning in the mid-term future. Using daily output from the PRECIS RCM, we examine changes in impact sectors closely linked to and affected by climate change. The aim is to identify regions in the study area that are likely to undergo significant changes in impact sectors, such as energy requirements, agriculture and thermal comfort. More specifically, vulnerable regions per sector of interest are identified, using different indices for the evaluation of climate change impacts in agriculture, thermal comfort or energy. Results from these runs yield vulnerability maps in each sector for each region.

2 Impacts

Agriculture. Climate change can affect agriculture directly through the meteorological conditions that influence crop growth and yield. We used the PRECIS output to calculate the growing season length, defined as the number of days between the last spring frost and the first autumn frost. In the control period, the length of the growing season starts from around 200 days in the greatest parts of Greece and Turkey and extends to 300 days or even the whole year for the Arabian Peninsula and North Africa. The model results indicate that by mid-century (2040–2069) the length of the growing season may increase by about 1 month/year in Turkey, the Balkans and part of Iran (Fig. 1). Some crops, such as winter

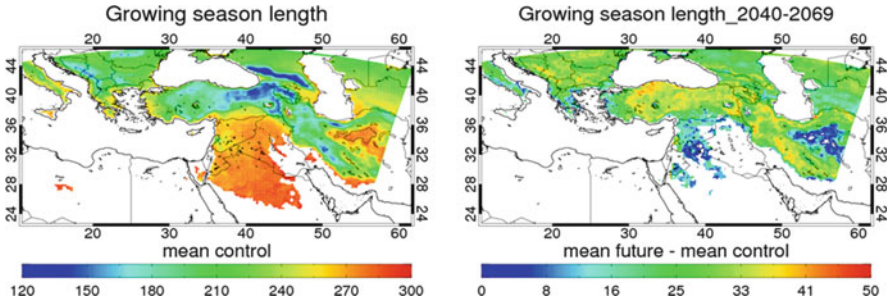

Fig. 1 *Left*: The length of the growing season in days for the control period 1961–1990. Note that frost free areas appear *white*. *Right*: Changes in the length of the growing season between the future and the control period

wheat, will profit from the milder winters whereas others, such as sunflower, are more prone to heat stress (Moriondo et al. 2010). Most importantly for crop cultivation, climate change will likely be associated with a higher frequency of extreme weather conditions. Our results (not shown) suggest that in the above regions over the same period the occurrence of very hot days (TX $>$ 35°C) will increase by 2–4 weeks/year, which could even seriously damage high-temperature sensitive crops grown in the region (e.g. corn). On the other hand, heavy precipitation events will increase by several days per year in the northern part (e.g. Balkans, N-Turkey), whereas their number decreases in South Turkey and Greece. Increases in heat extremes and droughts may counteract the beneficial effects of the increases in growing season length due to the inability of certain crops to cope with heat stress and drought (Evans 2010).

Energy. The demand for energy in the built environment is directly related to climatic conditions. However, the relationship is not linear. Changes in energy consumption are to a large degree linked to the variability of ambient air temperatures, and the maximum energy demand is closely connected to extreme values of air temperature. Considering the expected strong temperature increases in the EMME region, this section addresses the consequences for energy requirements, using the PRECIS climate projections.

To gain insight about the relationship between temperature and energy use we use the concept of degree-days, defined as the difference (in °C) of the diurnal mean temperature compared to a base temperature at which the energy consumption is at minimum. Consequently, the degree-day index is positive in the summer and negative in the winter. However, instead of positive and negative values for this index, the following definitions are used: heating (HDD) and cooling degree days (CDD): $HDD_i = \max(T^* - T_i, 0)$ and $CDD_i = \max(T_i - T^{**}, 0)$ where T^* and T^{**} are the base temperatures for HDD and CDD, respectively, and T_i is the mean temperature of day i. The HDD_i and CDD_i values are typically cumulated over a specified period (annual or seasonal) to provide an indication of the severity of

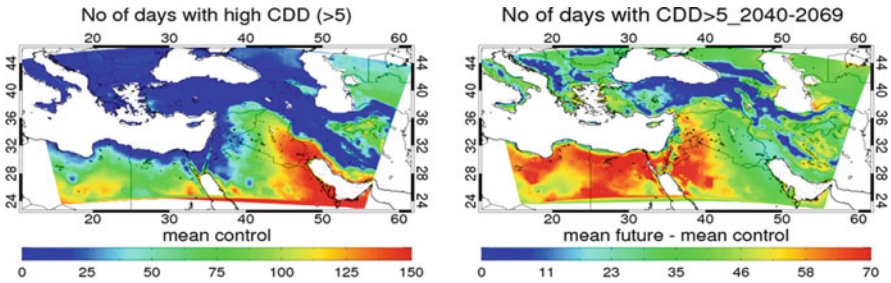

Fig. 2 *Left*: Number of days requiring large cooling (CDD $>$ 5°C) in the control period. *Right*: Changes in the number of days requiring large cooling (CDD $>$ 5°C) between the future and the control period

winter (summer) conditions at a particular location in terms of the outdoor dry-bulb air temperature, which in turn offers a guide to the likely aggregate energy demand for sensible heating (cooling) during that period. Here, we use 25°C for CDDs of particular interest for the EMME region, as defined by Giannakopoulos et al. (2009a). An illustrative and relevant view of the increasing cooling demands in the EMME is provided by the mean number of days per year during which cooling will need to exceed 5°C (CDD $>$ 5°C), comparing the control and mid-century periods. It indicates the additional strong cooling needed to provide comfortable living conditions and cope with heat waves. Figure 2 shows that during the control period the CDD $>$ 5°C in the northern and coastal EMME is typically less than a few weeks to 1 month, while this is 2–3 months in the southern desert areas and up to 5 months around the Persian Gulf. Further, the model projects quite dramatic changes in CDD for the period 2040–2069, with 3–6 weeks in the northern and coastal areas, 1 month around the Gulf region, up to 2 months in parts of Syria, southern Israel, Jordan, parts of Saudi Arabia, Egypt and Libya.

For comparison, Alcamo et al. (2007) and Giannakopoulos et al. (2009a) state that by the end-of-century along most of the northern Mediterranean coast an additional 2–3 weeks and further inland up to 5 more weeks of intense cooling will be needed. Moreover, the study of Giannakopoulos et al. (2009b) showed that in North Africa more than one additional month of heavy cooling will be required whereas in eastern Greece, western Turkey and Cyprus 15 additional days of heavy cooling will be needed.

The peak additional cooling energy demand during the warm and dry future summers coincides with a deficit in water supply, which reduces energy production by hydroelectric plants, e.g. in Turkey, where hydropower currently accounts for about 30% of the electricity production (Alcamo et al. 2007). It will also coincide with a growing demand for desalinated water. To put this into perspective, in Israel about 3% of national energy production is currently used for desalination, which may change approximately proportionally with the increasing water requirements. In EMME countries with limited resources, the anticipated increasing need for space cooling and fresh water demand will lead to a growing disparity in the power

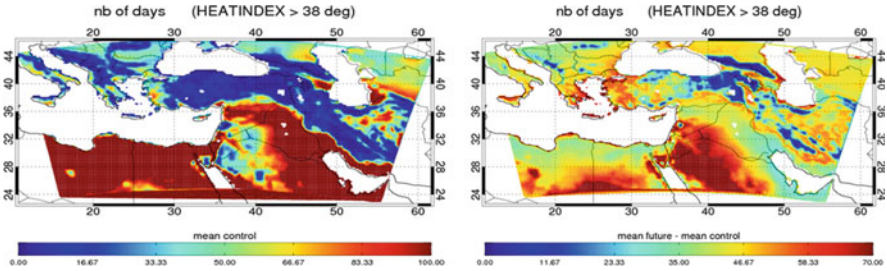

Fig. 3 *Left*: Number of days with high thermal discomfort (humidex $> 38°C$) in the control period. *Right*: Changes in the number of days with high thermal discomfort (humidex $> 38°C$) between the future and the control period

supply, and a growing need for innovative solutions, such as the co-generation of electricity and desalinated seawater by concentrated solar power.

Thermal comfort. There is growing evidence that the EMME already experiences impacts of climate change on public health (Confalonieri et al. 2007). Heat effects on thermal comfort (or discomfort) are assessed by computing the humidex (Masterton and Richardson 1979), an index employed to express the temperature perceived by people. Humidex is applied in summer and generally warm periods and describes the temperature felt by an individual exposed to heat and humidity. More specifically, humidex (in °C) is calculated on the basis of the following equation: $T(h) = Tmax + 5/9 * (e - 10)$, where $Tmax$ is the maximum air temperature (°C) at 2 m, e is vapour pressure $(6.112 * 10\hat{}(7.5 * Tmax/(237.7 + Tmax)) * h/100)$, and h is the relative humidity (%). Additionally, six humidex categories have been established, to inform the general public for discomfort conditions (http://www.eurometeo.com/english/read/doc_heat):

- $<29°C$: no discomfort
- 30–34°C: some discomfort
- 35–39°C: discomfort; avoid intense exertion
- 40–45°C: great discomfort; avoid exertion
- 46–53°C: significant danger; avoid any activity
- $>54°C$: imminent danger, heatstroke

Figure 3 presents projected changes in the number of days for the largest period of each year when the humidex exceeds 38°C. In the control period, most parts of Greece and Western Turkey have around a month of thermal discomfort days for the population. The number of days with humidex $> 38°C$ reach or exceed a 3 months high in North Africa and south parts of the Arabian Peninsula. Interestingly, unlike the case of heat waves, where continental regions show more substantial changes, in this case coastal and island regions are equally vulnerable. Specifically as regards coastal regions in the Eastern parts of Greece, Crete, western/central Turkey and Cyprus, the duration of the period with humidex $> 38°C$ is projected to increase by as many as 50 days in 2040–2069. Even larger increases of 70 days are projected for the Arabian Peninsula. Naturally, this should have an impact

Table 1 Changes in the impacts indices under consideration for each sub-region in the EMME

	Greece	West Turkey	East Turkey	Arabian Peninsula	North Africa
Growing season length	30	30	35	10	0
Large cooling demand days	35	35	25	50	60
Thermal discomfort days	45	45	35	60	50

on discomfort and, subsequently on population health. This parameter shows smaller changes in mountainous areas (e.g. Balkans, Anatolia), i.e. their cool summer climate should be maintained.

3 Conclusions

We have used daily climate projections based on the Hadley Centre PRECIS RCM to assess climate change impacts in the Eastern Mediterranean and Middle East (EMME). The PRECIS uses boundary and initial conditions from the HadCM3Q0 global climate model, employing the IPCC SRES A1B emission scenario. The control run represents the period 1961–1990 and has been used here as reference for comparison with future projections of the period 2040–2069, specifically chosen for the needs of policy makers, so as to assist their planning in the mid-term future. The overall findings of this analysis regarding projected changes in the impacts related indices for each region in the EMME are summarised in Table 1.

References

Alcamo J, Moreno JM, Nováky B et al (2007) Europe. Climate change 2007: impacts, adaptation and vulnerability. In: Parry ML, Canziani OF, Palutikof JP, van der Linden PJ, Hanson CE (eds) Contribution of working group II to the fourth assessment report of the intergovernmental panel on climate change. Cambridge University Press, Cambridge

Confalonieri U, Menne B, Akhtar R et al (eds) Climate change 2007: impacts, Adaptation and vulnerability. Contribution of working group II to the fourth assessment report of the intergovernmental panel on climate change. Cambridge University Press, Cambridge

Evans JP (2010) Global warming impact on the dominant precipitation processes in the middle East. Theor Appl Climatol 99:389–402. doi:10.1007/s00704-009-0151-8

Giannakopoulos C, Le Sager P, Bindi M, Moriondo M, Kostopoulou E, Goodess CM (2009a) Climatic changes and associated impacts in the Mediterranean resulting from a 2°C global warming. Global Planet Change 68:209–224

Giannakopoulos C, Hadjinicolaou P, Zerefos C, Demosthenous D (2009b) Changing energy requirements in the Mediterranean under changing climatic conditions. Energies 2(4):805–815. doi:10.3390/en20400805

Jones RG, Noguer M, Hassell DC, Hudson D et al (2004) Generating high resolution climate change scenarios using PRECIS. Met Office Hadley Centre, Exeter

Masterton JM, Richardson FA (1979) Humidex: a method of quantifying human discomfort due to excessive heat and humidity. Atmospheric Environment Service, CLI. Downsview, Ontario/ Environment Canada, Atmospheric Environment, pp 1–79

Moriondo M, Giannakopoulos C, Bindi M (2010) Climate change impact assessment: the role of climate extremes in crop yield simulation. Clim Change 104:679–701. doi:10.1007/s10584-010-9871-0

Nakićenović N, Swart R (eds) (2000) IPCC special report on emissions scenarios. A special report of working group III of the intergovernmental panel on climate change. Cambridge University Press, Cambridge

Spatial Variability of Daily Extreme Surface Air Temperatures Over Europe During 1950–2009

A. Gkikas, E. Mastrapostoli, F. Stamatoukou, B.D. Katsoulis, and N. Hatzianastassiou

Abstract The spatial variability of extreme surface air temperature has been studied across Europe over the 60-year period 1950–2009. Data of daily maximum and minimum temperature, T_{max} and T_{min}, respectively, taken from the European Climate Assessment & Dataset (ECA&D), were used to investigate their spatial variability, through parameters, $DT_i = [\max(T_i) - \min(T_i)]$ and $STDV(T_i)$, standard deviations, where i = max,min, expressing the absolute and overall spatial variability, respectively. The data are measurements from 181 stations uniformly distributed over Europe with adequate availability. Our results indicate that there is a significant spatial variability of daily T_{max} and T_{min} values over Europe. The computed values of $DT_{max,min}$ range from about 17°C to 58°C, whereas those of $STDV(T_{max,min})$ range from about 3.0–11.5°C, depending on the year and season. It is found that the spatial variability of maximum temperatures over Europe has decreased from 1950 to 2009, as indicated by the computed values $D(DT_{max}) = -0.008$°C and $D[STDV(T_{max})] = -0.003$°C. Similarly, the overall spatial variability of minimum temperatures over Europe has decreased as well, as indicated by our computed values $D(DT_{min}) = -0.016$°C and $D[STDV(T_{min})] = -0.006$°C. The seasonal analysis, however, reveals contrasting tendencies, with decreasing $D(DT_i)$ and $D[STDV(T_i)]$ in winter and spring and increasing in summer.

1 Introduction

Europe has been experiencing rising temperatures during the twentieth century, while a continuing warming is projected, associated with increasing extreme climate events (IPCC 2007). Heat and cool waves, i.e. extreme maximum and

A. Gkikas • E. Mastrapostoli • F. Stamatoukou • B.D. Katsoulis • N. Hatzianastassiou (✉)
Laboratory of Meteorology, Physics Department, University of Ioannina, Ioannina, Greece
e-mail: nhatzian@cc.uoi.gr

C.G. Helmis and P.T. Nastos (eds.), *Advances in Meteorology, Climatology and Atmospheric Physics*, Springer Atmospheric Sciences,
DOI 10.1007/978-3-642-29172-2_66,

minimum temperatures (T_{max} and T_{min}) are among the most dangerous extreme weather and climate events. A number of studies (e.g. Brown et al. 2008) reported increases of extreme daily maximum and minimum temperatures since 1950 over global land areas, Europe included.

Despite the progress that has been made on the topic still little is known quantitatively about the nature of the extreme temperature events and a number of issues still remain open. For example, because of the limited availability and inhomegeneity of observed daily extreme temperatures, fewer studies have been published on changes of these variables than for mean extreme temperatures (Brown et al. 2008). Moreover, concerning Europe, most of studies have been published after 2000, focusing either on individual or just on a few European countries. Consequently, a coherent picture for Europe as a whole lacked until recently. However, the situation has improved recently. Thus, daily gridded datasets, using adequate interpolation techniques, are available from the European Climate Assessment and Dataset (ECA&D, Haylock et al. 2008), which offer a great opportunity for more extended and representative analyses. Such spatially complete datasets allow us to assess new aspects of extreme European temperatures emphasizing their geographical variability.

In the present study, we examine a new aspect of extreme temperature features which has not been tackled in the existing literature. More specifically, we investigate the spatial variability of European extreme daily temperatures and the associated changes with time. On a specific day, large T_{max} and T_{min} differences can be observed throughout Europe, thus creating strong spatial gradients and variability. Here, by making use of spatio-temporally complete and coherent ECA&D daily T_{max} and T_{min} data, we aim at quantifying the spatial variability of extreme temperatures and examining whether or not this variability changes with time. Answering these questions can be of special interest for the currently changing European climate.

2 Data and Methodology

We used ECA&D daily data of T_{max} and T_{min} for the 60-year period from 1950 to 2009. The original data consist in time series of data from 272 stations across Europe as well as in series of gridded (50 × 50 km) data. Royal Netherlands Meteorological Institute (KNMI) has collected the ECA&D data from series of daily observations at meteorological stations throughout Europe and the Mediterranean. The utilized dataset includes 272 stations with a uniform spatial distribution. The ECA&D blended data were used, which are near complete by in-filling from nearby stations, they are updated using synoptical messages, and tested for homogeneity (http://eca.knmi.nl/dailydata/index.php). Gridded ECA&D data are also based on these blended series. The gridded data have been produced using interpolation uncertainty estimates based on the spatial correlation structure of the

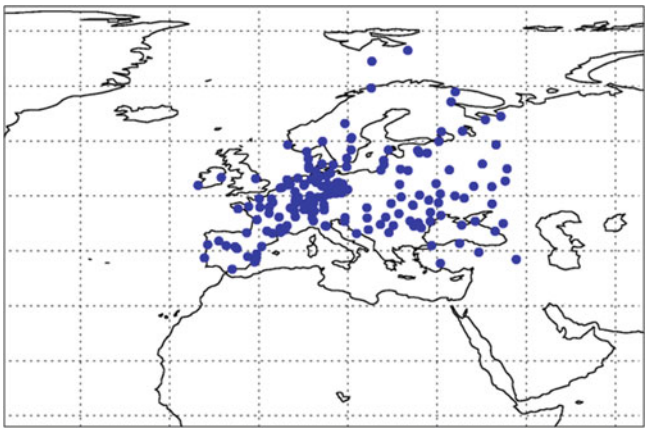

Fig. 1 Geographical distribution of 181 selected ECA&D stations included in the analysis

data (Haylock et al. 2008). In the present study, only the results of the analysis using the ECA&D stations (and not gridded) data are shown, due to space limitations.

A special care was taken to ensure as much as temporally homogeneous and spatially complete coverage of the stations used. Thus, we have tested/applied different criteria concerning the minimum availability of daily data over the entire study period (21,915 days). Very severe criteria, requiring complete (100%) availability, resulted in very few and spatially limited stations, whereas very soft criteria allowed large numbers of stations, but no representative data for time-series analysis. Therefore, here, we present the results of a criterion consisting in a compromise between an adequate availability of data, i.e. at least 99% available daily data for all stations over the whole period, and maximum possible spatial coverage of stations. This has resulted in 181 stations distributed over most of European land areas (Fig. 1). The largest density of stations is in west Europe, but relatively remote areas, such as the Nordic countries, Great Britain, Russia, and Anatolian peninsula are also covered. On the other hand, the southern Italian and Balkan peninsulas are not covered, and therefore the drawn conclusions from this study are valid over Europe except for those regions.

For the 181 selected stations, we defined the following variables to study the spatial variability of extreme, maximum and minimum, temperature values, T_{max} and T_{min}, respectively:

$$DT_{max} = [\max(T_{max}) - \min(T_{max})] \tag{1}$$

$$DT_{min} = [\max(T_{min}) - \min(T_{min})] \tag{2}$$

DT_{max} and DT_{min} yield the spatial variability of extreme (minimum and maximum) daily temperatures across Europe, by means of the absolute differences between the highest and lowest observed values, regardless of where they are

observed. In addition, as an alternative parameter yielding the spatial variability of extreme temperatures, the daily standard deviations of T_{max} and T_{min}, i.e. $STDV_{Tmax}$ and $STDV_{Tmin}$, respectively, were also used. The two defined variables are different in that STDVs represent the overall spatial variability of the extreme minimum/maximum European temperatures, whilst DT_{max} and DT_{min} represent the absolute (extreme) variability of their values.

3 Results

Figure 2a displays the time-series of the computed absolute and complete spatial variability of extreme (maximum and minimum) daily temperatures across Europe, over the 60-year period from 1950 to 2009. The absolute spatial variability, i.e. difference between highest and lowest T_{max} values over Europe, ranges from about 22–50°C, with an average value of 33.6 ± 5.3°C. However, it reaches limit values equal to 18.3°C to 60.1°C. Not a significant seasonal variability of DT_{max} values is found, with seasonal long-term average values ranging from 31.5°C (autumn) to 35.4°C (winter). As for the inter-annual variability of DT_{max}, it is seen that according to the applied linear regression fit, there has been a slight decrease over the 60-year period 1950–2009, by about 0.01°C or 0.02%. According to the performed *t*-test, although this trend is not significant at the 95% level, it tends to be so at somewhat lower significance level (p-value equal to 0.092) and indicates that maximum daily temperatures have become more spatially coherent and consistent across Europe from the mid-1900s to the early 2000s. It should be reminded that this trend is not related to the long-term changes of maximum temperatures, since the two variables, i.e. T_{max} and DT_{max}, as defined in (1), are irrelevant. Indeed, we estimated an overall, statistically significant (99% level), increase of mean (181 stations) T_{max} equal to 0.05°C or 0.38%, despite the determined decrease of DT_{max}.

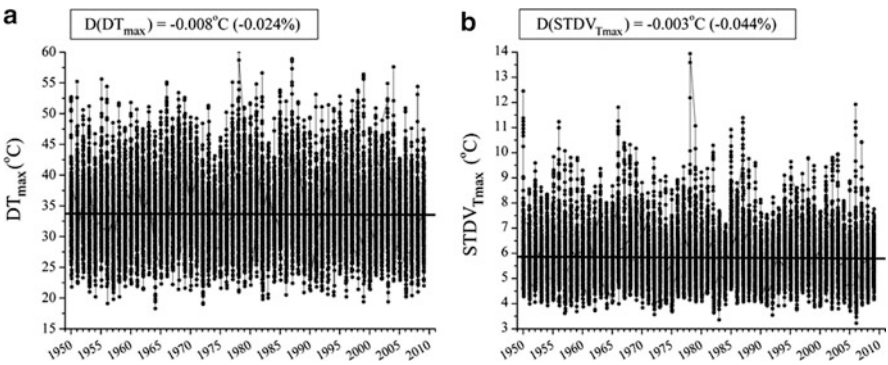

Fig. 2 Time series (1950–2009) of: (**a**) absolute spatial variability of DT_{max}, and (**b**) complete spatial variability ($STDV_{Tmax}$ and $STDV_{Tmax}$) of extreme daily temperatures across Europe (stations of Fig. 1). Linear regression fits (*black solid lines*) are also shown

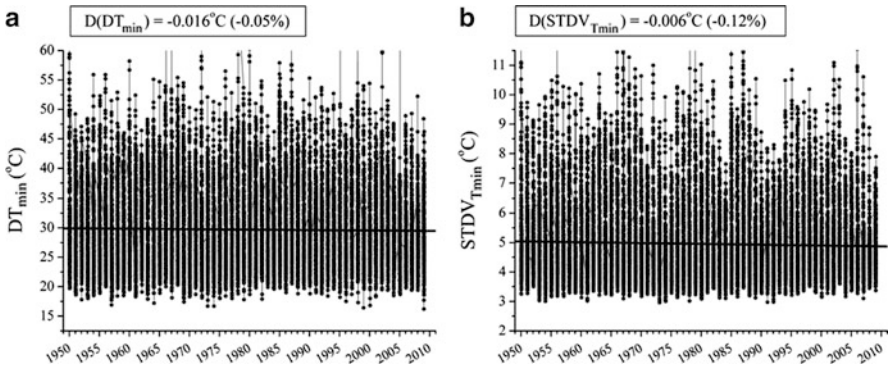

Fig. 3 As in Fig. 2, but for daily minimum temperatures, T_{min}

The findings, regarding the spatial variability of T_{max} values over Europe, based on DT_{max}, are verified from our analysis using $STDV_{Tmax}$ values (Fig. 2b). A similar long-term decrease of $STDV_{Tmax}$ is found, equal to −0.003°C or −0.044%, indicating a reduction of spatial variability of T_{max}. However, in this case, the decrease of $STDV_{Tmax}$ is statistically significant at the 99% level. The background $STDV_{Tmax}$ values range from about 2–3°C to 8–9°C (absolute limits 3.2°C and 13.9°C) with a long-term mean value equal to 5.8°C. These values are clearly smaller than the corresponding ones of DT_{max}, as expected, since they take into account a much larger number of stations, i.e. 181 instead of 2. Nevertheless, it is interesting that the two parameters yielding the spatial variability of maximum temperatures, DT_{max} and $STDV_{Tmax}$, although doing it in a slightly different way, both provide similar results, indicating that over Europe, from the mid-1950s till the early 2000s, the daily maximum temperatures have become more coherent and spatially consistent, i.e. more homogeneous geographically.

The corresponding results for the spatial variability of daily minimum temperatures, DT_{min}, across Europe, and its year-by-year and long-term (1950–2009) changes, are shown in Fig. 3. According to our computations, the background DT_{min} values range roughly between 20°C and 45°C (limit values 16.2°C and 72.4°C) with a 60-year mean value equal to 29.7 ± 6.9°C, and have undergone a decrease equal to −0.016°C or −0.05%, which is statistically significant at the 99% level. At the same time, the spatial variability of minimum temperatures, by means of $STDV_{Tmin}$ values, also presents a statistically significant (at 99% level) decrease equal to −0.006°C or −0.12%. Hence, it appears that not only the maximum, but also the daily minimum temperatures have gradually become more homogeneous spatially over Europe, over the 60-year period 1950–2009.

Moreover, our seasonal analysis (Table 1) shows that different trends are encountered for the four seasons. Thus, both DT_{min} and $STDV_{Tmin}$ have decreased in winter (−0.09% and −0.1%) and spring (−0.04 and −0.06%), whereas they increased in summer (0.04% for both parameters) and less in autumn (0.001% and

Table 1 Seasonal and annual percent (%) changes of the spatial variability of daily minimum and maximum temperatures across Europe, by means of $D(DT_{max,min})$ and $D(STDV_{Tmax,min})$, from 1950 to 2009

	Year	Winter	Spring	Summer	Autumn
$D(DT_{max})$	*−0.02*	*−0.02*	*−0.02*	0.02	<-0.001
$D(STDV_{Tmax})$	*−0.04*	*−0.05*	*−0.02*	0.03	0.01
$D(DT_{min})$	*−0.05*	*−0.09*	*−0.04*	0.02	0.001
$D(STDV_{Tmin})$	*−0.12*	*−0.1*	*−0.06*	0.04	0.01

Italic numbers indicate decreasing trends while *non italic numbers* increasing

0.01%). Therefore, we can conclude that the identified 60-year trends for the spatial variability of minimum European temperatures are mainly attributed to the winter season.

4 Conclusions

The spatial variability of daily minimum and maximum temperatures across Europe has been studied for the 60-year period 1950–2009, using data from 181 ECA&D stations uniformly distributed over the study region. Two parameters have been defined that quantify the spatial variability: the absolute variability, $DT_{max,min}$, and the overall variability, $STDV_{Tmax,min}$. Our results indicate that both parameters have decreased from the mid-1900s to the early 2000s, indicating thus more spatially homogeneous extreme daily temperatures across Europe. However, different trends are found on a seasonal basis, indicating a decrease mainly in winter, but also in spring, in line with the annual trends, and an increase in summer. The computed long-term changes of $DT_{max,min}$, and $STDV_{Tmax,min}$ were found to be statistically significant in most cases, especially for $STDV_{Tmax,min}$. The identified changes of the spatial variability of extreme temperatures are irrelevant to the computed increasing trends of extreme temperatures over the same period, i.e. 1950–2009 (by 0.38% and 1.0% for T_{max} and T_{min}), and their reasons as well the implications for European climate change need to be further investigated.

References

Brown SJ, Caesar J, Ferro CAT (2008) Global changes in extreme daily temperatures since 1950. J Geophys Res 113:D05115. doi:10.1029/2006JD008091

Haylock MR, Hofstra N, Klein Tank AMG, Klok EJ, Jones PD, New M (2008) A European daily high-resolution gridded dataset of surface temperature and precipitation for 1950–2006. J Geophys Res 113:D20119. doi:10.1029/2008JD010201

Intergovernmental Panel on Climate Change (IPCC) (2007) Climate change 2007: the physical science basis. Summary for policymakers, Paris, February 2007

Comparisons of Air Temperature Summer Conditions Between an Urban Forest Park and Its Surrounding Built-Up Area with Their Nearby Mountainous Forest, in the Greater Athens Area, Greece

V. Gouma

Abstract The impacts of diurnal forest cooling effect and the nocturnal mountain katabatic flows (2:00–7:00 LST) to the average air temperature summer conditions inside an urban forest park in Athens, Greece, comparing also to the urban heat island (UHI) effect intensities formed in the surrounding built-up area were shown. The park is situated at the end part of a high greenbelt that starts from the western foothills of the Mt. Hymettus and penetrates into the city of Athens. The park is affected by the UHI between 16:00 and 1:00 h, with a maximum just after sunset at 21:00 LST.

1 Introduction

It was on 1985, that the thought for such a study was first established, as the building of FRIA, is located inside the Syngros Park, Ilissia (size: 14 ha) which is located at the eastern part of the Greater Athens Area, Greece at the northwestern foothills of the Mount Hymettus (alt: 1,024 m). It is considered an urban forest park, as it is mainly covered by high and dense pine stands. The park is situated at the end part of a high greenbelt that starts from the foot of the mountain and penetrates into a built-up area which is densely populated (about 500.000 inhabitants), and extends up to the center of the city of Athens (Fig. 1). So, the questions raised were if and how the mountain and the city affects the microclimate of this park and its impact to the urban heat island (UHI) created in the area. It is well known the cooling effects of vegetation and even more of the forest, which is one of the main ways to ameliorate the UHI phenomenon that is more pronounced during night and its intensity depends on city population (Oke et al. 1989; Bonan 2008). The nocturnal

V. Gouma (✉)
Forest Research Institute of Athens (FRIA), Hellenic Agricultural Organization-DEMETER, Hymettus Avenue & 1, N. Chlorou Street, GR-11528 Ilissia, Athens, Greece
e-mail: gouva@fria.gr

C.G. Helmis and P.T. Nastos (eds.), *Advances in Meteorology, Climatology and Atmospheric Physics*, Springer Atmospheric Sciences,
DOI 10.1007/978-3-642-29172-2_67,

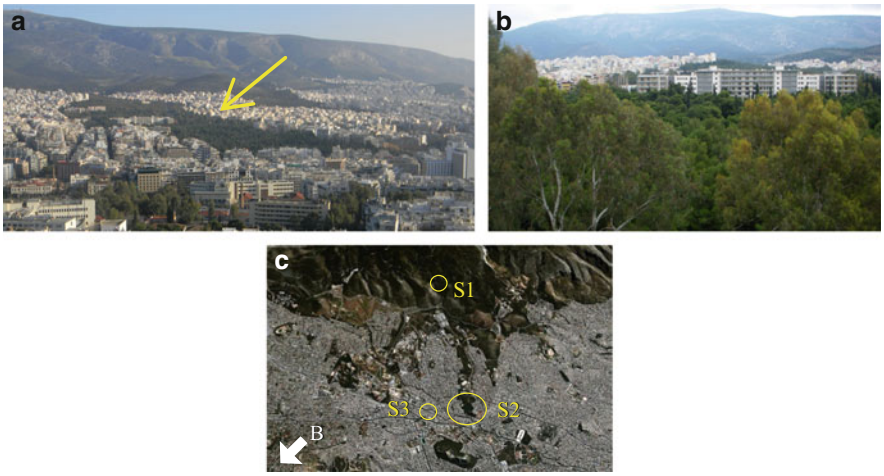

Fig. 1 Study areas: (**a**) the greenbelt 'Mt. Hymettus-Syngros Park', Athens, Greece, (**b**) view of the mountain from the Park and (**c**) the three study sites (Google Earth)

cold downslope air flow (Barry 2008) from the Mt. Hymettus to the Syngros Park was first indicated by Horbert et al. (1988). During the summer of 1984, the Park was cooler (mean minimum air temperature difference: 0.3°C) from a site situated at an altitude 150 m higher, near the mountain-residential interface. Nocturnal katabatic flows have also been defined at a northern west side of the Mt. Hymettus, which there were arrived weakly at a distance of 1.5 km inside the neighbouring residential area (Flocas et al. 1998).

The purpose of this paper is to contribute to the questions posed above by defining and comparing the air temperature summer conditions in the urban forest park, at its nearby forested mountain, and at the surrounding built-up area.

2 Data and Methodology

The first study site (S1) is located at a western forested slope of the Mt. Hymettus (alt. 390 m, asp. NW) and the other two (S2–S3) at the neighbouring urban area (Fig. 1c). From the latter, site (S2) is inside the Syngros Park, Athens (alt. 128 m, asp. W), while the other one (S3) in the nearby dense built-up area called Ambelokipi (alt. 123 m, asp. W). The horizontal distances among them are approximately 4 km (S2–S1) and 4.25 km (S3–S1) and 0.8 km (S2–S3).

The micrometeorological measurements were made at 2 m height above surface level. At the S1 site, a weather station (HOBO type, accuracy 0.2°C/resolution 0.02°C for summer air temperatures) which was located at a small opening of the medium to low height pine forest was used. In the Park, an air temperature data logger (HOBO Pro-v2, 0.2°C/0.02°C) inside a solar radiation shield was placed

under the canopy of the high pine stands. Also, data taken from the Ambelokipi urban station (S3) of the National Observatory of Athens were used. The station (DAVIS, 0.3°C/0.1°C) is mounted on the roof of a building with a height of 13 m. The comparisons were based on the 10-min measurements of the three sites taken during June–July–August of the years 2010 and 2011. Air temperature data, measured at the three sites, were used as well as wind velocity, direction and rain data from the sites S1 and S3. The comparisons were made by applying statistical paired t-tests (sl: 5%). In order to compare the air temperature conditions between the park and the mountain, the differences $\Delta T1 = S2–S1$ were calculated. The differences $\Delta T2 = S3–S1$ were used to define the magnitude of the UHI between the urban-mountain area at the Urban Canopy Layer (UCL) (Oke 2006). Days with rain recordings were excluded from the data bases eliminating also the probability of cloudy ones i.e. conditions unfavourable to define the higher air temperature differences. In order to determine the intensity of differences between the sites, the ΔT values were put in classes. It was assumed that values $<2°C$, were due to the influence of the altitude differences between the sites and the bioclimatic effects of forest vegetation. Values $\geq 2°C$, were indicated the formation and effect of UHI. The diurnal comparisons were made by calculating the mean hourly values from the 10-min measurements. The time of summer sunrise and sunset were considered to be on average at 6:10 and 20:00 LST, respectively.

3 Results

The coldest site, during the summer period, was on average the mountainous peri-urban (S1: 25.6°C) and the warmer the urban built-up (S3: 28.5°C) (Table 1). The paired t-tests have shown that the forest park, is on average warmer 1.5°C (sig 5%) from the mountain site, which is explained by their altitude difference. The average temperature difference ($\Delta T2$: 2.9°C) between the built-up site and the mountain shows the formation of UHI effect. Moreover, the ΔT intensity analyses indicate that the Park site behaves bioclimatically like a part of the mountainous forest most of the summer time ($\Delta T1 < 2°C$ at 42.4%). There were also cases ($\Delta T1$: $\geq 2°C$ at 41.3%) that seems to be affected by the heat produced at its nearby built-up area. The UHI magnitude that was formed between the urban-mountain sites was up to 8.4°C. The mountainous site was in some cases warmer than the Park (16.3%) and the built-up site (6.5%). Regarding the local wind conditions during summer, the S1 compared to the S3, recorded, on average, lower wind speeds, with less variation (S1: 0.9 m/s, std: 0.6 and S2: 1.3, std: 1.1) and higher calm percentages (S1: 20.4% and S2: 16.6%). On the mountain, the prevailing wind directions were from the N and SE sectors and at the city (S3) from the NE and S-SSE.

According to the hourly mean values (Fig. 2a), at 7:00 LST, the Park appears slightly warmer (0.6°C) than the mountain site (22.2°C). The following 2–3 h, the mountain begins to warm faster than the Park and the produced $\Delta T1$ values are the lower of the diurnal cycle. Then, the Park presents faster heating rate until both sites

Table 1 Description of air temperature and ΔT values at the three sites during the study period

Air temperature (°C): Summer period (June–July–August) (2010–2011) (N = 23,862)										
Sites		Max	Min	Mean	Std	25th		50th		75th
S1		38.8	13.7	25.6	4.54	22.3		25.5		29.0
S2		38.7	15.3	27.1	4.35	23.9		27.1		30.4
S3		39.9	18.2	28.5	3.78	25.9		28.3		31.2
						ΔT Intensity (°C)				
						<0	0–2	2–4	4–6	>6
Pairs	ΔT	ΔT (°C) (sl: 5%)				(%)				
S2–S1	ΔT1	6.0	−4.4	1.5	1.48	16.3	42.4	39.1	2.2	–
S3–S1	ΔT2	8.4	−3.4	2.9	1.90	6.5	27.7	37.0	23.7	5.1

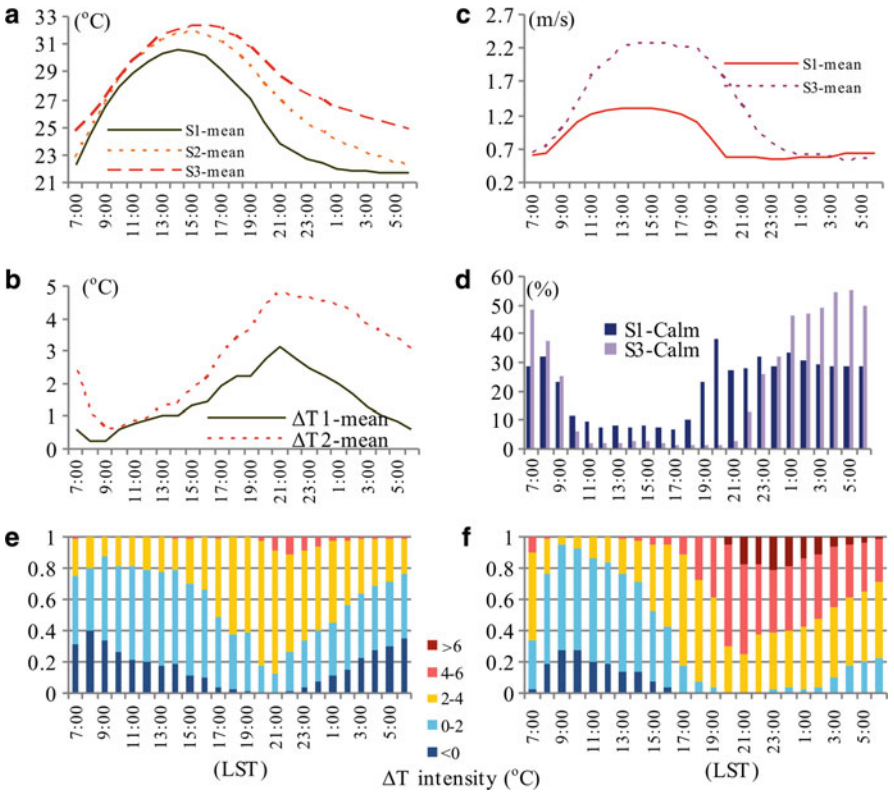

Fig. 2 Average hourly summer values at the study sites of (**a**) air temperature, (**b**) ΔT, (**c**) wind velocity and (**d**) wind calm percentage and also, cumulative relative percentage ΔT intensity of (**e**) ΔT1 (S2–S1) and (**f**) ΔT2 (S3–S1)

reach the highest daily mean values. Thus, at 14:00 h the air temperature at the mountain is on average 30.7°C and in the Park 31.8°C at 15:00. After 15:00 h, the Park appears a continuous nocturnal cooling phase. It is cooling quicker until

21:00, and then relatively slowly up to sunrise that approaches the temperature of the mountain. The mountainous site has a quick cooling phase up to sunset, a slower until 2:00 h and then maintains an almost constant temperature until sunrise. The lower daily mean temperature of the mountain (21.6°C) was formed at 5:00 h and in the Park (22.3°C) the next hour. Thus, the Park appears warmer than the mountain, all the hours of an average summer day. At 8:00 h, the smallest difference (0.2°C) is formed. At the next hour, a temperature difference builds up rapidly, reaches a maximum value (3.1°C) at 21:00 h and then decline towards sunrise, giving small ΔT1 values. The diurnal city-mountain average ΔT2 values in summer follow the differences of the heating-cooling rates at the two sites (Fig. 2b), and define the hours that the UHI effect is formed. During the night period, the ΔT2 values continuous to reduce but they remain high up to the sunrise (2.4°C). The most intense difference (4.8°C) is formed at 21:00 h and the lower (0.6°C) the hours 8:00–9:00. Differences ΔT2 lower than 2°C, between 2–4°C and ≥4°C were calculated during the periods 8:00–15:00, 16:00–19:00 and 2:00–4:00, correspondingly.

The local wind direction data have resulted that during summer, at the mountain site during the period 21:00–8:00 h, katabatic winds (SE/SSE) of low intensity were dominated and the remaining hours from N/NNE/NNW. At the city site, the prevailing winds were from NNE/N/NNW sectors during night and in day, from NNE/NE/NNW (7:00–13:00 h) and NE/SSE/S (14:00–20:00 h). The wind data at the sites S1 and S3 that were recorded during summer on average per hour (Fig. 2c, d) have shown that the lower velocities (S1: 0.6 and S2: 0.7 m/s) and the significant calm percentages (S1: up to 33.5% and S2: up to 55.4%) are associated with the higher ΔT values. The changes of ΔT1 values regarding the wind are best associated to the data at the S1 site. So, the hours of lower (8:00) and higher (21:00) ΔT values are coincide with the morning and evening transition phases, when slope winds reverse from downslope to upslope and the opposite.

From the above, it is concluded that, the air temperature differences between the park-mountain sites for the period 2:00–7:00 h are mainly due to topoclimatic (altitude and mountain downslope flows) and forest cooling impacts, for the 13:00–16:00 h due to topoclimatic (altitude) and forest cooling impacts and for the hours 17:00–1:00 due to the UHI effect (ΔT1 ≥ 2°C). Concerning the low ΔT values during morning hours (8:00–12:00) which are produced by a quick heating of the mountain site, there is a reference below.

The cumulative relative frequencies (%) per hour of the ΔT intensities in an average summer day are shown at Fig. 2e and f. The UHI impact to the Park stops at about 1:00 h and the following night hours up to the morning, the cool mountain katabatic flows contribute to its further cooling. The cases (9.4%) that the Park is colder than the mountain site (23:00–8:00 h) is an indication for that. The daytime hour that, the downslope flow arrives to the Park and then stops, cannot be well defined due to lack of data. During the day (about up to 16:00 h), the tall and dense pine stands of the Park, contribute to maintaining positive differences mainly lower than 2°C. The ΔT1 intensities of 0–2°C, 2–4°C and ≥4°C, were identified for day (max 5.2°C) and night (max 6.0°C) hours with respective frequencies 28.3–19.7–0.3% and 14.1–19.4–1.9%. The S3 site does not seem to be favored

by the cool nocturnal mountain flows as no negative ΔT2 values were determined. The ΔT2 intensities of 0–2°C, 2–4°C, 4–6°C and ≥6°C, were produced for day (max 7.7°C) and night (max 8.4°C) hours with respective frequencies 24.3–20.2–7.0–0.2% and 3.4–16.8–16.6–4.8%. The negative ΔT values (ΔT1: 6.9% and ΔT2: 6.5%) that were generated during day hours (for ΔT1 after 9:00 h) when the mountain site appeared to have a more intense heating comparing to the urban ones, seems to be due to specific summer weather conditions (i.e. on extremely hot days) as well as other reasons, the study of which are out of the purposes of this paper.

4 Conclusions

In summer the average air temperature conditions of the urban forest park (Syngros Park, Ilissia, Athens, Greece) are affected by its nearby mountainous forested area (Mt. Hymettus) and the surrounding build-up land due to topoclimatic (altitude etc.), forest cooling and heat effects. The UHI which is formed in the urban area comparing to the mountain during the period 16:00–7:00 LST, affects the Park for the hours 16:00–1:00, with a maximum just after sunset (21:00 h). The following hours of the night up to sunrise (2:00–7:00), cool downslope flows arrive up to the Park, through the high greenbelt which connects it to the mountain foothills and speeds up its cooling rate. Such nights the green belt behaves like a cool belt that starts from the Mt. Hymettus and arrives through the built-up areas up to the Park, which is near the eastern part of the Athens center. The above conclusions are in agreement and enhance an older but still valid suggestion (Valentien et al. 1999), which supports that the greenbelt Mt. Hymettus-Syngros Park can be regarded as a model for the urban planners. This has shown that the connection of the peri-urban mountainous forests of the Athenean Great Area with the green areas inside the built-up area can improve the urban thermal environment and on general the urban climate, of the city of Athens, especially during the hot Mediterranean summers.

References

Barry RG (2008) Mountain weather and climate, 3rd edn. Cambridge University Press, Cambridge, 506pp

Bonan G (2008) Ecological climatology. Concepts and applications. Cambridge University Press, New York

Flocas HA, Helmis CG, Blikas SN, Asimakopoulos DN, Bartzis JG, Deligiorgi DG (1998) Mean characteristics of the katabatic flow of a 1,024 m high knife mountain. Theor Appl Climatol 59:237–249. doi:10.1007/s007040050027

Horbert M, Kirchgeorg A, Chronopoulou-Sereli A, Chronopoulos J (1988) Impact of green on the urban atmosphere in Athens. Kernforschungsanlage Juelich GmbH (KFA), Berlin. http://hdl.handle.net/10068/247990

Oke TR (2006) Towards better scientific communication in urban climate. Theor Appl Climatol 84:179–190. doi:10.1007/s00704-005-0153-0

Oke TR, Crowther JM, McNaughton KG, Monteith JL, Gardiner B (1989) The micrometeorology of the urban forest (and discussion). Phil Trans R Soc Lond B 324:335–349. doi:10.1098/rstb.1989.0051

Valentien Ch, Papageorgiou-Venetas A, Kroitzsch M (1999) Planning of open spaces and green areas in Athens Basin. Technical Study, Volkswagen Foundation, Munich (in Greek)

Relationship of South-Eastern Europe Winter Precipitation with North Atlantic SST

M. Hatzaki and R. Wu

Abstract As the North Atlantic region shows variations that influence the regional climate, this study aims to investigate the relationship between the North Atlantic SST and the winter precipitation of south-eastern Europe and, furthermore, explore whether this relationship has changed in the past. Such change may be of significant importance for understanding the impacts of global warming on regional climate. The data used involve observational precipitation of 54 stations for 1958–2000 provided by the ECA&D database and the STARDEX EU Project, together with the NOAA Extended Reconstruction SST with $2.0^\circ \times 2.0^\circ$ resolution. The study focuses on interannual variations and a harmonic analysis is applied to the time series to exclude possible contamination of interannual relationship by interdecadal changes. The EOF analysis on winter precipitation data shows that the first EOF explains about 44% of interannual variability and indicates a uniform behaviour over the whole examined area. This EOF is highly correlated with the tropical North Atlantic SST anomalies with a time lag reaching up to two seasons. Moreover, the correlation between winter precipitation and tropical North Atlantic SST seems to weaken from mid-1970s to mid-1980s, and the possible reasons for that change need to be further investigated.

M. Hatzaki (✉)
Department of Environmental Physics and Meteorology, University of Athens, University Campus, Athens, Greece

Institute for Environmental Research and Sustainable Development, National Observatory of Athens, Athens, Greece
e-mail: marhat@phys.uoa.gr

R. Wu
Institute of Space and Earth Information Science, The Chinese University of Hong Kong, Shatin, N.T., Hong Kong

C.G. Helmis and P.T. Nastos (eds.), *Advances in Meteorology, Climatology and Atmospheric Physics*, Springer Atmospheric Sciences,
DOI 10.1007/978-3-642-29172-2_68,

1 Introduction

Observational studies have shown that the North Atlantic sea surface temperature (SST) exhibits substantial interannual to decadal variability (e.g., Bjerknes 1964; Czaja and Marshall 2001). SST variations are related to the atmosphere through evaporation, precipitation and atmospheric-heating processes, leading to changes in temperature, precipitation and storminess over Europe (Rodwell et al. 1999). As the main aspect of the North Atlantic influence on the European climate is through the North Atlantic Oscillation (NAO) variability, many studies have investigated the association of the SSTs with the NAO, and furthermore the changes of the Atlantic storm tracks over the North Atlantic (e.g. Marshall et al. 2001; Hurrel et al. 2003). The causes and mechanisms of North Atlantic variability, however, have not been fully understood. Furthermore, the influence of the variations in the North Atlantic SST has been investigated onto European and African precipitation (e.g. Vizy and Cook 2001; Rodriguez-Fonseca and de Castro 2002).

The purpose of this research is to investigate the response of the winter precipitation field in the southeastern Europe and Near East to the SST anomalies over Atlantic, which is an integral part of the factors governing rainfall sensitivity. Here, we demonstrate that the tropical North Atlantic SST is related to the winter precipitation of south-eastern Europe, through the atmospheric circulation.

2 Datasets and Methods

The present study uses the daily precipitation of 54 meteorological stations in Balkan Peninsula, Turkey and Cyprus from 1958 to 2000, which is provided by the STARDEX EU Project (www.cru.uea.ac.uk/projects/stardex) and the ECA&D database (eca.knmi.nl). The spatial distribution of the stations is presented in Fig. 1.

The sea surface temperature in the present study is the NOAA Extended Reconstruction SST, version 3 (Smith et al. 2008) and it is provided by NOAA/OAR/ESRL Physical Science Division (http://www.cdc.noaa.gov/). The data set maintains a resolution of $2.0^\circ \times 2.0^\circ$ and is available from 1854 to present.

The NCEP/NCAR reanalysis winds at 200 and 850 hPa (Kalnay et al. 1996) on $2.5^\circ \times 2.5^\circ$ grid, available from 1948 to date, together with the gridded monthly mean terrestrial air temperature and precipitation from the University of Delaware (Matsuura and Willmott 2009) with $0.5^\circ \times 0.5^\circ$ resolution for the period 1900–2008 are also used.

The spatial patterns of the winter precipitation anomaly are explored in the empirical orthogonal function (EOF) space. The EOF loadings are indicators of the correlation between the temporal fluctuation of the EOF eigenvectors and the precipitation anomalies.

The analysis is focused on interannual variations. For this purpose, a harmonic analysis is applied to all time series, and only variations with periods shorter than

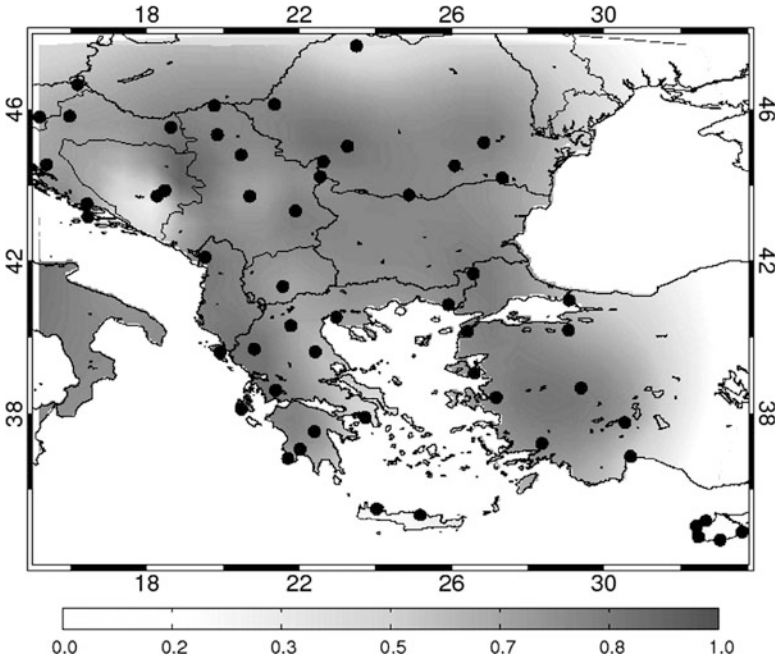

Fig. 1 Geographical chart of the examined area; *black dots* indicate the positions of the meteorological stations; the *shading* refers to the loadings of the first PC of the DJF precipitation

8 years have been retained to reconstruct the resulting time series. This excludes any possible contamination of interannual relationship by interdecadal changes (Wu et al. 2011). This study focuses on the identification of winter (DJF) relationship between south-eastern Europe precipitation and North Atlantic SST. In addition, the time lag of this relationship on seasonal basis is also examined.

3 Results

Based upon the loadings of the first EOF, a typical spatial pattern of the winter precipitation has resulted (Fig. 1). The first EOF explains about 44% of interannual variability, while the whole examined area exhibits a uniform behaviour, with higher loadings for inland and northern regions. The time series of the first EOF will represent the DJF precipitation for the analysis that follows.

Figure 2 shows the correlation of the DJF precipitation with the Atlantic SST of the same winter (DJF), the previous autumn (SON) and the previous summer (JJA) for the period 1958–2000. Positive correlations cover the tropical North Atlantic

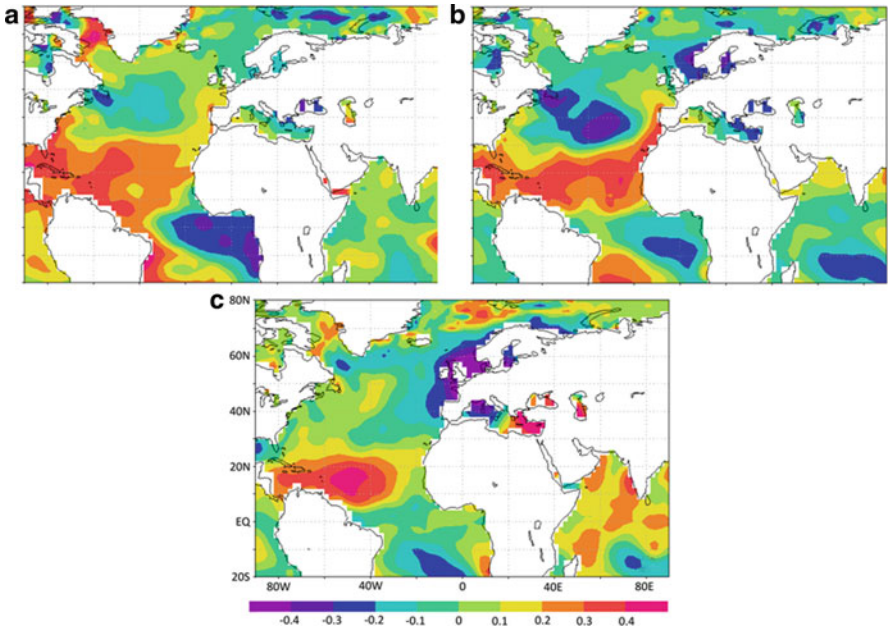

Fig. 2 Correlation between DJF first precipitation EOF and JJA North Atlantic SST (**a**), SON North Atlantic SST (**b**) and DJF North Atlantic SST (**c**)

region during DJF (Fig. 2c), which are still evident during SON (Fig. 2b) and JJA (Fig. 2a) with slightly weaker magnitude compared to DJF. This finding suggests the possibility of predicting the occurrence of significantly dry or rainy winters in the south-eastern Europe area with several months in advance. Rodriguez-Fonseca and de Castro (2002) also showed a possible connection between the anomalous Iberian winter precipitation and the previous summer SST anomalies over the North Atlantic basin.

The DJF SSTs of the tropical North Atlantic (hereafter TNA) that exhibit the higher correlation with DJF precipitation cover approximately the area between 60°W and 30°W and between 5°N and 25°N. The TNA area-mean is obtained by averaging the corresponding SST values. This time series is used as a reference to investigate the relation of SST with atmospheric circulation.

In order to demonstrate the robustness of this connection, a cross-validation analysis is performed using the correlation of the TNA area-mean SST with winter global precipitation (Fig. 3), with the use of gridded global precipitation data. The positive correlations of TNA SSTs with the DJF precipitation of the examined area are evident, along with the precipitation of Western Europe and Africa.

This TNA area-mean SST is then correlated with the wind at 200 and 850 hPa (Fig. 4). At 850 hPa (Fig. 4b), it is related with an increased cyclonic circulation over northern Europe along with a convergent flow from the Middle East leading to

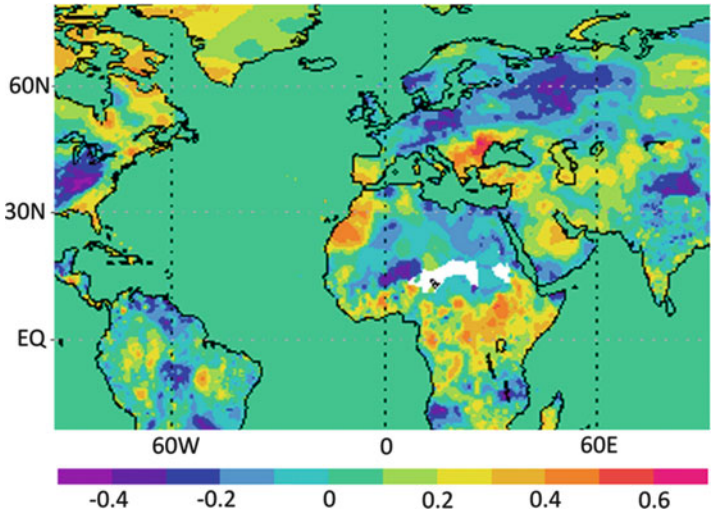

Fig. 3 Correlation between TNA area-mean SST and precipitation

an increased anomalous southwestern flow. This circulation increases the moisture over the examined area leading to enhanced winter precipitation over the eastern Mediterranean and the Balkan Peninsula. As evident from Fig. 4a, this circulation is still maintained at the upper levels.

Finally, the sliding correlation between DJF precipitation first EOF and TNA area-mean SST was calculated with a time window of 21 years (Fig. 5). It was found that for both filtered and unfiltered time series, the correlation is weaker from mid-1970s to mid-1980s. Future work will examine the reasons of this change in possible variations of the NAO and the position of the North Atlantic storm track.

4 Conclusions

As the predictability of the atmosphere on interannual to decadal time-scales is related to the ocean, an attempt is made to investigate the response of the winter precipitation field in the southeastern Europe to the SST anomalies over North Atlantic. With this study we have demonstrated that the winter precipitation of the examined area is strongly correlated to the tropical North Atlantic SSTs, with a time lag reaching up to two seasons, while this correlation seems to weaken from mid-1970s to mid-1980s. Furthermore, the tropical North Atlantic SSTs are linked to an atmospheric circulation that forms an increased anomalous southwesterly flow leading to enhanced winter precipitation over the eastern Mediterranean and the Balkan Peninsula. The results suggest the possibility of predicting the occurrence of significantly dry or rainy winters in the south-eastern Europe area with several months in advance.

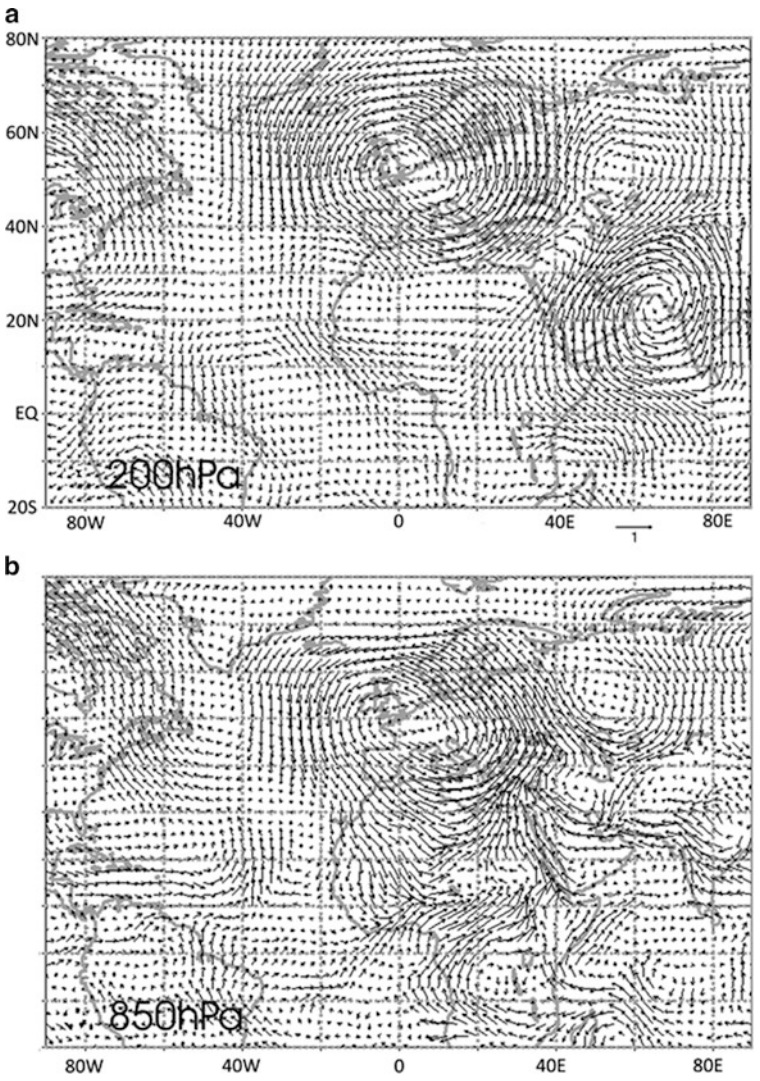

Fig. 4 200 hPa winds (**a**) and 850 hPa winds (**b**) obtained by regression on the DJF North Atlantic SST

Understanding the dynamic mechanisms that drive the atmospheric circulation is key in establishing the connection of various atmospheric components between distant regions. The preliminary work presented here provides a useful constraint towards understanding and explaining these mechanisms that control the interannual relationship between southeastern European climate and North Altlantic, as well as any interdecadal variations of this relationship.

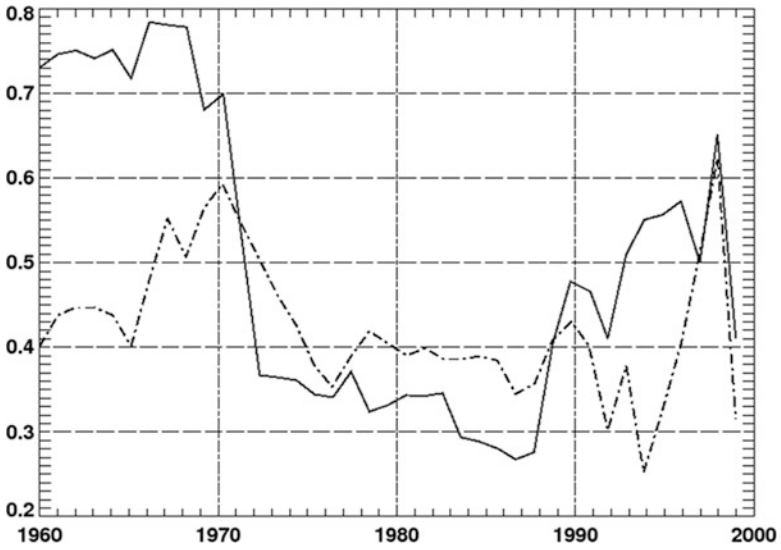

Fig. 5 Sliding correlation between DJF precipitation and TNA SST displayed at the central year of 21-year window for filtered (*dashed*) and unfiltered (*solid line*) time series

Acknowledgments This work was realized during the visit of Dr. Hatzaki at the Center for Ocean-Land-Atmosphere Studies (COLA), MD, USA, which support is greatly acknowledged.

References

Bjerknes J (1964) Atlantic air-sea interaction. Adv Geophys 10:1–82

Czaja A, Marshall J (2001) Observations of atmosphere-ocean coupling in the North Atlantic. Q J R Meteorol Soc 127:1893–1916. doi:10.1002/qj.49712757603

Hurrel JW, Ottersen G, Kushnir Y, Visbeck M (2003) An overview of the North Atlantic Oscillation. In: Hurrel JW, Ottersen G, Kushnir Y, Visbeck M (eds) The North Atlantic Oscillation: climatic significance and environment impact, vol 134, Geophysical monograph series. American Geophysical Union, Washington, DC, pp 1–35

Kalnay E, Kanamitsu M, Kistler R et al (1996) The NCEP/NCAR 40-year reanalysis project. Bull Am Meteorol Soc 77:437–471. doi:10.1175/1520-0477(1996) 077<0437:TNYRP> 2.0.CO;2

Marshall J, Johnson H, Goodman J (2001) A study of the interaction of the North Atlantic Oscillation with the ocean circulation. J Clim 14:1399–1421. doi:10.1175/1520-0442(2001) 014 <1399:ASOTIO>2.0.CO;2

Matsuura K, Willmott CJ (2009) Terrestrial air temperature: 1900–2008 gridded monthly time series (version 2.01). Center for Climatic Research, Department of Geography, University of Delaware, Newark

Rodriguez-Fonseca B, de Castro M (2002) On the connection between winter anomalous precipitation in the Iberian Peninsula and North West Africa and the summer subtropical Atlantic sea surface temperature. Geophys Res Lett 29:1863. doi:10.1029/2001GL014421

Rodwell MJ, Rowell DP, Folland CK (1999) Oceanic forcing of the wintertime North Atlantic Oscillation and European climate. Nature 398:320–323. doi:10.1038/18648

Smith TM, Reynolds RW, Peterson TC, Lawrimore J (2008) Improvements to NOAA's historical merged land-ocean surface temperature analysis (1880–2006). J Clim 21:2283–2296. doi:10.1175/2007JCLI2100.1

Vizy EK, Cook KH (2001) Mechanisms by which Gulf of Guinea and Eastern North Atlantic sea surface temperature anomalies can influence African rainfall. J Clim 14:795–821. doi:10.1175/1520-0442(2001) 014<0795:MBWGOG>2.0.CO;2

Wu R, Yang S, Liu S, Sun L, Lian Y, Gao Z (2011) Northeast China summer temperature and North Atlantic SST. J Geophys Res 116:D16116. doi:10.1029/2011JD015779

Phenological Response of Pear and Orange Trees to Air Temperature at Regions of Thessaly and Peloponnesus, Greece

A. Kamoutsis, A. Matsoukis, P. Kouzounas, and A. Chronopoulou-Sereli

Abstract This research assessed the phenological response of pear (*Pyrus communis* L. cv. Krystalli) and of orange (*Citrus sinensis* L. cv. Washington Navel) trees to air temperature at the regions of Kato Lechonia in Thessaly and at Agiorgitika, Ligourio and Amycles in Peloponnesus, Greece. Phenological observations took place in order to evaluate the start dates of various phenophases of the studied cultivars, from the "end of bud swelling" to the "fruit development" stages. Also, air temperature data were monitored from meteorological stations located near the experimental orchards. The results showed that the warmer conditions at Kato Lechonia in comparison with those of Agiorgitika caused an earlier appearance of pear tree phenophases. The timing of the "end of bud swelling" at Kato Lechonia and Agiorgitika correlated negatively with the air temperature of the late winter (February) as did the timing of "bud burst" and of "appearance of flower buds" at Kato Lechonia. As regards to the orange tree, similar phenological behavior during the examined period was observed between the regions of Ligourio and Amycles due to their "similar" thermal conditions.

1 Introduction

Phenology is the study of the timing of seasonal plant and animal activities driven by environmental factors (Zhao and Schwartz 2003). Phenological observations consist a part of sensitive data for the investigation of the plant response to the local climate conditions and to climate changes (Chmielewski and Rötzer 2001). Higher temperatures during the late winter and spring accelerate the development of plants and lead to an advanced timing of phenological events (Chmielewski et al. 2004;

A. Kamoutsis (✉) • A. Matsoukis • P. Kouzounas • A. Chronopoulou-Sereli
Laboratory of General and Agricultural Meteorology, Department of General Sciences, Agricultural University of Athens, Athens 118 55, Greece
e-mail: akamoutsis@aua.gr

C.G. Helmis and P.T. Nastos (eds.), *Advances in Meteorology, Climatology and Atmospheric Physics*, Springer Atmospheric Sciences,
DOI 10.1007/978-3-642-29172-2_69,

Matsoukis et al. 2010). Phenological observations have a great value in agricultural practice in order to define the optimal cropping areas and to select the most suitable cultivated plants in given regions (Chmielewski 2003).

The objective of this study is to investigate the phenological response of pear and orange trees to air temperature at regions of Thessaly and Peloponnesus in Greece.

2 Data and Methodology

This study was conducted at representative regions of pear (*Pyrus communis* L. cv. Krystalli) and of orange (*Citrus sinensis* L. cv. Washington Navel) trees cultivation, in Thessaly and Peloponnesus, Greece (Table 1, Fig. 1).

Table 1 Phenological observation regions of pear and orange trees in Thessaly and Peloponnessus, Greece

Plant species	Region	Prefecture (periphery)	Latitude	Longitude	Elev. (m)	Dist. (km)
Pyrus communis L. cv. Krystalli	Kato Lechonia	Magnesia (Thessaly)	39°19′49.5″N	23°02′16.5″E	41	2
	Agiorgitika	Arcadia (Peloponnessus)	37°29′52.4″N	22°28′54.2″E	694	22
Citrus sinensis L. cv. Washington Navel	Ligourio	Argolida	37°36′33.7″N	23°02′26.6″E	347	12
	Amycles	Laconia (Peloponnesus)	37°02′27.5″N	22°26′02.3″E	213	25

Elev. elevation, *Dist*. distance from the sea

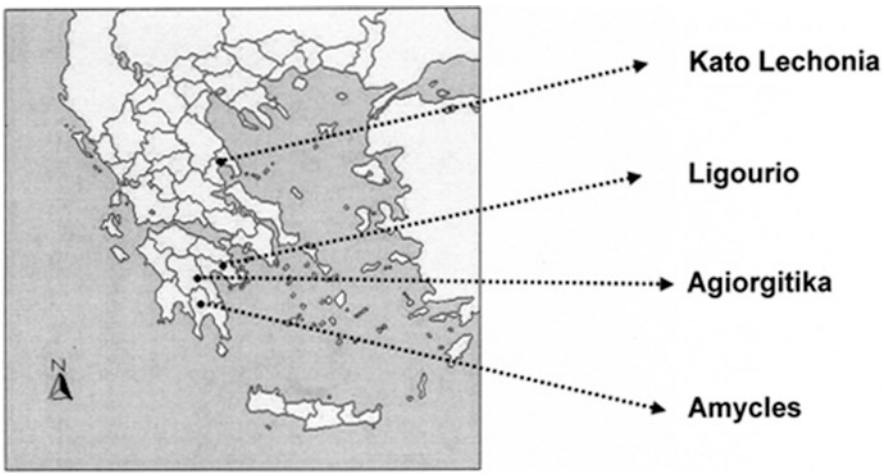

Fig. 1 Location map of the examined pear and orange tree cultivations (as shown by *dot lines*) in Greece

Phenological observations data from the Peripheral Centers of Plant Protection and Quality Control of Volos and Nafplion were collected every week in order to evaluate the start dates of the pear and orange trees phenophases from the "end of bud swelling" to the "fruit development" stages. The selection of phenophases took place according to BBCH scale (Meier 2003). The aforementioned observations were carried out from February to May during the period of 1998–2005 for pear tree and from March to July during the period of 2002–2006 for orange tree.

Air temperature data for the regions Ligourio and Amycles as well as for Kato Lechonia were monitored by meteorological stations of the Peripheral Centers of Plant Protection and Quality Control of Nafplion and Volos, respectively. These meteorological stations covered the study regions from which phenological observations took place. Additionally, air temperature data were used from meteorological stations of Hellenic National Meteorological Service for Tripolis located in the same plateau, 7.7 km northeast of the pear orchards for Agiorgitika region.

Analysis included *t*-tests for the comparison of the start dates of the same phenophases of the pear tree between Kato Lechonia and Agiorgitika and of orange tree between Ligourio and Amycles. Also, these tests were used to compare the average monthly values of air temperature for the same months between the respective regions for each examined plant species.

Pearson's correlation analysis was conducted in order to investigate the relationships between average start dates of the examined plant phenophases and the respective average values of air temperature during the period where these phenophases appeared. For statistical analysis, SPSS 18 and MS Excel were used with a level of significance ≤ 0.05.

3 Results

T-tests showed that the onset of the same pear tree phenophases at the region of Kato Lehonia was significantly different in comparison with those at Agiorgitika. The phenophases of the pear tree at Kato Lechonia appeared earlier than those at Agiorgitika (Fig. 2a).

This could be attributed to the significantly higher air temperature values at Kato Lechonia than those of Agiorgitika (Fig. 2b) from February to May, which is the period where the examined phenophases appeared. Similar results have been reported by Matsoukis et al. (2010) in the case of *Malus domestica* Borkh. cv. Starking Delicious at the regions of Agia and Zagora in Thessaly, Greece.

The different thermal conditions between the aforementioned regions could be explained mainly by lower elevation at Kato Lechonia compared to Agiorgitika and by the effect of topography. More specifically, Kato Lechonia is adjacent to the sea and Agiorgitika is located at the eastern part of Tripolis plateau between the two mountains of Mainalon and Artemision. Thus, the examined regions have different topography which plays an important role on the thermal conditions (Seeman 1979; Schimidli et al. 2009).

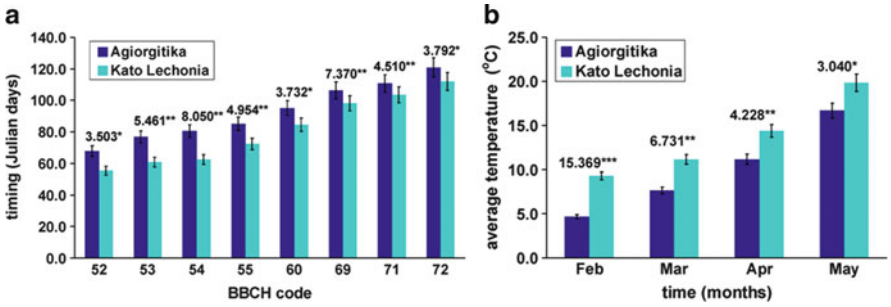

Fig. 2 Average start dates (Julian days) of the studied phenophases of pear tree cultivar Krystalli (**a**) and average monthly temperature values (**b**) in Agiorgitika and Kato Leconia, during the period 1998–2005. The *number above each pair of bars* indicates the *t*-test value between the same phenophases (**a**) and between the studied regions for the same month (**b**). The *vertical line in each bar* represents the Standard Error of the Mean. *, **, ***: significant at $p \leq 0.05$, 0.01 and 0.001, respectively. BBCH codes: 52: end of bud swelling, 53: Bud burst, 54: first leaves separating, 55: appearance of flower buds, 60: first bloom, 69: end of flowering, 71: fruit size up to 10 mm, 72: fruit size up to 20 mm

The average timing of the "end of bud swelling" (BBCH 52) at the two study regions as well as of the "bud burst" (BBCH 53) and of "appearance of flower buds" (BBCH 55) at Kato Lehonia correlated negatively with the air temperature of February (Table 2). This means that higher temperatures in the late winter promote an earlier appearance of the aforementioned pear tree phenophases.

As it can be seen, air temperature in February could be considered as the crucial factor for the occurrence of the "inflorescence emergence" stages (BBCH 52, 53 and 55) in the pear tree cv. Krystalli. Linear relationship between the extreme temperatures and the timing of the aforementioned phenophases was found in the case of *Malus domestica* Borkh. cv. Starking Delicious at the region of Agia, in Greece (Matsoukis et al. 2010).

Also, our results are in accordance with the research of Chmielewski and Rötzer (2001), as regards to the timing of leafing unfolding phenophases of various fruit trees in Europe.

The comparison of the same phenophases on orange trees (*Citrus sinensis* L. cv. Washington Navel), using the *t*-test technique, between the regions of Ligourio and Amycles, did not revealed significant changes (Fig. 3a). Also, there was an absence of significance of monthly average air temperature between the two study regions during the period in which the examined phenophases appeared (Fig. 3b). This fact could be attributed mainly to the effect of topography. The orange orchards in Ligourio are located inside a small valley among the mountain Arachnaion and other hills while those in Amycles are situated in a narrow valley with its borders between the mountains of Taygetos and Parnon. So, in these regions we can suppose that "similar" thermal conditions dominated resulting in a similar phenological behavior of the orange tree. The average air temperature during the period of the occurrence of the examined phenophases did not correlated with the start dates of phenophases in orange trees.

Table 2 Correlation between air temperature (February–May) and timing of the various phenophases of pear tree cultivar Krystalli at the regions of Kato Lechonia (a), in Thessaly and Agiorgitika (b), in Peloponnesus, Greece during the period 1998–2005

BBCH code	T_2	T_3	T_4	T_5	T_{23}	T_{24}	T_{34}	T_{45}
Kato Lechonia (a)								
52	−0.899*	−0.333			−0.707			
53	−0.896*	−0.369			−0.730			
54	−0.623	0.186			−0.113			
55	−0.920**	−0.366	−0.316		−0.739	−0.801	−0.482	
60		−0.494	−0.305				−0.588	
69		−0.634	−0.283				−0.699	
71			−0.259	0.717				−0.027
72			−0.322	0.762				−0.026
Agiorgitika (b)								
52	−0.872*	−0.051			−0.423			
53		−0.239						
54		−0.490	0.106				0.027	
55		0.021	0.151				0.117	
60		−0.137	0.349				0.108	
69			0.234	0.125				0.218
71			0.215	0.025				0.157
72			−0.226	−0.027				−0.171

T_2, T_3, T_4, T_5: average monthly temperature (°C) for February, March, April and May, respectively. T_{23}, T_{24}, T_{34}, T_{45}: average temperature from February to March, February to April, March to April and April to May, respectively. *, ** significant at $p \leq 0.05$ and 0.01, respectively. The empty cells of the table indicate the absence of the respective phenophases. The absence of asterisks indicates non-significance

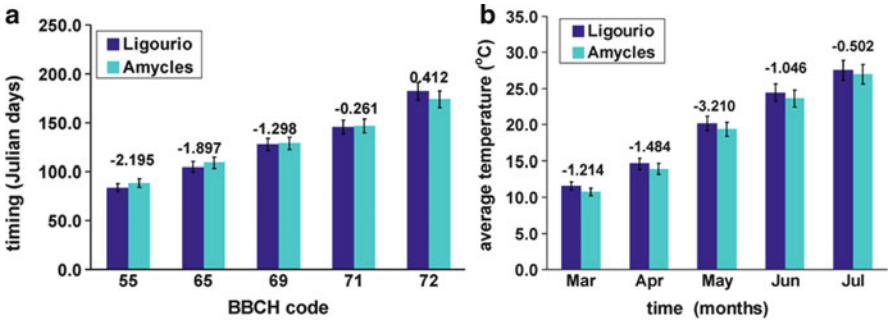

Fig. 3 Average start dates (Julian days) of studied phenophases of orange tree cultivar Washington Navel (**a**) and average monthly temperature values (**b**) in Ligourio and Amycles, during the period 2002–2006. The *number above each pair of bars* indicates the *t*-test value between the same phenophases (**a**) and between the studied regions for the same month (**b**). The *vertical line in each bar* represents the Standard Error of the Mean. BBCH codes: 55: Fist individual flowers visible, 65: full flowering, 69: end of flowering, 71: fruits reached 10% of final size, 72: fruits reached 20% of final size

4 Conclusions

The main findings of the present study concluded as follows:

1. An earlier appearance of the pear tree cv. Krystalli phenophases at the warmer region of Kato Lechonia (Thessaly) in comparison with those at Agiorgitika (Peloponnesus) was observed.
2. The timing of the "end of bud swelling" at Kato Lechonia and Agiorgitika as well as of "bud burst" and of "appearance of flower buds" at Kato Lechonia correlated negatively with the air temperature of February. Thus, higher temperatures during this month accelerated the onset of the aforementioned pear tree phenophases.
3. Similar phenological behavior of orange tree during the examined period was observed at Ligourio and Amycles due to the "similar" thermal conditions which were dominated at the aforementioned regions in Peloponnesus.

Acknowledgments The authors thank the observers of the Peripheral Centers of Plant Protection and Quality Control of Volos and Nafplion for their valuable work regarding the pear and orange trees phenophases. Thanks are also due to the agronomists Mr. C. Pinnas, G. Zegginis and, Mrs. D. Balomenou of the aforementioned Centers of Volos and Nafplion, respectively for providing the phenological and meteorological data as well as the Hellenic National Meteorological Service for providing the meteorological data.

References

Chmielewski FM (2003) Phenology and agriculture. In: Schwartz MD (ed) Phenology: an integrative environmental science. Kluwer Academic Publishers, Dordrecht

Chmielewski FM, Rötzer T (2001) Response of tree phenology to climate change across Europe. Agric Forest Meteorol 108:101–112. doi:http://dx.doi.org/10.1016/S0168-1923(01)00233-7

Chmielewski FM, Müller A, Bruns E (2004) Climate changes and trends phenology of fruit trees and field crops in Germany, 1961–2000. Agric Forest Meteorol 121:69–78. doi:http://dx.doi.org/10.1016/S0168-1923(03)00161-8

Matsoukis A, Kamoutsis A, Chronopoulou-Sereli A, Kiokakis L (2010) Evaluation of the phonological behavior of *Malus domestica* Borkh. cv. Starking Delicious in relation to air temperature in Greece. Agric Mediterr 137:146–158

Meier U (2003) Phenological growth stages. Mono- and dicotyledonous plants. In: Schwartz MD (ed) Phenology: an integrative environmental science. Kluwer Academic Publishers, Dordrecht

Schimidli J, Poulos GS, Daniels MH, Chow FK (2009) External influences on nocturnal thermally driven flows in a deep valley. J Appl Meteorol Clim 48:3–23. doi:http://dx.doi.org/10.1175/2008JAMC1852.1

Seeman J (1979) Agrotopoclimatology. In: Seeman J, Chirkov YI, Lomas J, Primault B (eds) Agrometeorology. Springer, Berlin/Heidelberg

Zhao T, Schwartz MD (2003) Examining the onset of spring in Wisconsin. Clim Res 24:59–70. doi:10.3354/cr024059

Regional Climate Models' Future Simulations of Mean Air Temperature in Greece

J. Kapsomenakis, P.T. Nastos, K. Douvis, C.M. Philandras, G. Tselioudis, and C.S. Zerefos

Abstract The future projections of mean air temperature in Greece for the near future 2021–2050 and distant future 2071–2100 relative to the reference period 1961–1990 are studied, analyzing the simulations from 12 Regional Climate Models (RCMs) within the ENSEMBLES European project. The simulations of the future climate were carried out on annual and seasonal basis under SRES A1B. The results showed that the mean annual air temperature in Greece will present an increase of 1.5°C and 3.2°C, for the periods 2021–2050 and 2071–2100 respectively, based on the average of the 12 climatic simulations. This increase is projected to be larger during summer and smaller during winter. Additionally, the projected warming varies among the different climatic simulations concerning the continental regions of the country especially during summer.

1 Introduction

The impact of the anthropogenic greenhouse gas emissions on air temperature concerns not only the mean warming itself, but also the changes in temperature variability. A number of studies have pointed out the significant effects of extreme temperature on human health and human life (Kalkstein 1993; McGregor 2005; Nastos and Matzarakis 2011), on energy consumption (Giannakopoulos et al. 2009), tourism and bioclimatic comfort of human beings (Subak et al. 2000; Nastos and Matzarakis 2008; Matzarakis and Nastos 2011). Besides, although there is a

J. Kapsomenakis (✉) • K. Douvis • C.M. Philandras • G. Tselioudis • C.S. Zerefos
Research Centre for Atmospheric Physics and Climatology, Academy of Athens, Omirou 24, Athens GR-10672, Greece
e-mail: johnkaps@geol.uoa.gr

P.T. Nastos
Laboratory of Climatology and Atmospheric Environment, University of Athens, Panepistimiopolis, Athens GR-15784, Greece

C.G. Helmis and P.T. Nastos (eds.), *Advances in Meteorology, Climatology and Atmospheric Physics*, Springer Atmospheric Sciences,
DOI 10.1007/978-3-642-29172-2_70,

quite clear evidence for abrupt climate changes, the mechanisms driving these changes are less clear and they are still the subject of very active research (Cracknell and Varotsos 2007). The Mediterranean region is characterized by large temporal and spatial climate variability, due to its geographical position. The influence of mesoscale features result to large climate gradients in a region which would otherwise have a more homogeneous climate (Lionello et al. 2008). Thus, the study of climate on a more local scale is considered very important. Regional climate models (RCMs) have been developed for the application of dynamical downscaling methods to enhance the regional information provided by (GCMs) or by the large scale reanalysis fields (NCEP/ERA-40) (Dickinson et al. 1989; Giorgi et al. 1990). RCMs represent in more detail surface features, such as complex mountain topographies and coastlines as well as small islands and peninsulas, which in a global model could not even appear.

This study aims to present the future projections of mean air temperature in Greece for the near future 2021–2050 and distant future 2071–2100 relative to the reference period 1961–1990, using the simulations from 12 Regional Climate Models (RCMs) within the ENSEMBLES European project.

2 Data and Methodology

The temperature datasets of a total of 12 simulations from Regional Climate Models (RCM) carried out by the European program ENSEMBLES (http://ensemblesrt3.dmi.dk/) were used in this study. More specifically, the results of the following simulations were analyzed: RCA3 (HadCM3Q), RM5.1 (ARPEGE), HIRHAM5 (ARPEGE), HIRHAM5 (ECHAM5), HIRHAM5 (BCM), CLM (Hadcm3Q0), RegCM3 (ECHAM5), RACMO2 (ECHAM5), REMO (ECHAM5), RCA (BCM), RCA (ECHAM5), RCA (HadCM3Q3); the name of the General Circulation Model (GCM), from which data were used as input in the simulation process for each RCM, appear in brackets, while the name of RCM used for the mentioned simulations appear in front of the bracket. The spatial resolution of the 12 RCMs is 0.22° longitude × 0.22° latitude. The assessment of the climatic conditions within the twenty-first century was based on SRES A1B (Nakićenović et al. 2000).

3 Results

Concerning the future projections of the RCMs for Greece the ensemble mean change of the 12 RCMs for the mean annual air temperature between the near future period (2021–2050) and the control period (1961–1990) for the Greek domain ranges from 1.6 to 1.7°C in the continental country, 1.2–1.3°C in the Ionian Sea to 1.5°C in the north Aegean Sea and 1.3–1.4°C in the South Aegean Sea (Fig. 1).

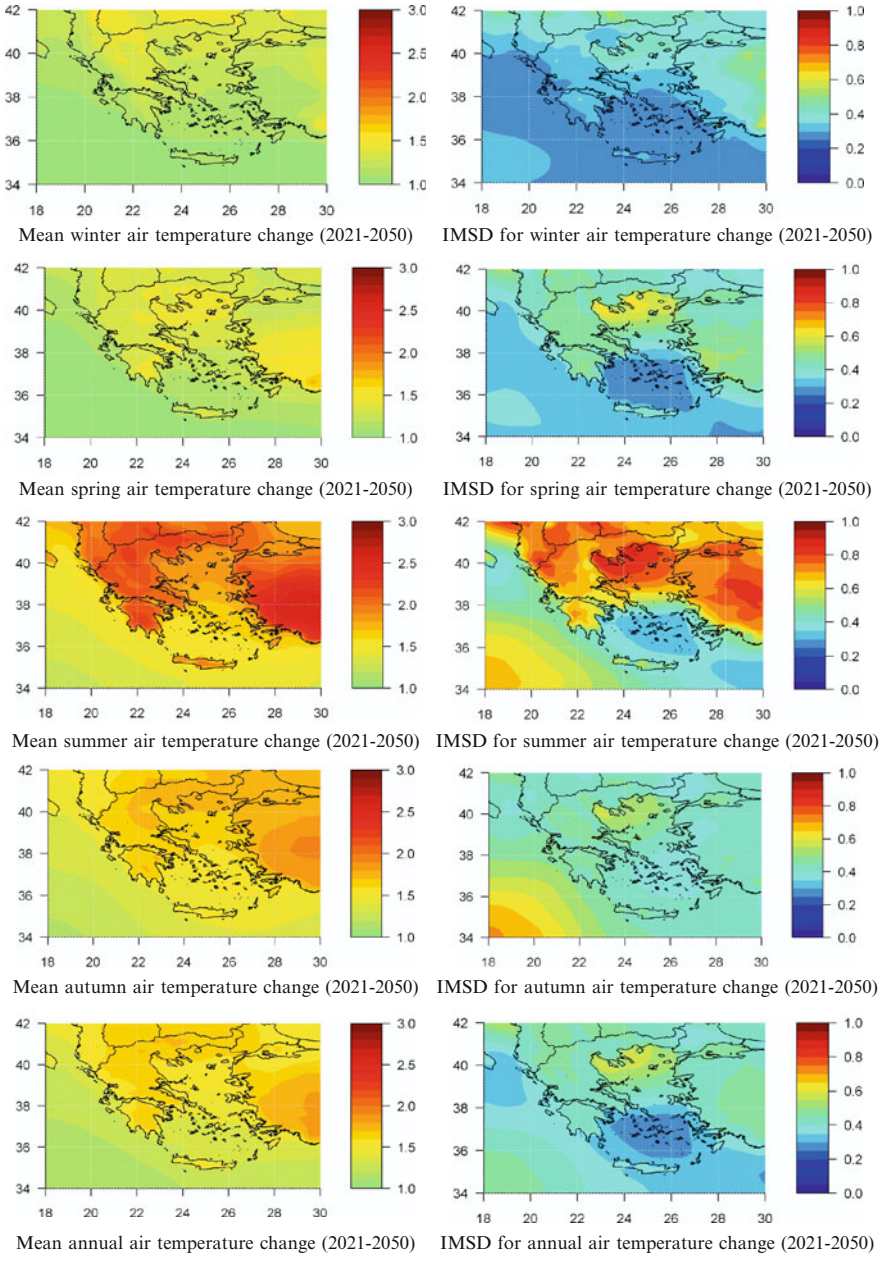

Fig. 1 Spatial distribution of ensemble mean seasonal and annual air temperature change (*left graphs*) and inter model standard deviation (*IMSD*) (*right graphs*) for the near future 2021–2050

The Inter Model Standard Deviation (IMSD) is about 0.4°C over the majority of the country, depicting higher values (~0.5°C) over north Aegean Sea in contrast to central Aegean sub regions (~0.2°C). Taking into account the results for the distant future (2071–2100), the projected change in air temperature ranges from 3.2–3.6°C over land and the north Aegean to 2.6–3.0°C over the rest maritime sub regions (Fig. 2). The IMSD is about 1.0°C over land, while higher values are evident over the north Aegean (1.2°C) and lower values (~0.7°C) over the south Aegean and Ionian Sea sub regions.

During winter and for the near future, the changes of air temperature range from 1.0°C to 1.4°C all over the country, with the highest values in the continental Greece and northern Aegean Sea. The IMSD ranges from 0.25–0.35°C over land to 0.35–0.40°C over the northern Aegean Sea and 0.25°C over the south Aegean and Ionian Sea.

The simulations for the distant future show increases of 2.8–3.0°C over the continental country and 2.4–2.6°C over western regions, Peloponnese, Crete and Aegean/Ionian Sea. The IMSD presents higher values 0.8–0.9°C over central continental Greece and north Aegean compared to 0.5–0.7°C for the rest of the country.

The projected changes of air temperature for spring in the near future are higher (1.4°C) in north Aegean Sea and eastern continental parts than the rest of the country (1.2–1.3°C). The IMSD appears to be higher over northern Aegean Sea (0.6°C) and continental regions (0.4°C) than central Aegean Sea (0.25°C) and Ionian Sea (0.35°C). Taking into account the distant future, the simulated changes range from 2.8°C at the west sub regions to 3.2°C at the eastern regions of continental Greece. The north Aegean Sea appears to be warmer (3.0°C) than the rest maritime areas (2.6–2.8°C). The simulations of the applied models show higher IMSD values over the north Aegean Sea (0.9–1.1°C) and lower values over land (0.8°C) and the south Aegean Sea (0.5°C).

During summer in the near future, the air temperature changes appear to be higher in continental (1.9–2.2°C) than in the maritime sub-regions (from 1.4°C in the south to 1.8°C in the north Aegean Sea while the Ionian Sea seems to be slightly cooler with values from 1.4°C to 1.5°C). The IMSD increases over land and north Aegean Sea (0.6–0.9°C) against 0.4–0.6°C over sea. Concerning the distant future, the projected changes range from 3.8–4.8°C over land to 3.1–3.8°C over sea. The IMSD depicts high values (1.0–1.5°C) over continental and north Aegean sub regions in contrast to 0.5–0.9°C over south Aegean and Ionian Seas.

During autumn, in the near future, the air temperature changes range from 1.6°C to 1.7°C over continental areas and northern Aegean Sea, while the south Aegean and Ionian Seas appear to be slightly cooler (1.3–1.5°C). The IMSD appears to vary from 0.3°C to 0.5°C with the lower values over central/south Aegean Sea. Larger increases are projected in the distant future; namely 3.2–3.6°C over land, while the Ionian Sea/north Aegean Sea and east coasts of the Aegean Sea and islands appear to be warmer (3.2°C) than the south (3.0°C). The IMSD for the projected change ranges from 0.9–1.2°C over land against 0.6–0.9°C over sea.

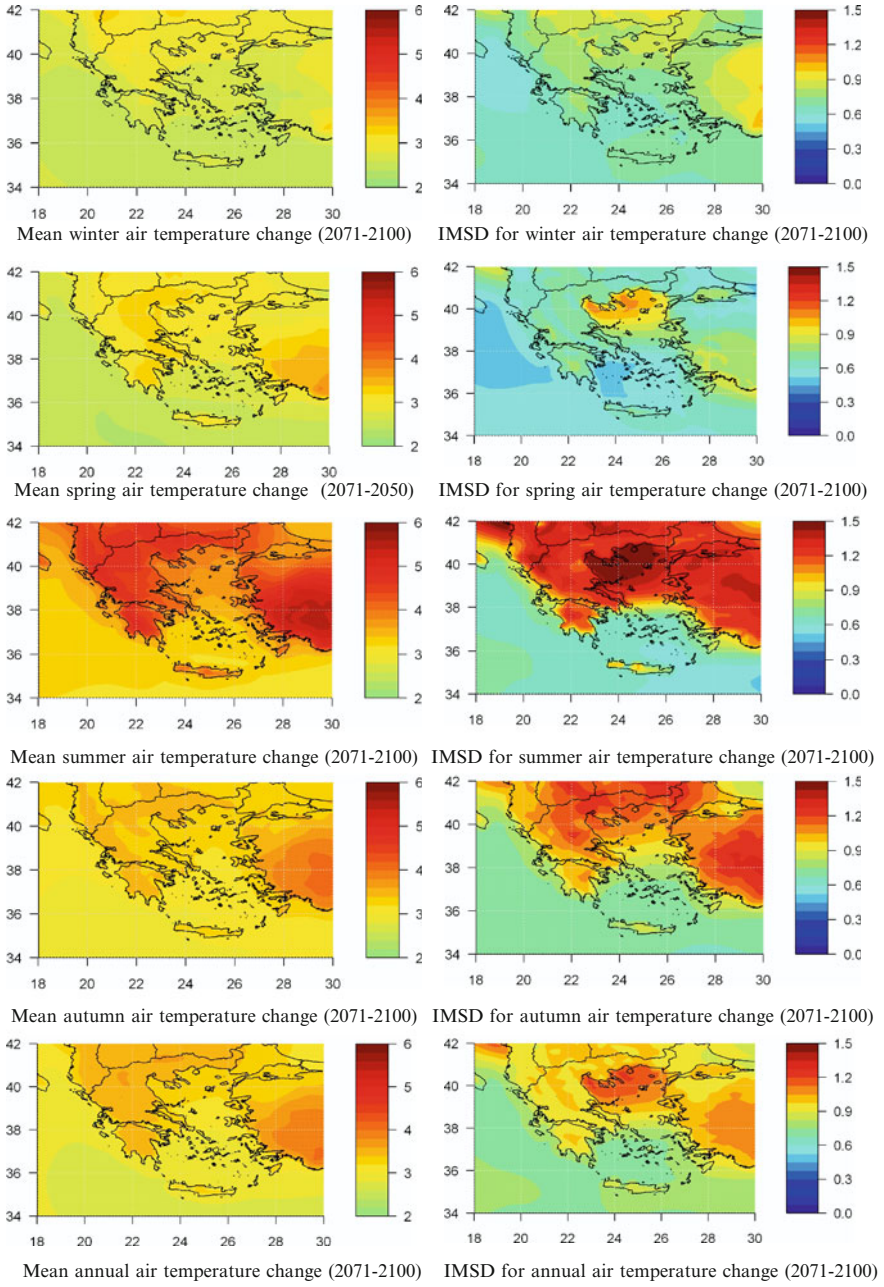

Fig. 2 Spatial distribution of ensemble mean seasonal and annual air temperature change (*left graphs*) and inter model standard deviation (*IMSD*) (*right graphs*) for the distant future 2071–2100

The above findings are in agreement with Zanis et al. (2009), who found that the mean change of the nine RCMs (PRUDENCE project) for the mean air temperature between the future period 2071–2100 (under SRES A2) and the control period 1961–1990 for the Greek domain is 3.4°C for winter and 4.5°C for summer with the changes being larger in continental than in the marine sub-regions.

4 Conclusions

Results showed that the ensemble mean change of the 12 RCMs (SRES A1B, ENSEMBLE project) for the mean air temperature, between the near future (2021–2050)/distant future (2071–2100) and the control period (1961–1990) for the Greek domain presents higher values in the continental Greece and northern Aegean Sea than in the maritime sub-regions. The simulations indicate that the summer air temperature changes in the distant future range from 3.8–4.8°C over land to 3.1–3.8°C over sea. Furthermore, the inter model standard deviation in the future simulations is generally larger in the continental sub-regions and northern Aegean Sea than in maritime sub-regions of Greece.

Further research is needed concerning the assessment of the various factors underlying the air temperature variability derived from the different climatic simulations by the RCMs.

References

Cracknell AP, Varotsos CA (2007) The IPCC fourth assessment report and the fiftieth anniversary of Sputnik. Environ Sci Pollut Res 14:384–387

Dickinson R, Errico R, Giorgi F, Bates G (1989) A regional climate model for the western United States. Clim Change 15:83–422. doi:10.1007/BF00240465

Giannakopoulos C, Hadjinicolaou P, Zerefos C, Demosthenous D (2009) Changing energy requirements in the Mediterranean under changing climatic conditions. Energies 2(4):805–815. doi:10.3390/en20400805

Giorgi F, Marinucci MR, Visconti G (1990) Use of a limited-area model nested in a general circulation model for regional climate simulations over Europe. J Geophys Res 95(D11):18413–18431. doi:10.1029/JD095iD11p18413

Kalkstein LS (1993) Health and climate change. Direct impacts in cities. Lancet 342:1397–1399

Lionello P, Planton S, Rodo X (2008) Preface: trends and climate change in the Mediterranean region. Global Planet Change 63:87–89. doi:10.1016/j.gloplacha.2008.06.004

Matzarakis A, Nastos PT (2011) Human-biometeorological assessment of heat waves in Athens. Theor Appl Climatol 105:99–106. doi:10.1007/s00704-010-0379-3

McGregor GR (2005) Winter North Atlantic Oscillation, temperature and ischaemic heart disease mortality in three English counties. Int J Biometeorol 49:197–204. doi:10.1007/s00484-004-0221-7

Nakićenović N, Alcamo J, Davis G, de Vries B, Fenhann J, Gaffin S, Gregory K, Grübler A, Jung TY, Kram T, La Rovere EL, Michaelis L, Mori S, Morita T, Pepper W, Pitcher H, Price L, Raihi K, Roehrl A, Rogner H-H, Sankovski A, Schlesinger M, Shukla P, Smith S, Swart R,

van Rooijen S, Victor N, Dadi Z (2000) IPCC special report on emissions scenarios. Cambridge University Press, Cambridge

Nastos PT, Matzarakis A (2008) Variability of tropical days over Greece within the second half of the twentieth century. Theor Appl Climatol 93:75–89. doi:10.1007/s00704-007-0325-1

Nastos PT, Matzarakis A (2011) The effect of air temperature and human thermal indices on mortality in Athens. Theor Appl Climatol. doi:10.1007/s00704-011-0555-0

Subak S, Palutikof JP, Agnew MD, Watson SJ, Benthan CG, Cannell MGR, Hulme M, McNally S, Thornes JE, Waughray D, Woods JC (2000) The impact of the anomalous weather of 1995 on the UK economy. Clim Change 44:1–26

Zanis P, Kapsomenakis I, Philandras C, Douvis K, Nikolakis D, Kanellopoulou E, Zerefos C, Repapis C (2009) Analysis of an ensemble of present day and future regional climate simulations for Greece. Int J Climatol 29(11):1614–1633. doi:10.1002/joc.1809

Evaluation of the Canadian Fire Weather Index in Greece and Future Climate Projections

A. Karali, A. Roussos, C. Giannakopoulos, M. Hatzaki, G. Xanthopoulos, and K. Kaoukis

Abstract Current trends in the Mediterranean climate and more specifically in Greece indicate longer and more intense summer droughts that even extend out of season. In connection to this, the frequency of forest fire occurrence and intensity is on the rise. In the present study, the Canadian Fire Weather Index (FWI) is used in order to investigate the correlation between fire risk and meteorological conditions in Greece. FWI is a daily meteorologically-based index designed in Canada and used worldwide (including the Mediterranean basin) to estimate fire danger in a generalized fuel type, based solely on weather observations. Here, an evaluation of the index is initially performed for the Greek territory using fire observations that cover a 15-year period. Two threshold values of extreme fire risk are established; FWI = 15 and FWI = 30 increasing from the north-west to the south-east of Greece. Subsequently, a regional climate model is used to provide input for the FWI system to investigate the impacts of climate change on fire risk for two future time periods, 2021–2050 and 2071–2100. Days with extreme fire risk are expected to increase by as many as 45 days per fire season by the end of the century.

1 Introduction

Forest fires have always been present in the Mediterranean ecosystems, thus they constitute a major ecological and socioeconomic issue. Throughout history, human induced or naturally caused forest fires have imposed their impact on natural

A. Karali (✉) • A. Roussos • C. Giannakopoulos • M. Hatzaki
Institute for Environmental Research and Sustainable Development, National Observatory of Athens, I. Metaxa and V. Pavlou Street, Palaia Pendeli, Athens 15236, Greece
e-mail: akarali@meteo.noa.gr

G. Xanthopoulos • K. Kaoukis
Institute of Mediterranean Forest Ecosystems and Forest Products Technology, National Agricultural Research Foundation, Hymettus Avenue & N. Chlorou 1, Athens 11528, Greece

C.G. Helmis and P.T. Nastos (eds.), *Advances in Meteorology, Climatology and Atmospheric Physics*, Springer Atmospheric Sciences,
DOI 10.1007/978-3-642-29172-2_71,

environment, affecting all types of forests and adjacent rural lands. The last few decades though, the number of forest fires has significantly increased, as well as their severity and impact on the environment. An average of 50,000 fires sweep away from 700 × 103 to 1,000 × 103 ha of Mediterranean forests per annum (FAO 2007), causing enormous ecological and socioeconomic destruction. In particular, the data collected reveal that, according to the average burnt area per fire, Greece has the most severe forest fire problems among the European Union countries (EU 2001) during the last three decades (Schmuck et al. 2011). It has been estimated that the average area burnt per fire is 39.4 ha in Greece, 28.47 ha in Spain, 19.74 in Italy and 15.29 in Portugal (Iliadis et al. 2002).

Forest fires are highly sensitive to climate change because fire behaviour responds immediately to fuel moisture (Weber and Flannigan 1997; Stocks et al. 2001). Thus, the projected increase in temperature increases fuel dryness and reduces relative humidity and this effect worsens in those regions where rainfall decreases. Accordingly, increases in climate extreme events are expected to have a great impact on forest fire vulnerability (Beniston 2003). The contribution of meteorological factors to fire risk is simulated by various non-dimensional indices of fire risk. Viegas et al. (1999) validated several such indices in the Mediterranean against observed fire occurrence, with the Canadian Fire Weather Index (FWI, van Wagner 1987) being amongst the best performers. The FWI model is non-dimensional, based on physical processes and has been used at several locations; thus it seems a sensible basis for exploring the mechanisms of fire risk change.

In this study, an evaluation of the index applied to current fire data for Greece is initially performed. The study aims to establish whether FWI values can adequately reflect fire risk as judged by actual fire occurrence and subsequently to estimate the projected changes in fire risk due to climate change.

2 Data

In this study, the fire data were provided by the Forest Special Secretariat of the Ministry of Environment, Energy and Climate Change. Some 23,150 fire events are documented in the period 1983–1997 throughout Greece. Meteorological data for 11 stations covering the same 15-year period were obtained from the Hellenic National Meteorological Service and used in this study.

Forest fire risk was assessed using the Canadian Fire Weather Index (FWI). FWI is a daily meteorological-based index used worldwide to estimate fire danger in a generalized fuel type. Although it has been developed for Canadian forests, several studies have shown its suitability for the Mediterranean basin (Moriondo et al. 2006). The FWI System provides numerical ratings of relative fire potential based solely on weather observations. FWI components depend on daily noon measurements of dry-bulb temperature, air relative humidity, 10 m wind speed and 24 h accumulated precipitation and are described in detail in van Wagner (1987). FWI consists of six standard components each measuring a different aspect

of fire danger. The first three are fuel moisture codes that follow daily changes in the moisture contents of three classes of forest fuel with different drying rates. The remaining components are fire behaviour indices representing the rate of spread, fuel weight consumed and fire intensity.

This study focused on the fire season (April–October) and mean daily values of the meteorological parameters mentioned above were used for the calculation of FWI daily values.

3 FWI Evaluation

In order to evaluate FWI, fire data from the forest services adjacent to the available meteorological stations were used. The index was classified in categories of bin with size 1 and the average value of the number of fires that occurred at each category was calculated for each station. The best estimated polynomial fit was applied on the data.

A pattern seems to emerge from the results analysis which classifies the domain into two distinct areas of different fire behaviour; the Western and Eastern Continental Greece (WCG and ECG), respectively. Specifically, in WCG one fire per day occurs when FWI $= 15$ (Fig. 1a), while in ECG the same is true when FWI $= 30$ (Fig. 1b). This rate of occurrence can be considered as extreme fire risk. This distinct behaviour can be attributed to the different meteorological regimes prevalent in each of the two regions. Specifically, WCG is characterized by high precipitation amounts (resulting in higher fuel moisture content), while in ECG, precipitation amounts are substantially lower and dry northern winds mostly prevail during the warm period of the year.

An evidence of the above is the distribution of the FWI as a function of the meteorological parameters; here shown as a function of wind speed and temperature (Fig. 2) for days without rain ($r < 1$ mm) and with low relative humidity ($rh < 60\%$). The distribution is shifted to lower wind speed values and FWI takes substantially lower values for Ioannina (in WCG) compared to Elliniko (Athens, in ECG).

The results for the islands of the Aegean do not seem to fit into a pattern as they show great variability in the relationship between fire events and FWI values, probably due to the small total number of fires and the complex local topography. Crete exhibits a distinct behaviour on its own, as an enhanced fire risk (i.e. about one fire every 2 days) occurs for FWI ≥ 30, while the extreme fire risk (i.e. one fire per day) occurs when FWI ≥ 40 (not shown). Our results signify that as we move further south and further east, i.e. to hotter and drier conditions, higher values of FWI are needed to reach our threshold for extreme fire risk of one actual fire per day. This probably means that forest ecosystems to the south are more adapted and less sensitive to fire risk as the forest ecosystems further north.

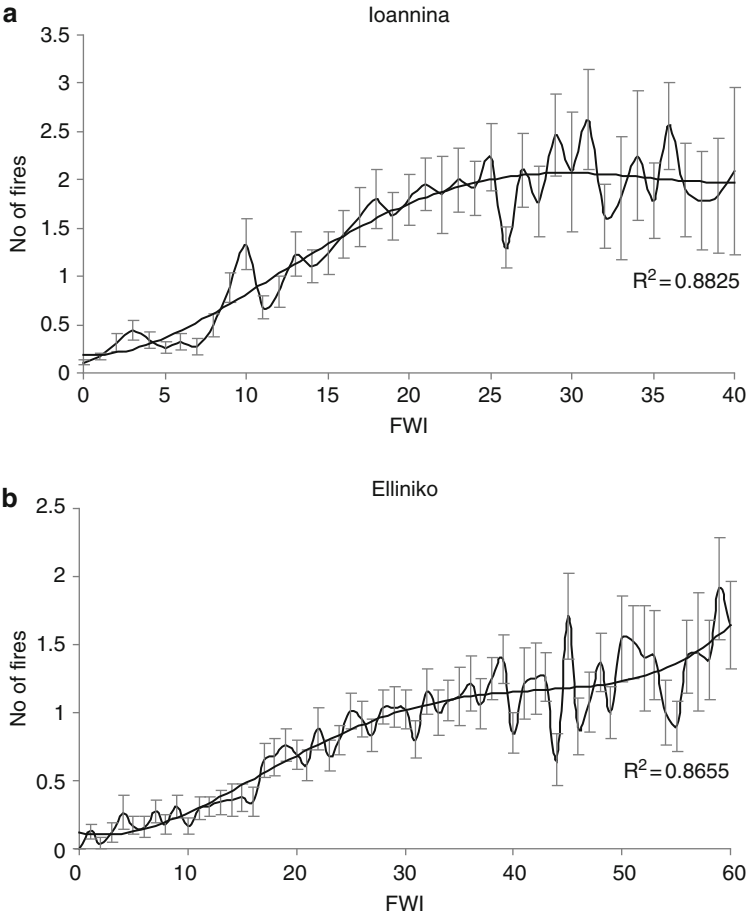

Fig. 1 Mean number of fires per day against FWI and the respective polynomial fit for two indicative stations: (**a**) Ioannina (WCG) and (**b**) Elliniko (ECG) for the 1983–1997 period

4 Future Projections

Present and future model output from the Regional Climate Model RACMO2 were used in this study. This model was developed within the framework of the EU ENSEMBLES project (www.ensembles-eu.org), by the Royal Netherlands Meteorological Institute (KNMI), running at 25 km horizontal resolution. The control run represents the base period 1961–1990 and is used here as reference for comparison with future projections for the periods 2021–2050 and 2071–2100. The future period simulations of the model are based on the IPCC SRES A1B scenario (Nakicenovic et al. 2000) which provides a good mid-line estimate for carbon dioxide emissions and economic growth (Alcamo et al. 2007). For the study region,

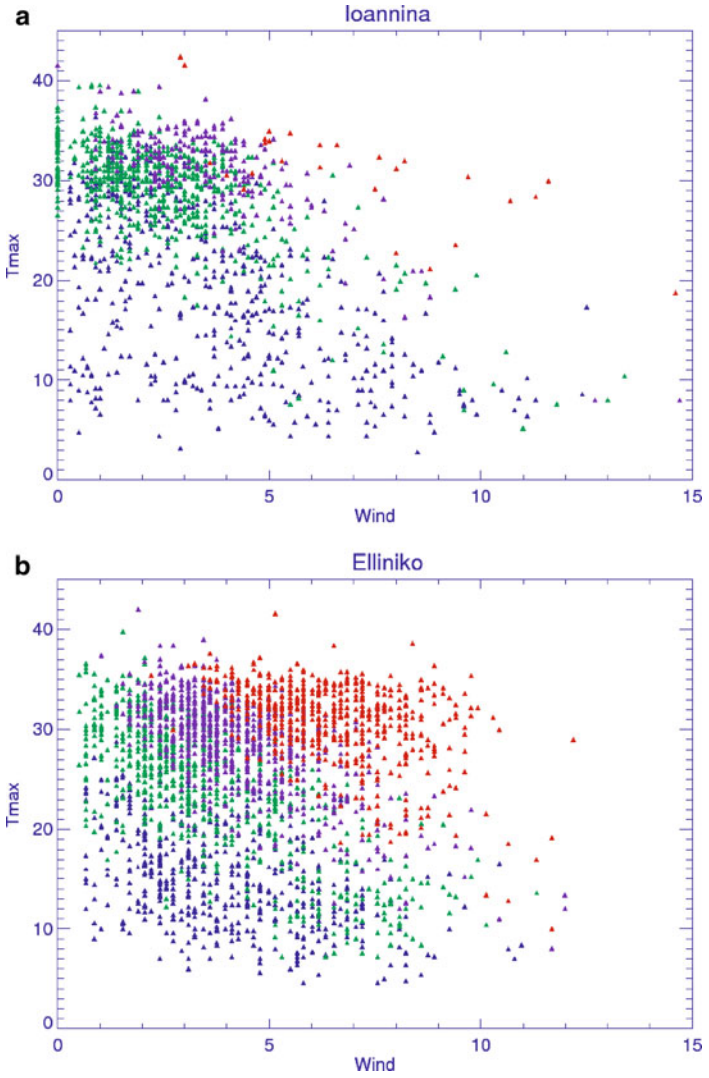

Fig. 2 FWI as function of wind speed and temperature for days with r $<$ 1 mm and rh $<$ 60% for (**a**) Ioannina (WCG) and (**b**) Elliniko (ECG); *blue* for FWI $<$ 15, *green* for 15 $\leq$ FWI $<$ 30, *violet* for 30 $\leq$ FWI $<$ 45, *red* for FWI $\geq$ 45

the maps produced illustrate the change in the number of days with extreme fire risk between the reference and the two future periods (Fig. 3).

In the eastern part of Greece, for the near future (2021–2050) an increase of up to 20 more days of extreme fire risk (FWI $>$ 30) per year is expected (Fig. 3a). The most notable increases are estimated in the Attica peninsula, Eastern Peloponnese, Central Macedonia Thessaly and central parts of Crete. By the end of this century,

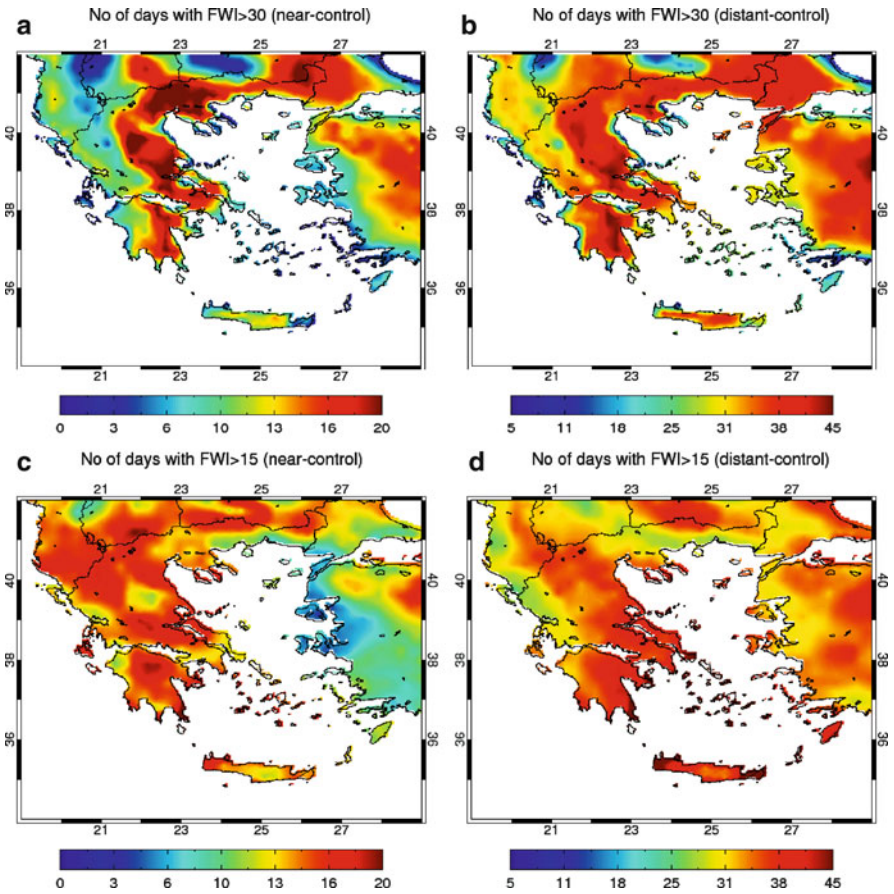

Fig. 3 Projected changes in the number of days with extreme fire risk during near future (*left*) and distant future (*right*), for ECG (*top*) and WCG (*bottom*)

even greater increases are evident for the same area reaching 45 more extreme fire risk days per year (Fig. 3b). As far as western Greece is concerned, the pattern remains the same with an increase in the days with extreme fire risk (FWI $>$ 15) of up to 20 more days per year (Fig. 3c). This increase is higher for the distant future (2071–2100), with values ranging between 25 and 40 days (Fig. 3d).

5 Conclusions

In this study, an evaluation of the FWI was performed using current fire observations for Greece for a 15-year period and the index was confirmed to be skilful at predicting fire occurrence. The values of FWI indicating extreme fire risk

(one fire per day) vary spatially, increasing as we move from the north-west to the south-east of Greece. Two threshold values of extreme fire risk can be established; FWI $\geq$ 15 for western continental Greece and FWI $\geq$ 30 for eastern continental Greece. These thresholds are not applicable for the Greek islands due to the complex local terrain and the small number of fire events.

Future projections suggest a general increase in fire risk over the domain of interest with a very strong impact in the eastern Peloponnese, Attica, Central Macedonia, Thessaly and central parts of Crete. For the near-future period (2021–2050), the number of days with extreme fire risk increases up to 20 more days per year almost in the entire domain. This increase is higher for the distant future (2071–2100) ranging between 25 and 40 more days per year in the western and eastern part of Greece, respectively.

Acknowledgments This paper was prepared in the framework of EU project CLIM-RUN (www.climrun.eu) whose support is gratefully acknowledged. Regional climate model data was provided in the framework of EU project ENSEMBLES (www.ensembles-eu.org).

References

Alcamo J, Moreno JM, Nováky B et al (2007) Europe. In: Parry ML, Canziani OF, Palutikof JP et al (eds) Climate change 2007: impacts, adaptation and vulnerability. Contribution of working group II to the fourth assessment report of the intergovernmental panel on climate change. Cambridge University Press, Cambridge, pp 541–580

Beniston M (2003) Climatic change in mountain regions: a review of possible impacts. Clim Change 59:5–31. doi:10.1023/A:1024458411589

EU, European Union (2001) Forest fires in southern Europe. Report no. 1. European Commission, Brussels, 45pp

FAO, Food and Agriculture Organization (2007) Fire management – global assessment 2006. FAO forestry paper no. 151, Rome, Italy, 121pp

Iliadis LS, Papastavrou AK, Lefakis PD (2002) A computer-system that classifies the prefectures of Greece in forest fire risk zones using fuzzy sets. Forest Policy Econ 4:43–54. doi:10.1016/S1389-9341(01)00079-X

Moriondo M, Good P, Durao R, Bindi M, Giannakopoulos C, Corte-Real J (2006) Potential impact of climate change on fire risk in the Mediterranean area. Clim Res 31:85–95. doi:10.3354/cr031085

Nakicenovic N, Alcamo J, Davis G et al (2000) Special report on emission scenarios, Working group III of the intergovernmental panel on climate change (IPCC). Cambridge University Press, Cambridge, 595pp

Schmuck G, Ayanz JSM, Camia A, Durrant T, Oliveira SS, Boca R, Whitmore C, Giovando C, Libertà G, Corti P, Schulte E (2011) Forest fires in Europe 2010. Report no 11. Joint Research Centre, Institute for Environment and Sustainability, Land Management and Natural Hazards Unit, Publications Office of the EU, Luxembourg, pp 8–11

Stocks BJ, Wotton BM, Flannigan MD, Fosberg MA, Cahoon DR, Goldammer JG (2001) Boreal forest fire regimes and climate change. In: Beniston M, Verstraete MM (eds) Remote sensing and climate modeling: synergies and limitations. Advances in global change research. Kluwer Academic Publishers, Dordrecht/Boston

Van Wagner CE (1987) Development and structure of a Canadian forest fire weather index system. Forestry technical report 35. Canadian Forestry Service, Ottawa

Viegas DX, Bovio G, Ferreira A, Nosenzo A, Sol B (1999) Comparative study of various methods of fire danger evaluation in southern Europe. Int J Wildland Fire 9:235–246. doi:10.1071/WF00015

Weber MG, Flannigan MD (1997) Canadian boreal forest ecosystem structure and function in a changing climate: impact on fire regimes. Environ Rev 5:145–166. doi:10.1139/a97-008

Spatio-Temporal Analysis of Extreme Anomalous Hot and Dry Weather Events in Israel

O. Karo and H. Kutiel

Abstract This study analyzes extreme anomalous hot and dry weather events in Israel based on new definition for those events. Four thresholds of extreme hot and dry weather conditions are proposed. Thus, an extreme anomalous hot and dry day is defined when two conditions are fulfilled: The standard score of the temperature is above one of the four thresholds and the standard score of the relative humidity is below one of the four thresholds. The main conclusion of this study is that differences in temperature and relative humidity in various geographic regions require a new definition for extreme anomalous hot and dry weather based on a regional basis and not on a unique one for the entire country throughout the year. More precise definitions can be obtained by adopting several levels of deviations from the mean values.

1 Introduction

Several studies have analyzed trends in maximum temperatures (Tmax, hereafter) and/or minimum relative humidity (RH, hereafter) trends in the Mediterranean region (e.g., Quereda et al. 2000; Serra et al. 2001; Founda et al. 2004; Zhang et al. 2005; Ziv and Saaroni 2009) and in Israel (Ben-Gai et al. 1999; Saaroni et al. 2003).

Extreme hot and dry weather conditions in Israel have been the subject of many studies, most of them dealing with the Sharav phenomenon. In some studies, the synoptic conditions were analyzed (Alpert and Ziv 1989; Levin and Saaroni 1999; Alpert et al. 2004a, b; Porat 2004), while other studies provide a range of definitions of the Sharav phenomenon, based on temperature and RH thresholds (Winstanley 1972).

O. Karo • H. Kutiel (✉)
Department of Geography and Environmental Studies, University of Haifa, Haifa, Israel
e-mail: kutiel@geo.haifa.ac.il

C.G. Helmis and P.T. Nastos (eds.), *Advances in Meteorology, Climatology and Atmospheric Physics*, Springer Atmospheric Sciences,
DOI 10.1007/978-3-642-29172-2_72,

Table 1 Various definitions of Sharav

	Sharav		Severe Sharav	
	RH	Tmax	RH	Tmax
IMS (until 1994)	<50% (coast) <45% (inland)	–	<30% (coast) <20% (inland)	$>\overline{Tmax_m}$
IMS (since 1994)	<30% (coast) <20% (inland)	$\overline{Tmax_{10d}} - 5°C$ and >27°C	<30% (coast) <20% (inland)	$\overline{Tmax_{10d}} + 10°C$ and >27°C
		Light Sharav	Medium Sharav	Severe Sharav
	RH	Tmax	Tmax	Tmax
Gat and Lomas (1990)	<20%	33.0–35.9°C	36.0–38.9°C	≥39.0°C

Table 2 Mean monthly Tmax and mean monthly minimum RH in January, April, July and October in four stations representing various climatic regions

Station	January		April		July		October	
	Mean Tmax (°C)	Mean RH (%)	Mean Tmax (°C)	Mean RH (%)	Mean Tmax (°C)	Mean RH (%)	Mean Tmax (°C)	Mean RH (%)
Har Kenaan	9.4	68	19.3	42	29.8	36	23.8	42
Beit Dagan	17.8	52	24.6	44	30.9	53	28.2	48
Jerusalem	11.7	56	21.2	36	28.9	35	24.8	39
Sedom	20.4	40	29.8	27	39.6	23	32.4	33

Table 1 lists the various definitions for Sharav events. There are some drawbacks in these definitions, which some of the researchers were aware of:

1. Differences of the mean Tmax and RH among the various regions are not taken into account apart from a rough separation between the coastal plain and the inland in the Israel Meteorological Service (IMS hereafter) definition.
2. Differences of the mean Tmax and RH among the different seasons are completely ignored.
3. Differences between the severities of the Sharav conditions depend solely on the temperature as the threshold of the RH remains constant in all Sharav levels in both definitions of the IMS (the later) and of Gat and Lomas (1990).

As Tmax and RH vary a great deal among the various regions of Israel and across the year (Table 2), in some hot and dry regions, the conditions during several months fit into the above definitions, whereas in other, these definitions are obtained rarely although in some cases, very unusual conditions for the region and the season exist, but yet not enough to be regarded as a Sharav event.

The present study suggests a new approach for defining and identifying extreme anomalous hot and dry weather events in Israel regardless if they were defined as a Sharav event according to one of the presented definitions. Our approach takes into

Table 3 Definitions of extreme anomalous hot and dry days

		Tmax z scores			
		$z < 1$	$1 \le z < 3$	$3 \le z < 5$	$5 \le z$
RH z scores	$z < \lvert -1 \rvert$	no extreme conditions	no extreme conditions	very mild conditions	mild conditions
	$\lvert -1 \rvert \le z < \lvert -3 \rvert$	no extreme conditions	very mild conditions	mild conditions	medium conditions
	$\lvert -3 \rvert \le z < \lvert -5 \rvert$	very mild conditions	mild conditions	medium conditions	extreme conditions
	$\lvert -5 \rvert \le z$	mild conditions	medium conditions	extreme conditions	most extreme conditions

consideration the spatial and temporal variability of Tmax and RH in the different regions, which were ignored in the previous definitions.

2 Data and Methodology

Daily Tmax and minimum RH for the years 1964–2008 from 12 meteorological stations in various regions of Israel from the IMS network were used (only 4 are presented).

For each station, the monthly means and the standard deviations for both parameters (Tmax and minimum RH) were calculated. Then, all daily values were standardized, both for the Tmax and for the RH. For each parameter four thresholds of extreme conditions were defined according to their standard scores. Extreme anomalous hot and dry conditions were defined as a combination of the two i.e., when the standard score of the Tmax was above one of the four thresholds and the standard score of the RH was below one of the four thresholds (Table 3).

3 Results

Table 4 presents the mean annual number of days with extreme anomalous hot and dry weather according to the above thresholds.

Previous studies have shown that spring is the season with the largest number of days with extreme anomalous hot and dry weather conditions followed by the autumn (Porat 2004). In this study spring is also found to be the season with the largest number of days with extreme anomalous hot and dry weather conditions in 9 of the 12 meteorological stations. However, winter is the second season with

Table 4 Mean annual number of days with extreme anomalous hot and dry conditions

Har Kenan	Tmax z score			
RH z score	z <1	1≤ z <3	3≤ z <5	5≤ z
z <|-1|	195	22	2	<1
|-1| ≤ z < |-3|	38	34	9	1
|-3| ≤ z < |-5|	12	20	15	4
|-5| ≤ z	2	4	4	4

Beit Dagan	Tmax z score			
RH z score	z <1	1≤ z <3	3≤ z <5	5≤ z
z <|-1|	208	33	4	<1
|-1| ≤ z < |-3|	37	12	4	1
|-3| ≤ z < |-5|	14	10	6	3
|-5| ≤ z	6	6	6	13

Jerusalem	Tmax z score			
RH z score	z <1	1≤ z <3	3≤ z <5	5≤ z
z <|-1|	194	22	3	0
|-1| ≤ z < |-3|	37	31	10	1
|-3| ≤ z < |-5|	12	20	16	6
|-5| ≤ z	2	3	4	4

Sedom	Tmax z score			
RH z score	z <1	1≤ z <3	3≤ z <5	5≤ z
z <|-1|	188	39	9	2
|-1| ≤ z < |-3|	43	23	11	3
|-3| ≤ z < |-5|	13	12	8	4
|-5| ≤ z	3	3	2	2

Background colors similar as in Table 3

extreme anomalous hot and dry weather conditions in 5 of 12 meteorological stations while autumn is the second season in just 2 meteorological stations. In the southern region of Israel (Beer Sheva, Sede Boker, Sedom and Eilat) summer is the first or the second season regarding the number of days with extreme anomalous conditions.

Analysis of the mean seasonal number of anomalous weather conditions, reveals that the extreme and most extreme conditions are obtained mainly in spring, whereas, the mild and very mild conditions mainly in winter. Furthermore, these tendencies are more pronounced in the coastal stations. It should be made clear, that in summer, despite the very high temperatures, there are only few anomalous cases due to the relatively small variability of Tmax and RH.

From a comparison of the relative contribution of the temperature's change versus the contribution of RH change (Fig. 1), it is evident that changes in RH are more effective in defining anomalous hot and dry conditions. This is true mainly in the coastal and inland regions, while in the Hula Valley and in the Negev, the role of the temperature in defining anomalous weather conditions is larger. This is due probably to the fact that in the coastal and the inland regions, the RH is relatively high and therefore during hot and dry episodes, the RH may decrease a great deal, whereas, in the Hula Valley and in the Negev, the RH is usually low which reduces the possibility of a further major decrease. This make the temperature rise to be more dominant as the main factor that causes a day to be with extreme conditions in these regions.

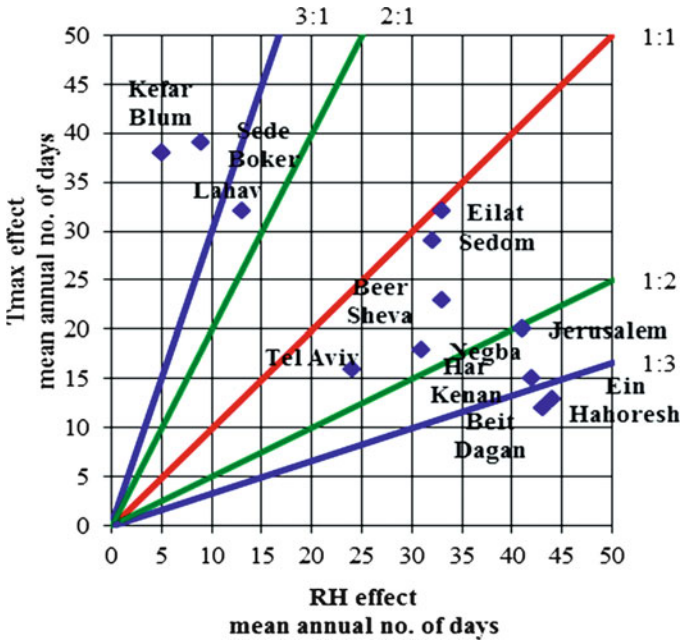

Fig. 1 The most effective factor in defining anomalous hot and dry weather conditions

4 Summary and Conclusions

This study presents a new approach based on monthly average of Tmax and minimum RH. Five severity degrees were defined. This approach is more suitable for Israel due to its large temporal and spatial variability. Anomalous hot and dry conditions are defined for each station and each month according to real measured values and are not subject to arbitrary thresholds.

The main advantage of this approach is that it deals with anomalous conditions in both RH and Tmax. This is extremely important as the normal conditions in each station along the year and its natural variability are taken into account. This is very crucial if one wishes to spot and analyze the extreme cases. It enables to analyze time series of anomalous conditions and the synoptic configuration that led to these anomalous conditions, which is a very difficult task in the conventional analysis way.

References

Alpert P, Ziv B (1989) The Sharav cyclone – observations and some theoretical considerations. J Geophys Res 94:495–514. doi:10.1029/JD094iD15p18495

Alpert P, Osetinsky I, Ziv B, Shafir H (2004a) Semi-objective classification for daily synoptic systems: application to the Eastern Mediterranean climate change. Int J Climatol 24:1001–1011. doi:10.1002/joc.1036

Alpert P, Osetinsky I, Ziv B, Shafir H (2004b) A new seasons definition based on classified daily synoptic systems: an example for the Eastern Mediterranean. Int J Climatol 24:1013–1021. doi:10.1002/joc.1037

Ben-Gai T, Bitan A, Manes A, Alpert P, Rubin S (1999) Temporal and spatial trends of temperature patterns in Israel. Theor Appl Climatol 64:163–177. doi:10.1007/s007040050120

Founda D, Papadopoulos KH, Petrakis M, Giannakopoulos C, Good P (2004) Analysis of mean, maximum, and minimum temperature in Athens from 1897 to 2001 with emphasis on the last decade: trends, warm events, and cold events. Global Planet Change 44:27–38. doi:10.1016/j.gloplacha.2004.06.003

Gat Z, Lomas Y (1990) Analysis of the spring Sharav in the coastal region. Research report 90/4. IMS, Beit Dagan, pp 1–33 (in Hebrew)

Levin N, Saaroni H (1999) Fire weather in Israel – synoptic climatological analysis. GeoJournal 47:523–538

Porat A (2004) The Sharav in Israel. Ph.D. thesis, Tel-Aviv University, 227 pp (in Hebrew)

Quereda SJ, Gil AO, Perez AC, Olcina JC, Rico A, Monton EC (2000) Climatic warming in the Spanish Mediterranean: natural trend or urban effect. Clim Chang 46:473–483. doi:10.1023/A:1005688608044

Saaroni H, Ziv B, Edlson J, Alpert P (2003) Long-term variations in summer temperatures over the Eastern Mediterranean. Geophys Res Lett 30(18):1–4. doi:10.1029/2003GL017742

Serra C, Burgueno A, Lana A (2001) Analysis of maximum and minimum daily temperatures recorded at Fabra observatory (Barcelona, NE Spain) in the period 1917–1998. Int J Climatol 21:617–636. doi:10.1002/joc.633

Winstanley D (1972) Sharav. Weather 27:146–168

Zhang X, Aguilar E, Sensoy S, Melkonyan H, Tagiyeva U, Ahmed N, Kutaladze N, Rahimzadeh F, Taghipour A, Hantosh TH, Albert P, Semawi M, Ali MK, Al-Shabibi MHS, Al-Oulan Z, Zatari T, Khelet IAD, Hamoud S, Sagir R, Demircan M, Eken M, Adiguzel M, Alexander L, Peterson TC, Wallis T (2005) Trends in Middle East climate extreme indices from 1950 to 2003. J Geophys Res-Atmos 110:1–12. doi:10.1029/2005JD006181

Ziv B, Saaroni H (2009) The contribution of moisture to heat stress in a period of global warming: the case of the Mediterranean. Clim Chang 104:305–315. doi:10.1007/s10584-009-9710-3

Assessing the Impact of Mineral Dust and Adsorption Activation on Cloud Droplet Formation

V.A. Karydis, P. Kumar, D. Barahona, I.N. Sokolik, and A. Nenes

Abstract Most aerosol-cloud-climate assessment studies assume that aerosol with a substantial fraction of soluble material are the sole source of Cloud Condensation Nuclei (CCN). However, insoluble species can also act as good CCN, even if they lack appreciable amounts of soluble material. The source of hygroscopicity in these particles is the adsorption of water vapor onto the surface of the particle. Moreover, during atmospheric transport, fresh dust undergoes aging which results in a coating of soluble material on its surface that augments its CCN activity. Given that dust may affect precipitation in climate-sensitive areas, the ability to capture the complex impact of mineral dust on cloud droplet formation is an important issue for global and regional models. The "unified dust activation framework" of Kumar et al. (2011) can be used to calculate the CCN activity of both fresh and aged dust. In this study, simulations of droplet number are carried out with the GMI chemical transport model. GMI simulates global atmospheric composition which is used to drive the droplet number calculations of Kumar et al. (2011) parameterization. This new framework is a comprehensive treatment of the inherent hydrophilicity from adsorption and acquired hygroscopicity from soluble salts in dust particles and is

V.A. Karydis (✉) • I.N. Sokolik
School of Earth and Atmospheric Sciences, Georgia Institute of Technology, Atlanta, GA, USA
e-mail: vlassis@gatech.edu

P. Kumar
School of Chemical and Biomolecular Engineering, Georgia Institute of Technology, Atlanta, GA, USA

D. Barahona
NASA Goddard Space Flight Center, Greenbelt, MD, USA

A. Nenes
School of Earth and Atmospheric Sciences, Georgia Institute of Technology, Atlanta, GA, USA

School of Chemical and Biomolecular Engineering, Georgia Institute of Technology, Atlanta, GA, USA

C.G. Helmis and P.T. Nastos (eds.), *Advances in Meteorology, Climatology and Atmospheric Physics*, Springer Atmospheric Sciences,
DOI 10.1007/978-3-642-29172-2_73,

used to assess the impact of dust and adsorption activation on the predicted global droplet number concentration.

1 Introduction

Mineral dust is a major component of particulate matter in the atmosphere, accounting for more than 50% of the global aerosol load. The long-range transport of dust particles can influence the composition and dynamic state of the atmosphere thousands of kilometers downwind of their source region. Dust can interact with sea salt, anthropogenic pollutants and secondary organic aerosol, forming particles that consist of a "core" of insoluble mineral dust with coatings of soluble material (Levin et al. 2005). Dust particles with a soluble coating are typically very efficient CCN (Levin et al. 2005).

Current theory used to describe droplet formation in atmospheric models assumes that the CCN activity of aerosols depends on their curvature and the fraction of soluble material. However, Kumar et al. (2009a) showed that insoluble species (like freshly emitted mineral dust) can also act as good CCN, even if they lack appreciable amounts of soluble material. The source of hygroscopicity in these particles can attributed to the strong adsorption of water vapor onto the surface of the dust particles and not to the presence of soluble ions in the material.

Global models and studies to date that include dust impacts on droplet number (Hoose et al. 2008; Manktelow et al. 2010; Pringle et al. 2010) assume that dust act as CCN only when a fraction of soluble material exists in the particles (and determines its hygroscopicity). This study assesses for a first time the impact of water adsorption on the CCN activity of insoluble (dust) aerosol and the resulting contribution to global cloud droplet number concentration (CDNC). Simulations are carried out with the NASA Global Modeling Initiative (GMI) Chemical Transport Model using offline wind fields and an online aerosol simulation coupled with the Kumar et al. (2011) activation parameterization. This new framework is a comprehensive treatment of the inherent hydrophilicity from adsorption and acquired hygroscopicity from soluble salts in dust particles.

2 Data and Methodology

The NASA GMI (https://gmi.gsfc.nasa.gov/gmi.html), used in this study, is a state-of-the-art modular 3-D chemistry and transport model (CTM), with the ability to carry out multi-year simulations for impact assessment studies. The detailed description of the framework can be found in Considine et al. (2005). The GMI aerosol model was contributed by Liu et al. (2005) and coupled to the GMI-CTM advection core.

2.1 Data

The model results presented here are based on a 1-year simulation with an initial 1 month spin up. Model inputs include emissions of SO_2 (fossil fuel and natural), DMS, H_2O_2, black carbon (from biomass burning and natural sources), organic carbon (fossil fuel, biomass burning, and natural), mineral dust (four size bins), and sea salt (four size bins) which are provided from Liu et al. (2005). The meteorological fields used in the simulations were taken from the Goddard Institute for Space Studies version II' (GISS II') GCM which includes a slab (Q-flux) ocean model to represent the ocean-atmospheric coupling. The horizontal resolution is 4° latitude by 5° longitude. The vertical resolution is 23 vertical layers.

The concentration of particles that can experience hygroscopic growth, is given as an input from the aerosol module to the cloud droplet formation parameterization and is distributed in four aerosol types: fossil fuel (sulfate, organic mass, and black carbon), biomass burning (organic mass and black carbon), marine (natural sulfate and sea salt), and mineral dust. Fossil fuel, biomass burning, and marine aerosols are assumed to follow the Köhler Theory (KT) for CCN activation whereas mineral dust is assumed to follow the "unified dust activation framework" of Kumar et al. (2011) based on the FHH adsorption activation theory (FHH-AT). Particles within each aerosol type are internally mixed and assumed to follow a prescribed number size distribution shape following the recommendations of Karydis et al. (2011). Parameters used by the cloud droplet formation parameterization also include the accommodation coefficient of 0.06, the updraft velocity representative of typical stratocumulus clouds, $V = 0.3$ m s^{-1} over land, and $V = 0.15$ m s^{-1} over ocean, and "basecase" FHH adsorption parameters, AFHH = 2.25 and BFHH = 1.2 (Kumar et al. 2011).

2.2 Methodology

Calculation of CDNC is carried out in two conceptual steps, one involving the determination of the "CCN spectrum" (i.e., the number of CCN that can activate to form droplets at a certain level of supersaturation), and another one determining the maximum supersaturation, s_{max}, that develops in the ascending cloudy parcels used to represent droplet formation in the general circulation model (GCM). The CDNC is then just the value of the CCN spectrum at s_{max}.

The "CCN spectrum" is computed following Kumar et al. (2009b) and assumes that particles can be described either by KT or FHH-AT. The "CCN spectrum" for an external mixture of lognormal particle size distributions is given by:

$$F^s(s) = \int_0^s n^s(s)ds = \sum_{i=1}^{n_m} \frac{N_i}{2} erfc\left[-\frac{\ln\left(\frac{s_{g,i}}{s}\right)}{x\sqrt{2}\ln(\sigma_i)}\right] \quad (1)$$

where s is the level of water vapor supersaturation, sg,i is the critical supersaturation of the particle with a diameter equal to the geometric mean diameter of the mode i, σi is the geometric standard deviation for mode i, and x is an exponent that depends on the activation theory used. For modes following Köhler theory, $x = -3/2$ (Fountoukis and Nenes 2005), while for particles following FHH theory, x depends on AFHH and BFHH (Kumar et al. 2009b). The adsorption parameter BFHH expresses the long range interactions of adsorbed water layers with the dust surface. AFHH primarily represents the interaction between the first water monolayer and the dust surface.

The maximum supersaturation, s_{max}, in the ascending parcel is calculated from an equation that expresses the supersaturation tendency in cloudy air parcels, which at the point of maximum supersaturation becomes (Fountoukis and Nenes 2005),

$$\frac{2aV}{\pi\gamma\rho_w} - Gs_{\max}I(0, s_{\max}) = 0 \tag{2}$$

where V is the updraft velocity, ρ_w is the density of water, and α, γ, G are parameters defined in Fountoukis and Nenes (2005). $I(0,s_{max})$ is known as the "condensation integral" (Kumar et al. 2009b; Karydis et al. 2011) and it expresses the condensational depletion of supersaturation upon the growing droplets at the point of s_{max} in the cloud updraft. Once s_{max} is determined by numerically solving (2), $N_d = F(s_{max})$ from (1).

3 Results

The predicted annual mean cloud droplet number concentrations at 920 mb are shown in Fig. 1a. As expected, higher CDNC concentrations are predicted over the mid-latitudes of the Northern Hemisphere (i.e., over China, Europe, and eastern U.S.; Fig. 1a), consistent with the high concentration levels of aerosol associated with industrialized regions. CDNC over the remote oceans and in the Polar Regions

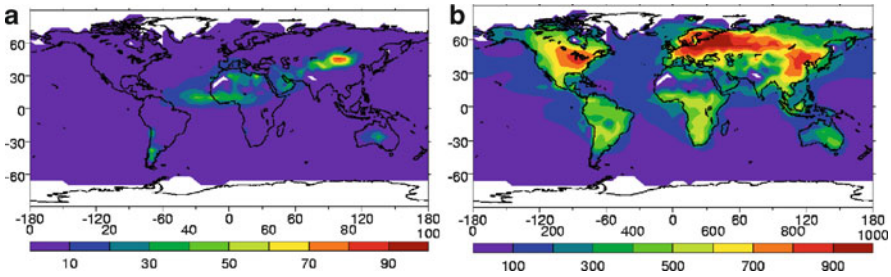

Fig. 1 Predicted annual mean (**a**) CDNC (cm^{-3}) and (**b**) mineral dust fractional contribution on CDNC at 920 mb

are lower. The effects of trade winds off the subtropical west coasts of Africa and America, and westerlies in midlatitude east coasts of North America and Asia are clearly depicted in Fig. 1a. In these regions CDNC increase, as clouds are influenced by long-range transport of continental air masses into adjacent ocean areas. In contrast to the North Hemisphere, lower droplet number concentrations are found over the oceans of the Southern Hemisphere (Fig. 1a) as a result of the cleaner air masses characterizing these regions (Fig. 1b). Over the Southern Ocean larger CDNC are predicted due to the enhanced production of sulfate, from dimethyl sulfide (DMS) oxidation, and the high concentrations of sea salt, which is stirred up from the intense winds travel eastward around the Antarctic. Over the continents of the Southern Hemisphere, larger CDNC appears over regions affected by biomass burning such as South America and Africa.

Cloud droplets formed from the activation of both soluble and insoluble aerosols. Even if the contribution of dust to the predicted CDNC is not significant on a global scale, it can be regionally important as it can affect not only the local air quality but also the nearby and long distance regions due to its ability to remain aloft for several days and travel thousands of kilometers (e.g. the transport of Saharan dust to the tropical Atlantic Ocean). The contribution of dust particles to the predicted CDNC on areas close to mineral dust sources (i.e. deserts) is up to 90 cm^{-3} (Fig. 1b). Mineral dust also has a small contribution on the annual average predicted CDNC across the Atlantic Ocean, as far as the Caribbean Sea (up to 50 cm^{-3}). Nevertheless, this effect can be even more important in specific dust storm episodes.

4 Conclusions

This study is a first attempt to assess the contribution of freshly emitted insoluble particles on global cloud droplet number. Simulations of droplet number are carried out with the NASA Global Modeling Initiative (GMI) Chemical Transport Model using wind fields computed with the Goddard Institute for Space Studies (GISS) general circulation model. GMI simulates global distributions of fossil fuel, biomass burning, marine, and dust aerosols; particles within each aerosol type are internally mixed and assumed to follow a prescribe size distribution shape. Particles with a significant amount of soluble fraction (the CCN activity of which is given by Köhler theory) are assumed to be sulfate, organic carbon, and sea salt. Dust is assumed to follow the "unified dust activation framework" of Kumar et al. (2011); parameters required to constrain the theory are obtained from activation experiments of resuspended desert soil samples (Kumar et al. 2011). Calculation of droplet number from the aerosol simulation is done online in GMI, using the Kumar et al. (2011) parameterization, which considers a comprehensive treatment of the inherent hydrophilicity from adsorption and acquired hygroscopicity from soluble salts in dust particles. This new framework is used to assess the impact of dust and adsorption activation on the predicted droplet number concentration.

According to the results of this study, mineral dust contribution to cloud droplet number concentration is relatively important in areas with high dust concentrations (i.e. deserts). Furthermore, Saharan dust impacts the predicted CDNC across the tropical Atlantic Ocean. The effect of mineral dust on the annual average CDNC is up to 90 cm^{-3} while the impact on the predicted CDNC across the tropical Atlantic Ocean is up to 50 cm^{-3}. Given that the results on this study are expressed as annual averages, this contribution can be even more important during specific dust storm episodes.

Acknowledgments We would like to acknowledge support from NASA-ACMAP, CONOCO-Phillips, and NOAA.

References

Considine DB, Bergmann DJ, Liu H (2005) Sensitivity of Global Modeling Initiative chemistry and transport model simulations of radon-222 and lead-210 to input meteorological data. Atmos Chem Phys 5:3389–3406. doi:10.5194/acp-5-3389-2005

Fountoukis C, Nenes A (2005) Continued development of a cloud droplet formation parameterization for global climate models. J Geophys Res 110(D11):D11212. doi:10.1029/2004JD005591

Hoose C, Lohmann U, Bennartz R, Croft B, Lesins G (2008) Global simulations of aerosol processing in clouds. Atmos Chem Phys 8(23):6939–6963. doi:10.5194/acp-8-6939-2008

Karydis V, Kumar P, Barahona D, Nenes A (2011) On the effect of insoluble dust particles on global CCN and droplet number. J Geophys Res 116:D23204. doi:10.1029/2011JD016283

Kumar P, Nenes A, Sokolik IN (2009a) Importance of adsorption for CCN activity and hygroscopic properties of mineral dust aerosol. Geophys Res Lett 36:L24804. doi:10.1029/2009GL040827

Kumar P, Sokolik IN, Nenes A (2009b) Parameterization of cloud droplet formation for global and regional models: including adsorption activation from insoluble CCN. Atmos Chem Phys 9(7):2517–2532. doi:10.5194/acp-9-2517-2009

Kumar P, Sokolik IN, Nenes A (2011) Measurements of cloud condensation nuclei activity and droplet activation kinetics of wet processed regional dust samples and minerals. Atmos Chem Phys 11(4):8661–8676. doi:10.5194/acp-11-8661-2011

Levin Z, Teller A, Ganor E, Yin Y (2005) On the interactions of mineral dust, sea-salt particles, and clouds: a measurement and modeling study from the Mediterranean Israeli Dust Experiment campaign. J Geophys Res 110(D20):D20202. doi:10.1029/2005JD005810

Liu XH, Penner JE, Herzog M (2005) Global modeling of aerosol dynamics: model description, evaluation, and interactions between sulfate and nonsulfate aerosols. J Geophys Res 110(D18):D18206. doi:10.1029/2004JD005674

Manktelow PT, Carslaw KS, Mann GW, Spracklen DV (2010) The impact of dust on sulfate aerosol, CN and CCN during an East Asian dust storm. Atmos Chem Phys 10(2):365–382. doi:10.5194/acp-10-365-2010

Pringle KJ, Tost H, Pozzer A, Poschl U, Lelieveld J (2010) Global distribution of the effective aerosol hygroscopicity parameter for CCN activation. Atmos Chem Phys 10(12):5241–5255. doi:10.5194/acp-10-5241-2010

An Investigation of Iran's Precipitation Anomalies in Relation with Atmospheric Blocking

G. Azizi and M. Khalili

Abstract Atmospheric blocking is a synoptic-planetary scale system that disrupts the prevailing westerlies. An important feature of this phenomenon is that in addition to being large-scale, it is quasi-stationary, which could lead to climatic anomalies within regions upstream and downstream of the main occurrence. In the present study, using CBS, blocking occurrences were identified for region 60° W to 50° E for a period of 1978–2007. To determine precipitation anomalies, standard scores were used. For doing so, standard scores higher than 0.5 and lower than −0.5 were defined as precipitations with anomalies. Standard scores defined covering more than half of all stations, were considered as positive and negative precipitation anomalies for Iran. The coincidence of positive and negative precipitation anomalies with dates of blocking occurrences has revealed using components of atmospheric circulation such as zonal and meridional wind, vorticity advection and omega. The results indicated that if a southern trough of dipole blocking places over a region, it will lead to precipitation in longer period. In addition, the quasi-stationary nature of blocking increases vorticity advection and will retain the positive value of vorticity during a blocking occurrence in front of a cyclone.

1 Introduction

Interruption of westerly circulation is called blocking (Barry and Carleton 2001). The relationship between regional climatic anomalies and circulation features has been investigated in previous studies. Regions under the blocking anticyclone experience dry/wet conditions for a long period of time (Triedl et al. 1981). When westerly winds are replaced by easterlies, the mean cyclone track and precipitation patterns are diverted towards polar or subtropical latitudes (Rex

G. Azizi • M. Khalili (✉)
Department of Physical Geography, University of Tehran, Tehran, Iran
e-mail: khalili.m@alumni.ut.ac.ir

C.G. Helmis and P.T. Nastos (eds.), *Advances in Meteorology, Climatology and Atmospheric Physics*, Springer Atmospheric Sciences,
DOI 10.1007/978-3-642-29172-2_74,

1950). Buehler et al. (2011), by using extreme statistic, showed that the extent of cold/dry spells were strongly associated with blocking frequency. They also showed that the number of cold spell days increased with the duration of blocking. Examining the relationship between blocking occurrence and cold occurrence of January of 1964 and 2008, Azizi and Khalili (2011) found that intensity and position of blocking event played an important role in extreme cold occurrence. Konrad and Colucci (1988) showed that blocking contributed to intensification of surface cyclone and the movement of middle-level trough toward northeast. In addition, Colucci and Alberta (1996), in a climatic study of the blocking and cyclogenesis, demonstrated that in the presence of blocking, atmospheric flux display positive anomalies in meridional vector and negative anomalies in zonal vector. Here, the climatology of a 30-year period (1978–2007) for blocking occurrence based on Lupo et al. (2008) categorised under Atlantic blockings is presented (sweeping a region between 60°W and 50°E). The rationale for selection of the northern hemisphere lies on its focus on blockings wielding impact on Iran weather (Azad 2007). On the other hand, precipitation displays fluctuations in terms of time and place especially in arid and semiarid regions like Iran, where precipitation coefficient of variation is more than 40% in most stations of the country. The main purpose of the present study is to answer the question of possible relationship between blocking occurrence and precipitation anomalies in Iran.

2 Data

The first and most basic dataset included the archive of blocking events including complete information as to when and where they occurred, and their intensity as defined by Wiedenmann et al. (2002). The centre for blocking studies was made this archive for global blocking events (http://weather.missouri.edu) (Lupo et al. 2008). This archive is available for public use. The NCEP-NCAR gridded reanalyses were used (www.cdc.noaa.gov/cdc/data.ncep.reanalysis.html) that cover a much longer period (30 years) of consistent data. Monthly/daily precipitation datasets of Iran (1978–2007) were used. Components of atmospheric circulation included mean geopotential height at 500 hPa, horizontal component of the zonal/meridional wind, vorticity advection and omega.

3 Methodology

The present study was based on the study by Lupo et al. (2008) to detect blocking occurrence and its characteristics, on Lupo and Smith (1995), on Lejenas and Okland's (1983) criterion LO = z(40°) − z(60°), and on the adjusted criterion by Wiedenmann et al. (2002) BI = 100.0[(MZ/RC) − 1.0], where MZ was the maximum 500-hPa height in the closed anticyclone region or on a line associated with

Table 1 Kutiel classification

z scores	Wet month	z scores	Dry month
$1.5 < z$	Strong	$-1.5 < z$	Strong
$0.5 \leq z \leq 1.5$	Weak	$-0.5 \leq z \leq -1.5$	Weak
$0 < z < 0.5$	Moderate	$0 < z < -0.5$	Moderate

Table 2 Relative frequency (%) of the number of precipitation anomalies from 1978 to 2007 due to Kutiel classification

Wet			Dry		
Weak	Moderate	Extreme	Weak	Moderate	Extreme
14.64	11.59	13.13	27.63	26.75	6.25

the ridge axis, and RC the subjectively chosen representative contour (Glisan and Lupo 2008). Using the archive, the whole blocking events occurred in this region was detected. In addition, the precipitation anomalies were determined using z scores and Kutiel Classification Criterion (Table 1). The standard score is: $z = (x_i - \bar{x})/sd$. Standard scores over 0.5 and less than -0.5 were defined as positive and negative precipitation anomalies, respectively.

In the next step, the relationship between blocking occurrence and precipitation anomalies was investigated based on synoptic analysis and examination of vorticity advection field and vertical motion (Omega) of the air. Because blocking event has a quasi-stationary nature, during blocking, the atmospheric flux will show an enduring time-and-place feature. Konrad and Colucci (1988) and Lupo et al. (2008) showed that the enduring and quasi-stationary nature of the blocking is effective on climatic upstream and downstream of the blocking.

4 Precipitation Anomalies

Standard scores of monthly precipitation of the synoptic stations of Iran were divided to six categories based on Kutiel (1996) classification (Table 2). The results show that the most percentage of frequency of the occurrence of positive precipitation anomalies is observed in the class with extreme humidity ($z \geq 1.5$), while the most percentage of frequency of the occurrence of negative precipitation anomalies is observed in the class of moderate and low humidity ($z \leq -0.5$ and $-0.5 \geq z \leq -1.5$).

It is obvious that in the overall negative and positive z scores, the frequency of occurrence of negative precipitation anomalies is more than that for positive precipitation anomalies, indicating that precipitation in Iran displays negative skewness. On the other hand, the occurrence of positive anomalies/wet months is more intense (Table 3).

Table 3 Frequency of the number of precipitation anomalies from 1978 to 2007 for each month due to subjective classification

Frequency	Jan	Feb	Mar	Apr	May	Oct	Nov	Dec	Total
Wet months	10	8	7	11	5	5	7	7	60
Dry months	7	10	9	14	13	8	12	10	83

5 Relationship Between Abnormal Rainfall and Blocking Episodes: Case Study of the Blocking of 7–17 November 1993

As mentioned before, the records of the occurrence of the blocking was obtained from CBS archive. In this section, the blocking event that occurred in November 7–17 1993 and contributed to the occurrence of positive precipitation anomaly, are examined for illustration as the case study. Coincided with dipole blocking, in November 13th, when blocking displayed its maturity, the total of daily precipitation of half of the synoptic stations of Iran such as Rasht, 83 mm, Kermanshah, 37 mm, and Isfahan, 37 mm has been recorded.

Analysing the map 500 hpa, it is observed that in the day November 13, the centre of anticyclone is superimposed on the longitude of 40°. Due to quasi-stationary and large scale of the blocking nature, when blocking occurs, it is expected that circulatory fluxes such as vorticity advection display prolonged time-and-place feature. Humidity and ascending air are integral parts. In November 13, the maximum value of the vorticity advection was observed as 10.5 R/s, indicating that situations conducive to ascension under the trough in the period of maximum cyclonic circulation of the air. This value is also observed in centre of closed low (Fig. 1a).

Stationarity of positive vorticity advection around closed cell of southern low and also of blocked period of November, 7–17 1993 is indicative of the quasi-stationary nature of blocking system and sustainability of positive vorticity advection. In the same day, the ascension speed of the air on the vertical motion map of the air (Omega) shows settling of a centre of maximum air ascension as −0.3 Pa/s between level of 500 and 850 hpa in front of the southern trough of dipole blocking (Fig. 1b). In the wind and specific humidity composite map, drawn between 700 and 850 hpa, a route of wind direction and consequently, humidity advection is identified around cyclonic circulation (Fig. 1c). The important point is that, although humidity advection is negligible in this day, the cause to which precipitation in November 13th can be attributed is the maximum ascension of the air around cyclonic circulation. It is justified based on the maximum value of vorticity advection and vertical motion of the air. So, following the quasi-stationary nature of the system and proper placing of the trough integral to blocking, contribute to the continuation of the ascension situation. If the front of southern/eastern trough of the dipole/omega blocking is superimposed on a region, due to the quasi-stationary feature of the system, the prolonged precipitation will be possibility. In contrast, if in the same model, the same region is under northern/western high in dipole/omega blocking, a prolonged dry spell (negative precipitation anomaly) will occur.

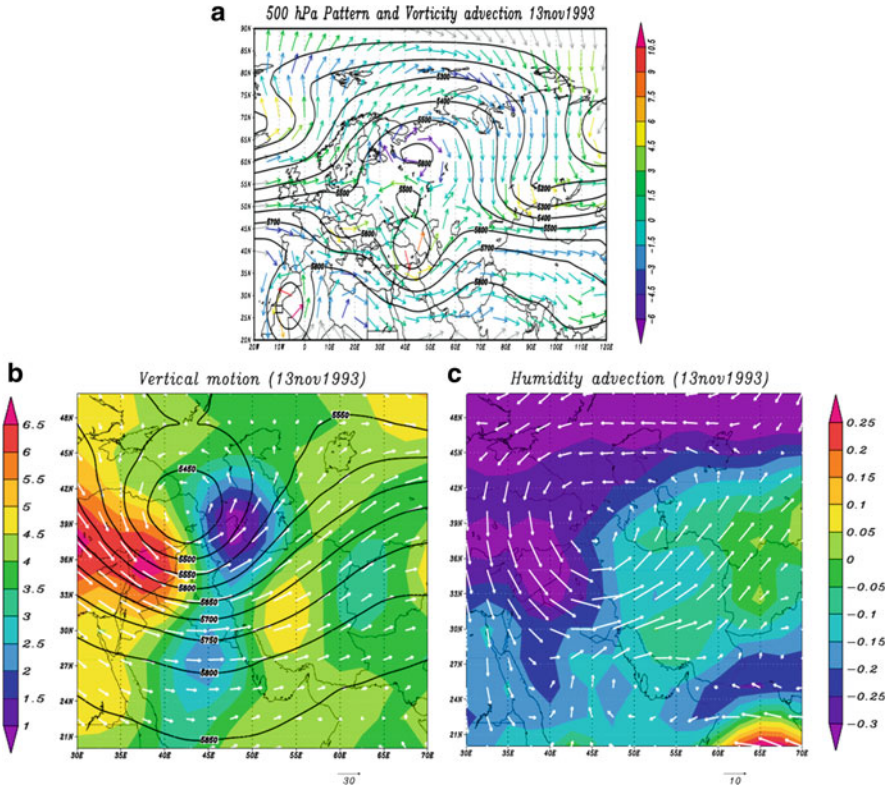

Fig. 1 (**a**) Vorticity advection (R/s) (derived by U/V wind) and NCEP-NCAR daily 500-hPa gridded (2.5° lat. × 2.5° long.). Geopotential height (in m), (**b**) Vertical motion/Omega (in Pa/s) between 850, 700 and 500 hPa and (**c**) Humidity advection (in g/kg) and wind (in m/s) between 850 and 700 hPa on 13 November 1993

According to Konrad and Colucci (1988), due to blocking, the surface cyclone intensified and the trough created in middle levels moves to northeast. Therefore, the conditions contributing to precipitation anomalies for Iran are highly dependent to the geographical occurrence of the blocking and the type of the occurrence, i.e. the trough/ridge position.

6 Conclusions

We found precise results by using blocking events and precipitation anomalies that can be summarized as follows: z scores obtained for the period of 1978–2007 are different for positive/negative classification. During the examined period, the frequency of occurrence is greater for negative anomalies, than for wet months, i.e. positive anomalies. The positive anomalies exhibited higher occurrence

frequency for extreme classification. Thus, the positive anomalies are stronger than negative anomalies. In general, the overall changes in geopotential height, especially in vorticity advection and vertical motion of the air (omega) can contribute to formation, duration, and diminishing of the blocking phenomenon and can help identify the maximum cyclonic/anticyclonic circulation period in the centers of synoptic systems. On the relationship between blocking and precipitation anomalies in Iran, it was found that due to the quasi-stationary nature of blocking system, atmospheric fluxes such as vorticity advection displays positive anomaly in the cyclonic region and negative anomaly in anticyclonic region. These results are in agreement with other previous studies obtained using different methods (Khalili 2011).

References

Azad R (2007) Dynamic and climatic study of blocking on Eurasia. MSc thesis, Geophysics Institute, Tehran University, Iran

Azizi GH, Khalili M (2011) Roles of blocking cold in extreme cold events over Iran. Geogr Res J 72:1–19

Barry RG, Carleton AM (2001) Synoptic and dynamic climatology. Routledge, London

Buehler A, Raible CC, Stocker TF (2011) The relationship of winter season North Atlantic blocking frequencies to extreme cold or dry spells in the ERA-40. Tellus 63A:212–222

Colucci SJ, Alberta TL (1996) Planetary-scale climatology of explosive cyclogenesis and blocking. Mon Weather Rev 124:2509–2520

Glisan JM, Lupo AR (2008) An extreme case of atmospheric blocking over western Europe. In: Proceedings of the 20th conference on climate variability and change/88th annual meeting of the American Meteorological Society, New Orleans, LA, USA, 20–24 Jan 2008

Khalili M (2011) Relationship between blocking and precipitation anomalies in Iran. MSc thesis, University of Tehran, Iran

Konrad CE II, Colucci SJ (1988) Synoptic climatology of 500 mb circulation changes during explosive cyclogenesis. Mon Weather Rev 116:1431–1443

Kutiel H (1996) Circulation and extreme rainfall conditions in the eastern Mediterranean during the last century. Int J Climatol 16:73–92

Lejenas H, Okland H (1983) Characteristics of Northern Hemisphere blocking as determined from a long time series of observational data. Tellus 35A:350–362

Lupo AR, Smith PJ (1995) Climatological features of blocking anticyclones in the Northern Hemisphere. Tellus 47A:439–456

Lupo AR, Clark J, Hendin AM, Kelly A, Mihalka S, Perrin KB, Puricelli LM (2008) The global increase in blocking occurrences. In: Proceedings of the 20th conference on climate variability and change, New Orleans, LA, USA

Rex DF (1950) Blocking action in the middle troposphere and its effects upon regional climate. I: An aerological study of blocking action. Tellus 2:196–211

Triedl RA, Birch EC, Sajecki P (1981) Blocking action in the Northern Hemisphere: a climatological study. Atmos Ocean 19:1–23

Wiedenmann JM, Lupo AR, Mokhov II, Tikhonova E (2002) The climatology of blocking anticyclones for the Northern Hemisphere: block intensity as a diagnostic. J Clim 15:3459–3474

Changes of Pan Evaporation Measurements and Reference Evapotranspiration in Greece

G. Kitsara, G. Papaioannou, and P. Kerkides

Abstract In this study daily pan evaporation measurements made at 13 sites in Greece are analyzed for evidence of long-term changes. Furthermore, the similarities between magnitude and trends in observed pan evaporation (Epan) and daily estimated Penman-Monteith reference evapotranspiration (ETp-m) are examined within the same period (1979–2004), for investigating the use of ETp-m estimates as a guide for future changes in evaporation. The results show that ETp-m and Epan are well correlated on a yearly, seasonal, warm and cold period and monthly basis. Trends in Epan and ETp-m are found positive for most of the stations on a yearly or warm and cold period or during the seasons (except of autumn). When examining Epan or ETp-m trends for every month separately, increases are mainly concluded for most of the months. Median trends in yearly and seasonal ETp-m and Epan are similar in sign. ETp-m and Epan median trends for each month are in agreement (mostly positive) for 75% of the months. When all stations are considered 'as a whole', annual, seasonal, warm and cold period Epan and ETp-m estimates show insignificant increases, while rainfall trends are significantly negative.

1 Introduction

Contrary to the expectation that a warmer climate will increase evaporation, many studies have reported decreasing or increasing pan evaporation over the past 50 years or so, for many places of the world as summarized by Roderick et al.

G. Kitsara • G. Papaioannou (✉)
Department of Physics, University of Athens, Panepistimioupolis Zographos, Phys-5 Building, Athens 15784, Greece
e-mail: gpapaioa@phys.uoa.gr

P. Kerkides
Department of Water Resources Management, Agricultural University of Athens, Iera Odos 75, Athens 1185, Greece

C.G. Helmis and P.T. Nastos (eds.), *Advances in Meteorology, Climatology and Atmospheric Physics*, Springer Atmospheric Sciences,
DOI 10.1007/978-3-642-29172-2_75,

(2007); Kirono et al. (2008); Fu et al. (2009) and Papaioannou et al. (2011). The interpretation mainly of negative trend has been controversial, either explained by the complementary relationship (Brutsaert and Parlange 1998) or attributed in decreasing solar irradiance (global dimming) (Cohen et al. 2002; Roderick and Farquhar 2002; Ohmura and Wild 2002; Liu et al. 2004; Wild et al. 2004). It has been shown that both effects (global dimming and the complementary relationship) can be combined (Brutsaert 2006) or even decreasing actual evapotranspiration with decreasing pan evaporation in regions with ample supply of water and increasing evapotranspiration with decreasing pan evaporation can be encompassed (Teuling et al. 2009). Recently, 'stiling' (the declining rates of observed near-surface wind speed) has been identified as a key factor reducing pan evaporative rates (as summarized by McVicar et al. 2012).

Trends in reference evapotranspiration have been also reported negative for some regions and positive for other ones (as summarized by Kirono et al. 2008) and they have been found as decreasing and increasing following the global dimming/brightening periods (Papaioannou et al. 2011). Recently, modeled Penman potential evaporation over all land areas of the globe has been found as following closely the trends of energy availability and not the trends of the atmospheric capability for vapor transfer (Matsoukas et al. 2011).

The present study focuses on the relationship, for Greece, between pan evaporation measurements and Penman-Monteith reference evapotranspiration values or their trends in order to investigate the use of ETp-m estimates as a useful guide for future changes in evaporation. The similarities between either their magnitudes or their trends are examined. Temporal analysis is presented for daily pan measurements (Epan) and reference evapotranspiration (ETp-m), as well as, for other meteorological attributes, as daily precipitation and wind velocity on yearly, seasonal or monthly basis.

2 Data and Methodology

In this study daily measurements of precipitation and evaporation from class-A pans (Epan) provided by the National Meteorological Service for 13 stations in Greece, during the period 1979–2004, are used. The stations, chosen on the basis of the records, being available for as long as possible are: Serres (41° 05′, 23° 34′), Trikala Im. (40° 36′, 22° 33′), Mikra (40° 31′, 22° 58′), Alex/poli (40° 51′, 25° 26′), Larisa (39° 39′, 22° 26′), Aghialos (39° 13′, 22° 48′), Agrinio (38° 37′, 21° 33′), Adravida (37° 55′, 21° 17′), Pirgos (37° 40′, 21° 26′), Kalamata (37° 04′, 22° 06′), Iraklio (35° 20′, 25° 11′), Ierapetra (35° 00′, 25° 24′), Tymbaki (35° 00′, 24° 46′).

Daily measurements of dry- and wet-bulb temperature, wind velocity and sunshine hours, for the above mentioned 13 stations, during the same period are also considered, for estimating ETp-m by Penman-Monteith method. The daily ETp-m is calculated as potential evapotranspiration from hypothetical reference

grass with an assumed height of 0.12 m, a fixed surface resistance of 70 s m^{-1} and an albedo of 0.23, according to Allen et al. (1998).

Trends in pan evaporation values, ETp-m estimates, precipitation and wind velocity for all stations considered as individuals or as a 'whole', are estimated on annual, cold (November–April) and warm (May–October) period, seasonal and monthly basis during the period 1979–2004. Having established their significance by the nonparametric Mann-Kendall test, recommended by the World Meteorological Organization, the magnitude of the time trends is determined using standard parametric regression methods.

3 Results

The correlation coefficient (r) between Epan and ETp-m and their mean and standard deviation values (as averaged across the 13 sites, for each month or year) are presented in Table 1. It is obvious that the mean values of Epan are higher than the ones of ETp-m and the magnitude of the variability of Epan is higher than ETp-m as indicated from its standard deviation values being almost twice the ETp-m ones, for most of the months. The correlation between Epan and ETp-m ranges from 0.57 to 0.81 for each month and equals to 0.80 on an annual basis.

The slopes of the trends of Epan and ETp-m are calculated for each station and various time periods. Table 2 shows the number of the stations with negative and positive sign (with the ones having trends at the 95% level of significance shown in parenthesis). The signs of the Epan trends were found positive in 9 or 7 and 8 or 9 or 10 or 8 sites on annual or warm and cold period basis, or during winter, spring and summer, respectively. In addition, 7 sites show positive ETp-m trends on annual

Table 1 Mean and standard deviation of monthly and annual, pan measurements (Epan) and Penman-Monteith evapotranspiration (ETp-m), as averaged across the 13 sites and correlation coefficient r between Epan and ETp-m

	Mean (mm/month)		St.-dev (mm/month)		r
	Epan	ETp-m	Epan	ETp-m	
January	45.16	32.79	31.79	14.32	0.77
February	52.85	42.28	30.10	12.54	0.75
March	88.18	66.99	29.44	14.25	0.73
April	123.29	93.85	26.46	14.94	0.68
May	176.81	135.33	34.07	17.56	0.59
June	239.13	174.91	42.69	22.39	0.57
July	281.25	195.63	58.11	36.11	0.73
August	253.66	172.94	55.57	33.68	0.77
September	179.47	117.74	42.98	25.82	0.75
October	116.48	72.98	36.14	21.33	0.81
November	64.90	40.36	30.70	16.77	0.80
December	49.86	30.51	33.33	14.64	0.76
Annual	139.25	98.03	29.40	17.74	0.80

Table 2 Total number of stations with positive and negative trends in pan measurements (Epan), Penman-Monteith evapotranspiration (ETp-m), precipitation (P) and wind speed (U)

	Trend direction							
	Epan		ETp-m		P		U	
	(+)	(−)	(+)	(−)	(+)	(−)	(+)	(−)
January	8(0)	5(3)	2(0)	11(3)	6(0)	7(0)	2(0)	11(5)
February	10(2)	3(0)	8(4)	5(1)	0	13(1)	4(1)	9(3)
March	9(1)	4(0)	7(1)	6(0)	2(0)	11(0)	5(2)	8(2)
April	6(1)	7(1)	7(0)	6(0)	1(0)	12(1)	5(1)	8(2)
May	10(3)	3(1)	13(3)	0	4(0)	9(0)	6(3)	7(1)
June	9(5)	4(2)	12(4)	1(0)	3(0)	10(1)	7(3)	6(2)
July	7(3)	6(1)	7(3)	6(0)	7(0)	6(0)	6(2)	7(2)
August	7(3)	6(1)	8(0)	5(0)	7(0)	6(0)	5(0)	8(3)
September	3(0)	10(3)	2(0)	11(6)	12(3)	1(0)	5(1)	8(2)
October	6(1)	7(3)	5(0)	8(0)	3(0)	10(1)	4(0)	9(0)
November	6(1)	7(0)	8(1)	5(1)	0	13(2)	4(1)	9(1)
December	3(0)	10(1)	4(0)	9(3)	9(0)	4(0)	4(1)	9(4)
Winter	9(2)	4(1)	7(2)	6(0)	8(0)	5(0)	5(1)	8(6)
Spring	10(2)	3(1)	11(3)	2(0)	1(0)	12(2)	7(3)	6(2)
Summer	8(3)	5(2)	10(4)	3(0)	5(0)	8(0)	5(2)	8(3)
Autumn	4(0)	9(3)	3(0)	10(2)	1(0)	12(0)	5(1)	8(3)
Warm seas.	7(3)	6(2)	7(3)	6(0)	4(0)	9(0)	5(2)	8(3)
Cold seas.	8(2)	5(0)	9(3)	4(0)	5(0)	8(0)	5(1)	8(7)
Annual	9(2)	4(2)	7(3)	6(0)	2(0)	11(2)	4(2)	9(4)

The ones with significant trends are shown in parenthesis

and warm season basis, and 9 sites, during the cold period. During winter, spring and summer ETp-m trends are mainly increasing in 7 or 11 or 10 sites respectively. On the contrary, 10 sites show negative ETp-m trends during autumn. The median trends of Epan and ETp-m have been found positive for yearly, warm and cold period, winter, spring and summer and negative during autumn in the majority of the cases. Precipitation (P) or wind speed (U) indicates negative trends in most of the stations (Table 2) for all periods except of winter or spring, respectively.

Epan or ETp-m trends calculated for each month are positive for 8 or 11 months, respectively (Fig. 1a). The signs of Epan and ETp-m median trends are positive and they are found in agreement, on average, at 75% of the sites for most of the months (7 or 8, respectively). An agreement between positive Epan and ETp-m median trends has been achieved for more months (6) as compared to the negative ones (3). Precipitation or wind speed trends are found (insignificantly) negative in almost all months except September or June, respectively.

When all stations are considered 'as a whole', the slopes of the trends of the Epan, ETp-m and P annual values averaged over the 13 sites are shown in Fig. 1b. Epan and ETp-m trends are positive (0.92 and 0.71 mm/y^2, respectively) and P trends are statistically significant negative (−4.45 mm/y^2).

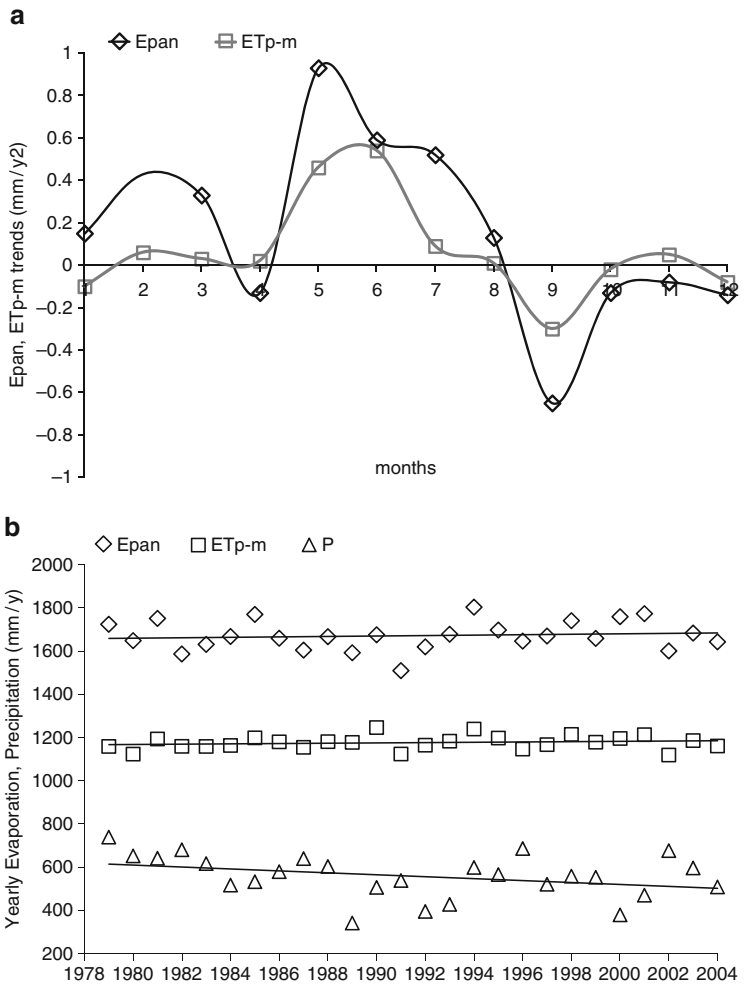

Fig. 1 Median trends of monthly pan measurements (Epan) and Penman-Monteith reference evapotranspiration (ETp-m) for any given month, as obtained from 13 stations (**a**). Trends of annual Epan, ETp-m and precipitation (P) based on the all stations average time series (**b**)

4 Conclusions

The behavior of Epan and ETp-m may not always be similar throughout time since Epan measures evaporation from a small open water surface, whereas ETp-m measures evaporation from a small land surface with unlimited water. Thus, the temporal and spatial variability of Epan has been found higher than that of ETp-m. Monthly, seasonal and annual Epan measurements and ETp-m estimates are rather related and the trends in observed Epan are partly reproduced by the trends in calculated ETp-m.

Epan and ETp-m trends are found mainly positive during all examined periods (except of autumn) for most of the sites and this is also verified from their median trend values. Almost all rainfall trends have been found negative for all timescales (except of winter). Wind speed trend is found mainly decreasing. When the analysis is performed on a monthly basis Epan (or ETp-m) trends and their median values are also found positive for most of the months. The analysis for all stations considered 'as a whole' results in statistically insignificant positive trends for Epan or ETp-m, but significant negative for precipitation.

The positive Epan or ETp-m trends may be attributed to the 'brightening' period, which is mainly included in the examined period (1979–2004). The observed wind speed trend has been found mainly negative. Decreases in wind speed have been combined mainly with declining pan measurements or Penman-Monteith estimates, whereas increases in wind speed have been combined, with increases in Epan. In this study, the negative wind speed trend has rather counteracted the brightening effect resulting in a smaller positive trend.

Acknowledgments The authors wish to express their thanks, to the National Meteorological Service of Greece, for providing the data. This research has been co-financed by the European Union (European Social Fund – ESF) and Greek national funds through the Operational Program 'Education and Lifelong Learning' of the National Strategic Reference Framework (NSRF) – Research Funding Program: Heracleitus II. Investing in knowledge society through the European Social Fund.

References

Allen RG, Pereira LS, Raes D, Smith M (1998) Crop evapotranspiration: guidelines for computing crop water requirements. FAO Irrigation and Drainage Paper 56. FAO, Rome

Brutsaert W (2006) Indications of increasing land surface evaporation during the second half of the 20th century. Geophys Res Lett 33:L20403. doi:10.1029/2006GL027532

Brutsaert W, Parlange M (1998) Hydrologic cycle explains the evaporation paradox. Nature 396:29–30

Cohen S, Ianetz A, Stanhill G (2002) Evaporative climate changes at Bet Dagan, Israel, 1964–1998. Agric Forest Meteorol 111:83–91. doi:10.1016/S0168-1923(02)00016-3

Fu G, Charles SP, Yu J (2009) A critical overview of pan evaporation trends over the last 50 years. Clim Chang 97:193–214. doi:10.1007/s10584-009-9579-1

Kirono DGC, Jones RN, Cleugh A (2008) Pan-evaporation measurements and Morton-point potential evaporation estimates in Australia: are their trends the same? Inter J Climatol 29 (5):711–718. doi:10.1002/joc.1731

Liu B, Xu M, Henderson M, Gong W (2004) A spatial analysis of pan evaporation trends in China, 1955–2000. J Geophys Res 109:D15102. doi:10.1029/2004JD004511

Matsoukas C, Benas N, Hatzianastassiou N, Pavlakis KG, Kanakidou M, Vardavas I (2011) Potential evaporation trends over land between 1983–2008: driven by relative fluxes or vapour-pressure deficit? Atmos Chem Phys 11:7601–7616. doi:10.5194/acp-11-7661-2011

McVicar T, Roderick M, Donohue R, Li L, Van Niel T, Thomas A, Grer J, Himri Y, Mahowald N, Mescherskaya A, Kruger A, Rehman S, Dinpashoh Y (2012) Global review and synthesis of the trends in the observed terrestrial near-surface wind speed: implications for evaporation. J Hydrol 416–417:182–205. doi:10.1016/j.jhydrol.2011.10.024

Ohmura A, Wild M (2002) Is the hydrologic cycle accelerating? Science 298:1345–1346. doi:10.1126/science.1078972

Papaioannou G, Kitsara G, Athanasatos S (2011) Impact of global dimming and brightening on reference evapotranspiration in Greece. J Geophys Res 116:D09107. doi:10.1029/2010JD015525

Roderick ML, Farquhar GD (2002) The cause of decreased pan evaporation over the past 50 years. Science 298:1410–1411

Roderick ML, Rotstayan LD, Farquhar GD, Hobbins MT (2007) On the attribution of changing pan evaporation. Geophys Res Lett 34:L17403. doi:10.1029/2007GL031166

Teuling AJ, Hirschi M, Ohmura A, Wild M, Reichstein M, Ciaias P, Buchmann N, Ammann C, Montagnani L, Richardson AD, Wohlfahrt G, Seneviratne SI (2009) A regional perspective on trends in continental evaporation. Geophys Res Lett 36:L02404. doi:10.1029/2008GL036584

Wild M, Ohmura A, Gilgen H (2004) On the consistency of trends in radiation and temperature records and implications for the global hydrological cycle. Geophys Res Lett 31:L11201. doi:10.1029/2003GL019188

Homogenization of Temperature Time Series of Western Greece

K.V. Kolokythas and A.A. Argiriou

Abstract Time series of climatic data are the basis in research on climate behavior and climate change. Climatic time series have to be as complete as possible and also as homogeneous as possible, in the sense that their variations should reflect changes in climate and not changes due to other reasons. Nevertheless, there are a number of factors that affect measurements of climatic parameters which may have as impacts abrupt or smother shifts and trends in the corresponding time series. Several methods have been developed in order to detect and correct these non-homogeneities. In this paper the Multiple Analysis of Series for Homogenization (MASH) method is applied to monthly mean temperature time series from a network of meteorological stations in Western Greece aiming at indentifying probable break-points, outliers and trends, and adjusting them in order to have a quality controlled and homogenized temperature time series for the specific area.

1 Introduction

A time series of a climatic variable (air temperature, humidity, pressure, wind speed and direction, etc.) is considered homogeneous if its variability is due only to changes of the regional weather and climate. However, collection of climatic data is often exposed to artificial influences such as relocation of weather stations, replacement of observers and/or instruments, changes in the environment or even changes in the observation rules. As recognized and widely accepted that long and reliable observation series are required to address climate change issues and impact studies, the knowledge of any inhomogeneity existing in climatic time series is vital (Aguilar et al. 2003).

K.V. Kolokythas (✉) • A.A. Argiriou
Laboratory of Atmospheric Physics, University of Patras, University Campus,
Patras GR-265 00, Greece
e-mail: ckkolmet@yahoo.gr

C.G. Helmis and P.T. Nastos (eds.), *Advances in Meteorology, Climatology and Atmospheric Physics*, Springer Atmospheric Sciences,
DOI 10.1007/978-3-642-29172-2_76,

Different statistical tests can be used for the detection of artificial changes – inhomogeneities – of the statistical properties of climatic variables such as long-term averages, trends or standard deviations. Homogenization methods can be classified into two groups: *absolute* and *relative ones* (Pandžic and Likso 2010). In this paper the Multiple Analysis of Series for Homogenization (MASH) method (Szentimrey 2008) – a relative method – is used for the examination of a network consist of 8 WMO weather stations of Western Greece, for the period 1955–2003. The aim is to test the homogeneity of the time series, detect probable breakpoints, outliers and trends and correct them in order to obtain a set of temperature data series for the region for a relatively long period (49 years) as precise as possible, without artificial shifts and/or biases, that would give us a more reliable outline of the climate and its provoked changes in Western Greece.

2 Method

The MASH method is a relative homogeneity test that does not assume the reference series as homogeneous. Its mathematical principle relies on difference time series which are constructed by subtracting the candidate time series from the weighted reference time series. Since all difference time series are calculated with respect to the candidate series, the breakpoints detected simultaneously in all time series can be attributed to the candidate one. This is achieved by multiple comparisons of a set of optimal difference time series take place each time. This set is presented below:

$$Z_j(t) = X_j(t) - \sum_{i \neq j} \lambda_i X_i(t) = IH_j(t) - \sum_{i \neq j} \lambda_i IH_i(t) + \varepsilon_{z_j}(t), (\mathrm{j} = 1, 2, \ldots \mathrm{N}) \quad (1)$$

In (1) Z_j are the optimal difference time series, X_j the candidate time series and $\sum_{i \neq j} \lambda_i X_i(t)$ the sums of reference series built for the candidate $X_j(t)$. The best weighting factor λ_i is defined the one which eliminates the variance of difference time series (reduces the noise $\varepsilon_{Zj}(t)$) resulting in increasing of the effectiveness of test statistics, and is a vector of the following shape:

$$\lambda_i = C_{ref}^{-1} \left(c_{c,ref} + \frac{\left(1 - 1^T C_{ref}^{-1} c_{c,ref}\right)}{1^T C_{ref}^{-1} 1} 1 \right) \quad (2)$$

with $c_{c,ref}$ a covariance vector of candidate and reference time series, and C_{ref} covariance matrix of reference series.

The detection of breakpoints is based on the examination of hypothesis for a significance level, taking into account both type one (false detected inhomogeneity) and type two (existence of a real break point that we could not detect) errors.

3 Stations Network and Tested Time Series

The MASH method is applied on time series of mean ambient temperatures measured in eight WMO weather stations (Table 1) of Western Greece belonging to the Hellenic National Meteorological Service (H.N.M.S.), for the period 1955–2003. All stations belong to the same climatic type defined as humid Mediterranean (Flokas 1992).

In this work a modified version of the MASH method was applied. The homogenization procedure is divided in two parts. First the parts of the time series with no or very few missing values (1970–2003) are homogenized. Then those homogenized parts are merged with the remaining parts of time series (1955–1969) where larger data gaps exist. Finally the homogenization procedure is applied on the merged time series, resulting to their overall homogenization.

At the beginning, correlation coefficients for all time series are computed based on mean monthly temperatures before homogenization. As shown, time series have in general very good cross correlation, with a mean correlation coefficient equal to 0.87. An exception is the time series of Zakynthos, which doesn't show so good correlation with those of Kerkyra and Aktio. Therefore, during homogenization procedure Kerkyra and Aktio time series were not considered as reference series for the time series of Zakynthos. Similarly the series of Zakynthos was not considered as reference for the series of Kerkyra and Aktio as well.

During the whole procedure, the defined significance level for the test statistics is 0.05. The length of the time series is 49 years (≈50), corresponding to a critical value for test statistics before homogenization (TSB) and after homogenization (TSA) of 20.86 (scores over that critical value mean that the tested time series are inhomogeneous, while equal or bellow that value the time series consider homogeneous).

4 Conclusions

1. The total number of the detected breakpoints in all time series varies among stations for the different time scales (monthly, seasonal, and annual). Considering the results of test statistics performed at the final stage of homogenization (TSAs), the examined time series at the end of the procedure appear to be homogeneous. Figure 1 shows the annual time series of all stations before (top) and after homogenization (down).
2. The majority of time series show a decreasing mean temperature after homogenization. Furthermore the linear trend of the mean temperature of the annual

Table 1 Description of the characteristics of the meteorological stations

Station	WMO code	Latitude	Longitude	Station altitude (m)	Begin	End	Years with missing data
Kerkyra (KR)	16641	39°5N	19°8^{E}	4	1955	2003	–
Aktio (PZ)	16643	38°9N	20°7^{E}	4	1971	2003	17
Agrinio (AG)	16672	38°6N	21°3^{E}	47	1956	1968	2
					1970	2003	
Kefalonia (KF)	16685	38°1N	20°4^{E}	22	1970	1987	17
					1989	2003	
Zakynthos (ZA)	16710	37°7N	20°8^{E}	3	1957	1957	6
					1959	1965	
					1969	2003	
Araxos (RX)	16687	38°1N	21°3^{E}	15	1955	2003	–
Andravida (AD)	16682	37°5N	21°3^{E}	12	1959	2002	5
Kalamata (KL)	16726	37°N	21°9^{E}	8	1956	2003	1

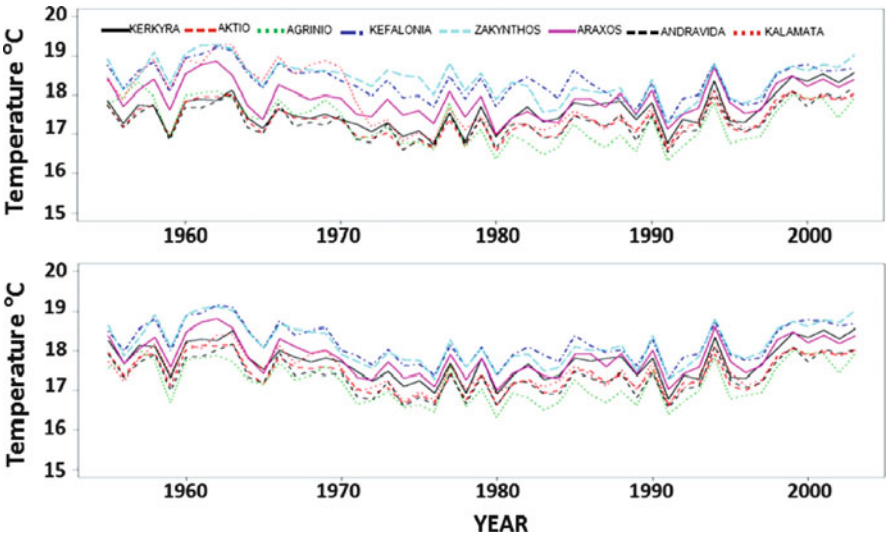

Fig. 1 *Top graph*: annual time series before homogenization. *Down graph*: annual time series after homogenization

time series of all stations for the period 1955–2003 is slightly declining but with a lower slope than before homogenization (Fig. 2). On Fig. 2 are also illustrated the linear regression lines of the total mean temperature before and after homogenization and the corresponding regression equations.

3. Examining the time series in relation to the total mean, the period 1955–2003 can be divided into three parts. In the first part, from 1955 till the beginning of 1970, the mean temperature of all stations is higher than the total mean. In the second one (early 1970 to middle 1990) – which differs among stations – the mean temperature is lower than the total mean, while in the last part

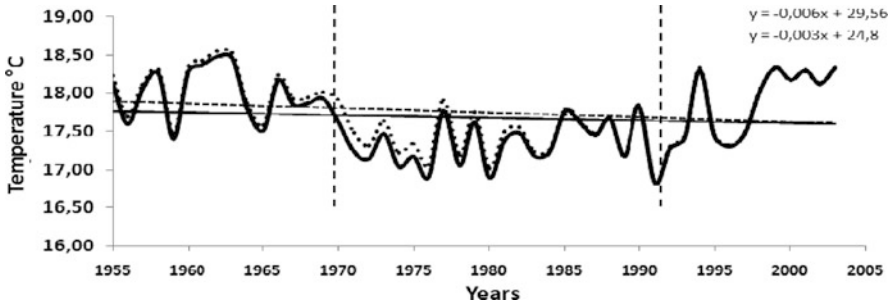

Fig. 2 Variation of the mean temperature (mean of the means of all time series) for the period 1955–2003. *Dotted line* presents the variation of total mean before homogenization and *solid line* after homogenization. Also the corresponding linear regression lines with their equations are shown

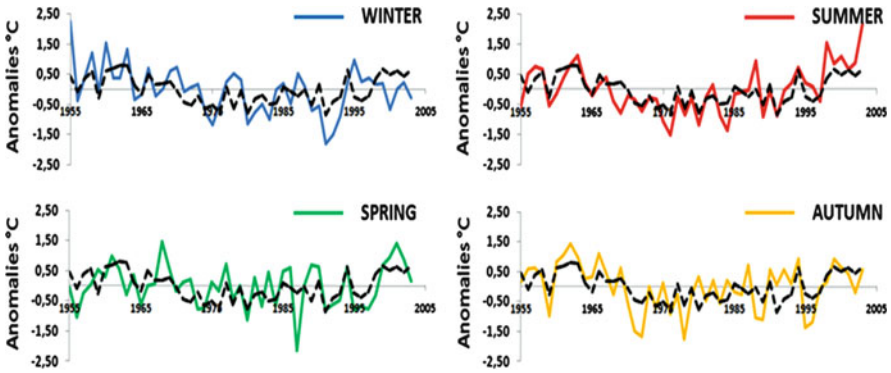

Fig. 3 Anomalies of the total mean temperature (*black dashed line*) and of the mean temperatures of all time series per season for the period 1955–2003

(common for all stations) the temperature has a constantly increasing trend. This division is also represented by the two dashed lines in Fig. 2.

4. In Fig. 3 there are four graphs representing the anomalies of mean temperature of the complete network for each season together with the anomalies of the annual mean. From these graphs it appears clearly that the mean temperature of the summer time series has almost the same variability as the annual mean. This fact reveals that the influence of the summer temperature on the total mean temperature may account for the total temperature fluctuation.

Based on these results, it is estimated that the explicit and constant increasing trend of summer temperature as well as the lack of another trend (of the same magnitude) in the three other seasons, are the main reasons causing the abrupt increase of the annual mean temperature from the beginning of 1990s, in all time series. This is also supported by a number of scientific works studying the temperature variation in Greece for the last 100 years (Proedrou et al. 1997; Feidas et al. 2004; Akilas et al. 2005).

5 Discussion

The correction of time series of climatic data may be a difficult and demanding work. However, taking into account the inhomogeneities these time series probably have, this work is considered to be of major importance regarding research on climate change. The homogenization of climatic time series, except for the detection and adjustment of inhomogeneities, leads in the filling of missing values, either sparse or systematic. So, the completed and homogenized series may be used for the better and more reliable studying of the climate of a significant region, as reference time series for the homogenization of other series, or even for comparing homogenization results with those of previous or future works.

Acknowledgments The authors would like to thank T. Szentimrey and M. Lakatos of the Hungarian Meteorological Service for their helpful and useful comments for better understanding and operating of M.A.S.H. used in this work and E. Anadranistakis and A. Mamara of the Hellenic National Meteorological Service for providing all the necessary data.

References

Aguilar E, Auer I, Brunet M, Peterson TC, Wieringa J (2003) Guidelines on climate metadata and homogenization. World Meteorological Organization WMO/TD No. 1186

Akilas E, Likoudis S, Lalas D (2005) Climatic change in Greek region. Analysis of observations: trend of the late 100 years. Observatory climatic changes. National Observatory of Athens, Chapter 5, pp 23–38

Feidas H, Makrogiannis T, Bora-Senta E (2004) Trend analysis of air temperature time series in Greece and their relationship with circulation using surface and satellite data: 1955–2001. Theor Appl Climatol 79:185–208. doi:10.1007/s00704-004-0064-5

Flokas A (1992) Meteorology and climatology. Zitis Publishers, Thessaloniki

Pandžic K, Likso T (2010) Homogeneity of annual air temperature time series for Croatia. Int J Climatol 30:1215–1225. doi:10.1002/joc.1922

Proedrou M, Theoharatos G, Cartalis C (1997) Variations and trends in annual and seasonal air temperature in Greece determined from ground and satellite measurements. Theor Appl Climatol 57. doi:10.1007/BF00867977

Szentimrey T (2008) Multiple analysis of series for homogenization (MASH v3.02). In: Proceedings of the second seminar for homogenization of surface climatological data, Budapest, Hungary, WMO, WCDMP-No. 41, pp 27–46

Evaluation of Cloud Description in General Circulation Models Using A-Train Observations

D. Konsta, H. Chepfer, and J.L. Dufresne

Abstract The representation of clouds and cloud feedbacks remain very different from one model to another, and they still constitute a major limitation to the reliability of climate change projections. It is therefore imperative to improve the representation of cloud processes in models. Until recently, the evaluation of several fundamental aspects of the cloudiness as the three-dimensional distribution of the cloud cover has been largely indirect, based on passive remote sensing satellites (e.g. ERBE, Scarab, ISCCP) which measure the TOA radiative fluxes. The A-train observations constitute exceptional tools to characterize the cloud properties. We will show that due to errors compensations, the climate models produce correct top-of the atmosphere fluxes. The A-train observations (CALIPSO, PARASOL, CERES) are used to unravel the errors compensations and to evaluate quantitatively the clouds description in various climate models using the COSP (CFMIP Observation Simulator Package) within the CFMIP (Cloud Feedback Model Intercomparison Program). A process oriented evaluation is conducted by analysing statistically the co-located A-train observations at high spatial resolution to built pictures of the cloud properties at the scale of the cloud process. This multi-instrument dataset at high spatial resolution is then used to assess the cloud parametrization in a climate model.

1 Introduction

The description of clouds in climate model remains one of the main uncertainties for future climate predictions (Soden and Held 2006; Bony et al. 2006; Dufresne and Bony 2008). The evaluation of cloud description in climate models is largely

D. Konsta (✉)
Academy of Athens, Athens 10672, Greece
e-mail: dimitra.konsta@lmd.polytechnique.fr

H. Chepfer • J.L. Dufresne
LMD/IPSL, CNRS, Universite Pierre et Marie Curie, Paris, France

C.G. Helmis and P.T. Nastos (eds.), *Advances in Meteorology, Climatology and Atmospheric Physics*, Springer Atmospheric Sciences,
DOI 10.1007/978-3-642-29172-2_77,

based on the observation of the radiative budget at the top of the atmosphere in monthly mean (Webb et al. 2001, Bony et al. 2004), making the vertical structure of clouds and the instantaneous cloud properties difficult to assess. The A-train observes jointly the cloud radiative properties with passive remote sensors PARASOL, MODIS, CERES and the cloud vertical distribution with the new generation of satellites carrying radar and lidar instruments CloudSat and CALIPSO. It constitutes a unique opportunity to make quantitative evaluation of GCM cloudiness in constraining simultaneously different key cloud variables: cloud cover, cloud vertical distribution, cloud optical depth. It is also a key step to evaluate not only the mean properties of clouds, but also how different cloud variables change simultaneously at the instantaneous time scale for a same environmental change which would increase our confidence in the ability of models to predict properly the variation of clouds under environmental changes and the response of clouds to anthropogenic forcing (Konsta et al. 2012b). A-train observations contain the different information required to improve our knowledge of cloud processes at high spatial resolution and allow to build pictures of cloud processes well suited for the evaluation of model's parameterization.

In Sect. 2 we shortly describe the A-train observations and the observation simulators used. In Sect. 3 the cloud properties simulated by LMDZ5 climate model are evaluated using firstly monthly mean observations and then correlations between instantaneous cloud properties.

2 Methodology

Observations: A CERES instrument (Wielicki et al. 1996) is on board Aqua platform within the A-train and measures broadband radiances in the SW and LW domains. Here we use CERES-EBAF to measure the shortwave albedo.

The CALIOP lidar (Winker et al. 2007) thanks to its highly sensitivity to optically thin atmospheric layers and to its high horizontal resolution (333 m) is well suited to document the cloud vertical distribution in the atmosphere. To compare with GCM results, a dedicated product has been developed on a $2^\circ \times 2^\circ$ grid, called CALIPSO-GOCCP, to be fully consistent with the lidar simulator (Chepfer et al. 2010).

PARASOL (Parol et al. 2004) provides measurements of reflectance at 6×6 km^2. We use the collocated to the CALIPSO trace of this level-1 product and analyze it choosing one constant direction so that the reflectance is used as a surrogate of the cloud optical depth. In every grid box of $2^\circ \times 2^\circ$ the cloud reflectance (CR) is calculated statistically from the values of the total reflectance and the cloud fraction (CF) observed by PARASOL and CALIPSO respectively at the same time (Konsta et al. 2012a).

The LMDZ5 climate model and CFMIP simulator: The climate model used in the evaluation is LMDZ5 (Hourdin et al. 2012), the atmospheric component of the IPSL-CM5 climate model. The horizontal resolution is 1.895° (latitude) $\times$ 3.75°

(longitude) and the vertical resolution is 39 vertical levels. To make consistent comparison between the observations and model outputs we use COSP (CFMIP Observational Simulator Package, Bodas-Salcedo et al. 2011) simulator that uses the models outputs to diagnose certain variables as they would be observed from space if the satellite flew over an atmosphere similar to that predicted by the model. Here we use PARASOL (Konsta et al. 2012b) and CALIPSO simulators that simulate PARASOL radiances and the lidar signal respectively.

3 Results

Evaluation of cloud properties on monthly mean statistics: Fig. 1 shows the zonal mean SW albedo (Fig. 1a), cloud reflectance (Fig. 1b) and total cloud fraction (Fig. 1c) observed and simulated by LMDZ5. The model reproduces well the mean value of the albedo. However, this is the result of two combined errors that almost compensate: model creates clouds that are optically too thick (CR $\approx$ 0.35 i.e. Cτ $\approx$ 6.8 in LMDZ5, versus CR $\approx$ 0.3 i.e. Cτ $\approx$ 5.5 in observations) but they are too few (CF $\approx$ 50% for LMDZ5, versus $\approx$70% in observations).

Evaluation of tropical clouds using instantaneous cloud properties: The relationship between cloud fraction and optical thickness over the tropical oceans is shown in Fig. 2. When using monthly mean data (Fig. 2a, b) the observations show that as the cloud fraction increases, the cloud optical depth increases too. The model simulates a more flat relationship and does not simulate the highest values of cloud fraction. Using instantaneous data gives a significantly different but more precise picture (Fig. 2c, d). In observations clouds are gathered in two clusters, one where clouds have a low to mid fraction (CF $<$ 60%) and a low reflectance (CR $<$ 0.2) and one with a fraction close to 1 and cloud reflectance that spans from 0.1 to 0.9. The model does not reproduce these two clusters as almost no cloud with a very high fraction is simulated. Also, in the observations there is a general trend of increasing cloud reflectance with increasing cloud fraction; this trend is of wrong sign in LMDZ5.

The vertical distribution of clouds is plotted as function of the cloud reflectance (Fig. 3). Observations show that optically thin clouds (CR $<$ 0.1, i.e. Cτ $<$ 1.5) are mainly low level clouds with low values of cloud fraction. As cloud reflectance increases, the cloud fraction at all levels increase. Clouds with a large reflectance (CR $>$ 0.6, i.e. Cτ $>$ 16.5) are mainly high. However we should be aware that the fraction of low level clouds may be underestimated for high cloud reflectance values due to the attenuation of the lidar signal. For LMDZ5 high clouds strongly dominate, with their fraction being quite low and uniform (10% $<$ CF $<$ 20%). The model fails to simulate high clouds with a high fraction and a high reflectance. It also strongly underestimates the presence of low clouds (CF $<$ 10%) and simulates only those that have a high reflectance (CR $>$ 0.3). This feature is amplified by the masking effect of high clouds but is still present when looking at the actual cloud cover simulated by the model.

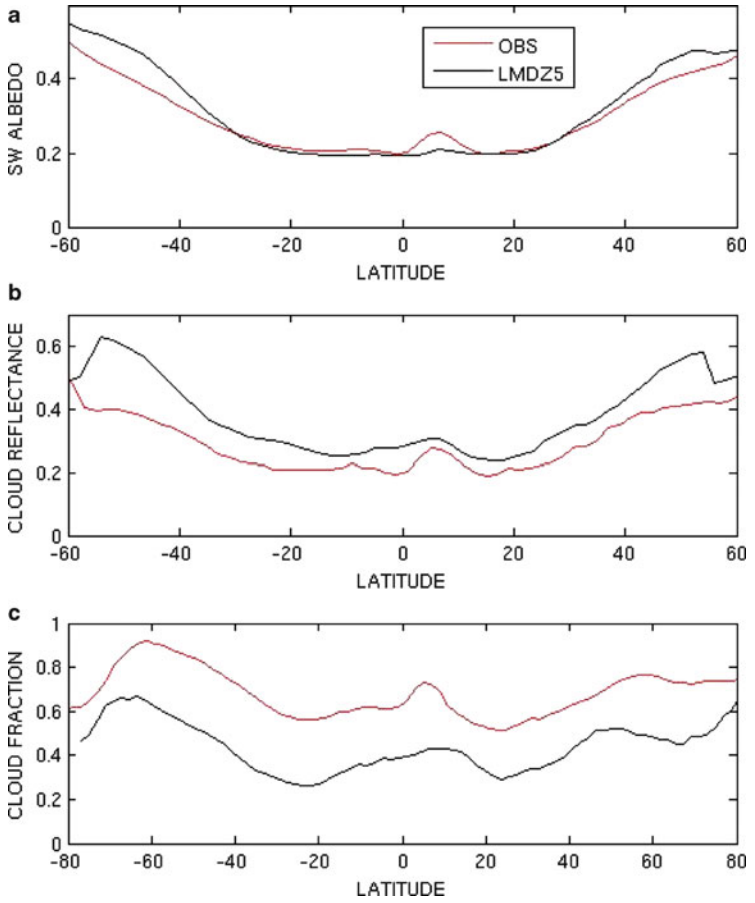

Fig. 1 Zonal mean of (**a**) diurnal SW albedo, (**b**) mono-directional cloud reflectance, and (**c**) total mean cloud fraction over ocean observed (*red line*) with CERES-EBAF and simulated (*blue line*) with LMDZ5

4 Conclusions

This study uses the A-train observations collected by CERES, PARASOL and CALIPSO to built pictures of cloud properties containing information at the cloud scale and to evaluate the characteristics of clouds simulated by the LMDZ5 atmospheric GCM on monthly mean statistics and on instantaneous and high spatial resolution. The comparison between the GCM and observations helped to identify the following biases in LMDZ5: The model underestimates the cloud fraction and overestimates the cloud reflectance so that the mean SW albedo is generally well reproduced. It overestimates the high level clouds and underestimates the low and mid level tropical clouds. It underestimates high optically thick clouds and

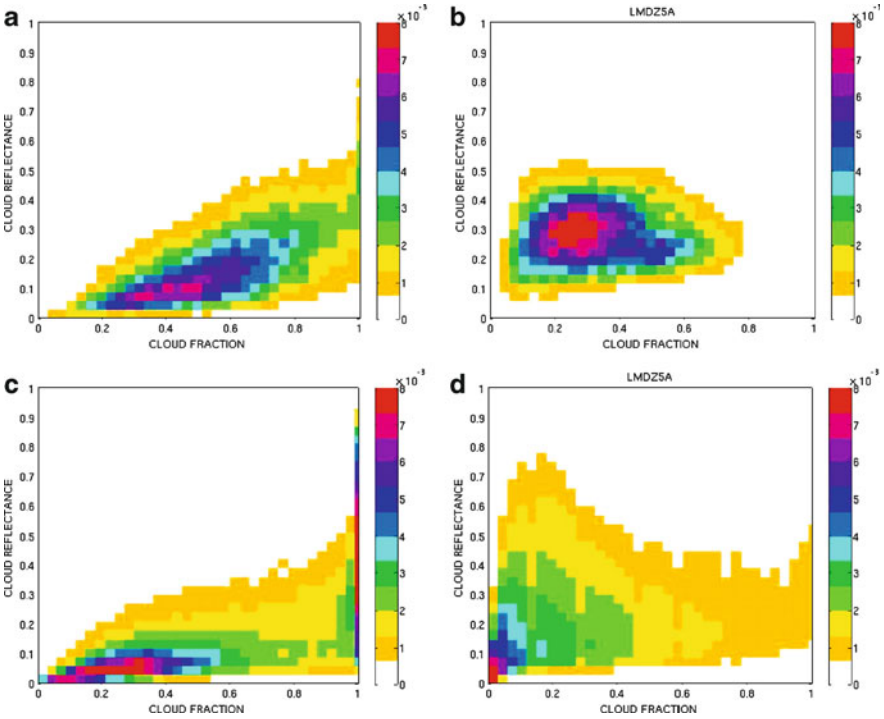

Fig. 2 2-D histograms of cloud reflectance and cloud fraction (**a**, **c**) observed with PARASOL and CALIPSO-GOCCP, (**b**, **d**) simulated with LMDZ5 and the simulator over the tropical oceans with (**a**, **b**) monthly mean values and (**c**, **d**) instantaneous values. The *colorbar* represents the number of points at each box (cloud fraction – reflectance) divided by the total number of points

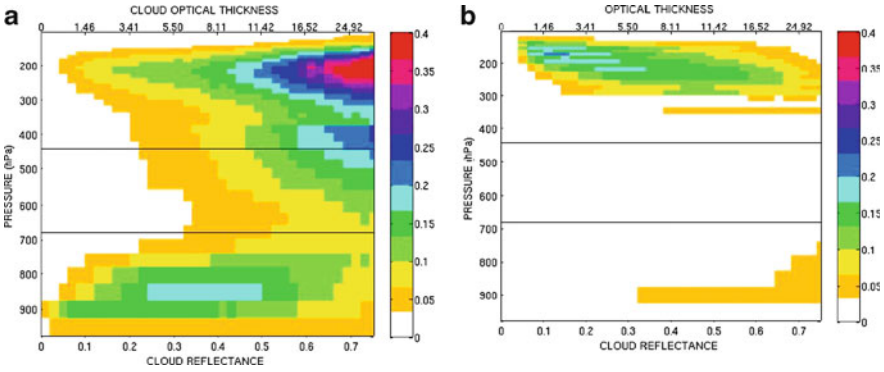

Fig. 3 Statistical relation between instantaneous cloud reflectance and vertical distribution of cloud fraction over the tropical ocean (**a**) observed with PARASOL and CALIPSO-GOCCP, (**b**) simulated with LMDZ5 and the simulator

overestimates high thin clouds. As a conclusion thanks to the A-Train observations and the COSP simulator, it is now possible to study the cloud properties at high resolution and have a powerful tool to constrain cloud description in climate models.

Acknowledgments Thanks are due to G. Cesana for providing CALIPSO-GOCCP, A. Idelkadi for running COSP simulator and S. Bony for useful discussions. CNES and NASA are acknowledged for PARASOL and CALIPSO data. Climserv/ICARE for the computing resources used.

References

Bodas-Salcedo A, Webb MJ, Bony S, Chepfer H, Dufresne J-L, Kein SA, Zhang Y, Marchand R, Haynes JM, Pincus R, John VO (2011) COSP: satellite simulation software for model assessment. Bull Am Meteorol Soc 92(8):1023–1043. doi:10.1175/2011BAMS2856.1

Bony S, Dufresne J-L, Le Treut H, Morcette J-J, Senior C (2004) On dynamic and thermodynamic components of cloud changes. Clim Dyn 22:71–86. doi:10.1007/s00382-003-0369-6

Bony S et al (2006) How well do we understand and evaluate climate change feedback processes? J Clim 19:3445–3482. doi:http://dx.doi.org/10.1175/JCLI3819.1

Chepfer H, Bony S, Winker D, Cesana G, Dufresne J-L, Minnis P, Stubenrauch CJ, Zeng S (2010) The GCM-oriented CALIPSO cloud product (CALIPSO-GOCCP). J Geophys Res 115: D00H16. doi:10.1029/2009JD012251

Dufresne J-L, Bony S (2008) An assessment of the primary sources of spread of global warming estimates from coupled atmosphere–ocean models. J Clim 21(9):5135–5144

Hourdin F, Foujols M-A, Cordon F, Guemas V, Dufresne J-L, Bony S, Denvil S, Guez L, Lott F, Ghattas J, Braconnot P, Marti O, Meurdesoif Y, Bopp L (2012) Climate and sensitivity of the IPSL-CMA coupled model: impact of the LMDZ atmospheric grid configuration. Clim Dyn (submitted)

Konsta D, Chepfer H, Dufresne J-L (2012a) A process oriented representation of tropical oceanic clouds for climate model evaluation, based on a statistical analysis of daytime A-train high spatial resolution observations. Clim Dyn (submitted)

Konsta D, Dufresne J-L, Chepfer H, Idelkadi A, Cesana G (2012b) Evaluation of clouds simulated by the LMDZ5 GCM using A-train satellite observations (CALIPSO-PARASOL-CERES). Clim Dyn (submitted)

Parol F, Buriez JC, Vanbauce C, Riedi J, Labonnote LC, Doutriaux-Boucher M, Vesperini M, Seze G, Couvert P, Viollier M, Breon FM (2004) Capabilities of multi-angle polarization cloud measurements from satellite: POLDER results. Adv Space Res 33:1080–1088

Soden BJ, Held IM (2006) An assessment of climate feedbacks in coupled ocean–atmosphere models. J Clim 19:3354–3360. doi:http://dx.doi.org/10.1175/JCLI3799.1

Webb M, Senior C, Bony S, Morcette JJ (2001) Combining ERBE and ISCCP data to assess clouds in the Hadley Center, ECMWF and LMD atmospheric climate models. Clim Dyn 17:905–922. doi:10.1007/s003820100157

Wielicki BA, Barkstrom BR, Harrison EF, Lee RB III, Smith GL, Cooper JE (1996) Clouds and the Earth's Radiant Energy System (CERES): an earth observing system experiment. Bull Am Meteorol Soc 77:853–868. doi:http://dx.doi.org/10.1175/1520-0477(1996)077<0853:CATERE>2.0.CO;2

Winker D, Hunt W, McGill M (2007) Initial performance assessment of CALIOP. Geophys Res Lett 34:L19803. doi:10.1029/2007GL030135

Assessment of Climate Change Extremes Over the Eastern Mediterranean and Middle East Region Using the Hadley Centre PRECIS Regional Climate Model

E. Kostopoulou, C. Giannakopoulos, M. Hatzaki, A. Karali, P. Hadjinicolaou, J. Lelieveld, and M.A. Lange

Abstract Regional-scale climate projections based on the Hadley Centre PRECIS climate model have been used to assess future changes of rainfall and temperature extremes in the Eastern Mediterranean and Middle East region (EMME). Model output was evaluated by comparison with stations located in the western part of the study region. The area of interest is particularly vulnerable to extreme climate events such as droughts and heat waves. Extreme climate indices were calculated for three future 30-year time slices and compared to the reference period (1961–1990). Overall, model projections for the different future time periods reveal a continual and gradual future warming trend while conditions characterised as exceptional hot summers during the control period are found to become "typical" by the end of the twenty-first century. In agreement with previous studies, our results point to a drying tendency in the study domain, and indicate a decline in annual precipitation by 5–30% by the end of the twenty-first century relative to the reference period. The model projects larger precipitation reductions in the northern EMME, while the number of days with heavy precipitation is expected to decrease in the high-elevation areas of the region.

E. Kostopoulou (✉)
Department of Geography, University of the Aegean, Mytilene 81100, Greece
e-mail: ekostopoulou@aegean.gr

C. Giannakopoulos • M. Hatzaki • A. Karali
Institute for Environmental Research and Sustainable Development, National Observatory of Athens, Athens, Greece

P. Hadjinicolaou • J. Lelieveld • M.A. Lange
Energy, Environment and Water Research Center, The Cyprus Institute, Nicosia, Cyprus

C.G. Helmis and P.T. Nastos (eds.), *Advances in Meteorology, Climatology and Atmospheric Physics*, Springer Atmospheric Sciences,
DOI 10.1007/978-3-642-29172-2_78,

1 Introduction

Recent studies on present and future climate have shown that the Eastern Mediterranean and the Middle East (EMME) are among the most vulnerable regions to climate change with pronounced warming and precipitation reductions (IPCC 2007; Giorgi and Lionello 2008; Sheffield and Wood 2008). Arnell (2004) showed that the countries most prone to increasing water stress are located around the Mediterranean and the Middle East. Evidence from observations and modelling results suggests that climate extremes tend to become more frequent and longer-lasting, which could threaten vital socio-economic sectors (IPCC 2007). This paper presents an assessment of climate change in the EMME. The average patterns of temperature and precipitation for the present-day period are described and their trends are calculated. Future climate change is assessed by spatial patterns of change for selected extreme temperature and precipitation indices.

2 Model Description and Evaluation

The study uses daily output data from the Hadley Centre PRECIS regional climate model (driven by HadCM3P, Collins et al. 2005). The model simulations were performed at the Cyprus Institute within the framework of the CIMME project (www.cyi.ac.cy/climatechangemetastudy), which studies "Climate Change and Impacts in the Eastern Mediterranean and Middle East". The area of interest extends from 22°N to 46°N and from 10°E to 62°E, covering large portion of the EMME region. We define the "present-day" reference period as 1961–1990, and "future" as the time period from 2070 to 2099.

Lelieveld et al. (2012) compared monthly CRU averages with PRECIS, and showed that the model realistically reproduces climatic patterns and indices of extremes. In this study daily bias is calculated between model and stations' maximum (TX), minimum (TN) temperature and precipitation (RR). The 30-year average bias for both TX, TN varies from 0°C to −3.5°C, indicating that the model has a cold bias at high altitudes. The correlation coefficients are 0.71–0.85 for TX and 0.68–0.82 for TN. The PRECIS daily precipitation does not correlate well with the observational series ($r < 0.5$). The representation of annual cycles by PRECIS was examined for each station by calculating the mean value for each calendar-day over the reference period. The averages for TX and TN are well represented for most stations, except for few model underestimations (overestimations) in winter TN (summer TX). The biases are confined to continental and high elevation stations and are possibly related to local effects (e.g. pronounced surface topography). The modelled annual precipitation cycles reproduce the observed wet/dry seasonal precipitation distribution in most cases. Nevertheless, for few sites the daily RR indicates a systematic underestimation of the model simulated precipitation.

3 Model Simulation of Present-Day Climate

The mean climate conditions for the control period 1961–1990 over the study region confirm the known contrasting temperature and precipitation patterns between the northern and southern parts of the EMME region (maps could not be included due to space limitations). According to the model simulations, the annual mean temperature ranges from 0°C in mountainous areas to 10–15°C in most parts of the northern Mediterranean region. The southern part of the region, i.e. N-Africa and the Middle East, shows the warmer temperature pattern with averages in the range of 18–28°C. Several sub-regions exhibit diverging distributions in precipitation, with annual totals ranging from over 1,500 mm in the humid north (W-Balkans, NW-Turkey), to approximately 500 mm in Mediterranean lowlands (S-Balkans, W-Turkey), to less than 200 mm in the arid south (Arabian Peninsula). Highly elevated areas receive large precipitation amounts indicating the predominant influence of orography on the spatial distribution of rainfall. The average patterns in relation to extreme temperature conditions are investigated based on the spatial distribution of winter TN and summer TX patterns. The winter average TN may reach as low as −10°C in the mountainous areas and around 0°C in continental parts north of 38°N latitude. In S-European winter TN ranges from −5°C to 10°C, while further south it approximates 10°C. The temperature contrasts between the northern and southern EMME sub-regions are particularly evident in the average summer TX, which ranges between 22°C and 30°C in the north, while further east and south it exceeds 40°C.

Annual and seasonal temperature and precipitation trends are assessed for the reference period. The 30-year linear trend was determined for each grid point and the Kendall-tau test was employed to estimate the statistical significance of trends. Maps were constructed depicting only grids with significant trends in TX and TN (Fig. 1). Strong positive trends in TN are found over the eastern Balkan Peninsula, Turkey and the Arabian Peninsula. The annual TN increases by 0.4–0.5°C/decade in a large part of the domain, while during summer trends between 0.6°C/decade and 0.7°C/decade are found in the E-Balkans and W-Turkey. The most prominent TN warming trends are seen in spring at a rate of about 0.7–0.8°C/decade. The overall strongest warming over the reference period is found for spring TX reaching up to 0.9°C/decade mainly occurred in the S-Balkans and Turkey. The trends in annual and summer TX are estimated at approximately 0.5°C/decade and 0.6°C/decade especially in W-Turkey. The model results do not show an overall statistically significant trend in precipitation during the reference period, except for individual sub-regions, indicating decreases in the annual number of wet days and the amount of annual precipitation, particularly over Turkey.

To assess extreme temperature and precipitation conditions in the EMME for the reference period (1961–1990) climate indices are calculated and expressed as the annual occurrence of a variable exceeding a certain threshold. The warming conditions are expressed by the number of ¨warm¨ days, which defines the annual count of days with TX $>$ 25°C, the number of ¨hot¨ days are defined as those with TX $>$ 35°C, and the number of tropical nights are days per year with TN $>$ 20°C. The number of frost nights are defined by days with TN $<$ 0°C. Regarding precipitation we use the average

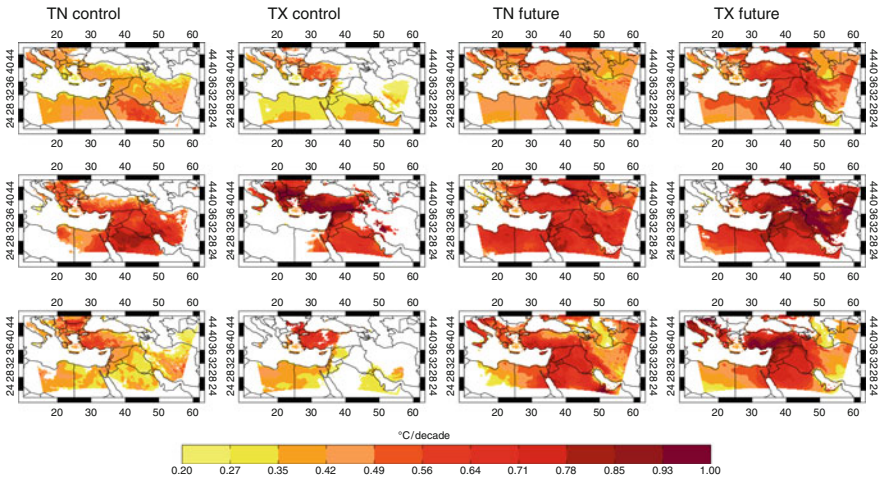

Fig. 1 Annual (*top row*) spring (*middle row*) and summer (*bottom row*) statistically significant trends for minimum (*TN*) and maximum (*TX*) temperatures over the period 1961–1990 (*first, second columns* respectively) and 2070–2099 (*third, fourth columns* respectively)

number of days (number of wet days) with RR $>$ 1.0 mm, and heavy precipitation is defined by the annual number of days with RR $>$ 10 mm.

The geographical patterns of the selected indices for the reference period, based on PRECIS output are presented in Fig. 2. Between the north and south of the EMME there can be a considerable difference in temperature, which is evident in the number of warm and hot days. The annual average number of days with TX exceeding 25°C ranges from 1 month (in elevated areas) to 3 months in the northern EMME, while in the south two thirds of the year can be considered as warm days. Moreover, hot days occur at a maximum 30–50 days/year in low elevation areas of the north and less than a month in areas of higher altitudes. In the southern EMME, days with temperature $>$ 35°C are common occurring up to 5 months/year (Gulf region). In contrast, continental (above 36°N) and high-altitude areas experience up to 150 frost days/year, while in the south the number of frost days does not exceed 20 days/year. Further, tropical nights (TN $>$ 25°C) are rare (up to a month/year) in the northern EMME, whereas in the south occur typically 1–2 months and more than 3 months/year around the Persian Gulf. The north–south contrast becomes most evident from the precipitation indices patterns. Precipitation is typically heavier on the western slopes of the mountain ranges, while rainfall amounts decrease rapidly with latitude in the semi-arid southern EMME. The number of wet days (RR $>$ 1 mm/day) during the reference period ranges from 200 days/year in high altitudes and approximately 100 days/year in the northern parts, to less than 40 days/year in the southern parts. Along the western edge of the Balkan Peninsula and other high-elevation areas (e.g. Caucasus), heavy precipitation occurs during maximum 50 days/year. About 30–40 days/year this occurs over the Taurus mountain range in S-Turkey, and the Zagros Mountains, which extend along southern and

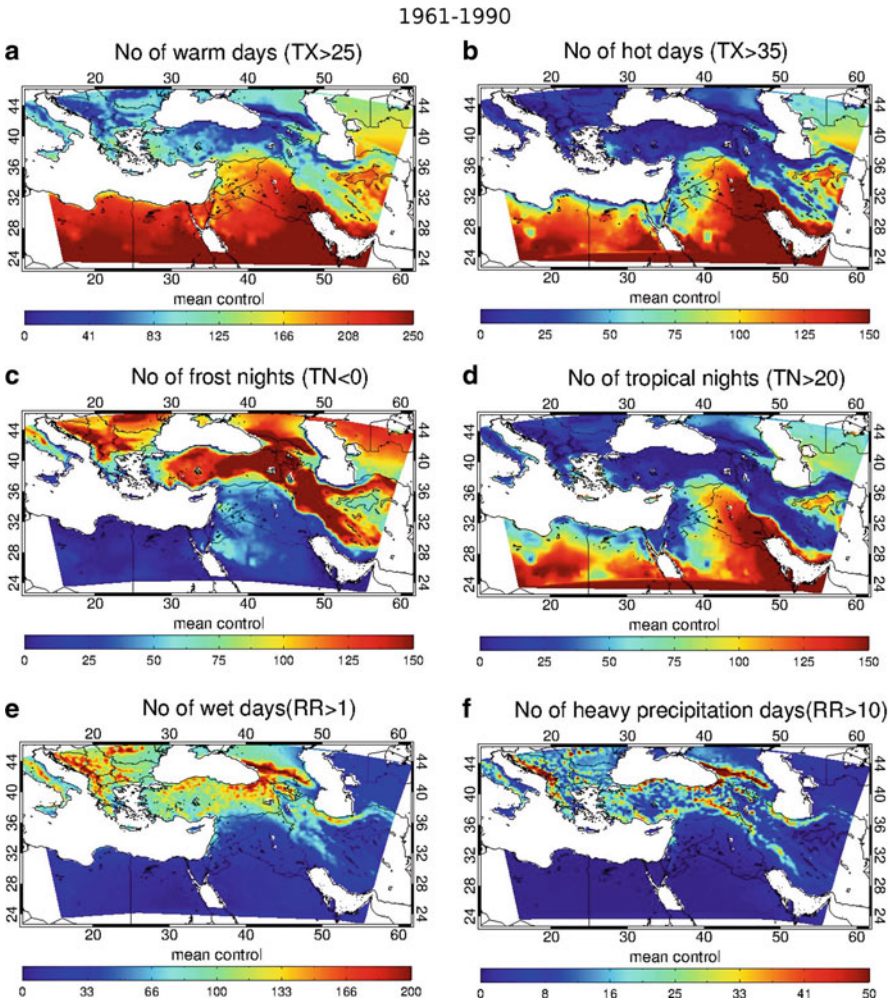

Fig. 2 (continued)

western Iran into northern Iraq. Over the reference period the occurrence of heavy precipitation days is unusual in the southern EMME region.

4 Predicted Temperature and Precipitation Changes

The mean climate change for 2070–2099 is analysed and Fig. 1 (third, fourth columns) provides key insights in the projected temperature change, presenting the distribution of statistically significant trends in annual, spring and summer TX

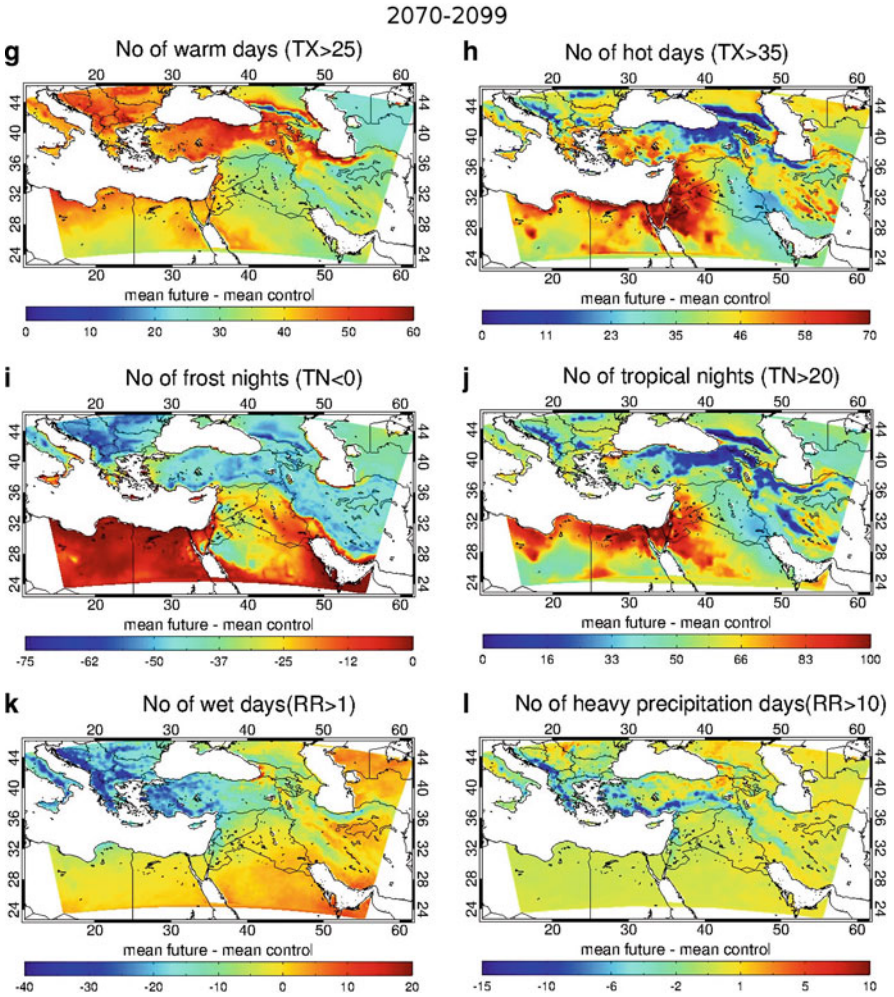

Fig. 2 Patterns of temperature and precipitation indices, showing the mean number of days per year during the control period 1961–1990 (**a**–**f**), and patterns showing their mean changes for the future period 2070–2099 relative to the control period 1961–1990 (**g**–**l**)

and TN. Trends are estimated to be positive in all cases and statistically significant in nearly the entire study region. The annual trend patterns for TN, TX show similar warming rates of approximately 0.4–0.6°C/decade. Consistent with the findings for the reference period, the model projections suggest prominent trends in spring TN and TX, which increases by 0.6–0.8°C/decade and 0.7–0.9°C/decade, respectively, with pronounced warming over the Middle Eastern countries. Summer temperatures reveal a gradual warming (0.5–0.9°C/decade) over much of the region.

We defined the "present-day" period as 1961–1990 and "future" as the time period from 2070 to 2099, and computed differences in climate indices between these two periods (Fig. 2g–l). The number of warm days is found to increase in particular in the northern part of EMME by 50–60 additional days/year by the end of the twenty-first century. Hot days are estimated to occur much more frequently in the EMME. In particular, low-elevation and coastal regions in the northern part are estimated to experience about 1–2 extra months with TX $>$ 35°C, while the southern parts are expected to face severe warm conditions with two additional months of hot days/year. It is estimated that the warmer future of the area will also include strong increases in the occurrence of warm nights. The change in the number of tropical nights translates to 1–2 additional months of tropical nights/year in the north and to 3 additional months in the southern EMME by the end of the twenty-first century. Towards a warmer future climate in EMME, the number of frost days is found to decline within a range of 1–2 months of fewer frost days/year (in high-latitude continental and high-altitude locations). Regarding precipitation, PRECIS shows that in the northern EMME, the number of wet days may decrease by 10–30 days/year, while heavy precipitation is likely to decrease in the high-elevation areas by 15 days/year by the end of the twenty-first century.

5 Conclusions

Calculated trends based on PRECIS model indicate statistically significant warming over land in the EMME of approximately 0.5–0.6°C/decade, which is projected to continue into the future. The warming trends are found in annual and seasonal daily TX and TN, with the spring temperatures increasing at a faster rate. Towards a warmer and drier climate in EMME the PRECIS results suggest increases of warm, hot days, and tropical nights. The projected increase of TX is most rapid in the northern EMME, by up to 2 months of additional warm days/year by the end of the twenty-first century. In contrast, frost days and wet days are projected to decrease. The combination of long-term changes and the greater frequency of extreme climate events can have adverse impacts on many economic sectors in EMME while excessive heat stress and reduced water resources will have important negative consequences for human health and ecosystems.

References

Arnell NW (2004) Climate change and global water resources: SRES emissions and socio economic scenarios. Global Environ Change 14:31–52. doi:10.1016/j.gloenvcha.2003.10.006

Collins M, Booth BBB, Harris GR, Murphy JM, Sexton DMH, Webb MJ (2005) Towards quantifying uncertainty in transient climate change. Clim Dyn 27:127–147. doi:10.1007/s00382-006-0121-0

Giorgi F, Lionello P (2008) Climate change projections for the Mediterranean region. Global Planet Change 63:90–104

IPCC (2007) Climate Change 2007 The physical science basis. In: Solomon S, Qin D, Manning M, Chen Z, Marquis M, Averyt KB, Tignor M, Miller HL (eds) Contribution of working group I to the fourth assessment report of the intergovernmental panel on climate change, Cambridge University Press, Cambridge

Lelieveld J, Hadjinicolaou P, Kostopoulou E, Chenoweth J, Giannakopoulos C, Hannides C, Lange MA, El Maayar M, Tanarhte M, Tyrlis E, Xoplaki E (2012) Climate change and impacts in the Eastern Mediterranean and the Middle East. Clim Chang. doi:10.1007/s10584-012-0418-4

Sheffield J, Wood EF (2008) Projected changes in drought occurrence under future global warming from multi-model, multi scenario, IPCC AR4 simulations. Clim Dyn 31:79–105. doi:10.1007/s00382-007-0340-z

Viticulture: Climate Relationships in Greece and Impacts of Recent Climate Trends: Sensitivity to "Effective" Growing Season Definitions

G. Koufos, T. Mavromatis, S. Koundouras, and N.M. Fyllas

Abstract Recent research has shown significant shifts in the phenological stages of grapevines (*Vitis vinifera* L.) due to temperature changes. That study investigated the relation between temperature and harvest time in grape growing regions of Greece. Harvest dates were collected on eight different varieties and regions: four island [Muscat of Alexandria (Limnos), White Muscat (Samos), Assyrtiko (Santorini), Athiri (Rodos)] and four inland [Roditis (Anchialos), Agiorgitiko (Nemea), Mavrodafni (Pyrgos), Xinomauro (Naoussa)] areas. In two cases (Limnos, Pyrgos), must sugar concentration (baumé degrees) were also collected. Climatic primary (precipitation, mean, maximum and minimum temperature) and secondary (growing degree days, diurnal temperature range and extreme events) data were computed for three periods [calendar year, growing season (April–October) and ripening (according to variety)]. The most frequent significant trends of climatic parameters and crop-climate relationships were observed for island regions compared to inland ones. Calendar year and growing season-based analyses presented the most frequently significant viticulture-climate relationships, with mean, maximum air temperature and growing degree days. The direction and magnitude of harvest time responses were not particularly sensitive to the choice of "effective" growing season definition. A negative harvest response was identified for all variables except for DPrec in three island stations and $DT_{max} > 35°C$ in Rodos.

G. Koufos (✉)
Department of Environment, University of the Aegean, Mitilini 81100, Greece
e-mail: envm08039@env.aegean.gr

T. Mavromatis
School of Geology, Aristotle University, Thessaloniki, Greece

S. Koundouras
School of Agriculture, Aristotle University, Thessaloniki, Greece

N.M. Fyllas
School of Geography, University of Leeds, Leeds, UK

C.G. Helmis and P.T. Nastos (eds.), *Advances in Meteorology, Climatology and Atmospheric Physics*, Springer Atmospheric Sciences,
DOI 10.1007/978-3-642-29172-2_79,

1 Introduction

Grapevine experiences direct effects of climate changes by shifting of its phenological stages. *Vitis vinifera* L. has four basic developmental stages: (1) budburst, (2) flowering, (3) veraison and (4) full ripeness (harvest). The time between these stages varies greatly with grape variety, climate and location (Jones and Davis 2000). Recent studies that investigated grapevine growth-climate relations showed shorter duration of between-stages periods (Duchene and Schneider 2005). Moreover, previous studies showed that warming during growing season has contrasting effects on wine quality depending on the variety and region (Jones et al. 2005).

A recent study (not published) investigated the relationships between viticulture and climate data including precipitation, mean (T_{mean}), maximum (T_{max}) and minimum (T_{min}) temperature, diurnal temperature range (DTR), growing degree days (GDD) and a set of extreme events ($T_{max} > 35°C$ and $T_{min} < 0°C$), with linear regression models over the last 18–37 years, for eight major grape varieties grown in Greece.

The trend of climate variables was similar for most of the regions. The temperature trends and more specifically these of T_{max}, T_{min} and GDD were the most frequently significant (Table 1). DTR trends weren't significant in most cases. Even though extreme events ($T_{max} > 35°C$ and $T_{min} < 0°C$) occurred more frequently, they didn't present significant trends (except for $T_{max} > 35°C$ in Samos and Anchialos). Finally, precipitation trends were not significant in any station (Table 1).

The objective of this study was to investigate the role of the definition and choice of the "effective" growing season on the direction and magnitude of viticulture-climate relationships. Three different "effective" growing seasons for each region were used: the calendar year (CY), the growing season (GS) and the ripening period (RP).

2 Data and Methodology

2.1 Data

Viticulture data in Greece consists mainly of harvest dates and must sugar concentration (baumé degrees) due to poor records saved from the wineries throughout the country. Thus, harvest-dates with the longest time series from eight different grape varieties and regions were gathered: four island [Muscat of Alexandria (Limnos), White Muscat (Samos), Assyrtiko (Santorini), Athiri (Rodos)] and four inland [Roditis (Anchialos), Agiorgitiko (Nemea), Mavrodafni (Pyrgos), Xinomauro

Table 1 Descriptive statistics for climate parameters over the calendar year (bold letters show the statistically significant relations between harvest date and the respective climate parameter)

Region	T_{max}	T_{min}	GDD	DTR	Prec.	$T_{max} > 35°C$	$T_{min} < 0°C$
	Mean/sd	Mean/sd	Mean/sd	Mean/sd	Mean/sd	Mean/sd	Mean/sd
Limnos	**19.5 (0.6)**	**11.6 (0.5)**	2,516 (141)	7.8 (0.4)	512 (176)	0.7 (1.5)	9.6 (6.1)
Samos	**22.5 (0.6)**	**14.2 (0.8)**	**3,368 (200)**	8.3 (0.5)	633 (167)	**20.5 (9.9)**	2.2 (3.0)
Santorini	**21.4 (0.5)**	**16.1 (0.6)**	3,291 (194)	5.3 (0.3)	330 (123)	1.1 (1.3)	0.1 (0.2)
Rodos	**22.3 (0.5)**	**16.8 (0.5)**	**3,541 (169)**	5.5 (0.3)	608 (206)	1.0 (1.6)	–
Anchialos	**20.9 (0.6)**	**10.9 (0.5)**	2,670 (146)	10 (0.4)	–	**7.2 (5.0)**	16.7 (7.2)
Nemea	19.9 (0.8)	7.0 (1.0)	2,000 (333)	12.9 (0.8)	685 (197)	10.4 (6.2)	59.2 (17.6)
Naoussa	**20.0 (1.2)**	**9.4 (0.5)**	**2,420 (140)**	10.7 (1.3)	–	8.5 (6.0)	45.4 (11.6)
Pyrgos	22.7 (0.7)	10.8 (1.1)	2,882 (165)	11.9 (0.8)	–	12.5 (7.3)	14.8 (8.3)

sd standard deviation

(Naoussa)] and, in two cases, baumé data (Limnos, Pyrgos). The time series ranged from 18 to 37 years.

Meteorological data such as: mean (T_{mean}), maximum (T_{max}) and minimum (T_{min}) daily air temperature (°C) as well as daily precipitation (Prec/mm) were collected from the nearest (to the vineyard) weather station (maximum distance <30 km). These data sets were provided by the Hellenic National Meteorological Service.

2.2 Methodology

T_{mean}, T_{max}, T_{min} and Prec were computed for each: (1) calendar year (CY: Jan. 1–Dec. 31), (2) growing season (GS: Apr. 1–Oct. 31) and (3) ripening period (RP: depending on the variety). Secondary variables, commonly used in viticulture studies, were calculated from primary data (Jones and Davis 2000) including: (1) growing degree days $T_{base} = 10°C$ (GDD: a useful tool to describe the timing of biological processes, McMaster and Wilhelm 1997) by using the formula GDD (°C) = $(T_{max} - T_{min})/2 - T_{base}$, (2) the number of days of extreme heat and cold, i.e. with maximum and minimum temperature above 35°C and below 0°C, respectively, and (3) diurnal temperature range (DTR) which is calculated as $T_{max} - T_{min}$.

The collected harvest-dates were transformed and used as difference variables. First, 1st of August was selected arbitrarily as the day-count reference baseline. Then, the calendar difference between real harvest date (as recorded in wineries' database) and 1st of August for each year (e.g. 16 Sep.–1 Aug. = 45) was calculated. Finally, the mean difference between the sum of mean calendar difference (e.g. 45 + 41 + … + 33 = 36.9) and calendar difference for each year (45−36.9 = 8.1) was computed for each station.

Linear regression models (Y = a + bX) were used to investigate harvest-dates (difference), baumé and climate trends through time. The statistical significance at $p = 0.05$ was estimated using the Pearson correlation method. To explore climate-viticulture relationships, a common approach was used based on the first-difference time series (Tao et al. 2008) both for viticulture (Δdifference, Δbaumé) and climate data (year to year changes) (DT_{mean}, DT_{max}, DT_{min}, DGDD, DDTR, DPrec, $DT_{max} > 35°C$, $DT_{max} < 0°C$). Finally, a sensitivity analysis of the results using the three periods (CY, GS and RP) was performed.

3 Results

Calendar year and growing season-based analyses presented the most frequently significant viticulture-climate relationships (26 vs. 27 significant cases, respectively). DT_{mean}, DT_{max}, DGDD and DT_{min} were the most dominant climate factors

Table 2 Frequency of significant viticulture (harvest dates, baumé)-climate relationships for the three definitions of "effective" growing season

	CY:tot[a] (inl.[b]/isl.[c])	GS:tot (inl./isl.)	RP:tot (inl./isl.)
DT_{mean}	5(2/3)	5(2/3)	2(0/2)
DT_{max}	5(2/3)	5(2/3)	1(0/1)
DT_{min}	3(0/3)	3(0/3)	4(1/3)
DGDD	4(1/3)	5(2/3)	3(1/2)
DDTR	2(1/1)	1(1/0)	2(1/1)
Dprec	2(0/2)	3(1/2)	1(1/0)
$DT_{max} > 35°C$	3(1/2)	3(1/2)	1(0/1)
$DT_{min} < 0°C$	2(1/1)	2(1/1)	1(1/0)
Total	26(8/18)	27(10/17)	15(5/10)

CY calendar year, *GS* growing season, *RP* ripening period

[a]Total number of significant viticulture (harvest-dates, baumé)-climate relationships

[b]Inland: total number of significant viticulture-climate relations for Nemea, Naoussa, Pyrgos and Anchialos

[c]Islands: total number of significant viticulture-climate relations for Limnos, Samos, Santorini and Rodos

for the islands while the former three were the most important ones for the inland areas (Table 2).

On the contrary, the number of significant viticulture-climate relationships was reduced when analysis was based on RP (15 significant cases were identified) and mainly represented by DT_{min} and DGDD. The most frequent significant trends of climatic parameters and viticulture-climate relationships were observed for island regions (Table 2).

The direction and magnitude of harvest time responses were not particularly sensitive to the choice of "effective" growing season definition (Table 3). A negative harvest response was identified for all variables except for DPrec in three stations (Santorini, Rodos and Nemea) and $DT_{max} > 35°C$ in one case (Rodos). Very weak responses were found to DGDD (>0.01) and $DT_{max} > 35°C$ trends. Slightly higher, on magnitude, mean harvest responses to the recent climate trends of DT_{mean}, DT_{max} and DT_{min} were found in four stations (Limnos, Samos, Santorini and Naoussa) when the analysis was based on GS than CY periods. In these regions harvest day was moved forward, on average, by 2.2% (almost by 5 days) as a result of the growing season trend in the above-mentioned climate parameters. The respective number due to CY trends was 1.7% (almost 6 days). Much higher harvest responses (almost 8.5%, on average) were found in two stations (Limnos, Samos) when the analysis was based on the RP (harvest day was moved forward by 2 days). A significant negative harvest time response to the trends of DDTR (ranged from −2.2% to −3.0%) was found only in one station (Naousa).

No significant relationship between climate variables and must baumé degrees was found for any region regardless of the "effective" growing season used as base.

Table 3 Direction (bold letters show negative trend) and magnitude of harvest time response (expressed as percentage of days showing significant relationship with the specific climate variable) to the "effective" growing season definitions

	Per.[a]	DT_{mean}	DT_{max}	DT_{min}	DGDD	DDTR	DPrec	$DT_{max} > 35°C$
Limnos	CY	**–1.8**	**–1.2**	**–2.0**	**0**[b]			
	GS	**–2.3**	**–1.6**	**–2.8**	**0**			
	RP	**–7.1**		**–6.0**	**–0.1**			
Samos	CY	**–1.4**	**–1.4**	**–1.2**	**0**			**0**
	GS	**–1.6**	**–1.4**	**–1.5**	**0**			**0**
	RP	**–9.6**	**–8.8**	**–8.4**	**–0.2**			**–0.1**
Santorini	CY	**–1.9**	**–1.8**	**–1.8**	**0**		0	
	GS	**–2.2**	**–1.9**	**–2.3**	**0**		0	
Rodos	CY						0	0.3
	GS						0	0.4
Nemea	GS						0	
	RP						0.2	
Naousa	CY	**–1.6**	**–2.0**		**0**	**–2.2**		**–0.1**
	GS	**–2.7**	**–3.4**		**0**	**–3**		**–0.2**

Only significant viticulture-climate relationships shown on the table
[a]Periods: *CY* calendar year, *GS* growing season, *RP* ripening period
[b]*0* correspond to lower than 0.01

4 Conclusions

The definition and effect of growing season on the direction and magnitude of harvest dates on eight major grape varieties was investigated in four island and four inland grape growing regions of Greece. Three different "effective" growing seasons for each region were used as base: the calendar year, the growing season of grapevine (Apr. 1–Oct. 31) and ripening period of each variety.

Calendar year and growing season-based analyses presented the most frequently significant viticulture-climate relationships, mainly with DT_{mean}, DT_{max}, DGDD. The most frequent significant trends of climatic parameters and crop-climate relationships were observed for island regions compared to inland ones. The direction and magnitude of harvest time responses were not particularly sensitive to the choice of "effective" growing season definition. A negative harvest response was identified for all variables except for DPrec in three island stations and $DT_{max} > 35°C$ in Rodos.

References

Duchene E, Schneider C (2005) Grapevine and climatic changes: a glance at the situation in Alsace. Agron Sustain Dev 25:93–99. doi:10.1051/agro:200405

Jones GV, Davis RE (2000) Climate influences on grapevine phenology, grape composition, and wine production and quality for Bordeaux, France. Am J Enol Vitic 51(3):249–261

Jones GV, White MA, Cooper OR, Storchmann K (2005) Climate change and global wine quality. Clim Chang 73:319–343. doi:10.1007/s10584-005-4704-2

McMaster GS, Wilhelm WW (1997) Growing degree-days: one equation, two interpretations. Agric For Meteorol 87:291–300. doi:http://dx.doi.org/10.1016/S0168-1923(97)00027-0

Tao F, Yokozawa M, Liu J, Zhang Z (2008) Climate-crop yield relationships at provincial scales in China and the impacts of recent climate trends. Clim Res 38:83–94. doi:10.3354/cr00771

On the Dynamics of Mediterranean Explosive Cyclogenesis

J. Kouroutzoglou, H.A. Flocas, M. Hatzaki, K. Keay, and I. Simmonds

Abstract In this study, a first attempt is made to examine the mechanisms contributing to the explosive cyclogenesis in the Mediterranean basin during the cold period of the year. Surface explosive cyclones and their vertical characteristics were defined with the aid of the University of Melbourne Cyclone Tracking and Vertical Tracing Software, using the 6-hourly ERA-40 datasets at the resolution of $1^\circ \times 1^\circ$ for a 40-year period (1962–2001), separately for the western (WM), central (CM) and eastern Mediterranean (EM). Composite anomalies of various thermodynamic parameters verified the strong baroclinic character of the phenomenon and the decisive role of the upper level dynamics during the time of explosive cyclogenesis. Moreover, an interesting differentiation characterizes the low level thermodynamic structure of the WM and mainly CM cases in relation to the EM ones, since explosive cyclogenesis in the former areas seem to occur as cold low – level air warms from below, penetrating the Mediterranean from NW, while in the EM cold and high – PV upper level air moves over areas of warm and moist low level environment. Nevertheless, a synergy of the lower and the upper levels is implied for all parts of the Mediterranean basin with different relative importance.

1 Introduction

Explosive cyclogenesis in the Mediterranean is a rather rare phenomenon as compared to the oceanic events (Sanders and Gyakum 1980). ς synoptic climatology of the Mediterranean bombs was carried out by Conte (1986) based on daily

J. Kouroutzoglou (✉) • H.A. Flocas • M. Hatzaki
Department of Environmental Physics-Meteorology, University of Athens, Building PHYS-5, University Campus, 157 84 Athens, Greece
e-mail: kourou.john@yahoo.gr

K. Keay • I. Simmonds
School of Earth Sciences, University of Melbourne, Victoria 3010, Australia

C.G. Helmis and P.T. Nastos (eds.), *Advances in Meteorology, Climatology and Atmospheric Physics*, Springer Atmospheric Sciences,
DOI 10.1007/978-3-642-29172-2_80,

synoptic charts. The first objective climatology of Mediterranean explosive cyclones was performed by Kouroutzoglou et al. (2011a) with the aid of the University of Melbourne cyclone tracking algorithm, employing 2.5° × 2.5° data from ERA-40. A comparison of this climatology with a higher resolution one of the same assimilation model is presented by Kouroutzoglou et al. (2011b).

The objective of this study is to examine the mechanisms contributing to the explosive cyclogenesis in the Mediterranean at the upper and lower levels, employing composite maps of dynamic parameters separately for western, central and the eastern Mediterranean.

2 Data and Methodology

The dataset used in this study include the 6-hourly analyses of mean sea level pressure and geopotential, wind components and temperature at five isobaric levels (850, 700, 500, 300 and 200 hPa) on a 1° × 1° regular latitude–longitude grid, interpolated from the respective 1.125° × 1.125° grid for the cold period (October–March) of 1962–2001, as derived from the ERA-40 Reanalysis of the ECMWF.

Mediterranean area was divided in three regions, as follows (Maheras et al. 2001): western Mediterranean (WM) area, extending between 350°W–10°E and 30°N–47°N, central Mediterranean (CM) area, extending between 10°E–20°E and 30°N–47°N and eastern Mediterranean (EM), extending between 20°E–38°E and 30°N–47°N (Fig. 1).

The identification and tracking procedure of the surface Mediterranean cyclones was performed with the aid of the Melbourne University cyclone finding and tracking scheme (hereafter, MS scheme; Murray and Simmonds 1991a, b). Explosive cyclones were identified following the criterion of Sanders and Gyakum (1980), in terms of normalized central pressure deepening rate (Lim and Simmonds 2002) over 24 h. Details can be found in Kouroutzoglou et al. (2011b).

Then, the vertical tracing of the surface explosive cases was performed and the composite anomalies of a set of thermodynamic parameters were calculated during the explosive cyclogenesis phase, including: potential vorticity (PV), potential temperature at 2PVU, potential temperature and equivalent potential temperature at 850 hPa and static stability.

3 Results: Discussion

As an attempt to evaluate the effect of the upper level dynamics on the explosive cyclogenesis for the WM, CM and EM explosive deepeners, respectively, the composite anomalies of PV at 315 K (Fig. 2) and potential temperature at the iso-potential vorticity surface of 2PVU (Fig. 3) were calculated. For the WM, a

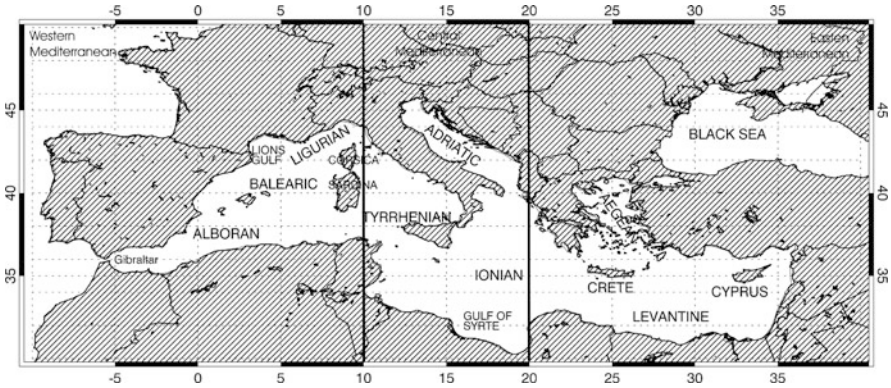

Fig. 1 Geographical chart of Mediterranean region; the western (WM), central (CM) and eastern Mediterranean (EM) areas are displayed

strong positive PV anomaly is evident in northwest Europe, with maximum over the British Isles, coinciding with a cold anomaly at tropopause. For the CM, a positive PV anomaly can be also seen over Central Europe, including Alps and Italy. For the EM, a shallow positive PV anomaly covers the Balkans. The advection of cold – high PV upper tropospheric air is favorable for the initiation of surface cyclogenesis (Bosart and Lin 1984), implying the existence of a tropopause folding and stratospheric intrusion upstream of the developing surface cyclone (Uccellini 1986). These findings are further supported taking into account that the majority of Mediterranean explosive cyclones follow the KF type of development (Kouroutzoglou et al. 2011a), being characterized by cyclone penetration in the Mediterranean from W-NW and further deepening inside the Mediterranean during their southward movement (Karacostas and Flocas 1983).

Moreover, the composite anomalies of geopotential and the respective composites of the wind vectors at 500 hPa (not shown), for each part of Mediterranean, reveal maxima of the upper level northwesterly winds at the rear of the cyclonic centres and define the existence of an upper level diffluent trough (Prezerakos and Flocas 1997), suggesting a tendency for further deepening. Moreover, the W-NW vertical tilting of the composite cyclonic centres at 850, 700, 500 and 300 hPa, as these are defined through the composites of vector winds (not shown) in the WM and CM, reveals the importance of baroclinicity of the explosive deepeners.

The composite anomalies of static stability for the 850–700 hPa layer (Fig. 4) demonstrated negative values that correlate to weak stability for all parts of Mediterranean, being induced by the relatively warm sea in low level cold air advections (Trigo et al. 2002). It is clear that the areas of maximum negative composite anomalies of static stability almost coincide with the peak positive PV anomalies located in the areas of maximum explosive cyclogenesis in all parts of Mediterranean basin. On the contrary, the respective distributions of the 500–300 hPa layer (not shown) present stronger static stability being attributed to the high PV air over those regions (Hoskins et al. 1985).

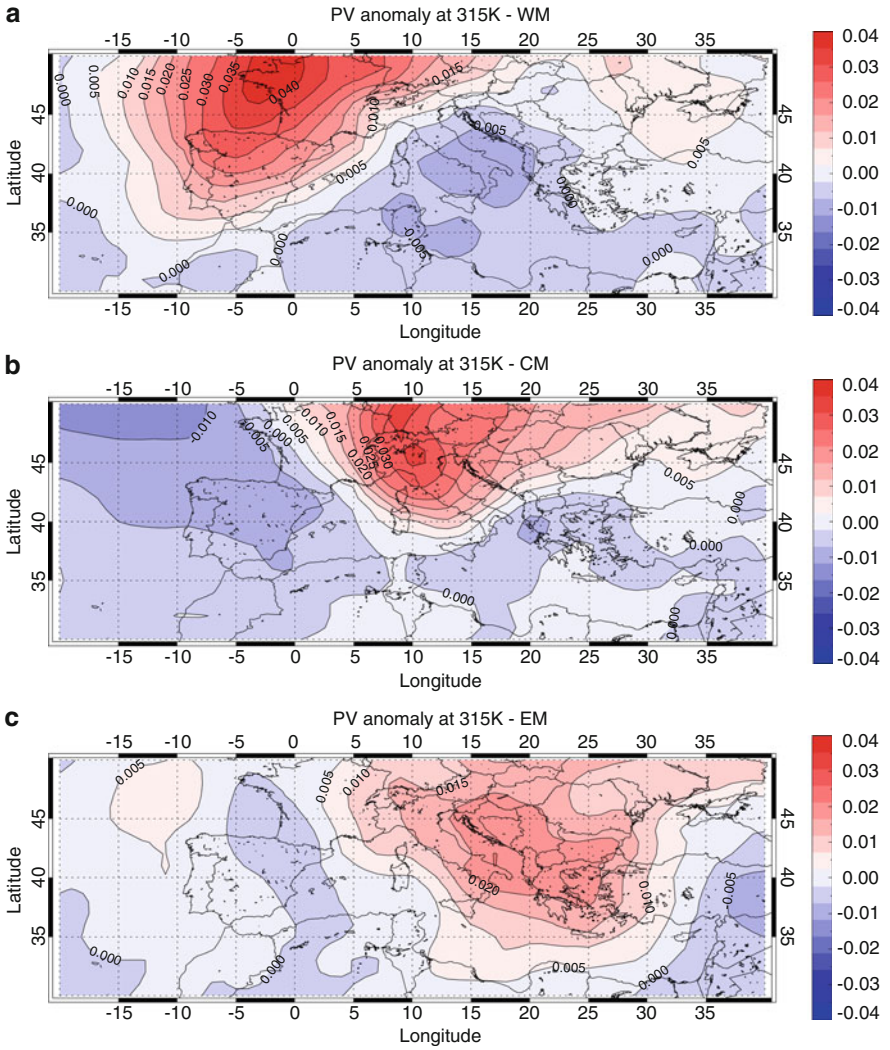

Fig. 2 Composite anomalies of potential vorticity at 315 K during the time of explosive cyclogenesis for the WM, CM and EM; contour interval is 0.009 $m^2\ s^{-1}\ K\ kg^{-1}$

The distributions of potential temperature (hereafter, Θ) at 850 hPa (not shown) for the explosive cases of WM and CM negative anomalies (cold low-level air) are located in the Northern strongly baroclinic Mediterranean coastal areas of the WM and CM (more intense in the CM), helping in the heating from below of the cold air after entering the warmer Mediterranean sea surface. On the contrary, positive Θ anomalies (warm air) are evident in the EM with higher values in South Ionian and south Aegean Sea, where deeper explosive cyclones were detected (Kouroutzoglou et al. 2011a). Nevertheless, Θ represents potential warming due to adiabatic

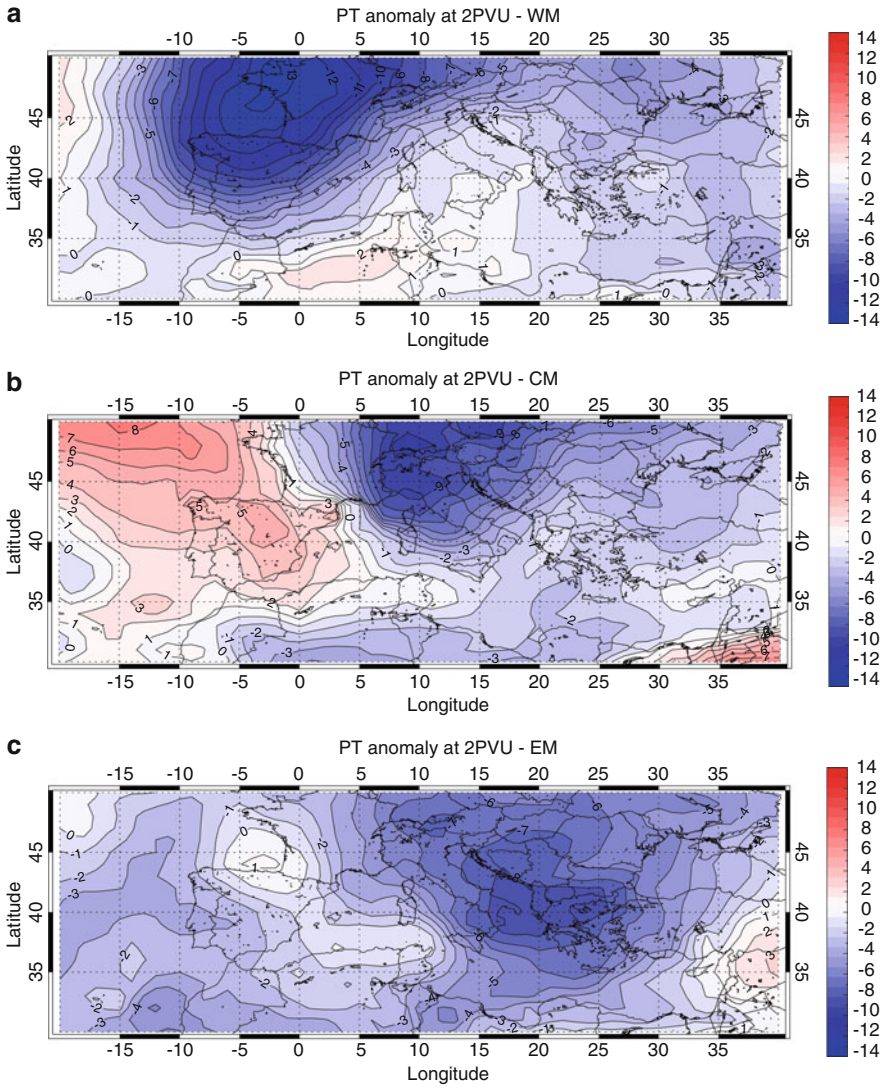

Fig. 3 Composite anomalies of potential temperature at 2PVU surface during explosive cyclogenesis for the WM, CM and EM; contour interval is 1.8 K

compression, while equivalent potential temperature (hereafter, Θe) describes potential warming due to condensation as well, allowing the consideration of the moisture of the parcel in relation to the stability conditions (Holton 2004). In the Mediterranean, which is affected by NW intrusions of cold air masses of polar origin, following the KF mechanism, the horizontal variations of Θe can be considerably significant, during the cold period of the year, since the sea warms and moistens the air passing over it, resulting in enhanced values of evaporation, allowing the development of vertical instability (Petterssen 1956).

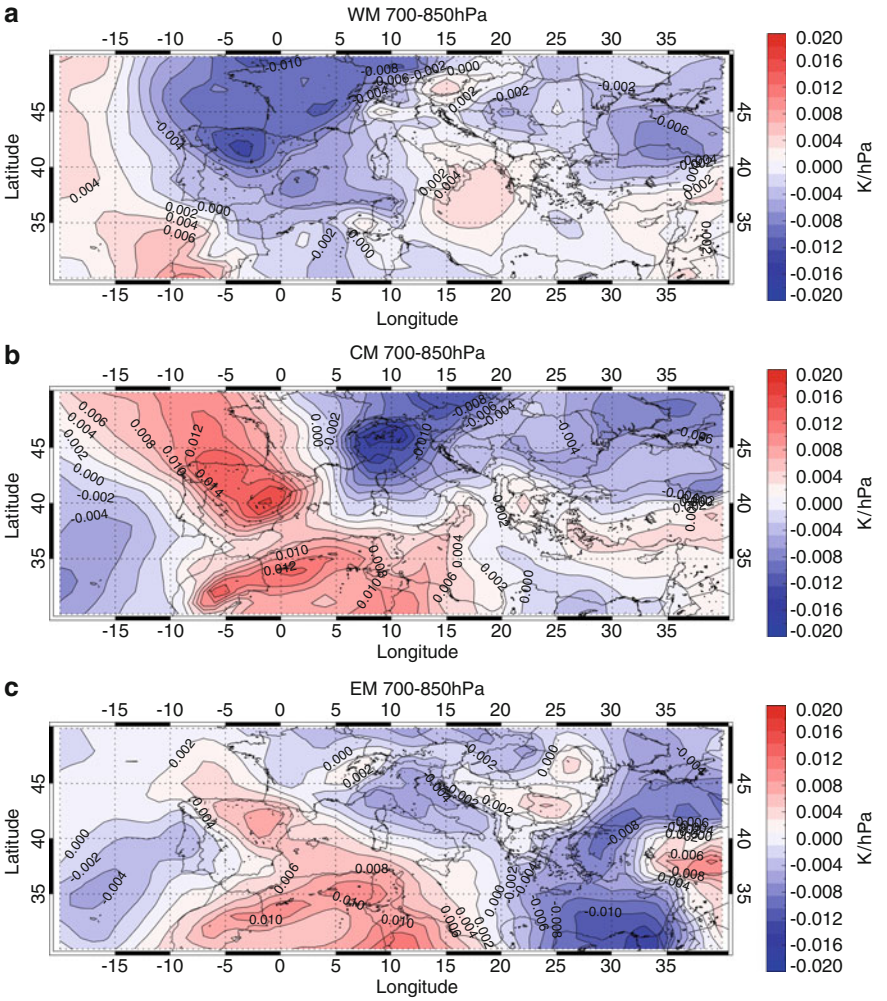

Fig. 4 Composite anomalies of the static stability at the 850–700 hPa layer for the WM, CM and EM during the time of explosive cyclogenesis; contour interval is 0.01 K hPa^{-1}

The examination of the composite anomalies of Θe (not shown) reveal some interesting characteristics compared to the pre-described anomalies of Θ: For the WM explosive cases an extended warm anomaly covers all the maritime parts from the Balearic Islands and the Alboran Sea up extending northeastwards to the Gulf of Genoa, implying a potential low level warming, while negative anomalies cover the NW Europe and North Atlantic regions. The increased temperature gradient between the above areas – and mainly the orientation of the isotherms being parallel to the axis NE-SW, constitutes a strong implication of the major synoptic scale frontal systems entering the Mediterranean area from northwest that control WM

cyclogenesis during the cold period of the year (HMSO 1962). Moreover, the composite anomalies of the vector wind at 850 hPa (not shown) reveal a W-SW flow from the Alboran up to Sardinia – Corsica enhancing the potential low level advection of warm and moist air, explaining, thus, the positive anomalies of Θe.

Similar patterns can be found in the CM. Moreover, the effect of the Alpine barrier can be seen through the increased temperature gradients along Gulf of Lions and Gulf of Genoa – North Italy (Trigo et al. 2002). Moreover, the maximum of the Θe in the area between south Italy and south Ionian Sea almost coincides with the area of maximum explosive deepening (Kouroutzoglou et al. 2011b). Thus, the importance of diabatic heating in this part of the Mediterranean can be stressed.

In the EM, both positive anomalies of Θ and Θe are evident in the Aegean Sea and mainly its southern part, implying the importance of the W-SW flow that form ahead of the synoptic scale cyclonic systems moving from South Italy towards the EM and advect low level warm and moist area within the EM. Therefore, in the EM the cold and high PV upper level air, penetrating from W-NW moves over low level warm and moist air, producing enhanced upward motions and surface cyclogenesis.

4 Conclusions

In this study, a first attempt is made to examine the mechanisms contributing to the explosive cyclogenesis in the WM, CM and EM basin. It was found that the upper level processes play an important role in all parts of Mediterranean basin through a tropopause folding. The effect of the cold – high PV upper level air in the destabilization of the lower levels was also highlighted. Baroclinicity seems to be important mainly in WM and CM. Nevertheless, explosive cyclogenesis in the WM and CM seems to result from the low level cold air penetrations from north in the Mediterranean basin, while in the EM, the upper level forcing seems to act in warmer low level environment, most likely explaining the occurrence of deeper explosive cyclones in this part of Mediterranean. A more comprehensive view of the low level forcing, the possible generation of low level PV due to the diabatic processes and the possible effect of the sea surface temperature variations in each part of Mediterranean is the subject of future work.

References

Bosart LF, Lin SC (1984) A diagnostic analysis of the Presidents' Day storm of February 1979. Mon Weather Rev 112:2148–2177. doi:10.1175/1520-0493

Conte M (1986) The meteorological "bomb" in the Mediterranean: a synoptic climatology. Riv Meteorol Aeronaut 46:121–130

HMSO (1962) Weather in the Mediterranean. Vol 1, 2nd Ed, Meteorological Office, London

Holton JR (2004) An introduction to dynamic meteorology, 4th edn. Academic, San Diego

Hoskins BJ, McIntyre ME, Robertson AW (1985) On the use and significance of isentropic potential vorticity maps. Q J R Meteorol Soc 111:877–946

Karacostas TS, Flocas AA (1983) The development of the "bomb" over the Mediterranean area. Climat méditerranéen & ressources en eau: actes de la Conference "Eau verte, eau bleue", Marseille, 6–8 Septembre 1983, La Météorologie 34:351–358

Kouroutzoglou J, Flocas HA, Simmonds I, Keay K, Hatzaki M (2011a) Climatological aspects of explosive cyclones in the Mediterranean. Int J Climatol 31:1785–1802

Kouroutzoglou J, Flocas HA, Simmonds I, Keay K, Hatzaki M (2011b) Assessing characteristics of Mediterranean explosive cyclones for different data resolution. Theor Appl Climatol 105:263–275. doi:10.1007/s00704-010-0390-8

Lim EP, Simmonds I (2002) Explosive cyclone development in the Southern Hemisphere and a comparison with Northern Hemisphere events. Mon Weather Rev 130:2188–2209. doi:10.1175/1520-0493

Maheras P, Flocas HA, Patrikas I, Anagnostopoulou C (2001) A 40 year objective climatology of surface cyclones in the Mediterranean region: spatial and temporal distribution. Int J Climatol 21:109–130

Murray RJ, Simmonds I (1991a) A numerical scheme for tracking cyclone centres from digital data. Part I: development and operation of the scheme. Aust Meteorol Mag 39:155–166

Murray RJ, Simmonds I (1991b) A numerical scheme for tracking cyclone centres from digital data. Part II: application to January and July general circulation model simulations. Aust Meteorol Mag 39:167–180

Petterssen S (1956) Weather analysis and forecasting. Vol I: motion and motion systems. McGraw Hill, New York

Prezerakos NG, Flocas HA (1997) The role of a developing upper diffluent trough in surface cyclogenesis over central Mediterranean. Meteorol Z 6:108–119

Sanders F, Gyakum JR (1980) Synoptic-dynamic climatology of the "bomb". Mon Weather Rev 108:1589–1606. doi:10.1175/1520-0493

Trigo IF, Bigg GR, Davies TD (2002) Climatology of cyclogenesis mechanisms in the Mediterranean. Mon Weather Rev 130:549–569. doi:10.1175/1520-0493

Uccellini LW (1986) The possible influence of upstream upper level baroclinic processes on the development of the QE II storm. Mon Weather Rev 114:1019–1027. doi:10.1175/1520-0493

On the Climate Characteristics of Convection Contribution to Precipitation in Southeastern Europe

C.J. Lolis, A. Bartzokas, and B.D. Katsoulis

Abstract The spatial and temporal variability of the convective percentage of precipitation in the Italian and Balkan peninsulas and the surrounding areas are examined for autumn, winter and spring. The data used consists of monthly grid point values of Convective Precipitation Rate (CPR) and Total Precipitation Rate (TPR) in the southeastern Europe for the 60-year period 1950–2009. The seasonal values are calculated from the monthly ones and the Convective Precipitation Percentage (CPP) is calculated, dividing CPR by TPR. The seasonal average patterns of CPP are characterized by a maximum over the sea and a minimum over the northern continental areas. The CPP over the sea is highest in autumn and lowest in spring, while CPP over the land is highest in spring and lowest in winter. The inter-annual variability of CPP is examined by applying S-mode Factor Analysis to the three seasonal data matrices. Only 12, 11 and 10 factors are retained for autumn, winter and spring. For all seasons, statistical significant of CPP trends are found: a decrease in central Europe and northern Italy and an increase in the area west of Sicily. These trends are possibly connected to the variability of the large-scale synoptic systems affecting the region.

1 Introduction

Precipitation in the area of southeastern Europe is characterized by a remarkable spatial and temporal variability. This is due to the complicated relief, the significant annual cycle involving the atmospheric circulation regime and the variability of the medium and large scale circulation systems affecting the region (see e.g. Hurrel and van Loon 1997; Trigo 2006). Moreover, atmospheric circulation and precipitation

C.J. Lolis (✉) • A. Bartzokas • B.D. Katsoulis
Laboratory of Meteorology, Department of Physics, University of Ioannina, Ioannina 45110, Greece
e-mail: chlolis@cc.uoi.gr

C.G. Helmis and P.T. Nastos (eds.), *Advances in Meteorology, Climatology and Atmospheric Physics*, Springer Atmospheric Sciences,
DOI 10.1007/978-3-642-29172-2_81,

in this area are expected to be significantly influenced by the forthcoming climate change (see e.g. Anagnostopoulou et al. 2006; Beniston et al. 2007). This influence may refer to the amount and/or the intensity of precipitation. A change in the intensity of precipitation may be closely connected to a corresponding change in the frequency of convective clouds and thunderstorms, which are the main sources of the convective part of precipitation. The physical mechanisms being responsible for the convective and the non-convective parts of precipitation are generally different (see e.g. Luo et al. 2010). During the cold period, the total precipitation and its convective and non-convective parts are generally expected to be covariant, as the main large scale circulation systems affecting the region control both precipitation types at a high degree. This means, that a change of precipitation nature towards a more convective or non-convective type may be better revealed by examining the variability of the percentage of convective precipitation relatively to the total amount instead of the variability of the convective or the non-convective parts, separately. In the present work, the spatial and temporal variability of the convective percentage of precipitation in the Italian and Balkan peninsulas and the surrounding areas are examined. The study is carried out for autumn, winter and spring and not for summer, because summer precipitation is almost zero in the southern parts of the region.

2 Data and Methodology

2.1 Data

The data used consists of monthly values of Convective Precipitation Rate (CPR) and Total Precipitation Rate (TPR) at 126 grid points (1.875° × 1.905°) in south-eastern Europe (5.625°E–30°E and 33.333°N–48.570°N) for winter, spring and autumn, for the period 1950–2009 (60 years), obtained from the NCEP/NCAR Reanalysis data set (Kalnay et al. 1996; Kistler et al. 2001). The seasonal values are calculated from the monthly ones and the Convective Precipitation Percentage (CPP) values are calculated by dividing CPR and TPR values. Thus, a 60 (years) × 126 (grid points) CPP matrix is constructed for each season.

2.2 Methodology

At first, the patterns of the mean CPP values for the period 1950–2009 are constructed for each season. Then, the inter-annual variability of CPP is examined by applying S-mode Factor Analysis (FA) with varimax rotation to each 60 × 126 data matrix of CPP (Jolliffe 1986). The number of the retained factors is decided by taking into account the SCREE plots. The patterns of high (>0.6) loading isopleths

and the diagrams of the factor scores time series are constructed. The inter-annual variations of factor scores, in fact, represent the variation of CPP in the high-loading areas. The statistically significant (95% confidence level) linear trends of CPP are found by applying the Mann Kendall test to the factor scores time series.

3 Results

For winter, the average CPP pattern (Fig. 1) is characterized by a maximum over the sea (above 95%) and a minimum over the northern continental areas (below 5%). This spatial distribution is in agreement with the fact that in winter, convection is intense over the sea, because sea surface is, averagely, warmer than the air above it and the depressions usually move along the Mediterranean Sea axis. The application of FA leads to 11 factors accounting for 76% of the total variance. The spatial distributions of the factor loadings reveal the high loading areas, indicating the sub-regions that correspond to the 11 factors (Fig. 1). The time series of the factor scores, express the inter-annual variations of CPP in the 11 sub-regions. A statistical significant decrease of the CPP is found for central Europe, the northern Italy and the northern Adriatic Sea (factors 1 and 6), while a statistically significant increase is found for the northern Tunisia and the sea area south of Sardinia (factor 4) (Fig. 2). The actual CPP change during the 60-year period is about –7% for the areas of factors 1 and 6 and about +10% for the area of factor 4. The correlation coefficient between factor 4 scores and the NAO index is found to be 0.50 (statistically significant at 99% confidence level), indicating a connection between CPP variability in the area of factor 4 and the North Atlantic Oscillation. Specifically, a high NAO index is connected to precipitation of a more convective nature in the area west of Sicily. This can be attributed to the fact that during a positive phase of NAO, the northerly flows over this region are more frequent leading to higher instability conditions associated with the passage of cold air masses over the warm sea.

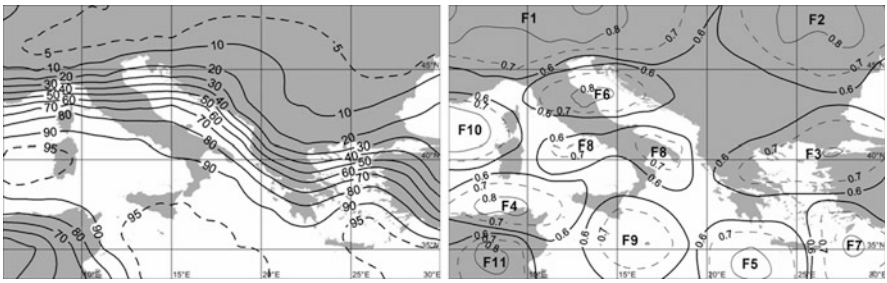

Fig. 1 (*Left*) The spatial distribution of mean winter Convective Precipitation Percentage CPP (%) for the period 1950–2009. (*Right*) The sub-regions of winter CPP covariability, defined by the spatial distribution of the factor loadings

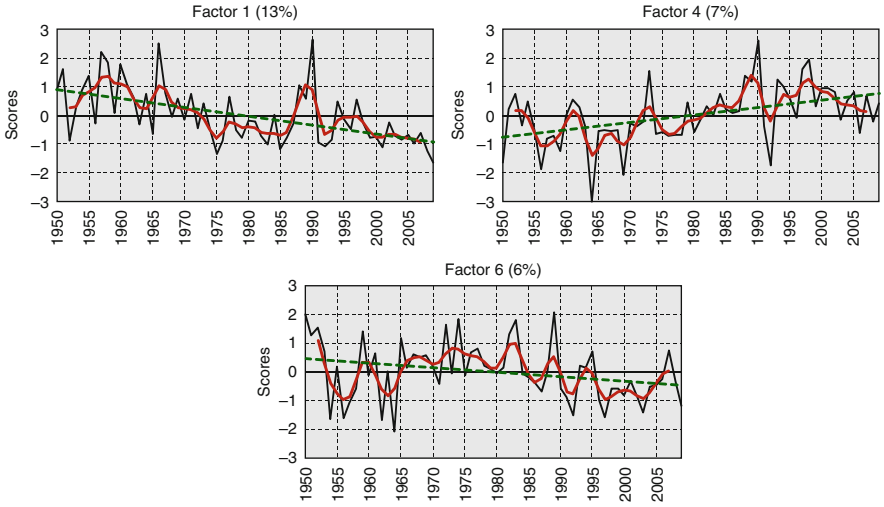

Fig. 2 Inter-annual variations of the winter factor scores, in fact CPP, that present statistically significant linear trends (*green dashed lines*), smoothed (*red bold lines*) by using 5-year moving averages with binomial coefficient weights. The percentage of variance explained is also shown

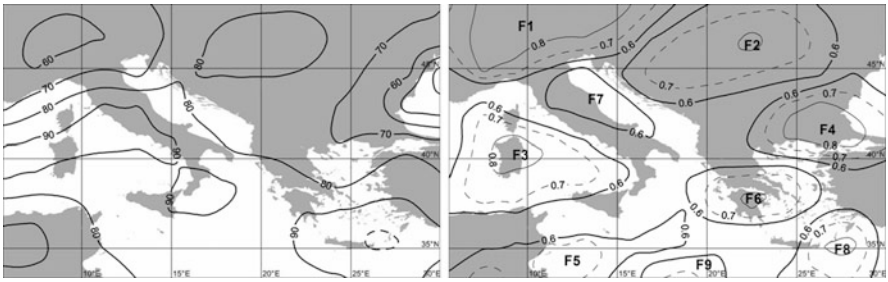

Fig. 3 As in Fig. 1, but for spring

For spring, the average CPP pattern (Fig. 3) shows a maximum over the sea, as it is the case for winter, but the CPP values over the northern continental regions are significantly higher than in winter (above 80%), because of the land warming and the associated high static instability conditions during late spring. FA leads to 10 factors, accounting for 70% of the total variance (Fig. 3). A statistically significant CPP decrease is shown over the northwestern continental areas of the central Europe and the Alps (factor 1), while an increase is found over Sardinia and the Tyrrhenian Sea (factor 3) (Fig. 4). The CPP change is about –35% for the area of factor 1 and about +7% for the area of factor 3.

For autumn, the average CPP pattern (Fig. 5) shows a maximum over the sea (above 95%) and a minimum over the northern continental areas, but the minimum values are higher than in winter (about 40%). FA leads to 12 factors accounting for

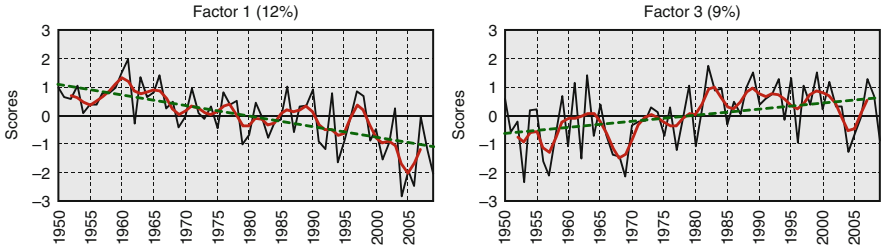

Fig. 4 As in Fig. 2, but for spring

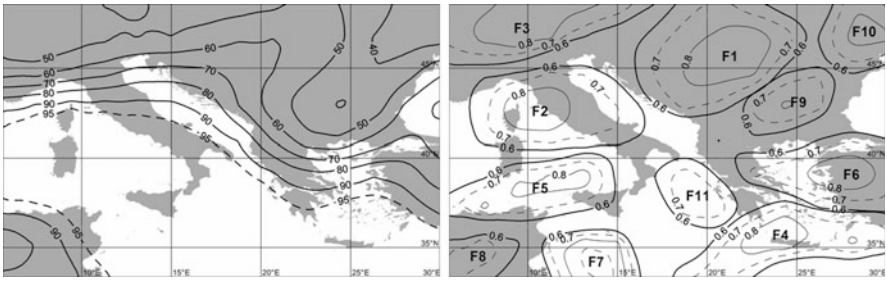

Fig. 5 As in Fig. 1, but for autumn

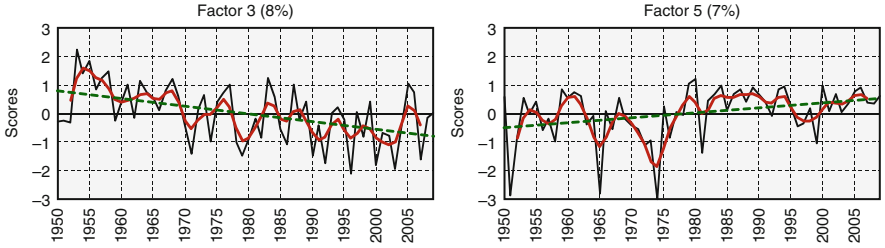

Fig. 6 As in Fig. 2, but for autumn

73% of total variance (Fig. 5). Statistical significant positive and negative trends are found for about the same areas of central Europe and the western Mediterranean (factors 3 and 5), slightly displaced relatively to those of winter and spring (Fig. 6). The CPP change is about –20% for the area of factor 3 and +2% for the area of factor 5.

The above convective precipitation characteristics could be partially explained by the fact, that cyclogenesis and precipitation are often promoted by land–sea temperature contrasts. Because land and sea have different effective thermal inertias, a large scale warming could affect this contrast, possibly reducing it in the winter period.

4 Conclusions

The variability of the convective percentage of precipitation (CPP) in southeastern Europe is studied for autumn, winter and spring and the following conclusions can be stated:

1. During the wet period of the year, which is characterized by the typical northwest Mediterranean cyclogenesis and depression activity, the spatial maximum of CPP is located over the Mediterranean Sea axis.
2. Among the three seasons, CPP over the sea is highest in autumn and lowest in spring, while CPP over the land is highest in spring and lowest in winter. This is in agreement with the intra-annual variation of static instability.
3. For the three seasons, a statistical significant CPP decrease is found for central Europe and northern Italy, while a statistically significant increase is found for the area west of Sicily.

References

Anagnostopoulou Chr, Tolika K, Flocas H, Maheras P (2006) Cyclones in the Mediterranean region: present and future climate scenarios derived from a general circulation model (HadAM3P). Adv Geosci 7:9–14

Beniston M, Stephenson DB, Christensen OB, Ferro CAT, Frei C, Goyette S, Halsnaes K, Holt T, Jylhä K, Koffi B, Palutikof J, Schöll R, Semmler T, Woth K (2007) Future extreme events in European climate: an exploration of regional climate model projections. Clim Chang 81:71–95. doi:10.1007/s10584-006-9226-z

Hurrel JW, van Loon H (1997) Decadal variations in climate associated with the North Atlantic oscillation. Clim Chang 36:301–326. doi:10.1023/A:1005314315270

Jolliffe IT (1986) Principal component analysis. Springer, New York

Kalnay E, Kanamitsu M, Kistler R, Collins W, Deaven D, Gandin L, Iredell M, Saha S, White G, Woollen J, Zhu Y, Leetmaa A, Reynolds B, Chelliah M, Ebisuzaki W, Higgins W, Janowiak J, Mo KC, Ropelewski C, Wang J, Jenne R, Joseph D (1996) The NCEP/NCAR 40-year reanalysis project. Bull Am Meteorol Soc 77:437–471

Kistler R, Kalnay E, Collins W, Saha S, White G, Woollen J, Chelliah M, Ebisuzaki W, Kanamitsu M, Kousky V, van den Dool H, Jenne R, Fiorino M (2001) The NCEP/NCAR 50-year reanalysis: monthly means CD-ROM and documentation. Bull Am Meteorol Soc 82:247–267

Luo Y, Wang Y, Wang H, Zheng Y, Morrison H (2010) Modeling convective-stratiform precipitation processes on a Mei-Yu front with the Weather Research and Forecasting model: comparison with observations and sensitivity to cloud microphysics parameterizations. J Geophys Res Atmos 115(18), art. no. D18117. doi: 10.1029/2010JD013873

Trigo IF (2006) Climatology and interannual variability of storm-tracks in the Euro-Atlantic sector: a comparison between ERA-40 and NCEP/NCAR reanalyses. Clim Dyn 26 (2–3):127–143. doi:10.1007/s00382-005-0065-9

Assessment on Temperature Extremes in Montenegro

J. Lukovic, D. Buric, V. Ducic, M. Doderovic, and I. Milevski

Abstract Montenegro so far has been poorly investigated in terms of climate extremes. The aim of this paper was analysis of extreme temperature indices in the Mediterranean region of Montenegro for the period 1951–2010. Four stations in the coastal area of Montenegro have been analysed Herceg Novi, Ulcinj, Budva and Bar. Due to well known great climate shift occurred in the late 1970 two periods (before 1980 and after 1980) were separately investigated. Six ETCCD indices of temperature extremes have been chosen. Indices and their trends are calculated on annual scale in order to identify possible temperature changes over the coastal region of Montenegro. The trend was analysed using Man-Kendall non parametric test while the slope is estimated using Sen's slope estimator.

1 Introduction

There has been considerable interest in the study of temperature and precipitation extremes (Zolina et al. 2008; Durao et al. 2010; Caesar et al. 2011) due to its great impact on the environment and society. Mediterranean region of Montenegro has been poorly studied regarding temperature extremes. This region is the smallest geographical area in the country. It is a typical Mediterranean area covering over

J. Lukovic (✉) • V. Ducic
Faculty of Geography, University of Belgrade, Belgrade 11000, Serbia
e-mail: jelenalu@yahoo.com

D. Buric
Hydrological and Meteorological Service of Montenegro, Podgorica, Montenegro

M. Doderovic
Faculty of Philosophy, University of Montenegro, Niksic, Montenegro

I. Milevski
University St. Kiril and Metodij, Skopje, FYR of Macedonia

C.G. Helmis and P.T. Nastos (eds.), *Advances in Meteorology, Climatology and Atmospheric Physics*, Springer Atmospheric Sciences,
DOI 10.1007/978-3-642-29172-2_82,

1,500 km^2. It is surrounded by Orijen Mountain (1,895 m), Lovcen Mountain (1,749 m), Sutorman Mountain (1,180 m) and Rumija Mountain (1,595 m).

Since 1951 there has been increasing temperature trend in Montenegro. World Meteorological Organization (WMO 2004), Intergovernmental Panel on Climate Change (IPCC 2007) stated that an increase in intensity of temperature, precipitation and other extreme weather events should be expected.

Therefore the aim of this paper is an analysis of temperature extremes in Mediterranean part of Montenegro. This highlights the interests for our study as it is the first one over the investigated area.

2 Data and Methodology

2.1 Data

In this paper daily temperature time series were used from meteorological stations Ulcinj, Bar, Herceg Novi and Budva (Table 1, Fig. 1) covering period 1951–2010. Data are obtained from Hydro-meteorological Service of Montenegro.

Table 1 List of the stations

Station name	WMO	Period	Latitude (N)	Longitude (E)	Elevation (m)
Budva	13458	1951–2010	42°17′	18°50′	2
Herceg Novi	13455	1951–2010	42°27′	18°31′	10
Bar	13461	1951–2010	42°06′	19°05′	5.7
Ulcinj	13464	1951–2010	41°55′	19°17′	3.6

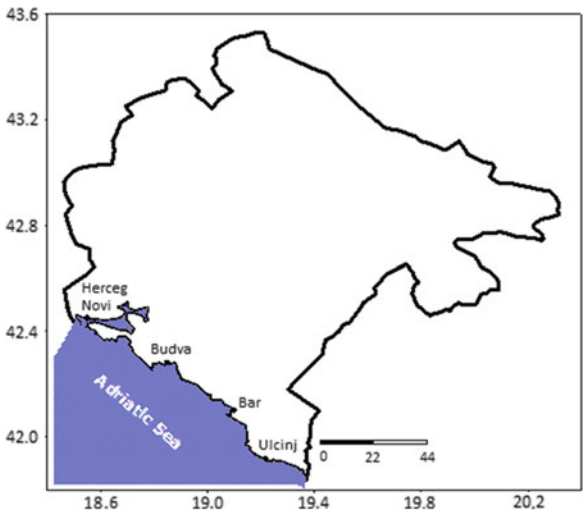

Fig. 1 Locations of the stations

Table 2 Definitions and abbreviations of the ETCCDI temperature indices used in this study

Index	Definition	Units
FD	Total number of frost days (days with absolute Tmin $< 0°C$)	Days
SU	Number of summer days: Annual count of days when TX (daily maximum temperature) $> 25°C$	Days
Tn10p	Days with Tmin $<$ 10th percentile of daily Tmin of the base period	%
Tx10p	Days with Tmax $<$ 10th percentile of daily Tmax of the base period	%
Tn90p	Days with Tmin $>$ 90th percentile of daily Tmin of the base period	%
Tx90p	Days with Tmax $>$ 90th percentile of daily Tmax of the base period	%

Definitions including formulas are available at http://cccma.seos.uvic.ca/ETCCDI/

Data are quality controlled for all stations following standards recommended by WMO (2004). Metadata were analysed regarding relocation, mal-operation. Missing data are corrected using nearby values. In assessing changes in temperature extremes timeseries homogeneity is a basic requirement. Unfortunately, an advanced correction method for daily temperature timeseries is not developed yet (Toreti et al. 2010). In this paper data are carefully evaluated applying a Multiple Analysis of Series for Homogenization (MASH v3.02) method, extended for homogenization of daily temperature data. Portions of time series with inhomogeneities were excluded from the analysis.

Expert team on Climate Change Detection and Indices (ETCCDI) which is supported by World Meteorological Organization (WMO) Commission for Climatology, the Joint Commission for Oceanography and Marine Meteorology (JCOMM) and the Research Program on Climate Variability and Predictability (CLIVAR) developed list of temperature and precipitation indices. In this paper we selected a set of six indices of temperature extremes (Table 2).

2.2 Methodology

The statistical significance of the calculated trends of the indices was tested using a Mann-Kendall test. This method has been applied because it is more suitable for non-parametric distributions. Man-Kendall test is used for trend analysis in ETCCDI workshops (Zhang et al. 2005). For trend estimation of indices has been used Sen's (1968) slope estimator. This is more robust approach for trend estimation of indices based on daily data.

3 Results

Six temperature indices have been assessed for the coastal region of the Montenegro. Stations have been analysed individually and then trend for the whole region has been calculated. Three indices are associated with cold

Table 3 Trends in temperature indices in the period 1951–2010 in days per decade (with statistical significance values)

Index	Bar	Ulcinj	Herceg Novi	Budva	Region (1951–2010)	Region (1951–1980)	Region (1981–2010)
FD	−3.75*	−0.97	−0.98	−0.84	−1.72**	−0.38	0.46
Tn10p	−3.35*	−0.52	−1.06	−0.06	−1.54	−0.21	−0.32
Tn90p	5.02*	1.96**	3.31*	5.27*	4.99*	−1.87**	4.25*
SU	3.34*	2.78***	1.62	3.68*	3.21***	−1.79**	2.87***
Tx10p	−1.88**	−1.92**	−1.67**	−1.42	−1.77**	−0.55	−1.16
Tx90p	3.76*	1.86**	1.12	4.15*	3.43*	−0.80	3.93*

*0.1% level; **10% level; ***1% level

temperatures and three for warm temperatures. All stations indicate statistically significant increase in the Tn90p index over the period 1951–2010 showing the most consistent pattern of trends. There has been an increase in whole region as well (Table 3).

Very strong increase is also in Tx90p as more than half stations indicated significant increase. Percentile-based indices have shown an agreement in sign and significance of trend for stations individually and whole region compared to global results. In coastal Montenegro the frequency of warm nights and warm days increased and frequency of cold nights and cold days decreased. Percentile indices are more robust over large areas as they account for local climates effects (Caesar et al. 2011). Cold nights (Tn10p) have shown negative trend significant only for Bar. Similar to this, small and negative trends are calculated for cold days (Tx10p) significant for all stations except for Budva.

In number of frost days (FD) decrease has occurred in all stations. Most trends are not significant with the exception of Bar station and whole region. Frich et al. (2002) have found uniform decrease in FD in the second half of the twentieth century. Results for the coastal region of Montenegro are consistent with those from Frich et al. (2002). Kostopoulou and Jones (2005) have found increase in number of frost days over the area of Serbia and Montenegro at annual and seasonal scale for the period 1958–2000.

Summer days have shown strong statistically significant increase for all stations with the exception of insignificant trend for Herceg Novi station. This reveals increased number of days with daily maximum temperature above 25°C over the study area during the warm season.

Trends calculated for Mediterranean part of Montenegro have generally shown tendency towards wormer conditions. Changes in warm indices are higher than changes in cold indices. Negative trends are calculated for cold nights but the most significant trends are obtained in terms of warm conditions over the study area. Bar station pronounced the strongest significance in general. This could be due to several reasons. In last few decades process of urbanization has happened which may lead to urban island of heat. Results for Ulcinj and Herceg Novi may indicate the impact of urban island of heat. These meteorological stations are located far

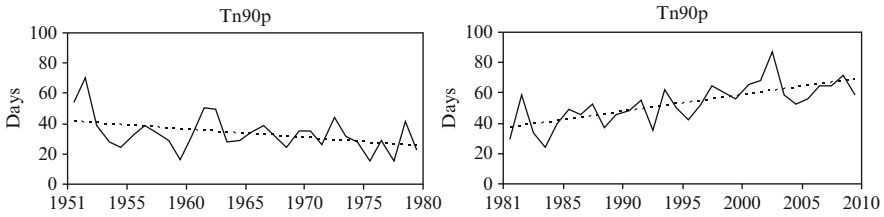

Fig. 2 Regional time series for warm nights (units: days) in (*left*) 1951–1980 period and (*right*) 1981–2010 period. *Dashed line* indicates Sen's slope estimator

from the town center, and trend change for them is showing less significant results comparing to urban stations in Bar and Budva.

However, in Montenegro in the second half of the twentieth century there has been statistically significant increase in temperature (Buric 2011). So far, there is no unique scientific opinion regarding the cause of such temperature increase. Prevails opinion that greenhouse effect is not always responsible for temperature and precipitation variations, internal oscillations may also contribute (Lukovic et al. 2010).

Due to well known great climate shift occurred in the late 1970 two periods (before 1980 and after 1980) were separately investigated (Table 3) on regional scale. For the period 1951–1980 all indices have shown decrease. Statistically significant decrease is calculated for summer and warm nights. Decrease in cold indices is insignificant. However, in the period 1981–2010 results are showing strong significant increase in warm days and warm nights (Fig. 2), including summer days. Insignificant decrease is calculated in cold days and cold nights. Regional indices calculated for the period 1981–2010 are in accordance to those calculated for the whole period as well as to global analysis of Alexander et al. (2006). For the Tn90p index there is no agreement in sign and significance of trend in 1951–1980 compared to 1981–2010 and global results.

4 Conclusions

In this paper six indices have been analysed in order to assess temperature extremes in the Mediterranean part of Montenegro. So far, whole country has been poorly documented in terms of climate extremes.

Results presented in this paper are in agreement with global analysis of Alexander et al. (2006). In all stations number of frost days decreased at annual scale. Negative trend has been calculated for cold nights and cold days as well. The most significant trends are obtained for warm conditions over the investigated area in the period 1951–2010.

However, separately investigated period 1951–1980 for region has shown opposite tendencies and contrasting trend to period 1951–2010 as well as 1981–2010.

Possibly due to well known climate shift occurred in late 1970s there has been change in sign of trend for warm days and warm nights. These two separately investigated periods have shown contrasting temperature trends.

Future investigation should take into analysis other temperature indices as well as seasonal scale of the investigation.

References

Alexander LV, Zhang X, Peterson T, Caesar J, Gleason B, Klein Tank AMG, Haylock M, Collins D, Trewin B, Rahimzadeh F (2006) Global observed changes in daily climate extremes of temperature and precipitation. J Geophys Res 111:D05109. doi:10.1029/2005 JD006290

Buric D (2011) Indices of temperature and precipitation extremes in Podgorica 1951–2008: Collection of papers of Institute of Geography "Jovan Cvijić", SANU, 61(1):31–41

Caesar J, Alexander LV, Trewin B, Tse-ring K, Sorany L, Vuniyayawa V, Keosavang N, Shimana A, Htay MM, Karmacharya J (2011) Changes in temperature and precipitation extremes over the Indo-Pacific region from 1971 to 2005. Int J Climatol 31(6):791–801. doi:10.1002/joc.2118

Durao R, Pereira M, Costa MJ, Delgado AC, del Barriod J, Soares A (2010) Spatial–temporal dynamics of precipitation extremes in southern Portugal: a geostatistical assessment study. Int J Climatol 30:1526–1537. doi:10.1002/joc.1999

Frich P, Alexander LV, Della-Marta P, Gleason B, Haylock M, Klein Tank AMG, Peterson T (2002) Observed coherent changes in climatic extremes during the second half of the twentieth century. Clim Res 19:193–212. doi:10.3354/cr019193

Intergovernmental Panel on Climate Change (2007) Climate change: mitigation. Contribution of working group 1 and 3 to the fourth assessment report of the intergovernmental panel on climate change. Cambridge University Press, Cambridge

Kostopoulou E, Jones PD (2005) Assessment of climate extremes in the Eastern Mediterranean. Meteorol Atmos Phys 89:69–85. doi:10.1007/s00703-005-0122-2

Lukovic J, Manojlovic P, Mustafic S (2010) Temperature change in Serbia and NAO. Bull Serb Geogr Soc 90(1):123–130

Sen PK (1968) Estimates of the regression coefficient based on Kendall's tau. J Am Stat Assoc 63:1379–1389

Toreti A, Kuglitsch FG, Xoplaki E, Maraun D, Wanner H, Luterbacher J (2010) Characterization of extreme winter precipitation in the Mediterranean and associated anomalous atmospheric circulation patterns. Nat Hazards Earth Sys Sci 10:1037–1050

World Meteorological Organization (2004) Report of the CCI/CLIVAR expert team on climate change detection, monitoring and indices (ETCCDMI). World Meteorological Organization, Geneve

Zhang X, Aguilar E, Sensoy S, Melkonyan H, Tagiyeva U, Ahmed N, Kutaladze N, Rahimzadeh F, Taghipour A, Hantosh TH, Alpert P, Semawi M, Ali MK, Al-Shabibi MHS, Al-Oulan Z, Zatari T, Al Dean Khelet I, Hamoud S, Sagir R, Demircan M, Eken M, Adiguzel M, Alexander L, Peterson TC, Wallis T (2005) Trends in Middle East climate extreme indices from 1950 to 2003. J Geophys Res 110:D22104. doi:10.1029/2005JD006181

Zolina O, Simmer C, Kapala A, Bachner S, Gulev S, Maechel H (2008) Seasonally dependent changes of precipitation extremes over Germany since 1950 from a very dense observational network. J Geophys Res 113:D06110. doi:10.1029/2007JD008393

Trend Analysis for Climatic Time Series for Greece

G. Marougianni, D. Melas, I. Kioutsioukis, H. Feidas, P. Zanis, and E. Anadranistakis

Abstract A database of climatic time series from the network of Hellenic National Meteorological Service has been developed under the research program GEOCLIMA. Initially a quality test was applied to the raw data and then missing data have been imputed with a regularized expectation–maximization algorithm to complete the climatic record. Next, a quantile-matching algorithm was applied in order to verify the homogeneity of the data. The processed time series were used for trend analysis of the time series of maximum and minimum air temperature and precipitation. It is shown that peak temperature extremes are becoming warmer, especially for the minimum temperatures, while precipitation is decreasing over the area with variable local significance though.

1 Introduction

There is currently a strong scientific interest concerning the issue of climate change. Many studies examine time series of a climate variable in order to investigate whether it contains a trend that might indicate if, by how much and in what direction climate has changed (Kioutsioukis et al. 2010).

In this study, the datasets of maximum and minimum air temperature and precipitation obtained from a number of meteorological stations in Greece for the

G. Marougianni • D. Melas (✉) • I. Kioutsioukis
Laboratory of Atmospheric Physics, Physics Department, Aristotle University of Thessaloniki, Thessaloniki 54124, Greece
e-mail: melas@auth.gr

H. Feidas • P. Zanis
Department of Meteorology and Climatology, School of Geology, Aristotle University of Thessaloniki, Thessaloniki 54124, Greece

E. Anadranistakis
Hellenic National Meteorological Service, Athens, Greece

C.G. Helmis and P.T. Nastos (eds.), *Advances in Meteorology, Climatology and Atmospheric Physics*, Springer Atmospheric Sciences,
DOI 10.1007/978-3-642-29172-2_83,

years 1955–2010 were used for trend analysis. Prior to trend analysis of the time series, missing observations have been imputed by using an *expectation–maximization* algorithm (Schneider 2001), in order to complete the climatic database. The observations were also examined to verify their homogeneity.

The scope of this study is to examine the trends in the annual and seasonal time series of precipitation and air temperature observations for all available stations in Greece, for the longest common time period of homogenous data, applying the Mann-Kendall test, as suggested by Sneyers (1992).

2 Data and Methodology

The available data consist of monthly values of 27 variables from 68 stations obtained from the database of the Hellenic National Meteorological Service (HNMS). The time series of the data extend from 1955 to 2010. In the present study solely the trend analysis for maximum and minimum air temperature and precipitation is presented which exhibit the most significant trends. The monthly values were not estimated by HNMS if more than 10 daily values or 5 consecutive days were missing, according to the guidelines of WMO. These data were subjected to a series of quality control tests by the HNMS, namely:

- Internal consistency checks, to ensure that the monthly means follow a consistent seasonal cycle,
- Between-variable consistency tests, to ensure for example that monthly minimum, mean and maximum temperatures are consistent and that months with zero precipitation have zero wet days,
- Identification of outliers in the monthly values, in order to ensure that predefined absolute limits are not exceeded.

Trends calculated from incomplete datasets can be biased. Thus, an expectation–maximization algorithm was applied in order to compute the missing values in the time series, while using the criterion that a year is considered to be "complete" when at least 8 monthly values are recorded (Peterson et al. 1998). Moreover, totals and averages were only estimated for the time series of the stations that values were available for at least 80% of the 30-year period, with no more than 3 consecutive years missing.

Annual precipitation totals were conventionally made to correspond to the period from September 1st to August 31st and dated by the year in which January occurred, to ensure that the rainy season is retained as one continuous period that ends with the dry summer season (Feidas et al. 2007). Similarly, annual mean temperature was conventionally made to correspond to the period from December 1st to November 30th (Feidas et al. 2004).

For the trend analysis, datasets from the time period from 1955 to 2010 were used for a number of stations that is different according to the meteorological variable. The spatial distribution of the stations with data coverage over 90% is

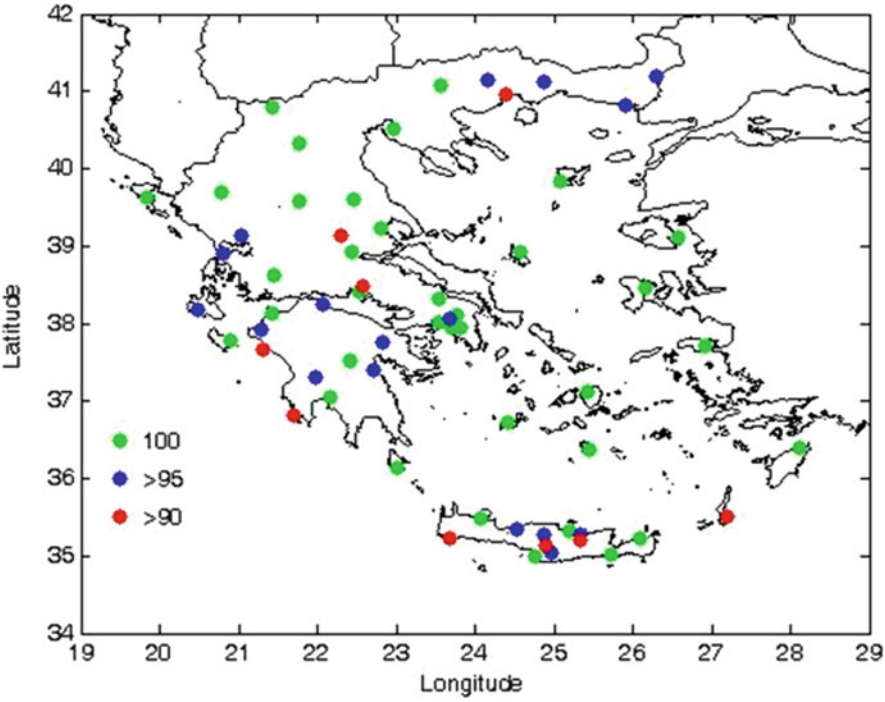

Fig. 1 Spatial distribution of the stations with data coverage ≥90%

Table 1 Annual and seasonal trends estimated for the time period 1955–2010 for precipitation

Station	Annual trend		Winter trend		Summer trend	
	Trend value	p-value	Trend value	p-value	Trend value	p-value
Alexandroupoli	−1.52	0.07	−0.87	0.12	0.05	0.97
Helliniko	0.22	0.58	−0.13	0.81	0.08	0.17
Heraklio	−1	0.44	−0.23	0.76	−0.02	0.17
Corfu	**−3.63**	0.03	−2.2	0.14	0.67	0.15
Larissa	0.06	0.86	0.34	0.51	−0.1	0.9
Thessaloniki (Mikra)	−0.85	0.31	−0.01	0.84	−0.08	1
Milos	0.77	0.52	0.45	0.14	0.04	0.33
Mytilene	−1.96	0.26	−1.78	0.17	−0.02	0.94
Rhodos	**−3.19**	0.04	**−2.43**	0.05	−0.05	0.23
Skyros	−1.54	0.11	−1.19	0.06	0.004	0.54
Tripoli	−2.25	0.08	−1.63	0.11	0.42	0.2

shown in Fig. 1. The data for the time period 2005–2010 derived from the database of the National Oceanic and Atmospheric Administration (NOAA) as well as the European Climate Assessment Database, which is initiated by the European Climate Support Network. This is due to the fact that the database of HNMS has not been fully updated for the period 2005–2010.

Table 2 Annual and seasonal trends estimated for the time period 1955–2010 for maximum temperature (°C/year)

Station	Annual trend		Winter trend		Summer trend	
	Trend value	p-value	Trend value	p-value	Trend value	p-value
Alexandroupoli	0.02	0.28	0.002	0.6	**0.03**	0
Helliniko	0.006	0.82	**−0.02**	0.017	**0.03**	0.01
Heraklio	0.005	0.69	**−0.02**	0.018	**0.02**	0.02
Corfu	0.008	0.63	−0.009	0.24	**0.03**	0
Larissa	0.01	0.6	−0.003	0.9	0.01	0.08
Naxos	0.015	0.17	−0.01	0.18	**0.03**	0
Milos	**0.03**	0.04	−0.006	0.63	**0.06**	0
Mytilene	0.025	0.16	−0.004	0.7	**0.05**	0
Rhodos	−0.02	0.15	−0.009	0.21	**−0.04**	0
Skyros	0.002	0.85	**−0.02**	0.04	**0.02**	0

Table 3 Annual and seasonal trends estimated for the time period 1955–2010 for minimum temperature (°C/year)

Station	Annual trend		Winter trend		Summer trend	
	Trend value	p-value	Trend value	p-value	Trend value	p-value
Alexandroupoli	0.02	0.12	0	0.97	**0.05**	0
Helliniko	0	0.75	0	0.61	0.01	0.08
Heraklio	0.02	0.1	0	0.73	**0.03**	0
Corfu	**0.04**	0.002	0.02	0.06	**0.06**	0
Larissa	0.02	0.16	0	0.79	**0.04**	0
Naxos	**0.03**	0.009	0.01	0.09	**0.04**	0
Milos	0	0.51	0	0.26	**0.02**	0
Mytilene	0.01	0.41	−0.01	0.25	**0.03**	0
Rhodos	**0.08**	0	**0.08**	0	**0.08**	0
Skyros	0	0.74	−0.01	0.06	**0.02**	0

3 Results and Discussion

The results from the trend analysis of the meteorological variables of special interest (air temperature and precipitation) are presented in Tables 1–3.

For the majority of the stations, an overall decreasing trend is evident in annual and seasonal precipitation series. There is a clear downward trend in winter and annual precipitation. It seems that after 1984 Greece entered a dry period which is responsible for the decreasing trend found for the whole period 1955–2010 (Feidas et al. 2007). However, there are no statistically significant cases, with the exception of the stations of Corfu and Rhodes.

A distinct overall trend in winter and summer maximum temperatures is exhibited in Table 2. However, the pattern of the trend is different by season. Winter shows a slight cooling trend, statistically significant only for a small number of stations, whereas summer shows a distinct overall warming trend, statistically significant for most stations (Figs. 2 and 3). The magnitude of the trend is higher in the summer

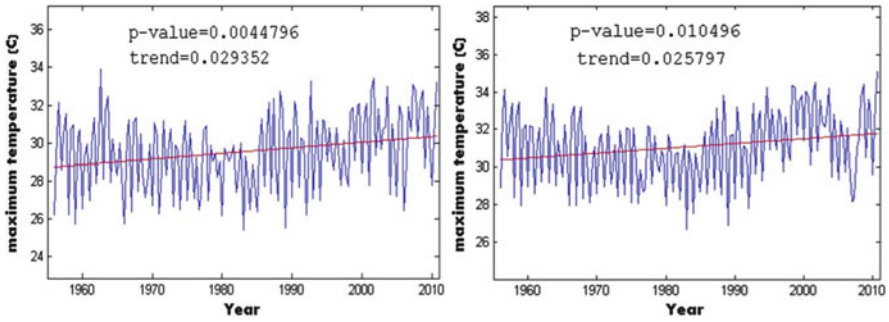

Fig. 2 Trend line of summer maximum temperature at the stations of Alexandroupoli (*left*) and Helliniko (*right*) for the 1955–2010 period

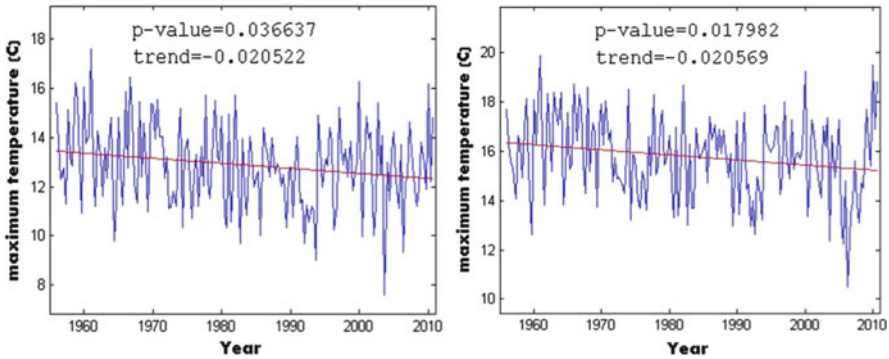

Fig. 3 Trend line of winter maximum temperature at the stations of Skyros (*left*) and Heraklio (*right*) for the 1955–2010 period

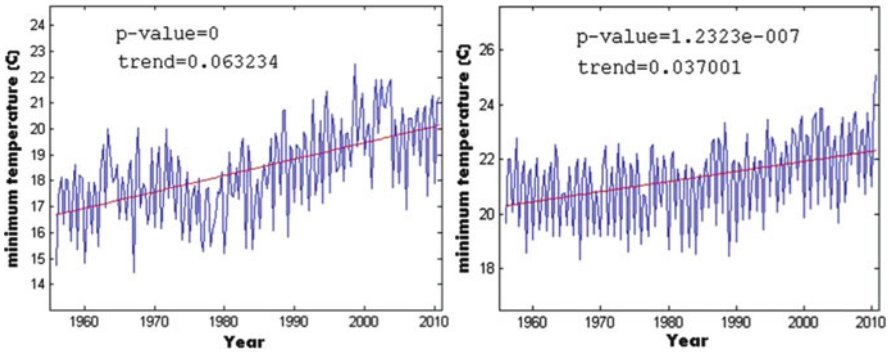

Fig. 4 Trend line of summer minimum temperature at the stations Corfu (*left*) and Naxos (*right*) for the 1955–2010 period

(mean value = 0.024) than in winter (mean value = −0.010). The absence of a distinct overall trend in the annual values is the result of the counterbalance of the two opposite trends in summer and winter. Although a clear warming trend is also observed for summer minimum temperatures (mean value = 0.038), winter temperatures remain unchanged (Table 3). This results to an overall positive trend in their annual values (Fig. 4). Further, peak minimum temperatures warm faster than peak maximum temperatures, as documented elsewhere (Kioutsioukis et al. 2010).

4 Conclusions

To summarize, between 1955 and 2010:

- Ninety percent of the examined stations showed a significant increase in the summer maximum and minimum temperatures; this could be physically linked to the Etesian winds because of the less frequent expansion of the low over the southeastern Mediterranean (Feidas et al. 2004),
- Summer minimum temperatures have been increasing at a faster rate than that of summer maximum temperatures, reflecting an asymmetric change of extreme temperature distributions (Kioutsioukis et al. 2010),
- Total annual precipitation has been significantly decreased at the stations located in western Greece as well as in the southeast, while the remaining areas exhibit a non-significant downward trend. This reduction is linked to the positive phase of the NAO that resulted in an increase in the frequency and persistence of anticyclones over the Mediterranean.

Acknowledgments The research has been co-financed by the European Union (European Regional Development Fund) and Greek national funds through the Operational Program "Competitiveness and Entrepreneurship" of the National Strategic Reference Framework (NSRF) – Research Funding Program COOPERATION 2009 (no. 09COP-31-1094, Title "Development of a Geographic Climate Information System").

References

Feidas H, Makrogiannis T, Bora-Senta E (2004) Trend analysis of air temperature time series in Greece and their relationship with circulation using surface and satellite data: 1955–2001. Theor Appl Climatol 79:185–208. doi:10.1007/s00704-004-0064-5

Feidas H, Noulopoulou Ch, Makrogiannis T, Bora-Senta E (2007) Trend analysis of precipitation time series in Greece and their relationship with circulation using surface and satellite data: 1955–2001. Theor Appl Climatol 87(1–4):156–177. doi:10.1007/s00704-006-0200-5

Kioutsioukis I, Melas D, Zerefos C (2010) Statistical assessment of changes in climate extremes over Greece (1955–2002). Int J Climatol 30(11):1723–1737. doi:10.1002/joc.2030

Peterson TC, Easterling DR, Karl TR et al (1998) Homogeneity adjustments of in situ atmospheric climate data: a review. Int J Climatol 18(13):1493–1517. doi:10.1002/(SICI)1097-0088(19981115)18:13<1493::AID-JOC329>3.0.CO;2-T

Schneider T (2001) Analysis of incomplete climate data: estimation of mean values and covariance matrices and imputation of missing values. J Climate 14:853–871. doi:10.1175/1520-0442(2001) 014<0853:AOICDE>2.0.CO;2

Sneyers R (1992) On the use of statistical analysis for the objective determination of climate change. Meteorol Z 1(5):247–256

Transferring Climate Information for Application and Planning: The Climate-Tourism/Transfer-Information-Scheme

A. Matzarakis

Abstract A new approach based on climate thresholds, the Climate-Tourism-Information-Scheme CTIS, which is appropriate for destination analysis of present climate conditions and for future climate changes is shown here. In particular, the method combines meteorological and tourism related components. All factors are included in one single information scheme in order to describe these factors in a high temporal resolution. The CTIS intends to integrate and simplify climate information for tourism. It contains detailed climate information which can be used by tourists to anticipate thermal conditions (including thermal comfort, cold stress, heat stress, cold stress and sultriness) as well as aesthetical (sunshine) and physical conditions (wind, rain) when planning their vacations. CTIS provides all-seasonally frequency classes and frequencies of extreme weather events on a 10-day or monthly time scale. The included factors and parameters are shown in terms of thresholds and frequencies. In general, the definitions of the threshold values do not necessarily correspond to universal meteorological threshold values and are adjusted to applied climatology purposes e.g. tourism, health and urban planning.

1 Introduction

It is a fact that weather/climate and several economic braches like tourism/recreation are interconnected in diverse ways. Tourists, tour organizers, travel agencies, tourism planners, and stakeholders for example need to be reliably informed and educated about the role of weather and climate in tourism and health issues (Matzarakis 2006). The knowledge of weather and information about climate and

A. Matzarakis (✉)
Meteorological Institute, Albert-Ludwigs-University Freiburg, Werthmannstr. 10, Freiburg D-79085, Germany
e-mail: andreas.matzarakis@meteo.uni-freiburg.de

C.G. Helmis and P.T. Nastos (eds.), *Advances in Meteorology, Climatology and Atmospheric Physics*, Springer Atmospheric Sciences,
DOI 10.1007/978-3-642-29172-2_84,

its application can assist tourism planning and tourism industries to reduce the adverse effects in the economy sector (Scott et al. 2009). General knowledge of climate parameters (based on thresholds) and their appropriateness for tourism and recreation are basic information, i.e. if too high sun intensity or strong winds. Climate extremes, e.g. heat waves or storms are most relevant because of the possible damages on infrastructure and human life. A useful climate advisory service will help to prepare and protect tourists and groups at risk (e.g. retirees, sick people, and children).

2 Methodological Approaches

The effects of specific climate conditions in tourism areas occur not only in the meso scale but more in the micro scale, where visitors and local population spend most of their time during day and night (Matzarakis 2006; Matzarakis et al. 2010). Therefore information about climate in high temporal and spatial resolution is of importance and interest. In addition, the knowledge of possibilities for mitigation and adaptation of current and expected climate conditions require interdisciplinary approaches and solutions. Many climate phenomena and conditions have been adequately studied qualitatively but not quantitatively so far. Current research focuses on the quantification of strategies for reductions of extremes and frequencies as well as thresholds in tourism areas.

The interactions of weather and climate in tourism are shown in Fig. 1. It is known that tourism, especially summer tourism, can be described by the triple S (sun, sea and sand). Many of the tourism factors creating the triple S are dependent on weather and climate (Fig. 1). An additional factor that can be added to the triple S, or used as single winter S, is snow, the main decision factor for winter tourism. Figure 1 shows the relevance and importance of weather and climate factors in the tourism sector.

In order to assess the climatic tourism potential for human health air temperature and precipitation are not sufficient. For example, winter sports enthusiasts and tourists desire snow as well as sunshine, beneficial thermal conditions, and recreation in their holidays. Nowadays, the assessment can be performed by facets (Fig. 2) of climate in tourism (thermal, aesthetical and physical facet) (de Freitas 2003). The thermal facet of climate is based on a complex thermal index, e.g. PET, which is based on the human energy balance. It describes the effect of the climate not only for cold but also for warm conditions. In general, PET (physiologically equivalent temperature) describes the effect of the thermal surroundings of the human body and includes the energy exchange between humans and environment and assesses the effect of the thermal environment. The other two facets, the aesthetical and physical, can be covered by simple and easily extracted parameters and factors, e.g. snow height and daily sunshine duration from data records or networks (Matzarakis 2006; Matzarakis et al. 2010).

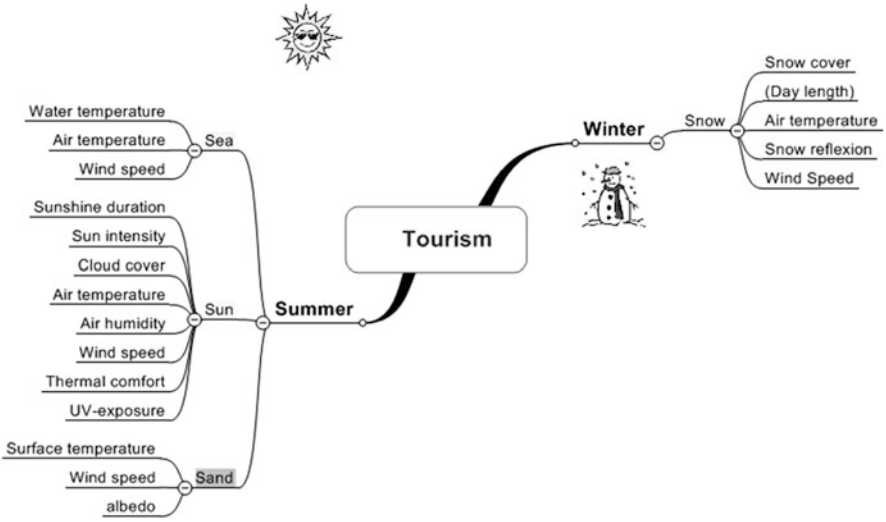

Fig. 1 Relations between climate and tourism and important parameters and factors (Matzarakis 2006)

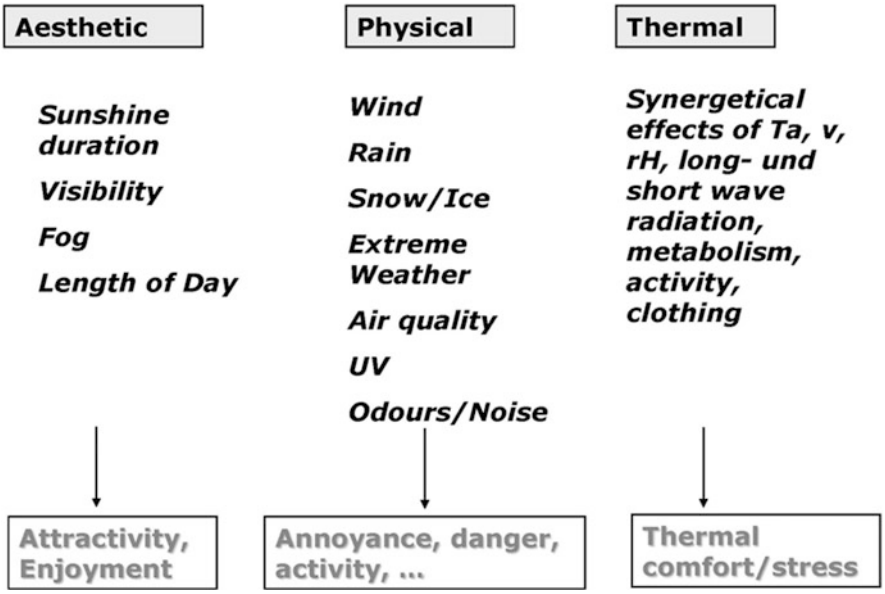

Fig. 2 Facets of climate in tourism (After Matzarakis et al. 2010)

Depending on the objectives of the evaluation, these meteorological parameters can be measured or calculated in a grid-net by numerical models. The most relevant parameters and factor important for tourism and recreation can be found in Fig. 2.

In order to quantify and visualize the facets of climate in tourism, a new approach based on climate thresholds (Climate-Tourism-Information-Scheme) has been developed. The method combines meteorological and tourism related components. It integrates and simplifies climate information for tourism. Thus, besides the two variables most frequently used in impact assessment studies (air temperature and precipitation), also physiologically equivalent temperature (PET), cold stress (PET $< 0°C$), heat stress (PET $> 35°C$), thermal acceptability ($18°C <$ PET $< 29°C$), sunshine/cloud cover conditions in terms of the number of days with a cloud cover <5 octas, vapour pressure >18 hPa, wind velocity >8 m/s, relative humidity >93%, precipitation <1 mm as well as precipitation >5 mm, and snow cover >10 cm are considered. In general, the definitions of the several threshold values do not necessarily correspond to the universal meteorological threshold values and are adjusted to applied tourism climatology and human health applications. For example, under meteorological aspects, a stormy day is given by a wind strength of at least 8 Bft, which corresponds to a wind velocity greater than 17.2 m/s, while in tourism climatology a wind velocity of 8 m/s (5 Bft) is perceived as unpleasant and uncomfortable. All the above-mentioned factors have been included in an information scheme in order to describe these factors in a high temporal resolution (Matzarakis 2007).

CTIS contains detailed climate information which can be used by tourists to anticipate thermal comfort as well as aesthetical and physical conditions for planning their vacations. CTIS provides all-seasonal frequency classes and frequencies of extreme weather events on a 10-day or monthly time scale (Matzarakis 2007). This method is preferred for analyzing climate stations or grid points. Since the results presented here are based on models and thus influenced by the models' uncertainties, a temporal resolution finer than 1 month is not considered to be useful.

3 Results

For the integral quantification of climate and tourism purposes in terms of a destination analysis the CTIS builds a valuable method, because it includes the most relevant parameters and factors in high temporal resolution (Matzarakis 2007; Lin and Matzarakis 2008; Zaninovic and Matzarakis 2009).

Each coloured column describes the corresponding frequency of any parameter or factor (Fig. 3). A frequency of 100% indicates that each day in a month is characterized by the respective condition listed on the right hand side. A frequency of 50% corresponds to an occurrence of the indicated condition during 15 days, 10% to 3 days of the considered month etc. Considering the second row in Fig. 4, heat stress occurs from June to September with an average frequency between 20%

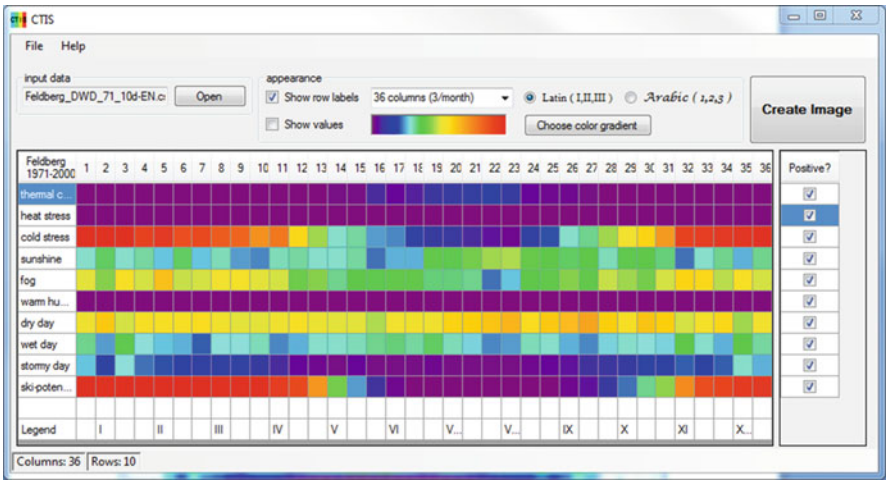

Fig. 3 CTIS main window for import of data, visual options and preparation of the factors (positive or negative)

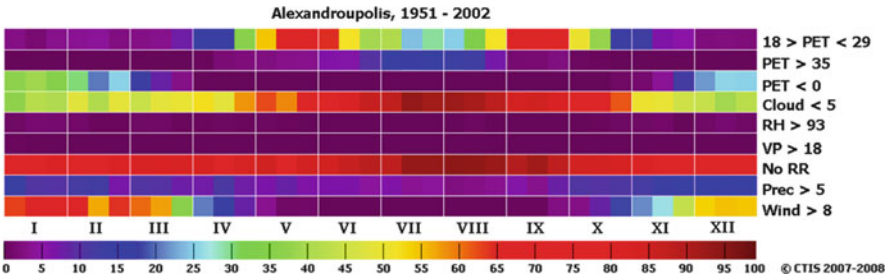

Fig. 4 CTIS for Alexandroupolis for the period 1951–2002

Table 1 Description of the range of rating for CTIS

color	range of per cent values	description
	< 14%	very poor
	14 % - 28 %	↕
	28 % - 42 %	↕
	42 % - 56 %	moderate
	56 % - 70 %	↕
	70 % - 84 %	↕
	> 84 %	ideal

and 40%, meaning that approx. 6–12 days are characterized by heat stress. In Fig. 4 the CTIS for Alexandroupolis for the period 1951–2002 is presented as an example.

As seen in Fig. 3 factors may be rated as positive or negative resulting in an inversion of the assessment scale for those rows. To make the information provided by the CTIS diagrams easier to understand a probability scale (Zaninovic and Matzarakis 2009) expressed in seven climate classes (with 14% probability in each class) from "very poor" to "ideal", is incorporated (Table 1). This rating is intended for use with classification coloring.

A small software module which is able to provide the graphs has been developed in a user friendly way (Matzarakis et al. 2010). It reads text based data files that contain frequencies of all climatic factors the user wants to present in his diagram. These factors have to be scaled on a uniform scale like 0–1 or 0–100. The CTIS program consists of two parts: the main window including data import and basic preparation and second, the report window for fine tuning the resulting image in size and font with real-time preview.

CTIS-software can be also used for other kind of analysis and visualizations in applied climatology and related disciplines.

4 Conclusions

Climate and climate relevant information has to be presented and visualized in an easily understandable way for non experts. Because of different forms of tourism and the diverse requirements on climate information an integral assessment of weather and climate in one single factor or value is very difficult and too complex to understand. A single value would fail to consider all factors and information. This lack can be filled by CTIS including the most relevant factors based on the climate facets in tourism and recreation.

Current and expected climatic conditions can nowadays be described with methods from human biometeorology and tourism climatology. Specific kinds of tourism possibilities based on CTIS can be assessed and quantified for different destination. Periods with occurrences of specific extremes, e.g. heat waves or periods of strong wind, can detected. Based on results such as these, tourists, the tourism industry, health resorts and authorities can be prepared or protected in order to avoid negative consequences in the economic sectors of tourism, recreation and health.

References

de Freitas CR (2003) Tourism climatology: evaluating environmental information for decision making and business planning in the recreation and tourism sector. Int J Biometeorol 48:45–54. doi:10.1007/s00484-003-0177-z

Lin TP, Matzarakis A (2008) Tourism climate and thermal comfort in Sun Moon Lake, Taiwan. Int J Biometeorol 52:281–290. doi:10.1007/s00484-007-0122-7

Matzarakis A (2006) Weather and climate related information for tourism. Tour Hosp Plann Dev 3:99–115. doi:10.1080/14790530600938279

Matzarakis A (2007) Assessment method for climate and tourism based on daily data. In: Matzarakis A, de Freitas CR, Scott D (eds) Developments in tourism climatology. Commission Climate, Tourism and Recreation. International Society of Biometeorology, Freiburg, pp 52–58

Matzarakis A, Schneevoigt T, Matuschek O, Endler C (2010) Transfer of climate information for tourism and recreation – the CTIS software. In: Matzarakis A, Mayer H, Chmielewski FM (eds) Proceedings of the 7th conference on biometeorology. Ber Meteorol Inst Univ Freiburg no. 20, pp 392–397

Scott D, de Freitas CR, Matzarakis A (2009) Adaptation in the tourism and recreation sector. In: McGregor GR, Burton I, Ebi K (eds) Biometeorology for adaptation to climate variability and change. Springer, Dordrecht, pp 171–194

Zaninovic K, Matzarakis A (2009) The biometeorological leaflet as a means conveying climatological information to tourists and the tourism industry. Int J Biometeorol 53:369–374. doi:10.1007/s00484-009-0219-2

Climatic Classification of an Industrial Area of Eastern Mediterranean (Thriassio Plain: Greece)

A. Mavrakis

Abstract The purpose of this work is to investigate the possible differentiations of the climatic parameters of an industrial basin of the Eastern Mediterranean. For this purpose, the monthly average values of temperature, relative humidity and precipitation as well as the climatic indices of Kerner, Johansson, de Martonne, Pinna, SPI and the Discomfort Index were examined. The data cover the period from 1958 to 2008. In order to detect a possible trend in the aforementioned data we used the non-parametric test of Mann – Kendall. The results for the climatic indices show a trend towards characterizing the climate as warmer and drier, but also an increase of the variation range of the climatic values. The results for the meteorological parameters show a warming trend, declining rainfall and a very significant reduction in relative humidity. The latter conclusion is consistent with intense land use change in the area of interest, and is due to a shift in the management of surface waters used for crops irrigation in the region.

1 Introduction

The Thriassio Plain is located 20 km northwest of Athens and includes the municipalities of Elefsis, Aspropyrgos, Mandra and the community of Magoula. Although Thriassio Plain extends over an area of 500 km^2, all activities are concentrated in an area of 120 km^2. The presence of several mountains in close proximity to the sea and the local climatic conditions produce local regressive atmospheric circulation patterns that greatly inhibit the capability of atmospheric self-cleaning through dispersion and transport mechanisms. Temperature inversion heights are especially low during the cold period of the year, frequently being lower

A. Mavrakis (✉)
Institute of Urban Environment and Human Resources, Department of Economic and Regional Development, Panteion University, 136 Syngrou Av., Athens 176 71, Greece
e-mail: mavrakisan@yahoo.gr

C.G. Helmis and P.T. Nastos (eds.), *Advances in Meteorology, Climatology and Atmospheric Physics*, Springer Atmospheric Sciences,
DOI 10.1007/978-3-642-29172-2_85,

than the surrounding hills and comparable to the highest chimneys of the large industrial compounds. This means that air pollutants are trapped within a shallow layer resulting in high (daily and hourly) pollution concentrations. The Thriassio Plain exhibits the higher (a) industrial activity concentration, (b) fuel consumption and (c) pollution related to the production processes, in Greece (Mavrakis et al. 2011). The area after WWII was industrialized urbanized and became a logistics center while agriculture was abandoned without any plan. This kind of development caused serious pollution problems making the area an example to avoid.

The purpose of this work is to investigate possible differentiations of the climatic parameters of the area due to that kind of development. For this purpose, we examine monthly and annual mean values of temperature, relative humidity and precipitation as well as the climatic indices of Kerner, Johansson, de Martonne, Pinna, Discomfort Index (Zambakas 1992) and the SPI (McKee et al. 1995).

2 Data and Methodology

The data used, covering the period from 1958 to 2008, were provided from the Hellenic National Meteorological Service and refer to Elefsis station (LGEL). Data includes monthly and annual average values of air temperature, relative humidity, precipitation, and annual (sum) precipitation.

The Kerner Oceanity Index identifies if the air masses have an oceanic origin, utilizing the fact that air masses in marine climates are colder during spring than in autumn. The index is expressed as:

$$Z = 100^{*}(T_O - T_A)/R \tag{1}$$

where: T_O and T_A are the mean air temperatures of October and April respectively and R is the annual temperature range (difference between average temperatures in the warmest and coldest month) in °C. Small values of the index indicate a continental climate while values higher than 10 indicate oceanic climate.

Johansson Continentality Index is used to discriminate between continental and oceanic climates. The index is calculated by the following formula:

$$K = (1.7^{*}R/\sin\varphi) - 20.4 \tag{2}$$

where R, is the annual temperature range, in °C, and φ is the station's latitude.

The de Martonne index is a measure of the aridity of a region and is given by the following relationship:

$$I = P/(T + 10) \tag{3}$$

where P is the monthly sum of precipitation and T the monthly mean air temperature. When the value of I is lower than 20 then the land in this month needs to be irrigated (de Martonne 1926). Pinna has proposed the following index (Zambakas 1992):

$$I = 1/2\,((P\ /\ T + 10) + (12\ Px\ /\ Tx10)) \tag{4}$$

where P, T are the annual precipitation and mean air temperature and Px, Tx are the precipitation and mean air temperature of the driest month. This index describes, in a better way, the regions and seasons where irrigation is necessary since it takes into account the precipitation and air temperature of the driest month. For $I < 10$, the climate is characterized as dry and for $10 \leq I \leq 20$ the climate is considered semi-dry Mediterranean with formal Mediterranean vegetation.

The Standardized Precipitation Index (SPI) normalizes anomalies in the temporal and spatial distribution of precipitation, thus enabling the comparison of drought severity among areas reflecting different hydrological regimes and quantifies the precipitation deficit for multiple time scales. These time scales reflect the impact of drought on the availability of the different water resources. The index was calculated using the SPI_SL_6 program (NDMC 2011). SPI was applied for five time scales in order to map the monthly, seasonal and annual variations of the phenomenon and examine in depth the effect of drought episodes. In particular, it was calculated for 1, 2, 3, 6 and 12 months.

For the calculation of Discomfort Index (DI) we used the formula (Paliatsos and Nastos 1999):

$$DI = Ta - 0.55\,(1 - 0.01RH)(Ta - 14.5) \tag{5}$$

where Ta is the air temperature, in °C, and RH is the relative humidity (in %).

In order to detect possible trends in the aforementioned data we used the non parametric test of Mann – Kendall (Sneyers 1990).

3 Results

Temperature is the main meteorological parameter that determines the climatic character of an area. In Thriassio, the hottest months are July and August with climatic (1961–1990) average temperature 28.6 and 28.2°C respectively. The highest temperature was recorded on 10th July 1977 (48.0°C) and the second higher temperature was recorded on 26th June 2007 (46.5°C) (Mavrakis et al. 2011). The absolute minimum temperature (−7.5°C) was recorded on February 21st 2008, while the next lower (−5.0°C) on 6th January 2002. The warmest and driest years were 2007 and 1989. During the summer of 2007, four heat waves events were observed (Theoharatos et al. 2010). Moreover, during 2007 low values of total rainfall were recorded while the average monthly value of the ambient temperature exceeded the average of the period under review by 0.7°C. The annual temperature range appears to be higher during the last 15 years compared to the respective

values in previous years, indicating a general tendency for warmer climate (hot summers and colder winders). The annual temperature range, namely the difference between average temperatures in the warmest and coldest month, is 19.4°C, which is in the range of the optimum temperature for human activity (18–20°C). There isn't any clear crossing of the stepwise curves u(t) and u'(t) and the Mann-Kendall test gives a value of −1.19, indicating a non-statistically significant trend (Fig. 1a). The relative humidity shows a clear continuous decline during the last 20 years (Fig. 1b) confirmed by a statistically significant value (−3.62) of the Mann-Kendall test, whereas the crossing of the stepwise curves u(t) and u'(t) suggests the turn point year to be 1972. The average precipitation shows a declining trend (Fig. 1c), but this doesn't concern the annual precipitation (Fig. 1d). The Mann-Kendall statistic is −0.47 and 0.11 respectively, which are not statistically significant. The starting point of the decrease seems to be around 1977 (for monthly precipitation) and 1972 (for annual).

The Kerner index (Fig. 1e) shows a positive yet non-significant trend (Mann-Kendall value 1.18) whereas the crossing of the stepwise curves u(t) and u′(t) indicates 1989 as a possible turn point year. According to the results, the climate of Thriassio Plain cannot be characterized as a marine climate, despite its proximity to the sea (Bay of Elefsis). Although the appearance of the sea breeze is very regular in Thriassio, it does not appear to affect significantly the climate of the region, maybe due to the specific geomorphology of the terrain (Mavrakis 2009). According to the Johansson index (Fig. 1f), the climate is characterized as marine when K varies between 0 and 33, as continental when K varies between 34 and 66, and as exceptionally continental when K varies between 67 and 100. According to results, Thriassio Plain is "very continental". The estimated values were $K > 90$: 41 years and $K < 90$: 7 years. For a number of years we cannot draw any conclusion. Mann-Kendall test value was 1.19 and the crossing of the stepwise curves u(t) and u′(t) suggests the turn point year to be 1989. The de Martonne climate index shows a normal course with the absence of extreme fluctuations. During 2 years (1964 and 1989) the calculated values were 7.2 and 6 respectively, while annual precipitation was less than 200 and 150 mm, suggesting significant dryness of the area, to such an extent as to reach the stage of desertification. Furthermore, a very impressive result is that the climate is characterized as "Mediterranean" only during 2 years, while in one case the climate is classified as "semihumid". In most cases we are led to the designation 'semi'. Mann-Kendall test value was 0.16 and the crossing of the stepwise curves u(t) and u′(t) suggests the turn point year to be 1972 and 2007. The Pinna index best describes the areas and the seasons that the irrigation is necessary. The application of the Pinna index gives values of $I > 5$: 41 years and $I < 5$: 9 years (semi-dry Mediterranean climates with typical Mediterranean vegetation). Mann-Kendall test value was −0.09 and the crossing of the stepwise curves u(t) and u′(t) suggests turn point years to be 1972 and 2007. SPI index (Fig. 1i) gives us the most significant signal concerning temporal and spatial distribution of precipitation. Mann-Kendall test value was −7.63 and the crossing of the stepwise curves u(t) and u′(t) suggests the turn point year to be in 1986. This means that the area is becoming arid. The latter conclusion is consistent with the intense land use changes that happened during last decades.

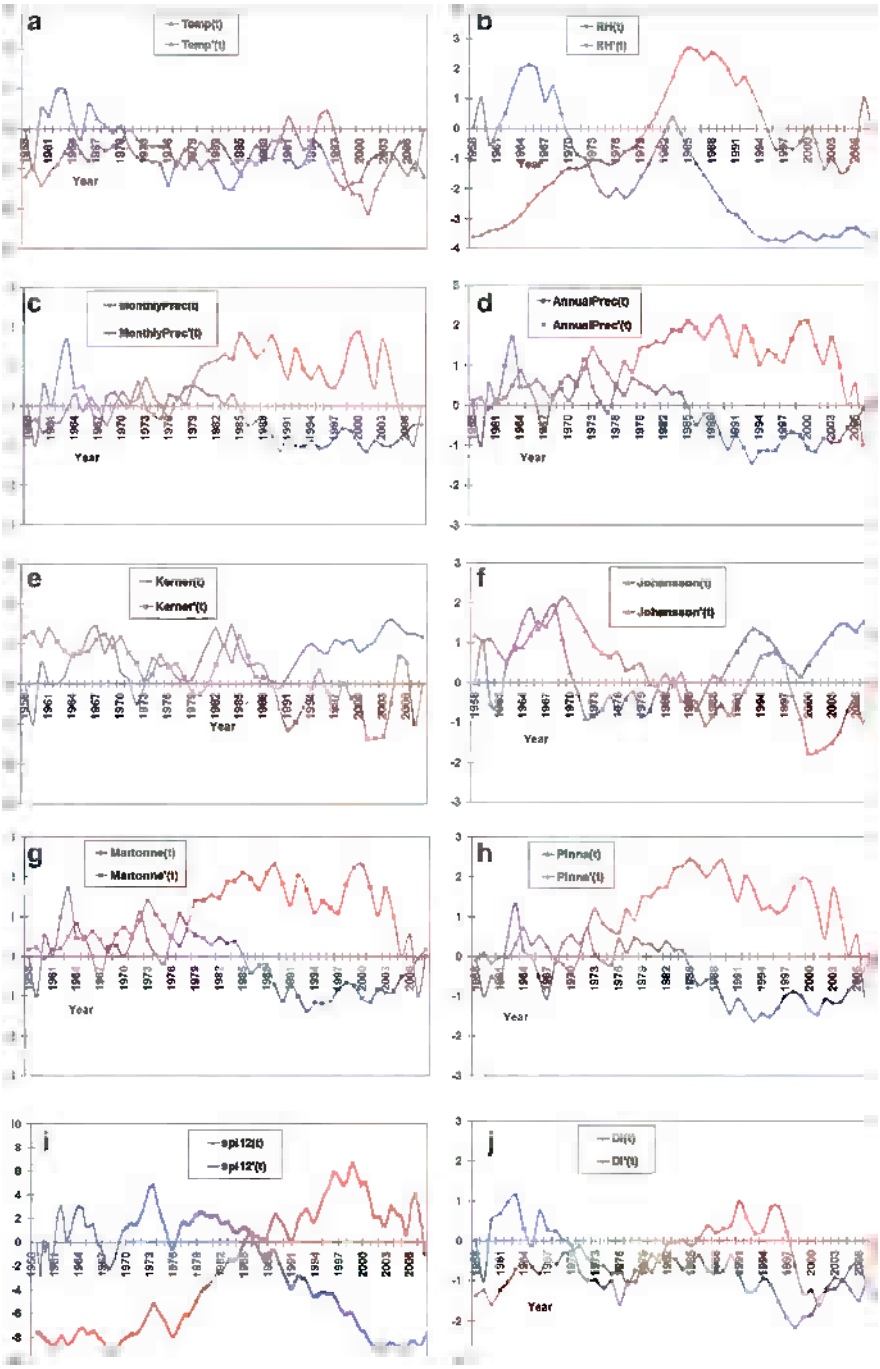

Fig. 1 Mann-Kendal test for annual: (**a**) air temperature, (**b**) relative humidity, (**c**) average precipitation, (**d**) annual precipitation, (**e**) Kerner index, (**f**) Johansson index, (**g**) de Martonne index, (**h**) Pinna index, (**i**) SPI index and (**j**) Discomfort Index

Finally for DI index (Fig. 1j) Mann-Kendall statistic is −1.38 (non significant) and the crossing of the stepwise curves u(t) and u′(t) suggests possible turn point years in 1982 and 2000.

4 Conclusions

The analysis of the meteorological parameters shows a warming trend, less precipitation and a strong, statistically significant reduction in relative humidity.

According to Kerner and Johansson climatic indices, the area exhibits continental characteristics. A more realistic description of the climate was achieved by applying the de Martonne index that classifies the climate of Thriassio Plain as semi-arid. The same result was confirmed by Pinna index. According to the SPI index there is a strong and statistically significant reduction of precipitation both in temporal and spatial terms. The aforementioned indices indicated that possible turning points could be identified during: 1964, 1972, 1977, 1986, 1989, 2000 and 2007.

The tendency towards a warmer and drier climate, suggested by the above analysis is consistent with intense land use change in the area of interest, and is due to a shift in the management of surface water used for crop irrigation in the region. This result could be a strong indication of the future climate of the area. From all the above results, it is reasonable to wonder about whether desertification is becoming a major problem of the area.

References

De Martonne E (1941) Nouvelle carte mondiale de l'indice s'aridité. Météorol 3–26

Mavrakis A (2009) Assessment of the spatial distribution of air pollution and its relation with land uses: the case of the Thriassion Plain. PhD thesis, Department of Economic and Regional Development, Panteion University. http://phdtheses.ekt.gr/eadd/handle/10442/17470

Mavrakis A, Spanou A, Pantavou K, Katavoutas G, Theoharatos G, Christides A, Verouti E (2011) Biometeorological and air quality assessment in an industrialized area of eastern Mediterranean-Thriassion Plain-Greece. Int J Biometeorol. doi:10.1007/s00484-011-0475-9

McKee TB, Doesken NJ, Kleist J (1995) Drought monitoring with multiple time scales. In: Ninth conference on applied climatology. American Meteorological Society, Boston, pp 233–236

National Drought Mitigation Center (2011) SPI-SL_6 program. Available at http://drought.unl.edu/MonitoringTools/DownloadableSPIProgram.aspx. Accessed on 2 October 2011

Paliatsos A, Nastos P (1999) Relation between air pollution episodes and Discomfort Index in the greater Athens area, Greece. Global Nest Int J 1(2):91–97

Sneyers R (1990) On the statistical analysis of series of observations. WMO Tech No 143, p 192

Theoharatos G, Pantavou K, Mavrakis A, Spanou A, Katavoutas G, Efstathiou P, Mpekas P, Asimakopoulos D (2010) Heat waves observed in 2007 in Athens, Greece: synoptic conditions, bioclimatological assessment, air quality levels and health effects. Environ Res 110 (2):152–161. doi:10.1016/j.envres.2009.12.002

Zambakas J (1992) General climatology. Department of Geology, National and Kapodistrian University of Athens, Athens, Greece

Climate-Cereal Crop Relationships in Greece and the Impacts of Recent Climate Trends: The Role of the Effective "Growing Season" Definition

T. Mavromatis

Abstract The role of the definition of the effective "growing season" on the direction and magnitude of four major cereal (hard and soft wheat, maize and barley) responses to recent climate trends is investigated, on periphery scale, throughout Greece, using two effective "growing seasons" for each crop: the full growing season (GS) and the grain filling (GF) period. Historical interpolated data of maximum (Tx) and minimum temperature (Tn), diurnal temperature range (Tr), precipitation (Prec) and solar radiation, over the period 1978–2005, were provided by the MARS-STAT Data Base. The direction of yield and, to a lesser extent, the magnitude of negative yield response to trends of Tx and Tr was not sensitive to the choice of the effective "growing season". On the other hand, the responses of barley, hard and soft wheat to the warming trends of Tn and decreasing trends of Prec in central Macedonia and Thrace were positive in the case of GS and negative in the case of GF period. The difference of crop responses to the definition of the "effective" growing season, however, was significantly larger to Tn than to Prec trends.

1 Introduction

The crop-climate relationships and the impacts of growing season climate (maximum (Tx) and minimum temperature (Tn), diurnal temperature range (Tr), precipitation (Prec) and solar radiation (Rad)) trends over the period 1978–2005 on yields of major cereals (hard and soft wheat (*Triticum turgidum L. var. durum and Triticum aestivum L.* respectively), maize (*Zea Mays L.)* and barley (*Hordeum vulgare*), at peripheral scale throughout Greece, were recently investigated with

T. Mavromatis (✉)
Department of Meteorology and Climatology, School of Geology, Aristotle University of Thessaloniki, Thessaloniki, Greece
e-mail: thmavrom@geo.auth.gr

C.G. Helmis and P.T. Nastos (eds.), *Advances in Meteorology, Climatology and Atmospheric Physics*, Springer Atmospheric Sciences,
DOI 10.1007/978-3-642-29172-2_86,

linear regression models. The direction of yield response of all crops to the recent climate variations was similar. The impacts of temperature trends and particularly these of Tr and Tx were the most significant, both in terms of frequency (~29% and 25% of peripheries were effected), respectively) and magnitude (yields declined on average by 2–8.1%/°C with increasing Tx and by 1.9–7.7%/°C with decreasing Tr). The warming trends of Tn caused a yield enhancement, weaker in magnitude, however (yields increased by 0.1%/°C for soft wheat to 4%/°C for barley, on average), in three crops (except for maize which was insensitive to this climatic variable) in eight out of eleven regions. The effects of Prec trends were almost as important, on frequency terms, as were the effects of Tn (10 vs. 11 peripheries). The few significant yield-solar radiation relationships (five cases or ~10% of peripheries only) were associated with a substantial yield fall that ranged from 2.2% MJ/m^2/day for maize to 10.9% MJ/m^2/day for hard wheat.

The objective of this study is to investigate the role of the effective "growing season" definition on the direction and magnitude of statistically significant crop responses to the abovementioned meteorological parameters. Two different effective "growing seasons" for each crop were used: the full growing season (from planting to maturity: GS) and the grain filling (GF) period.

2 Data and Methodology

2.1 Meteorological and Yield Data

Historical data on climate were provided by the MARS-STAT Data Base. This data base contains meteorological interpolated data from 1975, covering the European Union (EU) member states, the central European eastern countries, the new Independent states, and the Mediterranean countries (e.g. Baruth et al. 2007). These data consist of daily values of maximum and minimum temperature, global radiation and rainfall, interpolated from meteorological station data towards the centers of a 25 × 25 km climatic grid (Baruth et al. 2007) (Fig. 1). More details on the acquisition, checks and processing of meteorological data, including the interpolation procedure, are given by Baruth et al. (2007).

The administrative regions of the EU, the so called NUTS regions were used in this study. Two NUTS levels were used: the regional level (NUTS 2) (Fig. 1) and the sub-regional level (NUTS 3) which broadly comprises of the prefectures the NUTS 2 regions are divided in. Greece consists of 13 administrative regions (peripheries), nine of which belong to the mainland of Greece and four insular. These regions correspond to the NUTS 2 level. The peripheries are further subdivided into the 51 prefectures (nomoi) which match the NUTS 3 level. Since yield data are available on NUTS 3 level, these units (prefectures) were used to relate the meteorological interpolated data to the time series of yields for barley, hard and soft wheat from 1979 to 2005 and for maize for the period 1978–2005

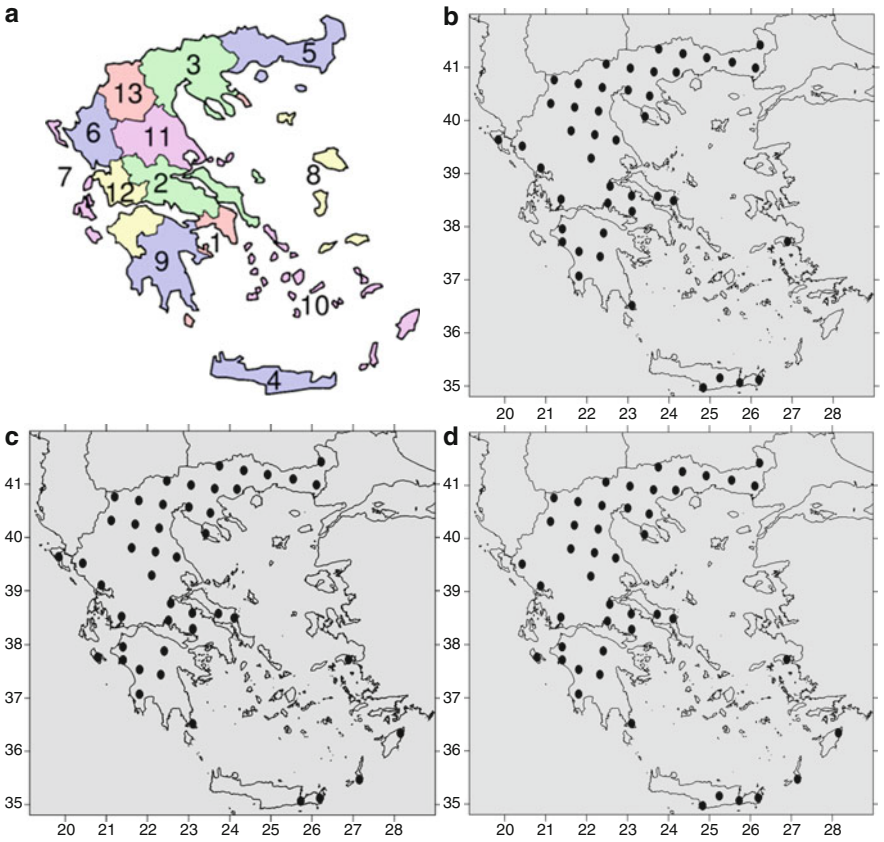

Fig. 1 Sub-regions (NUTS 2 level) of Greece: *1* Attica, *2* Central Greece, *3* Central Macedonia, *4* Crete, *5* East Macedonia and Thrace, *6* Epirus, *7* Ionian Islands, *8* North Aegean, *9* Peloponessos, *10* South Aegean, *11* Thessaly, *12* West Greece and *13* West Macedonia (**a**). The grid centers used for soft wheat (**b**), maize (**c**) and hard wheat (**d**) are also shown

(Fig. 1). Yields of these crops were obtained from published reports (Agricultural Statistics of Greece 2003). Only the regions where these crops are grown extensively (more than 5% of the cultivated surface) were selected: 36 prefectures in the case of soft wheat and 37 for the other three crops. The sets of climatic grid centers in Fig. 1 are very similar and sufficiently cover the selected prefectures for each crop.

2.2 Methodology

Typical cropping system, planting date and growing season for each crop were obtained from international (e.g. Russell and Wilson 1994) and national (e.g.

Kamoutsis et al. 2008) experts sources. For each crop a similar growing season was assumed throughout the country and study period. Averages of each climate variable for each climatic grid center were computed for the full growing season (from planting to physiological maturity) for each crop: Apr 20th–Sep 13th (for maize), Nov 20th–Jun 7th (for barley and hard wheat) and Nov 20th–Jun 30th (for soft wheat). To explore the climate-yield relationships by regions (NUTS 2 level), a common approach (e.g. Tao et al. 2008) based on the first-difference time series for yield (DYield) and climate (i.e. year to year changes) (DTx, DTn, DTr [where Tr is the diurnal temperature range Tx-Tn], DPrec and DRad) was used. The sensitivity of the results to the definition of the "effective" GS was explored by employing the grain filling period for each crop instead of the full GS: Jul 12th–Sep 13th for maize, Apr 15th–Jun 7th for hard wheat and barley and May 1st–Jun 30th for soft wheat.

Once the detrended time series of yield and climate were aggregated from NUTS 3 to NUTS 2 level (from prefecture to periphery) the relationships between DYield and DTx, DTn, DTr, DPrec and DRad were evaluated using the basic linear regression-based model analysis. Due to the limited historical sample size, a bootstrap resampling approach was used to estimate the sampling uncertainty associated with the derived regression coefficients. Specifically, the original data was resampled with replacement of the original data, a new regression model was computed, and this was repeated for 10,000 times. In order to examine any possible trend in the time series of meteorological parameters a two-tailed Student's *t* test, with 95% level of significance was applied on the slope (b) of the same regression approach ($Y = a + bX$), where time (years) was taken as the independent variable X and the meteorological Y as the dependent. The least-squares fitting process was used to fit the line.

3 Results

Maize appeared relatively insensitive to the choice of growing season definition (Table 1). Even though soft wheat, on the other hand, presented the same number of significant crop-climate relations (14 significant cases for each definition), it was, however, affected more often by the impacts of DTx during the grain filling period than during the full growing season. The opposite was true for DTr and DPrec. Hard wheat was more frequently vulnerable to the recent climate variations of DTr, DPrec and DRad during the GS and of DTx and DTn during GF. In contrast to DTr and DPrec, the impacts of temperature extremes, and particularly these of DTx (20 cases, in total, for GF vs. 14 for GS), were most frequently significant to cereals' productivity during GF. The direction of climate trends did not depend on the choice of growing season definition (not shown). In one case only (barley in central Macedonia), opposite trends for DTr were found.

The direction and, to a lesser extent, the magnitude of negative (ranged from 1.7% to 8.1%) yield response of all crops, but soft wheat, to warming (11 crop-region combinations) and cooling (hard wheat in Aegean) trends of DTx (Table 2)

Table 1 Sensitivity of the frequency of significant crop-climate relationships for the two definitions of "effective" growing seasons (GS: from planting to maturity and GF: grain filling period)

		DTx	DTn	DTr	DPrec	DRad	Sum
Hard wheat	GS	5	4	4	3	1	17
	GF	6	5	2	1		14
Soft wheat	GS	2	4	3	4	1	14
	GF	5	5	1	2	1	14
Maize	GS	4		4	1	1	10
	GF	4		4		1	9
Barley	GS	3	3	4	2	2	14
	GF	5	3	4	1	2	15

Table 2 Direction (the *grey cells* show negative trends) and mean yield response (expressed as % of the 2001–2005 yield average in the peripheries (Per.) showing simultaneous significant relationship to the specific meteorological parameter) to the "effective" growing season definitions

		DTx	DTn	DTr	DPrec	DRad
Hard wheat	Per.[a]	CM,TH,CG	CM,TH	CG	CM	
	GS	−7.2	7.5	−3.5	1.4	
	GF	−6.7	−13.9	−3.6	−0.1	
Soft wheat	Per.	CM,TH	CM,TH	CM	CM	
	GS	−8.1	4.9	−11.1	0.8	
	GF	−5.3	−7.0	−4.0	−0.1	
Maize	Per.	CM,CG,WG		CM,WG,PE		
	GS	−2.0		−1.7		
	GF	−1.7		−1.5		
Barley	Per.	CM,TH,CG	CM,TH	CG,PE		
	GS	−5.7	4.5	−2.9		
	GF	−6.2	−7.7	−2.8		

[a]Peripheries: *CM* central Macedonia, *TH* Thrace, *CG* central Greece, *WG* west Greece, *PE* Peloponessos

were not particularly sensitive to the definition of the "effective" growing season. A similar, to direction but weaker to magnitude (varied from 1.5% to 3.6%), crop response to the narrowing trends of DTr (six crop-region combinations) was found. Only the response of soft wheat in central Macedonia was substantially different (by more than 7%) during GS.

On the other hand, the responses of barley, hard and soft wheat to the warming trends of DTn (six crop-region combinations) and decreasing trends of DPrec (three crop-region combinations) in central Macedonia were positive in the case of full GS and negative in the case of GF period (Table 2). Despite the resemblance in the direction, the difference of crop response to the definition of the "effective" growing season was significantly larger to DTn (>11%) than to DPrec (>1.5%) trends. The multi-collinearity observed between all climate parameters in this region makes it almost impossible to explain this disagreement.

No common periphery with a significant relationship between any crop and DRad was found applying the two growing season definitions.

4 Conclusions

The role of the definition of the effective "growing season" on the direction and magnitude of major cereal crops' (hard and soft wheat, maize and barley) productivity in Greece was investigated. Two different effective "growing seasons" for each crop were used: the full growing season and the grain filling period. The direction and, to a lesser extent, the magnitude of negative yield response of all crops, but soft wheat, to warming trends of DTx were not particularly sensitive to the definition of the "effective" growing season. A similar, to direction but weaker to magnitude crop response to the narrowing trends of DTr was found. On the other hand, the responses of barley, hard and soft wheat to the warming trends of DTn and decreasing trends of DPrec in central Macedonia were positive in the case of full growing season and negative in the case of grain filling period. Despite the resemblance in the direction, the difference of crop responses to the definition of the "effective" growing season was significantly larger to DTn than to DPrec trends.

References

National Statistical Service of Greece (2003) Agricultural statistics of Greece Year 2001. Hellenic republic, National statistical service of Greece, Athens

Baruth B, Genovese G, Leo O (2007) CGMS version 9.2. User manual and technical documentation. JRC scientific and technical reports. EUR 22936 EN, Office for Official Publications of the EU, Luxembourg

Kamoutsis A, Matsoukis A, Chronopoulou-Sereli A, Katafygiotis L (2008) Effect of air temperature on start dates of wheat (Triticum aestivum) phenophases in Greece. In: Proceedings of the 9th conference of meteorology, climatology and atmospheric physics. Thessaloniki, 28–31 May 2008, pp 895–900

Russell G, Wilson GW (1994) An agro-pedo-climatological knowledge-base of wheat in Europe. EUR Publication N 15789 EN of the Office for Official Publications of the EC, Luxembourg

Tao F, Yokozawa M, Liu J, Zhang Z (2008) Climate-crop yield relationships at provincial scales in China and the impacts of recent climate trends. Clim Res 38:83–94. doi:10.3354/cr00771

Soil Temperature Prediction Using Time-Delay Neural Networks

E. Mazou, N. Alvertos, and I.X. Tsiros

Abstract Neural networks are widely used for time series prediction in the recent years. In particular, dynamic neural networks with embedded time delays are the most appropriate models for the simulation of nonlinear processes since they make use the effect of past input values. The purpose of this study is to predict soil temperature in various depths, by using dynamic neural networks. The dynamic networks used are recurrent neural networks with feedback loop that includes time-delay elements. The data used for the neural network's training, validation and testing were hourly values obtained from the weather station at the Agricultural University of Athens, for the period 2002–2005. Error statistics of the results showed a good fitting of the models.

1 Introduction

Neural networks have been widely used as time series forecasting such as economics, meteorology and biology. Accuracy for soil temperature values is very important, so neural network models have been used for soil temperature prediction. Artificial neural networks have been used for the prediction of hourly mean values of ambient temperatures 24 h in advance (Tasadduq et al. 2002). The Multilayer Perceptron neural network using soil temperatures data has also tested three algorithms (Scaled Conjugate Gradient, Levenberg-Marquerdt and Resilient) and had satisfactory mean errors during simulations except for the Scaled Conjugate Gradient (Veronez et al. 2006). Diamantopoulou et al. (2010) used neural networks to estimate the daily evapotranspiration.

There are two neural network categories: static (feedforward) and dynamic (recurrent). Feedforward networks have no feedback elements and contain no

E. Mazou (✉) • N. Alvertos • I.X. Tsiros
Agricultural University of Athens, Athens 11855, Greece
e-mail: jennymazou@aua.gr

C.G. Helmis and P.T. Nastos (eds.), *Advances in Meteorology, Climatology and Atmospheric Physics*, Springer Atmospheric Sciences,
DOI 10.1007/978-3-642-29172-2_87,

delays so the output is calculated directly from the input through feedforward connections. In recurrent networks, there is at least one feedback loop so the network may consist of a single layer of neurons with each neuron feeding its output signal back to the inputs of all other neurons so the output depends not only on the current input of the network, but also on the current or previous inputs, outputs, or states of the network. That is why recurrent neural networks are very appropriate for the simulation of nonlinear processes. A nonlinear AR and linear autoregressive moving average (ARMA) modeling by feedforward and recurrent networks respectively compared and showed that recurrent networks have an advantage over feedforward networks (Connor et al. 1994); and also three neural network models constructed and showed that the nonlinear autoregressive approach (NARX) was the best model for forecasting the soil temperature of the day (AbdAlKader and AL-Allaf 2011).

The purpose of this study is to predict soil temperature in various depths by using dynamic neural networks. The dynamic networks used are recurrent networks with feedback loop that includes time-delay elements.

2 Data and Methodology

2.1 Data

The data used as input for neural network's training and validation were obtained from the Automatic Weather station at the Agricultural University of Athens and represent soil temperature hourly values at soil depths of 0, 2, 5, 10, 20 and 30 cm.

Soil temperature measurements were used as input data from October 2002 at depths 2, 5, 10, 20 and 30 cm, from October 2003 at depths 2, 5, 10, 20 and 30 cm and from April 2002 at depths 2 and 5 cm and as target data soil temperature measurements from October 2003, October 2004 and April 2003 respectively.

2.2 Methodology

A typical neural network consists of three layers: input layer, hidden layer and output layer. The input refers to the available data that enters the system. The number of input layer neurons is equal to the number of parameters that contribute to the simulation.

In a time series problem we would like to predict future values of a time series from past values of that time series and past values of a second time series. This form of prediction is called nonlinear autoregressive with exogenous (external) input, or NARX so it's a recurrent model with time delays. The standard NARX network is a two-layer feedforward network, with a sigmoid transfer function in the

hidden layer and a linear transfer function in the output layer. This network has two inputs, one is an external input and the other is a feedback connection from the network output. For each of these inputs there is a tapped delay line to store previous values. The presence of feedback loops has a profound impact on the learning capability of the network on its performance (Neural Network Toolbox Getting Started Guide R2011b, Beale et al. 2011). The Levenberg-Marquardt algorithm has been used for the training of the NARX model.

For the purposes of the present study, in the Matlab's platform (Neural Network Toolbox Getting Started Guide R2011b) the data were randomly divided into two subsets, the training set (corresponding to 70% of the patterns), the validation and testing set (corresponding to 30% of the patterns), so that the generalization capacity of network could be checked after training phase. The determination of the optimal neural network architecture was achieved through trial and error. The default number of hidden neurons is set to 10. The default number of delays is 2. Generally, in order to improve the network performance, we can to retrain the network so it will initialize the weights and biases to new values, or increase the number of hidden neurons or delays, or increase the number of training vectors, or increase the number of input values.

Moreover, in the present study we changed the number of neurons and the number of delays in the input layer (retraining had improved results in some cases only) and tested the model for the following architectures:

1. 10 neurons, 2 delays
2. 10 neurons, 4 delays
3. 8 neurons, 4 delays

3 Results

Three statistical measures used in the present study: the mean square error (MSE) performance function, the plot of error autocorrelation function and the values of correlation coefficient R.

The regression plots showed a good relationship between network outputs and network targets. In Tables 1, 2, and 3 the results of the statistical error analysis are presented. It is shown that the best MSE values correspond to the first and third model where the number of delay elements is increased. We observe that the values of MSE error were decreased as we move to greater depths.

Figures 1 and 2 display the error autocorrelation function. The pattern of this function describes how the prediction errors are related to time. It is shown that by increasing the number of delay elements, the correlations, with the exception of the one at the zero lag, fall approximately within the 95% confidence limits around zero. These results imply that the model seems to be adequate and encourage the further use of the model for predictions.

Table 1 MSE values of the models for October 2002 and 2003 (October 2002: input; October 2003: target)

Depth	2 cm	5 cm	10 cm	20 cm	30 cm
MSE 1 (°C)	0.1	0.08	0.02	0.002	0.0003
MSE 2 (°C)	0.2	0.08	0.005	0.0002	0.0001
MSE 3 (°C)	0.3	0.08	0.003	0.0003	0.00009

Table 2 MSE values of the four models for October 2003 and 2004 (October 2003: input; October 2004: target)

Depth	2 cm	5 cm	10 cm	20 cm	30 cm
MSE 1 (°C)	0.1	0.06	0.01	0.002	0.0004
MSE 2 (°C)	0.01	0.08	0.004	0.0003	0.0001
MSE 3 (°C)	0.1	0.05	0.004	0.0002	0.0001

Table 3 MSE values of the four models for April 2002 and 2003 (April 2002: input; April 2003: target)

Depth	2 cm	5 cm
MSE 1 (°C)	0.2	0.1
MSE 2 (°C)	0.2	0.1
MSE 3 (°C)	0.3	0.2

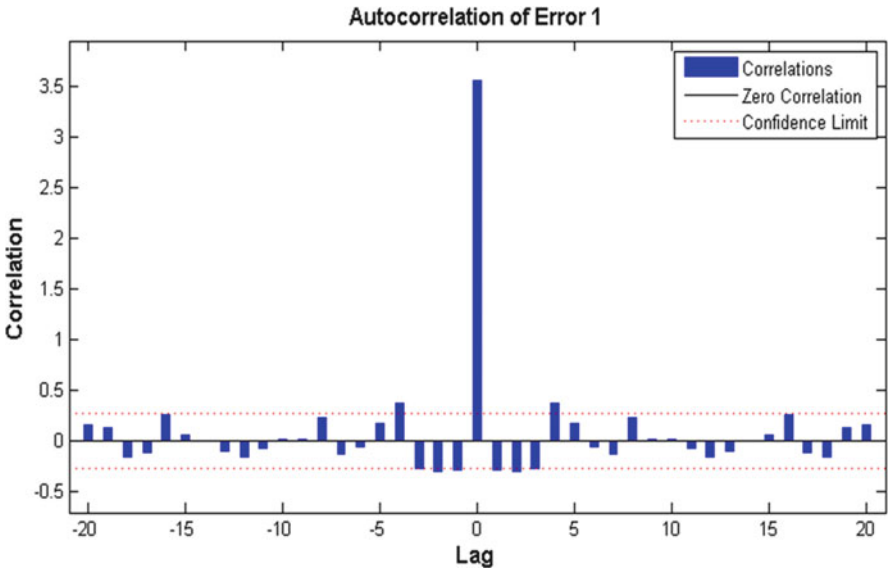

Fig. 1 Correlation plot of the third model for the depth of 5 cm

4 Conclusions

The results of the present study showed that the number of hidden layer neurons ranging between 8 and 10 may give satisfactory results in the case of soil temperature predictions. In addition, by the increase of the number of delays from 2 to 4, better results can be achieved, in terms of error statistics. Finally, it was shown that,

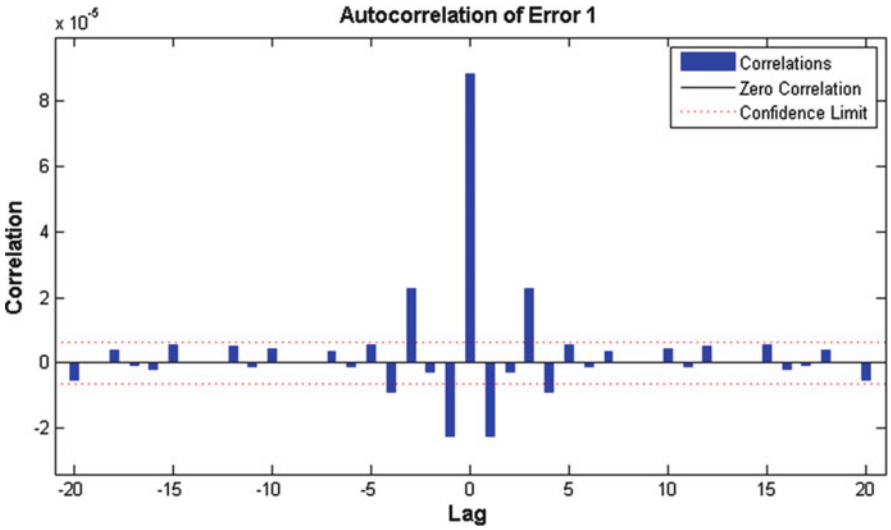

Fig. 2 Correlation plot of the third model for the depth of 30 cm

for all the examined models, the statistical errors were gradually decreased from the surface soil down to the various depths. Further studies should focus on more testing for various seasons of the year with focus on cold and hot weather conditions and also on improving and predictability.

References

AbdAlKader SA, AL-Allaf ONA (2011) Backpropagation neural network algorithm for forecasting soil temperatures considering many aspects: a comparison of different approaches. In: Proceedings of the 5th international conference on information technology, Amman, 11–13 May 2011

Beale MH, Hagan MT, Demuth HB (2011) Neural network toolbox getting started guide R2011b. http://mathworks.com/help/pdf_doc/nnet/nnet_gs.pdf. Accessed on 25 November 2011

Connor J, Martin D, Atlas L (1994) Recurrent neural networks and robust time series prediction. IEEE Trans Neural Networks 5:240–254. doi:1045-9227/94S04.00

Diamantopoulou MJ, Georgiou PE, Papamichail DM (2010) Performance evaluation of artificial neural networks in estimating reference evapotranspiration with minimal meteorological data. Global NEST J 13:18–27

Tasadduq I, Rehman S, Budshait K (2002) Application of neural networks for the prediction of hourly mean surface temperatures in Saudi Arabia. Renew Energ 25:545–554. doi:10.1016/S0960-1481(01)00082-9

Veronez MR, Thum AB, Luz AS, da Silva DR (2006) Artificial neural networks applied in the determination of soil surface temperatures – SST. In: Proceedings of 7th international symposium on spatial accuracy assessment in nature resources and environmental sciences, Lisbon

An Objective Classification of Synoptic Types over Europe

C. Michailidou, P. Maheras, C. Anagnostopoulou, and I. Tegoulias

Abstract A synoptic classification scheme is developed for Europe based on an automated two-step cluster analysis. It employs daily NCEP-NCAR reanalysis data over 62 years (1948–2009) in creating synoptic types from surface and upper air (1,000, 850, 700 and 500 hPa) temperature and humidity data as well as geopotential height and winds aloft. The synoptic types that have been created exhibit distinct seasonal preferences.

1 Introduction

Identification and analysis of synoptic and larger scale circulation patterns and their impact on regional and local climates is a major research theme in the field of synoptic climatology for the purposes of identifying potential air-pollution situations, long-range forecasting, and the study of rainfall and other weather phenomena (Alpert et al. 2004). Weather and circulation types can be determined from hydrodynamic measures, such as surface pressure variability, geopotential heights, or wind flow patterns and represent the dominant modes of atmospheric flow. Automated classifications are generally based on statistical techniques (in order to reduce large, multivariate datasets into distinct synoptic categories), such as principal component analysis (PCA) and cluster analysis (CA) (Barnston and Livezey 1987) and more recently fuzzy logic techniques and neural networks (Michaelides and Pattichis 1998). The use of PCA and CA has helped identify hemispheric weather regimes using geopotential height data (Mote 1998). Huth (2001) presents a method for the classification of circulation types over Europe based on a T-mode PCA combined with the *k*-means method of CA.

C. Michailidou (✉) • P. Maheras • C. Anagnostopoulou • I. Tegoulias
Department of Meteorology – Climatology, School of Geology, Aristotle University of Thessaloniki, Thessaloniki, Greece
e-mail: chrismichailidou@gmail.com

C.G. Helmis and P.T. Nastos (eds.), *Advances in Meteorology, Climatology and Atmospheric Physics*, Springer Atmospheric Sciences,
DOI 10.1007/978-3-642-29172-2_88,

In the present study a synoptic climatological weather classification scheme incorporating both surface and upper-air data is developed for Europe based on an automated two-step cluster analysis (TSCA). Coleman and Rogers (2007) developed a synoptic classification based on both surface and upper air data using an automated TSCA for the central United States. Michailidou et al. (2009) had used TSCA in order to group weather types that occur over two Greek cities combining meteorological parameters, reflecting air mass characteristics at the surface, with synoptic conditions prevailing over an area.

2 Data and Methodology

The study area encompasses the broad region of Europe from the northern part of Africa to the Baltic Sea (20–65°N) and is flanked on the west and east by the eastern part of the Atlantic Ocean and Black Sea respectively (20°W–50°E). The study area consists of 551 grid points.

2.1 Data

Daily mean NCEP-NCAR reanalysis data over all seasons of 62 years (1948–2009) are used in order to create synoptic types from surface and upper air (1,000, 850, 700 and 500 hPa) temperature and humidity data, as well as geopotential height and winds (zonal – u and meridional – v) aloft. The grid size resolution is 2.5° × 2.5° latitude – longitude grid. The initial data set consists of 11,020 variables and 22,646 cases-days.

2.2 Methodology

The selected NCEP–NCAR reanalysis data matrix is subjected to a correlation matrix based S-mode PCA, which reduces the dimensionality of the dataset such that the first few PCs retain most of the variance of the original data matrix. PCA reduces the number of variables under examination and allows one to detect and recognize groups of interrelated variables. The seasonal cycle was kept in the data analysis so as to help identify and demonstrate the overlap in some of the patterns between for example, autumn and winter, or between winter and spring. PCA is separately conducted for each variable at each level due to the large data set. Finally 636 PCs were retained in the study in order to explain more than 90% of the cumulative variance. Extraction communalities are 0.75 or higher for all variables and effectively represent the variability of the individual data points.

The daily unrotated PCA scores are used in a TSCA that generates groups of cases with similar component scores. The primary objective of cluster analysis is to establish relatively uniform groups of cases (e.g., weather patterns or synoptic types) from the input data (which may be PCA based), such that within-group

variance is minimized while between-group variance is maximized. Cluster analysis techniques are often classified as hierarchical and nonhierarchical (Chan 2005). TSCA is designed to handle very large data sets and the number of clusters can be selected automatically based on statistical criteria (Chan 2005; Michailidou et al. 2009). In order to find the number of clusters that provide the best groups for the data used in the present study, the BIC (Bayesian information criterion) is calculated for each cluster within a specified range which is then used to generate an initial estimate of the number of clusters. The second step refines the initial estimate by determining the greatest change in distance between the two closest clusters in each hierarchical clustering stage. However, if it is not possible to interpret the resultant clusters physically, the researcher can also ask for a range of solutions. Further reading regarding TSCA is provided by Michailidou et al. (2009).

3 Results

In the present study a series of TSCA was conducted in order to use several combinations of factors that are derived from different sets of variables or to produce different number of clusters. Finally, due to the relatively larger change in BIC values nine clusters were derived based on factors reflecting geopotential height at 500 and 1,000 hPa, temperature at 500 and 850 hPa, relative humidity at 850 hPa and wind at 500 and 850 hPa. Cases or days assigned to the same cluster possess comparable component scores and thus represent an atmospheric circulation regime (synoptic type, ST) distinct from that of other cluster memberships. The final cluster analysis (CA) solution is designed to show more typical synoptic situations rather than to identify exceptional weather events (e.g., winter cold waves) due to the small number of clusters.

3.1 Frequencies of the Synoptic Types

The frequency of occurrence of each of the nine clusters in the entire 62-year period studied is shown in Fig. 1 (left).

The most frequent is ST_1 while ST_4 is the one appearing less. Each year was divided in three periods considering the Mediterranean climate as a reference (Michaelides et al. 2010). It is worth noting that the "transitional" months (MASO) include patterns from all of the nine clusters (lower frequency at ST1, 7.6%). Certain clusters are present in the "warm and dry" season but almost absent in the "cool and dry" season and vice versa (Fig. 1 right).

3.2 Description of the Synoptic Types

For each of the 9 STs identified, the mean values of each variable (temperature, relative humidity, geopotential height, and wind) are plotted for each of the 551 grid

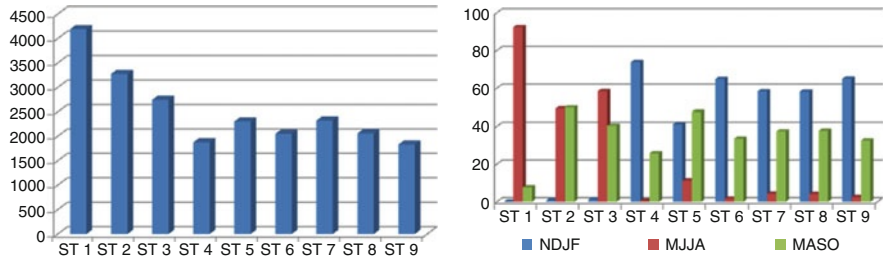

Fig. 1 Frequency of occurrence of the 9 STs (*left*); seasonal appearance (%) of the 9 STs (*right*)

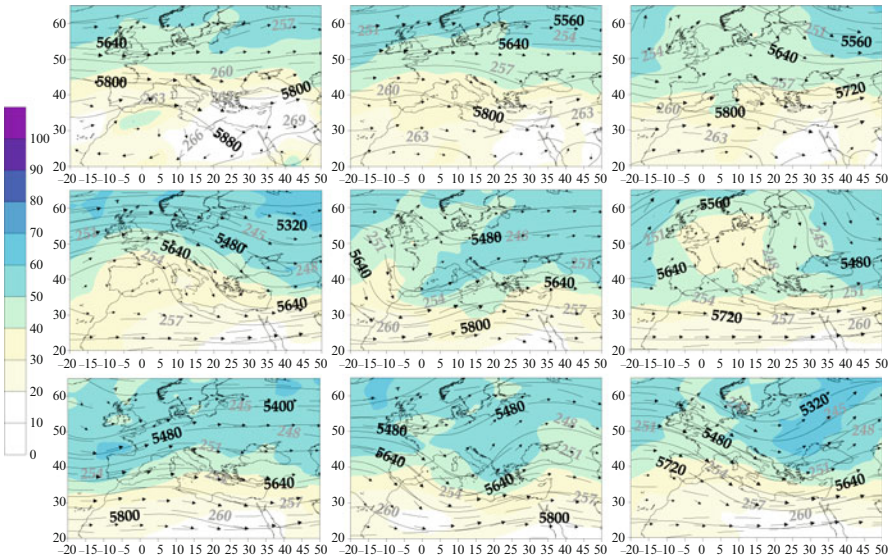

Fig. 2 Mean meteorological conditions for each synoptic type at 500 hPa. Mean temperature (°C, *digits in grey color*) is shown in *dashed lines* in 5°C intervals. *Solid lines* indicate mean geopotential height. Mean wind direction and speed are shown as wind bars (one for ten grid points). Mean relative humidity is shown as *shaded contours*

points at all levels. Due to space limitations, only the synoptic situation for the 1,000 and 500 hPa levels are shown for each ST (Figs. 2, 3).

Synoptic Type 1 (ST1) appears during the warm-dry period and presents the highest frequency of all STs for the study period (Fig. 1). At 500 hPa level (Fig. 2), low values of geopotential heights occupy the area at the NW of England while another system with the opposite behavior is observed over South Africa. Winds are principally westerly and are on the order of 20 ms^{-1} over the west part of central Europe. Relative humidity is rather low especially over South Europe. At the 1,000 hPa level (Fig. 3) a trough is extended over the eastern part of the Mediterranean and a ridge of high pressure is observed over central Europe. Temperature

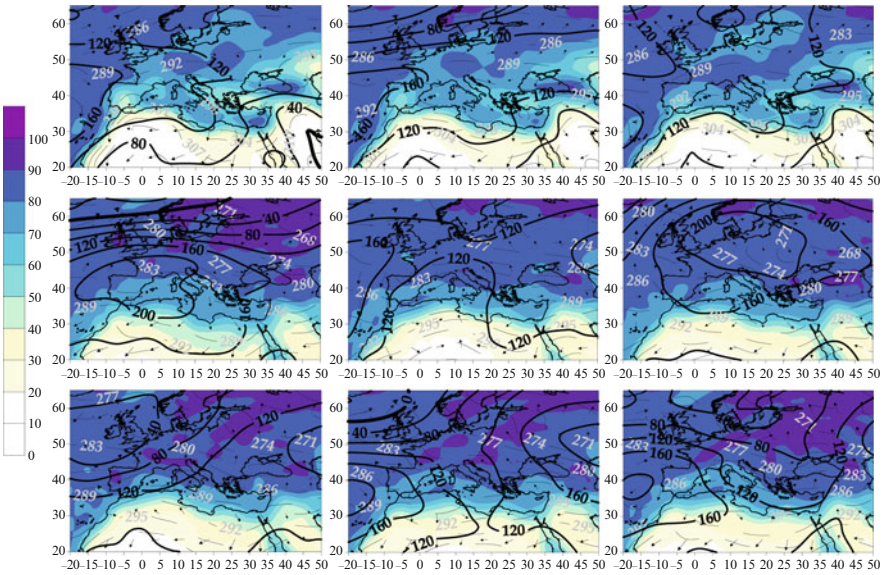

Fig. 3 As in Fig. 2 at 1,000 hPa. Mean temperature (°C) are shown in *shaded contours* in 3°C intervals

values are one of the highest of all STs. ST2 and ST3 occur both at the warm and at the transitional sub-period. ST2 presents no significant centre of action at the 1,000 hPa while the picture at 500 hPa is similar to ST1 but weaker. ST3 presents strong winds over the Mediterranean at midlevel.

The following 6 STs appear mainly during the cold period (exception: ST5 highest frequency at the transitional sub-period). For ST4 a ridge of an anticyclonic centre (1,000 hPa) is extended over the west Mediterranean while relative humidity is relatively high at the northeast and strong NW winds occupy the southwest. ST5 is characterized by zonal flow (westerly winds) at 500 hPa with the exception of the west part of the region where the winds are from the northern sector. ST6 is observed when an anticyclonic pattern is present over the central Europe (1,000 hPa) at the 500 hPa an omega blocking pattern is observed. When ST7 is predominant at midlevel the flow is almost zonal and at the 1,000 hPa level a cyclonic pattern is observed over England resulting to strong winds at the west of the Iberian Peninsula. The field of geopotential heights at 500 hPa for ST8 is governed by two centers of high values at the south part of the area of study (west and east) and one trough of low values at the north. The winds at this level are strong and mainly from the western sector. Finally, CT9 presents at the midlevel the same picture as ST8 shifted though to the east. At 1,000 hPa relative humidity receives high values at the NE Europe and central Europe is under the influence of a cyclonic pattern that extends a trough up to Greece.

4 Conclusions

A method for classification of synoptic types is proposed that utilizes variables from several isobaric levels. The surface and low level temperature and moisture conditions are used for their thermodynamic properties and as a tool in identification of the prevailing air mass, while the upper and low level dynamic wind and geopotential heights variables provided information about associated pressure and atmospheric circulation changes. Nine synoptic types have been created using a statistical method (TSCA) that has the ability to deal with mixed-type variables and large data sets and also determines the optimum number of clusters based on a statistical criterion. The synoptic types that have been created exhibit distinct seasonal preferences and the typing scheme generates synoptic patterns largely characterized by distinctive surface circulations and baroclinic vertical structure. The results are considered very satisfactory.

References

Alpert P, Osetinsky I, Ziv B, Shafir H (2004) Semi-objective classification for daily synoptic systems: application to the eastern Mediterranean climate change. Int J Climatol 24:1001–1011. doi:10.1002/joc.1036

Barnston AG, Livezey RE (1987) Classification, seasonality and persistence of low-frequency atmospheric circulation patterns. Mon Weather Rev 115:1083–1126. doi:10.1175/1520-0493(1987) 115<1083:CSAPOL>2.0.CO;2

Chan YH (2005) Biostatistics 304. Cluster analysis. Singapore Med J 46(4):153–159

Coleman JSM, Rogers JC (2007) A synoptic climatology of the central United States and associations with Pacific teleconnection pattern frequency. J Clim 20:3485–3497. doi:10.1175/JCLI4201.1

Huth R (2001) Disaggregating climatic trends by classification of circulation patterns. Int J Climatol 21:135–153

Michaelides S, Pattichis C (1998) Classification of rainfall distribution with the use of artificial neural networks. In: Proceeding of the 3rd national conference meteorology – climatology – physics of the atmosphere, Athens, pp 251–256 (in greek)

Michaelides S, Tymvios F, Charalambous D (2010) Investigation of trends in synoptic patterns over Europe with artificial neural networks. Adv Geosci 23:107–112. doi:10.5194/adgeo-23-107-2010

Michailidou C, Maheras P, Arseni-Papadimititriou A, Kolyva-Machera F, Anagnostopoulou C (2009) A study of weather types at Athens and Thessaloniki and their relationship to circulation types for the cold-wet period. Part I: two-step cluster analysis. Theor Appl Climatol 97:163–177. doi:10.1007/s00704-008-0057-x

Mote TL (1998) Mid-tropospheric circulation and surface melt on the Greenland ice sheet. Part II: synoptic climatology. Int J Climatol 18:131–145. doi:10.1002/(SICI)1097-0088(199802)18:2<131::AID-JOC228>3.0.CO;2-S

Optimization of a Regional Climate Model for High Resolution Simulations over Greece

S. Mystakidis, P. Zanis, C. Dogras, E. Katragkou, I. Pytharoulis, D. Melas, E. Anadranistakis, and H. Feidas

Abstract A set of six yearly high resolution (10 × 10 km) regional climate simulations were carried out over Greece using RegCM3 in the framework of the project GEOCLIMA based on different setups for the convective scheme. Specifically, the simulations comprised two experiments using the Grell convective scheme with Fritsch-Chappell (FC) closure assumption and four experiments using the Emanuel convective scheme. The aim of the study is the optimization of the model for Greece by comparing simulated values of near surface temperature, precipitation and cloudiness with the respective observed values at 84 Greek stations. The model domain is nested to a coarser RegCM3 European domain (at a resolution of 25 × 25 km) driven by the ERA-40 reanalysis dataset. Simulations using the modified Emanuel convective scheme reduce mean bias (and RMSE) in temperature over 25% (20%), in cloudiness over 20% (10%) and in precipitation over 70% (40%). Results show that the model for the Greek area is more sensitive to changes in autoconversion threshold than changes in relaxation rate.

S. Mystakidis (✉) • P. Zanis • C. Dogras • I. Pytharoulis • H. Feidas
Department of Meteorology and Climatology, School of Geology, Aristotle University of Thessaloniki, Thessaloniki 54124, Greece
e-mail: smystaki@auth.gr

E. Katragkou
Department of Meteorology and Climatology, School of Geology, Aristotle University of Thessaloniki, Thessaloniki 54124, Greece

Laboratory of Atmospheric Physics, Physics Department, Aristotle University of Thessaloniki, Thessaloniki, Greece

D. Melas
Laboratory of Atmospheric Physics, Physics Department, Aristotle University of Thessaloniki, Thessaloniki, Greece

E. Anadranistakis
Hellenic National Meteorological Service, Ellinikon, Greece

C.G. Helmis and P.T. Nastos (eds.), *Advances in Meteorology, Climatology and Atmospheric Physics*, Springer Atmospheric Sciences,
DOI 10.1007/978-3-642-29172-2_89,

1 Introduction

Regional climate models (RCMs) have become in the last few decades the most popular tools for studying regional climate. RCMs provide information in regions where the climate variables are strongly regulated by the underlying topography and the surface heterogeneity (Giorgi 1990). One of the primarily physical parameterizations on RCMs is the parameterization of convective processes. The adequate representation of convective processes is particularly important in RCMs, but there is no universally accepted framework for representing convection in numerical simulation models operating with grid scales that prohibit fully explicit representation (Segele et al. 2009; Zanis et al. 2009). The aim of the study is the optimization of the regional climate model RegCM3 for high resolution simulations over Greece by comparing observations with model results using different setups for the convective scheme.

2 Data and Methodology

The model used for the regional climate simulations in this work is RegCM3. RegCM was originally developed at the National Center for Atmospheric Research (NCAR) and has been mostly applied to studies of regional climate and seasonal predictability around the world (Pal et al. 2007). Six high resolution (10 $\times$ 10 km) regional climate simulations were carried out over Greece for the period December 1999–December 2000 using RegCM3 with 1 month for spin up. The model domain is nested to a coarser RegCM3 European domain (at a resolution of 25 $\times$ 25 km) driven by the ERA-40 reanalysis dataset. The simulations were carried out using two configurations for the convective scheme: (a) the Grell convective scheme with Fritsch-Chappell closure assumption GRFC (Grell 1993; Fritsch and Chappell 1980) and (b) the Emanuel convective scheme MIT (Emanuel 1991). The simulations comprised two experiments using the GRFC scheme and four experiments using MIT scheme (Table 1). Simulations using MIT convective scheme include changes in (1) the relaxation rate a (kg/m^{2}sK) which determines the rate at which the cloud-base upward mass flux is relaxed to steady state and in (2) the warm cloud autoconversion threshold l_0 (kg/kg) which determines the amount of cloud water available for precipitation conversion (Segele et al. 2009).

In order to evaluate and optimize RegCM3 for high resolution simulations over Greece the simulated values of near surface air temperature, precipitation and cloudiness are compared with the respective observed values at 84 Greek meteorological stations from the network of the Hellenic National Meteorological Service (Fig. 1b). The model domain (Fig. 1a) is nested within a coarser RegCM3 European domain with resolution of 25 $\times$ 25 km driven by the ERA-40 reanalysis dataset.

The statistical metrics used for the model evaluation with observations include: (a) the mean bias, (b) the mean absolute error (MAE), (c) the root mean square error

Table 1 Model experiments with different convective schemes

Convective parameterization scheme	Enclosure	Simulation
Grell (default)	Fritsch-Chappell	GRFC-D
Grell (beta version)	Fritsch-Chappell (Torma et al. 2011)	GRFC-B
Emanuel (default)	$l_0 = 0.0011$, a = 0.2	MIT-D
Emanuel	$l_0 = 0.01$, a = 0.1 (Segele et al. 2009)	MIT-B1
Emanuel	$l_0 = 0.01$, a = 0.2 (Segele et al. 2009)	MIT-B2
Emanuel	$l_0 = 0.01$, a = 0.3 (Segele et al. 2009)	MIT-B3

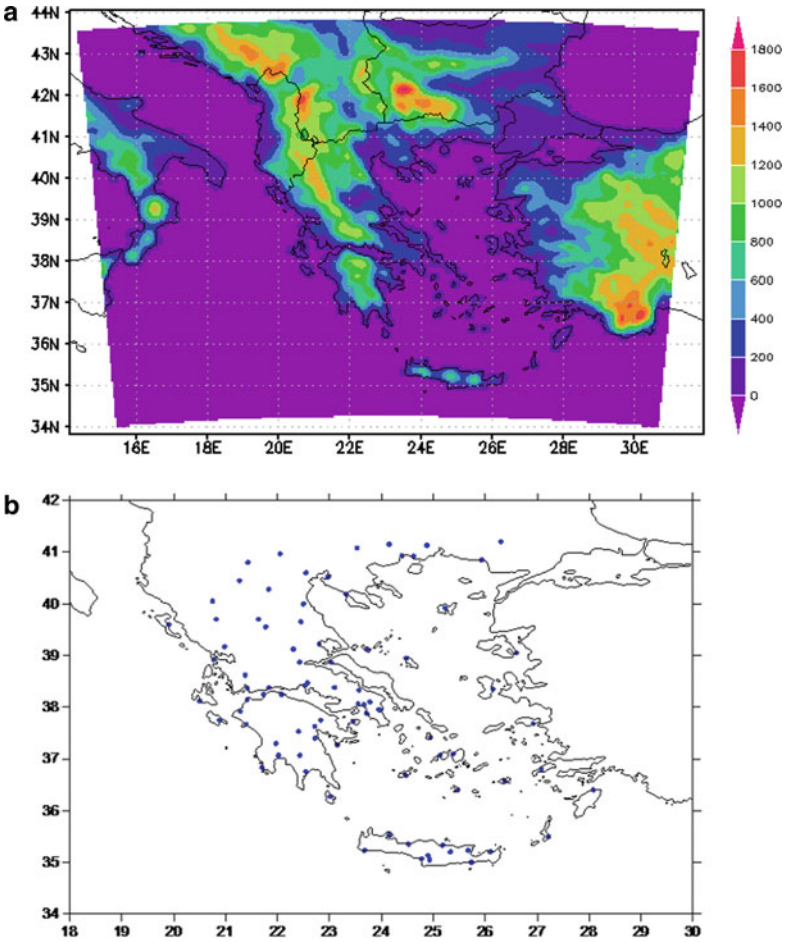

Fig. 1 (**a**) Topography of the model domain (33.82–44.04°N, 14.14–31.96°E) with a grid resolution of 10 × 10 km and (**b**) the network (34–42°N, 18–30°E) of the 84 stations of National Hellenic Meteorological Society

(RMSE), (d) the correlation coefficient (R) and (e) the normalized standard deviation (NSD) being the ratio of the standard deviation of simulated values over the standard deviation of observed values.

3 Results

Simulations reproduce the observed mean annual temperature distribution over the Greek area for all convective schemes. As an example Fig. 2 shows the observed and MIT-B1 temperature fields. The observed minimum in temperature over the northwestern Greece and central Peloponnesus is well reproduced but overall the model underestimates temperature. From Table 2 it is obvious that model bias, MAE and RMSE are larger when GRFC-D convective scheme is used while bias (and RMSE) is reduced by about 28% (21%) with the MIT-B1 convective scheme compared to GRFC-D. Correlation with observations is high for all simulations.

The observations (Fig. 3a) locate the major centers of precipitation maxima over western Greece while drier conditions prevail at regions of eastern Greece and

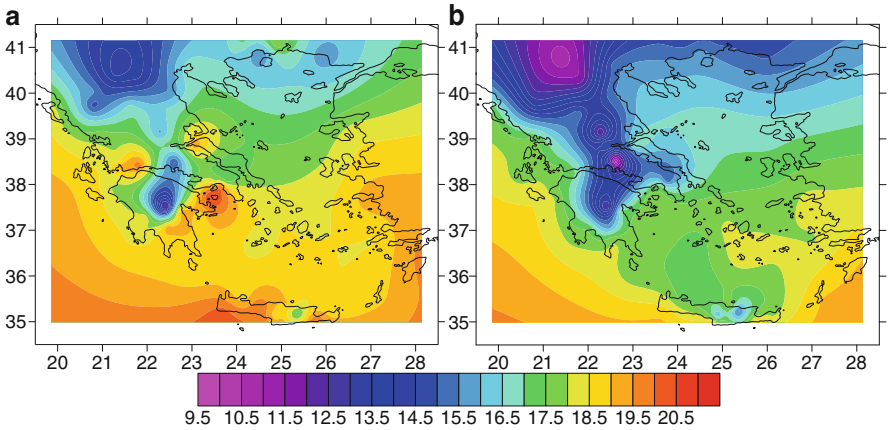

Fig. 2 Mean annual temperature (°C) distribution for (**a**) observations and (**b**) MIT-B1

Table 2 Bias, MAE, RMSE, correlation, NSD and standard deviation values for temperature simulations using different convective parameterization schemes.

	Bias (°C)	MAE (°C)	RMSE (°C)	R	NSD	STD (°C)
Observations						1.76
GRFC-D	−2.02	2.02	2.29	0.85	1.17	2.05
GRFC-B	−1.99	1.99	2.25	0.85	1.11	1.95
MIT-D	−1.62	1.63	1.95	0.86	1.19	2.1
MIT-B1	−1.46	1.48	1.8	0.86	1.16	2.05

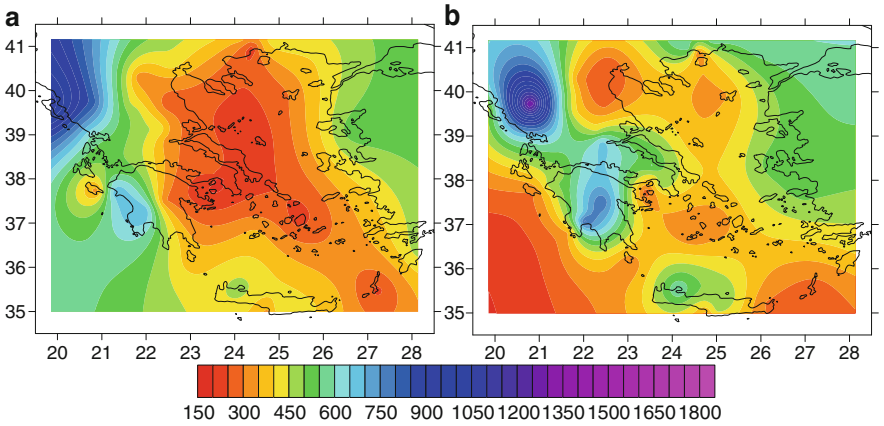

Fig. 3 Total annual precipitation (mm) distribution for (**a**) observations and (**b**) MIT-B1

Table 3 Bias, MAE, RMSE, correlation, NSD and standard deviation values for precipitation simulations using different convective schemes

	Bias (mm)	MAE (mm)	RMSE (mm)	R	NSD	STD (mm)
Observations						178.1
GRFC-D	235.8	266.3	327.0	0.51	1.45	258.1
GRFC-B	73.9	139.1	201.8	0.54	1.13	202.0
MIT-D	178.2	212.6	273.8	0.47	1.23	219.6
MIT-B1	60.6	136.2	197.7	0.44	1.05	186.8

Aegean Sea. The simulations reproduce the major observed characteristics of the precipitation field but overestimate precipitation in most Greek areas. The simulations MIT-B1 (Fig. 3b) and GRFC-B (not shown) are closer to the observed pattern of precipitation. Statistically the simulation MIT-B1 has the lowest values of bias, MAE and RMSE (Table 3). Simulation GRFC-B reduces the bias and RMSE by 69% and 38% respectively compared to the default GRFC-D while shows the highest correlation with observations. Model bias and RMSE are larger for GRFC-D and MIT-D.

According to the observations (Fig. 4a) maximum cloud cover is located over northwestern Greece while total cloud cover is reduced from northwestern to southeastern Greece. All simulations reproduce the major features of observed mean annual cloud cover spatial distribution over the Greek area (e.g. see Fig. 4b for MIT-B1). Statistically simulation MIT-B1 has the lowest values of bias, MAE and RMSE (Table 4) while all model simulations underestimate total cloud cover except from GRFC-B. Correlation with observations is higher than for precipitation and simulation MIT-B1 reduces bias and MAE by 22% and RMSE by 19% compared to the default convective scheme GRFC-D.

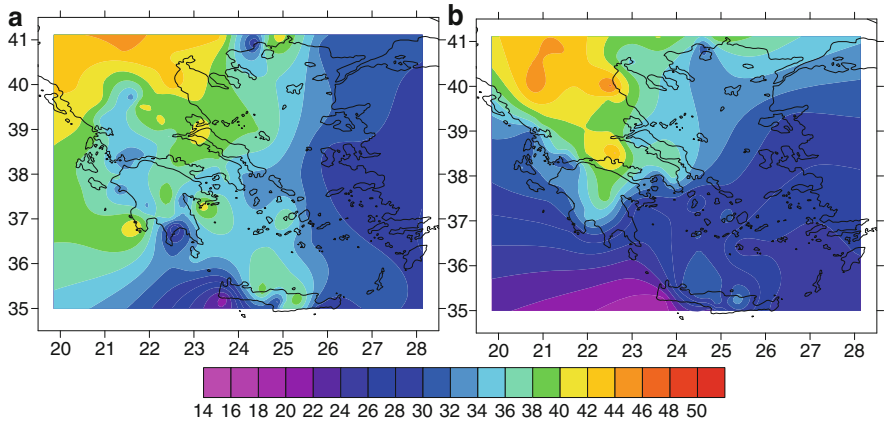

Fig. 4 Mean annual cloud cover (%) distribution for (**a**) observations and (**b**) MIT-B1

Table 4 Bias, MAE, RMSE, correlation, NSD and standard deviation values for cloud cover simulations using different convective parameterization schemes

	Bias (%)	MAE (%)	RMSE (%)	R	NSD	STD (%)
Observations						4.75
GRFC-D	−2.85	−3.6	5.81	0.62	1.34	6.34
GRFC-B	4.22	5.67	6.19	0.64	1.21	5.74
MIT-D	−4.94	−6.53	6.86	0.62	1.24	5.89
MIT-B1	−2.21	−2.93	5.21	0.62	1.24	5.88

Simulations MIT-B2 and MIT-B3 do not differ significantly compared to MIT-B1 according to t-test and Wilcoxon's test.

4 Conclusions

Aiming to the optimization of RegCM3 for high resolution regional climate simulations over Greece, a set of six yearly simulations were performed with different configurations for the Grell and Emanuel convective schemes.

It is evident that RegCM3 reproduces well the major characteristics of the observed annual distribution of temperature, precipitation and cloud cover over Greece. However, the best model performance is reached primarily with MIT-B1 and secondarily by GRFC-B schemes.

Specifically, simulations using the MIT-B1 convective scheme reduce mean bias in temperature by 28%, in cloudiness by 20% and in precipitation by 74% compared to the default scheme GRFC-D. It is evident also that the model is more sensitive to changes in autoconversion threshold than changes in relaxation rate.

Acknowledgments The research has been co-financed by the European Union (European Regional Development Fund) and Greek national funds through the Operational Program "Competitiveness and Entrepreneurship" of the National Strategic Reference Framework (NSRF) – Research Funding Program COOPERATION 2009 (no 09ΣΥΝ-31-1094, Title "Development of a Geographic Climate Information System"). The later boundary conditions for our simulations were provided by Earth System Physics Section, ICTP, Trieste, Italy.

References

Emanuel KA (1991) A scheme for representing cumulus convection in large-scale models. J Atmos Sci 48:2313–2335. doi:10.1175/1520-0469(1991) 048<2313:ASFRCC>2.0.CO;2

Fritsch JM, Chappell CF (1980) Numerical prediction of convectively driven mesoscale pressure systems. Part I: convective parameterization. J Atmos Sci 37:1722–1733. doi:10.1175/1520-0469(1980)037<1722:NPOCDM>2.0.CO;2

Giorgi F (1990) On the simulation of regional climate using a limited area model nested in a general circulation model. J Clim 3:941–963. doi:10.1175/1520-0442(1990) 003<0941:SORCUA>2.0.CO;2

Grell GA (1993) Prognostic evaluation of assumptions used by cumulus parameterizations. Mon Weather Rev 121:764–787. doi:10.1175/1520-0493(1993) 121<0764:PEOAUB>2.0.CO;2

Pal JS et al (2007) Regional climate modeling for the developing world: the ICTP RegCM3 and RegCNET. Bull Amer Met Soc 88:1395–1409. doi:10.1177/BAMS-88-9-1395

Segele TZ, Leslie LM, Lamb JP (2009) Evaluation and adaptation of a regional climate model for the Horn of Africa: rainfall climatology and interannual variability. Int J Climatol 29:47–65. doi:10.1002/joc.1681

Torma C, Coppola E, Giorgi F, Bartholy J, Pongrácz R (2011) Validation of a high-resolution version of the regional climate model RegCM3 over the Carpathian basin. J Hydrometeorol 12:84–100. doi:10.1175/2010JHM1234.1

Zanis P, Douvis C, Kapsomenakis I, Kioutsioukis I, Melas D (2009) A sensitivity study of the Regional Climate Model (RegCM3) to the convective scheme with emphasis in central eastern and southeastern Europe. Theor App Climatol 97:327–337. doi:10.1007/s00704-008-0075-8

Future Projections of Heat Waves in Greece. Extreme or Common Events?

P.T. Nastos and J. Kapsomenakis

Abstract The aim of this study is to analyze and quantify the future projections of heat waves in Greece. For this reason, specific climatic indices were used in the analysis, and concern percentile and absolute indices defined by the CCl/CLIVAR/JCOMM Expert Team (ET) on Climate Change Detection and Indices (ETCCDI). The future projections (SRES A1B) of these indices were carried out using six regional climate models from the ENSEMBLES project, concerning the near future 2031–2050 and the far future 2071–2100 compared to the reference period 1961–2000. The findings of this analysis are discussed against recent recorded heat waves in order to understand if such events are even more extreme or common in the future.

1 Introduction

It is a great consensus within the scientific community that the frequency and/or intensity of some extreme weather events have changed over the last 50 years; namely it is very likely that cold days, cold nights and frosts have become less frequent, while hot days and hot nights have become more frequent and heat waves have become more frequent over most land areas (IPCC 2007). Heat wave is commonly defined as a period of abnormally and uncomfortably hot weather with high air humidity. Typically, a heat wave lasts at least 2 days (Koppe et al. 2004). A recent research has given evidence that 'Mega-heatwaves' such as the 2003 and

P.T. Nastos (✉)
Laboratory of Climatology and Atmospheric Environment, University of Athens, Panepistimiopolis, Athens GR-15784, Greece
e-mail: nastos@geol.uoa.gr

J. Kapsomenakis
Research Centre for Atmospheric Physics and Climatology, Academy of Athens, Omirou 24, Athens GR-10672, Greece

C.G. Helmis and P.T. Nastos (eds.), *Advances in Meteorology, Climatology and Atmospheric Physics*, Springer Atmospheric Sciences,
DOI 10.1007/978-3-642-29172-2_90,

2010 events broke the 500-year long seasonal temperature records over approximately 50% of Europe. According to regional multi-model experiments, the probability of a summer experiencing 'megaheatwaves' will increase by a factor of 5–10 within the next 40 years (Barriopedro et al. 2011). Study of heat waves in Greece from synoptical and human-biometeorological point of view has been carried out by many researchers (Giles et al. 1990; Matzarakis and Mayer 1991; Katsouyanni et al. 1988; Prezerakos 1989; Philandras et al. 1999; Kostopoulou and Jones 2005; Nastos and Matzarakis 2008, 2011; Founda and Giannakopoulos 2009; Theoharatos et al. 2010; Matzarakis and Nastos 2011). It is worthy to note that the increase of mortality is strongly associated not only with the frequency but the duration of heat waves. Matzarakis and Nastos (2011) concluded that a statistically significant (at confidence level 95%) increasing trend of the maximum duration of heat waves within the year ($b = 1.33$ days/year, $p = 0.000$) is observed since 1983. In addition, the number of heat waves (HW) within the year appears a statistically significant (at confidence level 95%) trend ($b = 0.26$ HW/year, $p = 0.000$), since 1983.

The objective of this study is to quantify the future projections (SRES A1B) of heat waves in Greece, based on specific defined climatic indices, and to examine if observed heat waves (summer 2007) are even more extreme or common in the future.

2 Data and Methodology

The indices used can be divided in two categories: percentile and absolute indices defined by the joint CCl/CLIVAR/JCOMM Expert Team (ET) on Climate Change Detection and Indices (Alexander et al. 2006). The percentile indices concern: warm days, TX90p (the number of days with maximum temperature above the 90th percentile calculated for each calendar day, on basis of 1961–1990, using running 5 day window); warm nights, TN90p (the number of days with minimum temperature above the 90th percentile calculated for each calendar day, on basis of 1961–1990, using running 5 day window). The absolute indices concern: summer days, SU25 (number of days with daily maximum temperature above 25°C); tropical days, SU30 (number of days with daily maximum temperature above 30°C); tropical nights, TR20 (number of days with daily minimum temperature above 20°C); maximum daily maximum temperature, TXx; maximum daily minimum temperature, TNx.

The future projected change in the aforementioned indices was accomplished using the output of the simulations of an ensemble of six regional climate models (RCMs), which were carried out within the European project "ENSEMBLES" (http://ensemblesrt3.dmi.dk/). Thus, the mean daily air temperatures were used from the following six RCMs: CNRM-RM5.1(ARPEGE), DMI-HIRHAM5 (ARPEGE), ETHZ-CLM(HadCM3Q0), METO-HC_HadRM3Q0 (HadCM3Q0), KNMI-RACMO2 (ECHAM5), MPI-M-REMO (ECHAM5). The models' simulations used as initial and boundary conditions the output data of various

General Circulation Models (GCMs), which are presented in the above parentheses after each RCM. All six RCMs have spatial resolution $0.22^\circ \times 0.22^\circ$ (approximately 25×25 km). The simulations of the six RCMs for the near future (2031–2050) and the far future (2071–2100) were made under the A1B emissions scenario, while the simulations for the reference period (1961–1990) were made under the 20C3M emissions scenario, which represents a 20th century simulation using historical GHG concentrations (note this is actually 1871–2000).

Furthermore, the climatic indices were assessed for recent heat stress conditions, using daily maximum and minimum air temperature from 55 meteorological stations of the Hellenic Meteorological Service, for the summer 2007, when three strong heat waves were recorded.

3 Results

The results showed that summer days (SU25) range from 70 days in mountainous continental regions (Pindus range) to 140 days in eastern/western parts of the continental Greece and central Crete, while from 30 days in central Aegean Sea to 70 days in coastal areas. Moving to the near future (2031–2050), an increase in SU25 days appears from 18 to 27 days in mountainous continental regions and central Crete and from 35 days in coastal areas to 53 days in south Aegean Sea (Fig. 1). The inter model standard deviation (IMSD) with respect to the projected changes varies from 1 to 11 days. The increase in SU25 for the far future (2071–2100) appears higher from 32 to 48 days (continental regions and central Crete) and from 52 days (coastal areas) to 72 days (south Aegean Sea) with IMSD from 1 to 7 days. Taking into consideration the summer days in 2007, a year with three heat waves (Fig. 2), one can assume that the recorded 160 days for SU25 will be a common event and not so extreme for the far future. Concerning tropical days (SU30), the increase in the near future ranges from 22 to 30 days for continental Greece and from 2 days (Aegean Sea) to 14 days in coastal areas, having IMSD with 1–7 days appeared in the majority of the country and 10–14 days in the coastal areas. Greater increase will take place for the projections in the far future; namely 36–52 days for continental Greece and 12 (Aegean Sea) – 36 days in coastal areas. The IMSD for the projected change ranges from 5 days in continental Greece to 19 days in eastern coasts of Aegean Sea. Concerning warm days (TX90p) in the near future, the increase of TX90p over sea will reach the 180 days in contrast to 50 days over land, while in the far future the 270 days and 110 days respectively. Similar results have been extracted with respect to maximum daily maximum temperature, TXx.

Taking into account the tropical nights (TR20), they range from 0 days in central mountainous Greece (Pindus range), due to altitude forcing, up to 70 days in coastal areas. The sea appears to be warmer in nights than the interior continental country reaching 120 days in the south. In the near future the projected increase in TR20

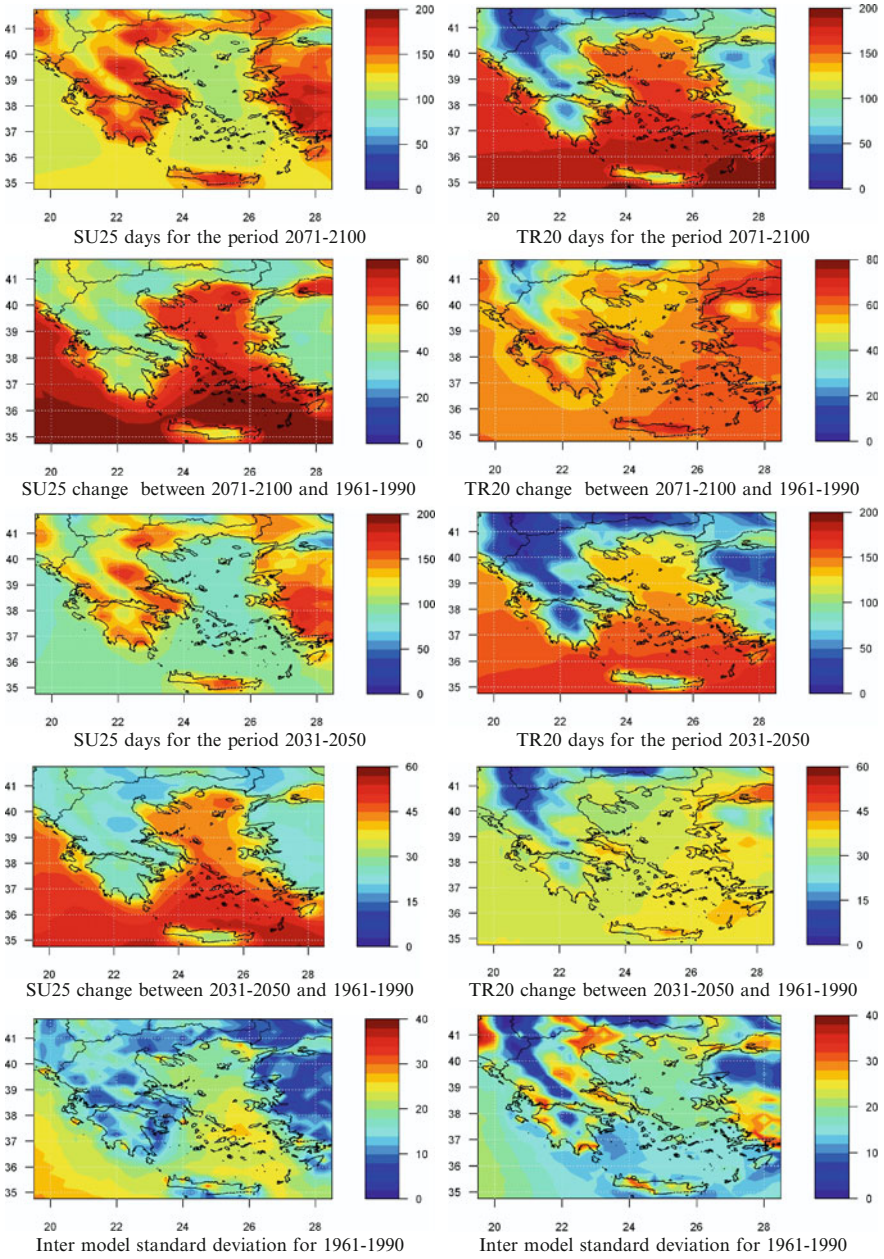

Fig. 1 Spatial distribution of summer days (SU25) and tropical nights (TR20) for the near future (2031–2050) and far future (2071–2100), along with changes from the reference period and the inter model standard deviation for the reference period 1961–1990

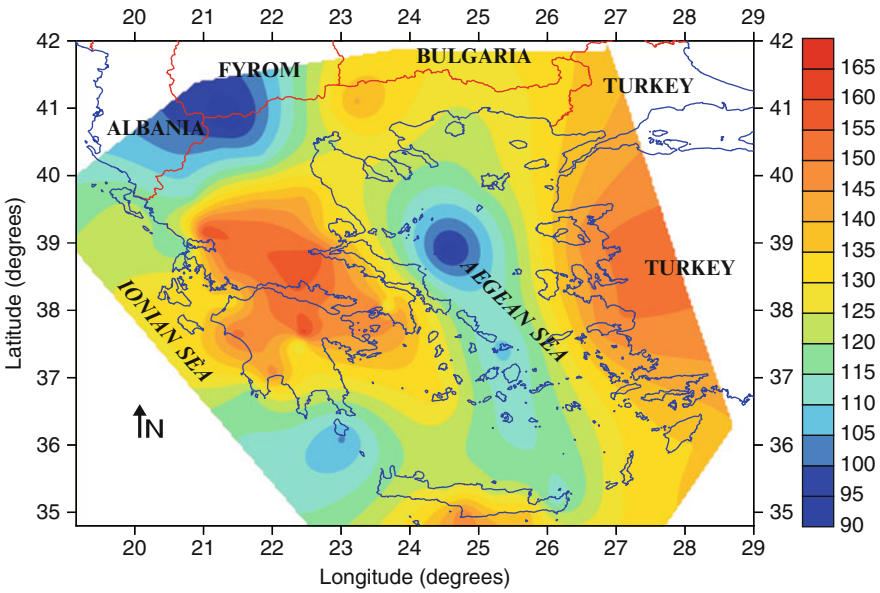

Fig. 2 Spatial distribution of summer days (SU25) during 2007

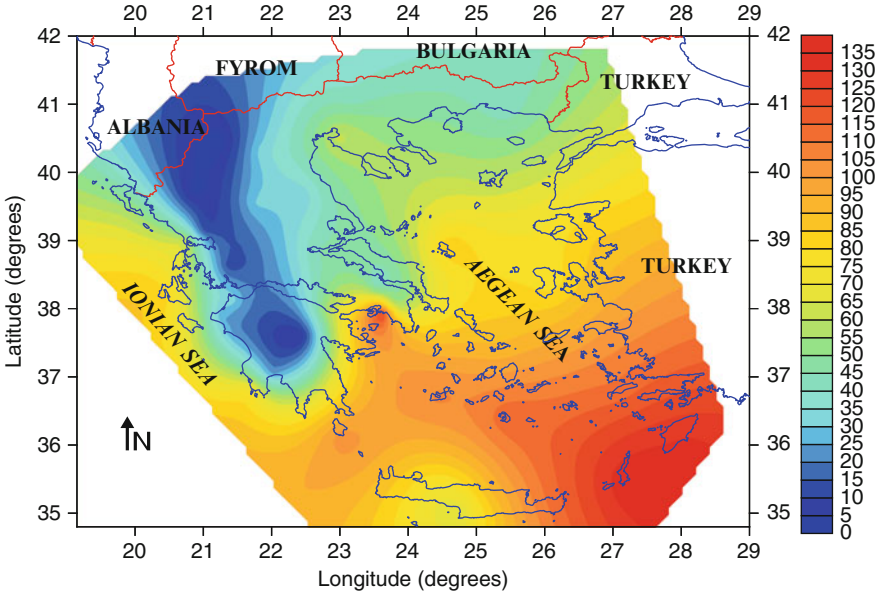

Fig. 3 Spatial distribution of tropical nights (TR20) during 2007

ranges from 9 days (continental Greece) to 39 days (southeastern Aegean Sea), with IMSD between 1 day (continental country) and 12 days over sea (Fig. 1). The increase in the far future range from 28 to 60 days within the aforementioned regions respectively, with IMSD between 5 and 19 days. The recorded pattern of

TR20, during summer 2007, when TR20 reached 135 days at the southeastern parts, shows an extreme situation, but so common for the projected pattern in the far future (Fig. 3).

Regarding warm nights (TN90p), the increase in the near future ranges from 60 days over land to 170 days over sea, while in the far future from 130 to 180 days respectively. Similar results have been found for maximum daily minimum temperature, TNx.

4 Conclusions

Results showed widespread significant changes in temperature extremes associated with projected warming in the near (2031–2050) and the far (2071–2100) future under SRES A1B, especially for those indices derived from daily minimum temperature. The findings of this study give evidence that extreme events such as summer 2007 will be more common and frequent in the future.

References

Alexander LV, Zhang X, Peterson TC, Caesar J, Gleason B, Klein Tank AMG, Haylock M, Collins D, Trewin B, Rahimzadeh F, Tagipour A, Rupa Kumar K, Revadekar J, Griffiths G, Vincent L, Stephenson DB, Burn J, Aguilar E, Brunet M, Taylor M, New M, Zhai P, Rusticucci M, MVazquez-Aguirre JL (2006) Global observed changes in daily climate extremes of temperature and precipitation. J Geophys Res 111:D05109. doi:10.1029/2005JD006290

Barriopedro D, Fischer EM, Luterbacher J, Trigo RM, García-Herrera R (2011) The hot summer of 2010: redrawing the temperature record map of Europe. Science 332:220–224. doi:10.1126/science.1201224 224

Founda D, Giannakopoulos C (2009) The exceptionally hot summer of 2007 in Athens, Greece – a typical summer in the future climate? Glob Plan Change 67:227–236

Giles BD, Balafoutis C, Maheras P (1990) Too hot for comfort: the heat waves in Greece in 1987 and 1988. Int J Biometeorol 34:98–104

IPCC (2007) The physical science basis. Contribution of working group 1 to the fourth IPCC assessment report. Chapter 11 regional climate projections, IPCC

Katsouyanni K, Trichopoulos D, Zavitsanos X, Touloumi G (1988) The 1987 Athens heatwave. Lancet 2(8610):573

Koppe C, Jendritzky G, Kovats S, Menne B (2004) Heat-waves: risks and responses, vol 2, Health and global environmental change. Regional Office for Europe, Copenhagen

Kostopoulou E, Jones PD (2005) Assessment of climate extremes in the Eastern Mediterranean. Meteorol Atmos Phys 89:69–85

Matzarakis A, Mayer H (1991) The extreme heat wave in Athens in July 1987 from the point of view of human biometeorology. Atmos Environ 25B:203–211

Matzarakis A, Nastos PT (2011) Human-biometeorological assessment of heat waves in Athens. Theor Appl Climatol 105(1):99–106. doi:10.1007/s00704-010-0379-3

Nastos P, Matzarakis ς (2008) Variability of tropical days over Greece within the second half of the twentieth century. Theor Appl Climatol 93:75–89. doi:10.1007/s00704-007-0325-1

Nastos PT, Matzarakis A (2011) The effect of air temperature and human thermal indices on mortality in Athens. Theor Appl Climatol. doi:10.1007/s00704-011-0555-0

Philandras CM, Metaxas DA, Nastos PT (1999) Climate variability and urbanization in Athens. Theor Appl Climatol 63:65–72

Prezerakos NG (1989) A contribution to the study of the extreme heat wave over the south Balkans in July 1987. Meteor Atmos Phys 41:261–271

Theoharatos G, Pantavou K, Marakis A, Spanou A, Katavoutas G, Efstathiou P, Mpekas P, Asimakopoulos D (2010) Heat waves observed in 2007 in Athens, Greece: synoptic conditions, bioclimatological assessment, air quality levels and health effects. Environ Res 110:152–161. doi:10.1016/j.envres.2009.12.002

Composite Mean and Anomaly of Synoptic Conditions for Tornadic Days over North Ionian Sea (NW Greece)

P.T. Nastos and I.T. Matsangouras

Abstract Tornadoes and waterspouts are violent phenomena of local scale, which are able to cause damages and in many cases loss of life. Recent studies have given evidence that west Greece is a vulnerable area for tornadoes, waterspouts and funnel clouds to occur. In this study, the composite mean and anomaly of synoptic conditions for tornadic days over the north Ionian Sea were quantified. The daily composite mean of synoptic conditions were based on NCEP/NCAR Reanalysis datasets for the period September 1, 1948 to December 12, 2010, while the composite anomalies were calculated with respect to 30 years climatology (1981–2010) of the synoptic conditions. The analysis of composite mean and anomaly of synoptic conditions was carried out in terms of seasonal variability of phenomena, over the north Ionian Sea, for specific barometric pressure level of 500 hPa and the sea level pressure (SFC). Additionally, the dynamic LI INDEX was analyzed and discussed.

1 Introduction

Tornadoes (TR), waterspouts (WS) and funnel clouds (FC) could be characterized as the most spectacular natural phenomena revealing the nature's force in a small scale. Wind whirl events occur in many parts of the world (Fujita 1973) and the performed research during the last two decades indicate their occurrence in Europe (Dessens and Snow 1987; Dotzek 2001; Holzer 2001). Regarding tornado activity in Greece, significant research has been carried out within the last years, such as the 300 years (1709–2010) historical records of tornadoes – waterspouts – funnel clouds (Matsangouras et al. 2011b), the 10 year climatology (Sioutas 2011) and

P.T. Nastos (✉) • I.T. Matsangouras
Laboratory of Climatology and Atmospheric Environment, University of Athens, Panepistimiopolis, Athens GR-15784, Greece
e-mail: nastos@geol.uoa.gr

C.G. Helmis and P.T. Nastos (eds.), *Advances in Meteorology, Climatology and Atmospheric Physics*, Springer Atmospheric Sciences,
DOI 10.1007/978-3-642-29172-2_91,

the twentieth century climatology (Nastos and Matsangouras 2010). Additionally to the above climatological publications, analysis of several catastrophic case studies have been carried out from synoptic scale point of view (Sioutas 2002, 2003; Matsangouras and Nastos 2010; Matsangouras et al. 2010, 2011a).

The authors consider tornadic daily composite mean of synoptic conditions and the composite anomalies as a valuable tool not only from the academic point of view but for the operational forecasters of Hellenic National Meteorological Service (HNMS). In this study, the composite mean and anomaly of synoptic conditions for tornadic days over the north Ionian Sea were quantified.

2 Data and Methodology

The Laboratory of Climatology and Atmospheric Environment (LACAE, http://lacae.geol.uoa.gr) of the University of Athens has begun a systematic effort in recording tornadoes, waterspouts and funnel clouds in Greece since 2007. LACAE developed in 2009 an open-ended online tornado report database web system (http://tornado.geol.uoa.gr) contributing in the study of climatology of these extreme weather events. All database's records have been confirmed by photos, video, eyewitness reports, literature reports and synoptical reports by Hellenic National Meteorological Service (HNMS). Based on this extensive dataset we investigated the seasonal synoptic conditions of tornadic days over the Ionian Sea for specific barometric pressure levels, in order to identify any synoptic patterns.

The daily composite mean of synoptic conditions were based on NCEP/NCAR Reanalysis datasets for the period September 1, 1948 to December 12, 2010, while the composite anomalies were calculated with respect to 30 years climatology (1981–2010) of the synoptic conditions.

2.1 Climatology of Tornadoes and Waterspouts

Matsangouras et al. (2011b) suggested that the annual mean of tornadic events for the period 1709–2010 over NW Greece is equal to 0.31 events per year. Noth Ionian area is the most favorable region for tornadic events with a density equal to 0.36 events $y^{-1}10^{-4}$ km^2. Taking into consideration the last 10 years (2001–2010), the density over north Ionian Sea area increases dramatically to 9.42 events $y^{-1}10^{-4}$ km^2 that is 1.16 tornadoes $y^{-1}10^{-4}$ km^2 and 7.56 waterspouts $y^{-1}10^{-4}$ km^2. More than 93 wind whirl events occurred (15 tornadoes, 72 waterspouts and 6 funnel clouds) in 74 days within the studied period September 1, 1948 to December 12, 2010. The spatial distribution (Fig. 1) reveals that south and central parts of Corfu are vulnerable to tornadoes occurrence. On the other hand waterspouts could be developed anywhere over north Ionian Sea, but it is remarkable that waterspouts were developed between Corfu Island and mainland of

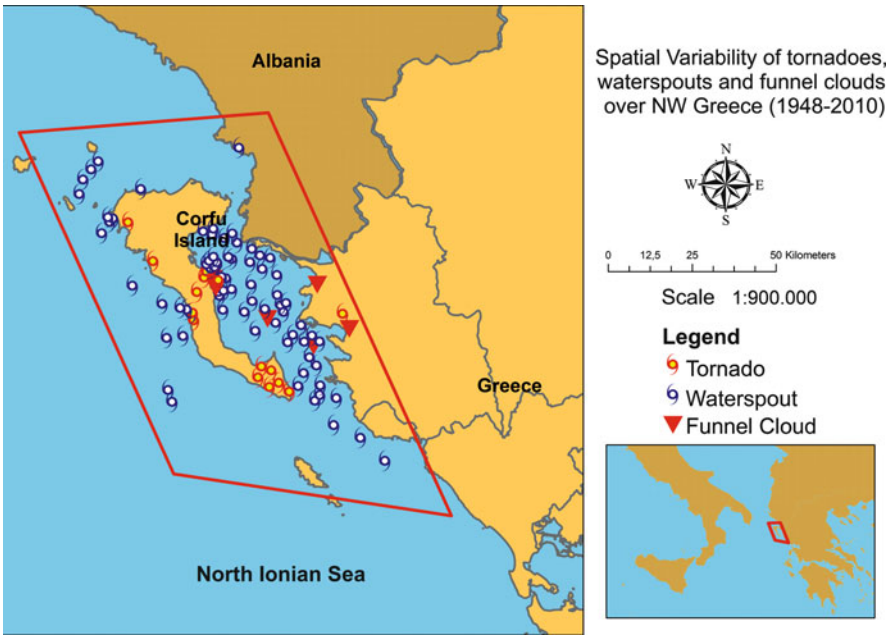

Fig. 1 Spatial variability of tornadoes, waterspouts and funnel clouds over north Ionian Sea from January 1, 1948 to December 31, 2010

Greece (almost 75% of recorded waterspouts). Funnel clouds were observed over the same area (between Corfu and NW mainland of Greece).

Autumn seems to be the most active season (for both tornadoes and waterspouts) followed by summer (Fig. 2), which is in agreement with the seasonal distribution presented by Matsangouras et al. (2011b). October and November are the months with the highest frequency of total tornadic events followed by September. Tornadoes are more frequent during November followed by October and September. On the contrary, waterspouts are frequent during September followed by October and November (Fig. 2).

2.2 Composite Mean and Anomaly of Synoptic Conditions

The composite mean synoptic conditions at 500 hPa barometric pressure level of tornadic days during autumn period (the most active season) reveals a long – wave trough from NW Italy to Sicily Island, causing a SW upper air flow over the area of interest (Fig. 3a). The composite anomaly at this barometric pressure level during autumn (Fig. 3b) presents a deepening of geopotential height at least equal or higher to 80 gpm over central Mediterranean Sea (between Sicily and central Italy). Studying the SFC composite mean of tornadic synoptic conditions during autumn

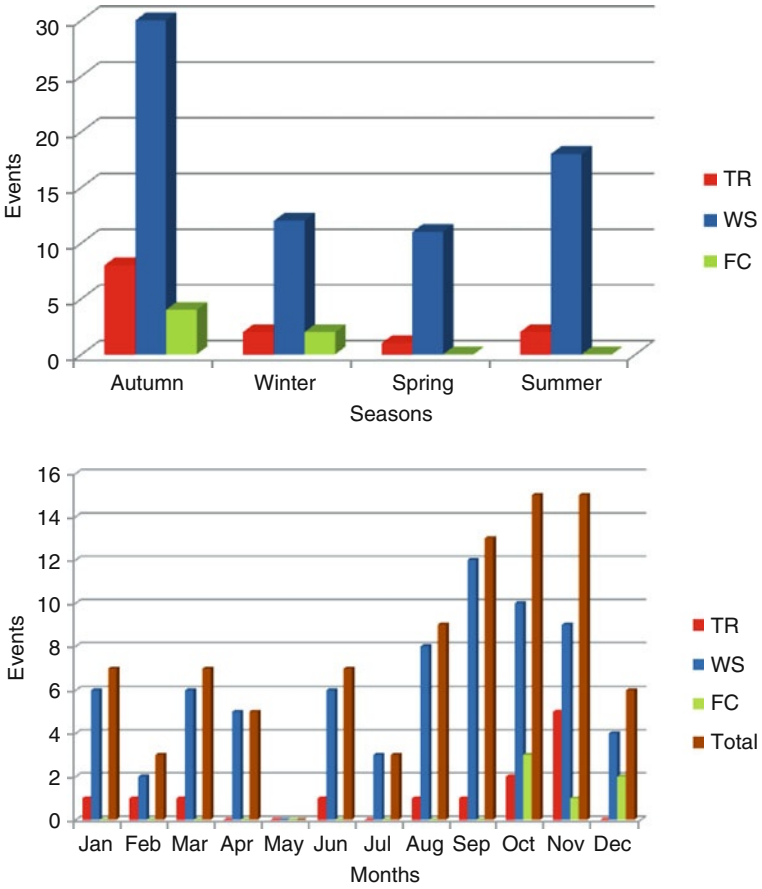

Fig. 2 Seasonal (*upper*) and monthly (*lower*) variability of tornadoes, waterspouts and funnel clouds over north Ionian Sea from January 1, 1948 to December 31, 2010

season, a shallow cyclonic circulation over central Italy (1,005 hPa) permits a S-SW air flow (Fig. 3c). The composite anomaly at SFC reveals a region with barometric pressure fall equal to −5 hPa over central Italy, north Ionian Sea, Adriatic Sea and Albania (Fig. 3d). The composite mean Lifted Index (LI) during the examined period is lower than 0°C, covering except the area of interest an extending area over east Mediterranean Sea, as well (Fig. 3e). This is in agreement with Sioutas (2011), who found that the mean value of LI for tornadoes over Greece (concerning 10 years period) is approximately −1.6°C. The composite anomaly (Fig. 3f) of LI value over north Ionian Sea ranges from −3.5°C to −4°C.

During winter the 500 hPa composite mean synoptic condition suggests a long wave trough over NE Europe implying a W-SW upper air flow (not shown) over north Ionian Sea. The composite anomaly at this level during winter's tornadic days is at least equal to −120 gpm over central Europe (not shown). The composite mean

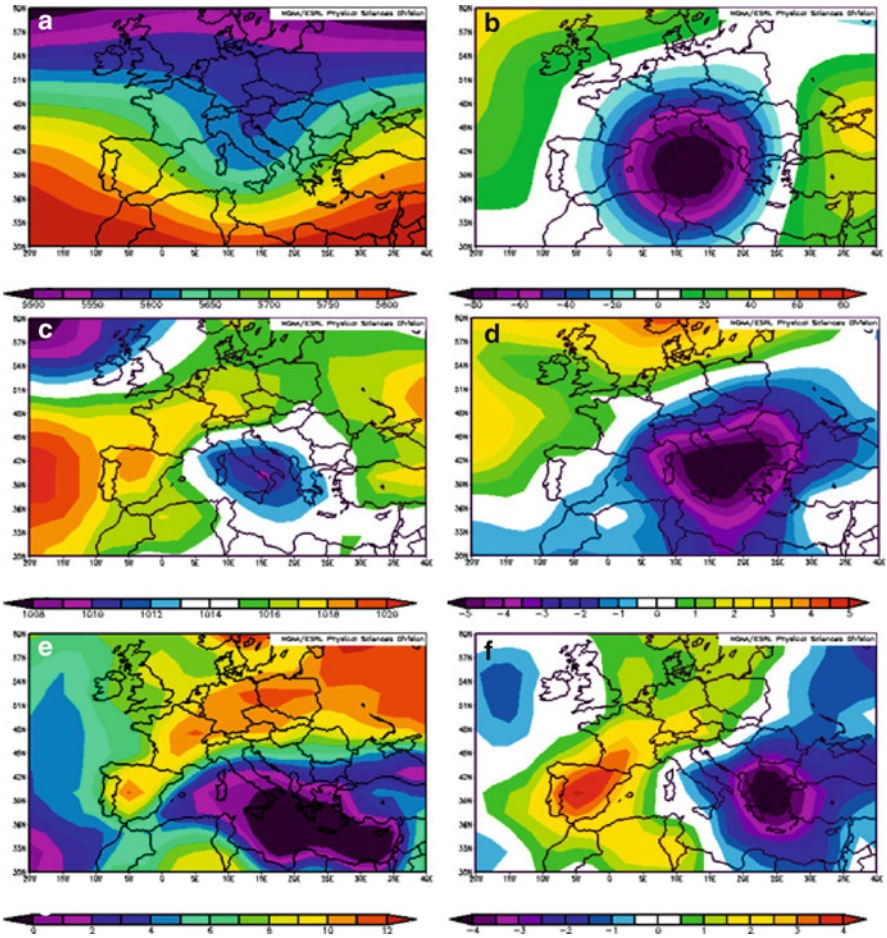

Fig. 3 Composite mean (*left graphs*) and anomaly (*right graphs*) of tornadic days during autumn for 500 hPa (*upper graphs*), SFC (*middle graphs*) and Lift Index (*lower graphs*)

of LI is equal to 4°C, covering an extended area over east Mediterranean Sea, while the composite anomaly presents −4°C over north Ionian Sea with the maximum fall over Balkans. The SFC composite mean (not shown) depicts a cyclonic circulation centered over the area of interest (and north of it). The daily composite anomaly during this season reveals a pressure decrease less than 8 hPa (not shown) over an extensive region at SE Europe (Italy-Balkans).

During Spring (the least active tornadic season), the composite mean at 500 hPa (not shown) reveals shallow and short wave successive troughs from north Romania to north Libya. The composite anomaly (not shown) presents a geopotential height fall of 60 gpm over a region including south Italy, north Libya and south Ionian Sea. The SFC composite mean (not shown) reveals that the high pressure system over Azores does not suggest any significant gradient field force over the area of interest,

combined with a shallow low pressure circulation over central Greece. During this season, the composite anomaly of tornadic days over north Ionian Sea is −4 hPa (not shown). The thermodynamic Lifted Index (LI) composite mean value of 3°C (and lower) appears in south Italy and south Greece (not shown), while the composite anomaly reveals a value of −2°C over north Ionian Sea (not shown).

Studying the composite mean of synoptic conditions at 500 hPa during summer season (the second most active season for waterspouts development over north Ionian Sea), an anticyclonic circulation over west Europe is revealed (not shown). It allows the existence of long wave trough from Poland to south Ionian Sea causing a W-SW upper air flow over the area of interest. The composite anomaly depicts a geopotential height fall of −60 gpm over Adriatic region (not shown).

A combination of high pressure system over west Europe (at least 1,018 hPa over south United Kingdom and north France) and low pressure system over east Mediterranean Sea (at least 1,006 hPa over Cyprus) is obvious. This composite mean synoptic condition permits over north Ionian Sea an E to SE surface wind flow (not shown). During this season the composite anomaly for tornadic events over north Ionian Sea appears to be less than −3 hPa, covering an extended area over south Italy and Balkans (not shown). The composite mean of the thermodynamic index LI over south Italy and Ionian Sea depicts values lower than −1°C (not shown). The LI composite anomaly appears to be −3°C over central Ionian Sea and −2°C over north Ionian Sea (Corfu Island).

3 Conclusions

North Ionian Sea (including Corfu island) could be characterized as a vulnerable area with respect to tornadoes, waterspouts and funnel clouds occurrence, with a frequency of 9.42 events $y^{-1}10^{-4}$ km^2 (considering the last 10 years).

Autumn is the most active season with the 45% of tornadic events (8 tornadoes, 40 waterspouts and 4 funnel clouds) in 32 days (including common days with multiple events). The composite mean of synoptic conditions reveals a long-wave trough from NW Italy to Sicily Island, causing a SW upper air flow at 500 hPa accompanied with a shallow cyclonic circulation over central Italy during autumn season. The composite mean of LI thermodynamic index is less than 0°C with a composite anomaly equal to −4°C over north Ionian Sea area.

Acknowledgments The authors would like to thank Hellenic National Meteorological Service (HNMS), state authorities, media (blogs, news site, TV and radio stations), the Hellasweather group and all anonymous people, who contribute to accomplish this extensive dataset of tornadoes, waterspouts and funnel clouds over north Ionian Sea area. Daily anomalies images were provided by the NOAA/ESRL Physical Sciences Division, Boulder Colorado.

References

Dessens J, Snow JT (1987) Tornadoes in France. Weather Forecast 4:110–132
Dotzek N (2001) Tornadoes in Germany. Atmos Res 56:233–251
Fujita TT (1973) Tornadoes around the world. Weatherwise 26:56–83
Holzer AM (2001) Tornado climatology of Austria. Atmos Res 56:203–211
Matsangouras IT, Nastos PT (2010) The 27 July 2002 tornado event in Athens, Greece. Adv Sci Res 4:9–13
Matsangouras IT, Nastos PT, Nikolakis DJ (2010) Study of meteorological conditions related to the tornado activity on 25-3-2009 over NW Peloponnesus, Greece. In: Proceedings of the 10th international conference on meteorology, climatology and atmospheric physics (COMECAP), 25–38 May 2010, Patra, pp 417–425 (in Greek)
Matsangouras IT, Nastos PT, Pytharoulis I (2011a) Synoptic-mesoscale analysis and numerical modeling of a tornado event on 12 February 2010 in northern Greece. Adv Sci Res 6:187–194
Matsangouras IT, Nastos PT, Sioutas MV (2011b) 300 years historical records of tornadoes waterspouts and funnel clouds over Greece. In: Proceedings of the sixth European conference on severe storms (ECSS), Palma de Mallorca, 3–7 Oct 2011
Nastos PT, Matsangouras IT (2010) Tornado activity in Greece within the 20th century. Adv Geosci 26:49–51
Sioutas MV (2002) Damaging tornadoes in Greece: July and September 2001. J Meteorol 27 (265):17–22
Sioutas MV (2003) Tornadoes and waterspouts in Greece. Atmos Res 67:645–656
Sioutas MV (2011) A tornado and waterspout climatology for Greece. Atmos Res 100(4):344–356

Effect of Sea-Air Interaction of Caspian Sea on Heavy and Super Heavy Precipitation Events in the Southern Coasts of Caspian Sea

H. Nouri, M. Azadi, and G. Ghasempour

Abstract Cloudiness and precipitation are the most important variables contributing to the formation of the climate of the southern coasts of Caspian Sea. The aim of this research is the investigation of the effect of air-sea interaction on the occurrence of the heavy and super heavy precipitation which is caused by convective and non-convective clouds. On the basis of daily precipitations and with regard to 25% and 50% probability, precipitation events are divided into heavy and super heavy and are also grouped into convective and non-convective cases based on the clouds synoptic codes. The maximum of each precipitation event, the mean and the coverage area was calculated using iso-rain maps for each of the four groups. The relationships among the mean of "2 m air temperature minus sea surface temperature (SST)", SST and precipitation events were studied. The results show that there are three conditions to occur heavy and super heavy precipitation including, SST increasing harmonically from the north to the south of the Caspian Sea, increased mean SST all over the Sea and increased mean of "2 m air temperature minus SST". The latter detected factor which is the most effective variable is less in convective than non-convective events and in heavy precipitation than in super heavy events.

H. Nouri (✉)
University of Malayer, Malayer, Iran
e-mail: hamidwatershed@yahoo.com

M. Azadi
Atmospheric Science and Meteorological Research Center, Tehran, Iran

G. Ghasempour
University of Mehr Alborz, Tehran, Iran

C.G. Helmis and P.T. Nastos (eds.), *Advances in Meteorology, Climatology and Atmospheric Physics*, Springer Atmospheric Sciences,
DOI 10.1007/978-3-642-29172-2_92,

1 Introduction

The Caspian Sea is the largest closed body of water on the surface of the Earth. The precipitation of the southern coasts of Caspian Sea (1,500 mm) is more than the rest of Iran (240 mm). Precipitation and the cloudiness are considered as the most significant climate factors in the area (Masoodian 2003). The Sea surface temperature (SST) and 2 m air temperature are the two major parameters to understand air-sea interaction process that lead to precipitation in coastal regions. Kawai and Wada (2007) reviewed the impacts of diurnal SST variation on the atmosphere at various time scales and suggested the potential importance of diurnal variations of SST on the sea breeze circulation in coastal areas. Zhou et al. (2009) and Zhou and Wu (2010), found that winter precipitation over South China has a significant correlation with Niño-3 and SST. The inter-annual variations of the East Asian summer monsoon are closely associated with SSTs in the tropical Pacific (Huang et al. 2003; Wu et al. 2003; Yang and Lau 2006; Lin and Lu 2009). Also, the relationship between SST and precipitation variability over South China has been studied (Chan and Zhou 2005; Lin and Lu 2009). Several studies have investigated the influences of SST on the precipitation over the Western Africa (Biasutti et al. 2004; Hunt 2000). Modeling studies confirmed statistical association between observed Sahel precipitation variability and tropical Atlantic SST, in the mid 1980s (Giannini et al. 2005). Therefore, large scales to regional SST were assumed by several researches to have an impact on the Sahel and more general African precipitation regimes. Thermodynamic parameters are the major factors to generate precipitation, particularly the heavy and super-heavy events, through the land-sea breeze mechanism (Moradi 2004; Khalili 1973). This research investigates the impacts of the SST and the "2 m air temperature minus SST" on the heavy and super heavy precipitation in the southern coasts of the Caspian Sea.

2 Data and Methodology

Some statistical methods such as regression were used for this study.

2.1 Data

The SST and 2 m air temperature data are extracted from the sites "www.ncdc.noaa.gov" and "www.dss.ucar.edu" for 719 points on the Caspian Sea from 1982 to 2006. Daily precipitation from 168 stations *and synoptic codes of clouds* from seven synoptic stations are taken *at the same time period* over the north of *Iran (*provided by the Iran Meteorological Organization).

2.2 Methodology

A precipitation event is a day or a number of days that precipitation has been recorded and its amount is more than 1 mm/day. The precipitation events are categorized into heavy and super heavy on the basis of daily precipitation and probabilities of 25% and 50% using Weibull method (Muraleedharan et al. 2007), for probability distribution (in which $p\% = m/(n + 1) \times 100$; m = row number after sorting, n = number of data). Therefore, it can be concluded that the heavy and super heavy precipitation events are corresponding to 40 and 95 mm per day, respectively. The events are grouped into convective and non-convective based on the clouds synoptic codes extracted from the stations. When the Synoptic codes of low clouds are 2, 3, 8 and 9 they are considered as convective clouds and when the codes are 4, 5, 6 and 7 they are regarded as non-convective clouds. Statistical precipitation parameters including the maximum of each precipitation event, the mean and the coverage area in North of Iran were calculated using iso-rain maps for each precipitation group (convective heavy, convective super-heavy, non-convective heavy and non-convective super-heavy precipitations). The relationships among the mean of "2 m air temperature minus SST" which will be termed "humidity absorption Index" (DTST) hereafter, the SST and the precipitation were studied. The average SST and DTST are calculated on the basis of the data over the grid points. The monthly regime and trend of the SST and the DTST were investigated within different precipitation groups over the long time period.

3 Results

The results show that there is a cold area in the middle of the Sea about 42–44°N where super heavy precipitation events occur during spring (Fig. 1a) when the Sea surface temperature is 6°C lower than the coastal waters in north of Iran. The SST is higher during summer than spring and the cold pond moves to the east of Caspian Sea about 41–43.5°N. The SST in summer is 5–6°C warmer than the SST in spring (Fig. 1b). In autumn (Fig. 1c), the SST gradually increases from the north to the south of the Sea. The cold area is located in the northern part of the Caspian Sea, so the length of the passage and the time for the absorbance of moisture are sufficient. The difference in SST between north and south is about 10°C. Despite the fact that the SST in the coastal water in autumn is about 4–6°C less than spring and summer, a lot of precipitation events specially the heavy and super heavy groups fall during this season, particularly in October, due to the increase in the passage the cold air mass moves through, the gradual increase of SST from the north to the south of the Sea, the strength of high pressure systems and their proper location. The SST gradient lines in winter are approximately similar to the SST gradient lines in autumn. The SST is less in winter than autumn (about its half), so precipitation is little, too (Fig. 1d). The studies on SST anomaly maps show that there are positive

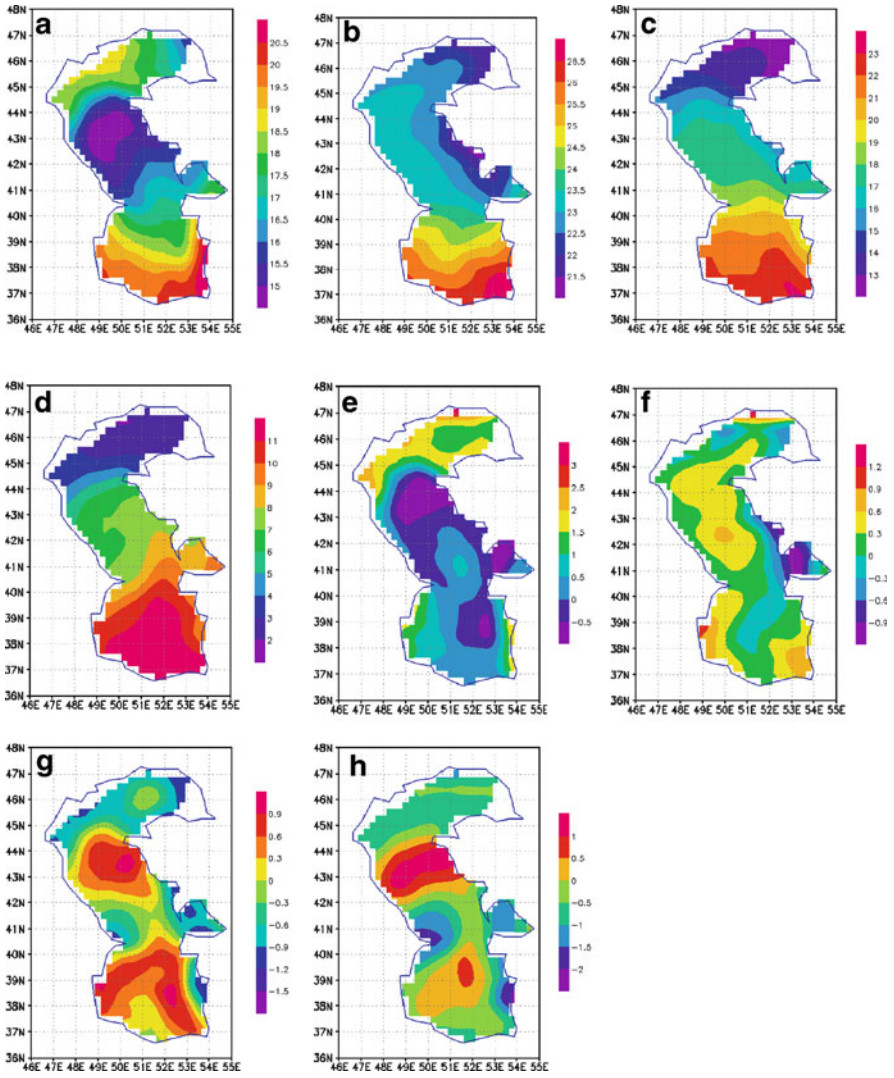

Fig. 1 Mean seasonally SST maps when super heavy precipitation events occur in (**a**) spring, (**b**) summer, (**c**) autumn, (**d**) winter and The SST seasonally anomaly maps when super heavy precipitation occur in (**e**) spring, (**f**) summer, (**g**) autumn, (**h**)winter

SST anomalies areas with appropriate locations above which the cold wind moves towards the north of Iran when super heavy precipitation events occur in coastal areas especially in autumn (Fig. 1e–h). Maximum, mean and coverage area of monthly precipitations have significant correlation coefficients with both the SST and DTST. The highest correlation coefficient is seen for the monthly precipitation mean and DTST average (61.3%). SST average over the sea and the monthly mean of coverage area precipitation (58.4%) and the maximum coverage area of monthly precipitations (52.9%) have the highest correlations. The results of the regression

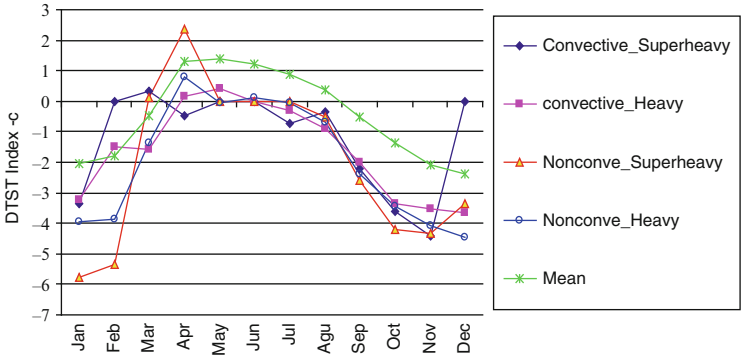

Fig. 2 The DTST index in different precipitation groups

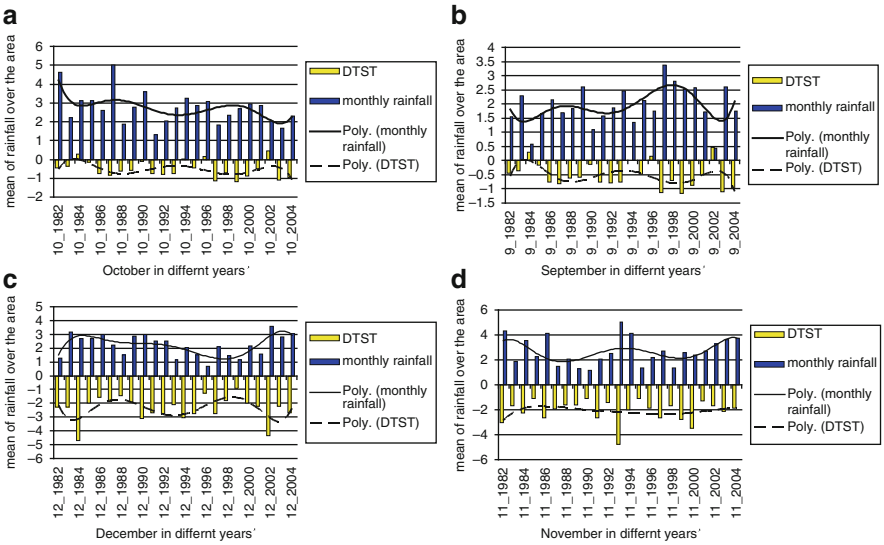

Fig. 3 The trend curves of the precipitation mean and the DTST index in (**a**) October, (**b**) September, (**c**) December and (**d**) November

analysis show that the highest R values are in September and October (66.5%). The DTST average is the only remaining variable in the regression equation; The SST variable was omitted from the equation. The negative values of DTST index are observed from September to March and positive values from April to August. The result show that 75%, 65%, 85% and 60% of convective super-heavy, convective-heavy, non-convective super-heavy, non-convective heavy precipitations respectively occur from September to December.

As can be seen from the Fig. 2a–d, the DTST average is less in super heavy and heavy precipitation than precipitation mean from May to November. According to Fig. 3a–d there are similar trends between monthly trend of precipitations and the

DTST index trend from September to February; the precipitation will increases or will decreases if the DTST index goes up or down while no similar trend reveals from March to August. DTST index is negative when super heavy and heavy precipitation occurs at the end of summer and during autumn in the southern coats of the Caspian Sea. In September when the DTST index is negative, the precipitation will increase. The monthly DTST index is usually greater than −1.2°C and the monthly SST ranges from 20.7°C to 24.2°C in September. During October, the DTST average is always negative and in its lowest value reaches to −2.4°C. The SST varies from 15.9°C to 20.8°C so it is warm adequately. DTST index is always negative in November and December and it reaches to −4.75°C. DTST index is positive during the other months so there is not a similarly trend between the DTST index and the precipitation. In general, in convective super-heavy precipitation, the DTST index is 0.4°C more than convective heavy precipitation. Similarly, The DSTS index is 0.7°C in non-convective super-heavy more than non-convective heavy precipitation. The DTST index reduces to −7°C in the super-heaviest precipitation.

4 Conclusions

In North of Iran, heavy and super-heavy precipitation events mostly occur from September to December. There are three important conditions which lead to formation clouds and precipitations especially convective and non-convective super heavy and heavy events in the southern coasts of Caspian Sea.

1. The SST average increase harmonically from the north to the south of the Caspian Sea; when cold air masses move above the Sea they absorb humidity adequately and ascend near the coasts.
2. The SST average from September to December is at least 6°C that is warm enough to produce heavy and super precipitation. After December, The SST reduces to 0°C and less in the northern half of the Sea.
3. The 2 m air temperature minus SST is the most important factor related to the precipitation in the area. Whenever the DTST average decreases, the precipitation increases and vice versa. The index is less in convective than non-convective events and in heavy precipitation than super heavy precipitation.

Acknowledgments The authors would like to thank the Institute of Meteorology, Free University, Berlin for their support in the frame of this work.

References

Biasutti M, Battisti D, Sarachik E (2004) Mechanisms controlling the annual cycle of precipitation in the tropical Atlantic sector in an atmospheric GCM. J Clim 17:4708–4723. doi:10.1175/JCLI-3235.1

Chan J, Zhou W (2005) PDO, ENSO and the early summer monsoon rainfall over South China. Geophys Res Let L08810. doi:10.1029/2004GL022015. 2005.10.5
Giannini A, Saravanan R, Chang P (2005) Dynamics of the boreal summer African monsoon in the NSIPP1 atmospheric model. Clim Dyn 25:517–535
Huang R, Zhou L, Chen W (2003) The progresses of recent studies on the variability of the East Asian monsoon and their causes. Adv Atmos Sci 20:55–69
Hunt B (2000) Natural climate variability and Sahel precipitation trends. Global Planet Chang 24:107–131
Kawai Y, Wada A (2007) Diurnal sea surface temperature, variation and its impact on the atmosphere and ocean. J Oceanogr 63:721–744
Khalili A (1973) Precipitation patterns of central Elburz. Theor Appl Climatol 21:215–232. doi:10.1007/BF02243729
Lin Z, Lu R (2009) The ENSO's effect on Eastern China precipitation in the following early summer. Adv Atmos Sci 26:333–342. doi:10.1007/s00376-009-0333-4
Masoodian A (2003) Climatic regions of Iran. J Geogr Dev 2:171–183
Moradi H (2004) The role of Caspian Sea in the southern coasts precipitation. Iran J Mar Technol Sci 2–3:77–88
Muraleedharan G, Rao A, Kurup P, Nair N, Unnikrishnan S (2007) Coastal engineering. Coast Eng 54(8):630–638. doi:10.1016/j.coastaleng DOI:dx.doi.org
Wu R, Hu Z, Kirtman B (2003) Evolution of ENSO-related precipitation anomalies in the East Asia and the processes. J Clim 16:3741–3757
Yang F, Lau K (2006) Trend and variability of China precipitation in spring and summer: linkage to sea surface temperatures. J Clim 19:4700–4718. doi:10.1002/joc.1094
Zhou L, Wu R (2010) Respective impacts of East Asian winter monsoon and ENSO on winter precipitation in China. J Geophys Res 115:D02107. doi:10.1029/2009JD012502
Zhou L, Chi-Yung T, Wen Z, Johnny C (2009) Influence of the SST and the ENSO on winter precipitation over South China. China J Nat Disasters 31:19–29

Evaluation of the Climate Change Impact on the Productivity of Portuguese Pine Ecosystems Using the Forest-BGC Model

L. Nunes, M.A. Rodrigues, and D. Lopes

Abstract The growth, survival and geographical distribution of plants are determined by climate, particularly temperature and precipitation. The actual tendency indicates a global climate change with direct negative impact on terrestrial ecosystems. Estimation of net primary production (NPP) allows a prediction of the impact of climate change on ecosystems. Studies on climate and dynamic modelling of stand development are being carried by the scientific community all over the world in order to assess the effects of global climate change. There is the question if that spatial scale of analysis is not overlooking local or regional information that can be important for smaller communities. The object of this study is to identify if the local scale is appropriate to analyse the impact of the climate change on the productivity of the local forest ecosystems. The Forest-BGC model was used to estimate the NPP in pine (*Pinus pinaster* Aiton) pure and mixed forest based on climate evolution scenarios derived from the analysis of past available climate series and its evolutionary trends for the Trás-os-Montes region, north of Portugal, which has three distinct climatic zones. We concluded that for the study areas temperature is the key variable influencing NPP under climate change scenarios.

L. Nunes (✉)
Agrarian School of Viseu (ESAV)/Polytechnic Institute of Viseu (ISPV), Estrada de Nelas, Quinta da Alagoa – Ranhados, Viseu 3550-606, Portugal

CITAB, University of Trás-os-Montes and Alto Douro (UTAD), Apartado 1013, Vila Real 5000-911, Portugal
e-mail: lnunes@esav.ipv.pt

M.A. Rodrigues
Physics Department, University of Aveiro, Campus Universitário de Santiago, Aveiro 3810-193, Portugal

D. Lopes
CITAB, University of Trás-os-Montes and Alto Douro (UTAD), Apartado 1013, Vila Real 5000-911, Portugal

C.G. Helmis and P.T. Nastos (eds.), *Advances in Meteorology, Climatology and Atmospheric Physics*, Springer Atmospheric Sciences,
DOI 10.1007/978-3-642-29172-2_93,

1 Introduction

Evidence of increased atmospheric CO_2 and mean annual temperature over the past century has prompted studies on their effect on the structure of the terrestrial ecosystems (Melillo et al. 1993; IPCC 2000; Su et al. 2007) to provide data for management support decisions. It is important to estimate production in Portuguese forests ecosystems to get information on carbon sequestration dynamics using net primary production (NPP), since it allows monitoring the impact of climate change on ecosystems at different ranges of spatial scales (local, regional and global). NPP is considered a complete and complex variable and reflects the growth of the whole ecosystem (Melillo et al. 1993).

Simulation models are essential tools to evaluate ecosystem productivity and to predict the effects of climate change (Ryan et al. 1996; Landsberg and Gower 1997). Forest-BGC is an ecosystem model which calculates the main NPP processes in forests ecosystems (Running and Coughlan 1988). The model was designed to be particularly sensitive to leaf area index (LAI), that is an important variable for calculating major physiological processes and measuring vegetation structure (Running and Coughlan 1988), carbon dynamics and climate change studies (Nemani and Running 1989; Gower et al. 1999).

This study was carried out in the Trás-os-Montes region, with three distinct climatic areas. The parameters of the Forest-BGC model are examined and used to simulate the NPP of pure and mixed pines forest in the north of Portugal and predict forest productivity under future scenarios of climate change.

2 Material and Methods

2.1 Study Area and Site Characteristics

Twenty-three study sampling plots of pine were selected in the Vila Real district, where 15 sampling plots are pure pines and eight mixed sampling plots are pine-oak (*Quercus pyrenaica* Willd.) with 500 m^2. Sampling sites were selected from natural forests in order to represent the entire distribution of the pines and oaks among the district and are identified in the National Forest Inventory (Fig. 1). All the sampling plots are private land and the soil is characterized as cambisols humic from schist (www.apambiente.pt).

The study area covers three climatic zones, however the sampling plots were located in Terra Fria (Bragança) and Terra Transição (Vila Real) only. Terra Fria is characterised by long and cold winters, with regular frost and snow and hot and short summers. Terra Transição is transitional between Terra Fria and Terra Quente. The altitude limits of these regions are located between the 400–700 m. The frost period extends from late October to mid April. Monthly climate information for both climate zones in the study area is given in Table 1.

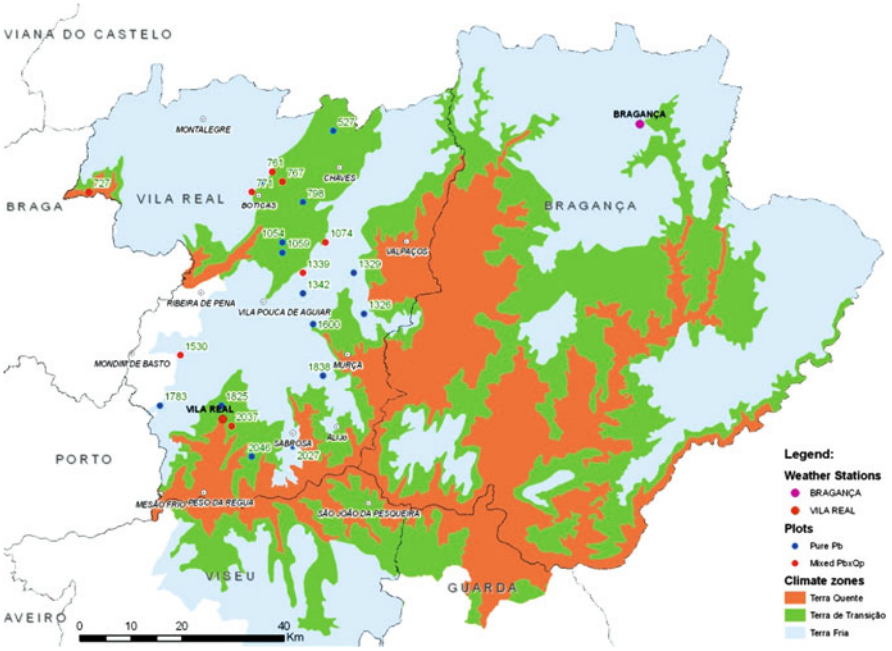

Fig. 1 Localization of the study area, meteorological stations in the Vila Real (TF) and Bragança (TT) districts and distribution of the different climatic zones

Table 1 Climate data for the Terra Fria (TF) and Terra Transição (TT); temperature in °C, precipitation in mm

Climate data	Climatic region	Jan	Feb	Mar	Apr	May	Jun	Jul
Average temperature	TT	4.6	5.3	10.2	12.2	15.7	21.8	21.9
	TF	2.9	3.8	8.8	11.1	14.6	21.4	22.5
Precipitation	TT	6.5	37.4	55.6	50.5	42.7	14.8	8.9
	TF	11.0	13.0	48.0	171.6	124.0	6.0	6.0

Climate data	Climatic region	Aug	Sep	Oct	Nov	Dec	Annual
Average temperature	TT	23.9	19.3	15.6	8.8	6.6	13.8
	TF	23.3	18.5	13.5	7.8	5.4	12.8
Precipitation	TT	2.4	24.5	143.2	66.3	117.1	569.9
	TF	6.0	3.0	161.0	27.0	57.0	633.6

Fieldwork measurements were taken in 2006, 2008 and 2009 in order to estimate the NPP and characterize stand density and individual parameters (Table 2).

2.2 Simulations of NPP Using Forest-BGC Model

The model Forest-BGC was parameterized taking in account daily climatic series for the meteorological stations of Vila Real (41°42′N, 7°42′W) and Bragança

Table 2 Mean values of pine pure and mixed sampling plots

Stand	N. plots	DBH (cm)	Density (tree ha^{-1})	LAI (m^2. m^{-2})	NPP (ton ha^{-1} $year^{-1}$)
Pure stand	15	22.6	511	3.7	11.7
Mixed stand	8	25.5	480	5.8	14.1

(42°21′N, 7°28′W) for the period 1941–2009, and the scenarios of climate change were based on the trend line parameters determined using the least squares method. The FOREST-BGC was run using the average figures for all the input parameters for each study area with only leaf carbon content changing.

3 Trends in Temperature and Precipitation Patterns

The trend line for the extreme values of temperature in the TF climatic zone shows an increase in maximum temperature of 0.26°C against 0.09°C in minimum temperature over a 10 year period. Analysis of average values shows a growing trend of 0.16°C in the annual mean temperature (Fig. 2a). The data for the TT climatic zone indicates a decrease of −0.02°C in the maximum temperature over a 10 year period. Analysis of average values shows a decreasing of around −0.044 C in the annual mean temperature over 10 years, which is almost insignificant (Fig. 2b). The TF data shows a growing trend of 4.49 mm/year (Fig. 2c) in accumulated annual precipitation probably caused by the amplitude of the oscillations. In TT there was a decreasing trend in precipitation of –2.46 mm/year (Fig. 2d). The annual amplitude of precipitation was higher in TT. Annual accumulated rainfall was over 1025.5 mm in TT and 667.8 mm in TF where 49.3% occurred in the months of winter.

4 Model NPP Simulations

Model NPP simulations were made for the year 2005, the latest for which climatic daily data was available. Changes were made first in temperature, then in precipitation and finally in both climatic parameters. Table 3 scenarios based on the trend series for TF climates showed that for pure and mixed stands the key variable affecting the NPP was temperature. Temperature increase resulted in decreased productivity in both pure and mixed stands, although the effect was more significant in the mixed stands. The scenario of increased precipitation did not seem to affect the productivity of both pure and mixed stands. When temperature and precipitation were simultaneously changed, the temperature effect prevailed resulting in e decrease of NPP. Our results agreed with findings published for productivity of *Picea glauca* populations in Québec (Andalo et al. 2005). The analysis of the TT shows that temperature was also the key variable affecting the NPP for both pure and mixed stands, nevertheless the decreasing trend of annual mean temperature was insignificant. When temperature decreased, the productivity tended to increase

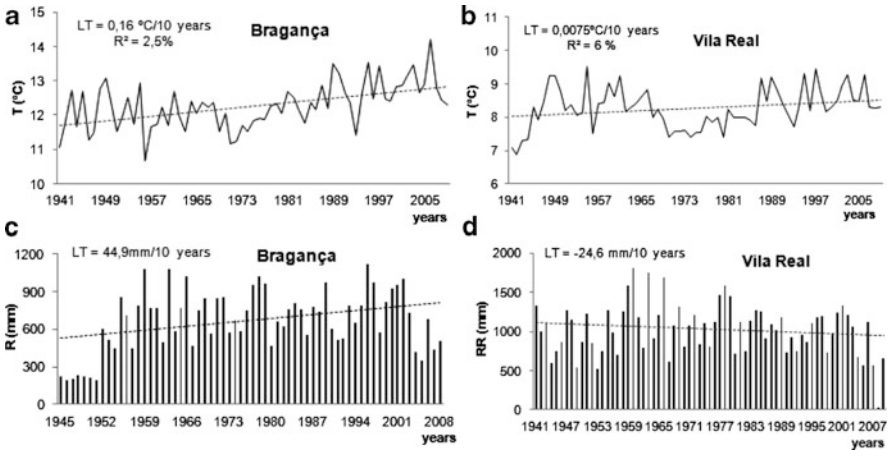

Fig. 2 Mean annual temperature series (**a**, **b**) and annual precipitation (**c**, **d**) for Bragança (TF) and Vila Real (TT) meteorological stations

Table 3 Results of NPP (ton ha^{-1} $year^{-1}$) obtained from the tested climate for TF and TT

		Pure pine		Pine oak mixed	
Terra fria	Temperature	No change	↑ 0.16°C in 10 years	No change	↑ 0.16°C in 10 years
Precipitation	No change	12.023	12.019 (↓ 0.033%)	9.610	9.599 (↓ 0.114%)
	↑ 44.9 mm in 10 years	12.023 (=)	12,019 (↓ 0.033%)	9.610 (=)	9.599 (↓ 0.114%)
Terra transição	Temperature	No change	↓ 0.044°C in 10 years	No change	↓ 0.044°C in 10 years
Precipitation	No change	11.138	11.140 (↑ 0.018%)	18.252	18.255 (↑ 0.016%)
	↓ 24.6 mm in 10 years	11.137 (↓ 0.009%)	11.139 (↑ 0.009%)	18.249 (↓ 0.016%)	18.253 (↑ 0.005%)

in both pure and mixed stands. However this tendency was more significant in pure stands. Decreases in precipitation resulted in decreased productivity in both pure and mixed stands. When both temperature and precipitation decreased, the effect of temperature prevailed, increasing NPP in both pure and mixed stands.

Analysis of the climate diagram for 2005 shows this to be an atypical year with higher precipitation values, especially for TF (3759 mm/year, against 570 mm/year in TT), with more frequent precipitation during the summer. In both meteorological stations, the highest levels of precipitation occurred in October and December and annual mean temperature was 11.73°C for TF and 13.87°C for TT. Cross referencing the climate diagram data and the results from the Forest-BGC simulations showed why temperature was more important for NPP estimations, in a year (2005) where precipitation was much higher than expected. The model was

able to adapt to these specific conditions and express results accordingly. This approach method can detect different climate scenarios and their impact on NPP. With changes in both temperature and precipitation, NPP increased approximately 18.6% although the main factor that contributed to increase NPP was an increase in precipitation.

5 Conclusions

In 2005 the temperature was the key variable driving NPP in the Trás-os-Montes region. Because 2005 was a year with higher precipitation, the use of this methodology should be repeated in order to clarify the importance of both climatic variables. However this methodology looks suitable for predicting NPP under climate change scenarios. Subsequent studies should be carried out over a longer period of time. One limitation for this kind of studies in Portugal is the difficulty in acquiring daily climatic data, which is essential for Forest-BGC based studies. The scale of analysis for this type of studies is another important factor. Climate change is a global phenomenon, but most analyses are carried out at different scales. This particular study shows that high variations in climate patterns, even in a small region, can exert different impacts on forest ecosystems. Stand complexity also plays an important role. Mixed stands are unquestionably more interesting in terms of ecology and biodiversity, and should be studied in greater depth in order to understand how differences in species composition and density are impacted by climate change.

Acknowledgments This study was funded by FCT research in projects PTDC/AGR-CF/68186/2006, PTDC/AGR-CF/69733/2006 and FCT Program SFRH/PROTEC/50127/2009.

References

Andalo C, Beaulieu J, Bousquet J (2005) The impact of climate change on growth of local white spruce populations in Québec, Canada. For Ecol Manag 205:169–182

Gower ST, Kucharik CJ, Norman JM (1999) Direct and indirect estimation of leaf area index, fAPAR, and net primary production of terrestrial ecosystems. Remote Sens Enviro 70:29–51

IPCC (2000) Land use, land-use change, and forestry. Intergovernmental panel on climate change. Cambridge University Press, Cambridge

Landsberg JJ, Gower ST (1997) Applications of Physiological Ecology to Forest Management. Physiological Ecology Series, Academic Press, San Diego, CA, pp 354

Melillo JM, Mcguire AD, Kicklighter DW, Moore IIIB, Vorosmarty CJ, Schloss AL (1993) Global climate change and terrestrial net primary production. Nature 363:234–240

Nemani RR, Running SW (1989) Testing a theoretical climate-soil-leaf area hydrologic equilibrium of forests using satellite data and ecosystem simulation. Agric For Meteorol 44:245–260

Running SW, Coughlan JA (1988) A general model of forest ecosystem processes for regional applications – I. Hydrologic balance, canopy gas exchange and primary production processes. Ecol Model 42:125–154

Ryan MG, Hunt ER Jr, Mcmurtrie RE, Ågren GI, Aber JD, Friend AD, Rastetter EB, Pulliam WM, Raison RJ, Linder S (1996) Comparing models of ecosystem function for temperate conifer forest. I. Model description and validation. In: Breymeyer A, Hall DO, Melillo JM, Ågren GI (eds) Global change: effects on forests and grasslands. Wiley, Chichester

Su H, Sang W, Wang Y, Ma K (2007) Simulating Picea schrenkiana forest productivity under climatic changes and atmospheric CO2 increase in Tianshan Mountains, Xinjiang Autonomous Region, China. For Ecol Manag 246:273–284

Decadal Analysis of Heat-Wave Events in Thessaloniki and Investigation of Impacts on PM10

N. Pakalidou, E. Katragkou, A. Poupkou, P. Zanis, A. Bloutsos, and T. Karacostas

Abstract The aim of this paper is to analyze the heat wave events during the decade 2001–2010 over Thessaloniki and the determination of their basic characteristics. Since extreme weather events are accompanied by serious pollution episodes, the potential linkages of heat wave events with high particulate matter (PM10) concentrations are investigated. In order to describe the heat wave events we use the Temperature Humidity Index (THI) and we classify accordingly the days fulfilling the heatwave criteria. PM10 measurements at two monitoring stations in Thessaloniki are used in order to investigate their potential linkage to the extreme meteorological events. In the urban background station of Panorama the distribution of PM10 is shifted to higher size bins and the mean of the distribution increases by 6 $\mu g/m^3$ during the heatwave days. At the urban station of Agia Sofia, the impact of heatwave on PM10 pollution on the PM10 distribution is weaker, due to masking effects of the local (traffic) emission sources.

1 Introduction

Heat wave is an extreme meteorological phenomenon which has been found to contribute to dangerously high levels of air pollution, especially at the large urban agglomerations. An analysis of air quality simulations for the 2003 summer heatwave (Vautard et al. 2005) suggested that the associated anticyclonic wind re-circulated the warm air throughout Europe and over the Mediterranean region,

N. Pakalidou (✉) • E. Katragkou • P. Zanis • A. Bloutsos • T. Karacostas
Department of Meteorology and Climatology, School of Geology, Aristotle University of Thessaloniki, Thessaloniki, Greece
e-mail: nikolettapakalidou@hotmail.com

A. Poupkou
Laboratory of Atmospheric Physics, School of Physics, Aristotle University of Thessaloniki, Thessaloniki, Greece

C.G. Helmis and P.T. Nastos (eds.), *Advances in Meteorology, Climatology and Atmospheric Physics*, Springer Atmospheric Sciences,
DOI 10.1007/978-3-642-29172-2_94,

leading to a build-up of pollutants together with a rise in temperature. A number of factors contributing to prolonged heatwaves in Europe and associated degradation of air quality have been discussed in the literature (Solberg et al. 2008). In the current work we aim at analyzing heatwave episodes over the greater Thessaloniki area along with the PM10 levels at two monitoring stations and try to identify potential linkages between the heatwave events and changes in distributions of PM10.

2 Data and Methodology

The meteorological data used in this study are from the Meteorological Station of Meteorology and Climatology, Aristotle University of Thessaloniki and refer to hourly temperature and relative humidity of the study area for the time period 2001–2010. In the greater Thessaloniki area, an official air pollution monitoring network is being operating by the Region of Central Macedonia (RCM). For the needs of the present study, hourly PM10 observational data for the years 2001–2010 from two air pollution stations of the RCM network were used. Agia Sofia station is located in the city center and represents urban traffic conditions while Panorama is a suburban background station.

A good effort to locate and study heatwave episodes is through the use of biometeorology Temperature-Humidity Index (THI-Temperature-Humidity Index). The index THI derives from the observed outdoor temperature and humidity and is defined as a measurement of apparent temperature, in particular how the man feels the temperature depending on the amount of water that evaporates into the air (Steadman 1979a, b). The calculation of THI is based on the relationship originally given by Thom (1959):

$$\mathrm{THI}\ (\mathrm{F}) = \mathrm{T}\ - (0.55 - 0.55^{*}\ \mathrm{RH})(\mathrm{T}\ - 58) \tag{1}$$

T is the temperature of dry bulb in °F and RH is the relative humidity in decimal.

Barrow and Karacostas (1996) suggested the THI steps showed in Table 1, referring to a person with normal clothing worker in an enclosed area.

Table 1 Levels of the Temperature – Humidity Index (THI) (From Barrow and Karacostas 1996)

THI (°F)	Characterization	Description
$69 \leq \mathrm{THI} < 75$	Mild	Few people feel discomfort
$75 \leq \mathrm{THI} < 80$	Moderate	Nearly 50% of people feel discomfort
$80 \leq \mathrm{THI} < 84$	Severe	Almost everybody feels discomfort
$84 \leq \mathrm{THI} < 92$	Intense	Rapid decrease in job performance
$92 \leq \mathrm{THI}$	Excellent	Extremely dangerous situation

3 Results

3.1 Heat Waves in Thessaloniki

The study of heat wave events is recorded per month (Fig. 1). The results reveal that June is characterized by a number of cases of mild discomfort throughout all the day, and from sunrise until 3–4 h after sunset, the discomfort becomes more intense, indicating its peak at noon (1400). In July, the state is resumed just like June, but with more pronounced features. In particular, severe discomfort is noted from early in the morning till sunrise (0800) and lasts until the change of day, whereas the intense discomfort in which there is serious dysfunction of individuals is identified early in the afternoon (1600–1900). In August it appears largely the second class throughout the 24 h of the day. Severe discomfort is emerging simultaneously with solar radiation and the intense discomfort is noted both in the morning (0700–0800) the midday (1200) and in the afternoon (1700). The image of September is quite different from the previous 3 months. It is observed mainly the first class THI, with minor occurrences of the second category, mainly in the summer hours, but without specific references.

The hourly occurrence of THI categories for each year of the study period shows that 2002 is considered the year with lower incidence rates of heatwave events, with small percentages of the first class rate and almost total absence of the other categories (results not shown). As similar is characterized the year 2008. Instead, 2003 is proved as one of the most intense heat wave incident years and therefore intense regarding the discomfort in Thessaloniki, especially during midday hours. Besides, that year are noted multiple episodes of heatwave events across Europe, resulting in multiple

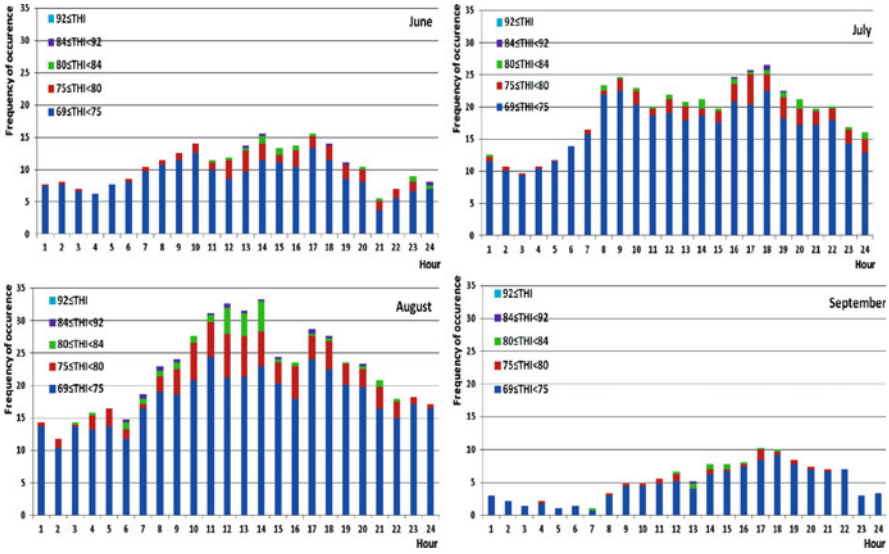

Fig. 1 Hourly occurrence of THI categories from June to September over the period 2001–2010

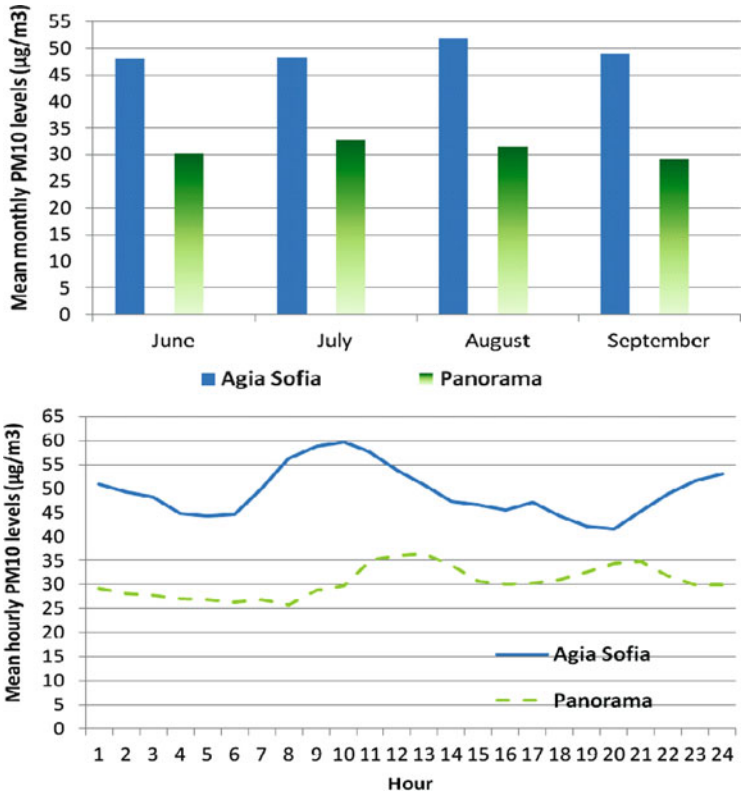

Fig. 2 Monthly PM10 concentrations (*upper*) and mean diurnal variation of PM10 levels (*lower*) for two monitoring stations in the greater Thessaloniki area for the months June to September of the years 2001–2010

deaths, particularly those who belong to the so-called vulnerable group. Finally, significant levels of distress are noted throughout 2010, during any time of the day.

3.2 PM10 in Thessaloniki

Figure 2 (upper) shows the monthly PM10 concentration values for the warm period of the year when heat-wave events can take place (months from June to September). In Agia Sofia and Panorama stations, monthly PM10 levels are in the order of 50 μg/m^3 and 30 μg/m^3 respectively and present a short range (48–52 μg/m^3 in Agia Sofia and 29–33 μg/m^3 in Panorama). In Agia Sofia station, monthly PM10 levels approximate the 24 h European Union limit value for PM10, which is equal to 50 μg/m^3, suggesting that particulate pollution can be an air quality issue in the city center in summer days.

Figure 2 (lower) depicts the mean diurnal variations of the PM10 observed values in Agia Sofia and Panorama stations, as they have been estimated for the

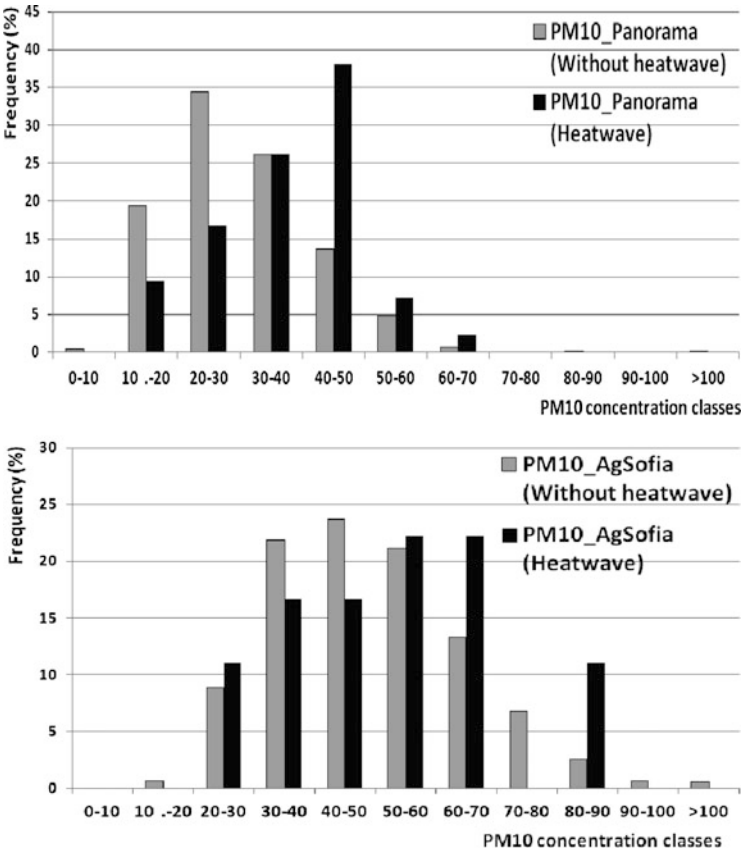

Fig. 3 Histogram with PM10 (μg/m^3) for days with and without heatwave at the Panorama (*upper*) and Ag.Sofia (*lower*) monitoring station

months June to September. In Agia Sofia station, the mean hourly PM10 concentrations range between 42 and 60 μg/m^3 and are maximum in the morning hours. In Panorama station, the mean hourly PM10 levels vary from 26 to 36 μg/m^3 and take higher values in the afternoon and late-evening/early-night hours.

3.3 PM10 in Thessaloniki Under Heatwave Conditions

Figure 3 shows the histograms of PM10 for Panorama and Agia Sofia monitoring station under heatwave and without heatwave days appearing in the time period 2001–2010. Table 2 summarizes the statistics of the distribution for each case for both stations. The mean (median) of the distribution at the background station of Panorama for non-heatwave days is 30 (29) μg/m^3 and increases by 7 (9) μg/m^3 during the heatwave days. The signature of the heatwave on the PM10 distribution

Table 2 Statistics of PM10 for the days with and without heatwave at the two stations

PM10 (μg/m3)	Heatwave		No heatwave	
	Mean	Median	Mean	Median
Ag Sofia	53	51	49	48
Panorama	37	38	30	29

is clear, since the frequency of the higher concentration classes (>40 μg/m^3) is higher during the heatwave days (8% vs. 20% during the non heatwave days). On the contrary, concentrations below 30 μg/m^3, which are quite typical in the non-heatwave days (frequency of appearance ~55%) are less often during the heatwaves.

At the Agia Sofia station the mean PM10 is considerably higher in comparison to the Panorama station since the station is affected mostly by the local (traffic) sources. The impact of the heatwave on the PM10 distribution is clear, but weaker in comparison to the Panorama station. During the heatwave days the mostly observed concentrations lie in the range of 50–70 μg/m^3 (total frequency 45%), while the mean of the distribution is shifted to 53 μg/m^3. During the no-heatwave days almost the 80% of the observed PM10 is below 60 μg/m^3.

4 Conclusions

In this work we analyze the heat wave events during the decade 2001–2010 over Thessaloniki and determine their basic characteristics. Since extreme weather events are accompanied by serious pollution episodes, the potential linkages of heat wave events with high particulate matter (PM10) concentrations are investigated. In order to describe the heat wave events the Temperature Humidity Index (THI) was used. According to this index the summer days (JJAS) of the time period 2001–2010 were classified to heatwave and no-heatwave days. Our analysis shows that in the urban background station of Panorama the distribution of PM10 is shifted to higher concentration bins and the mean of the distribution increases by 7 μg/m^3 during the heatwave days. The urban station of Agia Sofia, is mostly affected by the local (traffic) emission sources, still the impact of heat-wave could be seen on the PM10 distribution with an increase on the mean PM10 during the heatwave days by 4 μg/m^3 and a more often occurrence of high pollution episodes with daily PM10 values higher than 60 μg/m^3.

The higher PM10 levels during heatwaves might be related to photochemical produced secondary particles but very likely can be also related to lower dilution under the more stagnant conditions often associated with heatwave events. Also the differences between Agia Sofia and Panorama concerning the impact of heat waves on PM10 levels might be related to (a) less efficient dilution at Agia Sofia which is directly situated at the primary sources of aerosols (b) more secondary (photochemically produced) particles at Panorama whereas at Agia Sofia are emitted mainly primary particles.

References

Barrow EM, Karacostas TS (1996) The impact of greenhouse gas – induced climate change on the frequency and intensity of heat waves in Greece. University of East Anglia, Norwich

Solberg S, Hov O, Sovde A, Isaksen ISA, Coddeville P, De Backer H, Forster C, Orsolini Y, Uhse K (2008) European surface ozone in the extreme summer 2003. J Geophys Res 113:D07307. doi:10.1029/2007JD009098

Steadman RG (1979a) The assessment of sultriness. Part I: a Temperature – Humidity Index based on human physiology and clothing science. J Appl Meteor 18:861–873

Steadman RG (1979b) The assessment of sultriness. Part II: effects of wind, extra radiation and barometric pressure on apparent temperature. J Appl Meteor 18:874–885

Thom EC (1959) The discomfort index. Weatherwise 12:57–60. doi:10.1080/00431672.1959.9926960

Vautard R, Honore C, Beekmann M, Rouil L (2005) Simulation of ozone during the August 2003 heat wave and emission control scenarios. Atmos Environ 39:2957–2967. doi:10.1016/j.atmosenv.2005.01.039

A Study of Divergence and Convergence of the Wind Field over Europe and the Mediterranean

O. Pezoula and A. Bartzokas

Abstract In this work, the divergence and convergence of the wind field over Europe, the Mediterranean and North Africa is studied for the 60-year period 1950–2009. Mean monthly values (s^{-1}) are utilized at 273 grid points, spaced by 2.5° × 2.5°, at 10 atmospheric pressure levels from 1,000 hPa up to 100 hPa. It is found that on a seasonal basis considerable differences appear among the various European regions both near the surface of the Earth and in the upper atmosphere. During winter, near the surface, high values of convergence appear in the cyclogenesis areas and along the tracks of depressions. Specifically: in the Mediterranean, with maximum values in the Gulf of Genoa, the Black Sea and from the North Sea up to the Baltic Sea. On the contrary, over the rest of the areas divergence prevails. This situation is reversed above approximately 600 hPa with positive values (divergence) over the Mediterranean and the Seas of northern Europe and negative (convergence) over central Europe. During summer, over the seas, where air is cooler than over land, positive values are observed (divergence). This difference is more intense over lower latitudes. Similarly to winter, in the upper atmosphere, the convergence-divergence field becomes smoother changing signs at about 600 hPa.

1 Introduction

The divergence of the flux of a quantity expresses the time rate of depletion of the quantity per unit volume. Negative divergence is termed "convergence" and relates to the rate of accumulation. In meteorology, divergence/convergence is mostly used in relation to the velocity vector and so refers to the flux of air

O. Pezoula (✉) • A. Bartzokas
Laboratory of Meteorology, Department of Physics, University of Ioannina, Ioannina 45110, Greece
e-mail: opezoula@cc.uoi.gr

C.G. Helmis and P.T. Nastos (eds.), *Advances in Meteorology, Climatology and Atmospheric Physics*, Springer Atmospheric Sciences,
DOI 10.1007/978-3-642-29172-2_95,

particles themselves. The "divergence/convergence of velocity" is a three-dimensional property which expresses the time rate of expansion/contraction of the air per unit volume. In the atmosphere, divergence/convergence is small and is of little direct interest. The main concern is with the "horizontal divergence/convergence of velocity" (often simply referred to as the "divergence/convergence") and expresses the time rate of horizontal expansion/contraction of air per unit area (Meteorological Office 1972). Since the value of the three-dimensional property equals almost zero (1), horizontal divergence/convergence of air is closely associated with vertical velocities and contraction/expansion of an air column centred at the level concerned.

$$\nabla \cdot \vec{V} = 0 = \frac{\partial u}{\partial x} + \frac{\partial v}{\partial y} + \frac{\partial w}{\partial z} \Rightarrow \nabla_2 \cdot \vec{V} = \frac{\partial u}{\partial x} + \frac{\partial v}{\partial y} = -\frac{\partial w}{\partial z} \tag{1}$$

Thus, the combined effect of wind direction and speed is what produces divergent/convergent air flow. Divergence/Convergence is directly related to pressure changes at the surface and height changes of the constant-pressure level.

As the air accumulates in an upper atmosphere stratum over a region, greater pressure is exerted throughout the atmosphere. As the air flows into the stratum, the pressure increases. Barometric pressure at the surface rises, as do the heights of the constant-pressure levels. In other words, upper-level convergence causes pressure and height rises. The exact opposite effect takes place when air is depleted from an upper atmosphere stratum. As the air flows out of this stratum, pressure decreases. Barometric pressure at the surface falls, as do the heights of the constant-pressure levels. In other words, upper-level divergence causes pressure and height falls. Usually, in a column of air the sign of divergence/convergence changes more than once with height but, in general, its values are minimum at the level of 500–600 hPa, the so-called "level of non-divergence/convergence". Divergence and convergence are primarily used by forecasters to explain why systems are expected to fill or deepen during the forecast period.

The aim of the present work is a climatic study of the spatial distribution of divergence and convergence over Europe and the Mediterranean from the surface up to the upper atmosphere. The study is carried out on a seasonal basis, for winter and summer.

2 Data

The study is based upon mean monthly values of divergence/convergence (s^{-1}), at 273 grid points spaced by 2.5° in latitude and 2.5° in longitude covering Europe, the Mediterranean and North Africa from 10W to 40E and from 30N to 60N (Fig. 1). The study is carried out for 10 atmospheric pressure levels from 1000 hPa up to 100 hPa, for the 60-year period 1950–2009. The data basis has been obtained from the NCEP/NCAR Reanalysis project. From the monthly values (multiplied by 10^6), the mean winter (DJF) and summer (JJA) grid point seasonal values are calculated for the 60-year period.

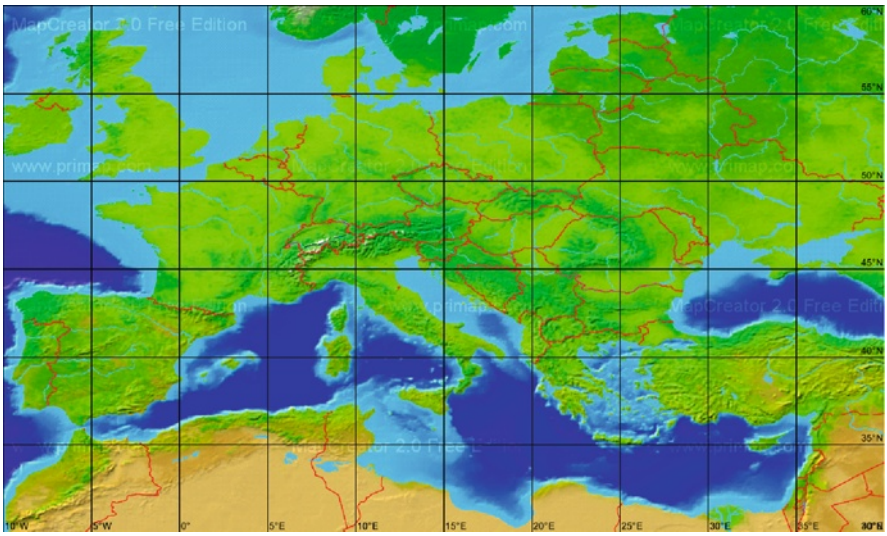

Fig. 1 The study area

3 Results

The results show that the climatic characteristics of divergence/convergence over Europe and the Mediterranean present considerable differences among the various regions of the study area. This is evident in all the atmospheric levels from the surface of the earth up to the upper atmosphere, both, in winter (Fig. 2) and in summer (Fig. 3). In the following paragraphs, six out of the ten levels studied will be presented (1,000, 925, 850, 700, 500 and 400 hPa).

3.1 Winter

For winter, near the surface (Fig. 2a), in general, a large spatial variability is observed. High convergence (negative values) appears in the cyclogenesis areas and along the tracks of depressions (Alpert et al. 1990). Specifically, maximum (absolutely) values of convergence appear in the Gulf of Genoa (up to -4.7×10^{-6} s^{-1}), the Black Sea (-3.8×10^{-6} s^{-1}) and from the North Sea to the Baltic Sea (-5.5×10^{-6} s^{-1}). On the contrary, high divergence appears over a belt crossing Europe from southwest to northeast, an area which is frequently affected by the extensions of either the subtropical anticyclone of the Atlantic (Azores High) or the Siberian anticyclone. The high values over northern Balkans must be attributed to the tracks of the travelling anticyclones over the area (Makroyannis 1976). Ascending at higher pressure levels, the values of divergence/convergence weaken gradually and thus the spatial differences are also reduced. For example, the maximum divergence values of central Europe (47.5N, 10E) are reduced from

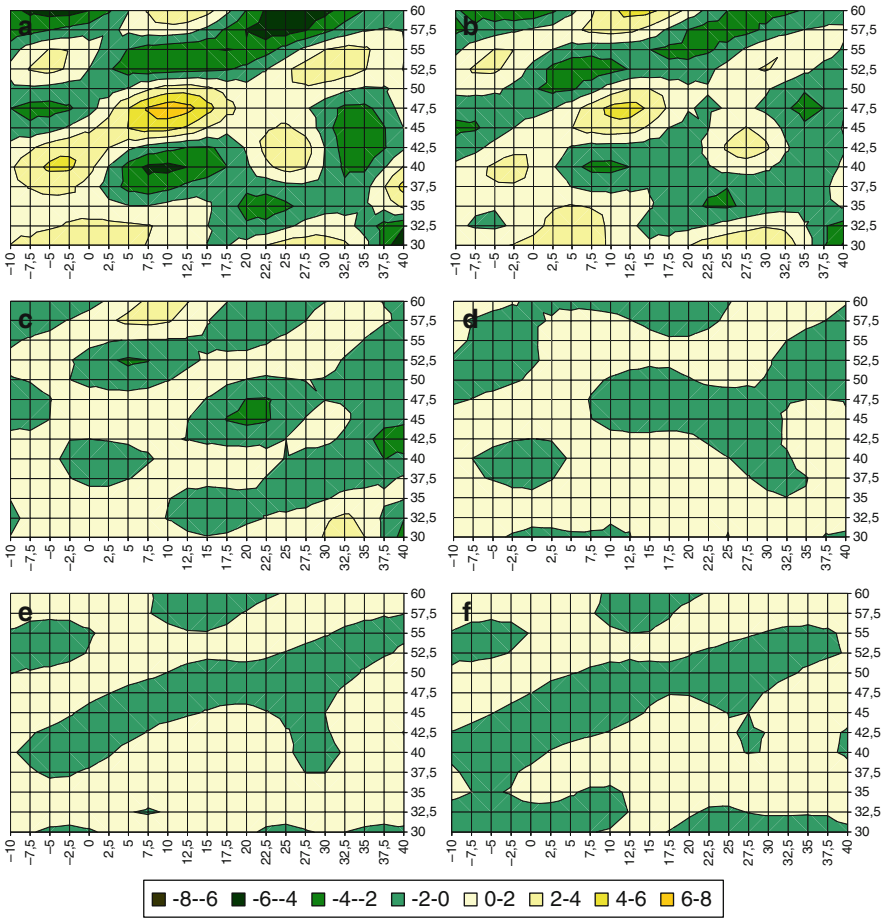

Fig. 2 Mean winter divergence/convergence ($\times 10^{-6}$ s^{-1}) over Europe and the Mediterranean at: (**a**) 1,000 hPa, (**b**) 925 hPa, (**c**) 850 hPa, (**d**) 700 hPa, (**e**) 500 hPa and (**f**) 400 hPa

7.3 at 1,000 hPa (Fig. 2a) to 4.6 at 925 hPa (Fig. 2b) and to 1.2 at 850 hPa (Fig.2c). Similarly, the maximum convergence values over the Baltic countries (57.5N, 25E) are reduced (absolutely) from −5.2 to −3.3 and to −1.0. Thus, the spatial divergence/convergence range is reduced from approximately 13 at 1,000 hPa to 5 at 850 hPa. At 600 hPa (not shown) these differences are minimized and gradually the sign of divergence/convergence starts reversing. This finding is in agreement with the ones of Varfi (2009) for cases of warm and cold invasion over the broader area of Greece. At 500 and 400 hPa (Fig. 2e, f) the pattern is completely opposite than on the surface with a convergence zone over Europe and divergence over the northern latitudes and the Mediterranean.

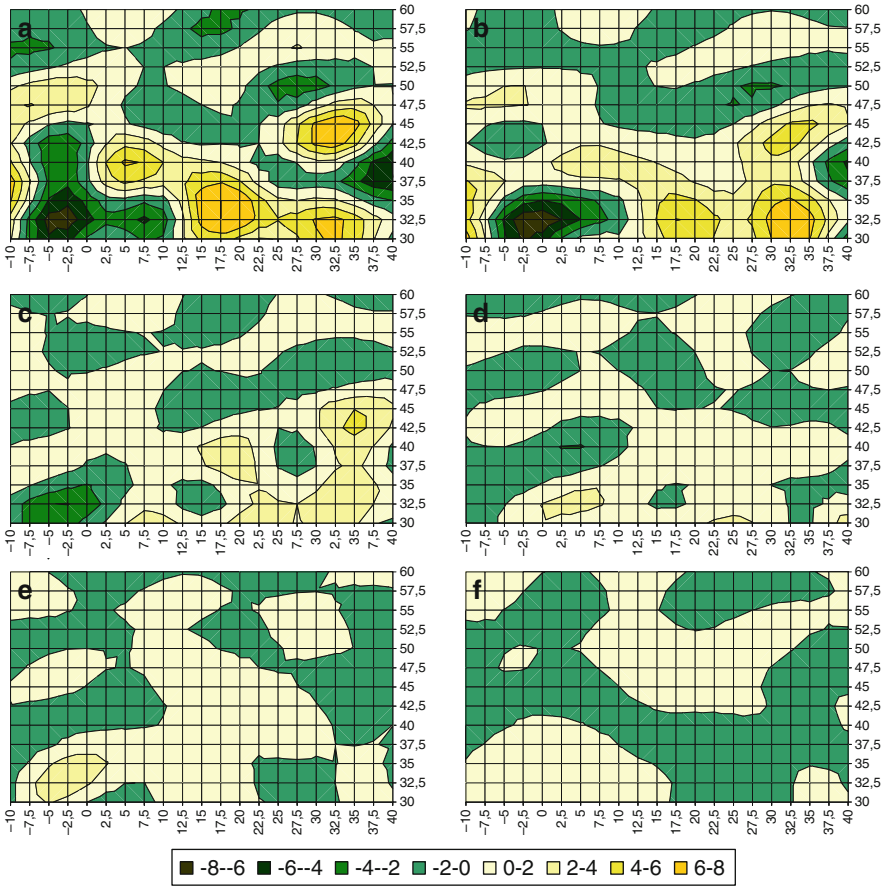

Fig. 3 As in Fig. 2 but for summer

3.2 Summer

During summer, the tracks of the depressions, travelling from west to east, are displaced northwards and the Mediterranean is very frequently under the influence of the enhanced and extended subtropical anticyclone of the Atlantic (Flocas et al. 2010). Because of the long duration of sunshine and the heat capacity difference between sea and land, the air over the sea is cooler than over the land. Thus, subsidence and stability is observed over the sea in contrast to the land where frequently instability prevails.

These conditions are portrayed in Fig. 3a, where, near the surface, high divergence values (up to 8×10^{-6} s^{-1}) are seen over the three Mediterranean basins (western, central and eastern), the Black Sea and the east Atlantic Ocean. On the contrary, central Europe is dominated by negative values (convergence) as it was expected. Strong convergence is also found in two other low latitude regions, in

NW Africa, southwest of the Atlas Mountains (minimum value −7.3) and over the Middle East. In the first region, the well known Saharan depressions are formed mainly during late spring and early autumn but also during summer, travelling eastwards along the North African Mediterranean coasts (Karoulias 1973; Schepanski and Knippertz 2011). In the latter, the low pressure system of SW Asia is built every summer over the warm land masses. Similarly to winter, the strong spatial differences (above 15) are reduced with height. This reduction is faster in summer as most of the prevailing atmospheric pressure systems, being of thermal origin, are "shallow", i.e. they present a relatively small vertical extend. At approximately 700 hPa (Fig. 3d) the sign starts reversing and at the higher pressure levels the pattern is completely opposite than on the surface (Fig. 3f).

4 Conclusions

In this work, the mean spatial distribution of divergence/convergence over Europe and the Mediterranean for 10 atmospheric levels, for winter and summer has been investigated. It has been shown that, near the surface of the Earth, positive/negative values (divergence/convergence) dominate in areas where mostly anticyclonic/cyclonic circulation prevails. As the height increases, the spatial differences are reduced and at approximately 600 hPa level divergence/convergence receives its lowest (absolutely) values. Above this level, the signs are reversed and at the upper atmosphere, the pattern presents completely opposite characteristics from the one near the surface of the Earth.

References

Alpert P, Neeman BU, Shay-El Y (1990) Inter-monthly variability of cyclone tracks in the Mediterranean. J Clim 3:1474–1478. doi:10.1175/1520-0442(1990) 003<1474:IVOCTI>2.0.CO;2

Flocas HA, Simmonds I, Kouroutzoglou J, Keay K, Hatzaki M, Bricolas V, Asimakopoulos D (2010) On cyclonic tracks over the eastern Mediterranean. J Climate 23:5243–5257. doi:http://dx.doi.org/10.1175/2010JCLI3426.1

Karoulias AS (1973) Saharan depressions. Dissertation, University of Thessaloniki (in Greek)

Makroyannis TJ (1976) Tracks of anticyclonic systems in the Greek area. Dissertation, University of Thessaloniki (in Greek)

Meteorological Office (1972) Meteorological glossary. Compiled by McIntosh DH, Her Majesty's Stationary Office, London

Schepanski K, Knippertz P (2011) Soudano-Saharan depressions and their importance for precipitation and dust: a new perspective on a classical synoptic concept. Q J R Meteorol Soc 137:1431–1445. doi:10.1002/qj.850

Varfi M (2009) Synoptic and dynamical study of warm and cold invasions in the broader area of Greece. Dissertation, University of Thessaloniki (in Greek)

Climatology of Upper Air Temperature in the Eastern Mediterranean Region

C.M. Philandras, P.T. Nastos, J. Kapsomenakis, and C.C. Repapis

Abstract The goal of this study is to contribute to the climatology of upper air temperature in the Eastern Mediterranean region, during the period 1965–2007. For this purpose, both radiosonde station and NCEP/NCAR reanalysis gridded datasets of upper air temperature were used for seven barometric levels at 850, 700, 500, 300, 200, 150, and 100 hPa. The impact of atmospheric circulation, by means of correlation between upper air temperature at different barometric levels and specific climatic indices such as Mediterranean Oscillation Index (MOI), North Sea Caspian Pattern Index (NCPI) and North Atlantic Oscillation Index (NAOI), is also quantified.

1 Introduction

In order to understand better the global warming, it is very important to quantify the trends and variability of upper air temperature at different barometric levels for as many locations as it is possible. The upper air temperature trends present relatively low confidence (Seidel et al. 2004), because of the sparse observational radiosonde

C.M. Philandras (✉) • J. Kapsomenakis
Research Centre for Atmospheric Physics and Climatology, Academy of Athens, 24 Omirou Str, GR-10672 Athens, Greece
e-mail: phatmcli@otenet.gr

P.T. Nastos
Laboratory of Climatology and Atmospheric Environment, University of Athens, Panepistimiopolis, GR-15784 Athens, Greece

C.C. Repapis
Research Centre for Atmospheric Physics and Climatology, Academy of Athens, 24 Omirou Str, GR-10672 Athens, Greece

Mariolopoulos-Kanaginis Foundation for the Environmental Sciences, 6 Coumbari Str, GR-10674 Athens, Greece

C.G. Helmis and P.T. Nastos (eds.), *Advances in Meteorology, Climatology and Atmospheric Physics*, Springer Atmospheric Sciences,
DOI 10.1007/978-3-642-29172-2_96,

network. Radiosondes have been used to monitor global changes since the International Geophysical Year (IGY) in 1958 (Thorne et al. 2005) and hence they are very important along with satellites in recording long term upper air temperature trends and variability. Angell and Korshover (1988) showed a significant increase (C.L. 95%) in mean annual global temperature at the surface and in the tropospheric 850–300 hPa layer in contrast to significant cooling trends (C.L. 99%) appeared in 300–100 hPa layer, for the period 1958–1987. Besides, most tropospheric temperature data sets show less warming in the global mean than that reported at the surface, being observed primarily in the tropics and Southern Hemisphere (Brown et al. 2000; Gaffen et al. 2000). Concerning the wider Greek area, significant research has been carried out in analyzing tropospheric air temperature trends (Metaxas et al. 1996; Bloutsos 1976).

This study presents the results of the analysis of the trends and variability in air temperature at various standard upper air pressure levels in several locations in the Eastern Mediterranean region. Furthermore, the impacts of atmospheric circulation on upper air temperature are also examined.

2 Data and Methodology

The upper air temperature data used in the analysis concern both radiosonde stations and NCEP/NCAR reanalysis datasets. More specifically, air temperature for seven pressure levels (850, 700, 500, 300, 200, 150, 100 hPa) from ten radiosonde meteorological stations (Athens, Ankara, Bet Dagan, Brindisi, Cagliari, Isparta, Istanbul, Izmir, Mafaq, Milano) within the examined region, were analyzed. The impact of atmospheric circulation is examined by applying Spearman correlation between upper air temperature at different barometric pressure levels and specific climatic indices such as Mediterranean Oscillation Index (MOI), North Sea Caspian Pattern Index (NCPI) and North Atlantic Oscillation Index (NAOI) (Nastos et al. 2011).

3 Results

The analysis of the time series of annual air temperature at the isobaric level of 850 hPa show a cooling trend since the beginning of the examined period until the late 1970s, especially westwards of Greece (Milano, Brindisi, Caliari), while eastwards the minimum is observed 5 years earlier. Thereafter, the air temperature rises until almost the end of 1980 depicting a secondary minimum about the end of the century, with respect to western stations from Greece. In the Middle East (Bed Dagan, Mafaq), the time series appear a stationary course with small fluctuations until now (Fig. 1). The linear trends for almost all the time series are positive and statistically significant (C.L. 95%) for the period 1965–2007 (Table 1). Accordingly, the time series of annual air temperature at the isobaric levels of 700, 500 and 300 hPa exhibit similar courses with statistically significant increasing trends, with

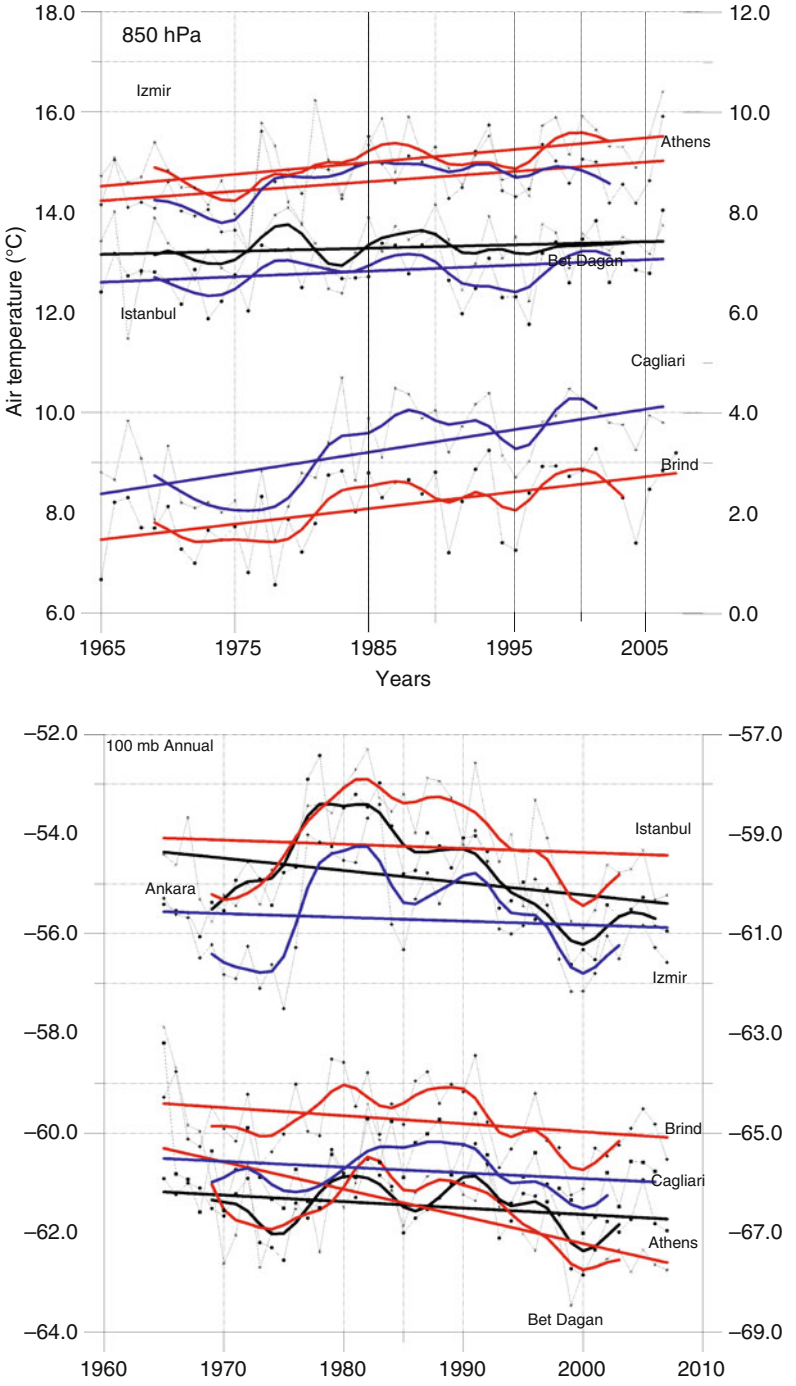

Fig. 1 Time series of annual upper air temperature for the isobaric level at 850 hPa (*upper*) and 100 hPa (*lower*) for representative radiosonde stations

Table 1 Trends of annual, summer and winter air temperature at 850, 700, 500, 300, 200, 150, and 100 hpa and correlations with NAOI, NCPI, MOI for the period 1965–2007

Level	Station	ANN				SUM				WIN			
		Trends	Correlation			Trends	Correlation			Trends	Correlation		
			NAOI	NCPI	MOI		NAOI	NCPI	MOI		NAOI	NCPI	MOI
850	Mafaq	.014*	−.44*	−.49*	−.08	.037*	−.29	−.52*	.36*	.008	−.27	−.65*	−.23
	Istanbul	.016*	.18	−.41*	.09	.046*	−.44*	−.30	−.01	−.009	−.28	−.47*	−.33
	Ankara	.029	.06	−.39*	.16	.045*	−.07	−.26	.19	.030	−.19	−.61*	−.09
	Izmir	.026*	.04	−.31	.26	.047*	−.30	−.23	.23	.010	−.17	−.55*	−.22
	Milano	.037*	.30	.34*	.25	.054*	−.11	.26	−.09	.029	.70*	−.36	.48*
	Brindisi	.030*	.21	−.02	.21	.062*	−.28	−.19	.06	.013	−.03	−.32	−.21
	Cagliari	.042*	.09	.06	.10	.049*	−.24	−.06	−.06	.009	.14	−.23	.02
	Isparta	−.065*	.33	−.20	.04	−.084*	.10	.07	.01	−.017	−.34*	−.57*	−.36*
	BetDagan	.001	−.10	−.50*	.04	.001	−.06	−.52*	.23	.002	−.43*	−.62*	−.37*
	Athens	.018*	.12	−.29	.26	.035*	−.37	−.52*	.10	.003	−.34*	−.61*	−.39*
700	Mafaq	.014·*	−.38*	−.50*	.06	.028*	−.14	−.27	.21	−.005	−.26	−.64*	−.21
	Istanbul	.016*	.12	−.35*	.04	.043*	−.36*	−.44*	.10	−.009	−.10	−.54*	−.20
	Ankara	.024	−.09	−.42*	.07	.038*	−.36*	−.48*	.24	.026	−.11	−.54*	−.07
	Izmir	.025*	.28	−.03	.01	.034*	−.28	−.36*	.25	.020	−.06	−.42*	−.14
	Milano	.040*	.33	.32	.24	.048*	−.12	.02	−.08	.039*	.58*	−.33	.34*
	Brindisi	.030*	.21	.02	.33	.041*	−.33*	−.36*	.05	.026*	.18	−.16	−.01
	Cagliari	.047*	.35*	.04	.19	.039*	−.20	−.21	−.06	.048*	.16	−.53*	.08
	Isparta	.001	.18	−.31	−.09	.027*	−.21	−.56*	.01	.011	−.16	−.57*	−.23
	BetDaga	.001	.04	−.34	.14	.014*	.04	−.36*	.08	.001	−.25	−.59*	−.24
	Athens	.018*	.12	−.26	.20	.025*	−.40*	−.60*	.16	.011	−.09	−.39*	−.27
500	Mafaq	.013	−.22	−.32	.16	.013	.04	.06	.23	−.002	−.13	−.63*	−.04
	Istanbul	.026*	.26	−.26	.15	.045*	−.35*	−.39*	−.07	.012	−.04	−.34*	−.15
	Ankara	.025*	−.03	−.37*	.18	.030*	−.40*	−.36*	.10	.019	−.15	−.60*	−.12
	Izmir	.031*	.06	−.13	.19	.032*	−.32	−.36*	.25	.028*	−.16	−.48*	−.19
	Milano	.046*	.10	.21	.06	.052*	−.18	−.02	−.19	.040*	.59*	.28	.38*

	Brindisi	.045·*	.20	−.01	.19	.044*	−.24	−.40*	−.04	.046*	.16	−.14	.02
	Cagliari	.052*	.14	−.01	.12	.040*	.12	−.02	−.06	.054*	.10	−.28	.08
	Isparta	.016	.15	−.28	−.08	.026*	−.22	−.57*	−.00	.022	−.14	−.51*	−.21
	BetDaga	.001	.01	−.20	.16	−.003	.20	−.14	.26	.007	−.22	−.65*	−.12
	Athens	.030*	.14	−.10	.20	.037*	−.06	−.25	−.21	.022	−.06	−.25	−.21
300	Mafaq	.018	.01	.00	.11	.009	.02	.12	.65*	−.005	.12	−.37*	−.01
	Istanbul	.026*	.26	−.25	.21	.029*	−.03	−.48*	.31	.016	−.05	−.07	−.13
	Ankara	.019	−.06	−.17	.14	.015	−.04	−.08	.60*	.017	.14	−.54*	.11
	Izmir	.032*	.17	−.12	.28	.026*	−.12	−.12	.55*	.033*	.10	−.46*	.06
	Milano	.054*	.13	.09	.16	.053·*	−.26	−.10	−.12	.074*	.54*	.15	.42*
	Brindisi	.047*	.06	−.05	.13	.040*	−.21	−.40*	−.01	.050*	.15	−.22	.12
	Cagliari	.122*	.06	.14	−.02	.119*	−.14	−.14	−.15	.133*	.30	.12	.26
	Isparta	.009	.17	−.02	.26	−.006	.00	−.17	−.66*	.015	.13	−.30	.02
	BetDaga	.003	−.03	.07	−.06	−.003	−.02	−.03	.37*	.015	.27	−.41*	.22
	Athens	.039*	.14	−.07	.26	.029	−.15	−.33*	−.55*	.040*	.13	−.14	.03
200	Mafaq	−.003	.50*	.28	.20	.000	.07	.05	.34*	.010	.65*	−.37*	.56*
	Istanbul	.012	−.01	−.07	.02	.019	.13	−.27	.39*	.016	.19	−.01	.15
	Ankara	.011	.19	−.08	.12	.005	−.08	−.23	.47*	.032	.25	−.02	.21
	Izmir	.018	−.02	−.04	.04	.028	−.21	−.05	.33*	.033*	.27	−.14	.27
	Milano	−.015*	.01	−.23	−.10	−.015	−.03	−.25	.35*	−.028*	−.26	−.14	−.26
	Brindisi	.017	−.12	−.20	−.09	.017	−.06	−.27	.41*	.011	.14	.04	.13
	Cagliari	.017	.20	.06	−.11	.019	−.05	−.28	.17	.032	.05	.32	−.04
	Isparta	−.005	.15	.29	.−.03	.010	−.11	−.22	.13	.004	.53*	.45*	.31
	BetDaga	−.004	.08	.32	−.14	−.014	.17	−.02	.21	.025	.65*	−.31	.48*
	Athens	.019*	.11	.09	.09	.038*	−.03	−.12	.39*	.022	.44*	.29	.36*
150	Mafaq	−.0193*	.43*	.02	.19	−.019*	−.07	.07	−.02	.011	.52*	.31	.47*
	Istanbul	.010	.25	−.02	−.11	.013	−.07	.11	−.44*	.009	.15	.06	.10
	Ankara	.001	.16	−.07	−.01	−.011	−.06	.15	−.02	.016	.06	.01	.06
	Izmir	.012	.14	−.04	.01	.017	−.12	.21	−.40*	.019	.18	.03	.22
	Milano	−.014*	.05	.04	−.15	−.021*	−.02	−.11	−.10	−.022*	−.18	.08	−.21

(continued)

Table 1 (continued)

Level	Station	ANN				SUM				WIN			
		Trends	Correlation			Trends	Correlation			Trends	Correlation		
			NAOI	NCPI	MOI		NAOI	NCPI	MOI		NAOI	NCPI	MOI
	Brindisi	.008	−.03	−.16	−.28	.006	.13	.02	−.40*	.003	.02	.07	.09
	Cagliari	.020*	.18	.08	−.20	.022	.04	.20	−.26	−.40*	.03	.24	.01
	Isparta	−.007	.28	.21	−.07	−.004	−.14	.01	−.52*	−.017	.48*	.54*	.35*
	BetDaga	−.027*	.46*	.26	.05	−.004	.14	−.11	−.18	−.011	.32	.45*	.23
	Athens	.016*	.14	.05	−.14	.030*	−.04	.10	−.45*	.017	.41*	.41*	.34*
100	Mafaq	−.022*	.23	.10	.00	−.032*	−.04	.12	−.16	−.018	.17	.41*	.47*
	Istanbul	−.011	.15	−.09	−.04	−.023	.39*	.03	−.17	−.015	.18	.08	.10
	Ankara	−.025*	.22	−.01	.04	−.058*	.11	.20	−.04	−.016	.05	−.01	.06
	Izmir	−.009	.25	−.08	−.07	−.020	.02	.16	−.46*	−.000	.05	.07	.22
	Milano	−.027*	.27	.03	.06	−.039*	.07	.17	−.36*	−.032*	−.08	−.05	−.21
	Brindisi	−.018*	.09	−.17	−.26	−.030*	.17	.20	−.59*	−.010	−.09	.02	.09
	Cagliari	−.011	.16	−.02	−.26	−.010	−.12	.16	−.61*	.016	−.02	.21	.01
	Isparta	−.027	.35*	.17	−.13	−.035*	−.09	.09	−.53*	−.041*	.39*	.44*	.35
	BetDagan	−.055*	.40*	.09	.02	−.055*	.12	.10	−.43*	−.049*	.29	.43*	.23

*Statistical significant values at 95%

an exception of the stations Mafaq and Betdagan appearing increasing trends but not statistically significant. Taking into account the higher isobaric levels, the trends begin to inverse from the isobaric level of 200 hPa and at 100 hPa all the time series of annual air temperature show increasing trends until the beginning of 1980s, and thereafter strong cooling. Concerning the whole examined period, cooling trends appear (Table 1), statistically significant.

During summer, the time series of air temperature at the isobaric levels from 850 to 300 hPa present almost similar patterns to the corresponding annual air temperatures, but with stronger increasing trends, statistically significant (C.L. 95%). At the isobaric level of 100 hPa, the trends for all stations being reversed to cooling and some of them, especially eastwards, are statistically significant. During winter, the time series of air temperature at all levels and for all the stations show increasing trends from early 1970s until early 1990s westwards of Greece, while eastwards the maximum occurs a decade earlier and thereafter a cooling trend appears across the region. At the Eastern Mediterranean, a stationary air temperature course is obvious since the beginning of the period to mid 1990s and in the process a small increase appears. The trends are positive but not statistically significant. The same pattern is depicted at the isobaric level of 700 hPa, while from 500 to 150 hPa the air temperature follows similar course as it appears westwards of Greece. Concerning the level of 100 hPa, a continuous statistically significant cooling trend is clear in all examined radiosonde stations.

The impact of atmospheric circulation on upper air temperature is examined in terms of specific climatic indices such as Mediterranean Oscillation Index (MOI), North Sea Caspian Pattern Index (NCPI) and North Atlantic Oscillation Index (NAOI). The influence of these indices appears at the isobaric level of 850 hPa (Table 1); namely, the examined indices are negatively correlated (statistically significant at C.L. 95%) with the air temperature, particularly eastwards of Greece (Fig. 2). NCPI dominates especially in winter throughout most of the area considered. This is in agreement with Nastos et al. (2011), who found similar results concerning the impacts of NCPI on the surface air temperature over Greece. Almost identical correlation patterns are depicted at the isobaric levels of 700 and 500 hPa, while at the higher levels the NCPI impacts exist, although weakened, in contrast to MOI, which appears to be stronger especially in summer (Fig. 2).

4 Conclusions

The results showed that significant warming trends appear from 850 to 300 hPa in contrast to significant cooling trends being clear from the 150 hPa isobaric level and higher. The atmospheric circulation impacts, by means of NAOI, NCPI and MOI, on upper air temperature are obvious at 850–500 hPa, while at higher levels MOI influence is predominant especially in summer.

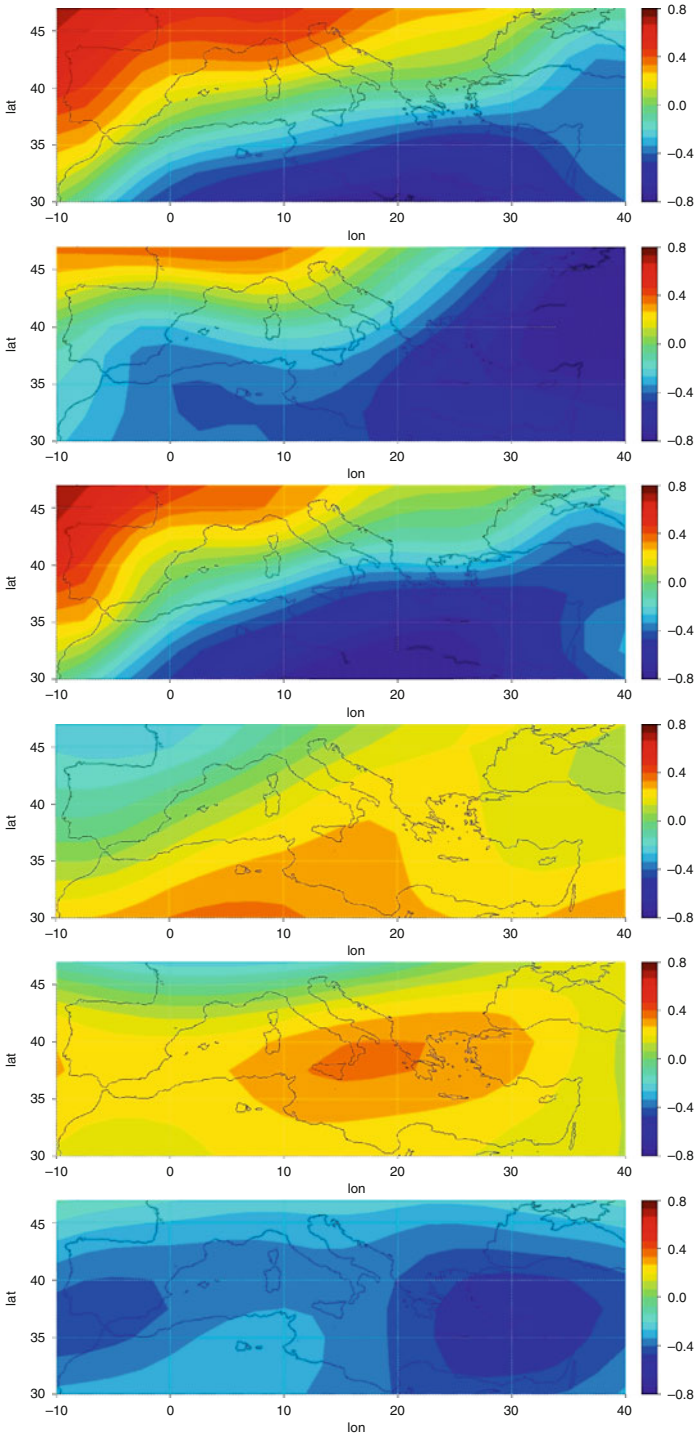

Fig. 2 Spatial distribution of correlation between mean air temperature at 850 hPa and the indices NAOI (**a**), NCPI (**b**), MOI (**c**), for winter (DJF) and between mean air temperature at 100 hPa and the indices NAOI (**d**), NCPI (**e**), MOI (**f**), for summer (JJA), during 1965–2007

References

Angell JK, Korshover J (1988) Variations and trends in troposphere and stratosphere global temperatures 1958–87. J Clim 1:1296–1313

Bloutsos AA (1976) The climate of the atmosphere over Athens. PhD, University of Athens

Brown SJ, Parker DE, Folland CK, Macadam I (2000) Decadal variability in the lower-tropospheric lapse rate. Geophys Res Lett 27:997–1000

Gaffen DJ, Santer BD, Boyle JS, Christy JR, Graham NE, Ross RJ (2000) Multidecadal changes in the vertical temperature structure of the tropical troposphere. Science 287:1242–1245

Metaxas AD, Philandras MC, Nastos TP, Repapis CC (1996) Tropospheric temperature trends over Athens for the period 1960–1994. In: Proceedings third panhellenic conference of meteorology, climatology and atmospheric physics, Athens, pp 97–104

Nastos PT, Philandras CM, Founda D, Zerefos CS (2011) Air temperature trends related to changes in atmospheric circulation in the wider area of Greece. Int J Remot Sens 32:737–750

Seidel DJ et al (2004) Uncertainty in signals of large-scale climate variations in radiosonde and satellite upper-air temperature datasets. J Clim 17:2225–2240

Thorne PW, Parker DE, Tett SFB, Jones PD, McCarthy M, Coleman H, Brohan P (2005) Revisiting radiosonde upper air temperatures from 1958 to 2002. J Geophys Res 110:D18105

Influence of Extreme Weather Events on Insects in Hungary

J. Puskás, L. Nowinszky, and É. Nagy

Abstract We investigated the influence of extreme weather events (thunderstorms and precipitation) on light-trap catch of European corn borer (*Ostrinia nubilalis Hbn.)* in Hungary. There were 560 thunderstorms in the afternoon and 222 at night during the examined period (between 1974 and 1990). The thunderstorms were determined according to the information of Daily Weather Report published by Hungarian Meteorological Service. According to our results if the thunderstorm is in the afternoon, the individuals of the European corn borer already fly in great number to the light-trap at previous night and if the thunderstorm is at night, the catching result is better at the same night. We also examined the influence of daily extreme precipitation (more than 50 mm). The seven investigated years were: 1980, 1982, 1986, 2004, 2005, 2006 and 2007. The light-trap catch of European corn borer was significantly lower on those nights when the precipitation was 50 mm or more at the environment of light-trap station. In both cases we used *t*-test to ascertain whether differences were significant in the examinations. Our results proved there are different influences on insects at the time of extreme weather events.

1 Introduction

It is well known, that the meteorological factors have significant influences on our environment. One of the most important factors is the precipitation. The precipitation can change the surface of lands, but it also has influence on people and other creatures.

J. Puskás (✉) • L. Nowinszky
Institute of Geography and Environmental Sciences, University of West Hungary, Szombathely 9700, Hungary
e-mail: pjanos@gmail.com

É. Nagy
Geomed Ltd, Szombathely, Hungary

C.G. Helmis and P.T. Nastos (eds.), *Advances in Meteorology, Climatology and Atmospheric Physics*, Springer Atmospheric Sciences,
DOI 10.1007/978-3-642-29172-2_97,

Most of the researchers reported in the entomological special literature, indicated that light-trap collecting is hindered by the rainfall. It is not easy to form an opinion of the modifying influence of precipitation in the various physical conditions and intensity. Papp and Vojnits (1976) had a collecting expedition in Korea. They had one of the most successful light-trap catching at night when there was a typical monsoon rainfall with flowing rain during some hours. The increase in number of caught insects was observed by some researchers on those days when there were thunderstorms during the day (Williams 1940; Hosny 1955). Wéber (1959) observed in Hungary, that the maximum value of collecting occurred more than 1 day before the thunderstorm. The light-trap results confirmed that armyworm moths were flying at the time of the hailstorms in Rhodesia (Rose and Law 1976). The supposed explanation for this is that the air pressure change before the thunderstorm increases the insects' activity (Wellington 1946). In one of our former publications (Nowinszky et al. 1994) it was shown that the light-trap collecting of straw point moth (*Rivula sericealis* Scop.) increases significantly at the time of thunder and lightning before the actual thunderstorm, but during the thunderstorm the value of catching decreases by about half and this low volume remains after discontinuance of thunderstorm.

In the past thunderstorms were accompanied with heavy rainfall. There was a remarkable change in intensity of precipitation during the last century. This tendency is probably related to climate change. According to Bartholy and Mika (2005) and Horváth (2009) the frequency of extreme precipitation increased in the Carpathian Basin in last 25 years significantly. The extreme quantity of precipitation in 2010 caused the summer flood damage (3901 ha) in the forests of Hungary. This was the most serious damage since 1995. This was partly flood, partly increased inland water due to the extremely rainy weather conditions (Hirka 2011).

We examined the light trap catch of European corn borer (*Ostrinia nubilalis* Hbn.) in connection with the thunderstorms and extreme precipitation in our present paper.

2 Material

The time of thunderstorms were determined in according to part of the day and taking notice of 11 light-trap stations from "Daily Weather Report" published by the National Meteorological Service between 1974 and 1990. We selected only those meteorological observing stations where there were light-trap stations, as well. They were as follows in Table 1.

9709 European corn borers (*Ostrinia nubilalis* Hbn.) were caught at the abovementioned observing stations during the indicated years. There were determined 560 thunderstorms in the afternoons and 222 at nights at observing stations in the

Table 1 The meteorological observing stations where there were light-trap stations, too

Light-trap stations	Latitude	Longitude	Years
Balassagyarmat	N48.078798	E19.293895	1974–1990
Békéscsaba	N46.684199	E21.086787	1974
Csopak	N46.978239	E17.918700	1959–1989
Eger	N47.903199	E20.373108	1978–1990
Kaposvár	N46.366530	E17.782483	1974–1990
Keszthely	N46.769569	E17.248142	1953–1967
Miskolc	N48.104385	E20.791356	1974–1975
Nyíregyháza	N47.953258	E21.726465	1974–1989
Pápa	N47.330815	E17.466030	1974–1990
Pécs	N46.071320	E18.233143	1977–1990
Zalaegerszeg	N46.845412	E16.847230	1974–1976

examined years. We did not include the 124 afternoon thunderstorms when we could not determine the exact time of their occurrence, this also applied to 21 thunderstorms that occurred sometime in the morning.

We also examined the influence of daily extreme precipitation (more than 50 mm). The seven investigated years were: 1980, 1982, 1986, 2004, 2005, 2006 and 2007. There were 17 days, when the precipitation was at least 50 mm at those light-trap stations where traps were in operation.

3 Method

The environmental factors were not the same at all places and at all times of trapping. Because of this it is sure, catching of the same number of individuals at two different observing stations or in two periods means other proportion of examined populations. To solve this problem, from the catch data we calculated the relative catch (RC) values for observation sites, species and generations. RC is the quotient of the number of individuals caught during the sampling interval (1 night or 1 h), and the mean values of the number of individuals of one generation counted for the sample interval. In this way, in the case of expected mean number of individuals, the value of relative catch was one.

We summarized and then made an average of the results of relative catches coming from several observing stations for each nights, also for the previous and following 2-2 nights in the flying period of European corn borer (*Ostrinia nubilalis* Hbn.) connected with the thunderstorms in the afternoons and during the nights. We also made investigation on the previous and following 3-3 nights in flight of European corn borer (*Ostrinia nubilalis* Hbn.) in connection with extreme precipitation (more than 50 mm). The collection modifying supposed influence was examined compared with light trapping results of previous and following days. We calculated the significance level of difference between the average values by means of the *t*-test.

4 Results and Conclusions

The results are shown in Tables 2 and 3.

We have no knowledge of the fact that diminishing cloudiness as well as thunder and lightning preceding a thunderstorm also enhance flying activity. Information regarding the modifying effect of precipitation has also become more accurate. The role of rain in impeding the flight of insects is well known, but it is new information that this hindering influence make its effect felt even after rain ceases. There is a significant rise in the catch during lightning and thunder preceding a storm, the catch drops by half during the storm and stays low even after the storm is over.

Our study gave the new result about the pieces information of this theme if the thunderstorm is in the afternoon, the individuals of the European corn borer (*Ostrinia nubilalis* Hbn.) already fly in great number to the light-trap at previous night and if the thunderstorm is at night, the catching result is better at the same night.

Table 2 Light-trap catch of the European corn borer (*Ostrinia nubilalis* Hbn.) in connection with thunderstorms

Days before and after the thunderstorms	Thunderstorms in the afternoon		Significance levels		
	Relative catch	Number of data	Between	t	P <
−2	1.032	560	−2 and −1	2.343	0.05
−1	1.236	560	−1 and 0	2.744	0.01
0	1.049	560			
1	0.936	560			
2	0.894	560			
Days before and after the thunderstorms	Thunderstorms at night		Significance levels		
	Relative catch	Number of data	Between	t	P <
−2	1.019	222			
−1	1.086	222	−1 and 0	2.167	0.05
0	1.289	222	0 and 1	1.995	0.05
1	1.048	222			
2	1.013	222			

Table 3 Light-trap catch of European corn borer (*Ostrinia nubilalis* Hbn.) in Hungary around the days when the precipitation was at least 50 mm

Days	Relative catch	Data	Between	t	P <
−3	0.870	17			
−2	0.886	17			
−1	1.020	17	−1 and 0	2.641	0.05
0	0.402	17	0 and 1	2.121	0.05
1	1.121	17			
2	1.455	17			
3	1.218	17			

The favourable catching result can most likely be explained with the higher flight activity anticipated directly due to the thunderstorms (Nowinszky et al. 1994) in this last case. If the thunderstorms are in the afternoon the higher catching results can be caused by the changing air pressure during the previous night as Wellington (1946) reported before.

The light-trap catch of European corn borer was significantly lower on those nights when the precipitation was 50 mm or more at the light-trap stations.

Our results proved that there are different influences on insects at the time of extreme weather events. Generally the light-trap catch was significantly lower during the days of extreme events.

References

Bartholy J, Mika J (2005) Weather and climate – is the bucket in drop? Hung Science 7:789 (in Hungarian)

Hirka A (ed) (2011) The biotic and abiotic forest damages in 2010 and expected damages in 2011. Hungarian Forest Research Institute, Budapest, Hungary

Horváth L (2009) Challenges and means of adaptation in the climate change's frame rules. Study for Hungarian Sustainable Development Council, Budapest (in Hungarian)

Hosny MM (1955) Notes on the effect of some secondary environmental conditions on the activity of nocturnal Macrolepidoptera. Bull Soc Entomol Egypte 39:297–314

Nowinszky L, Ekk I, Károssy Cs, Tóth Gy (1994) Weather elements. In: Nowinszky L (ed) Light trapping of insects influenced by abiotic factors. Savaria University Press, Szombathely

Papp J, Vojnits A (1976) Zoological collectings by the Hungarian Natural History Museum in Korea. Folia Entomol Hung 19:59–74

Rose DJW, Law AB (1976) The synoptic weather in relation to an outbreak of the African armyworm, Spodoptera exempta (Wlk.). J Entomol Soc S Afr 39(1):125–130

Wéber M (1959) Influence of meteorological front changes on insects attracted by light. Yearbook of Teachers' Training College Pécs, pp 259–275 (in Hungarian)

Wellington WG (1946) The effects of variations in atmospheric pressure upon insects. Can J Res 24:51–70

Williams CB (1940) An analysis of four years' captures of insects in light trap. Part II. The effect of weather conditions on insect activity and the estimation and forecasting of changes in the insect population. Trans R Entomol Soc Lond 40:227–306

Cloud Radiative Effects on Solar Radiation Over the Eastern Mediterranean Basin from 1984 to 2007

M. Pyrina, C.D. Papadimas, A. Fotiadi, C. Matsoukas, N. Hatzianastassiou, and I. Vardavas

Abstract The cloud radiative effect (CRE) on solar shortwave (SW) radiation is investigated over the broader Mediterranean basin, for the 24-year period from 1984 to 2007, using a deterministic spectral radiation transfer model (RTM) and quality monthly cloud data taken from the ISCCP-D2 satellite database. The model simulates the interaction of solar radiation with all relevant physical parameters, namely ozone, carbon dioxide, methane, water vapour, aerosols and atmospheric molecules as well as surface reflection. The ISCCP cloud model input data include cloud cover and optical depths for low-, mid-, and high-level clouds, separately for ice and liquid water clouds. The model computes CREs at the top of atmosphere (CRETOA), within the atmosphere (CREatmab), and at the surface (effects on downwelling and absorbed solar radiation, CREsurf and CREsurfnet). The determined perturbation of regional SW radiation budget by clouds is important, undergoing significant intra-annual and inter-annual changes.

M. Pyrina • C.D. Papadimas • N. Hatzianastassiou (✉)
Laboratory of Meteorology, Department of Physics, University of Ioannina, Agrinio, Greece
e-mail: nhatzian@cc.uoi.gr

A. Fotiadi
Laboratory of Meteorology, Department of Physics, University of Ioannina, Agrinio, Greece

Department of Environmental and Natural Resources Management, University of Ioannina, Agrinio 30100, Greece

C. Matsoukas
Department of Environment, University of the Aegean, Mytilene 81100, Greece

I. Vardavas
Department of Physics, University of Crete, 71110 Heraklion, Crete, Greece

C.G. Helmis and P.T. Nastos (eds.), *Advances in Meteorology, Climatology and Atmospheric Physics*, Springer Atmospheric Sciences,
DOI 10.1007/978-3-642-29172-2_98,

1 Introduction

Clouds reflect and absorb solar radiation resulting in a cooling of the Earth's surface, while emit and absorb thermal infrared radiation producing a natural greenhouse effect. The effect of clouds on radiative fluxes is referred to either as cloud radiative forcing (CRF) or cloud radiative effect (CRE) and can be defined as the difference between the radiative fluxes under clear-sky and cloudy-sky conditions. Given their critical role, the representation of clouds and their associated radiative processes, namely CREs, is a key issue in climate models. Besides, cloud feedbacks still remain the largest source of uncertainty in general circulation models (GCMs) and climate predictions (IPCC 2007).

Quantification of cloud CREs has been the subject of extensive research in the past (e.g. Ramanathan et al. 2000; Chen et al. 2000). The situation has been improved recently, due to rapid advance in satellite instrumentation, which made possible to determine accurately radiative fluxes and CREs, especially at the top-of-the atmosphere (TOA). However, a direct satellite based solution is not possible at the surface and within the atmosphere. The only safe alternative is to derive them using adequate and comprehensive radiative transfer models (RTMs). Such model computations, using satellite based input data, have the advantage to provide extended spatial coverage, which not ensured by local surface station measurements. Cloud input data, especially optical properties, are crucial for CREs computation. Such comprehensive climatological cloud data, separately given for low-, mid- and high-level clouds, have become available thanks to the International Satellite Cloud Climatology Project (ISCCP, Rossow et al. 1996) allowing thus calculation of CRE at TOA, surface and within the atmosphere.

In this work, the CREs on solar radiation are computed over the broader eastern Mediterranean basin (28.75–48.75, 16.25–38.75) with a $2.5^\circ \times 2.5^\circ$ spatial resolution, for the 24-year period from 1984 to 2007, using a deterministic spectral RTM and quality monthly cloud data taken from the ISCCP-D2 satellite database. Apart from other reasons, the choice of the study region was made because Mediterranean basin constitutes a climatically sensitive region that is systematically considered in climatic studies, while it is very interesting from the aspect of cloud properties, which are strongly influenced by the great irregularity of land and water distribution, as well as regional cloud formation mechanisms.

2 The Spectral Radiation Transfer Model and the Input Data

2.1 The Model

The spectral RTM computes solar radiative fluxes at 118 wavelengths for the ultraviolet–visible part of the spectrum, and for ten bands for the near-infrared part, using the modified Delta-Eddington method. The computations are performed

for each 2.5° latitude × 2.5° longitude cell of the region, considering ozone absorption, Rayleigh scattering, and absorption by water vapour, carbon dioxide and methane. Scattering and absorption by clouds (low, middle and high) and aerosols, and reflection from the Earth's surface are also taken into account. A complete description and detailed model considerations can be found in Hatzianastassiou et al. 2007 and Vardavas and Taylor (2007). The radiative fluxes, at various levels (-i), are computed with and without the presence of clouds and then the Cloud Radiative Effect (CRE) is given by: $CRE_i = F_{i,with} - F_{i,without}$. The accuracy of the model 2.5-° monthly fluxes has been successfully tested (Hatzianastassiou et al. 2005) against measurements from GEBA (Global Energy Balance Archive) and BSRN (Baseline Surface Radiation Network).

2.2 *The Input Data*

The model input data include cloud properties from ISCCP-D2 (Rossow et al. 1996), aerosol optical properties (from Global Aerosol Data Set) and vertical temperature and specific humidity profiles (from NCEP/NCAR global reanalysis project). The model takes into account Rayleigh scattering due to atmospheric gas molecules, as well as absorption by O_3, CO_2, H_2O and CH_4. Total O_3 column abundance (in Dobson units) is taken from Television Infrared Observation Satellite (TIROS) Operational Vertical Sounder (TOVS) archived in the ISCCP-D2 dataset. For CO_2 a fixed total atmospheric amount is taken, equal to 0.54 g cm^{-2}, corresponding to 345 parts per million by volume (ppmv). The water vapour data used are taken from the NCEP/NCAR Global Reanalysis Project. The mixing ratio of CH_4 is set equal to 1.774 ppmv, corresponding to 10^{-3} g cm^{-2}. The ISCCP-D2 cloud data include: cloud amount, cloud-top pressure, cloud-top temperature, liquid water path, and optical depth for total, but also for individual clouds, separately for liquid and ice phase. Cloud properties are subsequently grouped into three categories for low-, mid- and high-level clouds. For a more detailed explanation of the model input data and their treatment, the reader is referred to the work by Hatzianastassiou et al. (2005).

3 Results and Discussion

According to the model results, the annual regional mean cloud radiative effect on the outgoing (reflected) SW radiation at TOA (CRE_{TOA}) is equal to −32.9 Wm^{-2}, locally varying between −7 and −50 Wm^{-2}, indicating thus a "planetary" cooling of the study region caused by clouds. Clouds also uniformly increase the atmospheric absorption of SW radiation (CRE_{atmab}) over the region, by 11.6 Wm^{-2} (local values up to 17 Wm^{-2}) inducing thus a significant warming of the region's atmosphere, more in its northern than southern parts. As a result, clouds drastically

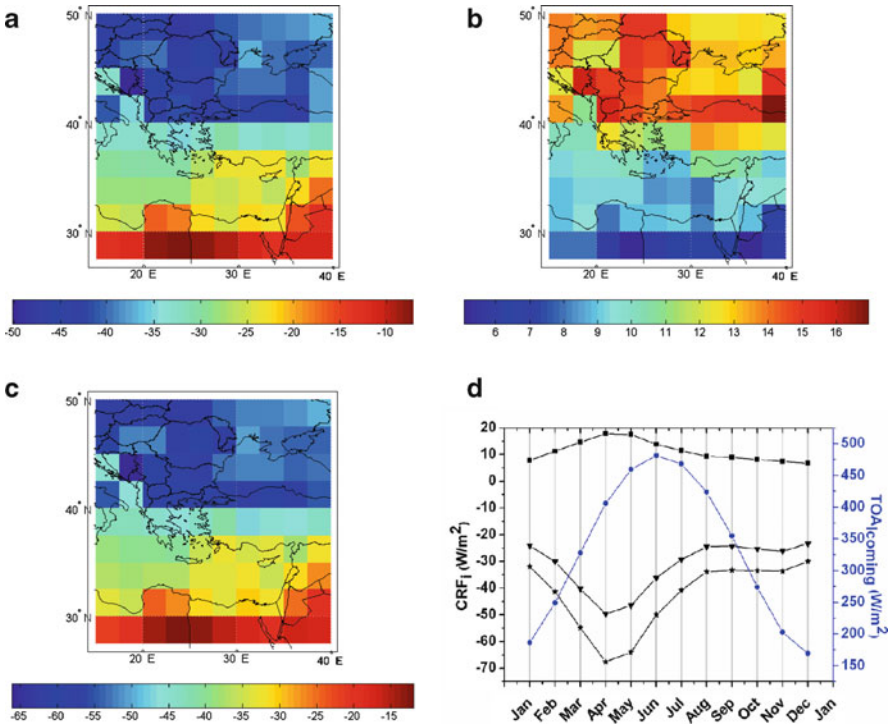

Fig. 1 Twenty-four year (1984–2007) results for average geographical distribution of CREs at: (**a**) TOA (CRE_{TOA}, *triangles*), (**b**) in the atmosphere (CRE_{atmab}, *squares*), and (**c**) at the surface ($CRE_{surfnet}$, *stars*) over the eastern Mediterranean basin. The intra-annual variability of CREs, as well as of the incoming solar radiation at TOA (*blue line*) are also shown in (**d**)

decrease the absorbed SW radiation at surface ($CRE_{surfnet}$) by −44.5 (with local values as large as −65 Wm^{-2}), inducing thus an important surface radiative cooling.

Based on the model computations, the contribution of high clouds to the mean annual regional radiative effects is equal to 32% (−10.5 Wm^{-2}) for CRE_{TOA}, 16% (1.9 Wm^{-2}) for CRE_{atmab} and 28% (−12.4 Wm^{-2}) for $CRE_{surfnet}$. The corresponding contributions of middle clouds are equal to 36% (−11.9 Wm^{-2}), 37% (4.3 Wm^{-2}) and 36% (−18.9 Wm^{-2}). Finally, the corresponding contributions of low clouds are 32%, 47% and 36% (−10.5, 5.4 and −15.9 Wm^{-2}). Therefore, a predominance of low and middle clouds is found, in terms of their effects on the SW radiation budget of the eastern Mediterranean basin.

The maximum values of all cloud radiative effects are observed in spring and not in summer as one might expect based on the highest available solar radiation amounts in this season (Fig. 1d). The spring maxima result from the combination of large cloudiness (≈65% till April, Fig. 2b) mostly attributed to low and middle clouds, and significant solar radiation amounts (350–450 Wm^{-2}, Fig. 1d) in the eastern Mediterranean basin during this season.

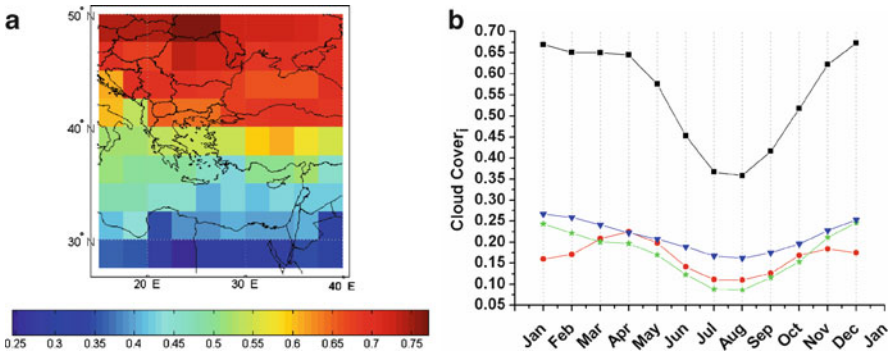

Fig. 2 Twenty-four year (1984–2007) average (**a**) geographical distribution of total cloud cover and (**b**) intra-annual variability of low (*blue line*), middle (*green line*), high (*red line*) and total cloud cover (*black line*) over the eastern Mediterranean basin

Given that questions arose in the past regarding the quality of ISCCP-D2 cloud cover, we performed a detailed comparison between the used monthly ISCCP-D2 cloud cover and similar ground based data from the European Climate Assessment and Dataset (ECA, http://eca.knmi.nl/). The ISCCP cloud cover data were satisfactorily correlated with measurements from nine uniformly distributed stations over the Greek region. Overall, the predicted coefficient of determination (R) for the nine sites is equal to 0.87, while the R values for independent sites ranges between 0.82 and 0.91.

In Fig. 3 are shown the computed changes of CREs over the study region for the period 1984–2007. The changes were computed by applying linear regression fits to the time series of deseasonalized anomalies of CREs for every pixel. Our results indicate that over most of the region, $CRE_{surfnet}$ has decreased by up to 6.5 Wm^{-2} or 32.5%, yielding a regional mean decrease of 4.15 Wm^{-2} or −10%. This decrease is equivalent to a warming of the region's surface (decreased surface cooling, $CRE_{surfnet}$) and is combined with a decreased atmospheric warming, i.e. regional atmospheric cooling, produced by the decrease of CRE_{atmab} by 1.4 Wm^{-2} or −9.3% (locally the decrease can be as large as 3 Wm^{-2} or more than 40%, Fig. 3c). Our analysis has shown that these changes are mainly due to a decreasing trend of cloud cover over the study region from 1984 to 2007 (Fig. 3d), equal to −4.9% in absolute or −9% in relative values (local decreases ranging up to −14% in absolute and 35% in relative values). The strong relationship between cloud cover and CREs is proven by the computed correlation coefficients, taking values from 0.5 to 0.9 over the greatest part of the study region (results not shown here).

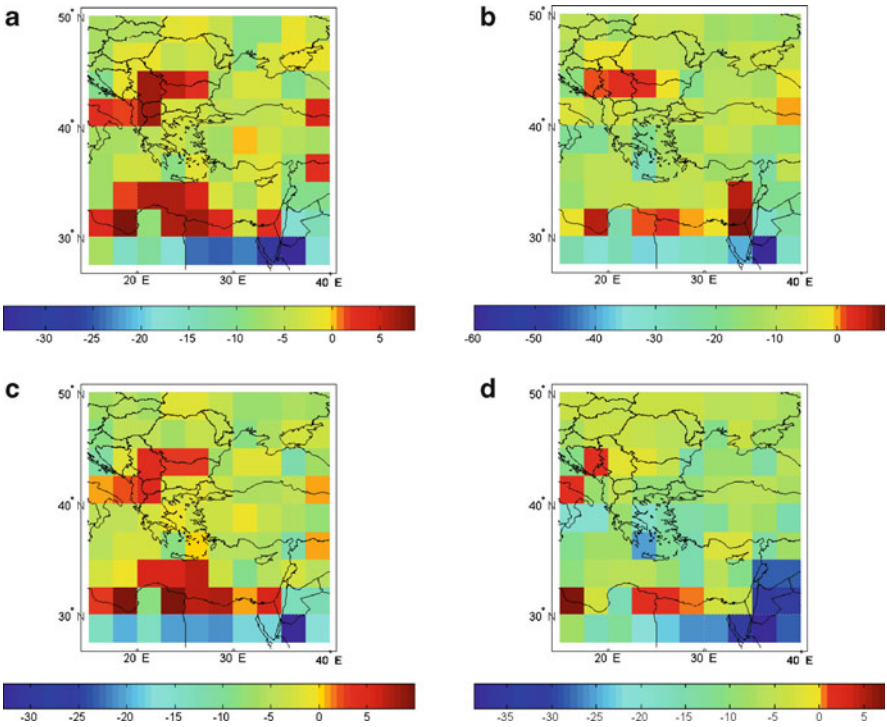

Fig. 3 Relative percent (%) changes of: (**a**) CRE_{TOA}, (**b**) CRE_{atmab}, (**c**) $CRE_{surfnet}$ and (**d**) total cloud cover, computed from the application of linear regression analysis to the corresponding time series (1984–2007) of mean regional monthly values

4 Conclusions

A detailed spectral radiative transfer model was used together with cloud properties from ISCCP to compute the cloud effects on the SW radiation budget of the eastern Mediterranean basin. According to our results:

1. Clouds produce a strong cooling effect at TOA over the region (-32.9 Wm^{-2}), they increase the atmospheric solar absorption by 17 Wm^{-2} and decrease the surface solar absorption by -44.5 Wm^{-2}, inducing thus an important radiative surface cooling and atmospheric warming over the eastern Mediterranean basin. The local CRE values are even larger, up to -65 Wm^{-2}, exhibiting a strong spatial variability.
2. The mid-level clouds have the greatest radiative effect at TOA, while low clouds exert the strongest effect on atmospheric solar absorption. Together, low and middle clouds, they mostly contribute to the cloud induced surface radiative cooling.

3. Decreasing cloud cover produced a planetary warming over the study region from 1984 to 2007, along with an atmospheric cooling and a surface warming.

References

Chen T, Rossow WB, Zhang Y (2000) Radiative effects of cloud type variations. J Clim 13:264–286

Hatzianastassiou N, Matsoukas C, Fotiadi A, Pavlakis KG, Drakakis E, Hatzidimitriou D, Vardavas I (2005) Global distribution of Earth's surface shortwave radiation budget. Atmos Chem Phys 5:2847–2867

Hatzianastassiou N, Matsoukas C, Drakakis E, Stackhouse PW Jr, Koepke P, Fotiadi A, Pavlakism KG, Vardavas I (2007) The direct effect of aerosols on solar radiation based on satellite observations, reanalysis datasets, and spectral aerosol optical properties from Global Aerosol Data Set (GADS). Atmos Chem Phys 7:2585–2599

Ramanathan V, Cess RD, Harrison EF et al (2000) Cloud-radiative forcing and climate: results from the Earth radiation budget experiment. Science 243:57–63

Rossow WB et al (1996) International Satellite Cloud Climatology Project (ISCCP). Documentation of new cloud datasets. Wold Meteorol. Org, Geneva

Vardavas IM, Taylor FW (2007) Radiation and climate, vol 138, International series of monographs on physics. Oxford University Press, Oxford

Large-Scale Variability Over Mediterranean Associated with the Indian Summer Monsoon

D. Rizou, H.A. Flocas, P. Athanasiadis, and A. Bartzokas

Abstract The objective of this study is the investigation of the large scale variability of the atmospheric circulation over the Mediterranean region in relation to the Indian summer monsoon. For this purpose composite anomalies of selected fields at various isobaric levels are analyzed for strong versus weak monsoon years. Gridded, monthly mean data, such as geopotential height, horizontal wind components, vertical velocity and relative vorticity at 300 hPa were used, as obtained from the ERA-40 Reanalysis Data Base, with 2.5° × 2.5° resolution for the boreal summer (June-September) and for a 44-year period (1958–2001). The standardized Dynamic Indian Monsoon Index by Wang and Fan (1999) was employed to determine the strong and weak monsoon years in the 44-year period. It was found that there are significant differences between *strong* and *weak* composites for all fields, especially in the upper troposphere. The results suggest that these differences may be related to the existence of Rossby wave trains as well as to the intensity and the meridional shift of the upper-level jet streams.

1 Introduction

El-Nino Southern Oscillation (ENSO), South Asian and African monsoons, tropical hurricanes and Sahara dust constitute some of the factors of the tropical and subtropical climate variability that influence the Mediterranean region. Rodwell and Hoskins (1996, 2001) studied the impact of the Asian monsoon

D. Rizou (✉) • H.A. Flocas • P. Athanasiadis
Division of Environmental Physics and Meteorology, Department of Physics, University of Athens, Athens, Greece
e-mail: desrizou@phys.uoa.gr

A. Bartzokas
Laboratory of Meteorology, Department of Physics, University of Ioannina, Ioannina 451 10, Greece

C.G. Helmis and P.T. Nastos (eds.), *Advances in Meteorology, Climatology and Atmospheric Physics*, Springer Atmospheric Sciences,
DOI 10.1007/978-3-642-29172-2_99,

on the Mediterranean and showed that the subsidence over the eastern Sahara/Mediterranean is influenced by the South Asian summer monsoon. More specifically, the strong diabatic heating associated with the rainfall in the South Asian summer monsoon region induces intensified easterlies in the equatorward portion of the North Pacific subtropical anticyclone, the Kelvin-wave response (Gill 1980), and a Rossby-wave response to the west of the monsoon region, which interacting with the southern flank of the mid-latitude westerlies, produces a region of adiabatic descent in the North African and Eastern Mediterranean (EM) regions. Ziv et al. (2004) proposed that the Etesian winds and the persistent subsidence over the region, which appear systematically during the summer, are linked to the Asian monsoon. They found that both of these features of the eastern Mediterranean circulation respond to the varying intensity of the Indian summer monsoon (ISM, also known as the Southwest Asian monsoon) on the inter-diurnal time-scale.

In this frame, the aim of the present study is to investigate the influence of the Indian summer monsoon on the atmospheric circulation over the greater Mediterranean region on a seasonal scale, during strong and weak monsoon years, as a first attempt to further examine the impact of the Indian summer monsoon on the EM climatic regime during summer and related large scale physical processes.

2 Data and Methodology

The dataset used in this work was the monthly mean ERA-40 Reanalysis Data of the European Center for Medium-Range Weather Forecast (ECMWF), on a $2.5^\circ \times 2.5^\circ$ grid and at standard pressure levels from 1,000 to 300 hP. Geopotential height, horizontal wind components data and several dynamic and thermodynamic parameters, covering boreal summers (June-September) from 1958 to 2001, were employed.

The Dynamic Indian Monsoon Index (DIMI) by Wang and Fan (1999) was used to select the extreme ISM years. DIMI is defined as the difference of 850 hPa zonal wind between a southern (5°N-15°N, 40°E-80°E) and a northern region (20°N-30°N, 70°E-90°E). Strong (weak) ISM years are defined as years when DIMI is above +0.65 sigma (below −0.65 sigma). As a result, 12 strong ISM years (1965, 1966, 1968, 1972, 1974, 1979, 1982, 1984, 1985, 1987, 1997, 1999) and 12 weak ISM years (1958, 1959, 1961, 1970, 1973, 1975, 1978, 1980, 1983, 1988, 1994, 1998) were derived.

Seasonal (JJAS) mean anomalies of the above mentioned data were calculated as the seasonal deviations from the climatological seasonal means for the period 1958–2001 separately for strong and weak ISM years. Derived *strong* and *weak* composites of representative fields (geopotential height, zonal and meridional wind components) are presented.

3 Results

The *strong* and *weak* composite anomalies of the zonal-wind component at 300 hPa are shown in Fig. 1. The examination of the *weak* composite (Fig. 1b) reveals a meridional shift of the subtropical jet (STJ) in the Asia region equatorward, as compared with its climatological mean position. On the other hand, the phases of the zonal wind anomaly in the strong ISM years (Fig. 1a) are opposite to those in the weak ISM years. In detail, the STJ is shifted to the north of its mean climatological position extending further to the west over EM. The STJ appears anomalously strengthened (weakened) over EM in the strong (weak) ISM years. The aforementioned STJ shift is also evident in the 300 hPa relative vorticity anomaly composite for the strong ISM years (not shown), where an anomalous positive vorticity is located poleward of the anomalous westerly zonal wind. It is well known that the

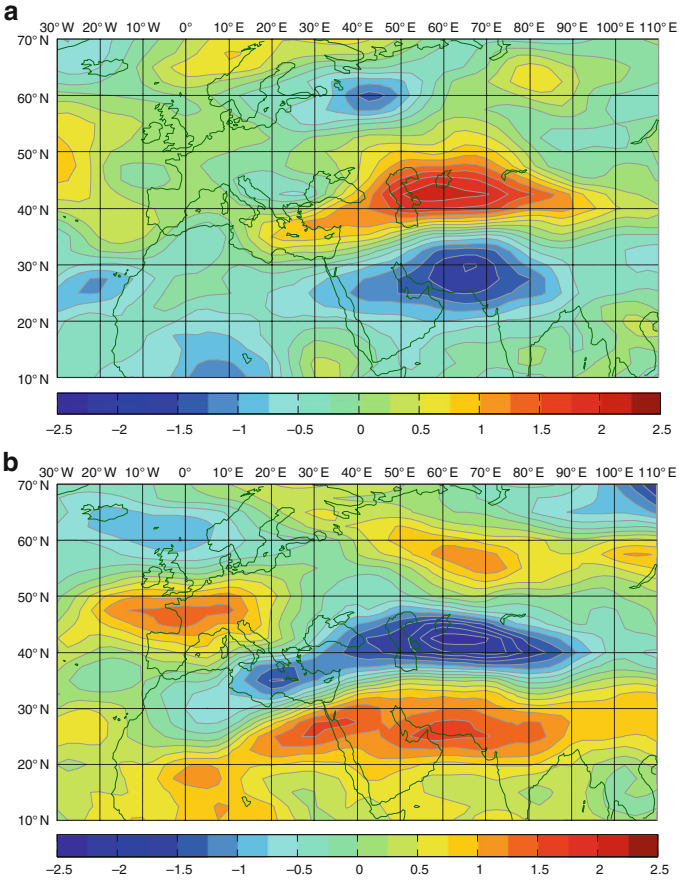

Fig. 1 Seasonal (JJAS) mean anomalies of zonal wind (m s^{-1}) at 300 hPa during (**a**) strong ISM years and (**b**) weak ISM years, from 44-year (1958–2001) climatology

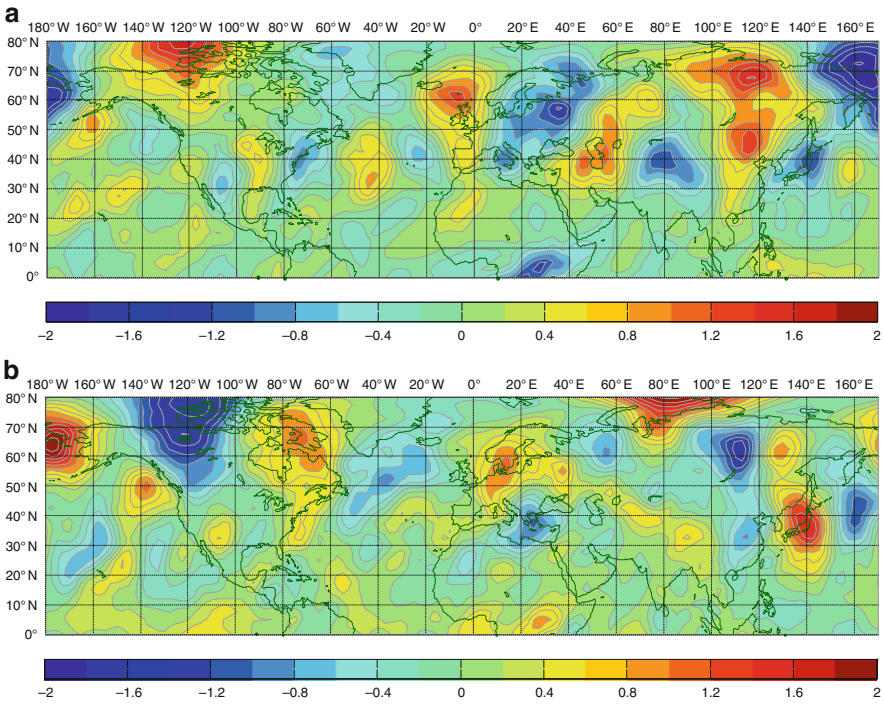

Fig. 2 Seasonal (JJAS) meridional wind component anomalies (m s^{-1}) at 300 hPa during (**a**) strong ISM years and (**b**) weak ISM years, from 44-year (1958–2001) climatology

position of the STJ is prominent for the development of the monsoon circulation cell (Yin 1949). As long as the STJ lies on the southern side of the Tibetan Plateau at about 30°N, it inhibits the development of summer monsoon. As the STJ slides to the north of Himalayas and Tibet at about 40°N and reforms over central Asia during the summer months, the summer monsoon cell finally develops. Additionally, the intensity and position of the STJ over the Mediterranean are key parameters for the climate variability over the region regarding heat wave events and precipitation (Prezerakos and Flocas 2002; Baldi et al. 2006; Gaetani et al. 2011).

The corresponding seasonal anomalies in the 300 hPa meridional wind field are displayed in Fig. 2. It is evident that the meridional wind anomalies in the strong ISM years are of significant magnitude over a large region, extending to the entire midlatitude band, whereas in the weak ISM years the anomalies are much weaker and of opposite sign. Furthermore, for the strong ISM years (Fig. 2a) the meridional wind anomalies depict a well-organized Rossby wave train of alternating southerlies and northerlies, propagating in mid-latitudes over the whole Northern Hemisphere and expanding to subpolar and polar latitudes over central and western Europe, east Asia, the Pacific Ocean and north-western America. The anomalies

become more intense over Eurasia continent and the wave train appears as emanating from the equatorial region and propagating on a great cycle, that is on a plane that intersects the center of the Earth.

It is interesting to note that the wave train propagation along the above region coincides with the position of the subtropical jet in the area (see Fig. 1). In fact, Fig. 2a reveals an anomaly pattern that is meridionally confined to the vicinity of the jets with anomalies that are zonally oriented, while the pattern in Fig. 2b appears unorganized with anomalies with no specific orientation. Many studies focus on the importance of the upper-level tropospheric jets as wave-guides for the observed low-frequency waves (e.g. Hoskins and Ambrizzi 1993; Branstator 2002).

According to the linear wave theory applied in these studies, the waveguide action of the jet has the potential to enhance the longitudinal extent of low-frequency disturbances, since they are meridionally confined and their energy propagates further before being dissipated. According to Branstator (2002), disturbances in the vicinity of the mean jets lead to covariability between widely separated areas.

Regarding the lower atmosphere, composites of geopotential height anomalies at 850 hPa are presented for both weak and strong ISM years in Fig. 3. In the geopotential height pattern of anomalies for the strong ISM years (Fig. 3a) an intense and extended positive anomaly is located over the Atlantic Ocean, western and central Europe and north-west Africa, while negative anomalies extend from the ISM region through the Persian Gulf and further along southern Turkey to the Aegean sea. According to this pattern, the Azores subtropical anticyclone and the Asian thermal low appear enhanced during strong ISM years. Greece lies in the middle of the two anomaly fields (enhanced baroclinicity), where anomalous northeasterly wind currents occur. Consequently, the strengthening of these two systems will have an impact on the Etesian winds as well, which result from the combination of the above mentioned systems (Ziv et al. 2004). These results are in agreement with the wind vector anomaly pattern at 850 hPa (see Fig. 3a) for strong ISM years, where an anomalous north current is prevalent over Eastern and central Mediterranean. The anomaly composite related to weak ISM years reveals a similar spatial distribution as in the strong years, though reversed. Accordingly, the wind vector anomalies for the weak ISM years (see Fig. 3b) present an opposite pattern, with anomalous southerlies dominating over EM, corresponding to weakened Etesian winds. On the other hand, the 500 hPa vertical velocity anomaly fields (not shown) depict anomalous subsidence over the EM for the strong ISM years and an anomalous upward motion in the weak ISM years. At the same time, the temperature anomalies at 1,000 hPa over the region, represent a regime characterized by negative (positive) values during strong (weak) ISM years (not shown), resulting from the combined action of two primary factors; the mid-tropospheric subsidence and lower-level cool advection, associated with the Etesians (Ziv et al. 2004).

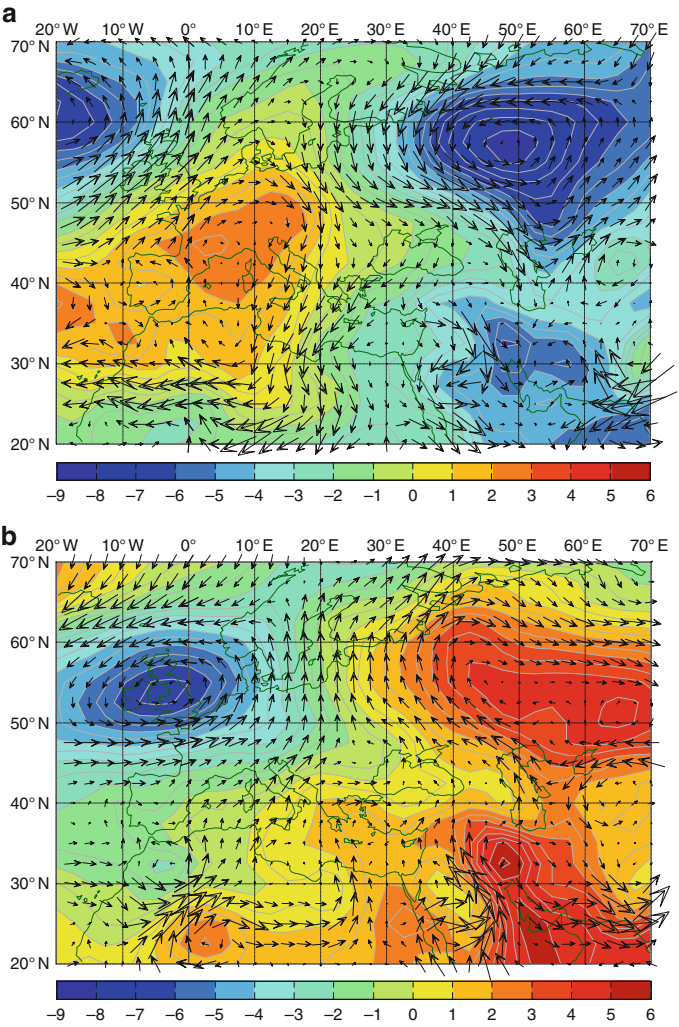

Fig. 3 Seasonal (JJAS) mean anomalies of geopotential height (gpm) and wind vector anomalies at 850 hPa during (**a**) strong ISM years and (**b**) weak ISM years. Anomalies are departures from the 1958–2001 climatology

4 Conclusions

In this study the anomalous characteristics of observed large-scale synoptic fields during extreme ISM years are analyzed and compared, as a first attempt to investigate the impact of the ISM on the EM region. The results indicate that the differences between the anomaly composites in strong and weak ISM years of examined fields are significant implying further analysis of the related dynamics.

In the strong ISM years the STJ over South Asia was found meridionally shifted poleward, compared with its climatological mean position, expanding enhanced over EM. On the contrary, it was found that the weak ISM years favor the equatorward shift of the STJ over South Asia and a weakening of its intensity over EM.

The meridional wind anomaly pattern at 300 hPa during strong ISM years revealed a well-organized Rossby wave train, zonally oriented and confined to the STJ along mid-latitudes. In the weak ISM years, the anomaly composite of 300 hPa meridional wind was completely different, scattered anomalies with no specific orientation. These preliminary results imply that a well-organized Rossby wave train is a response to the intensified Indian monsoon forcing, as Rodwell and Hoskins (1996) described.

Finally, the geopotential height anomaly patterns in the lower atmosphere for the extreme ISM years indicated the intensification of the Azores anticyclone and the Asian thermal low in the strong ISM years and the respective weakening of both systems in the weak ISM years. As a result, enhanced northerlies appear to be dominating over EM in the strong ISM years, as concluded from the 850 hPa meridional wind anomalies, with an impact on the temperature regime of the region.

Acknowledgments This research has been co-financed by the European Union (European Social Fund – ESF) and Greek national funds through the Operational Program "Education and Lifelong Learning" of the National Strategic Reference Framework (NSRF) – Research Funding Program: Heracleitus II. Investing in knowledge society through the European Social Fund.

References

Baldi M, Dalu G, Maracchi G, Pasqui M, Cesarone F (2006) Heat waves in the Mediterranean: a local feature or a larger-scale effect? Int J Climatol 26:1477–1487. doi:10.1002/joc.1389

Branstator G (2002) Circumglobal teleconnections, the jet stream waveguide, and the North Atlantic Oscillation. J Climate 15:1893–1910. doi:10.1175/1520-0442(2002) 015<1893:CTTJSW>2.0.CO;2

Gaetani M, Baldi M, Dalu GA, Maracchi G (2011) Jet stream and rainfall distribution in the Mediterranean region. Nat Hazard Earth Syst 11:1–14. doi:10.5194/nhess-11-2469-2011

Gill AE (1980) Some simple solutions for heat-induced tropical circulations. Q J R Meteorol Soc 106:447–462. doi:10.1002/qj.49710644905

Hoskins BJ, Ambrizzi T (1993) Rossby wave propagation on a realistic longitudinally varying flow. J Atmos Sci 50:1661–1671. doi:10.1175/1520-0469(1993) 050<1661:RWPOAR>2.0.CO;2

Prezerakos NG, Flocas HA (2002) Regional and global large-scale dynamics associated with a prolonged drought event in Greece. J Atmos Sol-Terr Phys 64:1841–1854. doi:10.1016/S1364-6826(02)00197-9

Rodwell MJ, Hoskins BH (1996) Monsoon and the dynamics of deserts. Q J R Meteorol Soc 122:1385–1404. doi:10.1002/qj.49712253408

Rodwell MJ, Hoskins BJ (2001) Subtropical anticyclones and summer monsoons. J Climate 14:3192–3211. doi:10.1175/1520-0442(2001) 014<3192:SAASM>2.0.CO;2

Wang B, Fan Z (1999) Choice of South Asian summer monsoon indices. Bull Am Meteorol Soc 80:629–638. doi:10.1175/1520-0477(1999) 080<0629:COSASM>2.0.CO;2

Yin MT (1949) A synoptic-aerologic study of the onset of the summer monsoon over India and Burma. J Meteorol 6:393–400. doi:10.1175/1520-0469(1949) 006<0393: SASOTO>2.0.CO;2

Ziv B, Saaroni H, Alpert P (2004) The factors governing the summer regime of the eastern Mediterranean. Int J Climatol 24:1859–1871. doi:10.1002/joc.1113

ECHAM5/MPI General Circulation Model Simulations of Teleconnection Indices Over Europe

E. Rousi, C. Anagnostopoulou, K. Tolika, P. Maheras, and A. Bloutsos

Abstract In this paper, a study of potential future changes of the atmospheric circulation over Europe is presented. Atmospheric circulation is studied through two teleconnection indices, the North Atlantic Oscillation (NAO) Index – which mostly affects the climate of western Europe – and the North Sea-Caspian Pattern (NCP) Index – mainly affecting eastern Mediterranean and the Balkan Peninsula. Firstly, the ECHAM5/MPI (Max Planck Institute) General Circulation Model's (GCM's) simulations for the two teleconnection indices are evaluated against NCEP/NCAR reanalysis data for the control run period 1971–2000, both in a temporal and a spatial scale. Secondly, the GCM's future simulations are studied. The main goals of this study are to validate the ECHAM5 GCM regarding the two teleconnection indices under consideration, and consequently to examine whether the current dominant circulation patterns change or not throughout the twenty-first century.

1 Introduction

Earth climate variability has long been considered to be strongly governed by variability in atmospheric circulation. A usual approach of studying atmospheric circulation is that of trying to identify and define certain patterns or cycles, such as atmospheric teleconnections.

North Atlantic Oscillation (NAO) is one of the most studied teleconnection patterns and it has long been recognized as strongly connected to the climate variability of the Northern Hemisphere and especially that of eastern America and Western Europe (Walker 1924). NAO is defined as the seesaw pattern of the

E. Rousi (✉) • C. Anagnostopoulou • K. Tolika • P. Maheras • A. Bloutsos
Department of Meteorology and Climatology, Aristotle University of Thessaloniki, Thessaloniki 54124, Greece
e-mail: erousi@geo.auth.gr

C.G. Helmis and P.T. Nastos (eds.), *Advances in Meteorology, Climatology and Atmospheric Physics*, Springer Atmospheric Sciences,
DOI 10.1007/978-3-642-29172-2_100,

geopotential heights (gph) or the sea level pressure (slp) between the North Atlantic Ocean and a zonal region at around 35–40° in the Atlantic. More specifically, the two poles taken under consideration are located over Iceland and over the Azores Islands (Rogers 1984) or over an eastern location, such as Lisbon or Gibraltar (Hurrell 1995). NAO has two different phases, a positive and a negative one, when in its positive phase, low pressure anomalies over the Icelandic region and throughout the Arctic combine with high-pressure anomalies across the subtropical Atlantic to produce stronger-than-average westerlies across middle latitudes. This phase of the oscillation is, consequently, associated with cold conditions over the northwest Atlantic and warm weather over Europe, as well as wet conditions from Iceland through Scandinavia and dry conditions over southern Europe. The negative NAO index phase shows a weak subtropical high and a weak Icelandic low. As a consequence, the reduced pressure gradient results in fewer and weaker winter storms crossing on a more west-east pathway. This way, moist air is brought into the Mediterranean and cold air to northern Europe.

The other teleconnection examined in this study is the North Sea-Caspian Pattern (NCP), which is evident at the 500 hPa level and was recognized by Kutiel and Benaroch (2002). NCP is measured by an index, NCPI, defined as the geopotential height (at the 500 hpa level) difference between the two poles of the NCP. The pattern is found to have three phases, the positive (NCP+), the negative (NCP-) and the neutral one when the pattern is not dominant. During NCP-, there is an increased southwesterly anomaly circulation towards the Balkans, western Turkey and the Middle East, causing above normal temperature and below normal precipitation in these regions. The opposite occurs with NCP + episodes.

Although General Circulation Models (GCMs) have already been used to assess present conditions and to predict future ones (Stoner et al. 2009), this study attempts to shed more light to the validation of ECHAM5/MPI GCM (Roeckner et al. 2006) regarding the NAO and NCP teleconnection indices, in both a spatial and temporal scale.

2 Data and Methodology

In this paper, NAO and NCP indices are studied. Firstly, they are calculated for the control run period, 1971–2000, using the NOAA NCEP/NCAR reanalysis data (Kalnay et al. 1996) and then for both the control run and a future period, 2071–2100, from the ECHAM5/MPI simulated model data. Both datasets have a spatial resolution of 2.5°latitude × 2.5°longtitude and model data is provided by the Max Planck Institute (Roeckner et al. 2006).

For the calculation of the NAO index (NAOI) the Iceland-Azores Sea Level Pressure (SLP) data were used and the procedure was similar to that in Rogers (1984). The NCP index (NCPI) was calculated according to Kutiel and Benaroch (2002), using the average geopotential height of the 500 hPa level of two grid points forming each of the two poles, over North Sea and Caspian Sea respectively.

Principal Component Analysis (PCA) was used as a statistical method to identify the existence of spatial patterns. Although for NAO unrotated PCA has shown satisfactory results, for NCP the Varimax method was used, since by maximizing the variance of the square correlation coefficients between each rotated component, it increases the discrimination among the loadings and makes them easier to interpret (Hatzaki et al. 2007).

3 Results

Regarding the spatial distribution of the NAO pattern during the cold period of the year, it seems to be rather well represented by the ECHAM5 GCM. Figure 1 shows the PCA loadings of the SLP (top) -the first factor is presented for each month, accounting for more than 40% of the total variance, and the differences produced by the GCM (middle). It can be seen that the two poles of the teleconnection pattern are represented as areas of low and high significant values respectively. In particular, for January and February, in the simulated dataset, the poles present a shift to

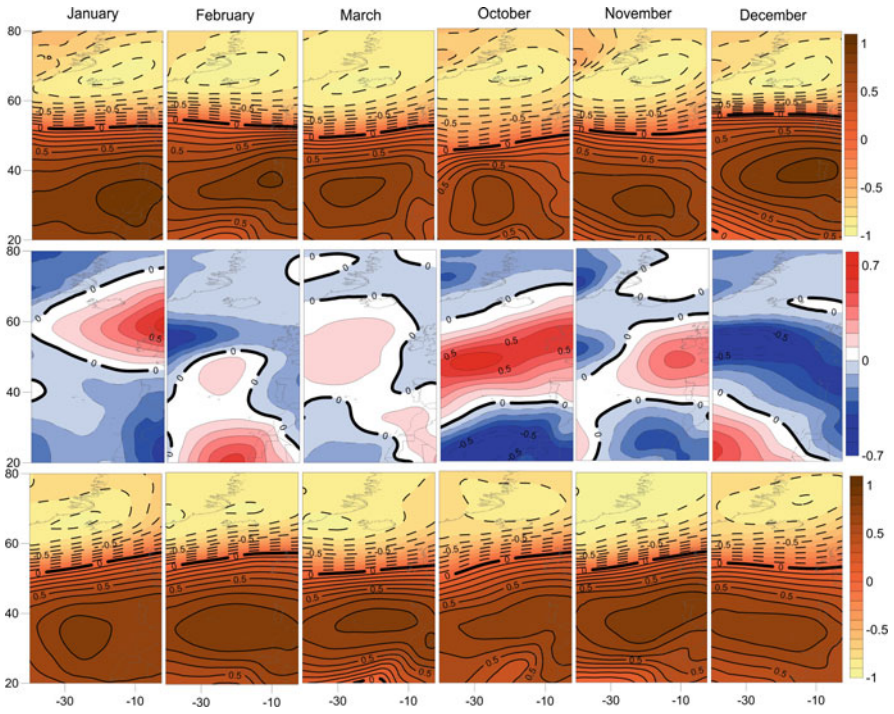

Fig. 1 PCA factor loadings for NCEP reanalysis SLP (*top*), differences between ECHAM5 model SLP and NCEP SLP (*middle*) for the control run period 1971–2000 and loadings for ECHAM5 model simulated SLP for the future period 2071–2100 (*bottom*)

the west of the domain, but the Iceland component is poorly recognized, especially in February. On the other hand, spatial distribution during March is very well represented by the model, as seen by the very small differences on Fig. 1. October and December are also rather well represented, but there is an overestimation and an underestimation of the loadings respectively. For November, although the negative pole over Iceland is well simulated, the southern pole seems to be shifted to the west and outside the limits of the study domain.

The future period chosen to be studied in this paper is 2071–2100. Figure 1 (bottom) shows the PCA loadings maps of the SLP for the cold period, according to the ECHAM5 GCM. In January, the pattern seems very similar to the one simulated by the model for the control run period, with the negative pole over Iceland being more pronounced in the future and this is also evident in February, whereas the pole over Azores is more extended during this month. In March, the pole over Iceland presents a westward shift in the future period, while the south component of the pattern does not seem to change much in position or intensity. On the other hand, the future simulations for October show a more scattered pattern, especially in its south component, where there is no defined pole. The spatial pattern for November also seems very different than that of the present period. The fact that the simulation of the control run period for this month has also presented some discrepancies with the real data, should be taken under consideration. For December a northward shift of the Iceland pole can be noticed.

As long as the temporal scale of the NAO index is concerned (Fig. 2), positive NAO phases prevail during the months of January, October and December. Though, the differences between the percentages of positive and negative phases do not seem important, with the exception of November, where negative phases predominate as compared to the positive ones. The temporal pattern of the NAO index is rather well represented by the ECHAM5 model for the control run period for most months but there is a general underestimation (overestimation) of positive (negative) NAO phases. During the future period, the temporal pattern does not change much but there is an increase (decrease) of positive (negative) NAO phases.

The spatial distribution of the North Sea-Caspian pattern is not so clear, since this teleconnection is not as pronounced as the NAO. Figure 3 shows the PCA loadings of the 500 hPa geopotential heights for January, November and December, but this time a rotation had to be made since the pattern was not evident in the unrotated PCA loadings. In particular, the Varimax rotation was used and then the factors depicting the NCP pattern where chosen, while each of them accounts for 15–20% of the total variance. In January, the ECHAM5 model captures the general pattern of the teleconnection but the pole over North Sea is spatially more extended and weaker. For February (not shown), the simulation is not very good, but what has to be taken into consideration is that even in the NCEP reanalysis geopotential fields, the pattern is not very clear. For March there is a rather good simulation of the positive pole over Caspian Sea, but the northern component of the teleconnection pattern is not so well represented, with its higher values shifted to a much western location, in the Atlantic Ocean. The spatial patterns for October and November are much better simulated, but there is a shift to the western part of the

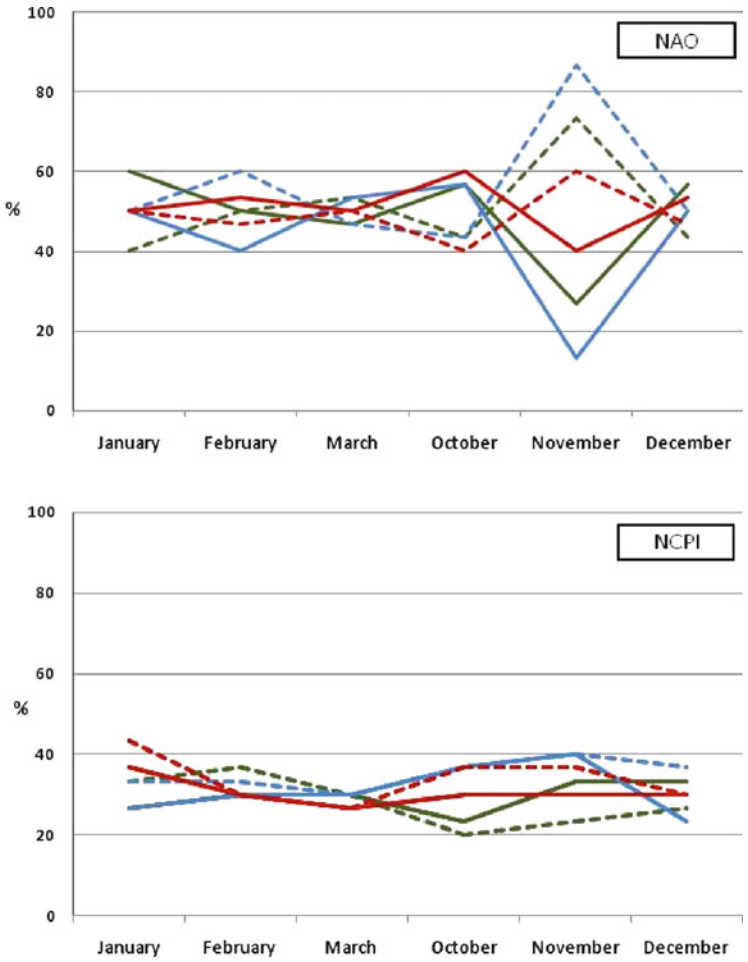

Fig. 2 Percentage of positive (*solid lines*) and negative (*dashed lines*) NAO (*upper*) and NCPI (*lower*) phases for each month and for three different datasets, NCEP reanalysis data (*green lines*), ECHAM5 control run period (*blue lines*) and ECHAM5 future period (*red lines*)

domain, especially of the northern component. In December the dipole is recognized but shifted to the north of the study area and as can be seen in the corresponding map (Fig. 1-middle row), the differences between modeled and reanalysis data are rather high.

Regarding the future simulations, for January the pattern is shifted to the north and east, while for February just the Caspian component seems to be located at a northern position and the dipole is very well pronounced. In March the spatial distribution doesn't change much compared to the model's control run period simulations. During October and November a different dipole seems to be the dominant one, with its northern component over Scandinavia and its southern one

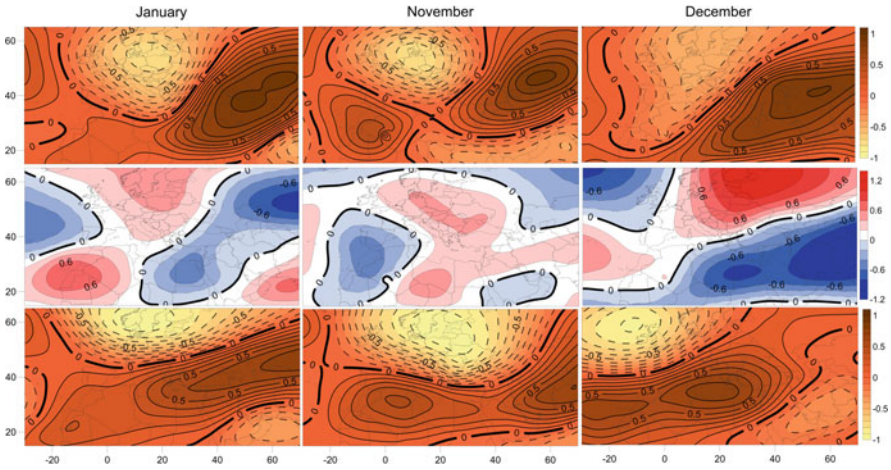

Fig. 3 PCA factor loadings for NCEP reanalysis gph (*top*), differences between ECHAM5 model gph (*middle*) and NCEP for the control run period 1971–2000 and loadings for ECHAM5 model simulated gph for the future period 2071–2100 (*bottom*)

over northern Africa. For December the pattern seems different in comparison to the control run simulation, since the poles have been shifted to the west.

The temporal scale of the NCPI is shown in Fig. 2 (lower). In general, the GCM provides a good simulation of the number of phases, especially for January, February and March. For the remaining months there is an overestimation of both positive and negative phases. In the future period, according to the model's simulations, the temporal variability of NCP is not very different than the present one, but there is a small increase mainly of negative phases during most months.

4 Conclusions

The general spatial pattern of the NAO is well represented by the model for the cold period months of the control run period 1971–2000, a fact that has also been pointed in other studies (Stoner et al. 2009). The main difference with the reanalysis data is a westward shift of the NAO centers of action. For the future period, an increase (decrease) of positive (negative) NAO phases was noticed. This actually indicates that warmer and wetter winters are expected to be more common in northern Europe, while more dry conditions are possible for the Mediterranean throughout the end of the twenty-first century.

NCP pattern is not as clear as NAO, resulting in a weaker representation by the model for the control run period. For the future period 2071–2100, a small intensification of its northern component is expected during most months, along with a general increase of both positive and negative phases, thus a more pronounced circulation resulting in more cases of below and above normal temperatures respectively over the eastern Mediterranean and the Balkans (Kutiel and Benaroch 2002).

References

Hatzaki M, Flocas HA, Asimakopoulos DN, Maheras P (2007) The eastern Mediterranean teleconnection pattern: identification and definition. Int J Climatol 27:727–737. doi:10.1002/joc

Hurrell JW (1995) Decadal trends in the North Atlantic Oscillation: regional temperatures and precipitation. Science 269:676–679. doi:10.1126/science.269.5224.676

Kalnay E et al (1996) The NCEP/NCAR 40-year reanalysis project. Bull Am Meteorol Soc 77:437–470

Kutiel H, Benaroch Y (2002) North Sea-Caspian Pattern (NCP) – an upper level atmospheric teleconnection affecting the Eastern Mediterranean: identification and definition. Theor Appl Climatol 71:17–28. doi:10.1007/s704-002-8205-x

Roeckner E, Lautenschlager M, Schneider H (2006) IPCC-AR4 MPI-ECHAM5_T63L31 MPI-OM_GR1.5 L40 SRESA1B run no.3: atmosphere 6 HOUR values MPImet/MaD Germany. World Data Center for Climate, Max-Planck Institute for Meteorology, Hamburg, Germany

Rogers JC (1984) The association between the North Atlantic Oscillation and the Southern Oscillation in the Northern Hemisphere. Mon Weather Rev 112:1999–2015

Stoner AM, Hayhoe K, Wuebbles DJ (2009) Assesing general circulation model simulations of atmospheric teleconnection patterns. J Climate 22:4348–4372. doi:0.1175/2009JCLI2577.1

Walker GT (1924) Correlations in seasonal variations of weather IX. Mem Ind Meteorol Dept 24:275–332

Atmospheric Circulation Characteristics Associated with high Static Instability Conditions Over the Athens Region

E. Serbis, C.J. Lolis, and P.A. Kassomenos

Abstract The main atmospheric circulation characteristics associated with high static instability conditions over the Athens region are examined for the period 1974–2004. The data used consist of daily (12UTC) values of: (1) 850, 700 and 500 hPa air temperature and dew point from radiosonde measurements at the Athens Hellinikon airport (BADC) and (2) 2.5 × 2.5 grid point 500 and 1,000 hPa geopotential height over the Mediterranean region (NCEP/NCAR), for the period 1974–2004. The stability index K (K-index) is calculated from the radiosonde measurements. Then, 5 % of the days (280 days) with the highest K values (highest instability days) are selected for the cold (16/10–15/4) and the warm (16/4–15/10) period of the year. For these days, a classification is applied to the geopotential height spatial distributions, by using Factor Analysis and K-means Cluster Analysis. The selected days are classified into nine clusters for the cold period and five clusters for the warm period. The mean 500 and 1,000 hPa geopotential height patterns are constructed for the days classified into each one of the clusters. According to the results, the clusters correspond to distinct circulation types associated with high instability conditions over the Athens region.

1 Introduction

Atmospheric stability is one of the most significant meteorological factors affecting weather. High atmospheric stability conditions are generally responsible for sunny and dry weather, while high instability favors convection which is responsible for extreme precipitation events, showers and thunderstorms. The latter phenomena affect significantly human life and their prediction is important. For the

E. Serbis (✉) • C.J. Lolis • P.A. Kassomenos
Laboratory of Meteorology, Department of Physics, University of Ioannina, 45110 Ioannina, Greece
e-mail: esermpis@cc.uoi.gr

C.G. Helmis and P.T. Nastos (eds.), *Advances in Meteorology, Climatology and Atmospheric Physics*, Springer Atmospheric Sciences,
DOI 10.1007/978-3-642-29172-2_101,

quantification of atmospheric stability, static stability indices have been introduced and developed. Radiosonde data can be used for the calculation of a variety of stability indices. Their estimation commonly requires computation based on several thermodynamic parameters (see e.g. Showalter 1953; Jacovides and Yonetani 1990; Lolis 2007) and their value shows the degree of convection which may vary, depending on factors like the synoptic conditions and the geographical position. Regarding the Mediterranean area, atmospheric stability is affected, mostly, by the humidity and thermal characteristics of the earth's surface, as well as the prevailing synoptic conditions. The atmospheric stability in Greece and specifically the case of high instability has been examined in the past from various points of view (see e.g. Dalezios and Papamanolis 1991; Karacostas et al. 1991; Marinaki et al. 2006). The main objective of the present study is the detection of the main synoptic types over the Mediterranean associated with high static instability over Athens.

2 Data and Methodology

2.1 Data

The data used in the present study consist of daily (1200 UTC) values of: (1) radiosonde measurements of 850, 700 and 500 hPa air temperature and 850 and 700 hPa dew point temperature at Hellinikon Athens airport obtained from BADC data base and (2) 1,000 and 500 hPa geopotential height (GH) at 189 grid points ($2.5^\circ \times 2.5^\circ$) covering the Mediterranean region, obtained from the NCEP/NCAR database, for the period 1974–2004 (Kalnay et al. 1996; Kistler et al. 2001).

2.2 Methodology

The daily radiosonde measurements are used for the calculation of K-index for Athens region according to the following formula (see e.g. Jacovides and Yonetani 1990):

$$K = (T_{850} + T_{Dew850}) - (T_{700} - T_{Dew700}) - T_{500} \quad (1)$$

where, T and T_{Dew} are the dry bulb and dew point temperatures respectively, and the subscripts refer to the pressure level in hPa. Generally, values of K greater than + 20°C over a region indicate a high possibility of thunderstorm events (see e.g. Andersson et al. 1989). The expected weather conditions for various classes of K are presented in Table 1.

In order to obtain the mean intra-annual variation of K, the 31-year (1974–2004) mean daily values are calculated for each of the 365 days in a year. Next, the

Table 1 The expected weather for various K-index classes

K-index (°C)	Expected weather
<15	No significant weather
15–25	Possible steady precipitation, isolated thunderstorms
26–30	Probable steady precipitation, widely scattered thunderstorms
31–35	Steady precipitation, scattered thunderstorms
>35	Steady precipitation, numerous thunderstorms

K-index and GH data sets are both separated into two subsets, one for the cold period (16/10–15/4) and one for the warm period (16/4–15/10) of the year (see e.g. Kassomenos et al. 2003). For each period, the days corresponding to the 5% (280 days) with the highest K values are selected. For these days, the corresponding 280 × 189 1,000 and 500 hPa GH data matrices are constructed. A methodology scheme including Factor Analysis (FA) and Cluster Analysis (CA) (Jolliffe 1986; Sharma 1995; Kalkstein et al. 1996) is applied to each of these matrices in order to reveal the main circulation types in the lower and the middle troposphere associated with high instability conditions over Athens for the cold and the warm period of the year. Specifically, S-Mode FA with varimax rotation (Richman 1986) is applied to the 280 × 189 matrices and then K-means CA is applied to the resultant factor scores in order to classify the days into groups characterized by common GH spatial distributions.

3 Results

The mean intra-annual variation of K is presented in Fig. 1 (upper). It is characterized by an early summer maximum and a late winter minimum. The early summer maximum is associated with the intense land warming and the persistence of cold air masses in the middle troposphere, while the late winter minimum is connected to the persistence of cold surface tropospheric layers. The distribution of daily values in the various K-index classes is presented in Fig. 1 (lower). It is seen, that almost 60% of the days are characterized by K lower than 15°C, while K is higher than 30°C in almost 2% of the days.

The application of FA to the daily values of 1,000 and 500 hPa GH leads to seven factors accounting for 85 % of total variance for the warm period and seven factors accounting for 87 % of total variance for the cold period. The application of CA to the resultant factor scores, results in five and nine clusters for the warm and cold period, respectively. The number of days classified into each cluster and the corresponding percentages are presented in Table 2.

For each cluster, the mean GH patterns are constructed for both 1,000 and 500 hPa. Thus the main circulation types associated with high instability conditions in Athens are revealed. In Figs. 2 and 3, the mean 500 and 1,000 hPa GH patterns and the inter-monthly variation of the classified days are presented for one

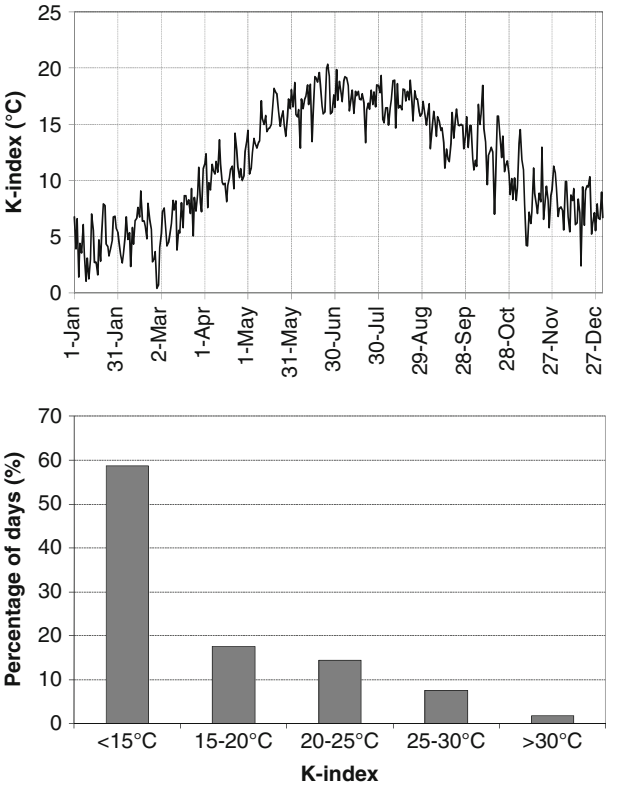

Fig. 1 (*upper*) The mean intra-annual variation of K-index in Athens for the period 1974–2004. (*lower*) The distribution of daily values of K-index in classes

Table 2 Cluster analysis results for the warm and the cold period

Warm period			Cold period		
Cluster	Num. of days	Num. of days (%)	Cluster	Num. of days	Num. of days (%)
1	24	8.6	1	20	7.1
2	33	11.8	2	20	7.1
3	54	19.3	3	21	7.5
4	75	26.8	4	30	10.7
5	94	33.5	5	32	11.4
			6	37	13.3
			7	39	13.9
			8	39	13.9
			9	42	15.1
Total	280	100	Total	280	100

characteristic cluster of each period. According to the results, for most of the clusters of the cold period, the main characteristics of atmospheric circulation associated with high static instability in Athens are a Mediterranean depression

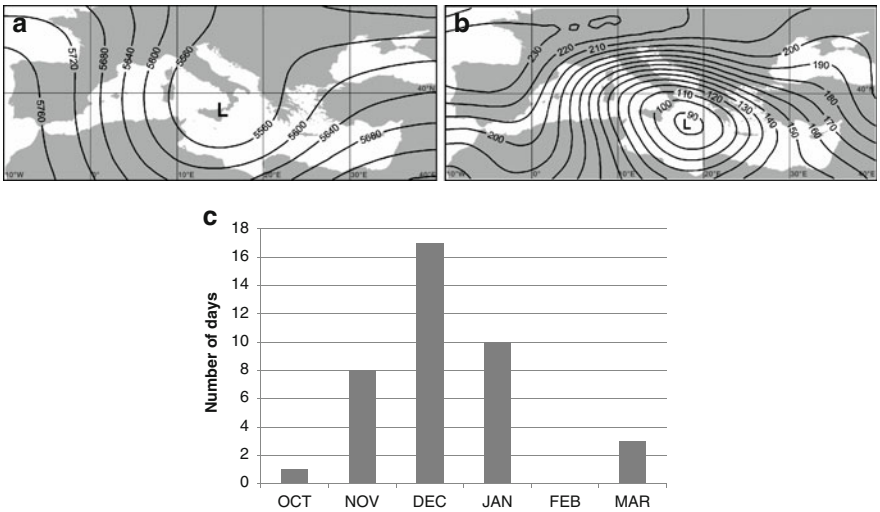

Fig. 2 Cluster 7 of the cold period – The mean geopotential height patterns for (**a**) 500 hPa and (**b**) 1,000 hPa and (**c**) the inter-monthly variation of the number of days

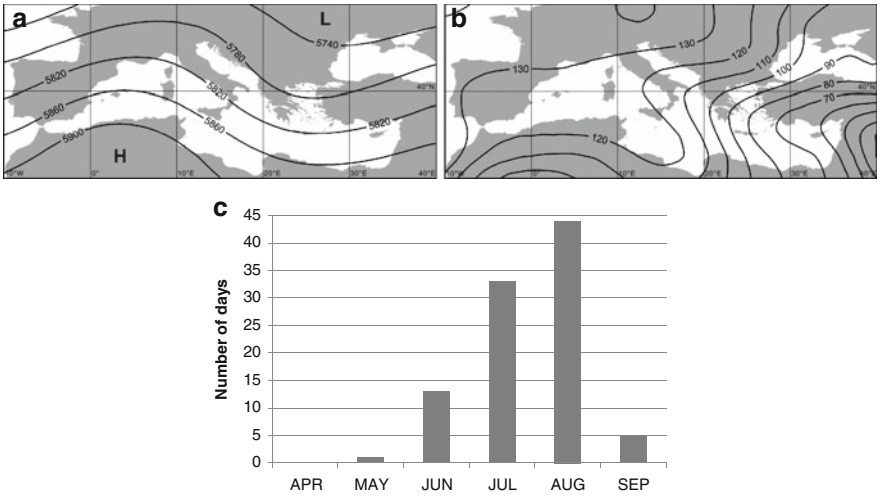

Fig. 3 As in Fig. 2, but for cluster 5 of the warm period

centered over Italy or the Ionian Sea and a warm and humid southeasterly flow over Athens at the surface. For most of the clusters of the warm period, a trough in the middle troposphere is mainly responsible for the high instability conditions, whereas near the surface the etesian winds almost dominate over the Aegean during this season. The differences among clusters refer mainly to the exact position and the intensity of the synoptic systems involved and most of them are characterized by a significant inter-monthly variation.

4 Conclusions

The main circulation types associated with high static instability in Athens are determined for the period 1974–2004 and the following conclusions can be stated:

1. The mean intra-annual variation of K is characterized by a maximum during early summer and a minimum during late winter, being mainly associated with the thermal characteristics of the earth's surface.
2. For the cold period, high instability conditions over Athens are mainly a result of a depression over Italy or the Ionian and a warm and humid south-easterly surface flow over Athens.
3. For the warm period, high instability conditions over Athens are mainly attributed to the presence of an upper air trough over Greece.

References

Andersson T, Andersson M, Jacobsson C, Nilsson S (1989) Thermodynamic indices for forecasting thunderstorms in southern Sweden. Meteorol Mag 118:141–146

Dalezios NR, Papamanolis NK (1991) Objective assessment of instability indices for operational hail forecasting in Greece. Meteorol Atmos Phys 45(1–2):87–100. doi:10.1007/BF01027477

Jacovides CP, Yonetani T (1990) An evaluation of stability indices for thunderstorm prediction in greater Cyprus. Weather Forecast 5:559–569

Jolliffe IT (1986) Principal component analysis. Springer, New York

Kalkstein LS, Nichols MC, Barthel CD, Greene JS (1996) A new spatial synoptic classification: application to air mass analysis. Int J Climatol 16:983–1004

Kalnay E, Kanamitsu M, Kistler R, Collins W, Deaven D, Gandin L, Iredell M, Saha S, White G, Woollen J, Zhu Y, Leetmaa A, Reynolds B, Chelliah M, Ebisuzaki W, Higgins W, Janowiak J, Mo KC, Ropelewski C, Wang J, Jenne R, Joseph D (1996) The NCEP/NCAR 40-year reanalysis project. B Am Meteorol Soc 77:437–471. doi:10.1175/1520-0477(1996)077<0437:TNYRP>2.0.CO;2

Karacostas TS, Kakaliagou OK, Flocas EA (1991) An objective evaluation of two instability indices associated with forecasting convective storms over the north and central Greece. Geofiz 8:51–59

Kassomenos PA, Sindosi OA, Lolis CJ (2003) Seasonal variation of the circulation types occurring over southern Greece: a 50-year study. Clim Res 24:33–46. doi:10.3354/cr024033

Kistler R, Kalnay E, Collins W, Saha S, White G, Woollen J, Chelliah M, Ebisuzaki W, Kanamitsu M, Kousky V, van den Dool H, Jenne R, Fiorino M (2001) The NCEP/NCAR 50-year reanalysis: monthly means CD-ROM and documentation. B Am Meteorol Soc 82:247–267

Lolis CJ (2007) Climatic features of atmospheric stability in the Mediterranean region (1948–2006): spatial modes, inter-monthly, and inter-annual variability. Meteorol Appl 14:361–379. doi:10.1002/met.36

Marinaki A, Spiliotopoulos M, Michalopoulou H (2006) Evaluation of atmospheric instability indices in Greece. European Geosciences Union. Adv Geosci 7:131–135

Richman MB (1986) Rotation of principal components. J Climatol 6:293–335

Sharma S (1995) Applied multivariate techniques. Wiley, New York

Showalter AK (1953) A stability index for thunderstorm forecasting. B Am Meteorol Soc 34:250–252

Construction of Winter Temperature Scenarios over Greece, Using an Alternative Statistical Downscaling Model Based on CCA

A. Skourkeas, F. Kolyva-Machera, and P. Maheras

Abstract In this study, an attempt is made to construct winter temperature scenarios over Greece, using an alternative statistical downscaling (Sd) model based on canonical correlation analysis. The proposed model derived, considering the long-term trends of the predictor variables (1,000–500 hPa thickness field geopotential heights) and the predictand variables (observed mean minimum winter temperatures over Greece). Both the trends of the above sets of variables were eliminated by using linear regression models based on generalized least square estimators. The Sd model is firstly calibrated for the period 1959–1978 and 1994–2000 and then it is validated for the intermediate years 1979–1993. Afterwards, the same model is applied in order to generate a present day scenario using the data from the General Circulation Model (GCM) HadAM3P, for the period 1961–1990 which is the control run period. In conclusion, a large scale output of IPCC – SRES is fed into these statistical models, in order to estimate the above temperatures in 2071–2100. The advantages of the proposed method to classical approach of CCA have been quantified in terms of a number of distinct performance criteria.

1 Introduction

General Circulation Models (GCMs) are one of the most considerable tools in the study of climate change. Even though, these models are thought to be capable of simulating the large-scale state of the climate in a general realistic matter, on the

A. Skourkeas (✉) • F. Kolyva-Machera
Section of Statistics and Operation Research, Mathematics Department, Aristotle University of Thessaloniki, Thessaloniki 54124, Greece
e-mail: askourke@gmail.com

P. Maheras
Department of Meteorology and Climatology, School of Geology, Aristotle University of Thessaloniki, Thessaloniki 54124, Greece

C.G. Helmis and P.T. Nastos (eds.), *Advances in Meteorology, Climatology and Atmospheric Physics*, Springer Atmospheric Sciences,
DOI 10.1007/978-3-642-29172-2_102,

regional climate their results are questionable (Von Storch et al. 1993). The global climate is to a great extent the response to the differential solar forcing, the earth rotation and the large-scale structure of the earth's surface, instead of the regional climates, the response of global climate in details. The idea of Statistical Downscaling (Sd) consists in using the observed relationships between the large-scale circulation and the local climates in order to construct statistical models that could translate anomalies of the large-scale flow into anomalies of some local climates (Von Storch and Navarra 1995).

In this paper, an attempt is made to construct reliable mean minimum winter temperature (hereafter temperatures) scenarios for Greece, using an alternative and more powerful Sd method, based on Canonical Correlation Analysis (Hotelling 1936). Although, many studies have been carried out, CCA in conjunction with EOF analysis (Barnett and Preisendorfer 1987) was found to give more reliable results than the CCA without the filtering of data or the SVD method (Bretherton et al. 1992). The proposed method (method A) consists in: (a) the elimination of statistically significant trend of the predictors and the predictands variables, by fitting a linear regression model using the generalized least squares and (b) the verification of the relationship between the canonical variates, by regression models, assuming that the errors are serially correlated. The findings of the proposed method are compared to those of classical approach (method B, Skourkeas et al. 2010).

2 Data and Methodology

2.1 Data Used and Study Region

The predictors assumed to be the values of the large-scale 1,000–500 hPa thickness field geopotential heights (gpm) from available NCEP/NCAR Re-Analysis archives for the period 1959–2000 (Kalnay et al. 1996). The 154 macro-scale variables covered the extended European area 0E-32.5EE and 30E-55EN with a spatial resolution 2.5E $\times$ 2.5Elat-long. The predictands' field represented by the mean minimum winter temperatures for 20 meteorological stations evenly distributed over Greece, derived from the Official Hellenic Meteorological Service. All the involved variables have been standardized, since anomalies of large-scale and regional variables were correlated to each other. The choice of 1,000–500 hPa thickness as the most appropriate predictor, is due to the fact that these variables are optimally correlated with the temperatures than other climatic parameters (Maheras et al. 2006). The Sd model is firstly calibrated for the period 1959–1978 and 1994–2000 and then it is validated for the intermediate years 1979–1993. Furthermore, simulated data derived from the GCM model HadAM3P, in order to generate a present day scenario for 1961–1990 (control run period). Finally,

an application of a large-scale output of IPCC-SRESS (A2, emission scenario, Cubasch et al. 2001) is carried out for estimating the temperatures over Greece, in 2071–2100.

2.2 The Proposed Statistical Method

A trend is a significant change over time exhibited by a random variable, detectable by statistical parametric and non-parametric procedures. For each predictand or predictor, we estimate the trend coefficient, using a simple linear regression model, so the estimators of the parameters in the model were given by the ordinary least squares method, if the errors are identically independent and normally distributed or by the general least squares method, if the errors are serially correlated (Draper and Smith 1998). De-trending is the statistical or mathematical operation of removing the statistically significant at 0.05 (hereafter st. sign.) trends from the series. De-trending is often applied to remove a feature thought to distort or obscure the relationships of interest.

The adapted variables are filtered, by retaining only a few leading EOFs, a fact that decreases the number of degrees of freedom in each field and renders the resulting modes more stable with respect to sampling variability. The statistically significant EOFs of each field are related to each other by means of CCA. According to the fact, that (a) the large-scale variables have to be found strongly correlated with the regional variables, (b) the large-scale variables are reliably simulated by the GCMs and (c) the relationship between the predictors and the predictands should be remain valid for future periods (Von Storch et al. 1993), the canonical variate of the predictands could be estimated by the canonical variate of the predictors, using a regression model with errors to be identically and independent normally distributed (ordinary least square estimators) or to be auto-correlated (general least squares estimators).

3 The Validation of the Sd Model (1979–1993)

From Table 1 (2a, 2b), the mean differences between the estimated and the observed temperatures for 20 stations over Greece, using the method A and the method B, are not found to be st. sign. Both, for two methods, in order to account the variability, the variances of the reconstructed temperatures are underestimated and found to be st. sign at most of the stations (Table 1 (3a, 3b)). Correlation coefficients (Table 1 (1a, 1b)) were computed individually for each pair of observations and downscaling values at each station and their values are found to be higher in method A, against to the method B. Finally, looking at the RMSEs (Table 1 (4a, 4b)), the sum of mean squared errors with method A (method B) is 18.12 (19.80), a fact that implies a decrease of 8.5%.

Table 1 Results of the period 1979–1993.Correlation coefficients (1), Mean differences (2), St. Dev. Ratios (3) and RMSEs (4) between the estimated and the observed temperatures with method A (columns a) and method B (columns b). Values in bold are st.sign. at 5% level

Stations	Corr. Coeff. (1a)	Corr. Coeff. (1b)	Mean Diff. (2a)	Mean Diff. (2b)	St. dev. ratios (3a)	St. dev. ratios (3b)	RMSEs (4a)	RMSEs (4b)
Agrinio	**0.61**	**0.59**	−0.09	−0.05	**0.29**	**0.23**	1.739	1.850
Alexandroupoli	**0.63**	**0.62**	−0.12	−0.09	0.71	0.70	1.124	1.135
Athens	**0.72**	**0.67**	−0.05	−0.03	0.66	0.65	0.392	0.441
Elliniko	**0.68**	**0.64**	−0.06	−0.06	**0.55**	**0.54**	0.587	0.637
Heraklio	**0.65**	**0.64**	−0.03	−0.03	**0.33**	**0.33**	0.412	0.420
Ierapetra	0.31	0.38	−0.09	−0.11	0.74	0.62	0.859	0.715
Ioannina	**0.51**	0.44	0.01	0.05	**0.40**	**0.36**	1.372	1.481
Kalamata	0.41	0.22	−0.09	−0.10	**0.36**	**0.53**	0.763	0.953
Kerkyra	**0.62**	**0.56**	−0.04	0.01	**0.35**	**0.40**	1.227	1.270
Kozani	**0.76**	**0.67**	−0.01	0.06	0.64	0.73	0.395	0.522
Kythira	**0.65**	**0.66**	−0.07	−0.03	0.73	0.75	0.397	0.388
Larissa	**0.48**	0.37	−0.01	0.01	**0.15**	**0.15**	1.713	1.778
Mylos	**0.69**	**0.63**	−0.06	−0.08	0.71	0.72	0.329	0.385
Mytilini	**0.71**	**0.71**	−0.14	−0.15	0.76	0.81	0.672	0.682
Naxos	**0.74**	**0.72**	−0.05	−0.02	**0.50**	**0.50**	0.266	0.275
Rhodes	**0.55**	**0.66**	−0.08	−0.08	0.61	**0.53**	0.602	0.510
Samos	**0.71**	**0.61**	−0.07	−0.13	**0.54**	0.65	0.541	0.662
Skyros	**0.64**	**0.68**	−0.08	−0.08	**0.48**	**0.05**	0.678	0.635
Tripoli	0.23	0.31	−0.02	0.01	**0.34**	**0.05**	1.680	1.704
Thessaloniki	**0.63**	**0.55**	−0.01	0.05	**0.52**	**0.57**	0.798	0.901

4 The Construction of a Present Day Scenario (1961–1990)

For the baseline period, even though both methods have revealed reliable representation of the mean differences between the simulated and the observed temperatures for 20 stations over Greece, the lower differences have been noticed at most of the stations, following the proposed method. (Table 2 (1a, 1b)).

Moreover, looking at Table 2 (2a, 2b), all the variance rations of the simulated to the observed temperatures are found to be st. sign., using both methods, a fact that implies the weakness of the Sd models, in order to capture the variability of the simulated temperatures.

5 The Construction of an Emission ScenarioA2 (2071–2100)

Finally, from Table 2 (3a, 3b) it is derived that for the period 2071–2100, using the method A, the average temperature response is 1.12EC, compared to 1.22EC with method B, i.e. a reduction of 8.2%. The range of the estimated temperatures (method A) is found to be more narrow than the corresponding with method B,

Table 2 Results of the scenarios. Mean differences (1), St. Dev. Ratios (2) between the simulated and the observed temperatures for 1961–1990 with method A (columns a) and method B (columns b). Mean differences (3), St. Dev. Ratios (4) between the simulated and the estimated temperatures for 2071–2100 with method A (columns a) and method B (columns b).Values in bold are st.sign. at 5% level

Stations	1961–1990				2071–2100			
	Mean Diff. (1a)	Mean Diff. (1b)	St. dev. ratios (2a)	St. dev. ratios (2b)	Mean Diff. (3a)	Mean Diff. (3b)	St. dev. ratios (4a)	St. dev. ratios (4b)
Agrinio	0.25	0.1	**0.59**	**0.35**	**1.53**	**1.47**	0.96	1.02
Alexandroupoli	0.26	0.24	**0.57**	**0.44**	**1.58**	**1.71**	0.97	0.95
Athens	0.20	0.20	**0.65**	**0.52**	**1.07**	**1.21**	0.97	0.93
Elliniko	0.20	0.15	**0.63**	**0.47**	**1.11**	**1.18**	0.97	0.98
Heraklio	0.15	0.16	**0.58**	**0.49**	**0.86**	**1.00**	0.97	0.94
Ierapetra	0.18	0.28	**0.45**	**0.55**	**1.38**	**1.68**	0.95	0.92
Ioannina	0.23	0.26	**0.64**	**0.44**	**1.09**	**1.31**	0.94	0.90
Kalamata	0.15	−0.01	**0.50**	**0.38**	**1.14**	**1.02**	0.97	1.05
Kerkyra	0.22	0.28	**0.63**	**0.54**	**1.14**	**1.38**	0.96	0.89
Kozani	0.19	0.38	**0.56**	**0.61**	**0.84**	**1.22**	0.93	0.89
Kythira	0.14	0.18	**0.58**	**0.60**	**0.85**	**1.01**	0.98	0.90
Larissa	0.26	0.27	**0.63**	**0.44**	**1.23**	**1.45**	0.94	0.91
Mylos	0.16	0.12	**0.58**	**0.48**	**0.99**	**1.06**	0.98	0.97
Mytilini	0.18	0.07	**0.54**	**0.45**	**1.35**	**1.30**	0.98	1.02
Naxos	0.15	0.20	**0.60**	**0.61**	**0.86**	**1.02**	0.97	0.90
Rhodes	0.16	0.21	**0.58**	**0.59**	**1.01**	**1.17**	0.98	0.91
Samos	0.22	−0.13	**0.45**	**0.44**	**1.39**	**1.07**	0.98	1.07
Skyros	0.15	0.07	**0.57**	**0.39**	**0.96**	**0.93**	0.97	1.00
Tripoli	0.17	0.06	**0.56**	**0.25**	**0.88**	**0.82**	0.93	1.00
Thessaloniki	0.23	0.36	**0.63**	**0.57**	**1.04**	**1.40**	0.93	0.89

since the first (second) one is 0.84EC (0.82EC)–1.58EC (1.71EC). Additionally, in both methods, the variability at all stations was found to be well simulated (Table 2 (4a, 4b)). Method A seems to give more homogeneous results than the method B, since the range of st. deviations in method B is wider than the range in method A.

6 Concluding Remarks

A framework for developing a temperature scenario for the future period, using a new Sd approach, based on CCA, concerning the de-trending of the predictor and the predictand variables and the detailed relationship between the canonical variates, has been introduced. As it seems from the validation and the control run period of the model, the trend factor plays an important role in the construction of the temperature scenarios. Basic point is that the sum of the mean squared errors in method A was reduced by 8.5%. From the future scenarios, the average temperature

response was reduced by 8.2%, according to the method A. In order to improve the Sd models, more robust and resistant estimators could be used to assess the relationship between the two fields.

References

Barnett T, Preisendorfer R (1987) Origin and levels of monthly and seasonal forecast skill for United States surface air temperatures determined by canonical correlation analysis. Mon Weather Rev 115:1825–1850. doi:10.1175/1520-0493(1987)115<1825:OALOMA>2.0.CO;2

Bretherton CS, Smith C, Wallace J (1992) An intercomparison of methods for finding coupled patterns in climate data. J Clim 5:541–560. doi:10.1175/1520-0442(1992)005<0541:AIOMFF>2.0.CO;2

Cubasch U, Meehl GA, Boer GJ, Stouffern MD, Noda A, Senior CA, Raper S, Yap KS (2001) Projections of future climate change. In: Houghton JT et al. (eds) IPCC WGI TAR. The Scientific Basis, pp 525–582, Cambridge University Press, NY

Draper NR, Smith H (1998) Applied regression analysis, 3rd edn. Wiley, New York

Hotelling H (1936) Relations between two sets of variates. Biometrika 28(3/4):321–377. doi:10.2307/2333955

Kalnay E, Karamitsou M, Kistler R et al (1996) The NCEP/NCAR 40-year reanalysis project. Bull Am Meteorol Soc 77:437–471

Maheras P, Flocas H, Tolika K, Anagnostopoulou C, Vafiadis M (2006) Circulation types and extreme temperature changes in Greece. Clim Res 30:161–174. doi:10.3354/cr030161

Skourkeas A, Kolyva-Machera F, Maheras P (2010) Estimation of mean maximum summer and mean minimum winter temperatures over Greece in 2070–2100 using statistical downscaling methods. Euro As J Sustain Dev Policy 2:33–44

Von Storch H, Navarra A (1995) Analysis of climate variability: application of statistical techniques. Springer, Berlin

Von Storch H, Zorita E, Cubasch U (1993) Downscaling of global climate change estimates to regional scales. An application to Iberian rainfall in wintertime. J Clim 6:1161–1171,10.1175/1520-0442(1993)006<1161:DOGCCE>2.0.CO;2

Climate Variability and Water Mass Formation in the Eastern Mediterranean Sea

S. Sofianos, V. Vervatis, N. Skliris, S. Somot, A. Lascaratos, and A. Mantziafou

Abstract Recent changes of the thermohaline circulation in the Eastern Mediterranean (i.e. the Eastern Mediterranean Transient) and older observations of the thermohaline structure of the Aegean-Levantine region (with events of dramatic changes of deep water characteristics) reveal the very sensitive character of the regional thermohaline circulation pattern. This and the long term variability of seawater characteristics in various Mediterranean basins show that the deep water mass formation processes in the region can be greatly affected by climate variability and the characteristics of the extreme atmospheric forcing events. Theoretical work and modeling experiments point out the effectiveness of extreme events and periods of abnormal atmospheric conditions to produce deep waters of different characteristics and different equilibrium depth. Studying the mechanisms involved in the air-sea interaction under extreme event conditions, with available observations and modeling techniques, and monitoring important sites of water mass formation becomes very important for understanding the regional dynamics of the water cycle and their effect on the climate of the whole Mediterranean Sea region.

S. Sofianos (✉) • V. Vervatis • A. Lascaratos • A. Mantziafou
Ocean Physics and Modeling Group, University of Athens, Athens, Greece
e-mail: sofianos@oc.phys.uoa.gr

N. Skliris
Ocean Physics and Modeling Group, University of Athens, Athens, Greece

National Oceanography Center Southampton, University of Southampton, Southampton, UK

S. Somot
Groupe d'Etude de l'Atmosphère Météorologique, Centre National de Recherches Météorologiques, Météo-France, CNRS, Toulouse, France

C.G. Helmis and P.T. Nastos (eds.), *Advances in Meteorology, Climatology and Atmospheric Physics*, Springer Atmospheric Sciences,
DOI 10.1007/978-3-642-29172-2_103,

1 Introduction

The Mediterranean Sea became a focal point of oceanic research during the last decades due to the discovery of an abrupt change in the thermohaline circulation pattern (Roether et al. 1996), namely the Eastern Mediterranean Transient (EMT). In contrast to the classical picture of the regional thermohaline circulation, the Aegean Sea became the major source of deep waters in the Eastern Mediterranean, with large amount of very dense waters outflowing and filling the deeper parts of the Eastern Mediterranean basins. Apart from trying to understand and explain the particular feature of climatic shift, the oceanographic community started posing questions on the sensitivity of the thermohaline circulation and the mechanisms involved. The effects of atmospheric forcing as well as the role of internal modes of variability are becoming major issues of oceanographic research, with special attention to the Eastern Mediterranean circulation.

The main purpose of the present paper is to investigate the dynamics of the Aegean-Levantine marine system during the EMT, using (recent and older) observed data of the deep-water thermohaline characteristics and a high-resolution ocean model coupled with the ARPERA dataset (Herrmann and Somot 2008). The investigation focuses on the mechanisms and the evolution of the thermohaline variability, along with the thermohaline coupling patterns between the two major basins.

2 Evolution of the Deep Water Thermohaline Characteristics

Although deep-water observations are difficult and costly, the accumulation of data from various expeditions during the last decades started revealing very interesting patterns of variability in the deep parts of the Eastern Mediterranean Sea. Figure 1 presents the yearly averaged temperature and salinity characteristics in the Levantine and Southern Aegean basins, derived from historical observations (MEDAR Group 2002), at the level of 2,000 and 1,000 m, respectively. These are the levels representing the deepest parts of the basins, which at the same time include statistically significant numbers of observations.

The time series of the thermohaline properties is characterized by episodic variability. The last event (early 90s) and most prominent corresponds to the EMT, while another episode can be located during the previous decades (1965–1975). Although the temperature and salinity changes follow a different pattern, indicating different mechanisms of variability, they both establish the idea that the thermohaline circulation is prone to intense changes and thus sensitive to external and internal modes of variability. In order to explore the mechanisms involved numerical model techniques are applied to the regional dynamics, at interannual time scales.

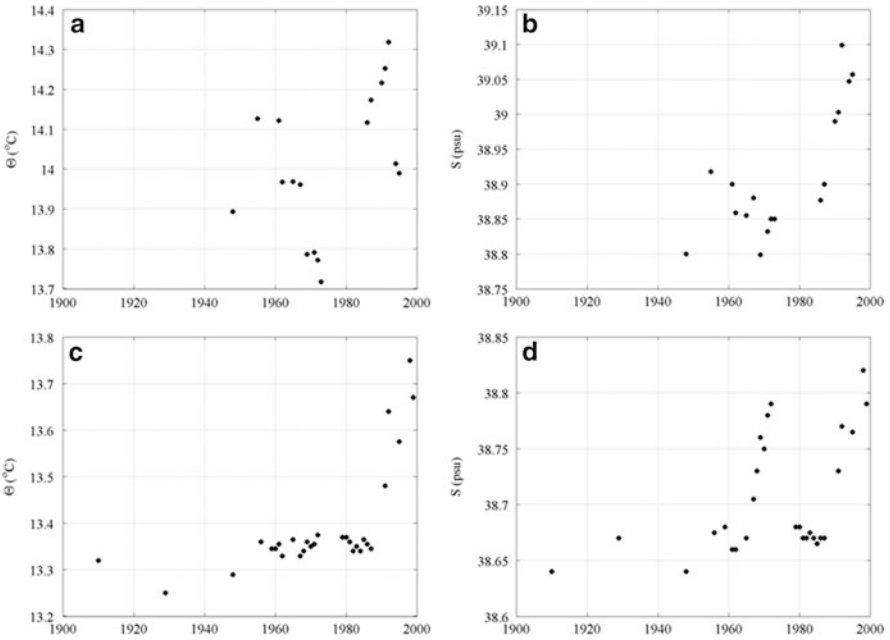

Fig. 1 Salinity and temperature evolution of the Cretan Sea 1,000 m (**a** and **b**) and Levantine 2,000 m (**c** and **d**)

3 Model Configuration

The ALERMO ocean model (Korres and Lascaratos 2003) has been used to deliver datasets filling the observational gaps. The domain covers the eastern part of the Mediterranean Sea and lies between 20 and 36.4°E and 30.7–41.2°N, with a horizontal resolution of 1/30th of a degree (~3.5 km). It is one-way nested to the coarse OPAMED model described in details in Somot et al. (2006) and incorporates a 6-hour atmospheric forcing provided from the ARPERA dataset (Herrmann and Somot 2008) for the 1960–2000 period.

4 Results

There is a clear evidence of a close relationship between latent heat-evaporation associated with intense northerly winds as the main mechanism of the buoyancy loss in the eastern Mediterranean (Fig. 2). These strong northerlies affect the Aegean and the northwestern Levantine. During extreme winters the buoyancy loss reaches 1.5 $\times$ 10−7 m^2/s^3 and the latent heat loss reaches 160 W/m^2.

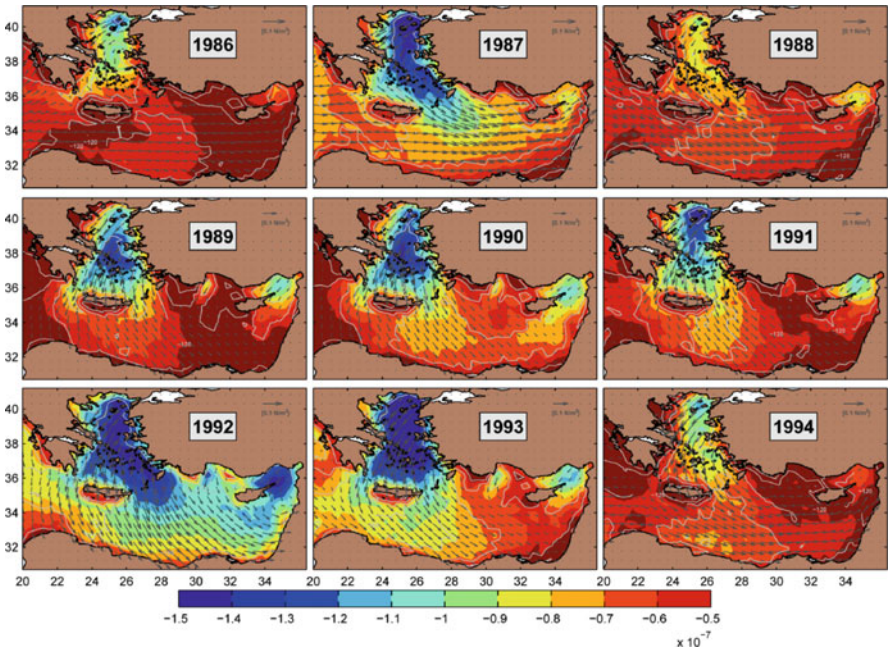

Fig. 2 Winter buoyancy flux (m^2/s^3) and wind stress (*dark gray arrows*) scaled in 0.1 N/m^2

The Dense Water Formation (DWF) processes visualized from the isopycnal outcropping of 29.2–29.3 kg/m^3, are dictated both by shelf and open ocean convection (Fig. 3). Shelf convection occurs in Lemnos-Lesvos plateau and in Cyclades plateau, while open ocean convection appears in central Cretan, Chios and Skyros dominated by equivalent cyclones (Vervatis et al. 2011). The extreme EMT winters are the 1987, 1989, 1990, 1992–1993. During the 1986 winter most of the Aegean concavities were filled with $\sigma_\Theta > 29.2$ kg/m^3, whereas in the sea-bed of the north-central Aegean lied a thin layer of $\sigma_\Theta > 29.3$ kg/m^3 trapped in Chios and Lemnos basins. These results deviate significantly from previous EMT studies (Nittis et al. 2003; Beuvier et al. 2010), with smaller quantities and less dense waters. However, Vervatis et al. (2011) using historical observations (MEDAR Group 2002), showed that prior to the EMT initiating DWF events in March 1987, the Lemnos basin deep layers were filled with water of $\sigma_\Theta > 29.3$ kg/m^3. Furthermore, they argued of an intermediate coupling across the Aegean sub-basins adequately reproduced from this modeling study. In addition, they introduced a possible replenishing mechanism of the deep layers under extreme DWF for the north and south Aegean, whereas for the central Aegean the V-shaped seabed allowed easier deep water replenishment by the thermohaline cell. Consequently, the deep layer replenishment introduces a dense water coupling through intermediate layers to the adjacent north and south Aegean basins, especially in the year following the extreme cascading events. This coupling appears to be straightforward in the north-central Aegean region, since both isopycnal lines of 29.2 and 29.3 kg/m^3 outcrop in

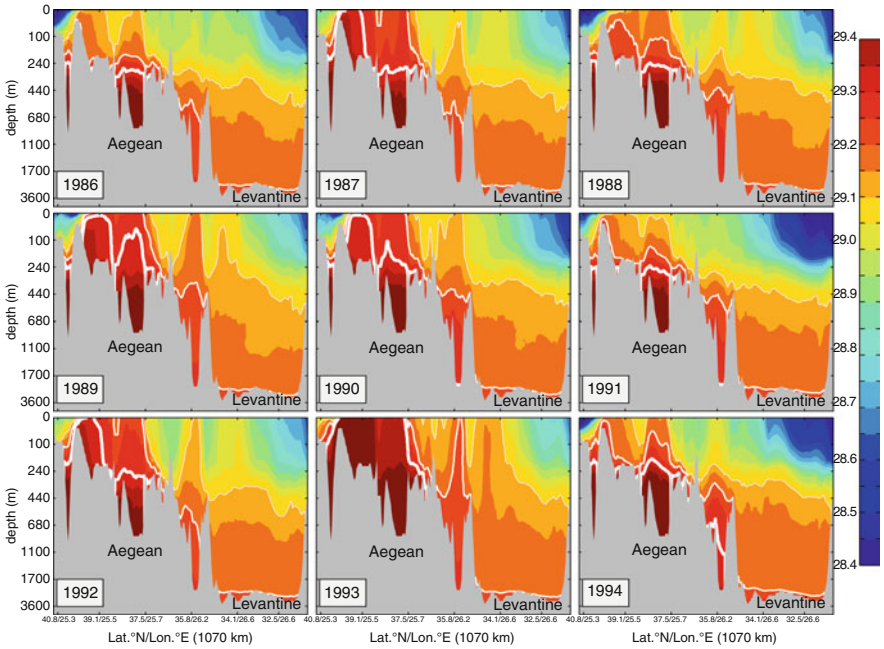

Fig. 3 Meridional transect of winter σ_Θ (kg/m^3) across the Aegean-Levantine basins. White contours are plotted at 29.2 kg/m^3 (*thin line*) and at 29.3 kg/m^3 (*thick line*)

Lemnos-Lesvos plateau and descend in Lemnos basin, while the south-central coupling appears to be more complex due to the irregular seabed. The bottom density of the central basin it is constantly higher than that in the south Aegean while the south Aegean does not form dense waters of 29.3 kg/m^3 or higher. Therefore it seems that the deep waters of the central basin act as a reserve supply of dense water for the deeper part of the southern basin.

Oceanographers have long puzzled how the Aegean managed to deliver such huge volumes of dense waters, determining the new state of the eastern Mediterranean deep layers. The predominance of the Kassos strait dense water outflow is clear in 1986 prior to the transient (Fig. 4). In the pre-EMT period occasional dense water outflow of 29.21 kg/m^3 or higher travelled westward and filled the Ptolemy-Pliny trench outside the Kassos strait. On the other hand, a small amount of the Aegean outflow propagated eastward through Karpathos strait in the Rhodes basin by diffusive processes or transported by deep eddies. The thermohaline characteristics of the Cretan Deep Water (CDW) outflow through Kassos and Karpathos straits vary in salinity between 38.78 and 38.82°C and 13.53–13.67°C. As the Aegean produced large amounts of dense waters during the severe EMT winters, a gradual change of the Ionian and Levantine deep layers occurred. The onset outflow of Kassos and Karpathos straits quickly filled the eastern Hellenic trench, bounded to the south from the east Mediterranean ridge, so that the flow could pass the sill south of Crete and proceed into the western Hellenic trench. The

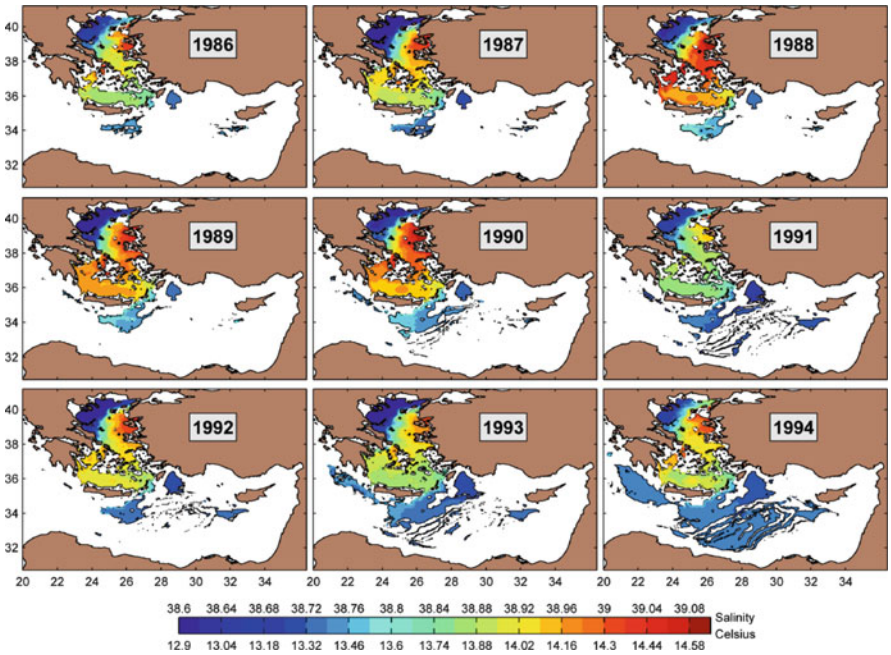

Fig. 4 Annual isopycnal surfaces of $\sigma_\Theta = 29.21$ kg/m^3. Contour colors depict both salinity and potential temperature (in °C) fields

latter argument is in accordance with the Coriolis steering mechanism, forcing the CDW to flow westward along the Cretan continental slope. Finally, the barrier of the east Mediterranean ridge outreached by the isopycnal 29.21 kg/m^3, allowing the Aegean's dense waters outflow to spread into the Levantine, after 1993 (Fig. 4).

5 Conclusions

Even though the EMT is turned out to be among the most studied climatic shifts in the last 20 years, and other modes of deep water climatic variability are now being addressed, there are still emerging novel hypotheses governing this transient, such as:

1. The latent heat/evaporation in the Aegean primarily driven by the wind, whereas in the Levantine SST-Tair differences regulating the air-sea fluxes.
2. Deep water mass formation and the variability of the thermohaline circulation are closely related to the regional climate variability (and related extreme events). It is the extreme EMT winter pulses of buoyancy loss and wind field variability that trigger events of abnormal circulation and water mass formation processes.

3. The north-central Aegean had been already filled up with dense waters ($\sigma_\Theta > 29.3$ kg/^{m3}) prior to the EMT mainly through shelf convection in Lemnos-Lesvos plateau; the perpetual formation above the V-shaped central Aegean, unveils a direct replenishment throughout the deepest channels of the Aegean's north-central region; the south Aegean accumulating dense waters imposed through the Myconos-Ikaria strait; due to complex topography and entrainment processes the central Aegean dense waters reach the deep layers of the south Aegean gaining buoyancy after the winter of 1993.
4. Internal mechanisms of intermediate/deep water exchange between basins can play a significant role in regulating the response of the Eastern Mediterranean Sea to the variability of the atmospheric forcing.

References

Beuvier J, Sevault F, Herrmann M, Kontoyiannis H, Ludwig W, Rixen M, Stanev E, Béranger K, Somot S (2010) Modeling the Mediterranean Sea interannual variability during 1961–2000: focus on the Eastern Mediterranean transient. J Geophys Res 115:C08017. doi:10.1029/2009JC005950

Herrmann MJ, Somot S (2008) Relevance of ERA40 dynamical downscaling for modeling deep convection in the Mediterranean Sea. Geophys Res Lett 35:L04607. doi:10.1029/2007GL032442

Korres G, Lascaratos A (2003) An eddy resolving model of the Aegean and Levantine basins for the Mediterranean forecasting system pilot project (MFSPP): implementation and climatological runs. Ann Geophys MFSPP Part I 21:205–220

MEDAR Group (2002) Mediterranean and black sea database of temperature, salinity and biochemical parameters and climatological atlas [CD-ROM]. Inst. Fr. de Rech. Pour l'Exploit. De la Mer Plouzane France [Available at http://www.ifremer.fr/sismer/program/medar/]

Nittis K, Lascaratos A, Theocharis A (2003) Dense water formation in the Aegean Sea: numerical simulations during the Eastern Mediterranean Transient. J Geophys Res 108:8120

Roether W, Manca BB, Klein B, Bregant D, Georgopoulos D, Beitzel V, Kovacevic V, Luchetta A (1996) Recent changes in eastern Mediterranean deep waters. Science 271:333–335. doi:10.1126/science.271.5247.333

Somot S, Sevault F, Déqué M (2006) Transient climate change scenario simulation of the Mediterranean Sea for the twentieth first century using a high-resolution ocean circulation model. Clim Dyn 27:851–879. doi:10.1007/s00382-006-0167-z

Vervatis VD, Sofianos SS, Theocharis A (2011) Distribution of the thermohaline characteristics in the Aegean Sea related to water mass formation processes (2005–2006 winter surveys). J Geophys Res 116:C09034. doi:10.1029/2010JC006868

Day to Day Variability of Air Temperature over Greece for the Period 1957–2002

V. Stathopoulos, A. Fotiadi, E.E. Houssos, N. Hatzianastassiou, and I. Vardavas

Abstract In the ongoing discussion of global warming and current climatic changes, an open issue is the increased variability of climatic parameters and the changing frequency and intensity of their extreme values. In this framework, the present work deals with the day-to-day variability of maximum (ΔTmax) and minimum (ΔTmin) air temperature and diurnal temperature range (Δ(DTR)) over the Greek area for the period 1957–2002. The data used are daily values from ten stations of the National Hellenic Meteorological Service (N.H.M.S.) which are uniformly distributed over the study area. The absolute values of the considered parameters, for each station, are analyzed in terms of intra-annual and inter-annual variation, whereas the existence of statistically significant trends on a seasonal and annual basis is also examined. The analysis reveals stations with common behaviour regarding temperature variability mainly determined by their geographical location and other geophysical characteristics. In many cases, especially for day-to-day variability of ΔTmin and Δ(DTR) there appear statistically significant trends, mainly increasing, either on a seasonal basis or annual.

V. Stathopoulos • I. Vardavas
Department of Physics, University of Crete, 71110 Heraklion, Crete, Greece

A. Fotiadi (✉)
Laboratory of Meteorology, Department of Physics, University of Ioannina, 45110 Ioannina, Greece

Department of Environmental and Natural Resources Management, University of Ioannina, 30100 Agrinio, Greece
e-mail: afotiadi@uoi.gr

E.E. Houssos • N. Hatzianastassiou
Laboratory of Meteorology, Department of Physics, University of Ioannina, 45110 Ioannina, Greece

C.G. Helmis and P.T. Nastos (eds.), *Advances in Meteorology, Climatology and Atmospheric Physics*, Springer Atmospheric Sciences,
DOI 10.1007/978-3-642-29172-2_104,

1 Introduction

The last decade, there is growing concern that climatic parameters present increased variability and their extremes may be changing in frequency and intensity as a result of human influences on climate. Besides, apart from the observed global warming, climate change may be perceived most through the impacts on extremes. For temperature extremes, minimum (T_{min}) and maximum (T_{max}) land-surface air temperature, the trend from 1950 to 2004, was 0.20°C/decade and 0.14°C/decade, respectively, with a trend in diurnal temperature range (DTR) of 0.07°C/decade (IPCC 2007). However, evidence for changes in observed interannual variability of temperature is still sparse. Especially, studies on the daily time scale are of regional and even local scale. Though they show patterns of changes in temperature extremes consistent with the general warming, uneven trends are observed for night time and day time temperatures or for different seasons.

In several scientific works, temperature trends have been studied for the Greek area, especially for the second half of the last century (e.g. Feidas et al. 2004; Philandras et al. 2008; Kioutsioukis et al. 2010; Nastos et al. 2011), but there is no respective information about long term temperature variability or it refers to very local scale.

In the present work, the day-to-day variability of daily maximum and minimum air temperature (ΔT_{max} and ΔT_{min}) and diurnal temperature range (Δ(DTR)) is studied for the period 1957–2002, based on daily values from ten stations which are uniformly distributed over Greece. Analysis is conducted in terms of intra-annual and inter-annual variation, while the existence of statistically significant trends on a seasonal and annual basis is also examined.

2 Data and Methodology

Daily values of surface maximum (T_{max}) and minimum (T_{min}) air temperature for 10 stations of the National Hellenic Meteorological Service (N.H.M.S.) in Greece are used for the period 1957–2002. Table 1 shows the coordinates and altitude of the stations.

Based on T_{max} and T_{min} values, diurnal temperature range (DTR) is also calculated. The day-to-day variability of temperature parameters is estimated as follow: $\Delta X = X_{i+1} - X_i$ where, X is the parameter considered, namely T_{max}, T_{min} and DTR, and i is the day of the year.

In order to examine whether any possible trend in time series is statistically significant, the Mann-Kendall statistic test is applied. In the following, absolute values of the estimated day-to-day variability of temperature parameters (ΔX) are considered.

Table 1 Geographical coordinates and altitude of the ten stations. Climatological mean value for the period 1957–2002 and the corresponding standard deviation are given for each parameter

Station	Lat. (°) N	Long. (°) E	Alt. (m)	Mean ± STD		
				ΔT_{max} (°C)	ΔT_{min} (°C)	Δ(DTR) (°C)
Alexandroupoli	40°51′	25°55′	7	1.88 ± 1.69	2.49 ± 2.05	2.84 ± 2.30
Thessaloniki	40°31′	22°58′	8	1.95 ± 1.67	2.19 ± 1.99	3.00 ± 2.57
Ioannina	39°42′	20°49′	480	1.94 ± 1.88	2.28 ± 1.96	3.03 ± 2.84
Larissa	39°38′	22°25′	73	2.17 ± 1.55	2.31 ± 1.56	3.38 ± 1.80
Mytilene	39°04′	26°36′	3	1.18 ± 1.41	1.74 ± 1.52	2.19 ± 2.04
Andravida	37°55′	21°17′	10	1.54 ± 1.38	1.91 ± 1.65	2.45 ± 2.05
Athens	37°44′	23°44′	28	1.57 ± 1.38	1.70 ± 1.42	2.04 ± 1.71
Tripoli	37°32′	22°24′	644	2.21 ± 1.85	2.38 ± 2.08	3.50 ± 2.97
Naxos	37°06	25°23′	9	1.55 ± 1.72	1.68 ± 1.88	2.25 ± 2.46
Heraklion	35°20′	25°11′	37	1.77 ± 1.83	1.81 ± 1.53	2.35 ± 2.02

3 Results

3.1 Intra-Annual and Inter-Annual Variation

The annual mean (climatological) values of the considered parameters, calculated over the period 1957–2002, summarized in Table 1, show that continental stations present the largest day-to-day variability (>2°C for ΔT_{min} and ΔT_{max} and >3°C for Δ(DTR)). Specifically, Tripoli which is a mountainous station at high altitude appears the greatest temperature variability. Ioannina station with the same geophysical characteristics also presents high values, whereas Larissa which displays the same large day-to-day variability is a continental station at low altitude located in a plain experiencing high temperatures in summer with frequent heat waves and relatively low temperatures in winter. The lowest variability in all parameters is observed at coastal and island stations such as Athens, Andravida, Naxos or Mytilene. However, though Thessaloniki and Alexandroupoli stations are close to sea, they present high variability for all temperature parameters. This can be attributed to cold spells that affect the northern part of Greece especially in winter time, as a result of the strengthening and extension of the Siberian anticyclone over the Balkan Peninsula. Note also that ΔT_{min} is in general higher than ΔT_{max}.

The inter-annual variation of ΔT_{min}, ΔT_{max} and Δ(DTR) for the period 1957–2002 is presented, only for some indicative stations, in Fig. 1 using timeseries of 5-days mean values. On the same plot the intra-annual variation for each year is also shown. All parameters exhibit an intra-annual variation with maximum during the cold period and minimum in summer and especially in August. The period of maximum in the ΔT_{min} seasonal variation corresponds to winter (December to February), but for some stations such as Alexandroupoli, Thessaloniki and Ioannina begins earlier in November. For ΔT_{max}, there are stations (Thessaloniki, Mytilene, Naxos and Heraklion) where the maximum of variability is displaced in spring (March-April), whereas continental stations (Tripoli, Ioannina and Larissa) present a double maximum. The strongest one appears in spring (March-April) and the secondary in autumn (mainly in October). Both maxima are found in the

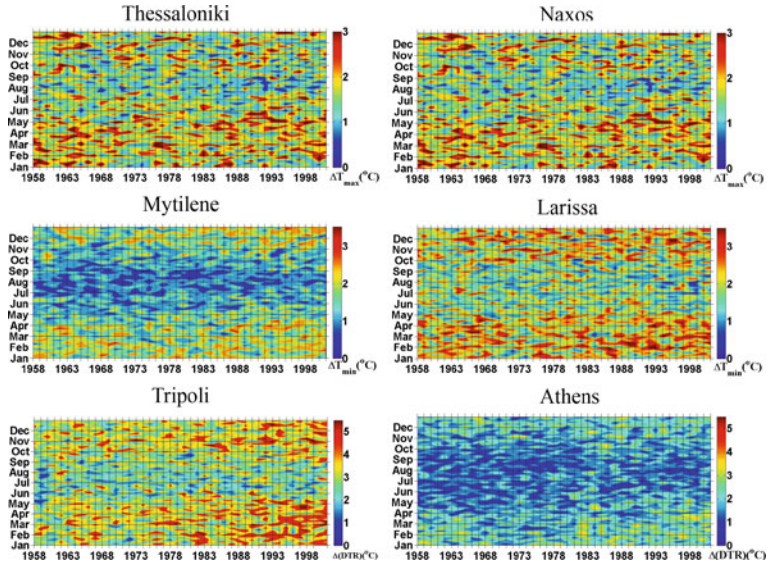

Fig. 1 Inter-annual and intra-annual variation of 5-days mean values of ΔT_{max} (*top panel*), ΔT_{min} (*middle panel*) and Δ(DTR) (*bottom panel*) for some indicative stations. Color bar is in °C

transitional seasons of the year which are characterized by variable weather conditions. The intra-annual variation of the Δ(DTR) seems to be determined by the T_{max} since, except for the Heraklion station, it has common features with ΔT_{max}. The summer minimum of all parameters seasonal variation is quite normal since extension of the subtropical high over Mediterranean basin in this period, ensures stable atmospheric conditions with high temperature and low humidity.

The inter-annual variation of the ΔT_{min}, ΔT_{max} and Δ(DTR) through timeseries of 5-days means, reveals values as high as ~5.5°C for Δ(DTR) and 4°C for ΔT_{min} and ΔT_{max} for many stations. Moreover, some common features can be recognized. For instance, the lower values in January regarding December or/and February, possibly due to the 10-days period on the second half of the month with fair and sunny weather (known as Alkyonides days) associated with persisting anticyclonic conditions over the Greek area. In all stations a period with low values is detected, spanning from late 60s till mid 70s. A respective period of low values of ΔT_{max} is found in the late 80s – early 90s for most of stations, whereas in some of them increased values appear after mid 90s.

3.2 Inter-Annual Trends of Day-to-Day Temperature Variability

In order to investigate the existence of trends in the inter-annual variation of ΔT_{min}, ΔT_{max} and Δ(DTR) over the period 1957–2002, timeseries of annual and seasonal mean values are used. The estimated linear trends are presented in Table 2, where the statistically significant ones (Mann-Kendall test at 95% significance level) are in bold.

Table 2 Linear trends based on annual and seasonal means over the period 1957–2002. Trends found statistically significant are in bold

Station	°C/decade	Year	Winter	Spring	Summer	Autumn
Alexandroupoli	ΔT_{min}	0.015	**0.068**	−0.006	−0.025	0.026
	Δ(DTR)	**0.042**	**0.086**	0.033	0.006	0.043
Thessaloniki	ΔT_{min}	**−0.093**	**−0.083**	**−0.095**	**−0.120**	**−0.072**
	Δ(DTR)	**−0.098**	**−0.110**	−0.026	**−0.150**	**−0.100**
Ioannina	ΔT_{min}	0.008	0.040	0.015	**−0.051**	0.028
	Δ(DTR)	0.020	**0.090**	0.055	**−0.071**	0.009
Larissa	ΔT_{min}	**0.042**	**0.084**	**0.069**	**−0.045**	**0.060**
	Δ(DTR)	**0.074**	**0.099**	**0.160**	−0.039	0.075
Mytilene	ΔT_{min}	**0.075**	**0.100**	**0.083**	**0.030**	**0.087**
	Δ(DTR)	**0.087**	**0.150**	**0.120**	0.030	**0.062**
Andravida	ΔT_{min}	−0.008	**0.045**	0.006	**−0.120**	**0.042**
	Δ(DTR)	0.001	0.031	0.051	**−0.088**	0.009
Athens	ΔT_{min}	**0.065**	0.042	**0.097**	**0.067**	**0.055**
	Δ(DTR)	**0.081**	**0.070**	**0.150**	0.043	**0.057**
Tripoli	ΔT_{min}	**0.130**	**0.230**	**0.150**	−0.016	**0.140**
	Δ(DTR)	**0.220**	**0.340**	**0.310**	**0.033**	**0.190**
Naxos	ΔT_{min}	**−0.079**	**−0.052**	**−0.114**	**−0.076**	**−0.073**
	Δ(DTR)	−0.013	0.023	−0.004	−0.015	−0.056
Heraklion	ΔT_{min}	**0.047**	**0.053**	**0.041**	0.026	**0.067**
	Δ(DTR)	**0.033**	0.007	**0.070**	0.007	**0.051**

For the majority of stations, day-to-day variability of T_{max} does not present any statistically significant trend on annual basis, except for Tripoli and Naxos with a positive trend and Andravida with a negative one (not shown in Table 2 due to lack of space). However, for most of stations an increasing trend (statically significant) appears in spring. ΔT_{min} on the other hand, mostly presents an increasing trend for all timeseries of annual and seasonal means, being stronger for the winter season. Thessaloniki and Naxos stations are exceptions since they appear systematically a decreasing trend (statically significant) on both annual and seasonal basis, whereas trends of summer period become negative for other stations as well. Δ(DTR) presents almost the same trends as the ΔT_{min}, but with fewer stations to have statically significant tendencies on seasonal level. Additionally, Δ(DTR) trends are stronger comparing to these of ΔT_{min} and ΔT_{max}. Note that Tripoli station consistently presents, for all temperature parameters, a statistically significant increasing trend, being usually stronger than these of the other stations (e.g. 0.13°C/decade and 0.22°C/decade for ΔT_{min} and Δ(DTR), respectively.)

4 Conclusions

The day-to-day variability of air temperature parameters, namely maximum (ΔT_{max}) and minimum (ΔT_{min}) temperature and diurnal temperature range (Δ(DTR)), has been studied in this work for 10 stations over the Greek area for

the period 1957–2002. Variability of all temperature parameters is higher for continental stations than for coastal or island regions, except for the two stations of northern Greece, Alexandroupoli and Thessaloniki, which are characterized by relatively large values. All parameters present an intra-annual variation with maximum during the cold period and minimum in summer (August). For continental stations the seasonal variation follows a double oscillation with the main maximum in spring and the secondary in autumn. The investigation for the existence of statistically significant trends shows that day-to-day variability of temperature extremes does not show a homogeneous trend over the Greek area. ΔT_{max} does not present any consistent trend, whereas the day-to-day variability of ΔT_{min} for the most of stations, has been increased from 1957 to 2002 especially in the winter season, inducing also a positive trend to Δ(DTR).

References

Feidas H, Makrogiannis T, Bora-Senta E (2004) Trend analysis of air temperature time series in Greece and their relationship with circulation using surface and satellite data: 1955–2001. Theor Appl Climatol 79:185–208. doi:10.1007/s00704-004-0064-5

IPCC (2007) The physical science basis. Contribution of working group I to the fourth assessment report of the IPCC. In: Forster P et al. (eds) Cambridge University Press, Cambridge, UK and New York

Kioutsioukis I, Melas D, Zerefos C (2010) Statistical assessment of changes in climate extremes over Greece (1955–2002). Int J Climatol 30:1723–1737. doi:10.1002/joc.2030

Nastos PT, Philandras CM, Founda D, Zerefos CS (2011) Air temperature trends related to changes in atmospheric circulation in the wider area of Greece. Int J Remote Sens 32:737–750. doi:10.1080/01431161.2010.517796

Philandras CM, Nastos PT, Repapis CC (2008) Air temperature variability and trends over Greece. Glob Nest J 10:273–285

Investigating with the Ceres-Wheat Model the Impacts of Soil and Climate Factors on Durum Wheat Performance and Earliness in Northern Greece

K. Symeonidis, T. Mavromatis, and S. Kotzamanidis

Abstract Understanding crop-climate relationships are an important step to the development of reliable management systems that could allow yield prediction and quality improvement. In the present study, the impacts of soil and climatic factors on phenological development and productivity of three varieties of durum wheat (*Triticum turgidum,* L. *var. durum*) have been examined. For this purpose, phenological observations and the final harvest from experiments conducted in the farm of the Cereal Institute in Thermi, Thessaloniki, during 2003–2010 were taken. Furthermore, the extent to which the CERES-Wheat model may predict the observed relations between soil-climatic factors and durum wheat has also been investigated. The root mean squared error (RMSE) for end ear growth ranged between 1.13 d and 1.88 d and from 0.52 to 1.27 d for model calibration and validation, respectively. The RMSE of final grain yield was, on average, 0.21 t ha^{-1} for model calibration and validation. This study showed that CERES-Wheat has the capacity for simulating satisfactorily the impacts of soil and climate factors on durum wheat performance and earliness in Northern Greece.

1 Introduction

Durum wheat (*Triticum turgidum,* L. *var. durum*) is one of the most important and valuable combinable cereal crops grown in the world. In the Mediterranean countries the importance of durum wheat is due to the particular utilization characteristic to the region and also because durum wheat constitutes the largest part of the staple food in these countries. In Greece, durum wheat is the main cereal produced, as the cropping area is about 17% of total agricultural area (NSSG 2007).

K. Symeonidis (✉) • T. Mavromatis • S. Kotzamanidis
Department of Meteorology and Climatology-School of Geology, Aristotle University of Thessaloniki, Thessaloniki 54124, Greece
e-mail: kon.simeonidis@windowslive.com

C.G. Helmis and P.T. Nastos (eds.), *Advances in Meteorology, Climatology and Atmospheric Physics*, Springer Atmospheric Sciences,
DOI 10.1007/978-3-642-29172-2_105,

The cultivation of durum wheat is heavily dependent on the prevailing environmental conditions during the crop growth which cannot be modified to a great extent under field conditions. The soil and climate has a substantial effect on both quality and quantity. The optimum level will not be achieved unless researchers manage to make better use of resources and new technology transfer. Researchers can change wheat cultivars, fertilizer levels and agricultural practices to maximize wheat crop yield under the current conditions. However, field experiments are time-consuming, requiring many years of trials. For this reason, researchers need to use a crop simulation model to reduce time, uncertainties and human resources required to decide the best management options for optimizing crop growth and yield.

The crop simulation model selected in this work is the CERES-Wheat model. This model simulates crop growth, development and yield taking into account the effects of weather, genetics, soil (water, carbon and nitrogen), planting, and irrigation and nitrogen fertilizer management (Soltani et al. 2004). The model is designed to have applicability in diverse environments and to utilize a minimum data set of field and weather data as inputs. CERES-Wheat is also one of the main models that have been incorporated in DSSAT v4.03 (Jones et al. 2003).

The aim of this research was to evaluate the capacity of CERES-Wheat to predict phenology stages and yield of wheat crops in a representative region of Central Macedonia.

2 Data and Methodology

CERES-Wheat is calibrated and validated for three durum wheat cultivars (Simeto, Mexicali and Sifnos). Field experiments were conducted at the farm of the Cereal Institute (40° 31′ N; 23° 00′ E; 15 m altitude) in Thermi, during 2003–2010. Field experiments were laid out in randomized complete block design (RCBD) with four replications. Plot in the fields has seven rows at 25 cm apart from each other. Recommended seed rate of 180 kg ha^{-1} was used. Phosphorous and nitrogen applied to all treatment. Diseases, weeds and pest infestations were controlled.

2.1 Data

Input requirements for CERES-Wheat include weather and soil conditions, plant characteristics, and crop management (Hunt et al. 2001). The minimum weather input requirements of the model, daily solar radiation, maximum and minimum air temperature, and precipitation, were obtained from the meteorological station of the experiment site. Soil surface parameters namely soil pH, organic carbon, nitrogen, cation exchange capacity and bulk density were estimated in Soil Science Institute of Thessaloniki. Albedo and drainage rate were determined

according to Jones and Kiniry (1986) and Suleiman and Ritchie (2001), respectively. Soil physical properties, namely the lower limit of soil water content, the water content at drained-upper limit, the saturation water content and the saturated hydraulic conductivity were estimated in Land Improvement Institute of Thessaloniki. Main management input information included plant population, planting depth, and date of planting. The available field observation, for all periods included emergence date, end ear growth date and final grain yield. Additional data and crop stages, including anthesis and physiology maturity date, 1,000 grain weight and individual grain weight, were collected in the last period (2009–2010).

2.2 Methodology

When using a crop model for any application, one first has to estimate the cultivar characteristics if they have not been previously determined. The seven genetic coefficients of the wheat cultivars required by the CERES-Wheat model derived using the experimental data from the 2004–2005, 2005–2006 and 2009–2010 field trials. The coefficients were estimated by adjusting coefficients until close match were achieved between simulated and observed phenology stages and yield (calibration). Then, to validate the prediction capabilities of the model, a separate, independent set of experimental data (2003–2004, 2006–2007, 2007–2008 and 2008–2009), not used for model calibration, was used for validation. To evaluate the association between predicted and observed values, several statistical measures were used including the coefficient of determination (R^2), root mean square error (RMSE), mean bias error (MBE) and mean absolute percentage error (MAPE) as follows:

$$RMSE = \left[\left(\sum_{i=1}^{n} (P_i - O_i)^2 \right) / n \right]^{0.5}$$

$$MBE = \frac{1}{n} \left[\sum_{i=1}^{n} (P_i - O_i)^2 \right]$$

$$MAPE = \frac{1}{n} \left[\sum_{i=1}^{n} \left(\left| \frac{O_i - P_i}{O_i} \right| \right)^2 100 \right]$$

where n is the number of observations, P_i is the model predictions and O_i is the observed value, for day i.

3 Results

Table 1 shows the values of the CERES-Wheat genetic coefficients for the three wheat cultivars obtained by fitting the model against the data from the experimental trials (2004–2005, 2005–2006 and 2009–2010).

These genetic coefficients simulated phenology stages and yield for all wheat cultivars matched well with the observed values of period 2009–2010 (Table 2). The model provided very satisfactory estimates for the end ear growth, flowering and physiological maturating (the predicted dates are same as the observed dates). Also, the model predicted the thousand grain weight very well and the grain yield very closed to observed values.

The simulated days to end ear growth and grain yields under the varied environmental conditions and management during 2004–2005 and 2005–2006 approximated very well with the observed values, as RMSE value ranged between 1.13 and 1.88 days after sowing (DAS). Regression analysis gave a R^2 between 0.976 and 0.988 during calibration. Days to end ear growth ranged between 129 to 160 and 132 to 160 days for observed and simulated, respectively (Fig. 1). With regard to grain yield, the differences between simulated and observed values ranged between 0.13 and 0.21 t ha^{-1}. However, the model tended to overestimate the grain

Table 1 Genetic coefficients of wheat cultivars

Cultivars	[a]P1V	[b]P1D	[c]P5	[d]G1	[e]G2	[f]G3	[g]PHINT
Simeto	62	37	560	14	56	2.1	90
Mexicali	52	32	490	14	58	1.7	91
Sifnos	55	34	500	14	58	2.1	93

[a]P1V: days for optimum vernalizing temperature required to complete vernalization
[b]P1D: percentage reduction in development rate in a photoperiod 10 h shorter than the threshold relative to that at the threshold
[c]P5: grain filling (excluding lag) phase duration (°C d)
[d]G1: kernel number per unit canopy weight at anthesis (number/g)
[e]G2: standard kernel size under optimum conditions (mg)
[f]G3: standard non-stressed dry weight (including grain) of a single tiller at maturity (g)
[g]PHINT: interval between successive leaf tip appearances (°C d)

Table 2 Calibration results and observed values for the examined wheat cultivars and for the period 2009–2010

Parameters	Simeto		Mexicali		Sifnos	
	Obs.	Pred.	Obs.	Pred.	Obs.	Pred.
End ear growth date[a]	152(±1.2[b])	152	147(±0.8[b])	147	148(±0.8[b])	148
Flowering date[a]	153(±1.0[b])	153	149(±1.3[b])	149	149(±1.0[b])	149
Physiological maturing date[a]	187(±0.5[b])	187	183(±0.5[b])	183	181(±1.4[b])	181
Thousand grain weight(g)	52	52	45.5	46	47	47
Grain yield (kg ha^{-1})	3800(±39[b])	3812	3690(±92[b])	3707	3475(±143[b])	3753

[a]Dates are in days after sowing (DAS)
[b]Standard deviation

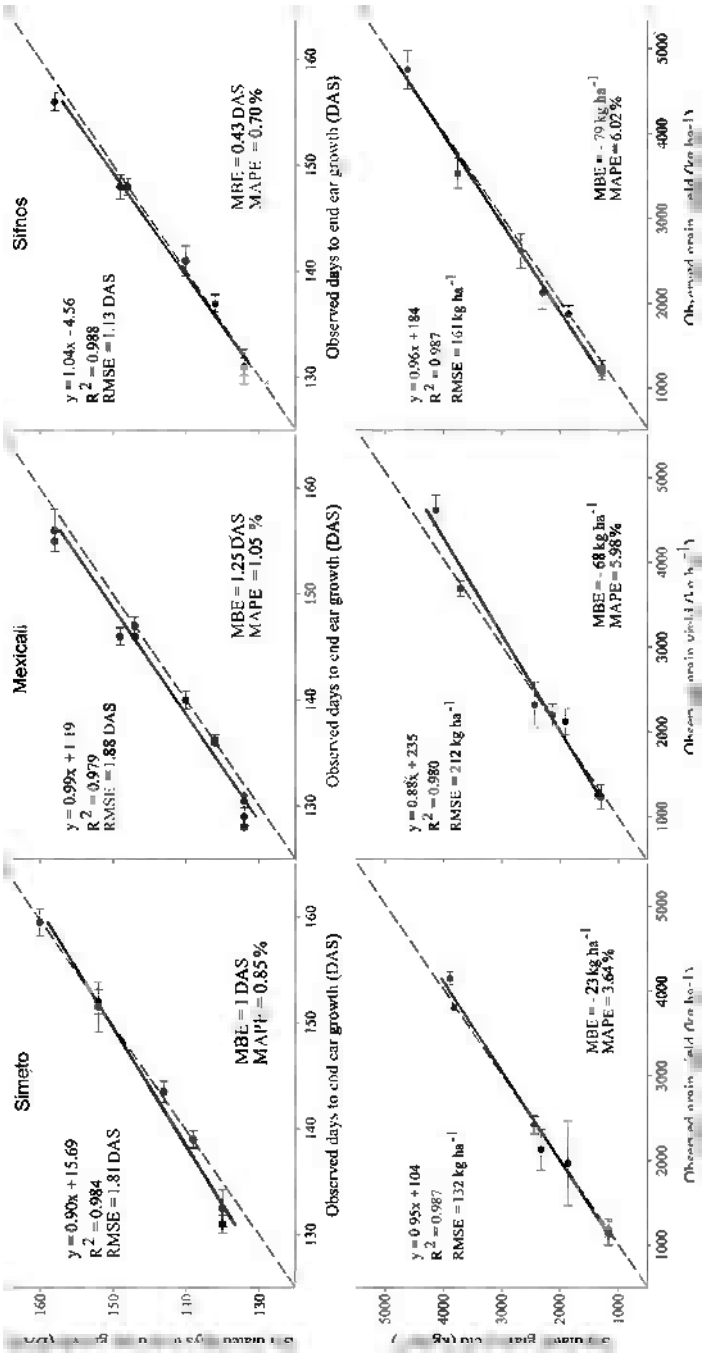

Fig. 1 Regression analysis of simulated and observed values (2004–2005, 2005–2006 and 2009–2010) for (*left*) end ear growth and (*right*) grain yield for the examined wheat cultivars. Bars indicate standard deviations of observations in relation to the average (•). The solid line represents the linear-regression fit to the data, while the dotted lines represent 1:1 linear correlation

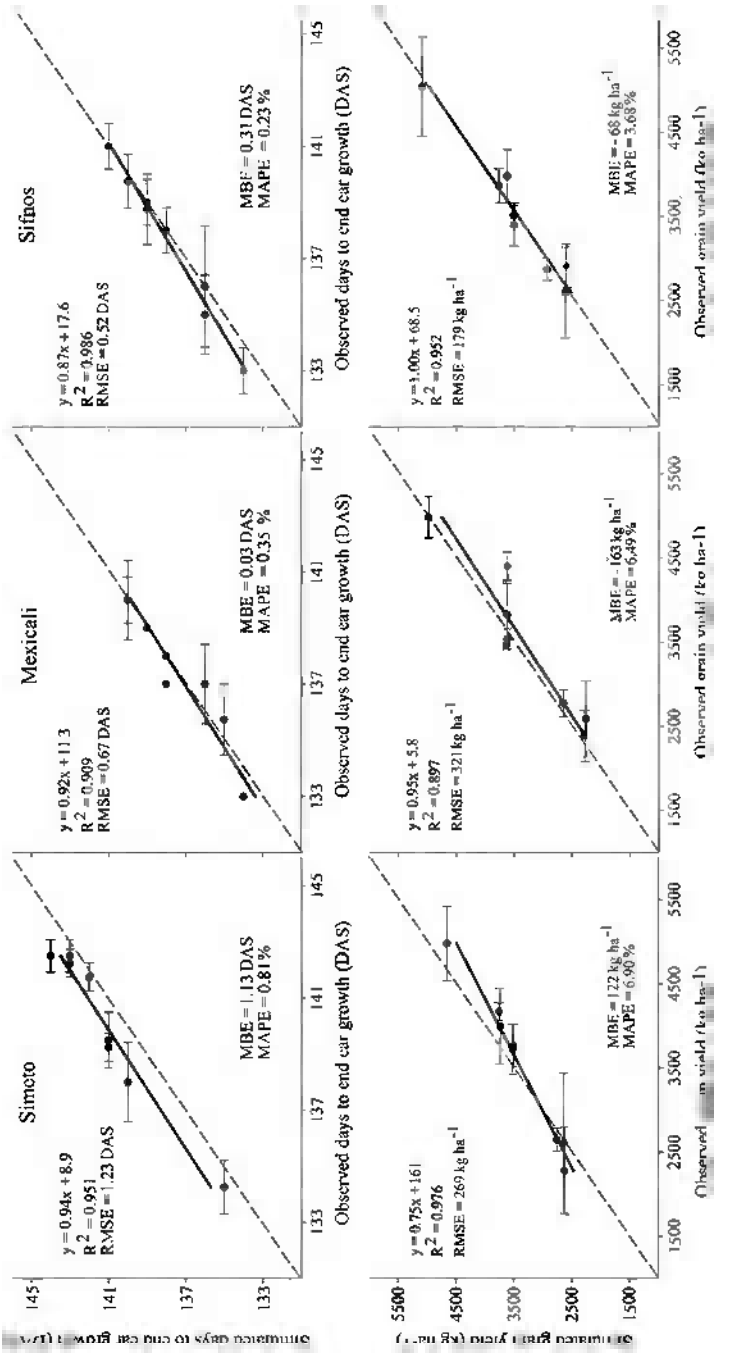

Fig. 2 Regression analysis of simulated and observed values (2003–2004, 2006–2007, 2007–2008 and 2008–2009) for (*left*) end ear growth and (*right*) grain yield for the examined wheat cultivars. Bars indicate standard deviations of observations in relation to the average (•). The solid line represents the linear-regression fit to the data, while the dotted lines represent 1:1 linear correlation

yield when experimental yields were low and to underestimate when experimental yields were high (Fig. 1).

Afterwards, the performance of the CERES-Wheat model was evaluated with the set of data of periods 2003–2004, 2006–2007, 2007–2008 and 2008–2009. Figure 2 shows the regression analysis of simulated and observed values and statistical measures of validation. In conclusion, the model gave good predictions of crop development and final grain yields, and for all cultivars. Prediction of end ear growth was satisfactory for each of the three cultivars with high R^2 (>0.90). The differences between the simulated and observed values for all cultivars were less than 2 days (with RMSE of 0.52–1.27 DAS). Also, the grain yield was underestimated by the model, with MBE value ranged between −68 and −122 kg ha^{-1}. The differences between the simulated and observed yield for all cultivars were less than 7%.

4 Conclusions

The CERES-Wheat model was calibrated and evaluated for durum wheat under the environmental conditions and agricultural practices found in Northern Greece, for which it had not been evaluated yet. The model simulated end of ear growth and grain yield with RMSE less than 2 days after sowing and less than 0.32 t ha^{-1}, respectively. The results of this study confirm that CERES-Wheat has the capacity for simulating satisfactorily the impacts of soil and climate factors on durum wheat performance and earliness in Northern Greece.

References

Hunt LA, White JW, Hoogenboom G (2001) Agronomic data: advances in documentation and protocols for exchange and use. Agr Syst 70:477–492. doi:10.1016/S0308-521X(01)00056-7

Jones CA, Kiniry JR (1986) Ceres-N Maize: a simulation model of maize growth and development. Texas A&M University Press, College Station

Jones JW, Hoogenboom G, Porter C, Boote K, Batchelor W, Hunt LA, Singh U, Gijsman A, Ritchie J (2003) The DSSAT cropping system model. Eur J Agron 18:235–265. doi:10.1016/S1161-0301(02)00107-7

NSSG, National Statistical Service of Greece (2007)

Soltani A, Meinke H, deVoil P (2004) Assessing linear interpolation to generate daily radiation and temperature data for use in crop simulations. Eur J Agron 21:133–148. doi:10.1016/S1161-0301(03)00044-3

Suleiman AA, Ritchie JT (2001) Estimating saturated hydraulic conductivity from soil porosity. Trans ASAE 44(2):235–239

Information System Regarding the Management and Processing of Data Base Software for Applications in Cases of Remote Sensing

A. Theodorou, K. Nicolaides, and F. Tymvios

Abstract Remote sensing is widely used in Synoptic Meteorology and Climatology. This is driving the needs for creating software able to handle, sort, store in suitable manner and process the relevant measurements. The present study refers to the design and construction of such software able to manage, and process all relevant measurements obtained by automatic meteorological stations currently installed at Larnaca and Paphos Int. Airports and by other automatic meteorological stations based elsewhere in Cyprus. The software is based on Visual Basic for Applications and all the products are either in the form of tables, or diagrams or either meteorological codes.

1 Introduction: The Need for Automated Weather Stations

In general, the society and its activities are related to the prevailing weather. In this manner, systematic weather and climate observation and consequently its analysis and forecast comprises a necessity for the day to day human activities. The need for instant weather information is also a request for the modern society.

Therefore, the present meteorological community has been directed towards novel technologies such as digital technology, telemetry and software engineering for creating sensitive automated instrumentation (Automatic Weather Stations, AWS) able to take continuous measurements that are, automatically saved on systems with great storage capacity and instantly available for demanding applications such as nudging into numerical weather prediction models, or early warning systems. The AWS are placed in remote areas with scarce coverage of information where human personnel has limited or difficult access, or in areas where a denser network with frequent measurements is required, such as airports.

A. Theodorou (✉) • K. Nicolaides • F. Tymvios
Meteorological Service, Nicosia, Cyprus
e-mail: atstavrou@gmail.com

C.G. Helmis and P.T. Nastos (eds.), *Advances in Meteorology, Climatology and Atmospheric Physics*, Springer Atmospheric Sciences,
DOI 10.1007/978-3-642-29172-2_106,

2 Automated Weather Stations: Advantages: Disadvantages

AWS possess several advantages when compared with personnel served stations but include also some disadvantages.

Among the advantages are included:

- The ability of high accuracy measurements in a small time step,
- The information is offered in a format ready for insertion into databases
- The relatively small initial cost and often low maintenance costs compared to the traditional observation methods.

The main disadvantage of these systems is their inability for cloud observations, since they are unable to precisely report the total cloud amount and the amount and type of each cloud at different levels (REF). This is a drawback in the case of AWS and this is the main reason the World Meteorological Organization recommends that in synoptic stations with automatic weather stations in operation the staff must serve towards the complement of the automated. This is essentially not a disadvantage for climatological weather stations.

3 Weather Observation Network. The Data Managing System

For the needs of the continuous monitoring of weather a network of 17 AWS was developed in Cyprus, while future plans include the operation of up to 65 stations that will gradually replace the traditional climatological stations. The AWS network is running in parallel with a network of three traditional synoptic stations (Larnaka Int. Airport, Paphos Int. Airport, and Athalassa area, where upper air observation is carried out). Weather information is also obtained from a synoptic station situated in the area of the British military base at Akrotiri, and from an automatic weather climatological station at the top of the Troodos mountainous range, called peak "Olympus", also property of the British Government. Additional weather information's (mainly concerning temperature and precipitation) are available from observations carried out by civilians which have an interest of the weather and are trained as meteorological observers.

3.1 Meteorological and Climatological Parameters. Data Transfer

Real time weather observation is realized through the technology of remote sensing and AWS. The data can be either stored on PCMCIA memory cards mounted on the AWS and collected monthly or transferred automatically to a centrally located information managing system, through analog connection (modems), ADSL internet connection (when available) or mobile connection (GPRS). The encoding format differs with each different type of weather station. In order to shape the

data uniformly, computer programs like Visual Basic (Microsoft Visual Basic Pro. 6.0) are employed, tuned for each station individually. In parallel, the observations are subject on quality control. Past experience shows that errors and missing values are often present in the transmission of data from AWS for computer data collection. Then the encoded data is fed into a new Visual Basic program that undertakes the transformation of meteorological observations in the PLOT format, which is easily recognizable by weather forecasters. Finally the data are stored in a database, easily accessible for recalling historical data.

3.2 The Database

Data collected from the automatic weather stations includes the following:

- Instantaneous temperature, 10-min average temperature and maximum and minimum temperature recorded in the 10 min
- Instantaneous relative humidity and 10-min average relative humidity
- Soil temperature
- Ten-minute average, the instantaneous intensity of the wind and maximum and minimum through the 10 min
- Wind run at 2 and 10 m
- Total solar radiation
- Total sunshine in minutes
- Ten-minute averaged amount of precipitation and intensity
- Instantaneous pressure value, 10-min maximum and minimum pressure values (Visual Basic pro 6.0; Meteorological Office 1982, 1956).

The configuration of each of the AWS differs according to the meteorological interest of the area.

3.3 System Parts

The system used for the management of the data collected is presented in Fig. 1. It consists of a Windows PC equipped with two modems with communication software for data transfer.

The Windows PC is running a stand-alone data quality control, transforms the information in the desired format and delivers the data for visualization of information and the completion of specialized weather forms. The last step is the data storage into a proprietary database for local use and the dissemination of the data into the main database of the Cyprus Meteorological Service (SQL). All the software is written in-house with Visual Basic for Windows. The programs operate autonomously without the need for the Parent Software (Access) and require little power for their customers (Win98, Pentium II and later).

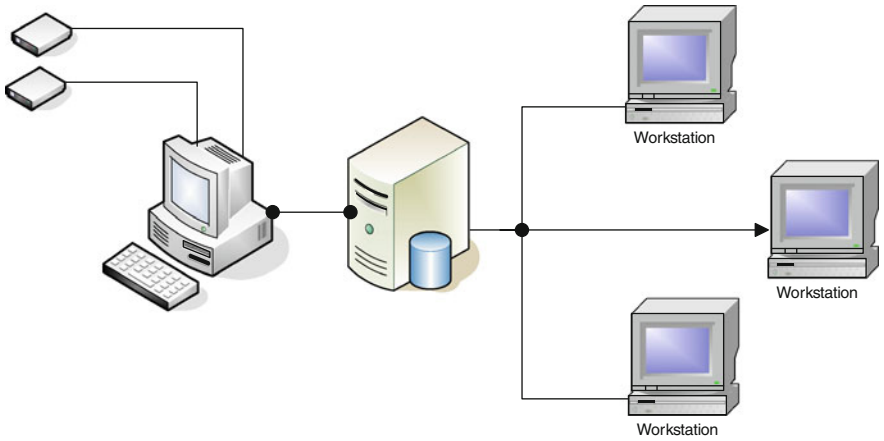

Fig. 1 A representation of the system

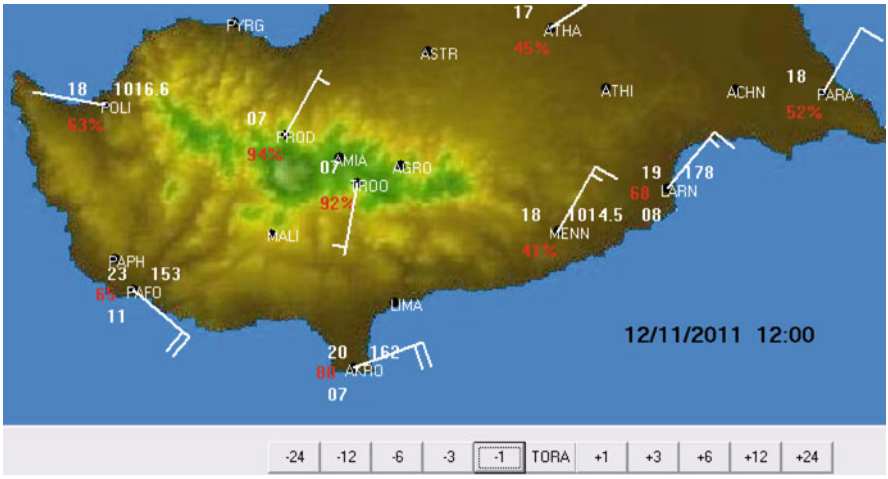

Fig. 2 The image available to the weather forecaster every hour

The data refresh rate is every hour for all automatic weather stations.

3.4 System Products

The system produces an image of the island every hour with the parameters graphically plotted in the WMO format, over the respective AWS positions. Figure 2 represents the image produced by the system which is available to the weather forecaster every hour (WMO 2008, 1987, 1975).

By using the control program the user can monitor the changes of wind, temperature, humidity and temperature (and soil temperature where available) and the heat index for each area. The above data are given in graphs for the last 36 h for quick comparison of the current day with the previous. Furthermore it is possible to navigate and retrieve data for any date in the system. Extreme values for any time which have been recorded by the system are also available on demand. Various climatological reports for the needs of the Climatology department are also prepared automatically and stored.

4 Conclusions. Systems Present Problems, Future Improvement and Development

The system is in operation in Cyprus Meteorological Service for more than 10 years. End users (either forecasters or climatology personnel) have concluded that the system improves their productivity and their ability to understand the weather parameters under focus. The weather forecasters do appreciate and use extensively the graphical products of the system. The benefit of a quick view of the weather as picked up from the entire AWS network (and not only from the three synoptic station) is really appreciable, while the climatology personnel enjoys the ability of the system to collect and store quality data into the database reducing the interference with the data into sampling information for random checks.

Nevertheless, several problems have been found in relation to the developed system such as:

- Several AWS, located in remote areas are difficult to communicate with, having problematic telephone networks.
- Gaps are introduced into the database due to data loss.
- The cost of data acquisition (telephone lines or wireless bandwidth); various routines are designed with linear logic and are not yet optimized in the local database so by increasing the data stored in database results in the increase of the average search time.

To improve and increase the performance of the system the following changes are proposed:

- Increase the stations of the system.
- The local database will be reimplemented in Microsoft SQL to avoid long searches.
- Increase the frequency of data acquisition through extensive usage of wireless technology (cheaper).
- Implement a Web application for visualization.

References

Meteorological Office (1956) Observer's handbook. HMSO, London Her Majesty's Stationery Office, London
Meteorological Office (1982) Handbook of meteorological instruments, 4th edn. Her Majesty's Stationery Office, London
Microsoft Visual Basic Pro 6.0
WMO (1975) International cloud atlas, Volume I, vol 407, Manual on the observation of clouds and other meteors. World Meteorological Organization, Geneva
WMO (1987) International cloud atlas, Volume II. World Meteorological Organization, Geneva
WMO (2008) Aerodrome reports and forecasts, a users' handbook to codes, vol 782, 5th edn. World Meteorological Organization, Geneva

Applications of Semi-Analytical Models for Estimating Soil Temperature

E. Thoma, I.X. Tsiros, S. Lykoudis, and B.E. Psiloglou

Abstract The present study deals with the application of various semi-analytical models to estimate ground temperature profiles. The models are based on the general formula of an analytical model which, considering a quasi steady state system, implements the superposition of annual and daily sinusoidal fluctuations. The models are then developed from the analytical model by replacing the steady state soil temperature with easily obtained daily average temperatures such as the average surface temperature, the average temperature of selected soil depths, the average soil temperature of the considered soil profile and, in the context of minimal data requirements, the average air temperature. Field measurements of soil temperatures at the surface and at various soil depths of the National Observatory of Athens station are used to evaluate the performance of the various models whereas the models' applicability is also discussed.

1 Introduction

Soil temperature and its variations in time and space are very important in describing several physical processes, such as evaporation, chemical reactions, and energy and mass exchange with the atmosphere (Luo et al. 1992), which in turn are of considerable interest to many disciplines ranging from forestry, micrometeorology and climatology to architecture and also building physics (e.g. Santamouris 2007).

E. Thoma • I.X. Tsiros (✉)
Division of Geological Sciences and Atmospheric Environment, Agricultural University of Athens, Iera Odos 75, 11855 Athens, Greece
e-mail: itsiros@aua.gr

S. Lykoudis • B.E. Psiloglou
Institute of Environmental Research and Sustainable Development, National Observatory of Athens, I. Metaxa and V. Pavlou, 152 36 P Pendeli, Greece

C.G. Helmis and P.T. Nastos (eds.), *Advances in Meteorology, Climatology and Atmospheric Physics*, Springer Atmospheric Sciences,
DOI 10.1007/978-3-642-29172-2_107,

The measurement of ground temperature profile is, however, not always easy, thus modeling can be a useful tool for providing knowledge of the diurnal and annual variations of the soil temperature at different depths. Modeling approaches include, in general, analytical, semi-analytical, numerical as well as statistical, Fourier and ANN based, and of course empirical models (e.g. Mihalakakou et al. 1995; Droulia et al. 2008; Yuan et al. 2008; Graham et al. 2010; Mazou et al. 2010). Despite the availability of so many modeling approaches, the balance between the accuracy of the model results and the availability of the required input data is always a major concern.

Analytical models are usually not very demanding in terms of input data, yet they are frequently limited to describing steady state conditions, therefore being unsuitable to describe the temporal evolution of the ground temperature profile. On the other hand, analytical models can be modified so as to include some degree of variation, usually by substitution of a steady state parameter by a dynamically varying counterpart. Following this approach, in this work we attempt to enhance the usability of the deterministic analytical model presented by Droulia et al. (2008). The model is based on a quasi steady state approach that takes into account the superposition of the annual and daily (diurnal) sinusoidal fluctuation around a constant value of the soil temperature.

$$\begin{aligned} T(z,t) = J &+ A_1 \cdot e^{-z/d_1} \cdot \sin\left(\frac{2\pi t}{8760} + \phi_1 - \frac{z}{d_1}\right) \\ &+ A_2 \cdot A_3 \cdot e^{-z/d_2} \cdot \sin\left(\frac{2\pi t}{24} + \phi_3 - \frac{z}{d_2}\right) \\ &- \frac{A_2}{2} \cdot e^{-z/d_3} \cdot \sin\left(\frac{364 \cdot 2\pi t}{8760} - \phi_2 + \phi_3 - \frac{z}{d_3}\right) \\ &- \frac{A_2}{2} \cdot e^{-z/d_4} \cdot \sin\left(\frac{366 \cdot 2\pi t}{8760} + \phi_2 + \phi_3 - \frac{z}{d_4}\right) \end{aligned} \tag{1}$$

$$\begin{aligned} d_1 = \sqrt{\frac{D \cdot 8760}{\pi}}, \quad d_2 = \sqrt{\frac{D \cdot 24}{\pi}} \\ d_3 = \sqrt{\frac{D \cdot 8760}{364\pi}}, \quad d_4 = \sqrt{\frac{D \cdot 8760}{366\pi}} \end{aligned} \tag{2}$$

In (1) and (2), $T(z,t)$ is the soil temperature at depth z and time t (hours), J is the long term steady state soil temperature, D is the soil diffusivity, t is time (hours) and A_1, A_2, A_3, φ_1, φ_2, φ_3 are amplitudes and phase shifts of the annual and diurnal components that can be estimated statistically.

Adopting the long term steady state soil temperature as the body upon which the diurnal and annual cycle variations are applied, limits the usability of this model, notably in cases where it would be more helpful i.e. in cases of incomplete or discontinued databases.

The purpose of this work is then to present simple semi-analytical models based on (1) and (2), incorporating easily available, dynamically varying parameters as replacements for the long term steady state ground temperature. Such models may allow the generation of realistically varying time series of ground temperature profiles.

2 Data and Methodology

2.1 Data

For the purpose of the present study, data for surface and soil temperatures, measured by electronic thermometers were obtained from the meteorological station located at the National Observatory of Athens for the period 1991–2006.

The data refer to hourly measurements in direct contact to bare soil at 0 (surface) 2, 5, 10, 15, 20, 30, 40, and 50 cm. During data recording, errors are introduced due to instrument malfunctions, as well as other factors including maintenance actions and unwanted shading by adjacent structures and vegetation, which mainly influence the outcome of the temperature measurements at the surface.

Therefore, prior to the development of the models, a detailed data quality analysis was performed. Extreme values were tracked and checked for consistency against the data for the rest of the depths at the same hour. Also data, especially surface values, were checked for complying with the expected diurnal variation. The values that were influenced by exogenous factors were considered as missing.

2.2 Methodology

Various semi-analytical models are introduced in an attempt to tackle the lack of temporal variation of the steady state soil temperature, J, which does not allow the use of the analytical model described in (1), in a dynamic manner. Thus, temporal variability is introduced by substituting J with some available or easily obtained hourly or daily temperatures, namely hourly air temperature (Tair), daily average air temperature from 24 hourly values (Tairav), daily average ground temperature from observations at 08:00, 14:00 and 20:00 (entered twice) (Tg3), daily average ground temperature from 24 hourly values (Tgav), and hourly ground temperature at 50 cm (Tg50).

The various models were fitted to the data using non-linear regression analysis. To test the performance of the various models, the fitting was performed on a training data set consisting of the 80% of the original data, whereas a randomly selected 20% of the data was reserved as a validation data set. The random selection was performed on each depth separately and the model developed will be referred

Table 1 Estimation of values and associated standard errors (S.E.) of the various model parameters (final models)

Model	Tair		Tairav		Tgav		Tg3		Tg50	
Parameter	Value	S.E.(±)	Value	S.E.(±)	Value	S.E. (±)	Value	S.E. (±)	Value	S.E. (±)
R^2	0.85		0.89		0.97		0.96		0.89	
A_1	1.594	0.005	1.512	0.004	0.065	0.003	−0.288	0.003	2.703	0.005
A_2	4.275	0.019	5.487	0.014	5.510	0.008	5.657	0.009	5.636	0.015
A_3	1.159	0.006	1.443	0.004	1.439	0.002	1.433	0.002	1.448	0.004
φ_1	4.317	0.003	4.298	0.003	4.189	0.038	4.585	0.009	4.869	0.002
φ_2	−6.513	0.004	−6.486	0.002	−6.483	0.001	−6.494	0.001	−6.498	0.002
φ_3	4.033	0.003	4.184	0.001	4.193	0.001	4.216	0.001	4.196	0.001
D	1.134	0.008	1.899	0.007	1.985	0.004	1.916	0.004	1.903	0.008

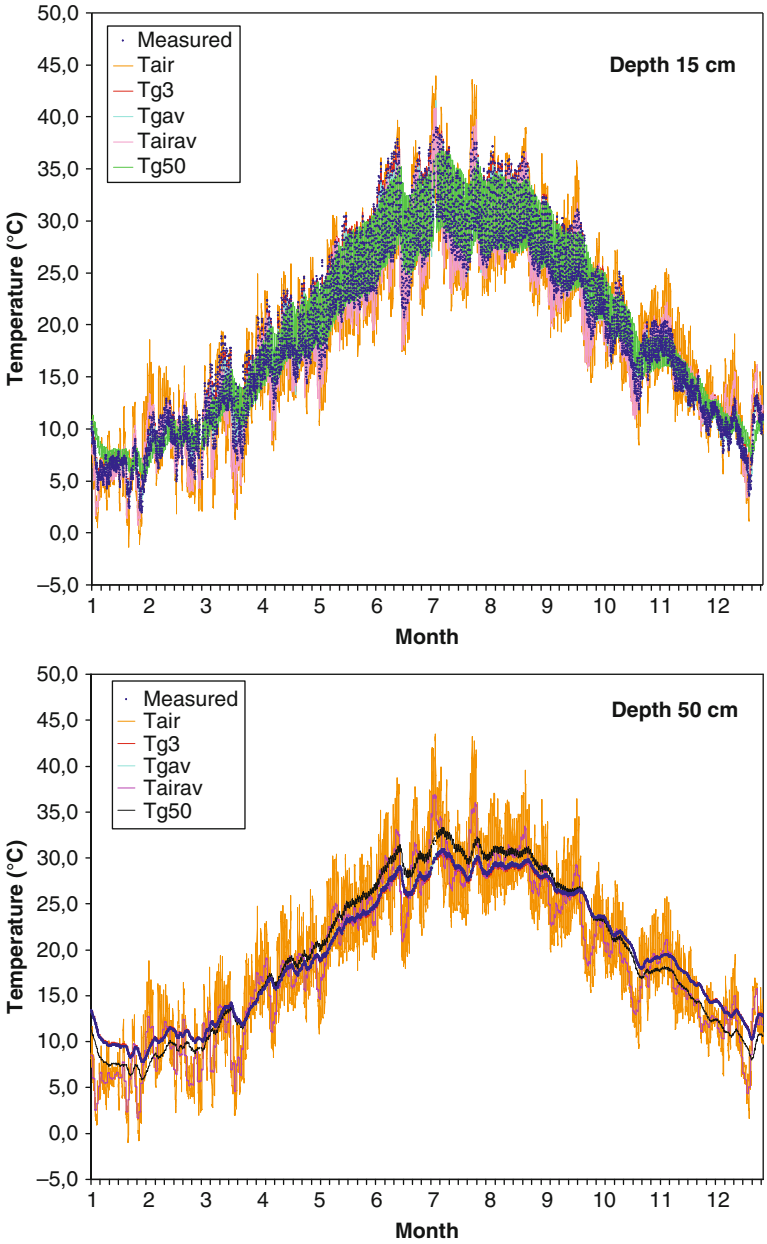

Fig. 1 Final models and measured data for the 15 cm (*upper*) and 50 cm (*lower*) depths

to as DevAll. Furthermore, since the surface (0 cm) measurements were found to be more susceptible to the influence of exogenous factors, these measurements were excluded and a second set of models was developed (denoted as Devno0).

Mean absolute error (MAE) and root mean square error (RMSE) were calculated for each model using the validation data set. Based on these results a set of models was developed using the entire dataset (denoted as Final).

3 Results

All models fitted to the training data set provided statistically significant parameter estimates. Models obtained with and without the surface (0 cm) measurements provided similar results in terms of R^2, whereas the estimated parameters' values even though statistically different in most cases, were very close to each other indicating a robustness of the obtained models. Models including 0 cm data (DevAll), using Tairav are performing better than those using Tair (overall RMSE 3.4 and 3.5°C respectively) which in turn is better than models using ground temperatures as a proxy for J (overall RMSE between 4.1°C and 4.6°C). This counterintuitive behavior is remedied in Devno0 models, with models using Tg3 and Tgav being significantly better that the rest, and very well in absolute terms: the overall RMSE is 1.6°C and 1.7°C respectively (dropping, for Tgav, from 3.4°C at 0 cm to 0.1°C at 0 cm) with similar MAEs.

Since the DEvno0 models performed better, this was the modelling approach adopted for the development of the Final models. The results are presented in Table 1 whereas data from the 15 cm and 50 cm depths for an indicative year (namely 2000) are presented in Fig. 1.

The majority of the parameters' estimates are pretty similar for all models, except for A1, the amplitude of the hourly variation, for models Tair and Tairav, and D, the thermal diffusivity, for model Tair.

Models using air temperature present, as expected, over exaggerated variation compared to the measurements, and the discrepancy is larger as we move deeper into the soil. On the other hand, models using Tgav are those performing best, with those using Tg3 coming second best. This was more or less expected since average ground temperature is the closest representative of the long term steady state ground temperature, J, initially required by the model ((1)).

4 Conclusions

Models using air temperature as a means to re-introduce temporal variability and add some forecasting capability to model described by (1) are, understandably, less successful than those using ground temperatures. Moreover, excluding soil surface temperatures from the data set, leads to greatly improved models regarding the rest

of depths, whereas the performance for surface (0 cm) ground temperatures is not significantly affected. Finally, a promising result of the present study is the good performance of the models based on the daily average ground temperature from observations at 08:00, 14:00 and 20:00 that can be used to reconstruct hourly time series for stations and periods having only 8-hourly measurements.

References

Droulia F, Lykoudis S, Tsiros I, Alvertos N, Akylas E, Garofalakis I (2008) Ground temperature estimations using simplified analytical and semi-empirical approaches. Sol Energy 83:211–219. doi:10.1016/j.solener.2008.07.013

Graham EA, Lam Y, Yuen EM (2010) Forest understory soil temperatures and heat flux calculated using a Fourier model and scaled using a digital camera. Agric Forest Meteorol 150:640–649. doi:10.1016/j.agrformet.2010.02.005

Luo Y, Loomis RS, Hsiao TC (1992) Simulation of soil temperature in crops. Agric Forest Meteorol 61:23–38. doi:10.1016/0168-1923(92)90023-W

Mazou E, Tsiros I, Alvertos N, Lykoudis S, Garofalakis I (2010) Estimation of soil temperature: time and frequency domain modeling. In: Proceedings tenth conference of meteorology, climatology and atmospheric physics. Hellenic Meteorological Society, Patras, pp 517–525

Mihalakakou G, Santamouris M, Asimakopoulos D, Argiriou A (1995) On the ground temperature below buildings. Sol Energy 55:355–362. doi:10.1016/0038-092X(95)00060-5

Santamouris M (2007) Advances in passive cooling, Buildings energy and solar technology series. Earthscan, Sterling

Yuan Y, Ji H, Du Y, Cheng B (2008) Semi-analytical solution for steady-periodic heat transfer of attached underground engineering envelope. Build Environ 43:1147–1152. doi:10.1016/j.buildenv.2007.03.001

Extreme Heat Wave Events in the Thessaloniki Region: Past, Present and Future Projections

K. Tolika and C. Anagnostopoulou

Abstract The present paper is the third part of a series of scientific researches concerning the extreme or anomalous high temperature conditions over the Greek region focusing especially on the Thessaloniki area. After the study of the three heat wave events during the summer of 2007 and the analysis of the exceptionally high maximum (Tmax) and minimum (Tmin) temperatures that occurred during November 2010, we aimed on the investigation of the temperature conditions of September of 2011 in Thessaloniki. This month was characterized by large departures of maximum temperatures from the long term mean values, reaching up to almost 4°C. Especially in the case of minimum temperatures, September of 2011 was found to have the highest Tmin average in comparison to the reference period 1958–2000. Analogous results were found for several stations over the domain of study. These temperature conditions are expected to occur more than 50% of the time by the end of the twenty-first century, according to the comparison with the future projections of seven different regional climate models. It should also be highlighted that several days in September 2011 exceeded even the 75th percentile of the simulated data.

1 Introduction

Several regions over Europe have experienced severe heat wave events, during the past decade. There is a growing scientific interest in the study of this kind of extremely high temperature conditions due to their intense consequences both to the environment and to society. The summer of 2003 was characterized by "record

K. Tolika (✉) • C. Anagnostopoulou
Department of Meteorology and Climatology, School of Geology, Aristotle University of Thessaloniki, Thessaloniki 54124, Greece
e-mail: diatol@geo.auth.gr

C.G. Helmis and P.T. Nastos (eds.), *Advances in Meteorology, Climatology and Atmospheric Physics*, Springer Atmospheric Sciences,
DOI 10.1007/978-3-642-29172-2_108,

breaking" high temperatures in several Central European countries (Beniston 2005; Beniston and Diaz 2004). Moreover, in 2007, the eastern Mediterranean, and especially the Balkan Peninsula and Greece, experienced a remarkably warm year (Busuioc et al. 2007; Founda and Giannakopoulos 2009; Tolika et al. 2009). The comparison of these results with the future projections of RCMs showed that this kind of temperature values are expected to occur more than 50% of the time in the future (Beniston 2007; Tolika et al. 2009).

Still, it is not only the summer months that are characterized by extreme high temperatures. During November 2010, Greece experienced a new "heat wave" event and anomalous high maximum and minimum temperatures were observed across the entire country and remained at high levels during the whole month with values which far exceeded the long term mean (Tolika et al. 2011).

Consequently the main scope of the present study is to conduct an analysis for the detection of other extreme high temperature events for the Thessaloniki region. It was found that September 2011 was also characterized by anomalously high maximum and minimum temperatures which exceeded the long term mean almost up to 4 °C in the case of maximum temperatures. Thus, aiming at a statistical analysis of the anomalously high temperatures during September 2011, we tried to identify if these warm conditions were detected all over Greece or it was just a regional extreme. Finally we compared the present results with the future projections of seven of the most up-to-date regional climate models.

2 Data and Methodology

Daily maximum and minimum temperature data (Tmax and Tmin respectively) were utilized for the period of September 2011 as well as for the long term period 1958–2000 for the station of Thessaloniki and for selected stations over the Greek region. Daily Tmax and Tmin screen-level temperatures were provided by the National Climatic Data Center (NCDC) of NOAA (http://www.ncdc.noaa.gov) with an exception of the station of Thessaloniki (data were recorded at the meteorological station located at the University of Thessaloniki (AUTh)). The data for the long term period were provided by the Hellenic Meteorological Service.

Moreover, regional climate Tmax and Tmin projections from seven RCMs developed during the ENSEMBLES European project were utilised. The grid points were selected based on their vicinity to the stations used in the study (the ones nearest (on land) to the station). Utilizing these simulated projections, several quantiles were computed for the last 30 years of the twenty-first century and compared with the corresponding observations. Basic information concerning the models used in this study is shown in Table 1 (http://ensembles-eu.metoffice.com/).

Table 1 The regional climate models used in the study

Model acronym	Institute	Driving GCM	Scenario	Resolution
CLM	ETHZ (Swiss Federal Institute of Technology, Zurich, Switz.)	HadCM3-Q0	A1B	25 km
HadRM3	HC (Hadley Centre for Climate Prediction and Research, UK)	HadCM3-Q0	A1B	25 km
HIRHAM	DMI (Danish Meteorological Institute, Denmark)	ECHAM5-r3	A1B	25 km
RACMO2	KNMI (Royal Netherlands Meteorological Institute, the Netherlands)	ECHAM5-r3	A1B	25 km
RCA	SMHI (Swedish Meteorological and Hydrological Institute, Sweden)	ECHAM5-r3	A1B	25 km
RegCM3	ICTP (The Abdus Salam International Centre for Theoretical Physics, Italy)	ECHAM5-r3	A1B	25 km
REMO	MPI (Max-Planck-Institute for Meteorology, Germany)	ECHAM5-r3	A1B	25 km

3 Results

Comparing the mean Tmax and Tmin during September, for the long term period 1958–2000 and for September 2011, for the station of Thessaloniki, it was found that the mean September temperatures were 27.1°C (Tmax) and 16.9°C (Tmin), yet for 2011 the equivalent values rise to 30.9°C and 19.3°C respectively. Thus, it is evident that especially in the Tmax case, the September 2011 value exceeded the climatological mean almost by 4.0°C (Fig. 1).

However it is the mean minimum temperature of September 2011(19.3°C) that is the highest recorded during the study period, while the second high Tmin value was observed in 1994 (18.9°C). Regarding Tmax, September of 1994 still remains the case with the highest mean maximum temperature (31.1°C), although it should be mentioned that this value is very close to the one of September 2011 (Fig. 1).

Moreover, from the study of the daily September time series it was found that both for Tmax and Tmin, almost all days presented temperatures that exceeded the mean daily values for the period 1958–2000. The exceptions is 1 day at the end of September for Tmin and two scattered days for Tmax which appear to be "colder" than the mean Tmax and Tmin values (Fig. 1).

Aiming at investigating if this anomalous warm September was an extended phenomenon all over Greece or if it characterized only the area of Thessaloniki, we also computed the mean September 2011 Tmax and Tmin to the equivalent long term mean of 1958–2000, for several stations over the domain of study. In the case of Tmax, the differences (TmaxSept2011 – TmaxSept(1958–2000)) are generally higher over the northern stations and vary from 1.2°C (Heraklio) to 5.1°C (Ioannina). The corresponding results for Tmin showed that the differences were lower than those for Tmax reaching up to 2.5°C (Alexandroupoli). It is worth mentioning that for the station of Ioannina the Tmin anomalies were negative

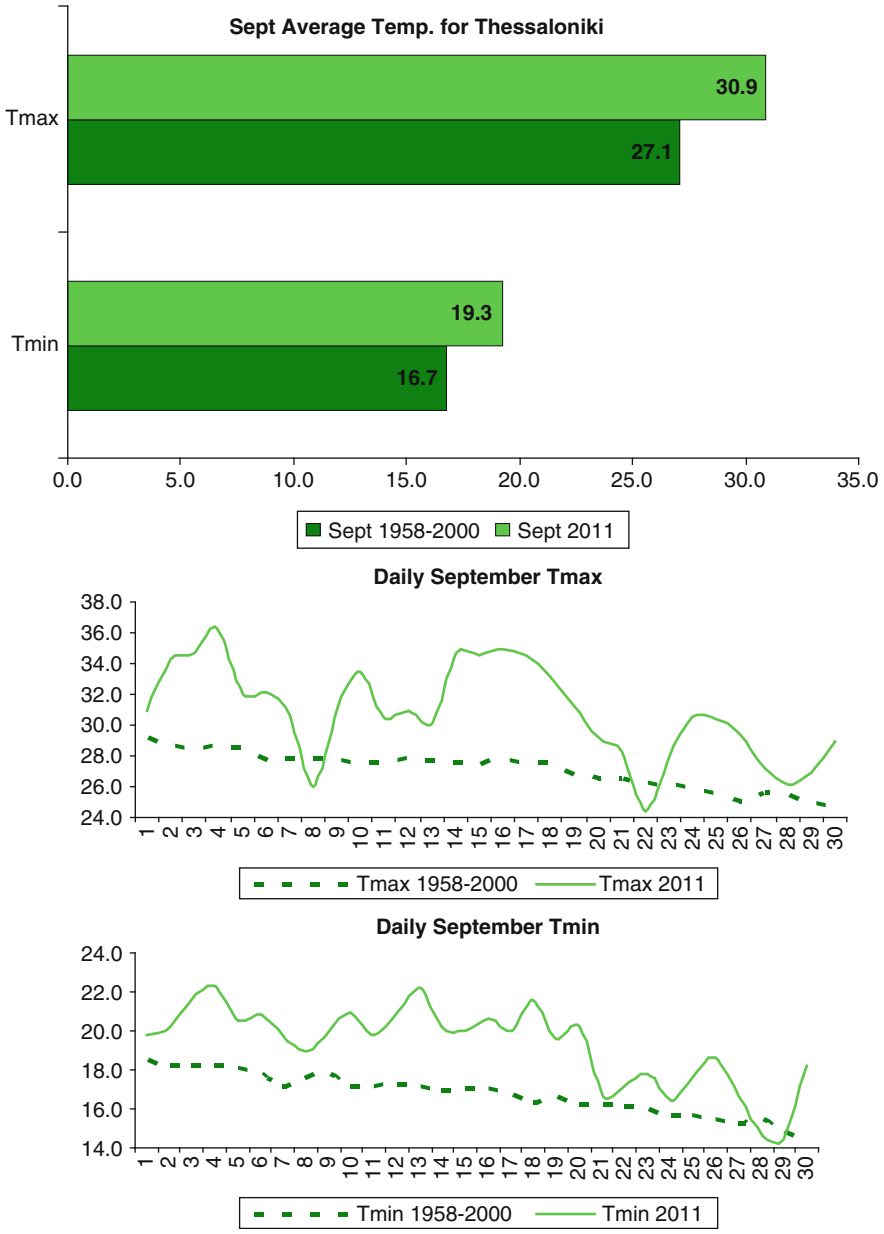

Fig. 1 Mean and daily September maximum and minimum temperatures for the station of Thessaloniki

(−0.3°C) meaning that the September 2011 minimum temperatures were a little lower than the long term mean, even though the same station was the one with the highest Tmax departures from the mean of the period 1958–2000 (Fig. 2).

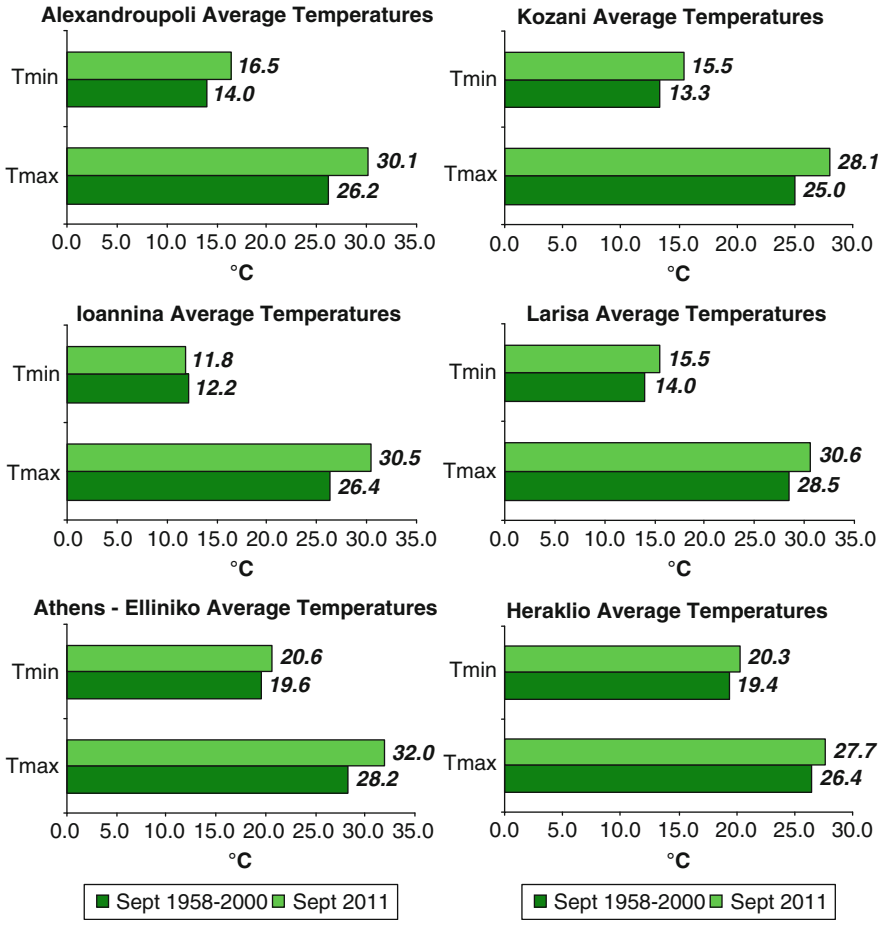

Fig. 2 Mean September maximum and minimum temperatures September 2011 (*light green*) September 1958–2000 (*dark green*) for selected stations over the domain of study

Furthermore, in order to accomplish a more detailed analysis of the intensity of the high temperature conditions during September 2011, daily September Tmax and Tmin data from seven up-to-date RCM models (the closest grid point on land to the station of Thessaloniki) were used for the computation of several quantiles (Q10, Q25, Q50, Q75 and Q90) for the last 30 years of the twenty-first century (2071–2100). The results were compared to the daily observational time series. Figure 3 illustrates the quantiles of every model in relation to the Tmax daily time series both for September 2011 as well as the mean daily values for the period 1958–2000, for the station of Thessaloniki. It was found that the observational values of September 2011 appear to be (several days) higher than Q10 and Q25 and for the majority of the models even higher than Q50. Also, for some days during the

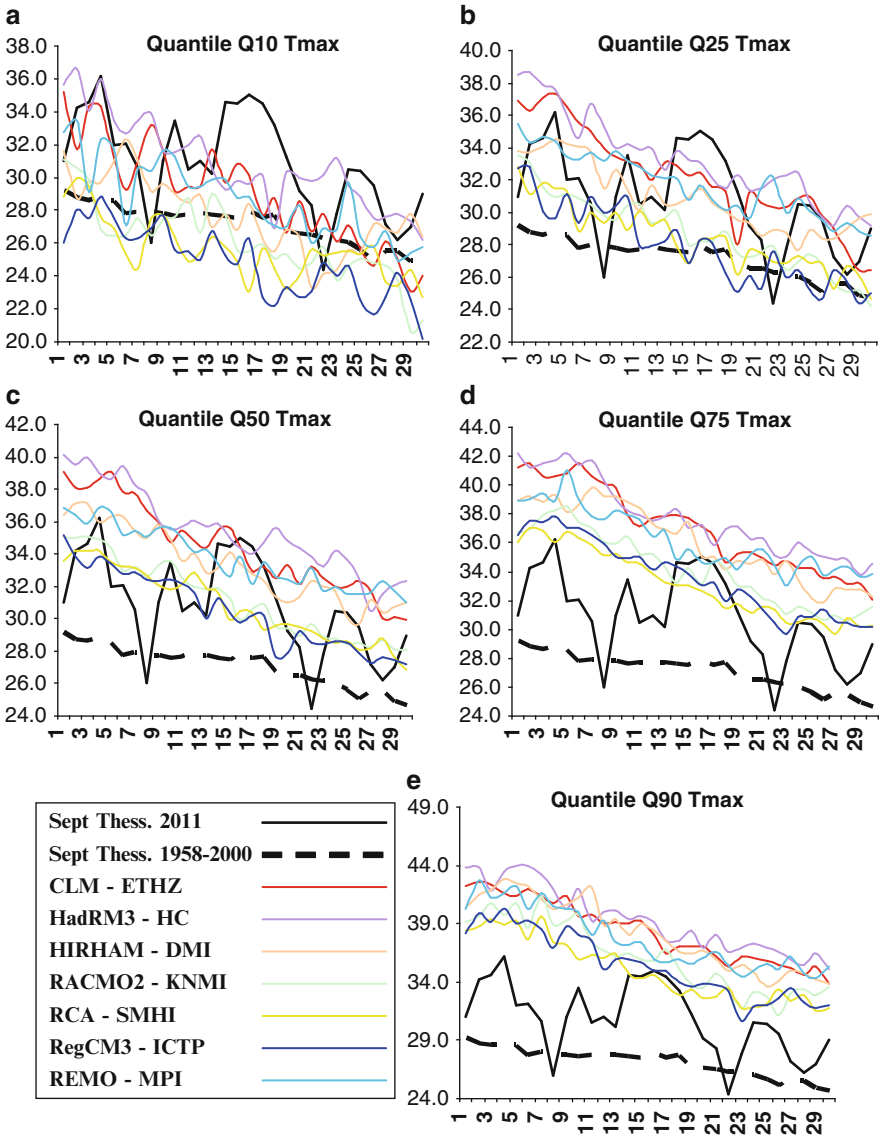

Fig. 3 Daily Tmax values for September 2011 (*solid lines*) and November mean Tmax values for the long term period 1958–2000 (*dashed lines*) for the station of Thessaloniki. Daily September Tmax quantiles (Q10, Q25, Q50, Q75 and Q90) for the future period 2071–2100 as derived from the seven selected RCMs under study

middle of the month, the observed Tmax are even higher than the 75-quantile of the RACMO2-KNNI, the RegCM3-ICTPand the RCA – SMHI model, which appear to be "*less warm*" than the other ones. It should be noted at this point that

the '*warmest*' model was found to be the one developed in Hadley Center (HadRM3-HC) and the observational September data of 2011 exceed the simulated values for some days for only the first two quantiles (Q10 and Q25). Conversely, the "coldest" model is the RCA – SHMI (Swedish Meteorological Center) for which September Tmax 2011, reach the 90-quantile of the model for a few days (Fig. 3). Analogous were the results for minimum temperature but due to space limitation are not presented in the present study.

4 Conclusions

The maximum and minimum temperatures of September of 2011 for the area of Thessaloniki were characterized by large departures from the reference period 1958–2000. More specifically, in the case of Tmax the anomalies from the long term mean reached almost 4°C. Analogous were the results for several other stations over the Greek region. Regarding Tmin, although the departures from the mean value were smaller, September 2011 presented the absolute highest minimum temperatures of all the study period for Thessaloniki. The comparison of the observed September 2011 Tmax with the future projections of 7 RCMs revealed that for a few days Tmax was even higher than the 50- quantile (for some models it exceeded the 75-quantile). This means that these temperature conditions are likely to occur, more than 50% of the time by the end of the twenty-first century. Analogous results were found by Tolika et al. (2009) for the extreme warm temperature conditions during the summer of 2007 in Thessaloniki. As a future work the authors plan to investigate the general atmospheric conditions that occurred during this extreme hot September as well as the links with the atmospheric circulation over the domain of study. Moreover, it would be of great interest to examine the precipitation conditions that occurred during September 2011.

Acknowledgments This study has been supported by the European Commission ENSEMBLES project (Contract number GOCE-CT-2003-505539) and the Research Committee of the Aristotle University of Thessaloniki.

References

Beniston M (2005) Warm winter spells in the Swiss Alps: strong heat waves in a cold season? A study focusing on climate observations at the Saentis high mountain site. Geophys Res Lett 32: L01812

Beniston M (2007) Entering into the "greenhouse century": recent record temperatures in Switzerland are comparable to the upper temperature quantiles in a greenhouse climate. Geophys Res Lett 34:L16710. doi:10.1029/2007GL030144, 2007

Beniston M, Diaz HF (2004) The 2003 heat wave as an example of summers in a greenhouse climate? Observations and climate model simulations for Basel, Switzerland. Global Planet Change 44:73–81. doi:10.1016/j.gloplacha.2004.06.006

Busuioc A, Dumitrescu A, Soare E, Orzan A (2007) Summer anomalies in 2007 in the context of extremely hot and dry summers in Romania. Romanina J Meteorol 9:1–17

Founda D, Giannakopoulos C (2009) The exceptionally hot summer of 2007 in Athens, Greece. Global Planet Change 67(3–4):227–236. doi:10.1016/j.gloplacha.2009.03.013

Tolika K, Maheras P, Tegoulias I (2009) Extreme temperatures in Greece during 2007: could this be a "return to the future"? Geophys Res Lett 36:L10813. doi:10.1029/2009GL038538

Tolika K, Pytharoulis I, Maheras P (2011) The anomalous high temperatures of November 2010 over Greece: meteorological and climatological aspects. Nat Hazards Earth Syst Sci 11:2705–2714. doi:10.5194/nhess-11-2705-2011

Anticyclonic Blocking Effects Over Europe from an Ensemble of Regional Climate Models in Recent Past Winters

K. Tourpali and P. Zanis

Abstract Anticyclonic blocking is an important factor for mid-latitude climate variability and is considered to play a key role on anomalous and extreme events. In this study we present an analysis of atmospheric blocking events on the output of a multi-model ensemble of Regional Climate Models (RCMs) simulations. The ensemble consists of a set of seven RCMs, nested on the European domain with a resolution of 50 × 50 km. All RCM simulations were driven by similar lateral boundary conditions, namely the ERA-40 reanalysis for the period 1961–2000, as part of the European project ENSEMBLES. The atmospheric blocking events are examined in terms of their frequency in the RCM outputs and compared to events detected in the ERA-40 data set. The aim is to investigate the ability of the different RCMs to reproduce the anticyclonic blocking events of the forcing reanalysis fields. Related effects on daily average temperature and precipitation are studied in the model results by means of composite maps and correlation analysis. The results are then compared to observations, with the aid of similar analysis performed on the daily mean temperature and precipitation data derived from the E-OBS gridded dataset.

1 Introduction

Global Circulations Models (GCMs) are the most advanced tools today available for climate simulations in past, present and future, but their resolution (100–300 km) is still too coarse to provide fine scale regional climate information

K. Tourpali (✉)
Laboratory of Atmospheric Physics, Physics Department, Aristotle University of Thessaloniki, Thessaloniki, Greece
e-mail: tourpali@auth.gr

P. Zanis
Department of Meteorology and Climatology, School of Geology, Aristotle University of Thessaloniki, Thessaloniki, Greece

C.G. Helmis and P.T. Nastos (eds.), *Advances in Meteorology, Climatology and Atmospheric Physics*, Springer Atmospheric Sciences,
DOI 10.1007/978-3-642-29172-2_109,

useful for impact studies. Regional climate models (RCMs) have been developed for the application of dynamical downscaling methods to enhance the regional information provided by GCMs (or by the large scale reanalysis fields) at resolutions ranging commonly between 50 and 10 km (Giorgi et al. 1990). RCMs represent in more detail surface features, such as complex mountain topographies, coastlines, small islands, lakes and peninsulas, and hence they have the ability to simulate atmospheric processes at a wide range of spatial and temporal scales.

When comparing the RCMs with their driving GCM, they generally reproduce the large-scale circulation of the GCM though in some cases there are substantial differences between regional biases in surface temperature and precipitation (Jacob et al. 2007). For the RCMs, the lateral forcing by the GCMs or reanalysis introduces a source of uncertainty. Even forced by the same lateral boundary conditions RCMs may simulate different atmospheric circulation patterns within the domain (Giorgi and Bi 2001; Christensen et al. 2001). This variability is often called the internal variability of RCMs and can be determined by the spread among the members in an ensemble of simulations driven by identical LBCs.

In this study we present an analysis of atmospheric blocking events on the output of a multi-model ensemble of Regional Climate Models (RCMs) simulations, all forced by similar lateral boundary conditions, namely the ERA-40 reanalysis for the period 1961–2000, as part of the European project ENSEMBLES. The aim is to investigate the ability of the different RCMs to reproduce the anticyclonic blocking events of the forcing reanalysis fields.

Previous studies showed a good performance of the RCMs participated in ENSEMBLES when forced by ERA40 meteorological fields. For example, Sanchez-Gomez et al. (2009) analysed the ability of an ensemble of 13 RCMs forced by ERA-40 data to reproduce weather regimes over the Europe-Atlantic sector during the period 1961–2000. They concluded that the RCMs reproduced the weather regimes behavior in terms of composite pattern, mean frequency of occurrence and persistence reasonably well. Furthermore, in another recent study based on 9 RCMs forced by ERA-40 fields it was showed that these models represented fairly well the seasonal mean spatial pattern and amount of precipitation over Europe at both 25 and 50 km horizontal grid spacing (Rauscher et al. 2010).

2 Data and Methodology

In this study we use data from 7 RCM simulations for the period 1961–2000 all forced by ERA-40. A summary of the models and their characteristics is shown in Table 1 (see also the ENSEMBLES project webpage: http://ensemblesrt3.dmi.dk). In particular we have used the 500 hPa geopotential height fields, the surface temperature and the surface precipitation fields. In addition, and in order to identify the atmospheric blocking anticyclones in the forcing field we have used the daily 500 hPa geopotential height fields from the ERA-40 reanalysis ($2.5^\circ \times 2.5^\circ$).

Table 1 Main features of the regional models used in this study

Institute	RCM	Grid points	Levels
DMI	HIRHAM	90 × 95	31
ETHZ	CLM	91 × 97	32
ICTP	RegCM	98 × 86	34
KNMI	RACMO	95 × 85	40
HADM (METOHC)	HadRM3	115 × 118	19
MPI	REMO	85 × 95	27
SMHI	RCA	85 × 95	24

The definition of atmospheric blocking requires the use of an objective definition. Here we use the objective blocking index described by Tibaldi and Molteni (1990), hereafter TM90. For the calculation of TM90 index the 500 HPa geopotential height gradients GHGS and GHGN are computed for each longitude as

$$GHGS = \frac{z(\varphi_o) - z(\varphi_s)}{\varphi_o - \varphi_s} \text{ and } GHGN = \frac{z(\varphi_n) - z(\varphi_o)}{\varphi_n - \varphi_o}$$

where $\varphi_0 = 60^\circ$ N + Δ, $\varphi_n = 80^\circ$ N + Δ, $\varphi_s = 40^\circ$ N + Δ and $\Delta = -2.5^\circ, 0^\circ, 2.5^\circ$. In our case, this index has been slightly modified to fit the central domain of the RCMs, so we set $\varphi_0 = 55^\circ$N, $\varphi_s = 40^\circ$ and $\varphi_n = 70^\circ$ N, keeping the grid spacing Δ the same. A given longitude is defined as blocked if both conditions $GHGS > 0$ and $GHGN < 10$ *m/deg latitude* are satisfied. A sector is assumed to be blocked if three or more adjustment latitudes are blocked, and a blocking episode is defined when blocking occurs for 5 or more consequent days. Here we compute the number of days belonging in blocking episodes for the winter period (December through February) from 1961 to 2000. This has been computed from the 500Z fields of ERA-40 as well as the equivalent fields from all RCMs in order to compare first the ability of the RCMs to reproduce wintertime blocking over the European sector. The 500Z fields from the RCMs were linearly interpolated to a 2.5 × 2.5 field to allow direct comparison to the ERA-40 results.

The days central to the episodes were defined from the ERA-40 results according to Barriopedro et al. (2006). These days were used then to perform a composite map analysis of the anomalies in temperature and precipitation fields associated with the presence of a blocking over the European sector. A separate analysis was conducted first, where we examined the 500 hPa geopotential height anomalies for the region of Europe from both the ERA-40 data set and the RCM data. Results (not shown) revealed that indeed the use of the number of days identified above as central key-dates leads to an anticyclonic blocking pattern centered over North-East Europe. Then, the anomalies of the temperature and precipitation fields were calculated for the winter months of the 40-year simulations of the RCMs with respect to their daily averages. Composite maps of anomalies were constructed from the fields of the RCMs as well as from the observational fields of E-OBS gridded dataset (Haylock et al. 2008) for the days central to the blocking episodes.

3 Results

Figure 1 presents the blocking frequency in the winter months calculated for the ERA-40 and RCMs. Only days belonging to blocking episodes lasting at least 5 days were taken into account. Our computations reveal that blocking, and in particular blocking episodes of more than 5 consequent days were reproduced by all RCMs. All models show that the largest number of blocking episodes occurs in the region between 2.5°E–7.5°E, same as in the ERA-40 data set. This region of highest frequency, as well as the general shape of the response in the Euro-Atlantic sector that we examine here is the same as the one calculated if the classic definition of TM90 is used (e.g. Barriopedro et al. 2006). The number of blocked days drops with the same pace as we move further than this sector, both to the east and the west. All RCMs show smaller blocking frequency at 7.5°W than ERA-40, as this area corresponds to almost all models western boundary. Some models show a smaller frequency of blocking events in general, a feature that is partly due to the strict definition of the blocking episode and the duration criterion.

Figure 2 presents the composite map of anomalies of surface temperature calculated from the E-OBS data set along with the corresponding maps of the RCM simulations. The analysis of the anomalies in observations reveals pronounced cold anomalies (on average ~ −3°C) over central Europe, at latitudes lower than 50°N. The coldest area (>−4°C) is found over western France, while the northern part of the Balkan Peninsula experiences low temperatures. Low temperatures of about the same magnitude are seen over Greece, too. Scandinavia and Iceland, on the other hand, show temperatures above the average, the highest anomaly reaching ~ 6°C located in the area of Norway/Sweden. The British Isles show a gradient in surface temperature response with low temperatures in south gradually increasing towards north. It is worth noting that the anomalies (positive and negative) are significant above the 95% confidence level, except for the transition area between 50°N–60°N in North-East Europe and Russia. This pattern

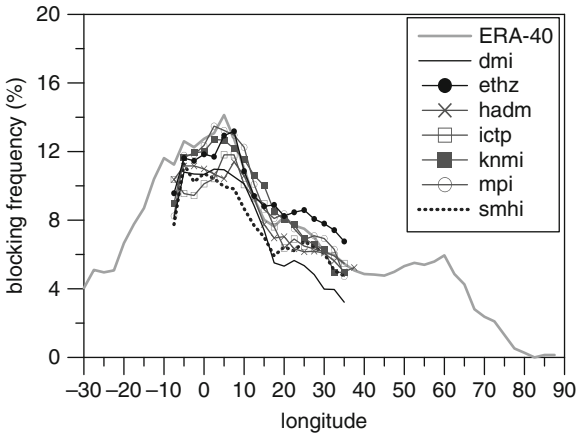

Fig. 1 Blocking frequency for the winter (Dec through February) as depicted in ERA-40 (*thick grey line*) and RCM simulations. Model names and corresponding lines are given in the figure

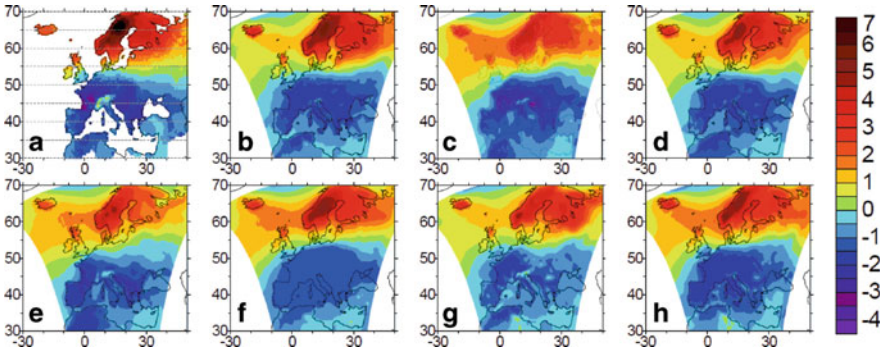

Fig. 2 Composite map of anomalies of surface temperature calculated from (**a**) the E-OBS dataset along with the composite maps of anomalies for the 7 RCMs. *Top panel*: (**b**) dmi, (**c**) ethz, (**d**) hadm and *bottom*: (**e**) ictp, (**f**) knmi, (**g**) mpi, (**h**) smhi (details in Table 1)

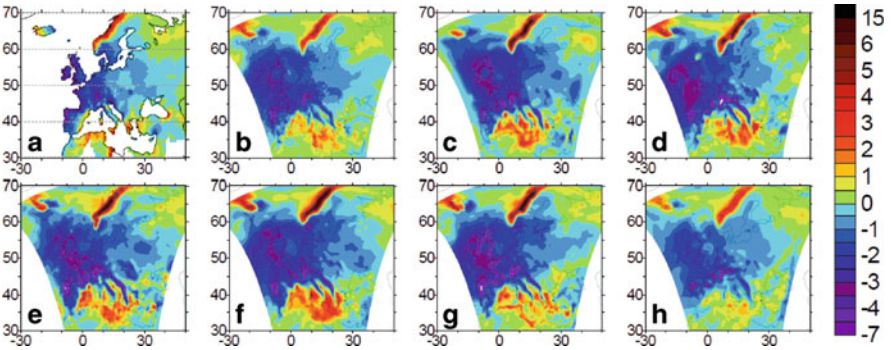

Fig. 3 Same as Fig. 2 but for precipitation anomalies

of response of surface temperature anomalies is seen in all RCMs. Anomalies of the same sign are seen in all models, and over the same regions, even though the absolute temperature response differs slightly from model to model, as does the area of the highest response in the lowest temperatures over France.

The composite maps of anomalies in precipitation are shown in Fig. 3. In E-OBS we see that the whole region of NW central Europe is under a negative precipitation anomaly field, the driest areas found over England and NW France. This area coincides with the region covered by the anticyclonic blocking and the associated anomalies in the flow, with cold and dry air in the region. Norway on the other hand has large positive precipitation anomalies, the same as the whole of the Mediterranean, Greece included. These anomalies in precipitation are seen in all model simulations. Models show that the area with the largest negative anomalies is located over the British Isles and France, and the areas located to the northern and southern parts of the blocking system show positive precipitation anomalies, thus more rain than the average.

4 Conclusions

The key conclusions can be summarized as follows:

1. Blocking episodes of more than 5 consequent days were reproduced by all RCMs as in the forcing field ERA-40 reanalysis.
2. The observed pattern of response of surface temperature and precipitation anomalies for the blocking episodes is also reproduced by all RCMs even though the absolute response differs slightly from model to model, as does the area of the highest response.

Acknowledgments This work has been funded by the European Community's Sixth Framework Programme as part of the project CECILIA (Central and Eastern Europe Climate Change Impact and Vulnerability Assessment) under Contract No. 037005. We acknowledge the RCM and E-OBS datasets from the EU-FP6 project ENSEMBLES (http://ensembles-eu.metoffice.com) and the data providers in the ECA&D project (http://eca.knmi.nl).

References

Barriopedro D, Garcia-Herrera R, Lupo AR, Hernandez E (2006) A climatology of Northern Hemisphere Blocking. J Climate 19:1042–1063. doi:10.1175/JCLI3678.1

Christensen OB, Gaertner MA, Prego JA, Polcher J (2001) Internal variability of regional climate models. Clim Dyn 17:875–887. doi:10.1007/s003820100154

Giorgi F, Bi X (2001) A study of internal variability of regional climate model. J Geophys Res 105:29501–29503. doi:10.1029/2000JD900269

Giorgi F, Marinucci MR, Visconti G (1990) Use of a limited-area model nested in a general circulation model for regional climate simulations over Europe. J Geophys Res 95 (D11):18413–18431. doi:10.1029/JD095iD11p18413

Haylock MR, Hofstra N, Klein Tank AMG, Klok EJ, Jones PD, New M (2008) A European daily high-resolution gridded dataset of surface temperature and precipitation. J Geophys Res 113: D20119. doi:10.1029/2008JD10201

Jacob D et al (2007) An intercomparison of regional climate models for Europe: model performance in present-day climate. Clim Chang 81:31–52. doi:0.1007/s10584-006-9213-4

Rauscher SA, Coppola E, Piani C, Giorgi F (2010) Resolution effects on regional climate model simulations of seasonal precipitation over Europe. Clim Dyn 35:685–711. doi:10.1007/s00382-009-0607-7

Sanchez-Gomez E, Somot S, Déqué M (2009) Ability of an ensemble of regional climate models to reproduce the weather regimes during the period 1961–2000. Clim Dyn 33:723–736. doi:10.1007/s00382-008-0502-7

Tibaldi S, Molteni F (1990) On the operational predictability of blocking. Tellus 42A:343–365

Thermal Comfort Conditions and Evaluation of the Thermal Bioclimate Index PET in Two European Cities During Summer

A. Tseliou, I.X. Tsiros, M. Nikolopoulou, and S. Lykoudis

Abstract This study examines the thermal comfort conditions in open urban areas of two European cities with different climatic characteristics. The aim is to obtain values of the neutral temperature based on data from field surveys that included microclimatic monitoring and structured questionnaires. The presented data covered summer measurements and conducted in Athens (Greece) and Kassel (Germany) while the actual thermal sensation votes (ASV) data expressed on a five-point scale. The values of air temperature in which occupants of two examined cities feel thermal comfort are estimated. Results show that higher neutral temperature values in comparatively warmer environments are indicative of adaptation of the occupants to the thermal environment. The results for the two examined cities show that people are well adapted to their local environment.

1 Introduction

The microclimatic effect on human thermal sensation in outdoor urban spaces presents continuously higher interest since, to a large extent, influences the use of these spaces by visitors. The application of bioclimatic indices used in many researches show that, despite the fact that these indices have mainly been developed to assess the human thermal comfort conditions, they are often incapable

A. Tseliou (✉) • I.X. Tsiros
Department of Geological Sciences and Atmospheric Environment, Agricultural University of Athens, Iera Odos, Athens 11855, Greece
e-mail: rea_geo@hotmail.com; Tseliou_a@aua.gr

M. Nikolopoulou
Kent School of Architecture, University of Kent, Canterbury CT2 7NR, UK

S. Lykoudis
Institute of Environmental Research and Sustainable Development, National Observatory of Athens, I. Metaxa & V. Pavlou, 152 36 P Pendeli, Greece

C.G. Helmis and P.T. Nastos (eds.), *Advances in Meteorology, Climatology and Atmospheric Physics*, Springer Atmospheric Sciences,
DOI 10.1007/978-3-642-29172-2_110,

to be precise and as a consequence their reliability is disputed (e.g. Lin and Matzarakis 2008; Tseliou et al. 2010; Lin et al. 2011). Previous research has shown that climatic characteristics, affect thermal sensation (e.g. Spagnolo and de Dear 2003; Nakano and Tanabe 2004; Tseliou et al. 2010). The present study focuses on thermal comfort and PET index estimations along with implications for adaptation and/or acclimatization. Two European cities with different climatic characteristics are examined in order to obtain values of the neutral temperature based on data from field surveys, which included microclimatic monitoring and structured questionnaires. The bioclimatic index PET also selected to be applied to estimate the air temperature range in which people feel thermal comfort.

2 Data and Methodology

Thermal comfort conditions were examined in two outdoor urban sites in two different cities in Europe within the RUROS project: Athens (sea-shore Alimos) and Kassel (Florentiner Platz) (Nikolopoulou and Lykoudis 2006; RUROS 2009). The Actual Sensation Votes (ASV) of the people interviewed during the campaigns were recorded using structured questionnaires, along with personal parameters such as sex, age, clothing, activity etc. that are required for a detailed calculation of the biometeorological indices. The actual question asked for ASV was "At the moment, how do you find the thermal environment" with possible answers: very cold (−2), cool (−1), neither cool nor warm (0), warm (+1), very hot (+2), whereas there was also another question about feeling comfortable with a yes/no answer. 393 questionnaires were totally completed. Detailed microclimatic monitoring was carried out with the use of portable mini-weather stations, while people were studied in their natural. Each site was monitored for a full week. The meteorological parameters monitored were air temperature and relative humidity measured through a psychrometer with forced ventilation, globe temperature with a Pt-100 thermometer in a gray ping pong ball, global solar radiation, and wind speed with an omni-directional hot-wire anemometer. A full description of the methodology employed is given in a previous work (Nikolopoulou and Lykoudis 2006). Climatic mean temperatures on seasonal basis for the two cities considered for the period 1961–1990 were obtained from the closest meteorological station available in the European Climate Assessment & Dataset (Tseliou et al. 2010). Table 1 shows the

Table 1 The mean monthly climatic air temperature of the examined cities based on European Climate Assessment & Dataset (Tseliou et al. 2010) as well as minimum, maximum and mean air temperature recorded at the portable mini weather station during the field surveys

	Mean climatic air temperature (°C)				Recorded temperatures(°C)		
Months	June	July	August	Mean summer Tair	Min	Max	Mean
Kassel	16.5	17.9	17.4	17.3	17.8	29.6	22.1
Athens	24.6	27.6	27.4	26.5	26.6	33.7	29.3

mean climatic air temperatures of summer for the two cities, as well as the min, max and mean temperatures recorded during the field surveys.

The widely used biometeorological index PET (Matzarakis and Mayer 1996; Höppe 1999) was selected to assess the thermal comfort conditions since it is a commonly applied index in similar urban environment studies. For PET calculations, air temperature, relative humidity, mean radiant temperature and wind speed data are required along with other personal parameters such sex, age, weight and height. PET was estimated using the equations of MEMI (Höppe 1999).

3 Results

3.1 The Neutral Temperature

Neutral temperature is the temperature at which an individual feels neither cold nor warm, but is in a state of thermal neutrality, frequently associated with thermal comfort. In order to obtain the air temperature at which an individual feels thermal comfort for the summer period, the mean ASV for each 1°C Tair interval was calculated. Figure 1 shows the linear regression equations for each city, as well as, the coefficient of determination R^2 between ASV and air temperature. It is shown that as the air temperature increases, there is an increase in ASV values. To obtain the neutral temperatures, the linear regression equation for ASV = 0 is solved. As shown in Table 2, the air temperature that thermal comfort is observed differs between the two cities, showing that an individual in warmer climates, like Athens, feels thermal comfort at higher air temperatures in comparison with those who live in cooler ones.

3.2 The PET Neutral Temperature

In order to find the PET values for neutral temperature for the two cities, the mean ASV for each 1°C PET interval was calculated. Figure 2 shows the linear regressions for each city, as well as, the coefficient of determination R^2 between mean ASV and PET. It is observed that an increase in mean ASV results in an increase in PET values for each of the examined cities. The equations of the fitted regression lines for the thermal sensations versus PET are shown in Fig. 2. The slope of the fitted lines can be used to indicate the sensitivity of thermal sensations of the individuals in the two cities since it can be used to examine the responses of thermal sensation votes for each 1-degree PET interval. For Kassel, the slope value of 0.049 corresponds to 20.4°C PET per sensation unit, indicating a rather wide range. Similarly, for Athens the slope value of 0.055 corresponds to 18.2°C PET per sensation unit. These values show that during summertime, the locals in both cities

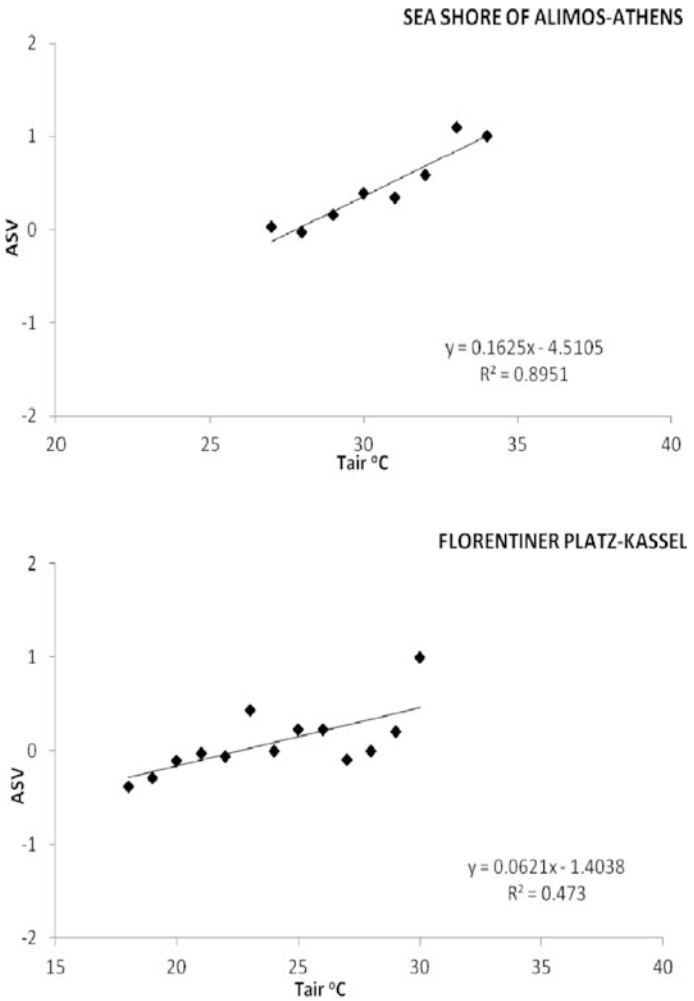

Fig. 1 Linear regressions between the air temperature and thermal sensation classes

Table 2 The neutral temperature for each city for the summer period based on Tair

Sites	Neutral temperature (°C)
Florentiner Platz-Kassel	22.6
Sea shore Alimos-Athens	27.8

are thermally comfortable at a fairly wide range of PET. It also seems that people have adapted to the heat, particularly when compared to the average air temperature for the season. The average air temperature during the surveys in Kassel is over 4°C higher than the climatic mean temperature for July, giving people the opportunity to

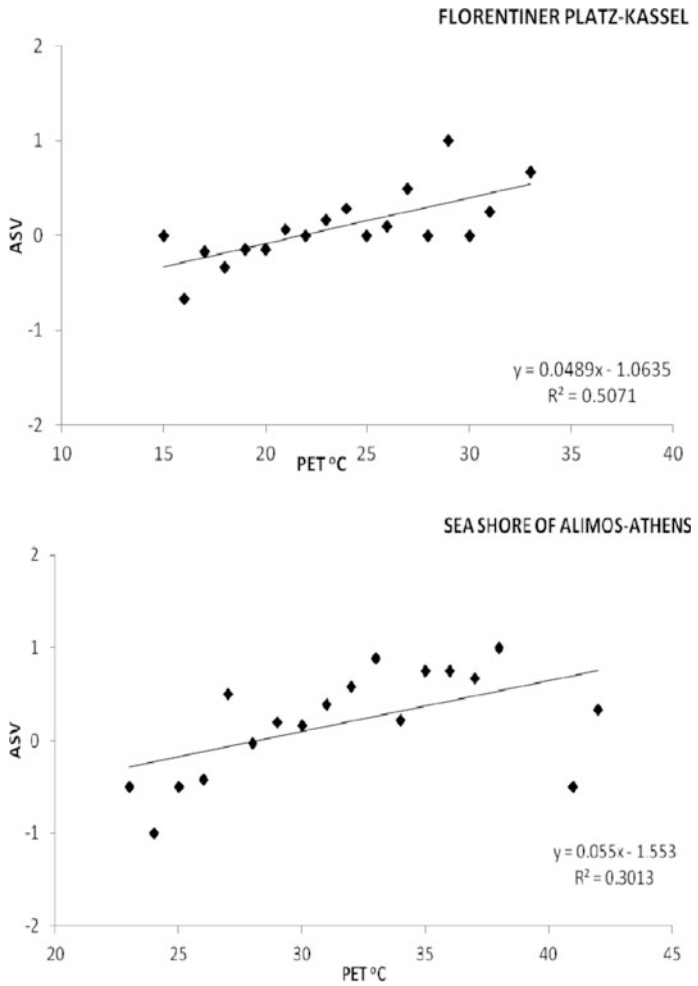

Fig. 2 The linear regression equations, revealing the PET values in which an individual feels thermal comfort during summertime

Table 3 PET neutral temperatures for the two cities for the summer period

Sites	Neutral temperature (°C)
Florentiner Platz-Kassel	21.8
Sea shore Alimos-Athens	28.2

adapt to the higher temperatures. In addition, following the methodology presented in Sect. 3.1 and substituting ASV = 0, the PET value can be calculated according to which an individual should feel thermal comfort the summer period of the year.

Table 3 shows these PET values in which people feel thermal neutrality for each city separately. The values of the neutral temperatures for the two cities clearly

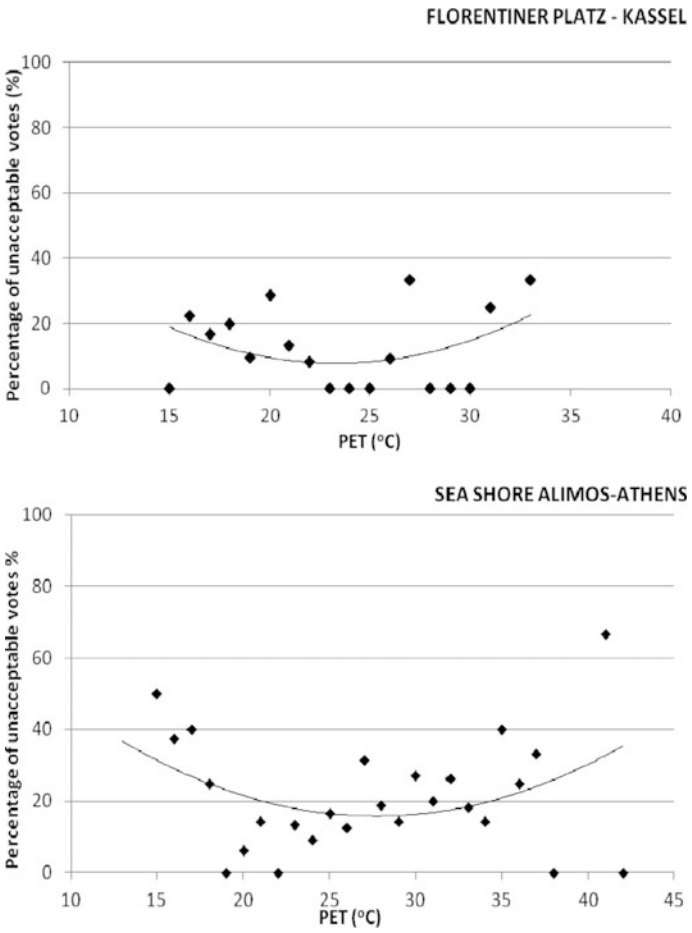

Fig. 3 Thermal acceptable ranges for the examined urban open spaces during summertime

support the fact that occupants of the open spaces are sensitive to PET variations to a different degree since higher neutral temperature values in comparatively warmer environments (see Table 1) indicates adaptation of occupants to the thermal environment.

3.3 PET Thermal Acceptable Range

To estimate the acceptable PET range for neutrality, comfort/discomfort votes, expressed in percentages, were analyzed for each city separately (Fig. 3). ASHRAE specifies the thermal comfort conditions, which are acceptable to 80% or more of the individuals in a space (ASHRAE 2004; Lin and Matzarakis 2008;

Table 4 PET range for ASV neither cold nor warm

ASV	Range (°C)	
	Florentiner Platz-Kassel	Sea Shore Alimos-Athens
Neither cold nor warm	20.3–26.1	25.5–30

Lin et al. 2011). The 80% acceptability limits are the intersections of the fitted curve and the 20% unacceptability line includes the range of values, which corresponds to −1(cold) to +1(warm) thermal sensation classes. In order to approach the thermal comfort range precisely the values ranges that are included in the three ASV classes were separated into three equal intervals from which the intermediate constitutes the thermal comfort values range.

Table 4 shows the PET resulting thermal comfort range for each examined city for summer. In accordance with what is shown in Sect. 3.2, this method also presents that higher neutral temperature values in comparatively warmer environments indicates adaptation of occupants to the thermal environment. That way, the thermal comfort range in Athens is found at higher temperatures comparatively with that of Kassel. For Athens the thermal comfort range is found between 25.5°C and 30°C whereas for Kassel this range is found at lower air temperatures, that is 20.3°C and 26.1°C. It is interesting to note that the two cities present a similar range of temperatures, representing thermal comfort; more specific, the PET thermal comfort range for Kassel is a 5.8°C interval (from 20.3°C to 26.1°C) with a similar thermal comfort interval obtained for Athens, that is 5.5°C (from 25.5°C to 30°C). This is in line with the results from Fig. 2, where the regression analysis for the different cities has similar slopes, implying a fairly well adaptation to the summer heat in their geographic location. Another interesting point, which arises, is the shift of the neutrality zone. Irrespective of the analysis employed, the summer neutral temperature in Kassel is around 5°C lower than in Athens, demonstrating the adaptation to the hotter climatic conditions.

4 Conclusion

This study investigated the thermal comfort conditions in two European cities during summer. Microclimatic and actual thermal sensation vote data were used to estimate values of air temperature in which occupants of the two examined cities feel thermally comfortable. Results show that higher neutral temperature values in comparatively warmer environments are indicative of adaptation of the occupants to the thermal environment. These results imply that people are well adapted to their local environment. Further studies should focus on evidence of adaptation during other seasons of the year and also on differences between them.

References

ASHRAE (2004) ASHRAE standard 55-2004. Thermal environmental conditions for human occupancy. American Society of Heating, Refrigerating and Air-Conditioning Engineers Inc., Atlanta

Höppe P (1999) The physiological equivalent temperature- a universal index for the biometeorological assessment of the thermal environment. Int J Biometeorol 43:71–75

Lin TP, Matzarakis A (2008) Tourism climate and thermal comfort in Sun Moon Lake, Taiwan. Int J Biometeorol 52:281–290. doi:10.1007/s00484-007-0122-7

Lin TP, de Dear R, Hwang RH (2011) Effect of thermal adaptation on seasonal outdoor thermal comfort. Int J Climatol 31:302–312. doi:10.1002/joc.2120

Matzarakis A, Mayer H (1996) Another kind of environmental stress: thermal stress. WHO News 18:7–10

Nakano J, Tanabe S (2004) Thermal comfort and adaptation in semi outdoor environments. ASHRAE Trans 110(2):543–553

Nikolopoulou M, Lykoudis S (2006) Thermal comfort in outdoor urban spaces: analysis across different European countries. Build Environ 41:1455–1470. doi:10.1016/j.buildenv.2005.05.031

RUROS (2009) Rediscovering the urban realm and open spaces. Nikolopoulou M. (Project Coordinator) http://alpha.cres.gr/ruros. Accessed May 2009

Spagnolo J, de Dear RJ (2003) A field study of thermal comfort in outdoor and semi-outdoor environments in subtropical Sydney Australia. Build Environ 38:721–738

Tseliou A, Tsiros I, Lykoudis S, Nikolopoulou M (2010) An evaluation of three biometeorological indices for human thermal comfort in urban outdoor areas under real climatic conditions. Build Environ 45:1346–1352

Connection of Heat Events in Cyprus with Synoptic Upper Air Patterns

F. Tymvios, S. Michaelides, D. Charalambous, A. Retalis, D. Paronis, D.G. Hadjimitsis, A. Agapiou, K. Themistokleous, and C. Skouteli

Abstract There is no widely accepted definition of heat wave. The definition recommended by the World Meteorological Organization and adopted in this research is "when the daily maximum temperature of more than 5 consecutive days exceeds the maximum temperature normal by 5°C". These periods of abnormally and uncomfortably hot and (usually) humid weather are very common in the Eastern Mediterranean during summer and early autumn. Expert examination of the synoptic patterns on upper air charts can reveal the potential for a heat wave event. In this respect, the research presented here attempts to identify height patterns favorable for heat events by using a neural network classification method, namely, the Kohonen Self Organizing Maps (SOM).

1 Introduction

The "climatic character" of a region is determined not only by the respective averages of meteorological parameters (temperature and precipitation being the most frequently used) but also by the type, frequency and intensity of weather events. Anthropogenic activities have the potential to alter the prevalence and severity of extremes such as heat waves, cold waves, storms, floods and droughts.

F. Tymvios (✉) • S. Michaelides • D. Charalambous
Cyprus Meteorological Service, Nicosia, Cyprus
e-mail: ftymvios@ms.moa.gov.cy

A. Retalis • D. Paronis
National Observatory of Athens, Athens, Greece

D.G. Hadjimitsis • A. Agapiou • K. Themistokleous
Cyprus University of Technology, Limassol, Cyprus

C. Skouteli
Open University of Cyprus, Nicosia, Cyprus

C.G. Helmis and P.T. Nastos (eds.), *Advances in Meteorology, Climatology and Atmospheric Physics*, Springer Atmospheric Sciences,
DOI 10.1007/978-3-642-29172-2_111,

Identifying and predicting changes in these types of events under a constantly evolving climate is difficult but critically important in order to understand the exposure to such changes that have a significant impact on human health, infrastructure and the economy, while simultaneously alter the ecosystem (Confalonieri et al. 2007). Heat waves have a distinct impact on society through increased mortality, change in energy consumption profile and the diversification of social behavior. The severity of the heat events may include the local climatological characteristics, the community design and the individual tolerance to heat. The frequency of appearances and the intensity of heat waves are both increasing in the Mediterranean area (Founda and Giannakopoulos 2009; Kuglitsch et al. 2010).

While the definition recommended by the World Meteorological Organization for a Heat Wave (WMO 2004) is "when the daily maximum temperature of more than 5 consecutive days exceeds the maximum normal (1961–1990) by 5°C", in most countries the definition of extreme heat events is based on the potential for hot weather conditions to result in an unacceptable level of adverse health effects, including increased mortality. Also, a threshold in maximum temperature is in practical use in many countries (Robinson 2001).

A strong relationship exists between large scale circulation patterns and regional surface variables such as surface pressure, dynamical rainfall, wind and temperature (Xoplaki et al. 2003; Tymvios et al. 2007, 2008, 2010). As a consequence, synoptic upper air charts at certain levels comprise a valuable tool for the operational weather forecaster to qualitatively predict occurrences of heavy rainfall over particular areas. The height pattern at 500 hPa is often used for this purpose. In order to take advantage of these semi-empirical methods and to simplify the statistical processing, stochastic downscaling methods are often applied to the actual weather patterns in order to generate clusters of synoptic cases with similar characteristics. Weather type classifications are simple, discrete characterizations of the current atmospheric conditions and they are commonly used in atmospheric sciences.

2 Data and Methodology

The island of Cyprus lies between latitude circles 34.6°N and 35.6°N and between meridians 32°E and 34.5°E, surrounded by the eastern Mediterranean Sea. Its Mediterranean climate is characterized by the succession of a single rainy season (November to mid-March) and a single longer dry season (mid-March to October). This generalization is modified by the influence of maritime factors, yielding cooler summers and warmer winters in most of the coastal and low-lying areas. Visibility is generally very good. However, during spring and early summer, the atmosphere is quite hazy, with dust transferred by the prevailing south-easterly to southwesterly winds from the Saharan and Arabian deserts, usually associated with the development of desert depressions (Michaelides et al. 1999).

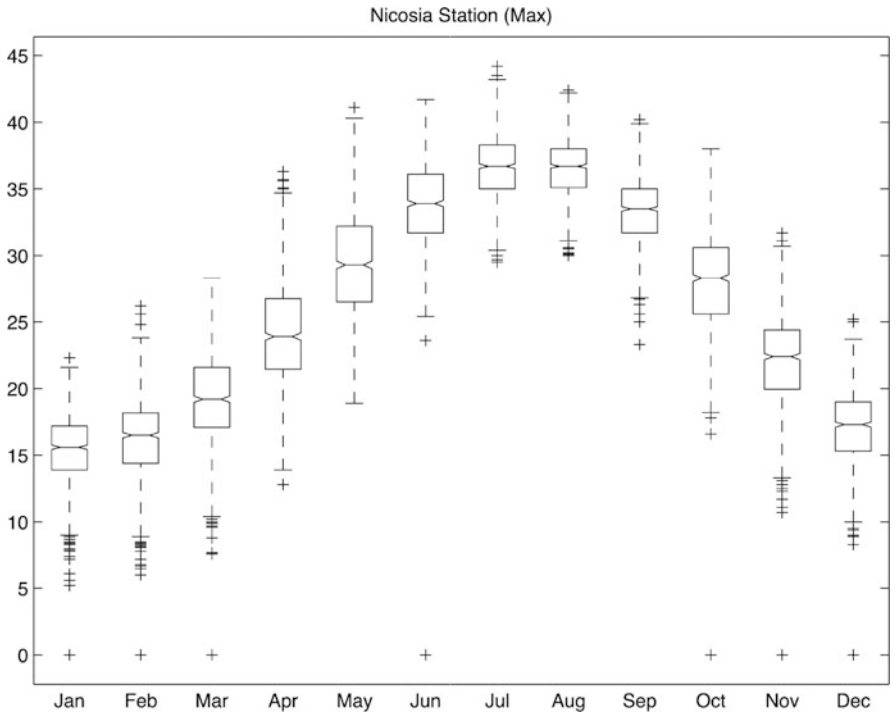

Fig. 1 Box and Whiskers plot of the maximum temperatures in Nicosia (1958–2000)

2.1 Data

As an indication of a possible heat event, the maximum temperature of Nicosia station was chosen. This station is located within the urban area of the city of Nicosia (latitude 35.17°, longitude 33.35°, altitude 170 m) and equipped with traditional instrumentation was operational from 1957 till 2001, when it was upgraded to an automatic station. The database used in this study comprises the maximum and minimum temperature records from this station and the weather classification results of the ERA40 reanalysis for the period of 1958–2000 (covering roughly the ERA40 time window). The maximum monthly temperature measurements are presented in Fig. 1.

The methodology used for the classification was presented in Michaelides et al. (2007, 2010). The temperatures database was checked for consistency and homogeneity against measurements from nearby stations while the maximum temperatures were also checked for normal distribution fitting.

2.2 Methodology

The maximum daily temperature at Nicosia station was checked against the climatological monthly average maximum value of the period 1961–1990. If the

difference was 5°C or more, then the period was characterized as "possible heat event". If the subsequent days were also positive against this temperature test for 3 days or more, then the period was considered as heat event. The heat events were checked against the weather classification patterns in order to identify connection among particular patterns and heat events. The same procedure was adopted for a difference of 3°C since events with a 5°C difference are rare during summer. Special care was taken when checking the last and the first day of the month where daily maximum temperature values were subtracted from the average climatological value of the 2 subsequent months.

3 Results

The distribution of the heat events in consecutive days for 3°C and 5°C difference is illustrated in Fig. 2. It is clearly evidenced that more than 75% of the events last 3–5 days. Most of the identified heat events occur in the transition periods (Spring and Autumn). This finding is also supported by the findings in Fig. 1, where the larger variation (the area between 25th and 75th percentile) of the average of the maximum temperatures is given for the same periods. With the exception of the periods 2/7/2000–14/7/2000 (13 days) and 12/7/1978–21/7/1978 (10 days), all incidents lasting more than 10 days for this station occurred in October, November, March, April and May.

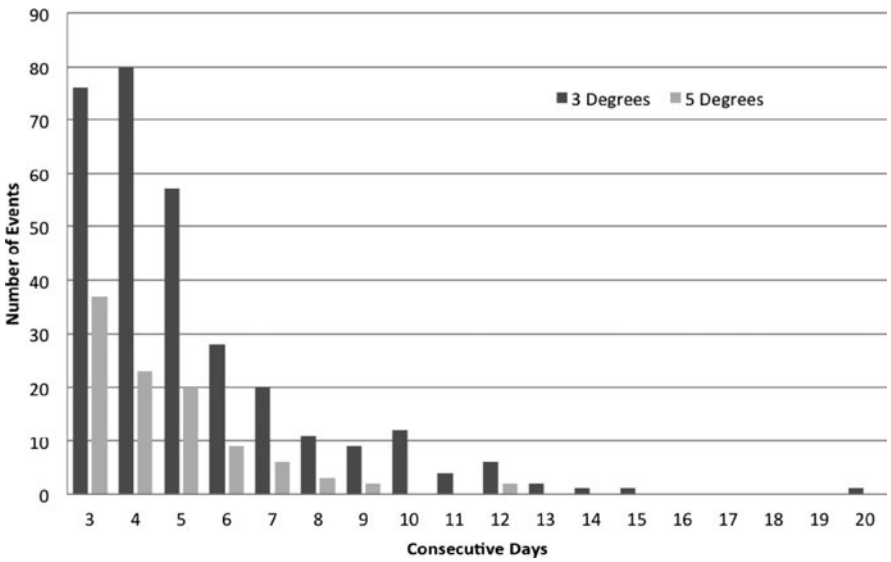

Fig. 2 Distribution of the heat events in consecutive days for 3°C and 5°C difference

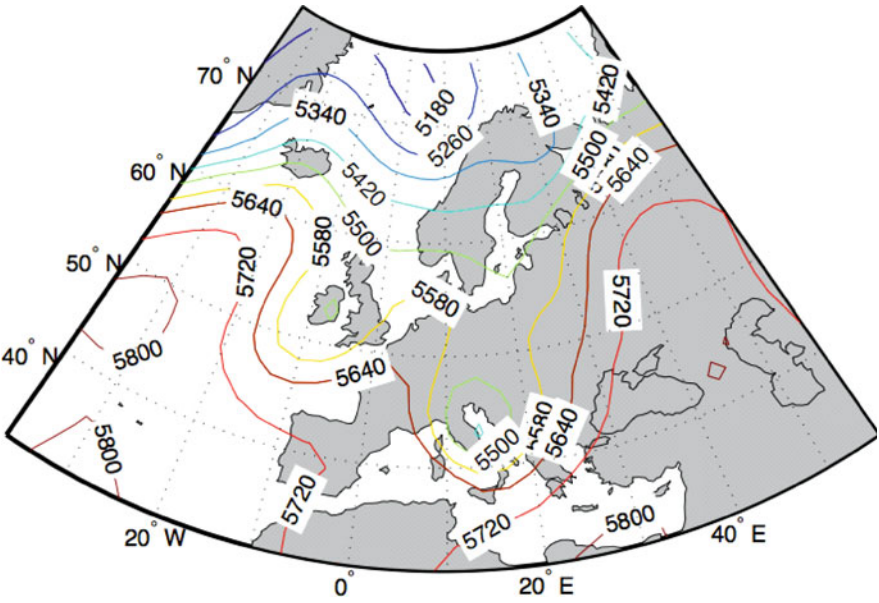

Fig. 3 The height pattern at 500 hPa (Cluster 5) from 24/11/1962

Clusters 5 and 34 share most of the heat event occurrences. They are both transition period clusters with similar characteristics, exhibiting an upper level ridge over eastern Mediterranean and a deep low west of the ridge; Cluster 5 belongs to the cold period and cluster 34 to the warm period. An example of a Cluster 5 member is illustrated in Fig. 3.

When these clusters appear during early Spring and late Autumn, the events last from 8 to 15 days, while when they appear just before or after Summer (May and September) they last around 5 days. Summertime appearances of heat events are equally shared between Clusters 12, 19, 24 and 36, all characterized by warm and dry conditions (Michaelides et al. 2010).

4 Conclusions

The connection between heat events and atmospheric circulation at 500 hPa did not give definite results about patterns that dominate heat event occurrences as it was possible to demonstrate in previous studies on rainfall and extreme rainfall events. There are two reasons for this inadequacy. The first is that the window that was chosen for the classification does not include the synoptic patterns that influence the area sufficiently; the second reason is that although upper air patterns at 500 hPa contribute significantly to the evolution of certain surface features (such as dynamical or extreme rainfall) such an association is not so clear for the

temperature field. In the search for associations of the temperature fields with synoptic patterns in the Mediterranean it is important to consider also the lower parts of the atmosphere.

Future research concerning the connection of the weather classification patterns will be focused into a new, much larger window that will include Northern Africa and the Middle East and a combination of classification of patterns over certain levels of the atmosphere (850, 700, 500 hPa).

Acknowledgments The results presented are part of an ongoing research project entitled "Study of the Phenomenon of Urban Heat Island in Cyprus", funded by the Cyprus Research Promotion Foundation of Cyprus, under contract No. AEIFORIA/ASTI/0308(BE)/01.

References

Confalonieri U, Menne B, Akhtar R, Ebi KL, Hauengue M, Kovats RS, Revich B, Woodward A (2007) Human health climate change 2007: impacts, adaptation and vulnerability. In: Parry ML, Canziani OF, Palutikof JP, van der Linden PJ, Hanson CE (eds) Contribution of working group II to the fourth assessment report of the intergovernmental panel on climate change. Cambridge University Press, Cambridge

Founda D, Giannakopoulos C (2009) The exceptionally hot summer of 2007 in Athens, Greece: a typical summer in the future climate. Global Planet Change 67:227–236. doi:10.1016/j.gloplacha.2009.03.013

Kuglitsch FG, Toreti A, Xoplaki E, Della-Marta PM, Zerefos CS, Türkeş M, Luterbacher J (2010) Heat wave changes in the eastern Mediterranean since 1960. Geophys Res Lett 37:L04802. doi:10.1029/2009GL041841

Michaelides SC, Evripidou P, Kallos G (1999) Monitoring and predicting Saharan desert dust transport in the eastern Mediterranean. Weather 54:359–365

Michaelides SC, Liassidou F, Schizas CN (2007) Synoptic classification and establishment of analogues with artificial neural networks. Pure Appl Geophys 164:1347–1364. doi:10.1007/s00024-007-0222-7

Michaelides S, Tymvios FS, Charalambous D (2010) Investigation of trends in synoptic patterns over Europe with artificial neural networks. Adv Geosci 23:107–112. doi:10.5194/adgeo-23-107-2010

Robinson PJ (2001) On the definition of heat waves. J Appl Meteorol 40:762–775

Tymvios FS, Constantinides P, Retalis A, Michaelides S, Paronis D, Evripidou P, Kleanthous S (2007) The AERAS project – database implementation and neural network classification tests. In: Proceedings of the 6th international conference on urban air quality, Limassol, Cyprus

Tymvios FS, Savvidou K, Michaelides SC, Nicolaides KA (2008) Atmospheric circulation patterns associated with heavy precipitation over Cyprus. Geophys Res Abstr 10:EGU2008-A-04720

Tymvios F, Savvidou K, Michaelides S (2010) Association of geopotential height patterns with heavy rainfall events in Cyprus. Adv Geosci 23:73–78. doi:10.5194/adgeo-23-73-2010

WMO (2004) In: Proceedings of the meeting of experts to develop guidelines on heat/health 53 warning systems. WCASP No. 63, WMOTD No. 1212

Xoplaki E, Gonzalez-Rouco JF, Luterbacher J, Wanner H (2003) Mediterranean summer air temperature variability and its connection to the large-scale atmospheric circulation and SST. Clim Dynam 20:723–739. doi:10.1007/s00382-003-0304-x

The Summer Circulation in the Eastern Mediterranean and the Middle East: Influence of the South Asian Monsoon and Mid-Latitude Dynamics

E. Tyrlis, J. Lelieveld, and B. Steil

Abstract The summer circulation in the Eastern Mediterranean and the Middle East (EMME) is dominated by persistent northerly winds (Etesians) whose ventilating effect counteracts the adiabatic warming induced by subsidence prevailing over the eastern Mediterranean. The ERA40 dataset is used to investigate the South Asian Monsoon and mid-latitude influences on the EMME circulation. Consistent with past modeling studies, in late spring an upper level warm structure and subsidence area expanding towards the EMME are identified, attributed to Rossby waves excited by monsoon convection. Steep sloping isentropes develop over the EMME with subsidence mainly over the eastern Mediterranean and Iran, where orographically induced circulation patterns enhance the mid-latitude northwesterly flow and the air mass subsidence along isentropes. These phenomena have a maximum in July and are strikingly synchronous to the convection over northern India where the background state favors a stronger Rossby wave response. The monsoon induced large-scale background state over the EMME is modified by synoptic activity originating in the Atlantic that introduces high frequency variability over the EMME. During 'etesian outbreaks' a ridge develops over the Balkans and sharp tropopause folds appear over the Aegean.

E. Tyrlis (✉)
The Cyprus Institute, EEWRC, 20 Constantinou Kavafi Street, Nicosia 2121, Cyprus
e-mail: e.tyrlis@cyi.ac.cy

J. Lelieveld
The Cyprus Institute, EEWRC, 20 Constantinou Kavafi Street, Nicosia 2121, Cyprus

Max Planck Institute for Chemistry, Mainz 55020, Germany

King Saud University, Riyadh 11451, Saudi Arabia

B. Steil
Max Planck Institute for Chemistry, Mainz 55020, Germany

C.G. Helmis and P.T. Nastos (eds.), *Advances in Meteorology, Climatology and Atmospheric Physics*, Springer Atmospheric Sciences,
DOI 10.1007/978-3-642-29172-2_112,

1 Introduction

As the South Asian summer monsoon heat low expands towards the Mediterranean forming the Persian trough, a sharp east–west pressure gradient builds up over the EMME resulting in persistent northerly winds in the Aegean Sea, known as the Etesians. The ventilating effect of the Etesians counteracts the adiabatic warming induced by subsidence (Ziv et al. 2004), which inhibits convection and results in a prolonged summer dry period. This subsidence is sometimes associated with the descending branch of the local Hadley Cell, while the disproportionately stronger descending branch, compared to its ascending one over the eastern Sahel region, is attributed to the influence of a monsoon driven zonal 'Walker type' circulation, which features ascent over southeastern Asia (Ziv et al. 2004). Such a closed circulation is not identified in the trajectory analysis by Rodwell and Hoskins (1996). Based on idealized simulations with primitive equation models, they proposed that the monsoon heating induces an equatorially trapped Rossby wave to its west, with a warm structure at its core. The interaction of this structure with the mid-latitude westerlies triggers further subsidence over the eastern Mediterranean (EMED), whereas orography focuses subsidence over specific areas. This study aims at the identification of the monsoon induced signal over the EMME and the assessment of the mid-latitude influence.

2 Data and Methodology

Six-hourly ERA-40 (Uppala et al. 2005) analyses of precipitation, MSLP, temperature and wind, interpolated onto a N80 full-Gaussian grid (~1° × 1.125°), are used. Daily mean precipitation and 500 hPa omega vertical velocity are constructed and then averaged over the areas shown in Fig. 1 to obtain regional monsoon intensity metrics of the four most active regions of the South Asian summer monsoon. ECMWF model forecasts for temperature, wind and diabatic heating are used for the quantification of the thermodynamic energy equation terms

$$\underbrace{\frac{\partial T}{\partial t}}_{LTT} = \underbrace{\frac{J}{C_p}}_{TPTT} + \underbrace{\frac{T}{\theta}\frac{\partial T}{\partial z}}_{VATT} + \underbrace{\underbrace{\left(-u\frac{\partial T}{\partial x}\right)}_{ZATT} + \underbrace{\left(-v\frac{\partial T}{\partial z}\right)}_{MATT}}_{HATT}$$

where T is temperature, θ is potential temperature, u and v are the horizontal wind components, J is the diabatic heating rate and Cp is the specific heat of dry air at constant pressure. The first term is the Local Temperature Tendency (LTT), J/C_p represents the total physics temperature tendency (TPTT), the third term gives the temperature tendency due to Vertical Advection (VATT), whereas the last term represents the temperature tendency due to horizontal advection (HATT) that can

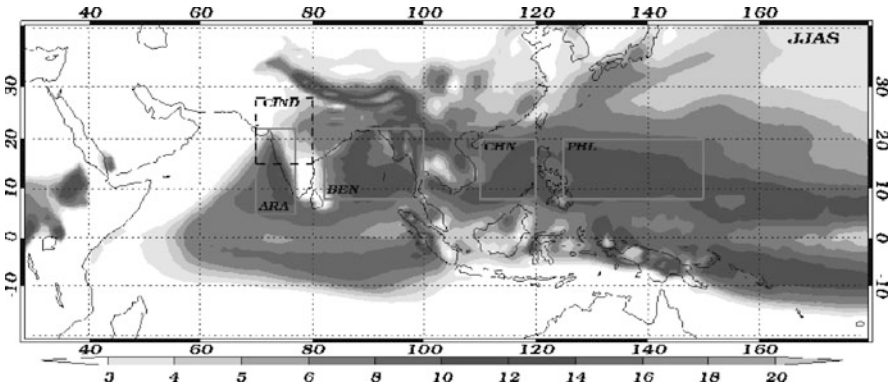

Fig. 1 Daily mean JJAS precipitation (mm/day)

be split into its zonal and meridional advection components ZATT and MATT, respectively. Since TPTT is available from the ECMWF model only as net temperature tendency from parameterized processes, all terms are calculated from 6 h model forecasts of temperature and wind components to acquire maximum consistency. The timeseries of daily mean values of all terms span the period 1 January 1958–31 August 2002.

3 Mechanisms Influencing the Summer EMME Circulation

An envelope area of subsidence extends from the central Mediterranean until Iran (Figs. 2 and 3b). The most intense subsidence is observed where the isentropes slope steeply so that even a small horizontal motion can be associated with a large vertical displacement. Subsidence is stronger over the central and eastern Mediterranean (Fig. 3a), with a 500 hPa maximum around Crete. Air masses converge above 500 hPa and diverge at lower levels while fanning out southwards and accelerate through (1) the Aegean Sea, (2) the Red Sea Straits and (3) the Iraq–Persian Gulf regions (Fig. 2a). Strong low and mid level subsidence is also apparent over areas (2) and (3). A distinct low level core of strong subsidence lies over the Aegean (Fig. 3a), while mainly mid level subsidence is found to the east of the Caspian Sea, also accompanied by an 'Etesian-like' northerly flow (Figs. 2a and 3b).

In late spring, monsoon convection is located over southeastern Bay of Bengal, below an upper level easterly jet leading to a weak Rossby wave response. As convection migrates to its northernmost location, over northern continental India in early July, below a weak easterly or even westerly flow, the Rossby wave structure amplifies (Lin 2009), impacting the EMME circulation, as implied by the strikingly synchronous seasonal cycles of the EMED subsidence and northerly flow with that

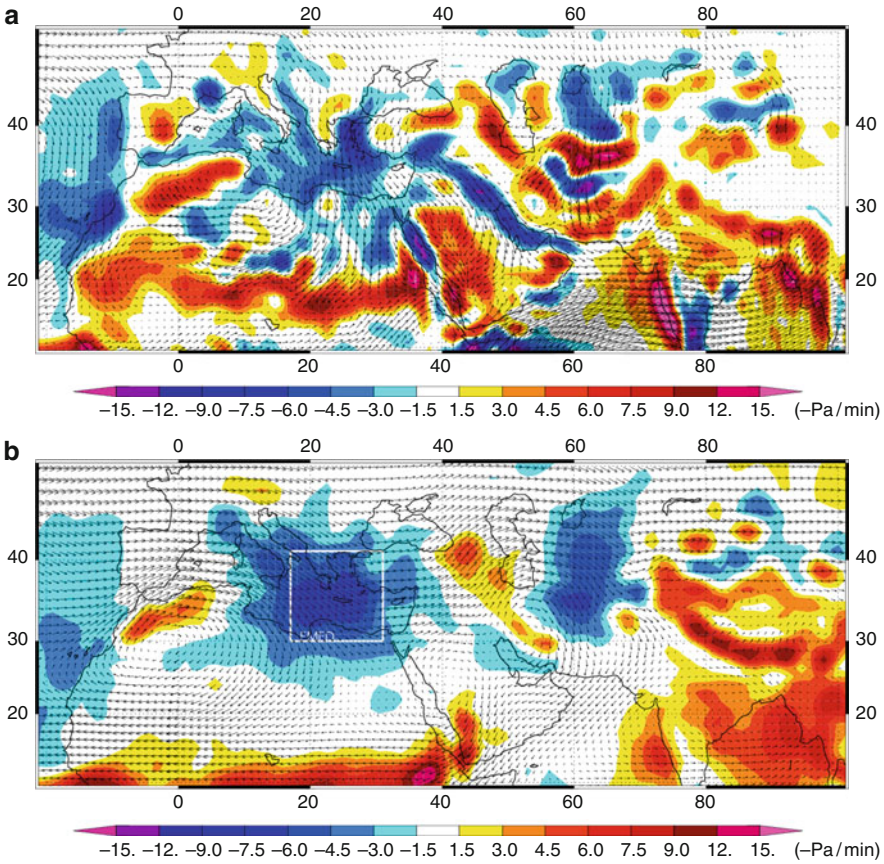

Fig. 2 July climatology of omega (−Pa/min) and wind at 850 hPa (**a**), and 500 hPa (**b**). The *white box* marks the EMED region (17–31°E, 30–41°N). *Blue* (*red*) colors denote subsidence (ascent)

of the monsoon activity (Fig. 4b). The monsoon induced zonally asymmetric circulation accounts for the anomalous latitude and strong free tropospheric subsidence observed over the EMME, in excess of the typical intensity and seasonal evolution of the descending branch of the Hadley Cell (Fig. 4a). The dynamics of the monsoon influence involve a westward expanding mid and upper level warming area (Fig. 5a), which can be directly linked to a Rossby wave signature, and results in sharp slopes of the isentropes over the EMME. This facilitates further subsidence and adiabatic warming in the western and northern periphery of the warm structure that is exposed to the mid-latitude westerlies (Fig. 5b). The Rossby wave response is characterized by a westward expanding baroclinic signature with an upper level ridge and a low level trough expanding westward that gives rise to the Etesians. Thus, subsidence and the northerlies over the EMME are reconciled manifestations of the monsoon influence (Tyrlis et al. 2012).

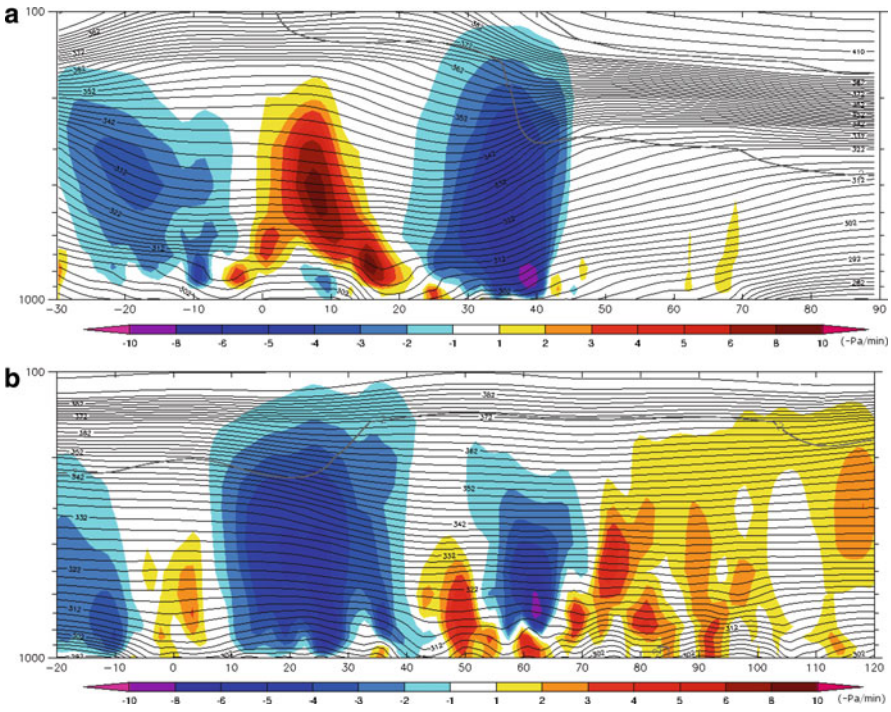

Fig. 3 Pressure-latitude (**a**) and pressure-longitude (**b**) profiles of July omega (*filled contours* in −Pa/min) and θ (contours in Kelvin) averaged over the sectors 24–28°E and 32–40°N, respectively. *Thick line* corresponds to the dynamical tropopause (2 PVU surface)

Apart from the direct influence of topography through the amplification of subsidence and the northerly flow over the Aegean, the Red Sea, the Iraq–Gulf region and to the east of the Caspian Sea, elevated surface heating over the high terrain contributes to the formation of the summer mid-level anticyclonic centers over northwestern Africa, central western Saudi Arabia and the Zagros mountains (Fig. 2b). Enhanced northerly flow and consequently stronger subsidence are induced to their east over the EMED and Iran leading in turn to enhanced adiabatic warming (Fig. 5c), which is opposed by horizontal advection cooling (Fig. 5d). Thus, the 500 hPa 'hot spots' over northern Saudi Arabia, Egypt and Afghanistan (Fig. 5b) are the indirect influence of topography on the thermodynamic state of the troposphere, as they are located downstream of the subsidence areas, marking the excess of VATT against HATT (Fig. 5c, d).

The distribution of all the JJA daily mean 1,000 hPa wind direction and speed, averaged over the Aegean (Fig. 6a), shows an elongated cluster protruding from the background distribution that can be associated with the 'Etesians regime'. Implementation of criteria for wind direction (40°W–30°E) and intensity (>4.5 m/s) allows us to identify periods of strong northerlies, namely the 'Etesian outbreaks'.

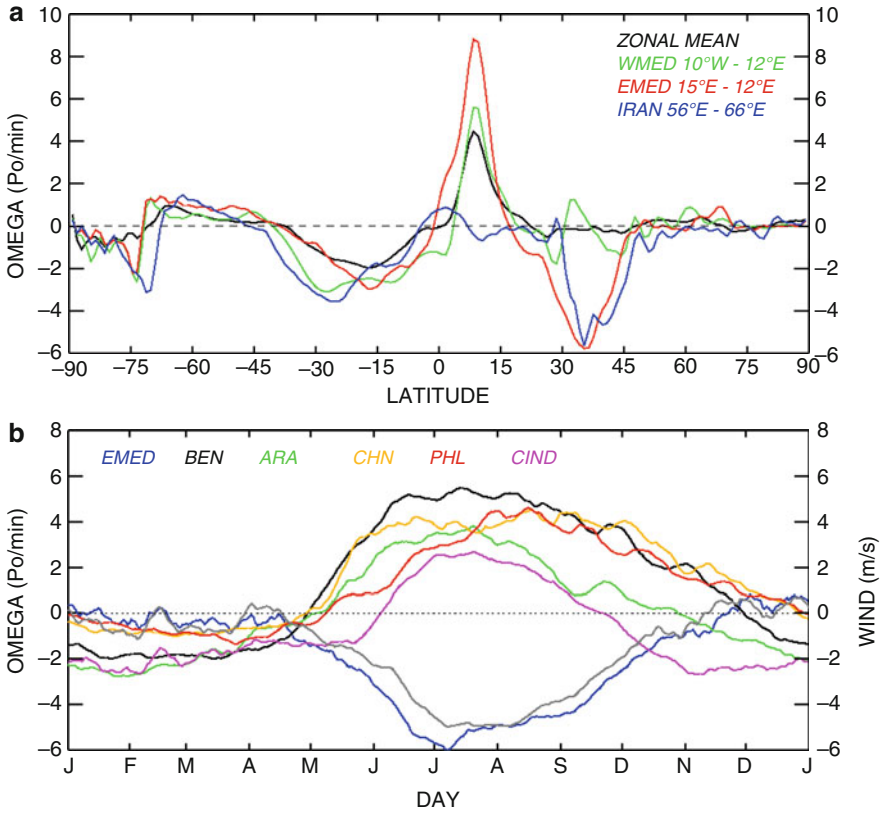

Fig. 4 (**a**) Latitudinal distribution of July omega (−Pa/min) averaged over the longitudinal sectors shown in the legend. (**b**) Seasonal evolution of 850 hPa meridional wind (*grey line*) and 500 hPa omega (−Pa/min) averaged over the EMED (Fig. 2b) and the areas depicted in Fig. 1

A wave originating in the North Atlantic 4–5 days prior to the outbreak onset (Fig. 6b) provides the 'seed' for ridge formation over the Balkans (Fig. 6c, d). During the outbreaks, stronger than normal subsidence (Fig. 6e) and intrusions of high PV of stratospheric origin (sharp tropopause folds) are observed (Fig. 6f).

4 Conclusions

The summer EMME circulation is characterized by persistent northerly winds and subsidence and is influenced by the South Asian Monsoon, which forms a large scale background state over the area. The dynamics of this interaction are explained by invoking the conceptual model of Rossby waves excited by monsoon

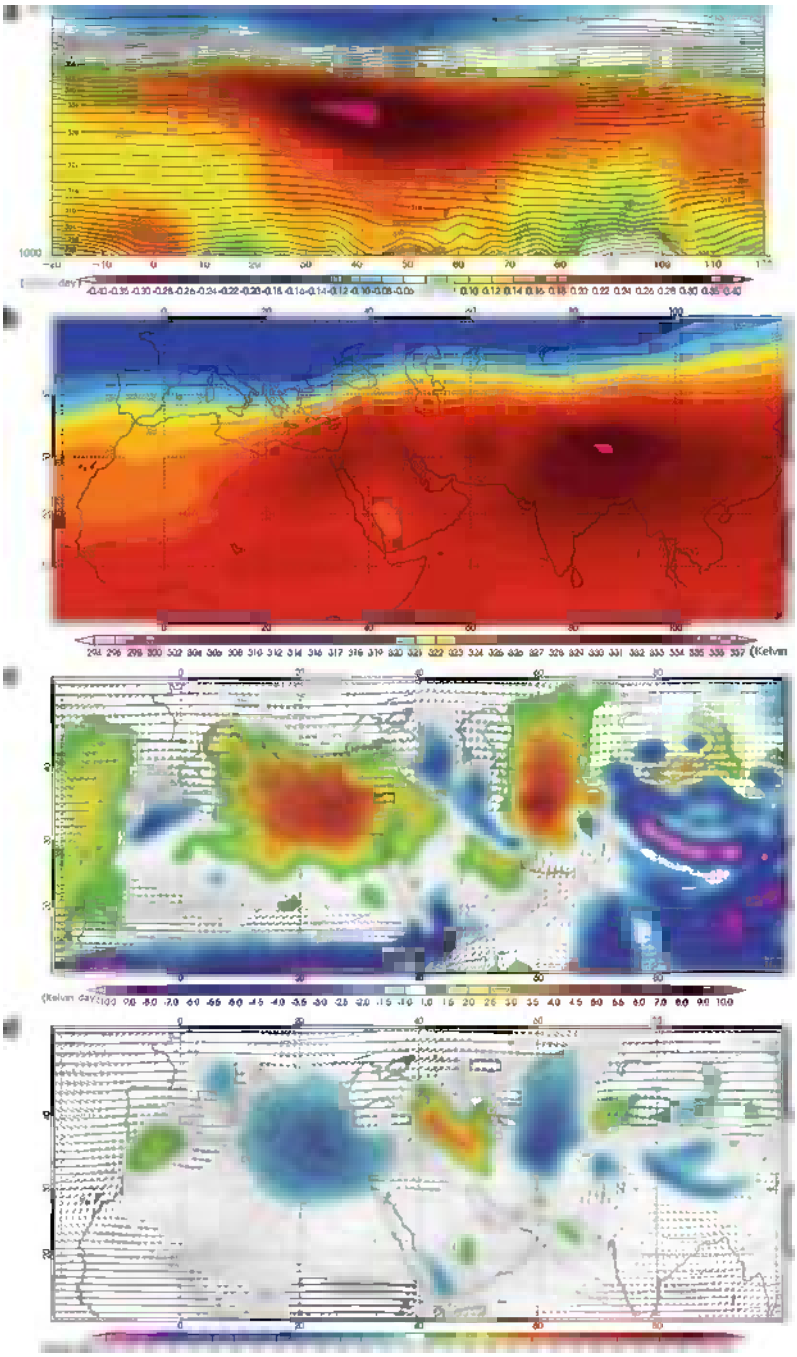

Fig. 5 (**a**) Pressure-longitude profile of mean June LTT averaged over the sector 32–40°N. 500 hPa θ (**b**) VATT (**c**) and HATT (**d**). Wind vectors and θ are also plot in **c**, **d**

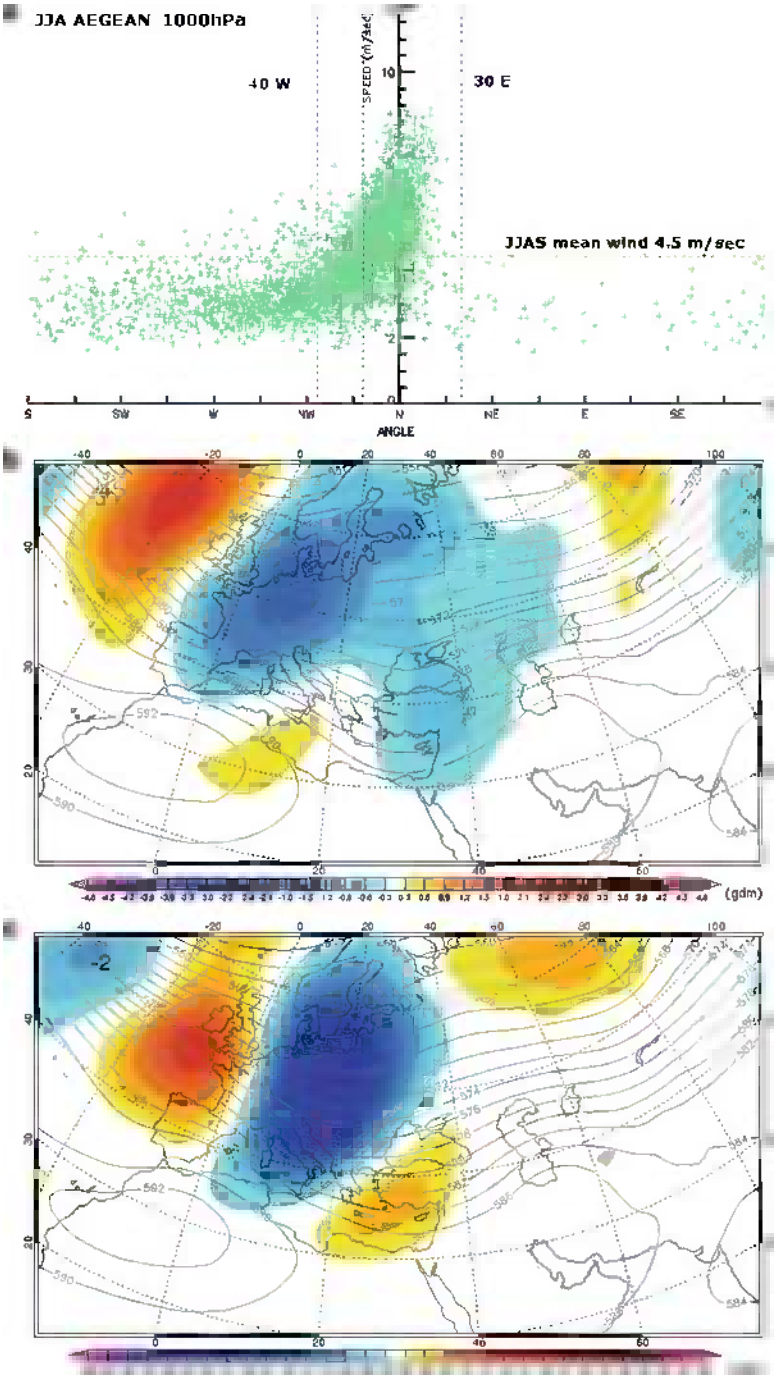

Fig. 6 (continued)

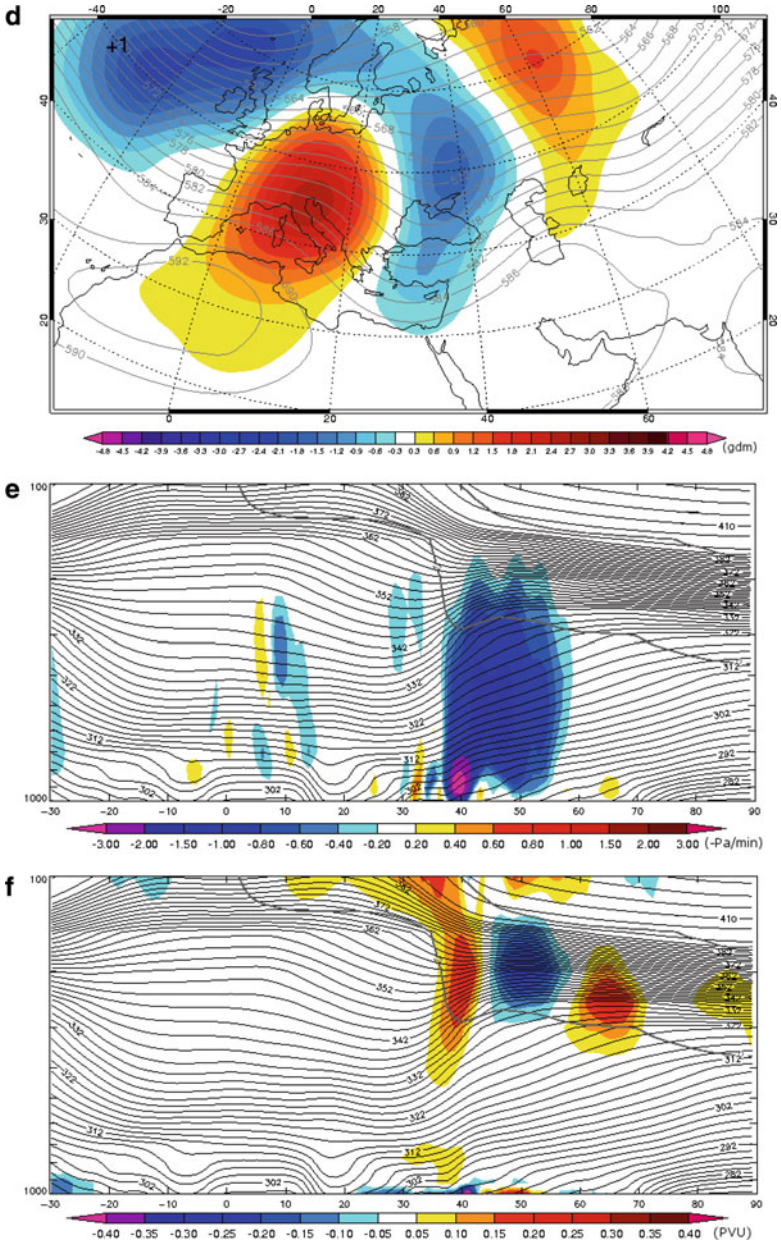

Fig. 6 (**a**) JJA daily mean 1,000 hPa wind direction and speed averaged over the Aegean Sea (23.5–28.5°E, 35–41°N). (**b**–**d**) Evolution of 500 hPa geopotential height (gdm) composite anomalies for −4, −2 and +1 days relative to the onset of July-August (JA) Etesian outbreaks, respectively. Contours depict the JA climate. (**e**, **f**) Pressure-latitude profiles of composite anomalies of omega (−Pa/min) and potential vorticity (PVU) during JA Etesian outbreaks, respectively. Thick line marks the dynamical tropopause and contours depict the θ JA climate

convection. Topography controls the location of the major mid-level anticyclones that focus the northerly flow and subsidence over the EMED and to the east of the Caspian Sea. Mid-latitude wave disturbances modify the background state and induce high frequency variability leading to circulation outbreaks over the area.

Acknowledgments The research leading to these results has received ERC funding under the European Union's Seventh Framework Program (FP7/2007-2013)/ERC grant agreement 226144.

References

Lin H (2009) Global extratropical response to diabatic heating variability of the Asian summer monsoon. J Atmos Sci 66:2697–2713. doi:10.1175/2009JAS3008.1

Rodwell MJ, Hoskins BJ (1996) Monsoons and the dynamics of deserts. Q J R Meteorol Soc 122:1385–1404. doi:10.1002/qj.49712253408

Tyrlis E, Lelieveld J, Steil B (2012) The summer circulation in the eastern Mediterranean and the Middle East: influence of the South Asian Monsoon. Clim Dyn Submitted

Uppala SM, Kallberg PW, Simmons AJ et al (2005) The ERA-40 reanalysis. Q J R Meteorol Soc 131:2961–3012. doi:10.1256/qj.04.176

Ziv B, Saaroni H, Alpert P (2004) The factors governing the summer regime of the eastern Mediterranean. Int J Climatol 24:1859–1871. doi:10.1002/joc.1113

Study of Frost Days in the Greek Region: Future Projections from the ENSEMBLES Models

K. Velikou and K. Tolika

Abstract According to the 2007 IPCC Report during the last decades an extensive reduction in the number of frost days has been observed mainly in the mid-latitude regions. Furthermore, the dynamical projections from several models estimate an additional decrease of the frost days all over Europe and especially in the Mediterranean region until the end of the twenty-first century. Thus, the main score of the present study is the statistical analysis of the frost characteristics in the Greek region. Maximum and minimum temperature daily data will be utilized for 21 meteorological stations uniformly distributed over the domain of study and the analysis of the number of frost days and the length of the frost-free period will take place. Finally, using the future projections of updated regional climate models, developed under the frame of the ENSEMBLES project, we will estimate the future changes of the aforementioned parameters due to the enhancement of the greenhouse effect.

1 Introduction

In recent years, scientific studies on changes in planet's temperature show a distinct upward trend. This temperature rise, which is expected to be quite intense in southern Europe and especially to the eastern Mediterranean, leads also to the reduction of frost days over those areas. According to the 2007 IPCC Report (Trenberth et al. 2007), a significant decrease in the number of frost days in a future climate is estimated mainly in the mid-latitude regions. Research on the climate of the USA until the end of twenty-first century (Meehl et al. 2004) showed that the number of frost days in this country decreases. This change is shown to depend partly on regional changes in atmospheric circulation. Moreover, research on changes in indices related to frost and snow in

K. Velikou (✉) • K. Tolika
Department of Meteorology and Climatology, School of Geology, Aristotle University of Thessaloniki, Thessaloniki 54124, Greece
e-mail: kvelikou@geo.auth.gr

C.G. Helmis and P.T. Nastos (eds.), *Advances in Meteorology, Climatology and Atmospheric Physics*, Springer Atmospheric Sciences,
DOI 10.1007/978-3-642-29172-2_113,

Europe by the end of the twenty-first century showed a distinct tendency towards fewer frost days and shorter frost seasons throughout Europe (Jylhä et al. 2007). Projections of changes in climate extremes showed that in the northwest region of North America and in Eastern Europe there are decreases in frost days over that continent related mainly to changes in atmospheric circulation (Tebaldi et al. 2006).

Thus, the present study aims on the statistical analysis of the number of semi frost and frost days, as well as the length of the frost free period over the Greek area and furthermore on the estimation of the future changes of the examined parameters until the end of the twenty-first century due to the enhanced greenhouse gas concentrations in the atmosphere.

2 Data and Methodology

The data used in the study consists of daily maximum and minimum temperature records from 21 stations that cover the entire Greek area (Fig. 1), for the period 1971–2000. Moreover, daily maximum and minimum simulated temperature data derived from the most updated regional climate models (RCMs), developed during the ENSEMBLES European Research project (http://www.ensembles-eu.org/), were also utilized. The models' simulations and projections cover the time period 1950–2100. ENSEMBLES constitutes of 14 RCMs, but due to space limitation the results only from the KNMI-RACHMO2 RCM are presented. The Royal Netherlands Meteorological Institute (KNMI) developed this dynamical model (KNMI-RACHMO2) with the GCM ECHAM5 as a "parent" model (Lenderink et al. 2003). For the future climate projections of this model, IPCC emission scenario A1B is being used. The spatial analysis of the model is 25 km × 25 km and covers the European area with 114 grid points in latitude and 124 grid points in longitude.

Semi frost day is defined as the day that the minimum temperature is lower than zero, while during a frost day also the maximum temperature remains below zero. Also, the frost free period is determined as the largest period during a year's time that the daily minimum temperature remains above zero. All the above parameters were calculated primarily for the reference period (1971–2000) for both the station

Fig. 1 The examined stations

Table 1 Observational data trends (+/−) for period 1971–2000

	Time series	Agrinio	Athens	Alex/poli	Argostoli	Chania	Elliniko	Heraklio	Ierapetra	Ioannina	Kalamata	Kerkyra
Semi frost days	1971–2000	+	−	+	+		−			+	−	−
Frost days	1971–2000		−	+						−		
Frost free period	1971–2000	−	+	+	−	+	+	+	+	−	−	+
	Time series	Kozani	Kythira	Larissa	Mylos	Mytilini	Naxos	Rodos	Samos	Skyros	Thes/niki	
Semi frost days	1971–2000	−	−	+	−	−	−		+	−	+	
Frost days	1971–2000	+		+							+	
Frost free period	1971–2000	+	+	+	+	+	+	+	−	+	+	

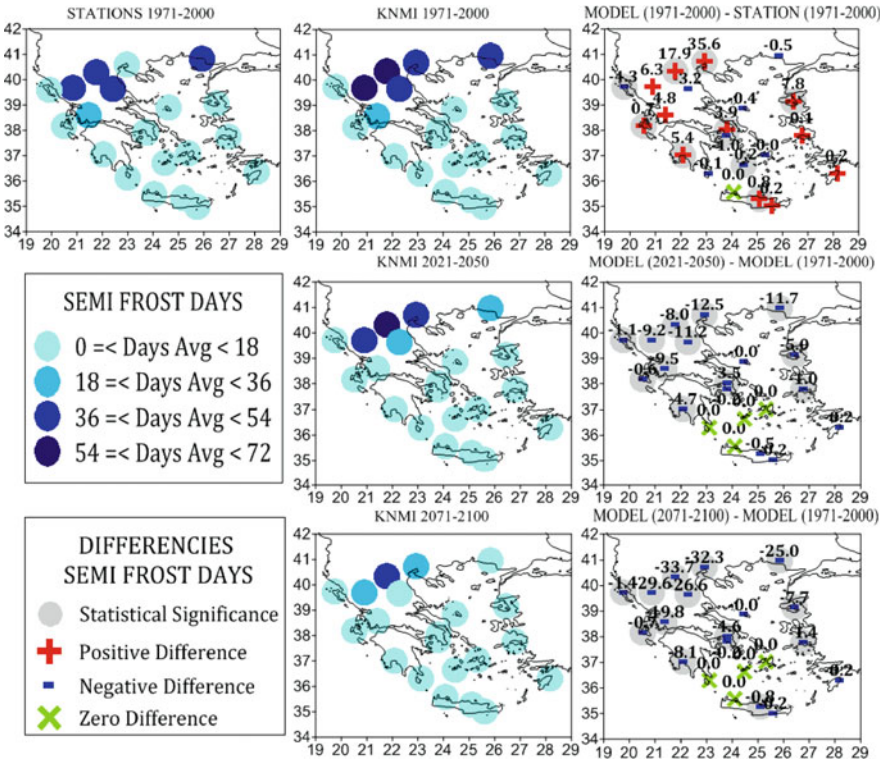

Fig. 2 Averages of semi frost days for all time series and their differences

and the corresponding simulated grid point (the nearest to the station and on land) temperature data and afterwards the statistical analysis was made for the model future projections for two future periods, 2021–2050 and 2071–2100. Moreover, the average values of semi frost days, frost days and frost free period were calculated for each station and grid point and for the time periods mentioned above. Kendall Tau test (Wilks 2005) was used in order to examine the statistical significance of the trends of each parameter for every station and grid point and for every time series. Finally, an attempt was made in order to find the differences between the future periods and the control period (2021–2050)–(1971–2000) and (2071–2100)–(1971–2000). The statistical significance of these differences was examined with the use of *T*-test (Wilks 2005).

3 Results

Regarding the semi frost days, the results from the analysis of the observational data show that Kozani has a maximum average of 53.1 semi frost days for period 1971–2000. Generally, stations in southern Greece are characterized by a negative

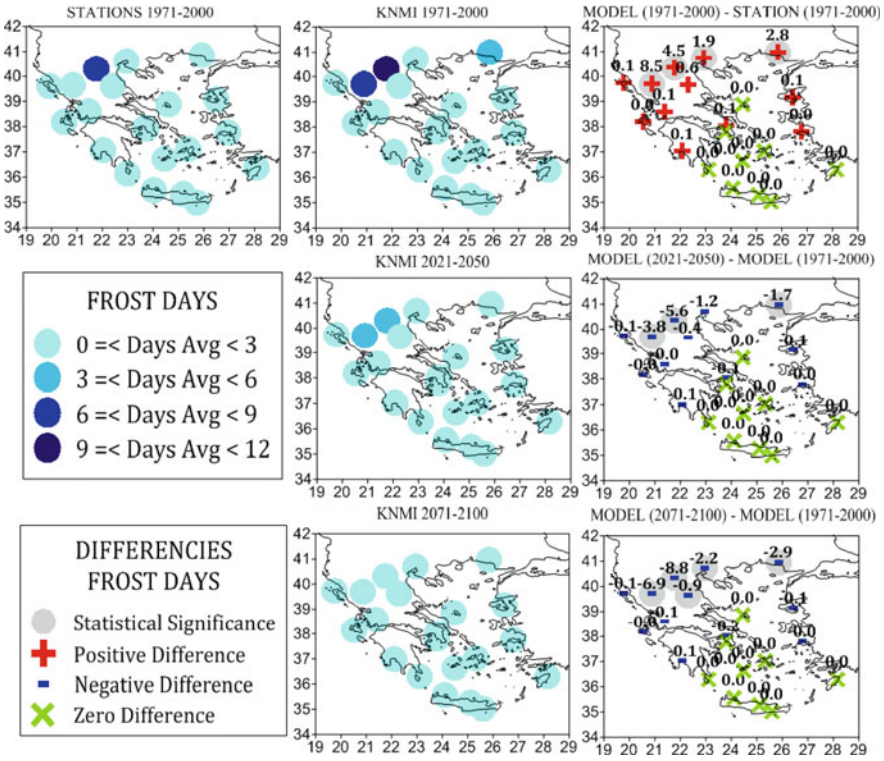

Fig. 3 Averages of frost days for all time series and their differences

trend, while for the stations in northern Greece semi frost days present positive trends, with an exception of Kozani station (Table 1). The equivalent results from KNMI-RACHMO2 model show that for the three examined periods (1971–2000, 2021–2050 and 2071–2100) Kozani has a maximum average of 71.1, 63.1 and 37.4 semi frost days respectively. During the last 30 years of the twenty-first century only 12 out of the 21 grid points (Agrinio, Athens, Alexandroupoli, Argostoli, Ioannina, Kalamata, Kerkyra, Kozani, Larissa, Mytilini, Samos and Thessaloniki) appear to have minimum temperatures below zero. Most of them are characterized by a downward trend in the number of semi frost days (not shown).

The greatest statistically significant differences between grid points and stations were observed for the station of Thessaloniki, where the model overestimates the observations (positive differences between model and observational data). Conversely, an underestimation of the observational data (negative differences between model and observational data) was found for Kerkyra. During the two future periods there is a decrease of semi frost days in the majority of the examined grid points compared to the control period 1971–2000. These results for semi frost days are shown in the maps of Fig. 2.

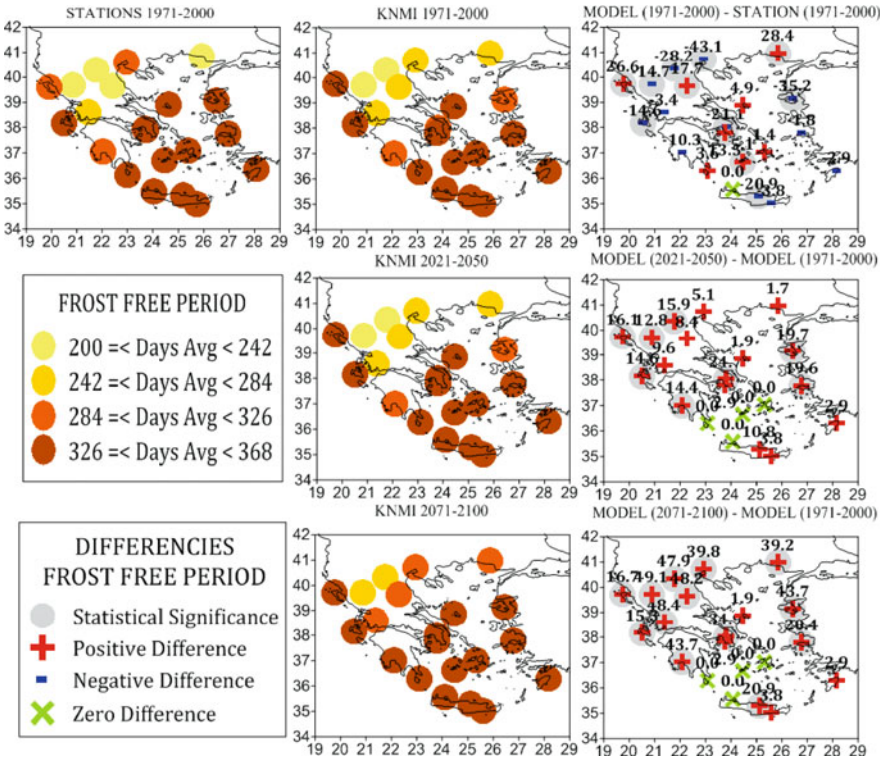

Fig. 4 Averages of frost free period for all time series and their differences

Concerning the analysis of the number of frost days in the domain of study it was found that the station of Kozani presented also the maximum average of 7.0 frost days for the period 1971–2000.

Only 6 stations, and more specifically Athens, Alexandroupoli, Ioannina, Kozani, Larissa and Thessaloniki, appear to have maximum temperatures below zero, four of which are characterized by an upward trend (Table 1). In the case of the simulated model data, for the three examined periods (1971–2000, 2021–2050 and 2071–2100) the grid point near the station of Kozani has a maximum average of 11.6, 5.9 and 2.8 frost days respectively. The majority of the simulated time series shows a negative trend (not shown) and at the end of twenty-first century only 4 out of the 21 grid points, corresponding to the stations of Alexandroupoli, Ioannina, Kozani and Mytilini, appear to have maximum temperatures below zero. The greatest statistically significant differences between the grid point and the observational data were observed in Ioannina showing that the model overestimates the observational frost-day number. Moreover, during the two future periods, there is a decrease of frost days compared to the period 1971–2000 (Fig. 3). Heraklio, Ierapetra, Rodos and Chania are the stations that have an annual frost free period for time series 1971–2000. With an exception of four stations in western Greece and

Samos where the trend is downward, all the other stations are characterized by an upward trend (Table 1).

For the simulated time series (1971–2000, 2021–2050, 2071–2100) the number of areas where the frost free period covers the whole year time is increasing as we reach the period 2071–2100. Most of the grid points under study are characterized by an upward trend (not shown). The greatest statistically significant differences were observed in Thessaloniki indicating that the model underestimates the observations. There is also an overestimation of the observations in Alexandroupoli. What is more, in periods 2021–2050 and 2071–2100 there is an increase of frost free period compared with control period 1971–2000. These results are illustrated in Fig. 4.

4 Conclusions

In conclusion, a general reduction of semi frost and frost days and an increase of frost free period are observed in the region of Greece. A similar pattern is observed in the mid-latitude regions and specifically throughout Europe and in the USA (IPCC Fourth Assessment Report 2007, Meehl et al. 2004, Jylhä et al. 2007; Tebaldi et al. 2006). In terms of semi frost and frost days the model primarily overestimates the observational data of the stations. On the other hand, regarding frost free period there seems to be an underestimation of the observational data of the stations. Nevertheless, there are many cases in the number of frost days, especially in southern Greece, where the differences between the model data and the observational data are zero. It is obvious that the number of semi frost and frost days will decrease throughout the Greek area until 2100, in addition to frost free period that appear to have a significant increase in all examined areas until 2100 according to the KNMI-RACHMO2 model.

Acknowledgments This study has been supported by the European Commission ENSEMBLES project (contract GOCE-CT-2003-505539)

References

Jylhä K, Fronzek S, Tuomenvirta H, Carter TR, Ruosteenoja K (2007) Changes in frost, snow and Baltic sea ice by the end of the twenty-first century based on climate model projections for Europe. Clim Chang 86:441–462. doi:10.1007/s10584-007-9310-z

Lenderink G, van den Hurk B, van Meijgaard E, van ulden A, Cuijpers H (2003) Simulation of present day climate in RACHMO2: first results and model developments. Technical report TR-252. Royal Netherlands Meteorological Institute, De Bilt

Meehl GA, Tebaldi C, Nychka D (2004) Changes in frost days in simulations of twenty first century climate. Clim Dyn 23:495–511. doi:10.1007/s00382-004-0442-9

Tebaldi C, Hayhoe K, Arblaster JM, Meehl G (2006) Going to extremes: an intercomparison of model-simulated historical and future changes in extreme events. Clim Chang 79:185–211. doi:10.1007/s10584-006-9051-4

Trenberth KE, Jones PD et al (2007) Observations: Surface and Atmospheric Climate Change. In: Contribution of Working Group I to the FAR of the IPCC. Climate Change 2007: The Physical Science Basis. Cambridge University Press, Cambridge, UK and New York, USA, pp 237, 252, 300–301

Wilks D (2005) Statistical methods in the atmospheric sciences, vol 91, 2nd edn, International geophysics series. Elsevier, Burlington

A Dynamic-Statistical Downscaling Approach for Simulating Air Temperature Time Series

I. Yiannikopoulou, D. Deligiorgi, H.A. Flocas, and K. Philippopoulos

Abstract A hybrid dynamic-statistical downscaling approach for gridded atmospheric data is presented, focusing on the regional variability of air temperature. Initially, NCEP Reanalysis 2 data are dynamically downscaled for the greater area of Eastern Mediterranean using the regional climate model RegCM-4.0. Subsequently the results are statistically downscaled at a single site via artificial neural networks (ANN). The methodology is applied for 3-month summer periods, focusing on the ability of the proposed methodology to detect and effectively represent ambient temperature at local scales. The RegCM-4.0 model with a 20 km spatial resolution is employed to improve and enhance the regional representativity of the dataset, while the ANNs are used as function approximators to model the relationship between a number of atmospheric predictor variables and the observed air temperature time series at a representative urban coastal site in Greece (Hellinikon). An insight of the ANN input-output transfer function is obtained by examining the relative contribution of each ANN input variable. The performance of the methodology is evaluated and the results indicate significant improvement from the inclusion of the statistical model in downscaling ambient temperature.

1 Introduction

Climate modeling is one of the most computationally intensive areas of scientific research and Global Climate Models (GCMs) are the main tools for assessing climate variability. Their horizontal resolution is roughly 150 km, leading to spatially averaged reconstructions and projections that do not correctly simulate the influence of mesoscale and microscale features on regional or local climate (Pasini 2008).

I. Yiannikopoulou • D. Deligiorgi (✉) • H.A. Flocas • K. Philippopoulos
Division of Environmental Physics and Meteorology, Department of Physics, National and Kapodistrian University of Athens, Athens, Greece
e-mail: despo@phys.uoa.gr

C.G. Helmis and P.T. Nastos (eds.), *Advances in Meteorology, Climatology and Atmospheric Physics*, Springer Atmospheric Sciences,
DOI 10.1007/978-3-642-29172-2_114,

Downscaling is the procedure of generating simulations of the climate system in finer spatial scales by employing dynamical, statistical or dynamic – statistical models, using the gridded output of GCMs or reanalysis datasets. Dynamical downscaling is performed using Regional Climate Models (RCMs), with their output being dynamically and thermodynamically fully self-consistent while the statistical methods exploit the statistical dependence of the climatic variable under investigation and the simulated large-scale fields. In the current study a combined dynamic – statistical method is employed in order to simulate the ambient temperature at a single site and compare it with in-situ meteorological observations from a characteristic urban coastal station.

2 Data and Methodology

The area under investigation is the Eastern Mediterranean basin (Fig. 1) and the study utilizes gridded reanalysis datasets along with meteorological observations for seven summer periods from 2001 to 2007. In detail, the four-times daily with a 2.5° × 2.5° latitude-longitude horizontal resolution NCEP Reanalysis 2 (NNRP2) dataset (Kanamitsu et al. 2002) and mean weekly on a 1-degree spatial resolution Optimum Interpolation Sea Surface Temperatures (OISST) (Reynolds et al. 2002) are used, along with air temperature observations from the Hellinikon meteorological station.

The proposed hybrid downscaling approach consists of two consecutive phases. Initially, climate data are downscaled in a finer spatial scale using the forth version of the ICTP Regional Climate Model (RegCM) and subsequently its outputs are statistically downscaled at a single site (Hellinikon) via Artificial Neural Networks (ANN). RegCM was developed by Giorgi et al. (1993a, b) and is a three-dimensional hydrostatic atmospheric model, which uses a sigma-pressure-based vertical coordinate system. The NNPR2 and OISST datasets are used for the

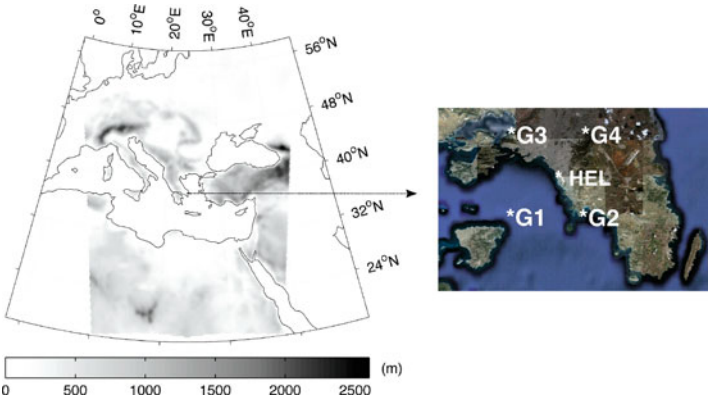

Fig. 1 RegCM domain and locations of nearest to the Hellinikon (HEL) grid points (G1–G4)

Table 1 RegCM surface model output variables used as ANN inputs

Variable	Description	Variable	Description
flw (Wm^{-1})	Net longwave	sina (Wm^{-1})	Solar incident
fsw (Wm^{-1})	Net solar absorbed	t2m (°C)	Temperature (2 m)
q2m	Specific humidity (2 m)	u10m (ms^{-1})	Eastward wind (10 m)
sena (Wm^{-1})	Sensible heat	v10m (ms^{-1})	Northward wind (10 m)

RegCM4.0 simulations as atmospheric boundary conditions and sea surface temperature input data respectively. The atmospheric component of the model is coupled with the Biosphere-Atmosphere Transfer Scheme BATS (Dickinson et al. 1993) while the subgrid explicit moisture scheme SUBEX (Pal et al. 2000) is used to handle non-convective clouds and precipitation. The RegCM domain in this study is centered at 37.97°N and 23.91°E and consists of 160 points in the longitude and 225 points in the latitude direction, with a 20km horizontal resolution (Fig. 1) and 18 vertical levels.

The ANN statistical downscaling scheme is based on the three hourly output values of the RegCM surface model and in total eight predictor variables (Table 1) are selected for estimating the ambient temperature at Hellinikon. In this study feed forward ANNs are used as function approximators due to their ability of estimating any measurable input-output function to any desired degree of accuracy (Hornik et al. 1989). The ANN consists of an input layer with 32 neurons, which are the input nodes of the predictor variables at the four nearest to the target station gird points (G1–G4), and a single neuron at the output layer, which is the output node of the mean three hourly air temperature target values at Hellinikon. The selected ANN architecture contains one hidden layer and the number of the hidden layer neurons is determined using the forward selection method. According to this method, an ANN is trained and tested using initially a small number of hidden neurons. Subsequently, the number of hidden neurons is increased and the process is repeated until the results indicate a satisfactory generalization ability of the network (Heaton 2005). The input–output dataset is divided into training, validation and test sets, with the 70% of the values used for training, 15% for validation and 15% (763 cases) for the test set. Multiple ANNs are trained with varying number of hidden layer neurons (from 2 to 60) and the optimum architecture is selected by examining, according to the forward selection method, the Mean Absolute Error (MAE) on the validation set. In all cases for avoiding the drawback of backpropagation algorithm of initial suboptimal set of weights, training is performed multiple times (25 repetitions).

The performance evaluation of the proposed downscaling scheme is based on a set of difference and correlation measures (Willmott 1982). The results of the MAE, the Root Mean Square Error (RMSE), the Mean Bias Error (MBE), the Mean Absolute Percentage Error (MAPE), the correlation coefficient (R), the coefficient of determination (R^2) and the index of agreement (d) are discussed and the scatter diagram of the observed versus the predicted values is presented. Furthermore, the residuals, which represent the portion of the test data that are not explained by the

downscaling methodology, are analyzed by examining their distribution using the Lilliefors normality test under the null hypothesis that the residuals come from a normally distributed population at the 5% significance level. An insight of the underlying input-output transfer function of the statistical downscaling element of the methodology is obtained by utilizing the Weights method (Garson 1991) for the selected ANN. The method determines the relative importance (RI) of the predictor variable inputs in estimating air temperature at Hellinikon.

3 Results

Figure 2a presents the RegCM simulated mean June to August (JJA) temperature field for the entire period. An initial analysis of the RegCM results includes the comparison of the observed temperature at Hellinikon against the corresponding simulated values at the four nearest grid points (Fig. 2b–e). The analysis reveals that better agreement is achieved for the two southern G1 and G2 grid points with 1.73°C and 1.72°C MAE respectively. Considerable discrepancies are observed for the G3 and G4 grid point simulations (2.24°C and 2.28°C MAE values), especially for the lower and higher temperature values. This underestimation of local ambient temperatures highlights the importance of incorporating sophisticated statistical models as post-processing elements of regional climate models.

The ANNs in this study are selected for their characteristic ability to model non-linear relationships between predictors and predictands, a feature highly desirable for modeling the non-linear climate system. According to the proposed methodology, 1,475 different ANNs are trained and tested and the optimum architecture contains 32 input neurons, 39 hidden layer neurons and a single neuron at the output layer. The overall results of the methodology are presented in Fig. 3a, where the low dispersion along the optimal agreement line illustrates the ability of the methodology to model sufficiently the effects of local topography in the temperature variation at Hellinikon. In detail, according to the model performance evaluation metrics (Table 2), the MAE is low (1.05°C) while the explained variation of ambient temperature at Hellinikon by the proposed downscaling procedure is 89% with minimal average bias (2×10^{-3}°C). This fact indicates that the methodology does not systematically over or under-estimate the observed temperature values, a finding which is consistent with the statistically significant normally distributed model residuals (Fig. 3b).

The relative contribution of each predictor variable from the application of the weights method is presented in Fig. 3c. The results denote the relevance of the selected predictors in estimating ambient temperature, with all predictors, except the net shortwave and the solar incident radiation, presenting RI values greater than 12% aggregated over all grid points.

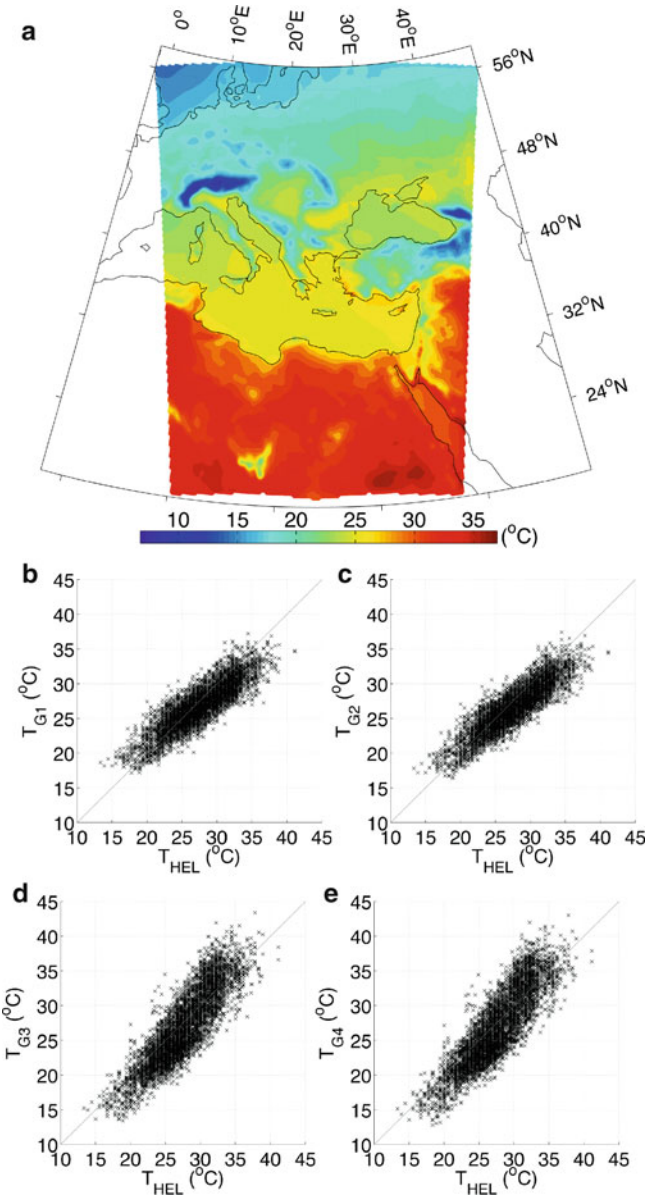

Fig. 2 RegCM JJA simulated temperature (**a**) and comparison of the G1–G4 points with the observations (**b**–**e**)

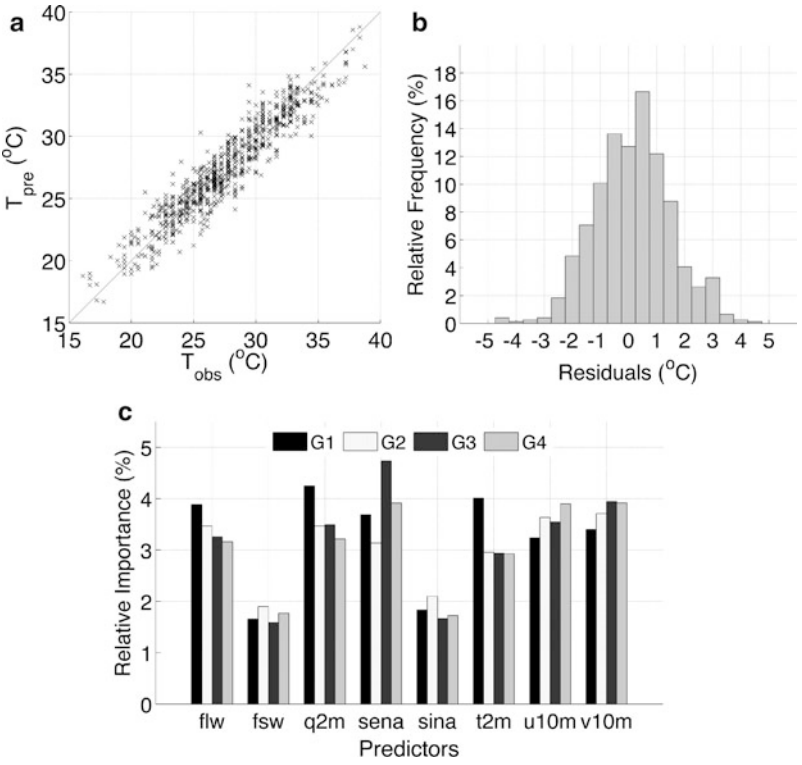

Fig. 3 Comparison of the predicted and observed values (**a**), residuals distribution (**b**) and relative importance of ANN input parameters (**c**)

Table 2 Performance evaluation results

MAE (°C)	RMSE (°C)	MBE (°C)	MAPE (%)	R	R^2	d
1.05	1.35	2×10^{-3}	3.96	0.95	0.89	0.97

4 Conclusions

This work highlights the importance of combining dynamic and statistical downscaling models for effectively estimating meteorological variables in local scales. The selected RegCM-ANN downscaling method gives promising results for providing site-specific ambient temperature values in an urban coastal site and the methodology can be applied by training different ANNs for climate impact studies in targeted locations. Future work is suggested on estimating the uncertainties and the related errors of regional climate models driven by GCMs for the Eastern Mediterranean and selecting the optimum statistical downscaling procedure for more reliable future projections of climate change at finer spatial scales.

Acknowledgments This research has been co-funded by the European Union and Greek national funds through the Operational Program "Education and Lifelong Learning" of the National Strategic Reference Framework (NSRF) – Research Funding Program: Heraclitus II: Investing in knowledge society through the European Social Fund.

References

Dickinson RE, Henderson-Sellers A, Kennedy PJ (1993) Biosphere-atmosphere transfer scheme (BATS) version 1e as coupled to the NCAR community climate model. National Center for Atmospheric Research, Boulder

Garson GD (1991) Interpreting neural-network connection weights. AI Expert 6:47–51

Giorgi F, Marinucci MR, Bates GT (1993a) Development of a second generation regional climate model (RegCM2) I: boundary layer and radiative transfer processes. Mon Weather Rev 121:2794–2813. doi:10.1175/1520-0493(1993) 121<2794:DOASGR>2.0.CO;2

Giorgi F, Marinucci MR, Bates GT (1993b) Development of a second generation regional climate model (RegCM2) II: convective processes and assimilation of lateral boundary conditions. Mon Weather Rev 121:2814–2832. doi:10.1175/1520-0493(1993) 121 <2814:DOASGR>2.0.CO;2

Heaton J (2005) Introduction to neural networks with Java, 1st edn. Heaton Research Inc., Chesterfield

Hornik K, Stinchcombe M, White H (1989) Multilayer feedforward networks are universal approximators. Neural Networks 2:359–366. doi:10.1016/0893-6080(89)90020-8

Kanamitsu M, Ebisuzaki W, Woollen J, Yang S, Hnilo JJ, Fiorino M, Potter GL (2002) NCEP-DEO AMIP-II Reanalysis (R-2). Bull Atmos Meteorol Soc 83:1631–1643. doi:10.1175/BAMS-83-11-1631(2002) 083<1631:NAR>2.3.CO;2

Pal JS, Small EE, Eltahir EAB (2000) Simulation of regional scale weather and energy budgets: representation of sub-grid cloud and precipitation processes within RegCM. J Geophys Res 105:29579–29594. doi:10.1029/2000JD900415

Pasini A (2008) Neural network modeling in climate change studies. In: Haupt SE, Pasini A, Marzban C (eds) Artificial intelligence methods in the environmental sciences, 1st edn. Springer, Dordrecht

Reynolds RW, Rayner NA, Smith TM, Stokes DM, Wang W (2002) An improved in situ and satellite SST analysis for climate. J Clim 15:1609–1625. doi:10.1175/1520-0442(2002) 015<1609:AIISAS>2.0.CO;2

Willmott CJ (1982) Some comments on the evaluation of model performance. Bull Amer Meteor Soc 63:1309–1313. doi:10.1175/1520-0477(1982) 063<1309:SCOTEO>2.0.CO;2

The Impact of Climate Change in Water Resources: An Example of Hard Rocks Aquifers in Mantoudi Area (Central Euboea Island, Hellas)

G. Yoxas and P.T. Nastos

Abstract There is a general consensus that climate change is an ongoing phenomenon. This will inevitably bring about numerous environmental problems, including alterations to the hydrological cycle, which is already heavily influenced by anthropogenic activity. The available climate scenarios indicate areas where rainfall may increase or diminish, but the final outcome with respect to man and environment will, generally, be detrimental. Groundwater resources and their long-term renewal are controlled by long-term climate conditions. Climate change will, therefore, have a great impact on groundwater resources. The main object of this research is to analyze the current situation and compare it with future projections in order to estimate the influence of climate change in the hard rocks aquifer of Mantoudi area (Central Euboea Island), from the quality point of view (i.e. electrical conductivity). Furthermore, the research is focused on those geoenvironmental parameters such as fracture density and degree of fracture interconnection that play the most important role to groundwater renewal. The conclusions of this analysis are based on future projections under SRES A1B scenario, using Regional Climate Models (RCMs) from the ENSEMBLES project, for the periods 2021–2050 and 2071–2100, compared to the reference period 1961–1990.

G. Yoxas (✉)
Department of Dynamic, Tectonic and Applied Geology, University of Athens, Panepistimiopolis, Athens GR-15784, Greece
e-mail: yoxas@geol.uoa.gr

P.T. Nastos
Laboratory of Climatology and Atmospheric Environment, University of Athens, Panepistimiopolis, Athens GR-15784, Greece

C.G. Helmis and P.T. Nastos (eds.), *Advances in Meteorology, Climatology and Atmospheric Physics*, Springer Atmospheric Sciences,
DOI 10.1007/978-3-642-29172-2_115,

1 Introduction

Climate change in combination with increased anthropogenic activities will affect water resources throughout the world. This paper gives information concerning the impacts of climate change on water resources, and particularly groundwater; such as those found in hard rocks. Climate variability and change can affect the quantity and quality of various components in the global hydrologic cycle (Milly et al. 2005).

According to the Intergovernmental Panel on Climate Change (IPCC 2007), global mean surface temperature has increased by $0.6 \pm 0.2°C$ since 1861, while an increase of 2–4°C over the next 100 years is projected. Moreover, global sea levels have risen between 10 and 25 cm since the late nineteenth century. As a direct consequence of warmer temperatures, the hydrologic cycle will undergo significant impact with accompanying changes in the rates of precipitation and evaporation. Predictions include higher incidences of severe weather events, a higher likelihood of flooding, and more droughts. The impact would be particularly severe in the tropical areas, which mainly consist of developing countries (Kumar 2005).

Although the most noticeable impacts of climate change could be fluctuations in surface water levels and quality, the greatest concern of water managers is the potential decrease and changes on quality of groundwater supplies, as it is the main available potable water supply source for human consumption and irrigation of agriculture produce worldwide (Stournaras 2008). Due to the fact that groundwater aquifers are recharged mainly by precipitation or through interaction with surface water bodies, the direct influence of climate change on precipitation and surface water ultimately affects groundwater systems (Stournaras et al. 2011).

Bearing in mind the complexity of the linkage between climate change and groundwater, it is necessary to adapt groundwater management accordingly and to consider the best options for developing and safeguarding groundwater resources.

Main scope of this paper is to estimate the flux of electrical conductivity of ground water due to climate change, in fissured rocks.

The underground water circulation is also a quite interesting matter since a large part of the Greek territory is consisted of permeable rocks, which accept the water through primary or secondary infiltration procedures and form the shape and the characters of the aquifers (Soulios 2010). Such cases can be identified in large continental basins or deltaic fans, the carbonate rocks of karst water tables (limestone, dolomites, marbles, and gypsum) and in extended igneous and metamorphic massifs (Stournaras et al. 2007).

2 Geological and Hydrogeological Setting

The encountered geologic formations belong to Sub-Pelagonian Zone. It is characterized by the intense lithological transformations within its whole extent. Clastic formations of Upper Jurassic – Lower Cretaceous are composed of radiolites, conglomerates, sandstones and shales with olistostromes of ophiolites.

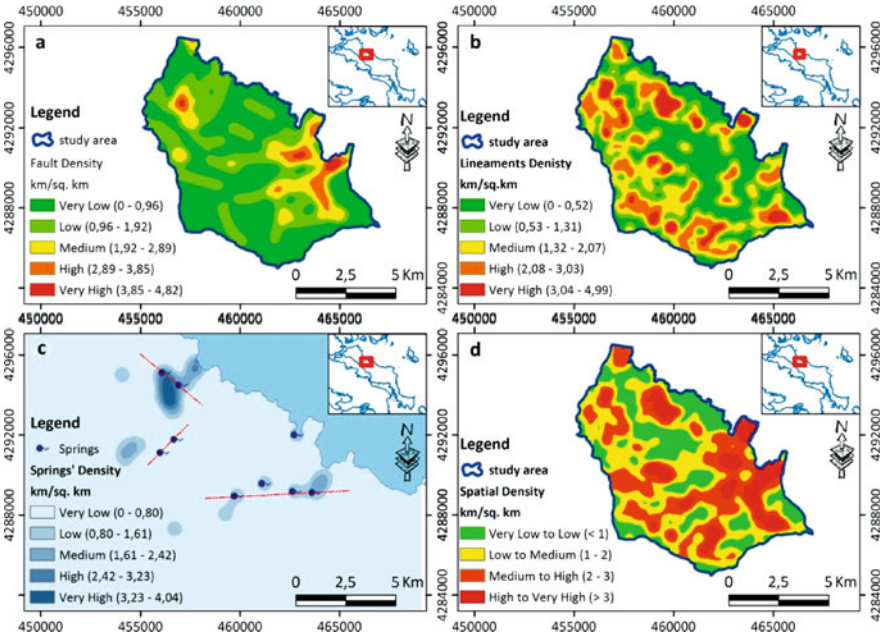

Fig. 1 (**a**) Fault density map, (**b**) lineaments/photolines density map, (**c**) Springs'density map, (**d**) spatial density map (Yoxas and Stournaras 2011)

The Euboea Island, especially the central part, corresponds to the typical Sub-Pelagonian Zone and consists of Paleozoic basement, covered by non-metamorphic Mesozoic formations, which present tectonic intercalations of ophiolites.

The main fracture aquifer seems to be (Yoxas 2011) the ophiolitic cover, presenting an intense differentiation related to the lithology, the geological structure and the tectonic regime. The hydrogeological conditions of the study area show that the distribution of the springs is related to the tectonical setting. Specifically, there are three main teams with a NE–SW, NW–SE and E–W orientation (Fig. 1c). This fact leads to the conclusion that the orientation of the springs is identical with the orientation of the fractures. In this frame, a correlation between the ruptures and the faults and plies has been attended. In the frame of the hydrogeological behaviour, the hydraulic characters of the simple porosity, double porosity, and multiple porosity fractured media are examined and evaluated. In the field of the remote sensing used in the tectonic approach, atmospheric and geometric correction, mosaic synthesis, and data integration led from the fault's density map (Fig. 1a) and lineament/fracture density map of several groups (Fig. 1b), to the statistical analysis of the discontinuities (Fig. 1d). Since field density is an important parameter for the delineation of the groundwater flow in hard rocks, density maps – which were also constructed in a GIS environment – represent the total length of lineaments/fractures per square kilometre of the area. The comparison of these two maps leads to the conclusion that the density pattern of lineaments/

fractures and faults in the study area is almost identical. The comparison of lineaments/fracture and fault density distribution led to the spatial density map of discontinuities, where these sub areas show a fine correlation with the three main fold axes, striking from NW to SE and from NNE to SSW respectively (Fig. 1d).

3 Data and Methodology

The majority of hydrological climate change impact studies focus on surface water, i.e. rainfall run off processes, whilst climate change in surface water dominated catchments affects river discharge directly through changes in the major long-term climate variables. The relationship between changing climate and groundwater is more complicated because of the indirect influence of the recharge process (Allen et al. 2004). Groundwater recharge is a function of meteorological input in combination with landscape characteristics, e.g. soil types, land use, and depth to the water table and human impacts such as drainage, groundwater abstractions, and flow regulation. The precipitation datasets of Regional Climate Model (RCM) carried out by the European Program ENSEMBLES (http://ensemblesrt3.dmi.dk) are analyzed in this study. Specifically the simulations of the used RCMs were carried out for SRES A1B and the interpretation of the results led to estimations of hydrologic balance parameters such as infiltration (I) and surface water (R) for the 2021–2050 and 2071–2100 periods respectively (Stournaras et al. 2011). According to lithological structure and geomorphological setting of the study area, a spatial distribution of R + I hydrological parameters for the future periods 2021–2050 and 2071–2100 was evaluated. The spatial resolution is 25 km × 25 km and the assessment of the climatic conditions within twenty-first century was based on SRES A1B (Nakicenovic et al. 2000). "The data derived from the ensemble mean simulations of the RCMs were compared with the gridded station observations for the reference period 1961–1990; the climatic data concerning air temperature and precipitation totals from the 57 meteorological stations were acquired from Hellenic National Meteorological Service (HNMS)." Moreover, in situ measurements of electrical conductivity in water samples, during the period 2006–2007 (Yoxas 2011), were used as reference value for depicting the climate change impact under the SRES A1B into groundwater bodies, for the future periods 2021–2050 and 2071–2100 respectively.

4 Results and Discussion

Analysis of the results, concerning the total surface and infiltrated water (R + I), concludes to a decrease of approximately 5–17% for the future period 2021–2050 and 14–37% for the 2071–2100 period respectively (Fig. 2).

Moreover, this decrease is projected to be highest in the Southwestern part of the study area for the 2021–2050, whilst for 2071–2100 the highest decrease seems to

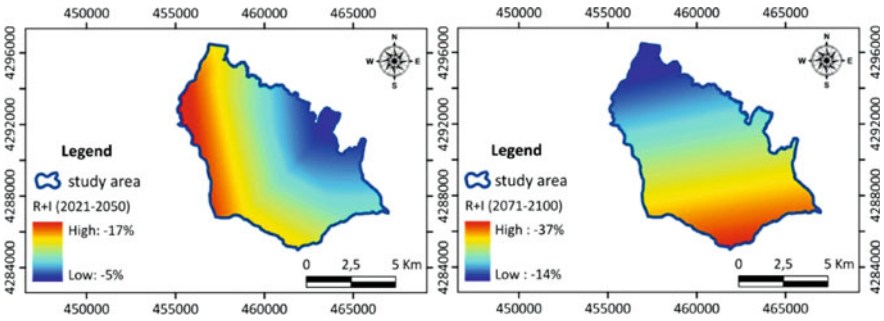

Fig. 2 Changes (%) in mean annual surface and infiltrated water between the future periods 2021–2050 (*left*), 2071–2100 (*right*) and the control period 1961–1990

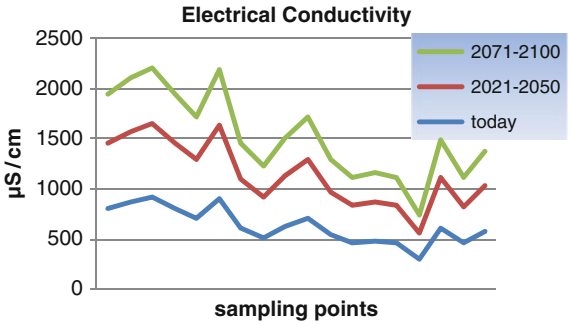

Fig. 3 Cross-plot diagram showing the electrical conductivity between future periods 2021–2050, 2071–2100 and the control period

be in the Southeastern part of the study area respectively. This result could be explained due to different landscape conditions (i.e. soil cover, geomorphological slope) which are remarkable in these parts of the study area (Fig. 1d).

The implication of climate change due to precipitation decrease is likely to affect the quality of groundwater. More specifically decrease of precipitation leads both to a decrease of surface water and infiltrated water respectively. According to the estimations of parameters R and I, electrical conductivity's projections were made respectively. Taking into account the current situation of electrical conductivity (Yoxas 2011) and the estimations made for the future periods 2021–2050 and 2071–2100, it is obvious the water degradation due to less rarefaction (Fig. 3).

5 Conclusions

Regional Climate Models under SRES A1B simulate a water volume (infiltration I and surface water R) deficit equal to −5% to −17% in the period 2021–2050 and −14% to −37% in 2071–2100 respectively with respect to the reference period 1961–1990.

According to calculations for the quality of groundwater, future estimations show an increase of salinization, as electrical conductivity shows an increase during the periods 2021–2050 and 2071–2100 respectively, especially in the coastal water bodies due to water shortage to less rarefaction.

A good knowledge of the geology and hydrogeology of the study system is an essential prerequisite to investigating the impact of climate change. The hydro chemical approach (i.e. electrical conductivity) presented here is the starting point for a further and more detailed study as it is obvious that variation of hydrological parameters are involved in the balance of water quality.

Acknowledgments This paper is presented on behalf of the Bank of Greece Scientific Committee for the Study of the Climatic Change in Greece (EMEKA). Acknowledgment is addressed to the Bank of Greece for its initiative and to the Academy of Athens for its coordination of the discussed project.

References

Allen DM, Mackie DC, Wei M (2004) Groundwater and climate change: a sensitivity analysis for the Grand Forks aquifer, southern British Columbia, Canada. Hydrogeol J 12:270–290. doi:10.1007/s10040-003-0261-9

IPCC (2007) Climate Change 2007: the physical science basis. In: Solomon S, Qin D, Manning M, Chen Z, Marquis M, Averyt KB, Tignor M, Miller HL (eds) Contribution of Working Group I to the fourth assessment report of the intergovernmental panel on climate change. Cambridge University Press, Cambridge, UK and New York, NY, USA, p 966

Kumar K (2005) High-resolution climate change scenarios for India for the 21st century. Curr Sci 90:334–345

Milly PCD, Dunne KA, Vecchia AV (2005) Global pattern of trends in streamflow and water availability in a changing climate. Nature 438:347–350

Nakicenovic N, Alcamo J, Davis G, De Vries B, Fenhann J, Gaffin S, Gregory K, Grubler A, Yong Jung T, Kram T, Lebre La Rovere E, Michaelis L, Mori S, Morita T, Pepper W, Pitcher H, Price L, Riahi K, Roehrl A, Rogner H-H, Sankovski A, Schlesinger M, Shukla P, Smith S, Swart R, Van Rooijen S, Victor N, Dadi Z (2000) Emissions scenarios. Special report of the Intergovernmental Panel on Climate Change. Cambridge University Press, Cambridge

Soulios G (2010) General hydrogeology, vol 1. University Studio Press, Thessaloniki

Stournaras G (2008) Hydrogeology and vulnerability of limited extension fissured rocks islands. Ecohydrol Hydrobiol 8(2–4):391–399. doi:10.2478/v10104-009-0031-y

Stournaras G, Migiros G, Stamatis G, Evelpidou N, Botsialas C, Antoniou V, Vassilakis E (2007) The fractured rocks in Hellas. In: Krasny J, Sharp J (eds) Groundwater in Fractured Rocks, pp 133–149, Taylor & Francis Group

Stournaras G, Yoxas G, Vassilakis E, Nastos PT (2011) Climate change implications on groundwater in Hellenic region. In: Lambrakis N, Stournaras G, Katsanou K (eds) Advances in the research of aquatic environment, vol 1. Springer, New York, pp 91–98

Yoxas G (2011) Hydrogeological, hydraulic and vulnerability mapping of ultra-mafic rocks. Application in Mantoudi – Central Euboea Island. PhD Dissertation. National and Kapodistrian University of Athens (in Greek)

Yoxas G, Stournaras G (2011) Evaluation of geological parameters for describing fissured rocks; a case study of Mantoudi – Central Euboea Island (Hellas). In: Lambrakis N, Stournaras G, Katsanou K (eds) Advances in the research of aquatic environment, vol 1. Springer, New York, pp 81–89

Efficient ANN Training for the Reconstruction of Isotopic Time Series

A. Zagouras, V. Salamalikis, A.A. Argiriou, and S. Lykoudis

Abstract Atmospheric circulation plays a major role in the stable isotopic composition of precipitation. In this study, the relationship between the synoptic patterns and the stable isotopic composition ($\delta^{18}O$ & $\delta^{2}H$) of precipitation is investigated using event-based rainfall data. The aim of this paper is the generation of isotopic time series using a combined synoptic classification technique. Using the classification software developed within the COST733 action, we generated synoptic catalogues utilizing various classification methods for two meteorological parameters: the geopotential height at the isobaric level of 500 hPa and the thickness (500–1,000 hPa) and we propose an efficient technique to generate a representative classification catalogue based on the above parameters. An ANN is trained using this catalogue in order to classify each one of the meteorological parameters. The output scheme is compared with the initial catalogues of the COST733 action using statistical indices both in terms of explaining the variance of the classified meteorological fields and in terms of providing classes with statistically distinct isotopic signatures. Finally, using the proposed classification, the isotopic composition of the synoptic classes is determined and used to reconstruct isotopic time series.

A. Zagouras (✉)
Laboratory of Atmospheric Physics, Department of Physics, University of Patras, Patras, Greece

Electronics Laboratory, Department of Physics, University of Patras, Patras, Greece
e-mail: thzagour@upatras.gr

V. Salamalikis • A.A. Argiriou
Laboratory of Atmospheric Physics, Department of Physics, University of Patras, Patras, Greece

S. Lykoudis
Institute of Environmental Research and Sustainable Development, National Observatory of Athens, Athens, Greece

C.G. Helmis and P.T. Nastos (eds.), *Advances in Meteorology, Climatology and Atmospheric Physics*, Springer Atmospheric Sciences,
DOI 10.1007/978-3-642-29172-2_116,

1 Introduction

Stable water isotopes are widely used as tracers of the hydrological cycle. The spatial and temporal variations of precipitation are associated with seawater evaporation and condensation history of the precipitating moisture (Daansgard 1964). Evaporation conditions at the water vapor source determine the initial isotopic composition of water vapor while the transportation of an air mass defines the rainout history. As described by the Rayleigh distillation process, the fractionation of stable water isotopes in rainfall is controlled by the progressive depletion of stable isotope values with decreasing temperature ("temperature effect"). The stable isotopic composition of precipitation is also affected from the synoptic circulation patterns and the prevailing weather conditions over the sampling area.

Several papers study the relationship between the isotopic composition of precipitation and the atmospheric circulation using a combination of air mass trajectories and the analysis of pressure fields (Gedzelman and Lawrence 1982; Burnett et al. 2004). Also, synoptic classification methods can be used to group precipitation events with identifiable signatures (Lykoudis et al. 2010). In this work the link between the synoptic circulation patterns and the isotopic composition of precipitation events is investigated using a combined synoptic classification technique.

Classifications catalogues derived using the classification software *cost733class* developed within the COST733 action were merged in a single representative catalogue by the Majority Classification (MC) algorithm presented in the following. The MC catalogue is used for training an ANN that classifies two parameters: the 500 hPa geopotential height (z500) and the 1,000–500 hPa thickness (k500). Based on this classification scheme daily isotopic time series of precipitation are generated.

2 Data and Methodology

Stable isotopic composition ($\delta^{18}O$ and $\delta^{2}H$) of precipitation events for the stations of Villacher Alpe, Austria (46° 36′ 00″/13° 40′ 00″/2,135 m a.s.l.) and Pendeli, Greece (38° 3′ 00″/23° 52′ 00″/498 m a.s.l.) were obtained through the GNIP/ISOHIS database (IAEA 2010). The temporal coverage of the corresponding isotopic data sets is limited and refers to the period of 2000–2003.

Daily gridded data from 1974 to 2003 of both the 500 hPa geopotential height and the 1,000–500 hPa thickness from NCEP/NCAR are also used (http://iridl.ldeo.columbia.edu), for the domain 27.5–52.5 N and 7.5–40 E. Each daily observation consists of groups of 154 data points. Catalogues of the most well known synoptic classification methods were generated using the *cost733class* (http://geo23.geo.uni-augsburg.de/cost733class-1.0), namely: Cluster Analysis of Principal Components (CAP), K-Means type (CKM), Erpicum (ERP), Kruizinga (KRZ), Lund (LND), T-mode Principal Components (PCT), Pseudo-random (RAC), SANDRA (SAN) (Philipp et al. 2010). The result of each classification is a catalogue of 10,957 labels,

Table 1 A multi-label dataset

Object	L_1	L_2	...	L_k
O_1	$\lambda_{1,1}$	$\lambda_{2,1}$	...	$\lambda_{k,1}$
O_2	$\lambda_{1,2}$	$\lambda_{2,2}$	...	$\lambda_{k,2}$
...	...	...	...	...
O_n	$\lambda_{1,n}$	$\lambda_{2,n}$	...	$\lambda_{k,n}$

varying from 1 to 27 in accordance with the desired number of classes. The routines and the experiments of this study were developed under MATLAB 7.9.

The Majority Classification (MC) algorithm is an efficient method for combining the catalogues of different classification methods to a single representative catalogue. A survey study of multi-label classification methods is introduced in (Tsoumakas and Katakis 2007). A classification catalogue is a list of labels assigned to n objects, defining their membership to a number of classes. Different classification methods may result in different labels for a specific class and each class could link together a diversity of objects. The basic concept of MC is based on the localization of the majority of linked objects among various catalogues. Let L be a multi-label dataset composed by k disjoint single-label sets as columns of n dimensions, n being the number of objects classified by k classification methods (Table 1).

The MC algorithm includes the following steps:

Step 1. As $S_i = \{O_j\}$, is defined the set of $j < n$ objects which have been assigned to the same label $\lambda_{i,1}$ with object O_1, where $1 \leq i \leq k$. The union of S_i sets, $S = \{S_1 \cup S_2 \cup ... \cup S_k\}$, gives a set of all p objects linked at least once with the first label $\lambda_{i,1}$ of each single-label set L_i.

Step 2. The frequency of participation of an object $O_p \in S$ in S is equivalent to a score of positive votes. The voting set is $V = \{v_1, v_2, ..., v_p\}$.

Step 3. All objects, with corresponding votes greater than the nearest approximation of the $\frac{k}{2}$ value are grouped together to an ultimate class c_s and they are excluded from dataset L.

Step 4. Dataset L is reassigned to the remaining objects; the algorithm repeats steps 1–3 until all objects are classified.

It should be noted that the final number of the c_s classes is not necessarily equal to the number of classes that the combined classifications consist of, since this depends on the algorithm's procedure. Additionally, the MC takes the advantage of the label independence considering that this is based on the links between the objects of a single label set, regardless of the label itself.

Given an MC catalogue, a feed-forward back propagation ANN is created, composed of two layers and five nodes in the hidden layer. The transfer function for both the hidden and the output layer is the tangent sigmoid, using a gradient descent momentum back propagation training function. A portion of up to 90% of the 10,957 input data points is used as a training set and the remaining 10% as the testing set, which coincides with the period 2000–2003 of the available isotopic data. The corresponding percentages of the MC catalogue are employed as the target set. Inputs are normalized within $[-1, 1]$. The initial 154 dimensions are reduced by Principal Component Analysis (PCA).

3 Results

Based on the combined classification method (*MC + ANN*) for both classification parameters, precipitation-amount weighted isotopic means are calculated for each class (Fig. 1).

Any given synoptic type is different in terms of isotopic composition of precipitation for each station. The weather conditions and the precipitation amounts corresponding to each class differ for either sampling site and this is reflected on the isotopes values. The altitude effect is clear in Fig. 1, since isotope values in Pendeli are higher than in Villacher Alpe.

The capability of each classification technique to represent the isotopic variation of event precipitation events is examined the Explained Variance (EV) and the Pseudo-F statistic (Fig. 2). The EV ranges from 0.0693 to 0.5126 and the Pseudo-F statistic from 0.2782 to 1.3014. Classifications with high number of classes have higher EV values.

Based on the isotopic information derived from the *MC + ANN* classification method daily isotopic time series are generated (Figs. 3 and 4).

The produced isotopic time series follow in general the measured values. However the isotopic values derived from the classification procedure have larger differences compared to the actual values. This is because the only information is included in the generation of the daily isotopic data is from the contribution of the classification scheme. The calculation of average isotope values for each class independently of the season smoothes seasonality out, and enhances the

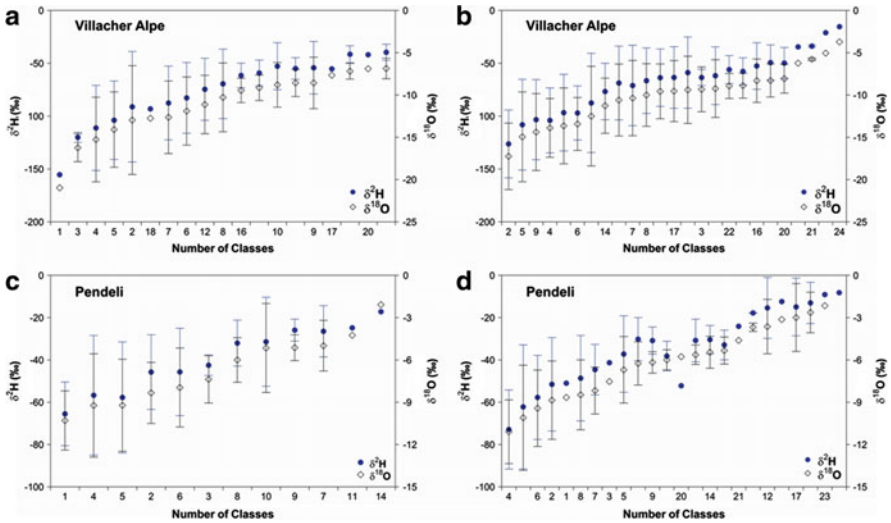

Fig. 1 Precipitation-weighted average isotope values for the *MC + ANN* classification method. (**a**, **c**) z500 and (**b**, **d**) k500

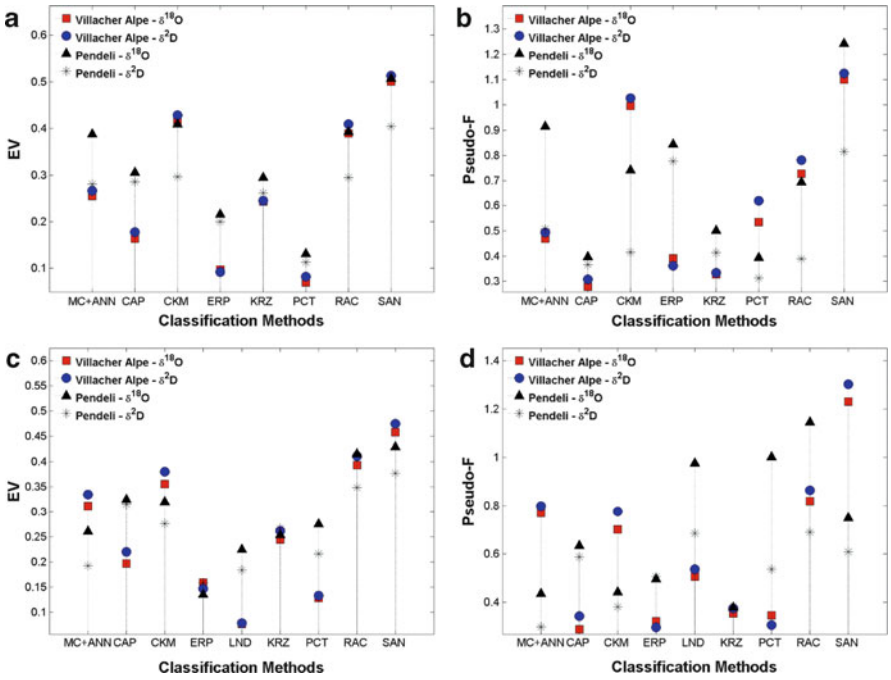

Fig. 2 Statistical indexes (EV and Pseudo-F) for the classification techniques. (**a**, **b**) k500, (**c**, **d**) z500

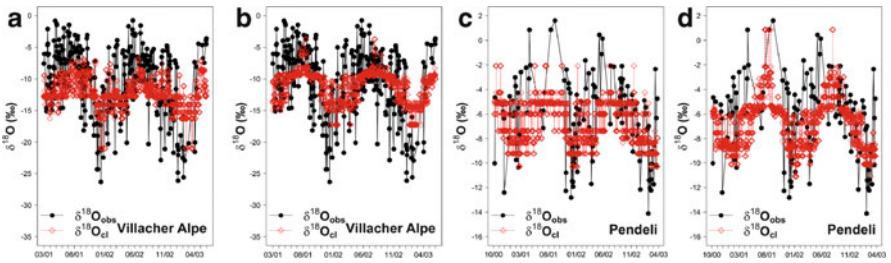

Fig. 3 Correlation between observed and predicted $\delta^{18}O$ time series from the *MC + ANN* method. (**a**, **c**) z500 and (**b**, **d**) k500

differences between the actual and the predicted isotopic time series. The use of the 500 hPa geopotential height as classification parameter provides better results than using thickness for both sampling sites and isotopic species as illustrated by Figs. 3 and 4.

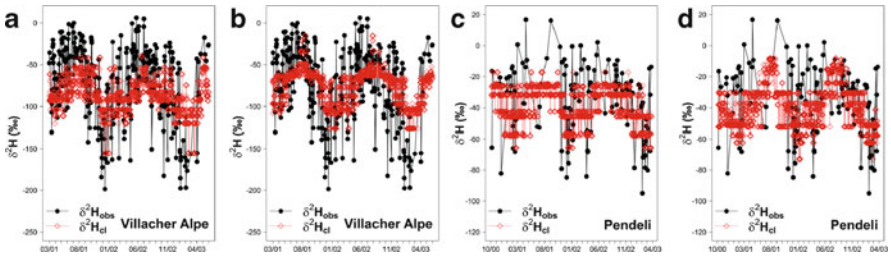

Fig. 4 Correlation between observed and predicted δ^2H time series from the *MC + ANN* method. (**a**, **c**) z500 and (**b**, **d**) k500

4 Conclusions

In this study the dependence of the isotopic composition of event-based precipitation on synoptic classification schemes is investigated. A combined classification procedure, *MC + ANN*, is proposed and then daily isotopic time series are generated. The isotopic signature for each class derived from the classification approach differs for each station since each synoptic type involves different air mass transportation pathways and induces different weather conditions for each location and this is imprinted on the isotope data. EV and Pseudo-F are calculated for all classification methods. Higher EV values appear when methods with high number of classes are used. The EV and Pseudo-F provide satisfactory values for the *MC + ANN* method. The daily isotopic times series produced by the *MC + ANN* method present discrepancies with measured data because the isotopic information derived only from the synoptic classification schemes cannot describe with high accuracy the daily isotopic composition of precipitation. Further investigation with longer dataset is required for a successful link between synoptic classification and the isotopic composition of precipitation events.

Acknowledgments This study is funded by the Research Committee of the University of Patras under the 'K. Karatheodori' grand (Project No. C.907).

References

Burnett AW, Mullins HT, Patterson WP (2004) Relationship between atmospheric circulation and winter precipitation δ^{18}O in central New York State. Geophys Res Lett 31:L22209. doi:10.1029/2004gl021089

Daansgard W (1964) Stable isotopes in precipitation. Tellus 16:436–468. doi:10.1111/j.2153-3490.1964.tb00181.x

Gedzelman SD, Lawrence JR (1982) The isotopic composition of cyclonic precipitation. J Appl Meteorol 21:1385–1404. doi:10.1175/1520-0450(1982) 021<1385:ticocp>2.0.co;2

IAEA (2010) Isotope Hydrology Information System: The ISOHIS database. Available from: http://isohis.iaea.org

Lykoudis SP, Kostopoulou E, Argiriou AA (2010) Stable isotopic signature under various synoptic classifications. Phys Chem Earth 35:530–535. doi:10.1016/j.pce.2009.09.002

Philipp A, Bartholy J, Beck C, Erpicum M, Esteban P et al (2010) COST733CAT – a database of weather and circulation type classifications. Phys Chem Earth 35:360–373. doi:10.1016/j.pce.2009.12.010

Tsoumakas G, Katakis I (2007) Multi label classification: an overview. Int J Data Warehous Min 3:1–13. doi:10.4018/jdwm.2007070101

Land-Atmosphere Coupling: The Feedback of Soil Moisture into Surface Temperature in Eastern Mediterranean and Middle East

G. Zittis, P. Hadjinicolaou, and J. Lelieveld

Abstract Future climate projections suggest that beside changes in mean climate there will also be shifts in extremes (i.e. droughts, floods, heat waves), partly due to enhanced interannual variability. In the already warm Eastern Mediterranean and Middle East (EMME) it is crucial to investigate possible changes in extreme temperature and try to understand all the relative mechanisms and feedbacks that cause or intensify severe heat events. One of these feedbacks is the soil moisture – atmosphere interaction. In general, when there is no sufficient water content in the soil, evapotranspiration is low, leading to higher near surface air temperatures, due to less evaporative cooling. In the present study, we explore this interaction, for the summer season. We identify sub-regions sensitive to this feedback in the EMME domain using the classical hydrology framework which defines evapotranspiration regimes as a function of soil moisture and latent heat flux. Moreover, we use the correlation of temperature and evapotranspiration as a diagnostic of this coupling. The data used cover the period 1951–2099 and come from the Hadley Centre's regional climate model PRECIS, driven by the A1B emissions scenario. Finally, we discuss possible alterations of the relationship between soil moisture and surface temperature throughout the twenty-first century.

G. Zittis (✉) • P. Hadjinicolaou
The Cyprus Institute, Nicosia, Cyprus
e-mail: g.zittis@cyi.ac.cy

J. Lelieveld
The Cyprus Institute, Nicosia, Cyprus

Max Planck Institute for Chemistry, Mainz, Germany

C.G. Helmis and P.T. Nastos (eds.), *Advances in Meteorology, Climatology and Atmospheric Physics*, Springer Atmospheric Sciences,
DOI 10.1007/978-3-642-29172-2_117,

1 Introduction

IPCC's fourth Assessment Report (2007) suggests that since 1950 the number and intensity of heat waves have increased. The identification of the Mediterranean region as a global climate change "hot-spot" (Giorgi 2006) raises concerns and the need for research on climate extremes in the area. Significant positive trends of temperature extremes in the region are indicated by a number of studies and heat stress intensification is very likely to continue through the twenty-first century.

The occurrence and intensity of heat waves are related to circulation patterns and certain atmospheric flow anomalies (Black et al. 2004; Kenyon and Hegerl 2008). Some studies though, indicate that circulation alone cannot explain the temperature anomalies (Seneviratne et al. 2006; Efthymiadis et al. 2011). Factors that may amplify extreme heat events include soil moisture feedbacks (Seneviratne et al. 2010) or anomalous warm SSTs (Black et al. 2004; Feudale and Shukla 2007).

In the present study we explore the role of soil moisture in the amplification of heat extremes in EMME. We focus on summer season, during which this mechanism appears to be stronger and the occurrence of such events most common.

2 Data and Methodology

2.1 Data

We used data of the summer mean temperature at 1.5 m above surface (T), net downward radiation ($R_{n\downarrow}$), surface latent heat flux (LE), soil moisture (SM) in the root zone as a degree of saturation (w) and evapotranspiration (ET). Since there are no consistent – in time and space – observations of most of the above mentioned variables we use model data. They are obtained from the Hadley Centre PRECIS (HadRM3P) Regional Climate Model (Jones et al. 2004), used to dynamically downscale the HadCM3 Global Circulation Model results to a $0.22^\circ \times 0.22^\circ$ km resolution over EMME. The simulation covers the period 1951–2099 and was forced by the A1B emissions scenario. The regional output by PRECIS has been extensively tested against observations in the EMME and ensemble model output for the European part of the domain (Lelieveld et al. 2012).

2.2 Methodology

Classical hydrology (Budyko 1956) defines two distinct evaporative regimes, the soil moisture and the energy limited. The first one encompasses relatively dry areas, where changes in SM lead to changes in ET, and the second relatively wet ones where ET is not sensitive to variations of SM. Koster et al. (2009), proposed a

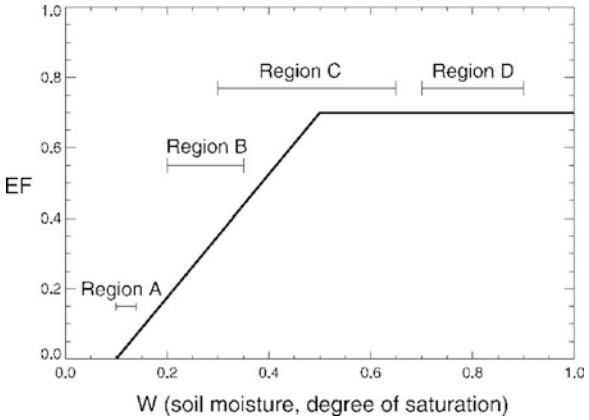

Fig. 1 Idealized relationship between evaporative fraction and soil moisture (From Koster et al. 2009)

refined classification of the evaporative regimes. Using the same basic concept they suggest a division in four evaporative regions (Fig. 1). Region A represents the SM controlled regime where the variation of SM is generally too small to cause changes in released latent heat flux. This flux is characterized by the evaporative fraction (EF), which is defined as the ratio of seasonal latent heat flux to total seasonal net radiation. Region D represents the wet energy-limited regime, where SM is abundant though ET is controlled by radiation. Region B is the transitional regime where increases (decreases) of SM lead to increases (decreases) in EF and to relatively lower (higher) surface air T. Region C can act either as region B or D depending on the available water content in any particular year.

As a first metric of the coupling between air T and SM we applied Koster's method using slightly different thresholds, adjusted to our region of interest and created the relevant maps. The four evaporative regimes are defined as:

Region A: Inter-annual SM variations are too small to affect inter-annual T variations ($\sigma_w < 0.02$), *Region B*: mean summer ET usually lies in the SM controlled regime ($\sigma_w > 0.02$, $|EF_{dry}| > 0.3$ and $|EF_{dry} + EF_{wet}| > 0.3$), *Region C*: summer averaged ET lies in the SM controlled regime during some years and in the energy-controlled regime during other years ($\sigma_w > 0.02$, $|EF_{dry}| > 0.3$ and $|EF_{dry} + EF_{wet}| < 0.3$), *Region D*: mean summer ET usually lies in the energy-controlled regime ($\sigma_w > 0.02$ and $|EF_{dry}| < 0.3$), where σ_w is the inter-annual standard deviation of SM and EF_{dry} and EF_{wet} are the wettest and driest deciles of normalized EF. As dry (wet) are considered the years with SM lower (higher) than the period 10th (90th) percentile.

In order to verify these relationships we calculated the means of all grid points of each evaporative type, and created the scatter plots of the anomalies of SM against T. The corresponding correlation coefficients and the LOWESS smoother curve are also shown.

Another widely used diagnostic of the land-atmosphere coupling is the correlation coefficient between ET and near surface air T. When ET is controlled by SM there is a strong anti-correlation between these two variables. On the other hand,

when there is soil moisture available and evaporation is controlled by atmospheric conditions this correlation is positive.

3 Results

Figure 2 represents the evaporative regimes derived from the model output for the 1951–2099 period. There is an apparent north-south gradient and in extended areas in the south there is no coupling between SM and T (A). In contrast, in the northern and wetter part of the domain ET can be controlled by SM variations (B, C), thus in relatively dry years we expect less ET and consequently relatively higher surface T due to less evaporative cooling. Regions in regime D, appear to be very limited in a few grid points at high elevation in the Caucasus Mountains.

In order to check if the spatial distribution of the evaporative regimes changes with time, we repeat the analysis for two sub-periods, the control period (1951–2000) and the end of the twenty-first century (2051–2099). It appears that the basic pattern remains similar (not shown), as about 96.6 % of all grid points are categorized in the same evaporative regime.

Figure 3 presents the scatter plots of SM versus T for the means of all grids of each evaporative regime. Strongest relationships are found for grids in B and C regimes. These correlations have negative sign, thus, in these regions we expect higher air T when SM is less than normal. For grids in A and D regimes the correlations are close to zero, indicating that SM and air T are not coupled.

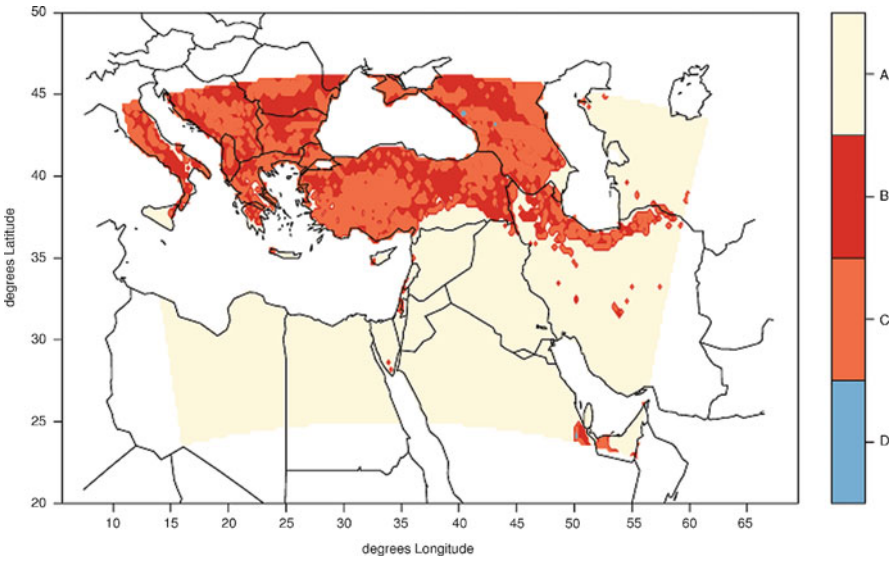

Fig. 2 Geographical distribution of evaporative regimes (A–D, see Fig. 1) on the basis of HadRM3P data for the period 1951–2099

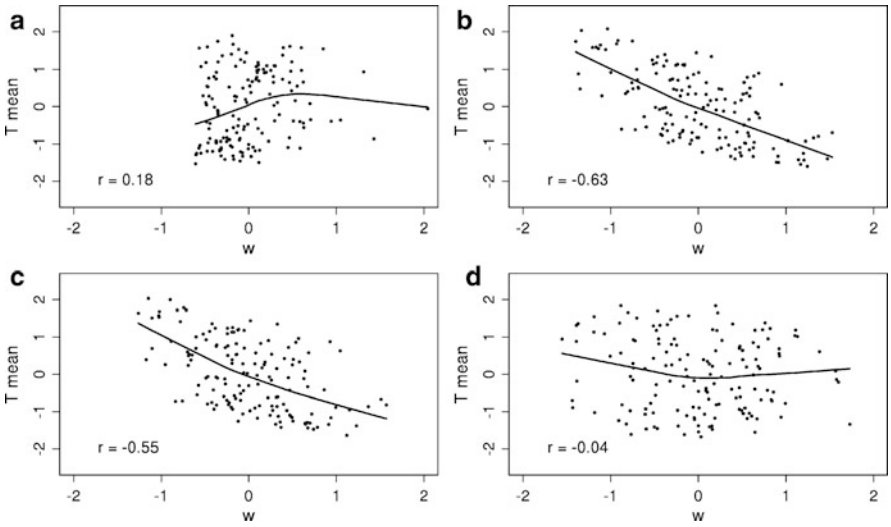

Fig. 3 Scatter plots of SM (w) and T anomalies for each evaporative regime

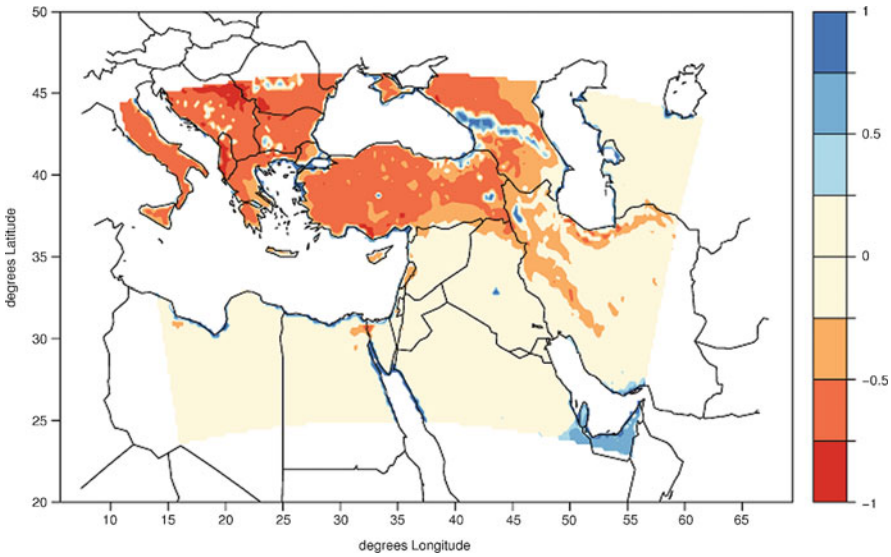

Fig. 4 Correlation coefficients between temperature and evapotranspiration (1951–2099)

The correlation coefficients between ET and T for the period 1951–2099 are shown in Fig. 4. Significant values are colored. Negative correlations, indicating a strong coupling between SM and T, are found over the Balkans and Turkey. In general, the method provides results consistent with the previous approach. In the southern and eastern parts of the domain correlations are low and not significant.

4 Conclusions

Combining the two diagnostic methods of the soil-temperature coupling (classification in evaporative regimes and correlation analysis), the northern part of the EMME domain appears to be more sensitive to this feedback. In Italy, the Balkans, Turkey and the region north and south of the Caucasus Mountains soil moisture deficits during dry years, possibly in addition to anticyclonic circulation patterns associated with subsidence, can potentially create or amplify extreme temperature conditions and contribute to heat waves. The scatter plots of these parameters verify the distinct characteristics of the intermediate "B" and "C" regimes in this region. According to our model projections the spatial distribution of the evaporative regimes does not seem to change significantly throughout the twenty-first century (Fig. 2 for 2051–2099 not different from the 1951–2000 one, not shown). Possibly this is connected to the non-dynamic vegetation scheme of PRECIS and the soil properties of the land scheme, which remain unchanged throughout the simulation. The only parameters interactively simulated by the model that can alter the evaporative regimes are either changes in the soil water content or in the amount of radiation that reaches the surface. It remains to be investigated if climate change induced regime alterations may occur in future, e.g. due to vegetation and soil transformations, which could potentially add to the feedbacks between soil moisture and temperature changes.

Acknowledgments The research leading to these results has received funding from the European Research Council under the European Union's Seventh Framework Programme (FP7/2007-2013) / ERC grant agreement n° 226144 (C8 Project).

References

Black E, Blackburn M, Harrison G, Hoskins B, Methven J (2004) Factors contributing to the summer 2003 European heatwave. Weather 59:217–223. doi:10.1256/wea.74.04

Budyko MI (1958) Heat balance of the earth's surface. U.S. Dept. of Commerce, Weather Bureau, Washington

Efthymiadis D, Goodess CM, Jones PD (2011) Trends in Mediterranean gridded temperature extremes and large-scale circulation influences. Nat Hazards Earth Syst Sci 11:2199–2214. doi:10.5194/nhess-11-2199-2011

Feudale L, Shukla J (2007) Role of Mediterranean SST in enhancing the European heat wave of summer 2003. Geophys Res Lett 34:L03811. doi:10.1029/2006GL027991

Giorgi F (2006) Climate change hot-spots. Geophys Res Lett 33:L08707

IPCC (2007) Contribution of working group I to the fourth assessment report of the intergovernmental panel on climate change. Cambridge University Press, Cambridge

Jones RG et al (2004) Generating high resolution climate change scenarios using PRECIS. Met Office Hadley Centre, Exeter

Kenyon J, Hegerl GC (2008) Influence of modes of climate variability on global temperature extremes. J Climate 21:3872–3889. doi:10.1175/2008JCLI2125.1

Koster RD, Schubert SD, Suarez MJ (2009) Analyzing the concurrence of meteorological droughts and warm periods, with implications for the determination of evaporative regime. J Climate 22:3331–3341. doi:10.1175/2008JCLI2718.1

Lelieveld J, Hadjinicolaou P, Kostopoulou E, Chenoweth J, El Maayar M, Giannakopoulos C, Hannides C, Lange M, Tanarhte M, Tyrlis E, Xoplaki E (2012) Climate change and impacts in the eastern Mediterranean and the Middle East. *Climate Change*, (pp. 1–21). http://dx.doi.org/10.1007/s10584-012-0418-4

Seneviratne SI, Lüthi D, Litschi M, Schär C (2006) Land-atmosphere coupling and climate change in Europe. *Nature*, 443(7108):205–209. doi:10.1038/nature05095

Seneviratne SI et al (2010) Investigating soil moisture–climate interactions in a changing climate: a review. Earth Sci Rev 99:125–161. doi:10.1016/j.earscirev.2010.02.004

Part III
Atmospheric Physics

Surface Ozone Spatial Distribution and Trends Over Europe During 1997–2006

D. Aggelis, P. Zanis, C.S. Zerefos, A.F. Bais, and P.T. Nastos

Abstract Surface ozone mixing ratio spatial distribution over Europe was constructed through kriging interpolation based on EMEP ground measurements during 1997–2006. The climatology, the annual and seasonal trends, the diurnal cycle and the altitude dependence were studied as well as the relation with the North Atlantic Oscillation (NAO). The mean seasonal cycle amplitude and maximum display an increasing gradient from northwest to southeast, with high levels in Austria and eastern Mediterranean. Trends are close to zero (−1.00 to +1.00 ppbv. year^{-1}), except for significant positive values in UK, Slovakia, S. Scandinavia and Austria, in winter and autumn. Diurnal amplitude decreases with latitude for low altitude stations (<1,000 m), due to enhanced photochemistry, with maximum in the afternoon. Elevated continental stations, usually in the free troposphere, exhibit diurnal variability close to zero and maximum around midnight. In winter about

D. Aggelis (✉)
Academy of Athens, Research Centre for Atmospheric Physics and Climatology, 24 Omirou str., 10672 Athens, Greece
e-mail: dvagg@teilam.gr

P. Zanis
Department of Meteorology and Climatology, School of Geology, Aristotle University of Thessaloniki, Thessaloniki, Greece

C.S. Zerefos
Academy of Athens, Research Centre for Atmospheric Physics and Climatology, 24 Omirou str., 10672 Athens, Greece

Navarino Environmental Observatory (N.E.O.), Messinia, Greece

A.F. Bais
Section of Applied and Environmental Physics, Department of Physics, School of Science, Aristotle University of Thessaloniki, Thessaloniki, Greece

P.T. Nastos
Laboratory of Climatology and Atmospheric Environment, National and Kapodistrian University of Athens, Athens, Greece

C.G. Helmis and P.T. Nastos (eds.), *Advances in Meteorology, Climatology and Atmospheric Physics*, Springer Atmospheric Sciences,
DOI 10.1007/978-3-642-29172-2_118,

40% of near surface ozone variability at the western edge of Europe may be attributed to circulation changes and ozone precursors' transport related to NAO.

1 Introduction

The surface ozone spatial distribution study would considerably contribute to the evaluation and better prediction of its effects on human health, ecosystems, material quality, atmosphere's oxidation capacity and climate change (Reid et al. 2008), focusing on seasonality, annual trends and diurnal variability.

Mean seasonal variability highlights ozone relationship to photochemistry, ozone precursors, transport patterns and hemispheric background. Annual linear trends, based on monthly mean deseasonalised values, reveal ozone change free of short-term meteorological variability. Diurnal course shows the influence of photochemistry or dynamical processes in the boundary layer where O_3 is formed.

Altitude above sea level (asl) was also investigated since elevated locations experience free tropospheric conditions and low altitude sites are mostly affected by solar radiation (Chevalier et al. 2007; Tarasova et al. 2007).

Intercontinental air pollution transport from North America to Europe (Li et al. 2002a), led to the correlation between surface ozone and North Atlantic Oscillation (NAO), i.e. the zonal westerly wind flux caused by the atmospheric pressure difference of the variable dipole between Azores high and Iceland low barometric fields (Hurrell et al. 2001).

2 Data and Methodology

2.1 Data

Primary hourly surface ozone density measurements ($\mu g.m^{-3}$), obtained by UV absorption at 89 ground-based rural stations of the European Monitoring and Evaluation Programme (EMEP, www.emep.int/ccc/), inhomogeneously spread mainly in western and central Europe, were reliable as accounting for more than 75% consecutive measurements during each year. Ozone data, reduced to the same temperature and pressure (1,013 hPa, 20°C), were converted to mixing ratio by volume (ppbv) with the approximation of the ideal gas equation (Fjaeraa and Hjellbrekke 2007).

NAO strength and zonality are expressed by the normalized NAO index, available at the Climate Prediction Center (www.cpc.Noaa.Gov/nao.html), as the difference of normalised pressure anomalies (departures of measured atmospheric pressure from the average atmospheric pressure in a long-term period at mean sea level, divided by standard deviation at each station) between Lisbon (Portugal) and Stykkisholmur/Reykjavik (S. Iceland), concerning monthly and daily values. When

the difference is greater than normal, the index is positive and the westerlies are more intense-positive phase-and when it's small, the index is negative and these winds are weaker-negative phase.

2.2 Methodology

Kriging interpolation, an acceptable method for atmospheric constituents' spatial distribution, produces unknown concentrations based on neighboring measurements, fitted with appropriate normalised weights chosen to minimize variance and bias of the estimate, using the variogramme depending on measurements' physical distance. In our study, the optimal solution is given by the Generalised Cross-Validation Model implementing smoothing parameter λ and Pearson's correlation coefficient ρ to minimise errors and reproduce primary individual data, in combination with Gaussian Kriging as they are conducted in r-project fields and climpact packages (r-project.org).

3 Results

Observed surface ozone mixing ratio mean seasonal cycle range (amplitude) varies between 11 and 35 ppbv, with higher levels in eastern Austria, Slovenia and Eastern Mediterranean. Interpolation reveals an increasing northwest to southeast gradient, 13–27 ppbv (Fig. 2). The maximum of surface ozone mixing ratio mean seasonal cycle exhibits similar behaviour to amplitude values, with levels greater than 50 ppbv, at elevated sites in Austria, S. Germany, Switzerland, Slovenia and Spain, as well as at Mediterranean coastal locations, ranging from 32 to 60 ppbv. Range and maximum generally decrease with altitude, especially over 2 km.

Mean seasonal cycle always peaks in spring followed at several stations by a secondary maximum in summer (Fig. 1), with gradual, from north to south, shift towards the warm season, roughly below the 48°N lat. The month of maximum is independent of altitude. The spring maximum dominates at sites lower than 1,000 m asl at latitude greater than 50°N.

Since springtime maximum is of background origin and summer peak is attributed to ozone precursors' emissions (Monks 2000; Tarasova et al. 2007) measurement sites can be distinguished into four basic types (Fig. 1):

Type I: Spring maximum with minimum in summer at remote sites as Mace Head (Ireland), Lough Navar (N. Ireland) and Strath Vaich Dam (Scotland-UK), Kårvatn (Norway), Esrange and Vindeln (Sweden), Oulanka (Finland).

Type II: Spring maximum with gradual decrease towards autumn, like Monte Velho (Portugal), Virolahti II (Finland), Sommerton (UK).

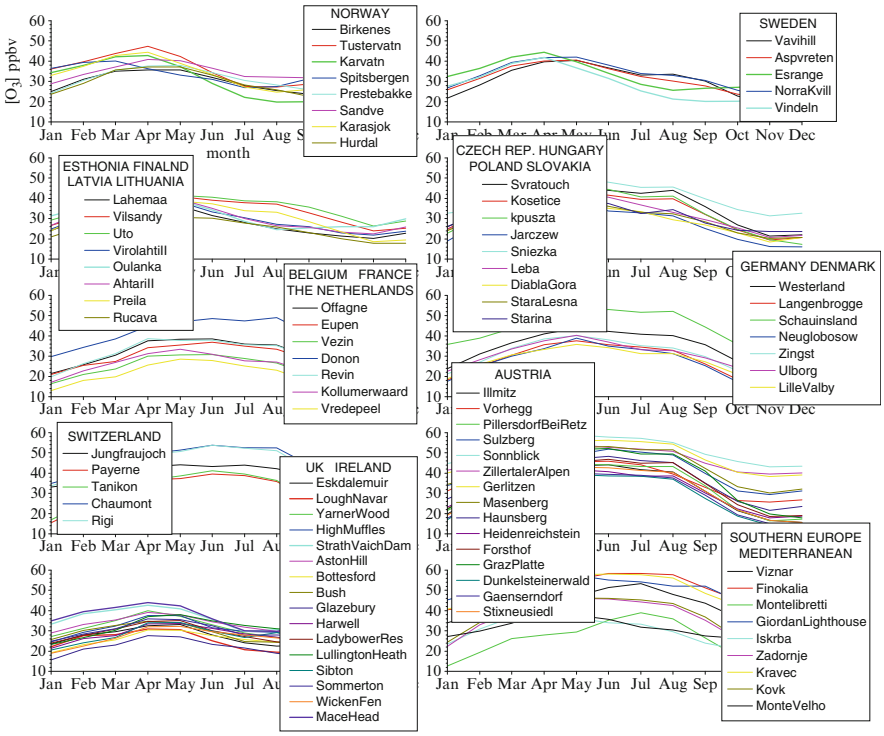

Fig. 1 Surface ozone mean seasonal cycle of 89 rural EMEP sites during 1997–2006

Type III: Broad spring – summer maximum, characteristic of elevated continental sites, Mediterranean and offshore island Utö in Finland and The Netherlands, Germany and Denmark.

Type IV: Pronounced summer maximum like elevated Viznar (Spain) and industrialised and populated Montelibretti (Italy) similar to urban and suburban sites.

Observations and estimates for mean annual linear trends vary between −1.24–(+1.13) and −1.00–(+1.00) ppbv.year^{-1} respectively. Positive statistically significant trends appear in eastern Austria (except for Sulzberg), the British Isles and S. Scandinavia-only in winter and autumn-and negative insignificant values at k-puszta (Hungary), Kårvatn (Norway), Utö and Vilsandy (Finland, Estonia). Low altitude sites determine prevailing close to zero trends in all seasons (Fig. 2).

Diurnal range, 1–19 ppbv, displays increasing gradient from north to south, (Fig. 2) diminishing with altitude above 1,200 m. Diurnal maximum, 29–50 ppbv, exhibits increasing gradient from NW to SE and highest values in Austria – Slovenia, Mediterranean, increasing above 1,200 m except for Jungfraujoch.

Diurnal ozone doesn't peak at sun zenith angle but usually in the afternoon (2–4 p.m. local time), because of the time required to restore equilibrium in the

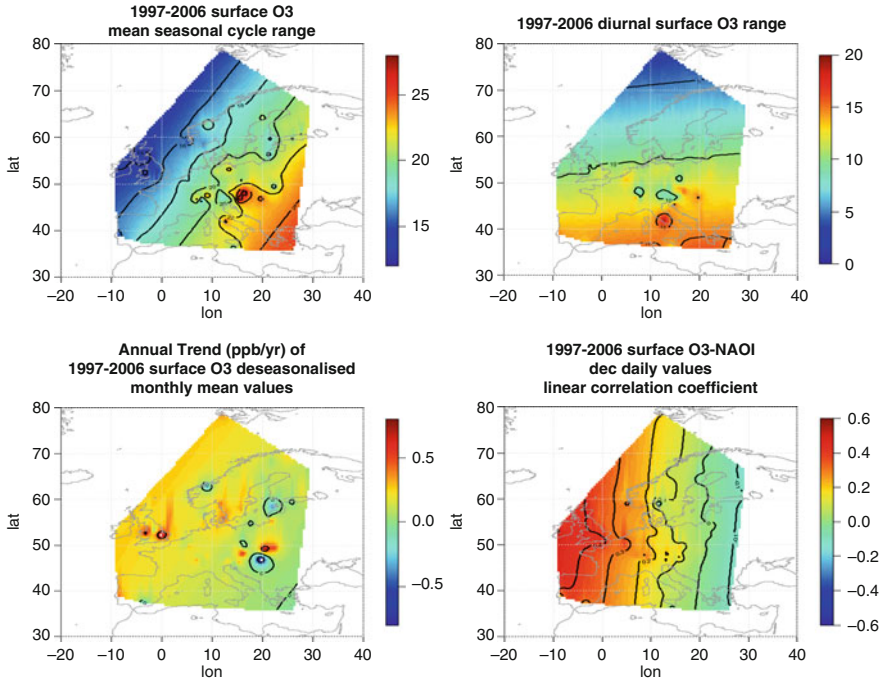

Fig. 2 Kriging interpolation values of surface ozone mixing ratio mean seasonal cycle range (*top left*), diurnal range (*top right*), annual trends (*bottom left*) and linear correlation coefficient to NAO index in December (*bottom right*) over Europe during 1997–2006

chemical reaction producing ozone from nitrogen oxides. Elevated inland sites peak around midnight, polar Spitsbergen early in the morning and Kravec (Slovenia), Sniezka (Poland) and Finokalia (Crete-Greece) in the evening. Diurnal variability is greater during the warm season (April–September).

Linear correlation coefficient r between observed deseasonalised monthly mean values of NAO index and surface ozone mixing ratio in all seasons show positive moderate correlation ($0.5 < r < 0.7$) at Mace Head (Ireland), Lullington Heath (UK), Birkenes and Sandve (Norway), Westerland (N. Germany), Ulborg (Denmark), Vorhegg and Sulzberg (Austria) and also at Rigi (Switzerland) in winter, at Sandve in summer and at Diabla Gora (Poland) in autumn. Kriging interpolation exhibits an increasing r gradient from west to east reproducing well r calculation in summer and autumn and sufficiently well in winter. Additionally daily values display positive moderate correlation in UK, Ireland and the Netherlands in December and January, confirmed by interpolation (Fig. 2). During 1997–2006 NAO Index mean seasonal cycle implies positive phase in NH winter months.

4 Conclusions

1. The highest ozone levels appear in Southeastern Europe probably due to enhanced photochemical activity and transport of ozone and ozone precursors by synoptic and regional scale winds. Mean seasonal variation in Northwestern Europe (Ireland, UK, Scandinavia) is characterised by springtime maximum, shifted to broad summer maximum in central mainland and farther south in the continent.
2. Trends are generally close to zero, within the limits 0.3–0.5 ppbv·year^{-1} in the overview of the last 30 years (Vingarzan 2004; Jonson et al. 2006), indicating O_3 stabilisation, maybe due to emissions reduction.
3. The diurnal amplitude of ozone variability is getting higher as we move from northern to southern latitudes due to enhancement of the photochemical ozone production.
4. During NH winter about 40% of near surface ozone variability at the western edge of Europe, as well as up to 20% in Scandinavia, Germany and Switzerland, maybe attributed to circulation changes and intercontinental transport of ozone and ozone precursors related to NAO.

After the 1990s emissions abatement strategies and despite the tendency for stabilization of ozone trends during the recent period 1997–2006, the lower tropospheric ozone in Europe remains high.

References

Chevalier A, Gheusi F, Delmas R, Ordonez C, Sarrat C, Zbinden R, Thouret V, Athier G, Cousin J-M (2007) Influence of altitude on ozone levels and variability in the lower troposphere: a ground-based study for western Europe over the period 2001–2004. Atmos Chem Phys 7:4311–4326. doi:10.5194/acp-7-4311-2007

Fjaeraa AM, Hjellbrekke A-G (2007) EMEP Co-operative programme for monitoring and evaluation of the long-range transmission of air pollutants in Europe, ozone measurements 2005, EMEP/CCC-Report 2/2007, O-99074

Hurrell JW, Kushnir Y, Visbeck M (2001) The North Atlantic oscillation. Science 291:603–605. doi:10.1126/science.1058761

Jonson JE, Simpson D, Fagerli H, Solberg S (2006) Can we explain the trends in European ozone levels? Atmos Chem Phys 6:51–66. doi:10.5194/acp-6-51-2006

Li Q et al (2002) Transatlantic transport of pollution and its effects on surface ozone in Europe and North America. J Geophys Res 107(D13):4166. doi:10.1029/2001JD001422

Monks PS (2000) A review of the observations and origins of the spring ozone maximum. Atmos Environ 34:3545–3561. doi:10.1016/S1352-2310(00)00129-1

Reid N, Yap D, Bloxam R (2008) The potential role of background ozone on current and emerging air issues: an overview. Air Qual Atmos Health 1:19–29. doi:10.1007/s11869-008-0005-z

Tarasova OA, Brenninkmeijer CAM, Jockel P, Zvyagintsev AM, Kuznetsov GI (2007) A climatology of surface ozone in the extra tropics: cluster analysis of observations and model results. Atmos Chem Phys 7:6099–6117. doi:10.5194/acp-7-6099-2007

Vingarzan R (2004) A review of surface ozone background levels and trends. Atmos Environ 38:3431–3442. doi:10.1016/J.Atmos Env. 2004.030030

Air Quality Simulations Over Europe for the Period 1996–2006 with Emphasis on Tropospheric Ozone

D. Akritidis, P. Zanis, E. Katragkou, I. Tegoulias, A. Poupkou, K. Markakis, T. Karacostas, and I. Pytharoulis

Abstract A modeling system based on the air quality model CAMx driven off-line by the regional climate model RegCM3 is used for assessing the impact of lateral boundary conditions and anthropogenic emissions on tropospheric ozone over Europe for the period 1996–2006. The RegCM3 and CAMx simulations were performed on a 50 km × 50 km grid over Europe with RegCM3 driven by NCEP reanalysis fields. Average monthly concentration values obtained from the global chemistry climate model ECHAM5-MOZ were used as chemical boundary conditions for the CAMx simulations. The present period (1996–2006) was simulated four times. The first run was forced with time and space invariable lateral chemical boundary conditions and EMEP emissions based on the year 1996. The second decadal simulation was based on ECHAM5-MOZ chemical boundary conditions and emissions both fixed for the year 1996. The third decadal simulation was based on ECHAM5-MOZ chemical boundary conditions with interannual variation but fixed emissions from the year 1996. Finally, the fourth decadal simulation was based on ECHAM5-MOZ chemical boundary conditions and emissions, both having interannual variation. Simulated ozone concentrations are compared against measurements from the EMEP network in order to evaluate the modeling system.

1 Introduction

Tropospheric ozone is a key species controlling the oxidation capacity of the atmosphere, while it acts as a greenhouse gas in terms of radiative forcing at the earth's surface. Furthermore elevated O3 concentrations are of major environmental

D. Akritidis (✉) • P. Zanis • E. Katragkou • I. Tegoulias • T. Karacostas • I. Pytharoulis
Department of Meteorology – Climatology, School of Geology, Aristotle University of Thessaloniki, University Campus, Thessaloniki, Greece
e-mail: dakritid@geo.auth.gr

A. Poupkou • K. Markakis
Laboratory of Atmospheric Physics, Aristotle University of Thessaloniki, Thessaloniki, Greece

C.G. Helmis and P.T. Nastos (eds.), *Advances in Meteorology, Climatology and Atmospheric Physics*, Springer Atmospheric Sciences,
DOI 10.1007/978-3-642-29172-2_119,

concerns because of its adverse effects on human health (Schlink et al. 2006) and on ecosystems (Fuhrer and Booker 2003). In Europe, even though high surface O3 events are decreasing, the O3 baseline appears to have increased at several surface sites (Monks et al. 2003). Emissions of ozone precursors from Europe have been substantially reduced over the last 10–15 years due to control strategies, but changes in ozone levels cannot be explained by changes in European emissions alone. More detailed information about anthropogenic and natural emission changes as well as information for intercontinental pollution transport is required in order to understand the issue of recent past trends and future changes in ozone.

In the recent years many studies based on regional climate-air quality models focusing on Europe, investigated climate change effects on tropospheric ozone (Katragkou et al. 2010), while other studies tried to evaluate the performance of the modelling system (Zanis et al. 2011). In this study a modeling system based on the air quality model CAMx driven off-line by the regional climate model RegCM3 is used for assessing the impact of lateral boundary conditions and anthropogenic emissions on tropospheric ozone over Europe for the period 1996–2006. Furthermore, simulated ozone concentrations are compared against measurements from the EMEP network in order to evaluate the modeling system.

2 Data and Methodology

The regional climate model simulations were performed with the regional climate model RegCM3 (http://www.ictp.trieste.it/~pubregcm/RegCM3/) driven by data from the NCEP reanalysis. RegCM3 was used to simulate the time period 1996–2006 for a large European domain with a grid resolution of 50 km $\times$ 50 km, in order to provide the meteorological forcing for the air quality simulations carried out by CAMx version 5.20.

CAMx (www.camx.com/) is a Comprehensive Air quality Model with extensions used is this study to simulate the time period 1996–2006 over Europe with a 50 km $\times$ 50 km spatial resolution. The vertical profile of the domain contains 12 layers of varying thickness with the uppermost layer extending to about 5.2 km. The chemistry mechanism used in CAMx is Carbon Bond version 4 (CB4) including 113 reactions and up 28 gas species, but not including aerosol chemistry. Photolysis rates were derived for each grid sell as a function of solar zenith angle, altitude, total ozone column, surface albedo and atmospheric turbidity, using a CAMx land-use file and average monthly satellite ozone column data from TOMS (Total Ozone Mapping Spectrometer) for the calculations.

Organic biogenic emissions are calculated with the use of an interface, using meteorological parameters from RegCM3 (temperature and radiation) and the available land-use categories according to Guenther et al. (1993). Anthropogenic emissions were processed (spatial disaggregation, temporal and chemical splitting) using the MOSESS emission model developed in the laboratory of atmospheric

physics in the Aristotle University of Thessaloniki. The emissions were provided in annual basis and the temporal analysis (monthly, weekly, diurnal) was completed using the profiles of Friedrich (1997) for all countries found inside the domain. Average monthly concentration values obtained from the global chemistry climate model ECHAM5-MOZ were used as chemical boundary conditions for the CAMx simulations, while the top boundary conditions are internally calculated from the model.

The first run (clean) was forced from constant lateral chemical boundary conditions and emissions based on the EMEP emissions of the year 1996. The second decadal simulation (run1) was based on ECHAM5-MOZ chemical boundary conditions and emissions fixed for the year 1996. The third decadal simulation (run2) was based on ECHAM5-MOZ chemical boundary conditions with interannual variation but fixed emissions from the year 1996. Finally, the fourth decadal simulation (run3) was based on ECHAM5-MOZ chemical boundary conditions and emissions both having interannual variation.

The simulated ozone concentrations are compared against measurements from the EMEP network. Since many of the stations of the EMEP network were not operating continuously during the time period of our study (1996–2006), we have used in the evaluation analysis only those stations that fulfill the criteria of 75% data availability for near surface ozone, choosing 87 stations from 23 European countries.

3 Results

Figure 1 shows the average surface ozone concentrations for the clean simulation. Model calculations for clean boundary conditions yield higher ozone concentrations over the Mediterranean basin, attaining values of around 60 ppb in summer and around 40 ppb in winter. Over continental Europe the summer averages range between 25 and 45 ppb and winter averages around 10–30 ppb. Figure 2 shows the average surface ozone concentrations for the run1 simulation. The different chemical boundary condition forcing resulted in changes of near surface ozone, with an increase ranging between 2 and 5 ppb in winter and a decrease ranging between 2 and 8 ppb in summer. The area showing the greater sensitivity in O3 during winter is northwest Europe while in summer north and west Europe.

In order to evaluate the ability of the RegCM3/CAMx modeling system, simulated ozone concentrations are compared against near surface ozone measurements from the EMEP network. Statistical metrics used for model evaluation are correlation coefficient (R), normalized standard deviation (NSD) (ratio of standard deviation of the simulated values versus standard deviation of observed values) and modified normalized mean bias (MNMB) which gives a measure of bias of simulated versus observed data bounded by the values -1 to $+1$ (-100% to 100%) performing with respect to under and over-estimation.

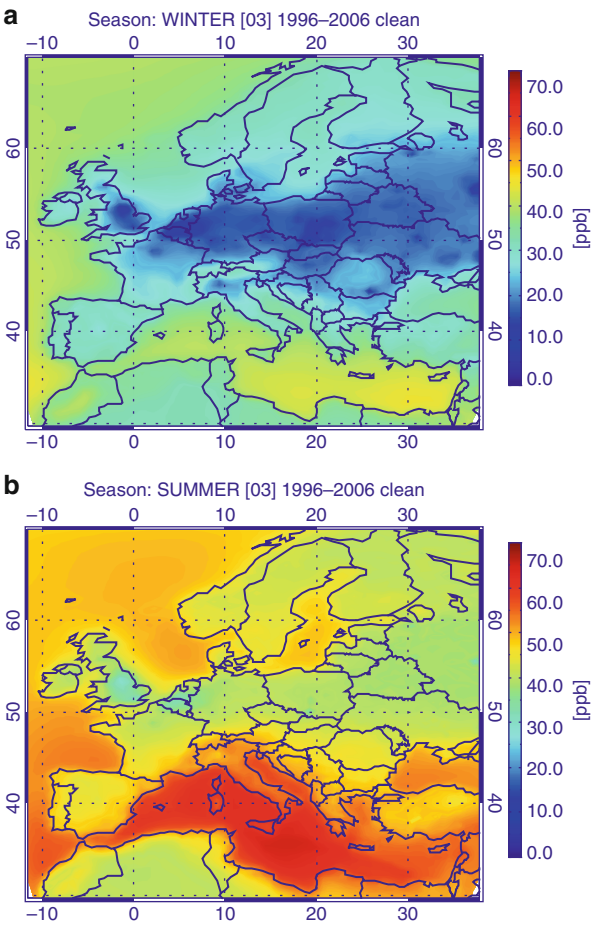

Fig. 1 Average (1996–2006) surface ozone concentrations for the clean simulation, for the winter (**a**) and the summer (**b**) season

Table 1 illustrates summary statistics of these metrics concerning data from the clean and run1 simulation, showing a good agreement between simulated and observed data.

In the case of clean simulation the 75% of the stations have a correlation $R > 0.75$ ($R > 0.48$ for clean simulation) capturing very well the monthly variability of ozone concentrations. For stations located near the north and north-west boundary of the domain the run1 simulation, unlike clean simulation, is capturing the spring maximum of ozone (Mace Head – Ireland, Fig. 3). Overall, the correlation between simulated and observed data is greater in the case of run1 simulation for the majority of the stations (Fig. 4a). Figure 4b illustrates a comparison between the correlations of run2 and run3 simulated data with the observed data, in order to examine the impact of varying anthropogenic emissions to ozone variability. The majority of the points (representing stations) are located near the

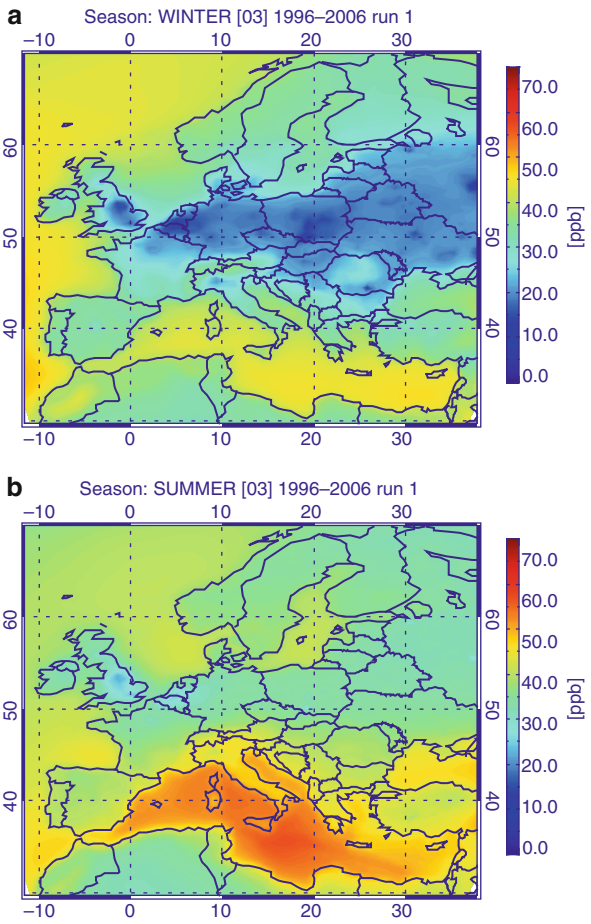

Fig. 2 Average (1996–2006) surface ozone concentrations for the run1 simulation, for the winter (**a**) and the summer (**b**) season

Table 1 Summary statistics of the evaluation metrics based on the comparison of clean and run1 simulated monthly surface ozone concentrations with the observed ozone from the EMEP network over the period 1996–2006

Summary statistics	R		MNMB (%)		NSD	
	Clean	run1	Clean	run1	Clean	run1
10%	0.26	0.62	−20.77	−19.99	0.80	0.54
25%	0.48	0.75	−7.41	−5.97	0.99	0.67
75%	0.78	0.84	15.41	15.91	1.30	0.87
90%	0.81	0.86	29.48	29.70	1.40	0.95
Min	−0.15	0.31	−43.66	−41.97	0.60	0.39
Max	0.85	0.89	79.18	76.23	1.67	1.15
Median	0.72	0.81	5.15	4.67	1.14	0.82

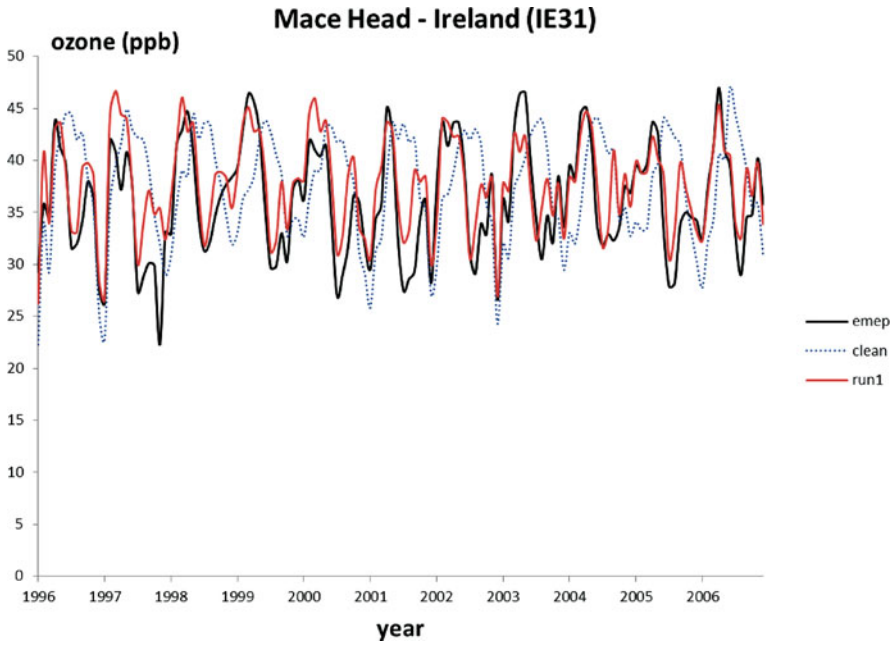

Fig. 3 Time series of clean simulation, run1 simulation and observed monthly ozone values at Mace Head (IE31, Ireland)

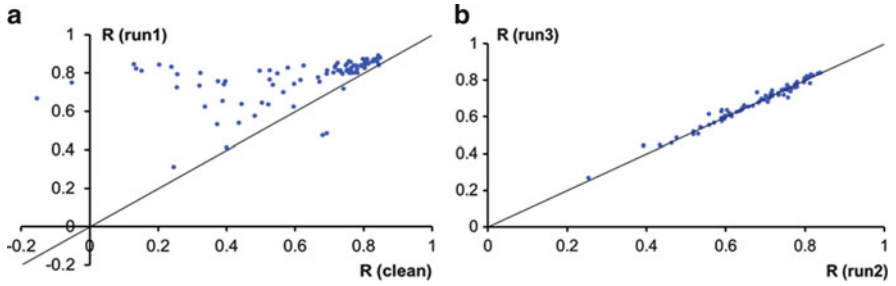

Fig. 4 Comparison between the correlations of (**a**) run1-emep data and clean-emep data, (**b**) run3-emep data and run2-emep data

line, showing that there is no significant improvement in R values between observed and simulated ozone values as a result of the varying from year to year anthropogenic emissions.

Concerning the amplitude of the ozone bias, a small tendency of model overestimation is found in both simulations (clean and run1) as the median MNMB is 5.15% and 4.67% respectively. For the run1 simulation the 50% of the stations have a MNMB value that range between −5.97% and +15.91%, while for the clean

simulation range between −7.41% and +15.41%. Concerning the NSD metric, for the clean simulation the modeling system seems to overestimate the amplitude of ozone variance (NSD $>$ 1 for the 75% of the stations), unlike the run1 simulation where the modeling system underestimates the amplitude of ozone variance (NSD $<$ 1 for the 93% of the stations).

4 Conclusions

The different lateral boundary conditions forcing resulted in changes of near surface ozone concentrations and variability. Using lateral boundary conditions obtained from the global chemistry climate model ECHAM5-MOZ (run1), the RegCM3/CAMx modeling system is capturing in a much better way the ozone monthly variability than using constant lateral boundary conditions (clean), especially for stations of northern and northwestern Europe. Concerning the correlation between simulated and observed monthly ozone values, the run1 simulation exhibits R values greater than the clean simulation for 95% of the stations. Furthermore, both clean and run1 simulations show a tendency of model overestimation concerning near surface ozone concentrations, as the MNMB median is 5.15% for clean and 4.67% for run1 respectively.

References

Friedrich R (1997) GENEMIS: assessment, improvement, temporal and spatial disaggregation of European emission data. In: Ebel A, Friedrich R, Rhode H (eds) Tropospheric modeling and emission estimation (Part 2). Springer, New York

Fuhrer J, Booker F (2003) Ecological issues related to ozone: agricultural issues. Environ Int 29 (2–3):141–154. doi:10.1016/S0160-4120(02)00157-5

Guenther AB et al (1993) Isoprene and monoterpene emission rate variability: model evaluations and sensitivity analyses. J Geophys Res 98:12609–12617. doi:10.1029/93JD00527

Katragkou E et al (2010) Decadal regional air quality simulations over Europe in present climate: near surface ozone sensitivity to external meteorological forcing. Atmos Chem Phys 10:11805–11821. doi:10.5194/acp-10-11805-2010

Monks PS et al (2003) Tropospheric ozone and precursors: trends, budgets and policy. In: Monks PS (ed) TROTREP Synthesis and Integration Report 91568, University of Leicester, UK

Schlink U et al (2006) Statistical models to assess the health effects and to forecast ground-level ozone. Environ Model Softw 21(4):547–558. doi:10.1016/j.envsoft.2004.12.002

Zanis P et al (2011) Evaluation of near surface ozone in air quality simulations forced by a regional climate model over Europe for the period 1991–2000. Atmos Environ 45:6489–6500

Trends of Shortwave and Longwave Surface Radiation in Europe: Spatiotemporal Analysis and Comparison of Satellite and Ground-Based Observations

G. Alexandri, C. Meleti, A.K. Georgoulias, and D. Balis

Abstract A detailed investigation of the shortwave (SW) and longwave (LW) up-welling and down-welling surface radiation trends over Europe is presented here. For the purposes of this work, satellite observations from the International Satellite Cloud Climatology Project (ISCCP) for the period 1984–2009 have been spatiotemporally analyzed at a ~280 × 280 km^2 resolution. A Fourier-based harmonic analysis technique has been used for the calculation of the trend also allowing for the assessment of its statistical significance. The results are compared to trends calculated from ground-based observations from several World Radiation Data Center (WRDC) stations. The stations have been categorized taking into account their position and the special characteristics of the surrounding region (rural/urban, high/low elevation, population, etc.). The variability of the SW and LW radiation within selected ISCCP grid cells is investigated with the use of ground-based observations. Observed trends and their significance depends on the area of study. Estimated trend for SW radiation over Europe as derived from ISCCP data for the period 1984–2009 is about −0.6 W/m^2 and for LW radiation is about 2.47 W/m^2.

G. Alexandri (✉) • C. Meleti • D. Balis
Laboratory of Atmospheric Physics, Aristotle University of Thessaloniki, 54124 Thessaloniki, Greece
e-mail: alexang@auth.gr

A.K. Georgoulias
Laboratory of Atmospheric Pollution and Pollution Control Engineering of Atmospheric Pollutants, Department of Environmental Engineering, Democritus University of Thrace, 67100 Xanthi, Greece

C.G. Helmis and P.T. Nastos (eds.), *Advances in Meteorology, Climatology and Atmospheric Physics*, Springer Atmospheric Sciences,
DOI 10.1007/978-3-642-29172-2_120,

1 Introduction

Solar radiation is a major determining factor of the climate conditions. Changes in the amount of solar radiation that reaches the Earth's surface have received prominent attention due to its potential influences on environmental, social and economic parameters (Pinker et al. 2005). These changes are affected by anthropogenic and natural factors. Many studies have examined the effect of these factors on solar radiation (Wild 2009). The aim of this work is to investigate the trend of shortwave and longwave solar radiation during the last decades.

2 Data and Methodology

Satellite and ground based data have been used to analyze the trends of shortwave (SW) and longwave (LW) radiation over Europe. The satellite datasets used here contain SW (0.2–5 μm) and LW (5.0–200 μm) down welling radiation at Earth's surface, as derived from International Satellite Cloud Climatology Project (ISCCP). Those data have spatial analysis 280 × 280 km^2, temporal analysis 3 h and cover the period 1984–2009. Zhang et al. (2004) put the uncertainty of the data set at 10–15 W/m^2 in the SW and 5–10 W/m^2 in the LW (compared with ERBE (Earth Radiation Budget Satellite and CERES (Clouds and the Earth's Radiant Energy System)).

The ground based observations were acquired from World Radiation Data Centre (WRDC) datasets and include 25 station of Global Radiation (SW) and 4 station of LW down welling radiation. The accuracy of the measurements depends on the type of instrument. SW radiation data cover the period 1994–2009 while LW radiation data the period 1999–2007.

For each grid cell and station timeseries of monthly averages of radiation are determined. In order to fit the time series a model with a linear trend and a seasonal component for the annual cycle of radiation has been used. The model proposed by Weatherhead et al. (1998) and described by the following function has been chosen:

$$Y_t = A + BX_t + \sum_{n=1}^{2}\left[a_n \sin\left(\frac{2\pi}{T} nX_t\right) + b_n \cos\left(\frac{2\pi}{T} nX_t\right)\right] + N_t \qquad (1)$$

where Y_t represents the monthly mean radiation of month t, X_t is the number of the month after the first month of each timeseries. Parameter A represents the monthly mean radiation of first month of each timeseries and B is the monthly trend of radiation. The seasonal component contains amplitude a_n, b_n and the time period T (1 year), while the symbol N_t is the reminder.

The reminder N_t in (1) is the difference between the model and the measured value. The reminder is given by the following formula (Weatherhead et al. 1998):

$$N_t = \varphi N_{t-1} + \varepsilon_t \tag{2}$$

where φ is the autocorrelation in the reminder and ε_t is the white noise. The autocorrelation in the reminder affects the precision of the trend. In the work of Weatherhead et al. (1998) a derivation is given for the precision of the trend as function of the autocorrelation φ, the length of the data set in months and the variance in the reminder σ_N.

The length of the datasets in years, m, is introduced to express the precision of the trend per year. For small autocorrelations the standard deviation σ_B of the trend per year can be approximated using the formula:

$$\sigma_B \approx \left[\frac{\sigma_N}{m^{3/2}} \sqrt{\frac{1+\varphi}{1-\varphi}} \right] \tag{3}$$

The precision of the trend on radiation is calculated using (3). It is common decision rule for trend detection that the significance level of the trend B is better than 95% if $|B/\sigma_B|$ is larger than 2.

3 Results and Discussion

For each ISCCP grid cell and WRDC station the model of (1) is applied, leading to a spatial distribution of each one of the fitting parameters. Two time periods considered for ISCCP data: The first includes the whole available satellite set and covers the period from 1984 to 2009, while the second period depends on the length of the ground based data timeseries and it is from 1994 to 2009 for SW radiation and from 1999 to 2007 for LW radiation.

3.1 Shortwave Radiation

Trend analysis of ISCCP SW radiation data over Europe shows a decrease of about -0.6 W/m^2 for the period 1984–2009. For the same period significant decrease is found over Central (~-1.81 W/m^2) and Central Eastern Europe (~-1.99 W/m^2), while increasing trends of SW observed over Southern-Western Europe (~1.36 W/m^2) and over Central Mediterranean (~1.6 W/m^2). The majority of results are statistically significant. The decrease is related to the observed increasing trend in aerosol loading (Chiacchio et al. 2011; Streets et al. 2006).

Trends of SW radiation were also calculated for the period 1994–2009, which is common between ISCCP and WRDC data timeseries (results presented in Table 1). Increases in SW radiation were observed in many WRDC stations. Responsible for the differences between the calculated trends from ground based stations and

Table 1 Observed trends of SW radiation for some WRDC stations and ISCCP grid cells

WRDC							ISCCP			
Station	Urban/rural	Elevation	Lat. (North)	Lon. (East)	Trend (W/m^2/year)	Significant?	Lat. (North)	Lon. (East)	Trend (W/m^2/year)	Significant?
Klagenfurt	Urban	448	46.65	14.33	0.65	Yes	46.25	12.60	0.06	Yes
Sonnblick	Rural	3106	47.05	12.95	−0.21	Yes	46.25	12.60	0.06	Yes
Graz	Urban	366	47.08	15.45	0.63	Yes	46.25	16.20	−0.10	Yes
Innsbruck	Urban	579	47.25	11.35	0.77	Yes	46.25	12.60	0.06	Yes
Bregenz	Rural	424	47.50	9.750	0.78	Yes	48.75	9.473	−0.22	Yes
Salzburg	Urban	420	47.78	13.05	0.90	Yes	48.75	13.26	−0.12	Yes
Wien/HoheWart	Urban	203	48.25	16.36	−0.01	No	48.75	17.05	−0.02	No
Uccle	Urban	100	50.80	4.350	0.48	Yes	51.25	6.00	−0.14	Yes
Melle	Rural	15	50.98	3.833	0.41	Yes	51.25	2.00	−0.03	No
Oostende	Rural	5	51.20	2.866	−0.08	No	51.25	2.00	−0.03	No
Kucharovice	Rural	334	48.88	16.08	0.42	Yes	48.75	17.05	−0.02	No
OstravaPoruda	Urban	342	49.81	18.15	0.61	Yes	48.75	17.05	−0.02	No
Praha	Urban	232	50.08	14.43	1.18	Yes	48.75	13.26	−0.12	Yes
HradecKralove	Urban	241	50.18	15.83	0.51	Yes	51.25	14.00	−0.05	No
Weihenstephan	Rural	470	48.40	11.70	0.47	Yes	48.75	13.26	−0.12	Yes
Trier	Urban	265	49.75	6.666	0.19	Yes	48.75	5.684	−0.16	Yes
Wuerzburg	Urban	268	49.76	9.966	0.23	Yes	48.75	9.473	−0.22	Yes
Braunschweig	Urban	81	52.30	10.45	0.20	Yes	51.25	10.00	−0.09	Yes
Hamburg	Urban	16	53.63	10.00	0.23	Yes	53.75	10.58	−0.04	No
Helsinki_arpt	Urban	51	60.31	24.96	0.06	No	61.25	61.25	−0.07	Yes
Sodankyla	Rural	199	67.36	26.65	0.05	No	66.25	66.25	−0.09	Yes
Goteborg	Urban	46	57.70	12.00	0.53	Yes	58.75	58.75	−0.12	Yes
Stockholm	Urban	30	59.35	18.06	0.32	Yes	58.75	58.75	−0.07	Yes
Borlange	Rural	153	60.43	15.50	0.0	No	61.25	61.25	−0.14	Yes
Ostersund	Rural	376	63.18	14.50	0.13	Yes	63.75	63.75	−0.14	Yes

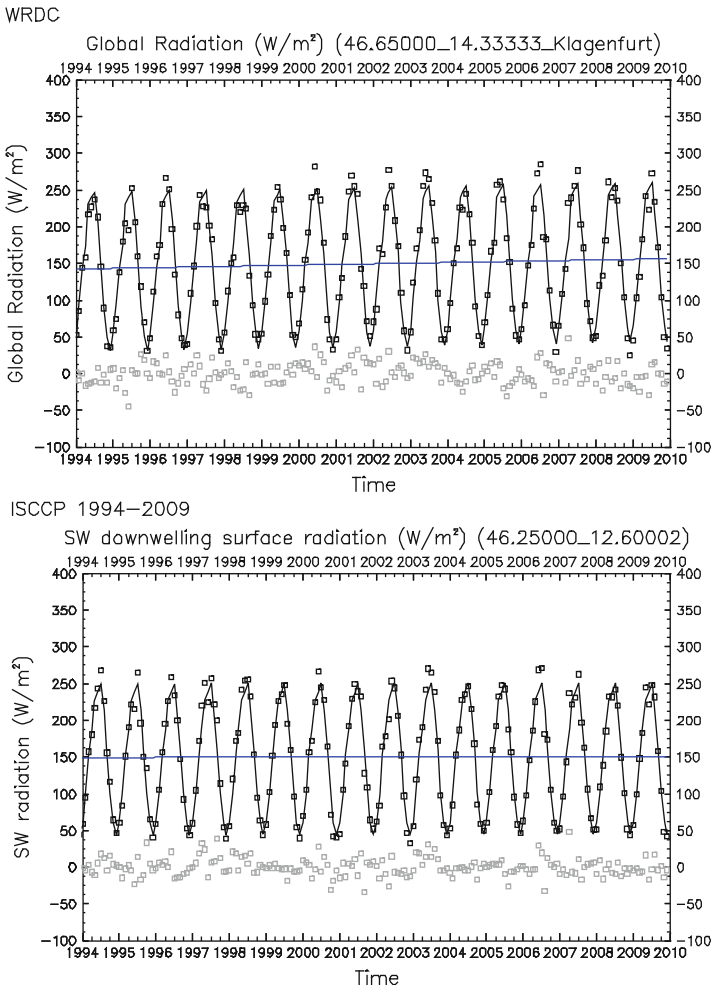

Fig. 1 An example of timeseries for the ground based station of Klagenfurt (*upper*) and for grid cell [lat: 46.25N – lon: 12.60E] (*lower*) The Y axis shows the monthly mean SW radiation and X axis shows the years. The *black* squares represent the observations. The *black* solid line presents the fitting result which consists of a linear growth and a seasonal component. The difference between model and observation is represented by the *gray* squares

satellite data is the size of satellite grid cell. Grid is large enough and in many cases includes regions with different topography, population density, industrial activity etc. Moreover, many ISCCP grids include more than one WRDC station, while ground based stations estimate well radiation trends on local scale. Analysis shows that the results from ground based data and satellite data are in good agreement for urban places situated on middle elevation, this is due to the fact that grids over Europe simulated better with urban areas on middle elevation. In Fig. 1 an example of trend analysis for a WRDC station (Klagenfurt station) and an ISCCP grid cell is presented.

Table 2 Observed trends of LW radiation for some WRDC stations and ISCCP grid cells

WRDC							ISCCP			
Station	Urban/rural	Elevation	Lat. (North)	Lon. (East)	Trend (W/m^2/year)	Significant?	Lat. (North)	Lon. (East)	Trend (W/m^2/year)	Significant?
LocarnoModi	Urban	366	46.18	8.78	−0.48	Yes	46.25	9.0	−1.56	Yes
Jungfraujoch	Rural	3,580	47.55	7.98	−1.39	Yes	46.25	9.0	−1.56	Yes
Davos	Rural	1,592	46.76	9.83	−0.64	Yes	46.25	9.0	−1.56	Yes
Payerne	Rural	490	46.81	6.93	−1.41	Yes	46.25	9.0	−1.56	Yes

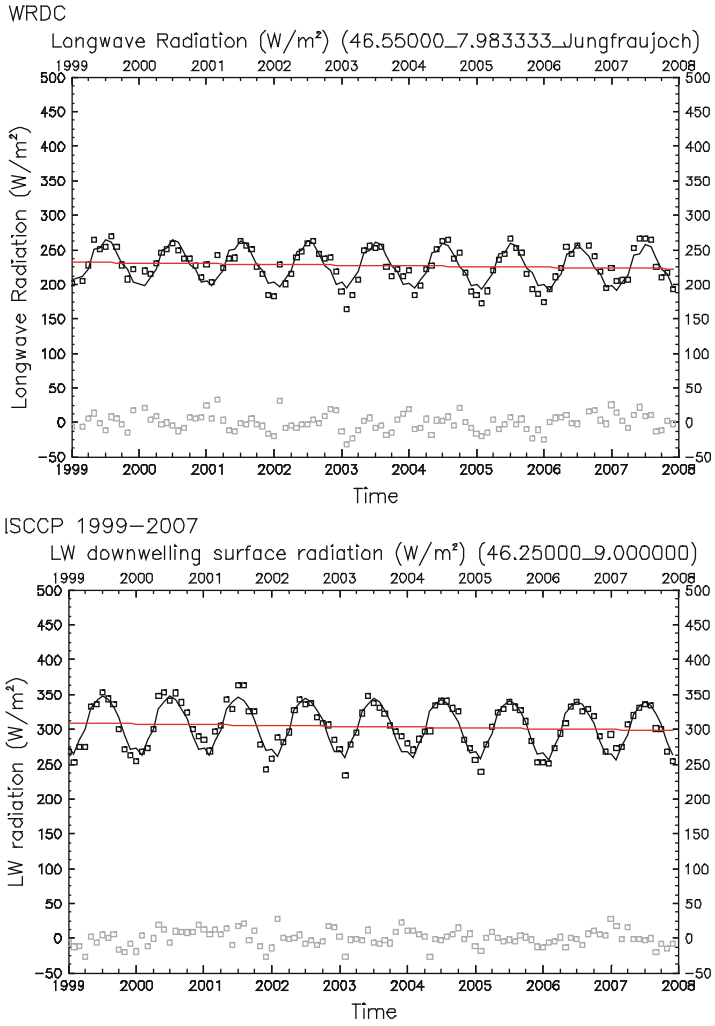

Fig. 2 An example of timeseries for the ground based station of Jungfraujoch (*upper*) and for grid cell [lat: 46.25N – lon: 9.0E] (*lower*). The Y axis shows the monthly mean LW radiation and X axis shows the years. The *black squares* represent the observations. The *black solid line* presents the fitting result which consists of a linear growth and a seasonal component. The difference between model and observation is represented by the *gray squares*

3.2 Longwave Radiation

ISCCP analysis revealed an increasing trend of LW radiation over Europe. For the period 1984–2009 LW radiation over Europe increases about 2.47 W/m^2. Significant increase has been observed over North-Eastern (~6.76 W/m^2) and Central Eastern Europe (~6.86 W/m^2). The increase of the greenhouse gasses over Europe

is considered to be responsible for the observed trend, since LW radiation is strongly affected by them (Schulze et al. 2009). Decreasing trends were found only over Central Mediterranean (~−0.9 W/m^2).

For the common period, 1999–2007, ISCCP and WRDC data also examined (results are presented in Table 2). All selected stations belonged to the same ISCCP grid. The satellite data analysis results were in agreement with those from ground based stations, particularly in rural regions. An example of trend analysis of LW radiation for a WRDC station (Jungfraujoch station) and an ISCCP grid cell is presented in Fig. 2. Differences in level of LW radiation between ISCCP and WRDC data (Fig. 2) due to the fact that ISCCP grid is large enough and includes area of different characteristics (population density, topography, etc.).

References

Chiacchio M et al (2011) Decadal variability of aerosol optical depth in Europe and its relationship to temporal shift of North Atlantic Oscillation in the realm of dimming and brightening. J Geophys Res 116:D02108. doi:10.1029/2010JD014471

Pinker RT, Zhang B, Dutton EG (2005) Do satellites detect trends in surface solar radiation? Science 308:850–854

Streets DG, Wu Y, Chin M (2006) Two-decadal aerosol trends as a likely explanation of the global dimming/brightening transition. Geophys Res Lett 33:L15806

Weatherhead EC et al (1998) Factors affecting the detection of trends: statistical consideration and application to environmental data. J Geophys Res 103:17149–17161

Wild M (2009) Global dimming and brightening: a review. J Geophys Res 114:D00D16

Zhang Y, Rossow WB, Lacis AA, Oinas V, Mishchenko MI (2004) Calculation of radiative fluxes from the surface to top of atmosphere based on ISCCP and other global data sets: refinements of the radiative transfer model and the input data. J Geophys Res 109:D19105

Evaluation of CALIPSO's Aerosol Classification Scheme During the ACEMED Experimental Campaign Over Greece: The Case Study of 9th of September 2011

V. Amiridis, E. Marinou, S. Kazadzis, E. Gerasopoulos, R.E. Mamouri, P. Kokkalis, A. Papayannis, N. Kouremeti, E. Giannakaki, E. Liakakou, D. Paraskevopoulou, M. Gratsea, G. Kouvarakis, K. Allakhverdiev, F. Huseyinoglu, A. Secgin, D. Balis, A.F. Bais, N. Mihalopoulos, I.A. Daglis, and C.S. Zerefos

Abstract In order to assess the validity of CALIPSO's aerosol classification scheme, an experimental campaign called ACEMED (Evaluation of CALIPSO's aerosol classification scheme over Eastern Mediterranean) has been organized over Greece on September 2011. In this study, we concentrate on the characterization of the aerosol load over Greece on 9th of September, using advanced in-situ aircraft instrumentation (onboard the FAAM-Bae146 aircraft of the UK Met Office).

V. Amiridis (✉) • E. Marinou • I.A. Daglis
Institute for Space Applications and Remote Sensing, National Observatory of Athens, Athens, Greece
e-mail: vamoir@noa.gr

S. Kazadzis • E. Gerasopoulos • E. Liakakou • D. Paraskevopoulou • M. Gratsea
Institute of Environmental Research and Sustainable Development, National Observatory of Athens, Athens, Greece

R.E. Mamouri • P. Kokkalis • A. Papayannis
National Technical University of Athens, Athens, Greece

N. Kouremeti • E. Giannakaki • D. Balis • A.F. Bais
Aristotle University of Thessaloniki, Thessaloniki, Greece

G. Kouvarakis • N. Mihalopoulos
Department of Chemistry, University of Crete, Heraklion, Greece

K. Allakhverdiev
Marmara Research Center (TUBITAK), Gebze, Turkey

Institute of Physics ANAS, Baku, Azerbaijan

F. Huseyinoglu • A. Secgin
Marmara Research Center (TUBITAK), Gebze, Turkey

C.S. Zerefos
Academy of Athens, Athens, Greece

Navarino Environmental Observatory, Messinia, Greece

C.G. Helmis and P.T. Nastos (eds.), *Advances in Meteorology, Climatology and Atmospheric Physics*, Springer Atmospheric Sciences,
DOI 10.1007/978-3-642-29172-2_121,

The analytical evaluation of CALIPSO's aerosol-type classification scheme that is performed using synchronous/collocated satellite/airborne measurements, show a qualitatively reasonable performance of the CALIPSO's aerosol classification scheme in the complex aerosol environment of the case under study, where smoke, continental, urban and dust aerosol components are present.

1 Introduction

CALIPSO satellite provides vertically resolved information of aerosol and cloud parameters since June 2006. In order to assess the validity of CALIPSO observations, the National Observatory of Athens (NOA) organized an experimental campaign over Greece on September 2011. The campaign, called "ACEMED – Evaluation of CALIPSO's aerosol classification scheme over Eastern Mediterranean", was coordinated by the National Observatory of Athens. Participants from the University of Crete (UoC), National Technical University of Athens (NTUA), Academy of Athens (AA), Aristotle University of Thessaloniki (AUTH), NCSR Demokritos, Marmara Research Center (TUBITAK) in Turkey and the Institute for Methodologies for Environmental Analysis in Potenza joined the campaign with their ground-based equipment. The campaign was supported by the European Facility for Airborne Research (EUFAR) through the provision of flight award on FAAM-BAe146 aircraft and the Mariolopoulos – Kanaginis Foundation for the Environmental Sciences. In a series of coordinated activities, ground-based measurements at various sites were carried out, whilst FAAM aircraft, equipped with specialized instrumentation, performed flights above the sites and also travelled along the path of CALIPSO satellite. The campaign has been followed also by ESA's mobile ground-based lidar that was operated in Crete during ACEMED. In this paper, a case study from ACEMED is analyzed, focusing on the detection of smoke from biomass burning aerosols in Eastern Mediterranean (e.g. Balis et al. 2003; Kazadzis et al. 2007; Amiridis et al. 2009), which is one of the CALIPSO subtypes associated with misclassifications.

2 Datasets

ACEMED provided a large dataset from the ground-based and airborne sector. In brief, multi-wavelength lidar measurements were performed in the EARLINET stations of NTUA and AUTH in Athens and Thessaloniki, but also in Crete using ESA's mobile lidar station. Sunphotometric measurements from the AERONET network in Greece were collected (Athens, Thessaloniki and Xanthi). NOA's Atmospheric Remote Sensing Station was additionally equipped with a Max-DOAS system kindly provided by AUTH.

In order to achieve the aim of ACEMED, aircraft lidar measurements of the vertical structure and in-situ aerosol measurements have been performed by

FAAM-BAe146 aircraft. Aerosol backscatter and depolarization vertical profiles, size distributions, scattering coefficients, aerosol absorption, chemical characterization and SSA airborne measurements have been conducted using the remote sensing and in-situ instrumentation of FAAM-BAe146 over Greece.

3 Results for the Case Study of 9th of September

FAAM's aircraft nighttime CALIPSO under-flight on 9th of September 2011 is analyzed here. Satellite overpass along with the aircraft flight track followed are presented in Fig. 1.

The flight included a high altitude leg flown as close as possible to the satellite track above all significant aerosol layers and centered on the overpass time. The flight altitudes along with aircraft lidar retrievals during the flight are presented in Fig. 2.

From the range corrected lidar signals (Fig. 2 – upper panel), the presence of an elevated layer is evident over Greece. Lidar retrievals show stable layering over Thessaloniki permitting the assumption of horizontal aerosol homogeneity. The aerosol extinction coefficient profile at 550 nm retrieved from aircraft's measurements is presented in Fig. 3. CALIPSO's extinction profile at 532 nm spatially averaged at 45 km distance is also presented for a first comparison.

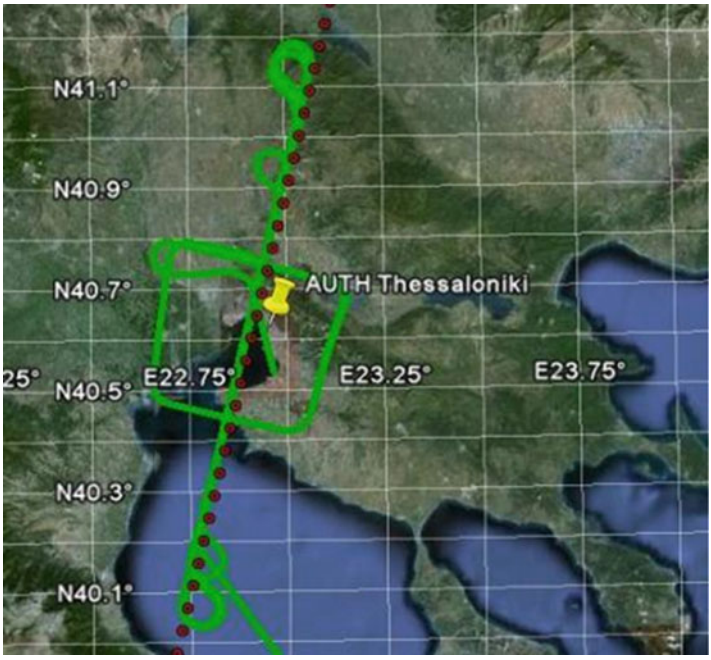

Fig. 1 CALIPSO overpass on 9th of September 2011 (00:45 UTC – *red dots*) followed by FAAM-BAe146 under-flights (*green line*). Thessaloniki's ground-based station is superimposed

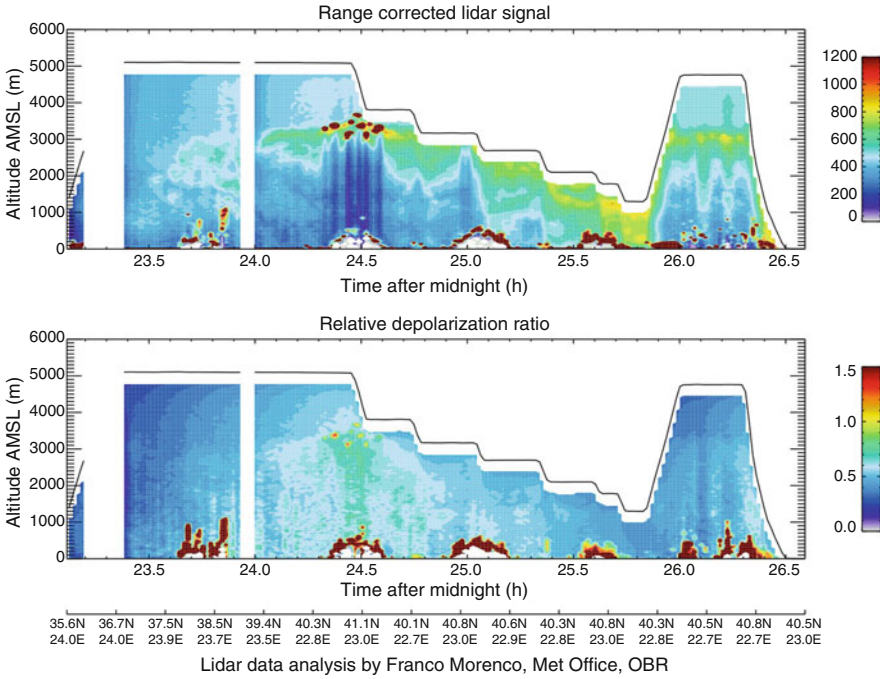

Fig. 2 Aircraft lidar retrievals during the ACEMED flight of 9th of September 2011. The range corrected lidar signal at 532 nm is presented (*upper panel*) along with the relative depolarization ratio (*lower panel*)

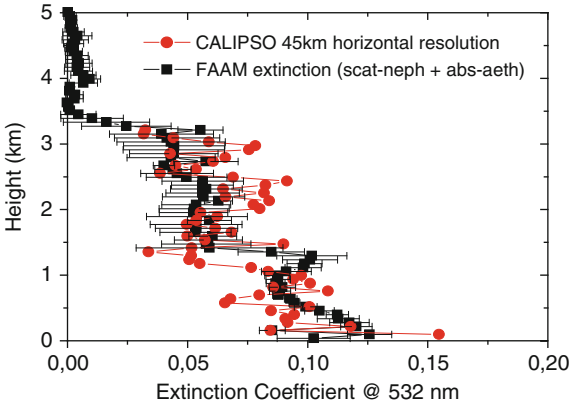

Fig. 3 Vertical distribution of the extinction coefficient at 550 nm (scattering + absorption) aircraft in-situ retrievals during the ACEMED flight of 9th of September 2011. Collocated CALIPSO extinction coefficient profile at 532 nm (45 km horizontal average) is superimposed

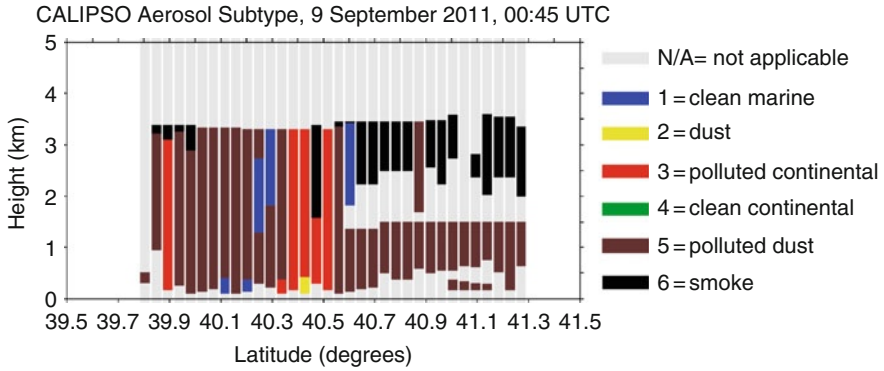

Fig. 4 Aerosol types over Thessaloniki during ACEMED's flights, as revealed by CALIPSO's aerosol classification scheme

The error bars represent the atmospheric variability in the horizontal distance covered by the aircraft to perform measurements in several heights. Assuming a negligible wavelength dependence of the extinction between 532 and 550 nm, CALIPSO and FAAM retrievals are in reasonable agreement.

During the flight under study, CALIPSO's aerosol classification scheme revealed a number of aerosol types during ACEMED, shown in Fig. 4. According to these retrievals, five of the six in total CALIPSO aerosol types were attributed to the aerosol load over the wider Thessaloniki area, indicating the complex aerosol mixing state over the city. An elevated layer over the city between 2 and 3 km is attributed to smoke according to CALIPSO's VFM. The polluted continental component is attributed mainly over and downwind the urban landscape. Polluted dust is the most frequently observed type in this snapshot.

FLEXPART simulations for the 9th of September (Fig. 5 upper), show that all the above classifications could be reasonable, since the air masses over the city are advected from various potential sources like the Saharan desert, the Mediterranean and regions with industrial activity in Central Europe. Active hot spots taken from MODIS fire product for the FLEXPART simulation period, show in addition fire activity in Albania and the Balkans (Fig. 5 lower), supporting the smoke presence over the area under study.

The smoke presence over Thessaloniki is additionally indicated by the intensive aerosol properties revealed from the in-situ FAAM's measurements, namely the vertical distributions of the single scattering albedo, the scattering-related Ångström exponent and AMS chemical composition retrievals (Fig. 6).

The SSA profile supports the presence of an absorbing aerosol layer between 2.2 and 3 km and Ångström exponent values indicate slightly larger particles. These values are typical for smoke, and this aerosol type is additionally supported by the AMS measurements (right panel), showing greater contribution of the organic compound in the height range under study.

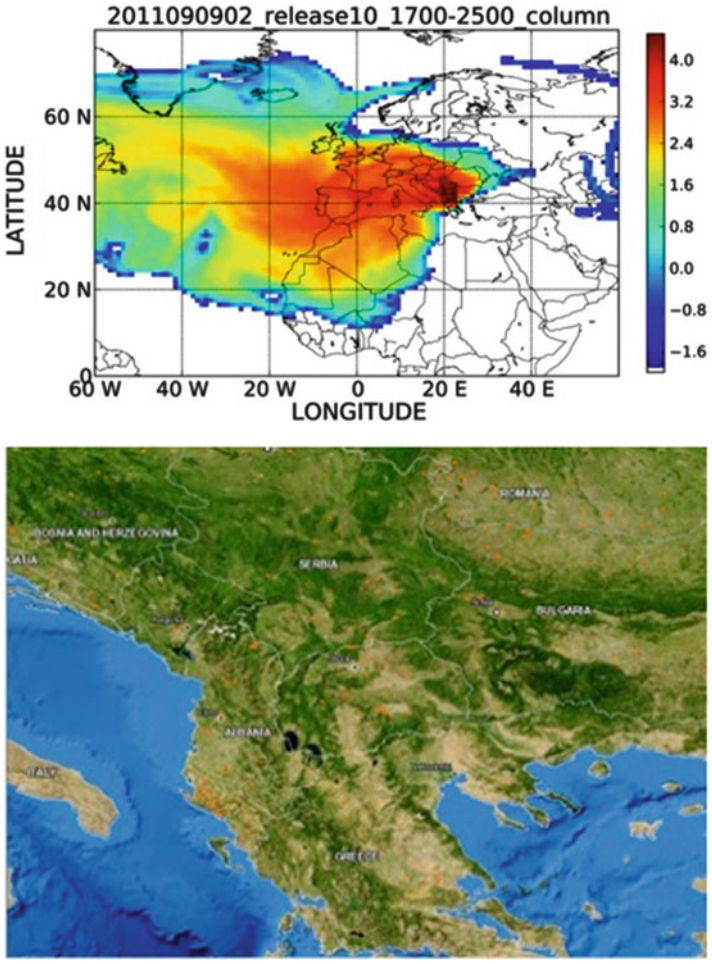

Fig. 5 FLEXPART simulations and MODIS hot spots

4 Conclusions

The first results from ACEMED campaign for the case study of 9th of September over the area of Thessaloniki, show a qualitatively reasonable performance of the CALIPSO's aerosol classification scheme. This scheme shows capability to qualitatively distinguish the smoke advected over Greece, as indicated by FLEXPART simulations. Moreover, the quantitative comparison between satellite and aircraft products shows a good agreement in terms of extinction retrievals.

A detailed analysis based on comparisons between CALIPSO's aerosol type attributions and collocated FAAM's in-situ retrievals will be performed in the

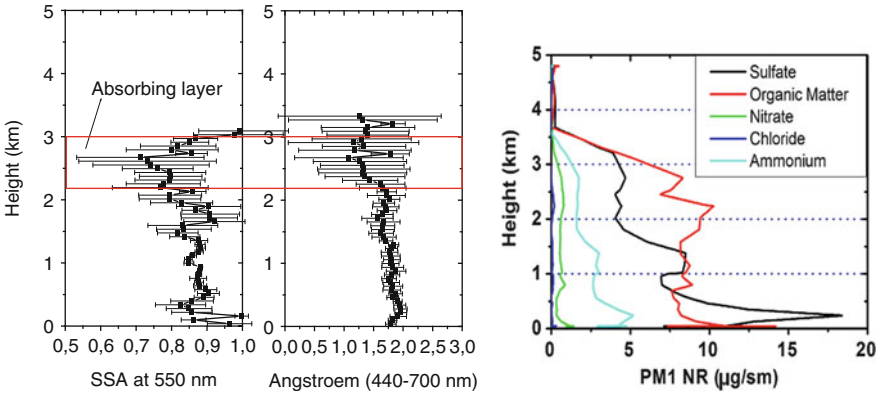

Fig. 6 Single scattering albedo at 550 nm (*left panel*) and scattering-related Angstrom exponent (440–700 nm – *center panel*) calculated from nephelometer/aethalometer aircraft measurements. AMS retrievals of the chemical composition (*right panel*)

future, for a comprehensive evaluation of CALIPSO's aerosol-type classification scheme.

Acknowledgments Authors acknowledge the support and research collaboration of EUFAR and Mariolopoulos – Kanaginis Foundation for the Environmental Sciences.

References

Amiridis V, Balis DS, Giannakaki E, Stohl A, Kazadzis S, Koukouli ME, Zanis P (2009) Optical characteristics of biomass burning aerosols over southeastern Europe determined from UV-Raman lidar measurements. Atmos Chem Phys 9:2431–2440. doi:10.5194/acp-9-2431-2009

Balis DS, Amiridis V, Zerefos C, Gerasopoulos E, Andreae M, Zanis P et al (2003) Raman lidar and sunphotometric measurements of aerosol optical properties over Thessaloniki, Greece during a biomass burning episode. Atmos Environ 37(32):4529–4538. doi:10.1016/S1352-2310(03)00581-8

Kazadzis S, Bais A, Amiridis V, Balis D et al (2007) Nine years of UV aerosol optical depth measurements at Thessaloniki, Greece. Atmos Chem Phys 7:2091–2101. doi:10.5194/acp-7-2091-2007

Estimating Direct Effects of Secondary Organic Aerosol Over Europe Using COSMO-ART

E. Athanasopoulou, H. Vogel, K. Lundgren, B. Vogel, C. Fountoukis, and S.N. Pandis

Abstract COSMO-ART is a recently developed regional model that couples meteorological and air quality processes online. It allows for a consistent chemical forecasting since it avoids temporal and spatial interpolation steps. Additionally, it enables the simulation of feedbacks between chemistry, aerosols and meteorology. Towards this direction, COSMO-ART has already incorporated the direct radiative forcing of aerosol processes. In the framework of this study, COSMO-ART is modified to include the volatility basis set (VBS) treatment of secondary organic aerosol (SOA) chemistry. The VBS approach assumes gas-to-particle partitioning of all (thousands) organics grouped by their saturation concentration and calculates their formation and chemical evolution (aging) into the atmosphere. COSMO-ART simulations are performed for May 2008 covering the greater European area with a horizontal resolution of 14 km and a vertical extend up to 20 km. Results are compared to PMCAMx predictions and are evaluated against EUCAARI measurements. Sensitivity simulations reveal the effectiveness of the VBS approach against a traditional SOA module and the fraction of anthropogenic SOA. Additional simulations excluding organic chemistry, aim at identifying the SOA effect on radiation and atmospheric temperature. An average radiative reduction is predicted over Europe, linked to a moderate temperature decrease.

E. Athanasopoulou (✉) • H. Vogel • K. Lundgren • B. Vogel
Institute for Meteorology and Climate Research, Karlsruhe Institute of Technology (KIT), Eggenstein-Leopoldshafen, Germany
e-mail: eleni.athanasopoulou@kit.edu

C. Fountoukis • S.N. Pandis
Institute of Chemical Engineering and High Temperature Chemical Processes, Foundation for Research and Technology Hellas (FORTH), Patras, Greece

C.G. Helmis and P.T. Nastos (eds.), *Advances in Meteorology, Climatology and Atmospheric Physics*, Springer Atmospheric Sciences,
DOI 10.1007/978-3-642-29172-2_122,

1 Introduction

Organic aerosol (OA) is measured to be a significant, if not the most important, fraction of submicron particles (PM1), on a global scale (Zhang et al. 2007). The deconvolution of OA into its hydrocarbon and oxygenated constituents, showed the importance of the latter, which reaches 83% and 95% of the total OA in urban downwind, and remote sites, respectively. A further analysis of the oxygenated constituents showed that they originate from the chemical transformation and condensation of volatile and semivolatile species (chemical aging). This reveals the important role of secondary organic aerosol (SOA) chemistry in the atmosphere.

Organic species in aerosol influence the Earth's radiation balance by varying the chemical composition, size distribution and water content of particles, thus by affecting their optical properties (Forster et al. 2007). Organic aerosol is usually considered as mildly absorbing (Kanakidou et al. 2005). When mixed with inorganics and soot, it contributes to a negative radiative forcing (Ming et al. 2005), which is intensified under clear-sky conditions.

Several recent field studies have shown that SOA may be strongly underestimated by current models based on "traditional" SOA precursors and chamber yields (Dzepina et al. 2009). On the other hand, modeling results after incorporating the chemical aging of organics are encouraging. An efficient way to incorporate this chemical evolution of organics into modelling is their group treatment by saturation concentrations (VBS scheme) (Donahue et al. 2006). Recent model applications using VBS confirm that the efficiency in predicting OA mass is improved (Murphy et al. 2011).

Although many models now include SOA, any overall estimate of their direct and indirect effects is still lacking. A recent study towards this direction (O'Donnell et al. 2011) is done on a global scale and by keeping SOA chemistry to a bare minimum. This, among others, means the lack of any chemical aging process, which, in turn, contributes to the systematic underestimation of OA.

In the framework of this study, the online coupled model COSMO-ART is applied over the European area during May 2008. Aerosol chemistry is modified to include the VBS treatment of SOA. Organic aerosol predictions are evaluated against EUCAARI measurements and compared to PMCAMx outputs. Sensitivity simulations give comparisons of VBS against the "traditional" SOA scheme SORGAM, reveal the role of biogenic sources of organics, and show the direct effects of SOA chemistry on atmospheric temperature and radiation.

2 Data and Methodology

In the framework of this study, organic PM1 predictions for May 2008 are compared against EUCAARI measurements of organic matter (Kulmala et al. 2009). Hourly mean values are calculated from four measurement ground sites: Cabauw (The

Netherlands), Finokalia (Greece), Mace Head (Ireland) and Melpitz (Germany). All observation sites are representative of regional atmospheric conditions.

COSMO-ART (Vogel et al. 2009) is a regional chemistry transport model (ART stands for Aerosols and Reactive Trace gases); online-coupled to the COSMO regional numerical weather prediction and climate model (Baldauf et al. 2011). In the version applied here, a modified Volatility Basis Set (VBS) module is used for the SOA treatment. SOA precursors are the aromatics, higher alkanes, higher alkenes, terpenes and isoprene. Their oxidation reactions by OH, O3 and NO3, produce four mixed sets of condensable species, grouped by their effective saturation concentration: 1, 10, 100 and 1,000 μg m^{-3}. Aerosol yields were identified during recent smog chamber experiments. The gas-to-particle mass transfer occurs when the above saturation concentrations, localized in respect to ambient air temperature, are exceeded. The subsequent chemical aging due to oxidation reactions by OH, is represented by making SOA less volatile by one order of magnitude.

The simulation area is covered by a grid over the greater European area with 14 km horizontal resolution and 20 km vertical extent. The meteorological initial and boundary conditions are achieved from the GME global model (Majewski et al. 2002). Boundary data for gas-phase species stem from MOZART predictions (Emmons et al. 2010). The boundary value for surface SOA is set to 1 μg m^{-3}, and vertically decreasing following the air density profile. The anthropogenic emission database used is the TNO/MACC (Kuenen et al. 2011), while biogenic VOC emissions are online calculated (Vogel et al. 1995).

3 Results

3.1 Organic Aerosol Performance

Overall, both the hourly and the diurnal variation of organics are well captured by the model during May 2008 at the four aforementioned sites (not shown). Average organic aerosol measurements are around 4–5 μg m^{-3} for the central European sites, while peripheral sites exhibit lower values (2.4–2.5 μg m^{-3}). Similar are the predicted findings (3.5–4.5 and 2.4–3.1 μg m^{-3}, respectively). Using the mean fractional bias and error metrics (Boylan and Russell 2006) a satisfactory performance is estimated for Mace Head, Finokalia and Melpitz, while Cabauw performs optimally. Noticeable discrepancies occur over Mace Head and Melpitz during short periods of NE winds. This implies an anthropogenic source of organics at N. Europe, currently unidentified by the applied emission database. The fraction of SOA to OA is predicted 80–95%, in consistency to global measurements in non urban areas (Zhang et al. 2007). This shows the preponderance of atmospheric chemical transformations of organic matter over emitted OA.

COSMO-ART to PMCAMx comparison of organic predictions (not shown) reveals neither large nor systematic differences. Their sources are the different emission databases applied, meteorology (online and offline treatment, respectively) and differences in the chemical oxidation of organic matter.

3.2 Sensitivity Studies

Apart from the 1-month base case application performed, three additional simulations were applied, which are shortly explained and presented below.

3.2.1 SORGAM Versus VBS Results

SORGAM is the so far official SOA module of COSMO-ART analytically described in Schell et al. (2001). The main differences from VBS are the exclusion of isoprene as a SOA precursor and the absence of any chemical aging procedure.

Predictions with both schemes show that SORGAM is satisfactory during night, but reaches unrealistically low values during day (not shown). Overall, it causes an OA underestimation of 100%. VBS is able to retain SOA mass throughout the day, mainly due to the applied aging. Furthermore, the VBS module is able to represent the delocalization of organic aerosol compared to emission areas, because it is able to simulate the chemical formation of SOA in the atmosphere.

3.2.2 Anthropogenic Versus Biogenic Origin of SOA

In order to calculate the fraction of SOA that originates from biogenic sources a simulation where only anthropogenic VOC's condense onto particles was subtracted from base case results. Contrary to what is found by global applications, anthropogenic exceed biogenic sources all over Europe. This reflects the strength of anthropogenic VOC emission inputs, compared to the lower biogenic, online-calculated VOC emissions. The biogenic-induced SOA is calculated 30–40% (maximum 50%) of PM1 SOA in central Europe, and 15–30% on the periphery.

3.2.3 SOA Direct Radiative Effects

In order to quantify the direct feedback mechanisms caused by the interaction of SOA and radiation, an additional 1-month simulation was performed, where the secondary organic aerosol chemistry was switched off (noSOA).

SOA mass (Fig. 1a) is predicted to cause a radiative cooling (Fig. 1b), which is up to -2.5 W m^{-2} on average. This is because condensation of organic matter onto

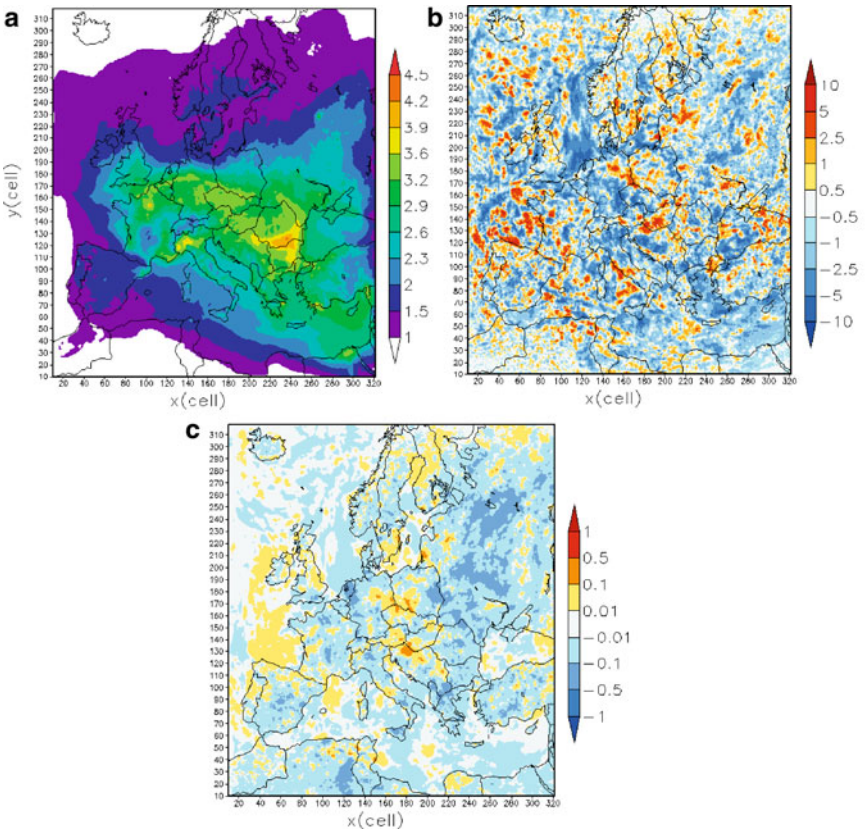

Fig. 1 Spatial distribution of average (May 2008) fields over Europe, predicted by COSMO-ART: (**a**) SOA concentrations (μg m^{-3}), (**b**) total surface radiation differences; base case – noSOA simulation (W m^{-2}), (**c**) temperature (2 m) differences; base case – noSOA simulation (K)

particles causes a shift of particles towards bigger sizes and subsequently modifies aerosol water content and cloud cover (not shown). A decrease in temperature (at 2 m altitude) up to −0.5 K is obvious at those areas where radiation is reduced by the SOA particles (Fig. 1c). Nevertheless, a spotty behavior, mainly in total surface radiation differences, is distributed all over the domain. This nonlinearity between mass and radiation changes is mainly caused by modifications in cloud properties due to changes in the thermodynamics that are initialized by the direct effect of SOA on radiation. Indeed, during May 2008, most areas are predicted to be covered with clouds by more than 50% (not shown). In areas where cloud cover intensification is imposed due to SOA, long wave radiation increases occur (not shown), which result in a moderate warming (Fig. 1c).

4 Conclusions

Organic aerosol is reasonably reproduced by COSMO-ART over Europe during May 2008. This is mainly due to the incorporation of secondary organic aerosol chemistry module VBS. Comparisons against simulations with the "official and traditional" module SORGAM quantify current SOA improvements. Contrary to what is commonly predicted by global models, SOA mass over Europe mainly originates from anthropogenic activities.

Online coupling performed by COSMO-ART enables the estimation of SOA interaction with radiation. Results in this study show a monthly average surface radiation reduction, followed by a moderate decrease in temperature. Nevertheless, cloudy conditions make the correlation between SOA mass and radiation poorer, due to the "spatial shift of clouds" phenomenon (Vogel et al. 2009), as well as by increasing long wave radiation and temperature.

Acknowledgments The authors would like to thank A. Mensah, A. Kiendler-Scharr, M. Dall'Osto, C. O'Dowd and L. Poulain concerning EUCAARI data.

References

Baldauf M, Seifert A, Forstner J, Majewski D, Raschendorfer M, Reinhardt T (2011) Operational convective-scale numerical weather prediction with the COSMO model: description and sensitivities. Mon Weather Rev. doi:10.1175/MWR-D-10-05013.1 (e-view)

Boylan JW, Russell AG (2006) PM and light extinction model performance metrics, goals, and criteria for three-dimensional air quality models. Atmos Environ 40(26):4946–4959. doi:10.1016/j.atmosenv.2005.09.087

Donahue NM, Robinson AL, Stanier CO, Pandis SN (2006) Coupled partitioning, dilution, and chemical aging of semivolatile organics. Environ Sci Technol 40:2635–2643

Dzepina K, Volkamer RM, Madronich S, Tulet P, Ulbrich IM, Zhang Q, Cappa CD (2009) Evaluation of recently-proposed secondary organic aerosol models for a case study in Mexico City. Atmos Chem Phys 9(15):5681–5709. doi:10.5194/acp-9-5681-2009

Emmons LK, Walters S, Hess PG, Lamarque JF, Pfister GG, Fillmore D, Granier C (2010) Description and evaluation of the model for ozone and related chemical tracers, version 4 (MOZART-4). Geosci Model Dev 3:43–67. doi:10.5194/gmd-3-43-2010

Forster P, Ramaswamy V, Artaxo P et al (2007) Changes in atmospheric constituents and radiative forcing. In: Solomon S, Qin D, Manning M (eds) Climate change 2007: the physical science basis. Contribution of working group I to the intergovernmental panel on climate change. Cambridge University Press, Cambridge/NY

Kanakidou M, Seinfeld JH, Pandis SN, Barnes I, Dentener FJ, Facchini MC, Van Dingenen R (2005) Organic aerosol and global climate modelling: a review. Atmos Chem Phys 5(4):1053–1123. doi:10.5194/acp-5-1053-2005

Kuenen J, Denier van der Gon H, Visschedijk A, van der Brugh H (2011) High resolution European emission inventory for the years 2003–2007. TNO-report TNO-060-UT-2011-00588

Kulmala M, Asmi A, Lappalainen HK, Carslaw KS, Pöschl U, Baltensperger U, Hov Ø (2009) Introduction: European Integrated Project on Aerosol Cloud Climate and Air Quality interactions (EUCAARI) – integrating aerosol research from nano to global scales. Atmos Chem Phys 9(8):2825–2841. doi:10.5194/acp-9-2825-2009

Majewski D, Liermann D, Prohl P, Ritter B, Buchhold M, Hanisch T, Paul G (2002) The operational global icosahedral–hexagonal gridpoint model GME: description and high-resolution tests. Mon Weather Rev 130:319–338. doi:10.1175/1520-0493(2002)

Ming Y, Ramaswamy V, Ginoux PA, Horowitz LH (2005) Direct radiative forcing of anthropogenic organic aerosol. J Geophys Res 110:12. doi:200510.1029/2004JD005573

Murphy BN, Donahue NM, Fountoukis C, Pandis SN (2011) Simulating the oxygen content of ambient organic aerosol with the 2D volatility basis set. Atmos Chem Phys 11:7859–7873. doi:10.5194/acp-11-7859-2011

O'Donnell D, Tsigaridis K, Feichter J (2011) Estimating the influence of the secondary organic aerosols on present climate using ECHAM5-HAM. Atmos Chem Phys Discuss 11(1):2407–2472. doi:10.5194/acpd-11-2407-2011

Schell B, Ackermann IJ, Binkowski FS, Ebel A (2001) Modeling the formation of secondary organic aerosol within a comprehensive air quality model system. J Geophys Res 106:28275–28293. doi:10.1029/2001JD000384

Vogel B, Fiedler F, Vogel H (1995) Influence of topography and biogenic volatile organic compounds emission in the state of Baden-Wurttemberg on ozone concentrations during episodes of high air temperatures. J Geophys Res 100:22907–22928. doi:10.1029/95JD01228

Vogel B, Vogel H, Baumer D, Bangert M, Lundgren K, Rinke R, Stanelle T (2009) The comprehensive model system COSMO-ART – radiative impact of aerosol on the state of the atmosphere on the regional scale. Atmos Chem Phys 9:8661–8680

Zhang Q, Jimenez JL, Canagaratna MR, Allan JD, Coe H, Ulbrich I, Alfarra MR (2007) Ubiquity and dominance of oxygenated species in organic aerosols in anthropogenically-influenced Northern Hemisphere midlatitudes. Geophys Res Lett 34:6. doi:200710.1029/2007GL029979

High Resolution Aerosol Optical Depth in the Broader Greek Area Using MODIS Satellite Data

G. Athanassiou, C.D. Papadimas, and N. Hatzianastassiou

Abstract We study the spatial (50 km × 50 km) and temporal distribution of aerosol optical depth (AOD) over the broader Greek area on a mean annual, seasonal and monthly basis. Daily visible Level-2 AOD data ($AOD_{550\ nm}$) from the MODIS database are used for the period March 2000–February 2008. The mean annual AOD values for the study region range from 0.13 to 0.37, with a mean annual regional AOD value equal to 0.19. Maximum *AOD* values are found in spring and late summer (August), and minimum in winter. The highest values occur in Eastern Greece (particularly during spring and summer) and near the Aegean coasts of Turkey (Smyrni) and Istanbul (during autumn and winter). The smallest AOD values are found in Western Greece, at some areas of the neighboring Balkan countries, and in the interior of Turkey (during all seasons) as well as in marine areas south and east of Crete (during summer). A decreasing tendency of regional AOD is found from 2000 to 2008, equal to $\Delta(AOD) = -0.05$, implying decreasing aerosol amounts over the study region.

1 Introduction

Aerosol particulate matter emitted by enhanced anthropogenic activities since the nineteenth century has been shown to have significantly affected the climate of the Earth, through their direct, indirect and semi-direct effects (IPCC 2007), while inducing a degradation of the quality of air, especially at areas close to important natural and anthropogenic aerosol sources. Therefore, a systematic monitoring of aerosols is required in order to minimize the consequences on health, but also to help in understanding the climatic implications of aerosols. More specifically, a warning has been made by the scientific community concerning the need for further

G. Athanassiou • C.D. Papadimas • N. Hatzianastassiou (✉)
Laboratory of Meteorology, Physics Department, University of Ioannina, Ioannina, Greece
e-mail: nhatzian@cc.uoi.gr

C.G. Helmis and P.T. Nastos (eds.), *Advances in Meteorology, Climatology and Atmospheric Physics*, Springer Atmospheric Sciences,
DOI 10.1007/978-3-642-29172-2_123,

and improved monitoring of aerosols in order to reduce the aerosol induced uncertainty of present and future climate, related to their strong spatial and temporal variability, largely associated with their short lifetime. Such a monitoring is valuable not only at global and synoptic, but also at regional scales.

In the present study, we investigate the spatial and temporal variability of aerosol optical depth (AOD) over the broader Greek area (19°E–30°E and 34°N–43°N). AOD is a very good indicator of aerosol loading in the atmospheric column, and critically determines the aerosol radiative and climatic effects (e.g. Hatzianastassiou et al. 2004). The choice of the broader Greek area for the present study of AOD is made because there is a lack in the literature for this specific region, lying in the eastern Mediterranean basin, which is an ideal study region for aerosol properties and climatic effects (Papadimas et al. 2008; Hatzianastassiou et al. 2009). In the past, studies on aerosol properties/effects over Greece have been performed only at local scale, mainly concerning the greatest urban centers like Athens and Thessaloniki (e.g. Balis et al. 2006; Gerasopoulos et al. 2011) or Crete island (Fotiadi et al. 2006; Kalivitis et al. 2007). All these studies were based largely on ground measurements, while studying AOD over the entire study region requires a complete spatial coverage by the data, which is only ensured by the utilized here MODerate resolution Imaging Spectradiometer (MODIS).

2 Data and Methodology

We used daily satellite-based AOD data at the mid-visible wavelength of 550 nm taken from the MODIS Collection 005 database (http://modis.gsfc.nasa.gov/). The Level 2 data, available at spatial resolution of 10 km × 10 km latitude-longitude, were obtained in their original HDF format, and were subsequently processed in order to extract the finally used AOD_{550} parameter. The MODIS AOD_{550} data over land and sea areas are derived based on different retrieval algorithms (Ichoku et al. 2002, Remer et al. 2005) having accuracies of $\pm 0.05 \pm 0.2AOD_{550}$ and $\pm 0.05 \pm 0.05AOD_{550}$, respectively.

The data used, which cover the 8-year period from March 2000 to February 2008, constitute time-series of 3696 daily values. Because of the required time overpass of the satellites, the original spatial resolution (10 km × 10 km) would not provide sufficient spatio-temporal coverage of the study region. Therefore, in order to ensure an increased coverage of data, we reprocessed them and computed spatially averaged products for 396 predefined geographical cells (pixels) of 50 km × 50 km over the entire study region. The daily AOD_{550} data were also averaged on a monthly, seasonal and annual basis, as well as on a regional mean basis, for an easier and more comprehensive management. In order to ensure better reliability of the computed results, we have applied specific criteria for the availability of AOD_{550} data. More specifically, in terms of spatial averages it was required to be available at least 40% of the overall number of 396 pixel-level data, while for temporal (monthly) averages the prerequisite was to have at least five (5) days with available data. A number of different

criteria, concerning the spatial and temporal availability of data, as well as of combinations of them, was also tried in order to investigate the sensitivity of the obtained results on them. Here, however, due to space limitations, only the results of the afore-mentioned criteria are presented.

3 Results

Figure 1 displays the spatial distribution of AOD_{550} over the broader Greek region. The values have a climatological sense, i.e. they are annual means computed over the entire 8-year period 2000–2008. The largest AOD_{550} values, up to 0.3–0.35, are found along the eastern coast of the Greek peninsula, as well as over Crete and along the western coast of Asia Minor. Given the known physico-geographical, social-political and meteorological conditions prevailing in the region, the large AOD_{550} values along the eastern and western coasts of the Aegean Sea should be associated with anthropogenic aerosol emissions, whereas those over Crete-island can be attributed to African dust frequently transported from the South (e.g. Fotiadi et al. 2006; Kalivitis et al. 2007). On the other hand, i.e. concerning the large anthropogenic aerosol loadings, indeed the Aegean coastal Greek and Turkish regions are the most populated ones for both countries, also hosting the largest industrial activities, thus explaining the increased AOD_{550} values, especially over the greatest national urban centers, namely Athens, Thessaloniki, Istanbul and Izmir (Smyrni). However, note that the centers which are located in the South, e.g. Athens or Izmir, also have a significant contribution of natural (dust) aerosols to their AOD_{550} values (Hatzianastassiou et al. 2009). The reported conclusions are also supported by the results of seasonal analysis shown in Figs. 2 and 3, as well as by the geographical distributions of MODIS Ångström exponent (not shown here)

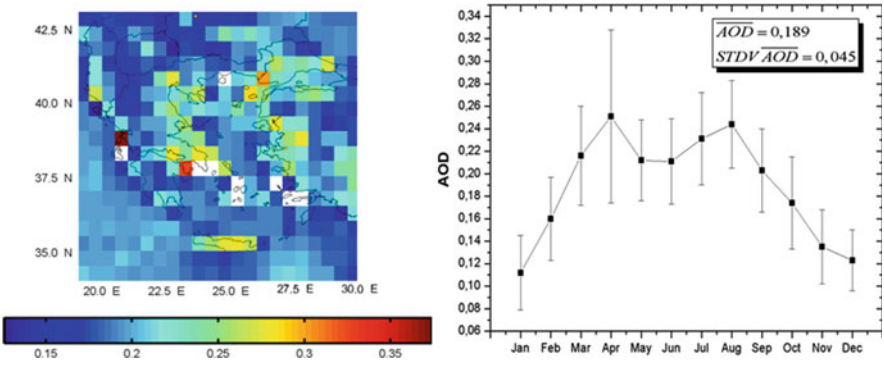

Fig. 1 (*Left*) Geographical distribution of 8-year (2000–2008) MODIS-Terra mean annual AOD_{550}. (*Right*) Intra-annual variation of 8-year mean AOD_{550} averaged over the broader Greek region. The geographical variability of AOD_{550} per month (standard deviations) is also given

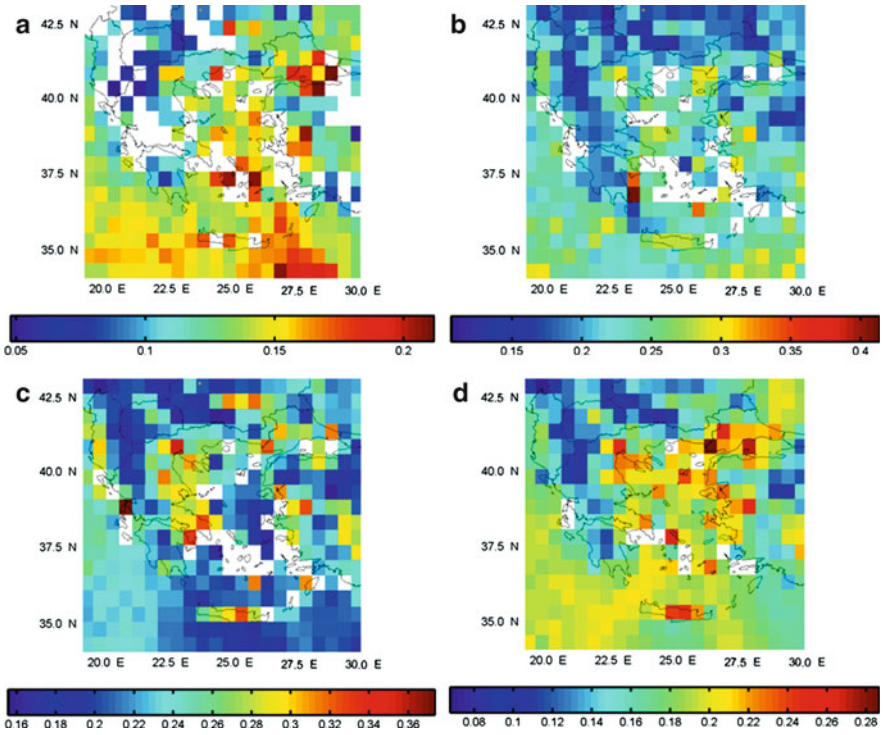

Fig. 2 As in Fig. 1, but for mean monthly AOD_{550} values for: (**a**) winter, (**b**) spring, (**c**) summer and (**d**) autumn. Note that the colorbar scales are different for each season. White shaded cells did not fulfill the temporal availability criterion for monthly AOD_{550} values (Sect. 2)

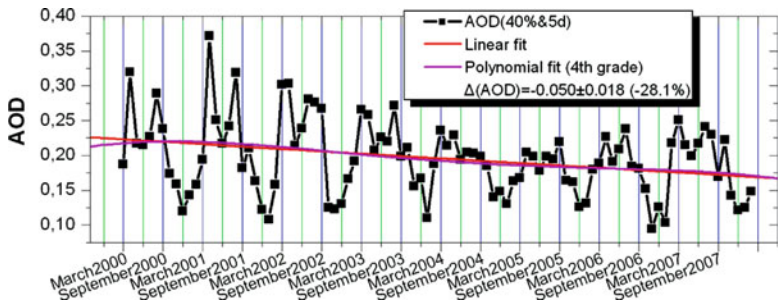

Fig. 3 Inter-annual variation of mean regional AOD_{550} (for the broader Greek region). The linear regression and fourth-order polynomial fits to the time-series as well as the computed change of AOD_{550} over the 8-year (2000–2008) period, are also shown

with smaller/larger values indicating coarse/fine aerosols of mostly natural and anthropogenic origin. Figures 2 and 3 indicate smallest AOD_{550} values in winter, due to the efficient wet removal processes (precipitation) against highest values in

spring and summer, when prevailing synoptic/meteorological conditions favor either the transport of African dust from the South (cyclonic conditions during spring) or the accumulation of aerosols in a stable atmosphere (anticyclonic conditions in summer). On the other hand, either on an annual or seasonal basis, the smallest AOD_{550} values are observed in western Greece, in the sea southern and eastern of Crete, as well as locally in the interior of Balkan countries northern of Greece and in the Anatolian peninsula. Note that when applying more severe criteria on the availability of AOD data, in Fig. 1, some isolated pixels with very large AOD_{550} values, like in Lefkas-island and Saronic Gulf, disappear, showing thus the importance of the selection criteria.

The seasonal variation of AOD_{550} values averaged over the study region is given in Fig. 2. There are two clear maxima, one in spring ($AOD_{550} = 0.25$, April) and another in late summer ($AOD_{550} = 0.245$, August), while the minimum values, down to 0.15, are observed in winter. The year-by-year variability, per month, is quantified by the error bars, which indicate that this variability is quite large, ranging from about 0.06 to 0.1. In particular, in spring (April) it is even larger, exceeding 1.5, an effect induced by the sporadic nature of African dust transport events that are most contributing to AOD regional levels during this season (Hatzianastassiou et al. 2009). The summer AOD maximum is mainly due to the built-up of significant aerosol loadings, because of the prevailing stable atmospheric conditions during this season and the absence of significant removal processes. This is verified by the occurrence of the maximum in late, and not in early or mid-, summer. Other reasons can be regional biomass burning events or long-range transport of aerosols, e.g. soot or sulfate, transported either from northern Balkans or from western and central Europe under the influence of synoptic conditions (Azores anticyclone) and associated wind systems, i.e. the Etesians. The computed mean annual value for the region is equal to 0.189, being slightly smaller than the corresponding values computed for the eastern Mediterranean (0.22 ± 0.05, Hatzianastassiou et al. 2009) and the entire Mediterranean basin (0.22 ± 0.07, Papadimas et al. 2008). The regional AOD levels are clearly larger than the corresponding global mean ($AOD_{550} = 0.12 \pm 0.04$, Ramanathan et al. 2001) based on satellite observations, verifying thus that the study region is a significantly aerosol loaded world region, with all the consequences that may this have.

Apart from the intra-annual variation of AOD, it is useful to examine the year-by-year variation of the annual cycle, given the significant temporal variability of aerosols and the activity of their sources and removal mechanisms. Indeed, as shown in Fig. 4, there is a considerable variation with time, consisting in varying minimum and maximum AOD_{550} values. Thus, the winter minimum values vary between about 0.1 and 0.13, whereas the maximum values range from 0.22 to 0.37, occurring primarily in spring and secondary in summer. It is interesting that in some years, e.g. 2005, the maximum values are observed in summer, opposite to Fig. 3. Beyond this, there appears to have been a decreasing tendency of AOD_{550} values from 2000 to 2008. This decrease is equal to -28.1%, and it is not a regional

phenomenon only, since a comparable decrease (−20.2%) was identified for the broader Mediterranean basin by Papadimas et al. (2008).

4 Conclusions

For the first time, the high spatial resolution (50 km × 50 km) distribution of aerosol loading, by means of aerosol optical depth, was studied over the broader Greek region for the 8-year period 2000–2008, using MODIS AOD data. It was found a significant spatial variability, despite the relatively small spatial extent of the region, with mean annual AOD_{550} values ranging from 0.12 to 0.37. There was also identified a significant seasonal cycle (monthly values varying between 0.11 and 0.25, with minima in winter and maxima in spring and summer) as well as an important year-by-year variability. Thus, our results verify and quantify the high spatial and temporal variability of aerosol properties, namely loading. The physical reasons for this variability can be sporadic aerosol emission and/or transport events that are of either local or remote nature, and will be the subject of a more extended study. They also indicate that the region is characterized by significant aerosol loads, with a mean annual regional value equal to 0.19, higher than the global mean (0.12) by 58%, which was found, however, to have undergone a decrease by 28%, inline with similar decreasing AOD trends for the Mediterranean or other global regions.

References

Balis D, Amiridis V, Kazadzis S et al (2006) Optical characteristics of desert dust over the East Mediterranean during summer: a case study. Ann Geophys 24(3):807–821

Fotiadi A, Hatzianastassiou N, Drakakis E et al (2006) Aerosol physical and optical properties in the Eastern Mediterranean Basin, Crete, from aerosol robotic network data. Atmos Chem Phys 6:5399–5413

Gerasopoulos E, Amiridis V, Kazadzis S et al (2011) Three-year ground based measurements of aerosol optical depth over the Eastern Mediterranean: the urban environment of Athens. Atmos Chem Phys 11:2145–2159

Hatzianastassiou N, Katsoulis B, Vardavas I (2004) Global distribution of aerosol direct radiative forcing in ultraviolet–visible wavelengths and consequences for the heat budget. Tellus Ser B 56:51–71

Hatzianastassiou N, Gkikas MN, Mihalopoulos N et al (2009) Natural versus anthropogenic aerosols in the eastern Mediterranean basin derived from multiyear TOMS and MODIS satellite data. J Geophys Res 114:D24202. doi:10.1029/2009JD011982

Ichoku C, Chu DA, Matoo S et al (2002) A spatio-temporal approach for global validation and analysis of MODIS aerosol products. Geophys Res Lett 29(12):8006. doi:10.1029/2001GL013206

Intergovernmental Panel on Climate Change (IPCC) (2007) Climate change 2007: the physical science basis. Summary for Policymakers, Paris

Kalivitis N, Gerasopoulos E, Vrekoussis M et al (2007) Dust transport over the eastern Mediterranean derived from TOMS, AERONET and surface measurements. J Geophys Res 112: D03202. doi:10.1029/2006JD007510

Papadimas CD, Hatzianastassiou N, Mihalopoulos N et al (2008) Spatial and temporal variability in aerosol properties over the Mediterranean basin based on 6-year (2000–2006) MODIS data. J Geophys Res 113:D11205. doi:10.1029/2007JD009189

Ramanathan V, Crutzen PJ, Kiehl JT et al (2001) Aerosols, climate, and the hydrological cycle. Science 294:2119–2124. doi:10.1126/science.1064034

The Application of a Mixed-Phase Statistical Cloud-Cover Scheme to the Local Numerical Weather Prediction Model COSMO.GR

E. Avgoustoglou and T. Tzeferi

Abstract An alternative to the COSMO model default sub-grid scheme for stratiform cloud-cover, based on relative humidity, is proposed for application. In the emerging sub-grid statistical mixed-phase scheme, a bivariate Gaussian distribution is invoked with respect to the quasi-conservative properties of saturation deficit and liquid-ice water potential temperature. The resulting stratiform cloud-cover from the implementation of the proposed scheme is realized in COSMO model through a two-parameter relation affecting the cloud-cover at saturation and the critical value for normalized over-saturation. The impact of cloud-ice on cloud-cover is accounted through the modification of condensation heat via an icing factor defined as the local ratio of cloud-ice over total cloud-water content. A comparison of the implementation of the relative humidity and the mixed-phase schemes is presented over the wider geographical domain of Greece for a representative test case with extended areas of stratiform clouds developed over a relatively weak wind field.

1 Introduction

The proper implementation of clouds in numerical weather prediction has turned out to be a formidable challenge, especially when it goes beyond the straightforward hypothesis that the air inside a grid box is either saturated or unsaturated (Schlesinger 1973; Sommeria 1976). This "all or nothing" assumption (according to Cotton et al. 2011) is essentially a first approximation to the several complex physical processes that take place in the atmosphere when cloud-condensate is considered (Mironov 2009). A shortcoming of this conjecture is the incorrect treatment of the initial cloud growth since latent heat is released after all grid-box volume is saturated. In addition, cumulus interiors may contain saturated air due to

E. Avgoustoglou (✉) • T. Tzeferi
Hellenic National Meteorological Service, 16777 Hellinikon, Greece
e-mail: euri@hnms.gr

C.G. Helmis and P.T. Nastos (eds.), *Advances in Meteorology, Climatology and Atmospheric Physics*, Springer Atmospheric Sciences,
DOI 10.1007/978-3-642-29172-2_124,

lateral merging of adjacent clouds and entrainment while cloud-cover might be affected by entrainment through grid box boundaries.

Under the effort to partially account for these processes in the radiation scheme of COSMO model, an alternative to the default sub-grid scheme (SGRH) based on relative humidity (Sandqvist 1978) is addressed to account for the stratiform cloud-cover. In the emerging sub-grid statistical liquid scheme (SGSL), a bivariate Gaussian distribution invoked for the quasi-conservative properties of saturation deficit and liquid water potential temperature (Sommeria and Deardorff 1977; Mellor 1977). The resulting stratiform cloud-cover from the implementation of SGSL in COSMO model was given by a two-parameter relation with respect to cloud-cover at saturation and the critical value of saturation deficit (Raschendorfer 2005; Avgoustoglou et al. 2006, 2010) complemented by the rather naive assumption that cloud-cover due to cloud-ice content is treated by simply stating cloud-cover equal to 100% if any cloud-ice is forecasted by the model. The SGSL scheme is currently used in the moist turbulence scheme of COSMO model and the goal is to justify its use also in the radiation scheme within the scope of UTCS (Unified Turbulence Closure Scheme) priority project of COSMO consortium (http://www.cosmo-model.org). However, the necessity to include consistently cloud-ice into the cloud-cover (Deardorff 1976; Smith and Del Genio 2002) led to a modification of SGSL towards a sub-grid statistical liquid-ice scheme (SGSLI) (Raschendorfer 2008) through the introduction of a mixed-phase condensation heat via an icing factor defined as the ratio of cloud-ice over total cloud-water content. A comparison of the implementation of SGSLI versus SGRH in the radiation scheme of COSMO model is presented over the wider geographical domain of the Balkans for a representative spring case with extended areas of stratiform clouds developed over a relatively weak wind field.

2 Data and Methodology

In this investigation, selected results of COSMO model are directly compared with satellite figures as well as observations of 2 m-temperatures of approximately 50 national meteorological stations. The METEOSAT (MSG) satellite data that were used in the present work include cloud analysis produced by Meteorological Products Extraction Facility Algorithms (MPEF). These products were visualized using the SYNESAT software available locally at the Hellenic National Meteorological Service. The methodology regarding the SGSLI scheme is based on the generalization of the SGSL scheme (Deardorff 1976) as it was implemented in a test version of COSMO model (Raschendorfer 2008; Avgoustoglou et al. 2010).

2.1 Data

A 48-h period was considered for this study, starting from 12 UTC of April 27, 2011. The boundary conditions came from a 3-h interval DWD Global Model

(GME) analysis on forty vertical levels and with horizontal grid of 0.5° (~50 km) while COSMO model run on a 0.0625° (~7 km) horizontal grid. In this work, we focus over the 24-h period of April 28 regarding the observations of the daily minimum and maximum 2-m temperatures. For the satellite data, we compare with the model cloud-cover of April 28 at 03 UTC. The domain under consideration, shown in the subsequent figures, covers the wider Balkan area centered on Greece.

2.2 Methodology

The adopted SGSLI cloud scheme enters as an extension to the SGSL cloud scheme (Sommeria and Deardorff 1977; Mellor 1977). The sub-grid stratiform cloud fraction $\boldsymbol{R}$ is estimated as

$$R = \int_{-\infty}^{+\infty}\int_{-\infty}^{+\infty} H(q_w - q_s)G dq_w d\theta_{li}, \quad H(x) = \begin{cases} 0, & x<0 \\ 1, & x \geq 0 \end{cases} \tag{1}$$

where $\boldsymbol{q_w}$ and $\boldsymbol{q_s}$ stand for the total-water and saturation specific humidity respectively while $\boldsymbol{G}$ is a bivariate normal function. The liquid-ice potential temperature $\boldsymbol{\theta_{li}}$, the total-water specific humidity $\boldsymbol{q_w}$ and the cloud-water $\boldsymbol{q_c}$ are defined as

$$\theta_{li} = \theta - \frac{\theta L_c}{T c_{p_d}} q_c, \quad q_w = \underbrace{q_v}_{vapour} + \underbrace{q_l}_{\text{liquid}} + \underbrace{q_i}_{ice} \quad \text{and} \quad q_c = q_l + q_i \tag{2}$$

The *mixed-phase* (Deardorff 1976) condensation heat $\boldsymbol{L_c}$ is defined as a linear combination of liquid water ($\boldsymbol{L_l}$) and ice ($\boldsymbol{L_i}$) condensation heats via an *icing factor* $\boldsymbol{r_i}$:

$$L_c = (1 - r_i) L_l + r_i L_i \quad \text{and} \quad r_i(T) = q_i / q_c \tag{3}$$

By using Clausius-Clapeyron equation, the cloud fraction $\boldsymbol{R}$ in SGSL scheme becomes (Sommeria and Deardorff 1977):

$$R \approx \frac{1}{2}\left(1 + \frac{Q}{1.6}\right), \quad 0 \leq \mathrm{R} \leq 1 \text{ with } Q = \frac{\bar{q}_w - \bar{q}_s}{\sigma} \quad \text{and}$$
$$\sigma = \left(\overline{q_w^2} + \overline{q_s^2} - 2\overline{q_w q_s}\right)^{\frac{1}{2}} \tag{4}$$

In analogy, the stratiform cloud-cover in the SGSLI scheme is approximated by a two-parameter relation (Raschendorfer 2008):

$$R \approx A\left(1 + \frac{Q}{B}\right), \quad 0 \leq \mathrm{R} \leq 1 \tag{5}$$

The parameter $\boldsymbol{A}$ refers to cloud-cover at saturation and $\boldsymbol{B}$ refers to the critical value of saturation deficit. The default values of these parameters are set 0.5 and 4.0 respectively. Under this analysis, it can be seen that SGSLI and SGSL coincide when $\boldsymbol{q_i}$ is set equal to zero. However, although there are certain shortcomings in the SGSLI scheme as a rather straightforward generalization of SGSL scheme regarding microphysics (Deardorff 1976), SGSLI scheme has an advantage from the operational standpoint, since it provides fractional cloud-cover when cloud-ice is present.

3 Results

From the direct comparison of low cloud-cover against the corresponding MSG picture (Fig. 1, fourth row panel), the SGSLI scheme shows a relative preponderance over the default SGRH scheme in the encircled area while in the rectangular areas the situation is reversed. Regarding medium cloud-cover, SGSLI scheme shows an overall preponderance over the default SGRH scheme in reference to the satellite image (Fig. 1, second row panel), especially in the encircled areas. It should also be noted that in reference to MSG picture, the SGSLI scheme provides a better tendency to resolve medium clouds, while the cloud structure of the SGRH scheme has the tendency to remain more compact.

Both cloud schemes overestimate high cloud-cover (Fig. 1, third row panel), especially over the West/South-West parts, addressing the issue of proper accounting of cloud-ice content. In contrast to medium cloud-cover, the SGRH scheme provides a better tendency to resolve high cloud-cover, while the cloud structure of the SGSLI scheme has the tendency to remain more compact. For the total cloud-cover both schemes are in very good agreement with each other as well as with the MSG picture (Fig. 1, first row panel). This feature demonstrates that the relative differences in low, middle and high cloud-cover layers between the two schemes are converging towards very similar total cloud-cover.

For the minimum daily 2-m temperatures of the 28th April 2011 (Fig. 2, upper graph), the vast majority of values from the SGSLI scheme are relatively closer to observations than the corresponding values of the SGRH scheme.

The values for the maximum daily 2-m temperatures from the implementation of the default SGRH scheme in COSMO model are relatively closer to observations than the analogous values of the SGSLI scheme (Fig. 2, lower graph); however the trend is more balanced towards both schemes.

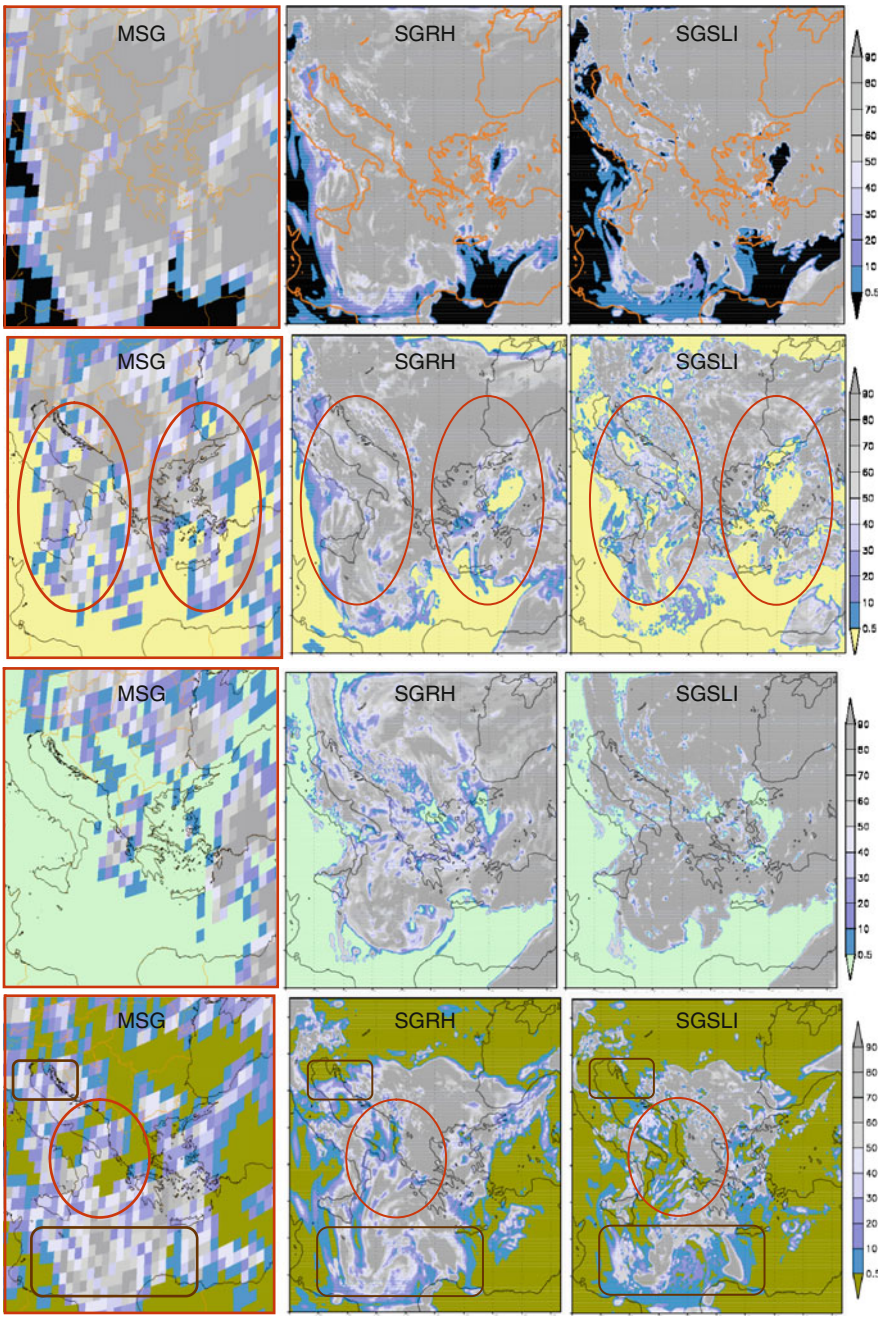

Fig. 1 Total, medium, high and low cloud-cover corresponding to *first*, *second*, *third* and *forth* row panels, respectively, for April 28, 2011 at 3 UTC. The *left* column refers to the satellite picture (MSG), while the *middle* and *right* columns refer respectively to SGRH and SGSLI implementations in COSMO model

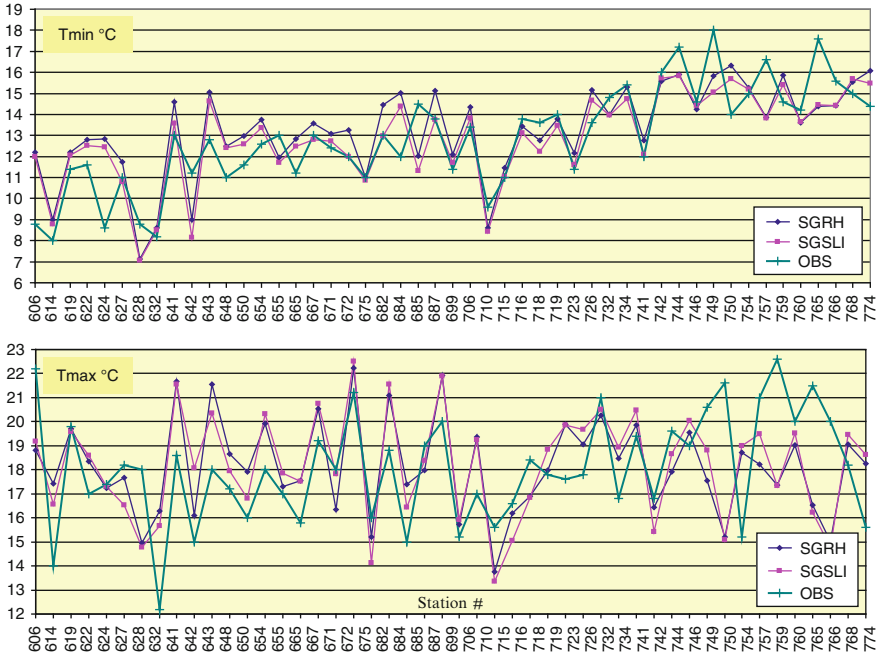

Fig. 2 Minimum (*upper graph*) and maximum (*lower graph*) 2-m temperature prognostic values for SGRH and SGSLI schemes against observations (OBS) for April 28, 2011

4 Conclusions

Due to the nature of the project, satellite data are of prime importance regarding the evaluation of the investigated sub-grid cloud schemes. The use of MSG data, as they were manipulated through the SYNESAT software provided a valuable insight to the relative value of the cloud-cover schemes under consideration. The overall cloud-cover is in excellent agreement compared with the satellite figures for both schemes. Regarding low clouds, it looks that SGSLI scheme preponderates over SGRH scheme in areas with relatively low cloudiness while the SGRH preponderates over more cloudy areas. On the basis of the current as well as past works, the overall effect regarding the operational implementation of the SGSLI scheme to COSMO model should be considered overall neutral. However, the overall slight improvements of minimum daily 2 m temperatures as well as middle cloudiness are some decent assets towards the SGSLI scheme. The implementation of the SGSLI scheme as an option to COSMO model will be of value for both operational and research purposes in the COSMO community.

Acknowledgments We gratefully thank Dmitrii Mironov and Matthias Raschendorfer for their continuous support over the several complexities of this work as well as Norbet Liesering for his help on the provision of boundary conditions.

References

Avgoustoglou E, Tzeferi T, Papageorgiou I (2006) Implementation of the statistical cloud scheme option; preliminary tests. COSMO Newsl 6:88–93

Avgoustoglou E, Charantonis T, Tzeferi T (2010) The investigation of a statistical cloud scheme in COSMO.GR local numerical weather prediction model. In: Proceedings of the 10th Panhellenic conference on meteorology, climatology and atmospheric physics, Patra, Greece Hellenic Meteorological Society, pp 169–177

Cotton WR, Bryan GH, van der Heever SC (2011) Storm and cloud dynamics. Elsevier Academic Press, London/San Diego

Deardorff JW (1976) Usefulness of liquid-water potential temperature in a shallow-cloud model. J Appl Meteorol 15:98–102

Mellor GL (1977) The Gaussian cloud model relations. J Atmos Sci 34:356–358

Mironov DV (2009) Turbulence in the lower troposphere: second-order closure and mass-flux modelling frameworks. Lecture Notes in Phys 756:161–221

Raschendorfer M (2005) A new TKE-based scheme for vertical diffusion and surface-layer transfer. DWD Internal Report (Draft Version)

Raschendorfer M (2008) Mixed water/ice phase in the SGS condensation scheme and the moist turbulence scheme. Presentation, 10th COSMO General Meeting, Cracow, Poland

Sandqvist H (1978) A parameterization scheme for non convective condensation including prediction of cloud water content. Q J R Meteorol Soc 104:677–690

Schlesinger RD (1973) A numerical model of deep moist convection: part I. Comparative experiments for variable ambient moisture and wind shear. J Atmos Sci 30:835–856

Smith SA, Del Genio AD (2002) A simple conceptual model of cirrus horizontal inhomogeneity and cloud fraction. Q J R Meteorol Soc 128:149–171. doi:10.1256/00359000260498833

Sommeria G (1976) Three-dimensional simulation of turbulent processes in an undisturbed trade wind boundary layer. J Atmos Sci 33:216–241

Sommeria G, Deardorff JW (1977) Sub-grid-Scale condensation in models of nonprecipitaining clouds. J Atmos Sci 34:344–355

Changes in Total Solar Irradiance Measured at Thessaloniki, Greece Since 1993 Associated with Changes in Aerosols

A.F. Bais, Th. Drosoglou, C. Meleti, and N. Kouremeti

Abstract Long-term changes in shortwave solar irradiance over Thessaloniki, Greece since 1993 are investigated, focusing on the influence of aerosols in relation to the solar zenith angle (SZA). Linear trends are computed for the entire dataset, for cloud free cases, and for different SZAs, separately for each season. The global upward trend in solar irradiance after 1990 is reconfirmed and is found to depend strongly on SZA, ranging from ~0.1% to +0.6% year^{-1}. Finally, we report signs of a stabilization of solar irradiance at the surface after about 2000.

1 Introduction

In recent decades, the amount of solar radiation incident at the Earth's surface has undergone significant variations, with associated impacts on climate. Trends in total solar irradiance (TSI) have been reported in several studies over the past two decades. Early studies indicate a worldwide decrease in the amount of solar radiation reaching the surface for the period 1960–1980 (Liepert and Tegen 2002; Stanhill and Cohen 2005), known as "global dimming". More recent studies have shown a reversing of this tendency since the late 1980s (e.g., Pinker et al. 2005; Romanou et al. 2007), known as "global brightening".

These variations in TSI at Earth's surface were found also under cloud free conditions, suggesting aerosols as a major factor affecting surface solar radiation. In Europe, long-term records of clear-sky atmospheric transmission measurements show consistent downward trend from the 1950s to the 1980s ranging between 4.9 and 6.7 W m^{-2} per decade and a partial recovery thereafter, indicative of aerosol changes (e.g., Ohvril et al. 2009; Wild 2009). Negative trends in the aerosol optical depth during the period 2000–2006 over the Mediterranean were found from the

A.F. Bais (✉) • T. Drosoglou • C. Meleti • N. Kouremeti
Physics Department, Aristotle University of Thessaloniki, Thessaloniki, Greece
e-mail: abais@auth.gr

C.G. Helmis and P.T. Nastos (eds.), *Advances in Meteorology, Climatology and Atmospheric Physics*, Springer Atmospheric Sciences,
DOI 10.1007/978-3-642-29172-2_125,

analysis of MODIS data (Papadimas et al. 2008; Koukouli et al. 2010). Negative trends in the aerosol optical depth at UV wavelengths were reported for Thessaloniki by Kazadzis et al. (2007), 3.5% year^{-1} at 355 nm for 1997–2005 and 2% year^{-1} at 320 nm for 1985–2006 (Zerefos et al. 2009).

In this study, we examine long-term trends in TSI over Thessaloniki, Greece since 1993 focusing on the influence of aerosols in relation to the solar zenith angle (SZA). Our dataset is shorter compared to the one used in Zerefos et al. (2009), because only since 1993 were the pyranometer measurements recorded at sufficiently high sampling rate to allow grouping of the data in SZA bins. In addition, this dataset is better quality controlled since it starts with a new instrument with a reconfirmation of its calibration during this period.

2 Data and Methodology

The data have been derived from continuous measurements at the Laboratory of Atmospheric Physics (LAP) of the Aristotle University of Thessaloniki (40°38′N, 22°57′E) with a Kipp & Zonen CM-21 pyranometer covering the period from January 1993 to March 2011. The monitoring site is located at the roof of the Physics Department, at the city centre and ~80 m above sea level. The horizon is clear of obstructions except for the range of azimuth angles 35–120° where obstacles below ~10° elevation block the direct irradiance in the morning for SZA larger than ~80°. These data points were excluded from the analysis. The data were recorded every 1 min together with the standard deviation of the samples during each minute. The stability of the CM-21 pyranometer quoted by the manufacturer is better than ±0.5% year^{-1}. However, a recalibration that was done at the Deutscher Wetterdienst – Meteorologisches Observatorium Lindenberg in 2005 revealed no change in its sensitivity (<0.1% during 12 years of operation).

Since the main focus of this study is the estimation of relative long-term changes in TSI, all data were adjusted to the mean Sun-Earth distance, using the inverse square law and then they were grouped into bins of 1° of SZA. The city experiences significant amounts of aerosols and air pollutants, originating both from local sources and from long range transportation from neighbouring countries (e.g., Kazadzis et al. 2007; Zerefos et al. 2009). In order to separate the effects of clouds from the effects of aerosols, measurements recorded under cloud-free skies were analyzed separately. To flag the clear-sky data we have used a radiative transfer model, libRadtran (Mayer and Kylling 2005), to estimate the upper and lower limits of the expected TSI under cloud-free conditions for representative high and low aerosol optical depths, as estimated in Kazadzis et al. (2007). These calculations were derived as a function of solar zenith angle. Then we assumed that all measured TSI data falling within the two limits refer to cloud-free cases. In addition, we have tested the variability of irradiance within a period of 5 min before and after each measurement, as in Vasaras et al. (2001).

For the analysis of long-term changes, linear trends were calculated for the different subsets of data as long as the subset contained more than 50 data points. It should be noted that there are no significant gaps in the dataset that would affect the calculation of trends. The significance of the trends was tested by using the Student's t-test.

3 Results and Discussion

From the long-term series of the pyranometer data departures of the daily sums from the climatological mean for each day of the year were calculated, to remove the natural annual variability of the measurements, caused by the annual variation of SZA and the length of the day. The derived linear trend in the departures is 0.33 W m^{-2} $year^{-1}$, statistically significant at the 99% confidence level. This positive trend is in accordance with earlier studies (e.g., Wild 2009 and references therin) reporting the start of a "brightening" (increasing of atmospheric transparency) since the late 1980s, resulting from changes in cloudiness and aerosols, but at least half of that at other European sites. There is clear evidence that the aerosol optical depth decreases in the 1990s and early 2000s (Kazadzis et al. 2007). Zerefos et al. (2009) have shown that for several years after the eruption of Mt. Pinatubo the aerosols remained elevated; therefore the first ~2 years of the data set used in this study may have been influenced by the volcanic aerosols.

To investigate whether the derived trend is consistent for the entire dataset, we recalculated the trends in TSI for smaller periods by removing every time 1 year from the start of the data series. The trends are stable for up to 4 years since 1993 and then gradually decrease as the starting year is shifted forward. Around year 2000 the sign of the trend reverses, indicating that the brightening of the 1980s and 1990s is probably changing to a diming, or, at least, levelling off. It seems that the lower troposphere in Thessaloniki has reached a point where aerosols no longer decrease and are levelling off (see Kazadzis et al. 2009) as the activities of the city are growing and the air quality measures can no longer lead to improvements, taking also into account that a good fraction of the aerosols are transported from other regions (e.g., Amiridis et al. 2005). The above pattern is systematic for all SZAs. No firm conclusions can be safely drawn with respect to the magnitude and the year of this reversal of the upward trend in TSI from this short dataset, until more years of observations are added in the future. At present, we report this change as an indication of a possible change in the well established "brightening" in the last few decades.

Linear trends of TSI were calculated also for different SZAs, separately for the morning and afternoon hours. This separation would reveal any detectable effects of the diurnal variation of the aerosols on the calculated trends. Usually the tropospheric aerosol load is more pronounced in the afternoon hours.

Figure 1 shows a general increasing trend in TSI from 1993 to 2011, for both cloud-free and all-sky conditions, respectively up to 0.4 and 0.6% $year^{-1}$,

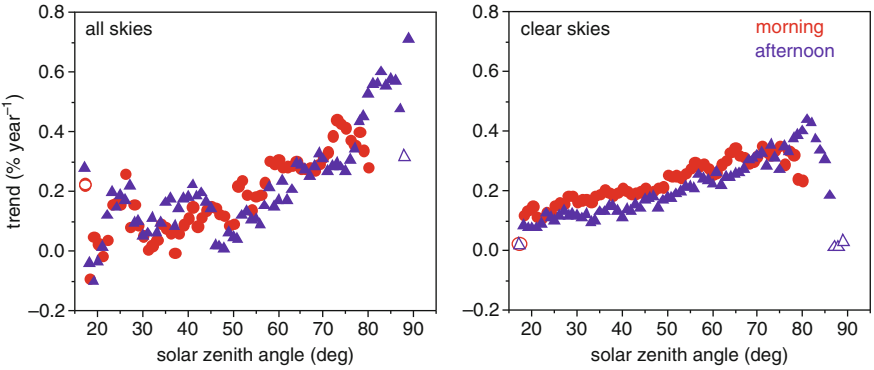

Fig. 1 Linear trends in total solar irradiance under all-sky (*left*) and clear-sky (*right*) conditions as a function of solar zenith angle. Trends are calculated separately for morning (*red circles*) and afternoon (*blue triangles*) hours. Filled symbols refer to trends with statistical significance higher than 99%

statistically significant at the 99% level, except for very large SZAs. For all-sky conditions the trends have greater uncertainty due to the interference of clouds and depict a noisier pattern, compared to clear-skies. Otherwise the magnitude of the trends is similar, at least for SZA smaller than about 70°.

With respect to SZA, the trend increases gradually, at higher rates for SZA larger than 50°. For clear skies at Thessaloniki, the only atmospheric parameter that can cause the dependence of the derived trends on SZA is a change in the amount and/or the optical properties of the aerosols, as surface reflectivity can be assumed constant during the period of study. A reduction in the optical depth of the aerosols increases the direct irradiance but reduces the diffuse component. The absolute, as well as the relative, magnitude of these changes depend strongly on SZA. Generally, the effect of a negative trend in the aerosol optical depth on TSI should be more pronounced at large SZAs. For example, model calculations reveal that for a reduction in the optical depth from 0.6 to 0.4 (typical values for Thessaloniki corresponding to the mean optical depth at 340 nm in the mid 1990s and mid 2000s, respectively), TSI increases by ~1.8% and ~5%, respectively for 20° and 70° SZA. Therefore in 10 years the decrease in the optical depth would result in larger increase in TSI at 70° SZA by about 3%, which is close to the difference in the trends between 20° and 70° SZA of Fig. 1. The larger trends in the all-skies dataset for SZA $> 70°$ imply that either the cloud-cover has been reduced over the years, or the clouds became optically thinner, resulting in increased TSI.

In addition to the amount of the aerosols, their type also influences TSI at the surface. Perhaps the most important factor is the single scattering albedo (SSA), which defines the absorption efficiency of the aerosols. Changes in SSA would modify the model-derived changes in irradiance discussed above, either to lower values, if the SSA increases during the period of the study, or to higher values if the SSA decreases. Although for the optical depth of aerosols there is a sufficiently long

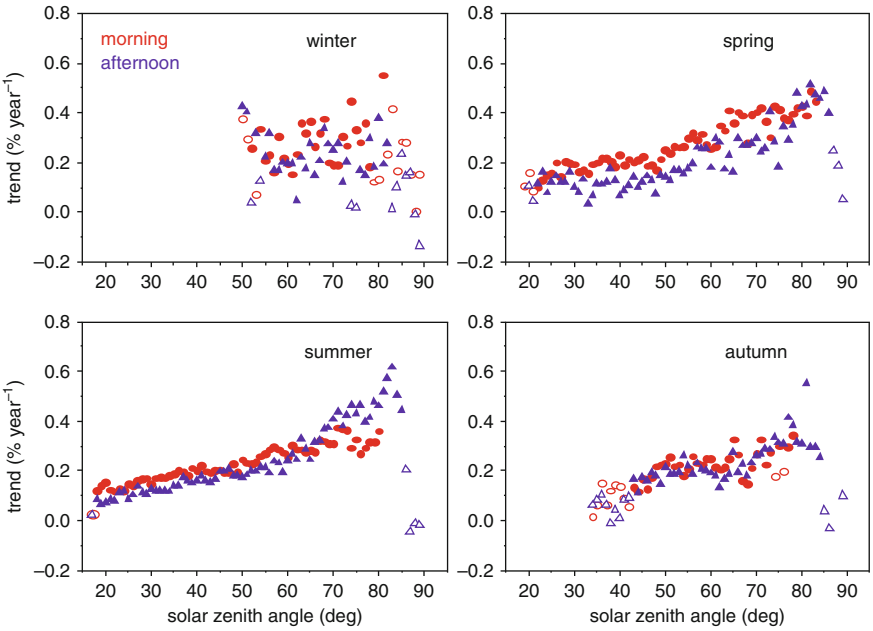

Fig. 2 Seasonal trends in total solar irradiance as function of solar zenith angle for clear skies, separately for morning (*red circles*) and afternoon (*blue triangles*) hours. *Filled symbols* refer to trends with statistical significance higher than 99%

time-series at Thessaloniki that reveals a negative trend, there is no robust information on the long-term changes in SSA.

For clear-skies, the trends are larger in the morning than in the afternoon; up to twice as much for SZAs between 30° and 40°. There is no clear evidence about the causes of this behavior. The optical depth of aerosols is usually larger in the afternoon; but this cannot be directly associated with its trend over the years.

The trends shown in Fig. 1 are biased from different seasons, since only SZAs larger that ~63° are present throughout the year. The trends for the smaller SZAs do not include data from the cold period; thus they are strongly influenced by the seasonal variation of the aerosols. For example, the dataset for 30° spans from mid-April to end of August; hence it is influenced by higher aerosol amounts and reduced cloudiness in this season.

Figure 2 shows the seasonal patterns of the derived trends as a function of SZA for clear skies to isolate the aerosols from the cloud effects. The general pattern found in the yearly trends remains also in the different seasons showing clearly that trends are increasing with increasing SZA. In spring and summer, the afternoon trends are slightly smaller, possibly associated with the built-up of the aerosols in the warm period that occurs mainly in the afternoon hours. The trends at large SZAs are by up to 0.2% year^{-1} larger compared to the annual trends (the maximum seasonal trend occurring at 80° SZA is about 0.6% year^{-1} instead of 0.4 for the

annual trend). As discussed above, the aerosol optical depth in the spring and summer is larger than in other seasons; therefore, the reduction in the optical depth that has occurred during the 1900s and 2000s results in larger trends in these seasons, particularly at large SZAs where the effect is more pronounced. The autumn trends follow the general tendency, but are slightly smaller and the morning to afternoon differences have now disappeared. Finally, there is no clear dependence of the winter trends on SZA, due to increased noise in this subset of data.

4 Conclusions

Total solar irradiance measurements conducted from 1993 to 2011 at Thessaloniki are used to investigate long-term changes. The daily averaged TSI increases with an average rate of 0.33 W m^{-2} $year^{-1}$ (or ~0.1% $year^{-1}$). Of similar magnitude are the trends for small SZAs, but they increase up to 0.4 and 0.6% $year^{-1}$ at large SZAs, respectively for cloud-free and all-sky conditions. The increasing trend of TSI for clear skies is attributed to cleansing of the atmosphere from aerosols. There are indications that TSI levels off in the 2000s or it even starts to decrease.

References

Amiridis V, Balis DS, Kazadzis S et al (2005) Four-year aerosol observations with a Raman lidar at Thessaloniki, Greece, in the framework of European Aerosol Research Lidar Network (EARLINET). J Geophys Res 110:D21203. doi:21210.21029/22005JD006190

Kazadzis S, Bais A, Amiridis V et al (2007) Nine years of UV aerosol optical depth measurements at Thessaloniki, Greece. Atmos Chem Phys 7(8):2091–2101

Kazadzis S, Kouremeti N, Bais A et al (2009) Aerosol forcing efficiency in the UVA region from spectral solar irradiance measurements at an urban environment. Ann Geophys 27(6):2515–2522

Koukouli ME, Kazadzis S, Amiridis V et al (2010) Signs of a negative trend in the MODIS aerosol optical depth over the Southern Balkans. Atmos Environ 44(9):1219–1228. doi:10.1016/j.atmosenv.2009.11.024

Liepert B, Tegen I (2002) Multidecadal solar radiation trends in the United States and Germany and direct tropospheric aerosol forcing. J Geophys Res-Atmos 107:4153. doi:10.1029/2001JD000760

Mayer B, Kylling A (2005) Technical note: the libRadtran software package for radiative transfer calculations – description and examples of use. Atmos Chem Phys 5:1855–1877

Ohvril H, Teral H, Neiman L et al (2009) Global dimming and brightening versus atmospheric column transparency, Europe, 1906–2007. J Geophys Res 114:D00D12. doi:10.1029/2008JD010644

Papadimas CD, Hatzianastassiou N, Mihalopoulos N et al (2008) Assessment of the MODIS Collections C005 and C004 aerosol optical depth products over the Mediterranean basin. Atmos Chem Phys Discuss 8(4):16891–16916. doi:10.5194/acpd-8-16891-2008

Pinker RT, Zhang B, Dutton EG (2005) Do satellites detect trends in surface solar radiation? Science 308(5723):850–854

Romanou A, Liepert B, Schmidt GA et al (2007) Twentieth century changes in surface solar irradiance in simulations and observations. Geophys Res Lett 34:L05713. doi:05710.01029/02006GL028356

Stanhill G, Cohen S (2005) Solar radiation changes in the United States during the twentieth century: evidence from sunshine measurements. J Clim 18:1503–1512

Vasaras A, Bais AF, Feister U et al (2001) Comparison of two methods for cloud flagging of spectral UV measurements. Atmos Res 57(1):31–42

Wild M (2009) Global dimming and brightening: a review. J Geophys Res 114:D00D16

Zerefos CS, Eleftheratos K, Meleti C et al (2009) Solar dimming and brightening over Thessaloniki, Greece, and Beijing, China. Tellus B 61(4):657–665. doi:10.1111/j.1600-0889.2009.00425.x

Forest Fire Aerosols: Vertically Resolved Optical and Microphysical Properties and Mass Concentration from Lidar Observations

D. Balis, E. Giannakaki, V. Amiridis, R.E. Mamouri, P. Kokkalis, G. Tsaknakis, and A. Papayannis

Abstract The influence of smoke on the aerosol loading in the free troposphere from EARLINET observations are examined in this paper. Several cases during 2001–2011 were identified over Thessaloniki and Athens, Greece, when very high aerosol optical depth values in the free troposphere were observed with a UV-Raman lidar. Particle dispersion modeling (FLEXPART) and satellite hot spot fire detection (ATSR) showed that these high free tropospheric aerosol optical depths are mainly attributed to the advection of smoke plumes from biomass burning regions. The biomass burning regions were found to extend across Russia in the latitudinal belt between 45°N and 55°N, as well as in Eastern Europe. The highest frequency of agricultural fires occurred during the summer season (mainly in August). Emphasis is also given on the 2007 wild fires surrounding Athens and earlier studies performed in the frame of EARLINET. The data collected allowed the optical and microphysical characterization of the smoke aerosols that arrived over Greece, where limited information has so far been available and in synergy with AERONET and CALIPSO observation a first attempt is made for the vertically resolved mass concentration of the smoke plumes.

D. Balis (✉) • E. Giannakaki
Laboratory of Atmospheric Physics, Aristotle University of Thessaloniki, Thessaloniki, Greece
e-mail: balis@auth.gr

V. Amiridis
Institute for Space Applications and Remote Sensing, National Observatory of Athens, Athens, Greece

R.E. Mamouri • P. Kokkalis • G. Tsaknakis • A. Papayannis
Laser Remote Sensing Laboratory, National Technical University of Athens, 15780 Athens, Greece

C.G. Helmis and P.T. Nastos (eds.), *Advances in Meteorology, Climatology and Atmospheric Physics*, Springer Atmospheric Sciences,
DOI 10.1007/978-3-642-29172-2_126,

1 Introduction

Biomass burning is a major source of air pollution and the second largest source of anthropogenic aerosols. The Fourth Assessment Report of the Intergovernmental Panel on Climate Change (Forster et al. 2007) reports a contribution of roughly +0.04 W/m^2 of biomass burning aerosol to the global radiative forcing (RF) with a standard deviation of 0.07 W/m^2. Textor et al. (2006) showed that there are still significant uncertainties in the aerosol vertical distribution in global aerosol models, information that is critical in assessing the magnitude and even the sign of the direct RF of biomass burning aerosols.

2 Data and Methodology

In this paragraph we present briefly the various data sources used in this study.

2.1 Ground Based Lidar Measurements

The ground-based lidar measurements were performed at the Laboratory of Atmospheric Physics (LAP-AUTH) in the Aristotle University Campus located in the centre of Thessaloniki. The lidar system is a 355 nm Raman/elastic lidar operating since May 2000. The LAP-AUTH lidar is based on the second and third harmonic frequency of a compact, pulsed Nd:YAG laser, which emits pulses of 300 and 120 mJ at 532 and 355 nm, respectively, with a 10 Hz repetition rate. The elastically backscattered signals at both 355 and 532 nm and the N_2 Raman shifted signal at 387 nm are collected with a Newtonian telescope of 500 mm diameter with 0.73 mrad adjustable field-of-view. The lidar system is part of EARLINET and has been intercompared both at algorithm and system levels (Böckmann et al. 2004; Matthais et al. 2004; Pappalardo et al. 2004). The Athens lidar station is based on a Quantel Brilliant Nd:YAG laser. The laser emits light pulses in the atmosphere, simultaneously at three wavelengths (1,064, 532 and 355 nm), with pulse energy of 360 mJ and repetition rate of 10 Hz. The outgoing beams of three wavelengths are directed to the atmosphere by two beam-folding mirrors – one for 355 nm and one for 532, 1,064 nm – to a 27° angle to the zenith. A 0.3 m-diameter reflecting Cassegrainian telescope pointing to 27° to the zenith, and having a focal length of 0.6 mm, is directly coupled through an optical fibre to the lidar signal multi-channel detection box. The v_1 vibrational Raman bands of nitrogen centered at 387 and 607 nm are used to determine the particle extinction coefficient vertical profile.

3 Results

Figure 1 (left) shows an aggregate plot of all ATSR and AATSR fire detections for the 10 days of the lidar measurements. Location of the burning regions was also verified by the MODIS Fire Product (http://modis-fire.umd.edu/products.asp). Symbols indicate the dominant land cover where the detection occurred based on a global land cover classification with a resolution of 300 m derived from the European Space Agency's Global Land Cover service for the production of global land-cover map for the year 2005, using ENVISAT MERIS Fine Resolution (300 m) data that replaced the GlobCover2000 product which had 1 km resolution (http://dup.esrin.esa.int/projects/-summaryp68.asp). Figure 1 (left) strongly suggests that smoke particles over Thessaloniki discussed in this paper were produced mainly by agricultural burning activities.

The above pattern almost systematically affects Greece during the warm period. However there are also extreme cases of forest fires in Southern Greece that affect the Greece. An example of such a case is e forest fire in Southern Greece which occurred during the second half of August 2007.

Vertical profiles of the extinction coefficient (355 nm), backscatter coefficient (355 and 532 nm), lidar ratio (355 nm) and backscatter-related Ångström exponent (355/532 nm) referring to smoke particles for the 10 days are presented for Thessaloniki in Fig. 2. The dates are specified on the label of the figure and follow the same colour-code as the profiles on the figure. Smoke layers, as they have been identified by emission sensitivities calculated for different arrival heights above the station, are indicated with different colour for each day. Only the smoke layers are indicated with colours, while black lines correspond to the complete vertical profile

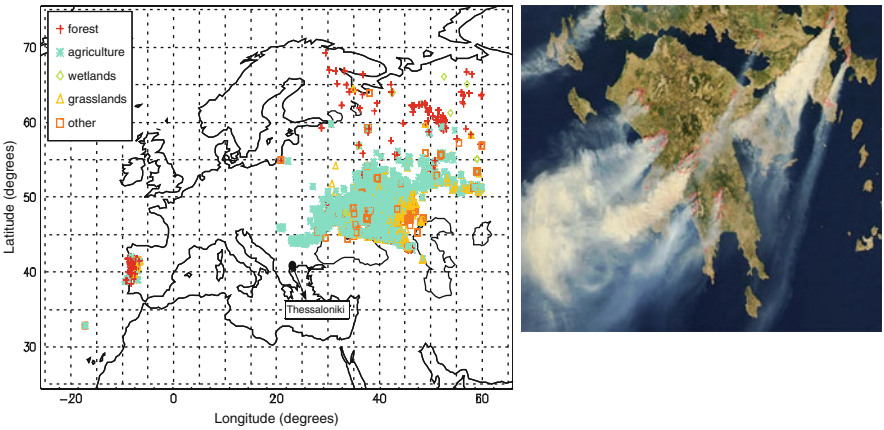

Fig. 1 Location of fires for the 10 days of lidar measurements over Thessaloniki as detected by ATSR. Symbols indicate the dominant land cover where the detection occurred. (*left*). Fires affecting the Lidar station at Athens during August 2007 location of fires for the 10 days of lidar measurements over Thessaloniki as detected by ATSR (*right*)

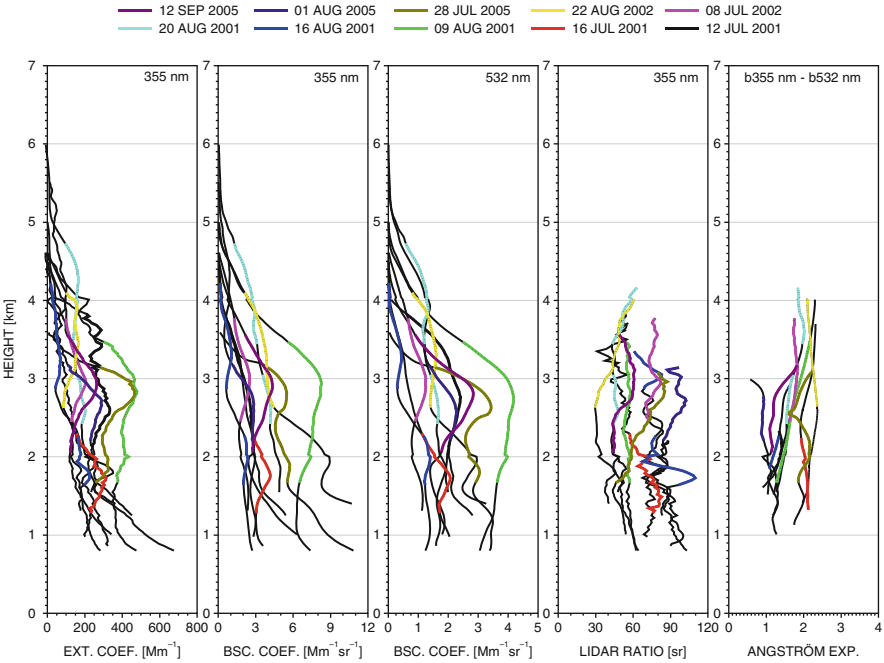

Fig. 2 Lidar derived vertical profiles of the extinction coefficient at 355 nm, the backscatter coefficients at 355 and 532 nm along with the lidar ratio at 355 nm and the backscatter-related Ångström exponent measured at Thessaloniki for 10 days that smoke presence was detected. *Black lines* correspond to the complete vertical profile measured for each day while height ranges indicated with different colour correspond to the smoke layers

measured for each day. The lidar ratio for smoke particles found to vary between 32 and 103 sr. The backscatter-related Ångström exponent ranged between 0.5 and 2.4.

Figure 3 presents the corresponding optical properties of the smoke aerosols during 27 August 2007 over the Athens during the extreme regional fire event. The variability of the lidar ratio and the Ångström exponent for smoke particles cannot be attributed to different source characteristics, since for most of the case studies discussed here the main and common source of smoke is the agricultural fires in Russia and Ukraine. In this region, farmers burn each year the crop stubble off recently harvested fields in anticipation of the next sowing. The variability in particle size can be attributed to the fact that the fire regions were located in variable distances from Thessaloniki which affects the optical characteristics of the observed smoke aerosols due to different ageing processes, depending also to the meteorological conditions responsible for the speed of the smoke plume. Calculated age averages of the air-masses (using CO as a tracer) when examined against vertical mean values of the backscatter related Ångström exponents show a correlation coefficient equal to -0.85 suggesting a strong anti-correlation. This suggests that smoke particles become larger with ageing. The observed anticorrelation between the lidar ratio and the backscatter related Ångström

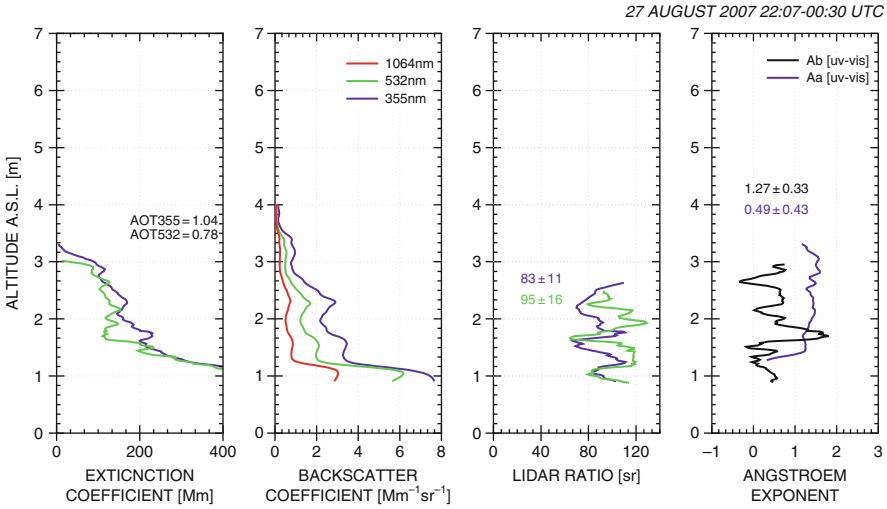

Fig. 3 Lidar derived vertical profiles of the extinction coefficient, backscatter coefficients and lidar ratio at 355 and 532 nm along with the lidar ratio at 355 nm and the related Ångström exponents measured at Athens during 27 August 2007

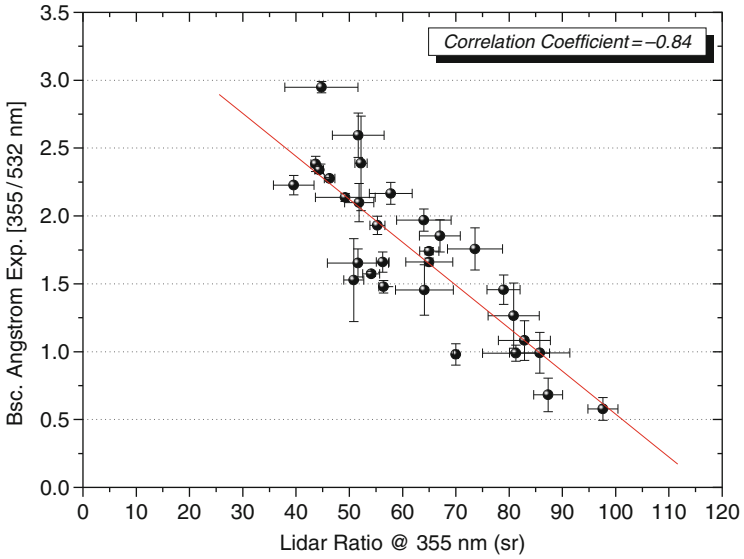

Fig. 4 Vertical mean values of the backscatter-related Ångström exponent calculated from the backscatter coefficients at 355 and 532 nm versus the vertical mean values of the lidar ratio at 355 nm

exponent shown in Fig. 4 indicates that the variability in the lidar ratio is positively correlated with the age of the smoke particles.

4 Conclusions

Many EARLINET stations are systematically affected by forest and large scale agricultural fires i.e. Russia, Siberia, N. Canada, Portugal, regional ones (Amiridis et al. 2009). The smoke plumes form these fires can travel for many days in the free troposphere and can result to very high optical depths and extinction coefficients (1.7 and 400 Mm^{-1} respectively). Estimated optical and microphysical properties for smoke show a wide range of values (lr355 = 30–90 sr, lr532 = 40–100 sr, lr355/lr532 < 1, $\mathring{A}_{a(355/532)}$ = 0.5–1.5, r_{eff} = 0.2–0.4 μm, ssa: the majority of cases 0.85–0.95). The ageing of the smoke plume and/or different source type can explain part of the observed variability.

Acknowledgments This work has been conducted in the framework of the projects EARLINET-ASOS under grant RICA-025991.

References

Amiridis V, Balis DS, Giannakaki E, Stohl A, Kazadzis S, Koukouli ME, Zanis P (2009) Optical characteristics of biomass burning aerosols over Southeastern Europe determined from UV-Raman lidar measurements. Atmos Chem Phys 9(7):2431–2440. doi:10.5194/acp-9-2431-2009

Böckmann C, Wandinger U, Ansmann A, Bösenberg J, Amiridis V, Boselli A, Delaval A, De Tomasi F, Frioud M, Grigorov IV, Hågård A, Horvat M, Iarlori M, Komguem L, Kreipl S, Larchevêque G, Matthias V, Papayannis A, Pappalardo G, Rocadenbosch F, Rodrigues JA, Schneider J, Shcherbakov V, Wiegner M (2004) Aerosol lidar intercomparison in the framework of the EARLINET project. 2. Aerosol backscatter algorithms. Appl Opt 43(4):977–989. doi:10.1364/AO.43.000977

Forster P, Ramaswamy V, Artaxo P, Berntsen T, Betts R, Fahey DW, Haywood J, Lean J, Lowe DC, Myhre G, Nganga J, Prinn R, Raga G, Schulz M, Dorland RV (2007) Changes in atmospheric constituents and in radiative forcing, in climate change 2007: the physical science basis. In: Solomon S, Qin D, Manning M, Chen Z, Marquis M, Averyt KB, Tignor M, Miller HL (eds) Contribution of working group I to the fourth assessment report of the intergovernmental panel on climate change. Cambridge University Press, Cambridge

Matthais V, Freudenthaler V, Amodeo A, Balin I, Balis D, Bösenberg J, Chaikovsky A, Chourdakis G, Comeron A, Delaval A, De Tomasi F, Eixmann R, Hågård A, Komguem L, Kreipl S, Matthey R, Rizi V, Rodrigues JA, Wandinger U, Wang X (2004) Aerosol lidar intercomparison in the framework of the EARLINET project. 1. Instruments. Appl Opt 43 (4):961–976. doi:10.1364/AO.43.000961

Pappalardo G, Amodeo A, Pandolfi M, Wandinger U, Ansmann A, Bösenberg J, Matthias V, Amiridis V, De Tomasl F, Frioud M, Iarlori M, Komguem L, Papayannis A, Rocadenbosch F, Wang X (2004) Aerosol lidar intercomparison in the framework of the EARLINET project. 3. Raman lidar algorithm for aerosol extinction, backscatter, and lidar ratio. Appl Opt 43 (28):5370–5385. doi:10.1364/AO.43.005370

Textor C, Schulz M, Guibert S, Montanaro V, Myhre G, Penner J, Pitari G, Reddy S, Seland Ø, Stier P, Takemura T, Tie X et al (2006) Analysis and quantification of the diversities of aerosol life cycles within AeroCom. Atmos Chem Phys 6(7):1777–1813. doi:10.5194/acp-6-1777-2006

Comparative Analysis of MERIS/AATSR Synergy Algorithm Aerosol Retrievals Versus MODIS Aerosol Product and Validation Against AERONET Observations

N. Benas and N. Chrysoulakis

Abstract Aerosol monitoring from space has been performed at mesoscale, for over two decades. Latest satellite aerosol products offer global daily coverage and a typical spatial resolution of 10 km × 10 km. A new synergy algorithm has been recently developed, to retrieve aerosol properties in higher spatial resolution, which may improve the study of aerosols at local scale, increasing the potential of Earth Observation to support local level air quality studies. The algorithm combines both spectral and angular information provided by MERIS and AATSR sensors, respectively. In the present study, the MERIS/AATSR synergy algorithm is validated by comparing the retrieved Aerosol Optical Thickness (AOT) with the respective AOT values observed at AERONET stations located in urban regions globally. AATSR, MERIS and AERONET data for the period August–September 2011 were analyzed. Comparisons with the respective AOT spatial distributions retrieved from MODIS aerosol product were also performed for the broader area of Athens. Results indicate that the retrieved AOT is in good agreement with the corresponding station measurements.

1 Introduction

Atmospheric aerosols are a crucial parameter in studies of the Earth-Atmosphere system. However, the quantification of the aerosol effects is more complex compared to greenhouse gases, due to their high spatial and temporal variability. In local scales, aerosols can also affect air quality and human health (e.g. Kaufman et al. 2002). The study of aerosols is based on two different approaches, namely ground measurements and satellite remote sensing. The most widely used ground

N. Benas (✉) • N. Chrysoulakis
Foundation for Research and Technology – Hellas, Institute of Applied and Computational Mathematics, N. Plastira 100, Vassilika Vouton, 70013 Heraklion, Greece
e-mail: benas@physics.uoc.gr

C.G. Helmis and P.T. Nastos (eds.), *Advances in Meteorology, Climatology and Atmospheric Physics*, Springer Atmospheric Sciences,
DOI 10.1007/978-3-642-29172-2_127,

data come from the Aerosol Robotic Network (AERONET), a network of ground based stations which provides a long term and continuous database of aerosol properties (Holben et al. 1998). However, this database is limited only over land and specifically over regions where stations are available and operational. Although the advantage of aerosol remote sensing compared to in-situ measurement is obvious, the spatial and temporal resolution of satellite retrieved aerosols remains a drawback in case of local scale studies.

Modern satellite aerosol products include Aerosol Optical Thickness (AOT), as well as other aerosol properties, at spatial resolutions reaching up to 10 km $\times$ 10 km. These products include NASA's Moderate Resolution Imaging Spectroradiometer (MODIS) Level 2 data products (Remer et al. 2005) and the GlobAEROSOL product (Thomas et al. 2006). These products are based on data from instruments with a single sampling of the angular domain. The main problem in AOT retrieval is to decouple the signal contributed by atmospheric scattering from that contributed by surface reflectance. This separation is always based on a priori knowledge about the spectral properties of the surface. Generally these methods are suitable only for dark targets, thus giving a sparse estimate of AOT. Use of multiple view-angle imagery allows an additional constraint to be placed, since the same area of surface is viewed through different atmospheric path lengths.

The present study aims to validate urban aerosol retrievals of a multiple view-angle approach, developed to make a synergistic use of the Advanced Along-track Scanning Radiometer (AATSR) and the Medium Resolution Imaging Spectrometer (MERIS) instruments (North et al. 2009). Both sensors are carried on board Envisat, launched in 2002, and provide complementary information, encompassing different spectral domains and viewing geometries. Its main advantage is the higher spatial resolution of the aerosol retrieval, offering new possibilities in discriminating aerosol spatial patterns, and generally studying spatial aerosol characteristics in areas of high interest, such as urban regions. For the validation purposes, aerosol data from AERONET stations in urban areas around the globe were used. A MODIS Level 2 AOT image was also used, to compare the aerosol spatial patterns derived by the algorithm with a similar product that has been tested and validated in the past and is known to perform well (Remer et al. 2002).

In the next section, MERIS and AATSR instruments, as well as the synergy algorithm are presented. Section 3 describes the methodology and procedure used for the validation of the synergy algorithm output against corresponding AERONET data. Results of the validation and comparison processes are presented in Sect. 4, before the summary and conclusions.

2 The MERIS/AATSR Synergy Algorithm for Aerosol Retrieval

MERIS is a medium resolution imaging spectrometer, operating in the solar reflective spectral range and possessing 15 spectral bands between 390 and 1,040 nm. Three of these bands are dedicated to the retrieval of aerosol properties.

The instrument's field of view around nadir covers a swath width of 1,150 km across-track. The Earth is imaged with a spatial resolution of 300 m × 300 m, in full resolution (Rast et al. 1999). AATSR is a scanning radiometer with 7 bands in visible, reflective infrared and thermal infrared. Special features of the AATSR include its use of a conical scan to give a dual view of the Earth's surface, thus improving the capacity for atmospheric correction. The AATSR swath covers approximately half of the MERIS swath (~500 km), with pixel sizes of 1 km × 1 km at the center of the nadir swath and 1.5 km × 1.5 km at the center of the forward swath. For the AATSR Level 1 products, forward pixels are resampled to 1 km^2 resolution, in order to be the same size as the nadir pixels (AATSR 2007).

The MERIS/AATSR synergistic algorithm for retrieval of aerosol properties has been described by North et al. (2009). A two-stage optimization process is employed by the algorithm: (1) Given a set of 21 satellite TOA (top of the atmosphere) radiances (from the 4 solar reflective AATSR bands (nadir and forward) and the 13 MERIS non-absorbing bands), and an initial guess of the atmospheric profile (which includes AOT at 550 nm and aerosol model), a corresponding set of surface reflectances is estimated. (2) Testing of this set against a constraint results in an error metric, where a low value corresponds to a set of surface reflectances (and hence atmospheric profile) which is realistic. The procedure is repeated using a refined atmospheric profile, until convergence to an optimal solution is achieved. The output of the algorithm includes AOT at 550 nm, Angstrom coefficient (α), aerosol model used and error estimates of AOT and α. The algorithm is capable of retrieving AOT in the spatial resolution of MERIS.

3 Validation Methodology

The MERIS/AATSR synergy algorithm is capable of retrieving aerosol properties in various spatial resolutions. Three different resolutions, corresponding to approximately 300 m × 300 m, 1 km × 1 km and 2 km × 2 km pixel size, were tested. For the validation of AOT against AERONET station measurements, the following procedure was used: in each algorithm output AOT image, pixels falling over AERONET stations were identified, using their geographical coordinates. Then an N×N pixel subset centered on each validation point was extracted, and the mean AOT and standard deviation were computed, representing the average value of AOT and its local spatial variability, respectively. Three subset sizes were tested: 1 × 1, 3 × 3 and 5 × 5 pixels. Performing all possible combinations of the subset sizes with the abovementioned spatial resolutions, the areas tested ranged between 300 m × 300 m and 10 km × 10 km. In each comparison, the AOT at 550 nm retrieved by the algorithm is compared to the AOT measured at the same wavelength. For several AERONET stations where measurements at this wavelength were not available, AOT was estimated by interpolation from measurements at 500 and 675 nm. Three temporal resolutions of AERONET measurements were also tested: instantaneous AOT values, 20-min and 1-h periods mean values centered on the satellite overpass time. All

AERONET data used in the present study are of quality level 1.5 (cloud screened). Level 2 quality data were not yet available for the period under study. To examine the performance of the algorithm in urban areas, we have categorized the AERONET stations into 8 groups, according to their land cover type. This categorization was based on the 2009 GlobCOVER product (Bicheron et al. 2008).

4 Validation of the AOT Against AERONET Observations

A total of 53 AOT measurements from 39 different AERONET stations were used for the validation of the synergy algorithm AOT over urban areas. All possible combinations between the algorithm's spatial resolution (300 m × 300 m, 1 km × 1 km and 2 km × 2 km pixel size), pixel subset sizes (1 × 1, 3 × 3 and 5 × 5 pixels mean values) and AERONET temporal resolutions were tested. The results show that the AOT computed by the algorithm is in good agreement with the corresponding AERONET measurements, presenting a slight overestimation of AOT, especially for higher AOT values.

Regarding the algorithm's spatial resolution, the best agreement for the 300 m × 300 m pixel size is found using instantaneous AERONET AOT values (slope = 0.70, R = 0.71, RMSE = 0.07), while for larger pixels (1 km × 1 km and 2 km × 2 km) the agreement is improved using 20-min and 1-h mean AOT values. These results show that increasing the pixel size, the AOT calculated becomes more representative of the AOT measured by the station over a larger period of time. Similar results are found when testing the pixel subset sizes (1 × 1, 3 × 3 and 5 × 5 pixels mean values): 20-min and 1-h mean measured AOT is in good agreement with spatially averaged AOT of an area 5 km × 5 km to 10 km × 10 km (slope = 0.82, R = 0.76, RMSE = 0.06 for 2 km × 2 km pixel size, 5 × 5 pixels mean value and 1-h station mean), whereas AOT from smaller areas is better compared with instantaneous values. Figure 1 shows the scatter plots of the algorithm AOT against AERONET measurements, for a pixel size of 300 m × 300 m and instantaneous station value and 2 km × 2 km pixel size and 20-min mean station value. The slope, correlation coefficient and RMSE for 1 km × 1 km pixel size and instantaneous station values are 0.80, 0.75 and 0.07 (not shown here). The correlation coefficients found, ranging between 0.71 and 0.78, compare well with the corresponding value found for MODIS AOT over land stations (0.80, Remer et al. 2005), showing a trade-off between algorithm performance and spatial resolution.

5 Comparison of the AOT Against MODIS Product

In order to compare the synergy algorithm derived AOT with the corresponding MODIS Level 2 product, a specific day was selected, when the two datasets almost coincide. Figure 2 shows the AOT distribution in the broader area of Athens, in

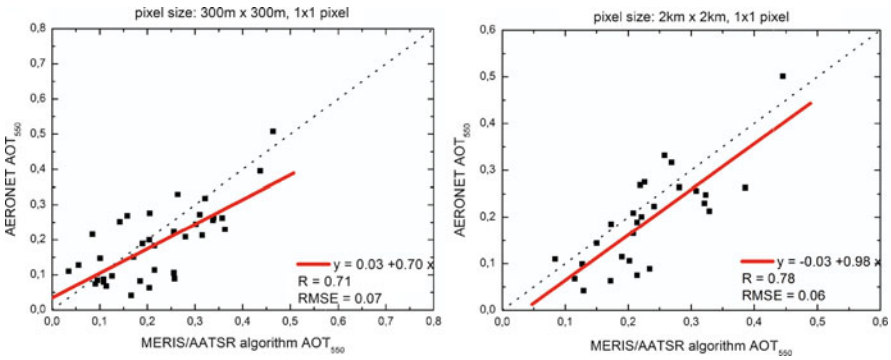

Fig. 1 Scatter plots of the AOT estimated by the synergy algorithm against AERONET station measurements: 300 m × 300 m pixel size versus in-situ instantaneous values (*left*) and 2 km × 2 km pixel size versus in-situ 20-min mean values (*right*)

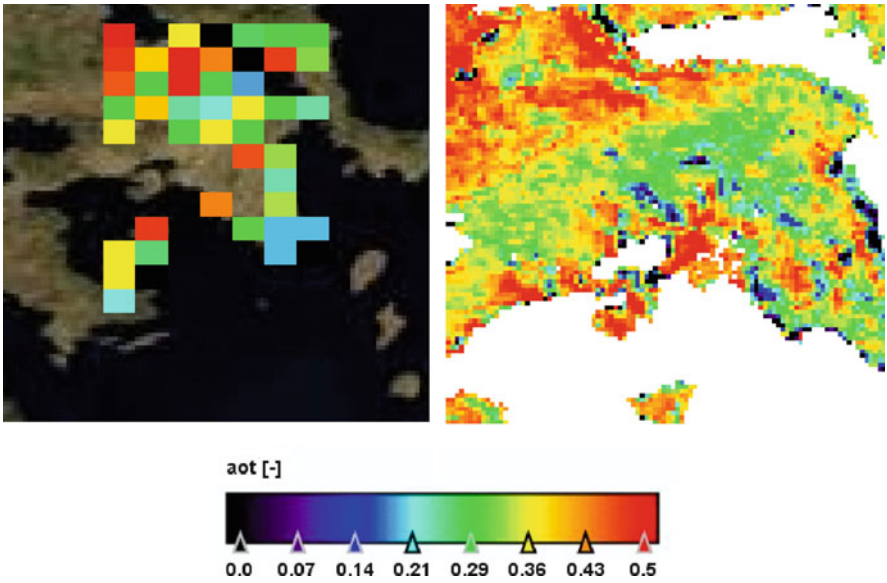

Fig. 2 Spatial distribution of the AOT in the wider area of Athens in August 18, 2011, derived by the MODIS Level 2 product (*left*) and the MERIS/AATSR synergy algorithm (*right*). The spatial resolutions are 10 km × 10 km and 1 km × 1 km, respectively

August the 18, 2011. The two datasets were acquired with 1 min difference (09:00 UTC for MODIS and 09:01 UTC for MERIS/AATSR).

The MODIS AOT has a spatial resolution of 10 km × 10 km, while the corresponding resolution of the synergy algorithm is 1 km × 1 km. In the areas where both datasets are available, there appears to be a general agreement. Nevertheless, more spatial details are available in the case of the synergy algorithm, while

the whole area, including the city of Athens, is covered almost without missing values.

6 Conclusions

A recently developed MERIS/AATSR synergy algorithm was used to estimate AOT over urban regions with high spatial resolutions. The computed AOT was validated against AERONET stations measurements. Various combinations of the algorithm's results pixel size, spatially mean AOT and temporally averaged measured AOT were tested. The output of the algorithm was found in general agreement with the AERONET AOT under all configurations examined. A spatial distribution of the algorithm AOT over the broader area of Athens was also compared to the corresponding MODIS Level 2 AOT, revealing the advantages of the synergy algorithm in terms of spatial resolution and coverage. The synergy algorithm offers new possibilities in the study of aerosols in local scale, increasing the potential of Earth Observation in air quality studies.

References

AATSR (2007) AATSR product handbook. European Space Agency – Envisat AATSR product handbook. (2.2) 27 Feb 2007

Bicheron P, Defourny P, Brockmann C, Schouten L, Vancutsem C, Huc M, Bontemps S, Leroy M, Achard F, Herold M, Ranera F, Arino O (2008) GLOBCOVER: products description and validation report. Toulouse, MEDIASFrance

Holben BN, Eck TF, Slutsker I, Tanré D, Buis JP, Setzer A, Vermote E, Reagan JA, Kaufman YJ, Nakajima T, Lavenu F, Jankowiak I, Smirnov A (1998) AERONET – a federated instrument network and data archive for aerosol characterization. Remote Sens Environ 66:1–16

Kaufman YJ, Tanré D, Boucher O (2002) A satellite view of aerosols in the climate system. Nature 419:215–223

North P, Grey W, Heckel A, Fischer J, Preusker R, Brockmann C (2009) MERIS/AATSR synergy algorithms for cloud screening, aerosol retrieval, and atmospheric correction. Algorithm theoretical basis document land aerosol and surface reflectance ATBD. ESRIN contract no. 21090/07/I-LG

Rast M, Bézy JL, Delwart S (1999) The ESA medium resolution imaging spectrometer (MERIS) – a review of the instrument and its mission. Int J Remote Sens 20:1681–1702

Remer LA, Tanré D, Kaufman YJ, Ichoku C, Mattoo S, Levy R, Chu DA, Holben BN, Dubovik O, Smirnov A, Martins JV, Li RR, Ahmad Z (2002) Validation of MODIS aerosol retrieval over ocean. Geophys Res Lett 29:MOD03. doi:10.1029/2001GL013204

Remer LA, Kaufman YJ, Tanré D, Mattoo S, Chu DA, Martins JV, Li RR, Ichoku C, Levy RC, Kleidman RG, Eck TF, Vermote E, Holben BN (2005) The MODIS aerosol algorithm, products and validation. J Atmos Sci 62:947–973

Thomas GE, Carboni E, Marsh SH, Dean SM, Grainger RG, Poulsen CA, Siddans R, Kerridge BJ (2006) GlobAEROSOL data user element: ATSR-2/AATSR algorithm theoretical basis document version 2.0. University of Oxford, UK

Aerosol Shortwave Direct Radiative Effect and Forcing Based on MODIS Level 2 Data in the Eastern Mediterranean (Crete)

N. Benas, N. Hatzianastassiou, C. Matsoukas, A. Fotiadi, N. Mihalopoulos, and I. Vardavas

Abstract A spectral radiative transfer model was used to quantify the aerosol direct radiative effect and forcing over the island of Crete in the Eastern Mediterranean. Computations were performed for the 11-year period from 2000 to 2010. MODIS Level 2 data (daily, 10 km $\times$ 10 km spatial resolution) were used as input to the model. Output includes the radiative fluxes and the aerosol direct radiative ffect at the top of the atmosphere, within the atmosphere and at the surface. The corresponding forcing components were evaluated based on MODIS fine mode aerosol data. Results show a decreasing trend of the aerosol radiative effect. The analysis of the contribution of anthropogenic and natural aerosols shows major peaks of natural aerosol effects occurring mainly in spring and autumn, while a summer maximum is attributed to anthropogenic aerosol.

1 Introduction

Amongst the different factors that can cause climate change, both greenhouse gases and aerosols play an important role. However, the quantification of the aerosol effects is more complex than the quantification of radiative forcing by greenhouse gases, because aerosol mass, chemical composition and particle number

N. Benas (✉) • I. Vardavas
Department of Physics, University of Crete, Herakleion 71003, Greece
e-mail: benas@physics.uoc.gr

N. Hatzianastassiou • A. Fotiadi
Department of Physics, University of Ioannina, Ioannina, Greece

C. Matsoukas
Department of Environment, University of the Aegean, Mytilene, Greece

N. Mihalopoulos
Department of Chemistry, University of Crete, Herakleion, Greece

C.G. Helmis and P.T. Nastos (eds.), *Advances in Meteorology, Climatology and Atmospheric Physics*, Springer Atmospheric Sciences,
DOI 10.1007/978-3-642-29172-2_128,

concentrations are highly variable in space and time (Kaufman et al. 2002). Better estimates of the aerosol radiative effects are required to reduce these uncertainties.

To reproduce successfully the distribution of the shortwave (SW) radiation budget through modeling studies on a local or regional scale, a complete description of the processes that govern the transfer of solar radiation within the Earth-atmosphere system is required. The Moderate Resolution Imaging Spectroradiometer (MODIS) instrument, on board NASA's Terra and Aqua satellites, provides most of the data sets needed for modeling the SW effects of aerosols (Chu et al. 2003; Remer et al. 2005). MODIS Level 2 data are provided each day at 10 km $\times$ 10 km latitude-longitude resolution.

In the present study, we focus on the direct radiative effect (DRE) of aerosols, which is the overall effect of natural plus anthropogenic aerosols, and the direct radiative forcing (DRF), which is the effect of anthropogenic aerosols only, on the radiative energy budget. We use MODIS Level 2 Collection 051 data separately from Terra and Aqua satellites, and detailed spectral radiative flux calculations performed with a radiative transfer model. The model is used to compute the local distribution of all shortwave radiation budget components above FORTH-CRETE AERONET station in Crete. The radiation budget components are calculated on an instantaneous basis (satellite overpass time), spanning the 11-year period from February 2000 through December 2010.

In the next section, the model, the methodology for deriving the aerosol radiative properties and the model input data are described. The results regarding the DRE and the DRF are given in Sect. 3, before the summary and conclusions.

2 Model, Methodology and Input Data Description

2.1 Model and Methodology

We use a deterministic spectral radiative transfer model developed from a spectral radiative-convective model (Vardavas and Carver 1984). Previous, spectral or simpler (broadband) versions of the model have been used in the past (e.g. Vardavas and Koutoulaki 1995; Hatzianastassiou et al. 2007). The computations are performed separately for 118 wavelengths in the range 0.2–1.0 μm, and 10 spectral bands in the range 1.0–10 μm. For each wavelength and spectral band, a set of monochromatic radiative flux transfer equations is solved for an absorbing and multiple-scattering atmosphere, using the Delta-Eddington approximation method (Joseph et al. 1976) based on the Henyey-Greenstein phase function, which is an extension of the Eddington method described in Shettle and Weinmann (1970). The model takes into account physical parameters and processes that affect significantly the solar radiation transfer: absorption by O_3 in the UV region between 0.2 and 0.35 μm (Hartley-Huggins bands) and in the visible, between 0.45 and 0.85 μm (Chappuis bands), and absorption in the near-infrared by water vapor (H_2O),

methane (CH_4) and carbon dioxide (CO_2). The model also includes scattering and absorption by clouds and aerosols, Rayleigh scattering and surface reflection.

The SW aerosol DRE (denoted henceforth as ΔF) is the direct effect of aerosols on the SW radiation budget at the top of atmosphere (TOA), at the Earth's surface and within the atmosphere, and is given by

$$\Delta F = F - F_{no-aerosol}$$

where F and $F_{no\text{-}aerosol}$ are the SW radiative fluxes (Wm^{-2}) computed with and without aerosols. The DRE components ΔF_{TOA}, ΔF_{AtmAb}, $\Delta F_{Surface}$ and $\Delta F_{NetSurface}$, represent the direct effect of aerosols on the net incoming (absorbed) radiation at TOA, within the atmosphere, and at the Earth's surface (DSR and surface absorption).

2.2 Model Input Data

In order to calculate the shortwave radiation budget using the model described above, various atmospheric, cloud and surface properties are required. The input data needed are available separately from the Terra and Aqua MODIS instruments, except for the aerosol single scattering albedo, which is taken from the FORTH-CRETE AERONET Station. MODIS Level 2 Collection 051 data come on a daily basis, at a 10 km × 10 km and 5 km × 5 km resolution for aerosol and all the other data, respectively. The data correspond to the specific overpass time of each satellite, which ranges from 10:20 to 12:00 for Terra and from 12:40 to 14:20 for Aqua (local time). MODIS Terra covers the period from February 2000, while MODIS Aqua data are available from July 2002. The model was run separately with Terra and Aqua MODIS input data, and the results correspond to the instantaneous satellite overpass times.

3 Results

3.1 Mean Monthly Time Series and Trends of DRE

To investigate the seasonal characteristics and possible trends of the aerosol DRE during the period examined, the monthly mean values were calculated from the instantaneous ones. The results of the monthly mean DRE at the surface (DSR and surface absorption), within the atmosphere and at TOA are shown in Fig. 1. From Fig. 1a it is obvious that the mean monthly aerosol DRE on the DSR can reach up to -60 Wm^{-2}. The corresponding monthly peak values for the DRE on the radiation absorbed by the surface (Fig. 1b) are -40 to -50 Wm^{-2}. The DRE increases the

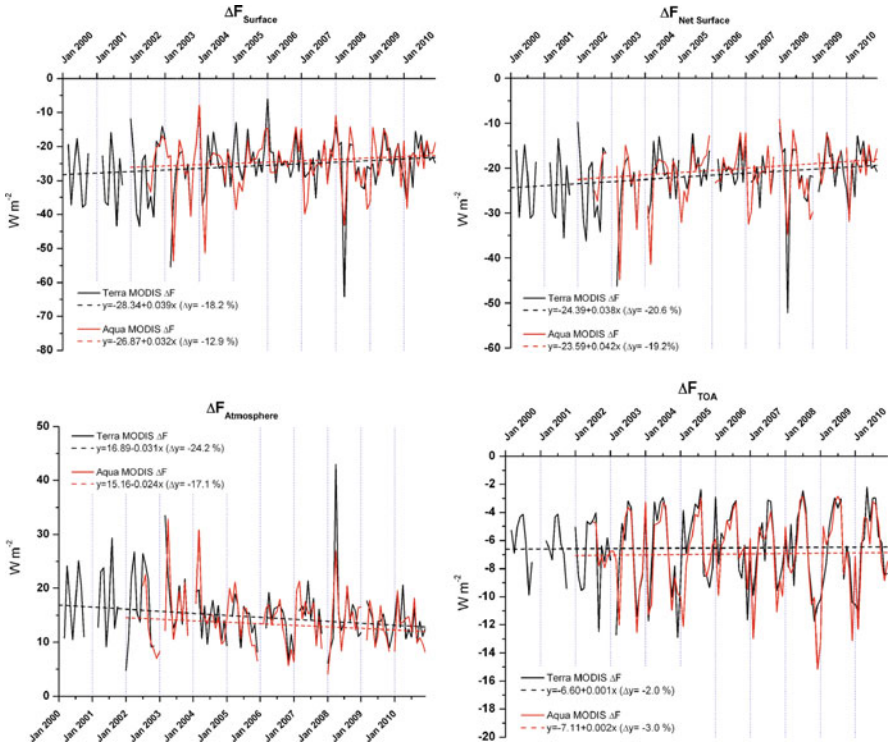

Fig. 1 Time series of the monthly mean aerosol DRE components (Based on Terra and Aqua MODIS Level 2 data, for the period 2000–2010, at the FORTH-CRETE AERONET station, Crete)

radiation absorbed by the atmosphere (Fig. 1c) by 10–20 Wm^{-2}, but can reach up to 40 Wm^{-2}. At TOA, the result of the DRE is an increase in the outgoing radiation, thus decreasing the net TOA incoming radiation by -4 to -12 Wm^{-2} (Fig. 1d). The results also show that almost every year there are two maxima in DRE, one occurring in spring (mainly April) and the other in late summer (August-September). This behavior is associated with the corresponding seasonal variation of AOT, as was shown by Fotiadi et al. (2006). The applied linear regression fits to both time series (from MODIS Terra and Aqua), are also given, along with the computed changes in the DRE ($\Delta y = \Delta(\text{DRE})$), over the period covered from each satellite. Linear fit that applied to the time series revealed that there is a decreasing trend from 2000 to 2010 in all DRE components.

3.2 Contribution of Anthropogenic and Natural Aerosols on DRE

To investigate the contribution of anthropogenic (mainly of fine mode) aerosols on the total DRE, we used the following method (see also Barnaba and Gobbi 2004):

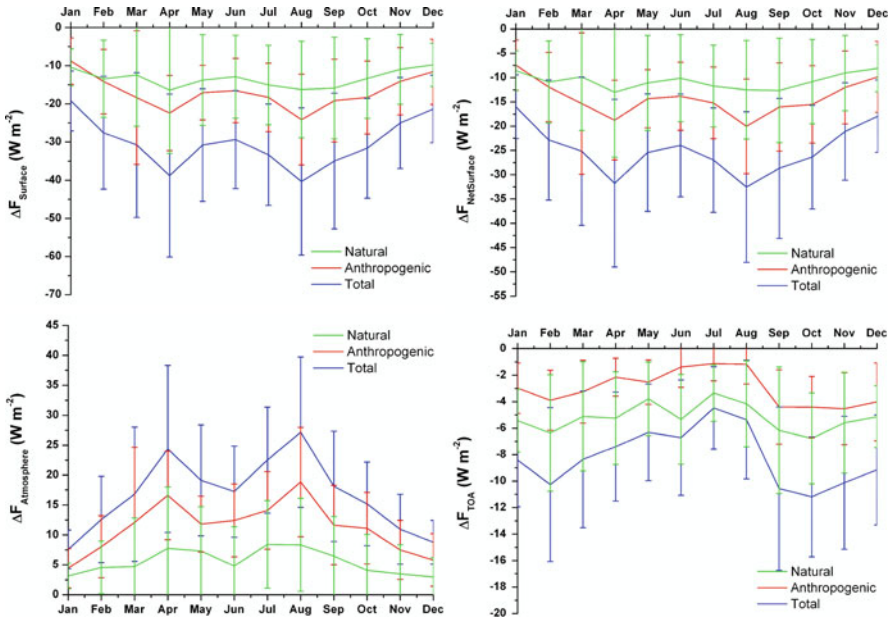

Fig. 2 Mean monthly aerosol DRE components (anthropogenic and natural) derived using Terra MODIS data

For each day, we divided the fine mode AOT given in MODIS data by the total AOT, to calculate the fine mode fraction (FMF). For the days that this fraction was greater than 0.7 we assumed that fine mode particles prevail. While fine mode AOT is already available from MODIS on a daily basis, we used monthly averaged values of fine mode g and ω, computed from the days when the fine mode particles prevailed (FMF greater than 0.7). Figure 2 shows the 11-year mean seasonal total aerosol DRE and DRF at the surface (DSR and surface absorption), within the atmosphere and at TOA, derived using Terra MODIS data. The results show that the contribution from anthropogenic aerosol particles at the surface (for both down welling and absorbed radiation) and within the atmosphere increases during summer and secondarily in spring, presenting maximum values mainly in August and April. Aerosols from natural sources show a similar behavior, with peaks appearing in April and late summer. These peaks can be attributed to dust events, which occur mainly during these seasons.

4 Summary and Conclusions

We have used a radiative transfer model, along with surface and atmospheric parameters from MODIS Level 2 products, to compute the instantaneous SW radiation budget and aerosol DRE and DRF at the surface, within the atmosphere

and at TOA, above FORTH-CRETE AERONET station in Crete, Greece. The model computations were performed for the 11-year period from 2000 to 2010, on a 10 km $\times$ 10 km pixel resolution. The linear regression analysis applied to the monthly mean DRE reveals a decreasing trend during the period examined. The contribution of anthropogenic aerosols is higher during spring and late summer (April and August), while that from natural sources (mainly dust events) peaks mainly in spring. In the future, the current version of the model could be used at various sites of specific interest, regarding the direct effect of aerosols on the radiation budget, to investigate the local patterns of the DRE.

Acknowledgments This work was supported in part by the Latsis Foundation and by the CityZen project in the frame of the European Union Seventh Framework Programme (Grant Agreement no. 212095).

References

Barnaba F, Gobbi GP (2004) Aerosol seasonal variability over the Mediterranean region and relative impact of maritime, continental and Saharan dust particles over the basin from MODIS data in the year 2001. Atmos Chem Phys 4:2367–2391

Chu DA, Kaufman YJ, Zibordi G, Chern JD, Jietai M, Chengcai L, Holben BN (2003) Global monitoring of air pollution over land from the Earth Observing System-Terra Moderate Resolution Imaging Spectroradiometer (MODIS). J Geophys Res 108:4661

Fotiadi A, Drakakis E, Hatzianastassiou N, Matsoukas C et al (2006) Aerosol physical and optical properties in the Eastern Mediterranean Basin, Crete, from Aerosol Robotic Network Data. Atmos Chem Phys 6:5399–5413. doi:10.5194/acp-6-5399-2006

Hatzianastassiou N, Matsoukas C, Fotiadi A, Stackhouse PW, Koepke P, Pavlakis KG, Vardavas I (2007) Modelling the direct effect of aerosols in the solar near-infrared on a planetary scale. Atmos Chem Phys 7:3211–3229. doi:10.5194/acp-7-3211-2007

Joseph JH, Wiscombe WJ, Weinmann JA (1976) The Delta-Eddington approximation of radiative flux transfer. J Atmos Sci 33:2452–2459

Kaufman YJ, Tanré D, Boucher O (2002) A satellite view of aerosols in the climate system. Nature 419:215–223

Remer LA, Kaufman YJ, Tanré D et al (2005) The MODIS aerosol algorithm, products and validation. J Atmos Sci 62:947–973

Shettle EP, Weinmann JA (1970) The transfer of solar irradiance through inhomogeneous turbid atmospheres evaluated by Eddington's approximation. J Atmos Sci 27:1048–1055

Vardavas I, Carver JH (1984) Solar and terrestrial parameterizations for radiative convective models. Planet Space Sci 32:1307–1325

Vardavas IM, Koutoulaki K (1995) A model for the solar radiation budget of the Northern Hemisphere: comparison with Earth radiation budget experiment data. J Geophys Res 100:7303–7314

Total Ozone Observations Made by Dobson Spectrophotometer at the Most SE Station in Europe the Last Twenty Years

J. Christodoulakis, C. Varotsos, D.N. Asimakopoulos, and C. Tzanis

Abstract Total ozone is closely connected with two crucial environmental problems: ozone depletion and global climate change. The Dobson spectrophotometer is the oldest measuring device (prototype) for total ozone observations in the atmosphere. The Dobson spectrophotometer No. 118 has been installed in Athens, Greece since 1989. We present a brief overview of the main activities of the instrument. According to the results of the intercomparison of the Athens Dobson spectrophotometer with World Standard Dobson Instruments, Dobson No. 118 is a reliable spectrophotometer and its measurements accurate and appropriate for further analysis. The comparison between Dobson measurements at Athens and all the available total ozone observations that have been performed using satellite-borne instrumentation revealed that it may be used as a ground-truth total ozone station for the validation of the satellite total ozone observations.

1 Introduction

Ozone in the troposphere–stratosphere affects climate in various ways. In the stratosphere, ozone is a strong absorber of ultraviolet (UV) solar radiation and also of upwelling thermal emission whereas in the troposphere, ozone, although it absorbs UV radiation, also plays an important role as a greenhouse gas (Alexandris et al. 1999; Varotsos et al. 1995; Kondratyev and Varotsos 1996). The ozone layer prevents harmful solar energy (the biologically damaging UV radiation) from reaching the Earth's surface (Zerefos et al. 1995, 1997; Feretis et al. 2002; Katsambas et al. 1997), strongly absorbs infrared thermal radiation (heating the stratosphere) and plays a major role in photochemistry (Cracknell and Varotsos 1994, 1995).

J. Christodoulakis (✉) • C. Varotsos • D.N. Asimakopoulos • C. Tzanis
Climate Research Group, Division of Environmental Physics and Meteorology, University of Athens, Panepistimiopoli-Zografou, 15784 Athens, Greece
e-mail: physjohn@yahoo.gr

C.G. Helmis and P.T. Nastos (eds.), *Advances in Meteorology, Climatology and Atmospheric Physics*, Springer Atmospheric Sciences,
DOI 10.1007/978-3-642-29172-2_129,

Ground-based measurements constitute a key component of the Global Ozone Network, both on their own account and by providing the ground truth for satellite-based instruments. However, the uneven geographical distribution of the existing ground-based network gives rise to a spatial sampling error, when attempts are made to determine the global distribution of the ozone content. The benefit of ground-based instruments is that it is easy to maintain them in good condition, while the benefit of satellite-based instruments is that they provide better temporal–spatial coverage and resolution (Tzanis 2009).

The Dobson Spectrophotometer is the oldest measuring device for the total ozone content (TOZ) in the atmosphere. Today, the observations of TOZ by this instrument are one of the longest geophysical measurements series in existence (TOZ over Arosa, Switzerland, since 1926) providing very useful information for ozone dynamics and its closely connected atmospheric variables (Varotsos 2002, 2005; Varotsos et al. 2005). The principle of operation of the instrument is based on making TOZ measurements in the Huggins bands by measuring the difference between the intensity of solar light at certain wavelength pairs. By using one pair of wavelengths, a differential measurement is made. One wavelength is significantly absorbed by ozone, and the other passes through a variable optical attenuator (wedge). This measured difference combined with the extraterrestrial constant and the ozone absorption spectrum indicates the TOZ. By using two pairs of wavelengths, the scattering effects can essentially be filtered out (Dobson 1957a, b). The pair most frequently used for more precise observations is the standard double-pair wavelengths designated AD, while the pair that is used less frequently for less precise observations is AC (A: 305.5 and 325.4 nm; C: 311.4 and 332.4 nm; D: 317.6 and 339.8 nm). Direct Sun AD observations generally provide the most precise measurements, if the secant of the solar zenith angle (z), 'μ', is less than 3 (Varotsos and Cracknell 1994; Christodoulakis et al. 2008).

The Greek Dobson station was installed at Athens in 1989. The station belongs to the Faculty of Physics of the National and Kapodistrian University of Athens. Laboratory of Upper Air is in charge of its operation. At the beginning, it was located at an urban area close to the centre of Athens. In the summer of 1997, the station was transferred to the University Campus which is located in a semirural area extended at the north-eastern part of the Athens basin, at a distance of about 5 km from downtown Athens. This station is the most south-eastern Dobson station in Europe and it has already been suggested in the literature as representative for the TOZ variations of the entire mid-latitude belt in the Northern Hemisphere (Chandra and Varotsos 1995; Efstathiou et al. 2003).

2 Participation in International Intercomparison Campaigns

The Athens Dobson spectrophotometer No. 118 has participated in three International Intercomparison Campaigns (held at Arosa, Switzerland in 1990; at Kalavryta, Greece in 1997 and at Hohenpeißenberg, Germany in 2006) since it was installed (Cracknell

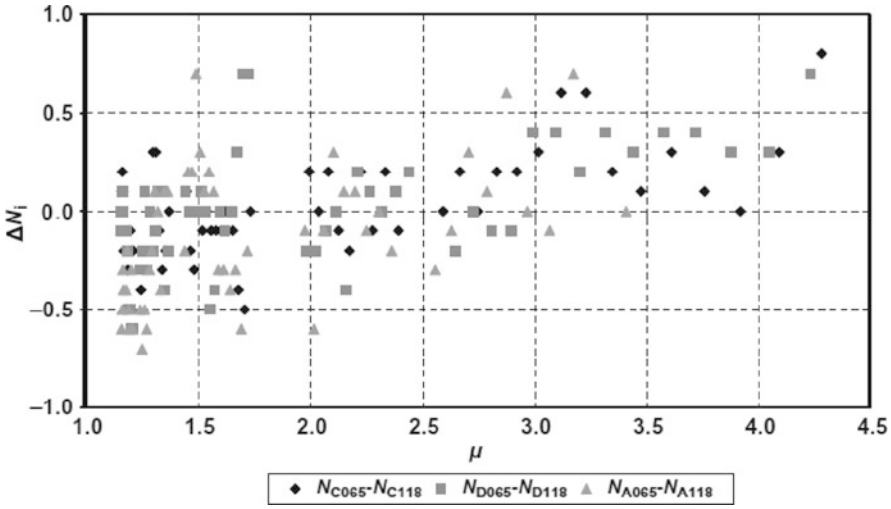

Fig. 1 $\Delta N_i = N_i$ for Dobson No. 065 – N_i for Dobson No. 118 (i = A,C,D wavelength pairs) versus μ

and Varotsos 1995; Varotsos et al. 2000; Tzanis et al. 2009). The first two campaigns were organized by the World Dobson Calibration Centre, part of the United States Department of Commerce, National Oceanic and Atmospheric Administration (NOAA) Climate Monitoring and Diagnostics Laboratory (CMDL) in Boulder, Colorado, which maintains the world primary (D083) and secondary Standard (D065) Dobson spectrophotometers. The third campaign was organized by the Regional Dobson Calibration Centre, Europe (RDCC/E) at Hohenpeißenberg, Germany, which maintains the Regional Standard (D064) Dobson spectrophotometer.

The Athens Dobson spectrophotometer No. 118 participated for the first time in the International Intercomparison Campaign at Arosa in Switzerland in 1990. The whole experiment was divided into two parts. In the first part, after some initial mercury and standard lamp tests, the necessary maintenance of the optical, mechanical and electronic subsystems was performed. In the second part the Dobson No. 118 was checked against the World Secondary Standard Dobson Instrument No. 065 to determine the existing calibration level. During this part both spectrophotometers made observations of total ozone at the same time, under clear-sky conditions. A part of the results of this procedure are presented in Fig. 1. In this figure are shown the differences in N values (ΔNi) for the A-C-D wavelength pairs vs. μ. The N values are calculated as: $N = \log\left[\frac{I_0}{I_0'}\right] - \log\left[\frac{I}{I'}\right]$ where I_0 and I_0' are the intensities outside the atmosphere of solar radiation at the short and long wavelengths, respectively, of the A–C–D wavelength pairs and I and I′ are the measured intensities at the ground of solar radiation at the short and long wavelengths, respectively. Parameter μ expresses the relative path length of sunlight, through the ozone layer, assumed to be 22 km. When $z = 0$ then $\mu = 1$. These

results confirm the dependence of the ΔN values by the solar zenith angle. This means that the precision of the TOZ measurements is also affected by the z and explains why the day to day measurements are taken for μ values less than 3.

The experimental results obtained from the intercomparison campaign at Arosa showed that TOZ observations made by Dobson spectrophotometer No. 118 had a deviation of 0.03% compared with TOZ observations made by the Standard Dobson No. 065, while μ ranged from 1.15 to 3.2.

The Kalavryta intercomparison (SSF/IC) of Dobson instruments consisted of the intercomparison of Dobson instruments with the World Secondary Standard Dobson Instrument No. 065. The procedure during this campaign was the same as at Arosa. According to the results of this experiment the differences between N for Dobson No. 065 and Dobson No. 118 versus μ were similar to those presented in Fig. 1. Specifically, the highest difference against the Standard Dobson (No. 065) using A-D pairs, in the μ range 1.15–3.2, was −0.4% in total ozone.

The intercomparison at the Meteorological Observatory of Hohenpeißenberg (MOHp), which acts as a European Ozone Centre including the task of a Dobson Calibration Centre, took place from 18 June to 11 July 2006. During the first phase of the campaign, new US-type electronics were installed and the shutter motor with its gear mechanism, responsible for adjusting the speed of the sector wheel, were replaced with a new motor free of the gear mechanism.

By the results of the intercomparison of D118 against the Standard Dobson spectrophotometer of this station (No. 064) was evidenced that the highest difference against the Standard Dobson No. 064 using A-D pairs, in μ range 1.15–3.2, was 0.6% in total ozone. According to the WMO, if the difference is less than 1%, then the test instrument is considered to be at the same calibration level as the Standard.

3 Comparison Between Dobson and Satellite Total Ozone Observations

In this section we present the comparison between the ground-based measurements obtained by Dobson spectrophotometer No. 118 during 1991–2011 and the observations made by the satellite-borne instruments TOMS (on board Nimbus-7 (1991–1993), ADEOS (1996–1997) and Earth Probe (1996–2005)), OMI (on board Aura, 2004-present) and SCIAMACHY (on board ENVISAT (2002-present); TOSOMI version 2.0 data) for the greater Athens area. TOMS and OMI were developed by the National Aeronautics and Space Administration (NASA) while SCIAMACHY was developed by the European Space Agency (ESA).

In Fig. 2a the TOZ measurements of the above mentioned instruments are presented. The differences between the satellite-borne observations and Dobson measurements are presented in Fig. 2b. To validate statistically the comparison between Dobson and satellite TOZ daily data, Spearman's and Wilcoxon's tests were used. The application of the Spearman's test, revealed that the correlation coefficients between Dobson and Nimbus-7, ADEOS, Earth Probe, OMI,

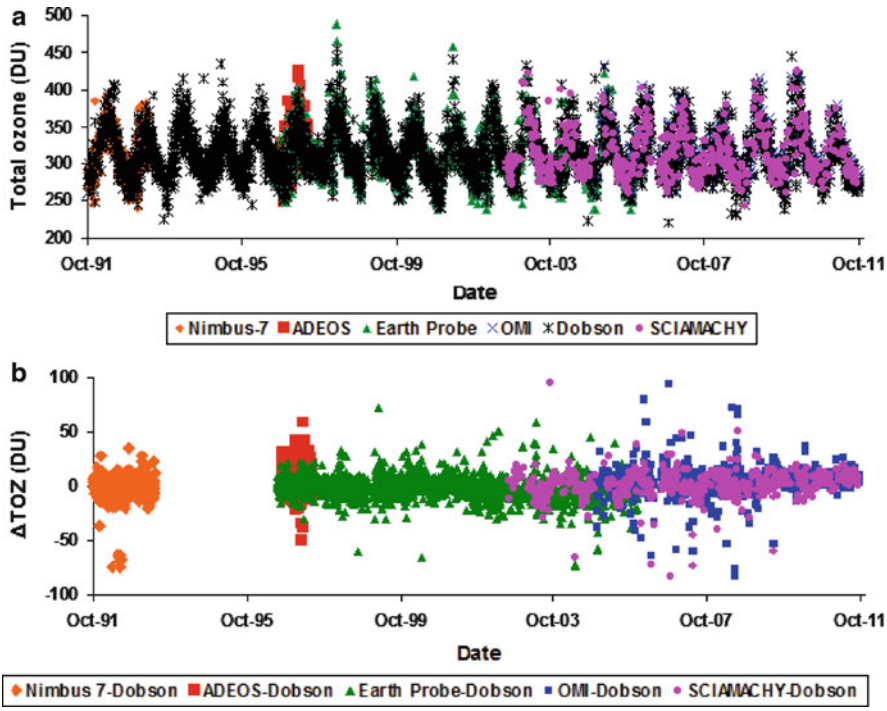

Fig. 2 (**a**) Total ozone daily observations performed by satellite-borne instruments and Dobson spectrophotometer No. 118 in Athens, Greece during 1991–2011. (**b**) The differences (ΔTOZ) between satellite and Dobson total ozone daily values in Athens, Greece during 1991–2011

SCIAMACHY TOZ data is 0.95, 0.96, 0.94, 0.92 and 0.93 (statistically significant at the 99% confidence level), respectively.

Wilcoxon's statistical test was applied to explore the deviation between the TOZ observations made by Dobson and satellite-borne instruments. The results obtained revealed that Dobson underestimates the TOZ with respect to Nimbus-7, OMI and SCIAMACHY by almost 5 DU, while with respect to Earth Probe and ADEOS by 0 and 10 DU, respectively. After removing the annual cycle by the Earth Probe observations and Dobson measurements the correlation coefficient was found to be 0.92 while the Dobson underestimates TOZ values by almost 6 DU. This means that the impact of the annual cycle on the correlation between satellite-borne observations and ground measurements is restricted.

4 Conclusions

The experimental results from the intercomparison campaigns at Arosa, Kalavryta and Hohenpeißenberg revealed that TOZ observations made by Dobson spectrophotometer No. 118 had a deviation less than 1% from the TOZ observations made

by Standard Dobson, when μ ranged from 1.15 to 3.2. Consequently, according to these results, Dobson spectrophotometer No. 118 installed at Athens, Greece, can be regarded as a reliable spectrophotometer and its measurements accurate and appropriate for further analysis.

Applying Spearman's test to the Dobson and Nimbus-7, ADEOS, Earth Probe, OMI, SCIAMACHY daily observations, it was found that the correlation coefficient ranged from 0.92 to 0.96. Application of Wilcoxon's test revealed that Dobson underestimates the total ozone with respect to satellite-borne observations by 0–10 DU. The results obtained confirm that the Athens Dobson station may be used as a ground-truth total ozone station for the validation of the satellite total ozone observations.

References

Alexandris D, Varotsos C, Kondratyev KY, Chronopoulos G (1999) On the altitude dependence of solar effective UV. Phys Chem Earth PT C 24:515–517

Chandra S, Varotsos CA (1995) Recent trends of the total column ozone: implications for the Mediterranean region. Int J Remote Sens 16:1765–1769

Christodoulakis J, Tzanis C, Varotsos C (2008) Technical report – Standardization of the Athens Dobson spectrophotometer versus reference Dobson spectrophotometer 064. Int J Remote Sens 29:1917–1920

Cracknell AP, Varotsos CA (1994) Ozone depletion over Scotland as derived from Nimbus-7 TOMS measurements. Int J Remote Sens 15:2659–2668

Cracknell AP, Varotsos CA (1995) The present status of the total ozone depletion over Greece and Scotland – A comparison between Mediterranean and more northerly latitudes. Int J Remote Sens 16:1751–1763

Dobson GMB (1957a) Observers' handbook for the ozone spectrophotometer. Ann Int Geophys Year 5:46–89

Dobson GMB (1957b) Adjustment and calibration of the ozone spectrophotometer, ibid. V, Part I. Pergamon Press, London, pp 90–113

Efstathiou MN, Varotsos CA, Singh RP, Cracknell AP, Tzanis C (2003) On the longitude dependence of total ozone trends over middle-latitudes. Int J Remote Sens 24:1361–1367

Feretis E, Theodorakopoulos P, Varotsos C, Efstathiou M, Tzanis C, Xirou T, Alexandridou N, Aggelou M (2002) On the plausible association between environmental conditions and human eye damage. Environ Sci Pollut Res 9:163–165. doi:10.1007/BF02987482

Katsambas A, Varotsos CA, Veziryianni G, Antoniou C (1997) Surface solar ultraviolet radiation: A theoretical approach of the SUVR reaching the ground in Athens, Greece. Environ Sci Pollut Res 4:69–73. doi:10.1007/BF02986280

Kondratyev KY, Varotsos CA (1996) Global total ozone dynamics – Impact on surface solar ultraviolet radiation variability and ecosystems. Environ Sci Pollut Res 3:205–209

Tzanis C (2009) Total ozone observations at Athens, Greece by satellite-borne and ground-based instrumentation. Int J Remote Sens 30:6023–6033

Tzanis C, Christodoulakis J, Efstathiou M, Varotsos C (2009) Comparison of the Athens Dobson spectrophotometer with World Standard Instruments. Int J Remote Sens 30: 3943–3950

Varotsos C (2002) The southern hemisphere ozone hole split in 2002. Environ Sci Pollut Res 9:375–376. doi:10.1007/BF02987584

Varotsos C (2005) Power-law correlations in column ozone over Antarctica. Int J Remote Sens 26:3333–3342. doi:10.1080/01431160500076111

Varotsos CA, Cracknell AP (1994) On the accuracy of total ozone measurements made with a Dobson spectrophotometer in Athens. Int J Remote Sens 15:3279–3283
Varotsos CA, Chronopoulos GJ, Katsikis S, Sakellariou NK (1995) Further evidence of the role of air-pollution on solar ultraviolet-radiation reaching the ground. Int J Remote Sens 16:1883–1886. doi:10.1080/01431169508954525
Varotsos CA, Kondratyev KY, Cracknell AP (2000) New evidence for ozone depletion over Athens, Greece. Int J Remote Sens 21: 2951–2955
Varotsos C, Ondov J, Efstathiou M (2005) Scaling properties of air pollution in Athens, Greece and Baltimore, Maryland. Atmos Environ 39:4041–4047
Zerefos CS, Bais AF, Meleti C, Ziomas IC (1995) A note on the recent increase of solar UV-B radiation over northern middle latitudes. Geophys Res Lett 22:1245–1247
Zerefos CS, Balis DS, Bais AF, Gillotay D, Simon PC, Mayer B, Seckmeyer G (1997) Variability of UV-B at four stations in Europe. Geophys Res Lett 24:1363–1366

Particulate Matter and Airborne Fungi Concentrations in Schools in Athens

P.V. Dorizas, E. Kapsanaki-Gotsi, M.N. Assimakopoulos, and M. Santamouris

Abstract Indoor Air Quality degradation is of exceptional concern due to the potential adverse effects indoor air pollutants have on human's health. Students are a susceptible group of people, who spend a lot of their time within classrooms. The purpose of this study is to investigate the concentration levels of particulate matter (PM) and total airborne fungi, in school classrooms. Further objective is to examine possible correlations between PM_{10}, $PM_{2.5}$, PM_1, ultrafine particles (UFPs, diameter <100 nm), and airborne fungi. The measurements were performed using fully automated instrumentation. The results indicate that a lot of PM_{10} concentrations exceeded the proposed daily limit of 50 $\mu g/m^3$. Also, in some cases the concentration of the total airborne fungi indoors, exceeded their concentration outdoors. There is evidence that certain correlations exist between PM and airborne fungi.

1 Introduction

In the recent years there has been a growing interest among the scientific community on the study of Indoor Air Quality (IAQ) as people spend approximately 90% of their time in indoor environments (EPA 1995a). People are largely exposed to indoor air pollutants for which there is evidence that cause adverse health effects when exceeding certain concentration thresholds. Exposures on indoor air pollutants such as UFP are linked with health effects such as asthma symptoms, allergies, respiratory and cardiovascular diseases (Pope and Dockery 2006).

P.V. Dorizas (✉) • M.N. Assimakopoulos • M. Santamouris
Department of Environmental Physics and Meteorology, University of Athens, University Campus, Athens 157 84, Greece
e-mail: pdoriza@phys.uoa.gr

E. Kapsanaki-Gotsi
Department of Ecology and Systematics, University of Athens, Athens 157 84, Greece

C.G. Helmis and P.T. Nastos (eds.), *Advances in Meteorology, Climatology and Atmospheric Physics*, Springer Atmospheric Sciences,
DOI 10.1007/978-3-642-29172-2_130,

Airborne fungi concentrations are also related to several health problems such as irritations, infections and allergies (Pongracic et al. 2010). However, there is limited number of studies in the literature concerning simultaneous measurements of PM and airborne fungi.

Children are more susceptible compared to adults due to the greater air inhaled in proportion to their body weight (EPA 1995b). Students in particular spend a considerable amount of their day time in classrooms (>6 h/day) (Silvers et al. 1994). Degraded IAQ in classrooms impacts students' performance, attendance and comfort (EPA 1995b). Thus, the quality of air inside school classrooms is of primary concern.

The present study (1) measures simultaneously concentrations of both PM and total airborne fungi in classrooms of two schools, in Athens (2) characterizes classrooms' indoor environments based on the proposed concentrations limit values by international certification bodies and (3) examines possible correlations between PM of different aerodynamic diameters and airborne fungi.

2 Measurement Methodology and Instrumentation

Two high schools from contiguous areas outside the city center of Athens were selected in order to perform the experimental campaign. The first is placed in the Kaesariani (K) urban area away from major highway and is close to a park. The second school is in the Ymittos (Y) urban area where the traffic in the adjoining streets is moderate. The measurements started in January 2011 lasted until May 2011 and were conducted once a week fortnightly in each school. Air sample was collected from eight sampling sites K1 to K8 and Y1 to Y8 for each of the two schools (K and Y respectively); one was the outdoor environment and the other seven were in classrooms as well as teachers' office. Certain classrooms were occupied by students during sampling.

Measurements of PM_{10}, $PM_{2.5}$, and PM_1 in units of $\mu g/m^3$ where performed using the OSIRIS airborne particulate monitor (Turnkey Instruments Ltd). UFPs (<100 nm in diameter) were measured using PTRAK (TSI, model 8525) in units of particles/cm^3. The sampling apparatus were placed at 0.8 m height above the floor and were synchronized to monitor with a sampling step of 1 s. The duration of each measurement per position was 10 min.

For the recovery of airborne fungi a Burkard (Burkard Manufacturing Co. Ltd. Hertfordshire, UK) portable air sampler for agar plates was used. Three plates with Malt Agar were exposed consecutively in each sampling site for 3 min/plate and then incubated for 2 weeks. The colony count was corrected and expressed as colony forming units per cubic meter CFU/m^3.

The statistical analysis was performed using SPSS 18 statistical software package as well as data analysis Microsoft Excel 2007. Average values and distributions of the measured parameters are characterized. Spearman's and Pearson correlation coefficients were calculated amongst different pollutants in order to understand the association between the measured variables. In the statistical analysis that follows, the average value of each 10 min measurement was taken into account.

3 Results

Figure 1 upper and right indicates the variation in time of PM_{10} concentrations at the two schools. Y-axis shows the average concentration per measurement, per sampling site, and X-axis shows the measurement dates. Intense fluctuations appear in some cases especially at school K (Fig. 1 upper K3, st.dev. = 46), whereas in school Y the variations are smoother (Fig. 1 lower Y3, st.dev. = 32). The monitored classrooms were naturally ventilated and the windows were kept closed

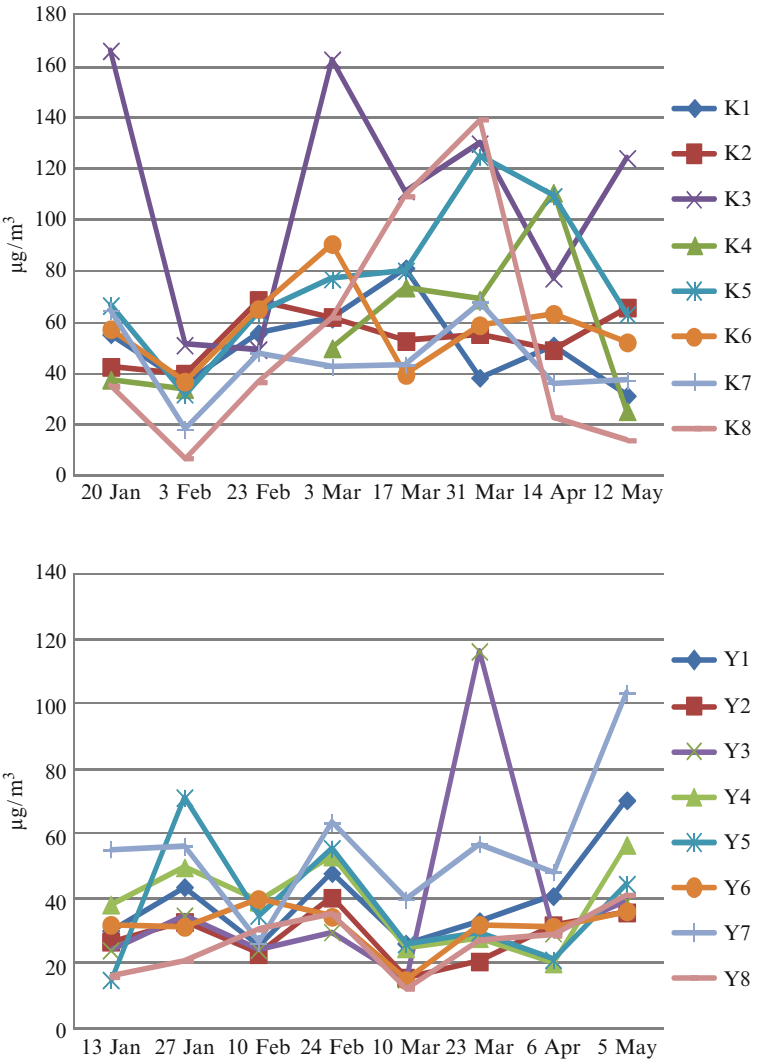

Fig. 1 PM_{10} concentration variation of school K (*upper*) and of school Y (*lower*)

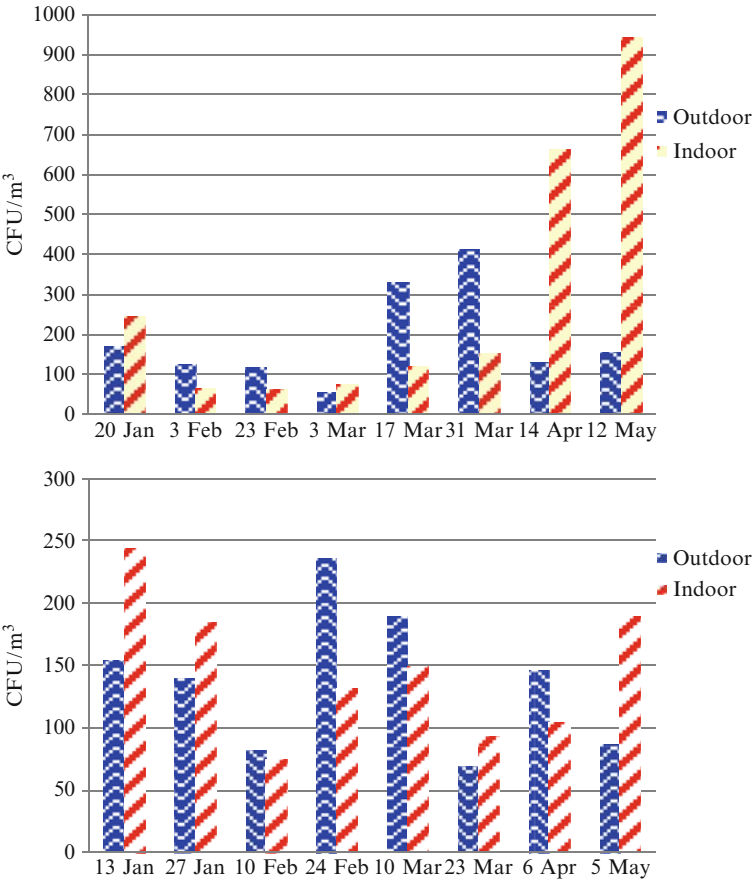

Fig. 2 Concentration of airborne fungi indoor versus outdoor in school K (*upper*) and in school Y (*lower*)

during the sampling time. Outdoor fresh air did not enter the classrooms so as to meet ventilation requirements and to remove odors and contaminants. Furthermore the increased concentrations for certain dates are possibly linked to the presence of a large number of students occupying the classrooms before or during the measurement. This could be attributed to the fact that the physical activity and presence of students may result in the resuspension of coarse particles and therefore affect their concentrations (Guo et al. 2010). However, there were cases with high concentrations but without students being present prior or during the measurement (e.g. Fig. 1 upper K3, March 3rd). Outdoor peak values at site K8 (17th and 31st of March) are due to the high relative humidity values as precipitation was observed on certain days. In addition, in these dates strong smell of smoke was detected which have also affected the concentrations. As for school Y, measurements do not fluctuate a lot (Fig. 1 lower). The exceptional peak of PM_{10} concentrations on

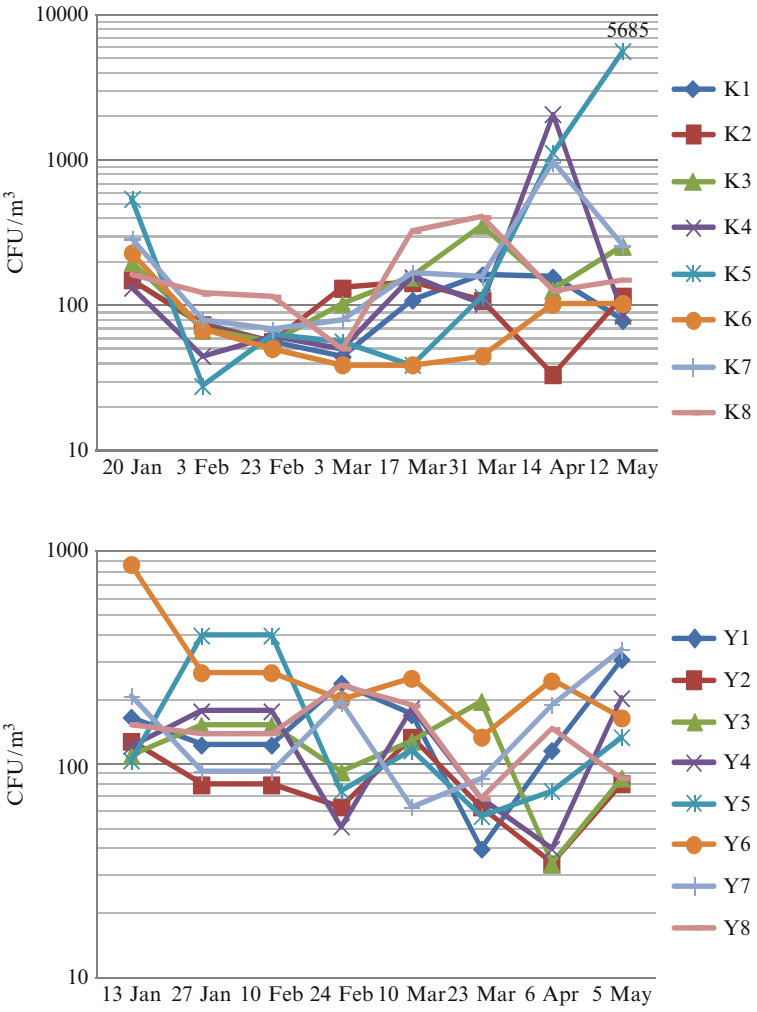

Fig. 3 Fluctuation of airborne fungi in school K (*upper*) and in school Y (*lower*)

the 23rd of March of Classroom Y3 (Fig. 1 lower) is due to the fact that this classroom was fully occupied by students that day right before the measurement, whose presence may have influenced the concentrations. It should be noted that this classroom was empty right before the rest of the measurement dates.

The percentages of the total average PM_{10} and $PM_{2.5}$ values that exceed the WHO recommended 24-h limit value of 50 and 25 μg/m^3 for school K are 60% and 5% respectively and for school Y are 17% and zero respectively.

The total concentration of the viable airborne fungi in the classrooms in each one of the schools, in several samplings is remarkably higher than that detected outdoors and this is an indication for the presence of amplification sources

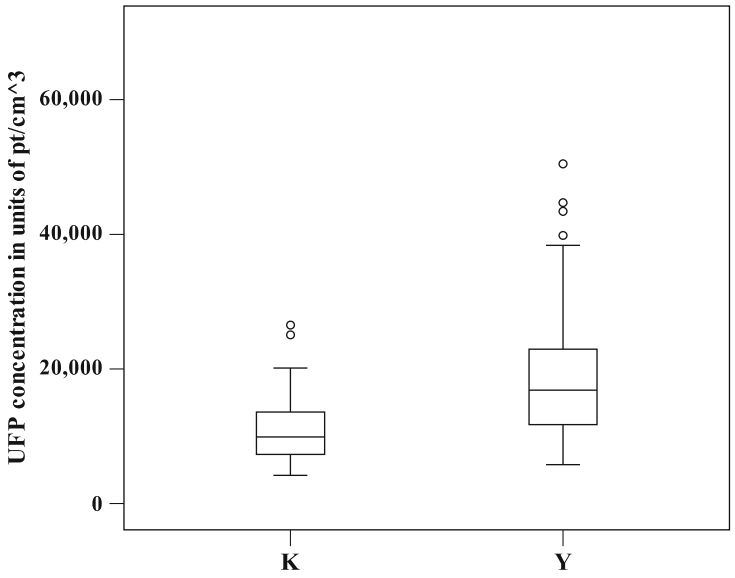

Fig. 4 UFP concentrations in particles per cubic centimeter for the two schools (K and Y)

indoors. The mean concentration of total fungi in the seven locations sampled indoors is presented versus the concentration outdoors, for the two schools (Fig. 2).

There is a spatio-temporal distribution in the concentration of fungi in the indoor air. The fungal load is presented in logarithmic scale (Fig. 3 upper and lower) in order to accommodate outliers. The concentration of fungi indoors ranged 28–548 CFU/m^3 excluding 4 extreme peaks in school K (Fig. 3 upper) and 28–402 CFU/m^3 excluding 1 extreme peak in school Y (Fig. 3 lower). There is not a universally acceptable threshold value limit for fungal concentration in relation to health impacts. It depends on several factors and mostly on the sensitivity of individuals.

Figure 4 presents the distribution of the total indoor average concentrations of UFP for the two schools in box plots. The centre line of the box is the median; the outer lines of the box represent 25th and 75th percentile and the dotted values are outliers. It can be seen that UFP concentrations in school Y are greater than the corresponding ones of school K and also present a stronger dispersion around the mean value. Vehicular emissions from the adjoining streets could have influenced the indoor concentrations of Y school. This is not consistent with the findings for school K which seemed to be mostly charged by larger particles.

As expected, from the statistical analysis that was performed it was found that PM_{10} are significantly correlated to $PM_{2.5}$ for both of the schools (Pearson correlation coefficient was approx. 0.7 at the 0.01 level for both schools). Thus, is in agreement with the findings of other research groups (Gaidajis and Angelakoglou 2009). As of the correlation between airborne fungi and PM, the statistical analysis shows that airborne fungi positively correlated to UFP for both schools. However, the correlations were weak as the correlation coefficients lie below 0.5 (0.310 and

0.356 at the 0.05 and 0.01 levels for schools K and Y respectively). It was found that PM_{10} concentrations correlated to the total fungi only in school Y (Spearman's correlation coefficient equal to 0.268 at the 0.05 level).

4 Concluding Remarks

A great percentage of the PM_{10} measurements exceeded the recommended limit values especially in school K. School K is rather surcharged from coarse particles compared to Y school. However, school Y had increased concentrations of particles in the ultrafine range. PM concentrations increased with the presence of students and smoke and were influenced by outdoor vehicle emissions. Some correlation coefficients found to be statistically significant; however, there could not be found a generalized correlation pattern for both schools. Further research should be made on the simultaneous measurements of PM and airborne fungi for longer measurement periods in order to develop a model for predicting the levels and interrelationships between PM and total airborne fungi.

Acknowledgments The authors would like to acknowledge all of the participants in the experimental campaign. In particular, we gratefully acknowledge the contribution of Antoniou Nikos, Antonopoulos George, Demertzi Marialena and Papakonstantinou Konstantinos. This research has been partly co-financed by the European Union (European Social Fund – ESF) and Greek national funds through the Operational Program "Education and Lifelong Learning" of the National Strategic Reference Framework (NSRF) – Research Funding Program: Heracleitus II. Investing in knowledge society through the European Social Funding.

References

EPA United States Environmental Protection Agency (1995) Indoor air quality tools for schools. US Environmental Protection Agency, Washington

EPA United States Environmental Protection Agency, Office of Radiation and Indoor Air, U S Consumer Product Safety Commission (1995) The inside story: a guide to indoor air quality. US Environmental Protection Agency, Office of Air and Radiation, Minnesota

Gaidajis G, Angelakoglou K (2009) Indoor air quality in university classrooms and relative environment in terms of mass concentrations of particulate matter. J Environ Sci Heal A 44:1227–1232. doi:10.1080/10934520903139936

Guo H, Morawska L, He C, Zhang YL, Ayoko G, Cao M (2010) Characterization of particle number concentrations and PM2.5 in a school: influence of outdoor air pollution on indoor air. Environ Sci Pollut Res 17:1268–1278. doi:10.1007/s11356-010-0306-2

Pongracic JA, O'Connor GT, Muilenberg ML, Vaughn B, Gold DR, Kattan M, Morgan WJ, Gruchalla RS, Smartt E, Mitchell HE (2010) Differential effects of outdoor versus indoor fungal spores on asthma morbidity in inner-city children. J Allergy Clin Immun 125:593–599. doi:10.1016/j.jaci.2009.10.036

Pope CA III, Dockery DW (2006) Health effects of fine particulate air pollution: lines that connect. J Air Waste Manage 56:709–742

Silvers A, Florence BT, Rourke DL, Lorimor RJ (1994) How children spend their time a sample survey for use in exposure and risk assessments. Risk Anal 14:931–944. doi:10.1111/j.1539-6924.1994.tb00062.x

On the SUVR Variability in Athens, Greece: An Overview

M. Efstathiou, C. Tzanis, C. Varotsos, P. Birmpakos, and M.N. Assimakopoulos

Abstract Changes in solar ultraviolet radiation (SUVR) have many different effects on global biogeochemistry. Nowadays, there is an increasing interest in the interactions and feedbacks between climate change and surface UV radiation. The amount of the UV radiation reaching the ground depends on a number of atmospheric and surface parameters such as the atmospheric ozone variability, the time of the day, the latitude, the season, the cloud cover, the meteorological conditions, the aerosol and gases concentrations. Ground-based and airborne measurements of the SUVR were carried out with various instruments in Athens, Greece to study the solar ultraviolet irradiance as a function of height and the influence of the air pollution and forest fires on the UV doses reaching the ground. Additionally, the relationship between SUVR at the Earth's surface and total ozone content during the summertime period has been investigated. To perform the above-mentioned studies a recently developed theoretical algorithm for the calculation of the UV irradiance at the Earth's surface was also employed. Finally, implications to the adverse human health effects will be discussed.

1 Introduction

The ultraviolet region of the electromagnetic spectrum emitted by the sun is very important from a biological viewpoint. The solar UV radiation reaching the Earth's surface can produce climatic, biologic and environmental effects on the humans, living organisms, plants and aquatic systems (Kondratyev and Varotsos 1996; Feretis et al. 2002). In order to study the biological effectiveness of the UV radiation, a variety of weighting functions or action spectra are often used for a

M. Efstathiou (✉) • C. Tzanis • C. Varotsos • P. Birmpakos • M. Assimakopoulos
Climate Research Group, Division of Environmental Physics and Meteorology, University of Athens, Panepistimiopoli-Zografou, Athens 15784, Greece
e-mail: efstathiou@avgouleaschool.gr

C.G. Helmis and P.T. Nastos (eds.), *Advances in Meteorology, Climatology and Atmospheric Physics*, Springer Atmospheric Sciences,
DOI 10.1007/978-3-642-29172-2_131,

specific biological or chemical effect. These weighting functions are necessary because solar UV radiation in the spectral region 290–320 nm (UV-B) increases steeply, towards longer wavelengths while the biological effectiveness often increases towards shorter wavelengths (Katsambas et al. 1997). So, different action spectra of weighted UV irradiances have different responses to atmospheric ozone changes (Cracknell and Varotsos 1994, 1995; Varotsos and Cracknell 1994).

It is also well recognized that complex relationships exist between the intensity of SUVR at the surface, the concentration of ozone in the stratosphere and troposphere, the abundance of aerosols at various altitudes and the spatio-temporal variations in cloud cover assessed in terms of fractional coverage (Varotsos et al. 1995a, b; Alexandris et al. 1999; Jacovides et al. 1994). Bruhl and Crutzen (1989) suggested that tropospheric ozone may act as a filter against SUVR, which implies that increased levels of tropospheric ozone due to photochemical reactions may compensate the increase in the amount of SUVR due to the ozone depletion at higher altitudes.

The current analysis attempts to present an overview of our researches on UV. In this respect we study the interaction between photochemical pollution and SUVR reaching the tropopause and the Earth's surface. In addition, a direct comparison of the erythemally effective UV irradiance (EUVI) observations reaching an urban and a suburban station is performed and the results are discussed by employing the parameters of the total reflectivity coefficient and photochemical air pollution. Additionally, the examination of the vertical gradient of the biological effective UV radiation from the sea level up to 5 km over Greece, is attempted. Finally, bearing the above in mind, the present study further investigates the correlation between the SUVR and the air quality that in its turn is further related with an intense forest fire.

2 Data and Methodology

The present study examines the amount of the UV radiation reaching the ground, based on SUVR measurements obtained from the UVB-1 pyranometer installed on the roof of the building of the University of Athens near the centre of Athens, Greece (Panepistimiopolis – 37.59°N, 23.44°E) as well as an automatic measurement system, the UV-501 Biometer (S/N 1915) installed at Penteli (another station located in the northern part of Athens). The UVB-1 pyranometer is a rugged instrument which measures both light transmitted directly through the atmosphere and light scattered by atmospheric gases and particulate matter in the atmosphere. As far as the UV-Biometer is concerned, this is a broad-band radiometer with a spectral response following the erythema action spectrum with the same principle as that for the Robertson–Berger meter.

Measurements of surface ozone concentration over the period 1993–2006, taken at monitoring stations of the National Air Pollution Monitoring Network located in the greater Athens area (Patision, Marousi and Panepistimiopolis), were also used.

Solar ultraviolet radiation was also measured by the Total Ultraviolet Radiometer (TUVR) which was also installed on the roof of the building of the University of Athens (Panepistimiopolis).

Radiometric data were also obtained in Greece, during the experimental campaign of the project entitled Radiation Field in the Troposphere (RAFT), in the framework of the EU project which is called Scientific Training and Access to Aircraft for Atmospheric Research Throughout Europe (STAAARTE). This campaign took place from 7 to 14 June 1997 and covered a large part of Greek territory. The research aircraft used in STAAARTE-RAFT was a Falcon 20-E5, D-CMET from DLR (German Aerospace Research Establishment).

Theoretical UV calculations were also made by using the UV-CALC program at the Laboratory of Upper Air, University of Athens and reflectivity coefficient data were collected by the Total Ozone Mapping Spectrometer (TOMS) flown on the Earth Probe satellite over Athens.

3 Discussion and Results

Figure 1 presents the comparison of the seasonal variation of EUVI values at the Penteli station with that at the Panepistimiopolis station, during the cloudless days of 1 March 2002 to 2020 September 2002.

By using the Wilcoxon test, the EUVI difference between Penteli and Panepistimiopolis (dEUV) was estimated to be 0.016 Wm^{-2} (Fig. 1a). That difference seems to be justified partly by the total reflectivity coefficient and partly by the increased concentration of the surface ozone (SOZ) at the Panepistimiopolis station. Over and above, a multiple regression was applied to the data of dEUV (between Penteli and Panepistimiopolis) and the data of SOZ and reflectivity. It was established that there is a significant anti-correlation (at 95% confidence level) only between dEUV

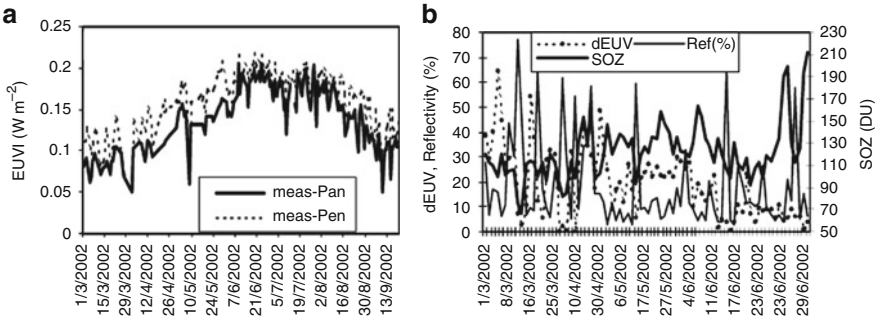

Fig. 1 (**a**) Comparison of the EUVI measured values between Penteli and Panepistimiopolis stations, for the cloudless days during 1 March 2002–20 September 2002. (**b**) The difference in EUVI values between Penteli and Panepistimiopolis and the corresponding contribution of the SOZ at the Panepistimiopolis station and the reflectivity coefficient

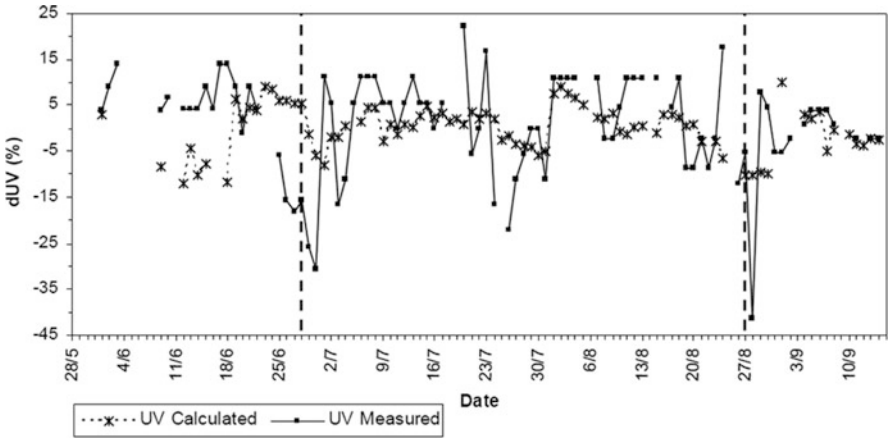

Fig. 2 Comparison of dUV (%) calculated values (From UV-CALC model at 280–320 nm) and the measured ones (Derived from Total Ultraviolet Radiometer at 295–385 nm), at local noon during 1 June 2007–14 September 2007, over Athens, Greece. The *dashed lines* correspond to the days when the two fires took place

and reflectivity coefficient and not between dEUV and SOZ (Efstathiou et al. 2005). In addition, the strength of the dEUV over some periods seems to be due to the mutual contribution of the SOZ of Panepistimiopolis and the reflectivity coefficient (Fig. 1b).

In the summer 2007, two forest fires took place in the greater Athens area. Figure 2 shows the march of the percentage deviation of the noontime UV values from the mean monthly noontime UV values during the period from June to September 2007, measured with the TUVR at the Panepistimiopolis station, as well as the calculated ones (UV-CALC program). According to Fig. 2, a downward shift in UV is observed for a few days after the date when the fires broke out (28 June 2007 and 27 August 2007). The observed variation between measured and calculated UV values is attributed to the fact that SUVR is filtered most probably by air pollution. The concentrations of various air pollutants like carbon monoxide, nitrogen oxides and ozone as well as aerosol density largely increase during the forest fire event. These parameters provide strong filtering of the solar UV radiation (Tzanis et al. 2009).

During the experimental campaign of the project entitled RAFT, radiometric data were also obtained in Greece. This campaign, as mentioned above, took place from 7 to 14 June 1997 and covered a large part of Greek territory. On 13 June 1997 the aircraft was flown over the greater city area of Athens (37.8°N). The measurements were taken during the ascent from 24 to 4,900 m and in the time interval from 11:07 to 12:26 UTC. The vertical gradient of the effective UV was 9.5% per km and the results are shown in Fig. 3a (Varotsos et al. 2001).

On 13 June 1997, at same time when measurements of the effective UV radiation were taken over the greater city area of Athens, ozonesondes were launched from the Athens ozonesounding station. The relation of the effective UV radiation and

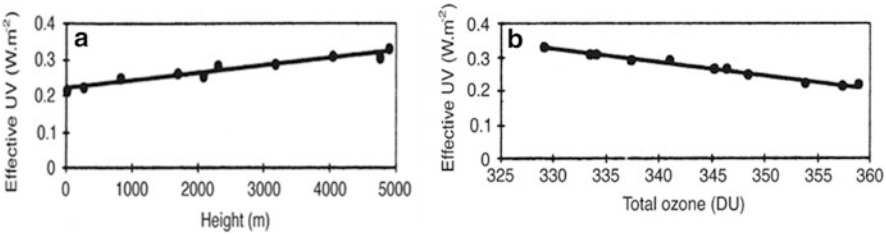

Fig. 3 (**a**) Variation of effective UV radiation with height, for 13 June 1997, (**b**) effective UV radiation and the integrated ozone content above each height level, for 13 June 1997

the integrated ozone content above each height level is shown in Fig. 3b. This analysis covered the height range from ground level up to 5,000 m and showed strong anti-correlation between the effective UV radiation and the overhead integrated ozone content (Varotsos et al. 2000). From the above analysis it appears that there exists a strong anti-correlation between the biologically effective UV radiation and the total ozone content above the measurement height level. The R^2 value of the linear regression is 0.98, while the relationship between ozone and UV becomes exponential for larger ozone values (Madronich et al. 1998). Schmucki and Philipona (2002) studying the altitude effect in the UV radiation field over Alps discussed the seasonal variations of the altitude effect, mainly influenced by changes of solar elevation, albedo values, turbidity levels and the Rayleigh scattering on UV.

4 Conclusions

The main conclusions deduced from the above-mentioned discussion are the following:

1. Comparing the seasonal variation of EUVI values at the Penteli station with that at the Panepistimiopolis station, during 1 March 2002–20 September 2002, it was found that the almost constant difference in EUVI values could probably be justified partly by the change in the total reflectivity coefficient and partly by the increased concentration of the surface ozone at the Panepistimiopolis station.
2. A decrease in UV irradiation was observed for a few days after the date when two forest fires broke out in the greater Athens area, during the summer 2007. This decrease seemed to be attributed to the air pollution filtering.
3. During the fifth day of the experimental campaign of the RAFT project, the obtained measurements showed a vertical gradient of the effective UV of 9.5% per km. On the same day and at same time ozonesondes were launched from the Athens ozonesounding station and the measurements showed a strong anti-correlation between the effective UV radiation and the overhead integrated ozone content, covering the height range from ground level up to 5,000 m.

References

Alexandris D, Varotsos C, Kondratyev KY, Chronopoulos G (1999) On the altitude dependence of solar effective UV. Phys Chem Earth PT C 24:515–517

Bruhl C, Crutzen PJ (1989) On the disproportionate role of the tropospheric ozone as a filter against solar UV-B radiation. Geophys Res Lett 16:703–706. doi:10.1029/GL016i007p00703

Cracknell AP, Varotsos CA (1994) Ozone depletion over Scotland as derived from Nimbus-7 TOMS measurements. Int J Remote Sens 15:2659–2668. doi:10.1080/01431169408954273

Cracknell AP, Varotsos CA (1995) The present status of the total ozone depletion over Greece and Scotland - A comparison between Mediterranean and more northerly latitudes. Int J Remote Sens 16:1751–1763. doi:10.1080/01431169508954515

Efstathiou MN, Feretis H, Tzanis C, Christodoulakis J (2005) Observed association between air pollution and the biologically effective solar ultraviolet irradiance. Int J Remote Sens 26:3487–3495. doi:10.1080/01431160500076566

Feretis E, Theodorakopoulos P, Varotsos C, Efstathiou M, Tzanis C, Xirou T, Alexandridou N, Aggelou M (2002) On the plausible association between environmental conditions and human eye damage. Environ Sci Pollut R 9:163–165. doi:10.1007/BF02987482

Jacovides CP, Varotsos C, Kaltsounides NA, Petrakis M, Lalas DP (1994) Atmospheric turbidity parameters in the highly polluted site of Athens basin. Renew Energy 4:465–470

Katsambas A, Varotsos CA, Veziryianni G, Antoniou C (1997) Surface solar ultraviolet radiation: a theoretical approach of the SUVR reaching the ground in Athens, Greece. Environ Sci Pollut R 4:69–73

Kondratyev KY, Varotsos CA (1996) Global total ozone dynamics – impact on surface solar ultraviolet radiation variability and ecosystems. Environ Sci Pollut R 3:205–209

Madronich S, McKenzie RL, Bjorn LO, Caldwell MM (1998) Changes in biologically active ultraviolet radiation reaching the Earth's surface. J Photochem Photobiol B 46:5–19

Schmucki DA, Philipona R (2002) Ultraviolet radiation in the Alps: the altitude effect. Opt Eng 41:3090–3095. doi:10.1117/1.1516820

Tzanis C, Tsivola E, Efstathiou M, Varotsos C (2009) Forest fires pollution impact on the solar UV irradiance at the ground. Fresen Environ Bull 18:2151–2158

Varotsos CA, Cracknell AP (1994) On the accuracy of total ozone measurements made with a Dobson spectrophotometer in Athens. Int J Remote Sens 15:3279–3283. doi:10.1080/01431169408954327

Varotsos CA, Chronopoulos GJ, Katsikis S, Sakellariou NK (1995a) Further evidence of the role of air-pollution on solar ultraviolet-radiation reaching the ground. Int J Remote Sens 16:1883–1886. doi:10.1080/01431169508954525

Varotsos C, Kondratyev KY, Katsikis S (1995b) On the relationship between total ozone and solar ultraviolet radiation at St Petersburg, Russia. Geophys Res Lett 22:3481–3484. doi:10.1029/95GL03172

Varotsos C, Kondratyev KY, AlexandrisD CG (2000) Aircraft observations of the vertical gradient of biologically effective ultraviolet radiation. Rad Prot Dos 91:161–163

Varotsos C, Alexandris D, Chronopoulos G, Tzanis C (2001) Aircraft observations of the solar ultraviolet irradiance throughout the troposphere. J Geophys Res-Atmos 106:14843–14854. doi:10.1029/2001JD900045

Comparison of Ozone Variations from Model Calculations (OsloCTM2) and Satellite Retrievals (SBUV)

K. Eleftheratos, I.S.A. Isaksen, C.S. Zerefos, K. Tourpali, and P.T. Nastos

Abstract In this study we analyse temporal and spatial variations of columnar ozone amounts over the northern and southern hemispheres, and calculate the correlation coefficients between total ozone and the equatorial zonal winds at 30 and 50 hPa, which were used as indices to study the impact of the Quasi-Biennial Oscillation (QBO) on ozone. Monthly mean total ozone amounts derived from improved chemical transport model simulations (OsloCTM2), were used to compute monthly zonal means over 10° latitude zones for the period 1998–2009, and compared with respective solar backscatter ultra-violet (SBUV) satellite observations over the northern and southern hemispheres. The correlations between ozone variations from the OsloCtm2 model calculations, ozone from SBUV satellite retrievals and the QBO are presented for the northern, tropical and southern latitudes.

K. Eleftheratos (✉)
Laboratory of Climatology & Atmospheric Environment, N.K.U.A, Athens, Greece

Atmospheric Environment Division, Biomedical Research Foundation of the Academy of Athens, Athens, Greece
e-mail: kelef@geol.uoa.gr

I.S.A. Isaksen
Department of Geophysics, University of Oslo, Oslo, Norway

C.S. Zerefos
Laboratory of Climatology & Atmospheric Environment, N.K.U.A, Athens, Greece

Atmospheric Environment Division, Biomedical Research Foundation of the Academy of Athens, Athens, Greece

Navarino Environmental Observatory (N.E.O.), Messinia, Greece

K. Tourpali
Laboratory of Atmospheric Physics, Department of Physics, Aristotle University of Thessaloniki, Thessaloniki, Greece

P.T. Nastos
Laboratory of Climatology & Atmospheric Environment, N.K.U.A, Athens, Greece

C.G. Helmis and P.T. Nastos (eds.), *Advances in Meteorology, Climatology and Atmospheric Physics*, Springer Atmospheric Sciences,
DOI 10.1007/978-3-642-29172-2_132,

1 Introduction

Ozone is an important constituent of the earth's atmosphere between 10 and 50 km height. It absorbs ultraviolet radiation from the sun, and protects the biosphere from harmful effects of ultraviolet radiation. Ozone column amounts in the atmosphere can be obtained from surface measurements and satellite observations (e.g., Zerefos 1997; Chipperfield et al. 2007), and can be calculated by chemistry-climate and chemistry-transport models (e.g., Eyring et al. 2006; Stolarski et al. 2006; Søvde et al. 2008). The ability of models to reproduce the observed atmosphere comes from the key physical and chemical processes included in the models. Today models are being improved to include comprehensive chemistry and physics of both the troposphere and the stratosphere, as has been done for the Oslo chemical transport model (CTM2). The updated version with improved microphysics and heterogeneous chemistry, and the extension of vertical layers to 60 has improved the capability to predict the distribution of ozone and precursors in the UTLS region, in the upper stratospheric region and in the troposphere (Søvde et al. 2008).

A recent study by Eleftheratos et al. (2011) provided additional evidence of improved simulations in total ozone columns by the updated Oslo CTM2 model. This has been achieved through a comparison of monthly mean, seasonal mean and annual mean total ozone, from the improved simulations for the period 2001–2007, with respective total ozone averages from SBUV satellite data. Here, we extend the period of record from 1998 to 2009 that includes several QBO cycles and examine whether ozone variations from improved Oslo CTM2 model simulations reproduce the well-known perturbation (QBO). Then we compare our results with respective SBUV satellite retrievals to test the consistency of the model calculations.

2 Data and Methodology

2.1 Oslo CTM2 Model

The Oslo CTM2 is a global off-line chemical transport model, driven by meteorological data from the European Centre for Medium-Range Weather Forecasts (ECMWF) Integrated Forecast System (IFS) model. In the IFS forecasts a spectral resolution of T319 is applied (T319 is approximately $0.5^\circ \times 0.5^\circ$ grid resolution, longitude/latitude, with 60 vertical layers). The horizontal resolution of the Oslo CTM2 can be varied between T21 (resolution of $5.6^\circ \times 5.6^\circ$, longitude/latitude), T42 ($2.8^\circ \times 2.8^\circ$), T63 ($1.9^\circ \times 1.9^\circ$) and $1^\circ \times 1^\circ$, into which the IFS spectral fields are truncated. The IFS data, available as gridded data, are averaged into the model grid. Here the T42 ($2.8^\circ \times 2.8^\circ$) horizontal resolution of Oslo CTM2 was used to calculate averages over 10° latitude zones.

The Oslo CTM2 has previously been applied in model/model comparisons and tested against observations (e.g., Isaksen et al. 1990, 2005; Gauss et al. 2003;

Andresen et al. 2006). The global chemical transport model Oslo CTM2 has been evaluated against measurements by satellite-based instruments, ozone sondes and aircraft (Søvde et al. 2008). All reactions and species in the Oslo CTM2 are described in detail in the study by Søvde et al. (2008). Further details can be also found in the study by Eleftheratos et al. (2011). The model was recently used to investigate the observed record ozone decline over the Arctic during wither/spring 2011 (Balis et al. 2011).

2.2 SBUV Satellite Data

The ozone satellite data used in this study come from the Solar Backscatter UltraViolet Instrument (SBUV/2) for the period 1998–2009. The SBUV/2 satellite data used here have been reprocessed with the version 8 algorithm and are available at http://www.cpc.ncep.noaa.gov/products/stratosphere/sbuv2to. The data are available as column ozone in Dobson Units (DU) for 13 layers. Details can be found in the study by Bhartia et al. (2004). Results of SBUV/2 ozone profile comparisons with other data sources are discussed by Petropavlovskikh et al. (2005), Nazaryan and McCormick (2005), Fioletov et al. (2006), and Terao and Logan (2007). In this study, total ozone was calculated by summing the profile ozone data for all 13 layers.

3 Results

Total ozone data from the Oslo CTM2 have been compared with the satellite SBUV data using linear regression analysis. Model and satellite total ozone data were used to compute monthly zonal means per 10° latitude zones. The time series obtained have been prewhitened to remove the annual cycle by subtracting from each month the long-term monthly mean of the 12 year period of record. The comparison of model calculations with satellite retrievals was performed using the obtained deseasonalized time series for the period 1998–2009. Figure 1 shows the total ozone anomalies (in per cent of the mean) from Oslo CTM2 model calculations and SBUV satellite retrievals averaged for the latitude zones of 10–60°N, 10°N–10°S, and 10–60°S. The correlation coefficients between the two data sets are presented in Table 1.

As can be seen from Fig. 1, there is a very good agreement between the Oslo CTM2 model and SBUV satellite ozone anomalies throughout the whole period of record. The correlation coefficients are highly significant over all latitude zones (Table 1). The dotted line in the middle of Fig. 1 shows the variations of zonal winds from over the equator at 30 and 50 hPa, which were used as indices of the QBO. The QBO indices were obtained by the Climate Prediction Centre of NOAA at http://www.cpc.ncep.noaa.gov/data/indices/. The general features of the QBO in

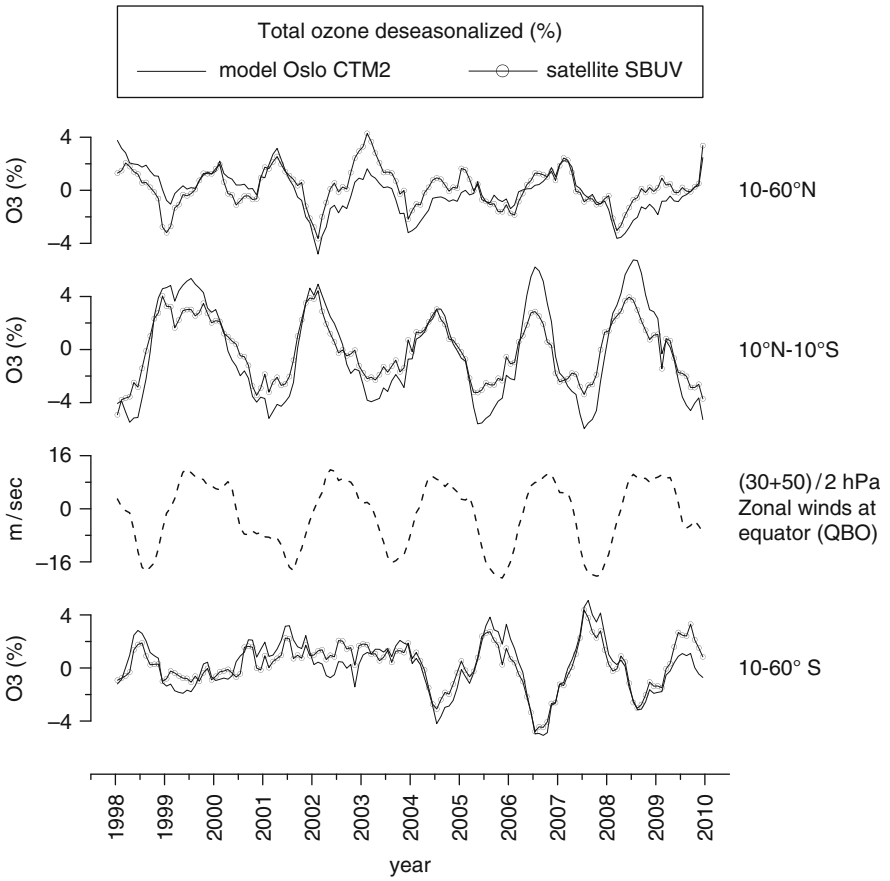

Fig. 1 Comparison between deseasonalized ozone anomalies (in %) from Oslo CTM2 model calculations (*solid line*) and SBUV satellite data (*circles*) for the period 1998–2009. The *dotted line* shows the zonal winds at equator at 30 and 50 hPa (in m/s) (QBO)

Table 1 Correlation coefficients between total ozone anomalies from Oslo CTM2 model calculations and SBUV satellite retrievals

	Correlation[a]	Number of data	Statistical significance (p-value)
10–60°N	+0.73	144	<0.0001
10°N–10°S	+0.95	144	<0.0001
10–60°S	+0.89	144	<0.0001

[a]Based on deseasonalized monthly data for the period 1998–2009

total ozone has been examined in a several studies dating back to 1964 (e.g. Zerefos 1983 and references therein). They include a QBO in total ozone at the equator (between 5° N and 5° S) which is nearly in-phase with the QBO in 50 mb temperature. The out-of-phase relation between the equatorial QBO and the middle latitude QBO is also seen in both hemispheres (Zerefos 1983). These features are evident in both OsloCTM2 model and SBUV satellite data sets.

4 Conclusions

This study analysed monthly averaged total ozone amounts from improved Oslo CTM2 model simulations for the period 1998–2009, and compared them with respective total ozone columns from SBUV satellite data. Total ozone columns from improved Oslo CTM2 model calculations compared well with the satellite data and the differences were within ±2%. Comparison of monthly mean total ozone anomalies from the model with satellite retrievals using linear regression analysis, showed statistically significant correlation coefficients between the two data sets at all latitude zones (correlations of +0.95 between 10°N and 10°S, +0.73 over 10–60°N, and +0.89 over 10–60°S). Correlations between modelled ozone and the QBO were found to be the order of +0.7 in the tropics. The impact of QBO was most pronounced at equatorial latitudes with amplitudes of +4% to –4%.

In summary, model results reproduced global observed ozone column well. Multiyear analysis gave good agreement between modelled and satellite-derived ozone column variations, and also revealed large scale impact of the QBO on the ozone column. These findings provide significant level of confidence when studying short and longer-term variations of ozone columns with the Oslo CTM2 model.

Acknowledgments The Navarino Environmental Observatory (N.E.O.), Messinia, Greece, and the SYNERGASIA 2009 PROGRAMME (Project code:09ΣΥΝ-31-867). Also, the FP6 EU projects SCOUT-O3 and QUANTIFY, the Network of Excellence ECATS, and the national project of NKUA-SARG Kapodistrias 2008–2009.

References

Andersen SB, Weatherhead EC, Stevermer A, Austin J, Brühl C, Fleming EL, de Grandpré J, Grewe V, Isaksen I, Pitari G, Portmann RW, Rognerud B, Rosenfield JE, Smyshlyaev S, Nagashima T, Velders GJM, Weisenstein DK, Xia J (2006) Comparison of recent modelled and observed trends in total column ozone. J Geophys Res 111:D02303. doi:10.1029/2005JD006091

Balis D, Isaksen ISA, Zerefos C, Zyrichidou I, Eleftheratos K, Tourpali K, Bojkov R, Rognerud B, Stordal F, Søvde OA, Orsolini Y (2011) Observed and modelled record ozone decline over the Arctic during winter/spring 2011. Geophys Res Lett 38:L23801. doi:10.1029/2011GL049259

Bhartia PK, Wellemeyer CG, Taylor SL, Nath N, Gopolan A (2004) Solar Backscatter Ultraviolet (SBUV) version 8 profile algorithm. In: Zerefos CS (ed) Ozone vol I, Proceedings of the XX quadrennial ozone symposium, 1–8 Jun 2004. Kos, pp 295–296

Chipperfield MP, Fioletov, VE (Lead Authors), Bregman B, Burrows J, Connor BJ, Haigh JD, Harris NRP, Hauchecorne A, Hood LL, Kawa, SR, Krzyscin, JW, Logan JA, Muthama NJ, Polvani L, Randel WJ, Sasaki T, Staehelin J, Stolarski RS, Thomason LW, Zawodny JM (2007) Global ozone: past and present, chapter 4. In: Scientific assessment of ozone depletion: 2006. Global ozone research and monitoring project, report no. 50. World Meteorological Organization, Geneva, pp 1–572

Eleftheratos K, Zerefos CS, Gerasopoulos E, Isaksen ISA, Rognerud B, Dalsoren S, Varotsos C (2011) A note on the comparison between total ozone from Oslo CTM2 ans SBUV satellite data. Int J Remote Sens 32:2535–2545. doi:10.1080/01431161003698401

Eyring V, Butchart N, Waugh DW, Akiyoshi H, Austin J et al (2006) Assessment of temperature, trace species, and ozone in chemistry climate model simulations of the recent past. J Geophys Res 111:D22308. doi:10.1029/2006JD007327

Fioletov VE, Tarasick DW, Petropavlovskikh I (2006) Estimating ozone variability and instrument uncertainties from SBUV(/2), ozonesonde, Umkehr, and SAGE II measurements: short-term variations. J Geophys Res 111:D02305. doi:10.1029/2005JD006340

Gauss M, Isaksen ISA, Wong S, Wang WC (2003) Impact of H2O emissions from cryoplanes and kerosene aircraft on the atmosphere. J Geophys Res 108:4304, doi:10.1029/2002JD002623

Isaksen ISA, Rognerud B, Stordal F, Coffey MT, Mankin WG (1990) Studies of Arctic stratospheric ozone in a 2-D model including some effects of zonal asymmetries. Geophys Res Lett 17:557–560. doi:10.1029/GL017i004p00557 DOI:dx.doi.org

Isaksen ISA, Zerefos C, Kourtidis K, Meleti C, Dalsøren SB, Sundet JK, Grini A, Zanis P, Balis D (2005) Tropospheric ozone changes at unpolluted and semipolluted regions induced by stratospheric ozone changes. J Geophys Res 110:D02302. doi:10.1029/2004JD004618

Nazaryan H, McCormick MP (2005) Comparisons of Stratospheric Aerosol and Gas Experiment (SAGE II) and Solar Backscatter Ultraviolet Instrument (SBUV/2) ozone profiles and trend estimates. J Geophys Res 110:D17302. doi:10.1029/2004JD005483

Petropavlovskikh I, Ahn C, Bhartia PK, Flynn LE (2005) Comparison and covalidation of ozone anomalies and variability observed in SBUV(/2) and Umkehr northern midlatitude ozone profile estimates. Geophys Res Lett 32:L06805. doi:10.1029/2004GL022002

Søvde OA, Gauss M, Smyshlyaev SP, Isaksen ISA (2008) Evaluation of the chemical transport model Oslo CTM2 with focus on arctic winter ozone depletion. J Geophys Res 113:D09304. doi:10.1029/2007JD009240

Stolarski RS, Douglass AR, Steenrod S, Pawson S (2006) Trends in stratospheric ozone: lessons learned from a 3D chemical transport model. J Atmos Sci 63:1028–1041

Terao Y, Logan JA (2007) Consistency of time series and trends of stratospheric ozone as seen by ozonesonde, SAGE II, HALOE, and SBUV(/2). J Geophys Res 112:D06310. doi:10.1029/2006JD007667

Zerefos CS (1983) On the quasi-biennial oscillation in stratospheric temperatures and total ozone. Adv Space Res 2:177–181

Zerefos CS (1997) Trends in stratospheric and tropospheric ozone. J Geophys Res 102:1571–1590

Simulating Ultrafine Particle Formation in Europe Using a Regional CTM: Contribution of Primary Emissions Versus Secondary Formation to Aerosol Number Concentrations

C. Fountoukis, I. Riipinen, H. Denier van der Gon, P.E. Charalampidis, C. Pilinis, and S.N. Pandis

Abstract A three-dimensional regional chemical transport model (CTM) with detailed aerosol microphysics, PMCAMx-UF, was applied to the European domain to simulate the contribution of direct emissions and secondary formation to total particle number concentrations. The model predicts nucleation events that occur over scales of hundreds up to thousands of kilometers especially in the Balkans and Southeast Europe. The model reproduces more than 70% of the hourly concentrations of particles larger than 10 nm (N_{10}) within a factor of 2. About half of these particles are predicted to originate from nucleation in the lower troposphere. Regional nucleation is predicted to increase the total particle number concentration by approximately a factor of 3. For particles larger than 100 nm the effect varies from an increase of 20% in the eastern Mediterranean to a decrease of

C. Fountoukis (✉)
Institute of Chemical Engineering and High Temperature Chemical Processes, Foundation for Research and Technology Hellas (FORTH), Patras, Greece
e-mail: cfountoukis@iceht.forth.gr

I. Riipinen
Department of Applied Environmental Science and Bert Bolin Centre for Climate Research, Stockholm University, Stockholm SE-11418, Sweden

H.D. van der Gon
TNO Built Environment and Geosciences, Princetonlaan 6, 3584 CB Utrecht, The Netherlands

P.E. Charalampidis • C. Pilinis
Department of Environment, University of the Aegean, University Hill, Mytilene 81100, Greece

S.N. Pandis
Institute of Chemical Engineering and High Temperature Chemical Processes, Foundation for Research and Technology Hellas (FORTH), Patras, Greece

Department of Chemical Engineering, Carnegie Mellon University, Pittsburgh, PA 15213, USA

Department of Chemical Engineering, University of Patras, Patras, Greece

C.G. Helmis and P.T. Nastos (eds.), *Advances in Meteorology, Climatology and Atmospheric Physics*, Springer Atmospheric Sciences,
DOI 10.1007/978-3-642-29172-2_133,

20% in southern Spain and Portugal resulting in a small average increase of around 1% over the whole domain. Nucleation has a significant effect in the predicted N_{50} levels mainly in areas where there are condensable vapors to grow the particles to larger sizes. A semi-empirical ternary sulfuric acid-ammonia-water parameterization performs better than the activation or the kinetic parameterizations in reproducing the observations.

1 Introduction

Aerosol nucleation is potentially important for the climate of our planet because the newly formed particles can grow through condensation of vapors (e.g., sulfuric acid and ammonia, organics) from a few nanometers up to cloud condensation nuclei (CCN)-relevant particle sizes of ~100 nm or more influencing the formation and properties of clouds. Nucleation also enhances atmospheric levels of ultrafine particles (those with diameter less than 100 nm) which are highly mobile within the human body and may be especially harmful to human health. Despite its importance, our understanding of the processes of formation and growth of atmospheric nanoparticles is currently limited mainly due to the ambiguous role of atmospheric species other than H_2SO_4 that could potentially control the frequency and rate of new particle formation events in the lower troposphere and contribute to aerosol growth. Proposed nucleation mechanisms differ in terms of which gas-phase species aid H_2SO_4 in forming the critical cluster. Recently, a strong correlation was found between measured aerosol nucleation rate and the gas-phase sulfuric acid concentration.

There have been a number of efforts in modeling new particle formation and growth on a large scale. Trivitayanurak et al. (2008) used a global model with detailed aerosol microphysics (GEOS-CHEM/TOMAS) to simulate the aerosol number concentration and found errors in N_{10} of 40–50% between 15°S and 45°S and between 45°N and 60°N highlighting the need for improved emission inventories. Jung et al. (2010) simulated in-situ ultrafine particle formation in the sulfate rich area of the Eastern United States and conducted a detailed comparison with data from the Pittsburgh air quality study. They found good agreement for particle number concentrations above 3 nm, however they stressed the need for more measurement data representative of different environments, and testing of more nucleation parameterizations. If the grid scale is large (e.g. on the order of 300 km which is usually the scale of a global model) the model has difficulties in tracking changes in the emitted particle number concentration and size distribution appropriately which could cause large uncertainty in its predictions. Regional-scale models are more suited for this task.

2 PMCAMx-UF Description

PMCAMx-UF is a newly developed (Jung et al. 2010) three-dimensional chemical transport model that simulates the aerosol number size distribution, in addition to the mass/composition size distribution. For the simulation of aerosol microphysics, PMCAMx-UF uses the DMAN model of Jung et al. (2006) which simulates the processes of coagulation, condensation/evaporation, emissions, and nucleation assuming that the aerosol is internally mixed. DMAN uses the Two-Moment Aerosol Sectional (TOMAS) algorithm of Adams and Seinfeld (2002) in which a sectional approach is used to track both aerosol number and mass. The aerosol size distribution is discretized in 41 sections covering the diameter range from 0.8 nm to 10 μm.

Three nucleation theories are tested along with their corresponding parameterizations for the simulation of new particle formation. The base case nucleation mechanism used here is based on the ternary H_2SO_4-NH_3-H_2O nucleation parameterization of Napari et al. (2002). The activation approach is also tested, in which the particle formation rate is proportional to the gas phase sulfuric acid concentration:

$$J_{act} = A[H_2SO_4]$$

where J_{act} is the formation rate ($cm^{-3}\ s^{-1}$) of stable clusters and A is a nucleation rate coefficient (s^{-1}). The value of A varies both spatially and temporally for reasons which are not well understood to date. Finally, the kinetic approach is also used, which is based on a square dependence of the new particle formation rate on the sulfuric acid concentration (Kulmala et al. 2006):

$$J_{kin} = k[H_2SO_4]^2$$

3 Model Predictions over Europe

The PMCAMx-UF modeling domain covers a 5,400 × 5,832 km^2 region in Europe with 36 × 36 km grid resolution and 14 vertical layers covering approximately 6 km. PMCAMx-UF was set to perform simulations on a rotated polar stereographic map projection. During May 2008 an intensive campaign of particle number size distribution measurements was performed in Europe. The model results are compared against hourly mean values from 7 measurement ground sites in Aspvreten, Cabauw, Hyytiala, Ispra, Mace Head, Melpitz and Vavihill. Particle size distribution measurements in all the sites were made using either a Differential Mobility Particle Sizer (DMPS) or a Scanning Mobility Particle Sizer (SMPS), both classifying particles above 10 nm in diameter. A simulation with

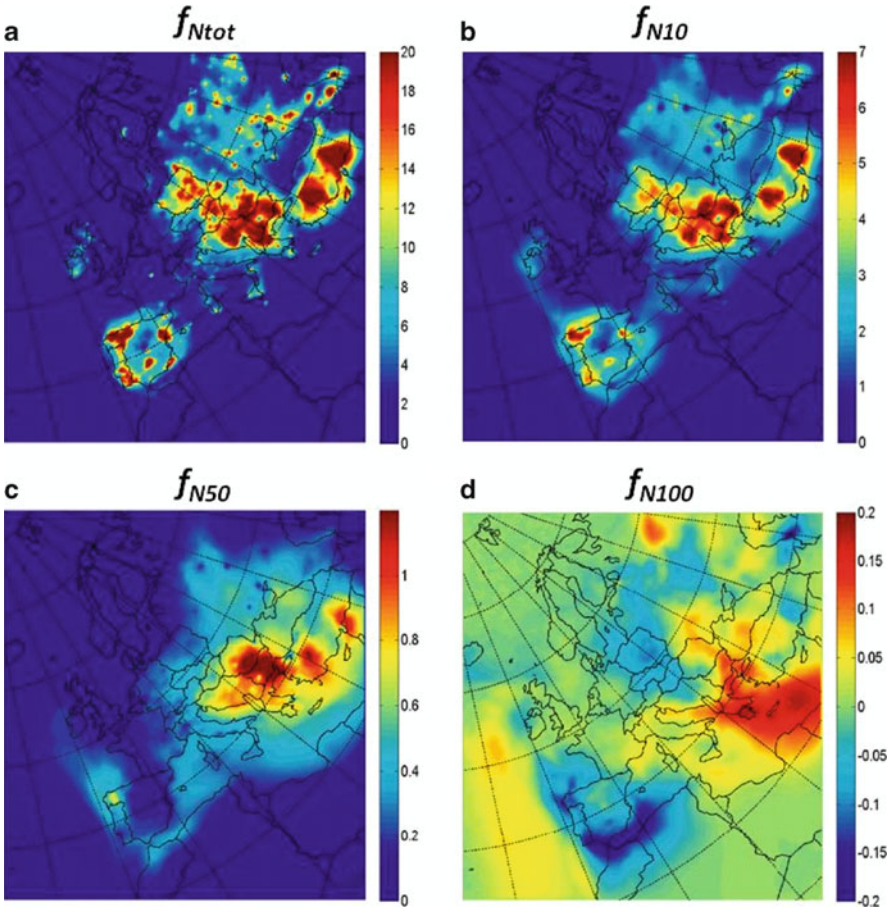

Fig. 1 Ground level average fractional increase of number concentration due to nucleation predicted during May 2008 for (**a**) all particles (f_{Ntot}), particles above (**b**) 10 nm (f_{N10}), (**c**) 50 nm (f_{N50}) and (**d**) 100 nm (f_{N100}). Different scales are used

nucleation turned-off was performed. The average fractional change of particle number concentration due to nucleation defined as $f_c = (N_f - N_i)/N_i$, where N_f and N_i are the predicted particle number concentrations with nucleation turned on and off, respectively is shown in Fig. 1. The average fractional increases are 3.0, 1.1, 0.2 and 0.005 for the N_{tot}, N_{10}, N_{50} and N_{100}, respectively, over the whole domain during May 2008 and the spatial pattern of these increases (mainly for N_{tot} and N_{10}) are similar to the corresponding average concentrations. Major nucleation areas include Turkey, Northern Spain, Romania, Bulgaria and Serbia while more localized new particle formation events are predicted over Estonia, Russia and South Spain. The model predicts that nucleation increases the total particle number concentration by a factor of 20 or more in some of these wide areas and by a factor of 6 or 7 for particles larger than 10 nm. Over some marine areas (e.g. the eastern

Mediterranean and across the coasts of Portugal and Spain) where SO_2 emissions from shipping are elevated, nucleation is predicted to significantly increase N_{tot} and N_{10} and to a less extent N_{50}. Interestingly, the situation is different for N_{100}. New particle formation events are predicted to increase the number concentration of particles above 100 nm by up to 20% over the Eastern Mediterranean and continental Greece. A simultaneous decrease of N_{100} is predicted over western Mediterranean and the north coast of Spain.

4 Comparison with Field Data

Overall, the model agreement with the particle number concentration ground measurements is encouraging (Fig. 2). More than 70% of the (hourly) data points for N_{10} and N_{50} are predicted within a factor of 2. The model predicts that direct emissions contribute only 30% to N_{10} in Melpitz with the rest coming from aerosol nucleation. Interestingly, nucleation is predicted to significantly affect N_{50} only in sites that are influenced by local pollution and have high aerosol number concentrations, namely in Melpitz (+33%), Cabauw (14%) and Ispra (+11%). In Cabauw and Ispra the predicted contribution of nucleation to particle number concentrations is lower compared to Melpitz. Including nucleation in the simulation in these two sites increases N_{10} by approximately 50% bringing the predictions closer to the measured values. Particle number concentrations measured in the two remote sites of Hyytiala and Aspvreten are the lowest among all sites, in agreement with the model predictions. Nucleation according to the model does not significantly affect N_{50} in these two remote sites (+5% on average in both sites). In Mace Head the model overestimates the frequency of nucleation thus overpredicting N_{10} during some days. N_{50} is well predicted by the model during most of the days in the four remote sites of Mace Head, Aspvreten, Hyytiala and Vavihill, contrary to the more polluted sites of Cabauw, Ispra and Melpitz in which the model systematically underpredicts both N_{50} and N_{100}.

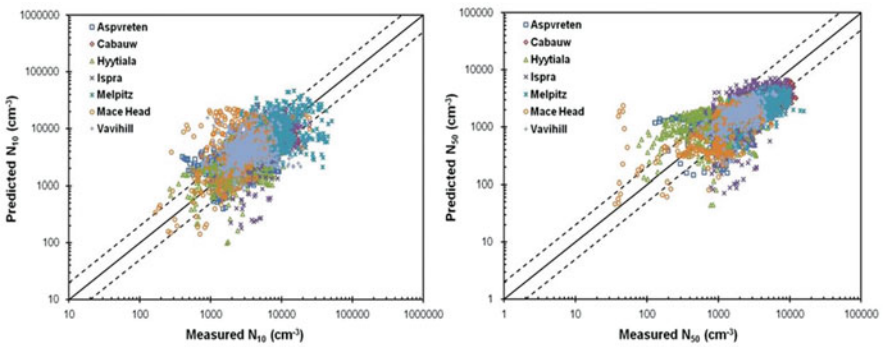

Fig. 2 Comparison of predicted versus observed particle number concentrations (cm-3) above 10 and 50 nm from 7 measurement stations during May 2008. Each point corresponds to a 1-h value

5 Conclusions

PMCAMx-UF, a 3-D regional chemical transport model with detailed aerosol microphysics, was applied to the European domain for the first time, in order to simulate particle number concentrations during the month of May 2008 during which an intensive campaign of measurements was performed in Europe. The model predicts nucleation events that occur over scales of hundreds up to thousands of kilometers mainly in the high SO_2 areas of the Balkans and Southeast Europe as well as more localized events in west and central Europe. Aerosol nucleation is predicted to increase the total particle number concentration by a factor of 20 or more in some of these wide areas and by a factor of 6.5 for particles larger than 10 nm. The effect of nucleation in the lower troposphere on particle number above 100 nm is, on average, small with the exception of the Mediterranean area where the model predicts that nucleation can increase the number concentration of CCN-sized particles by up to 20%. The model agrees encouragingly well with the particle number concentration ground measurements, reproducing more than 70% of the (hourly) data points for N_{10} within a factor of 2. Approximately 50% of particles above 10 nm are predicted to come from aerosol nucleation. Including nucleation in the simulation has a minor effect in the predictions of N_{100} at all studied sites, ranging from −4% to +3% while the effect on N_{50} is more pronounced only in sites that are influenced by local pollution and have high aerosol number concentrations (i.e. Melpitz, Ispra and Cabauw). Results from the 3 nucleation mechanisms that were tested suggest that (1) the ternary mechanisms performs better than the activation or the kinetic supporting the existence of ammonia in the newly formed particles, and (2) improvements in the diurnal and geographical split of the particle number emission inventory are needed.

Acknowledgments This work was funded by the European Community's 7th Framework Programme EU project PEGASOS (contract 265307). C. Fountoukis was partially supported by a Marie Curie International Reintegration Grant within the 7th European Community Framework Programme.

References

Adams PJ, Seinfeld JH (2002) Predicting global aerosol size distributions in general circulation models. J Geophys Res 107:D194370. doi:10.1029/2001JD001010

Jung J, Adams PJ, Pandis SN (2006) Simulating the size distribution and chemical composition of ultrafine particles during nucleation events. Atmos Environ 40:2248–2259. doi:10.1016/j.atmosenv.2005.09.082

Jung J, Fountoukis C, Adams PJ, Pandis SN (2010) Simulation of in situ ultrafine particle formation in the eastern United States using PMCAMx-UF. J Geophys Res 115:D03203. doi:10.1029/2009JD012313

Kulmala M, Lehtinen KE, Laaksonen A (2006) Cluster activation theory as an explanation of the linear dependence between formation rate of 3 nm particles and sulphuric acid concentration. Atmos Chem Phys 6:787–793

Napari I, Noppel M, Vehkamaki H, Kulmala M (2002) Parameterization of ternary nucleation rates for H2SO4-NH3-H2O vapors. J Geophys Res 107:D194381. doi:10.1029/2002JD002132

Trivitayanurak W, Adams PJ, Spracklen DV, Carslaw KS (2008) Tropospheric aerosol microphysics simulation with assimilated meteorology: model description and intermodel comparison. Atmos Chem Phys 8:3149–3168. doi:10.5194/acp-8-3149-2008

Effect of Atmospheric Temperature Variations on Total Ozone Measured with a Brewer MKII Spectrophotometer at Thessaloniki

K. Fragkos, A.F. Bais, and C. Meleti

Abstract The effect of atmospheric temperature and ozone profiles on the total ozone column (TOC) measurements of a Brewer spectrophotometer operating at Thessaloniki is investigated. The standard retrieval algorithm does not account for the temperature dependence of the ozone cross sections producing a bias in the measured TOC. The effect on TOC depends on the vertical profiles of temperature and ozone. For the Brewer at Thessaloniki, the temperature dependence of the instrument dependent effective ozone absorption coefficient ranges between 0.09%/°C and 0.13%/°C, resulting in up to 2% error in TOC. The marked annual variability of stratospheric temperature introduces an artificial annual cycle in the measured TOC. Removal of these effects improves the accuracy of TOC measurements at Thessaloniki.

1 Introduction

Stratospheric ozone is projected to return to its pre-1980 levels in the next few decades, as a result of the reduction in ozone depletion substances (ODS), from the implementation of the Montreal Protocol. Other factors, mostly related to the climate change, will influence the recovery of the ozone layer from the effects of ODSs affecting the detection and attribution of the recovery (WMO 2011). Thus, reliable and high quality measurements of total ozone column (TOC) are of great importance for scientific research and policy planning.

Total ozone is derived by remote-sensing techniques using ground-based and satellite instruments from spectral radiance measurements of solar UV radiation between 300 and 340 nm. Ground-based TOC measurements are performed regularly since 1958 by Dobson spectrophotometers (WMO/GAW 2003) and since

K. Fragkos (✉) • A.F. Bais • C. Meleti
Laboratory of Atmospheric Physics, Aristotle University of Thessaloniki, Thessaloniki, Greece
e-mail: kostasc@auth.gr

C.G. Helmis and P.T. Nastos (eds.), *Advances in Meteorology, Climatology and Atmospheric Physics*, Springer Atmospheric Sciences,
DOI 10.1007/978-3-642-29172-2_134,

early 1980s by Brewer spectrophotometers (Kerr et al. 1980). TOC measurements are based on the differential optical absorption spectroscopy technique, where the difference between the extraterrestrial and ground intensities, measured at different wavelengths, is compared with known, laboratory-based, ozone absorption cross sections. The cross sections by Bass and Paur (1984) (BP) are used systematically in Dobson and Brewer instruments. In the standard ozone retrieval algorithm of the Brewer spectrophotometers the temperature dependency of the ozone cross sections is not taken into account, resulting in a season-dependent bias in the measured TOC. In earlier studies the temperature sensitivity of the BP ozone cross sections was estimated in the range 0.001–0.11% per °C, strongly depending on instrument characteristics (Kerr et al. 1988; Van Roozendael et al. 1998; Kerr 2002; Scarnato et al. 2009). On the contrary, retrieval of ozone profiles from Brewer Umkehr measurements take in to account the temperature sensitivity of the ozone cross sections (Petropavlovskikh et al. 2011).

In this study we investigate the effect of the temperature dependence of the BP ozone absorption cross sections on the TOC measurements conducted at Thessaloniki with a Brewer MKII spectrophotometer, using measured profiles of temperature and climatological profiles of ozone.

2 Data and Methodology

A single-monochromator Brewer spectrophotometer MKII (SN 005, referred hereafter as B005) operates at the Laboratory of Atmospheric Physics, University of Thessaloniki, Greece (40.5°N, 22.9°E) since March 1982. During each day it performs several measurements of direct solar irradiance (DS) at five selected wavelengths. The TOC is then calculated with a relationship based on linear combinations of differential absorption and scattering coefficients and spectral irradiances, in the four longest wavelengths (Kerr et al. 1984).

The ozone absorption coefficient, used in the Brewer algorithm for the retrieval of TOC, is computed for a fixed temperature of −45°C, representative for the stratosphere (Savastiouk 2005). In reality, the absorption cross sections at any wavelength depend on temperature and as temperature changes with altitude, the absorption of solar radiation by ozone changes too. Therefore for accurate retrieval of TOC the actual temperature at all altitudes must be taken into account. The effective absorption cross section of ozone can be generally calculated from:

$$\alpha_{eff}(\lambda) = \frac{\int \alpha(\lambda, T(z)) \cdot O_3(z) dz}{\int O_3(z) dz} \tag{1}$$

where T(z) and O3(z) are the temperature and ozone profiles, a(λ,T(z)) is the wavelength and temperature dependent ozone cross section, while the integration is done between the surface and the top of the atmosphere.

The ozone absorption cross sections are usually measured in the laboratory at few discrete temperatures, while all other temperatures are derived by interpolation. Orphal (2003) showed that the best temperature fit for the ozone cross sections in the Huggins band is a quadratic polynomial. Here we used for the BP cross sections the parameterization of ASCO (http://igaco-o3.fmi.fi/ACSO/).

Temperature profiles are derived from radiosondes launched at the airport of Thessaloniki (~13 km south of the city centre) 2–3 times daily, depending on the period of the year. In this study we used profiles recorded from 2000 to 2010, downloaded from the Atmospheric Soundings portal of the University of Wyoming. As ozone profiles are not measured regularly at Thessaloniki, we used an extended version of the LLM ozone profile climatology (McPeters et al. 2007). This climatology offers dense vertical resolution and has been recently updated up to 2010, matching sufficiently the period of the available radiosonde data.

The effect of the temperature dependence of the ozone absorption coefficient on TOC calculation was investigated following an approach similar to that of Scarnato et al. (2009). The methodology retrieving TOC from ground measurements does not allow partitioning of the ozone absorption at different atmospheric levels through (1) as the actual temperature and ozone profiles are usually unknown. Instead, α(λ,Teff) is calculated from:

$$a(\lambda, T_{eff}) = c_0(\lambda) + c_1(\lambda) \cdot T_{eff} + c_2(\lambda) \cdot T_{eff}^2 \tag{2}$$

where c_0−c_2 are wavelength-dependent coefficients of the quadratic and T_{eff} is an effective temperature, which is derived from:

$$T_{eff} = \frac{\int_0^{30km} T(z) \cdot O_3(z) dz}{\int_0^{30km} O_3(z) dz} \tag{3}$$

In (3) the upper level for the integration is set to 30 km because most of the radiosondes do not reach higher altitudes. For those ending below 30 km we extrapolate to 30 km using temperature gradients from the US Standard Atmosphere. Due to the finite spectral resolution of the spectrophotometer the coefficients $\alpha(\lambda,T_{eff})$ are first convolved with the instrument's slit function and finally the differential effective ozone absorption coefficient is calculated from:

$$\Delta a(T_{eff}) = a(310, T_{eff}) - 0.5a(313.5, T_{eff}) - 2.2a(316.8, T_{eff}) + 1.7a \times (320, T_{eff}) \tag{4}$$

From a total of 4,978 temperature soundings the ozone effective temperature T_{eff} was calculated ranging from −40°C to −63°C, with a mean of −49.7°C. Obviously the actual temperature of the ozone absorption coefficient is by about 5°C lower than the usually assumed of −45°C, and shows a clear annual pattern that should be reflected in the retrieved TOC.

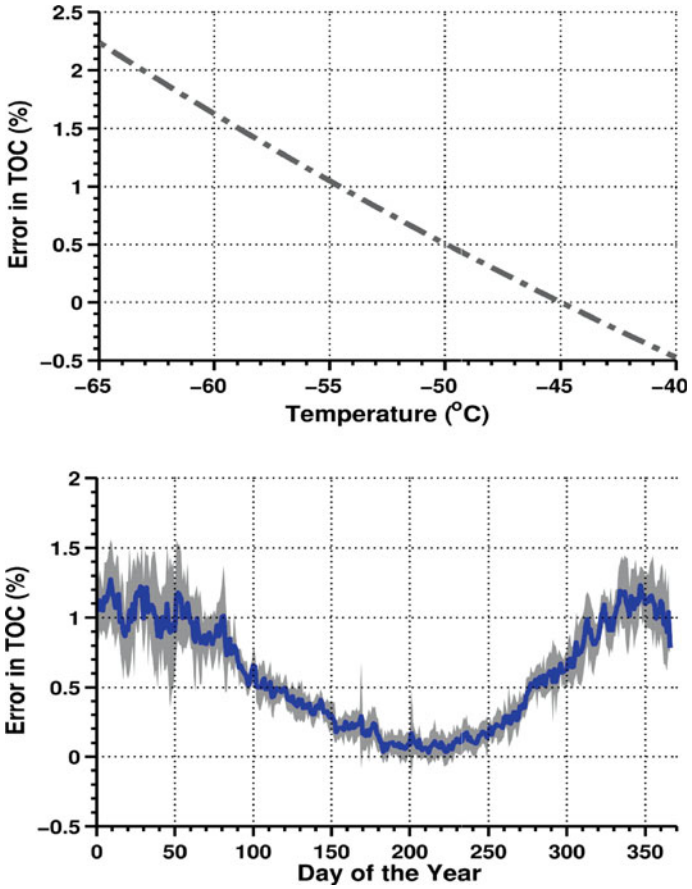

Fig. 1 Error in TOC due to temperature dependence of the ozone cross section as a function of the effective temperature (*upper*). Error in TOC as a function of day of year for the period 2000–2010 (*lower*), expressed by the mean $\pm 1\sigma$ of the individual daily data

3 Results and Discussion

To estimate the sensitivity of the differential ozone absorption coefficient on temperature, based on (4) we computed its temperature gradient $d(\Delta\alpha)/dT_{eff}$ for the entire range of Teff. Then the gradient is expressed as percentage from the relationship:

$$\frac{d(\Delta\alpha)}{dT_{eff}}(\%^{o}C^{-1}) = \frac{\left(d(\Delta\alpha)/dT_{eff}\right)_{T_{eff}}}{\Delta\alpha(T_{eff})} \times 100 \tag{5}$$

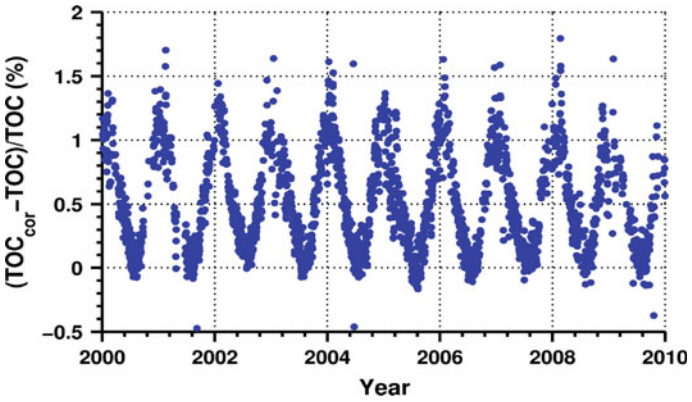

Fig. 2 Time series of the differences (in %) between the corrected and the original measurements of TOC at Thessaloniki, for the period 2000–2010

The percentage gradient ranges from 0.09% to 0.125% per °C, exhibiting a negative temperature dependence (increasing with decreasing temperature) for the ozone effective temperature range over Thessaloniki. These estimates are similar to those reported by Van Roozendael et al. (1998), 0.11−0.15% per °C, for a similar temperature range (−45°C to −70°C), and comparable with other estimates summarized in Table 4 of Scarnato et al. (2009). The observed differences of our estimates are mainly due to the different characteristics (slit function and operational wavelengths) of the instruments.

The percentage difference of the actual ozone absorption coefficient from the one that is calculated for a fixed temperature of −45°C is reflected directly on the error in the retrieved TOC, which is shown in Fig. 1. The error exhibits a quadratic dependence from temperature (upper panel) and can be up to 2%, for some extreme cases. The error as a function of the day of the year (lower panel) shows a marked annual cycle resulting form the annual variation of the temperature, mainly in the stratosphere. The error introduced by assuming constant temperature for the ozone cross section is always positive meaning that the Brewer at Thessaloniki always overestimates the TOC by up to ~1.5% in winter, while in summer the error is negligible, the order of 0.1%. This could possibly lead to systematic differences when the ground based ozone is compared against satellite data which use other ozone cross sections with different temperature sensitivity. Scarnato et al. (2009) showed that this annual variation of the error merely explains the systematic seasonal cycle in the difference of TOC measurements of Brewer and Dobson instruments, that has been documented at many midlatitudes sites (Vanicek 2006).

Based on the above correction factors, the TOC measurements at Thessaloniki for the period 2000–2010 were post-corrected for the temperature dependence of the ozone cross sections. The differences from the original series are shown in Fig. 2. This dataset comprises ozone data only for days with available radiosonde data which allow the calculation of T_{eff}. For the rest of the TOC measurements climatological temperature profiles may be used instead. The new TOC values are by up to 1.5% higher in winter, while in summer the change is negligible.

4 Conclusions

We have evaluated the effect of the temperature dependence of the ozone absorption cross sections used for the calculation of the total ozone column from measurements with a Brewer spectrophotometer at Thessaloniki. Daily temperature profiles from radio-soundings in the period 2000–2010 and climatological profiles of ozone were used to calculate an effective temperature for the absorption of solar UV radiation by ozone, and then to derive the effective ozone absorption coefficient. The derived changes in this coefficient are directly related to the error in the estimation of TOC. The effective temperature ranges between −45°C and −70°C; by far lower than the assumed −45°C in the standard Brewer TOC retrieval algorithm. This temperature variation results in up to ~1.5% error in TOC. The post corrected TOC measurements at Thessaloniki are higher by 1.5% in winter and practically the same in summer. These findings, in conjunction with results from earlier studies, indicate the need for post-processing and correction of global ground-based TOC measurements for the temperature dependence of ozone cross-sections, in order to achieve higher accuracy in TOC measurements and trends.

Acknowledgments The authors acknowledge the Atmospheric Soundings portal of the University of Wyoming (http://weather.uwyo.edu/upperair/sounding.html) for providing the radiosonde data and the TOMS GSFC NASA science team for the LLM ozone climatology (ftp://toms.gsfc.nasa.gov/pub/ML_climatology/).

References

Bass AM, Paur RJ (1984) The ultraviolet cross-sections of ozone: I. The measurements. In: Proceedings of the quadrennial ozone symposium. D. Reidel, Halkidiki, pp 606–610

Kerr JB (2002) New methodology for deriving total ozone and other atmospheric variables from Brewer spectrophotometer direct sun spectra. J Geophys Res-Atmos 107(D23):4731. doi:10.1029/2001JD001227

Kerr JB, McElroy CT, Olafson RA (1980) Measurements of ozone with the Brewer spectrophotometer. In: Proceedings of the quadrennial international ozone symposium, Boulder, pp 74–79

Kerr JB, McElroy CT, Wardle DI et al (1984) The automated Brewer spectrophotometer. In: Proceedings of the quadrennial ozone symposium. D. Reidel, Halkidiki, pp 396–401

Kerr JB, Asbridge IA, Evans WFJ (1988) Intercomparison of total ozone measured by the Brewer and Dobson spectrophotometers at Toronto. J Geophys Res-Atmos 93(D9):11129–11140. doi:10.1029/JD093iD09p11129

McPeters RD, Labow GJ, Logan JA (2007) Ozone climatological profiles for satellite retrieval algorithms. J Geophys Res 112:D05308. doi:10.1029/2005JD006823

Orphal J (2003) A critical review of the absorption cross-sections of O3 and NO2 in the ultraviolet and visible. J Photochem Photobiol A 157(2–3):185–209. doi:10.1016/S1010-6030(03)00061-3

Petropavlovskikh I, Evans R, McConville G, Oltmans S, Quincy D, Lantz K, Disterhoft P, Stanek M, Flynn L (2011) Sensitivity of Dobson and Brewer Umkehr ozone profile retrievals to ozone cross-sections and stray light effects. J Atmos Meas Tech 4:1841–1853. doi:10.5194/amt-4-1841-2011

Savastiouk V (2005) Improvements to the direct-sun ozone observations taken with the Brewer spectrophotometer. Dissertation, York University, Toronto

Scarnato B, Staehelin J, Peter T et al (2009) Temperature and slant path effects in Dobson and Brewer total ozone measurements. J Geophys Res 114:D24303. doi:10.1029/2009jd012349

Van Roozendael M, Peeters P, Roscoe HK et al (1998) Validation of ground-based visible measurements of total ozone by comparison with Dobson and Brewer spectrophotometers. J Atmos Chem 29(1):55–83. doi:10.1023/a:1005815902581

Vanicek K (2006) Differences between ground Dobson, Brewer and satellite TOMS-8, GOME-WFDOAS total ozone observations at Hradec Kralove, Czech. Atmos Chem Phys 6(12):5163–5171. doi:10.5194/acp-6-5163-200

WMO (World Meteorological Organization) (2011) Scientific assessment of ozone depletion: 2010. Ajavon A-LN, Newman PA, Pyle JA, Ravishankara AR. Geneva, Switzerland World Meteorological Organisation. Global ozone research and monitoring project – report no. 52:438

WMO/GAW (2003) Comparison of total ozone measurements of Dobson and Brewer spectrophotometers and recommended transfer functions. Staehelin KJ, Evans R, Vanicek K. WMO TD No. 1147

Summer Total Cloud Cover Weekly Variability over Europe: Sign of Aerosols' Indirect Effect?

A.K. Georgoulias, K.A. Kourtidis, G. Alexandri, and A. Sanchez-Lorenzo

Abstract The Day of Week (DoW) variability of total cloud cover (TCC) and aerosol optical depth (AOD_{550}) and its statistical significance over six European regions is investigated using 10 years of summertime satellite observations from TERRA and AQUA MODIS. In general, positive (higher values during midweek) weekly cycles in both AOD_{550} and TCC appear over Central Europe (CE), while a strong negative weekly cycle appears over the Iberian Peninsula and NE Europe (NEE). A very similar TCC and AOD_{550} weekly variability appears over CE, SW Europe (SWE) and NEE and a rather similar one over Central Mediterranean (CM). Possible scenarios that could explain the common weekly variability of aerosols and cloud cover through the aerosol indirect effects are discussed. An effort is made to verify our results and the proposed aerosol-cloud interaction scenarios with the use of independent satellite TCC data from the ISCCP and ground-based precipitation data from the ECA&D project.

A.K. Georgoulias (✉) • K.A. Kourtidis
Laboratory of Atmospheric Pollution and Pollution Control Engineering of Atmospheric Pollutants, Department of Environmental Engineering, Democritus University of Thrace, Xanthi 67100, Greece
e-mail: argeor@env.duth.gr

G. Alexandri
Laboratory of Atmospheric physics, Aristotle University of Thessaloniki, Thessaloniki 54124, Greece

A. Sanchez-Lorenzo
Institute for Atmospheric and Climate Science, ETH Zürich, Zürich 8092, Switzerland

C.G. Helmis and P.T. Nastos (eds.), *Advances in Meteorology, Climatology and Atmospheric Physics*, Springer Atmospheric Sciences,
DOI 10.1007/978-3-642-29172-2_135,

1 Introduction

Seven-day periodicities may be used as an index of the modification of weather and climate due to the human working cycle. Studying the weekly variability of pollution and meteorology is an old fashion, dating back to 1929. A detailed list of studies considering weekly cycles of photochemical parameters, ozone, NOx, CO, aerosols, etc., to the ground level in several urban centers in Central and North America, Europe and Asia from mid 70s to the present can be found in the recent work of Georgoulias and Kourtidis (2011) (hereafter referred to as GK11). The weekly variability of aerosols in the troposphere has been investigated with ground-based CIMEL measurements from the AERONET (e.g. Bäumer et al. 2008). The large scale weekly variability of aerosols in the U.S., Europe and Asia has been studied recently using satellite observations (Xia et al. 2008; Quaas et al. 2009, GK11). Several studies have also investigated the weekly variability of precipitation and its statistical significance with different and sometimes debatable results. Significant weekly cycles in other meteorological parameters (surface temperature, diurnal temperature range, cloud cover, surface radiation, etc.) have been shown around the globe (Sanchez-Lorenzo et al. 2012).

Nowadays, it is believed that the weekly cycles of meteorological variables may be partly explained through the aerosol direct radiative effect and the aerosol-cloud-precipitation interactions (indirect effects). It is widely accepted that enhanced aerosol concentrations lead to increased cloud droplet number concentrations which (under constant cloud liquid water paths) lead to smaller cloud droplet effective radii and consequently higher cloud albedo (first aerosol indirect effect). Smaller droplets are expected to delay precipitation formation and consequently to increase cloud lifetime and cloud cover (second aerosol indirect effect or cloud lifetime effect). When polluted convective clouds develop to greater heights cloud droplets may reach greater heights. Their freezing there can release additional latent heat and further invigorate the cloud updrafts. This can further suppress the precipitation and the development of downdrafts, prolong the growth of convective clouds allowing more water vapor ingestion and finally lead to more intense storms (Rosenfeld et al. 2008). Previous works, explained the observed cloudiness and precipitation weekly variability through the cloud lifetime and the storm invigoration effect (e.g. Bell et al. 2008).

Here, we present the summer weekly variability of the aerosol optical depth (AOD_{550}) and the total cloud cover (TCC) over Europe. We focus on summer for two main reasons: (1) as shown in GK11 the weekly variability of aerosols over Europe is driven by the summer weekly patterns and (2) convection, which favors the aerosol-cloud interactions, is larger in summertime. So, we expect that a possible effect of aerosols on the TCC weekly cycle would be more easily detectable in summer.

2 Data and Methods

TCC and AOD_{550} data from the level-3 MODIS TERRA (2/2000–2/2009) and MODIS AQUA (7/2002–12/2008) 1 × 1 daily gridded Collection 005 dataset are used. The data have been acquired through LAADS (Level 1 and Atmosphere Archive and Distribution System) (http://ladsweb.nascom.nasa.gov). In addition, data from the ISCCP (D1) cloud product at a spatial resolution of 250 × 250 km^2 for every 3 h on a daily basis were obtained from ISCCP's website (http://isccp.giss.nasa.gov/) (2000–2007). Data nearest to the MODIS TERRA and AQUA overpass were used.

The WCI, which was established in GK11, was used as a tool for the investigation of the summer weekly cycle spatial patterns over Europe. We further averaged spatially the TCC data over each of the 6 regions of interest selected in GK11 on a daily basis. From the emerging timeseries the average percent departure from the weekly mean was calculated for each day of the week. The statistical significance of the results was investigated with three different tests. (1) A two-tailed *t*-test was used to see if the average percent departures for the day of maximum and minimum are statistically significant at least at the 90% confidence level (c.l.). (2) The difference of the average percent departures between the day of maximum and minimum for the 7-day weeks were compared to results for artificial 6 and 8-day weeks. The time series are influenced by the synoptic weather noise (from few days-14 days) and the 7-day cycle may fluctuate by 1–2 days due to secondary aerosol formation. So, a 7-day signal much stronger than the 6 and 8-day signal indicates a local statistically significant weekly cycle connected to the local emission patterns. (3) Finally, the non-parametric test of Kruskal-Wallis (KW) was applied on the percent departure from the weekly average timeseries.

3 Results and Conclusions

As shown in GK11 the MODIS TERRA and AQUA WCI(AOD_{550}) patterns over Europe present a clear positive weekly cycle over CE and a clear negative weekly cycle over SWE and NEE in summer. GK11 showed that the aerosol weekly cycle patterns are mainly connected to continental aerosols. The WCI(TCC) patterns are characterized by a near-zero (TERRA) or positive (AQUA) weekly cycle in CE and strong negative weekly cycles in SWE and NEE (see Fig. 1).

The strong negative WCI(TCC) levels over SWE and NEE and the strong positive grid cells appearing around the highly industrialized region of "Black Triangle" in CE, are in general agreement to the WCI(AOD_{550}) results. To exclude the possibility that the TCC weekly variability is an artifact inserted by orbital and other technical features of MODIS we calculated the WCI(TCC) patterns using data from the International Satellite Cloud Climatology Project (ISCCP). Despite the differences between the two datasets (retrieval, data aggregation methods, spatial

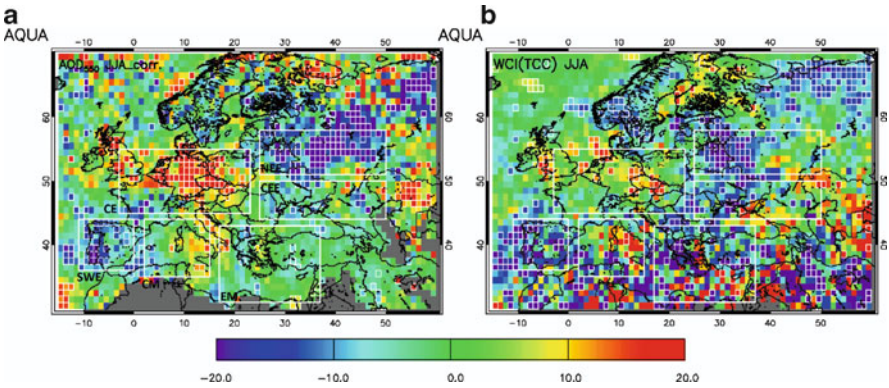

Fig. 1 (**a**) Summer WCI patterns calculated from AQUA MODIS AOD_{550} measurements for the period 7/2002–12/2008, (**b**) the same as (a) but for TCC data. Statistically significant at the 90% confidence level grid cells according to the two tailed *t*-test appear with a *thin white outline*. The six regions of interest are marked with a *thick white outline* in all the maps

resolution and time of observations) the ISCCP spatial patterns generally agree with that of MODIS.

The analysis of the spatially averaged MODIS data revealed a smooth weekly variability with a clear midweek peak/weekend low over CE. The day of maximum is Friday and the day of minimum is Monday (TERRA) or Tuesday (AQUA) with a maximum-minimum difference of the average percent departure from the weekly mean ~8% to 10%. Results for MODIS AQUA are shown in Fig. 2. The two-tailed *t*-test showed that the difference between the day of maximum and minimum was statistically significant at the 90% c.l. The 7-day signal is stronger than the 6 and 8-day signal. The KW test indicated statistical significance at the 95% c.l. only for MODIS AQUA. SWE presents a smooth weekly variability with a clear midweek low/weekend peak. The day of maximum/minimum is Tuesday/Thursday respectively. The maximum-minimum difference is ~11 to 14 with the results being statistically significant at the 90% c.l. The 7-day signal is stronger than the 6 and 8-day signal and the KW test indicated statistical significance at the 90% c.l. only for MODIS TERRA. The weekly variability over NEE presents a midweek low and weekend high, the day of maximum being Sunday and the day of minimum Friday (TERRA) or Thursday (AQUA) MODIS. The maximum-minimum difference is ~10% to 14% with the results being statistically significant at the 90% c.l.. The 7-day signal is stronger than the 6-day signal but lower than the 8-day signal and the KW test indicates statistical significance at the 95% (TERRA) and 90% (AQUA) c.l. For CM, there is a very striking difference between the day of maximum (Monday) and the day of minimum (Saturday). The maximum-minimum difference (~25%) is statistically significant at the 90% c.l., while the 7-day signal is much stronger than the 6 and 8-day signal. According to the KW test statistical significance is not indicated. The results for EM and CEE are not as clear as in the previous cases. The analysis done with the ISCCP data showed that there is a

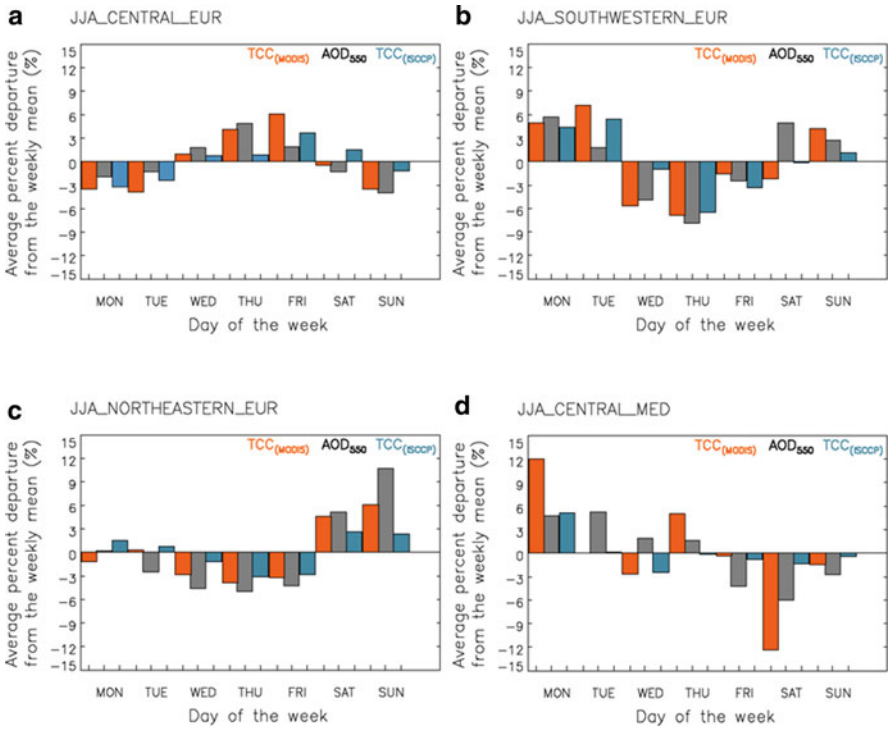

Fig. 2 TCC and AOD_{550} weekly variability for AQUA MODIS (7/2002–12/2008) and ISCCP (1/2002–12/2007) for: (**a**) CE, (**b**) SWE, (**c**) NEE, (**d**) CM. *Orange* colour is used for TCC from MODIS, *grey* for AOD_{550} from MODIS and *light blue* for TCC from ISCCP

general agreement between the ISCCP and MODIS TCC weekly variability over Europe, proving that the observed patterns are not an artifact originating from the special characteristics of the MODIS (see Fig. 2 for MODIS AQUA only). Despite the fact that statistical significance for the total of the three methods was indicated only in a few cases, the very good agreement between the weekly variability of aerosols and clouds in CE, SWE and NEE and the moderate agreement for CM could be a sign of the aerosol cloud lifetime effect.

Below, simple hypothetical scenarios that could explain the common TCC-AOD_{550} variability through the cloud lifetime and storm invigoration effect are discussed for CE, SWE and NEE. For a populated and industrialized region like Europe the general weekly variability of AOD_{550} is expected to correlate with the corresponding aerosol emission variability (see Bäumer et al. 2008). As shown in GK11 the transport of aerosols (e.g. 2–3 days from CE to NEE due to the dominating westerly winds) could change the sign of the weekly cycle of aerosols and this is taken into account here.

Particle concentrations are expected to decrease during the weekends due to decreased emissions in CE and increase thereafter during the week. Tropospheric aerosols start increasing in the beginning of the week delaying precipitation formation and increasing cloud lifetime and cloud cover (cloud lifetime effect). AOD_{550} peaks on Thursday and should be expected to stay high since emissions are not expected to vary significantly during the midweek. The TCC peaks 1 day after the aerosol peak (Friday). This could be due to the development of summer polluted convective clouds at greater heights where cloud droplets freeze, release additional latent heat, invigorate the cloud updrafts, suppress precipitation, extend cloud growth and finally lead to a delayed more intense storm sometime on Friday. On Friday the AOD_{550} levels drop due to the washing out by precipitation. On Saturday the AOD_{550} drops significantly followed by a clearer sky (decreased TCC) as it was expected. The washing out is followed by a decrease of the emissions during the weekend which gives even lower AOD_{550} on Sunday. This conceptual model is not expected to be valid for every week; however, we believe that it could possibly create a signal like the one seen in MODIS data.

Over the Iberian Peninsula clouds are of convective rather than frontal origin in summer. The dominating wind patterns do not favor the transport of aerosols from CE; hence they could not be responsible for the negative weekly cycle. As aerosol emissions increase on Monday a direct response of clouds through the cloud lifetime effect may increase TCC and suppress precipitation. This could finally lead to an intense precipitation on Tuesday-Wednesday (storm invigoration effect) washing out the aerosols. Thereafter the increase of aerosol concentrations starts again and TCC follows.

GK11 showed that due to the dominating westerly winds, air masses from CE are expected to arrive over NEE within 2–3 days. This phenomenon may create the negative aerosol weekly cycle observed over NEE since TCC follows aerosols due to the cloud lifetime effect.

An effort to see whether precipitation weekly cycles agree with the proposed scenarios has been made here using data from the ECA&D E-OBS gridded dataset at a $0.5^\circ \times 0.5^\circ$ resolution. The precipitation weekly variability agrees well with the observed TCC and AOD_{550} weekly variability over SWE and NEE. A strong negative weekly cycle is observed over SWE. In addition, a negative weekly cycle is observed over NEE and a positive weekly cycle over CE especially for the AQUA time period. These results seem to be in line with the scenarios suggested here.

Acknowledgments The authors acknowledge the use of data from LAADS (MODIS TERRA and AQUA level-3 data), the ISCCP website (ISCCP cloud data) and the ECA&D project website (E-OBS dataset from the EU-FP6 project ENSEMBLES)

References

Bäumer D, Rinke R, Vogel B (2008) Weekly periodicities of aerosol optical thickness over central Europe-evidence of an anthropogenic direct aerosol effect. Atmos Chem Phys 8:83–90. doi:10.5194/acp-8-83-2008

Bell TL, Rosenfeld D, Kim K-M, Yoo J-M, Lee M-I, Hahnenberger M (2008) Midweek increase in US summer rain and storm heights suggests air pollution invigorates rainstorms. J Geophys Res 113:D02209. doi:10.1029/2007JD008623

Georgoulias AK, Kourtidis KA (2011) On the aerosol weekly cycle spatiotemporal variability over Europe. Atmos Chem Phys 11:4611–4632. doi:10.5194/acp-11-4611-2011

Quaas J, Boucher O, Jones A, Weedon GP, Kieser J, Joos H (2009) Exploiting the weekly cycle as observed over Europe to analyse aerosol indirect effects in two climate models. Atmos Chem Phys 9:8493–8501. doi:10.5194/acp-9-8493-2009

Rosenfeld D et al (2008) Flood or drought: how do aerosols affect precipitation? Science 321 (5894):1309–1313. doi:10.1126/science.1160606

Sanchez-Lorenzo A et al. (2012) Assessing large large-scale weekly cycles in meteorological variables: a review. Atmos Chem Phys Discuss 12:1451-1491. doi:10.5194/acpd-12-1451-2012

Xia X, Eck TF, Holben BN, Phillippe G, Chen H (2008) Analysis of the weekly cycle of aerosol optical depth using AERONET and MODIS data. J Geophys Res 113:D14217. doi:10.1029/2007JD009604

Factors Controlling the Variability of Photolysis Rates of NO_2 and O^1D in the Complex Environment of the Eastern Mediterranean

E. Gerasopoulos, N. Mihalopoulos, S. Kazadzis, M. Vrekoussis, E. Liakakou, G. Kouvarakis, and N. Kouremeti

Abstract Time series of photolysis rates of ozone (JO^1D) and nitrogen dioxide (JNO_2), for the period 2002–2006, at the remote coastal Finokalia station on Crete Island (25°60′E, 35°24′N), were used in order to investigate the factors that control their levels and their temporal characteristics. The study focuses on the main climatological aspects of the photolysis rates and investigation of the factors that control their variability, with emphasis on the quantification of aerosol and total ozone effects. The average Aerosol Optical Depth in the area which equals to 0.27 ± 0.13, leads to percentage reduction of JNO_2 in the range 5–14% at 60° solar zenith angle (sza). For typical ozone column content (300–315 DU) the respective range of reduction for JO^1D is 8–24%. Overall, at regional AOD background levels (~0.1) the percentage reduction of both JNO_2 and JO^1D is lower than 6%, in the range of sza 15–75°. Dust is shown to be 1.5 times more efficient absorber than average aerosol types in the area. During high aerosol loads (AOD 0.5–0.7) the percentage reduction of Js can raise to 40% for high sza.

E. Gerasopoulos (✉) • S. Kazadzis • E. Liakakou
Institute for Environmental Research and Sustainable Development, National Observatory of Athens, Athens 15236, Greece
e-mail: egera@meteo.noa.gr

N. Mihalopoulos • G. Kouvarakis
Chemistry Dept, University of Crete, Heraklion, Greece

M. Vrekoussis
Center for Atmospheric Physics and Climatology, Academy of Athens, Athens, Greece

N. Kouremeti
Physics Department, Aristotle University of Thessaloniki, Thewssaloniki, Greece

C.G. Helmis and P.T. Nastos (eds.), *Advances in Meteorology, Climatology and Atmospheric Physics*, Springer Atmospheric Sciences,
DOI 10.1007/978-3-642-29172-2_136,

1 Introduction

The photolysis of trace gases in the atmosphere is a process of great importance for atmospheric chemistry. UV radiation drives the photolysis of several species, such as O_3 and NO_2, a process that controls their decomposition and removal from the atmosphere. The above control the formation of highly reactive radicals like hydroxyl-OH and hydroperoxyl-HO2 radicals (Kraus and Hofzumahaus 1998), which are essential for tropospheric ozone concentrations (e.g. Dickerson et al. 1997).

Eastern Mediterranean is a very sensitive area by means of intense photochemistry, high tropospheric ozone background (e.g. Gerasopoulos et al. 2006) and the presence of high aerosol concentrations of different types (e.g. Querol et al. 2009). The environmental terrain in the eastern Mediterranean is particularly complex regarding the effect of aerosols on photolysis rates, since even under conditions of reduced total ozone column, the encountered high levels of tropospheric ozone and absorbing dust aerosols, can cause a substantial decrease in the photolysis rates of ozone.

Apart from devoted campaigns, long term measurements of photolysis rates in the central/eastern Mediterranean do not exist (e.g. Casasanta et al. 2011). Other than that, this work presents the first long term (5 years, 2002–2006), continuous and direct measurements of two crucial for atmospheric chemistry photolysis rates, that of O_3 and NO_2, in an area well recognized for its particularities by means of photochemical activity. The great need for reliable values of photolysis rates as an input in chemical transport models (CTMs) is indisputable, since they are a parameter of particular importance for (photo)chemical process studies.

2 Data and Methodology

Continuous measurements of the photolysis rate of NO_2 (JNO_2) and ozone (JO^1D) were recorded for the period 2002–2006 by 2π commercially available filter radiometers (Meteorologie Consult, Metcon, Germany). The measurements were conducted at Finokalia (35° 20′ N, 25° 40′ E), a remote coastal site in the northeast part of the island of Crete, Greece. The sensors were calibrated yearly against a spectral radiometer at the Research Center Juelich, Germany (B. Bohn, pers. comm.). Total solar radiation measurements were performed by a pyranometer CM3 (Campbell Scientific, Inc.). The total ozone column has been obtained by TOMS (Total Ozone Mapping Spectrometer) until 2005 and OMI (Ozone Monitoring Instrument) for 2006. Aerosol optical properties performed with a CIMEL sun-photometer (AERONET level 2 data collection, http://aeronet.gsfc.nasa.gov/) carried out at FORTH-CRETE AERONET station, were also used.

For the detection of clouds, the shape of the diurnal course of solar radiation, recorded by the pyranometer, was examined. With the use of clear sky irradiance

calculations taken from a radiative transfer model, specific criteria were applied to extract clear sky data.

3 Results

3.1 Data Presentation

The maximum JO^1D value at local noon encountered in the data set is $4.04 \cdot 10^{-5}\ s^{-1}$ and the median value is $2.34 \cdot 10^{-5}\ s^{-1}$. Similarly, the maximum JNO_2 value at local noon encountered in the data set is $11.02 \cdot 10^{-3}\ s^{-1}$ and the median value is $8.01 \cdot 10^{-3}\ s^{-1}$. Regarding the seasonal variability of the photolysis rates a much broader pattern is revealed for JNO_2, with a 4 month plateau during April to July, and maximum in June. JO^1D is shifted to July due to masking of solar actinic flux sza dependence by the reduction of total ozone from June to July. The more abrupt change rate of JO^1D in the transition seasons, compared to that of JNO_2, is related to more efficient absorption by total ozone, and lesser by aerosols, at high solar zenith angles (sza) conditions that dominate towards winter time. Finally, the lower JNO_2 seasonal variability should be denoted with a max/min ratio of 1.5, when the respective ratio for JO^1D is 3.8.

3.2 Aerosol Effects

To quantify the impact of aerosols on JNO_2, we have plotted daily JNO_2 at 60° versus the AOD at 380 nm (Fig. 1). Dust episodes have been additionally distinguished by the criterion of AOD > 1 and Angström Exponent $AE_{340/440} < 1$. The slope of the linear regression indicates a reduction of JNO_2 by $2.2 \cdot 10^{-3}\ s^{-1}$ per AOD unit. This leads to a percentage reduction of about 10% at 60° sza, under typical urban conditions (mean $AOD_{380} = 0.3$, Gerasopoulos et al. 2011), and about 5% under regional background conditions (mean $AOD_{380} = 0.13$, Fotiadi et al. 2006).

The respective slope for dust aerosols, an efficient absorber, is calculated 1.5 times higher than that of non dust aerosols, indicating a reduction of JNO_2 by $3.1 \cdot 10^{-3}\ s^{-1}$ per dust AOD unit. This results to a percentage reduction of about 20% at 60° sza, under average dust loadings over the area (mean $A_{dust}OD_{380} = 0.45$, Gerasopoulos et al. 2011).

To investigate the impact of aerosols on JO^1D, daily JO^1D at 60° versus the AOD at 380 nm was plotted, for different total ozone bins (Fig. 2). For total ozone 300–320 DU, the slope is $-3.22 \cdot 10^{-8}\ s^{-1}$ per AOD unit, which, as in the case of JNO_2, results to a percentage reduction of about 13% at 60° sza, under typical urban conditions, and about 6% under regional background conditions. For the overall

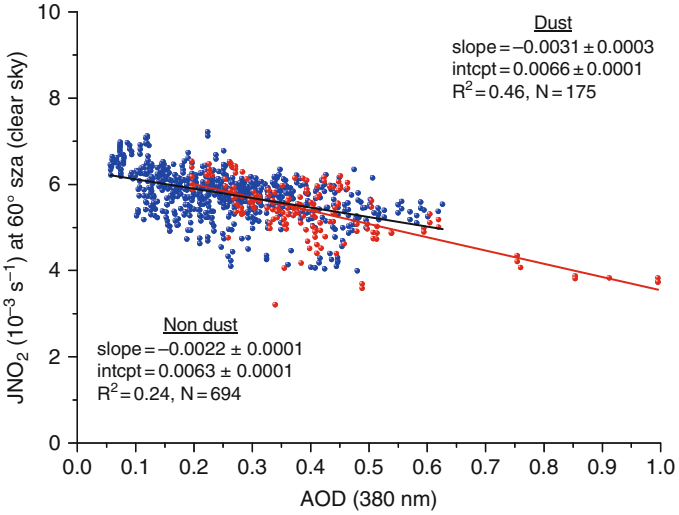

Fig. 1 JNO_2 at 60° versus AOD at 380 nm (*blue*). Dust episodes are denoted by *red points*

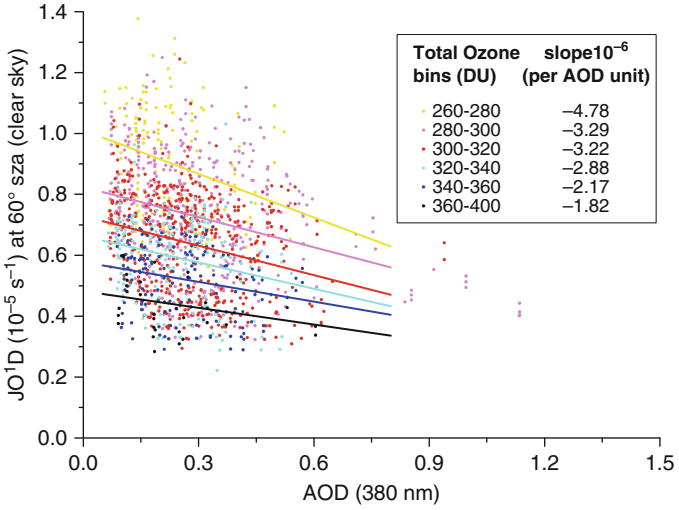

Fig. 2 JO^1D at 60° versus the AOD at 380 nm, for different total ozone bins

range of total ozone in this work the negative slopes are in good agreement with Casasanta et al. (2011) at Lambedusa (central Mediterranean), taking also into account the different AOD wavelength in the two studies.

It is worth noting that the slope linearly decreases with increasing total ozone column. This is mainly due to the fact that the slope, as derived from the Beer-Lambert law, is proportional to the incident radiation, which since it first propagates through the ozone layer it is inverse proportional to total ozone content.

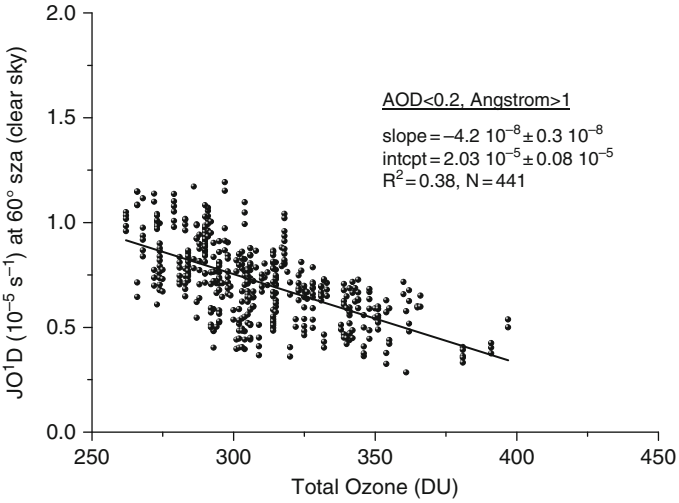

Fig. 3 JO^1D at 60° versus total ozone, for AOD < 0.2 and Angström Exponent ($AE_{340/440}$) > 1

3.3 Total Ozone Effects

To quantify the impact of total ozone on JO^1D, we have plotted daily JO^1D at 60° sza versus total ozone (Fig. 3), under aerosol cleaner (AOD < 0.2) and less absorbing (non dust, AE > 1) conditions. The slope of the linear regression indicates a reduction of JO^1D by $4.2 \cdot 10^{-8}$ s^{-1} per DU. This equals to a percentage reduction of about 30% at 60° sza, under typical spring conditions compared to the minimum total ozone fall conditions. The respective slope provided by Casasanta et al. (2011) at Lambedusa, is 3.38 10^{-8} s^{-1} per DU, calculated for the same sza, in the AOD (416 nm) range 0.1–0.2. Providing similar slopes for higher aerosol loads, they observe no particular trend, indicating that the ozone effect is basically de-coupled from the aerosol influence.

4 Conclusions

To address aerosol and total ozone effects at all sza, we have additionally performed linear regression analysis at steps of 5° for sza in the range 15–75°. From the extracted slopes we computed the percentage difference of Js from a reference J value per sza. For JNO_2 as reference value we used the value corresponding to AOD $= 0$, for each sza. The investigation of the impact of aerosols on JO^1D is confined to the 300–315 DU total ozone range, for AOD $= 0$, for each sza. Finally, the impact of total ozone on JO^1D is confined to AOD < 0.2 and AE > 1 (relatively clear conditions with no presence of dust) and the same

reference value for JO^1D as before (intercept for AOD = 0) is used. At regional AOD background levels (~0.1) the percentage reduction of JNO_2 ranges between 0.3% and 6% in the range of sza 15–75°. Under typical urban conditions (AOD ~ 0.3) the reduction is 10% at 60° sza and approaches 20% for higher sza. When considering specific high aerosol loads e.g. during dust events, then the reduction at 60° sza is 17% and 24%, for AOD 0.5 and 0.7, respectively, and it can raise to values 30–40% for higher sza. The percentage reduction of JO^1D at 60° sza for AOD 0.1, 0.3, 0.5 and 0.7 is 6%, 18%, 30% and 42%, respectively. It appears enhanced compared to JNO_2 as it includes the corresponding absorption by a total ozone column of 300–315 DU (most frequent distribution bin over the area). Finally, regarding the effect of O_3 absorption on JO^1D with respect to the absorption by a total ozone content of 300–315 DU, results to an almost constant percentage difference for sza < 35°. For higher sza it increases (for total ozone column < 300–315 DU) or decreases (for total ozone column > 300–315 DU) up to 60° sza, before it reaches a new plateau. The percentage change for a deviation by 20 DU is 11% at 60°, while for sza < 35° it lies around 7.5%.

Acknowledgments This work has been conducted within the framework of CIRCE project (Climate Change and Impact Research: the Mediterranean Environment), funded by the Commission of the European Union (Contract No 036961 GOCE), http://www.circeproject.eu/.

References

Casasanta G, di Sarra A, Meloni D, Monteleone F, Pace G, Piacentino S, Sferlazzo D (2011) Large aerosol effects on ozone photolysis in the Mediterranean. Atmos Environ 45:3937–3943. doi:10.1016/j.atmosenv.2011.04.065

Dickerson RR, Kondragunta S, Stenchikov G, Civerolo KL, Doddridge BG, Holben BN (1997) The impact of aerosols on solar ultraviolet radiation and photochemical smog. Science 278:827–830. doi:10.1126/science.278.5339.827

Fotiadi A, Hatzianastassiou N, Drakakis E, Matsoukas C, Pavlakis KG, Hatzidimitriou D, Gerasopoulos E, Mihalopoulos N, Vardavas I (2006) Aerosol physical and optical properties in the Eastern Mediterranean Basin, Crete, from Aerosol Robotic Network data. Atmos Chem Phys 6:5399–5413. doi:10.5194/acp-6-5399-2006

Gerasopoulos E, Kouvarakis G, Vrekoussis M, Donoussis C, Mihalopoulos N, Kanakidou M (2006) Photochemical ozone production in the Eastern Mediterranean. Atmos Environ 40:3057–3069. doi:10.1016/j.atmosenv.2005.12.061

Gerasopoulos E, Amiridis V, Kazadzis S, Kokkalis P, Eleftheratos K, Andreae MO, Andreae TW, El-Askary H, Zerefos CS (2011) Three-year ground based measurements of aerosol optical depth over the Eastern Mediterranean: the urban environment of Athens. Atmos Chem Phys 11:2145–2159. doi:10.5194/acp-11-2145-2011

Kraus A, Hofzumahaus A (1998) Field measurements of atmospheric photolysis frequencies for O_3, NO_2, HCHO, H_2O_2 and HONO by UV spectroradiometry. J Atmos Chem 31:161–180

Querol X, Alastuey A, Pey J, Cusack M, Perez N, Mihalopoulos N, Theodosi C, Gerasopoulos E, Kubilay N, Kocak M (2009) Variability in regional background aerosols within the Mediterranean. Atmos Chem Phys 9:4575–4591. doi:10.5194/acp-9-4575-2009

Vertical Separation of Aerosol Types Using of CALIPSO Level-2 Products

E. Giannakaki, D. Balis, and V. Amiridis

Abstract A first attempt is made to vertically separate profiles of optical parameters due to different aerosol types over Africa. The method applied makes use of particle backscatter profiles at 532 nm and vertically resolved linear particle depolarization ratio measurements at the same wavelength measured by space-borne CALIPSO lidar. Values of particle depolarization ratio of 'pure' aerosol types were taken from literature. A case of CALIPSO space-borne lidar system was selected on the basis of different mixing state of the atmosphere. To identify the origin of air-masses 4-day air mass back trajectories were computed using HYbrid Single-Particle Langrangian Integrated Trajectory (HYSPLIT) model, for different arrival heights, for the location and time under study.

1 Introduction

Mixtures of different aerosols play an important role over Europe. The mixing occurs because of the relatively long pathways of air masses across different aerosol source regions before the detection over European continent. Lidar measurements provide vertical profiling of aerosols with high resolution and permit the separation of aerosol types based on the optical properties. The determination of the extinction-to-backscatter ratio (the so-called lidar ratio) profile is possible using Raman-lidar technique for the independent determination of the particle extinction and backscatter vertical profiles (Ansmann et al. 2002). The lidar ratio contains information on the aerosol type, since it depends on the index of refraction and on the size of particles (Ackermann 1998).

E. Giannakaki (✉) • D. Balis
Laboratory of Atmospheric Physics, Aristotle University of Thessaloniki, Thessaloniki, Greece
e-mail: egian@auth.gr

V. Amiridis
Inst for Space Applications and Remote Sensing, National Observatory of Athens, Athens, Greece

C.G. Helmis and P.T. Nastos (eds.), *Advances in Meteorology, Climatology and Atmospheric Physics*, Springer Atmospheric Sciences,
DOI 10.1007/978-3-642-29172-2_137,

In the following, we present a case study to present the occurrence of such kind of aerosol mixtures and the way in which a better vertical separation can be performed using the methodology proposed by Tesche et al. (2009). After a brief description of data and methodology in Sect. 2, an example of aerosol mixture is presented in Sect. 3. In Sect. 4 we close our contribution with a summary and our conclusions.

2 Data and Methodology

2.1 Data

Multiwavelength aerosol Raman lidar in combination with polarization lidar at Praia, Cape Verde, were used to separate the optical properties of desert dust and biomass burning particles as a function of height in the mixed dust and smoke plumes over the tropical North Atlantic west of the African continent during SAMUM campaign (Tesche et al. 2009). In this paper, we study the possibility of using space-borne lidar data to vertically separate the aerosol types using the same case study.

In this study level 2 version 3.01 CALIPSO data are used. Flags that are stored in the level 2 aerosol profile products are used to screen our data for clouds and stratospheric features. Once the feature type has been decoded out of the Atmospheric Volume description, we keep those aerosol layers that have feature type equal to 2. CAD score reflects our confidence that the feature under consideration is either an aerosol or a cloud. In this study we screen out features with CAD score greater than −80. Finally, we use CALIPSO extinction quality control (QC) flags. We use solutions where the lidar ratio is unchanged during the extinction retrieval (extinction QC = 0) or if the retrieval is constrained (extinction QC = 1).

2.2 Methodology

The method used in this study makes use of lidar observations of the particle backscatter coefficient and the linear particle depolarization ratio at 532 nm in order to separate the backscatter contributions of the weakly light depolarizing aerosol components from the contribution of strongly light depolarizing particles.

Assuming that we have two aerosol types, the backscatter contribution of the first aerosol type, β_1 is obtained from the measured total backscatter coefficient β_t by (1),

$$\beta_1 = \beta_t \frac{(\delta_t - \delta_2)(1 + \delta_1)}{(\delta_1 - \delta_2)(1 + \delta_t)} \tag{1}$$

where δ_t, δ_1 and δ_2 are the observed particle depolarization ratio and the assumed particle depolarization ratios of the two pure aerosol types. The particle backscatter coefficient of the second aerosol type is given by $\beta_t - \beta_1$. The methodology is outlined in detail by Tesche et al. (2009).

3 Results

A case study that was extensively studied and presented at Tesche et al. (2009) has been used in this study. A lidar-based approach was proposed to separate profiles of optical parameters due to the influence of dust and smoke particles in the West African outflow plume. The case study of 31 January 2008 revealed a two layer aerosol system. A desert dust layer with optical depth of about 0.25 at 532 nm extended from the ground to 1.5 km height. That layer was topped by a lofted layer (from 1.5 to 5 km height) consisting of desert dust and biomass burning smoke (Tesche et al. 2009).

Here, we investigate the potential use of CALIPSO level-2 products for separating dust and smoke for the case of 31 January 2008. Figure 1 (left) illustrates the attenuated backscatter coefficient as measured from CALIPSO for 31 January 2008. Two layers can be identified; the first one is the deepest and extends from the ground up to 2 km. Above this layer, there is a thinner layer that extends up to almost 4 km. Trajectory analysis are shown in Fig. 1 (right, bottom) and indicate that dust has been transported from desert areas. MODIS satellite observations of fires within the period from 20 to 30 January 2008 (http://rapidfire.sci.gsfc.nasa.gov/firemaps) are shown in Fig. 1 (right, top).

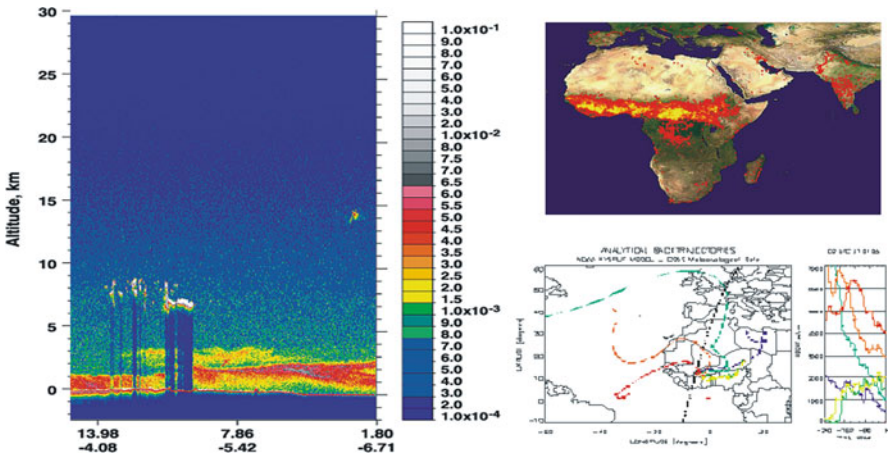

Fig. 1 Attenuated backscatter coefficient for 31 January 2008 (*left*), MODIS 10-day fire map that shows all location of fires (*red spots*) detected during the 21–30 January period (*right-top*), 10-day HYSPLIT backward trajectories ending at 11.67(lat) and −4.6 (lon) on 31 January, 02:00 UTC. CALIPSO orbit are also superimposed (*right-bottom*)

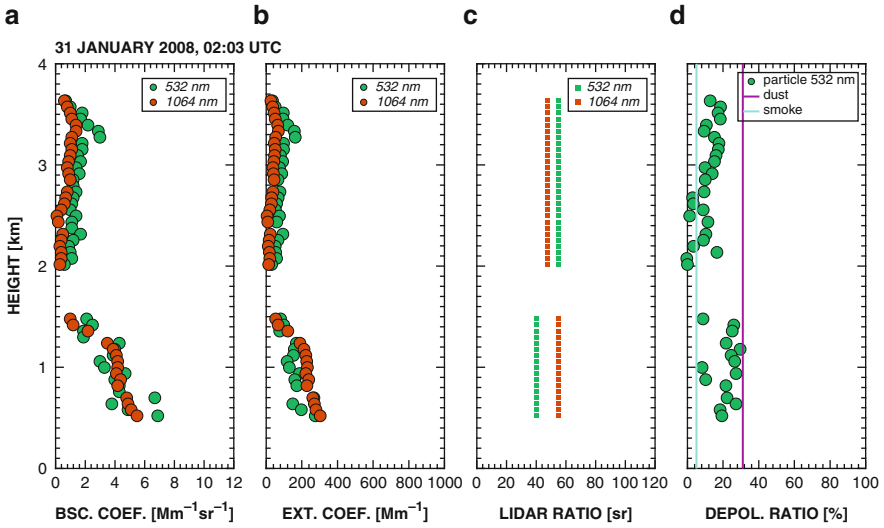

Fig. 2 (**a**) Backscatter coefficient at 532 and 1,064 nm, (**b**) extinction coefficient at 532 and 1,064 nm, (**c**) lidar ratio selected by CALIPSO at 532 and 1,064 nm, (**d**) depolarization ratio at 532 nm (*green*) and the input values of dust (*purple*) and smoke (*light blue*) particles

In Fig. 2 we present the backscatter and extinction coefficient at 532 and 1,064 nm, along with the lidar ratio selection and linear particle depolarization at 532 nm. Different aerosol properties of the two layer-structure can be recognized from particle depolarization profile. The lowest layer seems to have larger depolarization and probably this is the reason why CALIPSO selection scheme chooses a lidar ratio of 40 sr at 532 nm and 55 sr at 1,064 nm (see Omar et al. 2009).

To determine the backscatter coefficient of dust particles we use the particle depolarization ratio and backscatter coefficient at 532 nm as measured by CALIPSO level 2 aerosol product. Then, from the profiles of the particle backscatter coefficient and the dust backscatter coefficient we obtain the profile of the nondust (biomass burning aerosols) backscatter coefficient using (1).

For the computation of contribution of each aerosol type we need to estimate the 'pure' biomass burning depolarization ratio and the 'pure' dust depolarization ratio. These values have been taken from literature. Particle depolarization ratio of Saharan dust of 0.31 ± 0.03 at 532 nm (Freudenthaler et al. 2009) is in good agreement with the one of Asian dust of 0.35 as found from long-term observations over China and Japan (Sugimoto et al. 2003; Shimizu et al. 2004). According to the literature, non dust depolarization ratios can vary from 0.02 to 0.15 with an accumulation around 0.05 (e.g. Murayama et al. 1999). The value of 0.31 was considered for linear particle depolarization of pure dust (aerosol type 1) while the value of 0.05 was considered for the aerosol type 2 in our separation procedure.

Figure 3 shows profiles of the dust (purple) and smoke (light blue) backscatter coefficient. The separation procedure has revealed that the two layers are mixed, with the lower layer consisting mainly by dust particles and the upper layer consisting mainly with smoke particles. Our result is in agreement with those of

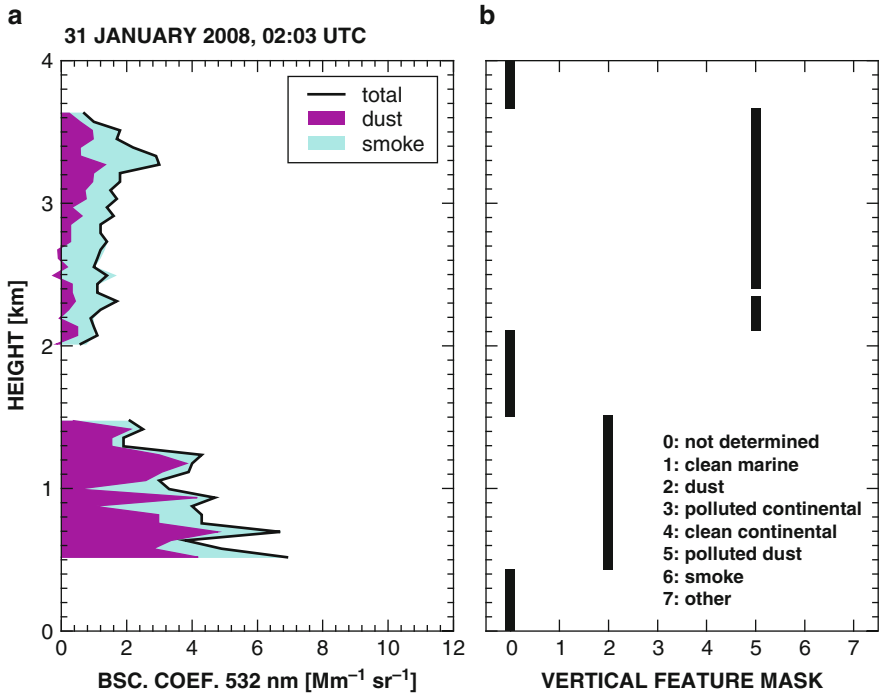

Fig. 3 (**a**) Separation of dust (*purple*) and smoke (*light blue*) particle backscatter coefficients at 532 nm, (**b**) Vertical Feature Mask as given by CALIPSO

Tesche et al. (2009) if we take into consideration that CALIPSO orbit intersects the area where fires occur and hence the contribution of smoke should be larger in our case. It is worth noting that according to CALIPSO selection scheme the first layer, was characterized as dust while the upper one was characterized as polluted dust. According to Omar et al. (2009), polluted dust is designed to account for episodes of dust mixed with biomass burning smoke, which are frequent in regions close to strong sources of both, for example on West Africa and Asia. It also accounts for instances of dust mixed with urban pollution as is frequently encountered in parts of Asia and Europe. According to trajectory analysis, polluted dust in this case is attributed to mixing of dust with biomass burning smoke particles.

The method is of value, since it can be applied to observations of next-generation space lidars such as high spectral resolution lidars measuring particle extinction at 355 and 532 nm, particle backscatter at 355, 532, and 1,064 nm and the depolarization ratio.

4 Conclusions

A lidar-based approach to separate profiles of optical parameters was applied to CALIPSO level-2 products. The technique was applied to estimate the contribution of dust and biomass burning smoke particles into the total backscatter coefficient

over West Africa. The case study of 31 January 2008 revealed a two layer aerosol system. Dust particles dominate in the lower layer, while smoke particles were significant to the upper layer. However, CALIPSO classification scheme showed two distinct layers of dust and smoke respectively.

In conclusion, mixtures of different aerosols have been presented as observed by CALIPSO. The mixing of different aerosol types result in quite different optical properties. We have shown that depolarization ratio can be a key parameter for separating these different aerosol mixtures, if we assume the depolarization ratio for pure aerosol types. From this perspective CALIPSO aerosol models can be improved.

Acknowledgments CALIPSO data were obtained from the NASA Langley Research Center Atmospheric Science Data Center. Elina Giannakaki acknowledges the support of Hellenic State Scholarships Foundation. This work has been conducted in the framework of the ACTRIS project.

References

Ackermann J (1998) The extinction-to-backscatter ratio of tropospheric aerosol: a numerical study. J Atmos Oceanic Technol 15:1043–1050. doi:10.1175/1520-0426(1998) 015<1043: TETBRO>2.0.CO;2

Ansmann A, Wagner F, Müller D, Althausen D, Herber A, Von Hoyningen-Huene W, Wandinger U (2002) European pollution outbreaks during ACE 2: optical particle properties inferred from multiwavelength lidar and star-Sun photometry. J Geophys Res D Atmos 107:4259. doi:10.1029/2001jd001109

Freudenthaler V, Esselborn M, Wiegner M, Heese B, Tesche M, Ansmann A, Müller D, Althausen D, Wirth M, Fix A, Ehret G, Knippertz P, Toledano C, Gasteiger J, Garhammer M, Seefeldner M (2009) Depolarization ratio profiling at several wavelengths in pure Saharan dust during SAMUM 2006. Tellus 61B:165–179. doi:10.1111/j.1600-0889.2008.00396.x

Murayama T, Okamoto H, Kaneyasu N, Kamataki H, Miura K (1999) Application of lidar depolarization measurement in the atmospheric boundary layer: effects of dust and sea-salt particles. J Geophys Res 104(D24):31781–31792. doi:10.1029/1999JD900503

Omar AH, Winker DM, Kittaka C, Vaughan MA, Liu Z, Hu Y, Trepte CR, Rogers RR, Ferrare RA, Lee KP, Kuehn RE, Hostetler CA (2009) The CALIPSO automated aerosol classification and lidar ratio selection algorithm. J Atmos Oceanic Technol 26(10):1994–2014. doi:10.1175/2009jtecha1231.1

Shimizu A, Sugimoto N, Matsui I, Arao K, Uno I, Murayama T, Kagawa N, Aoki K, Uchiyama A, Yamazaki AA (2004) Continuous observations of Asian dust and other aerosols by polarization lidars in China and Japan during ACE-Asia. J Geophys Res D Atmos 109(19):D19S17. doi:10.1029/2002jd003253, 11–14

Sugimoto N, Uno I, Nishikawa M, Shimizu A, Matsui I, Dong X, Chen Y, Quan H (2003) Record heavy Asian dust in Beijing in 2002: observations and model analysis of recent events. Geophys Res Lett 30(12):42–41. doi:10.1029/2002GL016349

Tesche M, Ansmann A, Müller D, Althausen D, Engelmann R, Freudenthaler V, Groß S (2009) Vertically resolved separation of dust and smoke over cape verde using multiwavelength Raman and polarization lidars during Saharan mineral dust experiment 2008. J Geophys Res D Atmos 114:D13202. doi:10.1029/2009jd011862

Air Pollution Monitoring Based on Remote Sensing and Simultaneous Ground PM 10 and PM2.5 Measurements: The 'WebAir-2 Project'

D.G. Hadjimitsis, A. Agapiou, K. Themistokleous, C. Achilleos, A. Nisantzi, R.E. Mamouri, C. Panayiotou, and S. Kleanthous

Abstract WebAir-2 EUREKA project aims to expand the basic air quality modelling technology (web-based client server) developed in E!3266 WebAir project. WebAir-2 will incorporate different technologies such as satellite remote sensing data and ground PM samples for monitoring air pollution and in addition 3G mobile phone technology will be used for personalized health related information, warnings and exposure reports. Emphasis will be given to the development of statistical models for PM against AOT derived from MODIS data. Due to inadequate spatial-temporal coverage of air pollution from existing air pollution stations, MODIS products can assist to this task both spatial and temporal. The statistical AOT model will be cross-validated during satellite overpass based on handheld sun-photometers and daily CIMEL sun-photometer (NASA/AERONET network) measurements. Moreover ground LIDAR measurements for vertical distribution of the aerosols will be carried out. Based on these data, a 3D nested grid Eurelian model CAMx will be used to generate the dynamic boundary conditions for the Cyprus model domain.

D.G. Hadjimitsis (✉) • A. Agapiou • K. Themistokleous • C. Achilleos • A. Nisantzi • R.E. Mamouri
Department of Civil Engineer and Geomatics, Cyprus University of Technology, Limassol 3603, Cyprus
e-mail: d.hadjimitsis@cut.ac.cy

C. Panayiotou
Atlantis Consulting LTD, Nicosia, Cyprus

S. Kleanthous
Department of Labour Inspection, Air Quality Sector, Nicosia, Cyprus

C.G. Helmis and P.T. Nastos (eds.), *Advances in Meteorology, Climatology and Atmospheric Physics*, Springer Atmospheric Sciences,
DOI 10.1007/978-3-642-29172-2_138,

1 Introduction

In the last 35 years a noticeable effort has been dedicated to urban air pollution research. However modeling air pollution especially in urban areas and even more in a regional scale is still pending (Pujadas et al. 2000). In many cases (Pummakarnchana et al. 2005; Pfeffer et al. 1995) a network of ground air pollutants stations is set in the area of interest in order to record air pollutants. However such methodology has a high cost (implementation and maintenance) while at the same time it is spatially limited (point measurements) (Ferradás et al. 2010).

On the other hand satellite remote sensing of air quality has evolved dramatically over the last decade (Randall 2008; Hadjimitsis et al. 2002; Hadjimitsis 2009). Spectral variations, recorded by satellite sensors are indicators of aerosol particles and therefore air pollution. When solar radiation undergoes through the atmosphere it produces a general decrease in the spectral irradiance which is related to the optical thickness of the atmosphere. These effects are due to the scattering and wide band absorption produced by both aerosol particles and atmospheric gases (Pujadas et al. 2000).

Air pollution is a serious problem in many heavily populated and industrialized areas For this reason many air pollution studies have appeared in the international literature (Kambezidis et al. 1998). The aim of the EUREKA project "WebAir2" is to expand the basic air quality modelling technology firstly in E!3266 WebAir project. WebAir-2 aims to combine different technologies such as satellite remote sensing data and ground PM samples for monitoring air pollution and in addition 3G mobile phone technology will be used for personalized health related information, warnings and exposure reports. The first case studies are located in areas of Cyprus and Croatia (Fig. 1)

2 Methodology

The overall methodology of the project is shown in Fig. 2. Both ground and satellite measurements will be acquired in order to evaluate the potential of satellite remote sensing for monitoring air pollutants. Indeed, the aim of WebAir-2 project is to develop statistical models for deriving the relationship between PM (2.5 PM or/and 10 PM) against Aerosol Optical Thickness (AOT) which is derived directly from satellite data such as the Moderate Resolution Imaging Spectroradiometer (MODIS) or indirectly from Landsat TM/ETM + images (see Hadjimitsis 2009, 2008). For validation purposes the AOT will be cross-validated by the following ground-based means for AOT measurements during the satellite overpass: (a) the handheld sun-photometer MICROTOPS II (b) the CIMEL sun-photometer which is part of the NASA/AERONET network (c) and the LIDAR.

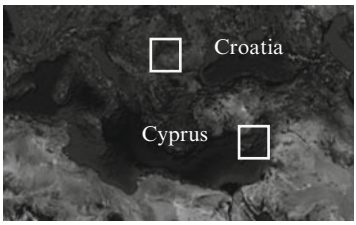

Fig. 1 Cases studies of the WebAir-2 project (Cyprus and Croatia)

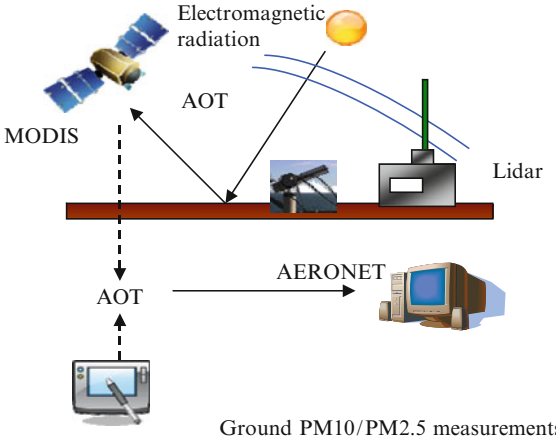

Fig. 2 Methodology for ground and satellite collection

3 Data

3.1 Ground PM Measurements

For the aims of the project several measurements will be carried out using either handheld sun-photometers or the Cimel sun photometer (Fig. 3). Sun photometers are handheld instruments that are used in order to retrieve Aerosol Optical Thickness – AOT, (at 500 nm), while the Cimel sun-photometer is an automatic sun-sky scanning radiometer. Cimel sun-photometer installed at the Cyprus University of Technology premises is part of the AERONET network (AErosol RObotic NETwork).

Daily measurements from these instruments will be used in order to correlate the AOT with the PM10 and/or PM2.5 data provided from ground stations For the Cyprus case study, air pollution data will be obtained from the Department of Labour and Inspection, Air Quality Control sector.

3.2 Lidar Measurements

The Lidar transmits laser pulses at 532 and 1,064 nm simultaneously and collinear with a repetition rate of 20 Hz. The two polarization components at 532 nm are

Fig. 3 CIMEL SUN-PHOTOMETER – hand-held Sun photometer – Microtops II (Cyprus University of Technology Premises-Remote Sensing Lab)

separated in the receiver by means of polarizing beamsplitter cubes (PBC). A special optomechanical designs allows the manual ±45°-rotation of the whole depolarization detector module with respect to the laser polarization for evaluating the depolarization calibration constant of the system. The receiver is ready to accommodate one more channel for detection of the Raman shifted radiation at 607 nm. Photomultiplier tubes (PMTs) are used as detectors at all wavelengths except for the signals at 1,064 nm (avalanche photodiode, APD). A transient recorder that combines a powerful A/D converter (12 Bit at 20 MHz) with a 250 MHz fast photon counting system (Licel, Berlin) used for the detection of 532 radiation, while only analog detection is used 1,064 nm. The raw signal spatial resolution is down to 7.5 m.

3.3 Satellite Data

Monitoring air quality for urban and sub-urban areas using conventional methods requires expensive equipment. Air pollution measurements are always related to the area where the air quality stations are located. However, remote sensing images can fill this gap since satellite images cover vast areas (Hadjimitsis 2008). This is possible to be performed if AOT values, retrieved from satellite sensors such MODIS, are related with PM10 and/or PM2.5.

The MODIS Aerosol Product (MOD 04) monitors the ambient aerosol optical thickness over the oceans globally and over a portion of the continents. Furthermore, the aerosol size distribution is derived over the oceans, and the aerosol type is derived over the continents. Daily Level 2 (MOD 04) data are produced at the spatial resolution of a 10 × 10 1-km (at nadir)-pixel array (HandBook MODIS).

4 Preliminary Results

PM10 were kindly provided from Department of Labour and Inspection, Air Quality Control sector, for a 5 year period 2005 and 2010. Figure 4 shows the distribution of PM10 for Nicosia and Limassol towns based on the ground stations of the Department of Labour and Inspection.

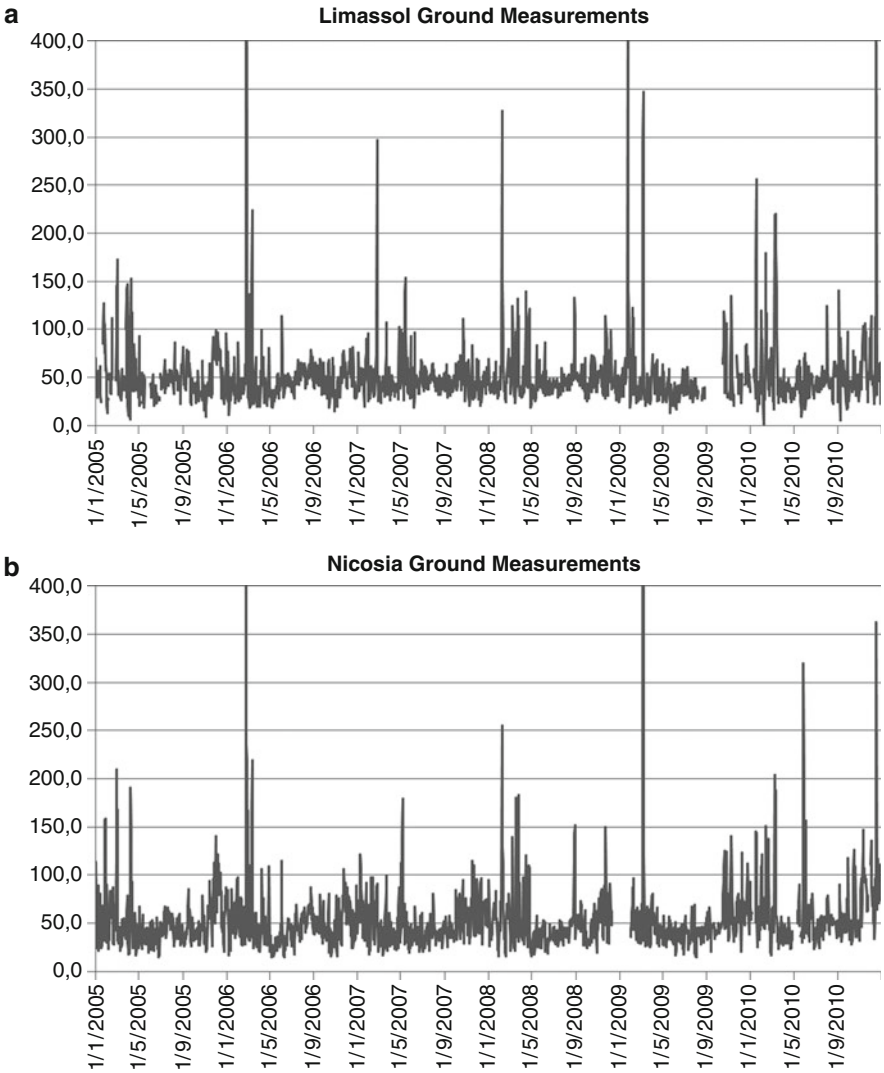

Fig. 4 PM10 measurements for Limassol and Nicosia towns (period 2005–2010)

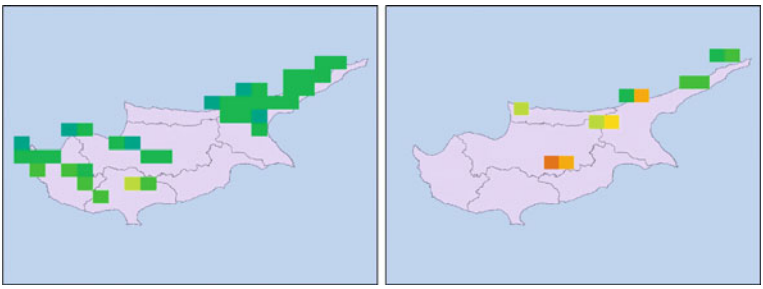

Fig. 5 AOT values from MODIS products

These data area going to be used in order to validate the correlation model between AOT (derived from MODIS products) and ground PM measurements. AOT values as found from MODIS images is shown in Fig. 5.

5 Future Work

When the data are collected and analyzed then for emissions, a dust entrainment model will be adapted from the EUREKA E! 3266 Webair (I), in order to generate dynamic source terms for the two cases studies. The results of the re-suspension model will be compared with ground measurements and from remote sensing data derived from satellite imagery (e.g. MODIS). This will also explore the potential of using the satellite data for data assimilation to improve the emission model performance. Model validation for the entrainment model will use selected episodes where monitoring data and/or satellite data are available for comparison of model results and observations.

Acknowledgments "WebAir-2" is a EUREKA project is funded by the Cyprus Promotion Research Foundation. Thanks are given to the Remote Sensing Laboratory of the Department of Civil Engineering and Geomatics at the Cyprus University of Technology for the support (http://www.cut.ac.cy/)

References

Ferradás GE, Miñarro DM, Morales MI, Terrés MMI, Martínez FJM (2010) An approach for determining air pollution monitoring sites. Atmos Environ 44(21–22):2640–264. doi:10.1016/j.atmosenv.2010.03.044

Hadjimitsis DG (2008) Description of a new method for retrieving the aerosol optical thickness from satellite remotely sensed imagery using the maximum contrast value principle and the darkest pixel approach. Trans GIS 12(5):633–644. doi:10.1111/j.1467-9671.2008.01121.x

Hadjimitsis DG (2009) Aerosol Optical Thickness (AOT) retrieval over land using satellite image-based algorithm. Air Qual Atmos Health 2(2):89–97. doi:10.1007/s11869-009-0036-0

Hadjimitsis DG, Retalis A, Clayton CRI (2002) The assessment of atmospheric pollution using satellite remote sensing technology in large cities in the vicinity of airports. Water Air Soil Pollut Focus 2(5–6):631–640. doi:10.1023/A:102130541700

Kambezidis HD, Weidauer D, Melas D, Ulbricht M (1998) Air quality in the Athens basin during sea breeze and non-sea breeze days using laser-remote-sensing technique. Atmos Environ 32 (12):2173–2182. doi:10.1016/S1352-2310(97)00409-3

Pfeffer HU, Friesel J, Elbers G, Beier R, Ellermann K (1995) Air pollution monitoring in street canyons in North Rhine-Westphalia, Germany. Sci Total Environ 169(1–3):7–15. doi:10.1016/0048-9697(95)04627-D

Pujadas M, Plaza J, Terés J, Artíñano B, Millán M (2000) Passive remote sensing of nitrogen dioxide as a tool for tracking air pollution in urban areas: the Madrid urban plume, a case of study. Atmos Environ 34(19):3041–3056. doi:10.1016/S1352-2310(99)00509-9

Pummakarnchana O, Tripathi N, Dutta J (2005) Air pollution monitoring and GIS modeling: a new use of nanotechnology based solid state gas sensors. Sci Technol Adv Mat 6(3–4):251–255. doi:10.1016/j.stam.2005.02.003

Randall VM (2008) Satellite remote sensing of surface air quality. Atmos Environ 42 (34):7823–7843. doi:10.1016/j.atmosenv.2008.07.018

On the Vertical Structure and Spectral Characteristics of the Marine Low-Level Jet

C.G. Helmis, G. Sgouros, and Q. Wang

Abstract The aim of this work is the study of the vertical turbulent structure and the spectral characteristics of the marine Low Level Jet (LLJ). The analyzed data are based on SODAR and in-situ instrumentation measurements, performed during summer 2003, in the frame of the Coupled Boundary Layers Air-Sea Transfer Experiment in Low Winds (CBLAST-Low), at Nantucket Island, MA, USA. The study of vertical profiles of the wind speed and temperature reveal the frequent development of marine LLJs, a modification of thermal stratification of the vertical structure of the marine Atmospheric Boundary Layer (MABL) and strengthening of LLJs depending on the meteorological conditions. In order to reveal the distribution of the intensity of wind variations in time scales corresponding to different physical processes, the Hilbert-Huang Transform (HHT) was applied to time series of the wind data from ground observations and SODAR data at different levels. Results are presented and discussed for a case study where the observed LLJ was formed on the top of the temperature inversion. It was persistent for several hours and the analysis of the wind speed data showed high amplitudes corresponding to contributions from the inertial motions but also from processes with a variety of time-scales.

C.G. Helmis (✉) • G. Sgouros
Department of Environmental Physics and Meteorology, University of Athens, University Campus, Zografou, Athens 15784, Greece
e-mail: chelmis@phys.uoa.gr

Q. Wang
Department of Meteorology, Naval Postgraduate School, Monterey, CA, USA

C.G. Helmis and P.T. Nastos (eds.), *Advances in Meteorology, Climatology and Atmospheric Physics*, Springer Atmospheric Sciences,
DOI 10.1007/978-3-642-29172-2_139,

1 Introduction

The study of the LLJ in the MABL has received considerable attention in several previous studies (Smedman et al. 1995; Munoz and Garreaud 2005) since it exhibits strong variations in space and time due to the land/sea surface forcing and the influence on the surface thermal and dynamical characteristics of the wind flow. Parish (2000) studying the LLJ along the California coast showed that the large-scale structure of the LLJ is related with the thermal circulation forced by the horizontal temperature contrast between land and ocean. Several mechanisms are responsible for the development and evolution of LLJs in general. These mechanisms include the local topography and/or baroclinicity resulting from large scale horizontal temperature gradient in the atmospheric boundary layer (Gerber et al. 1989), the mid-latitude fronts and synoptic gradients (Mori 1990), deformation frontogenesis (Blumen 1997) and the inertial oscillation due to the frictional decoupling (Banta et al. 2002). The present study focuses on the study of the vertical turbulent structure and the spectral characteristics of the marine Low Level Jet (LLJ). The measurements were made as part of the Coupled Boundary Layers and Air-Sea Transfer Low (CBLAST-Low) project aimed at the understanding of the air-sea interaction (Edson et al. 2007). The aim of this study is the contribution to the understanding of the LLJ development and evolution in the MABL by reporting and analyzing measurements of the upwind boundary layer as well as utilizing a newly developed signal processing technique, the Hilbert-Huang Transform.

2 Instrumentation and Data Analysis

The experimental campaign was carried out during the summer of 2003 (31 July to 27 August) at Nantucket Island, MA, USA. The CBLAST Nantucket measurement site was located on the southwest coast of the island within the complex of the Nantucket Waste Water Treatment Facility. The shortest distance (N-S direction) from the site to the waterfront is 94 m. Major instruments on the Nantucket site include a SOnic Detection And Ranging acoustic radar (SODAR – a commercial Remtech PA2), mean and turbulence measurements on a 20 m tower and a radiosonde system. The SODAR measurements yielded mean vertical velocity (w), horizontal wind speed and direction and the standard deviations of wind direction and vertical velocity at 30 min intervals. The vertical resolution of the SODAR is 40 m with a range of 500–700 m depending on the environmental acoustic noise and the atmospheric conditions, while the lowest measurement level was 50 m. Measurements of the mean wind, temperature and relative humidity and the corresponding standard deviations at 5, 10, and 20 m height, with a sampling frequency of 1 Hz and 10 min averaged output were carried out, while radiosondes were launched at the experimental site every 4–6 h.

Measurements of the vertical structure of the MABL from SODAR and radiosonde launches frequently indicated the development of a LLJ under steady

south-westerly (SW) wind conditions (upstream marine air) with moderate to high winds at the lower 500–600 m above the surface and northerly winds after the passage of cold fronts. The upwind MABL was characterized by a very stable surface layer at the first 100–150 m followed by slightly stable conditions at higher levels. In this paper, the presence of LLJs is identified following that of Banta et al. (2002) using the wind measurements from SODAR and radiosondes wind profiles. In addition, the profiles of potential temperature (θ), relative humidity (RH), horizontal wind speed and direction, from several radiosonde launches during these days were used. The HHT algorithm was applied to the estimated v and u components from the SODAR to reveal the temporal characteristics of the variations of the wind vectors at different levels. The recently developed HHT algorithm is an adaptive empirically-based data analysis method which has proved to be well-suited for studies of the ABL (Lundquist 2003; Sgouros and Helmis 2009). This method consists of two steps; the first one is the Empirical Mode Decomposition (EMD) that breaks the original time series into a finite number of Intrinsic Mode Function (IMF) components and the second one is the application of the Hilbert transform to the time series of each IMF component in order to obtain the best local fit of frequencies and amplitude variations as functions of time (Huang et al. 1999). The period of the inertial oscillation is $2\ \pi\ f_c^{-1}$ where fc is the Coriolis parameter ($f_c = 2\ \omega \sin \varphi$, where ω is the angular velocity of the earth and φ the latitude). For the Nantucket area (41 N, 70 W) the estimated inertial oscillation period is 18.36 h or a frequency of 0.027 cycles per 30 min (cp30 min).

3 Results and Discussion

During the summer period, North America is dominated by the anticyclones of the Pacific and the Bermuda-Azores in the North Atlantic. The Icelandic low appears much weaker than in winter, while in the desert regions of southwestern United States a thermal low appears. In the western fringes of the Bermuda High along the eastern coast of the U.S., southerly winds carrying moist air, which is lifted, cooled and condensed, produce showers and thunderstorms in the eastern coast. During the cold intrusions in the northeastern regions of the U.S., there are transported either continental polar air masses, very cold, dry and stable from Canada or maritime polar, cold, moist and unstable from the northwest Atlantic.

Figure 1 presents the 10 m height wind speed, direction and temperature time-series for the experimental period, 15–27 August 2003. During this period, four cases of LLJ events were observed, corresponding to episodes associated with the large scale southerly coastal flow and frontal events. The first event was a southerly large scale pre-frontal LLJ which lasted about 20 h from August 16, 2003–August 17 2003, while the second one was a post-frontal northerly jet from August 18, 2003–August 19 2003. The third LLJ event (19–23 August) was again a persistent southerly large scale one; while a pre-frontal (warm sector) LLJ event was reported over the experimental area, from August 25, 2003–August 26 2003 (Fig. 2).

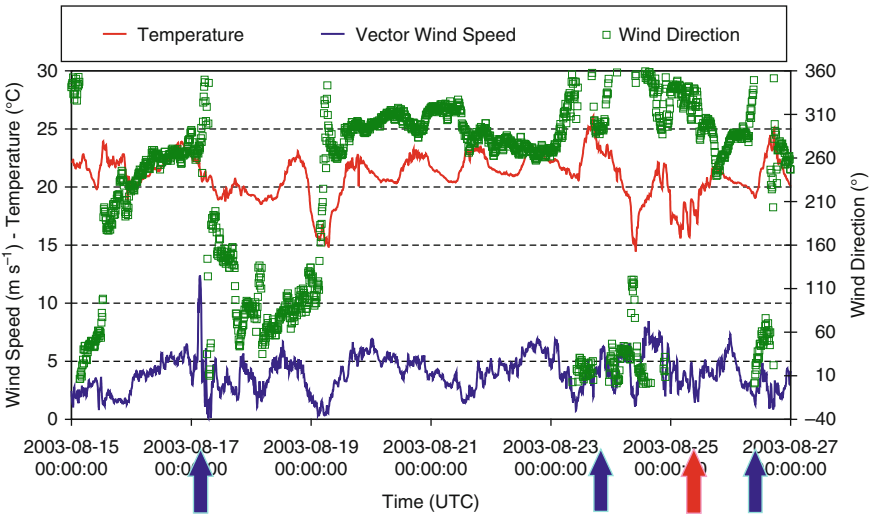

Fig. 1 Wind speed and direction at 10 m height and temperature for the period 15–27 August 2003 (*Arrows* denote warm (*red*) and cold (*blue*) frontal events)

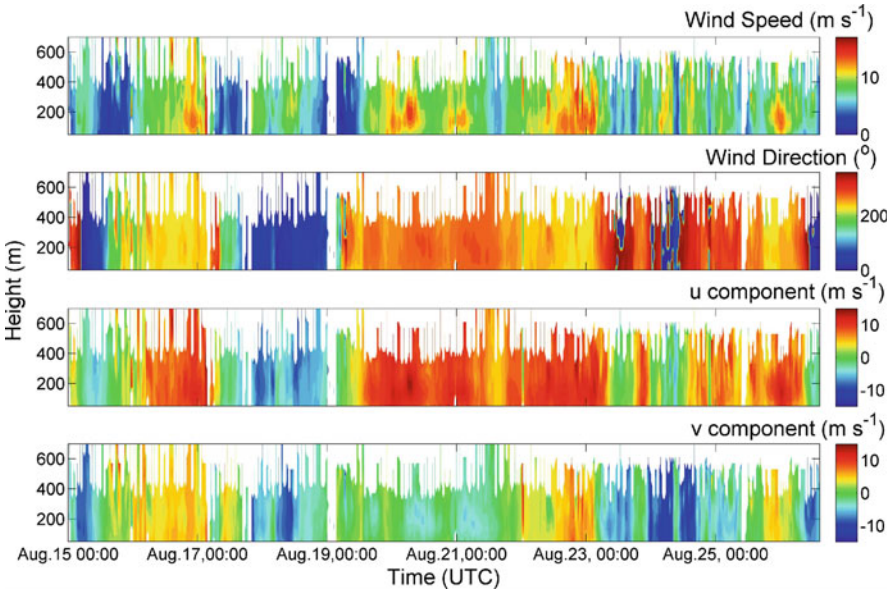

Fig. 2 Time-height plots of horizontal wind speed, direction, u and v components for the period 15–26 August 2003

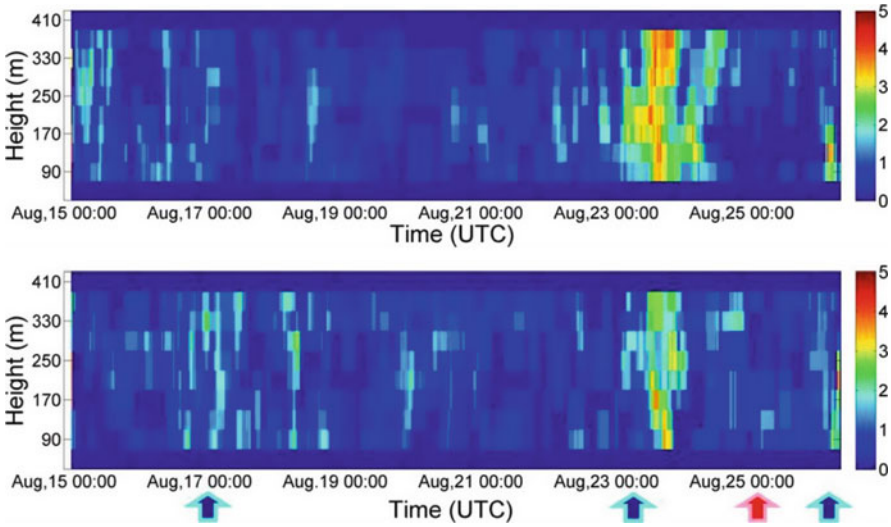

Fig. 3 Time – Height cross section of the inertial frequency amplitudes (ms^{-1}) calculated by the application of the HHT to the (*upper*) *u* and (*lower*) *v* component of the wind vector measured by the SODAR for the period 15–26 August 2003 (*Arrows* denote warm (*red*) and cold (*blue*) frontal events)

The wind LLJ maxima were found to be located above the MABL in relatively shallow layers showing that the studied southerly LLJs are associated with the shallow baroclinicity induced by the slopping MABL inversion. On the other hand, during the high duration LLJ case (19–23 August) an increase of the wind aloft produced a strong and persistent LLJ associated with the intensification of the pressure gradient at the eastern fringes of a low pressure center that was shifting eastward. It can be stated that the analyzed southerly LLJs are induced by the interaction of a slow moving cyclones over NE U.S. and the stationary high pressure system over the Atlantic Ocean as well as by the slopping inversion of the marine boundary layer. On the other hand, the northerly jets are linked with the cold frontal events. Figure 3 depicts the time-height distribution of the inertial frequency amplitudes, smoothed with a two-step vertical moving average window, calculated by the HHT for the period 15–26 August 2003. The *u* component depicts higher inertial motions then those calculated for the *v* component during the 23 and 26 August weaker frontal events (cold fronts), while the opposite is evident during the first frontal event (17 August). The increased strong absolute values of inertial amplitudes and their modification between the two wind components, for the periods of the cold and warm passages, are directly linked with the elliptical form of inertial motions caused by deformation frontogenesis (Blumen 1997; Sgouros and Helmis 2009). Weaker but significant inertial motions (greater than the mean values) are also observed in both components for the rest of the experimental period during the southerly LLJ events and especially after the 18th of August when frictional decoupling occurred with the shifted flow to the southerly sector. Diurnal

Table 1 Mean and standard deviation of the different scale amplitudes A (ms^{-1}) estimated by the HHT for the *u* and *v* components (August 15–26, 2003) for the analyzed levels

	Mesoscale motions (<12 h)	Inertial motions (~18 h)	Diurnal cycle (~24 h)	Synoptic scale (>48 h)
A_u (ms^{-1})	3.51+/−1.95	0.93+/−0.81	1.08+/−0.78	7.96+/−2.05
A_v (ms^{-1})	3.42+/−0.83	0.84+/−0.57	1.20+/−0.83	7.34+/−1.37

amplitudes for the two wind components (not shown) are imprinted in both components, while observed maxima at the layer between 100 and 300 m implies a correlation of this variation with the diurnal changes of the MABL height. Synoptic scale exhibits the highest amplitudes (Table 1), while increased are also the amplitudes of mesoscale motions, with very strong amplitudes observed during the frontal events (exceeding 10 ms^{-1}, not shown here).

4 Conclusions

For nearly all four LLJ cases the wind maxima are located just above the MABL in relatively shallow layers implying that the studied LLJs are associated with the shallow baroclinicity induced by the slopping MABL inversion. On the other the persistent LLJ case was associated with the large scale baroclinicity and the intensification of the pressure gradient at the eastern fringes of a low pressure center that shifted eastward. The complete set of the calculated complete Hilbert spectra was examined in order to identify the heights where amplitudes of inertial motions, diurnal variations and "mesoscale turbulence" are observed.

1. Increased strong inertial amplitudes for the periods of the warm and cold passages are linked with the elliptical form of inertial motions caused by deformation frontogenesis.
2. The observed maxima at the layer between 100 and 300 m regarding the diurnal cycle imply a correlation with the diurnal changes of the MABL height.
3. Strong mesoscale variations were observed during the frontal events.

References

Banta RM, Newsom RK, Lundquist JK, Pichugina YL, Coulter RL, Mahrt L (2002) Nocturnal low-level jet characteristics over Kansas during CASES-99. Bound-Lay Meteorol 105:221–252. doi:10.1023/A:1019992330866

Blumen W (1997) A model of inertial oscillations with deformation frontogenesis. J Atmos Sci 54:2681–2692. doi:10.1175/1520-0469(1997) 054<2681:AMOIOW>2.0.CO;2

Edson J et al (2007) The coupled boundary layers and air-sea transfer experiment in low winds (CBLAST-LOW). B Am Meteorol Soc 88:341–356

Gerber H, Chanf S, Holt T (1989) Evolution of a marine boundary layer jet. J Atmos Sci 46:1312–1326. doi:10.1175/1520-0469(1989) 046<1312:EOAMBL>2.0.CO;2

Huang NE, Shen Z, Long SR (1999) A new view of nonlinear water waves: the Hilbert spectrum. Annu Rev Fluid Mech 31:417–457. doi:10.1146/annurev.fluid.31.1.417

Lundquist JK (2003) Intermittent and elliptical inertial oscillations in the atmospheric boundary layer. J Atmos Sci 60:2661–2673. doi:10.1175/1520-0469(2003) 060<2661:IAEIOI>2.0.CO;2

Mori Y (1990) Evidence of inertial oscillations of the surface wind at Marcus Island. J Geophys Res 95:11777–11783. doi:10.1029/JD095iD08p11777

Muñoz RC, Garreaud RD (2005) Dynamics of the low-level jet off the West Coast of subtropical South America. Mon Wea Rev 133:3661–3677. doi:10.1175/MWR3074.1

Parish TR (2000) Forcing of the summertime low-level jet along the California coast. J Appl Meteorol 39:2421–2433. doi:10.1175/1520-0450(2000) 039<2421:FOTSLL>2.0.CO;2

Sgouros G, Helmis CG (2009) Low-level jet development and the interaction of different scale physical processes. Meteorol Atmos Phys 104(3):213–228. doi:10.1007/s00703-009-0028-5

Smedman AS, Bergstrom H, Horstrom U (1995) Spectra, variances and length scales in a marine stable boundary layer dominated by a low level jet. Bound-Lay Meteorol 76:211–232. doi:10.1007/BF00709352

Atmospheric Conditions Associated with High and Low Ozone Concentrations in the Boundary Layer and the Lower Troposphere over the Eastern Mediterranean (Aegean Sea)

P.D. Kalabokas

Abstract In this study the vertical ozone profiles during summertime (June to August) of the MOZAIC (Measurement of Ozone and Water Vapor by Airbus in Service Aircraft) Project over the eastern Mediterranean airports of Heraklion and Rhodes in Greece, have been analyzed in order to identify the major factors determining the ozone variability in the lower troposphere and the boundary layer over this area. In total 42 ozone profiles have been examined, which have been collected during a 10-year period (1996–2006). The corresponding vertical profiles of temperature, relative humidity and carbon monoxide have been also examined in parallel. It comes out that in the lower troposphere and to a certain extent within the boundary layer the role of the synoptic weather conditions and the associated large-scale transport of air masses seems to be more important in understanding the ozone variability than the local or regional short-term ozone photochemical production, for the examined area.

1 Introduction

It has been documented during the recent years that high rural background ozone levels, exceeding 60 ppb, have been observed in the lower troposphere and the boundary layer over mainland Greece, the Aegean Sea and other parts of the Eastern Mediterranean, especially during summertime (Varotsos et al. 1993; Kalabokas and Bartzis 1998; Kalabokas et al. 2000; Kourtidis et al. 2002; Kouvarakis et al. 2002; Kalabokas and Repapis 2004; Bossioli et al. 2007). The possibility for an influence of long-range pollution transport, mainly from the European continent, on ozone and its precursors over the Eastern Mediterranean has

P.D. Kalabokas (✉)
Academy of Athens, Research Center for Atmospheric Physics and Climatology,
24 Omirou str, Athens 10672, Greece
e-mail: pkalabokas@academyofathens.gr

C.G. Helmis and P.T. Nastos (eds.), *Advances in Meteorology, Climatology and Atmospheric Physics*, Springer Atmospheric Sciences,
DOI 10.1007/978-3-642-29172-2_140,

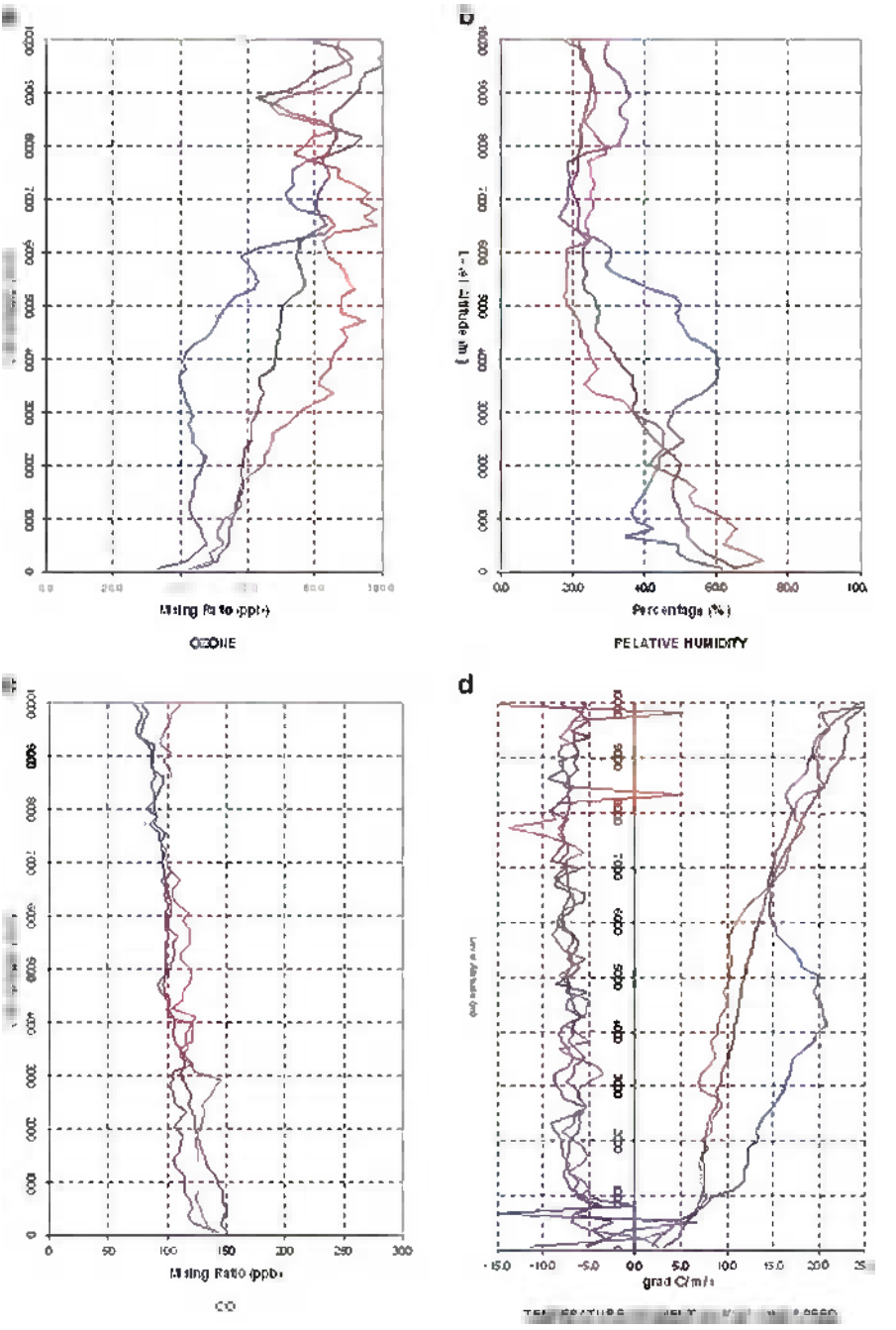

Fig. 1 (**a**) The averaged vertical summer (JJA) ozone profiles over the Eastern Mediterranean airports of Heraklion and Rhodes for the 10% highest (*red*) and the 10% lowest (*blue*) ozone

been discussed in several publications (Kallos 1995; Lelieveld et al. 2002; Zerefos et al. 2002; Volz-Thomas et al. 2003). In addition, the prevailing synoptic weather conditions seem to influence significantly the ozone levels in the lower troposphere and the boundary layer (Kalabokas et al. 2007; Kalabokas et al. 2008). The aim of this work is to further investigate the meteorological and pollution factors leading to high and low ozone levels in the boundary layer and the lower troposphere over the Aegean Sea.

2 Data and Methodology

Vertical MOZAIC (Measurement of Ozone and Water Vapor by Airbus in Service Aircraft, Marenco et al. 1998) profiles (42 in total) from ascending and descending flights over the Aegean airports of Heraklion (35.3°N, 25.2°E) and Rhodes (36.4°N, 28.1°E) have been analyzed (1996–2006). The analysis is focused on summertime (June to August) profiles. The analyzed parameters are: Ozone, carbon monoxide, relative humidity, temperature, and wind speed. The set of collected profiles is classified into groups of 10% highest and 10% lowest ozone levels for two vertical layers over the Aegean Sea: one layer within the boundary layer (500–1,000 m height) and one layer in the lower free troposphere (3,000–5,000 m).

3 Results and Discussion

The examination of the averaged vertical summer ozone profiles over Heraklion and Rhodes for the 10% highest and the 10% lowest ozone mixing ratios in the free troposphere, at 3,000–5,000 m, in parallel with the corresponding curves of relative humidity, carbon monoxide, temperature gradient and wind speed (Fig. 1), shows the following: The 10% highest ozone concentrations at 3,000–5,000 m over Heraklion and Rhodes are associated with low values of relative humidity and wind speed in that layer, indicating anticyclonic atmospheric conditions. On the other hand, the 10% lowest ozone concentrations at 3,000–5,000 m over the examined Aegean airports are associated with high values of relative humidity, wind speed and vertical temperature gradient indicating vertical instability and ascending movements of air masses. It is remarkable that, to the contrary of the large ozone and relative humidity differences in the lower troposphere, the observed over Heraklion and Rhodes average CO levels are comparable between

Fig. 1 (continued) mixing ratios at 3,000–5,000 m, (**b**) Same as (a) but for relative humidity, (**c**) Same as (a) but for carbon monoxide (CO), (**d**) (*left*), Same as (a) but for temperature gradient per km, (*right*), Same as (a) but for wind speed. The *black line* in (a), (b), (c), (d) shows the mean profile of the respective parameter (all profiles included) the figure legend

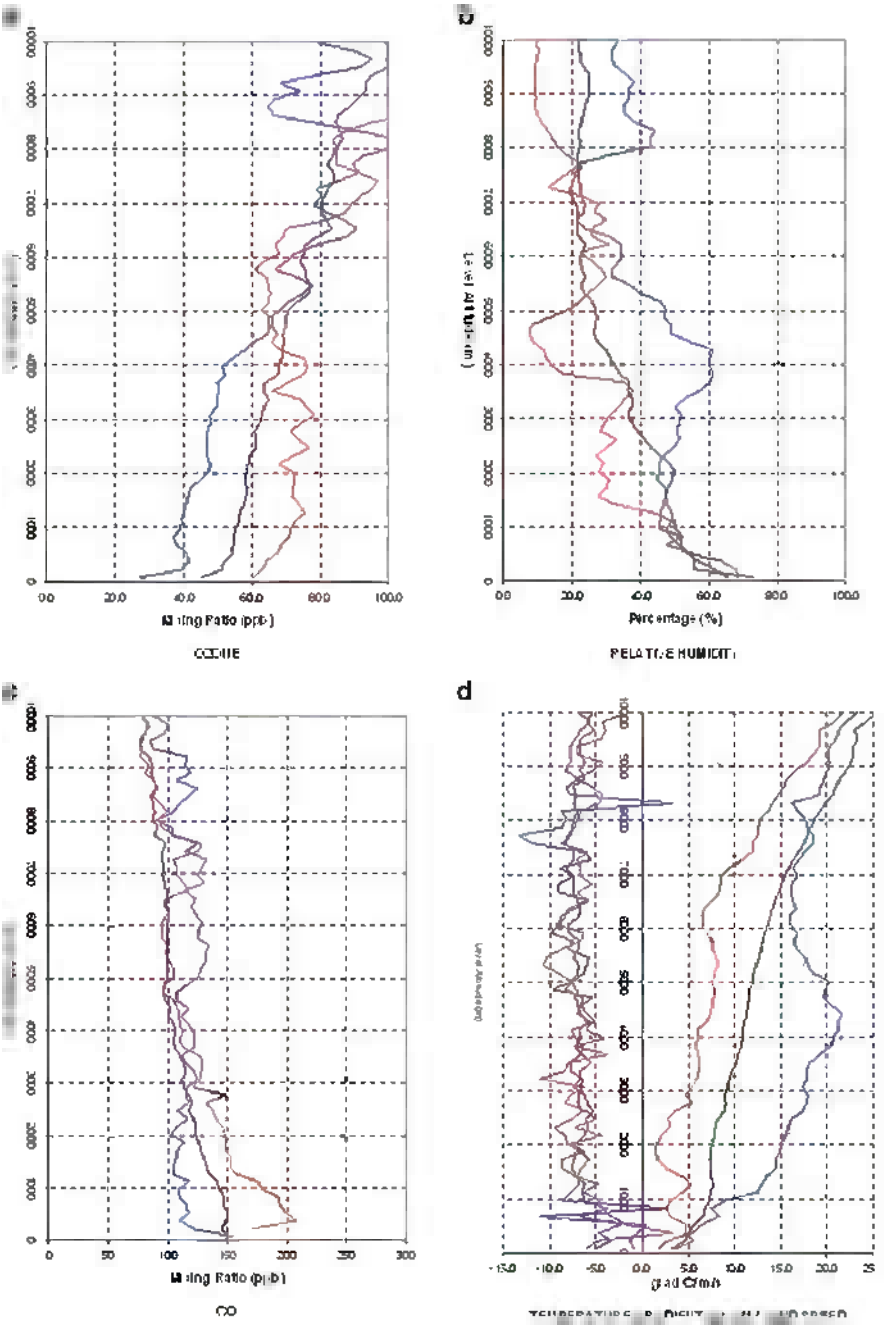

Fig. 2 (**a**) The averaged vertical summer (JJA) ozone profiles over the Eastern Mediterranean airports of Heraklion and Rhodes for the 10% highest (*red*) and the 10% lowest (*blue*) ozone

the highest and lowest ozone days over both airports, indicating comparable levels of primary pollution in the air masses under both examined conditions (highest-lowest ozone).

If the composite weather maps of geopotential heights at 500 hPa of the 10% of the days with the highest and the lowest ozone concentrations (at the 3,000–5,000 m layer) are plotted (not shown here), it is observed that the highest ozone concentrations in the lower troposphere and the boundary layer occur, in fact, during high pressure (anticyclonic) conditions prevailing over most of the European continent, which are associated with transport and subsidence of air masses from higher tropospheric layers leading to increase in ozone and decrease in relative humidity. On the other hand the lowest ozone values are associated with low-pressure systems covering Central and Eastern Europe leading to westerly circulation over Mediterranean towards the eastern region diffusing the air pollutants but also with the deepening and extension of the permanent summertime Middle-East low-pressure system.

The examination of the averaged vertical summer profiles over Heraklion and Rhodes for the 10% highest and the 10% lowest ozone mixing ratios within the boundary layer at 500–1,000 m (Fig. 2), shows that in the boundary layer almost no difference in relative humidity and a relatively small difference in wind speed is observed, to the contrary of the situation observed in the lower troposphere. The corresponding CO levels though are significantly higher during the highest ozone days in the boundary layer, indicating that high levels of ozone precursor pollutants (volatile organic compounds and nitrogen oxides) are also accumulated due to low atmospheric dispersion or stagnation and are susceptible to induce ozone photochemical production in the area under the favorable summertime conditions.

4 Conclusions

The analysis of the vertical summer ozone profiles measured in the period 1996–2006 in the framework of the MOZAIC project over the Eastern Mediterranean airports of Heraklion and Rhodes, shows that the highest ozone levels in the lower troposphere over the examined Eastern Mediterranean airports are associated with low relative humidity and wind speed. These measurements correspond to prevailing anticyclonic synoptic meteorological conditions. On the other hand, the lowest ozone levels are associated with high relative humidity and wind speed and occur during low pressure (cyclonic) meteorological conditions. In the free lower troposphere (3,000–5,000 m) the CO levels do not differ substantially between the

Fig. 2 (continued) mixing ratios at 500–1,000 m., (**b**) Same as (a) but for relative humidity, (**c**) Same as (a) but for carbon monoxide (CO), (**d**) (*left*), Same as (a) but for temperature gradient per km, (*right*), Same as (a) but for wind speed. The *black line* in (a), (b), (c), (d) shows the mean profile of the respective parameter (all profiles included)

highest and lowest ozone days, which shows that the high differences in tropospheric ozone (40–50 ppb) occur despite the comparable primary pollution levels in both examined situations, indicating the meteorological factor as predominant. Within the boundary layer, the CO levels are higher during the highest ozone days, implying that in addition to the influence of the rich in ozone higher tropospheric layers the local photochemical ozone production has a measurable contribution to the rural background boundary layer ozone levels during summertime over the area.

Acknowledgments The operators of the MOZAIC project (Dr. A. Volz-Thomas – Forschugszentrum Juelich, Germany, J.-P. Cammas and V. Thouret, Laboratoire d'Aerologie, CNRS and Universite de Toulouse, France) are gratefully acknowledged for providing data. Dr. C. Repapis (Academy of Athens and Mariolopoulos-Kanaginis foundation) is also acknowledged for helpful discussions and comments on the manuscript.

References

Bossioli E, Tombrou M, Dandou A, Soulakellis N (2007) Simulation of the effects of critical factors on ozone formation and accumulation in the Greater Athens Area. J Geophys Res 112:D02309. doi:10.1029/2006JD007185

Kalabokas PD, Bartzis JG (1998) Photochemical air pollution characteristics at the station of the NCSR-Demokritos, during the MEDCAPHOT-TRACE campaign, Greece (August 20th-September 20th, 1994). Atmos Environ 32(12):2123–2139

Kalabokas PD, Viras LG, Bartzis JG, Repapis CC (2000) Mediterranean rural ozone characteristics around the urban area of Athens. Atmos Environ 34(29–30):5199–5208

Kalabokas PD, Repapis CC (2004) A climatological study of rural surface ozone in Central Greece. Atmos Chem Phys 4:1139–1147. doi:10.5194/acp-4-1139-2004

Kalabokas PD, Volz-Thomas A, Brioude J, Thouret V, Cammas J-P, Repapis CC (2007) Vertical ozone measurements in the troposphere over the Eastern Mediterranean and comparison with Central Europe. Atmos Chem Phys 7:3783–3790. doi:10.5194/acp-7-3783-2007

Kalabokas PD, Mihalopoulos N, Ellul R, Kleanthous S, Repapis CC (2008) An investigation of the meteorological and photochemical factors influencing the background rural and marine surface ozone levels in the central and eastern Mediterranean. Atmos Environ 42:7894–7906

Kallos G (1995) Transport and transformation of air pollutants from Europe to the east Mediterranean region. Progress report, contract AVI-CT92-0005. European Commission on Environmental Research Programme Avicenne, Brussels.

Kourtidis K, Zerefos C, Rapsomanikis S, Simeonov V, Balis D, Perros PE, Thomson AM, Witte J, Calpini B, Sharobiem WM, Papayannis A, Mihalopoulos N, Drakou R (2002) Regional levels of ozone in the troposphere over eastern Mediterranean. J Geophys Res 107(D18):8140. doi:10.1029/2000JD000140

Kouvarakis G, Vrekoussis M, Mihalopoulos N, Kourtidis K, Rappenglueck B, Gerasopoulos E, Zerefos C (2002) Spatial and temporal variability of tropospheric ozone in the boundary layer above the Aegean Sea (eastern Mediterranean). J Geophys Res 107(D18):8137. doi:10.1029/2000JD000081

Lelieveld J, Berresheim H, Borman S et al (2002) Global air pollution crossroads over the Mediterranean. Science 298:794–799. doi:10.1126/science.1075457

Marenco A, Thouret V, Nedelec P, Smit H, Helten M, Kley D, Karcher F, Simon P, Law K, Pyle J, Poschmann G, Von Wrede R, Hume C, Cook T (1998) Measurements of ozone and water vapor by Airbus in-service aircraft: the MOZAIC airborne program, An overview. J Geophys Res 103:25631–25642. doi:10.1029/98JD00977

Varotsos C, Kalabokas P, Chronopoulos G (1993) Atmospheric ozone concentration at Athens. Greece. Part II: vertical ozone distribution in the troposphere. Atmos Res 30:151–155

Volz-Thomas A, Beekmann M, Derwent D, Law K, Lindskog A, Prevot A, Roemer M, Schultz M, Schurath U, Solberg S, Stohl A (2003) Tropospheric ozone and its control. In: Midgley et al. (Eds.) EUROTRAC-2 Final report, Part 1, Margraf Verlag, Weikersheim

Zerefos CS, Kourtidis KA, Melas D, Balis D, Zanis P, Katsaros L, Mantis HT, Repapis C, Isaksen I, Sundet J, Herman J, Bhartia PK, Calpini B (2002) Photochemical Activity and Solar Ultraviolet Radiation (PAUR) modulation factors: an overview of the project. J Geophys Res 107(D18):8134, doi: 10.1029/2000JD00134

A Case of African Dust Transport over Athens Captured by a Ceilometer

H.D. Kambezidis, A.G. Paliatsos, N. Kappos, and B. Kasselouri

Abstract The dust transport and its reaction with atmospheric pollution are increasingly gaining scientific interest as dust is considered to play a significant role in climate-change issues nowadays. The National Observatory of Athens has recently installed a ceilometer at the premises of its Actinometric Station (ASNOA). A ceilometer operates much like a lidar, but it only gives information about the laser-pulse energy (in the near IR) backscattered by clouds and atmospheric constituents (mostly airborne particles and less by molecules) in the form of attenuated backscatter coefficient; no information is given about absorption. Nevertheless, it is a useful instrument. The ASNOA ceilometer has been used in this work to record the laser-pulse echoes (backward-transmitted laser signals) on two occasions with and without African-dust transport over Athens (19 and 4 February 2010, respectively). Two methods for estimating the aerosol optical depth (AOD) for the 2 days are applied and compared. Conclusions are drawn about the applicability of the methods. Also, information about the free-troposphere transport (FTT) type of the dust aerosols is extracted from the analysis.

H.D. Kambezidis (✉) • N. Kappos
Atmospheric Research Team, Institute for Environmental Research and Sustainable Development, National Observatory of Athens, Athens, Greece
e-mail: harry@noa.gr

A.G. Paliatsos
General Department of Mathematics, Technological Education Institute of Piraeus, Athens, Greece

B. Kasselouri
School of Applied Arts, Hellenic Open University, Patras, Greece

C.G. Helmis and P.T. Nastos (eds.), *Advances in Meteorology, Climatology and Atmospheric Physics*, Springer Atmospheric Sciences,
DOI 10.1007/978-3-642-29172-2_141,

1 Introduction

It is well known that atmospheric aerosols play a significant role in the radiation budget of the earth-atmosphere climatic system (Haywood et al. 1999). Though this role has been extensively investigated and understood there are still large uncertainties for the aerosol radiative forcing at regional scale (Hougton et al. 2001). These uncertainties come from a lack of sufficient knowledge about aerosols' optical, physical and chemical properties and their large spatial and temporal variability. To reduce this uncertainty several measuring networks have been set up like AERONET (Holben et al. 2001), EARLINET (Pappalardo et al. 2010), MPLNET and REALM.

The vertical distribution of aerosols and their optical properties are two key parameters as inputs to various radiative-transfer models through which the aerosol radiative forcing can be calculated. Although lidars are good tools in estimating the spatial and temporal distribution of atmospheric aerosols, there is a difficulty in obtaining quantitative estimates of the aerosol extinction. Sources of error are the uncertainties in the lidar ratio (extinction-to-backscatter ratio) and the lidar-calibration constant. The lidar ratio depends upon the aerosol-phase function in the backscatter direction and the SSA. Other sources of uncertainty in the lidar (or ceilometer) measurements are related to the laser signal and the characteristics of the receiver. Nevertheless, there have been developed some calibration techniques (O'Conner et al. 2004), which rely on additional measurements.

One important type of atmospheric aerosols is dust aerosols from deserts. One of the bigger deserts close to Europe is Sahara. During dust outbreaks about 60% of the Saharan dust is transported into N. Atlantic and Mediterranean (Moulin et al. 1997; Kallos et al. 2006); often a significant amount reaches S. Europe (Papayannis et al. 2009), including Greece (Papayannis et al. 2005, 2009). Kalivitis et al. (2007) and Kaskaoutis et al. (2011) have identified three pathways of African-dust transport over Athens, Greece: (1) dust is transported in the layer from the surface up to the troposphere (vertical transport – VET), (2) dust is transported close to the surface and within the boundary layer (boundary-layer transport – BLT), and (3) dust is transported in the free troposphere (free-troposphere transport – FTT). The frequencies for all Saharan-dust events over Athens in the period 2000–2005 are 8%, 12% and 4% for BLT, VET and FTT, respectively.

This paper uses the recorded backscatter signal from a ceilometer (Vaisala CL31) installed at ASNOA premises located close to the Acropolis to identify the characteristics of such Saharan-dust event occurred on 19 February 2010. The purpose of the study is threefold. (1) it estimates AOD from the ceilometer readings using two methodologies; conclusions are drawn; (2) it compares AOD on the desert-dust day with ground-based PM_{10} measurements and draws conclusions; (3) verification of the FTT type over Athens is made.

2 Data and Methodology

The data used and the methodology applied are described in this section in a detail that is conceivable by non-experts in the fields of aerosol and remote-sensing research.

2.1 Data

The Vaisala CL31 ceilometer is a completely automated instrument to measure the ceiling of clouds up to a height of about 7.5 km. It incorporates an InGaAs laser source at 910 nm. The lidar transmits laser pulses at a frequency of 10 kHz. The ASNOA ceilometer operates by sending the laser pulses vertically. The echoes of the ceilometer are recorded as attenuated backscatter coefficients, $\beta(z)$.

Attenuated backscatter coefficients were measured on both 4 and 19 February 2010, 2 days characterised as Sahara-dust free and Saharan-dust events, respectively. For both days AOD was estimated from CL31 and SMARTS v2.95 code (see Sect. 2.2).

To compare the AOD values (estimated from SMARTS 2.95 and calculated from CL31) with ground-based PM_{10} values, the air-pollution measurements of the DEARTH network within the Athens basin were considered for the 2 days of interest. A first comparison of $\beta(z)$ between a vertical lidar and the ASNOA CL31 is given in Tsaknakis et al. (2011).

2.2 Methodology

$\beta(z)$ is a function of altitude, z. This coefficient is related to the extinction coefficient, $\sigma(z)$, through the relation:

$$\beta(z) = k * \sigma(z) \tag{1}$$

where k is the phase function having a typical value of 0.333 sr^{-1} (Münkel et al. 2007). The units of $\beta(z)$ and $\sigma(z)$ are $m^{-1}*sr^{-1}$ and m^{-1}, respectively. Since $\sigma(z)$ was not available from any other measurements (e.g. spectroradiometer) on the 2 days considered, the SMARTS v2.95 radiative-transfer code (Gueymard 1995) was used on both days, concurrently to the times of the ceilometer measurements to determine AOD. By taking the sum at both sides of (1) it is found that the sum of $\sigma(z)$ over all altitudes in the atmosphere is equal to AOD. This is a good approximation since $\Sigma\sigma(z)$ is done up to the altitude of 7.5 km. Therefore, (1) can be written as:

$$\sum \beta(z) = k * AOD \tag{2}$$

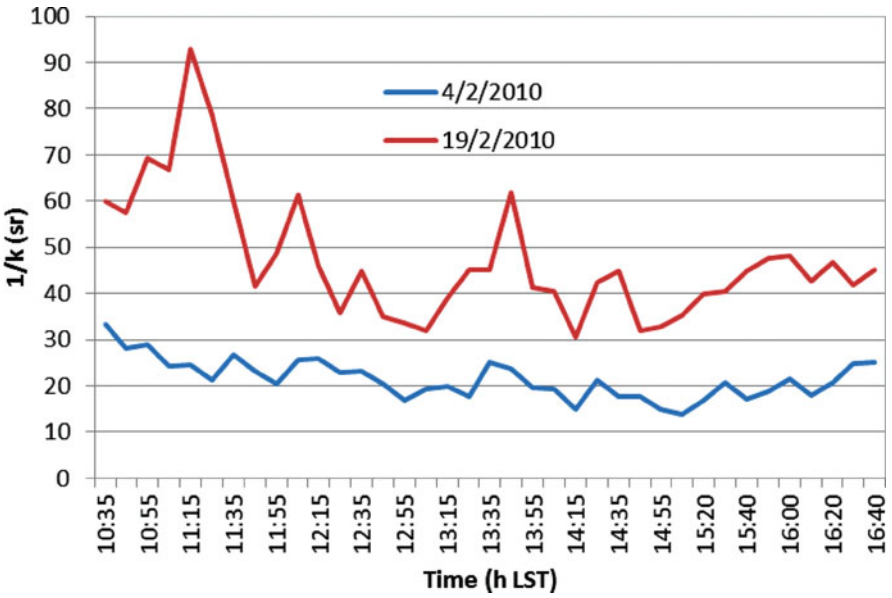

Fig. 1 Estimation of 1/k over Athens for 4 and 19 February 2010 derived from (2)

from which k can be estimated. The literature (e.g., Doherty et al. 1999; Papayannis et al. 2005, 2008) gives values of k ranging between as low as 0.1 sr^{-1} and as high as 0.01 sr^{-1} (for AOD ranging between 0.022 and 0.523, respectively).

3 Results

Figure 1 gives 1/k, the lidar ratio in sr, for 4 and 19 February 2010, respectively, as function of the time of the day.

It is seen from Fig. 1 that as the concentration of aerosols in the Athens' atmosphere was higher on that day, so was AOD; therefore, the CL31 (echoed) signal became higher, the noise buried in the signal was less (higher SNR) and the uncertainties connected with (2) became smaller. On the other hand, the 1/k values for 19 February 2010 were in the range of 40–90 sr and are in agreement with those found at Thessaloniki (Papayannis et al. 2008) and Athens (Papayannis et al. 2005) under Sahara-dust conditions (40–100 sr and 30–80 sr, respectively).

A variation of $\beta(z)$ versus height as derived from (2) is given in Fig. 2 for 4 and 19 February 2010. The presence of local aerosols over Athens at altitudes 1.5–2 km is clearly seen with very small values of $\beta(z)$ (Fig. 2a). To the contrary, Fig. 2b shows the day with the Sahara-dust event on 19 February 2010. The vertical distribution of the Sahara-dust aerosols has a peak at around 2.5 km, a finding that verifies the FTT type of transport, as said in the Introduction section. Indeed, near the surface the aerosol loading is not as high as above the boundary layer. The

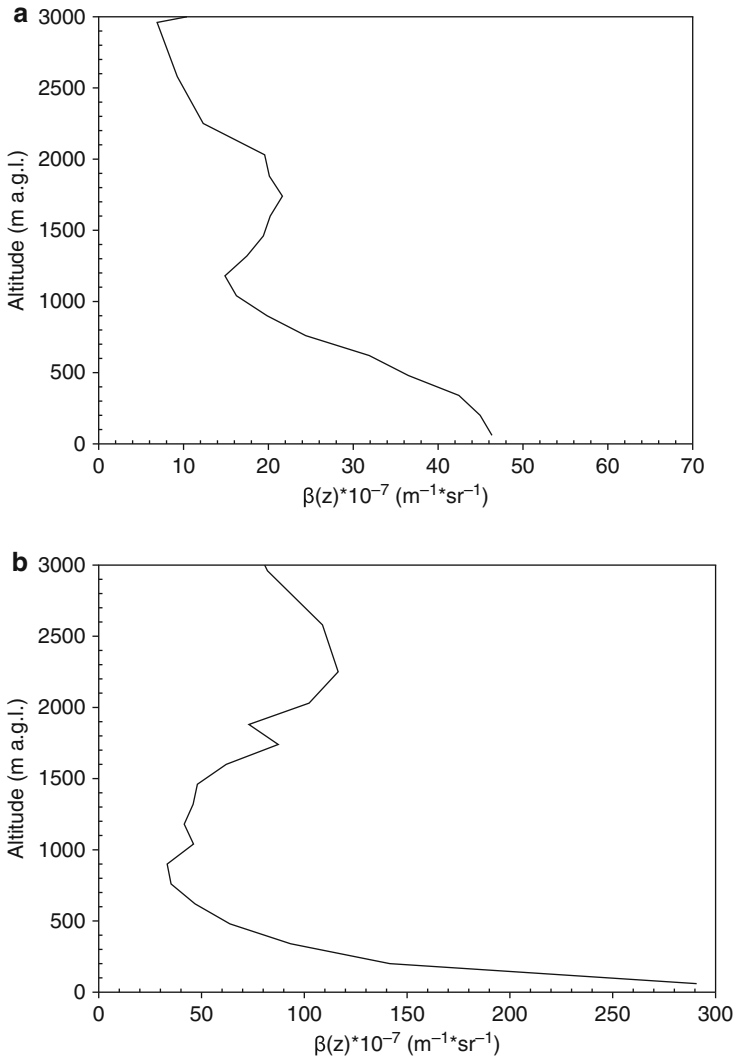

Fig. 2 Variation of β(z) versus altitude over Athens for (**a**) 4 February 2010 and (**b**) 19 February 2010

results of β(z) for 4 February 2010 are compared well with those of Tsaknakis et al. (2011), in terms of order of magnitude. Measurements by Tsaknakis et al. (2011) were taken at ASNOA with a vertical lidar and ASNOA CL31.

Figure 3 gives the horizontal distribution of the PM_{10} concentration over part of Athens on 19 February 2010 in comparison to the (reference) day of 4 February 2010. It is seen that the concentration of PM_{10} on the Sahara-dust event (Fig. 3, right panel) is much higher (at least twice) than the reference situation (Fig. 3, left panel). In both figures, the horizontal axis is geographical longitude (degrees) and the vertical one geographical latitude (degrees).

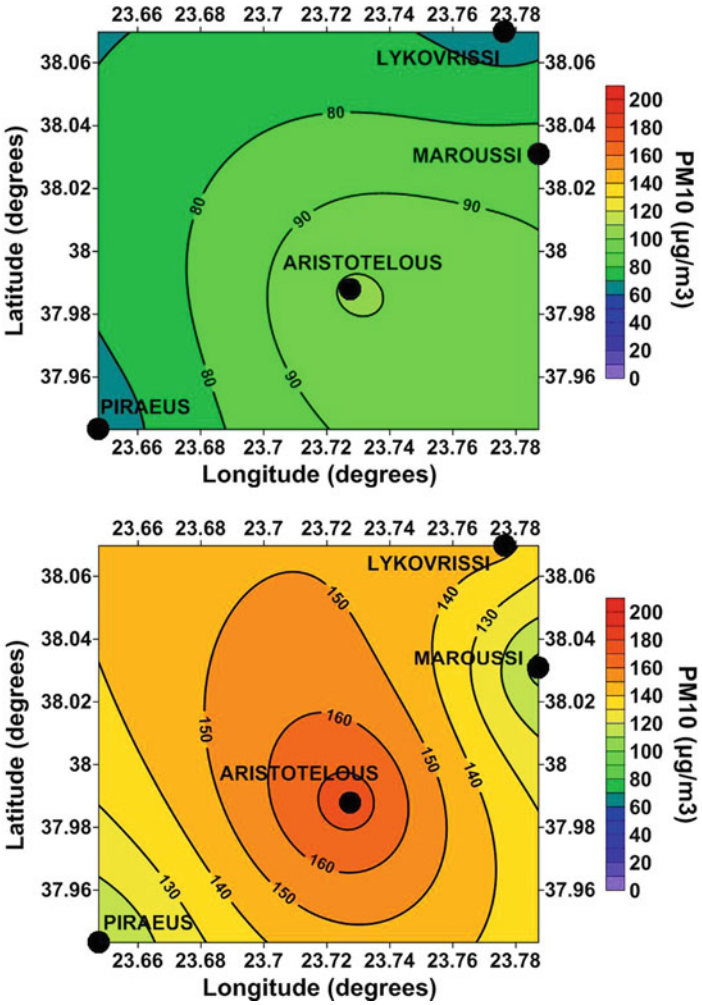

Fig. 3 Horizontal distribution of PM_{10} over part of Athens on 4 February 2010 (*upper*) and 19 February 2010 (*lower*) (Data source: DEARTH, Ministry of Environment, Energy and Climate Change [http://www.ypeka.gr/Default.aspx?tabid=490&language=el-GR])

4 Conclusions

Attenuated backscatter coefficient measurements from the ASNOA CL31 ceilometer have been used for two distinct cases of a clear day (4/2/2010) and a Sahara-dust event (19/2/2010) over Athens. From the profile of this parameter on the second case there was verified the FTT dust transport mechanism over Athens.

On the Sahara-dust day, increased PM_{10} concentrations were also measured at ground level giving a clear indication of the correlation between the dust aerosols above and particulate matter close to the surface (Münkel et al. 2007).

During 4/2/2010, β varied with altitude between almost $4 \cdot 10^{-6}$ m^{-1} sr^{-1} (surface) and $0.5 \cdot 10^{-6}$ m^{-1} sr^{-1} (3000 m). On 19/2/2010, β obtained greater values ranging from about $25 \cdot 10^{-6}$ m^{-1} sr^{-1} (surface) to $8 \cdot 10^{-6}$ m^{-1} sr^{-1} (3000 m).

References

Doherty SJ, Anderson TL, Charlson RJ (1999) Measurement of the lidar ratio for atmospheric aerosols using a 180 –backscatter nephelometer. Appl Optics 38(9):1823–1832. doi:10.1364/AO.38.001823

Gueymard C (1995) SMARTS2, a simple model of the atmospheric radiative transfer of sunshine: algorithms and performance assessment. FSEC report FSEC-PF-270-95

Haywood JM, Ramaswamy V, Soden BJ (1999) Tropospheric aerosol climate forcing in clear-sky satellite observations over the oceans. Science 283:1299–1303

Holben BN, Tanré D, Smirnov A et al (2001) An emerging ground-based aerosol climatology: aerosol optical depth from AERONET. J Geophys Res 106:12067–12097. doi:10.1029/2001JD900014

Houghton JT, Ding Y, Griggs DJ, Noguer M, van der Linden PJ, Dai X, Maskell K, Johnson CA (eds) (2001) Climate change 2001: the scientific basis. Cambridge University Press, Cambridge, UK/NY

Kalivitis N, Gerasopoulos E, Vrekoussis KG, Kubilay N, Hatzianastassiou N, Vardavas I, Mihalopoulos N (2007) Dust transport over the eastern Mediterranean derived from total ozone mapping spectrometer, aerosol robotic network, and surface measurements. J Geophys Res 112:D03202. doi:10.1029/2006JD007510

Kallos G, Papadopoulos A, Katsafados P, Nickovic S (2006) Transatlantic Saharan dust transport: model simulation and results. J Geophys Res 111:D09204. doi:10.1029/2005JD006207

Kaskaoutis DG, Kosmopoulos PG, Nastos PT, Kambezidis HD, Sharma M, Mehdi W (2011) Transport pathways of Saharan dust over Athens, Greece as detected by MODIS and TOMS. Geom Nat Haz Risk 3:35–54. doi:10.1080/19475705.2011.574296

Moulin C, Lambert CE, Dulac F, Dayan U (1997) Control of atmospheric export of dust from North America by the North Atlantic oscillation. Nature 387:691–694

Münkel C, Eresman N, Räsänen J, Karppinen A (2007) Retrieval of mixing height and dust concentration with lidar ceilometer. Bound Layer Meteorol 124:117–128. doi:10.1007/s10546-006-9103-3

O'Connor EJ, Illingworth AJ, Hogan RJ (2004) A technique for auto-calibration of cloud lidar. J Atmos Ocean Technol 21:777–786. doi:10.1175/1520-0426(2004) 021<0777:ATFAOC>2.0.CO;2

Papayannis A, Balis D, Amiridis V, Chourdakis G, Tsaknakis G, Zerefos C, Castanho AD, Nickovic S, Kazadzis S, Grabowski J (2005) Measurements of Saharan dust aerosols over the eastern Mediterranean using elastic backscatter-Raman lidar, spectrophotometric and satellite observations in the frame of the EARLINET project. Atmos Chem Phys 5:2065–2079. doi:10.5194/acp-5-2065-2005

Papayannis A, Amiridis V, Mona L, Tsaknakis G, Balis D, Boesenberg J, Chaikovski A, De Tomasi F, Grigorov I, Mattis I, Mitev V, Mueller D, Nickovic S, Perez C, Pietruczuk A, Pisani G, Ravetta F, Rizi V, Sicard M, Trickl T, Wiegner M, Gerding M, Mamouri RE, D'Amico G, Pappalardo G (2008) Systematic lidar observations of Saharan dust over Europe in the frame of EARLINET (2000–2002). J Geophys Res 113:D10204. doi:10.1029/2007JD009028

Papayannis A, Mamouri RE, Amiridis V, Kazadzis S, Pérez C, Tsaknakis G, Kokkalis P (2009) Systematic lidar observations of Saharan dust layers over Athens, Greece in the frame of EARLINET project (2004–2006). Ann Geophys 27:3611–3620

Pappalardo G, Wandinger U, Mona L et al (2010) EARLINET correlative measurements for CALIPSO: first intercomparison results. J Geophys Res 115:D00H19. doi:10.1029/2009JDO12147

Tsaknakis G, Papayannis A, Kokkalis P, Amiridis V, Kambezidis HD, Mamouri RE, Georgoussis G, Avdikos G (2011) Inter-comparison of lidar and ceilometers retrievals for aerosol and planetary boundary layer profiling over Athens, Greece. Atmos Meas Tech 4:1261–1273. doi:10.5194/amt-4-1261-2011

Drivers of Air Quality in the East Mediterranean

M. Kanakidou, N. Mihalopoulos, U. Im, S. Myriokefalitakis, and N. Daskalakis

Abstract Due to its location and the particularly warm and sunny climate, the East Mediterranean is receptor and chemical cooker of transported air pollution. Main local anthropogenic sources in the region are from traffic, combustion and energy generation concentrated in the large urban agglomerations in the region. These megacities local pollution emissions are added to high background regional air pollutant levels that are due to long range transport from upwind pollution or dust sources and to interactions of transported air masses with regional natural and anthropogenic emissions. Air quality in the East Mediterranean is strongly affected by sources other than the local anthropogenic sources. Thus, inter-country influences and natural contributions need to be documented. Improvement in air quality in the East Mediterranean requires coordinated effort between the countries surrounding the basin as well as the upwind located countries since their emissions affect the basin via long range transport and chemical aging of air masses. Our results clearly demonstrate significant imports of pollutants to the boundary layer via long range transport within the free troposphere followed by subsidence to the boundary layer. The impact of hot spot emissions in the area and its evolution in a warmer climate are evaluated and discussed.

M. Kanakidou (✉) • S. Myriokefalitakis • N. Daskalakis
Environmental Chemistry Processes Laboratory (ECPL), Department of Chemistry, University of Crete, P.O. Box 2208,Heraklion 71003, Greece

Institute of Chemical Engineering and High Temperature Chemical Processes (ICE-HT), Foundation for Research and Technology Hellas (FORTH), Patras 26504, Greece
e-mail: mariak@chemistry.uoc.gr

N. Mihalopoulos • U. Im
Environmental Chemistry Processes Laboratory (ECPL), Department of Chemistry, University of Crete, P.O. Box 2208,Heraklion 71003, Greece

C.G. Helmis and P.T. Nastos (eds.), *Advances in Meteorology, Climatology and Atmospheric Physics*, Springer Atmospheric Sciences,
DOI 10.1007/978-3-642-29172-2_142,

1 Introduction

The East Mediterranean region is an air pollution hotspot, located at a cross road of air masses from the surrounding regions that add to locally generated emissions. The warm and sunny climate of the area favors formation of secondary pollutants, such as ozone, compounding the air pollution problem. At the boundaries between the tropics and the mid-latitudes, the region is vulnerable to climate change. Main local anthropogenic air pollution sources are traffic, combustion, energy generation, open fire emissions. The East Mediterranean region has a high level of air pollution (Kanakidou et al. 2011) owing to:

- Local anthropogenic pollutant emissions from the region's megacities (Istanbul, Athens, Cairo),
- Significant natural emissions originating from within the region (i.e., sea salt, dust, plant emissions),
- Interactions of transported air masses with local/regional emissions
- Long range transport from upwind pollution (i.e., anthropogenic emissions from continental regions) or dust sources (i.e., Sahara desert).

Significant contributions to particulate matter originate from natural sources of dust (e.g., deserts) that are transported into the region and from within in the region itself. This influence is strongest in the southeast of the Mediterranean basin with a decreasing gradient of influence to the northwest.

Within the EU FP7 project CityZen, observational data analysis and modeling for the region have been performed. Mesoscale and global chemistry transport modeling has been used to distinguish and quantify the various impacts on air pollution. In the following the major results are outlined.

2 Methodology

The global 3-dimensional chemistry transport model TM4-ECPL has been operated on a $3^\circ \times 2^\circ$ horizontal resolution and 34 vertical layers from surface to the 10 hPa. The model is able to simulate gas and multiphase chemistry, accounting for carbon, nitrogen and sulfur chemistry, as well as all major primary and secondary aerosol components (Myriokefalitakis et al. 2011 and references therein). The model is driven by ECMWF ERA-iterim meteorology. For the present study simulations have been performed with the global model for the year 2008 (1) by using the anthropogenic emissions for the year 2008 derived from the Doering et al. (2009) developed for the CIRCE EU project; (2) by neglecting them and (3) by using the 2025 emission estimates. Import/export fluxes to and from the Eastern Mediterranean have been also derived from the TM4-ECPL model.

The mesoscale atmospheric modeling system used for this study consists of the Weather Research and Forecasting model (WRF-ARW v3.1.1) online coupled with the Model of Emissions of Gases and Aerosols from Nature (MEGAN) module of

the WRF-CHEM 3.1.1 for biogenic emissions, and off-line coupled with the U.S. EPA Community Multiscale Air Quality (CMAQ) model, v4.7. The domain and horizontal (30 × 30 km) and vertical (30 layers) resolutions of the mesoscale model, the physical and chemical options, the initial and boundary conditions and the scenarios adopted are described in Im et al. (2011). The anthropogenic emissions for the model domain are compiled using INERIS emissions for Europe to which, emissions for Greece on 10 × 10 km and for Istanbul and Athens on 2 × 2 km horizontal resolution have been merged (Im et al. (2011) and references within). The global chemistry transport model TM4-ECPL provides the initial and boundary conditions for the chemical tracers. For the present, several mesoscale simulations have been performed accounting and omitting the anthropogenic emissions of Athens and Istanbul extended areas as well as of the entire East Mediterranean. The effect of temperature changes on gaseous and particulate air pollutant levels in the Eastern Mediterranean has been investigated using the WRF/CMAQ mesoscale modeling system coupled with the MEGAN model for the processing of BVOC emissions. A set of temperature perturbations (spanning from 1°C to 5°C) has been investigated for July 2004 conditions.

3 Results

The result of the global and mesoscale simulations enabled the evaluation of the contribution of various sources to the air pollution levels in the East Mediterranean. The main results are here outlined and contrasted with relevant estimates derived from observations. They are also complemented by reference to other works.

3.1 Contribution of Local Anthropogenic Emissions to Air Pollution in Megacities

Analysis of SCIAMACHY satellite data enabled a first evaluation of the local anthropogenic contribution to the extinction of solar radiation by aerosols over the Greater Athens Area and Greater Cairo Area at 15–30% and 25–50%, respectively (Hatzianastassiou et al. 2009). This contribution maximizes during summer when at Cairo urban sites the contribution of local anthropogenic emissions to PM levels can reach almost 100%. Observations reveal that in the urban cores most fine mode particulate matter of local origin is dominated by organic matter and elemental carbon (up to ~60%; Theodosi et al. 2011), whereas in downwind locations the inorganic secondary components dominate particulate matter that is composed by larger particles.

Mesoscale simulations show that summertime fine particulate matter in Athens originates by 65% from local anthropogenic emissions, 10% from the regional biogenic emissions and 25% from long-range transport. For Istanbul, these

contributions are 75%, 3%, and 22%, respectively (Im and Kanakidou 2011). During summertime, Istanbul anthropogenic emissions are responsible for about 20% reduction in O_3 inside the extended megacity area itself, whereas they increase O_3 in the suburbs and downwind (Im and Kanakidou 2011). In contrast, Athens anthropogenic emissions have small impact on ozone in the Athens extended area (~7% increase). This difference is attributed to the elevated regional influence in Athens compared to Istanbul. The significant local influence in Istanbul is seen by the low carbon monoxide to nitrogen oxides molar ratios. High regional ozone is affected by different organic gases to nitrogen oxides ratios and organic gases speciation.

3.2 Pollution Inflow/Outflow

Air pollution outflow from megacities deteriorates the air quality of the region and can lead to an increased number of exceedances of the European Union limits for ozone and particulate matter. Istanbul anthropogenic emissions have significant regional impact in the outflow downwind the megacity over the Aegean Sea where in particular secondary air pollutants like ozone and secondary aerosols are increasing (Im and Kanakidou 2011). They contribute to regional aerosol concentrations (3% for fine particles) five times more than Athens emissions (0.6%). Similar case holds for gaseous pollutants with Istanbul emissions contributing slightly more to the regional mean concentrations (0.5% for ozone, 1.1% for carbon monoxide, 2.9% for PAN) than Athens emissions (0.4% for ozone, 1% for carbon monoxide, 2.5% for PAN). Interactions between anthropogenic and natural emissions in the region further enhance air pollution, producing ozone, particulate matter or changing the properties of atmospheric particles. For instance, coating by pollutants increases dust solubility and deposition of nutrients. Thus, organic aerosol in the urban sites is primary by 50% whereas downwind it has been chemically modified and is most secondary in nature. Global simulations show that the tropospheric ozone column in the East Mediterranean is largely maintained (>90%) by emissions from outside the region and long-range transport (Fig. 2a,c). In particular, large amounts of O_3 enter and leave the region through the free troposphere, whereas higher amounts of O_3 are penetrating the boundary layer form the free troposphere than are formed inside the boundary layer. The contribution of long range transport is smaller (~55%) for the shorter lived nitrogen dioxide column and for particulate matter (~40%) when excluding Saharan dust and sea-salt contributions (Myrokefalitakis et al. 2012).

3.3 Future Air Pollution Levels

Athens and particularly Istanbul urban centers are chemical sinks for O_3. These urban cores however emit large amounts of O_3 precursors (NO_x and NMVOCs)

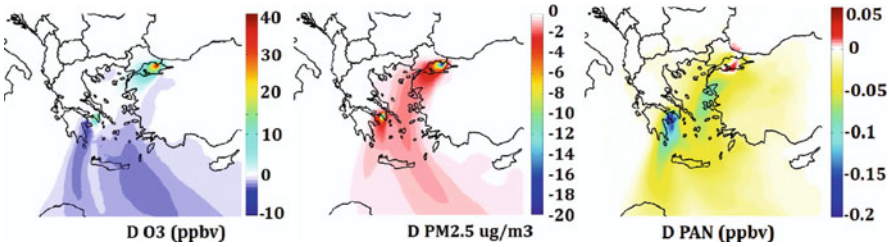

Fig. 1 Changes in surface concentrations of (*left*) ozone (ppbv), (*middle*) fine particles (μg/m^3) and (*right*) PAN (ppbv) resulting from omission of anthropogenic emissions from Athens and Istanbul extended areas

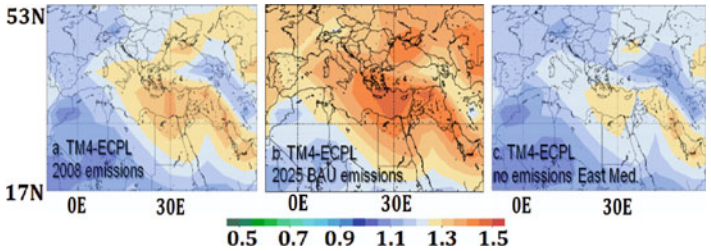

Fig. 2 Tropospheric O_3 column (in 10^{18} molecules/cm^2) simulated by the TM4-ECPL with 2008 ERA-iterim meteorology: (**a**) base case with 2008 emissions; (**b**) with 2025 BAU emissions (**c**) neglecting all East Med. emission (Myrokefaliakis et al. in preparation)

which lead to production of O_3 downwind (Fig. 1, see also in Im et al. 2011). According to our simulations, higher temperatures increase BVOC emissions by 9% K^{-1}. For the studied temperature perturbations, the regional O_3 mixing ratios increase almost linearly with the increases in ambient temperatures by 1 ± 0.1 ppb O_3 K^{-1}. Smaller increases (about half) are computed for the highly polluted Istanbul area (Im et al. 2011). In a warmer climate, lesser increases are expected for secondary organic aerosol and nitrate aerosols, while sulfate aerosols are expected to decrease in future summers with warmer temperatures (Im et al. 2012).

Global simulations assuming business as usual increase in the region and the global anthropogenic emissions and present climate, indicate that significant enhancements in the tropospheric ozone column (Fig. 2c) in the region have to be expected if no addition measures are taken to reduce air pollution.

4 Concluding Remarks

During the last two decades over the Greater Athens and Istanbul Areas significant improvements in air quality have been recorded. These improvements have been linked to a reduction in primary emissions owing to changes in transportation fuels

and industrial emissions controls. These improvements vary between megacities depending on the efficiency of measures adopted and the timing of implementation. However, future increases in emissions (e.g., owing to economic growth, shipping emissions) could counteract the current trend of improvements. The risk of open fires is also expected to increase in a warmer climate.

Our results show that regional characteristics should be taken into account when developing air pollution control strategies, considering the influence of natural sources and long-range transport. Improvement of air quality in the East Mediterranean will require a coordinated effort among the countries in the region and beyond. In addition to national legislation, a regional strategy for air quality and climate change mitigation should be pursued in order to be able to effectively achieve significant improvements.

Acknowledgments This work has been supported by the CityZen European Union FP7 programme.

References

Doering U, van Aardenne J, Monni S, Pagliari V, Orlandini L, San Martin F (2009) CIRCE report D8.1.3 Update of gridded emission inventories, addition of period 1990–2005 and the years 2010, 2015, 2050, Project FP6: 6.3 – No. 036961 – CIRCE

Hatzianastassiou N, Gkikas A, Mihalopoulos N, Torres O, Katsoulis BD (2009) Natural versus anthropogenic aerosols in the Eastern Mediterranean basin derived from multi-year TOMS and MODIS satellite data. J Geophys Res 114:D24202. doi:10.1029/2009JD011982

Im U, Kanakidou M (2011) Summertime impacts of Eastern Mediterranean megacity emissions on air quality. Atmos Chem Phys Discuss 11:26657–26690. doi:10.5194/acpd-11-26657-2011

Im U, Markakis K, Poupkou A, Melas D, Unal A, Gerasopoulos E, Daskalakis N, Kindap T, Kanakidou M (2011) The impact of temperature changes on summer time ozone and its precursors in the Eastern Mediterranean. Atmos Chem Phys 11:3847–3864. doi:10.5194/acp-11-3847-2011

Im U, Markakis K, Koçak M, Gerasopoulos E, Daskalakis N, Mihalopoulos N, Poupkou A, Kindap T, Unal A, Kanakidou K (2012) Summertime aerosol chemical composition in the Eastern Mediterranean and its sensitivity to temperature. Atmos Environ. doi:10.1016/j.atmosenv.2011.12.044

Kanakidou M, Mihalopoulos N, Kindap T et al (2011) Megacities as hot spots of air pollution in the East Mediterranean. Atmos Environ 45:1223–1235. doi:10.1016/j.atmosenv. 2010.11.048

Myriokefalitakis S, Tsigaridis K, Mihalopoulos N, Sciare J, Nenes A, Segers A, Kanakidou M (2011) In-cloud oxalate formation in the global troposphere: a 3-D modeling study. Atmos Chem Phys 11:5761–5782. doi:10.5194/acp-11-5761-2011

Myriokefalitakis S, Daskalakis N, Aan de Brugh JMJ, Krol M, Im U, van Ardenne J, Doering U, Kanakidou M (2012) On the contribution of long-range transport to Eastern Mediterranean air pollution: A 3-D modeling study, in preparation

Theodosi C, Grivas G, Zarmpas P, Chaloulakou A, Mihalopoulos N (2011) Mass and chemical composition of size-segregated aerosols (PM1, PM2.5, PM10) over Athens, Greece: local versus regional sources. Atmos Chem Phys 11:11895–11911. doi:10.5194/acp-11-11895-2011

Model for Estimating Atmospheric Ozone Content over Northern Europe for Use in Solar Radiation Algorithms

K. Karavana-Papadimou, B. Psiloglou, S. Lykoudis, and H.D. Kambezidis

Abstract Part of the attenuation to the incoming solar radiation by the atmosphere is attributed to absorption by ozone in the UV and visible portions of the spectrum. Ozone absorption typically accounts for only 2–3% of the global solar radiation depletion, but it is often 10–20% of the absorption of the direct component. Thus, broadband solar radiation models require atmospheric ozone content as input in order to correctly calculate the direct component. As reported by Heuklon (Sol Eng 22:63–68, 1979) described the general spatial and temporal characteristics of the ozone column in the atmosphere with an empirical mathematical relationship that can be easily incorporated into solar radiation transmission models (codes). The model requires only the day of the year, the latitude and longitude of the location of interest in order to calculate the total ozone column for that place and time, based upon observed climatological averages. In this study, the validity of van Heuklon's formula for the atmospheric ozone content estimation is tested against satellite measurements for a number of cities in Northern Europe. A new model based on the van Heuklon formula is fitted, with promising results.

1 Introduction

Solar radiation is absorbed by the lower troposphere and by the Earth's surface and is one of the major driving sources of tropospheric air motion. The prediction of solar radiation at the Earth's surface, using physical meteorological models,

K. Karavana-Papadimou
Dept. of Geology and Geoenvironment, National and Kapodistrian University of Athens, Athens, Greece

B. Psiloglou • S. Lykoudis • H.D. Kambezidis (✉)
Institute for Environmental Research and Sustainable Development, National Observatory of Athens, Athens GR-11810, Greece
e-mail: harry@noa.gr

C.G. Helmis and P.T. Nastos (eds.), *Advances in Meteorology, Climatology and Atmospheric Physics*, Springer Atmospheric Sciences,
DOI 10.1007/978-3-642-29172-2_143,

requires knowledge of the transmission functions of all atmospheric constituents, and a good estimation of their respective amounts in the atmosphere.

Though water vapour is the principal absorber of solar radiation in the atmosphere, the atmospheric ozone absorption is also of high importance, typically accounting for only 2–3% of solar radiation's attenuation, especially in the ultra violet B-region, but its contribution can reach up to 9–10% at high latitudes during summer. Several methods exist for calculating absorption due to ozone (Lacis and Hansen 1974; Hoyt 1978; Bird and Hulstrom 1981; Psiloglou et al. 1996), but they need the amount of ozone in the optical path as input. Consequently, the determination of ozone absorption relies upon the estimation of the ozone content of the atmosphere at a place and time.

Before the launch of satellites born instruments for measuring ozone's total column from space, Heuklon (1979) introduced a simple mathematical model, in order to represent the general spatial and temporal characteristics of ozone presence in the atmosphere. In fact, the van Heuklon model requires only the day of the year and the latitude and longitude of the location of interest to calculate the total ozone column. According to the model, the atmospheric amounts of ozone (in matm·cm) for any day of the year, and any location in the Earth's northern hemisphere, is the result of the combination of three variations around the equatorial annual average atmospheric ozone content, J:

$$\begin{aligned} O_3 = {} & J + A \cdot sin^2(\beta \cdot \varphi) + C \cdot sin[D \cdot (E + F)]\left[sin^2(\beta \cdot \varphi)\right] \\ & + G \cdot sin[H(\lambda + I)][sin^2(\beta \cdot \varphi)] \end{aligned} \tag{1}$$

where φ is latitude (degrees), and λ longitude (degrees), A represents the latitudinal, G the longitudinal and C the seasonal variation. The parameter β corrects for the latitude of maximum ozone content, E is the day of the year, D converts days to fractional parts of 360, F adjusts for the day of maximum and minimum ozone occurrence, H is set to 3 in order for the sine wave to repeat every 120°, and I depends on λ. The squared sine is used rather than the simple sine to produce the broad minimum of low latitudes and strongest gradients in the mid-latitudes in accordance to the observed spatial distribution. Therefore, (1) becomes for Northern Europe:

$$\begin{aligned} O_3 = {} & 235 + \{150 + 40 \cdot sin[0.9865 \cdot (E - 30)] + 20 \cdot sin[(3 \cdot (\lambda + 20)]\} \\ & \cdot \left[sin^2(1.28 \cdot \varphi)\right] \end{aligned} \tag{2}$$

Satellite measurements of atmospheric ozone in the last decades report an average atmospheric ozone amount of 300–400 matm·cm, reaching a minimum at equatorial latitudes and increasing pole wards, in both hemispheres, to a maximum of 400 matm·cm at the sub polar latitudes. Over the tropics the ozone vertical distribution is generally constant throughout the year, but at higher latitudes a marked seasonal variation is observed. Nevertheless, despite the wide use of this

model in solar radiation models up to mid-90s, its estimations are nowadays out of acceptable accuracy because average ozone levels declined during the 1980s and 1990s over Northern Europe. Therefore, its coefficients must be re-calculated.

Information derived from satellite measurements has been widely used in solar radiation models; however, there is still use for empirical ozone content models, for example in cases where satellite data are not available. The purpose of this study is to establish an empirical model for the ozone amount in the regions of Northern Europe, based on satellite measurements accumulated over the past decades. Moreover, we explore possible interrelationships between the seasonal and geographical variation of ozone amount across the examined region.

2 Data

NASA spacecrafts Nimbus-7 (1/11/1978 to 6/5/1993), Meteor-3 (22/8/1991 to 24/11/1994) and Earth Probe (25/7/1996 to 31/12/2005) have provided an extended database of daily total ozone column measurements over 206 locations worldwide, using the Total Ozone Mapping Spectrometer (TOMS).

For the needs of this analysis, TOMS measurements (version 8) from all three satellites were collected for 20 cities in Northern Europe (Table 1 and Fig. 2) covering the period from 1/11/1978 until 31/12/2005 (NASA 2011). These data have been corrected for a multitude of possible errors occurring under extreme conditions.

3 Methodology

In order to obtain an expression that better describes the ozone distribution across entire Northern Europe, a model based on van Heuklon's formula (1) was fitted to the entire Northern European data set, using non-linear regression analysis. In this analysis the parameters J, H, and β were considered as constants; J was taken as the average of the zone (−5°, +5° latitude) from the satellite data of the years 1978–2005, equal to 260 matm·cm, and following some initial exploratory analyses H retained its original value of 3, as did β (=1.28).

It also seemed interesting to further examine the geographical variation of the calculated parameters C and F, since they determine the ozone seasonal variation (S_{oz}), and possible relationships between those parameters and a location's (φ, λ) might account for some of the unexplained variance in the data.

Using the values of A, G and I obtained from the previous non-linear regression analysis of the entire database, new models based on the van Heuklon formulation were developed for every location separately, providing the spatial distribution of the C and F parameters in the examined region. An attempt to quantify this spatial

Table 1 Coordinates of the 20 cities selected across Northern Europe, along with the estimated values and standard errors (SE) of model parameters C and F

City	φ	λ	C	SE (±)	F	SE (±)
Amsterdam	52.37	4.90	55.3	0.6	−25.7	0.7
Copenhagen	55.65	12.57	54.4	0.6	−20.3	0.7
Frichtelberg	50.42	12.93	54.5	0.7	−19.1	0.7
Jokioinen	60.82	23.50	53.7	0.6	−15.2	0.7
Kaltennordheim	50.62	10.13	54.6	0.7	−20.7	0.7
Kiruna	67.52	20.13	53.6	0.6	−7.2	0.8
Langenbrugge	52.78	10.77	54.8	0.6	−21.2	0.7
London_Sibton	51.50	0.12	55.9	0.8	−27.1	0.8
Manchester	53.47	−2.13	53.9	0.5	−29.5	0.6
Minsk	55.82	27.47	53.1	1.0	−12.9	1.1
Norrkoping	58.6	16.12	54.2	0.6	−19.2	0.7
Oslo	59.92	10.72	54.4	0.6	−20.4	0.7
Riga	57.32	24.42	53.4	0.6	−15.9	0.7
Sodankyla	67.37	26.63	53.3	0.6	−8.8	0.8
St._Petersburg	59.97	30.28	53.0	0.6	−14.3	0.7
Strath-Vaich	57.72	−4.77	53.4	0.6	−28.0	0.7
Tromso	69.65	18.95	53.5	0.6	−3.8	0.8
Uppsala	59.83	17.62	54.4	0.6	−18.3	0.7
Vindelin	64.23	19.77	52.1	0.6	−14.4	0.7
Warsaw	52.25	21.00	50.6	0.9	−13.0	1.0

variation was made by an exploratory analysis of C and F dependence on φ and λ was performed using variations of the generic formula:

$$y = [a \cdot sin(\lambda + b)] \cdot [c \cdot sin^{d}(\varphi + e)] \tag{3}$$

4 Results

Fitting the van Heuklon model to the measured Northern European daily ozone amounts provided satisfactory results ($R^2 = 0.45$) especially considering that day-to-day variation may be more than 30% during the cold period (Fig. 1). This also suggests that even though the model is a fairly good representation of the dependencies of total ozone amount, there might be other relationships that remain hidden in the model's parameters. The final formula of the ozone model over Northern Europe, with parameters statistically significant at 95% confidence level, is:

$$\begin{aligned} O_3 = 260 + \{(74 \pm 0.7) + (53.7 \pm 0.1) \cdot \sin\{0.9865 \cdot [E - (18.4 \pm 0.2)]\} \\ + (8.0 \pm 0.5) \cdot \sin\{3 \cdot [\lambda + (35.8 \pm 1.5)]\}\}[\sin^2(1.28 \cdot \varphi)] \end{aligned} \tag{4}$$

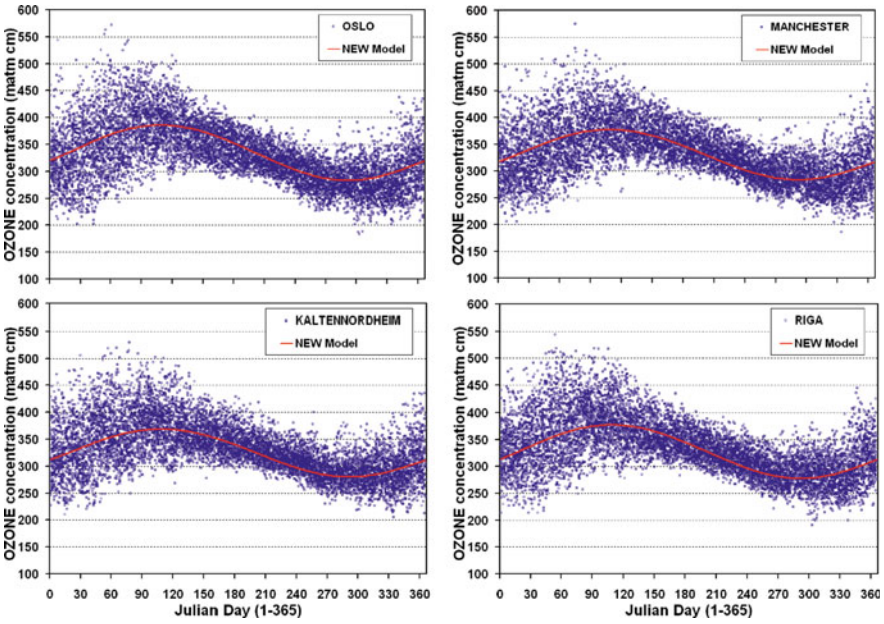

Fig. 1 The temporal variation of ozone amount for four chosen cities (Oslo, Manchester, Riga, Kaltennordheim) and the calculated values from the new model (4)

A comparison of the original model (2) with the one adjusted to Northern Europe (4) reveals some differences in the parameters' values caused by the restriction of the examined region. More specifically the main latitudinal (A) and longitudinal (G) components in the new model are about half of the original values, whereas the seasonal component (C) is about 30% larger. Also, the difference in F suggests that the ozone maximum appears somewhat earlier in the year, whereas the new value of I moves the location of that maximum westwards.

To further investigate possible hidden relationships we calculated city-specific values of the parameters C and F which control the seasonal component of the model. To that end the van Heuklon model was fitted to the ozone data of each city using the values of the new Northern European model with the rest of the parameters: J = 260, A = 74, G = 8, and I = 36. The results of the estimated values of parameters C and F for each location are given in Table 1 and also in Fig. 2.

It is evident from Fig. 2 that both C and F present systematic spatial patterns. F seems to depend more on λ, with a slightly tilted sigmoid pattern, increasing from west to north and northeast. C, on the other hand, has a less clear distribution, yet there is a decrease from south-southwest to north-northeast, indicating a higher dependence on φ. Examination of several variations of (3) showed that both parameters are best described by a model: $y = a \cdot sin(\lambda + b) \cdot sin^2(\varphi + e)$.

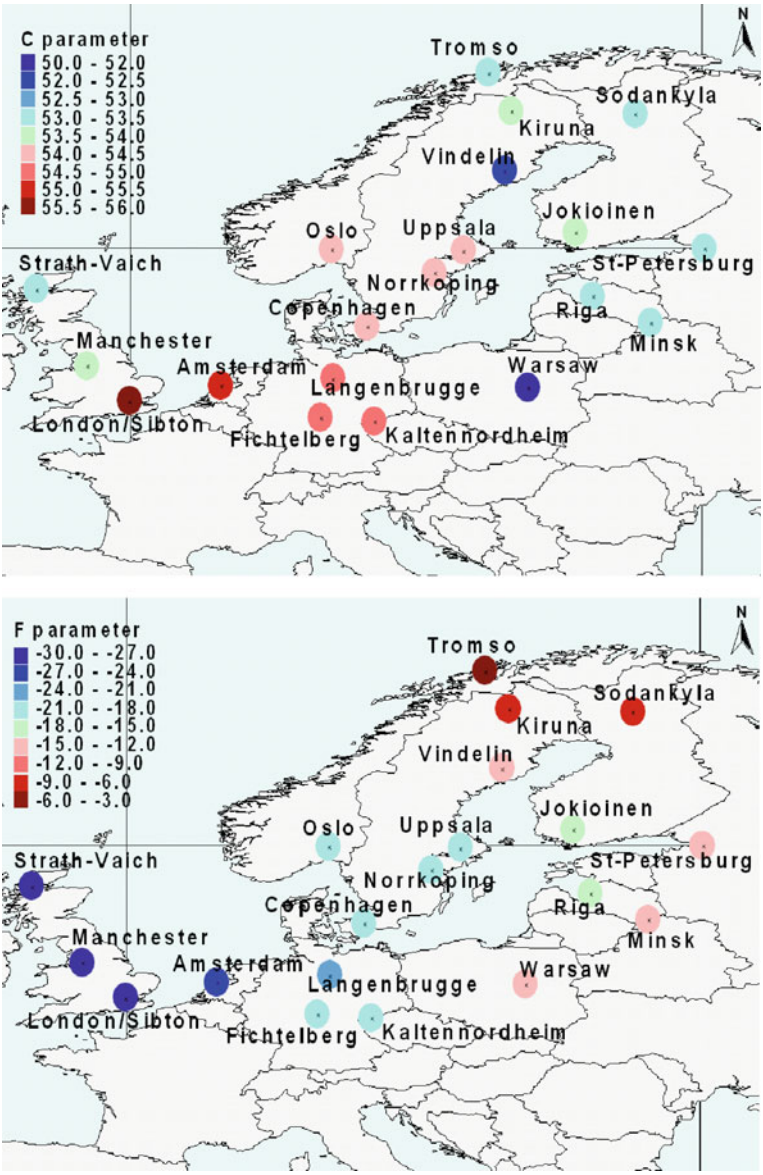

Fig. 2 Spatial variation of model parameters C and F, across Northern Europe

5 Conclusions

Utilising the large amount of data made available from the TOMS instruments aboard three satellites we attempted to adjust the model proposed by van Heuklon for the calculation of total atmospheric ozone, to the Northern European area.

The resulting model fits the satellite data quite well, whereas the differences observed between the new estimates of the model parameters and their original values were representative of the relatively restricted area considered in our study.

Furthermore, the phase and amplitude parameters of the seasonal component of the model were shown to have significant dependence on latitude and longitude. This indicates that, even though successful, van Heuklon's model might be ignoring some important modes of the total ozone variation, suggesting that, at least for specific regions are, other mathematical models might be worth exploring.

Acknowledgments The present study was conducted under traineeship and funded by the University of Athens grant traineeships program.

References

Bird RE, Hulstrom RL (1981) A simplified clear sky model for direct and diffuse insolation on horizontal surfaces. SERI/TR-642-761. Solar Energy Research Institute, Golden

Heuklon TK (1979) Estimating atmospheric ozone for solar radiation models. Sol. Energy 22:63–68

Hoyt DV (1978) A model for the calculation of solar global insolation. Sol Energ 21:7–35. doi:10.1016/0038-092X(78)90113-5

Lacis AL, Hansen JE (1974) A parameterization for the absorption of solar radiation in the Earth's atmosphere. J Atmos Sci 31:118–133. doi: http://dx.doi.org/10.1175/1520-0469(1974)031<0118:APFTAO>2.0.CO;2

NASA (2011) Earth Probe TOMS data & images. http://toms.gsfc.nasa.gov/eptoms/ep_v8.html. Accessed on June 15, 2011

Psiloglou BE, Santamouris M, Varotsos C, Asimakopoulos DN (1996) A new parameterization of the integral ozone transmission. Sol Energ 56:573–581. doi:10.1016/0038-092X(96)00030-8

Aerosol Characteristics over Bay of Bengal During W-ICARB Cruise Campaign

D.G. Kaskaoutis, P.R. Sinha, S.K. Kharol, P.G. Kosmopoulos, R.K. Manchanda, R.P. Singh, K.V.S. Badarinath, and S. Sreenivasan

Abstract Detailed observations of aerosol optical and physical properties were carried out to study variability at the sea surface, along vertical profiles and total column during the Winter-Integrated Campaign on Aerosols, Gases and Radiation Budget (W-ICARB) from 27 December 2008 to 30 January 2009 in the Bay of Bengal (BoB). The results show large heterogeneity in aerosol load and characteristics; dominance of anthropogenic aerosols over the northern BoB, along the eastern Indian coast and in Far East BoB region and higher fraction of coarse-mode aerosols over the southern parts of BoB. The aerosols over the area are highly influenced by the Indian continental outflow and the biomass burning in the Southeast Asia. On the other hand, the larger fraction of coarse-mode aerosols over the southern BoB is closely associated with intense sea-surface winds producing coarse-mode sea-salt aerosols. The vertical profiles of aerosols obtained via CALIPSO data also exhibit considerable vertical heterogeneities.

D.G. Kaskaoutis (✉)
Research and Technology Development Centre, Sharda University, Greater Noida 201 306, India
e-mail: dimitriskask@hotmail.com

P.R. Sinha • R.K. Manchanda • S. Sreenivasan
National Balloon Facility, Tata Institute of Fundamental Research, Hyderabad 500 062, India

S.K. Kharol • K.V.S. Badarinath
Atmospheric Science Section, Dept. of Space-Govt. of India, National Remote Sensing Centre, Balanagar, Hyderabad 500 625, India

P.G. Kosmopoulos
Laboratory of Meteorology, Department of Physics, National and Kapodistrian University of Athens, Athens GR-15784, Greece

R.P. Singh
School of Earth and Environmental Sciences, Schmid College of Science and Technology, Chapman University, Orange, CA 92866, USA

C.G. Helmis and P.T. Nastos (eds.), *Advances in Meteorology, Climatology and Atmospheric Physics*, Springer Atmospheric Sciences,
DOI 10.1007/978-3-642-29172-2_144,

1 Introduction

Recent cruise campaigns (e.g. INDOEX, ARMEX, ICARB) focused on region-specific characterization of the aerosol properties in oceanic regions surrounding India. Results from these campaigns have shown that large amounts of wind-blown dust particles and other anthropogenically-produced aerosols get transported from the Asian landmass over oceanic regions, thousands of kilometers away from their sources. To investigate the aerosol field in more detail the Winter-ICARB (W-ICARB) was scheduled from the Indian Space Research Organization Geosphere Biosphere Program (ISRO-GBP) to be conducted over BoB. The achievements of W-ICARB are: (1) this campaign was performed during a different season (December-January) when the synoptic winds are of continental origin, (2) none of the earlier cruises covered the eastern part of BoB (beyond ~93°E), (3) the interesting observations of high aerosol optical depth (AOD) and α values associated with a large fine-mode component in east BoB are brought out for the first time during W-ICARB.

2 Ship-Borne Measurements and Methodology

During the W-ICARB campaign plenty of instrumentation was in operation on board the oceanic research vessel focusing on investigating the aerosol optical, physical and chemical properties. Some of the initial results of the campaign have been recently published (Kumar et al. 2010; Moorthy et al. 2010) emphasizing on several columnar, vertical and surface aerosol characteristics. In the present study we mainly used spectral AOD measurements derived from the Microtops-II sun photometer (uncertainty of ± 0.03). In addition, we used Cloud-Aerosol Lidar and Infrared Pathfinder Satellite Observation (CALIPSO) images for the backscatter coefficient at 532 in a specific day of the cruise in order to show the intense outflow of aerosols and pollutants from Indian sub-continent towards BoB (Fig. 1).

3 Results

3.1 Temporal Variation of the Aerosol Optical Properties

Figure 2 shows the temporal variation of AOD_{500} (a) and $\alpha_{380-870}$ (b) over BoB during W-ICARB. High AOD is observed near the coasts (27–28 December, 1–2 and 7 January) and it was found to decrease when the ship moves away from the shore with lower values over pristine ocean (4–5 and 19–20 January). The high AOD_{500} values close to the coast arise mainly from the anthropogenic activities along the coastal regions, which are highly urbanized and industrialized. The mean AOD_{500} in the western part of BoB is found to be 0.45 ± 0.12. The AOD_{500} in west and north BoB is comparable in magnitude with that found during winter season

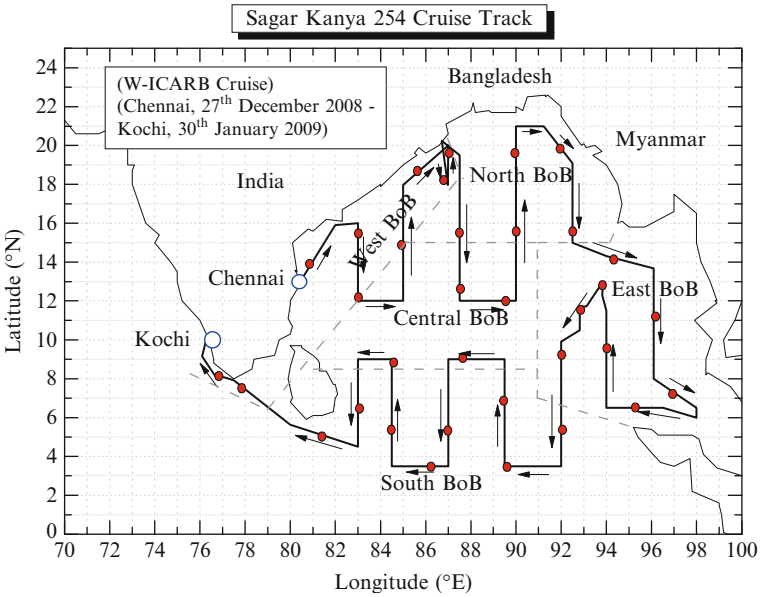

Fig. 1 The cruise track of Sagar Kanya 254 during W-ICARB, 27 December 2008–30 January 2009. The *arrow* shows the ship's direction of movement, while the *circles* the positions of the ship at 10:30 LST for each day. The entire BoB is divided into five sub-regions, namely (a) west, (b) north, (c) east, (d) central, and (e) south

over Hyderabad and over four urban Indian cities (Ramachandran 2007) indicating strong influence of these regions from the coastal urban centers. The mean AOD_{500} over south-central BoB (0.30 ± 0.11) is found to be lower than that of the other sub-regions. The high AOD_{500} value (0.39 ± 0.07) over far east BoB is found for the first time, since this region was remained unexplored during the former ICARB campaign. However, similar AODs were found over Port Blair associated with air masses from southeast Asia (Moorthy et al. 2003), where extensive biomass burning occurred during W-ICARB. The time series of α shows large day-to-day variability with a sharp gap on 4 January when the ship was cruising central BoB. These low α values are found to be mainly associated with coarse sea-salt aerosols over the area. The anthropogenic aerosols from fossil-fuel and bio-fuel combustion contribute to fine particles in winter, thus $\alpha > 1$ in the vast majority of the cases. The largest mean α is observed over east BoB indicating that this region is strongly affected by fine-mode aerosols coming from south-eastern Asia.

3.2 Classification of Aerosol Types

Figure 3 shows the scatter plot (upper panel) and the density plot (lower panel) of AOD_{500} vs $\alpha_{380–870}$ over the entire BoB. The density plot was constructed using 0.1

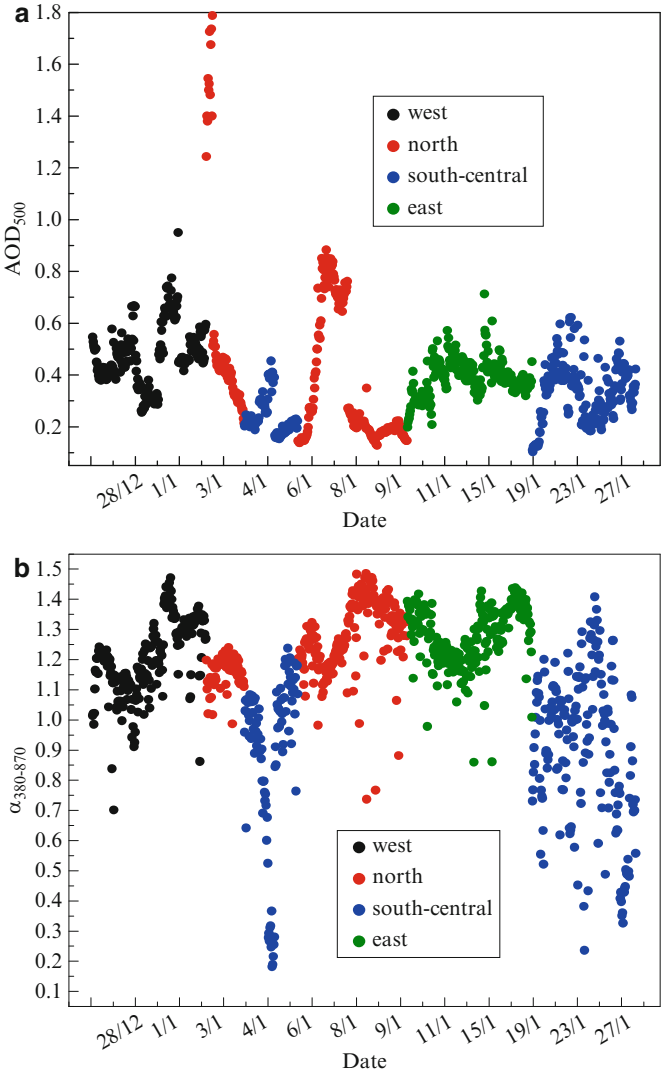

Fig. 2 Temporal variation of AOD_{550} (**a**) and $\alpha_{380–870}$ (**b**) values over different BoB sub-regions during W-ICARB cruise campaign. The mean values along with the standard deviations are given for each sub-region

step for both AOD_{500} and $\alpha_{380–870}$ values. There is a wide range of $\alpha_{380–870}$ values for low-to-moderate AOD_{500} (<0.4) suggesting large variability in the aerosol properties and type. The increasing values of $\alpha_{380–870}$ with increasing AOD_{500} in west BoB indicate significant contribution of fine particles in the atmospheric column, especially under high turbidity. There is an evidence of reduction of $\alpha_{380–870}$ as AOD increases over east BoB; this reflects the transition of fine-mode particles to accumulation-mode through coagulation, condensation and

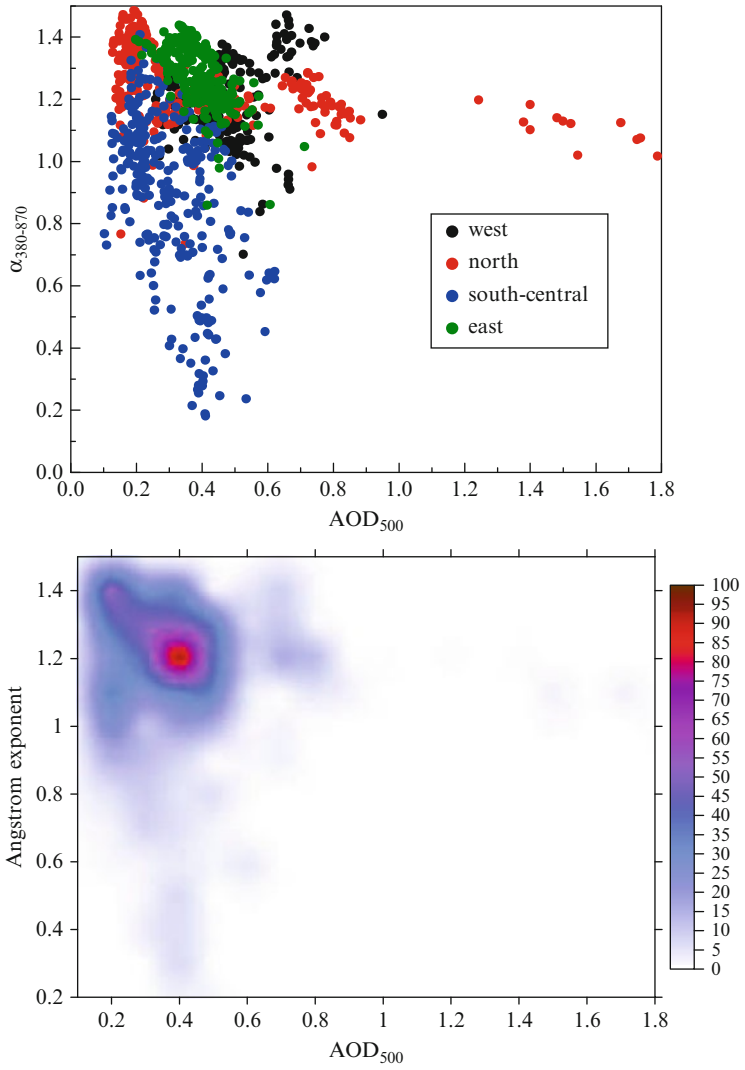

Fig. 3 Correlation between AOD_{500} and $\alpha_{380–870}$ in the different BoB sub-regions (*upper*) and density plot of AOD_{500} versus $\alpha_{380–870}$ correlation over entire BoB (*lower*)

gas-to-particle conversion. Viewing the density plot a clear-defined area of larger density is revealed for the (AOD_{500}, $\alpha_{380–870}$) pair of (~0.4, 1.2). This indicates that the aerosols over BoB during winter season are, in the vast majority of the cases, of anthropogenic origin with a large fine-mode fraction under turbid atmospheres. Other secondary large-density areas are those of (AOD_{500}, $\alpha_{380–870}$) = (~0.2, 1.4) corresponding to fine-mode aerosols for relative clean atmospheres and some hints of $\alpha_{380–870} < 0.8$ for $AOD_{500} = 0.4–0.5$, indicative of coarse-mode particles under turbid conditions.

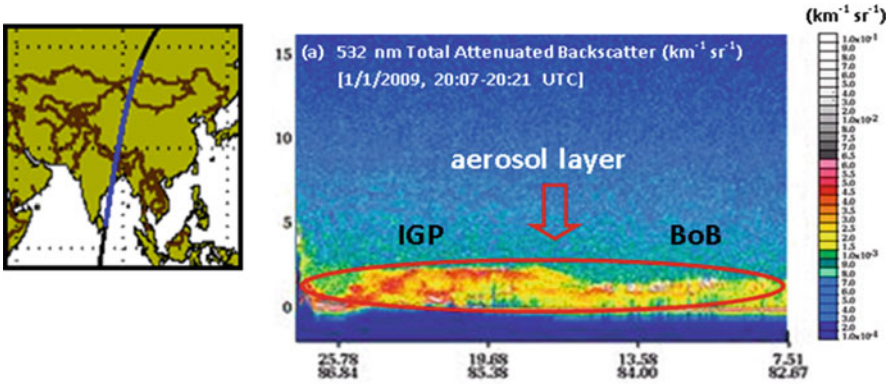

Fig. 4 (*Left*) CALIPSO trajectory on 1st January 2008. (*Right*) Total attenuated backscatter profiles (km^{-1} sr^{-1}) at 532 nm for nighttime conditions on 1st January 2009 obtained from CALIPSO observations. In the *bottom* of the figure the latitude (*above*) and the longitude (*below*) of the CALIPSO trajectory are also given

3.3 CALIPSO Observations

Lidar systems on board satellites (such as CALIPSO) have been increasingly available in the last years in order to identify the vertical extent of aerosols (Vaughan et al. 2004). A typical example of the vertical distribution of the aerosol plume over BoB on 1st January 2009 is shown in Fig. 4 for total attenuated backscatter coefficient at 532 nm. The nighttime CALIPSO overpass moving southwards covers Tibetan Plateau, eastern India and northwestern BoB. On that day the ship was crossing the northwestern BoB (18.3°N, 86.9°E) while the daily mean AOD_{550} and $\alpha_{380-870}$ values were 0.49 ± 0.05 and 1.28 ± 0.09, respectively.

The thick aerosol layer, extending from surface up to ~3 km, is quite detectable by CALIPSO covering Indo-Gangetic Plains (IGP) and northwestern part of BoB; this aerosol layer is developed just below the foothills of the Himalayas, into the topographic low basin of Ganges river. The backscatter profile is characterized by large attenuation values (0.002–0.005 km^{-1} sr^{-1}) within the aerosol layer. Note also the slight larger vertical extend of the aerosol layer over IGP, whose thickness is reduced over BoB (<~2 km) due to gravitational settling. The aerosol layer shows a continuous attenuation towards south BoB (7–8°N, 82–83°E) consisted with the results of Moorthy et al. (2010).

4 Conclusions

This study focused on the variability of aerosol properties and types over BoB during W-ICARB cruise campaign (27 December 2008 to 30 January 2009) using ship-borne measurements of spectral AOD. The results showed a large

spatio-temporal variation of the examined aerosol properties (e.g. AOD_{500}, $\alpha_{380–870}$) strongly affected by the continents, the outflow of pollutants, the meteorological parameters and the mixing processes (e.g. coagulation, humidification) in the marine atmosphere. The highest AOD_{500} was observed in western and northern BoB with lower values in the southern and parts of central BoB. The eastern BoB, which was investigated for the first time, presented concurrently high values of both AOD_{500} and $\alpha_{380–870}$. Large $\alpha_{380–870}$ values were also observed in the western and northern parts of BoB closely associated with high AODs indicating a large fraction of anthropogenic aerosols and/or biomass burning during winter season.

The classification of aerosols was achieved by means of the widely used method that relates AOD_{500} and $\alpha_{380–870}$. This correlation showed that the main aerosol type over BoB corresponded to the (AOD_{500}, $\alpha_{380–870}$) pair of (~0.4, 1.2), which is similar to that found over urban Hyderabad during winter season. The classification scheme indicated an extremely large fraction of fine-mode aerosols in turbid atmospheres, which is even larger than 90% in the western part of BoB and approaches 100% over eastern BoB. The clean maritime conditions were nearly absent, while quite interesting was the low fraction of mixed aerosols. CALIPSO observations show vertical extend of aerosols up to 2 km over BoB and significant outflow from Indian sub-continent and Ganges Basin. Therefore, it needs continuous and systematic efforts to monitor the aerosol field and properties over this region since the knowledge of their effects on the marine environment and in our changing planet is a real challenge.

Acknowledgments The authors are thankful to Director, NRSC and Dy. Director (RS&GIS-AA) for necessary help at various stages and ISRO-GBP via W-ICARB project for funding support. We also thank the Department of Ocean Development for giving the opportunity to conduct measurements on board Sagar Kanya.

References

Kumar A, Sarin MM, Srinivas B (2010) Aerosol iron solubility over Bay of Bengal: role of anthropogenic sources and chemical processing. Mar Chem 121:167–175. doi:10.1016/ j.marchem.2010.04.005

Moorthy KK, Babu SS, Satheesh SK (2003) Aerosol spectral optical depths over Bay of Bengal: role of transport. Geophys Res Lett 30(5):1249. doi:10.1029/2002GL016520

Moorthy KK, Beegum SN, Babu SS, Smirnov A, Rachel SJ, Kumar KR, Narasimhulu K, Dutt C, Nair VS (2010) Optical and physical characteristics of Bay of Bengal aerosols during W-ICARB: spatial and vertical heterogeneities in the MABL and in the vertical column. J Geophys Res 115:D24213. doi:10.1029/2010JD014094

Ramachandran S (2007) Aerosol optical depth and fine mode fraction variations deduced from Moderate Resolution Imaging Spectroradiometer (MODIS) over four urban areas in India. J Geophys Res 112:D16207. doi:10.1029/2007JD008500

Vaughan M, Young S, Winker D, Powell K, Omar A, Liu Z, Hu Y, Hostetler C (2004) Fully automated analysis of space-based lidar data: an overview of the CALIPSO retrieval algorithms and data products. Proc SPIE 5575:16–30

The Effect of Aerosol Absorption in Solar UV Radiation

S. Kazadzis, V. Amiridis, and N. Kouremeti

Abstract We have used a combination of a CIMEL sun-photometer and a UV multi-filter radiometer (MFR) in order to calculate columnar aerosol absorbing properties such as the single scattering albedo (SSA) in the Ultraviolet (UV) range in Athens area. Such calculations are hardly to be found since most UV related applications use SSA retrievals from the visible range assuming wavelength independent aerosol absorbing coefficients going from the visible to the UV range. Our results showed significantly reduced SSA values (higher absorption) comparing the CIMEL/AERONET SSA retrievals at 440 nm with the UV-MFR ones. In addition, we calculated lower SSA values for lower aerosol optical depth values and a seasonal variation of SSA with lower values for wintertime and higher in the summertime for all wavelengths. The effect of such SSA differences in the calculation of the UV spectral irradiances varies from 2% to10% and it is proportional to the solar zenith angle and the aerosol load.

1 Introduction

The role of aerosols, both natural and anthropogenic, is recognized as extremely important for regional and global climate change studies as well as for overall pollution mitigation strategies. A recent comprehensive review of the assessment of

S. Kazadzis (✉)
Institute for Environmental Research and Sustainable Development, National Observatory of Athens, Athens 15236, Greece
e-mail: kazadzis@noa.gr

V. Amiridis
Institute for Space Applications and Remote Sensing, National Observatory of Athens, Athens, Greece

N. Kouremeti
Physics Department, Aristotle University of Thessaloniki, Thessaloniki, Greece

C.G. Helmis and P.T. Nastos (eds.), *Advances in Meteorology, Climatology and Atmospheric Physics*, Springer Atmospheric Sciences,
DOI 10.1007/978-3-642-29172-2_145,

the aerosol direct effect, regarding both the current status and those outstanding issues that still urgently require further research, is given by IPCC (2007) and Yu et al. (2006). Both emphasize, that the significant aerosol absorption uncertainties, in global single scattering albedo (SSA), may constitute the largest single source of uncertainty in the current modeling estimates of aerosol climate forcing. SSA is the ratio of scattering to total extinction (scattering plus absorption). Since both quantities depend strongly on chemical composition, particle size, state of mixture, relative humidity and wavelength, comprehensive measurements are crucial to understand the effects and reduce SSA uncertainties, propagated into aerosol radiative forcing estimates.

Theoretically, SSA values can vary between 0 (totally absorbing aerosol) and 1 (totally scattering aerosol) but actual values range from 0.5 to 1.0 in the visible wavelengths. The difference of the SSA as calculated here with in situ SSA retrieved from absorption and scattering measurements at a single altitude level (e.g. at the ground), is that SSA calculated here can be considered as a columnar property. That means that it represents the "effective" SSA that is calculated in order to simulate the solar irradiance attenuation through the aerosol path.

For the Visible (VIS) range, advanced retrieval algorithms for microphysical aerosol properties have been developed in the framework of AERONET (e.g. Dubovik and King 2000). AERONET stations provide inversion based VIS-SSA retrievals. The weakness to retrieve SSA applies even more for the ultraviolet (UV) part of the spectrum. Compared to the visible spectral region, a little is known about aerosol absorption in the UV wavelength range (Bais et al. 2005; Krotkov et al. 1998; Corr et al. 2009). Moreover, solar UV variations caused by aerosol optical properties changes affect directly the tropospheric photochemistry:

- Increasing regional O_3 (10–20 ppb for Eastern USA) caused by increased UV levels, due to the presence of non-absorbing aerosols (Dickerson et al. 1997).
- Decreasing regional O_3 (up to 50 ppb for Mexico City and for particular days) caused by strong UV reduction due to absorbing aerosols (Castro et al. 2001).

2 Data and Methodology

In this work we present estimates of SSA at two independently retrieved wavelengths 332 and 368 nm for an urban site situated at Athens city area, Greece. The period of the measurement analysis was from January to December 2010. Since February 2009, the ground-based Atmospheric Remote Sensing Station (ARSS) is continuously operating to monitor radiation levels at ground and aerosol loadings over the city of Athens (Amiridis et al. 2009). ARSS is located on the roof of the Biomedical Research Foundation of the Academy of Athens *(37.9 N, 23.8E, 130 m a.s.l.)*. ARSS is equipped with a CIMEL CE318-NEDPS9 sunphotometer for the retrieval of aerosol optical depth (AOD) at 8 wavelengths from 340 to 1,640 nm, including polarization measurements and is a part of NASA's

AERONET (http://aeronet.gsfc.nasa.gov). ARSS is additionally equipped with an Ultraviolet Multi-filter Radiometer (UVMFR) instrument for radiation measurements in the UV spectral region. UVMFR measures both total and diffuse irradiance for seven specified wavelengths in the UV range. For this work we have used measurements of the two abovementioned instruments combined with radiative transfer model (RTM) calculations that have been performed using the LibRadTran Radiation Transfer code (Mayer and Kylling 2005).

Model calculations can be used for retrieving SSA when global and/or diffuse spectral irradiance, solar zenith angle (sza), total ozone and AOD are known (e.g. Kazadzis et al. 2010). For the retrieval methodology we have used measurements of the diffuse to global ratios (DGR) measured with the UVMFR instrument combined with AOD values that have been used as basic input parameters in the RTM for the calculation of the SSA at 332 and 368 nm. More specific, from the global and direct UVMFR measurements, the direct irradiance at 332 and 368 nm and then AOD has been calculated. CIMEL and UVMFR AOD retrievals showed an agreement within 0.02 for synchronous measurements. Furthermore, we have calculated look up tables (LUT) with the RTM, of DGR at 368 and 332 nm as a function of solar zenith angle, AOD, SSA, asymmetry parameter and ozone. Finally, we have used as inputs all the above parameters in order to calculate the matching SSA value for the given DGR. For the asymmetry factor we have used the mean daily value as retrieved at 440 nm from the CIMEL instrument measurements, when existed, otherwise the mean value of the period that equals with 0.70 (1 standard deviation of the period was 0.02).

3 Results

Using the methodology described in the previous section we have calculated SSA for 332 and 368 nm using the UVMFR 1 min data. In addition SSA's in the visible derived from Athens AERONET station have been used. Trying to investigate on the possible dependence of SSA and AOD, Fig. 1 shows the synchronous UVMFR and CIMEL SSA retrievals plotted against AOD at 440 nm. Low SSA values (high absorption) are associated with low AOD's. Such values are mostly wintertime cases. In addition, due to the low AOD's the uncertainties associated with both retrieval techniques (AERONET and UVMFR) are high. For higher AOD's CIMEL retrievals show an almost constant value of 0.88–0.9 while lower values have been calculated when moving towards shorter wavelengths. Similar results have been found in Krotkov et al. (1998) analyzing measurements derived at Washington DC, USA.

We found that SSA decreases with decreases in extinction optical thickness. We believe that this behavior reflects the changes from summer to winter months in the average aerosol composition at Athens. Indeed, the annual cycle of SSA is the same to AOD annual cycle: with a maximum in summer and a minimum in winter.

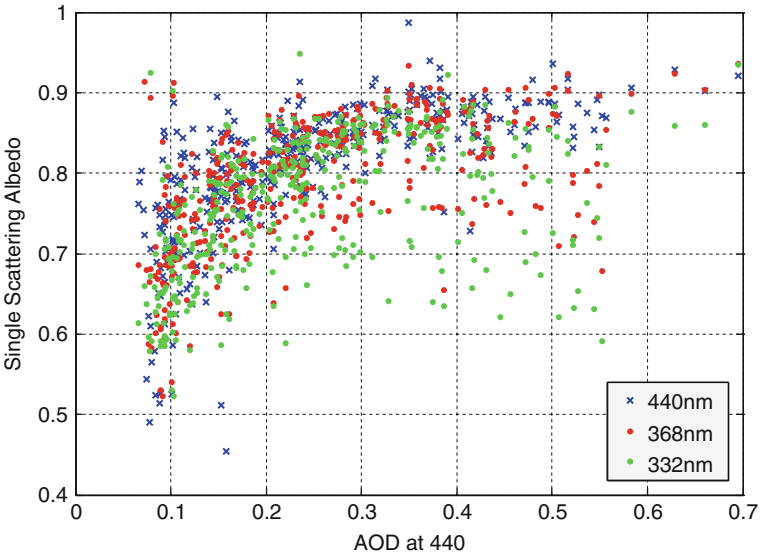

Fig. 1 Dependence of the calculated SSA from AOD measurements

Studies of the SSA annual variability for other cities such as Ispra, Italy and Thessaloniki, Greece (Arola et al. 2005) revealed the same feature.

In addition to the calculated SSA's from the CIMEL and the UVMFR measurement-based methodologies, in Fig. 2 we demonstrate other sources of SSA retrievals over Athens. Such retrievals are based on the Ozone Monitoring Instrument measurements and two modeling retrievals (OMAERO [2010] and OMAERUV [monthly SSA climatology from 2004 to 2009]). Finally, we have used the Aerocom initiative-based SSA (Kinne 2009). All SSA retrievals independent of wavelength range, revealed large deviations among the datasets. Data have been calculated and shown here as monthly means.

Since columnar SSA retrievals at UV wavelengths are not easy to be found worldwide, most of the RTM applications and users tend to assume that SSA is wavelength independent from VIS to UV. Under this assumption CIMEL SSA at 440 nm, which is a parameter that is provided by more than 200 AERONET stations worldwide, is practically used. However when trying to use RTM codes in order to simulate the UV solar irradiance, an uncertainty is introduced by the above assumption.

As an exercise we have used aerosol measurement data for Athens area and for year 2010 into the LibRadTran RTM in order to calculate the effect of the use of different SSA retrievals into the UVB (305–325 nm) and UVA (325–400 nm) solar irradiance. For such calculations the most important input parameter is the AOD and for that purpose we have used monthly mean AOD at 340 nm (superimposed in Fig. 2) and Ångström coefficient α values taken from the CIMEL/Athens measurements. The results of such RTM simulations are given in Fig. 3 below.

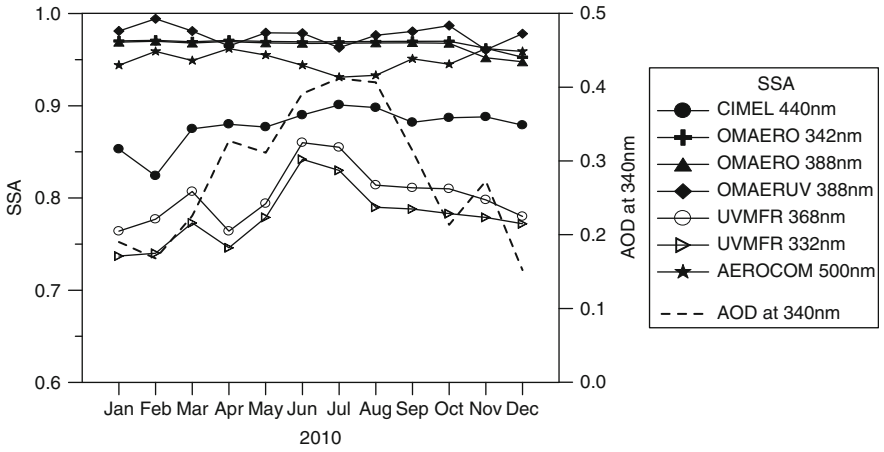

Fig. 2 Monthly mean SSAs from different measurement sources

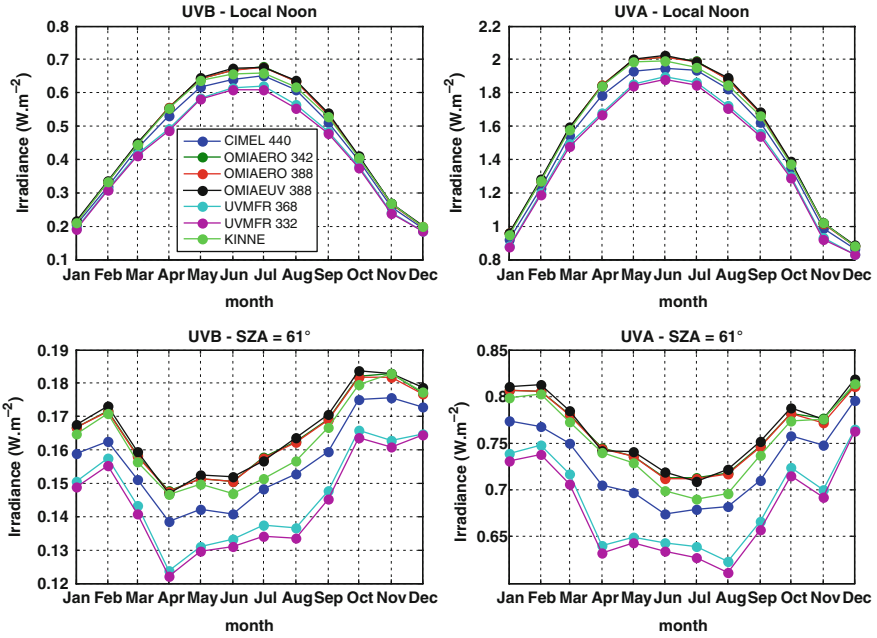

Fig. 3 UVB (*left panels*) and UVA (*right panels*) RTM simulations using different SSA datasets. Monthly mean local noon values (*up*) and monthly mean data at for constant solar zenith angle (*down*)

Results for UVB wavelengths show that compared with the CIMEL derived SSA (at 440 nm) UVMFR calculated SSAs for local noon lead to lower UVB values from 2% to 7%. For a constant solar zenith angle (here 61° – the minimum that can

be found throughout the year) the percentages drop from 5% to 10% depending on the aerosol load (maximum values at April and August). Aerocom and OMI Satellite related calculations show a UV overestimation of 2% and 5%, respectively, since SSA retrievals are always above 0.9. For UVA wavelengths the effect of using different SSAs is smaller. It is in the order of −2% to −5% for the local noon UVMFR related retrievals compared with the CIMEL, and 4–8% for the constant solar zenith angle, while for the satellite and Aerocom ones the overestimation is similar with the UVB range. Lower panels of Fig. 3 shows clearly the effects of: ozone (lower UV in the spring and higher in the autumn), the AOD (aerosol peaks for April and August and high AOD values for summertime) and the SSA described in detail above, to the UV radiation levels reaching the ground. It is notable that differences due to different SSA inputs are in the same magnitude (up to 10%) with the AOD related seasonal differences. The results presented in this study show the importance of other than AOD aerosol properties such as the SSA when trying to calculate UV solar irradiances. Especially for urban areas with a complex aerosol environment such as Athens the assumption and direct use of SSA from the visible range could lead to significant UV overestimation.

Acknowledgments SK would like to acknowledge the Marie Curie project ACI-UV, PERG05-GA-2009-247492.

References

Amiridis V, Kafatos M, Perez C, Kazadzis S, Gerasopoulos E, Mamouri RE, Papayannis A, Kokkalis P, Giannakaki E, Basart S, Daglis I, Zerefos C (2009) The potential of the synergistic use of passive and active remote sensing measurements for the validation of a regional dust model. Ann Geophys 27:3155–3164. doi:10.5194/angeo-27-3155-2009

Arola A, Kazadzis S, Krotkoc N, Bais A, Herman J, Lakkala K (2005) Assessment of TOMS UV bias due to the absorbing aerosols. J Geophys Res 110:D23211. doi:10.1029/2005JD005913

Bais AF, Kazantzidis A, Kazadzis S, Balis D, Zerefos CS, Meleti C (2005) Effects of aerosol optical depth and single scattering albedo on surface UV irradiance. Atmos Environ 39:1093–1102

Castro T, Madronich S, Rivale S, Muhlia A, Mar B (2001) The influence of aerosols on photochemical smog in Mexico City. Atmos Environ 35:1765–1772. doi:10.1016/S1352-2310(00)00449-0

Corr CA, Krotkov N, Madronich S, Slusser JR, Holben B, Gao W, Flynn J, Lefer B, Kreidenweis SM (2009) Retrieval of aerosol single scattering albedo at ultraviolet wavelengths at the T1 site during MILAGRO. Atmos Chem Phys 9:5813–5827. doi:10.5194/acp-9-5813-2009

Dickerson RR, Kondragunta S, Stenchikov G, Civerolo KL, Doddridge BG, Holben BN (1997) The impact of aerosols on solar ultraviolet-radiation and photochemical smog. Science 215:827–830. doi:10.1126/science.278.5339.827

Dubovik O, King MD (2000) A flexible inversion algorithm for retrieval of aerosol optical properties from Sun and sky radiance measurements. J Geophys Res 105 (D16):20,673–20,696. doi:10.1029/2000JD900282

IPCC (2007) Summary for policymakers. In: Solomon S, Qin D, Manning M, Chen Z, Marquis M, Averyt KB, Tignor M, Miller HL (eds) Climate change 2007: the physical science basis.

Contribution of Working Group I to the Fourth Assessment Report of the Intergovernmental Panel on climate change. Cambridge University Press, Cambridge/New York

Kazadzis S, Gröbner J, Arola A, Amiridis V (2010) Investigation of the accuracy for single scattering albedo retrieval from global UV irradiance measurements. Atmos Meas Tech Discuss 3:1303–1321. doi:10.5194/amtd-3-1303-2010

Kinne S (2009) Climatologies of cloud-related aerosols: part 1: particle number and size. In: Heintzenberg J, Charlson RJ (eds) Clouds in the perturbed climate system. MIT Press, Cambridge, MA, pp 37–57

Krotkov NA, Bhartia PK, Herman JR, Fioletov V, Kerr J (1998) Satellite estimation of spectral surface UV irradiance in the presence of tropospheric aerosols. 1: cloud-free case. J Geophys Res 103:8779–8793. doi:10.1029/98JD00233

Mayer B, Kylling A (2005) Technical note: the libRadtran software package for radiative transfer calculations – description and examples of use. Atmos Chem Phys 5:1855–1877

Yu H, Kaufman YJ, Chin M, Feingold G, Remer LA, Anderson TL, Balkanski Y, Bellouin N, Boucher O, Christopher S, DeCola P, Kahn R, Koch D, Loeb N, Reddy MS, Schulz M, Takemura T, Zhou M (2006) A review of measurement-based assessments of the aerosol direct radiative effect and forcing. Atmos Chem Phys 6:613–666. doi:10.5194/acp-6-613-2006

Estimation of the Cloud Modification Factor from Satellite and Ground Data at Thessaloniki, Greece

A. Kazantzidis, E. Nikitidou, and A.F. Bais

Abstract Clouds are one of the basic factors that influence Earth's climate and energy balance. Depending on their type and position they can reflect the incoming solar radiation or absorb the infrared radiation that is emitted by Earth. Their role in the climatic changes can be studied if their characteristics and variations are known with high temporal and spatial resolution. In this study, the cloud modification factor (CMF) is studied for the city of Thessaloniki, based on ground and satellite data. Given the radiation measurements at the ground station of Thessaloniki and model calculated values under cloudless conditions, the ground-based values of CMF are estimated. These are compared with data from the Meteosat Second Generation (MSG) satellite, provided every 15 min and from the Moderate Resolution Imaging Spectroradiometer (MODIS) instrument, on board the Terra and Aqua satellites which provides the data twice a day. The comparison covers the period of 2007–2010. The linear regression between the monthly values of MSG and ground CMF has a slope of 0.81, while MODIS data are in better agreement with the ground measurements (slope = 0.94). The higher differences between the MSG and ground data correspond to cases of broken or very thick clouds.

A. Kazantzidis (✉) • E. Nikitidou
Laboratory of Atmospheric Physics, Physics Department, University of Patras,
Patras GR-26500, Greece
e-mail: akaza@upatras.gr

A.F. Bais
Laboratory of Atmospheric Physics, Physics Department, Aristotle University of Thessaloniki,
Thessaloniki, Greece

C.G. Helmis and P.T. Nastos (eds.), *Advances in Meteorology, Climatology and Atmospheric Physics*, Springer Atmospheric Sciences,
DOI 10.1007/978-3-642-29172-2_146,

1 Introduction

The main factor that is responsible for the temporal and spatial variations of the solar radiation is cloudiness. The effect of clouds on solar radiation can be described by the cloud modification factor (CMF), which is defined as:

$$\mathrm{CMF} = \mathrm{I_{cloud}}/\mathrm{I_{clear}} \quad (1)$$

where $\mathrm{I_{cloud}}$ is the global irradiance under the presence of clouds and $\mathrm{I_{clear}}$ is the global irradiance for a cloud-free sky. CMF can ranges from 0 to 1, with 0 being the overcast situation and 1 representing the cloudless sky. Taking advantage of satellites global coverage, efforts have been made to estimate the global irradiance at the ground, based on cloud information from the satellite sensors and modeled irradiances under clear skies (Rigollier et al. 2004; Girodo et al. 2006; Deneke et al. 2008; Wang et al. 2008). Verdebout (2000) used the CMF retrieved from the Meteosat satellite to generate UV radiation maps over Europe. CMF is retrieved for every satellite signal, as a function of the solar and viewing zenith angles, the illumination and viewing azimuth angles, the effective surface albedo and the surface elevation. The CMF is depended on the solar zenith angle (sza) and the wavelength range where it is estimated. As the solar zenith angle increases, clouds have bigger influence on total radiation than the ultraviolet one. The algorithm for the retrieval of CMF from the Meteosat Second Generation (MSG) satellite has been operational at the Laboratory of Atmospherics Physics, University of Thessaloniki and the Laboratory of Atmospheric Physics, University of Patras since 2006. The MSG CMF is compared with ground-based and satellite-derived data from MODIS instrument (on board Terra and Aqua satellites) during the period 2007–2010.

2 Data and Methodology

2.1 Data

CMF data from the MSG satellite were used for the time period of 2007–2010. The Spinning Enhanced Visible and Infrared Imager (SEVIRI) sensor on MSG provides data at 12 different wavelengths, among which 0.6, 1.6 and 12 μm, with a spatial and temporal resolution of 0.05° x 0.05° and 15 min respectively. Pyranometer measurements, provided with 1-min step, for the same period at Thessaloniki were used to derive the ground CMF. Finally, cloud optical depth and cloud fraction data were used from the MODIS instrument to estimate the corresponding CMF. MODIS is on board the Terra and Aqua satellites which overpass Greece around 9.30 and 11.30 UTC respectively. Therefore, the data are available twice a day, with a spatial resolution of 1° x 1°.

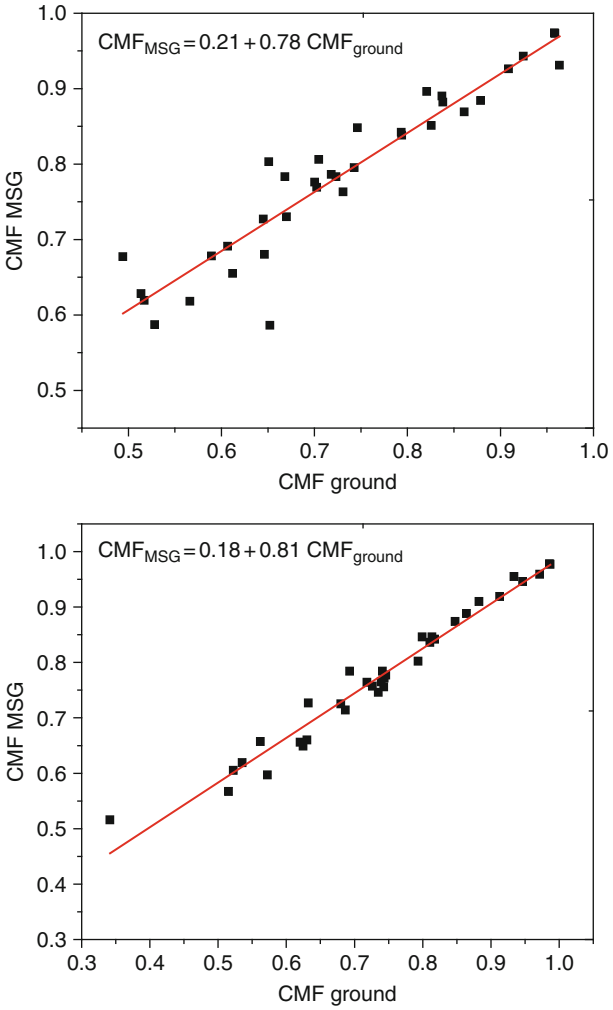

Fig. 1 Monthly values of MSG and ground CMF for the time period 2007–2010, when all the pyranometer measurements (*top*) and only the synchronous ones (*bottom*) are considered

2.2 Methodology

The CMF values from the ground-based data are estimated from the total irradiance measurements of the pyranometer and calculated irradiances for cloudless skies that match the conditions of the measurement. These are estimated by the LibRadtran radiative transfer model (Mayer and Kylling 2005). MODIS CMF is calculated from its cloud optical depth (COD) and the cloud fraction data. Model calculations

are also performed for the estimation of solar irradiance under cloudy and cloud-free conditions. CMF is calculated as:

$$\mathrm{CMF} = \mathrm{I}/\mathrm{I}_0 \tag{2}$$

where $\mathrm{I} = (1 - \mathrm{N})\mathrm{I}_0 + \mathrm{N} * \mathrm{I}_c$ and $\mathrm{I}_0, \mathrm{I}_c$ and N are the modeled irradiance under cloud-free conditions, the modeled irradiance for the specific COD value of the satellite and the cloud fraction respectively.

The original methodology for the calculation of the CMF from the MSG images is provided by Verdebout (2000). That algorithm was focused on the estimation of cloudiness in the ultraviolet (UV) spectral region. In our method, we modified the original algorithm to represent the cloud influence on the shortwave spectral region.

3 Results

The monthly averages of the MSG and ground-based CMF values have been estimated from 2007 until 2010 and are presented in Fig. 1. In the upper panel all the pyranometer measurements are taken into account (provided every minute). The comparison gives a slope of 0.78 between the monthly MSG and ground CMF. The slope increases (0.81, bottom graph) when only the synchronous CMFs are considered in the calculation of monthly values. This is expected because of the different temporal resolution of the two datasets. In general, the MSG values agree quite well with the ground-based measurements. The effect of cloudiness is overestimated in cases of low CMF values, where a systematic bias is revealed. The analysis of this

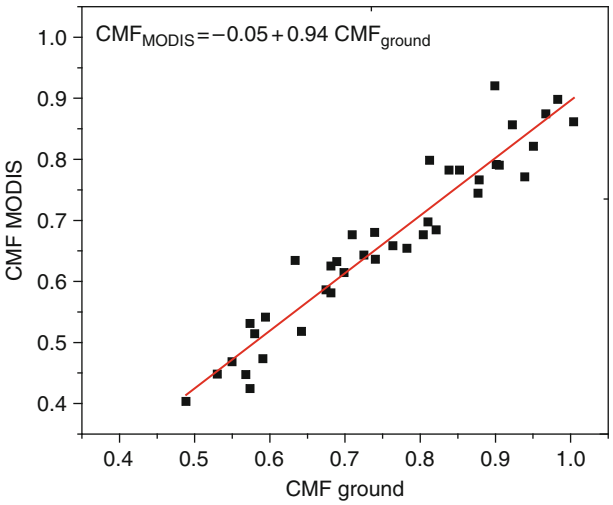

Fig. 2 Monthly values of MODIS and ground CMF for the time period 2007–2010

result showed that this is due to the existence of very thick clouds or the limited accuracy of the method for large solar zenith angles. For cloud-free skies, the differences in momentary values (not shown here) is within ±5%, due to the uncertainties introduced in model calculations for the estimation of the CMF from the ground-based measurements.

The monthly CMF values of MODIS for the 2007–2010 period are compared with the ground ones in Fig. 2. The slope between the two datasets is high, equal to 0.94. Monthly CMF values from MODIS seem to be in better agreement with the ground data, mainly due to the fact that the overpass time of MODIS is within ±1 h from the local noon (at relatively low solar zenith angles). Additionally, the different spatial resolution of the two satellite instruments (1° x 1° for MODIS and 0.05° x 0.05° for MSG) certainly affects our results.

4 Conclusions

The CMF is a key parameter in estimating the incoming solar radiation. Retrieved CMF values from the MSG satellite can be used in order to take advantage of the spatial and temporal resolution of the satellite. The linear regression between the monthly values of MSG and ground CMF has a slope of 0.81, while MODIS data are in better agreement with the ground measurements (slope = 0.94). MODIS data are provided twice a day therefore the temporal variability of clouds can't be captured as well as in the case of MSG. The higher differences between the MSG and ground data correspond to cases of broken or very thick clouds.

Acknowledgments The authors would like to thank NASA and EUMETSAT for providing the satellite data as well as the LibRadtran team (www.libradtran.org) for providing the model algorithm. Jean Verdebout (JRC, Ispra) is highly acknowledged for the original algorithm. This study was mainly conducted and funded by project "Hellenic Network of Solar Energy" (HNSE), funded by the General Secretariat for Research and Technology, Greek Ministry of Education, Lifelong Learning and Religious Affairs.

References

Deneke HM, Feijt AJ, Roebeling RA (2008) Estimating surface solar irradiance from METEOSAT SEVIRI-derived cloud properties. Remote Sens Environ 112:3131–3141. doi:10.1016/j.rse.2008.03.012

Girodo M, Mueller RW, Heinemann D (2006) Influence of three-dimensional cloud effects on satellite derived solar irradiance estimation – first approaches to improve the Heliosat method. Sol Energ 80:1145–1159

Mayer M, Kylling A (2005) Technical note: the libRadtran software package for radiative transfer calculations: descriptions and examples of use. Atmos Chem Phys 5:1855–1877. doi:10.5194/acp-5-1855-2005

Rigollier C, Lefèvre M, Wald L (2004) The method Heliosat-2 for deriving shortwave solar radiation from satellite images. Sol Energ 77:159–169. doi:10.1016/j.solener.2004.04.017

Verdebout J (2000) A method to generate surface UV radiation maps over Europe using GOME, Meteosat and ancillary geophysical data. J Geophys Res 105:5049–5058. doi:10.1029/1999 JD900302

Wang H, Pinker RT, Minnis P, Khaiyer MM (2008) Experiments with cloud properties: impact on surface radiative fluxes. J Atmos Ocean Tech 25:1034–1040. doi:10.1175/2007 JTECHO546.1

Aerosol Size over the Broader Greek Area Based on Satellite and Ground Measurements

M. Koras-Carraca, A. Gkikas, C.D. Papadimas, N. Mihalopoulos, and N. Hatzianastassiou

Abstract A first estimate of aerosol size over the broader Greek area (33.5°N-42.5°N and 18.5°E-29.5°E) is attempted by using satellite- and ground-based measurements for the 10-year period 2000–2010. A complete spatial coverage is ensured by daily gridded data derived from measurements taken from the MODerate resolution Imaging Spectroradiometer (MODIS) instrument onboard the NASA's Terra and Aqua satellites. More specifically, MODIS Collection 5.1 Ångström Exponent (α), Fine Fraction (FF) and aerosol Mean Effective Radius (reff) $1^\circ \times 1^\circ$ latitude-longitude data are used, over both land and sea. The obtained results reveal a geographical variability of aerosol size over the Greek area. Values of FF and α, are greater over the northern than southern part of the region, exhibiting a north-to-south gradient, as well as over land than sea. The smallest FF and α values ($\approx$0.1 and 0.5, respectively) appear over the southern Aegean and Ionian Sea, and south of Crete, indicating the influence of transported coarse dust particles from the Sahara desert. These patterns of aerosol size are also confirmed by the distribution of reff values (0.25–0.58 μm) over the region. The satellite-based results are evaluated against daily surface AERONET with the MODIS sea products providing a better agreement than the land ones.

M. Koras-Carraca • A. Gkikas • C.D. Papadimas • N. Hatzianastassiou (✉)
Laboratory of Meteorology, Department of Physics, University of Ioannina, Ioannina 45110, Greece
e-mail: nhatzian@cc.uoi.gr

N. Mihalopoulos
Environmental Chemical Processes Laboratory, Department of Chemistry, University of Crete, Heraklion, Crete 71110, Greece

C.G. Helmis and P.T. Nastos (eds.), *Advances in Meteorology, Climatology and Atmospheric Physics*, Springer Atmospheric Sciences,
DOI 10.1007/978-3-642-29172-2_147,

1 Introduction

The broader Greek area is a large part of the eastern Mediterranean basin, an area with very high aerosol loads. These loads are contributed by different types of natural and anthropogenic aerosol particles. Regarding to their size, which is a very important parameter for climate and human health, aerosols are primarily classified to fine (diameter, $d < 1$ μm) and coarse ($d > 1$ μm) ones. Urban, industrial or biomass burning aerosols are usually fine, while desert dust or sea-salt are basically coarse, making thus possible the establishment of a relationship between the type and the size of aerosols. Both fine and coarse particles are expected in the broader Greek area, given the existence of desert dust (e.g. Sahara), urban (e.g. Athens), sea-salt (e.g. Aegean, Ionian, Libyan Seas) and biomass burning (e.g. west coasts of Black Sea) aerosols around or within it. Moreover, the size (and load) of aerosols is also influenced by the variability of prevailing synoptic conditions. In the present study, for the first time, we attempt to determine the size of aerosol sizes all over the Greek area, and to examine their seasonal cycles. The representativeness of our results is ensured by the use of 10-year (2000–2010) MODerate resolution Imaging Spectroradiometer (MODIS) satellite data covering the entire study region, which are evaluated against ground based AERONET data.

2 Data

Daily satellite data of aerosol Ångström Exponent ($\alpha_{470-660\ nm}$, hereafter referred to as α), Fine Fraction (FF) and Mean Effective Radius (r_{eff}) have been obtained by the MODIS database. The MODIS radiometer on board the twin polar satellites Terra and Aqua provide daily measurements of physical and optical properties of aerosols for the periods 24 February 2000–22 September 2010 and 4 July 2002–18 September 2010, respectively. In this study, gridded ($1^\circ \times 1^\circ$) data from the latest available collection (Collection 5.1, C051) are used. The aerosol properties are provided separately over land (α, FF) and sea surfaces (α, FF, r_{eff}). The α and r_{eff} data are compared against corresponding daily measurements from 7 AERONET stations located within the study region. These are: (1) Athens-NOA, (2) Sindos-EIM, (3) Epanomi, (4) FORTH-Crete, (5) Lecce University (Italy), (6) Thessaloniki, and (7) Xanthi. The quality of surface data is ensured by using the Level 2 cloud screened AERONET data (Version 2).

3 Results

3.1 Geographical Distributions

The 10-year average geographical distributions of α, over continental and maritime parts of the broader Greek area, are presented in Fig. 1a, b, respectively. In addition, the corresponding distributions for r_{eff} and FF, over sea, are also given in Fig. 1c, d,

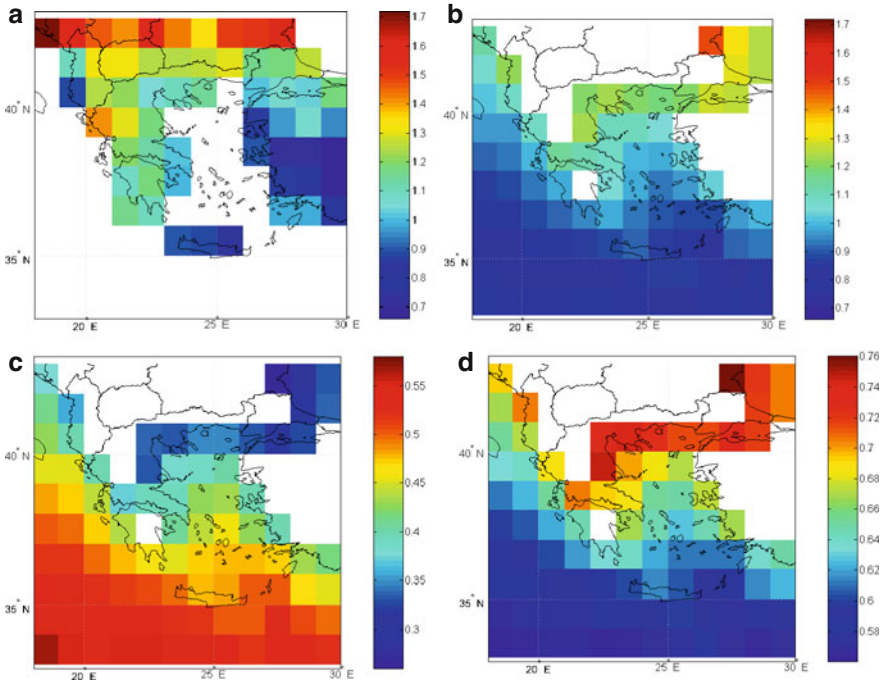

Fig. 1 Geographical distribution of: (**a**) Ångström exponent over land ($\alpha_{470–660\ nm}$), (**b**) Ångström exponent over sea ($\alpha_{550–865\ nm}$), (**c**) mean effective radius (r_{eff}, in μm) and (**d**) Fine fraction over sea, over the Greek broader area for the period 4 July 2002–18 September 2010, based on MODIS-Aqua measurements

respectively. Given that roughly similar results were obtained using both MODIS Terra and Aqua data, and that Aqua ones have been shown to be of slightly better quality than Terra, only MODIS-Aqua results are presented in this study. At a first glance, it is clear that fine particles (large α and FF values and low r_{eff} values) largely dominate in the northern continental areas of the study region, while coarse aerosols are mainly observed in the southern parts.

The geographical distribution of α (Fig. 1a) reveals a north-south gradient with maximum values (up to 1.7) over the northern parts of the study region and minimum ones (down to 0.6) over Crete. The high α values are attributed to fine aerosols originating from urban/industrialized areas or by biomass burning, extensively in northern Balkans, especially in summer (van der Werf et al. 2006). Such fine particles are transported in the Greek region from Europe or from the western coasts of the Black Sea under favourable synoptic conditions (i.e. etesians) or can be also produced locally (e.g. fires in Peloponnese, Attica and Euboea in August 2007). On the contrary, the low α values in South Greece can be explained by the presence of coarse desert dust, transported mainly from Sahara, and spreading out over the whole eastern Mediterranean, especially in spring (e.g. Hatzianastassiou et al. 2009). The distribution of α (for slightly different pair of wavelengths, i.e. 550

and 865 nm instead of 440 and 660 nm) over sea (Fig. 1b) indicates clearly smaller values than over land, which is explained by the coarse sea-salt particles there.

The geographical distributions for r_{eff} (Fig. 1c) and *FF* (Fig. 1d), only over sea areas, affirm the conclusions drawn from the Ångström exponent results. Thus, *FF* values decrease from North (0.76) to South (0.56), indicating decreasing particles' size. Note the higher FF values over Thessaloniki than Athens, despite the bigger size of the latter, due to the larger contribution of coarse (dust) particles for Athens than Thessaloniki. See also the quite higher FF values over the Black Sea (>0.7) than Aegean, as well as around Istanbul (Turkey). The main conclusions are strengthened by the seasonal analyses of α, r_{eff} and *FF* (not shown here).

3.2 Regional Means

Apart from the geographical, the seasonal variability of aerosol size over Greece, has been computed and is shown in Fig. 2 in terms of regional mean values of the selected three parameters. Over continental parts of the study region, the $\alpha_{470-660\ nm}$ values do not show a clear seasonal cycle (Fig. 2a) with values ranging from 1.03 ± 0.36 in August to 1.21 ± 0.26 in December. Given that a typical threshold value of Ångström exponent, for the discrimination of coarse and fine aerosols, is 1 (Dubovik et al. 2002) our results suggest that rather fine aerosols persist over continental Greece throughout the year. Over sea areas, however, $\alpha_{550-865\ nm}$ has a clear seasonal cycle with larger values in summer (1.14 ± 0.18) than winter (0.75 ± 0.16). There is also a secondary maximum in March, which is rather created by the associated minimum in late spring (April-May, 0.95 ± 0.18) due to transported Saharan dust (see Sect. 3.1).

According to the r_{eff} values, being lower than 0.6 (threshold value for the discrimination between fine and coarse aerosols, Tanré et al. 2001) for all months (Fig. 2c), fine aerosols prevail over the region throughout the year, in line with the results of Fig. 2a, b. There is however seasonal variability, with minimum r_{eff} values in summer (0.35 ± 0.06 n July) against maximum values in December (0.58 ± 0.09) indicating aerosols of smaller dimensions in this season. The results for fine fraction over sea surfaces (Fig. 2d) are very similar to those of α (Fig. 2b).

3.3 Comparison of Satellite and Ground Measurements

The satellite data for Ångström exponent and effective radius have been validated against corresponding reference data from ground measurements (AErosol RObotic NETwork, AERONET). Seven stations falling into the geographic limits of the study region have been selected, one in Italy (Lecce University) and 6 others in Greece. According to our comparison (Table 1 and Fig. 3) there is a relatively good agreement between MODIS and AERONET for the Ångström exponent and

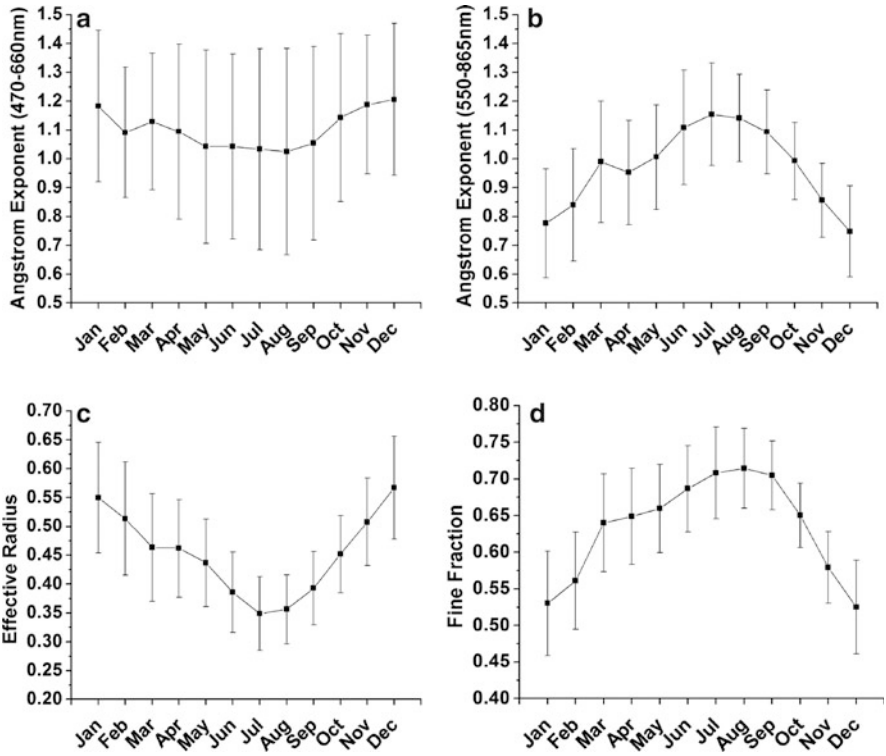

Fig. 2 Mean intra-annual variation of: (**a**) Ångström exponent over land ($\alpha_{470–660\ nm}$), (**b**) Ångström exponent over sea ($\alpha_{550–865\ nm}$), (**c**) mean effective radius (r_{eff}) and (**d**) Fine fraction over sea, over the Greek broader area for the period 4 July 2002–18 September 2010, based on MODIS-Aqua measurements. The error bars represent the spatial variability for each month

effective radius over sea, with slightly better statistics for Terra than Aqua ($R = 0.66$ and 0.67, respectively, against 0.63 and 0.66). In addition, all in all, the MODIS data are overestimated (by 0.24–0.27) for Ångström exponent, and underestimated for effective radius. On the contrary, over land, a very poor agreement is found for Ångström exponent, with very small correlation coefficients (0.28-Terra, 0.32-Aqua) and large bias (≈0.5). Our findings are in line with those of Levy et al. (2010), certifying that MODIS does not provide quantitative information about aerosol size over land.

A more detailed validation has been performed for the two AERONET sites of Athens and Crete (Fig. 3), for which an enough number of daily products is available (>3 years). The scatterplots confirm the conclusions of Table 1, with nice R values (0.66–0.73) over sea, but disappointingly low values of 0.16 and 0.08 over land. In terms of seasonal variation, there is again a good agreement between MODIS and AERONET over sea, with a similar annual cycle, against an obvious disagreement over land, produced by MODIS' failure to reproduce high α values in summer, both in Athens and Crete.

Table 1 Comparison between MODIS Ångström exponent and mean effective radius and ground-based measurements from 7 AERONET stations located into the study region, for the period 2000–2010. N is the number of matched data pairs and R is the correlation coefficient

	MODIS-Terra			MODIS-Aqua		
	N	R	Bias[a]	N	R	Bias[a]
$\alpha_{470–660\ nm}$ (land)	2,661	0.28	0.50	2,699	0.32	0.48
$\alpha_{550–865\ nm}$ (sea)	2,004	0.66	0.27	1,760	0.63	0.24
r_{eff} (sea)	2,004	0.67	−0.05	1,952	0.66	−0.03

[a]AERONET-MODIS

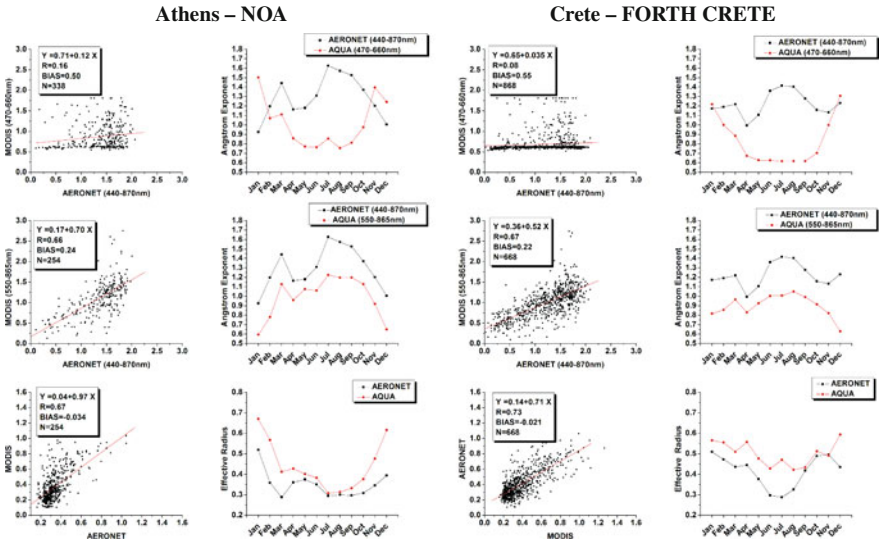

Fig. 3 Comparison, of daily MODIS-Aqua Ångström exponent over land (*first row*) and ocean (*second row*) and mean effective radius (*third row*) with corresponding AERONET data for Athens (NOA, *first–second columns*) and Crete (FORTH CRETE, *third–fourth columns*). For each station, the scatterplots and the mean intra-annual variation are presented

4 Conclusions

The spatial and temporal variability of aerosol optical properties describing the size of aerosols over the broader Greek has been investigated using satellite (MODIS) and ground (AERONET) measurements. The obtained results indicate the predominance of rather fine than coarse particles in the region, but with a significant land-sea and north-to-south gradients, with enhanced contributions of fine aerosols over land and in the northern part and coarse aerosols over sea and in the southern part of the region. The quality of MODIS data is satisfactory over sea but not so over land, limiting thus the validity of MODIS information there, especially during summer. Over sea surfaces, there is a clear annual cycle, with

more fine aerosols in summer, and enhanced contribution by coarse aerosols (dust) in late spring (April-May).

References

Dubovik O, Holben B, Eck TF, Smirnov A, Kaufman YJ, King MD, Tanré D, Slutsker I (2002) Variability of absorption and optical properties of key aerosol types observed in worldwide locations. J Atmos Sci 59:590–608

Hatzianastassiou N, Gkikas A, Mihalopoulos N, Torres O, Katsoulis BD (2009) Natural versus anthropogenic aerosols in the eastern Mediterranean basin derived from multiyear TOMS and MODIS satellite data. J Geophys Res 114:D24202. doi:10.1029/2009JD011982

Levy RC, Remer LA, Kleidman RG, Mattoo S, Ichoku C, Kahn R, Eck TF (2010) Global evaluation of the Collection 5 MODIS dark-target aerosol products over land. Atmos Chem Phys 10:10399–10420. doi:10.5194/acp-10-10399-2010

Tanré D, Kaufman YJ, Holben BN, Chatenet B, Karnieli A, Lavenu F, Blarel L, Dubovik O, Remer LA, Smirnov A (2001) Climatology of dust aerosol size distribution and optical properties derived from remotely sensed data in the spectral spectrum. J Geophys Res 106: D16:18205–18217. doi:10.1029/2000JD900663

van der Werf GR, Randerson JT, Giglio L, Collatz GJ, Kasibhatla PS, Arellano AF Jr (2006) Interannual variability in global biomass burning emissions from 1997 to 2004. Atmos Chem Phys 6:3423–3441

Experimental Study of the Turbulent Structure of the Surface Marine Atmospheric Boundary Layer over the Aegean Pelagos Under Etesian Winds

V.E. Kostopoulos, C.G. Helmis, and P.I. Raptis

Abstract In order to study the physical processes of the turbulent transportation of mass and energy within the surface Marine Atmospheric Boundary Layer over the Aegean Pelagos, field measurements were conducted on the island of Skyros, mainly under the etesian winds, during summer 2011. A meteorological mast was installed close to the shoreline, instrumented with fast anemometer (sonic) and hydrometer measuring the three components of the wind, the virtual temperature and water vapor at 10 m height with a sampling frequency of 20 Hz. At the same mast slow response sensors were measuring wind speed and direction, temperature and humidity at three levels (2, 6 and 10 m). Weak stable to near neutral flows were recorded during the experimental period. The eddy correlation analysis revealed the momentum and heat fluxes values which are presented and discussed. The estimated values are related both with stability and wind speed variations.

1 Introduction

The atmospheric surface layer is the layer within the Marine Atmospheric Boundary Layer (MABL) where significant exchanges of energy, momentum and mass occur with impact on the atmospheric and maritime circulations, in a whole spectrum of time and spatial scales. The fundamental importance of understanding the structure and the characteristics of the MABL has forced scientific expeditions over the last decades, mostly at open seas and oceans (Smith et al. 1996). Such experiments are still today considered compulsory in climate predictions since they provide modellers with essential parameterization schemes for surface turbulent

V.E. Kostopoulos (✉) • C.G. Helmis • P.I. Raptis
Department of Environmental Physics and Meteorology, University of Athens,
University Campus, Zografou, Athens 15784, Greece
e-mail: vkostopoulos@phys.uoa.gr

C.G. Helmis and P.T. Nastos (eds.), *Advances in Meteorology, Climatology and Atmospheric Physics*, Springer Atmospheric Sciences,
DOI 10.1007/978-3-642-29172-2_148,

fluxes of momentum, heat and water vapor (Brunke et al. 2003). Wind stress is usually parameterized in terms of drag coefficient (C_D), which is defined

$$C_D = \frac{\tau}{\rho \cdot U^2} \tag{1}$$

where τ is the wind stress at the sea surface, ρ is the air density and U is the mean wind speed at a reference height (10 m). The choice of using the drag coefficient regression equation under neutral conditions is regionally dependent (Geernaert and Plant 1990), while recent studies underline the need of improved surface fluxes parameterization (Edson et al. 2007). Short fetched flows wind stress is documented greater over young and developing wave fields compared to older wave fields, which are in more equilibrium with the wind. Since developing waves occur with atmospheric flow acceleration and fetch limited off-shore flow, it is expected that over the Aegean where complex topography and special oceanographic features exist, enhanced values of the momentum flux will be measured responding to air-sea interaction in much smaller spatial (10^2 km) and time scales comparing to the oceans (Sofianos et al. 2002).

It is worth mentioning that there are no published measurements over the semi closed sea of Aegean Pelagos up to now, while two expeditions in the Mediterranean Sea were reported, regarding mostly momentum flux response to regional sea state conditions (Drennan et al. 2003). Also the majority of past experiments took place on board ship platforms and it has been proved that such measurements suffer from various errors in flux measurements as well as from dependencies on assumptions of the applied methods (Frederickson et al. 1997). On the other hand, by measuring the marine ABL from land, the eddy correlation analysis can be utilised but the formation of the internal boundary layer should be taken under consideration.

The purpose of this work is to present the conducted experiment as well as the analysis of first results regarding the vertical transport of momentum and heat in relation with the atmospheric stability and the wind speed variations.

2 Experimental Area and Instrumentation

The island of Skyros of the Aegean Pelagos, hosted the experimental campaign which lasted 2 weeks, starting from the end of August 2011, under mainly etesian wind flows. This island is located at the centre of the Aegean Sea, is mountainous and at the north side a well distinguished prominence of 400 m height exists, covered by dense forests, followed by an almost leveled terrain with low hills (Fig. 1). The experimental site was located at the north-eastern part, an area of more than 1 km^2 with mean altitude less than 10 m, which expands to the sea surrounded mostly from shoreline with gentle slope and at a distance of several hundred meters to few kilometers from the ground elevation. The presence of three small reefs located few hundred meters off shore, is considered to create internal boundary layer (IBL) under certain wind directions.

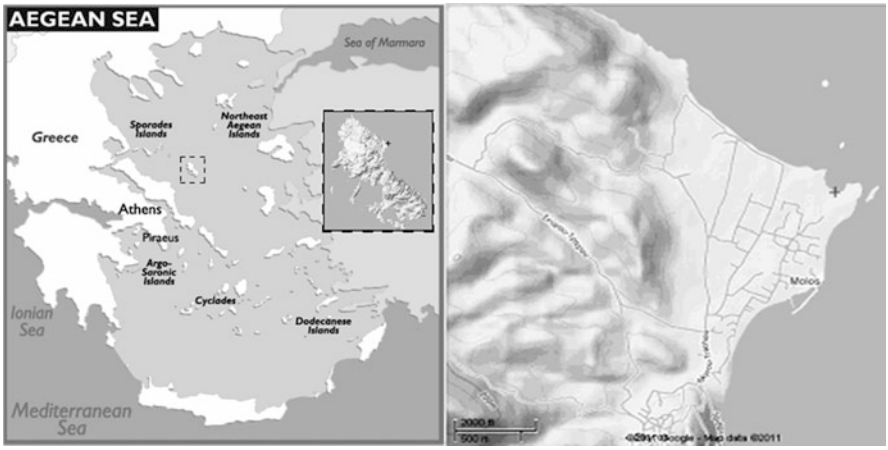

Fig. 1 The Aegean Pelagos and the island of Skyros (*left*). The location of the experimental site, indicated by *cross*, at the north eastern part of the island (*right*)

A three dimensional sonic anemometer (R3-50) and a fast hydrometer (Li-7500) measuring, with a sampling frequency of 20 Hz, the three components of the wind, virtual temperature, water vapour pressure and CO_2, were placed at 10 m height on a meteorological mast that was installed at 30 m distance from the shoreline. The mast was instrumented also with slow response sensors (1 Hz sampling frequency) at three levels (2, 6 and 10 m) measuring wind speed and direction, temperature and relative humidity. The selection of the mast location was based on the fact that the developed IBL, at a distance of 30 m from the shoreline, will be characterized with heights much less than 10 m (Savelyev and Taylor 2004). Additional analysis was conducted in order to include only cases of pure marine ABL using certain wind directions of open sea.

More than 100 h of open sea MABL flow data were recorded. Data was treated with quality control procedures proposed by the international literature (Lee et al. 2002) and subsets of data which were not characterized as pure marine data were excluded. Several records where identified as instrumentation problems mostly related with the water vapour caused probably by the sea spray. Tilt corrections were also applied using the planar fit method (Wilczak et al. 2001) and all records were furthermore examined for stationarity using the criterion suggested by Mahrt et al. (1996).

3 Flux Measurements Under Etesian Winds over the Aegean Sea

The etesian winds are seasonal winds, caused by the interaction of the thermal low of India and the high pressure field of the Azores or even by the dominance of one of them. They start from June and last until October and their sequence and

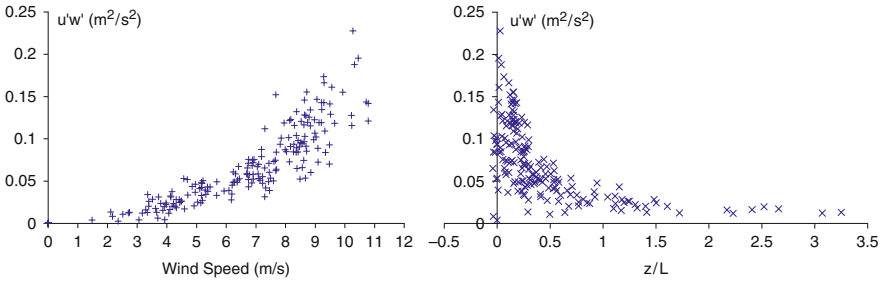

Fig. 2 Momentum flux towards wind speed and stability. Neutral conditions are considered for $z/L < |0.02|$

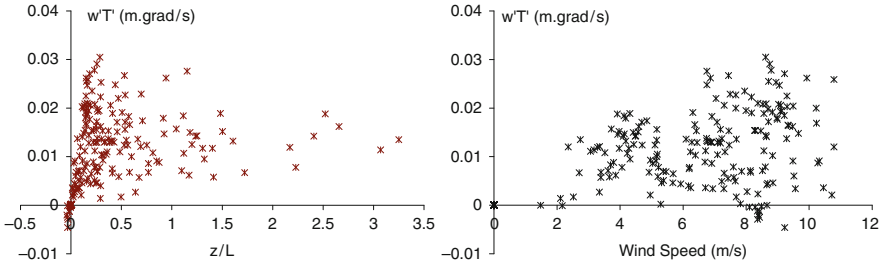

Fig. 3 Heat flux towards stability and wind speed

intensity increase and maintain high levels until the middle of September, when they start to decay. In general they blow from north to northeast directions and their highest intensities occur during daytime while at night the wind speed usually decreases. Moderate to strong etesian winds were recorded during the experimental period, ranging up to 12 m/s while temperature fluctuated from 25°C to 31°C and relative humidity from 50% to 85%. During the experimental period the sky was cloudless, apart from small mountain induced clouds at the south part of the island.

Eddy correlation analysis revealed momentum flux values ranged up to 0.2 m^2/s^2 increasing with the wind over the entire wind speed range (as shown in Fig. 2), which are close to the ones found over open sea (Helmis et al. 2006; Large and Pond 1981). The highest momentum flux values appear under neutral conditions, decreasing rapidly with stability reaching values of the order of 0.01 m^2/s^2.

Heat flux values are very small for neutral cases as expected (as shown in Fig. 3), while enhanced values appear mainly under slightly stable conditions, increasing with the increment of wind speed. Turbulent fluxes are generally expected to decrease under very stable conditions, reflecting the insufficient generation of turbulence needed to overcome the absorption of energy by buoyant forces. The maintained relatively high values of heat transport at stronger stability ($z/L > 1$) shown in Fig. 3, belong to light wind speed cases (less than 4 m/s) where dynamic processes are thought to be strongly modulated or even driven by thermal forcing (Edson et al. 2004).

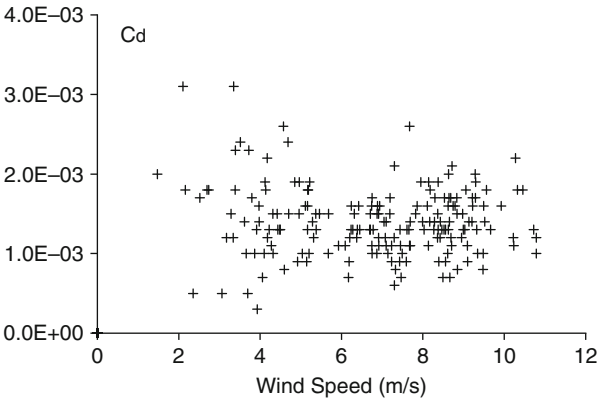

Fig. 4 Drag coefficient towards wind speed

In Fig. 4, the drag coefficient (C_d) gives high values at very low winds (<2.5 m/s) which might be attributed to viscosity effects even though the presented large scatter reflects the uncertainty of it's calculation caused by large random flux errors and the sensitivity on the method of calculation of the stress. At stronger winds when sea surface gradually shifts from aerodynamic smooth to rough, the values tend to enhance as expected (Edson et al. 2007).

Additional analysis will provide further insight to the physical processes as well as to the influence of the various meteorological factors to the turbulent transport of fluxes.

4 Conclusions

Micrometeorological measurements of the marine ABL were recorded under etesian winds. The results of this campaign reveal momentum flux values at the surface marine ABL, of the same order that were measured over ocean for the wind speed range recorded during this campaign. The turbulent fluxes are shown to increase with wind speed and are depended on the stability. High values of heat fluxes under light wind speed and stable conditions might reflect thermally driven dynamical processes.

Further research is needed towards the understanding of the physical processes related with the vertical transport of momentum, heat and humidity within the surface marine ABL of the Aegean Sea.

Acknowledgments This research has been co-financed by the European Union (European Social Fund – ESF) and Greek national funds through the Operational Program "Education and Lifelong Learning" of the National Strategic Reference Framework (NSRF) – Research Funding Program: Heracleitus II, Investing in knowledge society through the European Social Fund. The authors also gratefully acknowledge Dr. Halios C., Dr. Sgouros G. and Arnaoutis S., for their contribution in the frame of this work.

References

Brunke MA, Fairall CW, Zeng X, Eymard L, Curry JA (2003) Which bulk aerodynamic algorithms are least problematic in computing ocean surface turbulent fluxes? J Climate 16:619–635. doi:10.1175/1520-0442(2003) 016<0619:WBAAAL>2.0.CO;2

Drennan WM, Graber HC, Hauser D, Quentin C (2003) On the wave age dependence of wind stress over pure wind seas. J Geophys Res 108:1–13. doi:10.1029/2000JC000715

Edson J, Crofoot R, McGillis W, Zappa C (2004) Investigations of flux-profile relationships in the marine atmospheric surface layer during CBLAST. In: Proceedings of the 16th symposium on boundary layers and turbulence, Portland

Edson J et al (2007) The coupled boundary layers and air-sea transfer experiment in low winds (CBLAST-LOW). Bull Am Meteorol Soc 88:341–356. doi:10.1175/BAMS-88-3-341

Frederickson PA, Davidson KL, Edson JB (1997) A study of wind stress determination methods from a ship and an offshore tower. J Atmos Ocean Technol 14:822–834. doi:10.1175/1520-0426(1997) 014<0822:ASOWSD>2.0.CO;2

Geernaert GL, Plant WJ (1990) Surface waves and fluxes: current theory. Kluwer, Netherlands

Helmis CG, Wang G, Katsouvas G, Gao Z, Halios CH, Kalogiros JA, Wang S, Sgouros G, Edson J (2006) On the turbulent structure of the marine atmospheric boundary layer from CBLAST Nantucket measurements. Global Nest J 8:210–217

Large WG, Pond S (1981) Open sea momentum flux measurements in moderate to strong winds. J Phys Ocean 11:324–336, doi: http://dx.doi.org/10.1175/1520-0485(1981)011<0324:OOMFMI>2.0.CO;2

Lee X et al (2002) Handbook of micrometeorology: a guide for surface flux measurement and analysis. Kluwer, Dordrecht

Mahrt L, Vickers D, Howell J, Hojstrup J, Wilczak JM, Edson J, Hare J (1996) Sea surface drag coefficients in the Riso Air Sea Experiment. J Geophys Res 101:14327–14335. doi:10.1029/96JC00748

Savelyev S, Taylor P (2004) Internal boundary layers: I. Height formulae for neutral and diabatic flows. Bound Layer Meteorol 115:1–25. doi:10.1007/s10546-004-2122-z

Smith SD, Fairall CW, Geernaert GL, Hasse L (1996) Air-sea fluxes: 25 years of progress. Bound Layer Meteorol 78:247–290. doi:10.1007/BF00120938

Sofianos S, Johns W, Lascaratos A, Murray S, Olson D, Theocharis A (2002) Draft report of the Aegean Sea workshop. http://www.oc.phys.uoa.gr/workshop/Aegean_Draft_Report_f.htm Accessed 30 April 2012

Wilczak JM, Oncley SP, Stage SA (2001) Sonic anemometer tilt correction algorithms. Bound Layer Meteorol 99:127–150. doi:10.1023/A:1018966204465

Use of Shadowband Correction Models for Predicting Beam Solar Irradiance

M.C. Kotti and A.A. Argiriou

Abstract Beam solar irradiance can be calculated directly from global and diffuse horizontal radiation measurements. However diffuse radiation measurements need to be corrected because the pyranometer's shadowband does not obstruct only the solar disk but also an additional part of the sky vault. We present the results of normal beam irradiance calculated under different sky conditions from global and diffuse irradiance values corrected using shadowband correction models. The data consist of 1 min values of global and diffuse horizontal irradiance and also normal beam irradiance from the National Observatory of Athens, Greece. The results have been evaluated both graphically and statistically. It has been concluded that the Battles model performs best.

1 Introduction

Solar irradiance reaching the earth's surface has two primary streams of incoming radiation; the beam component, coming direct from the sun disc and the diffuse component, as a result of atmospheric scattering. The vector sum of beam and diffuse solar irradiance equals the global solar irradiance. The accurate assessment of beam solar irradiance arriving at the earth's surface is necessary for several applications and especially in energy meteorology, design and performance assessment of solar power plants and applications, agriculture etc.

Global solar irradiance is measured nowadays in many stations around the globe. Not all of these stations measure diffuse irradiance while beam irradiance is measured in a limited number of stations around the globe. Beam irradiance can be accurately calculated from global and diffuse horizontal irradiance, after

M.C. Kotti (✉) • A.A. Argiriou
Laboratory of Atmospheric Physics, Physics Department, University of Patras, Patras 26500, Greece
e-mail: mxkotti@upatras.gr

C.G. Helmis and P.T. Nastos (eds.), *Advances in Meteorology, Climatology and Atmospheric Physics*, Springer Atmospheric Sciences,
DOI 10.1007/978-3-642-29172-2_149,

correcting the diffuse irradiance measurements in order to compensate for the part of the sky vault obstructed by the shadowband used in pyranometers measuring diffuse irradiance. In this work four shadowband correction models namely the Drummond (Drummond 1956), LeBaron (LeBaron et al. 1990), Battles (Battles et al. 1995) and Muneer and Zhang (López et al. 2004) have been applied on diffuse irradiance data. The corrected diffuse irradiance values were then used in order to predict normal beam irradiance from global and diffuse irradiance values that have not been used for the correction model assessment.

2 Data and Instruments

One minute global horizontal, diffuse horizontal and beam irradiance data from the National Observatory of Athens, Greece, for the year 2001 were used. Global and diffuse irradiance was measured with a Kipp and Zonen CM 11 pyranometer and its compatible CM 11/121 shadowband and the direct solar irradiance was measured using a Kipp and Zonen CH 1 pyrheliometer.

3 Methodology

The measured data were first filtered to ensure the quality control of the solar radiation database (López et al. 2004). Diffuse irradiance readings were corrected using four shadowband correction models (López et al. 2004; Kudish and Evseev 2008). Shadowband correction models generally consider the shadowband's geometry and make an assumption regarding the sky radiance distribution. A correction factor, C, is estimated for each model.

Drummond's model assumes that the diffuse radiation is isotropically distributed in the sky hemisphere. Therefore the correction factor, C_D, can be estimated from the geometrical features of the pyranometer and of the shadowband (Duffie and Beckman 1991):

$$C_D = 1/(1 - X) \tag{1}$$

$$X = 2b\cos^3\delta(t_o \sin\phi \sin\delta + \cos\phi \cos\delta \sin t_o)/(\pi r) \tag{2}$$

b is shadowband's width (mm), δ is the sun's declination angle (rad), t_o is the hour angle at sunset (rad), ϕ is site latitude (rad).

LeBaron proposed a correction model that uses four parameters to describe both isotropic (geometric) and anisotropic (sky conditions) effects namely the geometric screening (as Drummond suggested), C_D, the solar zenith angle θ_z, the sky clearness, ε, and the sky brightness, Δ (Perez et al. 1990).

$$C_L = 1.245C_D + 0.522\log(\Delta) + 0.232\log(\varepsilon) + 0.322e^{-\frac{1}{\cos(\theta_z)}} \tag{3}$$

$$\varepsilon = (G_d + G_{btrue})/G_d \tag{4}$$

$$\Delta = G_d/(G_{on}\cos\theta_z) \tag{5}$$

The Battles model is based on the same parameters as the LeBaron model only using a piecewise procedure instead of parameterization, considering ε as the most significant parameter.

$$C_B = \begin{cases} 1.178C_D + 0.207\log(\Delta) + 0.422e^{-\frac{1}{\cos(\theta_z)}}, & \varepsilon \leq 3.5 \\ 1.454C_D + 0.655\log(\Delta) + 0.475e^{-\frac{1}{\cos(\theta_z)}}, & 3.5{<}\varepsilon \leq 8 \\ 1.486C_D + 0.495\log(\Delta), & 8{<}\varepsilon \leq 11 \\ 1.384C_D + 0.363\log(\Delta), & \varepsilon \geq 11 \end{cases} \tag{6}$$

The Muneer and Zhang model builds on sky patch radiance distribution work of Moon and Spencer (1942). The correction factor, C_M, is given from the expression:

$$C_M = 1/(1 - F/I_d) \tag{7}$$

$$F = wL_z\cos^3(\delta)\left[\frac{I_1 + bI_2}{1 + b_1}\right] \tag{8}$$

$$I_d = \left(\frac{\pi L_z}{6}\right)\left(\frac{3 + 2b_1}{1 + b_1} + \frac{3 + 2b_2}{1 + b_2}\right) \tag{9}$$

L_z is the zenith radiance ($W.m^{-2}\ sr^{-1}$), δ is the declination angle (rad), b_1 and b_2 parameters represent the radiance distribution indices for the two sky quadrants containing the sun and the opposed to the sun and w is the view angle of the shadowband subtended at the diffuse irradiance sensor (López et al. 2004).

The beam irradiance is then calculated from global and the corrected diffuse horizontal irradiance measurements using the equation:

$$G_{b(\text{calculated, i})} = \frac{G_g - G_{d(\text{corrected, i})}}{\cos(\theta_z)} \tag{10}$$

Index i denotes the uncorrected diffuse irradiance (u) and the corrected by the Drummond (D), LeBaron (L), Battles (B) and Muneer and Zhang (M) shadowband correction models.

4 Results

The calculated beam irradiance values were analyzed under all sky conditions and also under clear, partially cloudy and cloudy conditions (Kudish and Evseev 2008). Figure 1 shows the calculated beam irradiance data versus the beam irradiance

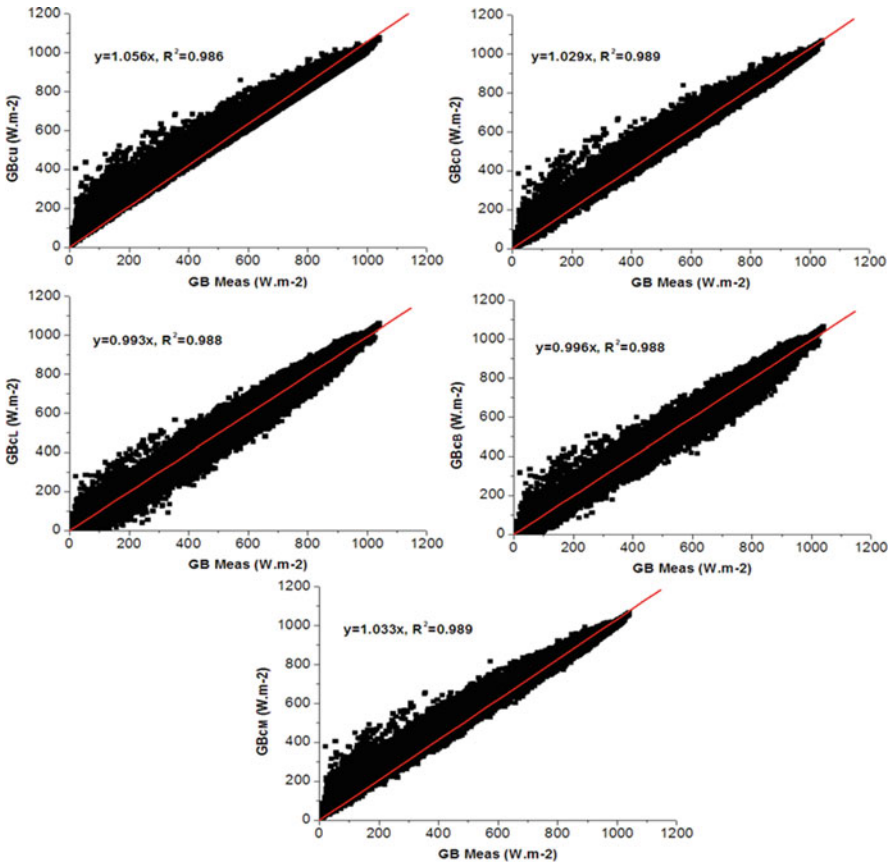

Fig. 1 Beam irradiance calculated using uncorrected, Drummond, LeBaron, Battles and Muneer – Zhang shadowband correction models versus measured beam irradiance for all sky conditions

measured directly by the pyrheliometer for all sky conditions. Similar graphs are also obtained for cloudy, partially cloudy and clear conditions. Calculated beam irradiance values are also statistically assessed. The statistical indicators used are shown in Table 1.

Results show that the slopes corresponding to the LeBaron and Battles models are closer to unity, for all sky, clear and partially cloudy sky conditions. Under cloudy conditions the Battles model performs better. The RMSE is lower for the LeBaron and Battles models under all types of sky conditions. The MBE values show that calculations of the beam irradiance without and with the Drummond and Muneer – Zhang shadowband correction models mostly overestimate the beam irradiance, while the LeBaron and Battles slightly underestimate it. According to the t-statistic (Stone 1993) the Battles model performs best under the various sky conditions.

Table 1 Statistical results of the beam irradiance data calculated from corrected diffuse irradiance data without and with the four shadowband correction models for all, clear, partially cloudy and cloudy sky conditions

All sky conditions: N = 12,0948 min, $\overline{G_{bMeas}}$ = 651.03 W/m^2					
Correction models	Slope	R^2	RMSE (W/m^2)	MBE (W/m^2)	t-Statistic
Uncorrected	1.056	0.986	60.8 (9.3%)[a]	50.1 (7.7%)[a]	504.59
Drummond	1.029	0.989	39.3 (6.0%)	26.3 (−3.4%)	302.98
LeBaron et al.	0.993	0.988	29.7 (4.6%)	−5.0 (−7.8%)	59.41
Battles et al.	0.996	0.988	29.0 (4.5%)	−2.7 (−7.5%)	32.30
Muneer and Zhang	1.033	0.989	42.8 (6.6%)	−30.9 (−2.7%)	262.17
Clear sky conditions: N = 97,446 min, $\overline{G_{bMeas}}$ = 760.57 W/m^2					
Correction models	Slope	R^2	RMSE (W/m^2)	MBE (W/m^2)	t-Statistic
Uncorrected	1.052	0.964	55.6 (7.3%)[a]	45.5 (6.0%)[a]	443.66
Drummond	1.026	0.967	36.2 (4.8%)	23.5 (3.1%)	266.16
LeBaron et al.	0.994	0.968	27.9 (3.6%)	−5.8 (−0.7%)	67.10
Battles et al.	0.996	0.963	28.1 (3.7%)	−3.1 (−0.4%)	34.71
Muneer and Zhang	1.030	0.970	38.1 (5.0%)	26.7 (3.5%)	306.65
Partially cloudy sky conditions: N = 18,158 min, $\overline{G_{bMeas}}$ = 245.92 W/m^2					
Correction models	Slope	R^2	RMSE (W/m^2)	MBE (W/m^2)	t-Statistic
Uncorrected	1.200	0.956	86.7 (35.2%)[a]	79.5 (32.3%)[a]	311.24
Drummond	1.109	0.961	55.2 (22.4%)	44.3 (18.0%)	181.87
LeBaron et al.	0.981	0.953	35.8 (15.7%)	−8.4 (−3.4%)	30.17
Battles et al.	0.999	0.958	35.4 (14.4%)	−1.6 (−0.6%)	6.17
Muneer and Zhang	1.136	0.963	64.0 (26.0%)	55.3 (22.4%)	230.49
Cloudy sky conditions: N = 5,344 min, $\overline{G_{bMeas}}$ = 30.18 W/m^2					
Correction models	Slope	R^2	RMSE (W/m^2)	MBE (W/m^2)	t-Statistic
Uncorrected	1.629	0.786	43.3 (143.3%)[a]	34.3 (113.5%)[a]	94.93
Drummond	1.335	0.823	26.9 (89.1%)	16.2 (53.5%)	54.93
LeBaron et al.	1.287	0.804	28.3 (93.7%)	22.1 (73.2%)	91.40
Battles et al.	1.089	0.842	18.1 (60.1%)	1.5 (5.1%)	6.18
Muneer and Zhang	1.469	0.811	33.9 (112.2%)	24.8 (82.2%)	78.59

[a]RMSE and MBE as percentage of $\overline{G_{bMeas}}$

5 Conclusions

Calculated beam irradiance from global horizontal and diffuse horizontal measurements using pyranometers and a shadowband are higher compared to beam irradiance measured using a pyrheliometer. Correction of diffuse irradiance is therefore required in order to compensate this obstruction.

In this work we studied the performance of several shadowband correction models by calculating beam irradiance from pyranometers comparing calculated values with pyrheliometer readings. It was found that the Battles model performs best under all kind of sky conditions, followed by the LeBaron model for all sky, clear and partially cloudy conditions and by Drummond model for cloudy conditions. Clear sky conditions cover the 68.6% of the database, cloudy conditions the 15.6% and partially cloudy the 15.8%. Therefore, for the Athens area, the Battles diffuse correction model should be preferred for predicting beam irradiance.

Acknowledgments The authors would like to thank the Institute for Environmental Research and Sustainable development of the National Observatory of Athens for providing the solar irradiance data used in this study.

References

Battles FJ, Olmo FJ, Alados-Arboledas L (1995) On shadowband correction methods for diffuse irradiance measurements. Sol Energ 54(2):105–114

Drummond AJ (1956) On the measurement of sky radiation. Arch Fur Meteorol Geophy Bioklimat Ser B 7:413–436

Duffie JA, Beckman WA (1991) Solar engineering of thermal processes. Wiley Interscience, New York

Kudish AI, Evseev EG (2008) The assessment of four different correction models applied to the diffuse radiation measured with a shadow ring using global and normal beam radiation measurements for Beer Sheva, Israel. Sol Energ 82:144–156

LeBaron BA, Michalsky JJ, Perez R (1990) A simple procedure for correcting shadowband data for all sky conditions. Sol Energ 44(5):249–256. doi:10.1016/0038-092X(90)90053-F

López G, Muneer T, Claywell R (2004) Assessment of four shadow band correction models using beam normal irradiance data from the United Kingdom and Israel. Energ Convers Manag 45:1963–1979. doi:10.1016/j.enconman.2003.11.001

Moon P, Spencer DE (1942) Illumination from a nonuniform sky. Illum Eng 37:707–726

Perez R, Ineichen P, Seals R, Michalsky JJ, Stewart R (1990) Modelling daylight availability and irradiance components from direct and global irradiance. Sol Energ 44:271–289

Stone RJ (1993) Improved statistical procedure for the evaluation of solar radiation estimation model. Sol Energ 51(4):289–291. doi:10.1016/0038-092X(93)90124-7

Investigating the GOME2/MetopA Total Sulphur Dioxide Load with the Aid of Chemical Transport Modelling over the Balkan Region

M.E. Koukouli, P. Valks, A. Poupkou, I. Zyrichidou, M. Rix, N. Hao, E. Katragkou, D. Balis, D. Loyola, and D. Melas

Abstract The current discerning capability of nadir viewing satellite instruments is mainly providing information on large volcanic events, such as the Kasatochi 2008 and the Eyjafjöll 2010 eruptions, and areas with high anthropogenic SO_2 sources such as Peruvian smeltering regions. Consequently, there exists a constant need to improve the algorithms in order to provide satellite information on the megacities' SO_2 levels for air quality purposes. In the current study, we aim to assess the observational capability of the GOME2/MetopA instrument by analysing the total SO_2 load estimated over the extended Balkan region with the use of the high spatial resolution Comprehensive Air Quality Model with extensions (CAMx) modelling results. Two years of satellite and modelling estimates have been analysed so as to pin-point locations of constantly high SO_2 loading, locations with a marked seasonal variability as well as locations with high expected loading that might not be visible from the satellite orbit. Regions of specific interest will be chosen for further investigation and algorithm development based on updated modelling input parameters such as the SO_2 loading profile.

1 Introduction

Sulphur dioxide, SO_2, enters the atmosphere as a result of both natural phenomena and anthropogenic activities, such as the combustion of fossil fuels, the oxidation of organic material in soils, volcanic eruptions, biomass burning, etc. Coal burning is the single largest man-made source of sulphur dioxide, accounting for about 50% of

M.E. Koukouli (✉) • A. Poupkou • I. Zyrichidou • E. Katragkou • D. Balis • D. Melas
Laboratory of Atmospheric Physics, Physics Department, Aristotle University of Thessaloniki, Thessaloniki, Greece
e-mail: mariliza@auth.gr

P. Valks • M. Rix • N. Hao • D. Loyola
German Aerospace Center (DLR-IMF), Munich, Germany

C.G. Helmis and P.T. Nastos (eds.), *Advances in Meteorology, Climatology and Atmospheric Physics*, Springer Atmospheric Sciences,
DOI 10.1007/978-3-642-29172-2_150,

annual global emissions, with oil burning accounting for a further 25–30%. Sulphur dioxide reacts on the surface of a variety of airborne solid particles (aerosols), is soluble in water and can be oxidised within airborne water droplets, producing sulphuric acid. This acidic pollution can be transported by wind over many hundreds of kilometres, and is deposited as acid rain.

Changes in the abundance of sulphur dioxide have an impact on atmospheric chemistry and on the radiation field, and hence on the climate (Hansen et al. 2005). Consequently, global observations of sulphur dioxide are important for atmospheric and climate research. In addition, SO_2 at high concentrations has negative effects on human health, in particular in combination with fog (smog).

In the current study we are combining information from remote sensing measurements of the atmospheric SO_2 load and chemical modelling predictions to assess both the satellite ability to sense the anthropogenic SO_2 levels but also the accuracy of the modelling SO_2 emission inventories.

2 Data

2.1 GOME-2/MetopA Total SO_2 Columns

The GOME-2 instrument is a 4 channels UV/visible spectrometer covering the spectral region from 240 to 790 nm with a spectral resolution of 0.26–0.51 nm (Munro et al. 2006). It was launched on MetOp-A in October 2006 and has been providing measurements since January 2007. The MetOp-A satellite is in a near polar sun-synchronous orbit with a descending node equator crossing time of 09:30 LT. The GOME-2 has a large swath of 1920 km, resulting in global coverage at the equator in 1.5 days and several overpasses per day at higher latitudes. The spatial resolution of the forward scan measurements is $80 \times 40\,km^2$ over most of the globe.

The operational GOME-2 total column SO_2 product is produced by the German Aerospace Center (DLR) in the framework of EUMETSAT's Satellite Application Facility on Ozone and Atmospheric Chemistry Monitoring (O3M-SAF), the PROMOTE and the Exupéry projects. SO_2 column retrieval is a two-step procedure (Valks and Loyola 2008). In a first step, slant column densities (SC) of SO_2 are determined using the well established Differential Optical Absorption Spectroscopy (DOAS) method (Platt 1994) in the wavelength region between 315 and 326 nm. Input parameters for the DOAS fit include the absorption cross-section of SO_2, for which the temperature is adjusted depending on the assumed height of the SO_2 plume, and the absorption cross-sections of interfering gases, ozone and NO_2. A further correction is made to account for the ring effect (rotational Raman scattering). In a second step, the corrected slant column densities of SO_2 are converted to geometry-independent vertical column (VC) amounts through division by an appropriate air mass factor (AMF) as $VC = SC/AMF$.

For SO_2, the AMF is strongly dependent on measurement geometry, surface albedo, clouds, aerosols, and most importantly, the shape of the vertical SO_2 profile

in the atmosphere. An *a priori* SO_2 profile is assumed with a predefined central plume height. The SO_2 column is computed for three different assumed plume heights: 2.5, 6 and 15 km above ground level. The lowest height represents either anthropogenic pollution or passive degassing of low volcanoes, the second height effusive volcanic eruptions or passive degassing of high volcanoes and the third height explosive eruptions. The AMFs are calculated with the radiative transfer model LIDORT (Spurr et al. 2001). An initial validation performed by Van Geffen et al. (2008) has yielded very promising results for the product.

2.2 CAMx Simulated SO_2 Columns

The simulated SO_2 vertical column densities are based on the results of the air quality forecast modeling system MM5-CAMx for Europe with 30 km spatial resolution. The domains' vertical profile contains 15 layers of varying thickness, extending up to about 300 hPa. The chemistry mechanism invoked is the Carbon Bond v4. The meteorological fields are derived from the fifth generation NCAR/Penn State University Mesoscale Model MM5 v3.6. MM5 is forced by the global 12:00 UTC GFS/NCEP forecast of 1° spatial resolution.

Annual anthropogenic emission data of gaseous (NOx, SO_2, NMVOC, CH_4, NH_3, CO) and particulate matter (PM_{10}) pollutants with reference year 2003 were provided by The Netherlands Organization (TNO) (Visschedijk et al. 2007) and have been used to support the photochemical model simulations. The emission spatial resolution was 1/8 by 1/16 degrees. The TNO annual emission data were temporally disaggregated (seasonal, weekly and diurnal temporal profiles) according to Friedrich (1997). Detailed emission data for Greece and for Athens and Thessaloniki were used according to Markakis et al. (2010). Ship emission data have been taken from the EMEP emission database. The global chemistry transport model MOZART-IFS (Flemming 2008) provides the CAMx chemical boundary conditions since January 2009.

3 Methodology

GOME-2 SO_2 columns have been extracted from the DLR orbit files for the domain of interest, i.e. from 30° to 65° N and from −10° to 45°E, to basically cover the wider Balkan region. The SO_2 is assumed to be in a 1 km thick layer centered around 2.5 km above sea level, i.e. the product associated either with anthropogenic or the passive degassing of low volcanoes. A very strict data acceptance policy was followed whereupon only zero flagged data are allowed, data with associated solar zenith angle of less than 70°, etc. The satellite data were transformed onto the CAMx Lambertian conformal projection with an approximate 50 × 50 km spatial resolution (depending on the latitude and longitude.)

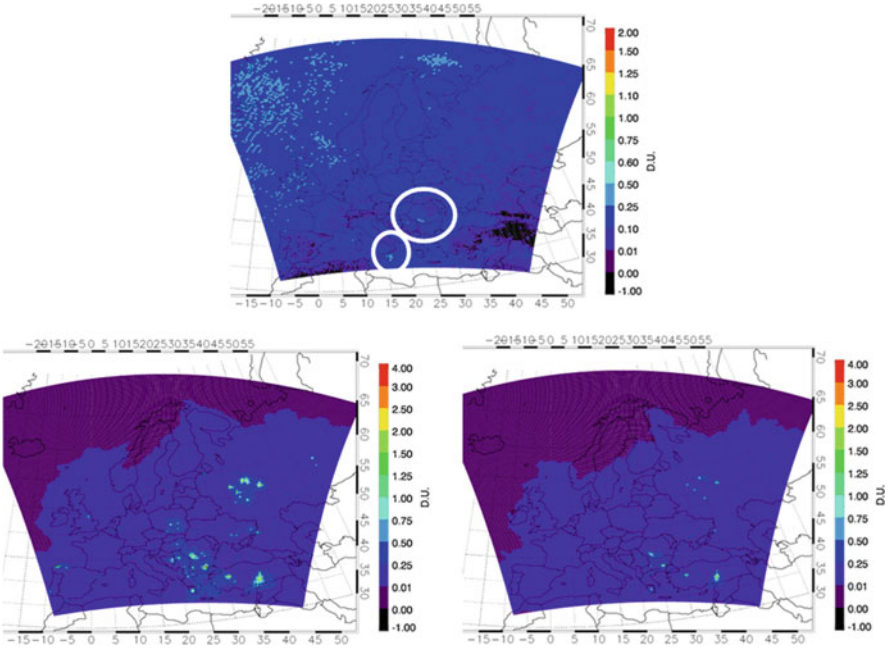

Fig. 1 The seasonal variability in summer from 2 years of data. *Upper*: GOME-2 total SO_2 columns. *Bottom left*: CAMx total SO_2 columns. *Bottom right*: CAMx SO_2 columns excluding the first 1,000 m of the PBL

Vertical profiles (15 levels up to ~7 km) of SO_2 in ppb units, every hour on a 30 by 30 km grid over Europe were extracted from the CAMx model results for the years 2008 and 2009. These were turned into tropospheric SO_2 columns as daily means & monthly means using an algorithm which integrating the 15 level concentrations while taking into account the number density in each level. The concentration during the hours closest to the GOME-2 overpass, namely between 8 and 10 UTC, was chosen.

From the two databases created, common days of data were found and used in studying the monthly mean, seasonal mean and yearly averages. An example of this process is shown and discussed in Fig. 1 below.

4 First Results

In Fig. 1 the total SO_2 columns from the GOME-2 satellite measurements (on the top) and the CAMx estimates (on the bottom) are shown for the summer season created from the common data points for years 2008 and 2009. A number of issues can be raised; first of all, almost all GOME-2 seasonal maps [not shown here] show artefacts with high value points in the north of the domain, over the North Sea & the Scandiavias, which are due to high SZA measurements resulting in unreasonable

SO_2 columns. A stricter filter has to be applied especially for the winter maps which appear to be entirely within the error range. The summer maps show some promising hot spots marked in the white circles. The larger of the two circles pin-points locations of major anthropogenic emission sources (possibly power plants), also seen in the equivalent CAMx maps on the bottom, with their high SO_2 column values, whereas the smaller circle shows the Mt Etna outgassing which is absent from the CAMx maps since the model does not contain volcanic SO_2 emission sources. The CAMx map on the left also show the dispersion of the gas in the near-surface PBL layers, which cannot be observed by the satellite instruments. Excluding the first 1,000 m from the model profile, this results in a different spatial distribution such as the one shown in the bottom right plot of Fig. 1. Only emission sources that disperse their SO_2 up to the top of planetary boundary layer are now seen. However, still not all equivalent hot spots are evident in the satellite map (upper); especially conspicuous is the absence of the emissions from a source in South-East Turkey.

5 Concluding Comments and Future Outlook

Sulfur dioxide monitoring from satellite instruments is a valuable tool in monitoring air quality and volcanic activity. The GOME-2 instrument provides the opportunity for monitoring long-range transport of volcanic clouds, detection of small eruptions, investigation of pre-eruptive degassing and monitoring anthropogenic pollution on a global scale and daily basis. Research in recent years has focused either on the study of volcanic outgassing (Carn et al. 2008), or large volcanic eruptions such as the August 2008 Kasatochi eruption (Krotkov et al. 2010) or on large scale anthropogenic emission sources, such as the daily sulfur dioxide emissions from copper smelters (Carn et al. 2007). This work represents an attempt which, to the best of our knowledge, is the first one to study this region on a detailed spatio-temporal grid using GOME-2/MetopA measurements and CAMx modeling estimates. This synergistic use of chemical & transport modeling estimates and satellite measurements permits the improvement on both types of scientific investigation and enhances the understanding on air quality issues.

Acknowledgments The research study was financed by the EU research projects MACC (Monitoring Atmospheric Composition and Climate: Grant Agreement no. 218793) and GEMS ('Global and regional Earth-system Monitoring using Satellite and in-situ data, contract no.: 516099). MEK would like to acknowledge the EUMETSAT *Satellite Application Facility on Ozone and Atmospheric Chemistry Monitoring* CDOP-2 phase.

References

Carn SA, Krueger AJ, Krotkov NA et al (2007) Sulfur dioxide emissions from Peruvian copper smelters detected by the ozone monitoring instrument. Geophys Res Lett 34:L09801. doi:10.1029/2006GL029020

Carn SA, Krueger AJ, Arellano S et al (2008) Daily monitoring of Ecuadorian volcanic degassing from space. J Volcanol Geotherm Res 176(1):141–150. doi:10.1016/j.jvolgeores.2008.01.029

Flemming J (2008) Technical description of the coupled forecast system IFS-CTM for global reactive gases forecast and assimilation in GEMS. http://gems.ecmwf.int/do/get/PublicDocuments/1534/1052?showfile=true Last date of access: April 30th, 2012

Friedrich R (1997) *GENEMIS: assessment, improvement, temporal and spatial disaggregation of European emission data. Tropospheric modelling and emission estimation (part 2)*. Ebel, A., Friedrich, R., Rhode, H., (Eds.). Springer, New York

Hansen J, Nazarenko L, Ruedy R et al (2005) Climate change: Earth's energy imbalance: confirmation and implications. Science 308(5727):1431–1435

Krotkov NA, Schoeberl MR, Morris GA et al (2010) Dispersion and lifetime of the SO_2 cloud from the August 2008 Kasatochi eruption. J Geophys Res 115:D00L20. doi:10.1029/2010JD013984

Markakis K, Poupkou A, Melas D et al (2010) A computational approach based on GIS technology for the development of an anthropogenic emission inventory of gaseous pollutants in Greece. Water Air Soil Poll 207:157–180. doi:10.1007/s11270-009-0126-5

Munro R, Eisinger M, Anderson C et al (2006) GOME-2 on METOP: from in-orbit verification to routine operations. In: Proceedings of the EUMETSAT meteorological satellite conference, Helsinki, 12–16 Jun 2006

Platt U (1994) Differential optical absorption spectroscopy (DOAS). In: Sigrist MW (ed) Air monitoring by spectroscopic techniques, vol 127, Chemical analysis series. Wiley, New York

Spurr RJD, Kurosu TP, Chance KV (2001) A linearized discrete ordinate radiative transfer model for atmospheric remote sensing retrieval. J Quant Spectros Radiat Transf 68:689–735. doi:10.1016/S0022-4073(00)00055-8

Valks P, Loyola D (2008) Algorithm theoretical basis document for GOME-2 total column products of ozone, minor trace gases, and cloud properties. DLR/GOME-2/ATBD/01, Iss./Rev.: 1/D. http://wdc.dlr.de/sensors/gome2/ Last date of access: April 30th, 2012

Van Geffen J, Van Roozendaal M, Rix M, Valks P (2008) Initial validation of GOME-2 GDP 4.2 SO2 total columns – ORR B, BIRA-IASB/DLR technical note TN-IASB-GOME2-O3MSAF-SO2-01

Visschedijk AJH, Zandveld PYJ, van der Gon D (2007) H.A.C.A. High resolution gridded European emission database for the EU Integrate Project GEMS. TNO-report 2007-A-R0233/B

Phaethon: A System for the Validation of Satellite Derived Atmospheric Columns of Trace Gases

N. Kouremeti, A.F. Bais, D. Balis, and I. Zyrichidou

Abstract Phaethon is a system for the retrieval of column densities of various atmospheric gases from the ground by applying the technique of Differential Optical Absorption Spectroscopy on direct sun and sky radiance spectral measurements. The system comprises a spectrograph with a CCD detector operating in the wavelength range 300–650 nm, the entrance optics with a field of view of 1°, equipped with a filter wheel, a temperature stabilization unit, and a solar tracker. The Phaethon system was validated against a MAX-DOAS system during a campaign at the High Altitude Research Station Jungfraujoch. The comparison of differential slant column densities derived from off-axis measurements showed an average agreement of 5–10% (±5%) depending on the viewing angle for NO_2, and 15–25% for O_4 (±2% for viewing angles <8°). Following the validation of Phaethon, direct solar irradiance and sky radiance spectral measurements are regularly performed at Thessaloniki, Greece, to derive atmospheric columns of various trace gases. The retrieved atmospheric columns of total and tropospheric NO_2 were compared to GOME-2 products revealing large discrepancies which are attributed to the large spatial variability of NO_2 due to the localized air pollution sources over the area.

1 Introduction

Phaethon is a low-cost ground based system for the retrieval of column densities of various atmospheric gases, through Differential Optical Absorption Spectroscopy (DOAS) analysis of direct sun and sky radiance spectral measurements. The development of the instrument took place within the ESA project "Building Infrastructure for the validation of satellite derived atmospheric parameters" and was

N. Kouremeti (✉) • A.F. Bais • D. Balis • I. Zyrichidou
Laboratory of Atmospheric Physics, Aristotle University of Thessaloniki, Thessaloniki, Greece
e-mail: nakour@auth.gr

C.G. Helmis and P.T. Nastos (eds.), *Advances in Meteorology, Climatology and Atmospheric Physics*, Springer Atmospheric Sciences,
DOI 10.1007/978-3-642-29172-2_151,

based on a prototype system that was developed for aerosol optical depth and solar radiation measurements (Kouremeti et al. 2008). The original system was upgraded by modifying its optical characteristics to fulfill the requirements for atmospheric gas retrievals with the DOAS technique (Platt and Stutz 2008).

In DOAS, spectral measurements of solar radiation (radiance) which has been absorbed by atmospheric constituents and then scattered by air molecules are compared with a reference spectrum which has undergone weaker absorption. The differences in the wavelength-dependent absorption features of the two spectra appear as a characteristic differential spectrum of proportional magnitude. This "differential" spectrum is analyzed by least-squares fits of cross sections, after the removal of slowly-varying spectral features by spectral smoothing. Spectrally resolved radiance and irradiance measurements acquired by the Phaethon system are analyzed with the QDOAS algorithm (Fayt and van Roozendael 2001), to derive differential slant column densities (DSCD) of atmospheric gases. The DSCD is converted to vertical column density with the aid of the airmass factors (AMF) which quantify the enhancement of attenuation of radiation due to absorption and scattering along its atmospheric path. The AMF is derived from radiative transfer model calculations taking into account information on the likely atmospheric composition and structure (e.g., Rozanov and Rozanov 2010).

2 The Phaethon System

The original Phaethon system was optimized for measurements of spectral solar irradiance and radiance in the spectral region 310–1000 nm, and subsequent retrieval of spectral aerosol optical depth. Details on this system can be found in (Kouremeti et al. 2008). The required modifications of the original system were determined by analyzing and comparing its characteristics with those required for achieving higher accuracy in the retrieved quantities. Additionally, the new system was designed to be portable, to take part in validation campaigns, and stable under different meteorological and weather conditions.

The spectrograph of the new system is a Maya 2000 Pro spectrometer manufactured by Ocean Optics, equipped with a back-thinned two dimensional FFT-CCD detector (Hamamatsu S10420). It is has high quantum efficiency in the UV where atmospheric radiation intensity is weak. An 8 m long and 1 mm thick UV graded light-guide, assembled from single quartz glass fibers to a bundle, assures high flexibility and constant light throughput. The new entrance optics results in a 1° field of view which fulfils the requirements for the retrieval of vertical distribution of atmospheric gases. A filter wheel with eight positions allows the use of different optical components required for the measurements (neutral density and band pass filters, one blocked for dark signal). A schematic of the system is shown in Fig. 1. The upgraded system was exhaustively tested and evaluated by laboratory and ambient radiation measurements in order to fully characterize its components and the sensitivity and stability of its optical characteristics.

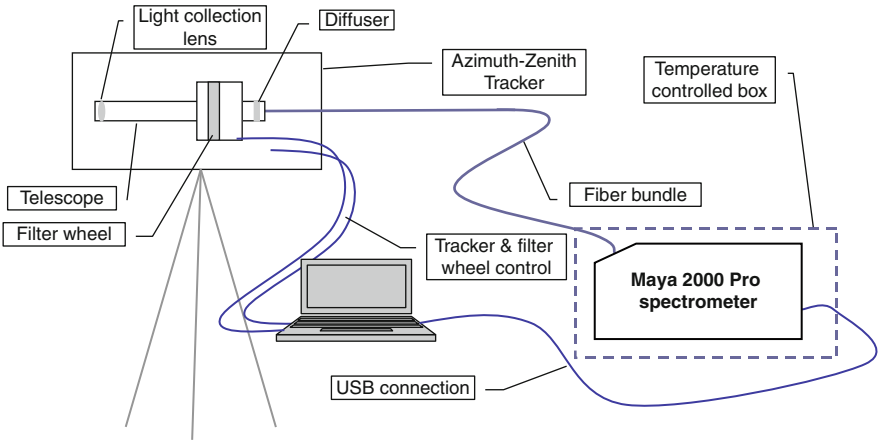

Fig. 1 Schematic diagram of the layout of the upgraded Phaethon system showing its major components (*bottom*) and photograph of the system (*top*)

3 The Validation Campaign

The validation of Phaethon was done at the High Altitude Research Station Jungfraujoch, ~3.5 km altitude, where a MAX-DOAS system is operating regularly by the Belgian Institute of Space Aeronomy (BIRA). The campaign lasted for 1 week in October 2010. The entrance optics of Phaethon and the tracker were mounted on the roof of the observatory, about 1 m far from BIRA instrument, at a location suitable for performing spectral sky radiance measurements from the zenith down to about -2° elevation angles, as well as, spectral solar irradiance measurements by pointing directly towards the solar disk. With this configuration both instruments were capable in pointing at the same locations on the sky without obstructing each other.

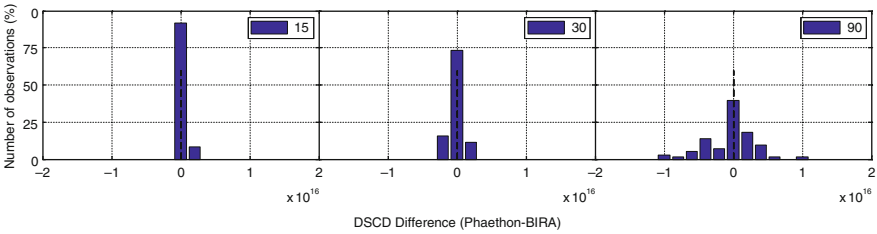

Fig. 2 Frequency distribution of differences of NO_2 DSCD measured by Phaethon and BIRA for SZA $< 85°$ for different viewing angles

Zenith sky radiance spectra were acquired at solar zenith angles larger than 85°, both in the morning and in the evening. During the rest of the day, alternating scans of direct solar irradiance and sky radiance at 14 viewing elevation angles and at 315° azimuth angle were recorded by both systems. Exact synchronization could not be achieved due to differences in the optical characteristics and operational details of the two systems, causing occasionally important uncertainties in the comparisons, due to the need for interpolation of data.

Comparison of the two systems revealed that Phaethon slightly overestimates the derived DSCD of NO_2 systematically, on average by 0.14×10^{16} molec cm^{-2}, and that its estimates are noisier. This behavior may be attributed to the weak absorption from NO_2 and the resulting uncertainty, which for Phaethon is more significant because its spectrometer is simpler and less accurate compared to BIRA. However, more than 75% of the data agree to within $\pm 0.1 \times 10^{16}$ molec cm^{-2}, and generally this offset is very small (Fig. 2). Despite this positive offset of Phaethon, the two instruments follow closely each other's variations, as the slopes of the regressions are close to unity (within ±5%).

4 Monitoring with Phaethon at Thessaloniki

Direct solar irradiance and sky radiance (zenith and off-axis) spectral measurements are regularly performed at Thessaloniki, Greece, with Phaethon from sunrise to sunset with emphasis in the time period 6:00–12:30 UT which covers the period of satellite overpasses. Total atmospheric columns of ozone and NO_2 as well as of tropospheric NO_2 are derived with the QDOAS algorithm from the recorded radiation spectra.

Comparisons with estimates of total and tropospheric columns of NO_2 from the GOME-2 instrument on board MetOp-A satellite, processed with GDP4.4, showed that although the agreement is rather poor, there is some correspondence in the day-to-day variability (Fig. 3 – upper). The correlation coefficient for daily averages is 0.84, slightly smaller of those reported in earlier studies (Valks et al. 2011). Concerning the tropospheric NO_2 (Fig. 3 – lower) the agreement is worse ($r = 0.78$), with cases where GOME-2 largely underestimates the ground-based

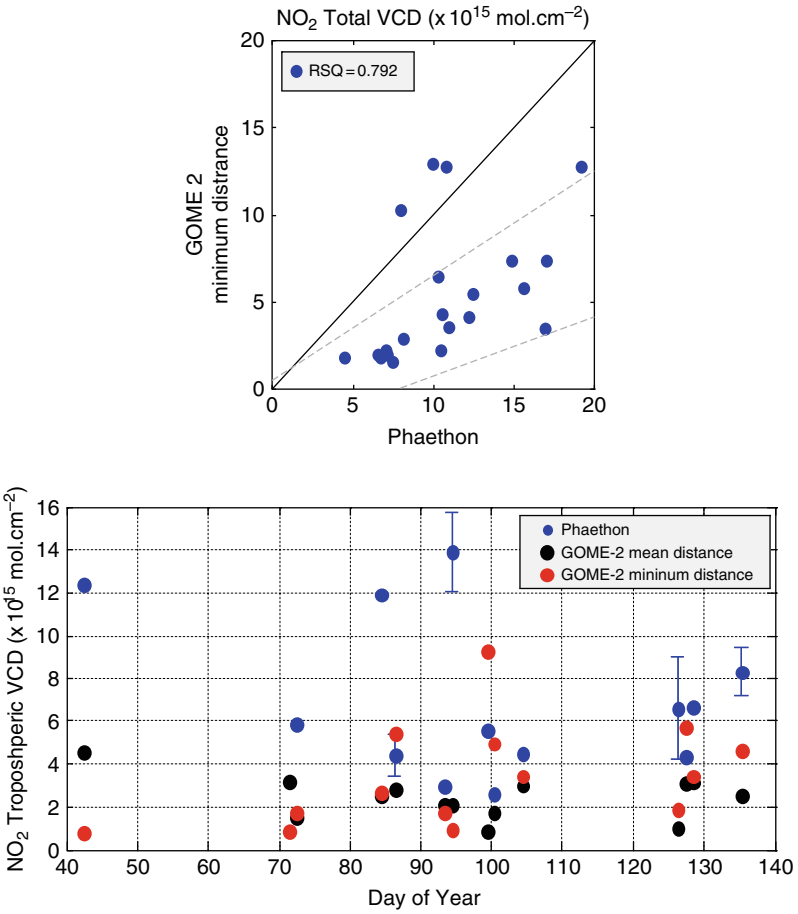

Fig. 3 Scatter plot between total VCD of NO_2 derived from Phaethon and GOME-2 (*upper*). Time series of daily averaged tropospheric VCD of NO_2 at Thessaloniki between days 40 and 140 of 2011 as derived from Phaethon, SCIAMACHY and GOME-2 (*lower*)

measurements, especially when averaging all pixels within 50 km distance from Phaethon's location. These discrepancies are attributed to the large spatial variability of NO_2 due to the localized air pollution sources (e.g., Pinardi et al. 2008).

The total O_3 column derived from Phaethon was validated by comparison of daily averages with the ozone derived from a collocated Brewer MKII spectrophotometer (Fig. 4 – upper). The two instruments correlate very well ($r = 0.977$), suggesting that Phaethon has the potential, with some further improvements to provide accurate total ozone measurements. Comparisons with estimates from the GOME-2 instrument, show that GOME-2 underestimates total ozone by ~2.5% compared to both ground-based instruments (Fig. 4 – lower), consistent with the

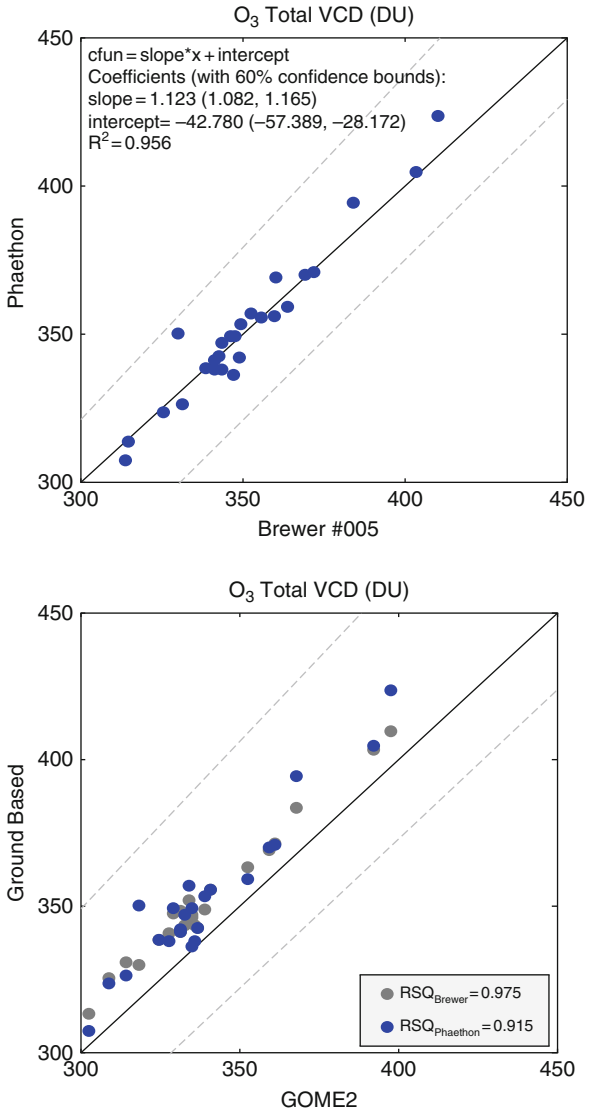

Fig. 4 Comparison of total ozone measurements derived from Phaethon and Brewer (*upper*). Comparison of total ozone measurements from the ground based systems, Phaethon and Brewer, with estimates from GOME-2 (*lower*). Both panels show data for the period January–May 2011

validation results reported in previous studies for Thessaloniki using 3 years of data (Balis et al. 2009; Loyola et al. 2011). The short time period of the common measurements does not allow the investigation of possible seasonal effects in the comparisons or solar zenith angle dependencies. At least a whole year of common measurements would be desirable to draw firm conclusions for the agreement of the

two ground-based data sets. In any case, the scatter of the existing comparisons is small, indicating that Phaethon provides total ozone with accuracy comparable to the Brewer spectrophotometer.

5 Conclusions

Phaethon was proven to provide satisfactory results in the retrieval of total and tropospheric columns of NO_2, O_4 and O_3 with acceptable accuracy. However, at this stage it cannot compete with other sophisticated MAX-DOAS systems. At locations with sufficient load of NO_2, as, e.g., over urban and industrial areas Phaethon is expected to have better performance, since the retrieval error of DSCD in Thessaloniki and for all viewing angles is less than 5% in contrast to Jungfraujoch which was between 5% and 30%. In this respect its permanent deployment at Thessaloniki would provide useful information on the validation of satellite products. An advantage of Phaethon is its capability to provide atmospheric columns both from direct solar irradiance and sky radiance spectra during the entire day. Consequently it will provide information on the diurnal course of the retrieved columns, information that satellite instruments are unable to deliver at present. In this respect Phaethon may prove a useful supplement to satellite monitoring of tropospheric gases. Extending of Phaethon's capabilities to derive additional products is already possible as the recorded spectra cover already the required spectral ranges. Retrieval of gases absorbing in the UV-B is more difficult, but still possible with reduced accuracy, due to the spectral resolution in this range.

Acknowledgments This project was funded under the Greek Industry Incentive Scheme (ESA-Greek Task Force), ESA Contract No. 22286/09/NL/CBI. The authors would like to thank M. van Roozendael, C. Fayt, G. Pinardi, for their substantial contribution in the validation of Phaethon and for providing the QDOAS algorithm. Also authors would like to thank D. Loyola for providing the GOME-2 data.

References

Balis D, Koukouli M, Loyola D, Valks P, Hao N (2009) O3MSAF validation report, SAF/O3M/AUTH/GOME-2VAL/RP/04

Fayt C, van Roozendael M (2001). WinDOAS 2.1: software user manual. http://bro.aeronomie.be/WinDOAS-SUM-210b.pdf, accessed on 30 April 2012

Kouremeti N, Bais A, Kazadzis S, Blumthaler M, Schmitt R (2008) Charge-coupled device spectrograph for direct solar irradiance and sky radiance measurements. Appl Opt 47:1594–1607. doi:10.1364/AO.47.001594

Loyola DG, Koukouli ME, Valks P, Balis DS, Hao N, Van Roozendael M, Spurr RJD, Zimmer W, Kiemle S, Lerot C, Lambert JC (2011) The GOME-2 total column ozone product: retrieval algorithm and ground-based validation. J Geophys Res Atmos 116. doi:10.1029/2010jd014675

Pinardi G, Hendrick F, Clémer K, Lambert JC, Bai J, Van Roozendael M (2008) On the use of the MAX-DOAS technique for the validation of tropospheric NO2 column measurements from satellite. In: Proceedings of the EUMETSAT meteorological satellite conference, Darmstadt

Platt U, Stutz J (2008) Differential optical absorption spectroscopy. Principles and applications. Springer, Berlin/Heidelberg

Rozanov VV, Rozanov AV (2010) Differential optical absorption spectroscopy (DOAS) and air mass factor concept for a multiply scattering vertically inhomogeneous medium: theoretical consideration. Atmos Meas Tech 3:751–780. doi:10.5194/amt-3-751-2010

Valks P, Pinardi G, Richter A, Lambert JC, Hao N, Loyola D, Van Roozendael M, Emmadi S (2011) Operational total and tropospheric NO2 column retrieval for GOME-2. Atmos Meas Tech Discuss 4:1617–1676. doi:10.5194/amtd-4-1617-2011

Effects of Albedo on Solar Irradiance

A. Kreuter, M. Blumthaler, A.R. Webb, A.F. Bais, R. Kift, and N. Kouremeti

Abstract The effects of ground albedo on solar radiation were investigated in a field campaign around Ny Alesund on Svalbard, Norway. In spring time this site exhibits high albedo gradients at the interface between sea water and snow covered land. Array spectroradiometers measuring global irradiance in the UV and visible wavelength range were installed at three field sites with increasing distance from the coastline towards the snow covered glaciers with a horizontal distance of about 20 km. For 3 weeks, quasi synchronous spectra were collected under clear sky and overcast sky conditions. At 320 nm, an enhancement of up to 15% of the global irradiance for clear sky was observed at the higher albedo site relative to the coastal site. Under overcast conditions this enhancement of irradiance was as high as 30%. The measurements agree well with a 1D radiative transfer model, considering an effective average albedo. Diurnal asymmetries of the irradiance have been observed and require a full 3D model treatment to account for the highly inhomogeneous albedo environment and the non-Lambertian reflectance of water (sun glint).

1 Introduction

The reflectivity of the earth's surface, the albedo, is a significant factor in the global radiation budget. While affecting the net energy balance of the atmosphere, reflected solar radiation also increases the sky's irradiance due to multiple

A. Kreuter • M. Blumthaler (✉)
Division for Biomedical Physics, Innsbruck Medical University, Innsbruck, Austria
e-mail: mario.blumthaler@i-med.ac.at

A.R. Webb • R. Kift
School of Earth Atmospheric and Environmental Sciences, University of Manchester, Manchester, UK

A.F. Bais • N. Kouremeti
Laboratory of Atmospheric Physics, Aristotle University of Thessaloniki, Thessaloniki, Greece

C.G. Helmis and P.T. Nastos (eds.), *Advances in Meteorology, Climatology and Atmospheric Physics*, Springer Atmospheric Sciences,
DOI 10.1007/978-3-642-29172-2_152,

scattering of air molecules, aerosols and clouds (Iqbal 1983). The amount of reflected solar radiation from the ground depends on surface, topography, solar zenith angle (SZA) and wavelength and may be highly variable in space and time (Degunther et al. 1998). The most extreme local albedo heterogeneities are found in polar coastal regions, where the low albedo of the ocean borders directly on the high albedo of snow covered land, creating a high albedo step transition. The arctic coast is thus an ideal test setting for studying the manifold impacts of albedo on the solar global irradiance. It has been shown from broadband measurements that ultraviolet (UV) irradiance can be considerably enhanced over snow covered terrain (Smolskaia et al. 1999; Mayer and Degünther 2000).

2 Methodology

Spectral measurements of the global irradiance were made during a 3-week field campaign around Ny Alesund on Svalbard in the spring 2009. Three diode array (DA) spectroradiometer systems (Kreuter and Blumthaler 2009) and a scanning grating spectroradiometer (Grobner et al. 2010) were used. All input optics had the same type of cosine-weighting diffusers. Quasi-synchronous spectra in the UV–visible (UV–VIS) spectral range were recorded every 5 min. The spectroradiometers were deployed at three sites, spatially distributed roughly along the direction of the albedo gradient, with increasing distance from the coast line towards the snow covered land with a horizontal distance of about 20 km. The first site (MS1) was set up at the coast of the Kongsfjord and was characterised by the lowest albedo surrounding. The next site (MS2) was 12 km to the south east, in Ny Alesund, were the second DA-system was set up at the Norwegian Polar Institute (NPI). Located close by, the scanning spectroradiometer was operated by the Alfred-Wegener-Institute (AWI). The third site (MS3), 7 km further to the southeast towards the Kongsvegen glacier, constituted the highest albedo surrounding.

Our global irradiance measurements were complemented by additional instruments: an all-sky imager (digital camera with a fish eye objective) was moved between the measurement sites to capture photos of the sky and record cloud conditions. A multi-filter radiometer was used as an independent stability check of the DA spectroradiometers. The infrastructure of the international research site at Ny Alesund is well established and supplied further atmospheric data such as aerosol optical depth (AOD). Detailed ice charts showing the ice condition of the Kongsfjord was available from the Norwegian Met service. We also used the webcam-images from the Zeppellin-mountain above Ny Alesund showing the Kongsfjord.

All DA spectroradiometers were radiometrically calibrated with the same calibration lamp as the absolute reference standard. While co-located at Ny Alesund before and after field deployment, all instruments were intercompared for several

days under various sky conditions. Regular calibrations were also performed for each instrument in the field, to monitor their stability.

3 Results

We first investigate the effect of increasing albedo on the global irradiance. We look at the spectral ratio of the global irradiance at two locations with a different albedo surrounding under cloudless conditions: Site MS1, located at the ice free sea with a lower effective albedo relative to MS2, surrounded by more snow covered land. To compensate for systematic errors due to differences in the calibration and cosine response, we take relative ratios relative to a reference day, i.e. we 'normalize' the spectra of each instrument with a spectrum of a clear sky reference day with the same SZA where both instruments were collocated. Figure 1a shows the relative spectral ratios between MS2 and MS1 for two clear sky days (120 and 128) for 70° (±1°) SZA in the afternoon and morning, respectively. On day 120, the Kongsfjord was fully frozen, resulting in a lower effective albedo difference between MS1 and MS2. At MS2 the global irradiance was about 3% higher at 450 nm and 9% at 320 nm, relative to MS1.

On day 128, after a temperature increase and change of wind direction to easterlies, the Kongsfjord was rapidly cleared of ice up to about the harbour of Ny Alesund. The albedo gradient between the coastal site MS1 and MS2 was therefore increased. The measured global irradiance at the higher albedo site of MS2 was about 8% higher at 450 nm to about 14% at 320 nm relative to MS1. Ratios are only shown up to a wavelength of 450 nm, which is the limit of the scanning grating spectroradiometer. For the corresponding SZA, no data was collected at MS3 because of an operational problem. The data is in good agreement with a 1D radiative transfer model, libRadtran (Mayer and Kylling 2005), using an effective (homogeneous) albedo at each site, with a difference of 0.2 and 0.3 for day 120 and day 128, respectively. The spectral increase of the albedo effect is associated with an increased scattering rate of the air molecules for smaller wavelengths (Rayleigh scattering). Below 320 nm ozone absorption becomes prominent and reduces the albedo effect again.

Now we extend our investigation of the albedo effect to cloudy conditions. Day 124 and 130 were fully overcast with roughly homogeneous stratus clouds. Again we consider the relative ratios of the locations MS3 and MS1. The ratio is an average of a few spectra with a range of SZA of 70°–85° and possibly slightly varying cloud thickness (the cloud cover looked constant to the human eye). We measured an increase of the global irradiance at the high albedo site MS3 of more than 25% relative to the coastal site MS1 (Fig. 1). The relative ratio is nearly independent of wavelength. The libRadtran 1D model calculation is in satisfactory agreement, assuming a reasonable cloud optical depth of 10. Under cloud cover the albedo effect is bigger than under a clear sky because the high density of water droplets (ice) in clouds backscatter light much more effectively than air molecules.

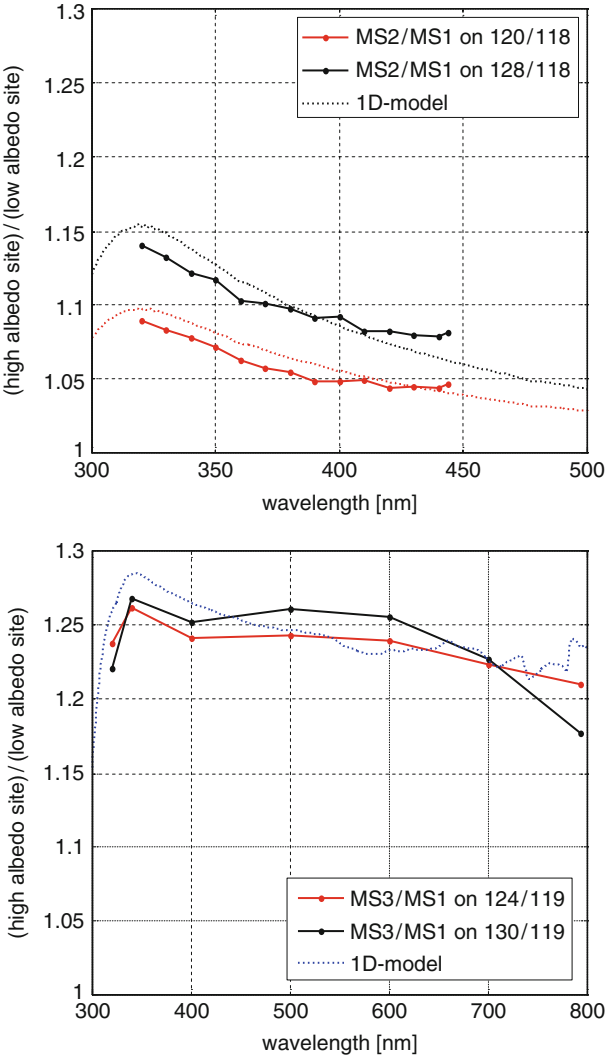

Fig. 1 Albedo effect under a clear sky (*upper*). Relative ratios of MS1 to MS2 for 2 days with a different albedo situation. The Kongsfjord was significantly cleared of ice after day 122. Albedo effect for an overcast sky (*lower*). Relative ratios of MS3 to MS1 (and the reference) for two overcast days

Scattering from the relatively large droplets is also very weakly dependent on wavelength.

While the spectral albedo effect described above is almost satisfactorily described by a simple 1D model considering only an effective, average albedo surrounding, other effects might actually arise from the complex surface distribution. On clear sky days we have noted an asymmetry in the daily variation,

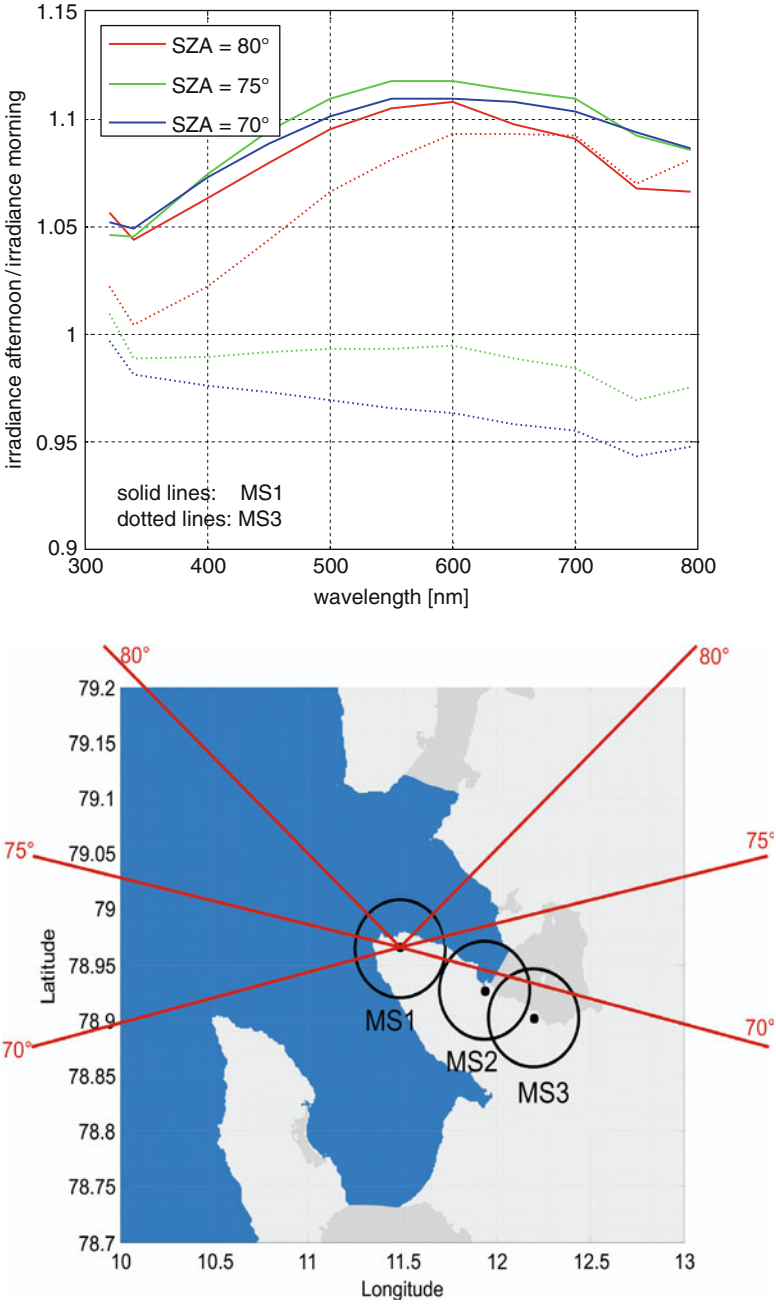

Fig. 2 Ratios of global irradiance spectra for clear sky conditions for the same solar zenith angle but different solar azimuth angle (morning/afternoon), showing a diurnal asymmetry (*upper*). Locations of the three measurement sites (*lower*). *Circles* have a 5 km radius and help visualize the effective albedo of each site (the *sketch* is representing conditions after day 122, when the fjord was cleared of ice). *Red lines* indicate solar azimuth angles for solar zenith angles of 70°, 75° and 80°

a systematic difference between the global irradiances measured at the same SZA in the morning and in the afternoon. The asymmetry is spectrally dependent and peaks at around 11% for 600 nm (Fig. 2). Furthermore, the spectral ratios depend on the SZA and location. Since the ratios are from spectra of the same instrument operating under constant conditions, calibration and cosine errors are highly unlikely to cause this effect. Azimuth errors of the global optics can also largely be excluded, since each input optics was characterized in the laboratory before the campaign and azimuth errors were below 2%. Atmospheric conditions were largely constant on day 120 and AOD was very low during the entire day at around 0.1 for 500 nm.

Since we are convinced that all instrument based biases can be excluded, we propose the following scenario to understand this effect. The only relevant difference between morning and afternoon with the same SZA is the azimuth of the sun. At the coastal station in the morning, at SZA of 70° the sun's position is over the snow covered land while in the afternoon it is over the sea. Figure 2b shows the geography with respect to the sun. When the sun is over the ocean, a pronounced sun glint was observed by eye on clear sky days from the site MS1. This specular reflection of the sun was also clearly visible on the photos from Zeppellin mountain overlooking the Kongfjord. It is well known that water is a non-Lambertian surface and a bidirectional reflectance distribution function (BRDF) should be considered (Cox and Munk 1954). The reflected solar radiation is then directed towards the part of the sky with underlying high albedo and could enhance the global irradiance in the afternoon relative to the morning. At MS3 close to the glaciers at 70° SZA the sun is over the snow both, in the morning and in the afternoon, and no difference in the global irradiance was detected. At MS3 the sun was over the water only for SZA around 80° in the afternoon when the ratio was also increased. Spectra measured at MS2 showed a similar behaviour.

First preliminary calculations have been performed with the 3D radiative transfer model MYSTIC (Mayer 2009). These first results confirm at least qualitatively that the albedo distribution in combination with the BRDF of water could cause such an effect. More detailed model studies are required and details will be published in another article.

4 Conclusions

We have presented spectral global irradiance data in the UV–VIS spectral range, measured in a campaign in the arctic coastal region on Svalbard. The area has a prominent albedo gradient from the low albedo ocean to the high albedo snow-covered land. Data were collected at three sites with increasing albedo to investigate the albedo effect on solar irradiance. The measured global irradiance at 320 nm in the UV was increased by up to 15% at the high albedo site under a clear sky. For a fully overcast sky, global irradiance in the UV was increased by up to 30%. The

albedo effect agrees quantitatively with a 1D radiative transfer model calculation, considering effective albedo only.

On clear sky days our global irradiance spectra show a diurnal asymmetry. As the asymmetry depends on the measurement location, we attribute this effect to the geographical asymmetry of water and snow distribution in combination with the non-Lambertian (BRDF) reflection of water, the so-called sun glint. This situation poses a challenging test case for 3D radiative transfer modelling to adequately account for inhomogeneous albedo and topography. For a final verification of this effect more detailed 3D model calculation using the MYSTIC code will be performed in the future

Acknowledgments The campaign was funded by ARCFAC project ID32. We thank S. Wuttke and the AWI for supplying the AWI UV-Data. We also thank B. Mayer and R. Buras for valuable discussions of 3D effects and first MYSTIC calculations.

References

Cox C, Munk W (1954) Statistics of the sea surface derived from sun glitter. J Mar Res 13:198–227

Degunther M, Meerkotter R, Albold A, Seckmeyer G (1998) Case study on the influence of inhomogeneous surface albedo on UV irradiance. Geophys Res Lett 25(19):3587–3590. doi:10.1029/98GL52785

Grobner J, Hulsen G, Wuttke S et al (2010) Quality assurance of solar UV irradiance in the Arctic. Photochem Photobiol Sci 9(3):384–391. doi:10.1039/B9 pp 00170k

Iqbal M (1983) An introduction to solar radiation. Academic Press, Toronto

Kreuter A, Blumthaler M (2009) Stray light correction for solar measurements using array spectrometers. Rev Sci Instrum 80(9):096108. doi:10.1063/1.3233897

Mayer B (2009) Radiative transfer in the cloudy atmosphere. EPJ Web Conf 1:75–99

Mayer B, Degünther M (2000) Comment on "Measurements of erythemal irradiance near Davis Station, Antarctica: effect of inhomogeneous surface albedo". Geophys Res Lett 27 (21):3489–3490. doi:10.1029/1999gl011171

Mayer B, Kylling A (2005) Technical note: the libRadtran software package for radiative transfer calculations – description and examples of use. Atmos Chem Phys 5:1855–1877. doi:10.5194/acp-5-1855-2005

Smolskaia I, Nunez M, Michael K (1999) Measurements of erythemal irradiance near Davis Station, Antarctica: effect of inhomogeneous surface albedo. Geophys Res Lett 26 (10):1381–1384. doi:10.1029/1999gl900190

The Impact of Wind Conditions on Particle Mass Concentrations in Athens, Greece

M. Lianou, I.G. Kavouras, T. Kopania, and A. Kotronarou

Abstract The aim of this study was to identify and quantify the effect of wind conditions (direction and speed) on the levels and variation of particulate matter. Daily PM_{10} and $PM_{2.5}$ samples were collected for 26 months (from October 2002 to December 2004) in an urban background site in Athens urban area, Greece. Harvard impactors were used to collect atmospheric particles on 37-mm Teflon filters. Particle mass was determined using analytical microbalance with precision of 1 μg. Meteorological data were obtained by the National Observatory of Athens station at Thissio. The relationships between PM_{10}, $PM_{2.5}$, $PM_{10-2.5}$ and wind conditions were analyzed using multivariate linear regression of PM concentrations against categorized wind conditions (direction and speed) for the non-rainy days during the study period. Significant fractions of PM_{10} and $PM_{2.5}$ mass concentrations were associated with low wind conditions blowing from south. Moderate correlations were observed between PM_{10} (and $PM_{2.5}$), and higher wind speeds. Conversely, coarse particles were poorly related to wind conditions although, they represent the majority of PM_{10} mass, indicating the possible contribution of non-wind related sources.

M. Lianou (✉) • T. Kopania • A. Kotronarou
Institute for Environmental Research and Sustainable Development, National Observatory of Athens, I. Metaxa & Vas. Pavlou, P. Penteli, Athens GR-152 36, Greece
e-mail: mlianou@meteo.noa.gr

I.G. Kavouras
Department of Environmental and Occupational Health, Fay W. Boozman College of Public Health, University of Arkansas for Medical Sciences, Little Rock, AR, USA

C.G. Helmis and P.T. Nastos (eds.), *Advances in Meteorology, Climatology and Atmospheric Physics*, Springer Atmospheric Sciences,
DOI 10.1007/978-3-642-29172-2_153,

1 Introduction

Winds have an important dual effect on particulate matter (PM) mass concentrations. Strong winds result in the dilution of air pollution and the cleaning of the lower troposphere (Lianou et al. 2004). They may also trigger resuspension of particles by wind erosion or abrasion from loose surfaces. Calm conditions usually favour the accumulation of air pollution. Athens is a large urban area with frequent air pollution events. Vehicular exhausts are considered as the main source of atmospheric particulate matter in the city (Lalas et al. 1982). Major industrial activities are located in the Thriasion pedion which is southwest of Athens. Manufacturing and shipping emissions are present in the harbor of Piraeus (south of Athens). Athens' topography (surrounded by mountains and an open alley to Saronic gulf to the south) induces the mixing and accumulation of particles on a daily basis, a phenomenon that is further enhanced by the air/sea breeze.

Here, we present the relationships between wind conditions (direction and speed) and PM_{10}, $PM_{2.5}$ and coarse particle mass levels using an empirical, semi-quantitative approach. The approach utilizes a multivariate linear regression model to extract the associations between PM levels and aggregated categorized wind conditions. To consider the non-linear relationship between PM concentrations and wind speed, wind conditions were aggregated into pre-defined bins. Ideally, wind speed bins would be as narrow as possible to fully represent the non-linearity. However, this analysis relies heavily on statistical regression and if bins are made too narrow (e.g. 1 m/s increments), then obtaining statistically significant regression results would not be possible (Kavouras et al. 2007). This analysis has been successfully used to estimate the fractional contribution of local PM sources in 70 background sites in the United States (Kavouras et al. 2009).

2 Data and Methodology

PM_{10} and $PM_{2.5}$ mass concentrations measured in an ambient fixed site conjointly with surface meteorological databases were analyzed to identify relationships between wind conditions (wind direction and speed) and particle mass in the greater Athens area. Twenty-four hours aerosol samples (noon to noon) were collected with Harvard impactors (Marple et al. 1987) from October 2002 to December 2004 in an urban background site in Athens (Lat.: 37° 59′ N, Long.: 23° 46′ E, Elev.: 155 m above MSL) (Lianou et al. 2007). Particle mass was determined by gravimetric analysis using an MX-5 analytical microbalance with a precision of 1 μg (Mettler-Toledo Inc.) (Puustinnen et al. 2007). Hourly meteorological data, precipitation (in mm), wind speed (in m/s) and direction (in degrees), were obtained from National Observatory of Athens station (Lat.: 37° 58′ N, Long.: 23° 43′ E, Elev.: 107 m above MSL). Owing to the detrimental effect of precipitation on particle

mass levels, we examined all days except for days when precipitation had occurred on that day or the prior day.

Hourly wind speed data (reported in m/s) were binned into one of three categories: $0 < \text{WS1} \leq 3.5$ m/s, $3.5 < \text{WS2} \leq 7.0$ m/s and WS3 >7.0 m/s. These wind speed bins were further divided into wind direction bins, each representing 90° centered about one of the four cardinal directions. The categorized wind conditions on a specific sample day were aggregated over a 24-h period to facilitate comparison with PM measurements. The linear regression analysis was applied to predict the value of a dependent variable from the values of n independent variables. The equation used in this study to describe the relationship between measured PM mass concentration, on a given sample day at the site (PM_m, in $\mu m/m^3$, dependent variable) and wind condition variables (x_i) was:

$$PM_m = a + \sum_{i=1}^{12} b_i \cdot x_i \tag{1}$$

where b_i are the regression coefficients of the 12 wind condition variables and α is the intercept. The intercept is the average PM concentration not associated with wind conditions. Least squares variable screening methods, including stepwise forward and backward procedures, were employed to objectively determine which variables were significant using 0.05 significance level t-value criteria. The estimated particle mass concentration at site for day j (PM_j) and the associated error (E_j) were calculated as:

$$PM_j = a + \sum_{i=1}^{12} \left(b_i \cdot x_{ij}\right) \tag{2}$$

and

$$E_j = \sum_{i=1}^{12} \left(e_i \cdot x_{ij}\right) \tag{3}$$

where e_i is the standard error of b_i regression coefficients. PM_j was calculated for each day when meteorological data were available. However, when PM_j values were associated with high levels of uncertainty (PM_j-$2E_j < 0$), it was assumed that the estimated PM concentration for that day was zero.

3 Results and Discussion

Statistically significant (p value <0.05) results were observed for models for all PM fractions. The computed particle mass concentrations were associated with high levels of uncertainty ($PM_j - 2E_j < 0$) only for a few days for PM_{10} (40 days) and

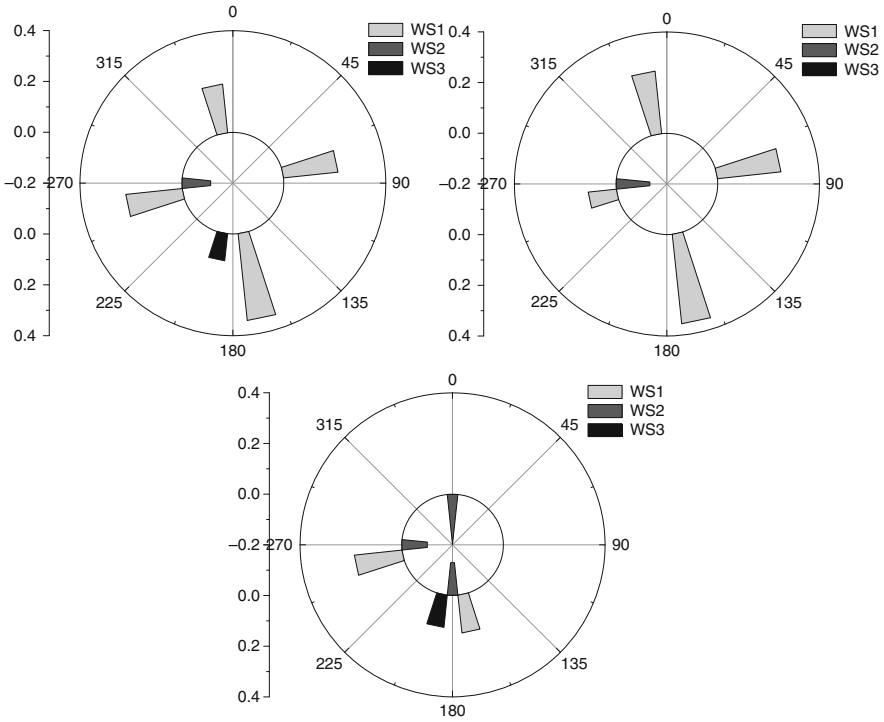

Fig. 1 Polar plots of standardized regression coefficients obtained from multivariate regression analysis of PM_{10} (*top left*), $PM_{2.5}$ (*top right*) and $PM_{10-2.5}$ (*down center*) concentrations and, wind conditions ($0 < WS1 \leq 3.5$ m/s, $3.5 < WS2 \leq 7.0$ m/s and $WS3 > 7.0$ m/s) in Athens, Greece, during 2002–2004 period

$PM_{2.5}$ (46 days) and about 385 days for coarse particles. This good correlation of PM_{10} and $PM_{2.5}$ with wind conditions, but not for $PM_{10-2.5}$, provided initial indication of the possible contribution of mechanically generated coarse particles as compared to windblown sources.

The orientation of the standardized regression coefficients for each PM fraction is illustrated in Fig. 1. Standardized coefficients provide a metric of the contribution of the individual coefficient on the estimated particle mass. The high (>0.25) standardized coefficients of regression for winds blowing from the south for both PM_{10} and $PM_{2.5}$ strongly suggested the presence of source areas located south of the site and required wind speeds, able to facilitate transport and/or resuspension.

Moderate contributions were observed for PM_{10} and $PM_{2.5}$ for low winds, blowing from the other directions. Stronger winds did not exhibit a statistically significant relationship with PM, with the exception of westerly winds. For coarse particles, moderate positive contributions were computed for southerly and westerly winds, while increased winds triggered reduced $PM_{10-2.5}$ levels.

Table 1 Mean (± propagated uncertainty) (in μg/m^3) of measured and of wind-related estimated PM_{10}, $PM_{2.5}$ and $PM_{10-2.5}$ concentrations in Athens, Greece, during 2002–2004 period

	Measured	Estimated
PM_{10}	59.2 ± 1.1	24.2 ± 0.2
$PM_{2.5}$	25.8 ± 0.6	13.1 ± 0.1
$PM_{10-2.5}$	33.5 ± 0.8	6.1 ± 0.2

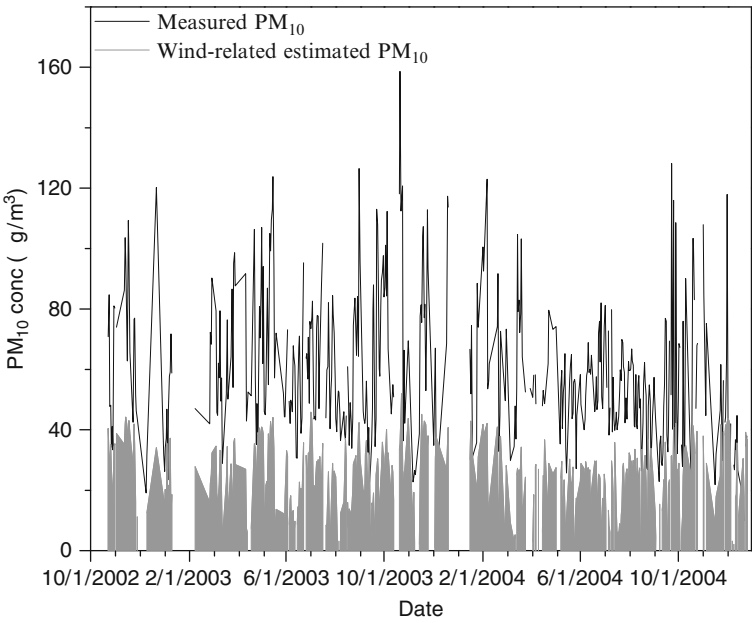

Fig. 2 Measured (*line*) and wind-related computed (*grey area*) PM_{10} mass concentrations during 2002–2004 period, in greater Athens region (Date: MM/DD/YYYY)

Table 1 show the average measured and estimated PM_{10}, $PM_{2.5}$ and $PM_{10-2.5}$ mass concentrations. Figures 2 and 3 present the daily variation of measured and wind-related estimated PM_{10} and $PM_{10-2.5}$ mass concentrations, respectively. On average, approximately 40% and 50% of measured PM_{10} and $PM_{2.5}$ mass concentrations were correlated with wind conditions, respectively. Conversely, a small fraction (18%) of coarse particles was attributed to specific wind conditions. It is noteworthy that measured coarse particles accounted for 56% of measured PM_{10} mass concentrations but, the estimated fraction of coarse particles on estimated PM_{10} mass concentration was only 25%.

The contribution of winds on particle mass levels (all fractions) appeared to be present throughout the monitoring period and followed the trends of measured particle mass levels. On a seasonal basis, no significant differences were observed for different periods of the year. The limitations of this approach include: (a) the

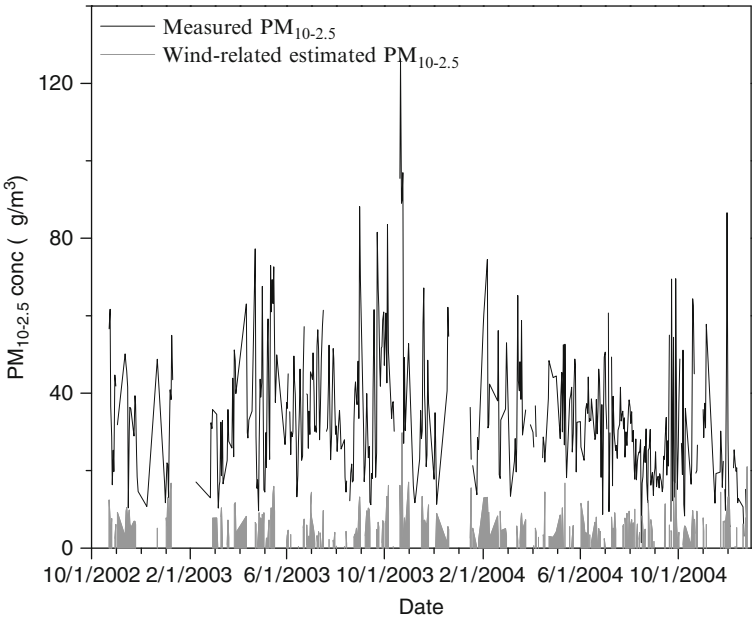

Fig. 3 Measured (*line*) and wind-related computed (*grey area*) $PM_{10-2.5}$ mass concentrations during 2002–2004 period, in greater Athens region (Date: MM/DD/YYYY)

seasonality of PM sources and (b) the relationships between synoptic scale weather systems and local wind conditions. The first assumption results in underestimated computed PM levels, while the second one leads to an overestimation of the PM levels. The impacts of these limitations are sidestepped by the rejection of the significance criteria (Kavouras et al. 2007).

4 Conclusions

Analysis of the relationships of particle mass with wind conditions showed that a large fraction of PM_{10} and $PM_{2.5}$ mass concentration was associated with low southerly winds. Stronger winds did not yield a statistically significant association (positive or negative) with PM levels. A low relationship was also observed for coarse particles, indicating the possible contribution of non-wind mechanically-generated sources.

Acknowledgments Financial support of this study was provided by the European Commission Quality of Life and Management of Living Resources program (contract: QLRT-2001000452).

References

Kavouras IG, Etyemezian V, Xu J, DuBois D, Green M, Pitchford M (2007) Assessment of the local windblown component of airborne dust in western United States. J Geophys Res Atmos 112:D08211. doi:101029/2006JD007832

Kavouras IG, Etyemezian V, DuBois D, Xu J, Pitchford M (2009) Source reconciliation of dust sources in western United States. J Geophys Res Atmos 114:D02308. doi:101029/2008JD009923

Lalas DR, Veirs VR, Karras G, Kallos G (1982) An analysis of SO_2 concentration levels in Athens, Greece. Atmos Environ 16:531–544

Lianou M, Kavouras I, Kotronarou ς (2004) Monitoring of PM_{10} and $PM_{2.5}$ levels in Athens and correlation with emission sources and meteorological conditions. In: Proceedings of the 7th conference on meteorology, climatology and atmospheric physics, Cyprus, 28–30 Sept 2004

Lianou M, Chalbot M-C, Kotronarou A et al (2007) Dependence of outdoor particulate mass and number concentrations on residential and traffic features in urban areas. J Air Waste Manag Assoc 57:1507–1517. doi:10.3155/1047-3289.57.12.1507

Marple VA, Rubow KL, Turner W, Spengler JD (1987) Low flow rate sharp cut impactors for indoor air sampling, design, and calibration. J Air Pollut Control Assoc 37:1303–1307

Puustinnen A, Hameri K, Pekkanen J et al (2007) Spatial variation of particle number and mass over four European cities. Atmos Environ 41:6622–6636

Emissions of Megacities and Their Impact on Air Quality Over Europe

A.G. Megaritis, C. Fountoukis, and S.N. Pandis

Abstract PMCAMx-2008, a three dimensional chemical transport model (CTM) was applied in Europe, to quantify the influence of emissions in European Megacities (Paris, London, Rhine-Ruhr, Po Valley) on the concentration of the major $PM_{2.5}$ components. Different emissions scenarios were applied (e.g. an "annihilation" scenario zeroing all anthropogenic emissions in Megacities), and the impact of Megacities emissions on air quality within Megacities and also in the surrounding regions was investigated. Two simulation periods were used, summer 2009 and winter 2010, to study the seasonal effect of Megacities emissions. The results show that the impact of the local emissions on the concentration of total $PM_{2.5}$ within Megacities is in the 10–60% range during wintertime depending on the chemical component and in the 5–40% range during summer. Local sources are especially important for black carbon (BC) contributing more than 40% of its concentration within Megacities, during both periods (up to 90% in Po Valley). Megacities emissions also influence the air quality of the surrounding regions within an average radius of 250 km from the Megacity.

A.G. Megaritis (✉)
Department of Chemical Engineering, University of Patras, Patras, Greece

Institute of Chemical Engineering and High Temperature Chemical Processes, Foundation for Research and Technology-Hellas (FORTH), Patras, Greece
e-mail: athmegaritis@chemeng.upatras.gr

C. Fountoukis
Institute of Chemical Engineering and High Temperature Chemical Processes, Foundation for Research and Technology-Hellas (FORTH), Patras, Greece

S.N. Pandis
Department of Chemical Engineering, University of Patras, Patras, Greece

Institute of Chemical Engineering and High Temperature Chemical Processes, Foundation for Research and Technology-Hellas (FORTH), Patras, Greece

Department of Chemical Engineering, Carnegie Mellon University, Pittsburgh, PA, USA

C.G. Helmis and P.T. Nastos (eds.), *Advances in Meteorology, Climatology and Atmospheric Physics*, Springer Atmospheric Sciences,
DOI 10.1007/978-3-642-29172-2_154,

1 Introduction

Over the past decades increasing urbanization has resulted in large urban agglomerations around the world, now hosting more than half of the world's population (UN 2007). These large urban agglomerations with more than ten million inhabitants, also known as Megacities (Gurjar and Lelieveld 2005) are characterized by high industrial activity, energy production, and other human activities in their extended areas. Megacities are thought to be substantial sources of anthropogenic pollutants having adverse effects on human health and ecosystems.

The influence of Megacities on the surrounding environment and the regional and global air quality have gained significant attention in the last decade. Several studies have focused on different Megacities around the world to examine their impact on regional and global air quality (Guttikunda et al. 2005; de Foy et al. 2006; Gurjar et al. 2008; Mena-Carrasco et al. 2009; Emmons et al. 2010). Gaffney et al. (1999) based on measurements and modelling in Mexico City, showed that Megacities can be important pollution sources for the surrounding areas. The peroxyacetyl nitrate (PAN) produced in Megacities can contribute to regional scale ozone (O_3) and secondary aerosols during long-range transport. Guttikunda et al. (2003) carried out a study covering a period of 25 years (1975–2000) examining the contribution of Megacities to sulfur emissions and pollution in Asia. They found that although Asian megacities cover <2% of the land area they emit ~16% of the total anthropogenic sulfur in Asia. Butler and Lawrence (2009) reported small impacts of Megacities on the oxidizing capacity of the atmosphere and larger on reactive nitrogen species on global scale.

In this study we apply a three-dimensional chemical transport model (CTM), PMCAMx-2008, in Europe in order to quantify how the European Megacities (Paris, London, Rhine-Ruhr, Po Valley) influence the air quality within Megacities and also in the surrounding regions. Two simulation periods were used, summer 2009 and winter 2010 to study the seasonal effect of Megacities emissions.

2 The PMCAMx-2008 CTM

2.1 Model Description

PMCAMx-2008 (Murphy and Pandis 2009; Tsimpidi et al. 2010; Karydis et al. 2010) uses the framework of the CAMx air quality model (Environ 2003) which simulates the processes of horizontal and vertical advection, horizontal and vertical dispersion, wet and dry deposition, and gas-phase chemistry. The gas-phase chemistry is described by the SAPRC99 mechanism (Carter 2000; Environ 2003) which includes 211 chemical reactions of 56 gases and 18 radicals. Three detailed aerosol modules are used: inorganic aerosol growth (Gaydos et al. 2003; Koo et al. 2003), aqueous phase chemistry (Fahey and Pandis 2001) and SOA formation and growth

(Koo et al. 2003). These modules employ a sectional approach that dynamically models the size evolution of each aerosol constituent across ten size sections varying from 40 nm to 40 μm.

PMCAMx-2008 includes a state-of-the-art organic aerosol module which is based on the volatility basis set framework (Donahue et al. 2006; Stanier et al. 2008). The model simulates the partitioning of primary emissions assuming primary organic aerosol to be semivolatile. Nine surrogate POA species with effective saturation concentrations at 298 K ranging from 10^{-2} to 10^{6} μg m^{-3} are used following the approach of Shrivastava et al. (2008). In addition, the model treats all organic species (primary and secondary) as chemically reactive. Chemical aging through gas-phase OH reaction of OA vapors is modeled.

2.2 Modeling Domain and Inputs

PMCAMx-2008 was applied over Europe covering a 5,400 × 5,832 km^2 region with 36 × 36 km grid resolution and 14 vertical layers covering approximately 6 km. The necessary inputs to the model include horizontal wind components, vertical diffusivity, temperature, pressure, water vapor, clouds and rainfall, all created using the meteorological model WRF (Weather Research and Forecasting) (Skamarock et al. 2005). In addition updated anthropogenic (Visschedijk et al. 2007) and biogenic (Guenther et al. 2006) gridded hourly emission fields were developed for the European domain for gases and primary particulate matter.

3 Results

We focus on the contribution that Megacities emissions, coming from anthropogenic sources, have on PM levels, within Megacities and also in the surrounding areas. For this purpose, we applied an "annihilation" scenario, reducing the emissions of Megacities by 100%, in two different simulation periods, summer 2009 and winter 2010. From the difference of the results of these simulations, we can determine the fraction of each PM component that comes from Megacities emissions and also the range of influence of the corresponding emission sources.

Figure 1 shows the fractional change of total $PM_{2.5}$ for this "annihilation" scenario of Megacities emissions. In Po Valley over 50% of total $PM_{2.5}$ originates from local sources during summer, while during winter the contribution of the local sources is even higher (up to 60%) Paris and Rhine-Ruhr emissions account for approximately 20% of total $PM_{2.5}$ within the corresponding Megacities during the summer while during winter their contribution on $PM_{2.5}$ levels is higher (30%). Local emissions in London do not seem to have a significant effect on $PM_{2.5}$, in both periods, contributing on average 6% to the $PM_{2.5}$ concentrations in London.

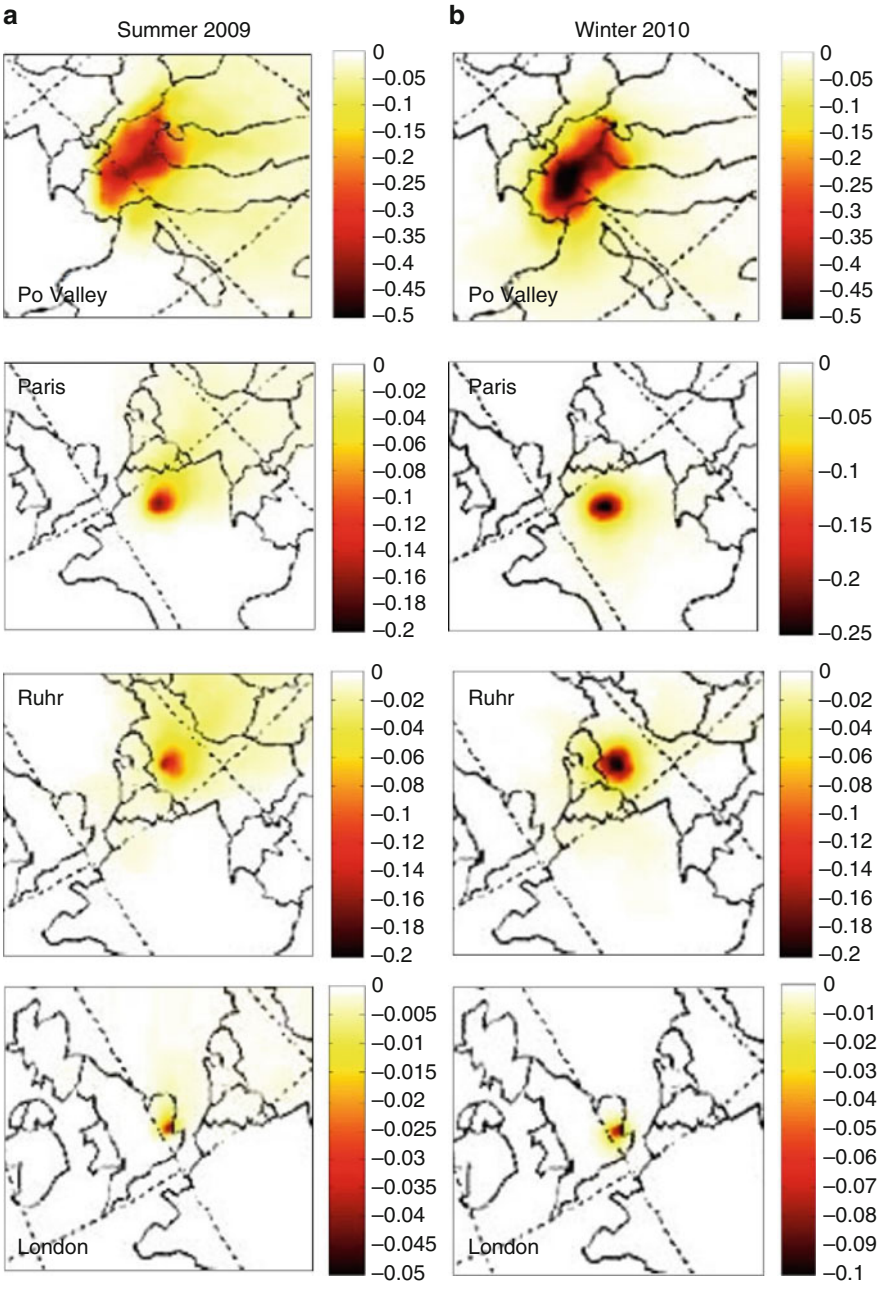

Fig. 1 Fractional change of total $PM_{2.5}$ for an "annihilation" scenario of European Megacities (Po Valley, Paris, Rhine-Ruhr, London) emissions during (**a**) summer 2009 and (**b**) winter 2010. A negative value corresponds to a decrease

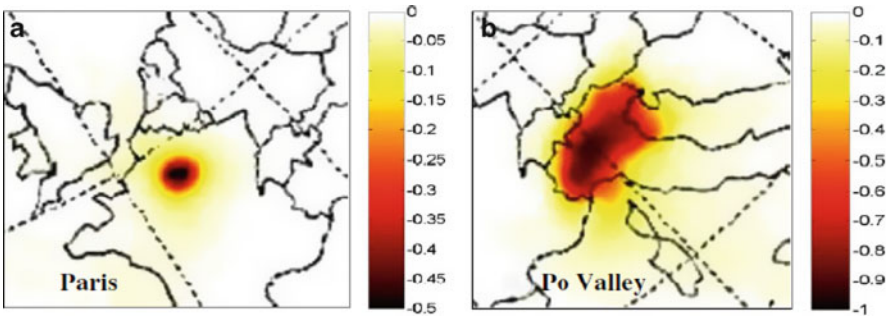

Fig. 2 Fractional change of BC in (**a**) Paris and (**b**) Po Valley after an emissions "annihilation" scenario during winter 2010. A negative value corresponds to a decrease

Megacities do not influence only their air quality, but their impacts extends to the surrounding regions up to an average distance of 200 km. Especially, Po Valley emissions could influence areas 600 km away from the source (Fig. 1).

Local emissions substantially impact BC levels in all the European Megacities. In both periods, more than 40% of the BC within Megacities is attributed to local sources. In Paris and Po Valley the contribution of local emissions to BC levels during winter, exceeds 60% and 90% respectively (Fig. 2). In addition, BC sources in Megacities could affect areas within 200 km of these urban areas.

4 Conclusions

In this study we applied a 3-D chemical transport model, PMCAMx-2008 over Europe, covering different simulation periods, to estimate how Megacities, based on an "annihilation" scenario of their anthropogenic emissions, influence the PM levels within Megacities and also to determine their contribution on the air quality in the surrounding areas.

In Po Valley, total $PM_{2.5}$ was found to be largely local in both periods (over 50% in summer and more than 60% during winter), while in Paris and Rhine-Ruhr the contribution of local sources is also significant mainly during winter. On the contrary, London emissions do not seem to have a significant effect on local $PM_{2.5}$ and long range transport of pollutants dominates.

Megacities emissions substantially impact mainly their BC levels. In both periods BC was found to originate from local sources in all the Megacities (more than 40%), while in Po Valley local sources accounted for approximately 90% of BC.

Megacities do not only influence their air quality, but they also impact areas several hundred kilometres away from the sources.

Acknowledgments This work was funded by the European Commission 7th Framework Programme project MEGAPOLI.

References

Butler TM, Lawrence MG (2009) The influence of megacities on global atmospheric chemistry: a modeling study. Environ Chem 6:219–225. doi:10.1071/EN08110

Carter WPL (2000) Programs and files implementing the SAPRC-99 mechanism and its associates emissions processing procedures for models-3 and other regional models: http://pah.cert.ucr.edu/~carter/SAPRC99.htm. Last accessed 31 Jan 2000

de Foy B, Varela JR, Molina LT, Molina MJ (2006) Rapid ventilation of the Mexico city basin and regional fate of the urban plume. Atmos Chem Phys 6:2321–2335. doi:10.5194/acp-6-2321-2006

Donahue NM, Robinson AL, Stanier CO, Pandis SN (2006) Coupled partitioning, dilution, and chemical aging of semivolatile organics. Environ Sci Technol 40:2635–2643

Emmons LK, Apel EC, Lamarque JF et al (2010) Impact of Mexico City emissions on regional air quality from MOZART-4 simulations. Atmos Chem Phys 10:6195–6212

ENVIRON (2003) User's guide to the comprehensive air quality model with extensions (CAMx), version 4.02, Report, ENVIRON International Corporation, Novato, CA. Available at: http://www.camx.com

Fahey K, Pandis SN (2001) Optimizing model performance: variable size resolution in cloud chemistry modeling. Atmos Environ 35:4471–4478. doi:10.1016/S1352-2310(01)00224-2

Gaffney JS, Marley NA, Cunningham MM, Doskey PC (1999) Measurements of peroxyacyl nitrates (PANS) in Mexico City: implications for megacity air quality impacts on regional scales. Atmos Environ 33:5003–5012

Gaydos T, Koo B, Pandis SN (2003) Development and application of an efficient moving sectional approach for the solution of the atmospheric aerosol condensation/evaporation equations. Atmos Environ 37:3303–3316. doi:10.1016/S1352-2310(03)00267-X

Guenther A, Karl T, Harvey P et al (2006) Estimates of global terrestrial isoprene emissions using MEGAN (Model of Emissions of Gases and Aerosols from Nature). Atmos Chem Phys 6:3181–3210. doi:10.5194/acp-6-3181-2006

Gurjar BR, Lelieveld J (2005) New directions: megacities and global change. Atmos Environ 39:391–393

Gurjar BR, Butler TM, Lawrence MG, Lelieveld J (2008) Evaluation of emissions and air quality in megacities. Atmos Environ 42:1593–1606. doi:10.1016/j.atmosenv.2007.10.048

Guttikunda SK, Carmichael GR, Calori G et al (2003) The contribution of megacities to regional sulfur pollution in Asia. Atmos Environ 37:11–22. doi:10.1016/S1352-2310(02)00821-X

Guttikunda SK, Tang YH, Carmichael GR et al (2005) Impacts of Asian megacity emissions on regional air quality during spring 2001. J Geophys Res. doi:10.1029/2004JD004921

Karydis VA, Tsimpidi AP, Fountoukis C et al (2010) Simulating the fine and coarse inorganic particulate matter concentrations in a polluted megacity. Atmos Environ 44:608–620

Koo B, Pandis SN, Ansari A (2003) Integrated approaches to modeling the organic and inorganic atmospheric aerosol components. Atmos Environ 37:4757–4768

Mena-Carrasco M, Carmichael GR, Campbell JE et al (2009) Assessing the regional impacts of Mexico City emissions on air quality and chemistry. Atmos Chem Phys 9:3731–3743

Murphy BN, Pandis SN (2009) Simulating the formation of semivolatile primary and secondary organic aerosol in a regional chemical transport model. Environ Sci Technol 43:4722–4728

Shrivastava MK, Lane TE, Donahue NM et al (2008) Effects of gas-particle partitioning and aging of primary emissions on urban and regional organic aerosol concentrations. J Geophys Res. doi:10.1029/2007JD009735

Skamarock WC, Klemp JB, Dudhia J, Gill DO, Barker DM, Wang W, Powers JG (2005) A description of the Advanced Research WRF version 2, NCAR technical note. http://www.mmm.ucar.edu/wrf/users/docs/arw_v2.pdf

Stanier CO, Donahue NM, Pandis SN (2008) Parameterization of secondary organic aerosol mass fraction from smog chamber data. Atmos Environ 42:2276–2299

Tsimpidi AP, Karydis VA, Zavala M et al (2010) Evaluation of the volatility basis-set approach for the simulation of organic aerosol formation in the Mexico City metropolitan area. Atmos Chem Phys 10:525–546. doi:10.5194/acp-10-525-2010

United Nations Population Fund, UNFPA, State of the world population (2007) Unleashing the potential of urban growth. http://www.unfpa.org/swp/2007/presskit/owp2007eng.pdf

Visschedijk AJH, Zandveld P, Denier van der Gon HAC (2007) TNO report 2007 A-R0233/B: a high resolution gridded European emission database for the EU integrated project GEMS. Organization for Applied Scientific Research, Netherlands

Stratospheric Responses to the 11-year Solar Cycle in MAECHAM5 with and without Ocean Coupling

S. Misios and H. Schmidt

Abstract The current generation of general circulation models (GCMs) faces major difficulties in reproducing, both qualitatively and quantitatively, the observed stratospheric response to the 11-year solar cycle. Because the majority of the previous studies used atmosphere-only GCMs without ocean coupling, it has been suggested that the inclusion of ocean dynamics may improve the simulated solar cycle signals. Our ensemble simulations with a coupled atmosphere-ocean GCM shows no indication that the ocean coupling alters significantly the solar cycle signals in the stratosphere. Although a measurable warming in the tropical oceans during solar maxima is detected in the coupled ensemble, its amplitude is too weak to affect the stratosphere. As such, the simulated temperature and zonal-mean zonal wind changes in the stratosphere are qualitatively similar both in the coupled and uncoupled ensembles. The simulated tropospheric response to the solar cycle forcing, however, differs significantly between the ensemble with and without ocean coupling.

1 Introduction

Stronger ultraviolet (UV) irradiance during the positive phase of the 11-year solar cycle produces higher ozone abundances in the upper stratosphere due to the enhanced photolysis of molecular oxygen. Higher UV and ozone levels should warm this region. Indeed, analyses of satellite observations indicated positive ozone

S. Misios (✉)
Max Planck Institute for Meteorology, Hamburg, Germany

International Max Planck Research School on Earth System Modelling, Hamburg, Germany
e-mail: stergios.misios@zmaw.de

H. Schmidt
International Max Planck Research School on Earth System Modelling, Hamburg, Germany

C.G. Helmis and P.T. Nastos (eds.), *Advances in Meteorology, Climatology and Atmospheric Physics*, Springer Atmospheric Sciences,
DOI 10.1007/978-3-642-29172-2_155,

and temperature changes on the order of 2.5% and 1°K, respectively (Randel et al. 2009; Soukharev and Hood 2006; Tourpali et al. 2007). Together with the temperature and ozone response maxima in the tropical (25°S–25°N) upper stratosphere, many studies indicated significant second response maxima in the tropical lower stratosphere (TLS). Increased ozone up to 4% and positive temperature anomalies up to 1°K have been reported in satellite datasets (Hood 2004; Soukharev and Hood 2006). Additionally, reanalysis products indicated a meridionally broad structure of positive temperature anomalies (up to 0.7°K) at 40 hPa, which takes the form of two separate lobes located at 25° latitude in each hemisphere (e.g. Crooks and Gray 2005).

Studies employing general circulation models (GCMs) with chemistry schemes to account for ozone photochemistry documented solar cycle responses in the upper stratosphere that lay within the observed range (Austin et al. 2008; Schmidt et al. 2010). Yet, with few exceptions (e.g. Schmidt et al. 2010), numerical modeling failed to reproduce the observed temperature and ozone response maxima in the TLS. Furthermore, GCMs still face difficulties in reproducing the observed solar signals during the boreal winter in the high-latitude stratosphere. These shortcomings may be related to the fact that the suggested relationship between the quasi-biennial oscillation of the equatorial stratosphere (QBO) and the 11-year solar cycle (Labitzke 2004; Matthes et al. 2010) is not successfully captured.

The majority of the aforementioned simulations were carried out with GCMs forced with climatological sea surface temperatures (SSTs) and time invariant solar spectral irradiances. Recent simulations forced with time varying spectral irradiances, observed SSTs, volcanic aerosols, and greenhouse gas concentrations, successfully produced a second response maximum in the TLS (Austin et al. 2008). This implies that the response of the TLS to the solar cycle forcing may depend on ocean coupling.

In this study, we aim to test the possible dependence of the solar signals in the stratosphere on ocean coupling. For this reason, we conduct ensemble simulations with an atmosphere GCM with and without ocean coupling. Influences from a) the increasing greenhouse gas concentrations and b) the aerosol loading from volcanic eruptions are deliberately excluded to ease interpretation.

2 Description of the Model, Experiments and Analysis Methods

We used the middle atmosphere version of the ECHAM5 (MAECHAM5) atmosphere GCM coupled to the Max Planck Institute Ocean Model (MPIOM). MAECHAM5 runs in T31L90 resolution, denoting spectral truncation at wavenumber 31 (equivalent to 3.75° × 3.75°grid) and 90 vertical levels (up to 0.01 hPa). The ocean curvilinear grid has 3° resolution at the Equator and 40 vertical levels. Greenhouse gas concentrations are fixed to values typical for the 1990s. To simulate realistic and transient solar cycle variability, spectral solar irradiance changes, conforming to those used in the CCMVal (Chemistry and

Climate Model Validation) activity, are implemented. Because MAECHAM5 is not coupled to a chemistry scheme as in the study of Austin et al. (2008), we add to the background ozone climatology the annual cycle of the solar-induced ozone anomalies taken from HAMMONIA simulations (Schmidt et al. 2010). The prescribed ozone anomalies are scaled with the daily 10.7 cm solar radio fluxes (F10.7) to introduce an 11-year variation.

An ensemble of nine realizations with MAECHAM5/MPIOM forced with solar spectral irradiance and ozone changes from 1955 to 2006 is carried out (hereafter CENS). Each ensemble member branches from different initial conditions taken from an unperturbed 140-year control simulation. A twin ensemble of nine realizations with the uncoupled MAECHAM5 is additionally conducted (hereafter AENS). The model setup is the same as in CENS except that the boundary conditions refer to SST and sea ice fraction climatologies of the control simulation.

Solar signals in every ensemble member are calculated with a multiple linear regression model that includes a first order autoregressive term (MRA-AR1). MRA-AR1, which complies with the suggestions of Crooks and Gray (2005), is applied on deseasonalized monthly temperature anomalies for every latitude and pressure level. MRA-AR1 includes four predictors: the F10.7 that describes the 11-year solar cycle variation, the Nino-3.4 index (SST anomalies averaged over 5°S–5°N and 170–120°W) that describes ENSO and two orthogonal indices to describe the QBO effects. Naturally, no ENSO predictor is used in AENS. All predictors are normalized to unit standard deviation except of F10.7, which is scaled to 100 solar flux units (sfu) to facilitate comparison with previous studies. A t-test statistic determines the statistical significance at 95%.

3 Results

In this section, the ensemble-mean annual temperature responses to the solar cycle forcing are documented first. Later, ensemble-mean zonal wind responses during the course of the boreal winter are presented. Ensemble-mean solar responses are calculated by averaging solar regression coefficients from all ensemble members.

As seen in Fig. 1, both CENS and AENS exhibit comparable temperature responses with magnitudes up to 0.5°K/100 sfu at 1 hPa. Significant changes are simulated throughout the tropical stratosphere with increasing magnitude with increasing altitude. Our model does not show a second temperature maximum in the TLS even though the prescribed ozone anomalies are characterized by a second response maximum (Schmidt et al. 2010). In both experiments, the TLS warms by about 0.15°K/100 sfu. Many individual ensemble members, however, do show well-formed temperature maxima in the TLS but we call for caution in interpreting these maxima as genuine solar signals. The collinearity between the Nino-3.4 and F10.7 predictors can considerably bias the solar cycle regression coefficients when short time series are analyzed with multiple regression models.

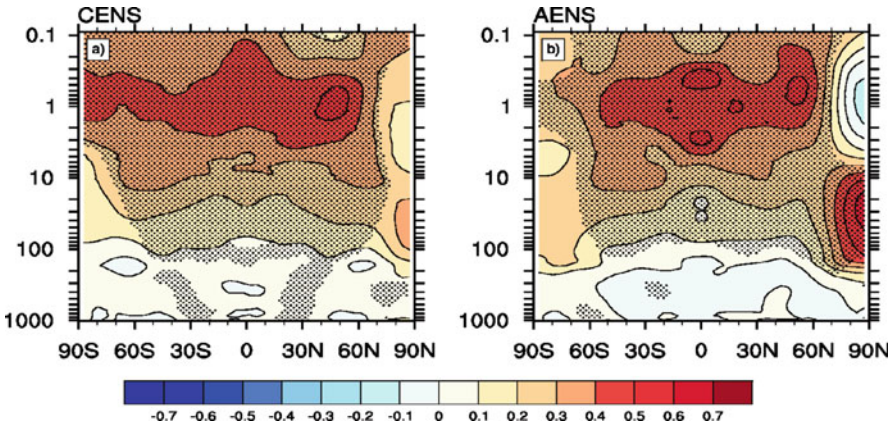

Fig. 1 Ensemble-mean regression coefficients of the annual temperature anomalies (K/100 sfu) onto F10.7 in (*left*) CENS and (*right*) AENS. Shading denotes 95% significance

At tropospheric heights, weak and generally insignificant temperature anomalies are simulated (less than ±0.1°K/100 sfu). In CENS, two significant vertical columns of positive temperature anomalies appear at mid-latitudes. In contrast, the significance is low in AENS and negative temperature anomalies are indicated. Interestingly, the multiple linear regression analysis of Haigh (2003) identified similar vertical columns of significant positive temperature anomalies at the same latitudes but with considerably higher magnitudes (~0.5°K). The much stronger response could be attributed to a contamination of solar cycle with volcanic-related signals. The latter have been deliberately excluded from our simulations.

The simulated upper stratospheric warming in previous studies ranges from 0.7 to 1.3°K, depending on magnitude of the ozone solar responses (Austin et al. 2008; Schmidt et al. 2010). In contrast, our model generates much weaker warming because the simulated solar heating rate anomalies in the stratosphere are unrealistically weak. The latter is associated to the coarse spectral resolution of the radiation scheme of MAECHAM5 (two only bands between 185 and 440 nm), resulting in approximately 45% weaker solar heating rates in the upper stratosphere compared to the heating rate changes in HAMMONIA.

Strong ocean responses to the 11-year solar cycle should influence the stratosphere. In CENS, the global-mean SST increases by merely 0.03°K/100 sfu but locally the signal is stronger. In the tropical Pacific, for instance, a basin-wide warming of 0.12°K/100 sfu is simulated. The amplitude and spatial characteristics of the tropical Pacific response are consistent with the signals detected by White et al. (1997) but oppose the La Niña-like cooling detected by van Loon et al. (2007). Apparently, the simulated SST responses in CENS are too weak to induce any measurable change in the stratosphere. Even in the tropical lower stratosphere, where the strongest sensitivity to surface changes in the tropical Pacific is anticipated, we find qualitatively and quantitatively comparable changes between the two model configurations (Fig. 1).

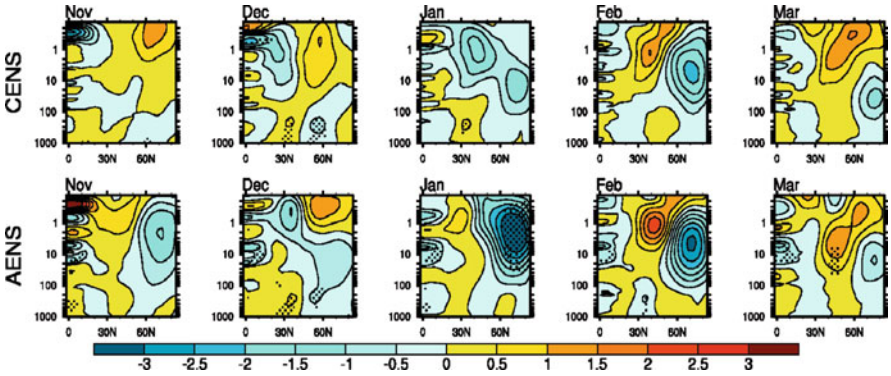

Fig. 2 November to March evolution of the ensemble-mean regression coefficients of the zonal-mean zonal wind anomalies (m/s/100 sfu) onto F10.7 in CENS and AENS

The comparison of the annual temperature changes in the stratosphere reveals negligible dependence on ocean coupling. The time evolution of the ensemble-mean zonal wind anomalies throughout the winter (November to March) further corroborates this notion (Fig. 2). The similarity between CENS and AENS, particularly in late winter (January to March) is remarkable. The polar vortex stays anomalously weak in January but anomalous westerlies moving poleward are simulated in the following months. Overall, the zonal wind changes in the high-latitude stratosphere are weak and hardly significant since the inter-annual variability in this region is much higher than the ensemble-mean solar cycle signals. Nevertheless, individual ensemble members do show much stronger positive or negative zonal wind anomalies of about 7 m/s/100 sfu (not shown).

Observation-based studies identified positive zonal wind anomalies in November that propagate poleward and downward within 3 months, resulting in negative anomalies in February and March (Kodera and Kuroda 2002). In our simulations, the westerly anomalies occur too late and their propagation is too slow. When the solar cycle UV heating in the stratosphere is deliberately amplified to match HAMMONIA heating rates (Schmidt et al. 2010), the simulated zonal wind responses are closer to those observed.

4 Conclusions

In this study, we conducted ensemble simulations with MAECHAM5 in two configurations, coupled and uncoupled to an ocean model, to inquire the possible dependence of the stratospheric response to the 11-year solar cycle on ocean coupling. We find trivial dependence given that the simulated solar cycle signals in the stratospheric temperature and zonal wind (both in annual and boreal-winter averages) do not critically depend on ocean coupling. Although a measurable

warming in the tropical oceans during solar maxima is detected in the coupled ensemble, its amplitude is too weak to affect the stratosphere. The response of the troposphere, however, is closely related to ocean changes given that in solar maxima the troposphere warms in the coupled but slightly cools in the uncoupled simulations. The latter means that ocean coupling does play an important role on the tropospheric response to the 11-year solar cycle. Our study suggests that the inclusion of ocean dynamics may not benefit general circulation models in reproducing the observed stratospheric response to the solar cycle forcing. Other factors such as the suggested non-linear relationship between the QBO and solar cycle forcing may improve the stratospheric response in future simulations.

Acknowledgments This work was funded by DFG under the ARTOS project.

References

Austin J, Tourpali K, Rozanov E, Akiyoshi H, Bekki S, Bodeker G, Brühl C, Butchart N, Chipperfield M, Deushi M, Fomichev VI, Giorgetta MA, Gray L, Kodera K, Lott F, Manzini E, Marsh D, Matthes K, Nagashima T, Shibata K, Stolarski RS, Struthers H, Tian W (2008) Coupled chemistry climate model simulations of the solar cycle in ozone and temperature. J Geophys Res Atmos 113:D11306. doi:10.1029/2007JD009391

Crooks SA, Gray LJ (2005) Characterization of the 11-year solar signal using a multiple regression analysis of the ERA-40 dataset. J Clim 18:996–1015. doi:10.1175/JCLI-3308.1

Haigh JD (2003) The effects of solar variability on the Earth's climate. Philos Trans Roy Soc A 361:95–111

Hood LL (2004) Effects of solar UV variability in the stratosphere. In: Pap J et al (eds) Solar variability and its effects of the Earth's atmosphere and climate system. American Geophysical Union, Washington, DC

Kodera K, Kuroda Y (2002) Dynamical response to the solar cycle. J Geophys Res Atmos 107:4749. doi:10.1029/2002JD002224

Labitzke K (2004) On the signal of the 11-year sunspot cycle in the stratosphere and its modulation by the quasi-biennial oscillation. J Atmos Sol Terr Phys 66:1151–1157

Matthes K, Marsh DR, Garcia RR, Kinnison DE, Sassi F, Walters S (2010) Role of the QBO in modulating the influence of the 11 year solar cycle on the atmosphere using constant forcings. J Geophys Res Atmos 115:D18110. doi:10.1029/2009JD013020

Randel WJ, Shine KP, Austin J, Barnett J, Claud C, Gillett NP, Keckhut P, Langematz U, Lin R, Long C, Mears C, Miller A, Nash J, Seidel DJ, Thompson DWJ, Wu F, Yoden S (2009) An update of observed stratospheric temperature trends. J Geophys Res Atmos 114:D02107. doi:10.1029/2008JD010421

Schmidt H, Brasseur GP, Giorgetta MA (2010) Solar cycle signal in a general circulation and chemistry model with internally generated quasi-biennial oscillation. J Geophys Res Atmos 115:D00I14. doi:10.1029/2009JD012542

Soukharev BE, Hood LL (2006) Solar cycle variation of stratospheric ozone: multiple regression analysis of long-term satellite data sets and comparisons with models. J Geophys Res Atmos 111:D20314. doi:10.1029/2006JD007107

Tourpali K, Zerefos CS, Balis DS, Bais AF (2007) The 11-year solar cycle in stratospheric ozone: comparison between Umkehr and SBUVv8 and effects on surface erythemal irradiance. J Geophys Res Atmos 112:D12306. doi:10.1029/2006JD007760

van Loon H, Meehl GA, Shea DJ (2007) Coupled air-sea response to solar forcing in the Pacific region during northern winter. J Geophys Res Atmos 112:D02108. doi:10.1029/2006JD007378
White W, Lean J, Cayan DR, Dettinger MD (1997) Response of global upper ocean temperature to changing solar irradiance. J Geophys Res Oceans 102:3255–3266

24-Hours Ahead Forecasting of PM_{10} Concentrations Using Artificial Neural Networks in the Greater Athens Area, Greece

K. Moustris, I. Larissi, P.T. Nastos, K. Koukouletsos, and A.G. Paliatsos

Abstract The study of atmospheric concentration levels at a local scale is one of the most important topics in environmental sciences. Multivariate analysis, fuzzy logic and neural networks have been introduced in forecasting procedures in order to elaborate operational techniques for level characterization of specific atmospheric pollutants at different spatial and temporal scales. Particularly, procedures based on artificial neural networks (ANNs) have been applied with success to forecast concentration levels of PM_{10}, CO and O_3. The present study deals with the development and application of ANN models as a tool to forecast daily concentration levels of PM_{10} in five different regions within the greater Athens area (GAA). Modeling was based on mean daily PM_{10} concentration, the maximum hourly NO_2 concentration, air temperature, relative humidity, wind speed and the mode daily value of wind direction from five different monitoring stations for the period 2001–2005. Model performance showed that the ANN models could successfully forecast the risk of daily PM_{10} concentration levels exceeding certain thresholds. In addition, despite the limitations of the models, the results of the study

K. Moustris (✉)
Department of Mechanical Engineering, Technological and Education Institute of Piraeus, Athens, Greece
e-mail: kmoustris@yahoo.gr; kmoustris@teipir.gr

I. Larissi
Laboratory of Environmental Technology, Electronic Computer Systems Engineering Department, Technological and Education Institute of Piraeus, Athens, Greece

P.T. Nastos
Laboratory of Climatology and Atmospheric Environment, Department of Geology and Geoenvironment, University of Athens, Athens, Greece

K. Koukouletsos • A.G. Paliatsos
General Department of Mathematics, Technological Education Institute of Piraeus, Athens, Greece

C.G. Helmis and P.T. Nastos (eds.), *Advances in Meteorology, Climatology and Atmospheric Physics*, Springer Atmospheric Sciences,
DOI 10.1007/978-3-642-29172-2_156,

demonstrated that ANN models, when adequately trained, could have a high applicability to predict the PM_{10} daily concentration 1 day ahead within the GAA.

1 Introduction

PM_{10} has been identified as one of the major air pollutants. Several epidemiological studies have demonstrated that PM_{10} are responsible for various health problems and especially with respiratory diseases (Schwartz et al. 1991; Dockery et al. 1992, 1993; Dockery and Pope 1994; Pope et al. 1995; Seaton et al. 1995; Ostro et al. 1999; Pope 2000; Grigoropoulos et al. 2008; Nastos et al. 2010).

During the last decade, many attempts have been made in order to model PM_{10} concentrations through the use of meteorological data as well as in order to predict PM_{10} concentration levels through the application of statistical methods and ANNs methodology (Perez and Reyes 2002; Hooyberghs et al. 2005; Papanastasiou et al. 2007; Shekarrizfard et al. 2011; Vlachogianni et al. 2011).

In this study, an effort was made to develop ANN models in order to predict 24-h ahead the mean daily PM_{10} concentrations in five different regions simultaneously within the GAA.

2 Data and Methodology

The city of Athens is located in an area of a complex topography within the Athens basin (~450 km^2). A detailed description of the Athens basin topography and climate is found in various publications (e.g. Larissi et al. 2010). The geography of the area does not favor the dispersion of air pollutants. The sources of atmospheric particles can be either natural or anthropogenic and car traffic is an important source in urban environments (Finlayson-Pitts and Pitts 2000).

The purpose of this study is the construction of models, using ANNs technique, which give the possibility of forecasting the mean daily value of PM_{10} for five different measuring sites of the GAA and for the next 24-h. The five examined monitoring sites belong to the monitoring network of the Hellenic Ministry of the Energy, Environment and Climatic Change (HMEECC) can be classified in two categories: The city-center station Aristotelous (ARI) and the peripheral stations Agia Paraskevi (AGP), Maroussi (MAR), Lykovrissi (LYK) and Thrakomakedones (THR). For each of the five stations hourly concentrations of ambient air pollutants, PM_{10} and NO_2 covering the period 2001–2005 as well as meteorological data concerning hourly values of the air temperature, relative humidity, wind speed, and wind direction for the period 2001–2005 have been used.

A question that always arises in prediction is what are the appropriate parameters-variables for the prognosis? For answering this question, the Stepwise Multi Linear Regression Analysis (SMLRA) was applied (Murtoniemi et al. 1994). The mean daily concentration of PM_{10} was considered as the dependent variable and the

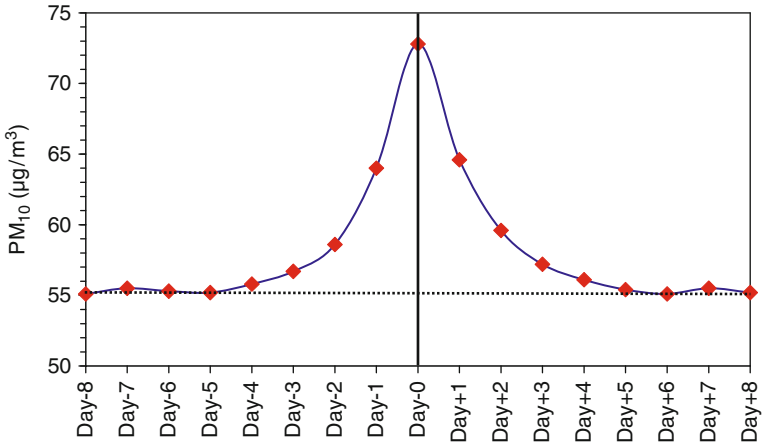

Fig. 1 PM_{10} concentration values from HMEECC monitoring network 8 days before and after the zero-day where a particulate episode occurs. Period 2001–2005

maximum hourly NO_2 concentration, the mean daily air temperature, the mean daily relative humidity, the mean daily wind speed and the mode daily wind direction, were considered as the independent variables. The SMLRA showed that the mode daily value of wind direction is not an important and appropriate variable for PM_{10} prediction.

In order to investigate how back to the history (how many days before), we have to train the ANN predictive model, daily PM_{10} concentrations during particulate episodes for the studied period, have been organized in superposed epoch analysis (SEA) illustrations and are depicted in Fig. 1 (Panofsky and Brier 1968).

The "zero" day represents the average value of PM_{10} concentrations when an episode day ($[PM_{10}] \geq 50$ μg/m^3) occurred in Volos. From Fig. 1, it is ascertained that the mean daily PM_{10} concentrations, during "zero" days, increased of about 27.7% (27.0%), in relation to the PM_{10} average magnitude 8 days before (after) the "zero" day. A clear decrease of the PM_{10} concentration after the "zero" days is obvious. Figure 1 shows that when an air pollution episode is expected, there is a significant increasing trend to the PM_{10} mean daily concentrations 3 days earlier. Furthermore, it appears that the phenomenon smoothed 3–4 days after the onset of the episode day.

After the application of both SMLRA and SEA, as input data, for the appropriate ANN model training, the number of the station (1–5), the number of the month (1–12), the mean daily PM_{10} concentration, the maximum hourly NO_2 concentration, the mean daily air temperature, the mean daily relative humidity and the mean daily wind speed from the three previous days, were used. Also, the mean daily temperature, the mean daily relative humidity and the mean daily wind speed of the next day were used as input parameters. In other words, the input layer consists of 20 processing elements, called artificial neurons (Moustris et al. 2010). There is only one hidden layer with 19 artificial

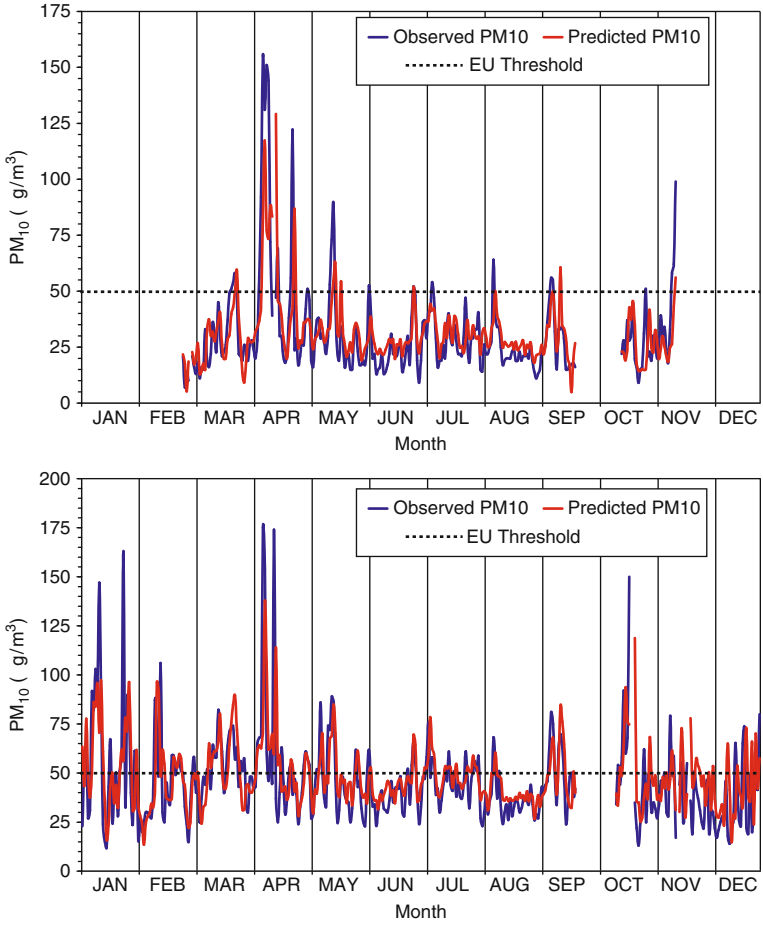

Fig. 2 The best (THR-*upper panel*) and the worst prediction (MAR-*lower panel*). Year 2005

neurons. Finally, the output layer has one artificial neuron, the mean daily PM_{10} concentration 24-h ahead (next day). The learning algorithm used in the present study was the back-propagation algorithm (Asadisaghandi and Tahmasebi 2011). The selected transfer function for both input and hidden layer was the hyperbolic tangent function (Moustris et al. 2010). The used data set was divided into two subsets. The first subset included data from the period 2001–2004 and used for the ANN model training, and the second subset included data for the year 2005 and was used for the evaluation of the forecasting ability of the developed ANN model.

Well known statistical indices such as the coefficient of determination (R^2), the index of agreement (IA), the mean bias error (MBE) and the root mean square error (RMSE) were used (Moustris et al. 2010) for the evaluation of the developed ANN forecasting model.

Table 1 Evaluation of the model forecasting ability

Station	Data completeness (%)	R^2	IA	MBE ($\mu g/m^3$)	RMSE ($\mu g/m^3$)
AGP	85.5	0.382	0.731	−0.8	16.9
ARI	82.6	0.332	0.731	−0.1	17.4
THR	81.2	0.447	0.776	+0.6	16.1
LYK	91.2	0.394	0.743	−4.0	19.9
MAR	78.1	0.284	0.697	+2.2	20.1

3 Results

Figure 2 shows, the best (upper panel) and the worst (lower panel) prediction of PM_{10} concentrations 24-h ahead. As presented in this figure, even in the case of the worst prediction MAR station (Fig. 2, right panel), the ANN model seems to have a significant ability to predict the days of exceedances according to the European Union daily threshold for the PM_{10} concentrations ($PM_{10} \leq 50\ \mu g/m^3$).

Table 1 presents the statistical indices between the observed and the predicted PM_{10} concentrations for the five examined stations and for the next 24-h, respectively. This table shows the data completeness during the examined period, and for the test year 2005 the coefficient of determination, the index of agreement, and finally, the MBE and RMSE values between the observed and predicted PM_{10} mean daily concentrations, 24-h ahead.

The values of the coefficient of determination range between 0.284 and 0.447. This means that the model is able to explain the 28.4–44.7% of the variation, respectively. The values of the IA range between 0.697 and 0.776. This means that the predictive values are close enough to the observed values that in combination to the MBE and RMSE values indicate a significant forecasting ability by the model.

4 Conclusions

In this work, ANN models developed and applied as forecasting models to predict the mean daily concentration of PM_{10}, 24-h ahead, in five different regions within the GAA. The extracted results of the performed analysis show that ANN models have a significant forecasting ability. It should be noted than by increasing the available input data and their quality (no blanks days), necessary for the model training, the application of ANN models could give more reliable forecasts for the PM_{10} concentration levels in the GAA.

References

Asadisaghandi J, Tahmasebi P (2011) Comparative evaluation of back propagation neural network learning algorithms and empirical correlations for prediction of oil PVT properties in Iran oilfields. J Petrol Sci Eng 78:464–475. doi:10.1016/j.petrol.2011.06.024

Dockery DW, Pope CA (1994) Acute respiratory effects of particulate air pollution. Annu Rev Public Health 15:107–132. doi:10.1146/annurev.publhealth.15.1.107

Dockery DW, Schwartz J, Spengler JD (1992) Air pollution and daily mortality: association with particulates and acid aerosols. Environ Res 59:362–373. doi:10.1016/S0013-9351(05)80042-8

Dockery DW, Pope CA, Xu X, Spengler JD, Ware JH, Fay ME, Ferris BG, Spizer FE (1993) An association between air pollution and mortality in six US cities. N Engl J Med 329:1735–1759

Finlayson-Pitts BJ, Pitts JN Jr (2000) Chemistry of the upper and lower atmosphere: theory, experiments and applications. Academic, San Diego, pp 608–611

Grigoropoulos KN, Nastos PT, Ferentinos G, Gialouris A, Vasiliou T, Mavroidakos J, Avgeri D, Kalabokis V, Saratsiotis D (2008) Spatial distribution of PM1 and sinus arrhythmias in Athens, Greece. Fresen Environ Bull 17:1426–1431

Hooyberghs J, Mensink C, Dumont G, Fierens F, Brasseur O (2005) A neural network forecast for daily average PM10 concentrations in Belgium. Atmos Environ 39:3279–3289

Larissi IK, Koukouletsos KV, Moustris KP, Antoniou A, Paliatsos AG (2010) PM_{10} concentrations levels in the greater Athens area, Greece. Fresen Environ Bull 19:226–231

Moustris KP, Ziomas IC, Paliatsos AG (2010) 3-Day-ahead forecasting of regional pollution index for the pollutants NO2, CO, SO2, and O3 using artificial neural networks in Athens, Greece. Water Air Soil Poll 209:29–43. doi:10.1007/s11270-009-0179-5

Murtoniemi E, Yliruusi J, Kinnunen P (1994) The advantages by the use of neural networks in modelling the fluidized bed granulation process. Int J Pharm 108:155–164. doi:10.1016/0378-5173(94)90327-1

Nastos PT, Paliatsos AG, Anthracopoulos MB, Roma ES, Priftis KN (2010) Outdoor particulate matter and childhood asthma admissions in Athens Greece: a time-series study. Environ Health 9:45. doi:10.1186/1476-069X-9-45

Ostro BD, Eskeland GS, Sanchez JM, Feyzioglou T (1999) Air pollution and health effects: a study of medical visits among children in Santiago, Chile. Environ Health Perspect 107:69–73. doi:10.1289/ehp.9910769

Panofsky HA, Brier GW (1968) Some applications of statistics to meteorology. University Park, Pennsylvania, pp 159–161

Papanastasiou DK, Melas D, Kioutsioukis I (2007) Development and assessment of neural network and multiple regression models in order to predict PM10 levels in a medium-sized Mediterranean city. Water Air Soil Poll 182:325–334. doi:10.1007/s11270-007-9341-0

Perez P, Reyes J (2002) Prediction of maximum of 24-h average of PM10 concentrations 30 h in advance in Santiago, Chile. Atmos Environ 36:4555–4561

Pope CA III (2000) Epidemiology of fine particulate air pollution and human health: biological mechanisms and who's at risk? Environ Health Perspect 108:713–723

Pope CA, Thun MJ, Namboodri MM, Dockery DW, Evans JS, Speizer FE, Heath CW Jr (1995) Particulate air pollution as a predictor of mortality in a prospective study of U.S. adults. Am J Respir Crit Care Med 151:669–674

Schwartz J, Slater D, Larson T, Pierson WE, Koeng JQ (1991) Particulate air pollution and hospital emergency room visits for asthma in Seattle. Am J Respir Crit Med 147:826–831

Seaton A, MacNee W, Donaldson K, Godden D (1995) Particulate air pollution and acute health effects. Lancet 345:176–178. doi:10.1016/S0140-6736(95)90173-6

Shekarrizfard M, Karimi-Jashni A, Hadad K (2011) Wavelet transform-based artificial neural networks (WT-ANN) in PM_{10} pollution level estimation, based on circular variables. Environ Sci Pollut Res Int 19:256–268. doi:10.1007/s11356-011-0554-9

Vlachogianni A, Kassomenos P, Karppinen A, Karakitsios S, Kukkonen J (2011) Evaluation of a multiple regression model for the forecasting of the concentrations of NO_x and PM_{10} in Athens and Helsinki. Sci Total Environ 409:1559–1571. doi:10.1016/j.scitotenv.2010.12.040

Aerosols Optical Properties and Their Effect on the UV Solar Irradiance at Uccle, Belgium

E. Nikitidou, V. De Bock, H. De Backer, and A. Kazantzidis

Abstract This study investigates the influences of aerosols optical properties on the UV solar irradiance reaching the ground. It does so using ground-based spectroradiometric measurements taken over the Uccle atmosphere during July 2006 to May 2010. Calculations with the radiative transfer code UVSPEC (LibRadtran package) are used in order to estimate the aerosol effect in the UV and the single scattering albedo. The results are compared with those from a collocated Cimel instrument, part of the AErosol RObotic NETwork (AERONET). The accuracy of the single scattering albedo estimation depends on the aerosol optical depth (AOD) and the solar zenith angle (SZA) at the time of the measurement and is higher for high AOD.

1 Introduction

Aerosols are tiny particles suspended in the atmosphere that may be of natural (desert dust, sea salt, volcanic aerosols) or anthropogenic origin (black carbon, sulphate). They affect the incoming solar radiation through scattering and absorption (direct effect) and change clouds reflectivity and lifetime (indirect effect). Their radiative forcing (RF) has a very high uncertainty (IPCC 2007). Aerosols effects incurring modifications on the incoming solar radiation are therefore of extreme importance to scientific research, mainly at the spectral UV portion of the spectrum (Kazadzis et al. 2009) where its variability may incur destructive effects in living organisms and atmospheric chemistry. Measuring the aerosol optical

E. Nikitidou (✉) • A. Kazantzidis
Laboratory of Atmospheric Physics, Physics Department, University of Patras, Patras GR-26500, Greece
e-mail: pnikit@upatras.gr

V. De Bock • H. De Backer
Royal Meteorological Institute of Belgium, Brussels, Belgium

C.G. Helmis and P.T. Nastos (eds.), *Advances in Meteorology, Climatology and Atmospheric Physics*, Springer Atmospheric Sciences,
DOI 10.1007/978-3-642-29172-2_157,

properties in the UV is more difficult that in the visible, due to the high dependence of the radiation to ozone variations. A key parameter in the interaction with radiation is the single scattering albedo (SSA), which determines the scattering and absorbing efficiency of aerosols. Retrieval of SSA in the UV is achieved with theoretically estimated irradiances under cloudless conditions and measurements of UV and AOD with an overall uncertainty of ±3–5% (Bais et al. 2005). The accuracy in the retrieved SSA depends on the AOD and the SZA and decreases with increasing AOD and SZA.

2 Data and Methodology

Measurements in the UV are used from the Brewer#178 instrument in Uccle, which is a southern suburb in Brussels, Belgium. The instrument is situated 100 m above sea level and the site is influenced by urban and continental aerosols and sea salt from the North Sea (De Bock et al. 2010). Measurements of UV, AOD and ozone are used along with theoretical calculations in order to derive the aerosols radiative forcing in the UV and SSA. The results are compared with data from a collocated Cimel instrument, part of the AEronet RObotic NETwork (AERONET).

2.1 Data

Ozone measurements were provided from Brewer#178, along with UV measurements in the range 290–363 nm with a step of 0.05 nm. The Langley Plot Method was used to retrieve the AOD from the instrument's direct sun observations at five wavelengths (306.3, 310.1, 313.5, 316.8 and 320.1) (Cheymol and De Backer 2003). The UV measurements are corrected for the cosine error. Comparison is made with AERONET data from the collocated Cimel. For that purpose the AERONET AOD at 340 nm and Angstrom exponent (340–400 nm) are used to estimate the AOD at 320 nm and compare with Brewer's 320.1 nm. The AERONET SSA at 440 nm is used to qualitatively compare with the retrieved SSA from the Brewer measurements. To avoid cloud contamination only quasi-simultaneous measurements from the two instruments are processed (maximum time difference of 3 min), based on the fact that the Cimel data are already cloud-screened. As a result the time period examined is from July 2006 until May 2010.

2.2 Methodology

The aerosol radiative forcing efficiency (RFE) is estimated in the 300–360 nm range. For this purpose theoretical calculations with the UVspec code of the

LibRadtran radiative transfer model (Mayer and Kylling 2005) are performed in order to derive the irradiance on the ground in the 300–360 nm range under cloud and aerosol free conditions. The model global (direct + diffuse) irradiances on the ground are estimated with a 0.05 nm step for the solar zenith angle and ozone conditions of the Brewer measurements and the integral of 300–360 nm is calculated. The percent RFE is given as

$$RFE(\%) = \left(\frac{I_{measured} - I_{\mathrm{mod}eled}}{I_{\mathrm{mod}eled}} \right) * 100 \quad (1)$$

per unit of AOD, where $I_{measured}$ and $I_{modeled}$ are the integrals of 300–360 nm range of the Brewer and modeled irradiances respectively.

Another set of theoretical calculations is performed with UVspec in order to derive the global irradiances in the 300–360 nm range that match the solar SZA, ozone and AOD conditions of the measurements. The irradiances are calculated for various SSA values and the accepted SSA values are those for which the measured and modeled irradiances agree to a percent better than 1. SSA values are derived at those wavelengths that are closer to the AOD measurements, that is 306.5, 310, 313.5, 316.5 and 320 nm.

3 Results

Comparison is made between the AOD of Brewer and Cimel at 320 nm, as can be seen in Fig. 1. There is very good agreement between the two datasets with the linear regression having an intercept of −0.0023 and a slope of 1.0008. The correlation coefficient is high, equal to 0.97 (95% confidence level).

The percent RF at the 300–360 nm wavelength range is shown in Fig. 2 versus the AOD of Brewer at 320 nm. The results have been grouped depending on the SZA at the time of the measurement, from 30 ± 2° to 60 ± 2°. The RFE% is given by the slope of the linear regression and ranges from −26.26% to −22.89% per unit of AOD.

The SSA has been estimated at 306.5, 310, 313.5, 316.5 and 320 nm. In Fig. 3, the monthly mean values of SSA from Brewer and Cimel with their standard deviations have been estimated, using only common measurements with AOD ≥ 0.4. Also the difference in the AOD from the two instruments was set to be lower than 5% so that any differences in the SSA values will be due to the different methodologies. The estimated monthly values of SSA from Brewer seem to better agree with Cimel data as the wavelength increases. The same is true for the corresponding standard deviations. The shorter UV wavelengths are subject to greater influence from uncertainties in the ozone measurements. At 320 nm, monthly mean Brewer SSA is in good agreement with Cimel, except in October where only three to four measurements were available. Estimated SSA monthly mean values at 320 nm range from 0.84 in October to 0.97 in August when they also have the lowest standard deviation. Lower SSA values are observed at 306.5 nm.

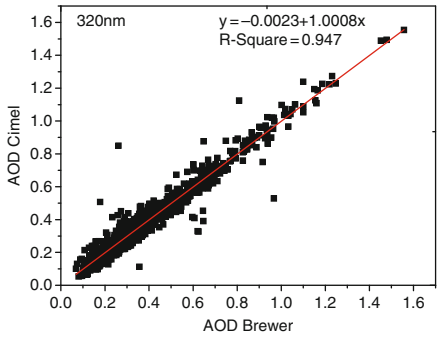

Fig. 1 Comparison of AOD from Cimel and Brewer#178 at 320 nm

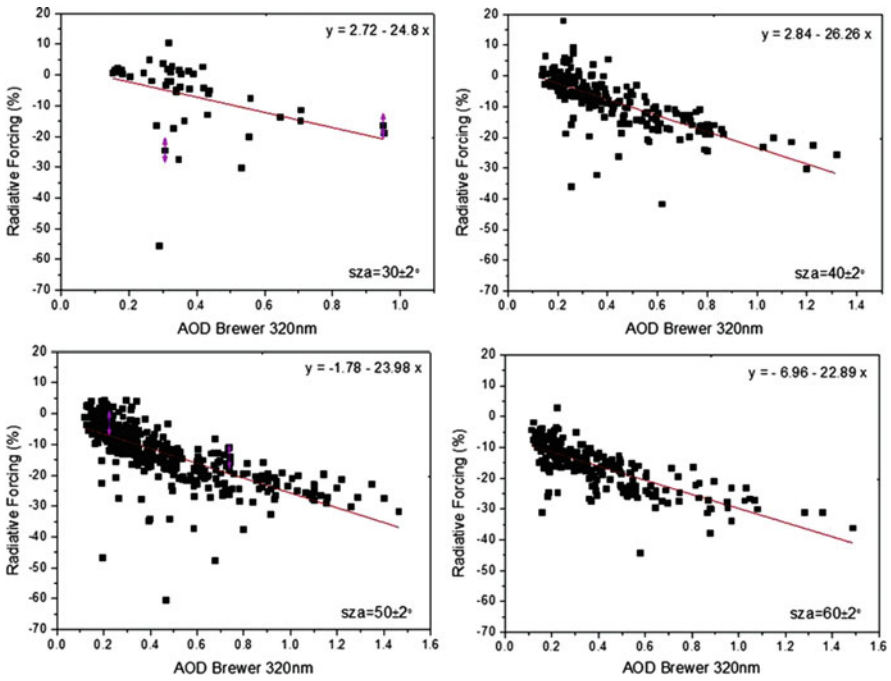

Fig. 2 Aerosols RFE% at the 300–360 nm wavelength range depending on the SZA range

This could be due to the higher uncertainties of the measurements at low UV wavelengths that introduce uncertainties to the retrieval method as well and partly due to the type of aerosols at Uccle that present higher absorption at lower wavelengths.

An example of the uncertainty of the SSA retrieval in low AOD conditions is provided in Fig. 4, where 2 days are presented (27/9/2009 and 17/4/2010) with high

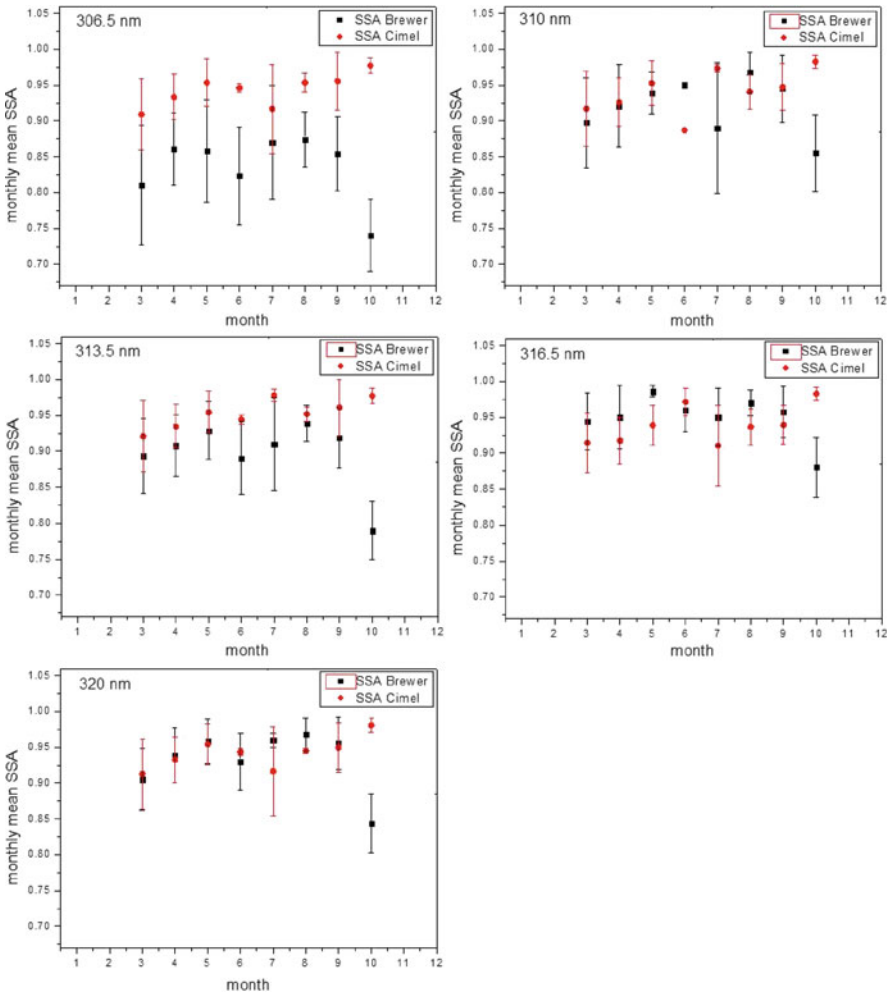

Fig. 3 Monthly mean values of SSA from Brewer at 306.5, 310, 313.5, 316.5 and 320 nm and Cimel at 440 nm and their standard deviations

and low aerosol load respectively. In the latter case there are higher uncertainties with the method providing up to three possible SSA values at 320 nm.

4 Conclusions

Aerosol properties from the Brewer#178 instrument at Uccle, Belgium have been used to study the effect of aerosols in the UV radiation. The AOD from Brewer at 320 nm is in high correlation (0.97) with the corresponding one from the collocated Cimel. The aerosol RFE% has been calculated in the 300–360 nm wavelength range

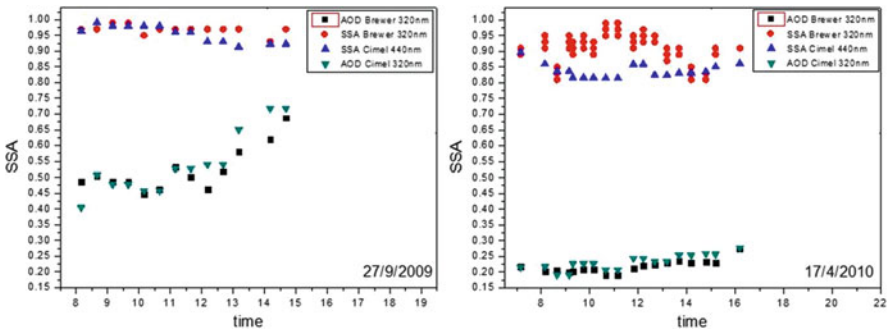

Fig. 4 SSA estimations from the Brewer method for 2 days with high (27/9/2009) and low (17/4/2010) aerosol load

with the UVspec code and ranges from −26.26% to −22.89% per unit of AOD, depending on the SZA at the time of the measurement. The SSA has been estimated at five wavelengths in the UV (306.5, 310, 313.5, 316.5, 320 nm) and when compared to Cimel data, the agreement is better as the wavelength increases. At 320 nm the estimated SSA values range from 0.84 in October to 0.97 in August. The uncertainty in the SSA estimations decreases as the AOD increases.

Acknowledgments The authors would like to thank the principal investigator of the AERONET site in Brussels, Christian Hermans, for providing the data and the LibRadtran team (www.libradtran.org) for providing the model algorithm.

References

Bais AF, Kazantzidis A, Kazadzis S, Balis DS, Zerefos CS, Meleti C (2005) Deriving an effective aerosol single scattering albedo from spectral surface UV irradiance measurements. Atmos Environ 39:1093–1102. doi:10.1016/j.atmosenv.2004.09.080

Cheymol A, De Backer H (2003) Retrieval of the aerosol optical depth in the UV-B at Uccle from Brewer ozone measurements over a long time period 1984–2002. J Geophys Res 108 (D24):4800. doi:10.1029/2003JD003758

De Bock V, De Backer H, Mangold A, Delcloo A (2010) Aerosol optical depth measurements at 340 nm with a Brewer spectrophotometer and comparison with cimel sunphotometer observations at Uccle, Belgium. Atmos Meas Tech 3:1577–1588. doi:10.5194/amt-3-1577-2010

IPCC (2007) Intergovernmental panel on climate change: climate change 2007. Working group I report: the physical science basis. Summary for Policymakers, Paris

Kazadzis S, Kouremeti N, Bais A, Kazantzidis A, Meleti C (2009) Aerosol forcing efficiency in the UVA region from spectral solar irradiance measurements at an urban environment. Ann Geophys 27:2515–2522

Mayer M, Kylling A (2005) Technical note: the libRadtran software package for radiative transfer calculations: descriptions and examples of use. Atmos Chem Phys 5:1855–1877. doi:1680-7324/acp/2005-5-1855

Study of Air Pollution with the Use of MODIS Data, LIDAR and Sun Photometers in Cyprus

A. Nisantzi, D.G. Hadjimitsis, E. Akylas, A. Agapiou, M. Panayiotou, S. Michaelides, F. Tymvios, D. Charalambous, S. Athanasatos, A. Retalis, D. Paronis, S. Perdikou, P. Koutrakis, J.S. Evans, and S. Achilleos

Abstract In the frame of 'AIRSPACE' project, ground-based measurements were conducted in the four main cities of Cyprus. Limassol, comprises the main test site as Lidar and CIMEL sun photometer (NASA/AERONET network) are located at the premises of CUT, while the other cities (Nicosia, Larnaca and Paphos) are used as validation sites. During data collection campaign, measurements from handheld sun-photometers, DustTrak (PM_{10}), Lidar and meteorological stations were used to extract an algorithm for relating satellite MODIS AOD retrievals and ground-based PM_{10} data for different types of geographical areas. For this purpose, the vertical distribution of atmosphere after the processing of daily lidar signals and meteorological parameters such as relative humidity, wind speed and direction were used.

1 Introduction

Over the last decades a great number of studies (Nicolantonio and Cacciari 2011; Boyouk et al. 2010) have focused their interest on remote sensing for monitoring air pollution. Aerosol Optical Depth (AOD) is defined as a measure of the extinction of

A. Nisantzi (✉) • D.G. Hadjimitsis • E. Akylas • A. Agapiou • M. Panayiotou
Cyprus University of Technology, Limassol 3036, Cyprus
e-mail: argyro.nisantzi@cut.ac.cy

S. Michaelides • F. Tymvios • D. Charalambous • S. Athanasatos
Cyprus Meteorological Service, Nicosia, Cyprus

A. Retalis • D. Paronis
National Observatory of Athens, Athens, Greece

S. Perdikou
Frederick Research Center, Nicosia, Cyprus

P. Koutrakis • J.S. Evans • S. Achilleos
Harvard University, Boston, MA, USA

C.G. Helmis and P.T. Nastos (eds.), *Advances in Meteorology, Climatology and Atmospheric Physics*, Springer Atmospheric Sciences,
DOI 10.1007/978-3-642-29172-2_158,

light from the ground to the top of the atmosphere. Particulate matter (PM) is another expression of aerosols loading within the atmosphere and is a crucial parameter due to its direct effect on public health. Exposure to $PM_{2.5}$ and PM_{10} has been associated with mortality and morbidity (Slama et al. 2007; Gent et al. 2003). Numerous studies have attempted to establish the relationship between columnar AOD and ground-based PM by using linear model (Pelletier et al. 2007; Koelemeijer et al. 2006). This relationship depends strongly on auxiliary parameters such as height of Planetary Boundary Layer (HPBL), Relative Humidity (RH), wind speed and direction (Ws, Wd) (Gupta et al. 2006). In this paper, the first systematic observations performed during the AIRSPACE project at the four urban areas in Cyprus, Limassol, Nicosia, Larnaca and Paphos, are presented. The data in Nicosia and Paphos were retrieved in July 2011, for Larnaca in August 2011 and for Limassol, which is the main study area, the data covered the period of March 2011 and July–September 2011 due to the availability of data for all the instruments used in the study. For each site, the PM_{10} readings in conjunction with MODerate resolution Imaging Spectro radiometer (MODIS) AOD data and sun-photometer measurements were analyzed.

2 Data and Methodology

2.1 Data

In order to retrieve AOD values at 500 nm, two Microtops II hand-held sun-photometers were used and measurements performed in Nicosia, Larnaca and Paphos. In Limassol the AOD values were retrieved from both Microtops II and CIMEL sun photometer. The CIMEL comprise part of the AErosol RObotic NETwork (AERONET) and the aerosol data are acquired during daylight and in clear sky conditions. In this study level 2 (March 2011) and level 1.5 (July–September 2011) data were used. Additionally, MODIS AOD data at 550 nm were retrieved from both EOS-Terra and EOS-Aqua satellites. Both instruments acquire data daily during daytime when they cross Europe near 1,030 and 1,330 h local solar time. The spatial resolution for both instruments is 10×10 km^2 and two different algorithms over land and sea surfaces are used due to the different radiative properties of water and land.

The TSI DustTrak (model 8,533 and 8,520) is a light scattering laser photometer that is used to measure PM mass concentrations. Specifically, measuring the amount of scattering light which is proportional to volume concentrations of aerosols it could obtain the mass concentration of them. In each site, it is located near the Microtops II sun photometer in the roof of a building chosen according to restrictions in order to avoid the local sources of pollution which may affect the measurements.

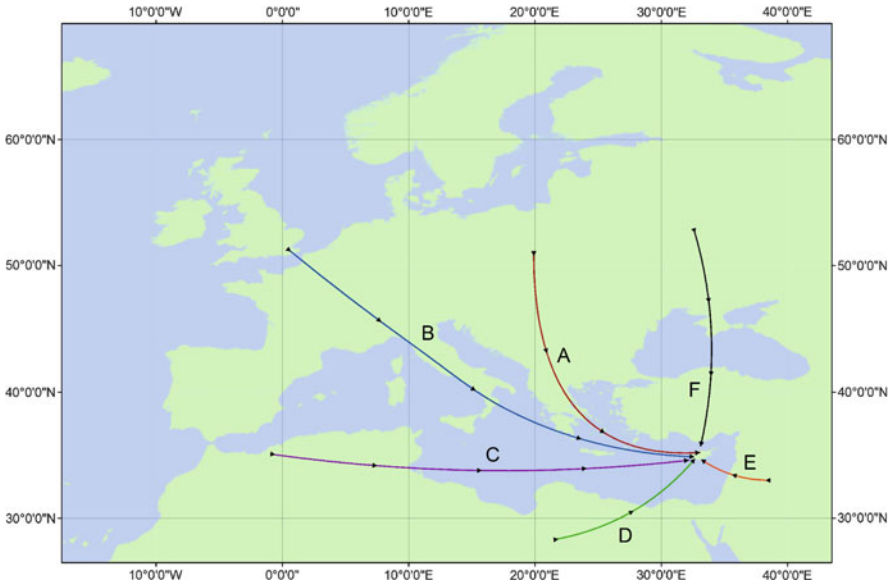

Fig. 1 Main trajectories ending over Cyprus

In order to examine the origin of air masses ending over Cyprus the HYSPLIT (Hybrid Single Particle Lagrangian Integrated Trajectory Model) model was used (Draxler and Hess 2004). The 2-day back trajectories of the air parcels arriving over Cyprus up to an altitude of 3 km were simulated. The simulation concerns three different height regions: 500, 1,500, 3,000 m a.s.l. (Fig. 1).

Meteorological data consist of HPBL, RH at the ground at 08.00 LST, hourly Ws and Wd. The Ws, Wd and RH obtained from the Cyprus Meteorological Services. HPBL has been estimated by using the first derivative of the Range Corrected Signal (RCS) (Menut et al. 1999) from lidar. The backscatter lidar provides aerosol or cloud backscatter measurements from a height beginning from 200 m up to tropopause height.

2.2 Methodology

Ground-based AOD data from CIMEL and Microtops II sun photometers and satellite AOD data are used in conjunction with PM_{10} measurements in order to retrieve a relationship between AOD and PM_{10} for the four main cities of Cyprus. Due to the fact that PM_{10} ground measurements are corresponded to a point whereas AOD data refers to the whole column of the atmosphere and MODIS AOD retrievals have spatial scale 10×10 km^2, this allows for the measurement of the vertical profile of aerosols using the lidar signals when available, as well as

meteorological data in order to increase the correlation between two study parameters. Lidar, sun photometer and DustTrak measurements were held daily during the Terra and Aqua MODIS overpass (06:00–11:00 UTC).

3 Results

Figure 2 shows the linear regression concerning AERONET–AOD and PM_{10} for the period March and July–September 2011 (for April–June 2011, the CIMEL sun-photometer had sent for the annually calibration) for Limassol. The following days with dust events occurring were excluded (29–30/3, 25/8, 7/9, 29/9/2011) from the statistical analysis, since no direct relation exists between columnar AOD and ground-based PM_{10} during dust intrusion (Nisantzi et al. 2011). According to the coefficient of determination ($R^2 = 0.2736$) the correlation coefficient for 1,146 measurements is 0.523 and it is statistical significant in the level of confidence $a = 0.005$. We used AERONET–AOD data instead of MODIS since MODIS-AOD retrievals for Limassol for the study period were limited ($n = 37$). However based on previous study (Nisantzi et al. 2011) the correlation coefficient between AOD derived from MODIS and AERONET is 0.82, so this led us to use AERONET–AOD in case of absent of MODIS-AOD and vice-versa.

In order to group the measurements we divide them according to Wd, Ws, HPBL, RH(%) and the six main trajectories ending over Cyprus. Table 1 presents the best correlation found for each category.

Regarding Wd and Ws, we noticed that high correlation between PM_{10} and AOD was established when prevailing wind from the north direction and with low speed. When RH is less than 40%, AOD values correlated better with PM_{10} values as also found in other studies (Gupta et al. 2006). Concerning HPBL it was expected that the higher correlation would happen for lower values (Gupta et al. 2006). This may

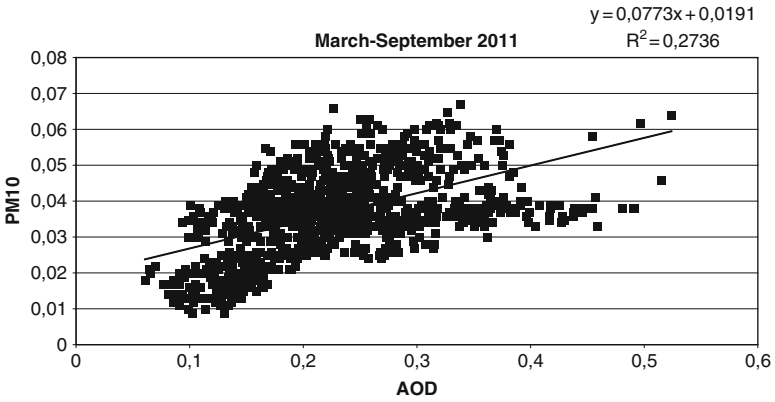

Fig. 2 Relationship between PM_{10} and AERONET–AOD

Table 1 Statistical elements for the best correlation for each study category

	Slope	Bias	R^2	R	n
Wd: North	0.148	0.004	0.596	0.77	108
Ws: 0–4 knots	0.159	0.004	0.568	0.75	100
RH: 0–40%	0.134	0.004	0.479	0.69	130
HPBL: 650–900 m	0.151	0.003	0.524	0.72	263
Trajectory: E	0.131	0.00008	0.786	0.89	66

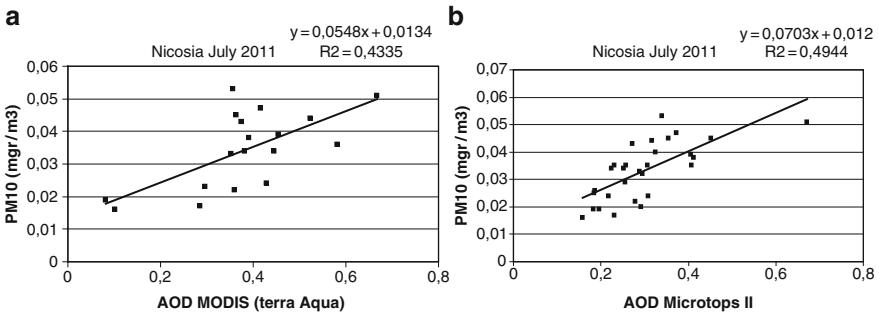

Fig. 3 Linear correlation between PM_{10} and (**a**) MODIS (Terra–Aqua)–AOD, (**b**) Microtops II-AOD

not present because during the measurements, frequently there was a layer above the PBL in Limassol area in a height of 1,500 m and this did not permit the usual procedure of PBL evolution. Thus AOD values remained high in contrast with PM_{10} values. While in case of low HPBL without any layer above it, low AOD values correspond to low PM_{10} values. Regarding the analysis of trajectories, it was found that when air masses move from the western part of Asia (see category E, Fig. 1), AOD and PM_{10} are better related.

During the 1 month of measurements for Paphos, Larnaca and Nicosia only the statistical analysis for Nicosia are shown the best correlation between the study parameters. Unfortunately during the 1 month of measurements for Larnaca and Paphos there were only two and five retrievals of AOD from MODIS, respectively. This did not allow any conclusion to be drawn about satellite AOD and ground-based PM_{10}. It is worth mentioning that for coastal cities of Limassol, Larnaca and Paphos both Aqua and Terra MODIS retrievals are limited. Additionally, for coastal areas, the relationship between AOD and PM_{10} did not present significant correlation; this may be due to the development of sea breeze during the summer months which diffuses the pollutants within the hinterland (Pokhrel and Lee 2011).

For the continental area, Nicosia, the first results have shown a well defined relation for both ground-based and satellite derived AOD and PM_{10} ($R = 0.7$ and $R = 0.66$ respectively), despite the short period of measurements (Fig. 3). Using

the meteorological data for the three validation sites there was not any clear evidence in order to classify the data due to the limited period of measurements.

4 Conclusions

This paper presented the analysis of the first measurements derived from an ongoing research project (AIRSPACE). It was found that the parameters that regulate the correlation in the highest level between PM_{10} and AOD are the north Wd, the low Ws (0–4 knots), the low RH value (<40%), the HPBL between 650 and 900 m and the trajectory category E. For the validation sites only Nicosia, possibly due to its geographical position, has given a good correlation between columnar AOD and ground-based PM_{10}. In a latter stage, more measurements are to be implemented using additionally the Harvard Impactors, designed by Pr. Koutrakis that have been installed to the four cities of Cyprus. Thus, PM_{10}, $PM_{2.5}$, EC-OC and Nitrate concentrations will be also available in the next months.

Acknowledgments The project is funded by the Cyprus Research Promotion Foundation in the frameworks of the project 'AIRSPACE'. In addition the authors would like to acknowledge the Cyprus University of Technology/Department of Civil Engineering and Geomatics (Remote Sensing Laboratory) for supporting this study.

References

Boyouk N, Leon JF, Delbarre H, Podvin T, Deroo C (2010) Impact of the mixing boundary layer on the relationship between PM2.5 and aerosol optical thickness. Atmos Environ 44:271–277. doi:10.1016/j.atmosenv.2009.06.053

Draxler RR, Hess GD (2004) Description of HYSPLIT-4 modelling system, NOAA technical memorandum ERL ARL-224. Air Resources Laboratory, Silver Spring

Gent JF, Triche EW, Holford TR, Belanger K, Bracken MB, Beckett WS (2003) Association of low-level ozone and fine particles with respiratory symptoms in children with asthma. JAMA 290:1859–1867. doi:10.1001/jama.290.14.1859

Gupta P, Christoper SA, Wang J, Gehrig R, Lee Y, Kumar N (2006) Satellite remote sensing of particulate matter and air quality assessment over global cities. Atmos Environ 40:5880–5892. doi:10.1016/j.atmosenv.2006.03.016

Koelemeijer RB, Homan CD, Matthijsen J (2006) Comparison of spatial and temporal variations of aerosol optical thickness and particulate matter over Europe. Atmos Environ 40:5304–5315. doi:10.1016/j.atmosenv.2006.04.044

Menut L, Flamant C, Pelon J, Flamant P (1999) Urban boundary layer height determination from lidar measurements over Paris area. Appl Opt 38:945–954. doi:10.1364/AO.38.000945

Nicolantonio W, Cacciari A (2011) MODIS multiannual observations in support of air quality monitoring in Northern Italy. Ital J Remote Sens 43:97–109

Nisantzi A, Hadjimitsis DG, Alexakis D (2011) Estimating the relationship between aerosol optical depth and PM10 using lidar and meteorological data in Limassol, Cyprus. SPIE Remote Sensing 2011, Prague, September 2011 (in press)

Pelletier B, Santer R, Vidot J (2007) Retrieving of particulate matter from optical measurements: a semiparametric approach. J Geophys Res 112:1–18. doi:10.1029/2005JD006737

Pokhrel R, Lee H (2011) Estimation of the effective zone of sea/land breeze in a coastal area. Atmos Pollut Res 2:106–115. doi:10.5094/APR.2011.013

Slama R, Morgensten V, Cyrys J, Zutavern A, Herbath O, Wichmann HE et al (2007) Traffic-related atmospheric pollutants levels during pregnancy and offspring's term birth weight: a study relying on a land-use regression exposure model. Environ Health Perspect 115:1283–1292

Ground-Based Aerosol Optical Depth Inter-Comparison Campaigns at EUSAAR Sites in Athens, Greece

S. Nyeki, C.H. Halios, K. Eleftheriadis, V. Amiridis, J. Gröbner, and C. Wehrli

Abstract This work summarises an aerosol optical depth (AOD) inter-comparison campaign conducted from June to September 2009 in Athens under the EUSAAR (European Super-Sites for Atmospheric Aerosol Research) Programme. A PFR (precision filter radiometer) travelling standard from the GAW-PFR network was first located at the NCSR "Demokritos" Institute (267 m asl), and then at the Institute for Space Applications and Remote Sensing of the National Observatory of Athens (ISARS/NOA, 191 m). ISARS/NOA has a CIMEL sun-photometer which is part of AERONET. Concurrent data at two co-incident channels showed that the $\lambda = 865$ nm but not the 500 nm channel at ISARS/NOA fulfilled the WMO Global Atmosphere Watch criterion of traceability.

S. Nyeki (✉) • J. Gröbner • C. Wehrli
Physical Meteorological Observatory of Davos/World Radiation Centre (PMOD/WRC), Davos, Switzerland
e-mail: stephan.nyeki@pmodwrc.ch

C.H. Halios
Physical Meteorological Observatory of Davos/World Radiation Centre (PMOD/WRC), Davos, Switzerland

Department of Environmental Physics and Meteorology, University of Athens, Athens 15784, Greece

K. Eleftheriadis
ERL, INT-RP, National Center of Scientific Research "Demokritos", GR-15310, Agia Paraskevi, Athens, Greece

V. Amiridis
Institute for Space Applications and Remote Sensing, National Observatory of Athens, Metaxa and Vas. Paulou Str., GR-15236 Penteli, Greece

C.G. Helmis and P.T. Nastos (eds.), *Advances in Meteorology, Climatology and Atmospheric Physics*, Springer Atmospheric Sciences,
DOI 10.1007/978-3-642-29172-2_159,

1 Introduction

The measurement of atmospheric trace gases and aerosols is an important step towards understanding their effect on climate and air quality. In order to further quantify key processes, and to harmonise, validate and provide a long-term database of measurements at European sites, the EUSAAR (European Super-sites for Atmospheric Aerosol Research) network was established. The monitoring network consists of 20 high-quality European ground-based stations or so-called "supersites", and covers a variety of representative locations. Amongst the numerous parameters measured at these sites, aerosol optical depth (AOD) is an important input to climate models. Several international and national AOD networks exist in Europe, each with different instruments, different algorithms to determine AOD and different archive formats. A harmonisation of these aspects among EUSAAR stations was therefore decided upon. Although the EUSAAR programme ended in 2011 the follow-on programme, ACTRIS, ensures that the network of stations continues.

This study summarises an AOD inter-comparison campaign conducted from June to September 2009. A PFR (precision filter radiometer; Wehrli 2000) travelling standard from PMOD/WRC (Physical and Meteorological Observatory of Davos, Switzerland) was located at the Demokritos Institute in Athens (DEM; 267 m asl), Greece. The site is designated as a Global Atmosphere Watch (GAW) Regional site and EUSAAR/ACTRIS Associate. AOD was also measured at the Institute for Space Applications and Remote Sensing of the National Observatory of Athens (ISARS/NOA; 191 m asl), which is located 3 km from Demokritos. ISARS/NOA has a CIMEL sun-photometer which is part of AERONET (Holben et al. 1998). Both sites are on the outskirts of the Athens Basin, and can be categorised as "sub-urban" in nature.

2 Methods

Measurements by the PFR travelling standard were taken at 1-min intervals, and evaluated according to GAW-PFR procedures to Level 3 data (McArthur et al. 2003; Nyeki et al. 2012). Measurements by CIMEL radiometers were run according to the standard AERONET measurement protocol, where the measurement frequency depends on the airmass and time. In practise, AOD measurements are available every 10–11 min. Level 1.5 AOD data using the AERONET Version 2 Direct Sun Algorithm were available, and are automatically cloud-screened (Holben et al. 1998). Both AERONET and GAW-PFR have near-real-time capability and provide online preliminary AOD data from the previous day.

Coincident GAW-PFR and CIMEL AOD measurements which occurred to within ± 30 s were used for further analysis. Comparison of individual channels was constrained by wavelength differences smaller than $\pm 1\%$ of the common mean

wavelength. This condition limits the comparison between CIMEL and PFR instruments to two wavelengths which are nominally $\lambda = 500$ and 865 nm.

3 Results

The total measurement period in Athens lasted 83 days, of which only several days were completely cloudy/rainy. Observed AOD values ranged up to 0.5 and are typical of sub-urban sites impacted by anthropogenic pollution. A total of at least 1,273 and 440, valid, cloud-free coincident data points ($\lambda = 500$ nm) were collected at Demokritos and ISARS/NOA, respectively.

An overview of the good agreement in AOD is presented in Fig. 1, where correlation coefficients >0.94 and slopes of 0.99–1.04 are found at both

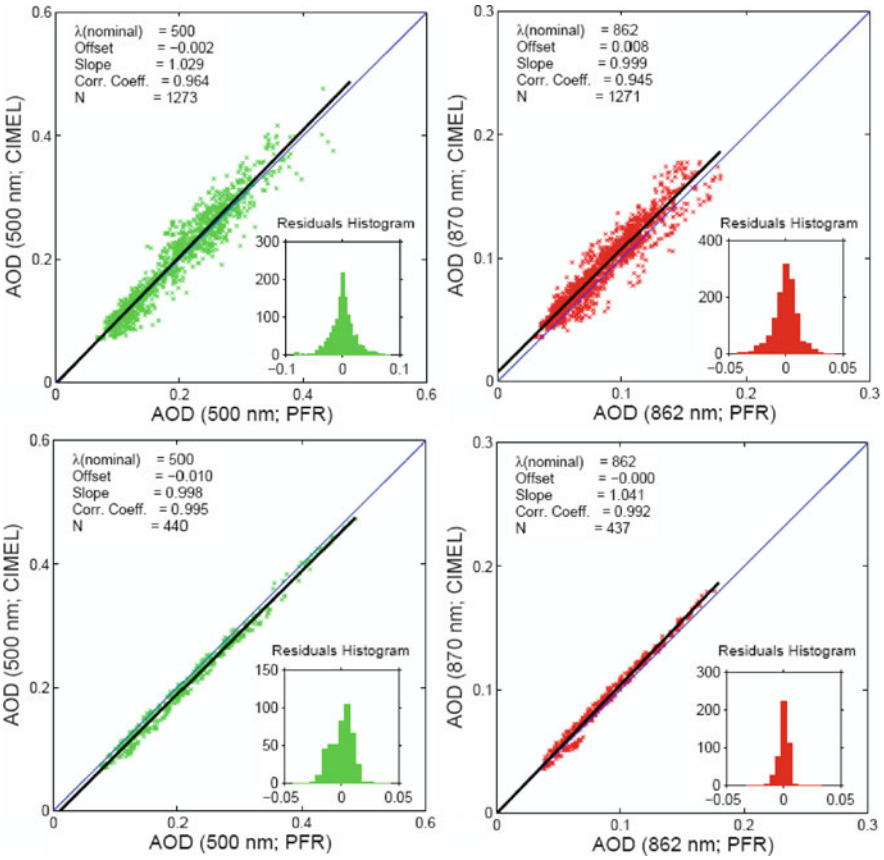

Fig. 1 Coincident AOD values at: (*upper panel*) Demokritos, (*lower panel*) ISARS/NOA. Coincident wavelengths are: (*left*) $\lambda = 500$ nm, and (*right*) 865 nm

wavelengths and sites. However, greater scatter in AOD is evident at Demokritos (±0.03) than at ISARS/NOA (+0.02 to −0.02). In addition, a small but significant positive offset in the AOD difference at $\lambda = 865$ nm but not at $\lambda = 500$ nm appears to exist at Demokritos.

These observations at Demokritos are most probably due to the difference in elevation and distance to the CIMEL at ISARS/NOA. The Athens basin is a considerable source of anthropogenic aerosols which are capped within the planetary boundary layer (PBL) by the local inversion at about 2,000–2,500 m during summer months. Inhomogeneities in the aerosol concentration will therefore exist due to local sources. In addition, the higher elevation of the Demokritos site by 76 m implies that less of the atmospheric column is measured which should result in slightly lower PFR AOD values. Assuming a 2,000 m PBL depth then 76 m represents 3% of the PBL depth. Three percent of the AOD average at 500 nm is therefore ~0.006 which would approximately account for the AOD difference at $\lambda = 865$ nm in Fig. 1b. However, this is not the case at $\lambda = 500$ nm where the AOD difference is negligible. As it seems reasonable that AOD would in general be higher at the lower altitude site (i.e. ISARS/NOA) this then suggests that either or both the CIMEL and PFR calibrations at $\lambda = 500$ nm were slightly non-optimal.

The quality of AOD data from the inter-comparison can be gauged by applying WMO criteria, discussed in WMO GAW report no. 162 (WMO 2005). The ability to trace the calibration to a primary reference(s), the so-called traceability, is not currently possible based on physical measurement systems. Report no. 162 states that, the initial form of traceability will be based on difference criteria, such that an inter-comparison or co-location traceability will be established if the AOD difference between networks is within specific limits. These limits will depend on the derivation methodology as each measurement system has a different uncertainty profile. Inter-comparison campaigns should be over a sufficient period of time to ensure that: (1) ≥1,000 coincident AOD data points are collected, (2) minimum of 5 clear sunny days occurs, (3) AOD at 500 nm should lie within the range 0.040–0.200.

If these conditions are met then for traceability to exist, 95% of the AOD difference should lie within certain defined limits. The definition of these limits depends in the first instance on the measurement method. In the present case, for "finite field-of-view" instruments such as the PFR and CIMEL, the limit is defined as $U95 < \pm(0.005 + 0.010/m)$ where m = airmass. The first term accounts for instrumental and algorithmic uncertainties while the second term represents the uncertainty δV in the exo-atmospheric calibration value V which corresponds to a requirement of a relative uncertainty in calibration of <1%. Figure 2 illustrates the AOD difference versus airmass at Demokritos and ISARS/NOA. The low CIMEL-PFR AOD difference (−0.011 and 0.003 at 500 and 865 nm; campaign average) at ISARS/NOA suggests that the overall goal of achieving an AOD measurement uncertainty <0.015 was attained. However, when looked at in detail, measurements at Demokritos did not fulfill the traceability standard while those at ISARS/NOA were only fulfilled by the 865 channel where 100% of points lay within the WMO

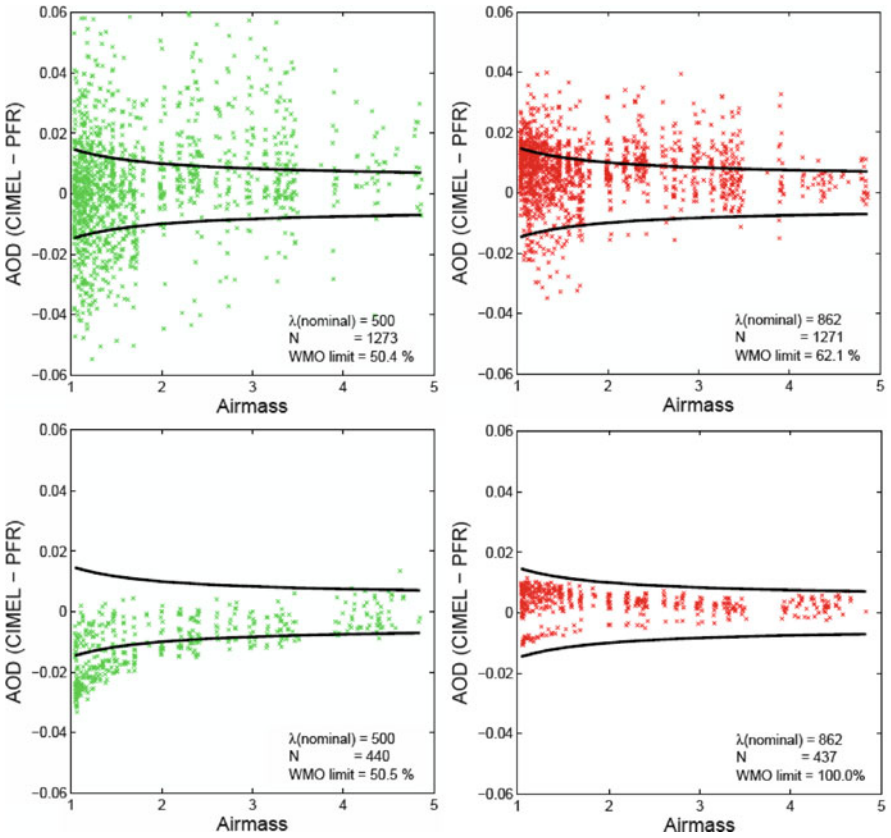

Fig. 2 AOD difference versus airmass illustrating the WMO criterion for traceability (*solid line*) at: (*upper panel*) Demokritos, and (*lower panel*) ISARS/NOA. Wavelengths are: (*left panel*) $\lambda = 500$ nm, and (*right panel*) 865 nm

criterion for AOD. However, it should be mentioned that only 440 rather than 1,000 valid, coincident data points were collected at ISARS/NOA due to logistical reasons.

4 Conclusions

An AOD inter-comparison campaign between a CIMEL instrument (AERONET) and PFR Travelling Standard (GAW-PFR) was conducted at two sites in Athens (Demokritos and ISARS/NOA sites) during the June–September 2009 period. The WMO criterion for traceability was met by the $\lambda = 865$ but not by the 500 nm channel at ISARS/NOA. Neither channel met the criterion at Demokritos. This case illustrates the well-known observation that aerosol concentrations are in general

only homogeneous over short distances. AOD and in-situ aerosol measurements that are too distant apart, as is the case at several EUSAAR super-sites, may therefore be difficult to interpret.

As an overall consideration, it is important to note that a lower limit exists beyond which the AOD difference is difficult to minimise. An AOD inter-comparison study conducted by McArthur et al. (2003) compared network PFR and CIMEL sun-photometers amongst other AOD instruments. It was demonstrated that only a marginal improvement in AOD uncertainty at the 0.005 level could be obtained.

Acknowledgments We thank EUSAAR for funding which was obtained as a sub-contractor of the Paul Scherrer Institute, Switzerland.

References

Holben BN, Eck TF, Slutsker I, Tanre D, Buis JP, Setzer A, Vermote E, Reagan JA, Kaufman YJ, Nakajima T, Lavenu F, Jankowiak I, Smirnov S (1998) AERONET – a federated instrument network and data archive for aerosol characterization. Remote Sens Environ 66:1–16. doi:10.1016/S0034-4257(98)00031-5

McArthur LJB, Halliwell DH, Niebergall OJ, O'Neill NT, Slusser JR, Wehrli C (2003) Field comparison of network sunphotometers. J Geophys Res 108(D19):4596. doi:10.1029/2002JD002964

Nyeki S, Halios CH, Baum W, Eleftheriadis K, Flentje H, Gröbner J, Vuilleumier L, Wehrli C (2012) Ground-based aerosol optical depth trends at three high-altitude sites in Switzerland and Southern Germany from 1995–2010. J Geophys Res in 2nd review

Wehrli C (2000) Calibrations of filter radiometers for determination of atmospheric optical depth. Metrologia 37:419–422. doi:10.1088/0026-1394/37/5/16

WMO (2005) WMO/GAW Experts workshop on a global surface-based network for long term observations of column aerosol optical properties, Davos 2004. Baltensperger U, Barrie L, Wehrli C (eds), GAW No. 162, WMO/TD-No. 1287

Regression of the Scattered Radiation Intensity with Precipitable Water Depth and Relative Atmospheric Mass

M.D. Panagiotopoulou, A.S. Rapti, and N.D. Panagiotopoulos

Abstract The precipitable water influences the radius size of the absorbent continental particles and maritime aerosols. The precipitable water depth and the scattered irradiance intensity were measured at the Atmospheric Physics Laboratory of the University of Patras during sunny days, at constant solar elevations, in the time period 2006–2009, exhibiting seasonal variation with a summer maximum and a winter minimum. The data analysis results in a higher scattered irradiance summer maximum and a lower winter minimum during the prevalence of continental air masses than that of maritime air masses. Two families of regression curves of the scattered irradiance intensity with precipitable water depth are being obtained, one for continental and one for maritime air masses. The aim of this work is the computation of the scattered irradiance intensity from the origin of the air masses, and the values of the precipitable water depth and relative atmospheric mass.

1 Introduction

The scattered irradiance is the result of the single and multiple scattering of the solar beam irradiation by the molecules of the clean-dry atmosphere and by the aerosols. The intensity of the molecular scattering, Rayleigh scattering, is inversely proportional to the fourth power of the wavelength λ in the ultraviolet region of the solar spectrum and does not depend on the atmospheric water vapor content. The sunlight scattering by aerosol, Mie scattering, which is being caused by the dusts included in the continental air masses and by the sea-salts in the maritime air masses, attenuates the near violet and visible spectral regions and depends on the precipitable water depth. The intensity of the scattered irradiance by the aerosol depends on the ratio r/λ of the particle radius r to the wavelength λ of the transmitted irradiation. Once

M.D. Panagiotopoulou • A.S. Rapti (✉) • N.D. Panagiotopoulos
Atmospheric Physics Laboratory, University of Patras, Patras 26 500, Greece
e-mail: arapti@physics.upatras.gr

C.G. Helmis and P.T. Nastos (eds.), *Advances in Meteorology, Climatology and Atmospheric Physics*, Springer Atmospheric Sciences,
DOI 10.1007/978-3-642-29172-2_160,

the aerosols have been formed there are dynamic processes that may result in evolution of the size distribution in time, and the variations in aerosols size influence their radiative properties such as the scattering phase function, single scattering albedo, and optical thickness (Eck et al. 1999). The presence of large dust particles in the atmosphere increases the scattered radiation intensity and it seems to be influenced by the atmospheric content in dust particles rather than in maritime aerosol (Rapti 2000). Light scattering efficiency is roughly proportional to the particle cross section (Ansmann et al. 2001). Tanré et al. (2001) have found that dust is being scattering material mainly and that even in the blue the single-scattering coefficient is 0.8. The atmospheric optical thickness in summer in the 0.280–0.525 μm spectral region and for the continental air masses was founded 0.8 (Rapti 2005). Radiative transfer properties of aerosols are sensitive to the scattering (Dubovik et al. 2002). The water uptake leads to an increase of the particle size, and the backscattering ratio increases with water vapour mixing ratio faster for the continental air mass from northern-eastern Europe (De Tomasi and Perrone 2003).

Precipitable water depths are being calculated by correlation of the specific humidity (g/kg) with precipitable water depth (cm) from Vaisala's radiosonde data by Rapti (2005) and by Rapti and Panagiotopoulou (2010).

2 Data

In this work the values of the scattered irradiance intensity were obtained at the Atmospheric Physics Laboratory of the University of Patras at the constant solar elevations 20°, 30°, 40°, 50°, 60° and 70°, during the sunny days of the 3-year measurement period. The measurements of the atmospheric pressure were performed with a microbarograph by Belfort, Instrument Company. The meteorological instruments were controlled against reference instruments i.e. the microbarograph against a Fortin type barometer, the thermograph against a mercurial thermometer and the hygrograph against an August type psychrometer.

3 Analysis

3.1 The Dependence of the Scattered Irradiance on the Precipitable Water Depth

Figure 1a, b, shows the 3 year time series of the scattered irradiance intensity I_D at the solar elevation angle 30° (Fig. 1a), and of the precipitable water depth w (cm) (Fig. 1b) with the beginning of the measurements in September. From Fig. 1a, b is evident that the scattered irradiance intensity and the precipitable water depth present the same seasonal variation with a summer maximum and a winter minimum.

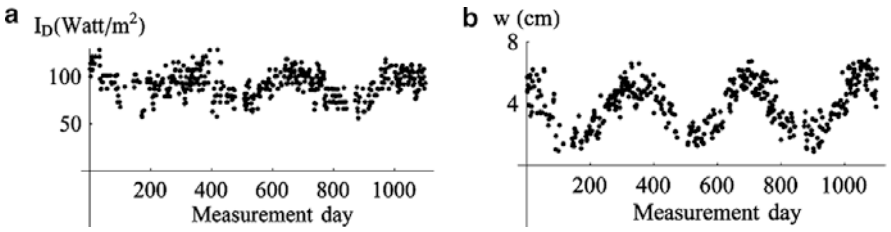

Fig. 1 (**a**, **b**) Seasonal variation of the scattered irradiance intensity I_D (W/m^2) at the solar elevation angle 30°, m = 2, and of the simultaneous data of the precipitable water depth w (cm)

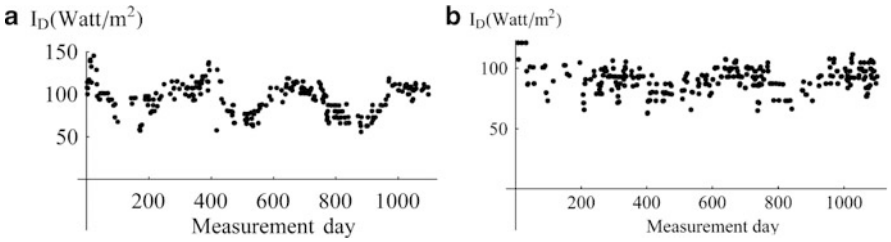

Fig. 2 (**a**, **b**) Seasonal variation of the scattered irradiance intensity I_D (W/m^2) at the solar elevation angle 30°, m = 2, with the measurement day, for (**a**) continental and (**b**) maritime aerosol

3.2 The Scattered Irradiance Intensity with Continental and Maritime Aerosol

Figure 2a, b shows the time series of the scattered irradiance during the prevalence of continental air masses (Fig. 2a) carried from the east-northeastern Europe by the continental east-northeastern winds, and during the prevalence of maritime air masses (Fig. 2b) carried by the maritime west-southwestern winds from the Atlantic Ocean.

From Fig. 2a is evident that the winter minimum of the scattered irradiance intensity with continental air masses is lower than that with maritime air masses (Fig. 2b), and that the summer maximum of the scattered irradiance intensity with continental air masses is higher than that with maritime air masses.

Figure 3a, b, c shows the best-fit regression curves to the measured data of the scattered irradiance intensity I_D (W/m^2) and precipitable water depth w (cm) in the prevalence of continental (Fig. 3a) and maritime (Fig. 3b) air masses.

From Fig. 3a is evident that the scattered irradiance increases fast with precipitable water in the prevalence of continental air masses, and from Fig. 3b that the scattered irradiance by maritime aerosol is higher than that by the dry dusts in winter. Indeed, the dry salt crystals are giant particles with dry radius $r \geq 1$ μm, while the dry dust particles are large particles with dry radius in the region 0.1 μm $\leq r \leq 1$ μm.

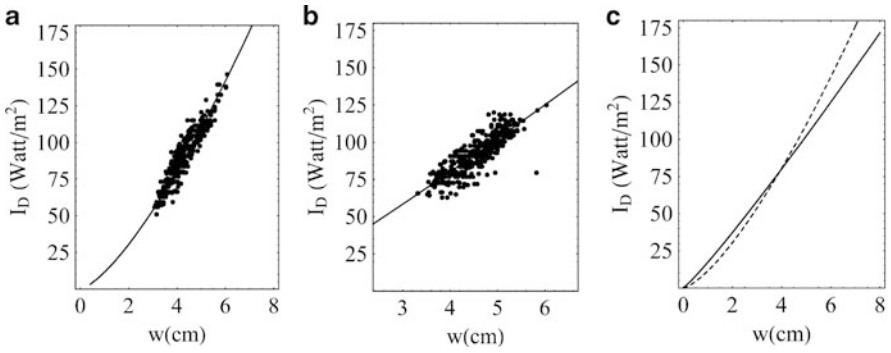

Fig. 3 (**a**, **b**, **c**) Regression of the scattered irradiance intensity I_D (W/m^2) at m = 2, with simultaneous data of the precipitable water depth, w (cm), for (**a**) continental and (**b**) maritime aerosol

3.3 Scattered Irradiance Dependence on Relative Atmospheric Mass

Figure 4a, b, c shows the regression of the scattered irradiance I_D (W/m^2) at m = 1.31 with precipitable water depth for continental (Fig. 4a) and maritime (Fig. 4b) air masses.

The correlation coefficient is R = 0.9199 and the R.M.S.E. = 0.0603 for the continental air masses, and R = 0.8797 and R.M.S.E. = 0.0601 for the maritime. From the regression curves shown in Figs. 3c (m = 2) and 4c (m = 1.31) it can be seen that the decrease of the relative atmospheric mass results in the increase of the scattered irradiance intensity. The result of the selective extinction of the solar beam by the atmosphere is the variation of the spectral distribution of the solar irradiance in the prevalence of continental and maritime aerosol (Rapti and Panagiotopoulou 2010).

Figure 5 shows the two families of the regression curves to the measured data of the scattered irradiance intensity I_D(m) at m = 1.31, 1.56, 2.00, regressed on the precipitable water depth w (cm), one family of curves for continental and one for maritime air masses, with the upper curves corresponding to relative atmospheric mass m = 1.31 and the following curves corresponding to m = 1.56, 2.00.

From Fig. 5 it can be seen that the high region of the sunlight scattering by the continental dust is observed simultaneously with the precipitable water depth summer maximum in the nearly low relative atmospheric mass m = 1.31. The intense sunlight scattering by the wet dust means that the transmitted irradiance undergoes maximum attenuation and the solar beam intensity falling on the earth's surface is very weak. That is why in some warm and dust-turbid summer days even when it is near noon it can be observed that "the sunrays are weak".

Also, from Fig. 5 is evident that the weak sunlight scattering is observed during the precipitable water depth winter minimum and in the prevalence of the clear and cold-dry continental air masses. The weak sunlight scattering due to cold-dry

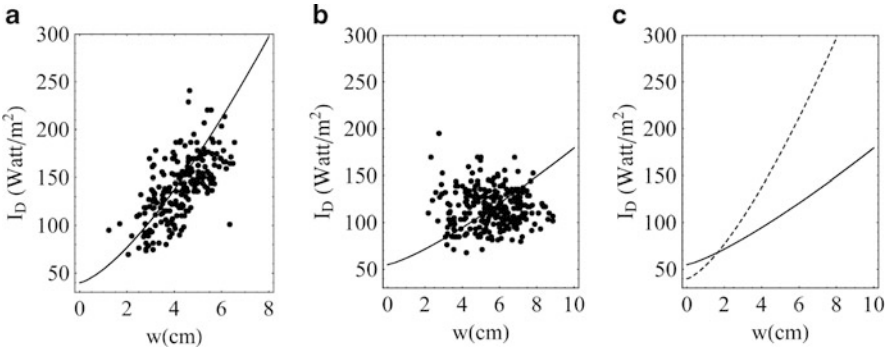

Fig. 4 (**a**, **b**, **c**) Regression of the scattered irradiance intensity I_D at the solar elevation angle 50°, m = 1.31, with precipitable water depth w (cm), for (**a**) continental and (**b**) maritime aerosol

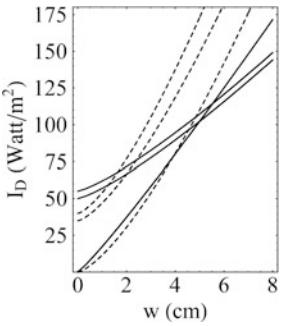

Fig. 5 Dependence of the scattered irradiance $I_D(m)$ (W/m^2) on relative atmospheric mass and precipitable water depth w (cm) in the prevalence of continental (- - -) and maritime (__) aerosol

continental air masses results in minor attenuation of the transmitted irradiance and so, the intensity of the solar beam remains strong. That is why in some clear and cold-dry winter days it can be observed that "the sunrays are intense".

4 Conclusions

The time series of the scattered irradiance intensity and precipitable water depth show the same annual variation with a summer maximum and a winter minimum. The regression analysis of the measured data results in two families of regression curves of the scattered irradiance intensity, at constant relative atmospheric mass, with precipitable water depth, one family of curves for continental and one for maritime air masses. Continental air masses carried by the east-northeastern winds include insoluble absorbent dust particles. Maritime air masses carried by the west-southwestern winds include soluble sea-salt crystals.

In summer the sunlight scattering by the wet grown dusts of the shorter wavelengths in the visible region of the solar spectrum is very strong, and this leads to higher scattered irradiance intensity maximum than that by the maritime

aerosol. In winter the scattered irradiance minimum is lower in the prevalence of cold-dry continental air masses than that in the prevalence of the moist maritime air masses, and the transmitted solar beam irradiance is appreciably strong. The dependence of the sunlight scattering on the relative atmospheric mass results in the increase of the scattered irradiance with the decrease of the relative atmospheric mass.

References

Ansmann A, Wagner F, Althausen D, Muller D, Herber A, Wandinger U (2001) European pollution outbreaks during ACE 2:1. Alofted aerosol plumes observed with Raman lidar at the Portuguese coast. J Geophys Res 106:723–733

De Tomasi F, Perrone MR (2003) Lidar measurements of tropospheric water vapor and aerosol profiles over southeastern Italy. J Geophys Res 108:4286–4298. doi:10.1029/2002JD002781

Dubovik O, Holben B, Eck T, Smirnov A, Kaufman Y, King M, Tanre D, Slutsker I (2002) Variability of absorption and optical properties of Key aerosol types observed in worldwide locations. J Atmos Sci 59:590–608

Eck T, Holben B, Reid J, Dubovik O, Smirnov A, O'Neill N, Slutsker I, Kinne S (1999) Wavelength dependence of the optical depth of biomass burning, urban, and desert dust aerosols. J Geophys Res 104:31333–31349

Rapti AS (2000) Atmospheric transparency, atmospheric turbidity and climatic parameters. Solar Energy 69:99–111

Rapti AS (2005) Spectral optical atmospheric thickness dependence on the specific humidity in the presence of continental and maritime air masses. Atmos Res 78:13–32

Rapti AS, Panagiotopoulou MD (2010) Seasonal evolution of the precipitable water depth and of the spectral irradiance with continental and maritime air masses. In Proceedings of the 10th international conference of meteorology, climatology and atmospheric physics, Patras, Greece

Tanré D, Kaufman Y, Holben B, Chatenet B, Karnieli A, Lavenu F, Blarel L, Dubovik O, Remer L, Smirnov A (2001) Climatology of dust aerosol size distribution and optical properties derived from remotely sensed data in the solar spectrum. J Geophys Res 106:205–217

Air Quality During Heat Waves

D.K. Papanastasiou, D. Melas, and H.D. Kambezidis

Abstract Meteorological and air pollution data observed during the last decade in Athens, Thessaloniki and Volos were analyzed to assess the air quality during heat waves. The identification of a heat wave day was based on two temperature criteria applied to the data recorded at the cities centre: the daily maximum and the daily average temperature value are at least 37°C and 31°C, respectively. Heat wave days were identified every year in Athens but only in 2007 in Thessaloniki and Volos. Air quality was aggravated during heat wave days, a fact that was verified by the means of the common air quality index. PM_{10} concentration levels increased 30% in the centre of Athens and more than 100% in Thessaloniki and Volos, while O_3 concentration levels increased 29% in Thessaloniki's suburb. The increase of pollution levels triggered exceedances of the air quality standards. Temperature and pollution levels during the heat waves occurred in 2007 were separately examined.

1 Introduction

Heat waves (HWs) induce adverse environmental impacts, which can affect human health, the degradation of air quality being one of them (Struzewska and Kaminski 2008; Theoharatos et al. 2010). Air pollution results from the combination of high

D.K. Papanastasiou (✉)
Laboratory of Agricultural Engineering and Environment, Centre for Research and Technology – Thessaly, Institute of Technology and Management of Agricultural Ecosystems, Volos, Greece
e-mail: dkpapan@cereteth.gr; dkpapan@auth.gr

D. Melas
Laboratory of Atmospheric Physics, School of Physics, Aristotle University of Thessaloniki, Thessaloniki, Greece

H.D. Kambezidis
Atmospheric Research Team, Institute for Environmental Research and Sustainable Development, National Observatory of Athens, Athens, Greece

C.G. Helmis and P.T. Nastos (eds.), *Advances in Meteorology, Climatology and Atmospheric Physics*, Springer Atmospheric Sciences,
DOI 10.1007/978-3-642-29172-2_161,

emissions and unfavourable weather. Higher temperatures and irradiance result in enhanced biogenic VOC emission and more intensive photochemical processes which increase O_3 formation (Sillman and Samson 1995). Additionally, stagnation of air masses allows the accumulation of pollutants in the atmospheric boundary layer and in the residual layer during the night (Solberg et al. 2008). Moreover, high ambient temperatures support the production of secondary aerosols (Boy and Kulmala 2002). Many studies have verified that HWs trigger a mortality increase. Some of the deaths attributed to high temperatures are probably caused by photochemical and particulate air pollution, combined or not with high temperatures. Fischer et al. (2004) showed that 400–600 deaths occurred during the 2003 HW in the Netherlands could be attributed to O_3 and PM_{10} exposure.

The objective of this paper is to assess the air quality in Athens (ATH), Thessaloniki (THE) and Volos (VOL), Greece, during HWs.

2 Data

Air pollution data (O_3, NO_2, PM_{10}) recorded at ATH, THE and VOL were used in this study. O_3 concentration was monitored at Marousi and Neohorouda stations, NO_2 concentration at Aristotelous and Agia Sofia stations, and PM_{10} concentration at Aristotelous, Agia Sofia and Volos stations. Aristotelous, Agia Sofia and Volos stations are located at the centre of ATH, THE and VOL, respectively, Marousi is close to the centre of ATH, while Neohorouda is a suburb of THE. All stations are members of the national network of air pollution monitoring. Temperature data recorded at the centre of ATH (Thissio, National Observatory of ATH), THE (campus of Aristotle University) and VOL were also used. Data cover the period 2001–2010 (THE's data does not include 2010).

3 Methodology

The identification of a HW day was based on two temperature criteria that have been suggested by Metaxas and Kallos (1980): the daily maximum (DM) and the daily average (DA) temperature value at the city centre are at least 37°C and 31°C, respectively. Air quality (PM_{10} and O_3 concentration levels) was assessed (1) taking into account the European Union's regulations in force (Directive 2008/50) and (2) by the means of the common air quality index (CAQI). Directive 2008/50 states that the DA value of PM_{10} concentration should not exceed 50 $\mu g/m^3$ on more than 35 days per year and also sets information (180 $\mu g/m^3$) and alert (240 $\mu g/m^3$) thresholds for hourly O_3 concentration. CAQI was developed under CITEAIR project (Van den Elshout et al. 2008). It is calculated according to a grid (Table 1), by linear interpolation between the class borders. The final index is the highest value of the sub-indices for each component. In this study, the CAQI developed for traffic monitoring sites was used, which comprises NO_2 and PM_{10} concentrations.

Table 1 Calculation grid for the CAQI

Index class	Grid	NO_2 concentration ($\mu g/m^3$)	PM_{10} concentration ($\mu g/m^3$)
Very low	0–25	0–50	0–12
Low	26–50	51–100	13–25
Medium	51–75	101–200	26–50
High	76–100	201–400	51–100
Very high	>100	>400	>100

As CAQI was used for a daily index, the DM hourly value of NO_2 concentration and the DA value of PM_{10} concentration were used.

4 Results

The application of the two temperature criteria resulted in the identification of 152 HW days in ATH (Table 2). More HW days were observed in 2007 and 2010, when the criteria were fulfilled in 28 and 29 days, respectively. Taking into account the date of the first and the last HW day observed in these years, the frequencies of HW day occurrence were 38% and 39%, respectively. HW days were identified every year in ATH but only in 2007 in THE and VOL. This fact supports the opinion that the HWs observed in 2007 were possibly the worst HW events recorded in Greece (Theoharatos et al. 2010).

The mean pollution levels during HW and non-HW summer days are presented in Table 3. It is revealed that pollution levels were significantly increased during HW days. PM_{10} concentration levels in ATH were 30% higher during HW days than during non-HW days, while they were more than double during HW days in THE and VOL. Maximum O_3 concentration levels increased 6% near the centre of ATH (Marousi station), while the increase was more pronounced (29%) at THE's suburb. The increase of pollution levels triggered exceedances of the air quality standards (AQS). Concerning PM_{10}, the threshold of 50 $\mu g/m^3$ was exceeded in 72% of the HW days in ATH and in all HW days in THE and VOL. The corresponding percentages for the non-HW days were 33%, 18% and 20% for ATH, THE and VOL, respectively. Concerning O_3, the information threshold in ATH was exceeded in 12% and 9% of the HW and the non-HW days, respectively. In THE, it was exceeded in 29% of the HW days and never during non-HW days. Figure 1 verifies the degradation of air quality in the cities centre during summer HW days by the means of CAQI. This figure shows a clear shift to higher CAQI classes during HW days.

Temperature and pollution levels during the warm period of 2007 (8/6–8/9) were studied separately, as in 2007 HW days were identified in all the cities included in this study. In ATH (Fig. 2a), the temperature criteria were met for 5 (24–28/6), 10 (18–27/7) and 5 (22–26/8) consecutive days in June, July and August, respectively. The higher temperature was observed on 26/6 (45.6°C), 25/7 (42.8°C) and 23/8 (39.4°C) during June's, July's and August's event. PM_{10} concentration levels remained higher than the limit value of 50 $\mu g/m^3$ during the periods 11–29/6

Table 2 HW days identified in ATH, THE and VOL

Year	City	HW days observed	First/last HW day observed
2001	ATH	19	June 13/August 11
2002		9	June 17/August 4
2003		12	June 15/September 1
2004		4	July 10/July 23
2005		9	July 20/August 13
2006		14	June 29/August 23
2007	ATH	28	June 21/September 1
	THE	7	June 24/August 25
	VOL	4	June 24/July 25
2008	ATH	17	July 6/August 26
2009		11	June 10/August 3
2010		29	June 15/August 27

Table 3 Mean values of DA PM_{10} and DM hourly O_3 concentrations during HW and non-HW summer days in ATH (2001–2010), THE (2007) and VOL (2007)

	PM_{10} concentration ($\mu g/m^3$)			O_3 concentration ($\mu g/m^3$)	
	Aristotelous	Agia Sofia	Volos	Marousi	Neohorouda
HW days	60	84	92	137	150
non-HW days	46	41	40	129	116

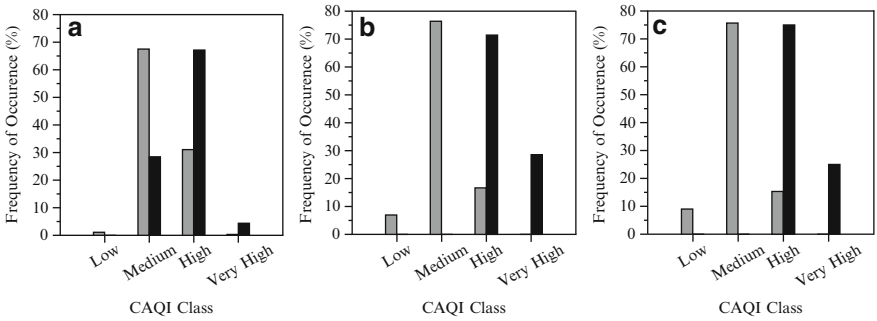

Fig. 1 Frequency of occurrence of CAQI classes during summer in the centre of ATH (**a**; 2001–2010), THE (**b**; 2007) and VOL (**c**; 2007) (*grey bars*: non-HW days; *black bars*: HW days)

(except on 17/6 when the DA PM_{10} concentration was 49 $\mu g/m^3$) and 21–27/7, while exceedances of the limit value were also observed during the HW days identified after 22/8. Summing up, the limit value was surpassed in 21 out of 28 HW days. Maximum O_3 concentration levels exceeded the information threshold during 4 and 2 consecutive days in June and August, respectively, (22–25/6, 30–31/8), while they surpassed the alert threshold during 2 consecutive days in July (24–25/7). In THE (Fig. 2b), HW days were identified in the same periods as in ATH. The higher temperature was observed on 27/6 (41.0°C), 25/7 (42.3°C) and 25/8 (38.5°C) during June's, July's and August's event. As it was mentioned earlier, AQS were also violated.

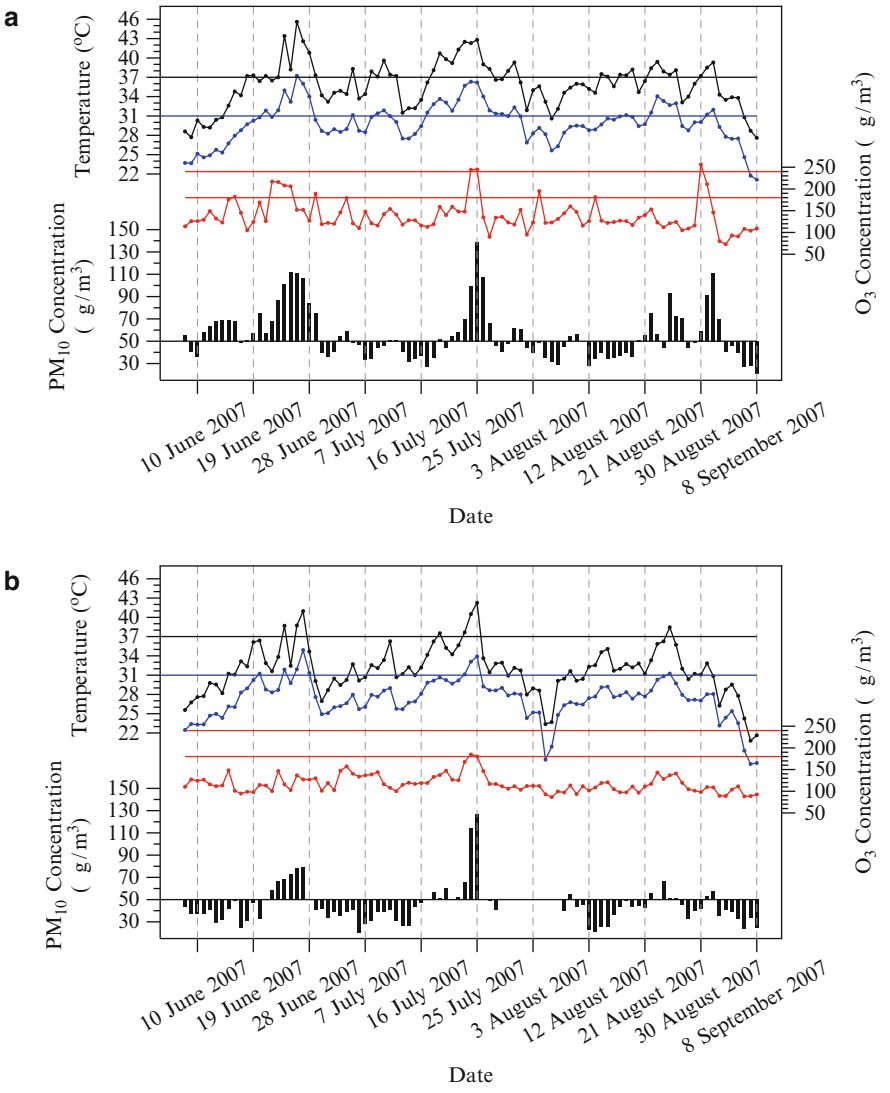

Fig. 2 Temperature and pollution levels, 8/6–8/9/2007 (**a**) ATH; (**b**) THE; *black curve*: DM temperature value; *blue curve*: DA temperature value; *red curve*: O_3 concentration; bars: PM_{10} concentration; *black*, *blue* and *red horizontal lines*: temperature thresholds (37°C and 31°C), O_3 information (180 μg/m^3) and alert (240 μg/m^3) thresholds)

The HW events observed in VOL in 2007 were studied by Papanastasiou et al. (2010). The temperature criteria were met on 24/6, 26/6, 27/6 and 25/7. The temperature peak during June's event was observed on 26/6 (42.5°C), while it reached 38.6°C on 25/7. Papanastasiou et al. (2010) showed that PM_{10} concentration exceeded the limit value of 50 μg/m^3 during the periods 23–29/6 and 22–27/7, the peaks being observed on 27/6 and 25/7.

5 Conclusions

HW days were identified every year in ATH in the period 2001–2010. Their number ranged between 4 and 29 days/year (mean value: 15 days/year). HW days were also identified in THE and VOL but only in 2007. This fact shows that the HWs occurred in 2007 influenced a great part of Greece, and therefore they are rightly considered as the worst events observed during the last years. Air quality was significantly deteriorated during HW days and AQS were usually exceeded.

Acknowledgments The research has been co-financed by the European Union (European Regional Development Fund) and Greek national funds through the Operational Program "Competitiveness and Entrepreneurship" of the National Strategic Reference Framework (NSRF) – Research Funding Program COOPERATION 2009 (no. 09COP-31-1094, Title "Development of a Geographic Climate Information System").

References

Boy M, Kulmala M (2002) The part of the solar spectrum with the highest influence on the formation of SOA in the continental boundary layer. Atmos Chem Phys 2:375–386. doi:10.5194/acp-2-375-2002

Fischer PH, Brunekreef B, Lebret E (2004) Air pollution related deaths during the 2003 heat wave in the Netherlands. Atmos Environ 38:1083–1085. doi:10.1016/j.atmosenv.2003.11.010

Metaxas DA, Kallos G (1980) Heat waves from a synoptic point of view. Riv Meteorol Aeronaut 40:107–119

Papanastasiou DK, Melas D, Bartzanas T, Kittas C (2010) Temperature, comfort and pollution levels during heat waves and the role of sea breeze. Int J Biometeorol 54:307–317. doi:10.1007/s00484-009-0281-9

Sillman S, Samson PJ (1995) Impact of temperature on oxidant photochemistry in urban, polluted rural and remote environments. J Geophys Res 100:11497–11508. doi:10.1029/94JD02146

Solberg S, Hov O, Sovde A, Isaksen ISA, Coddeville P, De Backer H, Forster C, Orsolini Y, Uhse K (2008) European surface ozone in the extreme summer 2003. J Geophys Res 113:D07307. doi:10.1029/2007JD009098

Struzewska J, Kaminski JW (2008) Formation and transport of photooxidants over Europe during the July 2006 heat wave – observations and GEM-AQ model simulations. Atmos Chem Phys 8:721–736. doi:10.5194/acp-8-721-2008

Theoharatos G, Pantavou K, Mavrakis A, Spanou A, Katavoutas G, Efstathiou P, Mpekas P, Asimakopoulos D (2010) Heat waves observed in 2007 in Athens, Greece: synoptic conditions, bioclimatological assessment, air quality levels and health effects. Environ Res 110:152–161. doi:10.1016/j.envres.2009.12.002

Van den Elshout S, Leger K, Nussio F (2008) Comparing urban air quality in Europe in real time a review of existing air quality indices and the proposal of a common alternative. Environ Int 34:720–726. doi:10.1016/j.envint.2007.12.011

Optical Properties of Aerosols Over Athens, Greece, and Their Relation with Chemical Composition

D. Paraskevopoulou, E. Gerasopoulos, E. Liakakou, M. Gratsea, P. Zarmpas, C. Theodosi, and N. Mihalopoulos

Abstract To investigate the relation between aerosol optical properties and their chemical composition, scattering and absorption of aerosols have been recorded on a routine basis during the last 4 years (2008–2011) at the Aerosol Monitoring Station of the National Observatory of Athens, at Penteli's premises, Athens, Greece. In parallel, monitoring of $PM_{2.5}$, $PM_{2.5–10}$, and PM_{10} fractions of particulate matter was performed. Samples were analysed for complete chemical characterization of aerosols, by means of ionic chromatography and the thermal–optical transmission method for EC/OC.

1 Introduction

Aerosols constitute a major environmental issue, and various studies have been performed worldwide on the optical properties of aerosols (e.g. Moffet and Prather 2009; Zhang et al. 2008). More specifically, the Mediterranean basin has been repeatedly suggested as one of the areas where aerosols are expected to play a significant climatic role (e.g. Vrekoussis et al. 2005). Particularly, in the city of

D. Paraskevopoulou
Institute for Environmental Research and Sustainable Development, National Observatory of Athens, I. Metaxa and Vas. Pavlou, P. Penteli, 15236 Athens, Greece

Environmental and Analytical Chemical Division, Department of Chemistry, University of Crete, P.O. Box 2208, 71003 Heraklion, Greece

E. Gerasopoulos • E. Liakakou • M. Gratsea
Institute for Environmental Research and Sustainable Development, National Observatory of Athens, I. Metaxa and Vas. Pavlou, P. Penteli, 15236 Athens, Greece

P. Zarmpas • C. Theodosi • N. Mihalopoulos (✉)
Environmental and Analytical Chemical Division, Department of Chemistry, University of Crete, P.O. Box 2208, 71003 Heraklion, Greece
e-mail: mihalo@chemistry.uoc.gr

C.G. Helmis and P.T. Nastos (eds.), *Advances in Meteorology, Climatology and Atmospheric Physics*, Springer Atmospheric Sciences,
DOI 10.1007/978-3-642-29172-2_162,

Athens, air pollution has been one of the main environmental problems, arising from the massive number of registered vehicles in circulation, which is growing at a rate of 7% yearly. Additionally, the vicinity with arid and desert areas (e.g. Sahara) and industrialized areas in the continental Europe, affects significantly the composition of aerosols (Koulouri et al. 2008).

2 Data and Methodology

2.1 Data

Filter sampling on a 24 h basis was conducted at the Aerosol Monitoring Station of the National Observatory of Athens (NOA), at Penteli's premises (38.3 N, 23.5 E, 527 m a.s.l), during the period from May 2008 to September 2011. Co-located absorption coefficient measurements were performed from February 2009 to September 2011 while scattering coefficients are reported from October 2008 to September 2011, both at 5-min resolution. Aerosol samples from March 2008 to April 2010 were analyzed for OC and EC and from May 2008 to December 2008 for main ions.

2.2 Methodology

NOA's Dichotomous Partisol and Partisol FRM-2000 air samplers were used for the sampling of $PM_{2.5–10}$, $PM_{2.5}$ and PM_{10} fractions of aerosols on a 24 h basis. Precombusted quartz fiber filters (Whatman QMA, diameter 47 mm) were used to collect samples for the OC, EC and IC analysis. All filters were pre- and post-weighed using a six-digit microbalance.

The quartz filters were cut into equal pieces (punches) of 1 cm^2 surface. 1 punch was analysed for OC and EC, with the Thermal-Optical Transmission (TOT) technique (Theodosi et al. 2010), using a Sunset Laboratory OC/EC Analyzer described in details by Koulouri et al. (2008), with small changes in temperature program (Theodosi et al. 2010). Two additional punches were extracted with nanopure water and analysed for the main ions following the technique described by Theodosi et al. (2010).

Aerosol light scattering coefficient was measured with a mono-wavelength portable integrating nephelometer (M903, Radiance Research, Seattle, USA), while a commercial instrument particle soot absorption photometer (PSAP, Radiance Research, Seattle, USA) was used for the monitoring of the light absorption coefficient of ambient aerosols at Penteli station.

Air mass origins for the duration of the filter sampling, were computed by applying 4-day back-trajectory analysis, with the Hybrid Single-Particle Lagrangian Integrated Trajectory (HYSPLIT) model (Draxler and Rolph 2003), which uses

the meteorological data, produced by the National Weather Service ETA Model, in order to compute advection and dispersion of air-parcels arriving over our site in Penteli.

3 Results

The whole period average values of PM_{10}, $PM_{2.5}$ (fine) and $PM_{2.5–10}$ (coarse) aerosol masses, were found to be 39 ± 18, 22 ± 10, and 19 ± 12 μg.m^{-3}, respectively. The average seasonal cycle of the three fractions is presented in Fig. 1.

The 5-min mean values of the scattering coefficient (530 nm) ranged between almost zero and 286 Mm^{-1}; presenting a mean value of 34.6 Mm^{-1}. The monthly mean scattering coefficients as well as the whole period seasonal cycle is presented in Fig. 2a, b, and maximum values are found in summer. On a daily basis, the highest values are found to be linked to pollution transported from northern Europe or transport of dust from Saharan, as observed from air mass back-trajectories. The 5-min mean absorption coefficient presented mean values 8.02, 9.46 and 11.86 Mm^{-1} at 660, 522 and 470 nm, respectively.

The absorption coefficient data were also analyzed on a seasonal basis (Fig. 3), indicating that there is maximum seasonal signal during late winter and spring while minimum is found in late summer to autumn. The Angstrom exponent calculated from the absorption coefficients at 470 and 660 nm, presented its maximum value (1.48) on February and minimum average value (0.80) on August, indicating fine fresh absorbing particles in the colder period.

Hygroscopic aerosol particles can be associated with a large amount of water, affecting the nephelometer measurements, which are performed at ambient RH (Sciare et al. 2005). In order to calculate the contribution of hygroscopic species (NH_{4x} + SO_{4y}) to the light scattering coefficient, we multiplied the concentration of NH_{4x} + SO_{4y} by a computed humidity-dependent, scattering enhancement factor,

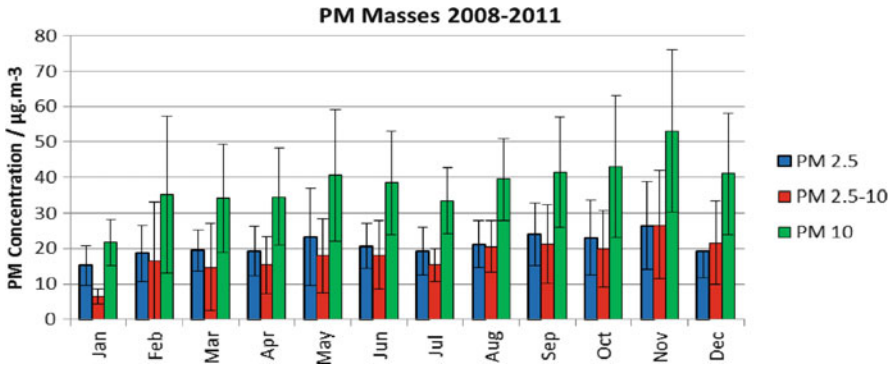

Fig. 1 Whole period seasonal cycle of $PM_{2.5}$, $PM_{2.5–10}$ and PM_{10} masses at Penteli, during the sampling period 2008–2011

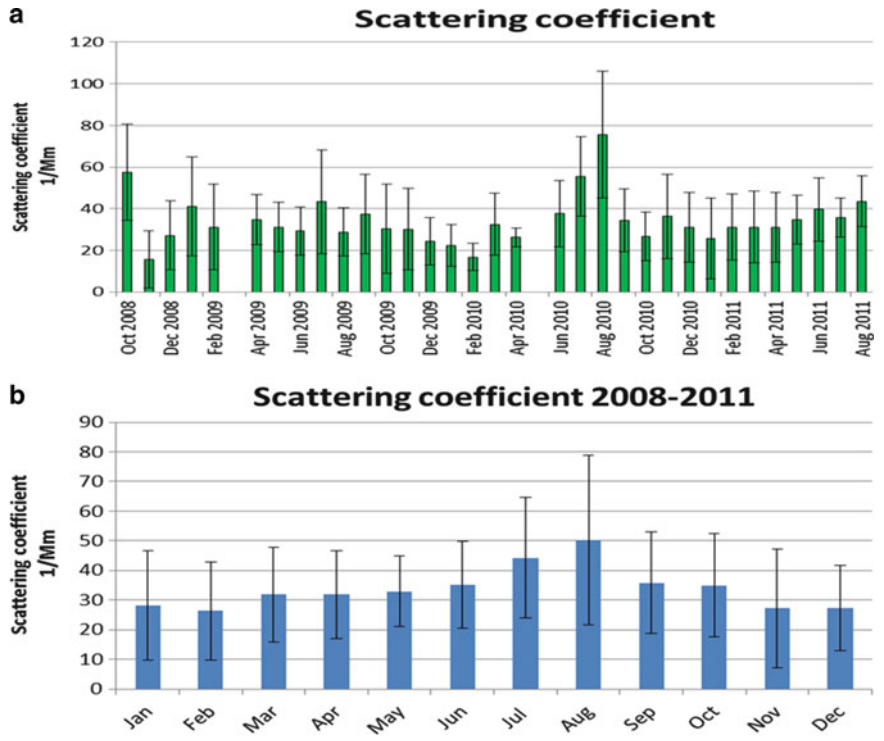

Fig. 2 Aerosol scattering coefficient at Penteli during the period 2008–2011: (**a**) monthly mean values, (**b**) whole period seasonal cycle

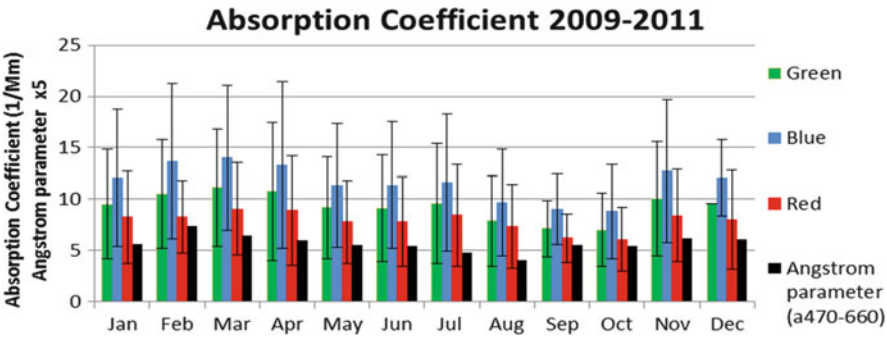

Fig. 3 Whole period seasonal cycle of the absorption coefficient at 660(*red*), 522(*green*) and 470 (*blue*) nm and the Angstrom parameter (470/660) at Penteli, during the period 2009–2011

f(RH) (Calculation of f(RH) is described in details by Sciare et al. 2005). The temporal variation of the scattering coefficient and $NH_{4x} + SO_{4y}$ concentrations seems to be similar during the investigated period (Fig. 4). The squared correlation coefficient from daily values improves from 0.49 to 0.62 ($N = 53$) when RH correction is applied. The seasonal variation of the scattering coefficient has been

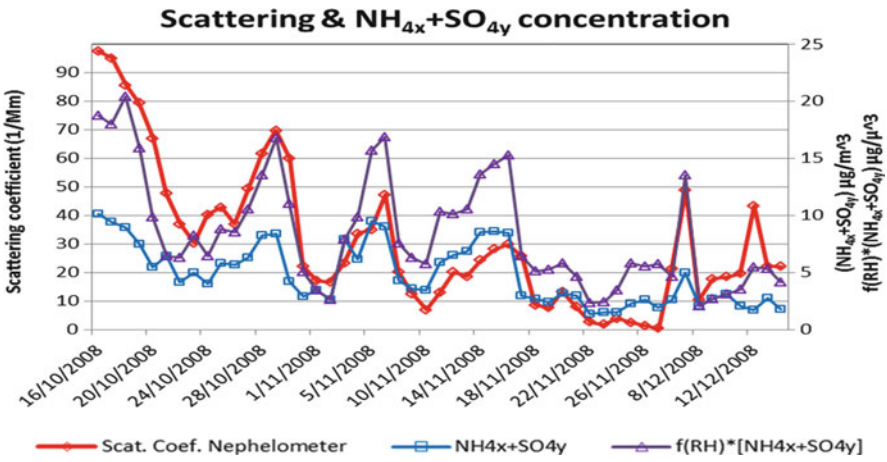

Fig. 4 Aerosol scattering coefficient and NH_{4x} + SO_{4y} concentration at Penteli, for the period October–December 2008. Correction of NH_{4x} + SO_{4y} concentrations for hygroscopic growth is also plotted (*green* line)

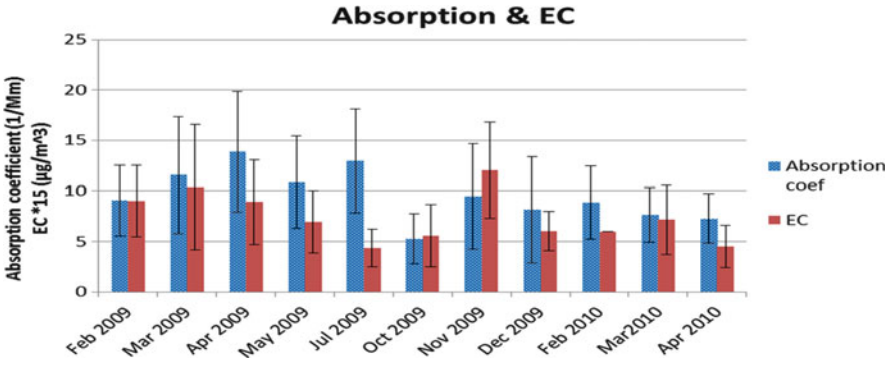

Fig. 5 Monthly means of the absorption coefficient and EC concentrations at Penteli, for the period February 2009–April 2010

compared to OC concentration, for the period October 2008–April 2010, with no obvious matching. The seasonality of the absorption coefficient and EC concentration, during the period February 2009–April 2010, is presented in Fig. 5, showing significant covariance (Squared correlation coefficient from daily values $R^2 = 0.28$, $N = 244$).

4 Summary and Conclusions

This paper presents the first long term study of the relation between optical and chemical properties of aerosols, in the region of Athens.

Ambient scattering coefficients at Penteli show significant seasonality with maximum values during summer. The mean scattering coefficient at Penteli is 34.6 Mm^{-1} and is highly correlated to NH_{4x} + SO_{4y} concentration which seems to contribute significantly to scattering. The covariance improves significantly if water uptake by NH_{4x} + SO_{4y} is taken into account and accordingly corrected.

The absorption coefficient recorded at Penteli shows mean values 8.02, 9.46 and 11.86 Mm^{-1} at 660, 522 and 470 nm, respectively; presents maximum during late winter and spring, while minimum is found in late summer to autumn. The Angstrom exponent calculated from the absorption coefficients indicates fine absorbing particles in the colder period. The high covariance between the absorption coefficient and EC concentrations is indicative of the significant absorbing role of the latter at urban environments. Additionally, the correlation between the mineral dust levels and the absorption coefficient could constitute the subject of our future study.

Acknowledgments This research has been co-financed by the European Union (European Social Fund – ESF) and Greek national funds through the Operational Program "Education and Lifelong Learning" of the National Strategic Reference Framework (NSRF) – Research Funding Program: Heracleitus II. Investing in knowledge society through the European Social Fund.

References

Draxler RR, Rolph GD (2003) HYSPLIT (HYbrid Single-Particle Lagrangian Integrated Trajectory) Model access via NOAA ARL READY Website (http://www.arl.noaa.gov/ready/hysplit4.html). NOAA Air Resources Laboratory, Silver Spring, MD

Koulouri E, Saarikoski S, Theodosi C, Markaki Z, Gerasopoulos E, Kouvarakis G, Mäkelä T, Hillamo R, Mihalopoulos N (2008) Chemical composition and sources of fine and coarse aerosol particles in the Eastern Mediterranean. Atmos Environ 42:6542–6550. doi:10.1016/j.atmosenv.2008.04.010

Moffet RC, Prather KA (2009) In-situ measurements of the mixing state and optical properties of soot with implications for radiative forcing estimates. Proc Natl Acad Sci 106:11872–11877. doi:10.1073/pnas.0900040106

Sciare J, Oikonomou K, Cachier H, Mihalopoulos N, Andreae MO, Maenhaut W, Sarda-Esteve R (2005) Aerosol mass closure and reconstruction of the light scattering coefficient over the Eastern Mediterranean Sea during the MINOS campaign. Atmos Chem Phys 5:2253–2265

Theodosi C, Im U, Bougiatioti A, Zarmpas P, Yenigun O, Mihalopoulos N (2010) Aerosol chemical composition over Istanbul. Sci Total Environ 408(12):2482–2491. doi:10.1016/j.scitotenv.2010.02.039

Vrekoussis M, Liakakou E, Koc-ak M, Kubilay N, Oikonomou K, Sciare J, Mihalopoulos N (2005) Seasonal variability of optical properties of aerosols in the Eastern Mediterranean. Atmos Environ 39:7083–7094. doi:10.1016/j.atmosenv.2005.08.011

Zhang R, Khalizov AF, Pagels J, Zhang D, Xue H, McMurry PH (2008) Variability in morphology, hygroscopicity, and optical properties of soot aerosols during atmospheric processing. PNAS 105:10291–10296. doi:10.1073/pnas.0804860105

Atmospheric Circulation Role on Air Pollutants (PM_{10}, NO_X, O_3): Two Different Approaches

St. Pateraki, D.N. Asimakopoulos, H.A. Flocas, Th. Maggos, and Ch. Vasilakos

Abstract Hourly PM_{10}, NO_X and O_3 samples were collected simultaneously, at a rural rapid developing area, the Mesogia Plain. The measurements took place both winter (10) and summer (10) days, at five different sites of the area, during the period of 2008. The influence of the synoptic and mesoscale circulation on the configuration of the obtained air pollution patterns, is the motivation of the specific work. Two different approaches were adopted. Following the first one, the day by day synoptic conditions were classified at the isobaric level of 850 hPa. The classification scheme resulted in six synoptic categories. Following the second approach, the experimental days were classified according to the prevailing pressure systems on the surface charts, resulting into three different types. Then, with the aid of hourly wind data, five different mesoscale patterns were identified. The data analysis verified the significance of the prevailing meteorological conditions. However, the key role of the emissions, the difference on the character of the air pollutants as well as the complicity of the aerosols sources proved to be determinant for the absence of significant relationship between the inorganic pollutants and PM_{10}.

S. Pateraki (✉)
Environmental Research Laboratory/INT-RP, National Centre for Scientific Research "DEMOKRITOS", 15310, Aghia Paraskevi Attikis, P.O.B. 60228, Athens, Greece

Department of Environmental Physics and Meteorology, University of Athens, University Campus, Building PHYS-5, 157 84 Athens, Greece
e-mail: stella@ipta.demokritos.gr

D.N. Asimakopoulos • H.A. Flocas
Department of Environmental Physics and Meteorology, University of Athens, University Campus, Building PHYS-5, 157 84 Athens, Greece

T. Maggos • C. Vasilakos
Environmental Research Laboratory/INT-RP, National Centre for Scientific Research "DEMOKRITOS", 15310, Aghia Paraskevi Attikis, P.O.B. 60228, Athens, Greece

C.G. Helmis and P.T. Nastos (eds.), *Advances in Meteorology, Climatology and Atmospheric Physics*, Springer Atmospheric Sciences,
DOI 10.1007/978-3-642-29172-2_163,

1 Introduction

Air pollution constitutes one of the major problems in urban areas due to their complex topography, the population shift, the increased industrialization as well as the continuously increasing emissions. Estimating the exposure of population to air pollutants levels is very important in order to identify the possible health effects as well as to take specific policy measures for pollution abatement where required (Chaloulakou et al. 2008). In line with such scientific demands, many studies have focused in the monitoring of the inorganic NO_X, the photochemical O_3 and especially the airborne particles which are thought to be one of the most important atmospheric pollutants in the European countries. Despite the increasing number of recent studies around the world, the understanding and the connection between the pollutants' behaviour and the meteorology, is still not clear. The aim of the specific work is not simply to quantify the concentrations of the NO_X, the O_3 as well as the PM_{10}, but also to investigate the role of atmospheric circulation on the obtained air quality status.

2 Data and Methodology

Measurements were conducted simultaneously at five different sites (1: Markopoulo, 2: Koropi, 3: Spata, 4: Glika Nera, 5: Palini) in the greater area of Mesogia, in the east direction of the Athens Basin (Fig. 1). The examined area is a rural but surprisingly rapid developing area, with significant interaction with the center part of the basin. Traffic is the only source for all the stations of our network with an additional existence of a quarry at Markopoulo.

2.1 Data

Thirty minutes averaged meteorological, inorganic pollutants (NO_X, O_3) as well as aerosol (PM_{10}) data were provided in continuous basis by the stations of the Environmental Services Department of the Athens International Airport S.A. The fieldwork took place in 2008, covering a 20 days period, both summer and winter.

2.2 Methodology

Two different approaches were followed in the specific work in order to explain the meteorology role on the observed aerosol patterns.

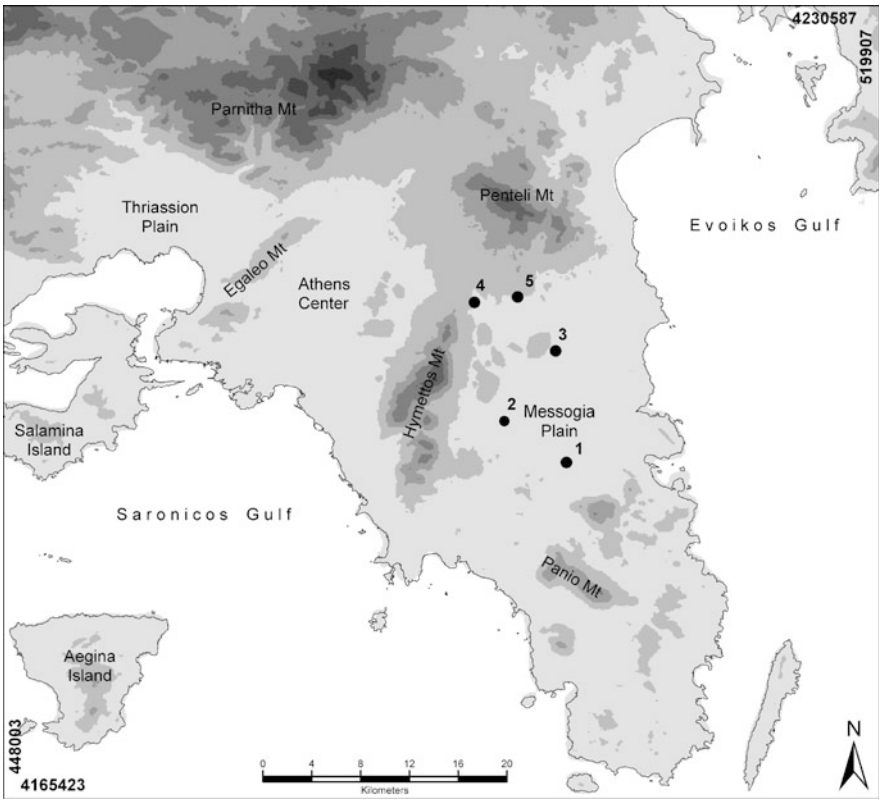

Fig. 1 Map of the sampling area

During the first approach, day by day synoptic conditions were classified over the Attica peninsula according to Kassomenos et al. (1998). The isobaric level of 850 hPa was selected because it is representative of the lower troposphere, independently of any topographic affects. This classification scheme results in six synoptic categories which are demonstrated to be statistically distinct for the greater Athens area: Southwesterly (SW) flow, Northwesterly (NW) flow, Long-wave trough (LW), ZONAL flow, Open anticyclone (OA) and High-low pressure (HL). More details on the description of the categories can be found in Kassomenos et al. (1998).

In the second approach, the environment-to-circulation approach was followed (Yarnal 1993), by identifying circulation schemes specifically assessed on the certain experimental days. For this purpose, surface synoptic maps at 0,000 and 1,200 UTC were employed, as derived from the European Meteorological Bulletin Archive. Specifically, the experimental days were classified according to the prevailing pressure systems on the surface charts. This classification results in the verification of Anticyclonic, Cyclonic and HL (Combination of High-Low) days. Then, the mesoscale wind regime was investigated following the classification of

Helmis et al. (1997). It was found that five different wind patterns influence the Plain: Type A: Pure sea breeze circulation (Saronikos and Evoikos gulf cells), Type B: Strong interaction of the sea breeze with northerly synoptic wind, Type C: Strong northerly component synoptic wind, Type D: Strong southerly component synoptic wind, Type F: Strong westerly component synoptic wind.

3 Results

The total mean NO_X, O_3 and PM_{10} levels, at all the stations, did not exceed 62.9, 132.7 and 78.1 μg/m^3, respectively. The flat terrain and the three mountains (Panio, Hymettos, Penteli) which surround the stations and cut them off from the Athens Basin might be the explanation for their homogeneity.

Generally, the most serious traffic problems (NO_X peaks) were obtained at Glika Nera and Spata. As it was expected, the ozone levels were the lowest at these two stations while the highest concentrations were recorded at Palini and Koropi. The maximum mean PM_{10} values were registered at Markopoulo maybe due to the quarry existence. It is well-known that emissions from the construction activities are related with bigger diameter particles (Pateraki et al. 2010).

During the winter period, the O_3 and PM_{10} problems concentrate mainly at Koropi and Markopoulo, respectively, while the highest NO_X values were recorded at Spata. During the summer period, the O_3, NO_X and PM_{10} peaks were obtained at Palini, Glika Nera and Koropi, respectively. It should be mentioned the increased summer O_3 values due to its photochemical nature as well as the decreased NO_X levels due to the less traffic emissions. With the only exception being Koropi, the increased winter emissions and the favourable meteorological conditions appeared to be responsible for the particles behaviour.

The hourly variations of the air pollutants are mainly caused by the changing emission differentiations and meteorological conditions. Local traffic emissions dominate the NO_X concentrations during the daytime and especially during traffic rush hours. Their daily cycles are characterized by a morning maximum or in other words ‘fresh emissions’, resulting from the traffic peak around 7:30–8:00 a.m. As far as O_3 is concerned, it usually reaches its higher values between 13:00 and 15:30 p.m., due to the enhancement of the solar radiation. It is important to highlight the differentiation and the complexity of the PM_{10} character (Fig. 2).

The different nature of the O_3, NO_X and PM_{10} being combined with the complex aerosols character and the variety of their sources might be the case for different dependence of the pollutants behavior to the different prevailing meteorological conditions. This assumption may be further supported by the usual absence of statistically significant associations between the investigated pollutants.

Following the categorization according the isobaric level of 850 hPa, the Open Anticyclone category prevails in the 40% of the whole experimental period, being followed by the Zonal flow category. PM_{10} and O_3 peaks were detected during the HL days with the only exception the Koropi station where the inorganic pollutants

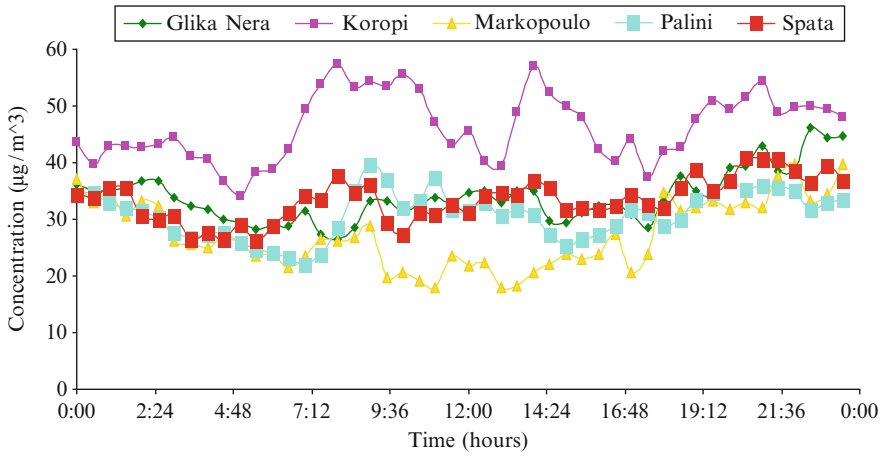

Fig. 2 Hourly variation of PM_{10} during the whole experimental period

were favored during the Open Anticyclone days. The result may be further explained by the increased temperature values during the specific days. It is well-known the photochemical nature of O_3 as well as the significant PM_{10} mass constitution by the secondary $PM_{2.5}$. As far as NO_X are concerned, the obtained picture was complicated maybe due to the non uniform distribution of the traffic emissions. Specifically, NW and SW days enhanced their levels at Glika Nera, Palini, Spata, and Markopoulo, respectively, while HL days at Koropi.

In accordance with the prevalence of the different pressure systems, cyclone days were dominant (40%), being followed by the Anticyclone (30%). With the only exception Palini where the Cyclone days enhanced the air pollutants accumulation, high pressure systems and HL days enhanced the NO_X and O_3 levels, respectively. A different behavior was obtained for PM_{10} with their maximum values being recorded during the Cyclone days, except for Koropi when this occurs under HL days. During different atmospheric surface circulation types, the specific pollutants' behavior was more complicated. A, B and D types increased NO_X values at Glika Nera and Spata, Koropi and Markopoulo as well as at Palini, respectively. A uniform behavior was obtained for O_3 and PM_{10} with their maximum values during the HL or type C days and Cyclone or type D days, respectively.

The seasonal dependence of the pollutants on the prevailing circulation type, the obtained picture is complicated highlighting the determinant role of the emissions. An indicative example is the PM_{10} behavior during the different experimental periods (Fig. 3).

Investigating the hourly variations of the three pollutants under different meteorological scenarios, a common behavior was not obtained. Irrespectively of the prevailing atmospheric circulation type, O_3 proved to be mainly governed by its photochemical nature, presenting its peaks from 12:00 to 17:00. For the other two pollutants, the variability of the emissions was determinant.

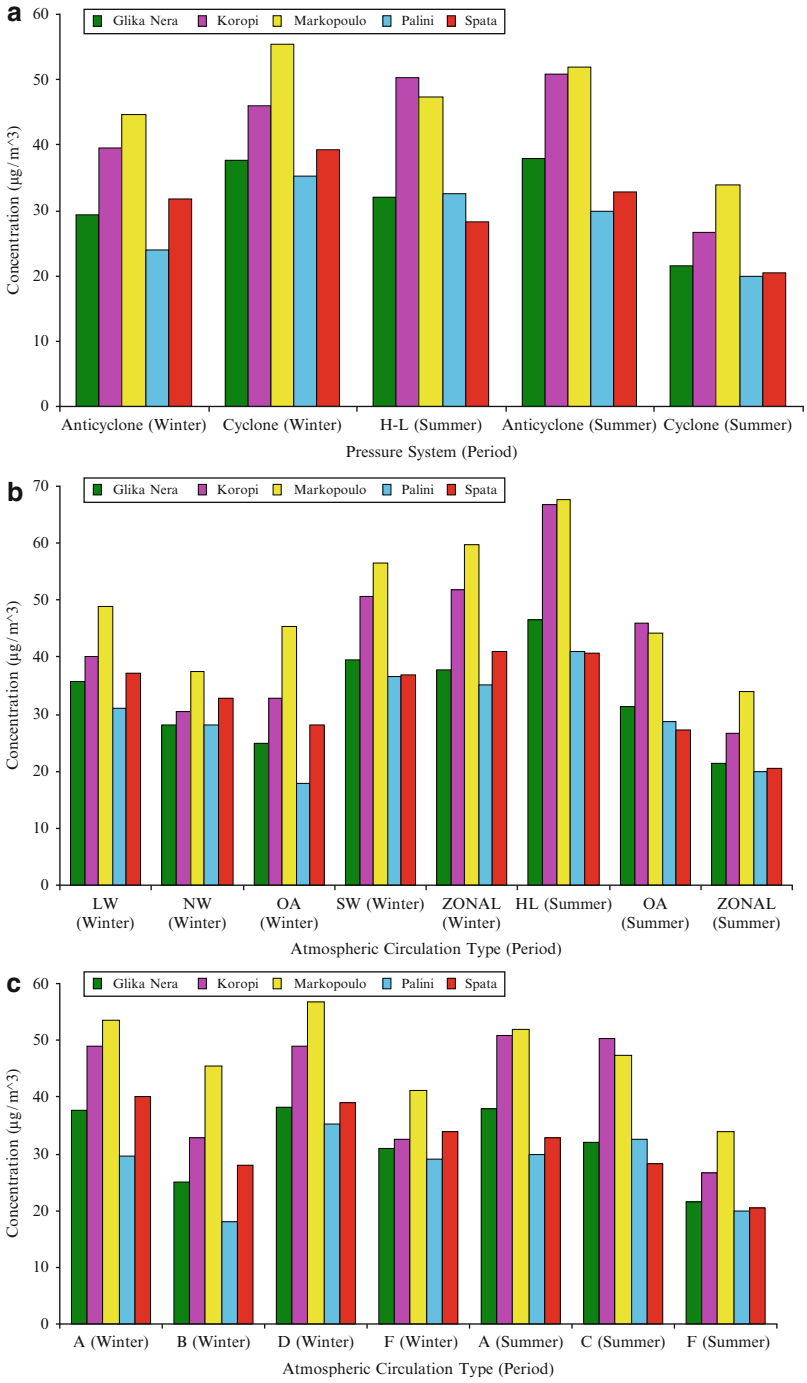

Fig. 3 Seasonal variation of PM_{10} during the different prevailing (**a**) atmospheric circulation types at 850 hPa, (**b**) pressure systems and (**c**) atmospheric circulation surface types

4 Conclusions

The data reported in this study constitute the results of 20 days parallel inorganic pollutants and aerosols measurements in five different sites across the west direction of the Athens Basin. The experimental campaign covered both cold and warm period while different meteorological scenarios were discussed in order to obtain a better picture for the pollution problems of the area.

The corresponding mean concentrations spatially ranged between 19.8 and 28.9 $\mu g/m^3$, 77.0–94.8 $\mu g/m^3$ and 31.0–50.0 $\mu g/m^3$ for NO_X, O_3 and PM_{10} respectively, between the network stations.

1. Irrespectively of the meteorological approach, the results clearly indicate the prevalence of emissions (local or non) over the meteorology, for the obtained particulate pollution picture. On the contrary, the inorganic pollutants behavior was equally governed by both emissions and meteorology.
2. The variability of the emissions as well as their strength being combined with the both primary and secondary PM origin might be the explanation not only for the insignificant associations with the inorganic pollutants but also for the different spatial and temporal particles behaviour.
3. With O_3 being the exception, the hourly variations of both NO_X and PM_{10} appeared to be closely dependant on the hourly variations of the emissions.

Acknowledgments The authors would like to thank the Environmental Services Department of the Athens International Airport S.A. for providing us the air pollution and the meteorological data.

References

Chaloulakou A, Mavroidis I, Gavriil I (2008) Compliance with the annual NO2 air quality standard in Athens. Required NOx levels and expected health implications. Atmos Environ 42:454–465. doi:10.1016/j.atmosenv.2007.09.067

Helmis CG, Asimakopoulos DN, Papadopoulos KH, Kassomenos P, Kalogiros JA, Papageorgas PG, Blikas S (1997) Air mass exchange between the Athens basin and the mesogia plain on Attica, Greece. Atmos Environ 31:3833–3849. doi:10.1016/S1352-2310(97)00169-6

Kassomenos P, Flocas HA, Lykoudis S, Petrakis M (1998) Analysis of mesoscale patterns in relation to synoptic conditions over an urban Mediterranean basin. Theor Appl Climatol 59:215–229. doi:10.1007/s007040050025

St P, Asimakopoulos DN, Maggos Th, Vasilakos Ch (2010) Particulate matter levels in a suburban Mediterranean area: analysis of a 53-month long experimental campaign. J Hazard Mater 182:801–811. doi:10.1016/j.jhazmat.2010.06.108

Yarnal B (1993) Synoptic climatology in environmental analysis. Belhaven Press, London

Annual Variation of Benzene Concentrations Over Western Athens Area During the Year 2009

M. Petrakis, B. Psiloglou, A.G. Paliatsos, L. Drivas, and G. Zotos

Abstract The Institute for Environmental Research and Sustainable Development of the National Observatory of Athens in collaboration with the Technological Educational Institute of Piraeus (TEIP) has installed a Differential Optical Absorption Spectroscopy (DOAS) system at the TEIP campus in order to study the atmospheric pollution impacts in the western Athens area, aiming at the representation of the air pollution levels in a particularly polluted urban area. This system, operating on a continuous basis, measures the concentration of the main pollutants (O_3, NO_2, SO_2) as well as BTX (benzene, toluene, xylene). The main objective of this study is to analyse the mean hourly benzene concentrations measured by the DOAS system for the whole of 2009 in order to study both the diurnal and the seasonal variation. The major finding is that the mean seasonal variation of the examined air pollutant presents a minimum during the warm period of the year and a maximum during the cold period. The mean diurnal variation of benzene concentrations is characterized by a double peak structure. The mean values of benzene concentration for the whole year were found equal to 5.97 $\mu g/m^3$, which is in accordance with the EU upper limit value of 6 $\mu g/m^3$ for the year 2009.

M. Petrakis • B. Psiloglou (✉)
Institute for Environmental Research and Sustainable Development, National Observatory of Athens, P. Penteli, GR-15236 Athens, Greece
e-mail: bill@meteo.noa.gr

A.G. Paliatsos
General Department of Mathematics, Technological Educational Institute of Piraeus, Athens, Greece

L. Drivas • G. Zotos
Electronic Computer Systems Engineering Department, Technological and Education Institute of Piraeus, Athens, Greece

C.G. Helmis and P.T. Nastos (eds.), *Advances in Meteorology, Climatology and Atmospheric Physics*, Springer Atmospheric Sciences,
DOI 10.1007/978-3-642-29172-2_164,

1 Introduction

The city of Athens, located in an area of complex topography within the Athens basin (~450 km^2), has an elongated shape in the NE-SW direction, surrounded by mountains with heights ranging from 400 to 1,500 m at the western, northern and eastern sides, and sea (Saronikos Gulf) at the south. To the east of the basin's axis, the city is less densely populated. To the west, the area is designated as 75% industrial and 25% residential. Urban traffic represents the main source of air atmospheric pollution in terms of gases and aerosols, in the greater urban area.

The prevailing winds in the Athens basin blow from N and NE in late summer, fall and winter and from SSW and SW in the spring and early summer. These NE and SW directions coincide with the major geographical axis of the basin. The ventilation of the basin is poor during the prevalence of local circulation systems, such as sea-land breezes along the major NE-SW geographical axis of the basin, making Athens to be considered as a typical example of a city with frequent episodes of photochemical air pollution. Various researchers examined the characteristics of inversions and the influence of various meteorological parameters on air pollution episodes (Katsoulis 1988).

In order to study the effects of the pollution cycle and especially benzene concentration, the Institute of Environmental Research and Sustainable Development of the National Observatory of Athens has installed a DOAS measuring system in the Athenian suburb of Aegaleo, at the TEIP facilities. This system, unique in the greater Athens area, monitors basic air pollutants (O_3, NO_2, SO_2), as well as other compounds such as benzene, toluene, p-m-xylene (BTX) using the DOAS method. A detailed description of the DOAS system is given elsewhere (Petrakis et al. 2003).

Traffic is the main source of aromatics in the urban atmosphere emitted in fuel type specific ratios, while the only significant atmospheric removal process is through the reaction with OH during daytime.

Due to the toxicity and carcinogenicity of benzene, the European Union (EU) has published a directive proposed the whittling down of ambient air benzene concentrations up to 2010 to negligible ones since there is no safe limit for benzene concerning the carcinogenicity of this toxic pollutant. Nevertheless, EU set a temporal annual limit value for benzene (5 $\mu g/m^3$) for December 2000 with a 100% (5 $\mu g/m^3$) tolerance. The latter must be reduced by 2006 to 4 $\mu g/m^3$ and every 12 months thereafter by 1 $\mu g/m^3$ to reach 0% by 1/1/2010. In the same directive an upper and lower assessment threshold introduced concerning the 70% and 40% of the annual limit value respectively (EU 2000).

The aim of this study is to analyse the mean hourly measurements for benzene concentration for the western Athens area using the DOAS method. Measurements were made in a heavy traffic area in the SW suburbs of Athens, in the vicinity of the TEIP in Aegaleo.

2 Methodology and Data

The DOAS technique, pioneered by Platt and his co-workers (Platt et al. 1979) is a non-contact air pollution monitoring technique. A full description of the DOAS technique is given elsewhere (Edner et al. 1993; Kourtidis et al. 2000; Petrakis et al. 2003; Triantafyllou et al. 2008).

In this work, mean hourly benzene concentration measurements, for a 1-year period, 2009, are used. The data obtained by the DOAS system (OPSIS AR-500) that was operating in the Athenian suburb of Aegaleo, inside the TEIP campus. A detailed description of the monitoring site is found in a relevant publication (Petrakis et al. 2003). Mean pollutant concentrations were averaged for each month, and day. For the diurnal variation study, seasonal averages for each hour of the day were also calculated.

3 Results

In Greece, the annual cycle can be divided climatologically in cold and wet period (October–March) and in warm and dry period (April–September), while the months of October and April can be characterized as transition months (Metaxas et al. 1999).

Figure 1 depicts that the seasonal variation of the examined air pollutant concentrations appears a minimum during the warm period of the year and a maximum during the cold period. Mean monthly values of benzene concentrations vary between 5.33 and 6.97 $\mu g/m^3$, with a mean value of 5.97 $\mu g/m^3$ for the whole year, which is in accordance with the EU upper limit value of 6 $\mu g/m^3$ for the year 2009.

The mean diurnal variation of the examined air pollutant concentrations appears a double peak pattern, as it is shown in Fig. 2. The dominant peak is observed during the morning hours and the secondary peak during evening hours, coinciding apparently with peaks of the local activities (e.g. traffic, open market hours). Similar patterns of benzene mean diurnal variation also have been observed in other Greek cities (Kourtidis et al. 2000; Triantafyllou et al. 2008).

With the aim of distinguishing weekly variations in the measurements, the diurnal profiles of benzene, as averaged for the entire period of observations, are shown in Fig. 3. Note that the diurnal cycle of benzene has a double-sinusoidal peak shape with levels of benzene comparatively higher on weekdays than at weekends. The two maxima correlate very precisely with the rush hours from Monday to Friday. However, the benzene profiles are significantly altered during the weekend indicating a change in the traffic pattern. Also, quantitatively, the decrease in the

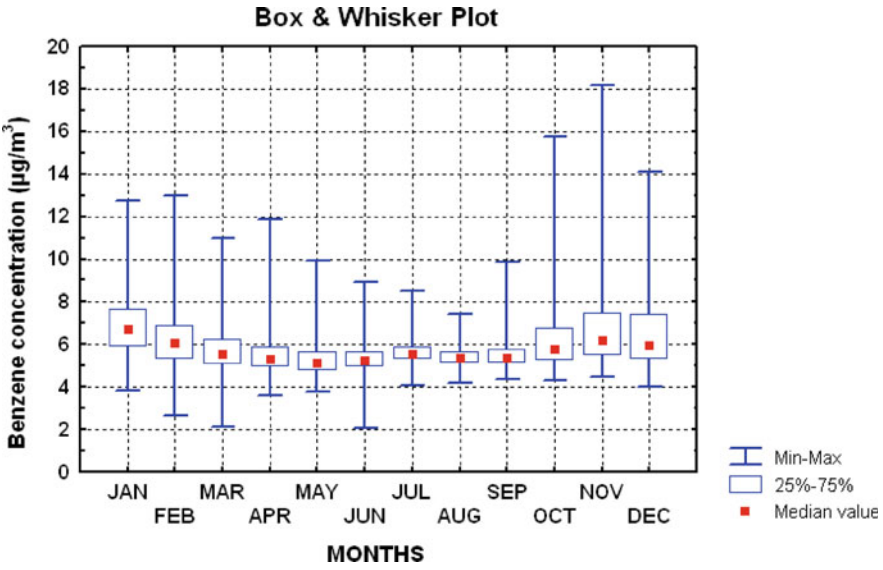

Fig. 1 Box & Whisker plots of benzene mean hourly concentrations, at TEIP measuring site, during the year 2009

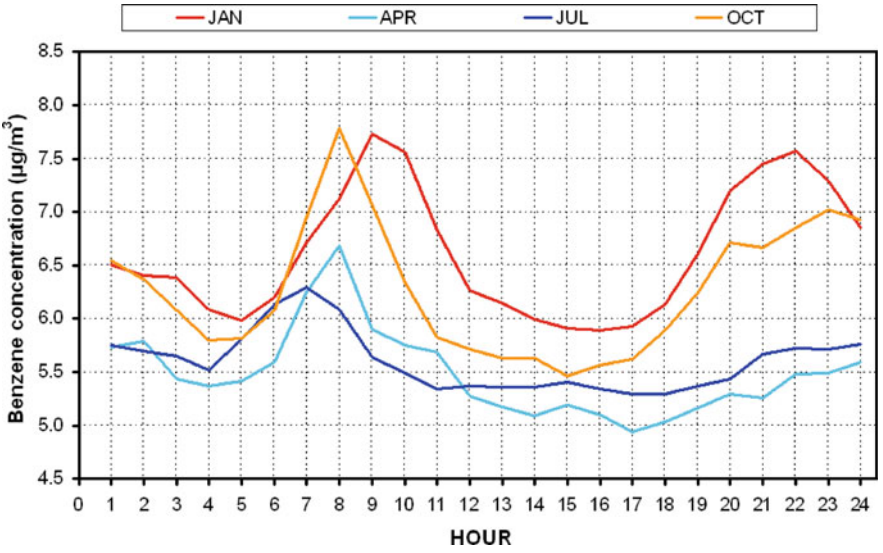

Fig. 2 Mean diurnal variation of the hourly averaged benzene concentrations, for the four characteristic months, January, April, July and October, at TEIP measuring site, during the year 2009 (1 = 0:01–1:00, 2 = 1:01–2:00, 3 = 2:01–3:00, . . ., 24 = 23:01–24:00 LST)

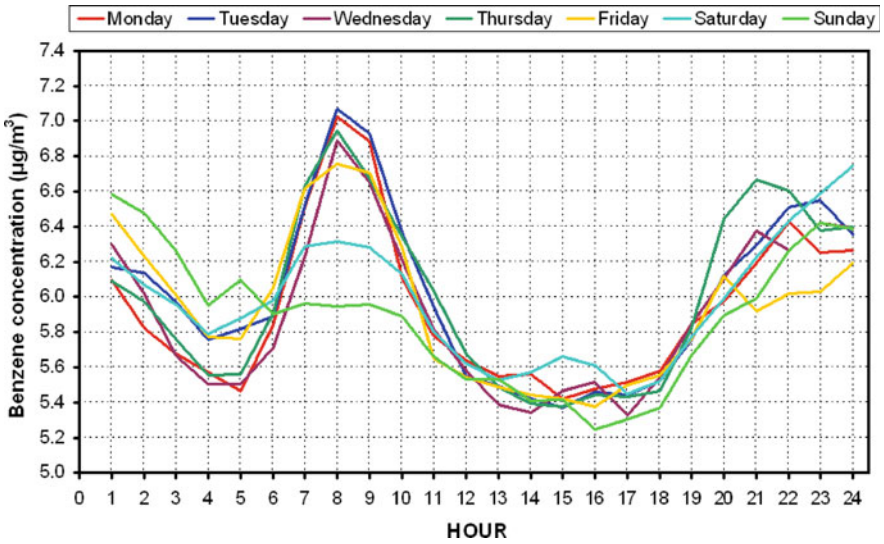

Fig. 3 Mean diurnal variation of benzene concentrations for each week day, at TEIP measuring site, during the year 2009 (1 = 0:01–1:00, 2 = 1:01–2:00, . . ., 24 = 23:01–24:00 LST)

benzene concentrations during weekends could be a consequence of the reduction in motor traffic on those 2 days of the week.

Figure 4 shows the frequency distribution of benzene mean hourly concentration values, measured during the four representative months (January, April, July and October) at TEIP measuring site.

As it can be seen from Fig. 4, most of the mean hourly values of benzene concentration vary between 4.5 and 6.5 μg/m^3, especially in the warm and dry period (July), as well as in the transition months (October and April), which can be attributed to the seasonal variation of the studied air pollutant.

4 Conclusions

The hourly benzene concentrations measured by the DOAS system for 2009 were examined in order to study both the diurnal and the seasonal variation. From this analysis the following major conclusions can be outlined:

1. The mean seasonal variation of the examined air pollutant concentrations presents a minimum during the warm period of the year and a maximum during the cold period.

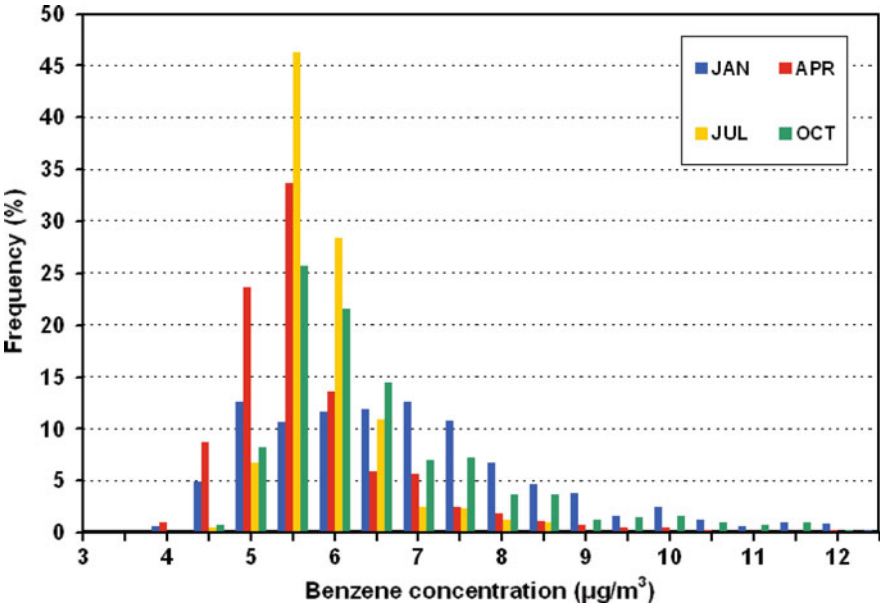

Fig. 4 Frequency distribution of benzene mean hourly concentrations monitored at TEIP measuring site, during the year 2009 (5 = 4.51–5.0 μg/m^3, 5.5 = 5.01–5.5 μg/m^3, 6 = 5.51–6.0 μg/m^3)

2. A pronounced diurnal structure is observed at the examined air pollutant, while local sources introduce differences in the amplitude of the diurnal variation observed at each examined month.
3. Mean monthly values of benzene concentrations vary between 5.33 and 6.97 μg/m^3, with a mean value of 5.97 μg/m^3 for the whole year, which is in accordance with the EU upper limit value of 6 μg/m^3 for the year 2009.

References

Edner H, Ragnarson P, Spannare S, Svanberg S (1993) Differential optical absorption spectroscopy (DOAS) system for urban atmospheric pollution monitoring. Appl Opt 32:327–333. doi:10.1364/AO.32.000327

EU (2000) Council Directive 2000/69/EC of the European Parliament and the Council (2000). Limit values for benzene and carbon monoxide in ambient air. Official Journal of the European Communities, L313 of 13/12/2000, pp 12–22

Katsoulis BD (1988) Some meteorological aspects of air pollution in Athens, Greece. Meteorol Atmos Phys 39:203–212. doi:10.1007/BF01030298

Kourtidis K, Ziomas I, Zerefos C, Gousopoulos A, Balis D, Tzoumaka P (2000) Benzene and toluene levels measured with a commercial DOAS system in Thessaloniki, Greece. Atmos Environ 34:1471–1780. doi:10.1016/S1352-2310(99)00375-1

Metaxas DA, Philandras CM, Nastos PT, Repapis CC (1999) Variability of precipitation pattern in Greece during the year. Fresen Environ Bull 8:1–6

Petrakis M, Psiloglou B, Kassomenos PA, Cartalis C (2003) Summertime measurements of benzene and toluene in Athens, using a DOAS system. J Air Waste Manage Assoc 53:1052–1064

Platt U, Perner D, Patz HW (1979) Simultaneous measurements of atmospheric CH_2O, O_3 and NO_2 by differential optical absorption. J Geophys Res 84:6329–6335. doi:10.1029/JC084iC10p06329

Triantafyllou AG, Zoras S, Evangelopoulos V, Garas S, Diamantopoulos C (2008) DOAS measurements above an urban street canyon in a medium sized city. Global Nest J 10:161–168

Properties of Aged Aerosols in the Eastern Mediterranean

M. Pikridas, L. Hildebrandt, E. Kostenidou, G.J. Engelhart, B.H. Lee, N. Mihalopoulos, and S.N. Pandis

Abstract Three month-long campaigns (FAME-07, -08, -09, -11) have been conducted at Finokalia in order to assess the water uptake, volatility and oxidation state of aged organic particulate matter (PM) along with aerosol nucleation. Finokalia is a remote coastal station located in the southeast of the Mediterranean Sea on the island of Crete, Greece. The site lacks local sources as there is no notable human activity at a range of approximately 15 km. The PM that reaches the site is heavily influenced by the surrounding source regions and the organic content highly oxidized. During the summer aerosols always contained water even under very low relative humidity (RH $<$ 20%) possibly due to their acidity. Organic aerosol was highly and almost uniformly oxidized and the resulting mass spectra did not change throughout the summer campaign, even after it was thermally treated, indicating a high oxidation state. An organic aerosol evaporation model was used to simulate the behaviour of the thermally treated aerosol and showed that aged organic PM was two or more orders of magnitude less volatile than laboratory-generated secondary organic PM. Nucleation is controlled by the gas phase ammonia levels and the resulting PM acidity, at least during the summer, resulting in low number of particle formation events per year.

M. Pikridas (✉) • E. Kostenidou
Institute of Chemical Engineering and High Temperature Chemical Processes, Patra, Greece
e-mail: mpikridas@chemeng.upatras.gr

L. Hildebrandt • G.J. Engelhart • B.H. Lee
Center for Atmospheric Particle Studies, Carnegie Mellon University, Pittsburgh, PA, USA

N. Mihalopoulos
Institute of Chemical Engineering and High Temperature Chemical Processes, Patra, Greece

Environmental Chemical Processes Laboratory, University of Crete, Heraklion, Greece

S.N. Pandis
Institute of Chemical Engineering and High Temperature Chemical Processes, Patra, Greece

Center for Atmospheric Particle Studies, Carnegie Mellon University, Pittsburgh, PA, USA

C.G. Helmis and P.T. Nastos (eds.), *Advances in Meteorology, Climatology and Atmospheric Physics*, Springer Atmospheric Sciences,
DOI 10.1007/978-3-642-29172-2_165,

1 Introduction

Even though the importance of particulate matter (PM) has been recognized for several decades, significant gaps remain in our understanding of its sources and atmospheric transformations. The greatest uncertainty concerns organic aerosol (OA) which is composed of thousands of species, many of them unidentified (Goldstein and Galbally 2007) originating from a myriad of sources. The volatility of atmospheric OA is one of its most important physical properties determining its ambient concentration, providing indirect information about its chemical composition and reflecting its origin and history in the atmosphere (Jonsson et al. 2007). The presence of OA complicates the effect of water in ambient PM, which can only be predicted accurately if the particles contain only simple inorganic salts.

New particle formation (NPF) in the atmosphere is frequently observed at many different sites around the world (Kulmala et al. 2004) and is of interest due to the particles' effect on radiative forcing, cloud formation and lifetime (Charlson and Heitzenberg 1995). Previous studies have suggested that NPF may be limited by: meteorological variables (Boy and Kulmala 2002), particle acidity (Jung et al. 2008) or the presence of organic gases (Kanawade et al. 2011).

A series of Finokalia Aerosol Measurement Experiments (FAME-07, -08, -09, -11) were conducted in order to improve our understanding of the physical and chemical properties of aged European aerosol as it is transported from central to south-eastern Europe. These experiments focused on the oxidation state of organics (Hildebrandt et al. 2010; Lee et al. 2010), the water uptake of aged particles under sub-saturated (Engelhart et al. 2011) and supersaturated (Bougiatioti et al. 2009) conditions as well as a mechanism behind NPF (Pikridas et al. 2012).

2 Site Description

Measurements were conducted at Finokalia (35° 240 N, 25° 600 E), a remote coastal area located in the southeast of the Mediterranean Sea on the island of Crete, Greece (Fig. 1). The station is located at the top of a hill at an elevation of 230 m facing the sea. There is no notable human activity at a range of approximately 15 km. A more detailed description of the site has been published elsewhere (Mihalopoulos et al. 1997).

3 Results

Due to the lack of strong local sources, Finokalia is heavily influenced by regional sources. During the FAME-08 campaign four main source regions were identified: Marine, Africa, Greece and other continental (Pikridas et al. 2010).

Fig. 1 Map of Greece and the island of Crete indicating the location of the sampling station

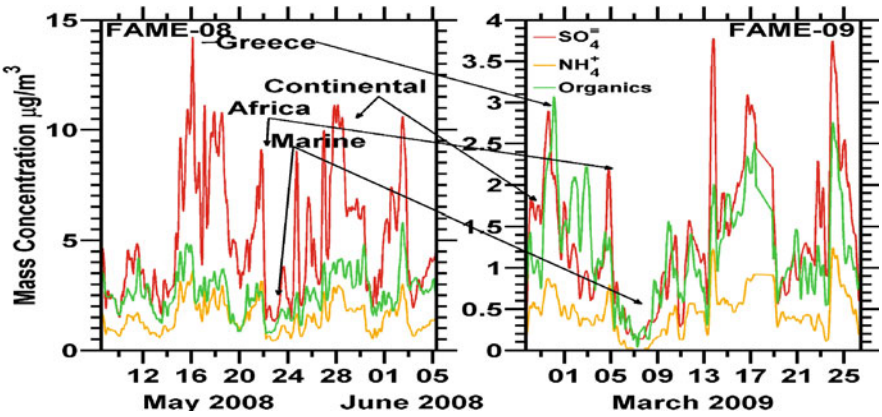

Fig. 2 Aerosol (PM_1) dry composition time series measured by the AMS for FAME-08 and -09. The effect of the surrounding source regions is noted

The concentration time series of the main dry PM_1 components, monitored by the aerosol mass spectrometer (AMS, Jayne et al. 2000; Jimenez et al. 2003), are depicted in Fig. 2. Previous studies have identified similar source regions and their influence on PM composition and visibility (Mihalopoulos et al. 1997; Sciare et al. 2003; Sciare et al. 2008). It has been shown that the air masses reach the site within 1–5 days typically from Europe because of the dominant northerly winds.

3.1 Aerosol Water and Cloud Condensation Nuclei

The PM water concentration was monitored via the Dry-Ambient Aerosol Size Spectrometer (DAASS, Stanier et al. 2004) under ambient conditions.

The particles during the summer showed no signs of efflorescence retaining as much as 10% of their water content at 20% RH, potentially because of their acidity.

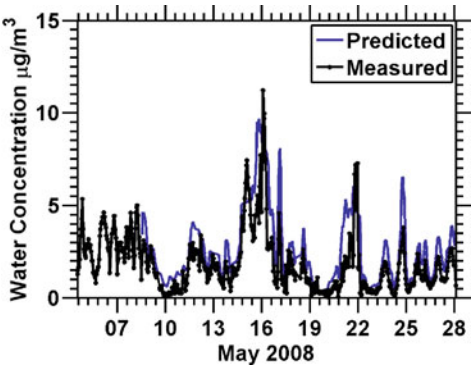

Fig. 3 Water concentration time series measured by the DAASS and calculated from E-AIM

At 50% RH, at which particulate matter mass is often measured in the European monitoring networks (Tsyro 2005), the particles still contained approximately 40% water by volume. DAASS measurements were in good agreement with aerosol thermodynamic theory (E-AIM Model II, Clegg et al. 1998) (Fig. 3) even though the effect of organics was neglected. Organics were found to increase the volume of PM by less than 5% on average which indicates a relatively small water uptake by them.

In supersaturated conditions, where particles can be activated to form cloud condensation nuclei (CCN), the effect can be quite different. The closure between predicted and measured CCN improved significantly (the error decreased 7 ± 11% to 0.6 ± 9%) when the water soluble fraction of organics was included in the calculations.

3.2 Aerosol Oxidation State

The oxidation state of organics can be accessed via the Q-AMS by following the contributions of certain mass fragments, such as f_{44} (mostly CO_2^+) and f_{57} (mostly $C_4H_9^+$), to the total organic mass. During the summer of 2008 (FAME-08) the relative contribution of f_{44} remained constant throughout the campaign indicating a high and uniform oxidation state of organics (Hildebrandt et al. 2010). The contribution of f_{44} did not change significantly as the source regions of PM shifted, nor as the aerosol was thermally treated. This suggests that 1 day of atmospheric aging – the minimum time for an air parcel to reach the site – suffices for the organic aerosol to reach an apparent oxidation plateau under the strong oxidizing conditions observed at Finokalia during the summer. Model calculations based on the thermally treated aerosol showed that the organic aerosol measured during FAME-08 is two or more orders of magnitude less volatile than laboratory-generated monoterpene (α-pinene, β-pinene and limonene under low NO_x conditions, Lee et al. 2010) as shown in Fig. 4.

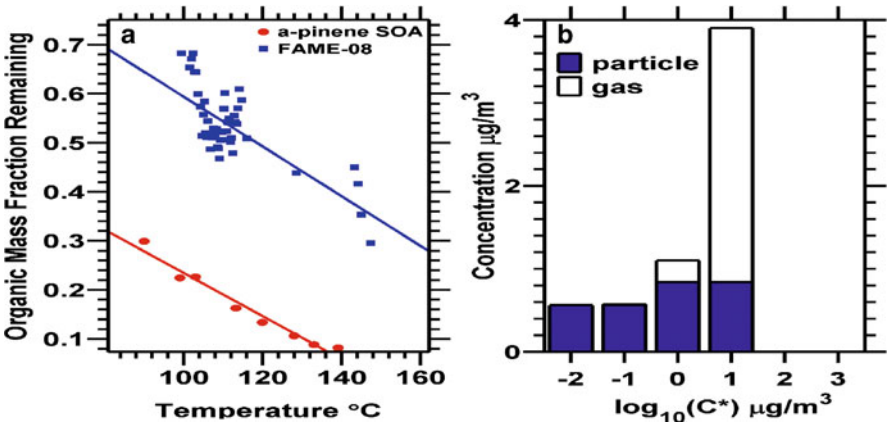

Fig. 4 (**a**) Mass fraction remaining after thermally treating aerosols for 14 s as a function of temperature during FAME-08 (*blue*) with thermogram of lab-generated α-pinene SOA (≈10 µg m^{-3}, 250 nm). Lines are linear fits to guide the eye and (**b**) the volatility distribution of aged ambient organic aerosol during FAME – 2008 for total (gas and particle phase) organic concentration of 6.2 µg m^{-3} and organic aerosol concentration of 2.8 µg m^{-3}

3.3 New Particle Formation

Nucleation under ambient atmospheric conditions is a photo induced phenomenon and is not frequent (once every 6 days on an annual average basis) at Finokalia. Surprisingly, particle formation events are more frequent during the winter than during the photochemically more active summer. This behavior is consistent with the lack of gas-phase ammonia during the summer. The high sulfate levels during this period result in acidic particles and transfer of all the available ammonia to the particulate phase. This is consistent with model calculations showing that ternary nucleation cannot occur when particles are acidic (Jung et al. 2008). Nucleation occurs more frequently in air masses that have spent significant time over land (source region Greece) before reaching the site because they are enriched with ammonia. If the ammonia levels are adequate to neutralize PM then nucleation may occur.

4 Conclusions

A series of experiments (FAME-07, -08, -09, -11) were conducted in order to assess the properties of aged aerosols. The mass spectra of OA, during the summer, remain unchanged even after thermal treatment suggesting an oxidation plateau. The volatility of these organics was at least two orders of magnitude lower than the volatility laboratory-generated SOA formed from the oxidation of monoterpenes.

Aged organics had a minor effect on the water uptake of PM under sub-saturated conditions but a non-negligible effect under supersaturated conditions. Nucleation was found to be controlled by PM acidity and the process was more frequent during the winter when particles are typically neutral.

References

Bougiatioti A, Fountoukis C, Kalivitis N, Pandis SN, Nenes A, Mihalopoulos N (2009) Cloud condensation nuclei measurements in the marine boundary layer of the Eastern Mediterranean: CCN closure and droplet growth kinetics. Atmos Chem Phys 9:7053–7066. doi:10.5194/acp-9-7053-2009

Boy M, Kulmala M (2002) Nucleation events in the continental boundary layer: influence of physical and meteorological parameters. Atmos Chem Phys 2:1–16. doi:10.5194/acp-2-1-2002

Charlson RJ, Heitzenberg RL (1995) Aerosol forcing of climate. Wiley, New York

Clegg S, Brimblecombe LP, Wexler AS (1998) A thermo-dynamic model of the system H^+-$NH4^+$-$SO42^-$-$NO3^-$-H2O at tropospheric temperatures. J Phys Chem A102:2137–2154. doi:10.1021/jp973043j

Engelhart GJ, Hildebrandt L, Kostenidou E, Mihalopoulos N, Donahue NM, Pandis SN (2011) Water content of aged aerosol. Atmos Chem Phys 11:911–920. doi:10.5194/acp-11-911-2011

Goldstein AH, Galbally IE (2007) Known and unexplored organic constituents in the Earth's atmosphere. Environ Sci Technol 41:1515–1521

Hildebrandt L, Engelhart GJ, Mohr C, Kostenidou E, Bougiatioti A, DeCarlo PF, Prevot ASH, Baltensperger U, Mihalopoulos N, Donahue NM, Pandis SN (2010) Aged organic aerosol in the Eastern Mediterranean: the Finokalia aerosol measurement experiment – 2008. Atmos Chem Phys 10:4167–4186. doi:10.5194/acp-10-4167-2010

Jayne JT, Leard DC, Zhang XF, Davidovits P, Smith KA, Kolb CE, Worsnop DR (2000) Development of an aerosol mass spectrometer for size and composition analysis of submicron particles. Aerosol Sci Technol 33:49–70

Jimenez JL, Jayne JT, Shi Q, Kolb CE et al (2003) Ambient aerosol sampling using the aerodyne aerosol mass spectrometer. J Geophys Res – Atmos 108:8425–8437

Jonsson AM, Hallquist M, Saathoff H (2007) Volatility of secondary organic aerosols from the ozone initiated oxidation of α-pinene and limonene. J Aerosol Sci 38:843–852

Jung JG, Pandis SN, Adams PJ (2008) Evaluation of nucleation theories in a sulfur-rich environment. Aerosol Sci Technol 42:495–504. doi:10.1080/02786820802187085

Kanawade VP, Tom Jobson B, Guenther AB, Erupe ME, Pressely SN, Tripathi SN, Lee S-H (2011) Isoprene suppression of new particle formation in mixed deciduous forest. Atmos Chem Phys Discuss 11:11039–11075. doi:10.5194/acpd-11-11039-2011

Kulmala M, Vehkamaki H, Petaja T, Dal Maso M, Lauri A, Kerminen V-M, Birmili W, McMurry PH (2004) Formation and growth rates of ultrafine atmospheric particles: a review of observations. J Aerosol Sci 35:143–176. doi:10.1016/j.jaerosci.2003.10.003

Lee B-H, Hildebrandt L, Kostenidou E, Riipinen I, Engelhart GJ, Donahue NM, Pandis SN (2010) Volatility of organic aerosol sampled during FAME-2008. Atmos Chem Phys 10:12149–12160. doi:10.5194/acp-10-12149-2010

Mihalopoulos N, Stephanou E, Kanakidou M, Pilitsidis S, Bousquet P (1997) Tropospheric aerosol ionic composition above the Eastern Mediterranean Area. Tellus B 49:314–326

Pikridas M, Bougiatioti K, Engelhart GJ et al (2010) The finokalia aerosol measurement experiments – 2008 (FAME-08): an overview. Atmos Chem Phys 10:6793–6806

Pikridas M, Riipinen I, Hildebrandt L, Kostenidou E, Manninen H, Mihalopoulos N, Kalivitis N, Burkhart JF, Stohl A, Kulmala M, Pandis SN. (2012) New particle formation at a remote marine site in the Eastern Mediterranean. J Geophys Res Atmos (accepted)

Sciare J, Bardouki H, Moulin C, Mihalopoulos N (2003) Aerosol sources and their contribution to the chemical composition of aerosols in the Eastern Mediterranean Sea during summertime. Atmos Chem Phys 3:291–302. doi:10.5194/acp-3-291-2003

Sciare J, Oikonomou K, Favez O, Liakakou E et al (2008) Long-term measurements of carbonaceous aerosols in the Eastern Mediterranean: evidence of long-range transport of biomass burning. Atmos Chem Phys 8:5551–5563. doi:10.5194/acp-8-5551-2008

Stanier CO, Khlystov AY, Chan WR, Mandiro M, Pandis SN (2004) A method for the in situ measurement of fine aerosol water content of ambient aerosols: the dry-ambient aerosol size spectrometer (DAASS). Aerosol Sci Technol 38:215–228

Tsyro SG (2005) To what extent can aerosol water explain the discrepancy between model calculated and gravimetric PM10 and PM2.5? Atmos Chem Phys 5:515–532. doi:10.5194/acp-5-515-2005

Study of the Impact of an Intense Biomass Burning Event on the Air Quality in the Eastern Mediterranean

A. Poupkou, K. Markakis, N. Liora, T.M. Giannaros, U. Im, N. Daskalakis, S. Myriokefalitakis, D. Melas, P. Zanis, M. Kanakidou, and C.S. Zerefos

Abstract Aim of this work is to study the impact of the intense forest fires that tookplace in Greece at the end of summer 2007 on the air quality in the Eastern Mediterranean. For this reason the meteorological model MM5 and the photochemical model CAMx are applied over the study area with 10 km spatial resolution. CAMx model is implemented for two emission scenarios; with and without biomass burning emissions. High spatial resolution wildfire emission data are used that are based on the Global Fire Emissions Database (GFED3). The CAMx chemical boundary conditions are taken from the TM4 global model. The nonradiative impact on the composition of the atmosphere and on environmental indices (e.g. Aggregate Risk Index) is quantified in regional scale. The impact of the atmospheric processes on the air pollution levels due to the biomass burning event is also studied giving more emphasis on the boundary layer. The intense biomass burning event in the Eastern Mediterranean at the end of August 2007 results in an enhancement of the CO, NOx and PM2.5 concentrations over almost all the study area, which can range from several times to two order of magnitude over the fire hot spots. The increases in O3 levels are less pronounced and are found mainly

A. Poupkou (✉) • K. Markakis • N. Liora • T.M. Giannaros • D. Melas
Laboratory of Atmospheric Physics, Aristotle University of Thessaloniki, Thessaloniki 54124, Greece
e-mail: poupkou@auth.gr

U. Im • N. Daskalakis • S. Myriokefalitakis • M. Kanakidou
Environmental Chemical Processes Laboratory, University of Crete, Irakleio 71003, Greece

P. Zanis
Department of Meteorology and Climatology, Aristotle University of Thessaloniki, Thessaloniki 54124, Greece

C.S. Zerefos
Research Centre for Atmospheric Physics and Climatology, Academy of Athens, Athens 10672, Greece

Navarino Environmental Observatory (N.E.O.), Costa Navarino, Greece

C.G. Helmis and P.T. Nastos (eds.), *Advances in Meteorology, Climatology and Atmospheric Physics*, Springer Atmospheric Sciences,
DOI 10.1007/978-3-642-29172-2_166,

downwind the burnt areas. On the 25th August 2007, when fire counts in the study area are maximum, in the daytime boundary layer, the inclusion of biomass burning emissions results in a change of the chemical regime from O3 destruction to O3 production.

1 Introduction

The summer of 2007 was among the worst fire seasons of the past decades for the Eastern Mediterranean. Large forest fires took place in Greece from late August to early September 2007. Apart from the direct tragic fire damage (human losses and a total of 195,000 ha of land burnt in Peloponnesus and Evia), large quantities of gaseous and particulate pollutants were emitted influencing the chemical composition of the atmosphere. Following, the nonradiative impact of this intense biomass burning event on the air quality in the Eastern Mediterranean is studied with the use of a modeling system.

2 Data and Methodology

A modeling system was applied that consisted of the photochemical air quality model CAMx (version 5.30), off-line coupled with the mesoscale meteorological model MM5 (version 3.7). Model runs were performed for a grid spacing over the Eastern Mediterranean with 10 km spatial resolution. There were 17 vertical layers extending up to 10 km. First model layer height was ~23 m. The gaseous and particulate daily varying chemical boundary conditions for CAMx were taken from the global model TM4-ECPL (Myriokefalitakis et al. 2011). The time period studied extends from 20 August to 5 September 2007. The modeling system was applied with a 1 week start-up period.

The gaseous and particulate matter anthropogenic emission data for the reference year 2007 were taken from the French National Institute for Industrial Environment and Risks (INERIS) database. Only for the energy sector, emission data for the reference year 2005 were taken from the The Netherlands Organisation (TNO) database. For the Istanbul megacity and the large Greek urban agglomerations of Athens and Thessaloniki detailed emissions were accounted for according to Markakis et al. (2012, 2010a, b). Anthropogenic emission data were temporally and spatially processed using the MOdel for the Spatial and tEmporal diStribution of emissionS (MOSESS). The Natural Emission Model (NEMO) driven by MM5 was applied for the calculation of biogenic NMVOCs, sea salt and windblown dust emissions (Poupkou et al. 2010).

The wildfire emission data were based on the Global Fire Emissions Database (GFED3). They had 0.1° spatial resolution and were available on a daily basis (Fig. 1). The following chemical species were included in CAMx runs: CO, NOx

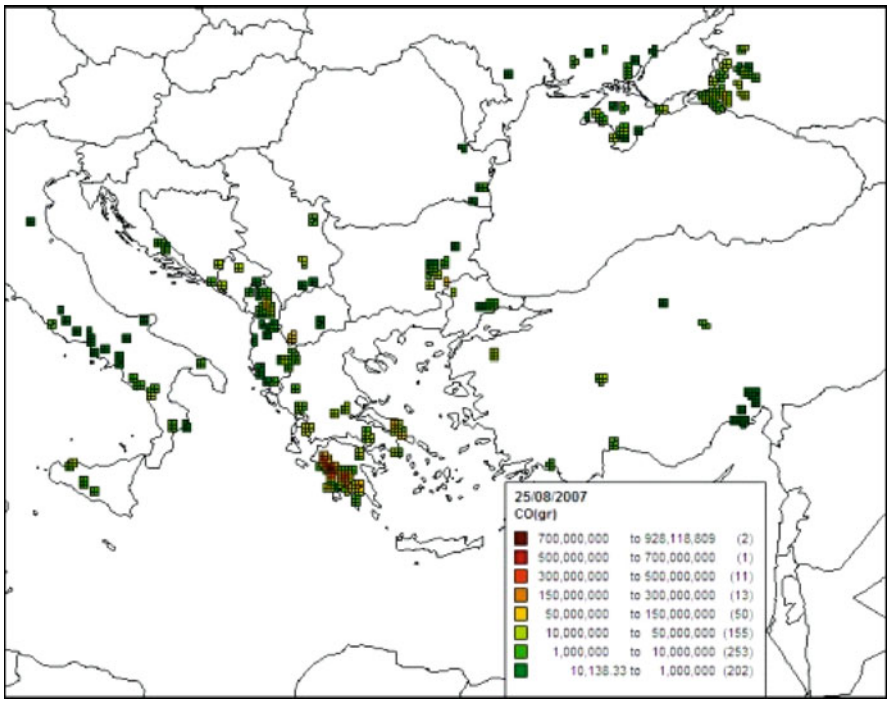

Fig. 1 Daily mean biomass burning CO emissions (gr/gridcell) on the 25th August 2007

(as NO), NH3, SO2, CH4, NMHCs and PM2.5. Sixty percent of the emissions were injected in the first 1,000 m and 40% of the emissions from 1,000 to 2,000 m (according to Dentener et al. 2006). There had been no diurnal variation of wildfire emissions in model runs.

The zero-out modeling method was used and two emission scenarios were examined: CAMx runs including and excluding biomass burning emissions.

The Aggregate Risk Index (ARI) is an air quality index based on the exposure-response relationship and relative risk (RR) of the well-established daily mortality, or morbidity. The use of ARI enables the assessment of additive effects of short-term exposure to the main air pollutants. Based on the recently proposed methodology of Sicard et al. (2011), the ARI can be computed using the following formula:

$$ARI = \sum_i a_i \cdot C_i$$

The index is defined to reflect the contribution of individual pollutants "i" to total risk. C_i is the corresponding time-averaged concentration (in $\mu g\ m^{-3}$) and "α_i" is a coefficient proportional to the respective incremental risk values ($RR_i - 1$). The pollutants that are considered for the calculation of ARI include NO_2, O_3, SO_2, and PM_{10}, while the values for the coefficients "α_i" are defined based on published RR_i values by the World Health Organization.

3 Results

Figure 2 shows the nonradiative impact of the biomass burning emissions on the air quality of the Eastern Mediterranean over the study whole time period for the first CAMx layer (the impact of temperature and radiation changes due to biomass burning on the air quality was not taken into account). Figure 2 upper left, right show that the biomass burning results to an increase of the spatially resolved CO and NOx mean concentrations that can be from 3.5 to 7 times for CO and from one to two orders of magnitude for NOx over the fire hot spots. Because of the biomass burning events, the domain-wide mean concentration is higher by 1.2 times for CO and by 1.3 times for NOx. Over the fire hot spots O3 levels are generally reduced (Fig. 2 lower left). However, there is an enhancement of O3 levels over the greater part of the modeling domain which is more pronounced downwind the burnt areas. Over an extended part of the modeling domain, PM2.5 mean levels are increased by 1.5–3 times. Over the fire hot spots, the corresponding increases can be more than five times (Fig. 2 lower right). Due to fires, the domain-wide mean PM2.5 concentration becomes 1.4 times higher.

Figure 3 shows the computed ARI over the study area for the different emission scenarios examined on the 25th August 2007 when fire counts in the whole domain and fire emissions in Greece were maximum. The inclusion of biomass burning

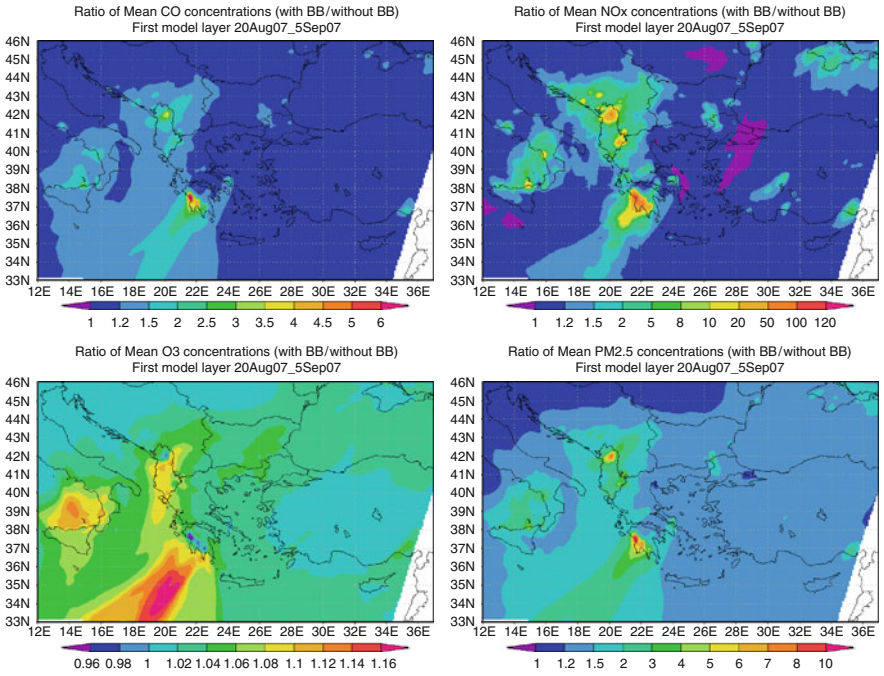

Fig. 2 The nonradiative impact of biomass burning on the air quality in the Eastern Mediterranean for the period 20 August–5 September 2007 for CO (*upper left*), NOx (*upper right*), O3 (*lower left*) and PM2.5 (*lower right*)

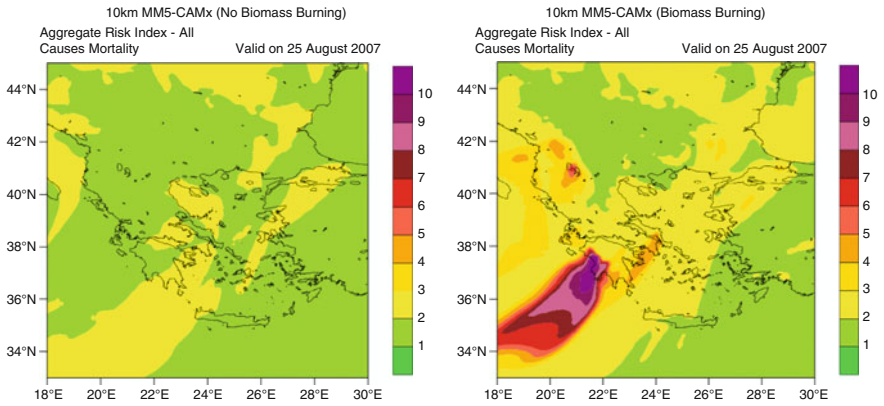

Fig. 3 Aggregate Risk Index for the 25th August 2007 without biomass burning (*left*) and with biomass burning (*right*)

emissions results to increased ARI values over the greater part of the study area. In particular, the highest ARI values are observed south-west of Peloponnesus, where the largest fires were burning. Such exceptionally high ARI values are found mainly over areas that are sparsely populated. The increased ARI values over the Attica basin should also be noted. As seen in Fig. 3, when accounting for biomass burning, ARI values over the Attica almost double. In an area as densely populated as the Attica basin, such an increase is important. The computed ARI values indicate that there is a moderate risk of increased mortality ranging from 7% to 12.1%. In the absence of fire emissions, the computed ARI values correspond to a relative risk of increased mortality between 1.7% and 6.9%.

Figure 4 shows the contribution of atmospheric processes in the determination of O3 levels in the study area up to 2,000 m a.g.l. on the 25th August 2007. Vertical transport of O3 results in positive changes in O3 levels throughout the day. Deposition represents an O3 loss process being more influential during daytime. Chemistry is a source for O3 during daytime when biomass burning emissions are accounted for. Almost the opposite is the case when biomass burning emissions are omitted in the CAMx run. In the later case, daytime O3 photochemical destruction rates are estimated which are linked to low daytime NOx levels being less than 90 pptv indicating a photochemical destruction regime for O3 (Zanis et al. 2000).

4 Conclusions

The results from the application of the MM5-CAMx modeling system reveal that the nonradiative impact of the intense biomass burning event in the Eastern Mediterranean at the end of August 2007 is an enhancement of the CO, NOx and PM2.5 concentrations over almost all the study area, which can range from several

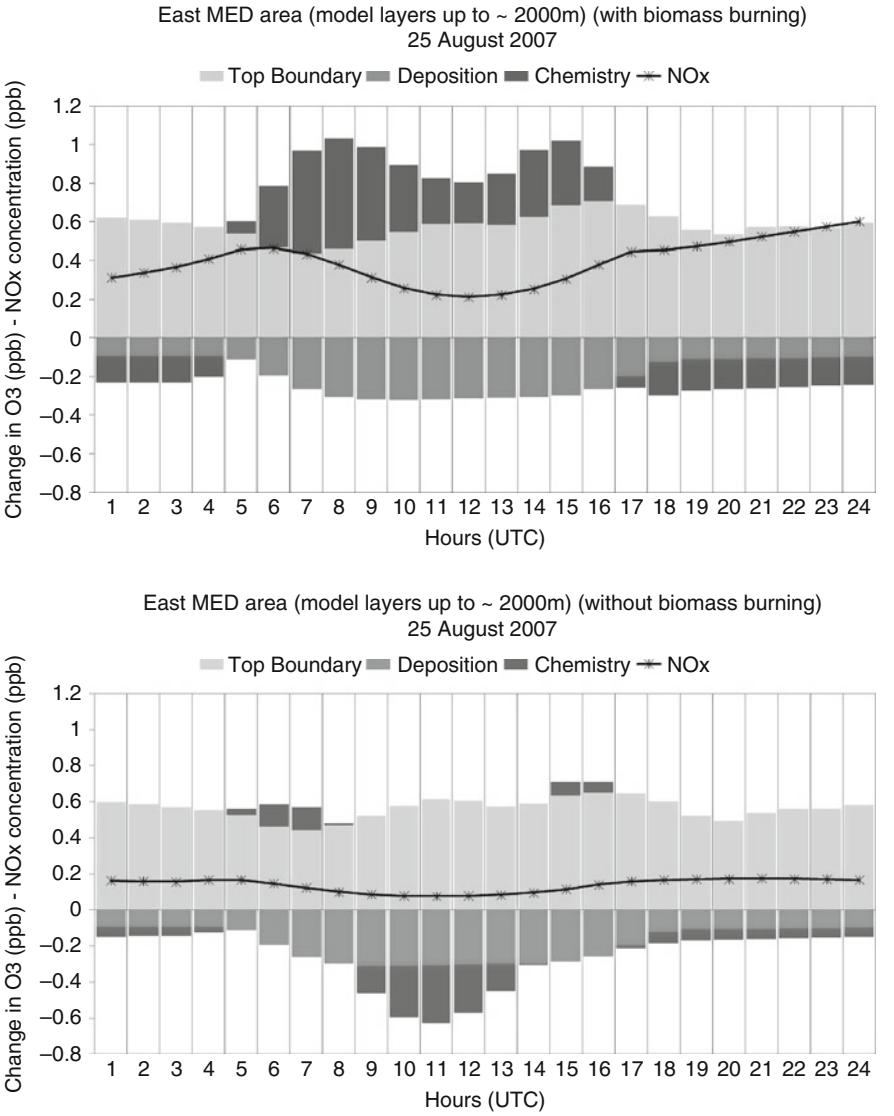

Fig. 4 Contribution of atmospheric processes in the determination of O3 levels in the Eastern Mediterranean on the 25th August 2007

times to two order of magnitude over the fire hot spots. The increases in O3 levels are less pronounced and are found mainly downwind the burnt areas. On the 25th August 2007, when fire counts in the study area are maximum, the risk of increased mortality increases in the densely populated Attica basin indicating possible health issues due to fire plumes. On the same day, in the boundary layer during daytime, the inclusion of biomass burning emissions results in a change of the chemical regime from O3 destruction to O3 production.

Acknowledgments This work was supported by the FP7 EU projects CityZen (megaCITY-Zoom for the Environment: Grant agreement no. 212095) and MACC (Monitoring Atmospheric Composition and Climate: Grant Agreement no. 218793) and by the MED-APICE project co-financed by the European Regional Development Fund in the framework of the MED Programme. We would like to thank the Research Committee of the Aristotle University of Thessaloniki for the 2011 Post-Doctoral Scholarships and Dr. Kaiser (ECMWF) for his help on processing the wildfire emission data.

References

Dentener F, Kinne S, Bond T, Boucher O, Cofala J, Generoso S, Ginoux P, Gong S, Hoelzemann JJ, Ito A, Marelli L, Penner JE, Putaud JP, Textor C, Schulz M, van der Werf GR, Wilson J (2006) Emissions of primary aerosol and precursor gases in the years 2000 and 1750 prescribed data-sets for AeroCom. Atmos Chem Phys 6:4321–4344. doi:10.5194/acp-6-4321-2006

Markakis K, Poupkou A, Melas D, Zerefos C (2010a) A GIS based anthropogenic PM10 emission inventory for Greece. Atmos Pol Res 1:71–81. doi:10.5094/APR.2010.010

Markakis K, Poupkou A, Melas D, Tzoumaka P, Petrakakis M (2010b) A computational approach based on GIS technology for the development of an anthropogenic emission inventory of gaseous pollutants in Greece. Water Air Soil Pollut 207:157–180. doi:10.1007/s11270-009-0126-5

Markakis K, Im U, Unal A, Melas D, Yenigun O, Incecik S (2012) Compilation of a GIS based high spatially and temporally resolved emission inventory for the greater Istanbul area. Atmos Pollut Res 3:112–125. doi:10.5094/APR.2012.011

Myriokefalitakis S, Tsigaridis K, Mihalopoulos N, Sciare J, Nenes A, Kawamura K, Segers A, Kanakidou M (2011) In-cloud oxalate formation in the global troposphere: a 3-D modeling study. Atmos Chem Phys 11:5761–5782. doi:10.5194/acpd-11-485-2011

Poupkou A, Giannaros T, Markakis K, Kioutsioukis I, Curci G, Melas D, Zerefos C (2010) A model for European biogenic volatile organic compound emissions: software development and first validation. Environ Model Softw 25:1845–1856. doi:10.1016/j.envsoft.2010.05.004

Sicard P, Lesne O, Alexandre N, Mangin A, Collomp R (2011) Air quality trends and potential health effects – development of an aggregate risk index. Atmos Environ 45:1145–1153. doi:10.1016/j.atmosenv.2010.12.052

Zanis P, Monks PS, Schuepbach E, Carpenter LJ, Green TJ, Mills GP, Bauguitte S, Penkett SA (2000) In situ ozone production under free tropospheric conditions during FREETEX '98 in the Swiss Alps. J Geophys Res 105:24223–24234. doi:10.1029/2000JD900229

Temporal Variability of Surface Ozone Concentrations in Volos, Greece

G. Proias, I. Larissi, K. Moustris, P.T. Nastos, and A.G. Paliatsos

Abstract The surface ozone is a pollutant of major concern due to its impact on receptors, at currently occurring ambient levels in many regions of the world. The aim of this work is to present the results derived from an analysis of hourly surface ozone concentrations, measured at the urban station of Volos, a coastal medium-sized city at the eastern seaboard of Central Greece, during the 10-year period 2001–2010. The regional climate, which is characterized by hot and dry summers with intense sunshine, plays an important role in the observed exceedances of the air quality ozone limits. The analysis showed that, ozone diurnal patterns depict daytime photochemical ozone built up, during the sunlight hours of the day. It is remarkable that the maximum daily 8-h averages often exceeded the standard value that is assigned by the EU Directive for human health protection, during almost the warm period of the year, mainly at noon and afternoon hours.

G. Proias (✉)
Department of Planning and Regional Development, University of Thessaly, 38334 Volos, Greece
e-mail: giproias@uth.gr

I. Larissi
Laboratory of Environmental Technology, Electronic Computer Systems Engineering Department, Technological and Education Institute of Piraeus, Athens, Greece

K. Moustris
Department of Mechanical Engineering, Technological and Education Institute of Piraeus, Athens, Greece

P.T. Nastos
Laboratory of Climatology and Atmospheric Environment, Department of Geology and Geoenvironment, University of Athens, Athens, Greece

A.G. Paliatsos
General Department of Mathematics, Technological Education Institute of Piraeus, Athens, Greece

C.G. Helmis and P.T. Nastos (eds.), *Advances in Meteorology, Climatology and Atmospheric Physics*, Springer Atmospheric Sciences,
DOI 10.1007/978-3-642-29172-2_167,

1 Introduction

Increased tropospheric (background) ozone concentrations are currently a matter of concern since the have more than doubled during the last decades (Volz and Kley 1988; Staehelin and Smith 1991). The importance of surface ozone effects on human health, animal population, plant growth, and its significant role in the energy budget of the troposphere have been reported in the literature (Lippmann 1991; Brauer and Brook 1997). The high background ozone values observed in Mediterranean regions may be attributed to the high levels of solar UV in combination with locally emitted anthropogenic ozone precursors. Since weather conditions (sunshine, high temperatures and low winds) significantly affect ozone formation, high concentrations occur mainly during the summer, in urban, suburban and rural areas. A number of scientific works on surface ozone regarding eastern Mediterranean regions underline the problem (Ziomas et al. 1989; Glavas 1999; Kalabokas et al. 2000; Dueñas et al. 2002; Paliatsos et al. 2006, 2008; Poupkou et al. 2008; Papanastasiou and Melas 2009).

The main objective of the present study is to reveal the surface ozone temporal variability patterns over the area of Volos, a city of average size on the eastern seaboard of Central Greece. Reasons for the observed temporal variations of ozone levels are discussed. In addition, the data is discussed in relation to the surface ozone thresholds for human health protection set by the European Union.

2 Data and Methodology

In the current work an attempt is made to give a statistical evaluation of surface ozone based on the data recorded at the urban station of Volos for a 10-year period starting in 2001. The air quality data were acquired from the Volos air pollution-monitoring station ($\lambda = 22^\circ\ 57'$E, $\phi = 39^\circ\ 22'$N, h = 2.6 m a.m.s.l.), a station provided with fully automated analyzers, that were installed by the Hellenic Ministry of the Environment, Energy and Climatic Change and were operated by the prefecture of Magnesia, in order to measure air pollution levels in Volos, which presents air pollution problems, like most urban areas in the world.

The city of Volos is located in Thessaly region, and extends along the northern part of the cove of the Pagassitikos Gulf on the eastern seaboard of Central Greece. The case of Volos is an interesting example, where the population shifts and the increased industrialization during the last decades have resulted in the degradation of the air quality in the area. Volos is a medium-sized city and has a population of about 120,000 inhabitants (census 2001). This city is a commercial and touristic city, the seaport of Thessaly with a great number of craft-based industrial, and commercial activities, as well as activities, that are related with tertiary sector services. A detailed description of the Volos topography and climate is found in various publications (e.g. Papaioannou et al. 2010).

The air pollution problems are enhanced by the topography of the area and the city planning. Due to topography, the air masses are trapped within the greater area of Volos, especially during south-south-western wind blow, because of the Pelion Mountain, located to the northeast of the city (Papaioannou et al. 2010). This wind blow is associated with the sea breeze, which occurs mainly during the hot period of the year and during the middle of the day, thus at the time when other parameters (temperature, sunshine duration) facilitate the formation of photochemical pollutants. The fact that, the formation of ozone is a complicated procedure in which complicated chemical reactions are involved, has as a result that, although the primary pollutants were drastically reduced during the last years due to the gradual substitute of old cars with new technology cars (Papaioannou et al. 2010), the ozone levels have not shown the same decreasing trend (Papanastasiou and Melas 2009).

3 Results

All data analyzed in this paper are based upon the mean hourly surface ozone concentrations from which, mean concentrations were computed for each day, month, and year during the 10-year period 2001–2010. Well-defined seasonal (Fig. 1) and diurnal (Fig. 2) patterns are revealed. These temporal fluctuations are further discussed. Figure 1 shows the seasonal variation of surface ozone concentrations at the urban station of Volos, for the examined 10-year period (2001–2010). The seasonal variation of ozone concentrations is characterized by a maximum during the warm period (April–September) and a minimum during the cold period of the year (October–March). The minimum value observed in December and the maximum value in July with a ratio 1:2.7.

The ozone concentrations in the troposphere follow a characteristic diurnal course with high concentrations in the early afternoon hours (when radiation and temperature favour ozone formation) and low concentrations during the late night hours until early in the morning (when only ozone distraction takes place). Using data for the period 2001–2010, the mean diurnal variation of surface ozone concentrations, separately during January, April, July and October, at the measuring site of Volos, is shown in Fig. 2. These months were chosen throughout this paper to contrast the surface ozone concentrations patterns from the climatic point of view. This peak is observed between 13:00–17:00 LST in January, 11:00–20:00 in April (Fig. 2, upper panel), 10:00–20:00 in July, and 12:00–18:00 in October (Fig. 2, lower panel). The amplitude of the diurnal variation ranges from 24 to 61 $\mu g/m^3$, for January and April respectively. The high amplitude of surface ozone diurnal variation, in July, is probably due to the high photochemical ozone production caused by the high solar insolation during the daytime period. It should be mentioned at this point that the diurnal variation pattern of surface ozone is consistent with the known built-up of ozone in the morning hours, which is caused partly by mixing down of the ozone-rich air from above and later on by

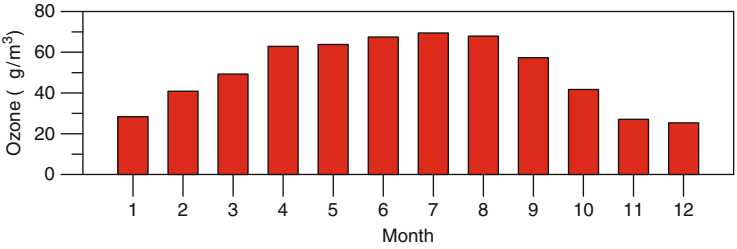

Fig. 1 Mean monthly variation of surface ozone concentrations at the measuring site of Volos, from 2001 to 2010

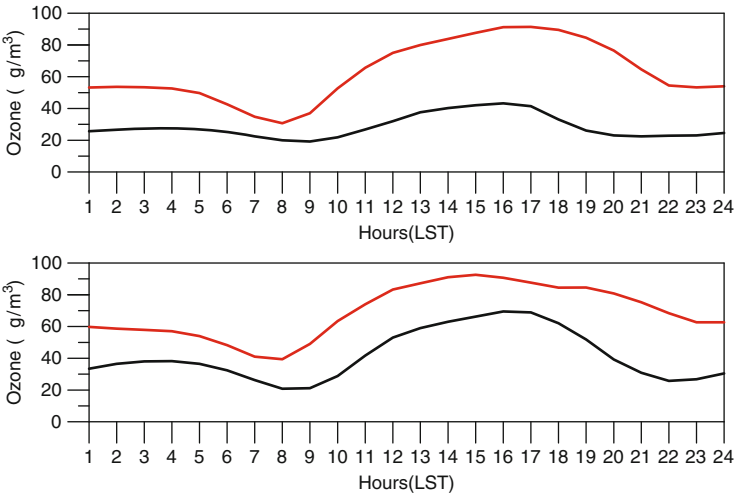

Fig. 2 Mean diurnal variation of surface ozone concentrations, for the period 2001–2010, at the measuring site of Volos for January–April (*black* and *red line*, respectively; *upper panel*) and July–October (*red* and *black line*, respectively; *lower panel*)

photochemical production (Kelly et al. 1984). During the evening and night hour's surface ozone is substantially decreased by chemical destruction and dry deposition (Ziomas et al. 1989). This result emphasizes the strong dependence upon the total UV-solar irradiance reaching the earth of the photochemical surface ozone production. Similar patterns of seasonal variation have also been observed in other Mediterranean sites (Ziomas et al. 1989; Dueñas et al. 2002; Paliatsos et al. 2006; Poupkou et al. 2008).

The urban ozone levels of Volos (especially during the afternoon hours of the warm season) are lower than the corresponding average levels in Athens (Kalabokas et al. 2000), but they are comparable with the corresponding average levels at rural cites such Aliartos (Kalabokas and Repapis 2004; Paliatsos et al. 2006, 2008).

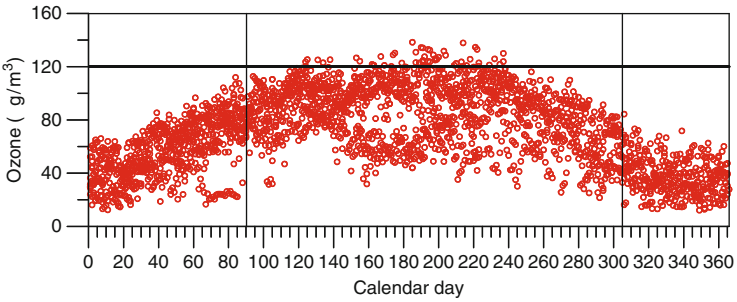

Fig. 3 Mean annual variation of surface ozone maximum daily 8-h averages at the measuring site of Volos (2001–2010; the *horizontal line* indicates EU target)

The mean annual course of maximum daily 8-h averages of surface ozone concentrations for the period 2001–2010 is shown in Fig. 3, with vertical lines making the warm period interval. It can be seen that the maximum daily 8-h averages often exceeded the standard value (horizontal line) that is assigned by the EU Directive (EU 2002) for human health protection, during almost the warm period of the year. This is in agreement with the results of Papanastasiou and Melas (2009) with respect to the area of Volos.

The fact that these violations are mainly observed during the warm period of the year is probably attributed more to meteorology (horizontal transport or vertical subsidence) than the photochemical ozone production caused by the high solar insolation during the daytime period of the season. It should be mentioned at this point that, the diurnal variation pattern of surface ozone is consistent with the known ozone built-up in the morning hours, which is caused partly by enriching the air with ozone from above and later on by photochemical production (Kelly et al. 1984; Paliatsos et al. 2008). Most of the violations are observed during the noon and afternoon hours at a station inside an urban area influenced by air of rural origin.

4 Conclusions

The hourly surface ozone concentrations measured at the urban station of Volos, continuously monitored for the 2001–2010 parcels, were examined in order to study both the seasonal and the diurnal variation. From this analysis the following conclusions can be drawn:

1. The seasonal variation of surface ozone concentrations presents a minimum during the cold period of the year and a maximum during the warm period.
2. The mean diurnal variation of surface ozone concentrations at this rural measuring site has a single peak structure. This peak is observed between 13:00–17:00 LST in January, 11:00–20:00 in April, 10:00–20:00 in July, and 12:00–18:00 in October. The amplitude of the diurnal variation ranges from 24 to 61 ppb, for January and April respectively.

3. The regional climate, which is characterized by hot and dry summers with intense sunshine, plays an important role in the observed exceedances of the 8-h averages of surface ozone standard value (120 μg/m^3) for human health protection, during the warm period of the year.

References

Brauer M, Brook JR (1997) Ozone personal exposures and health effects for selected groups residing in the Fraser Valley. Atmos Environ 31:2113–2121. doi:10.1016/S1352-2310(96)00129-X

Dueñas C, Fernádez MC, Cañete S, Carretero J, Liger E (2002) Assessment of ozone variations and meteorological effects in an urban area in the Mediterranean Coast. Sci Total Environ 299:97–113. doi:10.1016/S0048-9697(02)00251-6

EU (2002) Directive 2002/3/EC of the European Parliament and of the Council of 12 February 2002 relating to ozone in ambient air. Off J Eur Commun L 67:14–30

Glavas S (1999) Surface ozone and NO_x concentrations at a high altitude Mediterranean site, Greece. Atmos Environ 33:3813–3820. doi:10.1016/S1352-2310(98)00393-8

Kalabokas PD, Repapis CC (2004) A climatological study of rural surface ozone in central Greece. Atmos Chem Phys 4:1139–1147. doi:10.5194/acp-4-1139-2004

Kalabokas PD, Viras LG, Bartzis JG, Repapis CC (2000) Mediterranean rural ozone characteristics around the urban area of Athens. Atmos Environ 34:5199–5208. doi:10.1016/S1352-2310(00)00298-3

Kelly NA, Wolff GT, Ferman MA (1984) Sources and sinks of ozone in rural areas. Atmos Environ 18:1251–1266. doi:10.1016/0004-6981(84)90036-2

Lippmann M (1991) Health effects of tropospheric ozone. Environ Sci Technol 25:1954–1962. doi:10.1021/es00024a001

Paliatsos AG, Koronakis PS, Kaldellis JK (2006) Effect of surface ozone exposure on vegetation in the rural area of Aliartos, Greece. Fresen Environ Bull 15:1387–1393

Paliatsos AG, Viras LG, Moustris K (2008) Temporal variability of surface ozone at rural locations in Greece. Fresen Environ Bull 17:66–73

Papaioannou AB, Viras LG, Nastos PT, Paliatsos AG (2010) An analysis of selected air pollutants in the city of Volos, Greece. Environ Monit Assess 161:485–494

Papanastasiou D, Melas D (2009) Statistical characteristics of ozone and PM10 levels in a medium sized Mediterranean city. Int J Environ Pollut 36:127–138

Poupkou A, Symeonidis P, Lisaridis I, Melas D, Ziomas I, Yay OD, Balis D (2008) Effects of anthropogenic emission sources on maximum ozone concentrations over Greece. Atmos Res 89:374–381. doi:10.1016/j.atmosres.2008.03.009

Staehelin J, Smith W (1991) Trend analysis of tropospheric ozone concentration utilizing the 20 year data set of ozone balloon soundings over Payerne (Switzerland). Atmos Environ 25A:1739–1757. doi:10.1016/0960-1686(91)90258-9

Volz A, Kley D (1988) Evaluation of the Montsouris series of ozone measurements made in the nineteenth century. Nature 323:240–242. doi:10.1038/332240a0

Ziomas IC, Zerefos CS, Bais AF, Proyou AG, Amanatidis GT, Kelessis AG (1989) Significant increasing trends in surface ozone in Greece. Environ Technol Lett 10:1071–1082. doi:10.1080/09593338909384828

Air Pollution in Eastern Mediterranean: Nested-Grid GEOS-CHEM Model Results and Airborne Observations

A.P. Protonotariou, E. Bossioli, M. Tombrou, N. Mihalopoulos, G. Biskos, J. Kalogiros, G. Kouvarakis, and V. Amiridis

Abstract Trace gases concentrations in the boundary layer (BL) and the free troposphere are studied in the Eastern Mediterranean based on an updated nested-grid application of GEOS-CHEM global model and airborne observations that were collected over the Greek territory during the AEGEAN GAME airborne field campaign in September 2011. Modelled concentrations are studied against measurements along the flight tracks. Moreover, the spatial distribution of the pollutants over the study domain is examined in relation to the prevailing wind regime. The role of the long-range transport of pollution is investigated particularly through the northern and eastern boundaries due to the prevailing NE circulation. It is found that the model captures adequately carbon monoxide (CO) and ozone (O_3) levels within the troposphere. CO and O_3 concentrations over the Aegean Sea can exceed the background levels attributed either to transport downwind the local

A.P. Protonotariou (✉) • E. Bossioli • M. Tombrou
Division of Environmental Physics and Meteorology, Department of Physics, University of Athens, 157 84 Athens, Greece
e-mail: aprot@phys.uoa.gr

N. Mihalopoulos • G. Kouvarakis
Environmental Chemical Processes Laboratory, Department of Chemistry, University of Crete, Heraklion, Greece

G. Biskos
Department of Environmental Studies, University of the Aegean, Mytilini, Greece

Delft University of Technology, Delft 2628BL, The Netherlands

J. Kalogiros
Institute of Environmental Research and Sustainable Development, National Observatory of Athens, Athens, Greece

V. Amiridis
Institute for Space Applications and Remote Sensing, National Observatory of Athens, Athens, Greece

C.G. Helmis and P.T. Nastos (eds.), *Advances in Meteorology, Climatology and Atmospheric Physics*, Springer Atmospheric Sciences,
DOI 10.1007/978-3-642-29172-2_168,

sources or to long range transport particularly from the northern and eastern part of the domain under the strong NE Etesian winds.

1 Introduction

High concentrations of gaseous pollutants have been observed over the Aegean Sea in Greece under the prevailing strong northerly winds in summer (the so called 'Etesians'), due to the simultaneous contribution of local and distant sources (Salisbury et al. 2003; Kalabokas et al. 2008). Previous airborne campaigns in the study area showed that the role of the long range transport is crucial for air quality in the region (Formenti et al. 2002; Lelieveld et al. 2002). Thus, global models have been employed to assess the imported pollution (e.g. Roelofs et al. 2003; Tombrou et al. 2009).

In the present study, aircraft observations and the nested version of the GEOS-CHEM global 3-D chemistry transport model are employed (Wang et al. 2004; Chen et al. 2009; Protonotariou et al. 2010), in order to assess the chemical composition of the atmosphere over the Aegean Sea in Greece. The study particularly focuses on September 2011, when the UK BAe-146 research aircraft was deployed as part of the AEGEAN GAME campaign (Tombrou et al. 2012).

2 Data and Methodology

2.1 Data

Observations of atmospheric composition in the BL and free troposphere collected during the AEGEAN GAME campaign are integrated in the present study. Additionally, measurements from the rural station of Finokalia in Crete Island and one in Limnos Island were collected during the study period. More details about the AEGEAN GAME are presented in Tombrou et al. (2012).

2.2 Methodology

The nested-grid simulation of GEOS-CHEM is applied over Europe with horizontal grid resolution of 0.50° latitude by 0.67° longitude. The most updated GEOS-5 assimilated products from the NASA Global Modeling and Assimilation Office are employed, which include meteorological fields in 0.50° latitude by 0.67° longitude at 47 vertical layers. The model is initialized based on a 9-month global simulation at a horizontal resolution of 4° latitude by 5° longitude. During this run, boundary conditions around Europe are produced every 3 h for the

nested-grid simulation. The ozone-NOx-hydrocarbon-sulphur chemistry mechanism coupled to aerosol chemistry (Martin et al. 2003; Park et al. 2003; 2004) is considered in the present model's version (v8-03-01), described by 59 trace gases and aerosols. The model includes fossil fuel and ship emissions from the EMEP inventory for the European domain (Vestreng and Klein 2002), biofuel emissions (Yevich and Logan 2003), biogenic VOC emissions from vegetation based on the MEGAN (Guenther et al. 2006) and natural sources from the oceans (Spracklen et al. 2008), volcanic activity (Chin et al. 2000) and lightning (Price and Rind 1992). Biomass burning emissions are not included, as updated emissions were not available for 2011, which however is not expected to affect significantly model results as biomass burning activity in the greater area during September 2011 was relatively low.

In order to interpret aircraft observations during the campaign, model results are sampled along each flight track's time and location. First, the collected measurements are used to evaluate GEOS-CHEM nested-grid application. Then, model results and airborne observations are employed to interpret the chemical regime over the study area during the Etesian winds period.

3 Results

Based on statistical analysis calculated along the three plane flights of the AEGEAN GAME, modelled mean CO concentrations (107.2 ppbv) agree well with mean observations (97.5 ppbv, Table 1), showing an underestimation of ~10%, as evident by the negative mean bias (−9.8 ppbv) and the mean error (11.0 ppbv). On the other hand, O_3 modelled mean concentrations show a 15% underestimation in comparison to the observed values.

An example of CO and O_3 concentrations is given along the B637 flight on 1 September 2011 (Fig. 1). The highest CO levels (up to ~150 ppbv in the proximity of the airport; Fig. 1 upper) are observed at low altitudes, attributed to regional anthropogenic pollution. Moreover, increased CO concentrations (up to 140 ppbv) in relatively low altitude (~550 m at 9:42 UTC) probably reflect ship emissions as the aircraft flew through a ship plume. In this case, the model underestimates CO concentrations, as the heavy ship traffic in the Aegean Sea during summer is not accurately simulated due to the horizontal resolution of the model. CO in general decreases at higher altitudes (~70 ppbv). However, higher levels in comparison to the background values are measured between ~2.5 km and ~1 km around 9:20 UTC and 12.10 UTC over the south and north Aegean Sea respectively. The model results reveal that apart from the local pollution, the high levels over the northern edge are also attributed to long range transport of anthropogenic pollution, as evident from the spatial CO distribution (Fig. 2) and the corresponding plots at the boundaries (Fig. 3). In particular, significant CO concentrations are imported within the BL mainly from Eastern Europe.

Table 1 Statistic evaluation of the nested-grid application of GEOS-CHEM over Europe along flights B637, B640, B641 of the AEGEAN GAME campaign

	CO	O_3
Mean observation (ppbv)	107.2	58.4
Mean estimation (ppbv)	97.5	69.3
Mean bias (ppbv)	−9.8	10.9
Mean error (ppbv)	11.0	11.0

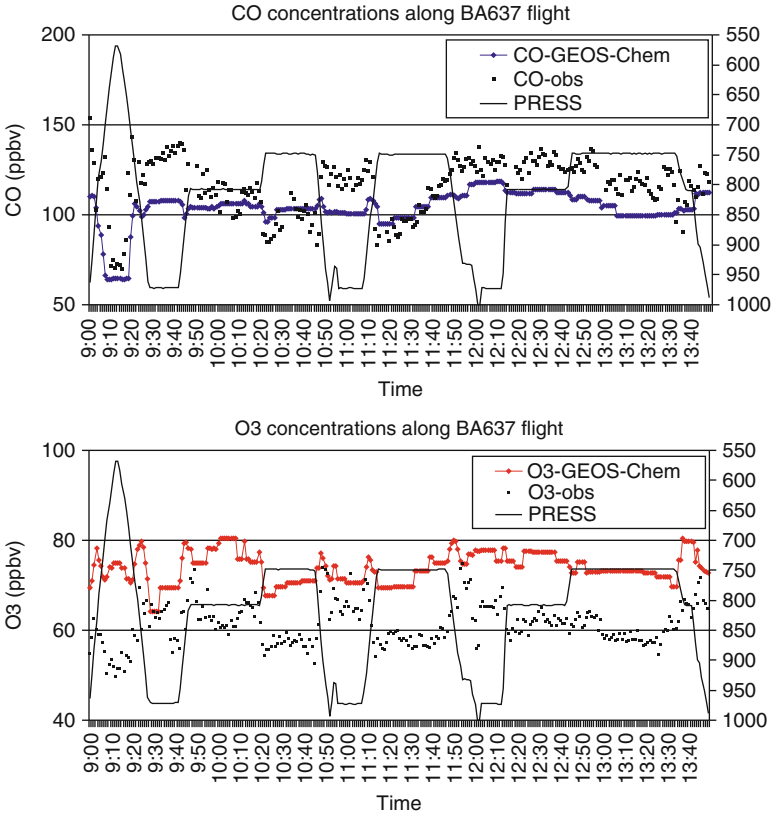

Fig. 1 Modeled (*lines* with *diamonds*) and observed (*squares*) (*upper*) CO and (*lower*) O_3 concentrations along the B637 flight on 1 September 2011. Concentrations are in ppbv and pressure (continuous lines) in hPa

4 Conclusions

Results from the nested-grid application of GEOS-CHEM over Europe were combined with aircraft observations in order to study the chemical composition over the Aegean Sea during the Etesian wind regime. The study particularly focused on September 2011, when the UK BAe-146 research aircraft was deployed as part of the AEGEAN GAME measurement campaign. The model captured adequately CO

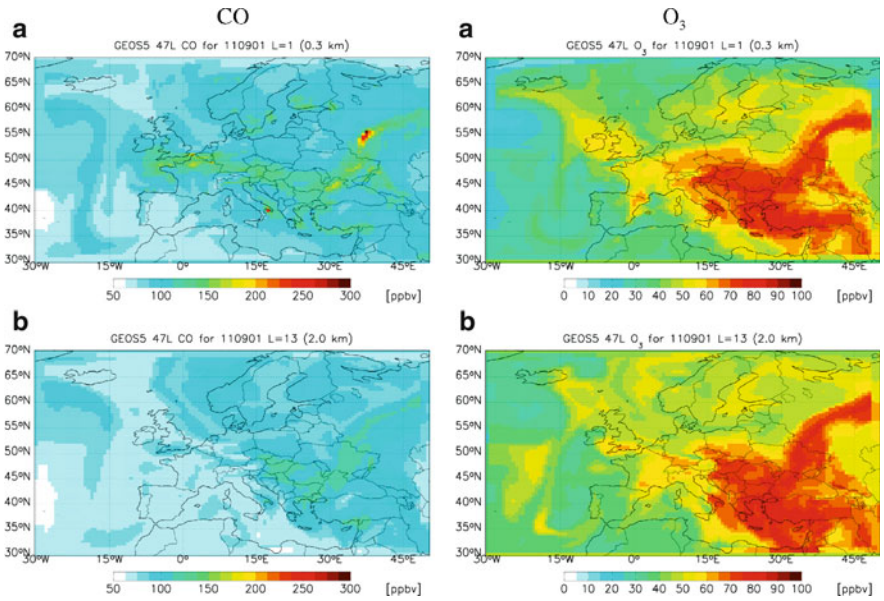

Fig. 2 Simulated spatial distribution of CO and O_3 concentration on 1 September 2011 at (**a**) surface and (**b**) 2 km (~800 mbar)

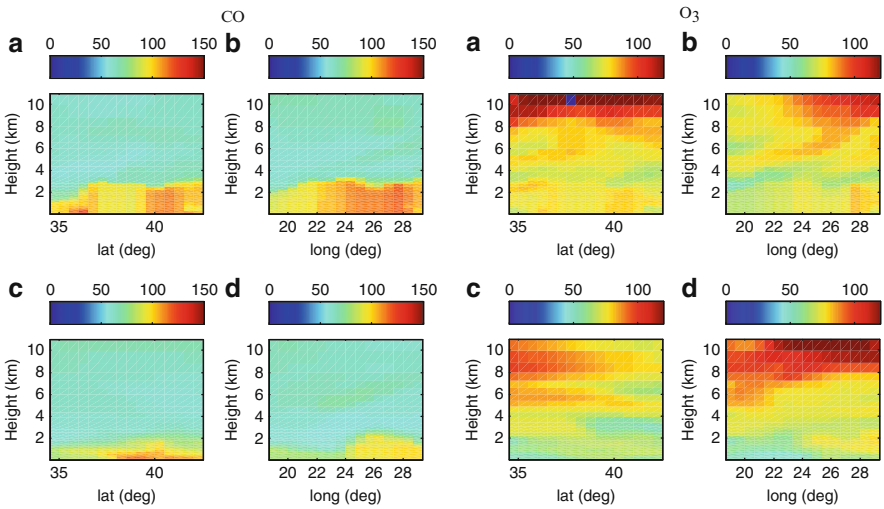

Fig. 3 Vertical distribution of CO and O_3 concentrations (ppbv) on 1 September 2011 at the (**a**) Eastern, (**b**) Northern, (**c**) Western and (**d**) Southern boundary around the Greek territory

and O_3 levels within the troposphere. It was found that under the strong NE Etesian winds, CO and O_3 concentrations over the Aegean Sea can exceed the background levels downwind local sources while the effect of long range transport is significant

in the northern and eastern part of the domain contributing by up to 150 ppbv and 120 ppbv for CO and O_3, respectively.

Acknowledgments This work is supported by the EUFAR (227159) EC Grant Agreement and the AEGEAN_GAME2 project. Authors acknowledge Aaron van Donkelaar, Konstantinos Varotsos, Luke Schiferl and Yiannis Georgiadis for technical support.

References

Chen D, Wang YX, McElroy MB et al (2009) Regional CO pollution in China simulated by the high-resolution nested-grid GEOS-Chem model. Atmos Chem Phys 9:3825–3839. doi:10.5194/acp-9-3825-2009

Chin M, Rood RB, Lin S-J et al (2000) Atmospheric sulfur cycle simulated in the global model GOCART: model description and global properties. J Geophys Res 105(D20):24671–24687. doi:10.1029/2000JD900384

Formenti P, Reiner T, Sprung D et al (2002) STAAARTE-MED 1998 summer airborne measurements over the Aegean Sea – 1. Aerosol particles and trace gases. J Geophys Res 107(D21):4450. doi:10.1029/2001JD001337

Guenther A, Karl T, Harley P et al (2006) Estimates of global terrestrial isoprene emissions using MEGAN (Model of Emissions of Gases and Aerosols from Nature). Atmos Chem Phys 6:3181–3210. doi:10.5194/acp-6-3181-2006

Kalabokas PD, Mihalopoulos N, Ellul R, Kleanthous S, Repapis CC (2008) An investigation of the meteorological and photochemical factors influencing the background rural and marine surface ozone levels in the Central and Eastern Mediterranean. Atmos Environ 42:7894–7906. doi:10.1016/j.atmosenv.2008.07.009, ISSN 1352–2310

Lelieveld J, Berresheim H, Borrmann S et al (2002) Global air pollution crossroads over the Mediterranean. Science 298:794–799

Martin RV, Jacob DJ, Yantosca RM, Chin M, Ginoux P (2003) Global and regional decreases in tropospheric oxidants from photochemical effects of aerosols. J Geophys Res 108(D3):4097. doi:10.1029/2002JD002622

Park RJ, Jacob DJ, Chin M, Martin RV (2003) Sources of carbonaceous aerosols over the United States and implications for natural visibility. J Geophys Res 108(D12):4355. doi:10.1029/2002JD003190

Park RJ, Jacob DJ, Field BD, Yantosca RM, Chin M (2004) Natural and transboundary pollution influences on sulfate-nitrate-ammonium aerosols in the United States: implications for policy. J Geophys Res 109:D15204. doi:10.1029/2003JD004473

Price C, Rind D (1992) A simple lightning parameterization for calculating global lightning distributions. J Geophys Res 97:9919–9933. doi:10.1029/92JD00719

Protonotariou AP, Tombrou M, Giannakopoulos C et al (2010) Study of CO surface pollution in Europe based on observations and nested-grid applications of GEOS-Chem global chemical transport model. Tellus B 62:209–227. doi:10.1111/j.1600-0889.2010.00462.x

Roelofs GJ, Scheeren B, Heland J, Ziereis H, Lelieveld J (2003) A model study of ozone in the eastern Mediterranean free troposphere during MINOS (August 2001). Atmos Chem Phys 3:1199–1210. doi:10.5194/acp-3-1199-2003

Salisbury G, Williams J, Holzinger R et al (2003) Ground-based PTR-MS measurements of reactive organic compounds during the MINOS campaign in Crete, July-August 2001. Atmos Chem Phys 3:925–940. doi:10.5194/acp-3-925-2003

Spracklen DV, Arnold SR, Sciare J, Carslaw KS, Pio C (2008) Globally significant oceanic source of organic carbon aerosol. Geophys Res Lett 35:L12811. doi:10.1029/2008GL033359

Tombrou M, Bossioli E, Protonotariou AP, Flocas H, Giannakopoulos C, Dandou A (2009) Coupling GEOS-CHEM with a regional air pollution model for Greece. Atmos Environ. doi:10.1016/j.atmosenv.2009.04.003

Tombrou M, Bossioli E, Kalogiros J, Biskos G, Coe H, Dandou A, Michalopoulos N, Kouvarakis G, Protonotariou AP, Triantafyllou E (2012) Physical and chemical processes of polluted air masses during Etesians: AEGEAN-GAME airborne campaign – an outline. In: Helmis CG, Nastos PT (eds) Advances in Meteorology, Climatology and Atmospheric Physics, Springer Atmospheric Sciences, Springer-Verlag, Berlin, Heidelberg

Vestreng V, Klein H (2002) Emission data reported to UNECE/EMEP: Quality assurance and trend analysis & Presentation of WebDab, MSC-W Status Report 2002. Norwegian Meteorological Institute, Oslo, Norway

Wang YX, McElroy MB, Jacob DJ, Yantosca RM (2004) A nested grid formulation for chemical transport over Asia: applications to CO. J Geophys Res 109:D22307. doi:10.1029/2004JD005237

Yevich R, Logan JA (2003) An assessment of biofuel use and burning of agricultural waste in the developing world. Global Biogeochem Cycles 17(4):1095. doi:10.1029/2002GB001952

Weekly Cycles in Meteorological Variables Over Large-Scales: Fact or Myth?

A. Sanchez-Lorenzo, P. Laux, H.J. Hendricks-Franssen, A.K. Georgoulias, J. Calbó, S. Vogl, and J. Quaas

Abstract Several studies have found weekly cycles of meteorological variables appearing over large domains, which can hardly be related only to urban effects, while other studies fail to reproduce these with statistical significance. In addition to the lack of unequivocal evidence for these cycles, their possible physical causes have been controversially discussed. We present a short summary of the main results about this topic published during the recent two decades. Also, a brief summary of the suggested reasons, especially focusing on the possible aerosol-cloud-radiation interaction as a result of the weekly cycles of anthropogenic activities, is presented.

1 Introduction

Although there are clear evidences of the anthropogenic impact in the recent change of the Earth's climate, there are still important uncertainties, especially related to the aerosol effects in the climate system (Solomon et al. 2007).

A. Sanchez-Lorenzo (✉)
ETH Zürich, Institute for Atmospheric and Climate Science (IAC), Zürich, Switzerland
e-mail: arturo.sanchez@env.ethz.ch

P. Laux • S. Vogl
Karlsruhe Institute of Technology (KIT), Institute for Meteorology and Climate Research (IMK-IFU), Garmisch-Partenkirche, Germany

H.J. Hendricks-Franssen
Forschungszentrum Jülich GmbH, Agrosphere Institute (IBG-3), Jülich, Germany

A.K. Georgoulias
Department of Environmental Engineering, Democritus University of Thrace, Xanthi, Greece

J. Calbó
Department of Physics, University of Girona, Girona, Spain

J. Quaas
Institute for Meteorology, University of Leipzig, Leipzig, Germany

C.G. Helmis and P.T. Nastos (eds.), *Advances in Meteorology, Climatology and Atmospheric Physics*, Springer Atmospheric Sciences,
DOI 10.1007/978-3-642-29172-2_169,

Because there is no evidence of natural processes with a constant 7-day cycle, the search of a weekly behavior in meteorological variables has become a traditional approach to link human activities, which are normally reduced during weekends compared to weekdays, and their impact on the climate. Initially, the study of weekly cycles of meteorological and air pollution variables was become a method to detect local climate modification (also known as urban effect) in urban and industrialised areas.

Since 1994, there is an ongoing interest in the detection of these weekly cycles in large-scale domains, which can be considered as areas not affected directly by urban effects. This urban effect can be defined as up to 10 km beyond the edge of urban land cover (Zhang et al. 2004). Consequently, these large-scale weekly cycles can hardly be related to local effects exclusively, and the possible role of the human activities in these cycles is still not clear as a different mechanism is required to explain their possible existence. The most common hypothesis links these large-scale weekly cycles to the direct and indirect anthropogenic aerosol effects, as the anthropogenic aerosols emissions normally also show a weekly signal in large-scale areas (e.g. Georgoulias and Kourtidis 2011 and references therein).

This short paper reviews some of the studies that have been published dealing with large-scale weekly cycles in meteorological variables. For an exhaustive review of the subject see Sanchez-Lorenzo et al. (2012), where also limitations in the methods, causes, and directions for future search are deeply discussed.

2 A Selection of Studies About Weekly Cycles

The first study suggesting their existence was published by Gordon (1994). His results showed significant weekly cycles in temperatures, with maximum (minimum) anomalies on Wednesday (Sunday) in the whole Northern Hemisphere, whereas no significant differences were found for the Southern Hemisphere.

Not too much attention was paid to Gordon (1994), and the next study was published after 4 years by Cerveny and Balling (1998). They found weekly cycles in rainfall over the Atlantic coast of the U.S., with a peak on Saturdays and lower values during the mid-week. They suggested that this weekly signal is due to an indirect aerosol effect, as a result of the downwind advection of pollutants emissions from the east-coast of the U.S.

More recently, Bell et al. (2008) (see Fig. 1) found significant weekly cycles in summer rainfall over the southern U.S. Specifically, they found high (lower) anomalies during the weekdays (weekends) in the continental south-eastern U.S. (region B in Fig. 1). An opposite behaviour over the nearby Atlantic Ocean (region C in Fig. 1) is also found, in agreement with the findings of Cerveny and Balling (1998) or posterior studies (e.g. Rosenfeld and Bell 2011). The authors attribute their results to the hypothesis that anthropogenic air pollution invigorates convective storms over land during the mid-weeks, whereas the opposite cycle over the nearby ocean is a compensatory response of the weekly cycles detected over land. Altogether, these studies provide the most solid evidence of significant large-scales weekly cycles in rainfall as a response of the anthropogenic activities.

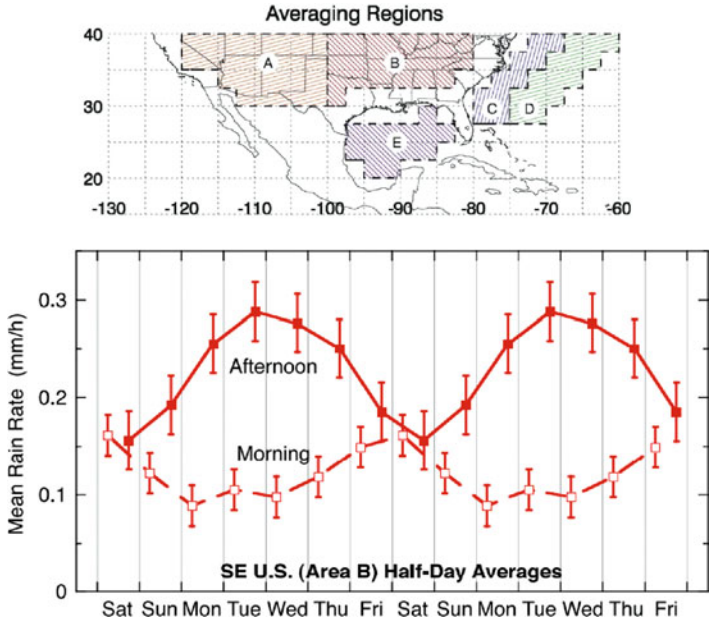

Fig. 1 (*Top*) Five averaging areas (*A*–*E*) chosen by Bell et al. (2008) in southern U.S. and adjacent waters. (*Bottom*) Summer mean values (1998–2005 period) of rain rate by day of the week in southern U.S. (area *B* in *top panel*) for the mornings and afternoons (From Bell et al. (2008). Copyright [2008] American Geophysical Union. Reproduced by permission of American Geophysical Union)

Regarding possible weekly cycles in temperature records, the most studied variable has been the diurnal temperature range (DTR). For example, Forster and Solomon (2003) analysed a possible weekend effect, which was defined as the difference between weekend (Saturday-Monday) and weekdays (Wednesday–Friday) for DTR over the major part of the Northern and also in some areas of the Southern Hemisphere. Their results (Fig. 2) showed significant positive differences (i.e. larger DTR during the weekends as compared to the weekdays) mainly over the south-western and east coast of the U.S., Mexico, south-western Canada, different locations over Russia, Mongolia, and eastern China. Oppositely, negative differences (i.e. lower DTR during the weekends) were observed for many stations placed in the central areas of Canada and Japan. Other areas such as Europe and Australia did not show any significant pattern. This implies that the weekly cycles is a large scale phenomenon, although the identified patterns are not spatially coherent neither in magnitude nor in sign. This strong spatial variability is difficult to explain, like for example the absence of significant results over Europe where the anthropogenic emissions and human activities are larger than in other areas showing significant differences (e.g. Canada, Mongolia, etc.).

In line with Forster and Solomon (2003), posterior studies showed no agreement in the reliability of possible weekly cycles over Europe (e.g. see Stjern 2011 and references therein) although a weekly cycle in temperatures is still likely for some countries (e.g. Laux and Kunstmann 2008).

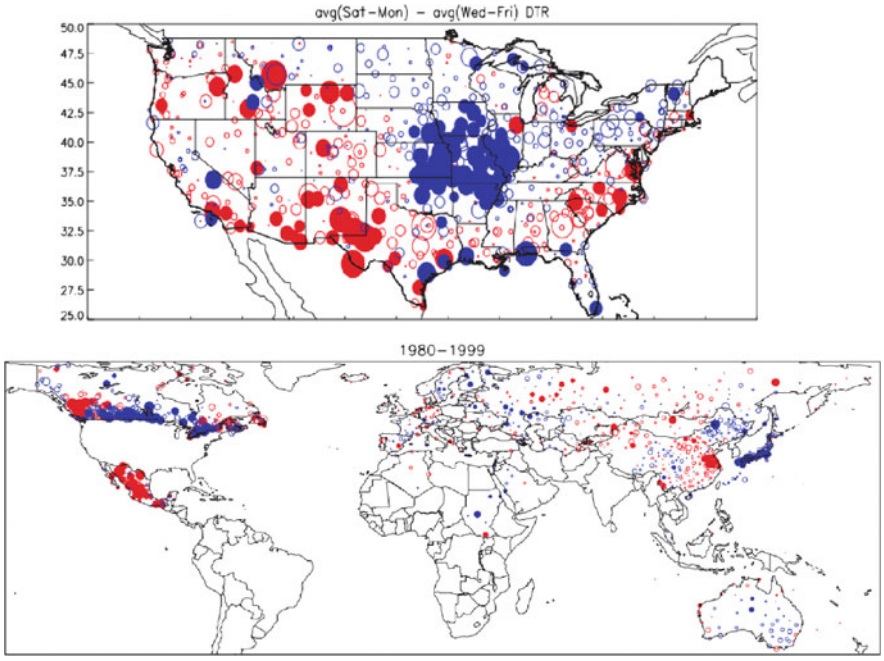

Fig. 2 (*Top*) Annual weekend effect in DTR over continental U.S., using series with more than 40 years of data. Filled circles are significant at the 95% confidence level, and the size of the circle is related to the magnitude of the DTR weekend effect. Positive (*negative*) anomalies are drawn in red (*blue*). (*Bottom*) As in left panel, but for the stations outside the U.S., using 1980–1999 data (From Forster and Solomon (2003). Copyright (2003) National Academy of Sciences, U.S.A)

Regarding Asia, different studies have been published during the last years, especially over China. Gong et al. (2006) analysed different meteorological variables in east China. They claimed for a similar annual weekend effect in DTR to Forster and Solomon (2003) in China, although they also found a seasonal opposite behaviour in the sign of the weekly cycle, with a tendency towards positive (negative) values in winter (summer). The authors suggested that the weekly differences would be physically related to the direct and indirect effect of anthropogenic aerosols. Similarly, Choi et al. (2008) found a similar weekly signal during summer in China, and they suggested a possible link of cloud formation and PM10 concentration on weekly scale to explain their results.

3 In Search of the Significance: Statistical Limitations

Although many studies claimed to find significant results, there are some general shortcomings in the methods used to assess the significance of the weekly cycles (e.g. Hendricks Franssen 2008), which are listed as follow:

1. To neglect the spatial autocorrelation of the data, and lack of a better understanding of the long-term persistence in the time series (Windsor and Toumi 2001; Varotsos and Kirk-Davidoff 2006).
2. The assumption of normality in the time series, which it is not always true in climate series, especially in daily records. Consequently, the uses of non-parametric tests are more flexible than the traditional parametric tests.
3. An additional problem is that several studies focus their analysis on a certain season, a certain region and a certain decade, and this always tends to provide significant results. If significant results are only found with this specific situation, a scientific reasoning would be desirable to explain the results.
4. Finally, it is also important to realize that results which did not result in a significant weekly cycle were in general not published in the scientific literature, whereas significant results are much more likely to have been published. This is well known under the name of "publication bias" in the literature.

4 In Search of the Cause: A Direct/Indirect Effect of Aerosols?

Even the limitations in the detection of large-scale weekly cycles, still there is an important number of papers claiming significant results, and consequently a cause to explain these possible periodicities is needed. Here we will briefly focus our attention on the role of the aerosols, which is the main mechanism suggested until now as the possible cause of the large-scale weekly cycles.

In fact, the major part of the studies reporting significant weekly cycles claimed that direct and, especially, indirect effects of anthropogenic aerosols are the main cause, with some studies showing clear evidence of this connection (e.g. Bell et al. 2008; Rosenfeld and Bell 2011). Aerosols impacts can be summarised as:

1. A "direct" effect on radiation: Aerosol particles scatter and absorb solar (and also, but to a much lesser extent, terrestrial) radiation.
2. The so-called "indirect" effects (Lohmann and Feichter 2005), as e.g.:
   (a) The anthropogenic aerosols serving as cloud condensation and ice nuclei enhance cloud droplet number concentrations (CDNC), and thus the scattering cross section that enhances cloud albedo (also called "first indirect effect").
   (b) It has been hypothesised for liquid-water clouds that with droplet size spectra of generally reduced size, precipitation formation is delayed, enhancing cloud lifetime and cloud fraction.
   (c) In a convective cloud, if precipitation is reduced for liquid-water clouds, more liquid water may reach the freezing level, and freezing is delayed to higher altitudes (also called convective invigoration effect). Such an effect would lead to deeper clouds, and more intense precipitation. This effect has been proposed as a cause for the cycles found in the south-eastern U.S. (Bell et al. 2008).

5 Conclusions

The main conclusions of this work are summarised as follows:

1. There is not a consistent spatial pattern in the results claiming for significant large-scale weekly cycles in meteorological variables. Consequently, they are difficult to discern from natural climate variability.
2. Significant weekly cycles over North America seem plausible, especially in the south-eastern of the U.S. Equally, for Asia a large number of evidences have been published recently pointing out the existence of significant weekly cycles, especially in eastern China.
3. More uncertainties exist in Europe as there is no general consensus about the reliability of studies suggesting significant results.
4. The assessment of the statistical significance faces a number of challenges that need to be taken into account when the analyses are applied to climate data sets in search of weekly cycles.
5. The direct and indirect effects of anthropogenic aerosols are the most probable cause of large scale weekly cycles.

Overall, more research is needed on this topic. Additionally it is necessary to identify, understand and quantify the physical mechanisms beyond these weekly cycles, e.g. through the use of climate model simulations (Quaas et al. 2009).

Acknowledgments This work was partially supported by the Spanish Ministry of Science and Innovation project NUCLIERSOL (CGL2010-18546). Arturo Sanchez-Lorenzo was granted by a postdoctoral position funded by the government of Catalonia, Spain (2009 BP-A 00035).

References

Bell TL, Rosenfeld D, Kim KM, Yoo JM, Lee MI, Hahnenberger M (2008) Midweek increase in U.S. summer rain and storm heights suggests air pollution invigorates rainstorms. J Geophys Res 113:D02209. doi:10.1029/2007JD008623

Cerveny RS, Balling RC (1998) Weekly cycles of air pollutants, precipitation and tropical cyclones in the coastal NW Atlantic region. Nature 394:561–563

Choi Y, Ho C, Chen D, Noh Y, Song C (2008) Spectral analysis of weekly variation in PM_{10} mass concentration and meteorological conditions over China. Atmos Environ 42:655–666

Forster PM, Solomon S (2003) Observations of a "weekend effect" in diurnal temperature range. Proc Natl Acad Sci USA 100:11225–11230

Georgoulias AK, Kourtidis KA (2011) On the aerosol weekly cycle spatiotemporal variability over Europe. Atmos Chem Phys 11:4611–4632

Gong DY, Guo D, Ho CH (2006) Weekend effect in diurnal temperature range in China: opposite signals between winter and summer. J Geophys Res 111. doi:10.1029/2006JD007068

Gordon AH (1994) Weekdays warmer than weekends? Nature 367:325–326

Hendricks Franssen H (2008) Comment on "An unexpected pattern of distinct weekly periodicities in climatological variables in Germany". Geophys Res Lett 35:L05802. doi:10.1029/2007GL031279

Laux P, Kunstmann H (2008) Detection of regional weekly weather cycles across Europe. Environ Res Lett 3:044005. doi:10.1088/1748-9326/3/4/044005

Lohmann U, Feichter J (2005) Global indirect aerosol effects: a review. Atmos Chem Phys 5:715–737

Quaas J, Boucher O, Jones A, Weedon GP, Kieser J, Joos H (2009) Exploiting the weekly cycle as observed over Europe to analyse aerosol indirect effects in two climate models. Atmos Chem Phys 9:8493–8501

Rosenfeld D, Bell TL (2011) Why do tornados and hailstorms rest on weekends? J Geophys Res 116:D20211. doi:10.1029/2011JD016214

Sanchez-Lorenzo A, Laux P, Hendricks-Franssen HJ, Calbó J, Vogl S, Georgoulias AK, Quaas J (2012) Assessing large-scale weekly cycles in meteorological variables: a review. Atmos Chem Phys Discuss 12:1451–1491

Solomon S et al (eds) (2007) Climate change 2007: the physical science basis. Cambridge University Press, Cambridge/New York

Stjern CW (2011) Weekly cycles in precipitation and other meteorological variables in a polluted region of Europe. Atmos Chem Phys 11:4095–4104

Varotsos C, Kirk-Davidoff D (2006) Long-memory processes in ozone and temperature variations at the region 60°S–60°N. Atmos Chem Phys 6:4093–4100

Windsor HL, Toumi R (2001) Scaling and persistence of UK pollution. Atmos Environ 35:4545–4556

Zhang X, Friedl MA, Schaaf CB, Strahler AH, Schneider A (2004) The footprint of urban climates on vegetation phenology. Geophys Res Lett 31:L12209. doi:10.1029/2004GL020137

Meteorological Influences Within the Context of Air Quality in Beijing

K. Schäfer, Y. Wang, S. Norra, R. Shen, J. Xin, H. Ling, G. Tang, C. Münkel, N. Schleicher, Y. Yu, J. Schnelle-Kreis, L. Shao, V. Dietze, K. Cen, R. Zimmermann, S. Schrader, and P. Suppan

Abstract Daily $PM_{2.5}$ samples were collected continuously with two high-volume samplers at the ground of CUGB from 06/2010 until 06/2011. The site is very near to the instrumentation for long-term investigation of the inorganic composition of $PM_{2.5}$ (DWD, KIT/IMG). The daily filter samples are analyzed for carbon fractions, organic compound speciation (HMGU, UR), inorganic

K. Schäfer (✉) • R. Shen • P. Suppan
Atmospheric Environmental Research (KIT/IMK-IFU), Karlsruhe Institute of Technology, Institute for Meteorology and Climate Research, Garmisch-Partenkirchen, Germany
e-mail: klaus.schaefer@kit.edu

Y. Wang • J. Xin • H. Ling • G. Tang
Institute of Atmospheric Physics, LAPC, Chinese Academy of Sciences (CAS), Beijing, P. R. China

S. Norra
Karlsruhe Institute of Technology, Institute of Geography and Geoecology (KIT/IGG), Karlsruhe, Germany

Karlsruhe Institute of Technology, Institute of Mineralogy and Geochemistry (KIT/IMG), Karlsruhe, Germany

C. Münkel
Vaisala GmbH, Hamburg, Germany

N. Schleicher • Y. Yu • S. Schrader
Karlsruhe Institute of Technology, Institute of Mineralogy and Geochemistry (KIT/IMG), Karlsruhe, Germany

J. Schnelle-Kreis
Joint Mass Spectrometry Centre, Cooperation Group Comprehensive Molecular Analytics, Helmholtz Zentrum München – German Research Center for Environmental Health (HMGU), Neuherberg, Germany

L. Shao
Department of Resources and Earth Sciences, China University of Mining and Technology (CUMTB), Beijing, P. R. China

C.G. Helmis and P.T. Nastos (eds.), *Advances in Meteorology, Climatology and Atmospheric Physics*, Springer Atmospheric Sciences,
DOI 10.1007/978-3-642-29172-2_170,

(KIT/IMG) and isotopic composition. Gaseous pollutants like NO, NO_2 and O_3 and compounds which are of interest for secondary aerosol formation like SO_2 were measured by a DOAS with three retroreflectors from 04/2009 until 03/2011 in Beijing at LAPC. By path-integrated measurements at different directions information about emission sources (motorway, small street) can be provided. The emitter/receiver unit is in 20 m distance to an air pollution monitoring station. The diurnal development and variation of the mixing layer height (MLH) is determined by a ceilometer. It is shown that the variations of the observed SO_2 and NO_2 as well as $PM_{2.5}$ concentrations are influenced by the MLH, apart from the meteorological (e.g. wind), emission (e.g. SO_2) and photochemistry dependences. High air pollution is coupled significantly with MLH lower than 1,000 m.

1 Introduction

Due to the geographic location of Beijing local and regional wind systems are able to bring fresh air masses or at least to limit air pollution over Beijing. These winds can be originated by the more than 2,000 m high mountain ridge of the northwestern Yundu and Xishan Mountains. On the other hand, this mountain ridge acts as a barrier for air masses coming from southern directions. During those meteorological conditions, air pollution can accumulate in the region of Beijing.

In Beijing and other Chinese cities aeolian mineral dust originated from the West and Northwest of China is of high peak in varying degrees during spring of each year. It is suggested that these dust storms not only transport large amounts of mineral elements but also significant quantities of pollutants and nutrients.

Particulate matter (PM) is an air pollutant associated with adverse effects on human health.

V. Dietze
German Meteorological Service (DWD), Research Center Human Biometeorology, Air Quality Department, Freiburg, Germany

K. Cen
State Key Laboratory of Geological Processes and Mineral Resources, China University of Geosciences (CUGB), Beijing, P. R. China

R. Zimmermann
Joint Mass Spectrometry Centre, Cooperation Group Comprehensive Molecular Analytics, Helmholtz Zentrum München – German Research Center for Environmental Health (HMGU), Neuherberg, Germany

Joint Mass Spectrometry Centre, Institute of Analytical Chemistry, University of Rostock (UR), Rostock, Germany

2 Data and Methodology

Continuous measurements and dedicated campaigns were performed in cooperation between German and Chinese groups. The data are used to show the meteorological influences and the role of emissions within the context of the air quality in Beijing relevant for measures to reduce the air pollution.

2.1 Data

KIT/IMG and DWD investigate the inorganic composition of $PM_{2.5}$ based on weekly active samples and passive samples for the coarse particle fraction in a continuous measurement series since 2005 (Norra et al. 2007).

Two campaigns were performed in 2009 to analyse the vertical distribution of atmospheric particles by various methods. Particles were sampled by passive sampling methods on adhesive acceptor plates in various heights at LAPC (DWD and KIT/IMG). $PM_{2.5}$ was sampled on quartz fibre filters (Whatman) by means of a mini-volume Sampler from Leckel GmbH. (KIT/IMG) and by TEOM instruments (CAS) during the same time. The filters were weighed before and after sampling to determine the mass concentration of sampled particulates. The quartz fibre filters were analysed by ICP-MS for trace elements and main elements.

Daily $PM_{2.5}$ samples are collected continuously with two high-volume samplers from Digitel in parallel at the ground of CUGB from June 2010 to June 2011 (KIT/IMK-IFU). Local meteorological data are determined by an ultra-sonic anemometer at the sampling site. The site is very near to the instrumentation of DWD and KIT/IMG for long-term investigation of the inorganic composition of $PM_{2.5}$. The daily filter samples are currently analyzed for carbon fractions, organic speciation (HMGU, UR), isotopic composition (KIT/IMK-IFU) and inorganic composition (KIT/IMG). Data will be used for source apportionment of PM, in order o investigate impact of meteorological conditions on source contributions.

To study the diurnal variation of gaseous pollutants like NO, NO_2 and O_3 and compounds which are of interest for secondary aerosol formation like SO_2 a DOAS (Differential Optical Absorption Spectroscopy) is operated from beginning of April 2009 until March 2011 (KIT/IMK-IFU) in Beijing at LAPC (Schäfer et al. 2010a). By path-integrated air pollution measurements at different directions information about different emission sources can be provided. The DOAS from OPSIS GmbH contains an emitter/receiver unit pointing to three retro-reflectors. One path is measured across a small street and a motorway (568 m path length) 10 m above the street level. Another path (126 m length) is in nearly the same direction but only across the small street. The third path (266 m length) is in the opposite direction of path1/path2. The emitter/receiver unit is located in a distance of about 20 m to an air pollution monitoring station at the roof of that building.

Furthermore, a ceilometer LD 40 from Vaisala is used (KIT/IMK-IFU) to analyse the diurnal development and variation of the mixing layer height (MLH) and boundary layers (Emeis et al. 2007). The performance of the compact lidar working with a diode laser at 855 nm wavelength called ceilometer is originally used to investigate cloud layers, vertical visibility, and cloud cover is sufficient to determine convective layer depths exceeding 2,000 m. It enables the detection of nocturnal stable layers down to 150 m. The two lens optical design of this ceilometer provides sufficient overlap of the transmitter and the receiver field-of-view over the whole measuring range and allows reliable detection of nocturnal stable layers. The instrument runs in fully automated, hands-off operation mode. Laser power and window contamination are permanently monitored to provide long-term performance stability. These results and their comparisons with radiosonde data (wind vector, relative humidity and potential virtual temperature) from a meteorological observatory in the southern suburb of Beijing are plotted in the same figure and described in detail in Schäfer et al. (2009).

2.2 Methodology

Air pollution episodes in urban areas often occur during periods with low wind speeds and low MLH and can not only be ascribed to increased local anthropogenic emissions. An important factor, which influences exchange processes of ground level emissions, is the MLH whose quantitative knowledge is important for the understanding and analysis of air pollution episodes (Schäfer et al. 2006). Air pollutants emitted from the ground can accumulate up to the MLH and if the MLH is located near to the ground air pollution can be high due to a strongly limited air mass dilution. To study these processes in more detail, the correlations of particulate concentrations with MLH are investigated.

One-hourly-mean and daily-mean-values are determined from these data as well as from the concentration data and applied for the correlation analyses.

An estimation of the total error of the correlation values is necessary to demonstrate the reliability of the determined correlation coefficients. The concentrations of $PM_{2.5}$ and trace gases are measured with a standard error in the order of 5% ($S_1 = 0.05$). The determination of MLH from ceilometer data has an error of about 10% ($S_2 = 0.10$) if MLH is within the detection range. Thus, the overall error of correlation between the concentrations and MLH can be estimated from the following equation:

$$\text{Overall Standard Error} = 1 - \{(1 - S_1) \cdot (1 - S_2)\}$$

which is giving a value of 14.5% for all compounds. Only such correlation coefficients between concentrations and MLH which are higher than this value are significant i.e. showing dependence between these data. More details of correlations are shown in Schäfer et al. (2010b).

Remote sensing capabilities were used here to monitor MLH (Emeis et al. 2004; Emeis and Schäfer 2006). The heights of the near surface aerosol layers and the MLH can be analyzed from optical vertical backscatter profiles (Emeis et al. 2008). Here the gradient method is used (Münkel 2007). In this method these heights are characterized by minima of the vertical gradient (the term 'gradient minimum' is used here to denote the most negative value of the gradient) of the optical attenuated backscatter intensity. This approach has been refined and extended to enable the calculation of up to five lifted inversions (Emeis et al. 2007).

For a better understanding of the results presented here, the applied method is shortly summarized in the following. Prior to the determination of gradient minima the overlap and range corrected attenuated backscatter profiles are averaged over time and height to suppress noise generated artefacts. Therefore the height values of the aerosol layers are determined in a two-step procedure. Between ground and 900 m height sliding averaging is calculated over 20 min for a variable height interval Δh. Up to 200 m height Δh is 80 m; every 100 m it is increased by 20 m. Above 900 m, Δh is 240 m. Two additional parameters have been introduced to further reduce the number of false hits. The minimum accepted attenuated backscatter intensity right below a lifted inversion is set to 300×10^{-9} m^{-1} sr^{-1}. Additionally, the threshold determining whether a vertical gradient minimum of the backscatter intensity is reported as a lifted inversion is set to $-\mathrm{MB} \times 0.625 \times 10^{-4}$ m^{-1}, where MB is the mean backscatter intensity up to a height of 1,000 m.

3 Results

High particulate ($PM_{2.5}$) load near the surface is coupled with MLH if it is much lower than 1,000 m (Fig. 1). During conditions characterised by MLH higher than 1,000 m a multiple layering of the planetary boundary layer was observed. The square of the correlation coefficient between concentration and MLH is up to 0.5 for $PM_{2.5}$, 0.3 for NO_2 and 0.2 for SO_2. The dependence of element concentrations from MLH is different and significant only for those compounds which are not emitted from sources nearby the measurement site as Cu and Zn. The most appropriate temporal averaging period for the correlation of concentrations with MLH are daily mean values. This is caused by missing data during certain weather situations like well-mixed conditions and some very rapid temporal variations of MLH.

In addition to the MLH also the wind direction had a considerable influence on the particle concentrations. During winds from westerly directions the air was relative dry and clean. Sometimes particulate clouds from desert regions were transported to Beijing so that the backscatter intensity increased rapidly. During winds from other directions, especially from the ocean, the relative humidity was

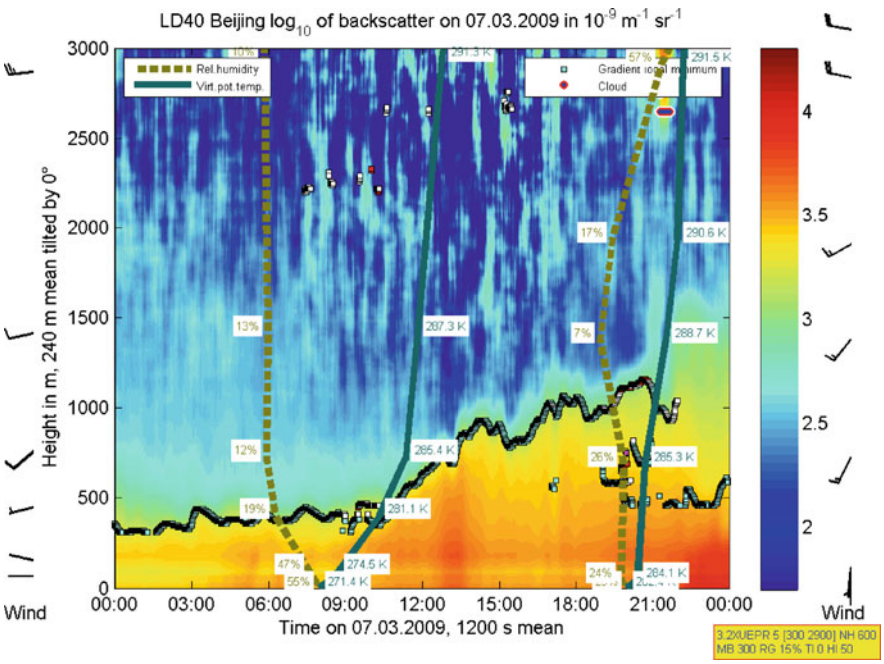

Fig. 1 Results of ceilometer at LAPC (backscatter intensities) together with radiosonde data (wind vector, relative humidity and potential virtual temperature) from meteorological observatory south of Beijing on 07/03/2009. MLH is given from local minimum of gradient of backscatter data. The time is local time. The backscatter intensity is presented in different colours

high. Higher particulate loads were observed during winds from southern directions which transported particulate loaded air masses. This is studied in more detail by backward trajectory calculations.

4 Conclusions

It can be concluded that an important part of the variance of the observed $PM_{2.5}$, SO_2 and NO_2 concentrations is caused by MLH and wind i.e. that the influences of MLH and wind upon $PM_{2.5}$, SO_2 and NO_2 concentrations are significant. Meteorological influences can explain these concentrations apart from emission (e.g. SO_2) and photochemistry dependences.

References

Emeis S, Münkel C, Vogt S, Müller W, Schäfer K (2004) Determination of mixing-layer height. Atmos Environ 38:273–286

Emeis S, Schäfer K (2006) Remote sensing methods to investigate boundary-layer structures relevant to air pollution in cities. Bound Lay Meteorol 121:377–385

Emeis S, Jahn C, Münkel C, Münsterer C, Schäfer K (2007) Multiple atmospheric layering and mixing-layer height in the Inn Valley observed by remote sensing. Meteorol Z 16:415–424

Emeis S, Schäfer K, Münkel C (2008) Surface-based remote sending of the mixing-layer height. Meteorol Z 17:621–630

Münkel C (2007) Mixing height determination with lidar ceilometers – results from Helsinki Testbed. Meteorol Z 16:451–459

Norra S, Hundt B, Stüben D, Cen K, Liu C, Dietze V, Schultz E (2007) Size, morphological and chemical characterization of aerosols polluting the Beijing atmosphere in January/February 2005. In: Rauch S, Morrison GM (eds) Highway and urban environment. Springer, Berlin

Schäfer K, Emeis S, Hoffmann H, Jahn C (2006) Influence of mixing layer height upon air pollution in urban and sub-urban areas. Meteorol Z 15:647–658

Schäfer K, Wang Y, Münkel C, Emeis S, Xin J, Tang G, Norra S, Schleicher N, Vogt J, Suppan P (2009) Evaluation of continuous ceilometer-based mixing layer heights and correlations with $PM_{2.5}$ concentrations in Beijing. In: Picard RH, Schäfer K, Comeron AT, Kassianov E, Mertens CJ (eds) Remote sensing of clouds and the atmosphere XIV, Proceedings of the SPIE, vol 7475. SPIE, Bellingham, pp 74750N-1–74750N-12

Schäfer K, Wang Y, Norra S, Shen, R, Xin J, Ling H, Tang G, Münkel C, Schleicher N, Yu Y, Emeis S, Suppan P (2010) Meteorological influences and role of emissions within the context of air quality in Beijing. In: Weilenmann M (ed) Proceedings of the 18th international symposium transport and air pollution (TAP2010). EMPA, Dübendorf, Proceedings CD, Poster Sessions, pp 119–124

Schäfer K, Wang Y, Xin, J, Ling H, Suppan P (2010) Long-term air quality study by DOAS within Beijing. In: Picard RH, Schäfer K, Comeron AT (eds) Remote sensing of clouds and the atmosphere XV, Proceedings of SPIE, vol 7827. SPIE, Bellingham, pp 78270I-1–78270I-7. doi: 10.1117/12.865112

Monitoring Cloud Coverage in Cyprus for Solar Irradiance Prediction

R. Tapakis and A.G. Charalambides

Abstract The penetration and acceptance of Renewable Energy Sources has already taken place in our lives. Solar Energy is the feedstock for various applications of Renewable Energy Systems (RES), thus, the knowledge of the intensity of the incident solar irradiance is essential for monitoring the performance of such systems. The only unpredictable factor in defining the solar irradiance and the performance of the systems is clouds. So far, various researchers proposed several models for the estimation of solar irradiance in correlation to cloud coverage and cloud type. The present work describes the development of a simple method for cloud detection and computation of short-term cloud motion using a Nikon D3100 camera with a 18–55 mm VR lens, positioned on a tripod in Limassol, Cyprus. The method used for distinguishing clouds from the sky is the "Red-Blue threshold". Additionally, the results of the cloud distinction are used to calculate the future position of clouds. The developed methodology will provide a useful tool for researchers that want to focus on the effect of small local clouds on the energy production of their solar RES. The maximum error in our model was 12% for the prediction of the cloud location eight time steps in advance with only two cloud images processed.

1 Introduction

During the past few years, there has been a major progress in the use of solar technologies, especially as Renewable Energy Systems (RES) for the production of electricity. Such technologies include residential and large scale photovoltaic (PV) parks (El Chaar et al. 2011), solar troughs and solar tower power plants, solar dish

R. Tapakis • A.G. Charalambides (✉)
Department of Environmental Science and Technology, Cyprus University of Technology, Lemesos 3603, Cyprus
e-mail: a.charalambides@cut.ac.cy

C.G. Helmis and P.T. Nastos (eds.), *Advances in Meteorology, Climatology and Atmospheric Physics*, Springer Atmospheric Sciences,
DOI 10.1007/978-3-642-29172-2_171,

technologies and the upcoming construction of commercial solar updraft towers (Thirugnanasambandam et al. 2010). Still, solar RES have not yet achieved to confront the use of fossil fuels mainly due to their dependency on the sun's irradiance, since in most cases there is not an affordable energy storage option. An effective independence from the solar irradiance can be achieved only in solar thermal power plants, using thermal storage; yet, the variable feed-in tariff option in many countries motivates the operators of solar thermal power plants to optimize the plant's performance over maximum profit. The continuous development of technologies that use solar energy, leads to the need of accurate knowledge of the amount of the incident solar irradiance on the surface of the earth.

Several researchers have proposed various models to calculate the solar irradiance, based on various parameters. Apart from the cloudiness, all the parameters that effect solar irradiance can be computed with very good accuracy using the existing numerical forecasting methods (Kasten and Czeplak 1980; Ahmad and Tiwari 2011). Earlier models take into consideration only the effect of the cloud coverage on the total solar irradiance whereas more recent models take into account the cloud class and whether the sun is obscured by clouds, resulting to the reduction of Direct Normal Irradiance (DNI) as well.

The aim of our research is to forecast the incident solar irradiance taking into consideration the reduction of solar irradiance from the presence and movement of the clouds. In this paper the results of our progress regarding the distinction of clouds from sky and the computation of the cloud movement will be presented.

2 Equipment

The equipment used in our research is a ground based digital camera, positioned at the roof of a building at the university campus in Limassol that photographs the sky at scheduled time intervals. The camera used was a Nikon D3100, with an 18–55 mmVR lens at an angle of view of 30° to the horizontal, facing towards north to avoid lens flare. The measurements of the camera were stored on a computer and for the evaluation of the measurements we have developed an algorithm in C++.

3 Methodology for Cloud Detection and Computation of the Cloud Trajectories

The technique used to distinguish clouds from sky is the Ratio Red/Blue (R/B) threshold technique. The principle of the technique is that the different spectrum colors that constitute sunlight are scatted in a different way by the particles of the sky. In a cloud-free atmosphere, which appears blue to our eyes, more light within

the blue spectrum is scattered by gas molecules. On the other hand, clouds consisting of water and ice particles, scatter the same amount of blue and red spectrum, and appear colorless (ranging from white to dark grey) to our eyes. Thus, clear sky sections of an image have relatively lower red pixel values compared to cloud sections, and thus they can be distinguished (Heinle et al. 2010; Roy et al. 2001). The exact value of the separating threshold depends on the camera and the atmospheric conditions, so it has to be determined empirically. Furthermore, the threshold limit should not be the same across the entire image but must be determined as a function of the relative position of the pixels towards the horizon and the sun (Long et al. 2006; Pfister et al. 2003). In our research we used the modified R/B threshold method, where instead of computing the ratio of red to blue, the criterion used was the difference of blue to red (B-R threshold). The three color compounds of the initial RGB (Red, Green and Blue) picture are isolated into three different images i.e. three grey-level images of the corresponding Red, Blue and Green layers of the original picture. The intensity of grey (ranging from 0 to 255) of every pixel of the isolated pictures represents the amount of the specific color at the same pixel of the original image. Afterwards, we compare the values of the corresponding pixels in the blue and red images. If the difference in the intensity of a pixel between blue and red is less than the threshold, then the pixel is classified as cloud, otherwise is classified as sky. A binary image of the same dimensions as the original image is then created, where every pixel classified as cloud has the value 1 and every pixel classified as sky has the value 0. After the distinction of the clouds from the sky, further calculations are carried out, to define the cloud coverage, the ratio of the contour to total cloud pixels and the designated cloud characteristics (cloud features).

The short-term cloud movement is calculated from a stack of sequential pictures, taken at scheduled time intervals from the camera. The principle used to estimate the cloud's trajectories is based on the assumption that the cloud is equivalent to a uniform object in a rectilinear trajectory. The cloud's motion is caused due to advection and is considered not be affected by the variation of cloud's characteristics in time. All the dynamical and microphysical properties of a cloud are considered to be applied at a single point in space that represents the location of the "equivalent cloud" (Koren et al. 2009). This point is called the Center Of Gravity (COG) of the cloud, and is defined from the location of the cloud in the sky plane in Cartesian or Polar coordinates, in two or three dimensional space. COG is the point in space at which we consider that the total mass is concentrated, and at which external forces may be applied. Thus, using equations of motion, the properties of the cloud are simplified, especially when the cloud is not a uniform mass, like Altocumulus or Cirrus clouds. Furthermore, adjacent clouds of the same class that have the same trajectories can be treated as a unique cloud with the same COG, in order to avoid the clustering of the image, simplifying the calculations of the properties of the clouds and making the physical description of cloud evolution clearer. Apart from the coordinates of the COG of the cloud, several statistical features that characterize the cloud have to be calculated. Such features are the spread, the effective area of the cloud (defined as the product of the x-axis and

y-axis spread) and the aspect ratio of the cloud (defined as the ratio of the x-axis over y-axis spread). These features, along with the features computed during the distinction of the cloud from the sky, are used to confirm that the same cloud is detected in consequent images.

4 Results

For demonstrating our methodology, ten sequential photographs of a cloud were used, taken at one minute intervals. Using the developed algorithm, the clouds were distinguished from the sky, a cloud that was present in all the photos was selected for processing and isolated and then, the location of the COG of the selected cloud was calculated in every image. The threshold value used was 60. Figure 1 presents

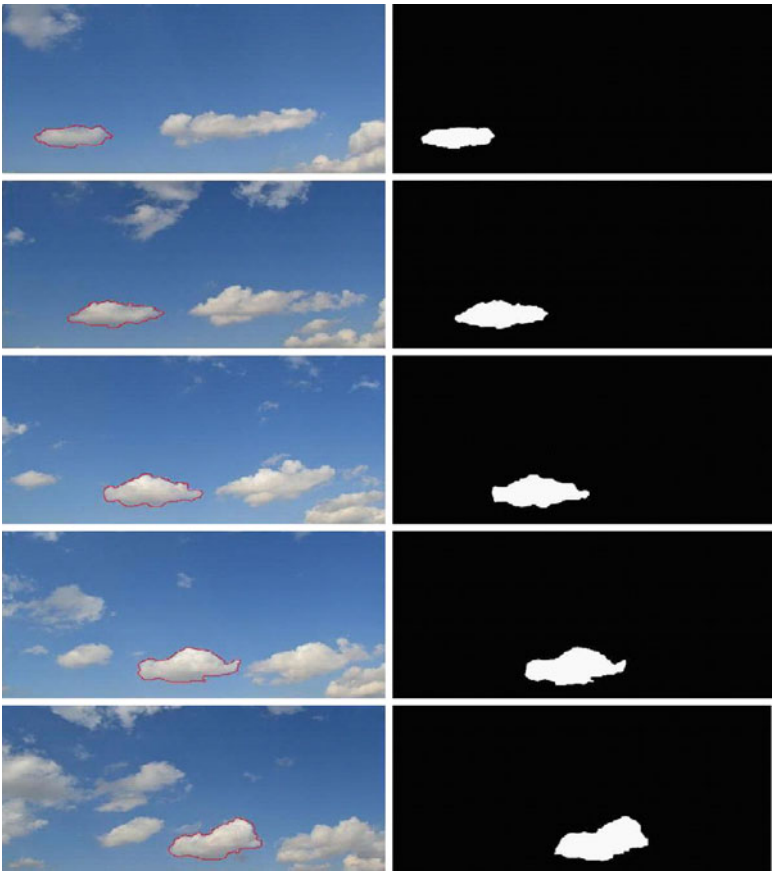

Fig. 1 Initial photograph and binary representation of the cloud/sky distinction for the first, third, fifth, seventh and ninth time step

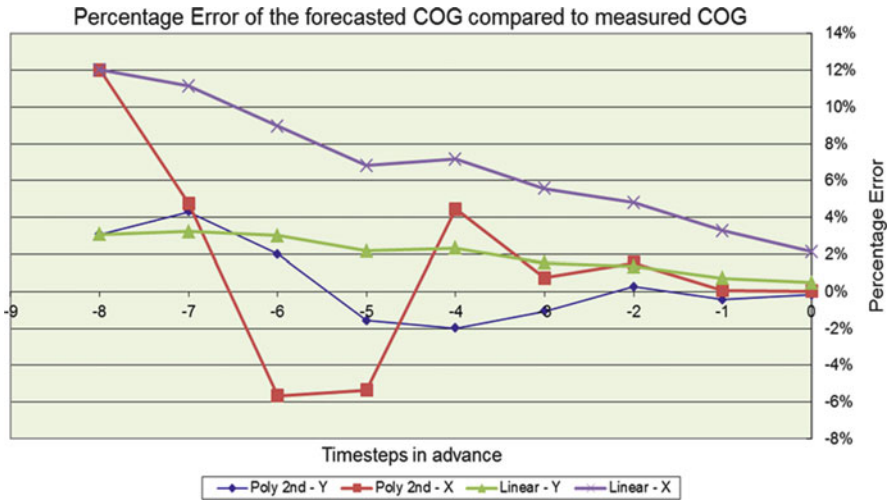

Fig. 2 Percentage error of the forecasted COG of the cloud in the tenth image compared to the measured COG of the same cloud

the initial picture where the preselected cloud is encircled in red contour and the binary representation of the distinction of clouds (white) from sky (black) for the first, third, fifth, seventh and ninth time step.

For each picture of the stack the COG and the statistical features of the cloud in the image were calculated. From the displacement of the COG of the cloud in the sequent images and the evaluation of the features of the cloud, the equation of motion of the cloud was calculated for both the vertical and horizontal axis using the following technique. Since the motion of clouds can be approximated as smooth deformation with local gradual variations in velocities (Zhou et al. 2001) the derived equations are in a linear or second degree polynomial form. At first the equation of motion of the cloud was estimated using the COG from the first two pictures. Using the derived equation the location of the COG for the next pictures was forecasted up to the last picture and compared to the true location of the COG as resulted from the pictures taken. Then this procedure was repeated in order to estimate the equation of motion using the first three pictures and so on, up to the penultimate picture. The aim of this procedure is the prediction of the location of the COG of the last picture, using as few pictures and as distant in time as possible.

Figure 2 above presents the accuracy of the forecasted location of the COG of the tenth photograph compared to the real location of the COG, for both the horizontal and vertical axis using a linear and a second degree polynomial equation. The vertical axis of the graph represents the accuracy, whereas the horizontal axis represents the last known photograph that was used to derive the equation of motion (i.e. at -8, 2 images were used to calculate the COG of the cloud, eight time steps in advance, at -7, 3 images were used to calculate the COG of the cloud, seven time steps in advance, and so on). As seen in the graph, the polynomial equation

simulates better the equation of motion of the cloud, achieving an absolute error of less than 6% by processing only four images and six time steps in advance of the "predicted" image.

5 Conclusions

The algorithm developed regarding cloud detection can distinguish clouds from sky. Yet, a variable threshold must be used to contain the angular dependence of the threshold for different zenith angles. The algorithm regarding the forecast of the future displacement of the cloud exhibits great dependence on the forecast period and the number of recorded images. As the forecast period decreases and the number of recorded images increases, the error in the estimation of the displacement of the cloud decreases. From our results we observe a low error in our calculation of the COG, thus the methodology can be further developed for longer intervals and other types of clouds.

References

Ahmad MJ, Tiwari GN (2011) Solar radiation models – a review. Int J Energy Res 35:271–290. doi:10.1002/er.1690

El Chaar L, Lamont LA, El Zein N (2011) Review of photovoltaic technologies. Renew Sustain Energy Rev 15:2165–2175. doi:10.1016/j.rser.2011.01.004

Heinle A, Macke A, Srivastav A (2010) Automatic cloud classification of whole sky images. Atmos Meas Tech 3:557–567. doi:10.5194/amt-3-557-2010

Kasten F, Czeplak G (1980) Solar and terrestrial radiation dependent on the amount and type of cloud. Sol Energy 24:177–189. doi:10.1016/0038-092X(80)90391-6

Koren I, Altaratz O, Feingold G, Levin Z, Reisin T (2009) Cloud's center of gravity – a compact approach to analyze convective cloud development. Atmos Chem Phys 9:155–161

Long CN, Sabburg J, Calbó J, Pagès D (2006) Retrieving cloud characteristics from ground-based daytime color all-sky images. J Atmos Ocean Tech 23:633–652. doi:10.1175/JTECH 1875.1

Pfister G, McKenzie RL, Liley JB, Thomas A, Forgan BW, Long CN (2003) Cloud coverage based on all-sky imaging and its impact on surface solar irradiance. J Appl Meteorol 42:1421–1434. doi:10.1175/1520-0450(2003) 042<1421:CCBOAI>2.0.CO;2

Roy G, Hayman S, Julian W (2001) Sky analysis from CCD images: cloud cover. Lighting Res Technol 33:211–222. doi:10.1177/136578280103300402

Thirugnanasambandam M, Iniyan S, Goic R (2010) A review of solar thermal technologies. Renew Sustain Energy Rev 14:312–322. doi:10.1016/rser: 2009.07.014

Zhou L, Kambhamettu C, Goldgof DB, Palaniappan K, Hasler AF (2001) Tracking nonrigid motion and structure from 2D satellite cloud images without correspondences. IEEE Trans Pattern Anal 23:1–7. doi:10.1109/34.969121

Carbonaceous Aerosols Over the Mediterranean and Black Sea

C. Theodosi, D. Smouliotis, P. Zarmpas, M. Kocak, and N. Mihalopoulos

Abstract The role of carbonaceous material (organic and elemental carbon) in the Mediterranean and Black sea atmosphere is yet to be unraveled. To fill this gap the present work is focused on the study of carbonaceous aerosols over the Mediterranean and Black Sea. Thus, aerosol samples were simultaneously collected at a remote site in Greece (Finokalia, Crete), a highly populated urban (Istanbul), a remote (Imbros) and two rural sites in Turkey (Sinop, Erdemli). Approximately 1,200 aerosol samples were collected and analyzed for Organic and elemental carbon (OC and EC), as well as water-soluble organic carbon (WSOC). Their seasonal variation, the factors controlling their variation and their relative contribution to aerosol mass is presented and thoroughly discussed. More specifically, organic matter constitutes a significant part of the total PM_{10} mass (21–33% of Particulate Organic Matter and 2–11% EC). The percentage of WSOC ranges from 37% to 40% of the OC for the four remote and rural regions, while in Istanbul constitutes 27% of OC and 10% of the total PM_{10} mass. Correlations with potassium and sulfate showed that the sources of organic matter in Istanbul are mainly due to the anthropogenic activities, while in rural and suburban areas to long range transport and biomass burning.

1 Introduction

Aerosols in the atmosphere arise from natural sources, such as windborne dust, sea-spray, volcanoes, and from anthropogenic activities, such as combustion of fossil fuels (Seinfeld and Pandis 1998). They are introduced into the atmosphere

C. Theodosi (✉) • D. Smouliotis • P. Zarmpas • N. Mihalopoulos
Department of Chemistry, University of Crete, P.O. Box 2208, 71003 Heraklion, Greece
e-mail: c_theodosi@chemistry.uoc.gr; mihalo@chmeistry.uoc.gr

M. Kocak
Institute of Marine Science, Middle East Technical University, Erdemli, Mersin, Turkey

C.G. Helmis and P.T. Nastos (eds.), *Advances in Meteorology, Climatology and Atmospheric Physics*, Springer Atmospheric Sciences,
DOI 10.1007/978-3-642-29172-2_172,

either directly (primary aerosols) or as a product of gaseous reactions in the atmosphere (secondary aerosols) and they play a significant role in the climate forcing.

Carbonaceous aerosols constitute an important fraction of aerosol mass and are classified into two types, elemental carbon (EC) and organic carbon (OC). EC is produced during incomplete combustion and emitted directly in the particle phase, whereas OC is not only emitted directly in particulate matter (primary) but it also forms by chemical reaction of volatile organic compounds in the atmosphere (secondary; Seinfeld and Pandis 1998). In general, secondary organic aerosol (SOA) compounds are water-soluble because they have polar functional groups (e.g. hydroxyl, carbonyl and carboxyl) produced by the oxidation reaction (Saxena and Hildemann 1996). Secondary OC can therefore be considered to be water-soluble organic carbon (WSOC), which in atmospheric particles influences aerosol behavior inside respiratory tracts and wet-scavenging processes in the atmosphere (Saxena and Hildemann 1996).

To evaluate the significance of carbonaceous material in the chemical composition of aerosols and identify their sources over the Mediterranean and the Black Sea, PM_{10} samples have been collected at five different locations around the two basins, during one year period. The aerosol samples were analyzed for organic, elemental carbon and dissolved organic carbon and main anions and cations.

2 Data and Methodology

PM_{10} particles were collected on Quartz filters (Quartz filter, QMA, 47 mm, Whatman) at five different sampling sites (Finokalia, Imbros, Erdemli, Sinop and Istanbul) on the frame of CITYZEN project, using a constant flow (16 L/min) Genk type sampler.

Sampling was conducted within the period April 2009–February 2010, with a 24-h sampling frequency, covering approximately more than 95% of each month.

2.1 Data

A map indicating the location of the aforementioned regions across the Mediterranean and Black Sea are depicted in Fig. 1.

2.2 Methodology

All filters were analyzed for Organic and elemental carbon (OC and EC), with the Thermal-Optical Transmission (TOT) technique (Birch and Cary 1996), using

Fig. 1 Location of the sampling sites: Finokalia (35°20′N, 25°40′E), Istanbul (41.12°N, 29.00°E), Erdemli (36.56°N, 34.25°E), Imbros (40.23°N, 254.90°E), Sinop (42.04°N, 35.04°E)

a Sunset Laboratory OC/EC Analyzer, while water-soluble organic carbon (WSOC) using an organic carbon analyser (TOC-VCSH, Shimadzu) as described in details by Theodosi et al. 2010. Water insoluble organic carbon (WIOC) concentrations were also calculated by subtracting WSOC concentrations from OC concentrations (WIOC = OC–WSOC). Secondary Organic Carbon (SOC) was determined by subtracting the OC/EC primary ratio multiplied by the EC concentrations from OC concentrations ($SOC = OC-(OC/EC)_{primary}*EC$ by Turpin and Huntzicker (1995), where the $OC/EC_{primary}$ ratio defined as the OC/EC from combustion sources and equal to 1). The particulate organic matter (POM) was estimated by multiplying the measured OC by a conversion factor (CF), which corresponds to the ratio of organic mass to organic carbon and depending on the site varies between 1.4 and 1.8 (Sciare et al. 2005).

3 Results

The OC, EC temporal variation (n = 260), representatively for Erdemli, one out of the five sampling sites are presented in Fig. 2.

Both OC and EC in the region of Finokalia, Istanbul, Sinop and Erdemli depict a distinct seasonal variability characterized by summer minimum and winter maximum concentrations, while in the region of Imbros the opposite seasonal variability is observed (Fig. 3).

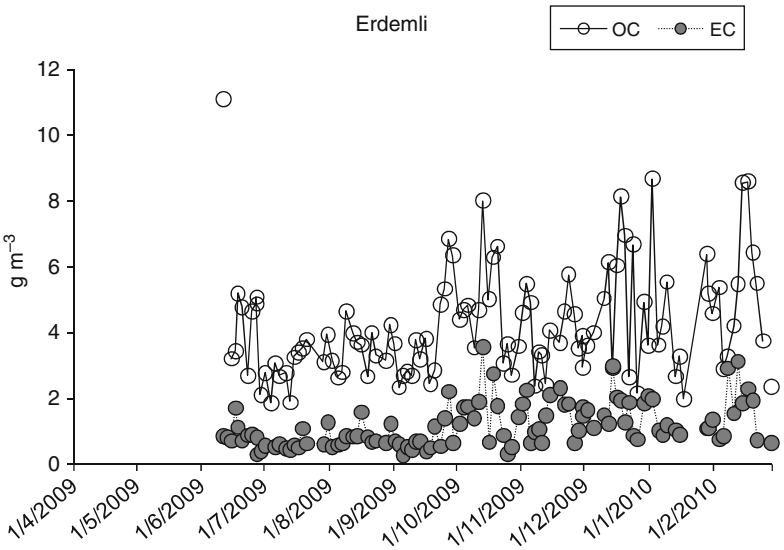

Fig. 2 Daily variation of OC and EC for PM_{10} levels collected at Erdemli

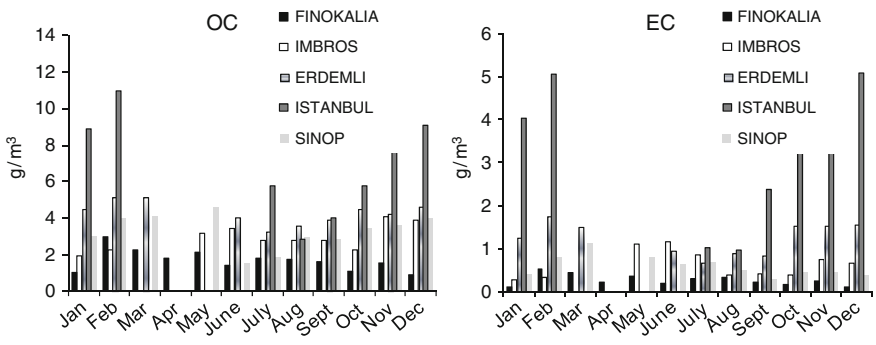

Fig. 3 Monthly average variations of OC and EC for all sampling sites in this study

The OC to EC carbon ratios, which are used to identify the presence of primary organic aerosols, indicate that in the case of Finokalia and Imbros (with OC/EC ratios exceeding 2; 3.2 and 2.3, respectively) OC is mostly secondary, whilst primary in Istanbul (OC/EC = 1.7).

The SOC percentages are higher for Finokalia, Sinop, Imbros and Erdemli (average 79%) than Istanbul's (average 53%) as presented in Fig. 4 (left). The low value of the Istanbul ratio underlines the major role of uncontrolled traffic-related or/and industrial originated emissions in Istanbul, as documented by Theodosi et al. (2010).

The determination of WSOC, WIOC and other elements can provide additional information regarding the carbon sources, such as the presence of secondary OC

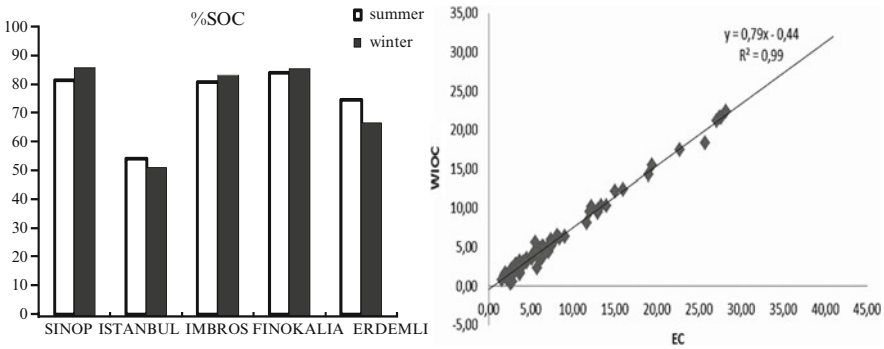

Fig. 4 The %SOC and WSIOC/EC ratio for Istanbul for summer and winter for all sampling sites, respectively

and primary emissions using WSOC and WIOC as indicators respectively (Theodosi et al. 2010).

A good correlation between WIOC and EC ($r^2 = 0.99$) was found in Istanbul indicating the influence of fossil fuel primary emissions (Fig. 4, right).

The WSOC to OC ratio in Istanbul during summer was found to be 0.36, slightly higher than the one observed in Cairo (0.33; Favez et al. 2008) indicating the existence of secondary (oxidised and more soluble) organic species, which increase water solubility. This ratio decreased during winter (0.25), due to the lack of photochemical oxidation, as well as to less wet depositional losses of WSOC relative to the insoluble carbon in winter (Kleefeld et al. 2002).

In addition the regression of OC and EC with no-sea-salt Potassium, showed that carbonaceous sources are mainly due to combustions of fossil-fuel especially those linked to traffic and vehicular exhausts. Moreover, during winter additional sources like household heating contribute to the total carbon loadings. In Sinop the main source of carbonaceous aerosol is biomass burning.

The total organic mass and the elemental carbon constitute a significant part in the PM_{10} mass of the measured samples (30% of POM and 11% EC in Istanbul, 33% of POM and 5% of EC in Imbros), while in Sinop and in Erdemli of relatively least (23% of POM and 2% of EC, 21% POM and 4% EC respectively).

4 Conclusions

This study reports on carbonaceous measurements of aerosols in the Mediterranean and Black Sea.

The average concentrations of OC and EC at Istanbul was much higher than the concentrations measured at the other sampling sites due to the abundance of anthropogenic sources at the greater Istanbul area.

OC and EC at Finokalia, Istanbul, Sinop and Erdemli demonstrate a clear seasonal variation with a minimum during summer and a maximum during winter.

In the case of Imbros the opposite tendency is observed. This can be explained by the fact that the aforementioned sampling site is located downwind of Istanbul, where the increased urbanization of megacities such as Istanbul can affect neighboring sites.

Regarding the carbonaceous composition, organic matter constitutes a significant part of the total mass of PM_{10} (21–33% POM and 2–11% EC). The percentage of WSOC ranges from 37% to 40% of the OC for the four remote regions, while in Istanbul constitutes 27% of OC and 10% of the total PM_{10} mass.

The correlation between OC and EC with no-sea-salt Potassium and with other ions (NO_3^-, Ox^-, SO_4^{2-}), showed that the sources of the OC and EC in Istanbul are due to combustions of fossil-fuels and vehicular exhausts, while in Sinop from biomass burning.

SOC values are higher in Finokalia, Sinop, Imbros and Erdemli than Istanbul's, reflecting the abundance of direct sources of pollution at the greater Istanbul area.

Acknowledgments This work has been funded by the EU project CITYZEN.

References

Birch ME, Cary RA (1996) Elemental carbon-based method for monitoring occupational exposures to particulate diesel exhaust. Aerosol Sci Technol 25:221–241. doi:10.1080/02786829608965393

Favez O, Cachier H, Sciare J, Alfaro SC, El-Araby TM, Harhash MA, Abdelwaha MM (2008) Seasonality of major aerosol species and their transformations in Cairo megacity. Atmos Environ 42:1503–1516. doi:10.1016/j.atmosenv.2007.10.081

Kleefeld S, Hoffer A, Krivacsy Z, Jennings SG (2002) Importance of organic and black carbon in atmospheric aerosols at Mace Head, on the West Coast of Ireland. Atmos Environ 36:4479–4490. doi:10.1016/S1352-2310(02)00346-1

Saxena P, Hildemann LM (1996) Water-soluble organics in atmospheric particles: a critical review of the literature and application of thermodynamics to identify candidate compounds. J Atmos Chem 24:57–109. doi:10.1007/BF00053823

Sciare J, Oikonomou K, Cachier H, Mihalopoulos N, Andreae MO, Maenhaut W, Sarda-Esteve R (2005) Aerosol mass closure and reconstruction of the light scattering coefficient over the Eastern Mediterranean Sea during the MINOS campaign. Atmos Chem Phys 5:2253–2265. doi:10.5194/acp-5-2253-2005

Seinfeld JH, Pandis SN (1998) Atmospheric chemistry and physics: from air pollution to climate change. Wiley, New York

Theodosi C, Im U, Bougiatioti A, Zarmpas P, Yenigun O, Mihalopoulos N (2010) Chemical composition of aerosols over Istanbul, Turkey. Sci Total Environ 408(12):2482–2491. doi:http://dx.doi.org/10.1016/S0269-7491(98)00186-9

Turpin BJ, Huntzicker JJ (1995) Identification of SOA episodes and quantification of primary and secondary organic aerosol concentration during the SCAQS. Atmos Environ 29:3527–3544. doi:http://dx.doi.org/10.1016/S1352-2310(99)00310-6

Physical and Chemical Processes of Polluted Air Masses During Etesians: Aegean-Game Airborne Campaign – An Outline

M. Tombrou, E. Bossioli, J. Kalogiros, J. Allan, A. Bacak, G. Biskos, H. Coe, A. Dandou, G. Kouvarakis, N. Mihalopoulos, A.P. Protonotariou, B. Szabó-Takács, and E. Triantafillou

Abstract Gaseous species and aerosol size distribution and chemical composition within the boundary layer during the Etesians is investigated, based upon airborne measurements, over the Aegean Sea, from Crete to Limnos islands (29/8–8/9 2011, Aircraft_BAe146–FAAM). Three flights of a similar route covered the eastern and western parts of the Aegean Sea. Two flights were performed on the same day to study the impact of the diurnal cycle. The sorties involved horizontal tracks mainly at 150 m a.s.l. and above the aerosol layer, at 2.5 km a.s.l., and profiles up to 4.5 km near the ground stations of Crete and Limnos and the Central Aegean Sea. Marked variations were detected in the vertical structure of aerosols and thermodynamic variables between the eastern and western segments flown around the Aegean.

M. Tombrou (✉) • E. Bossioli • A. Dandou • A.P. Protonotariou
Department of Meteorology and Atmospheric Physics, University of Athens, Athens, Greece
e-mail: mtombrou@phys.uoa.gr

J. Kalogiros
Institute of Environmental Research and Sustainable Development, National Observatory of Athens, Athens, Greece

J. Allan • A. Bacak • H. Coe
The School of Earth, Atmospheric and Environmental Sciences, University of Manchester, Manchester, UK

G. Biskos
Department of Environmental Studies, University of the Aegean, Mytilini, Greece

Delft University of Technology, Delft 2628BL, The Netherlands

G. Kouvarakis • N. Mihalopoulos
Environmental Chemical Processes Laboratory, Department of Chemistry, University of Crete, Heraklion, Greece

B. Szabó-Takács
Department of Soil Sciences and Climatology, University of Pécs, Pécs, Hungary

E. Triantafillou
Department of Environmental Studies, University of the Aegean, Mytilini, Greece

C.G. Helmis and P.T. Nastos (eds.), *Advances in Meteorology, Climatology and Atmospheric Physics*, Springer Atmospheric Sciences,
DOI 10.1007/978-3-642-29172-2_173,

Several discrete aerosol layers, separated by a clean slot, containing particles of different chemical composition were observed, with sulfates and organics being the dominant components. CO concentrations ranged from 80 ppb above the mixing layer, up to 140 ppb near the surface. O_3 ranged between 50 and 75 ppb, with higher values observed at surface upwind of Finokalia and in the mixing layer in Central and Northern Aegean Sea.

1 Introduction

Transport and transformation processes in the Eastern Mediterranean have been the topic of intensive studies that aim to evaluate their impact on regional air quality and visibility, climate and atmospheric composition change (e.g. Mihalopoulos 2007; Hildebrandt et al. 2010; Pikridas et al. 2010). In particular, during the Etesians, increased concentrations of gaseous pollutants and aerosol particles are observed, due to the simultaneous contribution of local and distant sources (Salisbury et al. 2003; Kalabokas et al. 2008). This complex mixture of fresh and aged pollution over the Aegean Sea is mainly controlled by the wind field that is modified by the numerous islands of the Aegean Sea, especially Crete during the Etesians (Kotroni et al. 2001). Recent simulations have shown that the existing dynamic and chemical processes in modelling systems could not always represent efficiently the observed physical and chemical atmospheric conditions in this area (Tombrou et al. 2009). These processes, therefore, warrant the availability of field measurements for the calibration of the models. In the present study we investigate the physical and chemical processing of polluted air transported over the Aegean troposphere during the Etesians based on airborne observations along the Aegean Sea, from Crete to Limnos islands (29/8–8/9 2011, Aircraft BAe146–FAAM).

2 Flight Measurements

The experiment involved flights of long legs; near surface and close to PBL top, along the direction from Lesvos to Crete sampling the spatial structure of the atmospheric parameters and of the chemical concentrations. Deep profiles exceeded the PBL top and included closed legs at the free troposphere both at the northern end above Limnos and at the southern part above Crete. The interpretation of the airborne measurements is enriched by the analysis of in situ continuous air pollution and meteorological measurements on the islands of Limnos and Crete. Furthermore, measurements were performed using instruments onboard commercial vessels commuting across the Aegean Sea. Measurements include three flights in the period from 29/8 to 8/9 of 2011. The flights (4–5 h each) were of similar route covering the eastern and western parts of the Aegean Sea. Two were performed on the same day to study the impact of the diurnal cycle. The sorties involved

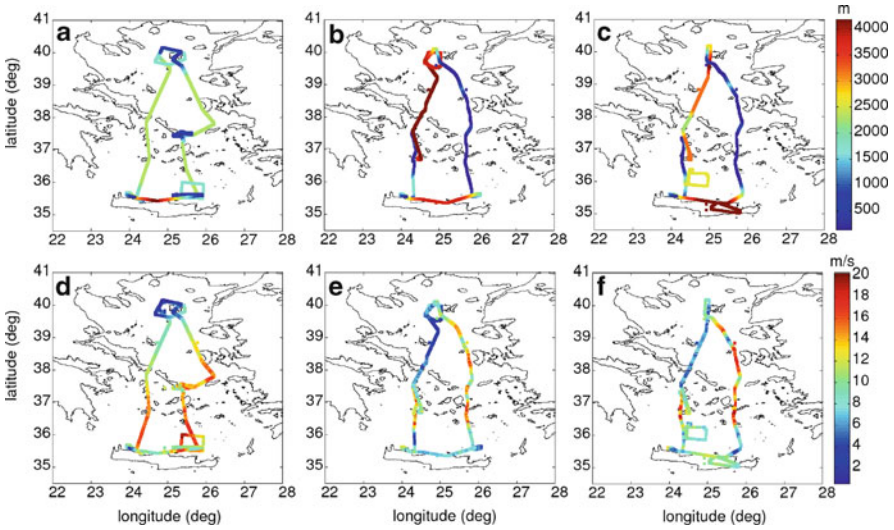

Fig. 1 Flight trajectories along with the flight altitude in color, for flight (**a**) B637 on 1 September 2011, (**b**) B640 on 4 September 2011 and (**c**) B641 on 4 September 2011 and along with the horizontal wind speed in color, for flight (**d**) B637, (**e**) B640 and (**f**) B641

horizontal tracks mainly at 150 m and above the aerosol layer, at 2.5 km above sea level (a.s.l.), and profiles up to 4.5 km near the sites of ground measurements, at Crete and Limnos and in the Central Aegean Sea (Fig. 1a, b, c).

2.1 Meteorological and Air Quality Data

On 1 September 2011 (flight B637), a large-scale surface anticyclone prevailed over the south-eastern Europe, that produced fair weather conditions and a moderate flow from the north-east sector over the Aegean Sea. On 4 September 2011, the low pressure pattern that prevailed over the southeastern Europe, in combination with the anticyclone over Balkans (flights B640 and B641) resulted in a strong channeled surface-wind flow over the Aegean Sea (not shown). Average wind speed of up to 20 ms^{-1} measured at 150 m a.s.l., while it diminished above 4.5 km (Fig. 1d, e, f).

Atmospheric turbulence measurements (32 Hz) were obtained with a radome probe, at the nose of the aircraft, combined with fast GPS/INS attitude angle measurements for the estimation of wind components and with fast temperature and humidity measurements. Vertical velocities were corrected for aerodynamic effects, which are significant at high frequencies (Kalogiros and Wang 2002).

Gaseous species, aerosol size distribution and chemical composition have been measured onboard. The University of Manchester AMS system was fitted to the three flights during the Aegean Game but it operated only during B637 and

Table 1 Instruments operating on BAe146–FAAM aircraft

Meteorology	Chemistry, cloud physics, aerosol
Rosemount/Goodrich type 102 total air temperature sensors (32 Hz)	TE49C UV photometric ozone analyzer (1 Hz)
Heimann IR brightness temperature (8–14 μm) (4 Hz)	AL 5002 VUV fast fluorescence CO analyzer (1 Hz)
General eastern hygrometer (4 Hz)	AQD dual channel chemiluminescence NOx (1 Hz)
Buck CR2 cryogenic hygrometer dew point (1 Hz)	Passive cavity aerosol spectrometer probe (0.1–3 μm) (1 Hz)
TWC Lyman-alpha hygrometer (64 Hz)	Cloud droplet probe (3–50 μm) (1 Hz)
Johnson Williams liquid water (4 Hz)	Particle soot absorption photometer 565 nm (1 Hz)
Broad band radiometers: clear and red (1 Hz)	TSI 3563 nephelometer at 450, 550 and 700 nm (1 Hz)
Position/dynamics: GPS, GIN (32 Hz), radar altimeter (2 Hz)	Aerosol mass spectrometer (AMS) (40–700 nm) (10 Hz)
Turbulence probe (32 Hz)	Scanning mobility particle sizer (SMPS) (10 Hz)

B641 flights. Table 1 summarizes the meteorological and air quality data obtained during the campaign.

3 Results

The turbulent quantities at 150 m a.s.l. were calculated using the eddy-correlation method and the horizontal averaging length was set to 5 km. Preliminary results show that the wind stress has a strong variation through the Aegean Sea but also within a short distance. In a few cases, over the area of West Cyclades, the wind stresses even exceed the value of 0.6 Nm^{-2}. Much lower values (of more than one order) are calculated in the northern part of Aegean (near Limnos). It is worth mentioning that the larger values of wind stress are not related with the higher wind speeds. The higher values of sensible heat flux are measured in the middle of Aegean Sea. Apart from a few cases of positive heat flux (up to 35 Wm^{-2} measured at East Cyclades), most of the area is characterized by negative heat flux. The higher negative values, where in some cases exceed 100 Wm^{-2}, are measured in the West Cyclades and are well related to the lower SST at this region.

The knowledge of the PBL evolution over the Aegean Sea, during an Etesian event, constitutes a main objective of this study. A first examination of the deep profiles at the northern and southern parts from the three flights shows that the boundary layer height is less than 1 km at the northern part while it even exceeds the height of 2.5 km at the area northern of Crete.

The spatial distribution of ozone and CO indicates large gradients in the concentrations. The ozone average measured concentrations is 61.22 $\pm$ 5.23 ppb, 56.01 $\pm$ 6.33 ppb and 57.80 $\pm$ 5.83 ppb for the B637, B640 and B641 flights, respectively. The higher values are observed near surface upwind of Finokalia station (75 ppb), in the mixing layer in the Central and Northern Aegean Sea

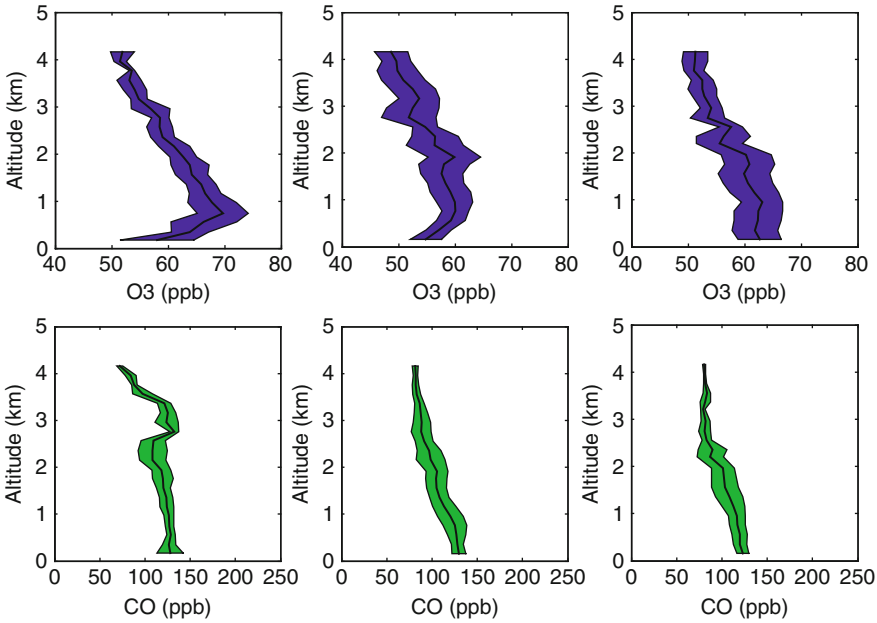

Fig. 2 Mean (± standard deviation) vertical profile of O_3 (*top*) and CO (*bottom*) over the Aegean Sea during flights B637 (*left*), B640 (*middle*) and B641 (*right*)

(65–75 ppb) and downwind of the Athens plume near Milos (65 ppb). The CO average measured concentrations are 115.87 ± 16.41 ppb, 108.26 ± 26.96 ppb and 98.74 ± 20.82 ppb for the B637, B640 and B641 flights, respectively. The higher CO concentrations are observed at the eastern side of the Aegean Sea (120–140 ppb). In Fig. 2, the mean vertical profiles of ozone and CO during the three flights are presented. The CO concentrations decrease up to 100 ppb at 2 km. During the B637 flight an enhancement is evident at 3 km (over Crete) while during the B641 flight enhanced CO concentrations were observed at 2 km (close to Finokalia). Above these altitudes, background concentrations of the lower troposphere were observed. The ozone profile reveals the presence of a lower tropospheric enhancement where the mean is above 60 ppb. Individual profiles show values of 70 ppb inside the PBL. On 4th September, both in the morning and afternoon flights, an ozone enhancement is evident at 2 km. Above 2 km the concentrations are 50–55 ppb.

Several discrete aerosol layers of different chemical composition were observed with the cToF-AMS throughout the Aegean. Sulphates and organics are the dominant components with mass fractions contribution 46.3% and 43%, respectively. Ammonium, nitrates and chloride contribute by 8.7%, 1.9% and 0.08%, respectively. The maximum and mean concentrations of the chemical components measured by AMS for flight B641 are presented in Table 2. Marked variations were evident in the vertical structure of aerosols and thermodynamic variables between the eastern and western segments flown around the Aegean.

Table 2 Maximum and mean concentrations for all the chemical compounds measured with AMS during B641 flight

	Max	Mean
Sulphates (μg sm^{-3})	15.345	5.005 ± 4.7965
Organic matter (μg sm^{-3})	12.684	4.170 ± 3.999
Ammonium (μg sm^{-3})	4.693	1.539 ± 1.607
Nitrate (μg sm^{-3})	1.608	0.179 ± 0.184
Chloride (μg sm^{-3})	0.331	0.017 ± 0.026

4 Conclusions

A strong variability on ABL physical and chemical structure was detected, during the Aegean-Game airborne campaign over the Aegean Sea. The measured physical parameters and chemical/aerosol concentrations will be compared with model predictions to assess their ability to capture various processes in the atmosphere over the Aegean Sea.

Acknowledgments This work is supported by the EUFAR (227159) EC Grant Agreement under the AEGEAN_GAME2 project. We thank the FAAM Team. Due to limited space we could not acknowledge in person each of the participants. This will be done in a future publication.

References

Hildebrandt L, Engelhart GJ, Mohr C et al (2010) Aged organic aerosol in the Eastern Mediterranean: the Finokalia aerosol measurement experiment-2008. Atmos Chem Phys Discuss 10:1847–1900. doi:10.5194/acpd-10-1847-2010

Kalabokas PD, Mihalopoulos N, Ellul R, Kleanthous S, Repapis CC (2008) An investigation of the meteorological and photochemical factors influencing the background rural and marine surface ozone levels in the Central and Eastern Mediterranean Atmos Environ 42(34):7894–7906

Kalogiros J, Wang Q (2002) Aerodynamic effects on wind turbulence measurements with research aircraft. J Atmos Oceanic Technol 19:1567–1576. doi:10.1175/1520-0426(2002) 019<1567:AEOWTM>2.0.CO;2

Kotroni V, Lagouvardos K, Lalas D (2001) The effect of the island of Crete on the etesian winds over the Aegean Sea. Q J R Meteor Soc 127(576):1917. doi:10.1002/qj.49712757604

Mihalopoulos N (2007) Long-range transport of pollutants above the Eastern Mediterranean: implications for air quality and regional climate In: Mellouki A, Ravishankara AR (eds) Regional climate variability and its impacts in the Mediterranean area. In: Proceedings of the NATO advanced research workshop on regional climate variability and its impacts in the Mediterranean area, Series: NATO Science Series: IV: Earth and Environmental Sciences, vol 79. Marrakech, 1 Sep 2006

Pikridas M, Bougiatioti A, Hildebrandt L et al (2010) The Finokalia Aerosol Measurement Experiment–2008 (FAME-08): an overview. Atmos Chem Phys 10:6793–6806. doi:10.5194/acp-10-6793-2010

Salisbury G, Williams J, Holzinger R et al (2003) Ground-based PTR-MS measurements of reactive organic compounds during the MINOS campaign in Crete, July-August 2001. Atmos Chem Phys 3:925–940. doi:10.5194/acp-3-925-2003

Tombrou M, Bossioli E, Protonotariou AP et al (2009) Coupling GEOS-CHEM with a regional air pollution model for Greece. Atmos Environ 43:4793–4804. doi:10.1016/j.atmosenv.2009.04.003

Lignite Power Plant's Contribution to the Particulate Pollution in the Grater Western Macedonia Area, Greece

A.G. Triantafyllou, A. Krestou, and V. Matthaios

Abstract Quantifying the contribution of individual sources to air pollution in one area is the first essential step in managing air quality in this region. The area of Western Macedonia is a very complex in terms of air quality management problem because of large and complex pollution sources operating in the region. The emissions from five lignite power plants (LPP) operating in this region, the corresponding opencast lignite mining, as well as the urban activities in the industrial axis, is a complex problem to quantify the contribution of these sources in a spatial and temporal scale in the region. This paper attempts to quantify the contribution of LPP to the particulate pollution of this region, using PM10 concentrations measurements and simulations. Specifically were used: (a) suspended particulate PM10 concentration measurements for a 4 years period (2007–2010) at various locations in the region and (b) simulations of atmospheric dispersion.

1 Introduction

An important step for the air quality management in a region and the consequent implementation of the necessary measures aiming towards the most effective treatment of atmospheric pollution problems, are source apportionment studies. Six methods for attributing ambient pollutants to emission sources are usually used: emissions analysis, trend analysis, tracer studies, trajectory analysis, receptor modeling and dispersion modeling (Blanchard 1999). Dispersion models are well suited for estimating quantitative source-receptor relationships, because the effect of individual emission sources or source regions on predicted ambient

A.G. Triantafyllou (✉) • A. Krestou • V. Matthaios
Laboratory of Atmospheric Pollution and Environmental Physics (LAP-EP),
Technological Education Institute of Western Macedonia, 50100 Kozani, Greece
e-mail: atria@airlab.teikoz.gr

C.G. Helmis and P.T. Nastos (eds.), *Advances in Meteorology, Climatology and Atmospheric Physics*, Springer Atmospheric Sciences,
DOI 10.1007/978-3-642-29172-2_174,

concentrations can be studied. This method was selected in this study for attributing ambient pollutants to emission sources in the Amyntaion–Ptolemais–Kozani Basin (APKB), a complex terrain area in NW Greece.

The area is characterized by an intensive industrial activity with five lignite combustion power plants and open pit mines. In addition the different types of pollution sources in this area related with urban and agricultural/burning biomass activities, result in huge amount of pollutants' emissions, mainly dust emissions, and high PM10 concentrations (Triantafyllou 2003). The variety of pollution sources and the topography complexity render the source apportionment study of this area an interesting case study. There are only a limited number of works which attempt to study the contribution of the different pollution sources to the PM10 concentrations in the area. Triantafyllou and Kassomenos (2002), investigated the atmospheric conditions which favor the pollutants' transport emitted by the LPP, by using a coupled atmospheric mesoscale model and Lagrangian dispersion model. Samara (2005), employed a CMB receptor model to determine contributions to ambient TSP levels at the different receptor sites in APKB, while Tolis et al. (2011), made a preliminary source apportionment study for the city of Kozani conducted through a PMF model application. The current study is focused on the investigation of the LPP emissions' contribution to the PM10 pollution in urban and agricultural areas of APKB. For this purpose meteorological observations, PM10 concentration measurements and simulations of atmospheric dispersion are used.

2 Data and Methodology

2.1 Study Area

APKB is located in the middle of Western Macedonia, GREECE, that is characterized as a broad, relatively flat bottom basin surrounded by tall mountains with heights 600-more than 2,000-m above Mean Sea level (Fig. 1, left). The climate of the area is continental Mediterranean with low temperatures during winter and high ones during summer. The winds in the center of the basin blow mostly along the NW/SE axis due to channeling of the synoptic wind, since the NW/SE axis coincides with the major geographical axis of the basin. Five lignite power stations (Fig. 1, left) operate in the basin with lignite mined in the nearby open pit mines, resulting in the greatest amount of the total electrical energy produced in Greece. One lignite power station 675 MW (PS6) also operates in Bitola/FYROM, close to the border with the area under interest. Considerable amounts of fly ash and fugitive dust are emitted from the LPPs stacks and mining operations (Triantafyllou 2003). In the two major towns of the area (Kozani and Ptolemais) about 100.000 people live and work. There are also several villages with population ranging from several 100 s to several 1,000 s of inhabitants.

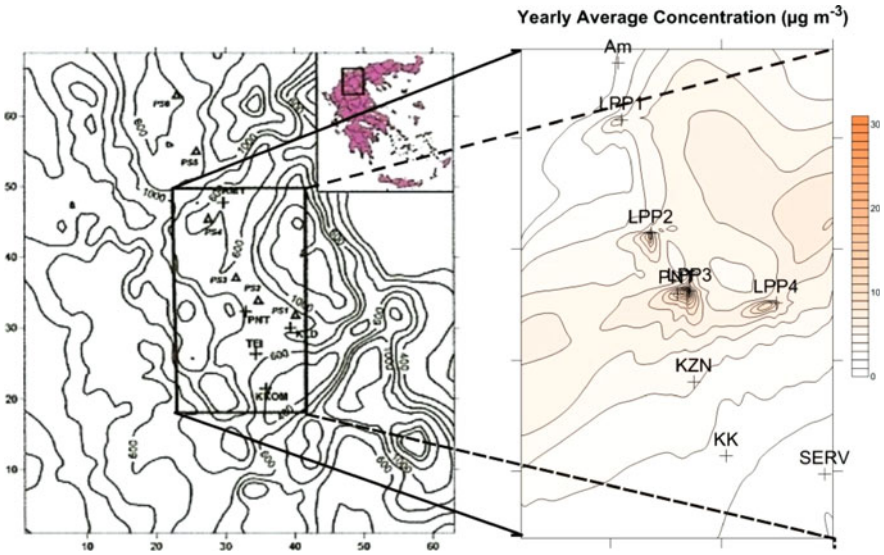

Fig. 1 (*Left*) The topography of the APKB showing the locations of the lignite power stations (PS1.6) and the monitoring stations. The location of the two major towns, Kozani and Ptolemais, is also shown. Elevations are in meters. (*Right*) Annual average concentration contours of PM10 originated from LPS, 2008. Concentrations are given in μg/m^3

2.2 The Dispersion Model (TAPM)

TAPM is a nestable, prognostic meteorological and air pollution model that solves fundamental fluid dynamics and scalar transport equations to predict meteorology and pollutant concentration for a range of pollutants important for air pollution applications. For computational efficiency, it includes a nested approach for meteorology and air pollution, with the pollution grids optionally being able to be configured for a sub-region and/or at finer grid spacing than the meteorological grid, which allows a user to zoom-in to a local region of interest quite rapidly. More information can be found in Triantafyllou et al. (2011), Hurley et al. (2005).

The model run for a 4 years' period using 25 vertical model levels, and three nested domains of 25 × 25 horizontal grid points at 30, 10 and 1-km spacing for the meteorology, and 141 × 221 horizontal grid points at 3, 1, and 0.3-km spacing for the pollution. NCEP synoptic analyses were used at the outer grid boundaries. The stacks of the 5 LPP in the APKB (3 stacks for Agios Dimitrios, 4 stacks for Kardia, 3 stacks for Ptolemaida and 1 stack for Amyntaion) were employed as emission sources, with their coordinates being obtained by the Universal Transverse Mercator. The LPP of Pontokomi was considered as the center (0,0,0).

3 Results and Discussions

3.1 PM10 Background Concentrations Computation

The PM10 background calculation is carried out either by subtracting the local sources contribution calculated by the model from the measured concentration in a distant station or by discriminating pollution measurements according to the wind direction (Kakosimos et al. 2011). The mean monthly background for the 4 years studied was calculated here following the first method for K. Komi (the most distant station), and the mean value was estimated 20 μg/m^3. This value was confirmed by the pollution rose of the same area (Fig. 2a), which gives the same value for wind blowing from the opposite (Fig. 2b) to the LPPs direction (19 μg/m^3). Since the results of both methods vary for only 1 μg/m^3, the first calculation method was preferred for the background estimation as the most straightforward.

3.2 Spatial Distribution of PM10 Concentrations

The spatial distribution of PM10 concentrations due to LPP contribution was calculated for each of the 4 years studied (2007–2010). Figure 1b shows the PM10 annual average concentration contours in APKB for 2008. The highest PM10 concentration calculated from TAPM model (17 μg/m^3) corresponded to receptors around the LPP sources. The same situation was true for all the studied years. On the other hand, the PM10 contribution of LPPs to receptors outside the basin was found much lower (3 μg/m^3) in both south and north areas.

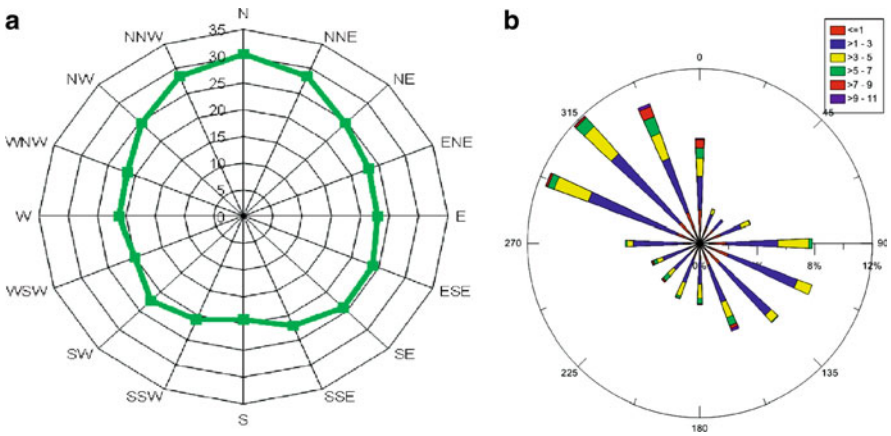

Fig. 2 (**a**) Pollution rose in K. Komi, (**b**) wind rose in K. Komi, for 2009–2010

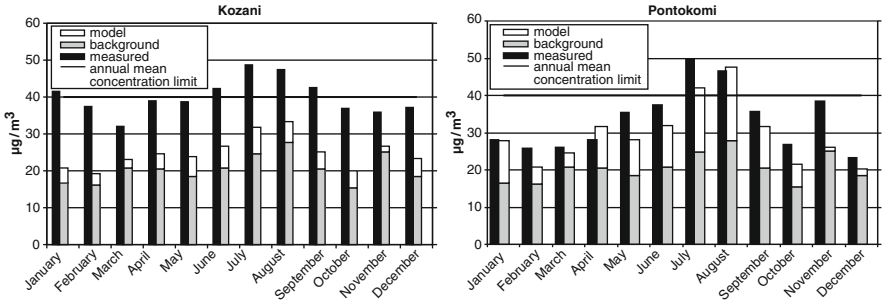

Fig. 3 Monthly average PM10 concentrations calculated by TAPM plus the background concentration compared to data from the monitoring station (*left*) in the center of Kozani and (*right*) in Pontokomi, from 2007 to 2010

3.3 Comparison with Measurements by Monitoring Stations

The mean monthly concentrations for the whole period for the urban area (Kozani), is presented in Fig. 3, left. The LPPs contribution to PM10 concentrations in the urban area for the whole period was about 10%. However, this percentage is raised to 19% if the background is not taken into consideration.

According to Tolis et al. (2011), a percentage of 23.7% of PM10 in Kozani is attributed to coal and lignite burning. The discrepancy in the results of the aforementioned study and the current one is explained by the fact that in the work of Tolis et al. (2011), fly ash together with coal from open pit mines is considered, while at the same time the results were obtained for a very short study period (from 20/12/2009 to 12/01/2010 and from 19/07/2010 to 30/07/2010). In the work of Samara (2005) the LPS contribution to TSP in Kozani is 6–8%. The higher corresponding contribution calculated by TAPM in Kozani is explained by the fact that the current work studied the PM10 dispersion from LPPs while the former work studied TSP dispersion from the same source. Since finer particulate matter can be dispersed in a larger area, and Kozani is far from LPPs (13 km), the results seam realistic. The highest contribution of LPPs (Fig. 3, right) was for Pontokomi (29%), a result that was expected since this area is the closest to LPP (1.7 km). This percentage is raised to 66% if the background is not taken into consideration. The agricultural areas (Amyntaio and K. Komi), seem to be affected by LPS PM10 emissions at the same extent (12–13%). This is also a reasonable result, since both receptor areas are in the boundaries of the basin (Fig. 1, left). According to Samara (2005) the LPPs contribution to TSP in Amyntaio is 7–8%. The higher corresponding contribution calculated by TAPM in Amyntaio could be attributed to the same reason as in the case of Kozani (see above).

The validation metrics as recommended by Schatzmann et al. (2010) in COST 732 provide a comparison between the sum of background and TAPM calculated concentrations and the monitoring stations measurements. The calculated values were Fractional Bias (FB) $= -0.26$ ($|FB| < 0.3$), Geometric Mean Bias

(MG) = 1.31 (0.7 < MG < 1.3), Geometric Variance (VG) = 1.11 (VG < 1.6). From the above results, the sum of background and TAPM calculated concentrations and the monitoring stations measurements are marginally agree.

4 Conclusions

The current study focused on the contribution of PM10 emissions from LPPs in three agricultural (Amyntaio, Pontokomi, K. Komi) and one urban (Kozani) areas in APKB. The study covered a 4 years period, from 2007 to 2010, and employed the atmospheric dispersion model TAPM. A comparison between the sum of background and TAPM calculated concentrations and the monitoring stations measurements using selected indices showed a marginal agreement. The highest contribution of PM10 emitted from LPPs was observed for Pontokomi, which is the closest to LPP receptor area. The LPPs contribution to Kozani was 10%, however this percentage raised to 19% when the background was not considered.

Acknowledgments The authors would like to thank the Greek Public Power Corporation for providing the data from its stations located in Amyntaio, Pontokomi, K. Komi.

References

Blanchard CL (1999) Methods for attributing ambient air pollutants to emission sources. Annu Rev Energy Environ 24:329–365. doi:10.1146/annurev.energy.24.1.329

Hurley P, Physick W, Luhar A (2005) TAPM – a practical approach to prognostic meteorological and air pollution modeling. Environ Model Softw 20:737–752

Kakosimos KE, Assael MJ, Katsarou AS (2011) Application and evaluation of AERMOD on the assessment of particulate matter pollution caused by industrial activities in the greater Thessaloniki area. Environ Technol 32:593–608. doi:10.1080/09593330.2010.506491

Samara C (2005) Chemical mass balance source apportionment of TSP in a lignite-burning area in Western Macedonia, Greece. Atmos Environ 39:6430–6443

Schatzmann M, Olesen H, Franke J (2010) COST action 732 model evaluation case studies: approach and results. University of Hamburg, Meteorological Institute Centre for Marine and Atmospheric Sciences, Hamburg

Tolis EI, Saraga DE, Amari GZ, Gougoulas T, Papaioanou CC, Sorioglou AK, Kougioumtzidis E, Sfetsos A, Bartzis JG (2011) Particulate matter (PM) and source apportionment studies during winter and summer period in the city of Kozani, Greece. In: 16th MESAEP international symposium, Ioannina, Greece. Poster

Triantafyllou AG (2003) Levels and trend of suspended particles around large lignite power stations. Environ Monitor Assess 89:15–34. doi:10.1023/A:1025829907390

Triantafyllou AG, Kassomenos PA (2002) Aspects of atmospheric flow and dispersion of air pollutants in a mountainous basin. Sci Total Environ 297:85–103. doi:10.1016/S0048-9697(02)00090-6

Triantafyllou AG, Krestou A, Hurley P, Thatcher M (2011) An operational high resolution local-scale meteorological and air quality forecasting system for Western Macedonia, Greece: some first results. In: Proceedings of the 12th international conference on environmental science and technology, Rhodes Island, Greece, pp A1904–1911

Assessment of the Impacts of Climate Change on Ozone Air-Quality in Europe

K.V. Varotsos, C. Giannakopoulos, and M. Tombrou

Abstract Although consensus exists among the scientific community that climate change could affect future air-quality through its linkages to weather meteorology, the evolution of the atmospheric composition in a changing climate needs to be further investigated. The objective of this study is to investigate the potential impact of future climate change on ozone air-quality in Europe. Simulations with the global chemical transport model GEOS-CHEM driven from the GISS III general circulation model are conducted for a present (1999–2001) and the future (2049–2051) 3-year period. To isolate the effects from changes in climate and anthropogenic emissions four types of simulations are performed: (1) present day climate and emissions (2) future climate following the IPCC SRES A1B scenario and present day anthropogenic emissions of ozone precursors (3) present day climate and future emissions and (4) future climate and emissions. Results indicate that the impact of climate change on its own leads to an increase of less than 3 ppb in western and central Europe. When both climate change and future emissions are implemented in the simulations higher changes in the ozone concentrations are evident reaching 12 ppb in the South west and east Mediterranean. Moreover, the ozone photochemical sensitivity to isoprene and nitrogen oxides (NOx) is also investigated.

K.V. Varotsos (✉)
Division of Environmental Physics and Meteorology, National and Kapodistrian University of Athens, Athens, Greece

Institute for Environmental Research and Sustainable Development, National Observatory of Athens, Athens, Greece
e-mail: kvarotso@phys.uoa.gr

C. Giannakopoulos
Institute for Environmental Research and Sustainable Development, National Observatory of Athens, Athens, Greece

M. Tombrou
Division of Environmental Physics and Meteorology, National and Kapodistrian University of Athens, Athens, Greece

C.G. Helmis and P.T. Nastos (eds.), *Advances in Meteorology, Climatology and Atmospheric Physics*, Springer Atmospheric Sciences,
DOI 10.1007/978-3-642-29172-2_175,

1 Introduction

Climate change impact on ozone air-quality is an area of research evolved over the last decade based on the assumption that air quality is strongly dependent on weather systems and therefore sensitive to climate change. The majority of the studies focus on areas with increased anthropogenic activities using 3D climate chemistry modeling systems with coarse or finer resolutions (Jacob and Winner 2009; Katragkou et al. 2011). A wide range of results exists in literature regarding the regional patterns of ozone, associated with the modeling systems used, the time slices investigated as well the future emissions scenario incorporated in the simulations. Although uncertainty exists, climate-chemistry modeling studies demonstrate a probable worsening of future air-quality and therefore become useful tools for minimizing the adverse health effects. The objective of this study is to investigate the impact of future climate change on ozone air-quality in Europe using a coupled global climate-chemistry model.

2 Methodology

The GEOS-CHEM chemical transport model driven by meteorological fields from the NASA/GISS III GCM is used to investigate ozone air quality in Europe under present and future climate. The horizontal resolution is $4^{o} \times 5^{o}$ with 23 vertical levels extending up to 0.02 hPa. For the purposes of this study four scenario simulations are performed: (a) present day climate and emissions (b) future climate following the IPCC SRES A1B scenario (Nakicenovic and Swart 2000) and present day anthropogenic emissions of ozone precursors (c) present day climate and future emissions and (d) future climate and emissions. The base year anthropogenic emissions inventory used in this study is 2000 while for the future anthropogenic emissions growth factors based on the A1B scenario are applied on the present day emissions as described in Wu et al. (2008). For instance, future NOx anthropogenic emissions are projected to increase both globally and in the European domain by about 97% and 15% respectively. Anthropogenic CO emissions are projected to increase by 26% globally whereas a decrease of 24% is expected in Europe.

The model's inventory also includes natural emissions of ozone precursors such as NMVOCs from vegetation and NOx from soil and lightning which are computed within the model and are allowed to vary with the meteorological variables. NMVOCs vary only with temperature and solar radiation. An extensive description of the model's emission inventory is provided in Wu et al. (2008).

The simulations performed here cover two 3-year time slices: 1999–2001 (2000) for the present day climate and 2049–2051 (2050) for future climate. The results presented are 3-year averages and are calculated over the period April 1–September 30 (AMJJAS).

3 Results

3.1 Temperature and Isoprene

Figure 1a shows that the highest temperatures are simulated by GISS-GCM at regions below 45° latitude for the present climate. Results from the changes between future and present day climate indicate that climate change affects mostly the western areas of the European domain whereas small changes are shown for the eastern ones (Fig. 1b).

More specifically, the mean temperature increase between the two periods is less than 0.9° with the highest, about 1.2°, evident at the Iberian peninsula and the British Isles. In central and northern Europe temperature increases vary from 0.5° to 1° whereas for the rest of the areas increases less than 0.5° are shown. Isoprene biogenic emissions increases in the future are less than 10% (Fig. 1d) compared to

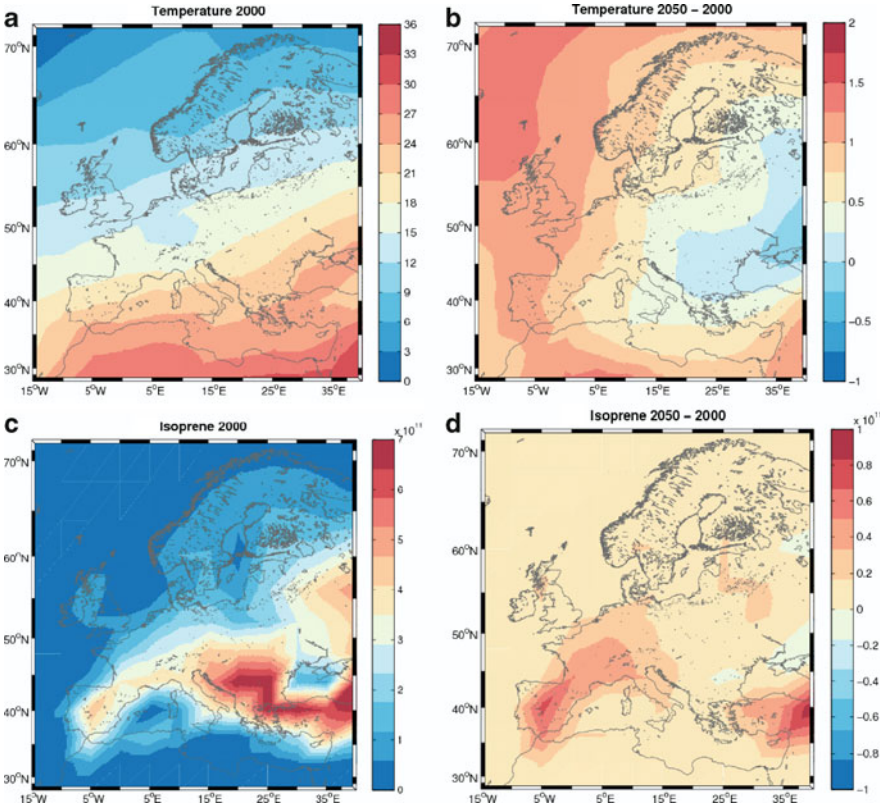

Fig. 1 Simulated average (**a**) temperature for the present day climate (1999–2001), (**b**) temperature changes between 2050 climate (2049–2051) and present day climate, (**c**) present day climate isoprene emissions and (**d**) isoprene emission changes for the AMJJAS period. Units for temperature are °C whereas for isoprene atomC/cm^2/s

the present day emissions (Fig. 1c) due to temperature increases with the highest increases evident at south west Europe.

3.2 *Surface O_3 and NOx*

In Fig. 2a–d results for the average daily maximum 8-h average ozone concentrations (AMJJAS period) under present climate (Fig. 2a) as well as changes between each of the scenario simulations and the present day simulation are shown (Fig. 2b–d).

From Fig. 2b it is evident that the impact of climate change on its own leads to an increase of less than 3 ppb in western and central Europe whereas smaller changes are shown for the rest of the areas. In north west and central Europe this increase is attributed, partly due to NOx abundance (Fig. 2e) as well as to the increase of isoprene biogenic emissions due to increased temperatures (Fig. 1d). In the south west Europe, where lower NOx concentrations are simulated, the increase is mostly attributed to the enhanced isoprene emissions. When future emissions are implemented in the simulations, larger changes in ozone concentration are evident (Fig. 2c, d). The highest increases over land are evident in the south west and south east Mediterranean (about 12 ppb). From Figs. 1c, d and 2e, f it is evident that in both areas ozone increases are attributed to the increased NOx in the model. Two other areas that exhibit interesting results are the southern areas of France and in north west Europe (London agglomerations, Channel region and parts of Benelux region). At both areas NOx anthropogenic emissions are projected to decline under A1B future emissions scenario by about 35% although an increase of about 15% is expected in Europe by 2050 (not shown). In the first area, a decrease in the simulated ozone concentrations is shown (Fig. 2c, about 2 ppb) whereas an increase of about 6 ppb is shown for the second one. It should be noted that similar results can be found in a previous study (Beekmann and Vautard 2010) where the authors examined the ozone formation chemical regime (sensitivity of ozone photochemical formation to volatile organic compounds (VOCs) and NOx emissions). In particular, it was found that a decrease of 30% in NOx emissions compared to the control run, leads to a decrease of 3–5 ppb in the Mediterranean and to an increase over 3 ppb in the greater Channel area.

In the extreme north European areas (above 60^{o} latitude), ozone concentrations show decreasing tendencies although temperature seems to increase under climate change. In this case, additional meteorological parameters should be considered such as mixing height and convective fluxes. Moreover, other chemical species that are associated to the ozone formation such as PAN need to be investigated.

4 Conclusions

In this study the impact of climate change on ozone air-quality in Europe was examined with the use of the GEOS-CHEM chemical transport model driven by meteorological fields from the NASA/GISS III GCM. A combination of

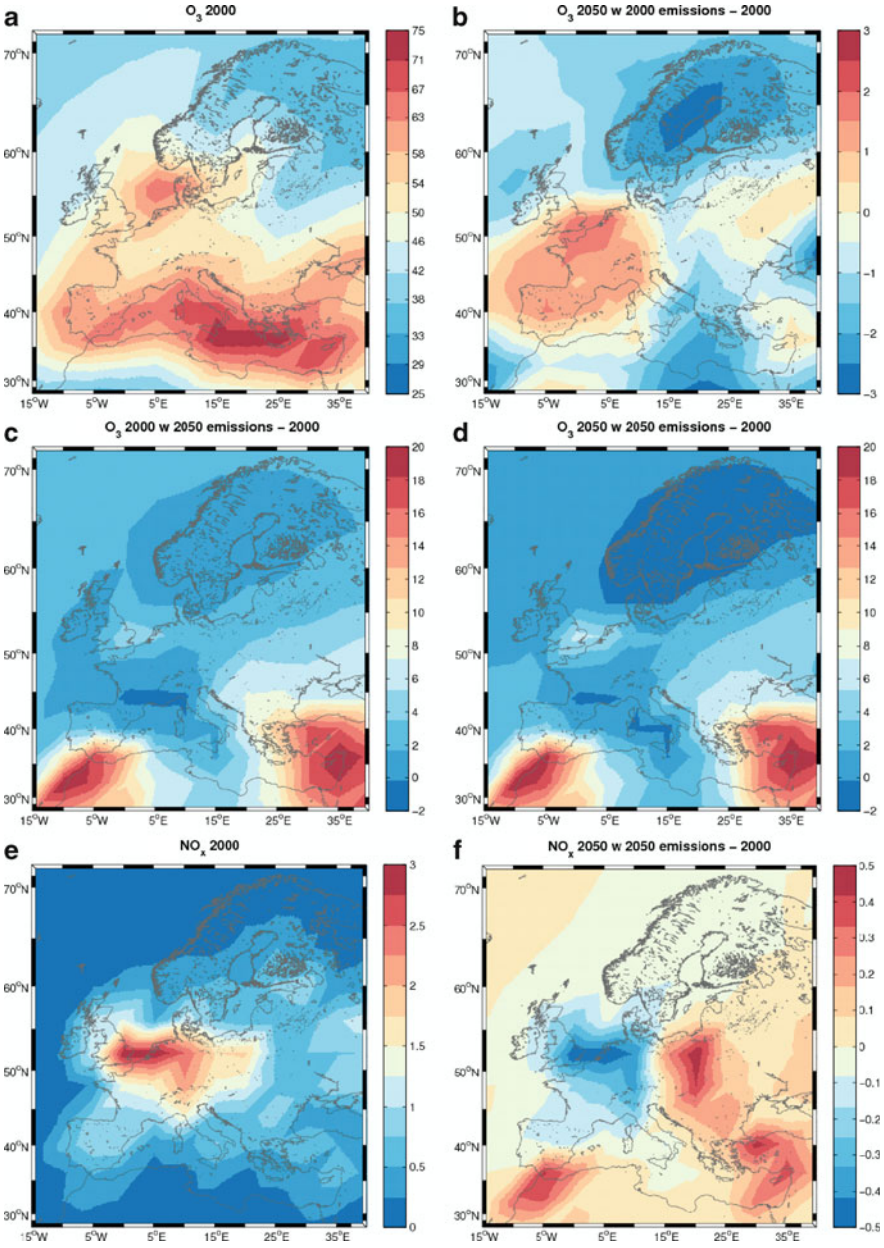

Fig. 2 Simulated daily maximum 8 h average O_3 for the AMJJAS period: (**a**) averaged under present day conditions, (**b**) changes between 2050 climate change and present day, (**c**) changes between 2000 climate with 2050 emissions and present day, (**d**) changes between 2050 climate and emissions and present day, (**e**) NOx concentrations averaged over AMJJAS for the present day climate and emissions and (**f**) changes between 2050 climate and emissions minus present day climate and emissions. All units are in ppb

simulations were conducted for a present (1999–2001) and a future (2049–2051) 3-year period. Results indicated that the impact of climate change on its own leads to an increase of less than 3 ppb in western and central Europe associated with increased isoprene emissions due to increased temperatures, whereas even smaller changes are shown for the rest of the areas. When both climate change and future emissions are implemented in the simulations higher changes in the ozone concentrations are evident mostly linked to the increased NOx under the A1B emissions scenario. The highest increases, over land are evident in the south west and south east Mediterranean (about 12 ppb). Finally, in the extreme north European areas (above 60^{o} latitude), future ozone tends to decline despite the rise in temperatures under climate change.

Acknowledgments This research has been co-financed by the European Union (European Social Fund – ESF) and Greek national funds through the Operational Program "Education and Lifelong Learning" of the National Strategic Reference Framework (NSRF) – Research Funding Program: Heracleitus II. Investing in knowledge society through the European Social Fund.

References

Beekmann M, Vautard R (2010) A modelling study of photochemical regimes over Europe: robustness and variability. Atmos Chem Phys 10:10067–10084. doi:10.5194/acp-10-10067-2010

Jacob DJ, Winner DA (2009) Effect of climate change on air quality. Atmos Environ 43:51–63. doi:10.1016/j.atmosenv.2008.09.051

Katragkou E, Zanis P, Kioutsioukis I, Tegoulias I, Melas D, Krueger BC, Coppola E (2011) Future climate change impacts on summer surface ozone from regional climate-air quality simulations over Europe. J Geophys Res 116:D22307. doi:10.1029/2011JD015899

Nakicenovic N, Swart R (2000) Special report on emissions scenarios (SRES) a special report of IPCC working group III. Cambridge University Press, Cambridge, UK

Wu S, Mickley LJ, Leibensperger EM, Jacob DJ, Rind D, Streets DG (2008) Effects of 2000–2050 global change on ozone air quality in the United States. J Geophys Res 108:D0630. doi:10.1029/2007JD008917

Regional Air Quality Simulations Over Europe in Present and Future Climate: Evaluation and Climate Change Impacts on Near Surface Ozone

P. Zanis, E. Katragkou, I. Tegoulias, I. Kioutsioukis, and D. Melas

Abstract Regional climate-air quality simulations were carried out over Europe with the RegCM3/CAMx modelling system for two future decades, 2041–2050 and 2091–2100 under IPCC A1B scenario and the control decade 1991–2000. The RegCM3/CAMx simulations for the present decade were driven either by ERA-40 reanalysis or the global circulation model (GCM) ECHAM5 while the simulations for the two future decades were driven by ECHAM. The simulations serve as a theoretical experiment to investigate the impact of changing climate on near surface ozone. The simulated ozone was evaluated with respect to near surface ozone measurements from the EMEP database for the control decade 1991–2000 indicating a relatively good performance of the RegCM3/CAMx modelling system in simulating near-surface ozone levels over Europe. Our projections in future suggest that the changes in near surface ozone imposed by climate change are small over the near future decade (2041–2050) but become significant over the end of twenty-first century. Specifically the ozone change over the future decade 2091–2100 is more intense over south-west Europe during summer, increasing by 6.2 ppbv as a result of the combination of relatively more stagnant conditions, increased temperatures and solar radiation within an anticyclonic anomaly.

P. Zanis (✉) • I. Tegoulias
Department of Meteorology and Climatology, School of Geology, Aristotle University of Thessaloniki, Thessaloniki, Greece
e-mail: zanis@geo.auth.gr

E. Katragkou
Department of Meteorology and Climatology, School of Geology, Aristotle University of Thessaloniki, Thessaloniki, Greece

Laboratory of Atmospheric Physics, Physics Department, Aristotle University of Thessaloniki, Thessaloniki, Greece

I. Kioutsioukis • D. Melas
Laboratory of Atmospheric Physics, Physics Department, Aristotle University of Thessaloniki, Thessaloniki, Greece

C.G. Helmis and P.T. Nastos (eds.), *Advances in Meteorology, Climatology and Atmospheric Physics*, Springer Atmospheric Sciences,
DOI 10.1007/978-3-642-29172-2_176,

1 Introduction

The scientific discussion of the potential sensitivity of air quality to climate change has increased in recent years with emphasis given on tropospheric ozone. To date, most studies investigating future tropospheric ozone changes have been based on global climate-chemistry models or global climate models coupled off-line to global chemistry-transport models (Hauglustaine et al. 2005; Stevenson et al. 2006). Only recently an increasing number of studies has appeared in the literature based on regional models focusing on Europe (Meleux et al. 2007; Zanis et al. 2011 and references therein). These studies investigated climate change effects on tropospheric ozone at the regional scale using off-line coupling of regional climate or meteorological mesoscale models with regional air quality models. It should be noted that the spatial distribution of lower tropospheric ozone is highly variable due to its relatively short lifetime (of the order of hours to days) and therefore a regional context is especially important to investigate climate change effects on tropospheric ozone (Giorgi and Meleux 2007).

The current work presents the impact of changing climate on surface ozone over Europe for the future decades 2041–2050 and 2091–2100 under the A1B IPCC scenario based on the RegCM3/CAMx modelling system. Results of the model evaluation with respect to ozone are also presented for the recent past decade 1991–2000.

2 Data and Methodology

The regional modelling system used in this work for long-term air-quality simulations over Europe is RegCM3/CAMx. It includes the regional climate model RegCM3 (http://www.ictp.trieste.it/~pubregcm/RegCM3/) to provide the meteorological forcing to drive air-quality simulations carried out by CAMx version 4.40 (http://www.camx.com/). CAMx is off-line coupled to RegCM3 with a Fortran-based interface which reads the basic meteorological parameters from RegCM3 in a six-hourly basis and exports them to CAMx-ready fields and format. Anthropogenic emissions were calculated with data from the UNECE/EMEP data base (http://webdab.emep.int/) for European emissions relative to the year 2000 and interpolated on the CAMx grid. Details for the modelling system, the chemistry mechanism, the emissions and the chemical lateral boundary conditions can be found in Katragkou et al. (2010) and Zanis et al. (2011).

RegCM3 was used to simulate the time period 1960–2002, forced at the lateral boundaries by ERA-40 reanalysis fields over Europe with a grid resolution of 50 km $\times$ 50 km and 18 vertical layers up to 50 hPa. Furthermore, RegCM3 was used for a transient simulation for the period 1950–2100 with a grid resolution of 25 km $\times$ 25 km forced by the general circulation model ECHAM5 under the A1B future scenario. These two long-term simulations of RegCM3 were carried out at

ICTP (International Centre for Theoretical Physics) within the framework of the EU project ENSEMBLES (http://ensembles-eu.metoffice.com/index.html) and provided the meteorological forcing to drive offline the air quality model CAMx for the following experiments:

(a) A perfect lateral meteorological boundary conditions experiment for the period 1991–2000 using as lateral boundary for RegCM3 the ERA-40 meteorological fields which is considered as an experiment closer to real atmospheric conditions. This simulation will be hereafter referred to as ERA run.
(b) Three decadal air quality simulations which were performed for the time slices 1991–2000, 2041–2050 and 2091–2100 with RegCM3 being forced by the ECHAM5 global climate model under the IPCC A1B scenario for the future decades. The RegCM3/CAMx simulation for the period 1991–2000 forced by ECHAM5 is considered the control experiment that can serve as a basis for comparison with future scenario simulations. The control experiment simulation ECHAM5/RegCM3/CAMx will be hereafter referred to as ECHAM run.

The simulated ERA and ECHAM ozone concentrations were evaluated using near surface ozone measurements from the EMEP database (http://tarantula.nilu.no/projects/ccc/emepdata.html). The database includes only rural stations throughout Europe, to enhance consistency with the 50 km $\times$ 50 km model data. Since many of the stations of the EMEP network were not operating continuously during the time period of our study (1991–2000), we have used in the evaluation analysis only those stations that fulfill the criteria of 75% data availability for near surface ozone. This criterion led to the selection of 68 stations from 17 European countries.

The statistical metrics used for the model evaluation include: (a) temporal correlation coefficient (R) of simulated versus observed values; (b) normalized standard deviation (NSD), i.e. the ratio of the temporal standard deviation of simulated values over the standard deviation of observed values and (c) the modified normalized mean bias (MNMB).

3 Results

As it is evident from summary statistics of Table 1 the ERA results are closer to observations than ECHAM. This can be justified from the fact that the ERA experiment is closer to real atmospheric conditions and hence its meteorology is expected to follow the synoptic scale variability in a more realistic way than the GCM based experiment.

Concerning the correlation between simulated and observed monthly ozone values, the majority of stations exhibit R values ranging between 0.7 and 0.9 in the ERA simulation and $R > 0.6$ in the ECHAM simulation. This indicates that the monthly variability of simulated ozone is in phase with the observed one in most cases. The MNMB values show a tendency of model overestimation, as the median

Table 1 Summary statistics of the major evaluation metrics based on the comparison of ERA and ECHAM simulated monthly near surface ozone with the respective observed ozone from the 68 EMEP stations over the period 1991–2000

	R		MNMB (%)		NSD	
	ERA	ECHAM	ERA	ECHAM	ERA	ECHAM
Median	0.80	0.72	3.95	15.50	1.08	0.94
First quartile	0.60	0.50	−6.70	4.95	0.95	0.82
Third quartile	0.85	0.79	14.23	30.18	1.25	1.06

The statistical evaluation metrics include: (**a**) the correlation coefficient of modelled versus observed values, (**b**) the modified normalized mean bias and (**c**) the ratio of the standard deviation of modelled values over the standard deviation of observed values

MNMB from the 68 stations is +3.9% in ERA simulation and +15.5% in ECHAM simulation. Hence the MNMB values in the ECHAM simulation are higher than in ERA indicating a shift to more frequent overestimated ozone values in ECHAM values versus the observed ones. Concerning the amplitude of the ozone variance a satisfactory agreement with observations is found for the majority of stations. For 50% of the stations, the NSD values range between 0.95 (first quartile) and 1.25 (third quartile) in ERA and between 0.82 (first quartile) and 1.06 (third quartile) in ECHAM. Hence the NSD values in the ECHAM simulation are shifted to slightly lower values than in ERA indicating a slight shift to more frequent underestimated amplitude of ozone variance in ECHAM values versus the observed ones. Overall, despite the presence of some systematic biases, all metrics considered indicate a relatively good performance of the RegCM3/CAMx modelling system in simulating near-surface ozone levels over Europe. More details concerning the evaluation of ERA and ECHAM simulated surface ozone can be found in Zanis et al. (2011).

The FUT1 simulations suggest that the changes in climate key-parameters affecting ozone are small until the 2040s in comparison to the control simulation. As a consequence the simulated FUT1 ozone changes in mid-century (Fig. 1a, b) are also very small ranging between −1 and +1 ppbv. The pattern of changes is better understood if inspected along with changes in temperature, solar radiation and biogenic emissions (see Katragkou et al. 2011). The bottom panel of Fig. 1 shows ozone changes between FUT2 simulation and the present decade. Changes in all meteorological parameters are more pronounced until the 2090s. By the end of twenty-first century climate change leads to increased ozone concentrations, the differences, however, vary for different parts of Europe with the changes being generally higher in summer than in winter. In winter (Fig. 1d), the Mediterranean Sea, the Iberian Peninsula and eastern Atlantic show an ozone increase ranging between 2 and 4 ppbv, while less sensitive appears to be central and eastern continental Europe. In summer (Fig. 1c), surface ozone increases mostly over south-western continental Europe (5–6 ppbv) and to a lesser extent over the eastern Mediterranean basin.

Figure 2 indicates that the highest ozone changes over south-western continental Europe by the end of twenty-first century is linked to: (a) increased solar radiation

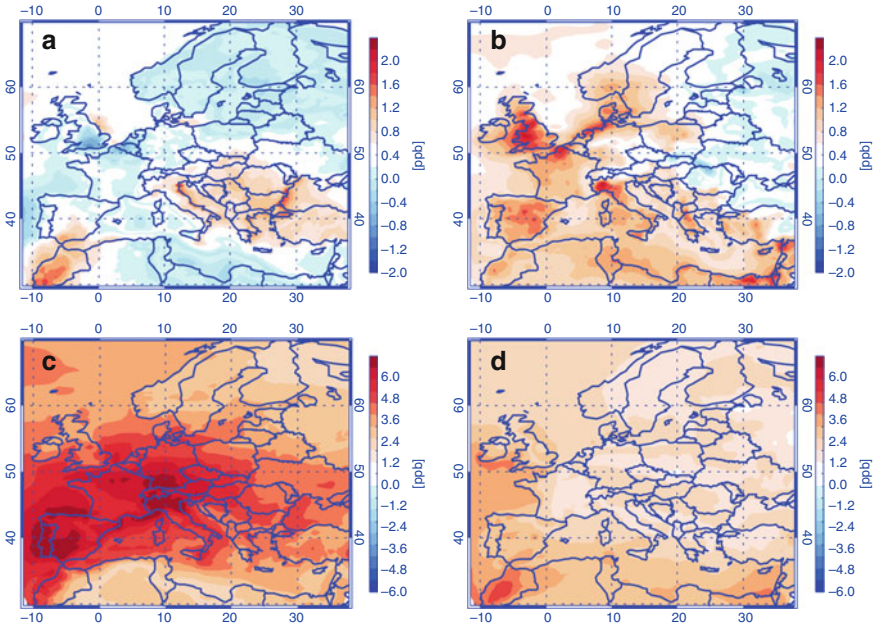

Fig. 1 Differences in simulated average ozone between FUT1 (2041–2050) and control simulation for (**a**) summer and (**b**) winter as well as between FUT2 (2091–2100) and control simulation for (**c**) summer and (**d**) winter. Mind the differences in color scales

(Fig. 2a), (b) positive geopotential height anomalies (Fig. 2b) and (c) decreased wind speed (Fig. 2c). The largest decrease of wind speed over Western Europe in association with the anticyclonic anomaly favours stagnant conditions. Hence, the combination of relatively more stagnant conditions, increased temperatures and solar radiation within an anticyclonic anomaly, favors enhanced ozone production in the western part of Europe where mean surface ozone increases mostly.

4 Conclusions

The key conclusions can be summarized as follows:

1. The evaluation results justify our overall assessment that the RegCM3/CAMx is suitable to be used for present and future regional climate-air quality simulations with emphasis on near surface ozone.
2. The simulated ozone changes in mid-century (2040s) are very small ranging between −1 and +1 ppbv.
3. By the end of twenty-first century climate change leads to increased ozone concentrations, the differences, however, vary for different parts of Europe between 2 and 6 ppbv with the changes being generally higher in summer than in winter.

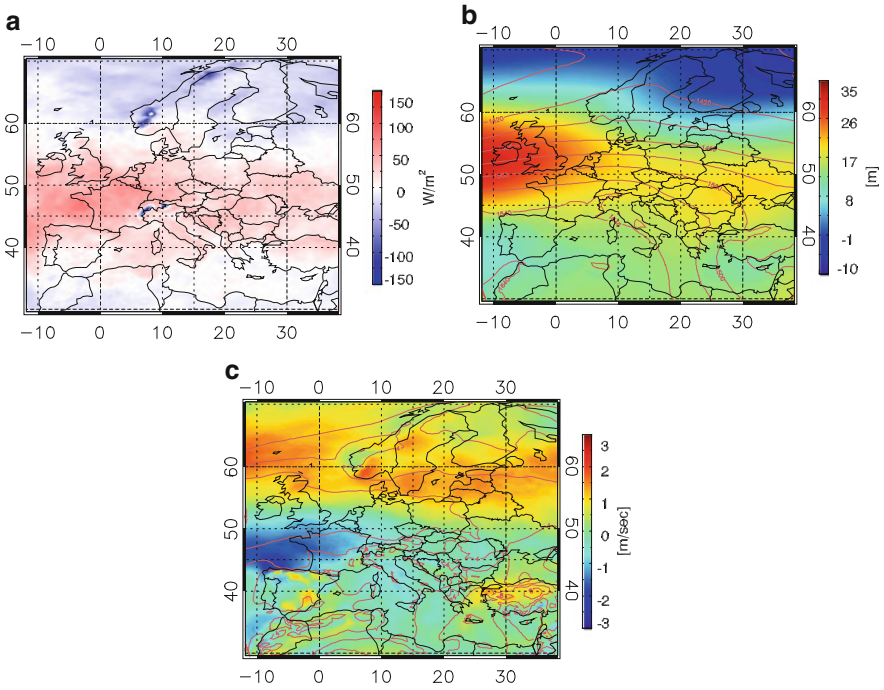

Fig. 2 Differences between FUT2 (2091–2100) and control simulation for the summer season in simulated average: (**a**) incoming solar radiation (W/m^2), (**b**) geopotential height at 850 hPa and (**c**) wind speed at 850 hPa

4. The combination of relatively more stagnant conditions, increased temperatures and solar radiation within an anticyclonic anomaly, favors enhanced ozone production in the western part of Europe where mean surface ozone increases mostly (5–6 ppbv).

Acknowledgments This work has been funded by the European Community's Sixth Framework Programme as part of the project CECILIA (Central and Eastern Europe Climate Change Impact and Vulnerability Assessment) under Contract No. 037005.

References

Giorgi F, Meleux F (2007) Modeling the regional effects of climate change on air quality. C R Geosci 339:721–733

Hauglustaine DA, Lathiere J, Szopa S, Folberth GA (2005) Future tropospheric ozone simulated with a climate-chemistry biosphere model. Geophys Res Lett 32:L24807. doi:10.1029/2005GL024031

Katragkou E, Zanis P, Tegoulias I, Melas D, Krüger BC, Huszar P, Halenka T, Rauscher S (2010) Decadal regional air quality simulations over Europe in present climate: near surface ozone

sensitivity to external meteorological forcing. Atmos Chem Phys 10:11805–11821. doi:10.5194/acp-10-11805-2010

Katragkou E, Zanis P, Kioutsioukis I, Tegoulias I, Melas D, Krüger BC, Coppola E (2011) Future climate change impacts on surface ozone from regional climate-air quality simulations over Europe. J Geophys Res 116:D22307. doi:10.1029/2011JD015899

Meleux F, Solmon F, Giorgi F (2007) Increase in summer European ozone amounts due to climate change. Atmos Environ 41(35):7577–7587. doi:10.1016/j.atmosenv.2007.05.048

Stevenson DS, Dentener FJ, Schultz MG, Ellingsen K, van Noije TPC, Wild O, Zeng G, Amann M, Atherton CS, Bell N, Bergmann DJ, Bey I (2006) Multimodel ensemble simulations of present-day and near-future tropospheric ozone. J Geophys Res 111:D08301. doi:10.1029/2005JD006338

Zanis P, Katragkou E, Tegoulias I, Poupkou A, Melas D, Huszar P, Giorgi F (2011) Evaluation of near surface ozone in air quality simulations forced by a regional climate model over Europe for the period 1991–2000. Atmos Environ 45:6489–6500. doi:10.1016/j.atmosenv.2011.09

Compilation of a NOx Emission Inventory for the Balkan Region Using Satellite Tropospheric NO_2 Columns

I. Zyrichidou, M.E. Koukouli, D. Balis, K. Markakis, I. Kioutsioukis, A. Poupkou, D. Melas, K.F. Boersma, and M. van Roozendael

Abstract The important improvements in the quality of space-born tropospheric trace gas estimates have permitted their use, in combination with inverse atmospheric modelling, to obtain evolved top-down pollutant emission estimates. In this study, inverse modeling is applied to the case of tropospheric nitrogen dioxide (NO_2) columns as seen by the OMI/Aura instrument and estimated by the Comprehensive Air Quality Model with extensions (CAMx). The main idea is to use the a priori information from the bottom up emission inventory used in the CAMx model, the tropospheric NO_2 quantities estimated by the CAMx runs and the tropospheric NO_2 columns deduced by the satellite observations to create an a posteriori NOx emission inventory. This new inventory, constrained in the top-down manner by the satellite estimates, can be used anew in the CAMx model to produce a new modeled NOx product. This work has identified biases in the original emission inventory for instance due to missing emission sources or over-estimation of the spread of emission sources and has proved an improved bottom-up emissions inventory.

I. Zyrichidou (✉) • M.E. Koukouli • D. Balis • K. Markakis • I. Kioutsioukis • A. Poupkou • D. Melas
Laboratory of Atmospheric Physics, Physics Department, Aristotle University of Thessaloniki, Thessaliniki, Greece
e-mail: ezyrichi@auth.gr

K.F. Boersma
Royal Netherlands Meteorological Service, De Bilt, The Netherlands

M. van Roozendael
Belgian Institute for Space Aeronomy, Brussels, Belgium

C.G. Helmis and P.T. Nastos (eds.), *Advances in Meteorology, Climatology and Atmospheric Physics*, Springer Atmospheric Sciences,
DOI 10.1007/978-3-642-29172-2_177,

1 Introduction

Nitrogen oxides, resulting from fossil fuel combustion, biomass burning, microbial processes in soils, lightning or transport from the stratosphere, control the formation of ozone in the troposphere and contribute to the local air quality (Logan 1983). The accurate estimation of NOx emissions is crucial for the better understanding of air pollution and climate change. However, the bottom-up approach of evaluating NOx emissions by integrating activity information and emission factors from diverse sources, is often subject to substantial uncertainties due to limited knowledge of emission data and characteristics (Streets et al. 2003).

Satellite instruments can provide a global and year-round coverage of NO_2 columns and offer additional constraints on global surface NOx emissions yielding an improved emission inventory, as shown in Martin et al. (2003). They developed an inverse modeling algorithm to derive a top-down NOx emission inventory linearly relating GOME tropospheric NO_2 columns to model surface NOx emissions. In this study we apply this methodology over the Balkan Peninsula using the CAMx model relationship between NO_2 columns and NOx emissions with the observations of the OMI/Aura satellite instrument.

2 Data and Methodology

2.1 Data

OMI onboard the NASA Aura satellite has a daily global coverage and crosses the equator at approximately 13:30 local time (Levelt et al. 2006). The nadir horizontal resolution of OMI is 24×13 km^2. In our analysis the tropospheric NO_2 column densities derived by the KNMI (Royal Netherlands Meteorological Institute) and BIRA/IASB (Belgian Institute for Space Astronomy) algorithm and are publicly available on a day-by-day basis via ESA's Tropospheric Emission Monitoring Internet Service at http://www.temis.nl/airpollution/no2.html. The retrieval algorithm is described elaborately in Boersma et al. (2007). Here we only consider pixels where clouds contribute to less than 50% of backscattered radiation (van der A et al. 2008). The monthly mean tropospheric NO_2 fields are derived from OMI observations for the period April 2009–March 2010. To achieve optimum comparability of the two different data sources, the satellite data have been fitted to the resolution of the model grid, $0.1^\circ \times 0.1^\circ$ (about 10×10 km for the area in question).

The a priori information (model simulations and bottom-up inventory) was given by the Comprehensive Air Quality Model with extensions (CAMx) version 4.40. The CAMx grid focuses on the Balkan Peninsula, has 10 km spatial resolution and consists of 15 vertical layers of varying thickness, extending up to about 300 hPa. The meteorological fields are derived from the fifth generation NCAR/Penn State

University Mesoscale Model MM5 version 3.7. MM5 is forced by the global 12:00 UTC *G*lobal *F*orecast *S*ystem (GFS)/*N*ational *C*enters for *E*nvironmantal *P*rediction (NCEP) forecast of 1° spatial resolution.

Annual anthropogenic emission data of gaseous and particulate matter pollutants provided by The Netherlands Organization (TNO) (Visschedijk et al. 2007) have been used to support the photochemical model simulations. The emission inventory was prepared in order to account for the year 2003 emissions in the European territory. The TNO annual emission data were temporally disaggregated (seasonal, weekly and diurnal temporal profiles) according to Friedrich (1997). The emission data for Greece are based on detailed emission inventories developed in national and urban scales according to Markakis et al. (2010). Ship emission data have been taken from the EMEP emission database. Biogenic NMVOC emissions are calculated from the biogenic emission model BEM (Poupkou et al. 2010). The global chemistry transport model MOZART-IFS (Flemming 2008) provides the CAMx chemical boundary conditions since January 2009. NO_2 tropospheric vertical column densities were extracted from integration from surface up to about 7 km and for the time period from 01/04/2009 to 31/03/2010.

2.2 *Methodology*

Following the mass balance method used by Martin et al. (2003), we compute the Balkan top-down (not shown with plot in this paper) surface NOx emissions for April 2009–March 2010 from the respective retrieved tropospheric NO_2 columns Et through the linear relationship, $E_t = a\Omega_t$ (1), where the linear coefficient a is determined from the simulation with a priori emissions as $a = E_a/\Omega_a$, where Ω_a is the NO_2 column from that simulation. This equation is applied over the total Balkan domain (land and sea).

The a posteriori inventory, E_p (2), is obtained by combining the top-down NOx emission inventory, E_t, and its relative error ε_t, with a priori estimates from the bottom-up inventory, E_a, and its relative error ε_a and ε_p is its relative error (3).

$$\ln E_p = \frac{\ln E_a (\ln \varepsilon_t)^2 + \ln E_t (\ln \varepsilon_\alpha)^2}{(\ln \varepsilon_t)^2 + (\ln \varepsilon_a)^2} \tag{2}$$

$$\frac{1}{(\ln \varepsilon_p)^2} = \frac{1}{(\ln \varepsilon_t)^2} + \frac{1}{(\ln \varepsilon_a)^2} \tag{3}$$

The uncertainty in the a priori inventory is not available and we consider it to be the 50% of the a priori value. The uncertainty in biomass burning and soil NOx

emissions is taken to be a factor of 3, reflecting the range of global estimates (Prather and Ehhalt 2001). The uncertainty in fossil fuel is taken from Jaegle et al. (2005) which is 1.7 for Europe. Finally, the uncertainty in the OMI retrievals is assumed to be equal to the standard deviation of the monthly mean error values.

3 Results and Discussion

Figure 1 depicts a 12-month spatial distribution of the NO_2 tropospheric columns derived from the CAMx model (left plot) and the OMI instrument (right plot). The discrepancies between model and satellite (for instance over Athens and Thessaloniki) may be attributed for e.g. to a specific parameterisation concerning the vertical mixing, used in this model. Moreover, CAMx lacks the NO_2 hotspots over Istanbul and the coast of Minor Asia. However, the CAMx model shows generally similar spatial NO_2 distribution patterns with the OMI instrument on yearly basis over the rest of the Balkan Peninsula.

Figure 2 presents the spatial distributions and regional totals of the NOx emissions for the a priori (top plot), and a posteriori (bottom plot) inventories computed from (2). The Balkan annual surface NOx emissions in the a posteriori inventory amount to 0.977 Tg N $year^{-1}$, which is not significantly different from the a priori (0.855 Tg N $year^{-1}$) values given in Table 1. From Table 1 it is also clear that Balkan surface NOx emissions constitute around 15% of the global value, comparing to Jaegle et al. (2005). In our study the a posteriori emissions are higher than the a priori inventory for the Balkan region by up to 12%. Enhancements are observed along the ship tracks, over industrial and remote regions and also over Istanbul, where the a priori EMEP-based inventory used provides unrealistically low estimates for the city that are not considered representative for this area.

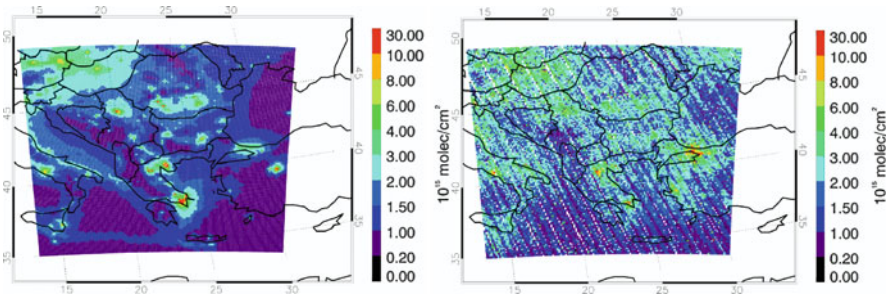

Fig. 1 Annual tropospheric NO_2 column as simulated by CAMx (Ω_α) (*left* plot) and observed by OMI (Ω_t) (*right* plot) over the Balkan region

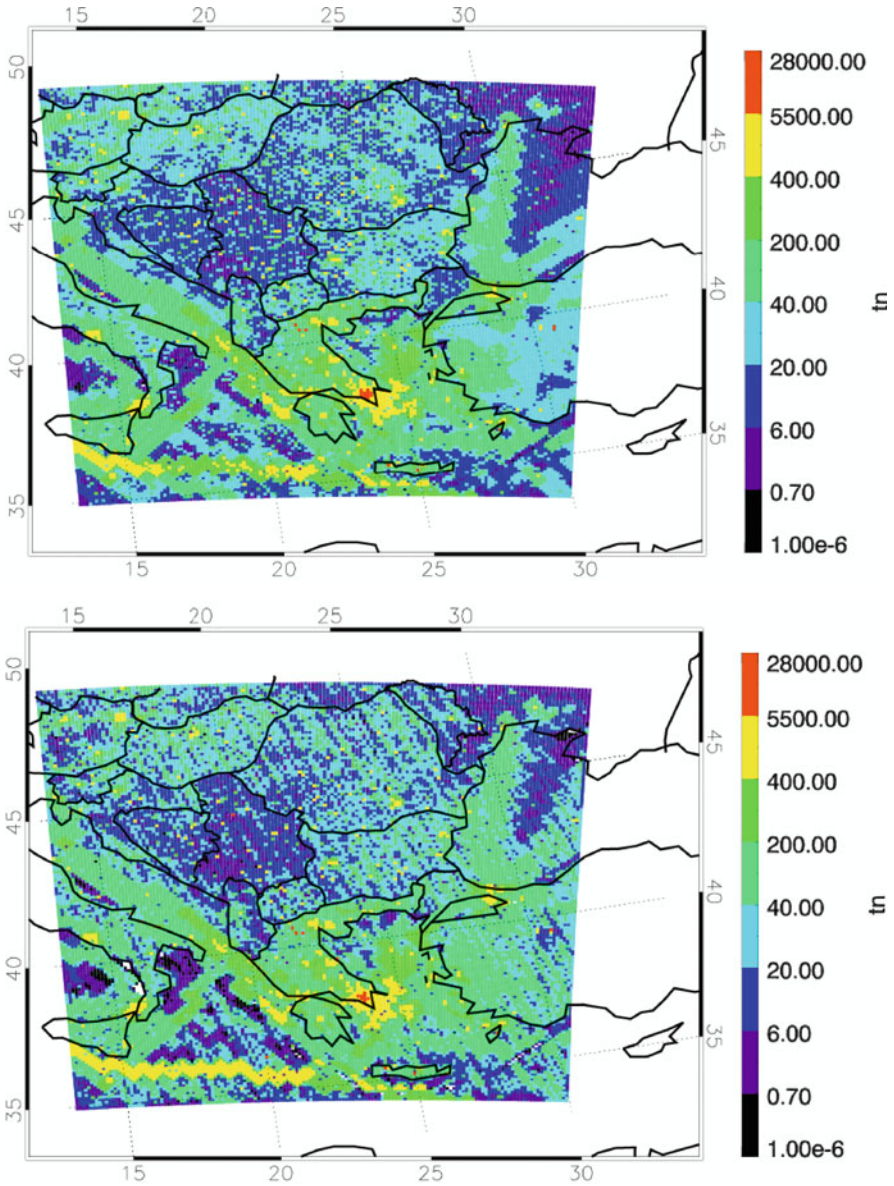

Fig. 2 Annual spatial distribution of NOx emissions over the Balkans of the a priori (E_a) (*top* plot) and a posteriori (E_p) (*bottom* plot) inventories

Table 1 Annual total surface NOx emissions

	Tonnes NOx/year	Tg N/year[a]
Balkan domain for 04/2009–03/2010 (our study)		
A priori (CAMx) [Ea]	1.90×10^6	0.855 (0.44)
Top down (OMI) [Et]	2.13×10^6	0.943 (4.29)
A posteriori [Ep]	2.20×10^6	0.977 (3.15)
Europe for 2000 (Jaegle et al. 2005)		
A priori (GEOS-CHEM) [Ea]	12.41×10^6	5.5 (1.7)
Top down (GOME) [Et]	13.99×10^6	6.2 (1.5)
A posteriori [Ep]	13.99×10^6	6.2 (1.4)
Europe for 09/1996–08/1997 (Martin et al. 2003)		
A priori (GEOS-CHEM) [Ea]	12.64×10^6	5.6 (2.0)
Top down (GOME) [Et]	13.09×10^6	5.8 (1.7)
A posteriori [Ep]	13.32×10^6	5.9 (1.5)

[a]The relative errors are indicated in parenthesis

4 Conclusions

The main findings of this study are summarized by the following:

1. Small differences have been found between the a priori (0.983 Tg N year^{-1}) and a posteriori (0.975 Tg N year^{-1}) emission inventories.
2. The high resolution simulations and satellite measurements enable observation of ship emissions, while there were no evident enhancements along ocean ship tracks in Martin et al. (2003).
3. In the a posteriori inventory the industrial and remote regions are better distinguished than in the a priori, where there were no soil and biomass burning emissions.
4. A posteriori emissions are higher than the a priori inventory for the Balkan region by up to 12%.
5. In future the seasonality of the emissions will be examined, soil and biomass burning emissions will be computed (currently not included in the a priori emission inventory) and the a posteriori inventory will be used anew in the CAMx model to produce a new NOx product.

Acknowledgments The research study was financed by the EU research projects: Monitoring Atmospheric Composition and Climate: Grant Agreement no. 218793 and Global and regional Earth-system Monitoring using Satellite and in-situ data, contract no.: 516099.

References

Boersma KF et al (2007) Near-real time retrieval of tropospheric NO_2 from OMI. Atmos Chem Phys 7:2103–2118. doi:10.5194/acp-7-2103-2007

Flemming J (2008) Technical description of the coupled forecast system IFS-CTM for global reactive gases forecast and assimilation in GEMS, available at http://gems.ecmwf.int/do/get/PublicDocuments/1534/1052?showfile

Friedrich R (1997) GENEMIS: assessment, improvement, temporal and spatial disaggregation of European emission data. In: Ebel A, Friedrich R, Rhode H (eds) Tropospheric modelling and emission estimation (Part 2). Springer, New York

Jaegle L et al (2005) Global partitioning of NOx sources using satellite observations: relative roles of fossil fuel combustion, biomass burning and soil emissions. Faraday Discuss 130:407–423. doi:10.1039/b502128f

Levelt PF et al (2006) The ozone monitoring instrument. IEEE Trans Geosci Remote Sens 44 (5):1093–1101. doi:10.1109/TGRS.2006.872333

Logan JA (1983) Nitrogen oxides in the troposphere: global and regional budgets. J Geophys Res 88:10785–10807. doi:10.1029/JC088iC15p10785

Markakis K et al (2010) A computational approach based on GIS technology for the development of an anthropogenic emission inventory of gaseous pollutants in Greece. Water Air Soil Poll 207:157–180. doi:10.1007/s11270-009-0126-5

Martin RV et al (2003) Global inventory of nitrogen oxide emissions constrained by space-based observations of NO_2 columns. J Geophys Res 108(D17):4537. doi:10.1029/2003JD003453

Poupkou A et al (2010) A model for European biogenic volatile organic compound emissions: software development and first validation. Environ Model Softw 25:1845–1856

Prather MJ, Ehhalt D (2001) In: Climate change 2001: the science of climate change, intergovernmental panel on climate change. Cambridge University Press, Cambridge, p 241

Van der A RJ et al (2008) Trends, seasonal variability and dominant NOx source derived from a ten year record of NO_2 measured from space. J Geophys Res 113:D04302. doi:10.1029/2007JD009021

Streets DG et al (2003) An inventory of gaseous and primary aerosol emissions in Asia in the year 2000. J Geophys Res 108(D21):8809. doi:10.1029/2002JD003093

Visschedijk A, Zandveld P, van der Gon DH (2007) A high resolution gridded European emission database for the EU integrated project GEMS. TNO report 2007-A-R0233/B

Index

C.G. Helmis and P.T. Nastos (eds.), *Advances in Meteorology, Climatology and Atmospheric Physics*, Springer Atmospheric Sciences,
DOI 10.1007/978-3-642-29172-2, © Springer-Verlag Berlin Heidelberg 2012